FRONTIERS IN EARTH SCIENCES

O. Lacombe · J. Lavé · F. Roure · J. Vergés (Eds.)

Thrust Belts and Foreland Basins

From Fold Kinematics to Hydrocarbon Systems

Springer

Frontiers in Earth Sciences

Series Editors:
J. P. Brun · O. Oncken · H. Weissert · C. Dullo

Olivier Lacombe
Jérôme Lavé
François Roure
Jaume Vergés
(Editors)

Thrust Belts and Foreland Basins

From Fold Kinematics to Hydrocarbon Systems

With 290 color figures

Springer

Olivier Lacombe
Laboratoire de Tectonique
Université Pierre et Marie Curie
Aile 45–46, Niveau 2, Case 129
4 Place Jussieu
75252 Paris
France

François Roure
Institut Français du Pétrole
1–4 Avenue de Bois-Préau
92852 Rueil-Malmaison
France

Jérôme Lavé
Laboratoire de Géodynamique
des Chaînes Alpines
Université J. Fourier
Maison de Géosciences
1381 rue de la piscine
38400 St-Martin-d'Hères
France

Jaume Vergés
Institut Ciencies de la Tierra
Jaume Almera
Cons. Sup. Invest. Cientificas
Calle Lluís Solé i Sabarís s/n
08028 Barcelona
Spain

Preface

Thrust belts and foreland basins record the main phases of orogenic evolution. They are shaped by the coupled influence of deep (flexure, plate rheology and kinematics) and surficial (erosion, sedimentation) geological processes, at different time scales. Thrust belts and foreland basins constitute important targets for scientists interested in both fundamental and applied (fluids, hydrocarbons) aspects.

In the framework of a new cycle of workshops of the ILP task force on "Sedimentary Basins", a three-day meeting on "Thrust Belts and Foreland Basins" was organized in December 2005 on behalf of the Société Géologique de France and the Sociedad Geológica de España, hosted by the Institut Français du Pétrole near Paris. The main purpose of the meeting was to offer the opportunity for Earth scientists from different disciplines, i.e. geologists, geophysicists and geochemists, to present and share their different knowledge on the processes governing the evolution of orogenic belts and adjacent forelands. A special emphasis had been given to make a "bridge" between the most recent advances in surface processes, geochemistry, provenance studies, field studies, analogue and numerical modelling, high resolution seismicity, and hydrocarbon prospect in forelands basins. The conference was successful in bringing together scientists from academia and industry from nearly 20 countries. New contributions using the geologic information recorded in thrust belts and foreland basins as well as stimulating key notes provided fertile ground for discussion, focusing on the orogenic evolution of adjacent mountain belts, on the stratigraphic records resulting from the coupled influence of deep and surficial geological processes, on exploration strategies for hydrocarbons in foothills areas, and on recent methodological and technical advances that have renewed our view on these important targets in both their fundamental and applied aspects.

The present volume addresses most of these topics. It comprises 25 key papers presented at the conference. The content of the volume reflects the diversity of the presentations and the success of the workshop, and is likely to promote new contacts between interdisciplinary Earth scientists. Volume architecture brings the reader from geodynamic considerations to general and specific issues of thrust belt description and hydrocarbon systems exploration through seismic imaging, fluid flow studies, and structural modelling. Given the focused attention that Zagros/Makran and Carpathian thrust belts received during the meeting and volume elaboration, contributions specific to these two important areas were put separately. The varied methodologies implemented when studying these two thrust belts examples, and the contrasted answers they bring, stress the importance of confronting independant approaches. These case studies also provide to any researcher interested by thrust belts a synthetic view on the modern techniques and recent advances developed for studying these major geological targets.

Olivier Lacombe, Jérôme Lavé, François Roure
and Jaume Vergés

Acknowledgments

Contents

Part VII
Tectonics, Sedimentation and Denudation in Thrust Belts

The Editors

Dr. Olivier Lacombe is professor of tectonics at the Pierre et Marie Curie University (Paris, France) since 2002. He obtained his PhD in Earth Sciences from this university in 1992.

Olivier is an expert in brittle tectonics, especially in the study of fracture populations and reconstruction of paleostress orientations and magnitudes using analysis of faults and calcite twins. His main interest relates to the understanding of the structure and the kinematic evolution of fold-thrust belt - foreland basin systems, with special emphasis on the style of deformation (basement-involved tectonics and inversion), timing of deformation and tectonic history. Olivier also recently focused on the characterization of the ductile to brittle transition during late stage exhumation of HP metamorphic rocks in orogen hinterlands. He has worked in various regions worldwide, i.e., in the Alps and Pyrenees-Provence, Taiwan, Zagros, and more recently in the Cyclades-Aegean.

Dr. Jérôme Lavé is research scientist at the CNRS (Centre National de la Recherche Scientifique) in the LGCA (Laboratoire de Géologie des Chaînes Alpines) in Grenoble (France) since 1999. He obtained his PhD in geophysics from the Denis Diderot University (Paris, France) in 1997.

Jérôme is an expert in seismotectonics and morphotectonics. He has been working on terrace deformation in relation to active folding in thrust belts, on erosion and river incision processes and on quantification of pebble and bedrock abrasion processes during fluvial transport. He recently developed a new paleo-altimetric method based on the cosmogenic nuclides. His general fields of interest are the coupling and feedback loops between tectonic, erosion and climate, the dating and modelling of fluvial and glacial landscapes in relation with paleoclimate, and the numerical modelling of landscape evolution. He has mostly worked in the Himalayas, Tibet, Zagros and Altiplano.

Dr. François Roure is currently professor at IFP (Institut Français du Pétrole) and VU-Amsterdam. He joined the CNRS (Centre National de la Recherche Scientifique) in 1980. After a PhD aiming at the study of the Mesozoic geodynamic evolution of the North American Cordillera in N California and Oregon, he moved to IFP in 1984, studying first the crustal architecture of the Alps, Pyrenees and Apennines, then the petroleum systems in foothills and foreland domains in the Carpathians, Albanides, Sicily, Alaska and Colombia.

More recently, François has focused his interest on the evolution of sub-thrust reservoirs in the Himalayan foothills in Pakistan, as well as in the sub-Andean basins, and the North American Cordillera again, i.e., in Mexico and in the Canadian Rockies. His last projects aimed at the study of the crustal architecture and petroleum evaluation of the United Arab Emirates and North Algeria.

Dr. Jaume Vergés is researcher at the Institute of Earth Sciences "Jaume Almera" of the CSIC (Consejo Superior de Investigaciones Científicas) in Barcelona (Spain). He has been working on many fold-and-thrust belts, i.e., the Pyrenees, Zagros, An-

des, NW Cuba and the Polish Carpathians, mostly on geometries of folding and thrusting and timing of deformation.

Jaume is presently co-director of the GDL (Group of Dynamics of the Lithosphere), a working group focusing on understanding the links between surficial and deep geodynamic processes through combination of geology, geophysics and numerical modelling.

List of Contributors

Riadh Ahmadi
Ecole Nationale d'Ingénieurs de Sfax, Laboratoire de Géologie
BP-W, 3038 Sfax, Tunisia
riadhahmadi@voila.fr

Faram Ahmadhadi
Iranian Offshore Oil Company, Geology and Petrophysics Department
IOOC Tower, 12th Floor, Tooraj St., Vali-e-Asr Avenue, Post Code 19395, Tehran, Iran
faram_ifp@yahoo.com
&
Institut Français du Pétrole, Direction Géologie-Géochimie-Géophysique
1-4 Avenue de Bois-Préau, 92852 Rueil-Malmaison Cedex, France

Khalid Amrouch
Université Pierre-et-Marie Curie, Laboratoire de Tectonique, CNRS UMR 7072
4 Place Jussieu, Case 129, T46-E2, 75252 Paris Cedex 05, France
Khalid.Amrouch@ifp.fr
&
Institut Français du Pétrole, Direction Géologie-Géochimie-Géophysique
1-4 Avenue de Bois-Préau, 92852 Rueil-Malmaison Cedex, France

Andrea Artoni
Universita degli Studi di Parma, Dipartimento di Scienze della Terra
Parco Area delle Scienze 157/A, 43100 Parma, Italy
art@unipr.it

Victor Avram
Rompetrol, Rompetrol Building
222 Calea Victoriei, 010099 Bucharest, Romania
Victor.Avram@rompetrol.com

Anne Battani
Institut Français du Pétrole, Direction Géologie-Géochimie-Géophysique
1-4 Avenue de Bois-Préau, 92852 Rueil-Malmaison Cedex, France
Anne.Battani@ifp.fr

Martin Bêche
Institut Français du Pétrole, Direction Géologie-Géochimie-Géophysique
1-4 Avenue de Bois-Préau, 92852 Rueil-Malmaison Cedex, France
Martin.Beche@ifp.fr
&
Université Laval, Département de Géologie et de Génie Géologique
Ste-Foy, Québec GIK 7P4, Canada

Nicolas Bellahsen
Université Pierre-et-Marie Curie, Laboratoire de Tectonique, CNRS UMR 7072
4 Place Jussieu, Case 129, T46-E2, 75252 Paris Cedex 05, France
nicolas.bellahsen@lgs.jussieu.fr

Massimo Bernini
Universita degli Studi di Parma, Dipartimento di Scienze della Terra
Parco Area delle Scienze 157/A, 43100 Parma, Italy
massimo.bernini@unipr.it

Giovanni Bertotti
Faculty of Earth and Life Science, Vrije Universiteit
De Boelelaan 1085, 1081 HV Amsterdam, The Netherlands
bert@geo.vu.nl

Giuseppe Bertozzi
Edison S.p.A.
Foro Buonaparte, 31 Milano, Italy
giuseppe.bertozzi@edison.it

Christophe Buret
Laboratoire de Géologie, Université de Picardie
33 rue St-Leu, 80039 Amiens, France
Christophe.Buret@sc.u-picardie.fr

Evgueni Burov
Université Pierre-et-Marie Curie, Laboratoire de Tectonique, CNRS UMR 7072
4 Place Jussieu, Case 129, T46-E2, 75252 Paris Cedex 05, France
evgenii.burov@lgs.jussieu.fr

Michael M. Buslov
Institute of Geology, Siberian Branch of the Russian Academy of Science
Novosibirsk, Russia
misha@uiggm.nsc.ru

Jean-Paul Callot
Institut Français du Pétrole, Direction Géologie-Géochimie-Géophysique
1-4 Avenue de Bois-Préau, 92852 Rueil-Malmaison Cedex, France
J-Paul.Callot@ifp.fr

Juan-Carlos Calvo
Repsol-YPF-Bolivia
Santa-Cruz, Bolivia
jcalvoc@repsolypf.com

Rossella Capozzi
Dipartimento di Scienze della Terra e Geologico-Ambientali, Universita di Bologna
Via Zamboni 67, 40127 Bologna, Italy
capozzi@geomin.unibo.it

Eugenio Carminati
Dept. of Earth Sciences, Univ. of Roma La Sapienza
Piazzale Aldo Moro 5, 001 85 Rome, Italy
eugenio.carminati@uniroma1.it

Raymi Castilla-Chacon
Institut Français du Pétrole, Direction Géologie-Géochimie-Géophysique
1-4 Avenue de Bois-Préau, 92852 Rueil-Malmaison Cedex, France
Raymi.Castilla@ifp.fr

Rosina Chaker
Institut Français du Pétrole, Direction Géologie-Géochimie-Géophysique
1-4 Avenue de Bois-Préau, 92852 Rueil-Malmaison Cedex, France

Louis Chérel
Institut Français du Pétrole, Direction Géologie-Géochimie-Géophysique
1-4 Avenue de Bois-Préau, 92852 Rueil-Malmaison Cedex, France
Louis.Cherel@ifp.fr

Jean-Marc Daniel

Institut Français du Pétrole, Direction Géologie-Géochimie-Géophysique
1-4 Avenue de Bois-Préau, 92852 Rueil-Malmaison Cedex, France
J-Marc.Daniel@ifp.fr

Muhammad Danish-Shaika

NIO, National Institute of Oceanography
Street 47, Block 1, Clifton, Karachi, Pakistan
niopk@cubexs.net.pk

Johan De Grave

Department of Mineralogy and Petrology, University of Gent
Krijgslaan 281, S8, B-9000 Gent, Belgium
Johan.DeGrave@UGent.be

Boris Dehandschutter

International Bureau for Environmental Studies, IBES
Leuvensesteenweg 4, B-3080 Tervuren, Belgium
bodehand@ibes.be

Vincent Delos

Institut Français du Pétrole, Direction Géologie-Géochimie-Géophysique
1-4 Avenue de Bois-Préau, 92852 Rueil-Malmaison Cedex, France
&
GIST
62bis avenue André Morizet, 92100 Boulogne-Billancourt, France
Delos@earthdecision.com

Damien Delvaux

Department of Geology and Mineralogy, Royal Museum of Central Africa
Leuvensesteenweg 13, B 3080 Tervuren, Belgium
damien.delvaux@africamuseum.be
&
ISES, Netherland Research Center for Integrated Solid Earth Science, Free University
De Boelelaan 1085, 1081 HV Amsterdam, The Netherlands

Guy Desaubliaux

Institut Français du Pétrole, Direction Géologie-Géochimie-Géophysique
1-4 Avenue de Bois-Préau, 92852 Rueil-Malmaison Cedex, France
Guy.Desaubliaux@ifp.fr

Eric Desaulniers

Université Laval, Département de Géologie et de Génie Géologique
Ste-Foy, Québec GIK 7P4, Canada

Eric Deville

Institut Français du Pétrole, Direction Géologie-Géochimie-Géophysique
1-4 Avenue de Bois-Préau, 92852 Rueil-Malmaison Cedex, France
Eric.Deville@ifp.fr

Carlo Doglioni

Dept. of Earth Sciences, Univ. of Rome La Sapienza
Piazzale Aldo Moro 5, 00185 Rome, Italy
Carlo.Doglioni@uniroma1.it

Piotr Dziadzio

Polish Oil and Gas Company
Jaslo, Poland
&
current address:
piotr.dziadzio@glinik.pl

Nadine Ellouz-Zimmermann
Institut Français du Pétrole, Direction Géologie-Géochimie-Géophysique
1-4 Avenue de Bois-Préau, 92852 Rueil-Malmaison Cedex, France
Nadine.Ellouz@ifp.fr

Jean-Luc Faure
Institut Français du Pétrole, Direction Géologie-Géochimie-Géophysique
1-4 Avenue de Bois-Préau, 92852 Rueil-Malmaison Cedex, France
J-Luc.Faure@ifp.fr

Jérémie Ferrand
Institut Français du Pétrole, Direction Géologie-Géochimie-Géophysique
1-4 Avenue de Bois-Préau, 92852 Rueil-Malmaison Cedex, France

Dominique Frizon de Lamotte
Univ. de Cergy-Pontoise, Dpt. Sc. de la Terre et de l'Environnement
5 Mail Gay-Lussac, Neuville/Oise, 95031 Cergy-Pontoise, France
dfrizon@geol.u-cergy.fr

Rocco Gennari
Universita degli Studi di Parma, Dipartimento di Scienze della Terra
Parco Area delle Scienze 157/A, 43100 Parma, Italy
rocco.gennari@nemo.unipr.it

Nicolaas J. Hardebol
Institut Français du Pétrole, Direction Géologie-Géochimie-Géophysique
1-4 Avenue de Bois-Préau, 92852 Rueil-Malmaison Cedex, France
nicolaas.hardebol@ifp.fr
&
Faculty of Earth and Life Science, Vrije Universiteit
De Boelelaan 1085, 1081 HV Amsterdam, The Netherlands
nico.hardebol@falw.vu.nl

Syed Imran Hasany
NIO, National Institute of Oceanography
Street 47, Block 1, Clifton, Karachi, Pakistan
niopk@cubexs.net.pk

Salman Jahani
Institut Français du Pétrole, Direction Géologie-Géochimie-Géophysique
1-4 Avenue de Bois-Préau, 92852 Rueil-Malmaison Cedex, France
Salman.Jahani@ifp.fr
&
National Iranian Oil Company (NIOC)
Yaghma Alley-Jomhouri Avenue, Tehran, Iran
Salman_Jahani@yahoo.com

Anne Jardin
Institut Français du Pétrole, Direction Géologie-Géochimie-Géophysique
1-4 Avenue de Bois-Préau, 92852 Rueil-Malmaison Cedex, France
Anne.Jardin@ifp.fr

Shahram Kargar
Geological Survey of Iran
Shiraz, Iran
shahram_kargar_geo@yahoo.com

Donna Kirkwood
Commission géologique du Canada, CGC-Québec
490 rue de la Couronne, Québec G1K 9A9, Canada
Donna.Kirkwood@rncan.gc.ca

Piotr Krzywiec

Polish Geological Institute
ul. Rakowiecka 4, 00-975 Warsaw, Poland
Piotr.Krzywiec@pgi.gov.pl

Pierre Labaume

Laboratoire Dynamiue de la Lithosphère, cc 060, CNRS-Univ. Montpellier-II
34095 Montpellier Cedex 5, France
Pierre.Labaume@dstu.univ-montp2.fr

Olivier Lacombe

Université Pierre-et-Marie Curie, Laboratoire de Tectonique, CNRS UMR 7072
4 Place Jussieu, Case 129, T46-E2, 75252 Paris Cedex 05, France
olivier.lacombe@lgs.jussieu.fr

Siegfried Lallemant

Univ. de Cergy-Pontoise, Dpt. Sc. de la Terre et de l'Environnement
5 Mail Gay-Lussac, Neuville/Oise, 95031 Cergy-Pontoise, France
siegfried.Lalleman@geol.u-cergy.fr

Jérôme Lavé

Laboratoire de Géodynamique des Chaînes Alpines, Université Joseph Fourier
BP53, 38041 Grenoble Cedex, France
Jerome.Lave@ujf-grenoble.fr

Federica Lenci

Dept. of Earth Sciences, Univ. of Rome La Sapienza
Piazzale Aldo Moro 5, 00185 Rome, Italy
fedelenci@yahoo.com

Grzegorz Lesniak

Polish Oil and Gas Institute
ul. Lubicz 25A, Pl. 31-503 Krakow, Poland
lesniak@inig.pl

Jean Letouzey

Institut Français du Pétrole, Direction Géologie-Géochimie-Géophysique
1-4 Avenue de Bois-Préau, 92852 Rueil-Malmaison Cedex, France
Jean.Letouzey@ifp.fr

Pascale Leturmy

Univ. de Cergy-Pontoise, Dpt. Sc. de la Terre et de l'Environnement
5 Mail Gay-Lussac, Neuville/Oise, 95031 Cergy-Pontoise, France
Pascale.Leturmy@geol.u-cergy.fr

Steven Lingrey

ExxonMobil Production Company, Production Geoscience, Special Studies
Room EMB 2717C, Houston, TX 77252-2180, USA
steve.lingrey@exxonmobil.com

Andreas Lückge

Bundesanstalt für Geowissenschaften und Rohstoffe, BGR
Stilleweg 2, 30665 Hannover, Germany
A.Lueckge@bgr.de

Geoffroy Mahieux

Laboratoire de Géologie, Université de Picardie
33 rue St-Leu, 80039 Amiens, France
Geoffroy.Mahieux@sc.u-picardie.fr

Vinicio Manzi

Universita degli Studi di Parma, Dipartimento di Scienze della Terra
Parco Area delle Scienze 157/A, 43100 Parma, Italy
vinicio.manzi@unipr.it

Daiana Marcantoni
Dept. of Earth Sciences, Univ. of Rome La Sapienza
Piazzale Aldo Moro 5, 00185 Rome, Italy

Georges Mascle
LGCA, CNRS-UMR 5025, Maison des Géosciences
BP 53, 38 043 Grenoble Cedex, France
gmascle@ujf-grenoble.fr

Irena Matyasik
Polish Oil and Gas Institute
ul. Lubicz 25A, 31-503 Krakow, Poland
matyasik@inig.pl

Eric Mercier
Université de Nantes, Laboratoire de Planétologie et Géodynamique UMR 6112
BP 92208, 44322 Nantes Cedex 3, France
Eric.Mercier@univ-nantes.fr

Isabelle Moretti
Institut Français du Pétrole, Direction Géologie-Géochimie-Géophysique
1-4 Avenue de Bois-Préau, 92852 Rueil-Malmaison Cedex, France
Isabelle.Moretti@ifp.fr

Fausto Mosca
Humble Geochemical Services
218 Higgins, Post Office Box 789, Humble, Texas 77338, USA
&
current address:
Devon Energy
1200 Smith Street, Houston, Texas 77002, USA
fausto.mosca@dvn.com

Nicolas Mouchot
Univ. de Cergy-Pontoise, Dpt. Sc. de la Terre et de l'Environnement
5 Mail Gay-Lussac, Neuville/Oise, 95031 Cergy-Pontoise, France
Nicolas.Mouchot@geol.u-cergy.fr

Frédéric Mouthereau
Université Pierre-et-Marie Curie
Laboratoire de Tectonique, CNRS UMR 7072
4 Place Jussieu, Case 129, T46-E2
75252 Paris Cedex 05, France
frederic.mouthereau@lgs.jussieu.fr

Peter Mühr
Bundesanstalt für Geowissenschaften und Rohstoffe, BGR
Stilleweg 2, 30665 Hannover, Germany
p.muehr@bgr.de

Carla Müller
6 Bis Rue Haute, 92 Rueil-Malmaison, France

Michal Mysliwiec
Polish Oil and Gas Company
Jaslo, Poland
&
current address:
michal.mysliwiec@petroinvest.pl

Alfredo Otero
Repsol-YPF-Bolivia
Santa-Cruz, Bolivia
Aoteror@repsolypf.com

Benham Oveisi
Geological Survey of Iran
Tehran, Iran
&
Laboratoire de Géodynamique des Chaînes Alpines, Université Joseph Fourier, BP53
38041 Grenoble Cedex, France
Oveisi@ujf-grenoble.fr

Giovanni Papani
Universita degli Studi di Parma, Dipartimento di Scienze della Terra
Parco Area delle Scienze 157/A, 43100 Parma, Italy
giovanni.papani@unipr.it

Vicenzio Picotti
Dipartimento di Scienze della Terra e Geologico-Ambientali, Universita di Bologna
Via Zamboni 67, 40127 Bologna, Italy
picotti@geomin.unibo.it

Anne-Catherine Pierson-Wickmann
Univ. of Rennes 1, Géosciences Rennes UMR 6118
Avenue du Gal Leclerc, 35042 Rennes, France
anne-catherine.pierson-wickmann@univ-rennes1.fr

Bogdan Popescu
Rompetrol
Rompetrol Building, 222 Calea Victoriei, 010099 Bucharest, Romania
bodgan.popescu@rompetrol.com

Silvain Rafini
Université de Nantes, Laboratoire de Planétologie et Géodynamique UMR 6112
BP 92208, 44322 Nantes Cedex 3, France
&
current address:
Département des Sciences de la Terre et de l'Atmosphère, Université de Québec à Montréal
Montréal, PQ, 201 rue du Président Kennedy, local PK6640, Canada
rafini.silvain@courrier.uquam.ca

Francesca Rizzini
Universita degli Studi di Parma, Dipartimento di Scienze della Terra
Parco Area delle Scienze 157/A, 43100 Parma, Italy
francesca.rizzini@unipr.it

Philippe Robion
Univ. de Cergy Pontoise, Dpt. Sc. de la Terre et de l'Environnement
5 Mail Gay-Lussac, Neuville/Oise, 95031 Cergy-Pontoise, France
robion@u-cergy.fr

François Roure
Institut Français du Pétrole, Direction Géologie-Géochimie-Géophysique
1-4 Avenue de Bois-Préau, 92852 Rueil-Malmaison Cedex, France
Francois.Roure@ifp.fr
&
Faculty of Earth and Life Science, Vrije Universiteit
De Boelelaan 1085, 1081 HV Amsterdam, The Netherlands

Marco Roveri
Universita degli Studi di Parma, Dipartimento di Scienze della Terra
Parco Area delle Scienze 157/A, 43100 Parma, Italy
marco.roveri@unipr.it

Jean-Luc Rudkiewicz
Institut Français du Pétrole, Direction Géologie-Géochimie-Géophysique
1-4 Avenue de Bois-Préau, 92852 Rueil-Malmaison Cedex, France
J-Luc.Rudkiewicz@ifp.fr

David Saucier
Université Laval, Département de Géologie et de Génie Géologique
Ste-Foy, Québec GIK 7P4, Canada
dave_saucier@hotmail.com
&
current address:
BP Exploration
Burnside Road, Farburn Industrial Estate, Dyce Aberdeen, AB21 7PB, United Kingdom
Dave.Saucier@uk.bp.com

Julien Schmitz
Institut Français du Pétrole, Direction Géologie-Géochimie-Géophysique
1-4 Avenue de Bois-Préau, 92852 Rueil-Malmaison Cedex, France
Julien.Schmitz@ifp.fr

Davide Scrocca
Istituto di Geologia Ambientale e Geoingegneria, c/o Dipartimento di Scienze della Terra
Universita degli Studi di Roma "La Sapienza"
Piazzale Aldo Moro 5, 00185 Rome, Italy
davide.scrocca@igag.cnr.it

Aamir Ali Shahzad
Pakistany Navy
11 Liaquat Barracks, Naval Headquarter, Karachi, Pakistan
seaali@yahoo.com

Shahram Sherkati
National Iranian Oil Company (NIOC)
Yaghma Alley-Jomhouri Avenue, Tehran, Iran
SSherkati@niocexp.org

Andrea Sitta
Edison S.p.A.
Foro Buonaparte, 31 Milano, Italy
andrea.sitta@edison.it

Akhter Mehmood Subhani
Geological Survey of Pakistan, GSP
P.O. Box No. 15, Sariab Road, Quetta, Pakistan

Piotr Such
Polish Oil and Gas Institute
ul. Lubicz 25A, Krakow 31-503, Poland
such@igng.krakow.pl

A. Tabreez
NIO, National Institute of Oceanography
Street 47, Block 1, Clifton, Karachi, Pakistan

Dorina Tambrea
Rompetrol
Rompetrol Building, 222 Calea Victoriei, 010099 Bucharest, Romania
dorina.tambrea@rompetrol.com

Mihai Tarapoanca
Rompetrol
Rompetrol Building, 222 Calea Victoriei, 010099 Bucharest, Romania
&
current address:
Danubian Energy Consulting
Rue Silvestru n° 2 apt. 6, Code Postal 020735, Bucharest, sector 2, Romania
mtarapoanca@danubianenergy.com

Julien Tensi
Université Pierre-et-Marie Curie, Laboratoire de Tectonique, CNRS UMR 7072
4 Place Jussieu, Case 129, T46-E2, 75252 Paris Cedex 05, France
Julien.Tensi@lgs.jussieu.fr

Maria Tornaghi
Edison S.p.A;
Foro Buonaparte, 31 Milano, Italy
maria.tornaghi@edison.it

Anna Travé
Departament de Geoquímica, Petrologia i Prospecció Geològica, Facultat de Geologia, Universitat de Barcelona
c/Martí i Franqués s/n, 08028 Barcelona, Spain
atrave@ub.edu

Peter Van der Beek
Laboratoire de Géodynamique des Chaînes Alpines, Université Joseph Fourier, BP53
38041 Grenoble Cedex, France
pvdbeek@ujf-grenoble.fr

Peter Van den Haute
Department of Mineralogy and Petrology, University of Gent
Krijgslaan 281, S8, B-9000 Gent, Belgium
Peter.Vandenhaute@ugent.be

Jaume Vergés
Group of Dynamics of the Lithosphere, Institute of Earth Sciences "Jaume Almera", CSIC
Lluís Solé i Sabarís s/n, 08028 Barcelona, Spain
jverges@ija.csic.es

Université Pierre-et-Marie Curie, Laboratoire de Tectonique, CNRS UMR 7072

Part I
Surficial and Deep Processes in Thrust Belts

Part I of the volume comprises two chapters which deal with several large-scale and first-order features of thrust belts and foreland basins.

Burov (Chapter 1) investigates the interactions between the surface and sub-surface processes by means of thermo-mechanical modelling. One main point is that advection of material at the Earth's surface and horizontal flow in the lower crust might be coupled so as to permit mountain growth in response to horizontal shortening. This mechanism is investigated on the basis of semi-analytical and numerical experiments in which the rheological layering of the lithosphere and surface processes are modelled. These ideas are tested on well-studied cases such us the Western Alps, the Tien Shan and the Himalaya. Some implications about the role of climate on continental tectonics and on the geomorphology of mountain ranges are derived.

In their paper, Lenci and Doglioni (Chapter 2) address the overall asymmetry of thrust belts by analyzing various convergent margins in terms of geographic polarity of the margin, age and composition of the subducting plate. They argue that the asymmetry between orogens or accretionary wedges is to the first-order global and related to geographically opposed (i.e., W- to E-NE directed) subduction zones, while local/regional stratigraphic-rheological characteristics which may vary along strike, such as the décollement depth, exert only second-order controls on each orogen

Coupled Lithosphere-Surface Processes in Collision Context

Evgueni Burov

Abstract. From the mechanical point of view, a mountain range that exceeds a certain critical height (of about 3 km in altitude, depending on rheology and width) should flatten and collapse within few My as a result of gravitational spreading of its ductile crustal root. Even if the crustal root does not collapse, the mountain range would be levelled by gravity sliding and other surface processes that, in case of static topography, lead to its exponential decay with a characteristic time constant on the order of 2.5 My. However, in nature, mountains grow and stay as localized tectonic features over geologically important periods of time (> 10 My). To explain the paradox of long-term persistence and localized growth of the mountain belts, a number of workers have emphasized the importance of dynamic feedbacks between surface processes and tectonic evolution. Indeed, surface processes modify the topography and redistribute tectonically significant volumes of sedimentary material, which acts as vertical loading over large horizontal distances. This results in dynamic loading and unloading of the underlying crust and mantle lithosphere, whereas topographic contrasts are required to set up erosion and sedimentation processes. Tectonics therefore could be a forcing factor of surface processes and vice versa. One can suggest that the feedbacks between tectonic and surface processes are realized via two interdependent mechanisms:

1. Slope, curvature and height dependence of the erosion/deposition rates
2. Surface load-dependent subsurface processes such as isostatic rebound and lateral ductile flow in the lower or intermediate crustal channel.

Loading/unloading of the surface due to surface processes results in lateral pressure gradients, that, together with low viscosity of the ductile crust, may permit rapid relocation of the matter both in horizontal and vertical direction (upward/downward flow in the ductile crust). In this paper, we overview a number of coupled models of surface and tectonic processes, with a particular focus on 3 representative cases:

1. Slow convergence and erosion rates (Western Alpes)
2. Intermediate rates (Tien Shan, Central Asia)
3. Fast convergence and erosion rates rates (Himalaya, Central Asia).

1 Introduction

Continental mountain belts, such as, for example, Tien Shan (Central Asia, Figure 1a), are characterized by highly localized topography elevations persistently growing over tens of millions of years. The fact that gravitational potential energy per unit surface $0.5\rho gh^2$ scales as h^2 implies that a thrust belt should grow more easily in width than in height (Molnar and Lyon-Caen, 1988, h is the mean topography elevation above sea level, ρ is density and g is acceleration due to gravity). A portion of continental crust submitted to quasi-static horizontal shortening should tend to thicken homogeneously. This can be put another way around by considering that a range results from thrusting on faults that cut through the upper crust and root into the lower crust. Uplift of the range implies an increase in the vertical stress acting on the fault. This acts to oppose further frictional sliding on the fault, inhibiting further thrusting. A new fault will then form farther away from the range front leading to widening of the range. In addition, erosion and sedimentation at the surface, together with flow in the lower crust, should favor smoothing of topographic irregularities. At the pressure and temperature conditions of the lower crust, most crustal rocks are thought to flow easily at very low deviatoric stresses (e.g., Brace and Kohlstedt, 1980; Wang et al., 1994, Fig. 2a). The deviatoric stresses associated with slopes of the topography and of the Moho (e.g., Fleitout and Froidevaux, 1982) should therefore be relaxed by viscoplastic flow in the ductile lower crust inducing decay of topographic irregularities (Kusznir and Matthews, 1988; Gratton, 1989; Bird, 1991, Fig. 1b).

The growth and maintenance of topographic features at the surface of continents might be taken to indicate that the strength of the crust exceeds the deviatoric stresses associated with slopes of the topography and of the Moho. Yet, as mentioned above, laboratory experiments indicate that at the pressure and temperature conditions of the lower crust, most crustal rocks should flow easily. Irregularities of the topography and of the Moho boundary should therefore be
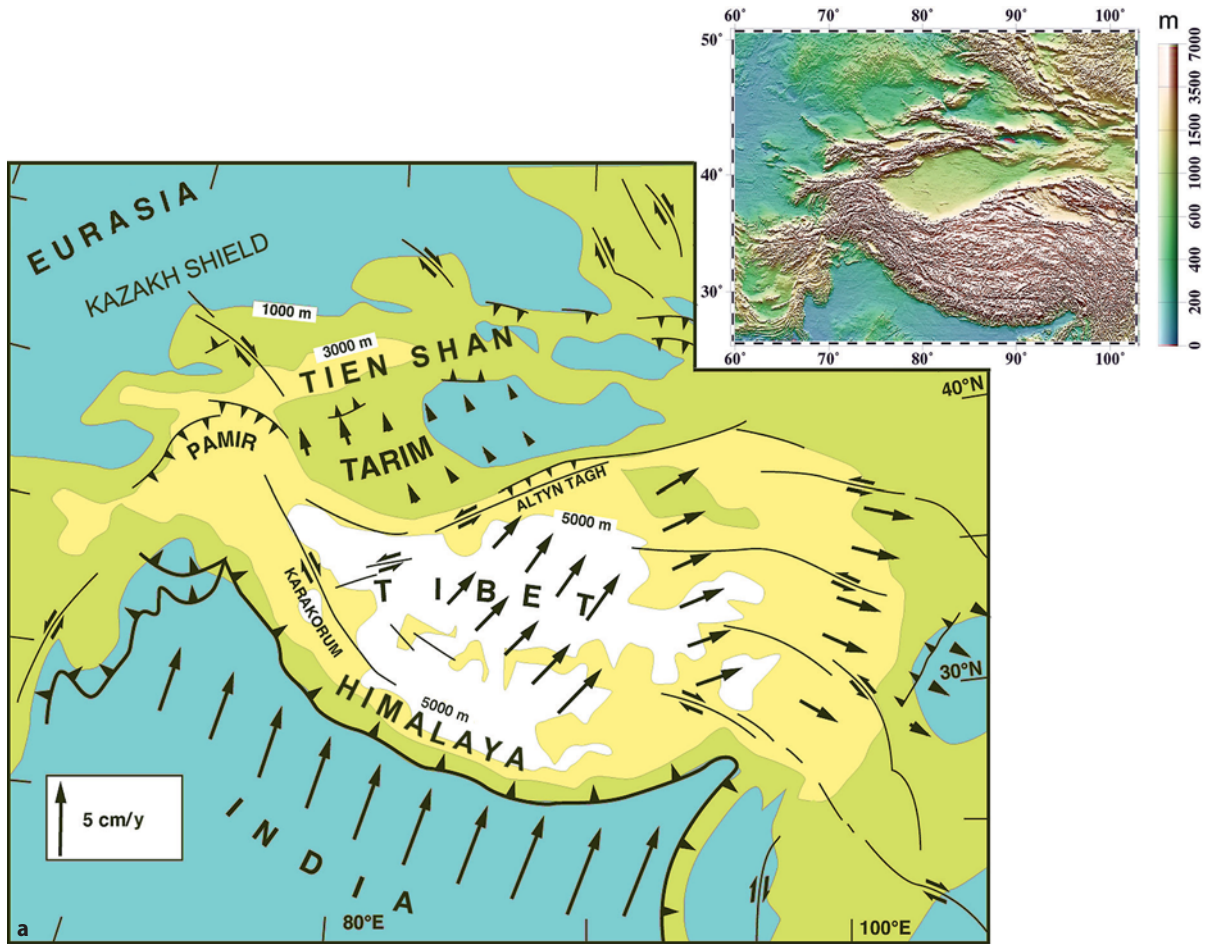
Fig. 1a. Actively growing intercontinental belts and plateaux: an example showing a schematic map of India-Eurasia collision with its main features such as the Himalayan mountain belt, Tibetan plateau, Tarim basin, Pamir and Tien Shan mountain belt. Insert shows a digital elevation map of the same area. The topography peaks to 8800 m in the Himalayas (Everest) and 7500 m in Tien Shan (Pobeda Peak). Modified after (Avouac and Tapponier, 1993)
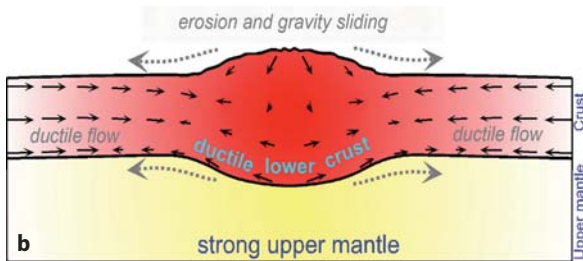
Fig. 1b. Erosional and gravity collapse of a mountain range (e.g., Gratton, 1989; Bird, 1991). In the conceptual model shown here, there is no balance between surface and subsurface processes. Even if such range was created somehow, it will not persist, as its root and topography will be flattened in about 2 My in the absence of some compensating mechanisms. Tectonic convergence may not solely compensate this flattening; it may only grant an overall thickening of the crust; some additional localizing mechanisms are needed to concentrate thickening in a narrow range.

relaxed by viscoplastic flow in the ductile lower crust and decay with time (Kusznir and Matthews, 1988; Gratton, 1989; Bird, 1991). Consider, for example, the Tien Shan range, which is, except for the Himalayas, the largest and most active intracontinental range in the world (Fig. 1a). Tien Shan (translated as "Heavenly Mountains") is 300–400 km wide in its central area, with a mean elevation of about 3500 m and local peaks of up to 7500 m, in a zone of relatively thick and tectonized crust (Moho depths from 50 to 70 km) (e.g., Avouac et al., 1993). The Tien Shan is a continuously growing range, that has started to rise 10–15 My ago. A simple dimensional analysis (Gratton, 1989) as well as numerical simulations (Bird, 1991; Avouac and Burov, 1996; Burov and Watts, 2006) show that the topography of such a range should, instead of growing, be reduced by half in a few My (Fig. 1b). This estimate is based on the assumption of ductile rheology of the
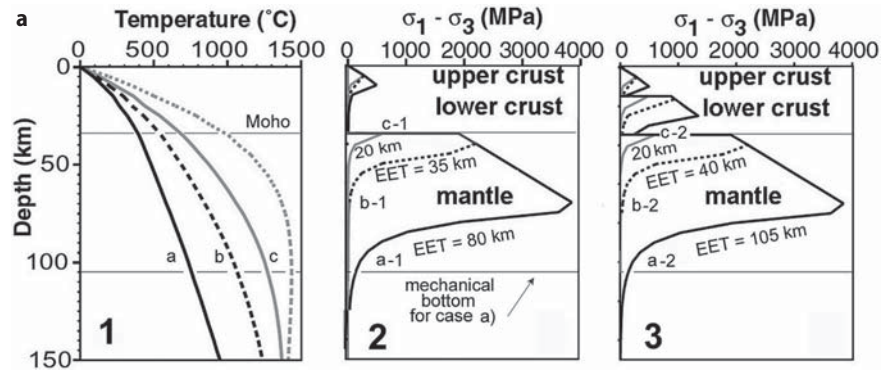
Fig. 2. a) Typical rheology profiles for continental lithosphere indicate the possibility for lower-crustal flow: (*1*) geotherms that yield YSEs shown in the middle and on the right; (*2*) yield stress envelope (YSE) for quartz-rich upper and lower crust and olivine mantle; (*3*) yield stress envelope (YSE) for quartz-rich upper crust , diabase lower crust, olivine mantle. EET – equivalent elastic thickness of the lithosphere computed for each of YSEs. **b**) Solution to the problem stated in Fig. 1b: a conceptual model of continental collision in which strong feedback between surface processes, isostatic reaction and subsurface crustal flow results in accelerated growth of topography in the area of strongest subsurface uplift

lower crust, which is supported for this area by multiple data starting from seismic data (Vinnik and Saipbekova, 1984; Makeyeva, 1992; Roecker et al., 1993; Vinnik et al., 2006) and ending by gravity-flexural analysis (Burov et al., 1990, 1993; Avouac and Burov, 1996). Only the short topographic wavelengths, typically less than a few tens of kilometers that can be supported by the strength of the upper crust would be maintained over geological periods of time, yet provided that they are not wiped out by erosion, which is faster on short wavelength features. In addition, surface processes might be thought to contribute to an even more rapid smoothing of the topography. Similarly, in the absence of strong rheological heterogeneities or of strain localization processes, a portion of a continental crust submitted to horizontal shortening should tend to thicken homogeneously, so that no mountain should form. The growth and maintenance of an intracontinental mountain range over long periods of time must therefore involve dynamical processes allowing for long-term localization of lithospheric strain below the mountain.

Several mechanisms have been advocated to explain localization of major thrust faults and, by its proxy, stability of mountain belts. Intrinsic strain softening properties of rocks could sustain localized thrust faulting at the crustal scale. Alternatively, a range could result from shear stresses at base of

the crust induced by lithospheric under-thrusting or by mantle dynamics (e.g., Beaumont et al., 1994; Ellis et al., 1995). Such a mechanism may be suggested for mountains associated with subduction zones or with hotspots (Vogt, 1991), but seems inappropriate to explain most intracontinental mountains. In the case of, for example, the Tien Shan belt, a particular mantle dynamics has been inferred from gravity modelling (Burov et al., 1990, 1993) and seismic anisotropy (Makeyeva, 1992; Roecker et al., 1993), but we contend that it might not be the key factor. Our point is instead that coupling between surface processes and flow in the lower crust could provide an alternative and more general explanation (Avouac and Burov, 1996; Burov and Cloetingh, 1997).

To explain the paradox of long-term mountain persistence and localized growth, a number of workers have emphasized the importance of dynamic feedbacks between surface processes and tectonic evolution (e.g., Molnar and England, 1990; Masek et al., 1994a; Avouac and Burov, 1996; Molnar, 2001). Indeed, surface processes modify the topography and redistribute tectonically significant volumes of sedimentary material (vertical, or normal loads) over large horizontal distances. This may result in dynamic loading and unloading of the underlying crust and mantle lithosphere, whereas topographic contrasts are required to set up erosion and sedimentation processes.

Tectonics therefore could be a forcing factor of surface processes.

In this paper, we first review the existing models of surface processes and the thermo-mechanical properties of the lithosphere that condition its response to surface and tectonic loading-unloading. We then review our own and other previous modelling studies that show that surface and tectonic processes are not independent processes and can interact. We show in particular that advection of material at the Earth's surface and horizontal flow in the crust might be coupled so as to permit mountain growth in response to horizontal shortening. This mechanism is then validated and investigated on the basis of semi-analytical and numerical experiments in which the rheological layering of the lithosphere and surface processes are modelled. We then find that, depending of the erosion rate compared to horizontal shortening, flow in the lower crust can be "outward" (from under the high topography) or "inward" (toward the crustal root of a high topography). When inward flow occurs, a mountain range can actually grow and no other mechanism is required to explain localized uplift. Some implications about the role of climate on continental tectonics and on the geomorphology of mountain ranges are then derived.

We suggest an additional feedback mechanism by lateral crustal flow (Fig. 2b). According to this mechanism, erosional removal of material from topographic heights (dynamic unloading) and its deposition in the foreland basins (dynamic loading) should result in horizontal ductile crustal flow that may oppose gravitational spreading of the crustal roots and may eventually drive a net influx of material towards the orogeny. We finally test our ideas on three representative and well-studied cases:

1. Slow convergence and erosion rates (Western Alpes),
2. Intermediate rates (Tien Shan, Central Asia), and
3. Fast convergence and erosion rates rates (Himalaya, Central Asia).

2   Interplays Between Surface and Tectonic Processes

2.1 Tectonic Forcing on Surface Processes

Surface topography elevations are required to set up erosion and sedimentation processes. Tectonics is therefore a forcing factor of surface processes. Following Ahnert (1970), and Pinet and Souriau (1988), Summerfield and Hulton (1994) have compiled rates of denudation at the scale of major river basins. These studies indicate that denudation is primarily influenced by basin topography so that rates of denudation appear to be systematically high in areas of active tectonic uplift. Common values of mean denudation rates in such areas would be of the order of a few 0.1 mm/y to about 1mm/y at the scale of large drainage basins. Such rates are generally consistent with estimates derived from balancing sediment volumes over geological periods of time (Leeder, 1991; Summerfield and Hulton, 1994). Thermochronologic studies indicate, however, local values as great as 1 mm/y (see Leeder, 1991 and Molnar and England, 1990, for critical reviews). The discrepancy between local and basin averaged estimates is due to the fact that tectonic uplift is probably distributed in brief pulses over localized domains within a drainage basin (Copeland and Harrison, 1990). In the absence of any tectonic feedback, common values of denudation rates should lead to the disappearance of a major mountain belt like the Alpes or Tien Shan in a few million years. Pinet and Souriau (1988) demonstrated that denudation leads to an exponential decay of the topography of a range with a characteristic time constant of the order of 2.5 m.y.

2.2 Coupling Between Denudation and Tectonic Uplift due to Isostasy

Many recent models have investigated coupling between the isostatic reaction and surface processes (e.g., Kooi and Beaumont, 1994; Snyder et al., 2000; Basile and Allemand, 2002; Garcia-Castellanos, 2002; Garcia-Castellanos et al., 2002; 2003; Simpson and Schlunegger, 2003; Persson et al., 2004; Casteltort and Simpson, 2006). Redistribution of surface loads by erosion and sedimentation must induce tectonic deformation to maintain isostatic balance. Vertical uplift is expected to partly compensate unloading in the area subjected to denudation while subsidence should occur in response to loading by sedimentation. This feedback mechanism may lead to some coupling between denudation and tectonic uplift (e.g., Ahnert, 1970). A first consequence is that the time needed to erode a topographic relief must take into account removal of the topographic relief and of the crustal root. If local isostasy is assumed and if horizontal strains are neglected, denudation is dynamically compensated by uplift and the characteristic time of decay of the topography would then be of the order of 10 m.y. (Leeder, 1991). In addition, it has been argued that a positive feedback may arise (Molnar and England, 1990; Masek et al., 1994b). If the slopes of valleys steepen during river incision, isostatic readjustment following denudation in a mountain range may result in a net uplift of the higher summits in spite of the average lowering of reliefs. Alternatively regional compensation due to the elasticity of the lithosphere might lead to the uplift of the

eroded edge of a plateau. Erosion might therefore induce some uplift of topographic summits leading in turn to enhanced erosion. The uplift of the Himalayan belt during the last few million years may have resulted from such a coupling rather than from thrusting at the Himalayan front (Burbank, 1992; Burbank and Verges, 1994). Note however that, while the peaks might reach higher elevations following isostatic adjustment, the net effect of erosion is crustal thinning. Thus, these models cannot explain the growth of mountains over long time periods.

The strongest feedback between erosion and isostatic reaction would be obtained for local isostasy. It will be mitigated in case of more regional compensation and become negligible for lithospheres whose equivalent elastic thickness exceeds 60 km. This is another reason to support the idea that more efficient mechanisms should also take place in collisional settings.

2.3 Coupling Between Surface Processes and Horizontal Strains

As mentioned in the introduction, small lateral variations of the crustal thickness should drive horizontal flow in the lower crust. Some studies have already pointed out to the importance of such a process in continental tectonics (e.g., Lobkovsky, 1988; Lobkovsky and Kerchman, 1991; Burov and Cloetingh, 1997). For example, Kruse et al. (1991) have shown that horizontal flow in the lower crust has regulated isostatic equilibrium during extension in the Basin and Range. The lower crust would have been extruded from under the high topography during that process. Following Westaway (1994) we will call this sense of flow "outward". On the other hand, Gregory and Chase (1994) inferred "inward" flow, toward the crustal root, during the Laramide orogeny of the Frontal Range, Colorado. The characteristic time associated with flow in the lower crust induced by the topography of a range a few thousands of meters high, a few hundreds of km wide, is in the order of a few m.y. The characteristic times of erosional decay of the topography of a range and of lateral collapse of a crustal root are thus of the same order of magnitude. Since both processes are driven by topographic slopes, some coupling may arise. Although it is not often pointed out, it has long been recognized that this kind of process might play a major role in elevation changes within continents (see Westaway, 1994 for an review of historical development of these ideas). Westaway (1994) made a case for such a coupling, with inward flow, in the context of extensional tectonics in western Turkey. He proposed that sediment loading in the sedimentary basins would have driven flow toward the uplifted area. This kind of process was first modelled by King and Ellis (1990), who modelled crustal extension using a thin elastic plate (upper crust) overlying an inviscid fluid (lower crust).

We propose that this kind of coupling might also appear in a compressional context. Let us consider a portion of a lithosphere, loaded with some initial range topography in regional isostatic balance, and submitted to horizontal compression. Horizontal stress gradients, resulting from the slopes of the topography and of the Moho, must drive horizontal flow. The lithosphere in the region of the range is weakened, since the crust is thick and hot, and because bending of the lithosphere beneath the mountain load tends to reduce its strength (Burov and Diament, 1992; 1995; Ranalli, 1995). Higher strain rates in the area below the range should therefore be expected. A low viscosity channel in the lower crust beneath the high topography might therefore allow lateral flow. In the absence of horizontal shortening and erosion, the lower crust below the range would be extruded laterally as discussed by Bird (1991). If erosion takes place, a regime may be established in which horizontal shortening would be preferentially accommodated by crustal thickening in the area below the range:

a) Surface processes remove material from the range and feed the adjacent flexural basins inducing isostatic imbalance.
b) This imbalance produces a temporary excess of normal stress below the foreland basins and deficit below the range favoring flow in the lower crust towards the crustal root. The range uplifts and the basins subside.

Ultimately this coupled regime might lead to some dynamic equilibrium in which the amount of material removed by erosion would balance the material supplied to the range by subsurface deformation.

Apart of the direct mechanical effect of erosion/sedimentation (loading-unloading) on the lithosphere, it also has very important thermal, and, by proxy, mechanical consequences, because the removal and accumulation of sedimentary matter modifies surface heat flux and thermal conditions in the upper crust (e.g., England and Richardson, 1977). Accumulation of sediments in the forelands leads to (1) cooling of the accretion wedge at a short term, in case of rapid advection/filling (initial stages of collision when the convergence rate is highest); (2) heating of the accretion wedge at a long term in case of slow advection (when collision rate slows down), due to heat screening (sediments have low thermal conductivity) and the abundance of heat producing radiogenic elements in the sedimentary matter. Furthermore, penetration of the mechanically weak sediment in the subduction channel should serve as lubrification and may enhance the conditions for subduction processes.

2.4 Coupling of Surface Processes and Tectonic Input/Reaction in Full Scale Mechanical Models: Major Stages

A number of earlier modelling studies (e.g., Beaumont, 1981; Beaumont et al., 1992; 1995; Willet, 1999) have investigated various relationships between erosion and tectonic processes. However, tectonic reaction was not fully accounted for, as most of these models that have exploited semi-kinematic formulations for the crust or the mantle lithosphere. One of the first full-scale parametric semi-analytical models was developed by Avouac and Burov (1996) in order to validate the coupled regime between surface and subsurface processes. For this purpose this model accounted for:

1. Surface processes.
2. The effect of topographic loads and variations of crustal thickness on the mechanical behavior of the lithosphere.
3. Ductile flow in the lower crust.
4. Depth-and-strain dependent rheology of the lithosphere.

In the following sections we first discuss the components needed to build a coupled tectonic model of orogenic building:

1. The existing models of surface processes.
2. The rheology data needed for proper account of the mechanical response of the lithosphere.
3. Thermal models of the lithosphere needed for proper account of thermally dependent ductile rheology.

We then describe the design and major results of the coupled semi-analytical model of Avouac and Burov (1996). This semi-analytical model has a number of limitations in terms of model geometry and its inability to account for some key deformation modes such as formation of major thrust faults. For this reason, in the final sections of this study, we go further by introducing an unconstrained fully coupled numerical thermo-mechanical model of continental collision/subduction similar to that used by Burov et al., (2001); and Toussaint et al. (2004a,b). This model takes into account more realistic (than in the previous studies) geometry of the convergent plates, accounts for large strains and brittle-elastic-ductile rheology including localized brittle (faulting) and ductile deformation.

3 Surface Processes Modelling: Principles and Numerical Implementation

3.1 Basic Models of Surface Processes

A growing amount of field and experimental studies have investigated and validated various forms of long-and-short range erosion and sedimentary transport laws and models (Ahnert, 1970; Beaumont, 1981; Beaumont et al., 1992;2000; Burbank, 1992; Burbank and Verge, 1994; Ashmore, 1982; Mizutani, 1998; Lavé and Avouac, 2001; Lague et al., 2000, 2003; Davy and Grave, 2000; Lague et al, 2000; Molnar, 2001; Grave and Davy, 2001; Densmore et al., 1997;1998; Pinet and Souriau, 1988).

Short-range erosion. A simple two-dimensional law may be used to simulate erosion and sedimentation at the scale of a mountain range. The evolution of a landscape results from the combination of weathering processes that prepare solid rock for erosion, and transportation by hillslope and stream processes (see Carson and Kirkby, 1972 for a review). Although many factors, depending on the lithologies and on climate (e.g., Fournier, 1960; Nash, 1980), may control this evolution, quite simple mathematical models describing the geometrical evolution of the morphology at the small scale have been proposed and tested successfully (e.g., Kirkby, 1971; Smith and Bretherton, 1972; Chorley et al., 1984; 1986; Luke, 1972; 1974; Kirkby et al., 1993). For example, the two-dimensional evolution of a scarp-like landform can be modelled assuming that the rate of downslope transport of debris, q, is proportional to the local slope, ∇h (Culling, 1960; 1965; Hanks et al., 1984; Avouac, 1993; Kooi and Beaumont, 1994; 1996; Braun and Sambridge, 1997).

$$q = -k\nabla h \qquad (1)$$

where k is the mass diffusivity coefficient, expressed in units of area per time [e.g., m²/y]. Assuming conservation of matter along a 2-D section and no tectonic deformation, h must obey:

$$dh/dt = -\nabla q \qquad (2)$$

With constant k, Eqs. (1) and (2) lead to the linear diffusion equation:

$$dh/dt = k\nabla^2 h \qquad (3)$$

This model of surface processes holds only for particular conditions. The regolith must form more rapidly than it is removed by surface transport and slopes

must not exceed the frictional angle of the material. Even for scarps formed in loose alluvium some complications arise when high scarps are considered. Scarps with height typically in excess of about 10 meters in arid climatic zones, tend to have systematically sharper curvatures at crest than at base (e.g., Andrews and Bucknam, 1987). Gravity-driven erosion processes such as hillslope landsliding impose strong limitations on the applicability of the diffusion equation since the processes are rather slope- then curvature-dependent, which basically requires to introduce slope-and-height dependent terms in the equation (3). At the larger scale, hillslope and stream processes interact and the sediment transport then depends nonlinearly on the slope and on other factors such as the slope gradient, the area drained above the point, the distance from the water divide, so that the simple 2-D linear diffusion does not apply in general (e.g., Gossman, 1976). In spite of these limitations, we have chosen to stick to a linear diffusion law to model erosion in the upland. This model does not accurately mimic the spatial distribution of denudation in the mountain range but it leads to a sediment yield at the mountain front that is roughly proportional to the mean elevation of the basin relative to that point (a rough approximation to the sediment yield resulting from a change of elevation h over a horizontal distance d is $k \times h/d$) and therefore accounts for the apparent correlation between elevation and denudation rates (Ahnert; 1970, Pinet and Souriau, 1988; Summerfield and Hulton, 1994). We did not apply the diffusion model to the whole system, however. We felt that we should take into account the major discontinuity in surface processes that occurs at the mountain front. As a river emerges into the adjacent basin its gradient is sharply reduced and deposition occurs. The streams shift from side to side and build up alluvial fans and tend to form a broad gently sloping pediment at the base of the mountain range. In addition, a lateral drainage often develops along the foothills of mountain ranges. The Ganges along the Himalayan foothills, the Parana along the Andes, or the Tarim along the Tien Shan are good examples. Altogether the formation of the pediment and lateral drainage tend to maintain gentle slopes in the foreland. There is therefore a sharp contrast between river incision that maintains a rugged topography with steep slopes in the mountain range and widespread deposition of alluvium in the foreland. This discontinuity of processes must be considered to model the sharp break-in-slope at the mountain front that is generally observed on topographic profiles across mountain belts. In order to simulate this major change in surface processes, sedimentation in the lowland is modelled assuming flat deposition by fluvial network: we assume that conservation of matter along the section and the sediment at the mountain front is distributed in order to maintain a flat horizontal topography in the foreland. We arbitrarily set the change from diffusional erosion to sedimentation ("flat deposition") at a differential elevation of 500 m, which is, however, representative for the transition from highlands to forelands.

We considered values for k varying between 10^2 to 10^4 m^2/y that yield denudation rates of the order of a few 0.01 mm/y to 1 mm/y for a 200–400 km-wide range with a few thousand meters of relief. In order to test the sensitivity of our model on the assumed erosion law we also considered non linear erosion laws of the form:

$$dh/dt = k^*(x,h,\nabla h)\nabla^2 h \qquad (4a)$$

where $k^*(x,h,\nabla h)= k(x)(\nabla h)^n$ (e.g., Gossman, 1976; Andrews and Bucknam, 1987). We will refer to the cases with n = 1, 2 as first-and second-order diffusion, respectively. In these cases we did not introduce the change in regime at the mountain front since the nonlinear effects already tend to form relatively smooth pediments. It should be noted that Eq. (4) differs from the one obtained assuming a non linear diffusion coefficient in Eq. (1). In that case conservation of mass would lead to an additional term $\nabla k^* \nabla h$:

$$dh/dt = k^*(x,h,\nabla h) \nabla^2 h + \nabla k^*(x,h,\nabla h)\nabla h \qquad (4b)$$

However, Eq. 4a is a phemenological one and may reflect the possibility of material loss from the system. It is also noteworthy that the existing nonlinear erosion laws are not limited to Eq. 4a (e.g., Newman, 1983; Newman et al., 1990), which only presents the simplest way to account for dependence of erodibility on the morphology.

Long-range surface processes. The long-range surface processes are associated with fluvial transport, i.e., with river incision, slope geometry, character of sediment matter, and conditions for deposition (Flint, 1973; 1974; Sheperd and Schumm, 1974; Hirano, 1975; Schumm et al., 1987; Seidl and Dietrich, 1992; Govers 1992a,b; Hairsine and Rose, 1992; Sklar and Dietrich, 1998;2001; Howard et al., 1994; Howard, 1998; Smith, 1998; Davy and Crave, 2000; Snyder et al., 2000; Snyder, 2001; Hancock and Willgoose, 2001; Simpson, 2004). The characteristic laws for this range are different as these mechanisms are dependent on the incision and transport capacity of the fluvial network, local slope, and type of sediment. Deep steep rivers can carry sediment longer distances as it can be caught in turbulent flow layer. Shallow rivers would deposit sediment rapidly resulting in rapid river blockage and frequent change of the direction of the fluvial network. There is also a strong dependence of transport capaci-

ty on the grain size and climate episodicity (e.g., Davy and Crave, 2000). The long-range fluvial models were used with success by Kooi and Beamount (1994; 1996), Garcia-Castellanos (2002), Garcia-Castellanos et al. (2002; 2003), Persson et al. (2004). The cumulative material flow, q_{fe}, due to the fluvial transport can be presented, in most simple form, as:

$$q_{\text{fe}} = -K_r\, q_r\, dh/dl \tag{4c}$$

where q_r is the river discharge, K_r is nondimensional transport coefficient and dh/dl is the slope in the direction of the river drainage with l being the distance along the transporting channel. The diffusion equation (4a), except if it is not strongly nonlinear, provides symmetrical, basically over-smoothed shapes whereas the fluvial transport equation (4c) may result in realistic asymmetric behaviors, because, locally, the direction of each bifurcation of the fluvial network is affected by negligibly small factors, even though the overall direction of the flow is controlled by the regional slope of topography (Fig. 3). Any important change in the regional slope of topography, such as at the transition from tectonically built steep highlands to flat sedimentary built forelands, may result, at some moment, in a drastic change of the direction of the fluvial network, which may choose a principally new stream direction orthogonal to the highland network (as it is the case for the Ganges river, for example). This happens when the sedimentary basin is filled to a point that the inclination of its surface in the direction of tectonic conver-

gence becomes less important than that in some other direction (basically in the direction of the boundary between the steep highlands and flat lowlands).

Although river networks in mountain ranges owe their existence to the competing effects of tectonic uplift and climate-controlled erosion, it was also argued that some universal geometric properties of river networks may be relatively independent of both tectonics and climate (Casteltort and Simpson, 2006). These authors have proposed that the geometry of river networks is established on the lowland margins of incipient uplifts, and is quenched into the erosion zone as the mountain belts widen with time. In that model, the geometry of river networks simply reflects the downward coalescence of alluvial rivers on undissected surfaces outside of mountain belts, and is therefore independent of erosion processes. Yet, the amount of the transported matter, incision rates, and other major dynamic parameters of the network are definitely tectonic-and-climate dependent.

3.2 Alternative Models of Surface Processes

The diffusion equation reflects an integrated effect of various processes acting at micro-and macroscale: chemical and physical erosion and weathering, gravity hillslope sliding etc. Some of these processes, for example, chemical erosion, are well described by the diffusion equation, since it reflects the physics of propagation of chemical interactions. On the other hand, gravity-driven processes are not diffusive. These processes are primarily slope dependent and thus do not fit well within the linear diffusion model (Densmore et al.,1997; 1998; Hasbargen and Paola, 2000; Roering et al., 2001; Schorghofer and Rothman, 2002; Pelletier, 2004). Indeed, it has been noted that the diffusion equation tends to over-smooth the predicted topography and fails to reproduce the usually sharp transitions from tectonically modified uplifted landscape to typically flat deposition surfaces in the foreland basins. To remedy this problem, either enhanced split (bi-mode) erosion models that discriminate between diffusion and gravity driven processes (e.g., Simpson and Schlunegger, 2003) or alternative stochastic (based on methods of artificial intellect such as cellular automates) and analogue models were proposed (Crave et al., 2000; Davy and Crave, 2000; Crave and Davy, 2001; Bonnet and Crave, 2003). Crave et al. (2001) or Tucker and Bras (1998; 2000), for example, used stochastic methods based on cellular automats that "learn" how to reproduce erosion/sedimentation from pre-imposed logical rules that establish relations between a given grid cell and its neighbors, as a function of the local slope, height, precipitation, regolith type and other conditions. If the rules and their rela-
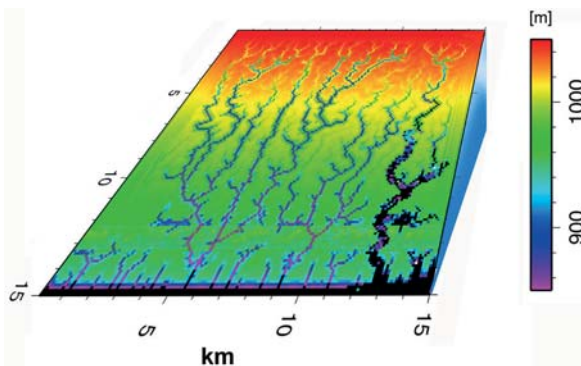
Fig. 3. Example of a typical numerical morphology model with surface erosion and sedimentation based on linear diffusion erosion equation and fluvial transport equation (Poisson, et al., 1996). Diffusion equation, except if it is not strongly non-linear, provides symmetrical shapes whereas fluvial transport equation may result in asymmetric behaviour because, locally, the direction of each bi-furcation of the fluvial network may be affected by negligibly small factors, even though the overall direction of the flow is controlled by the regional slope of topography

tions are well established, they may form the "vocabulary" and "grammar" (= "language") for description of topography evolution. This approach may eventually produce more realistic landscapes than the common diffusion-fluvial transport models. However, for each new application, it requires one to justify the local applicability of the previously established rules. Analogue (physical) erosion models were used to study erosional response to tectonic forcing (e.g., Lague et al., 2003). These models may produce naturally looking landscapes, yet their applicability is rather limited since it is highly difficult to control, scale and interpret their parameters.

Linear and nonlinear diffusion short-range models combined with fluvial transport long-range models (Fig. 3) remain to be most widely used for tectonic-scale modelling. In particular, diffusion and fluvial transport equations can be generalized (Simpson and Schlunegger, 2003) as following:

$$
\begin{cases}
\dfrac{dh}{dt} = \nabla \cdot \left((k + cq^{\mathrm{n}}) \nabla h \right) \\[2mm]
\nabla \cdot \left(\dfrac{\nabla h}{|\nabla h|} q \right) = -\alpha \\[2mm]
De = \dfrac{c\alpha^{n}L^{n}}{k}
\end{cases}
\tag{5}
$$

where c is sediment discharge, α is effective rainfall, q is surface fluid discharge, and $k + cq^{n}$ has a sense of a variable nonlinear diffusion coefficient that incorporates both the effects of diffusion-driven (k-term: chemical and physical erosion, weathering) processes and gravity-driven, i.e. fluvial, processes (cq^{n} term: slope-dependent flow, sliding, creep etc). The respective role of dispersive processes and hillslope creep processes is characterized by dimensionless De number (L is characteristic length scale).

4 Structure and Rheology of the Lithosphere

4.1 Rheology

Many studies of the interplay between erosion and tectonics have been conducted assuming either local isostasy (Ahnert, 1970; Leeder, 1991) or thin plate flexural behavior of the lithosphere (Beaumont, 1981; Flemings and Jordan, 1989;1990; Beaumont et al., 1992; Masek et al., 1994a,b; Garcia-Castellanos, 2002; Garcia-Castellanos et al., 2002; Garcia-Castellanos et al., 2003). Some authors have considered the possibility for ductile flow in the lower crust and treated the lower crust as an inviscid fluid overlaid by a thin elastic plate (King et al., 1988; King and Ellis, 1990; Avouac and

Burov, 1996; Burov and Cloetingh, 1997; Burov et al., 2001). The effect of variations in the surface loading and in the crustal thickness on the mechanical behavior of the lithosphere have been often neglected, except several studies (e.g., Beaumont et al., 1992, 2000; Avouac and Burov, 1996; Burov and Cloetingh, 1997; Burov et al., 2001; Toussaint et al., 2004a,b). The coupled erosion-tectonics regime described in the previous sections assumes that strain localization below a tectonic load, range or basin, results from weakening of the lithosphere due to crustal thickening and bending stresses. In order to account for this process one can treat the lithosphere neither as a one-layer elastic or visco-elastic plate with vertically integrated properties overlying an inviscid asthenosphere, or as a thin viscous sheet (e.g., England and McKenzie, 1983; Vilotte et al., 1982). We thus have to consider the lithological and mechanical rheological layering of the lithosphere. For the model demonstrated here, three lithological layers were defined: the upper crust, the lower crust, and the mantle (Fig. 2a). Each layer has specific properties (density, mechanical, and thermal constants) that are given in Table 1. We assume no compositional changes due to deformation or cooling. The lithological boundary between the upper and lower crust lies at a fixed depth of 20 km. The bottom of the mantle lithosphere is limited by the 1330°C isotherm at a depth of about 250 km. At small differential stresses the rocks behave elastically. In terms of principal components, the relationship between the stress tensor, σ, and the strain tensor, ε, can be written:

$$
\sigma_{j} = 2\mu_{e}\varepsilon_{j} + \lambda(\varepsilon_{1} + \varepsilon_{2} + \varepsilon_{3})
\tag{6}
$$

where j =1, 2, 3. λ and μ_{e} are Lamé's constants related to Young's modulus (E) and Poissons's ratio v as $\lambda = E\,v((1 + v)(1 - 2v))^{-1}$; $\mu_{e} = E/2(1 + v)$. Typical values for E and v are 6.5–8×10^{10} N/m^2 and 0.25, respectively (e.g., Turcotte and Schubert, 1982).

Weakening by brittle failure or ductile flow occurs when elastic stresses reach some threshold value that determines the condition for failure or significant ductile deformation. Above this threshold rocks no longer behave elastically, and unrecoverable strain may grow without increase of stress. The conditions of brittle failure are independent of rock type and temperature, but strongly controlled by pressure (Byerlee, 1978):

$$
\begin{aligned}
\sigma_{3} &= (\sigma_{1} - \sigma_{3})/3.9 \text{ at } \sigma_{3} < 120 \text{ MPa}; \\
\sigma_{3} &= (\sigma_{1} - \sigma_{3})/2.1 - 100 \text{ MPa at } \sigma_{3} \geq 120 \text{ MPa}
\end{aligned}
\tag{7}
$$

where σ_{1}, σ_{2}, σ_{3} are principal stresses [MPa]. This law corresponds to Mohr-Coulomb plastic behavior.

Ductile flow in the lithosphere essentially results from dislocation creep (e.g., Kusznir, 1991). This

Table 1a. Definition of variables

Variable	Values and units	Definition	Comments
$\tau_{xx}, \tau_{xy}, \tau_{yy},$	Pa, MPa	shear stress components	
$\sigma_{xx}, \sigma_{xy}, \sigma_{yy}$	Pa, MPa	full stress components	$\boldsymbol{\sigma} = \tau - P\mathbf{I}, \sigma_{xy} = \tau_{xy}$ etc.
P	Pa, MPa	pressure	
$\mathbf{v}$	m/s, mm/y	total velocity vector	
u	m/s, mm/y	horizontal velocity	x component of v
v	m/s, mm/y	vertical velocity	y component of v
μ	Pa s	effective viscosity	10^{19} to 10^{25} Pa s
k	m^2/y	coefficient of erosion	~ mass diffusivity
dh	m, km	topographic uplift	or subsidence
du	m, km	tectonic uplift	do not mix with u
de	m, km	erosion	or sedimentation
ψ	m^2/s	stream function	$u = \partial\psi/\partial y, v = \partial\psi/\partial y$
ξ	s^{-1}	vorticity function	$\partial u/\delta y - \partial v/\partial x = \Delta\psi$
ε		strain	
$\dot{\varepsilon}$	s^{-1}	average strain rate	$\dot{\varepsilon} = (\tfrac{1}{2}\dot{\varepsilon}_{ij}\dot{\varepsilon}_{ij})^{\tfrac{1}{2}}$
q	m^2/s	integrated flux	ductile crust
q_e	$(m^2$/s$)$ / m	erosional flux	per unit length
E	8×10^{10} N/m^2	Young's modulus	in the semi-analytical model
v	0.25	Poisson's ratio	in the semi-analytical model
λ, μ_e	N/m^2	Lamé's constants	
A^*	$Pa^{-n}\,s^{-1}$	material constant	power law
n	3 to 5	stress exponent	power law
H^*	kJ mol^{-1}	activation enthalpy	power law
R	8.314 J/mol K	gas constant	power law
T	C°, K	temperature	
$\gamma(y)$	Pa/m, MPa/km	depth gradient of yield stress	$\gamma(y) \propto d\sigma(\varepsilon)/dy,$
w	m, km	plate deflection	~ deflection of mantle lithosphere
$T_e, \tilde{T}_e (x, w, w', w'', t)$	m, km	effective elastic thickness	~ instant integrated strength
T_{ec}	m, km	effective elastic thickness of the crust	$T_e \approx (T_{ec}^3 + T_{em}^3)^{1/3}$ $T_{ec} \le h_{c_1}$
T_{em}	m, km	effective elastic thickness of mantle lithosphere	$T_e \approx (T_{ec}^3 + T_{em}^3)^{1/3}$ $T_{em} \le h_{c_2} - T_c$
$\tilde{M}_x$	N m / m	flexural moment	per unit length
$\tilde{T}_x$	N	longitudinal force	
$\tilde{Q}_x$	N / m	shearing force	per unit length
p^+	Pa, N/m^2	surface load	
p^-	Pa / m	restoring stress	per unit length
$h(x, t)$	m, km	surface topography	
$\tilde{h}(x, t)$	m, km	upper boundary of ductile channel	
h_c, T_c	m, km	Moho depth	Moho boundary
h_{c_2}	m, km	lower boundary of ductile crustal cannel	$h_{c_2} \le T_c$

Table 1a. *Continued*

Variable	Values and units	Definition	Comments
$h_{c_1}(x, t, w)$	m, km	maximal mechanical thickness of the upper crust	here, 10–20 km depending on stress
$\Delta h_{c_2}(x, t, w, u, v)$	m, km	thickness of crustal channel	
y_{ij}	m, km	depths to lithological and mechanical interfaces	i is number of a detached layer j is number of the mechanical sub-layer
ρ_{c_1}	2650 kg/m³	density	of upper crust
ρ_{c_2}	2900 kg/m³	density	of lower crust
ρ_m	3330 kg/m³	density	of mantle
a	degrees	inclination of upper boundary of channel	$a \sim \partial \tilde{h} / \partial x$
β	degrees	inclination of lower boundary of channel	$\beta \sim \partial w / \partial x$
g	9.8 m/s²	acceleration due to gravity	
T	°C	temperature	
t_a	m.y.	thermal age	$\leq$ geological age
a	250 km	thermal thickness of the lithosphere	
T_m	1330 °C	T at depth a	
χ	m²s⁻¹	thermal diffusivity	$\chi = k/\rho C_p$
χ_{c_1}	8.3×10⁻⁷ m²s⁻¹	thermal diffusivity	upper crust
χ_{c_2}	6.7×10⁻⁷ m²s⁻¹	thermal diffusivity	lower crust
χ_m	8.75×10⁻⁷ m²s⁻¹	thermal diffusivity	mantle
k_{c_1}	2.5 Wm⁻¹°K⁻¹	thermal conductivity	upper crust
k_{c_2}	2 Wm⁻¹°K⁻11	thermal conductivity	lower crust
k_m	3.5 Wm⁻¹°K⁻¹	thermal conductivity	mantle
h_r	10 km	decay scale of radiogenic heat production	upper crust
H_s	9.5×10⁻¹⁰ W kg⁻¹	surface radiogenic heat production rate per unit mass	upper crust
$H_{c_2} C_{c_2}^{-1}$	1.7×10⁻¹³°K s⁻¹	radiogenic heat	lower crust
ρC_p	J (m³K)⁻¹	density × specific heat	

mechanism is thermally activated and results in relationship between strain rate and stress which can be written:

$$\dot{\varepsilon} = A^* \exp(-H^*/RT)\,(\sigma_1 - \sigma_3)^n \qquad (8)$$

The material constants adopted for the creep law of lithospheric minerals are given in 1b. The ratio of the stress to strain rate defines an effective non-Newtonian viscosity:

$$\mu_{\text{eff}} = \left(\frac{\partial \varepsilon}{\partial t}\right)_{\text{II}}^{d\,(1-n)/n} (A^*)^{-1/n} \exp(H/nRT) \qquad (9)$$

where $\left(\dfrac{\partial \varepsilon}{\partial t}\right)_{\text{II}}^{d} = \left(Inv_{\text{II}}\left(\dfrac{\partial \varepsilon_{ij}}{\partial t}\right)\right)^{1/2}$

is the effective strain rate and $A^* = \frac{1}{2}A \cdot 3^{(n+1)/2}$ is the material constant, H is the activation enthalpy, R is the gas constant, n is the power law exponent. Although

Table 1b. Summary of rheology parameters used in model calculations

Parameter	Value
Lamé elastic constants $\lambda = G$	30 GPa (in numerical models)
Friction angle (Mohr-Coulomb criterion)	30°
Cohesion (Mohr-Coulomb criterion)	20 Mpa
Specific upper and weak lower-crust properties	
ρ (upper crust)	2800 kg m^{-3}
ρ (lower crust)	2900 kg m^{-3}
n	2.4
A	6.7×10^{-6} MPa$-$n$\cdot$s^{-1}
Q	1.56×10^5 kJ$\cdot$mol^{-1}
Specific strong lower-crust properties	
ρ	2980 kg m^{-3}
n	3.4
A	2×10^{-4} MPa$^{-n}\cdot$s^{-1}
Q	2.6×10^5 kJ$\cdot$mol^{-1}
Specific mantle properties	
ρ (lithosphere)	3330 kg m^{-3}
ρ (oceanic slab)	3350 kg m^{-3}
ρ (asthenosphere)	3310 kg m^{-3}
n	3
A	1×10^4 MPa$^{-n}\cdot$s^{-1}
Q	5.2×10^5 kJ$\cdot$mol^{-1}

Note: Compilation by Burov et al. [2001]. Q, n, A are parameters of the ductile flow law (activation energy, material constant, and power exponent, respectively). See also [Brace and Kohlstedt, 1980; Kirby, 1983; Kirby and Kronenberg, 1987; Kohlsted et al., 1995; Byerlee, 1978; Carter and Tsenn, 1987; Tsenn and Carter, 1987]

ductile deformation occurs even under low differential stresses, a ductile yield strength can be defined. If boundary conditions are given in terms of rate of displacement, a "basic" strain rate can be derived and represents the average strain rate in the medium (10^{-15} s^{-1} – 5×10^{-15} s^{-1}). This "basic" strain rate corresponds to a stress threshold defined from Eq. (8). Owing to the nonlinearity of rheology described by Eq. (8) the ductile deformation will process very slowly so that most of the imposed deformation will be absorbed elastically if the stress is slightly less than the yield level. For example, for olivine, strain rate decreases by a factor of 1000 if the stress lies 10–15% below the "threshold" level. This behavior differs from that of a Newtonian fluid where decrease in stress would lead to a directly proportional decrease of the strain rate. On the opposite, the stress level cannot exceed significantly this threshold since it would require a strain rate much higher that the one that is imposed from bound-

ary conditions. This threshold thus defines a ductile yield strength. A temperature of about 250–300°C must be exceeded for ductile deformation of quartz, whereas for olivine it should be 600–700°C (e.g., Brace and Kohlstedt, 1980; Carter and Tsenn, 1987; Kohlsted et al., 1995). It results in the yield stress envelope (YSE) being controlled by the conditions for brittle failure in the shallow crust and upper mantle, and by the condition for ductile failure in the deep crust and deep upper mantle. Combining rheological laws, Eqs. (6) to (9), form a piece-wise continuous yield-stress envelope (YSE) in $\Delta\sigma$-y space (Figure 2a, defined as a contour $\sigma^f = \sigma^f(x, y, t, \dot{\varepsilon})$ such that:

$$\sigma^f = sign(\varepsilon) \, \mathbf{min}(|\sigma^b(x, y, t, \dot{\varepsilon}, sign(\varepsilon))|, |\sigma^d(x, y, t, \dot{\varepsilon})|) \tag{10}$$

where $\sigma^b(x, y, t, \dot{\varepsilon}, sign(\varepsilon))$, $\sigma^d(x, y, t, \dot{\varepsilon})$ are the "brittle" and "ductile" yield stresses from Eqs. (6) and (7). sign(ε)=1 if $\varepsilon \geq 0$ and -1 if $\varepsilon < 0$. The differential stress $\sigma(x,y)$ at a point is taken to be equal to the minimum of σ^e and σ^f, computed as a function of the local strain $\varepsilon = \varepsilon(x, y, t, \dot{\varepsilon})$:

$$\sigma(\varepsilon) = sign(\varepsilon) \, \mathbf{min}(|\sigma^f|, |\sigma^e(\varepsilon)|) \tag{11}$$

where $\sigma^e(\varepsilon)$ is the elastic differential stress according to Eq. (5). If σ^e exceeds σ^f, the material is considered as ductile or brittle, depending on which rheology limits the yield strength. Due to asymmetry of the Byerlee's law (7), the yield stress depends on the mode of deformation, sign(ε) (for extension sign(ε)=1; for compression sign(ε)=−1). Equation (11) implies that the lithosphere remains elastic if imposed stress does not exceed the yield stress. Most of the upper crust remains elastic or brittle-elastic (depth interval between approx. 5 and 15–20 km). The crust is mostly ductile below 15–20 km. Depending on the geotherm and strain rates, first 30 to 70 km of the mantle lithosphere remains elastic. This formulation reflects the fact that the lithosphere gets weaker when submitted to increasing horizontal forces or flexural stresses and when the crust gets thicker.

4.2 Thermal Model

A thermal model is required to define the rheological profile of the lithosphere and to fully account for the effect of crustal thickening on the rheology of the lithosphere. In this paper, the initial geotherm is computed according to a half-space heat transfer model (for details see Burov et al., 1993 and Burov and Diament, 1995). For the following evolution, heat transfer equations are solved separately for the upper crust, lower

crust, and mantle with conditions of temperature and heat flux continuity across the interfaces. These equations have the form:

$$\dot{T} + uT_x' + vT_y' - \chi_f\Delta T = H_d + H_r + v\Omega \qquad (12)$$

where primes mean spatial differentiation by respective coordinate. The thermal diffusivity parameter χ_f equals to χ_{c1}, χ_{c2}, χ_m depending on the lithological layer (see Table 1). $H_r = \chi_{c1}k_{c1}^{-1}\rho_c H_s\exp(-yh_r^{-1})$ is the radiogenic heat. H_r equals to constant heat generation $H_{c2}C_{c2}^{-1}$ in the lower crust and to zero in the mantle. H_d refers to heat generation due to mechanical dissipation (e.g., frictional heating). The adiabatic temperature gradient in the asthenosphere, Ω, is 0.3°C/km (Turcotte and Schubert, 1982).

The boundary and initial conditions are: $T(x,0,t_a) = 0°C$ (temperature at the upper surface = const at time t_a, where t_a is the thermal age); $T(x,a,t) = T_m = 1350°C$ ($a \approx 250$ km is the depth to the thermal bottom, or thermal thickness of the lithosphere); $T(x,y,0) = T_m$ (homogeneous temperature distribution at the beginning). t_a is defined as the age of the last large-scale thermal event determined from geological data.

5 Implementation of Coupled Models

5.1 Semi-Analytical Model

In this section we describe the numerical procedure used in the semi-analytical model by Avouac and Burov (1996) and Burov and Cloetingh (1997).

In this model, we distinguish between competent and weak layers (Fig. 4, top). The competent layers are those which contribute significantly to the flexural strength of the lithosphere. This encompasses not only the elastic domains but also high stress (>5% of the lithostatic pressure) brittle and ductile domains (e.g., Burov and Diament, 1992; 1995). Only the competent

Fig. 4. Model Setups. Top: Setup of a simplified semi-nalytical collision model with erosion-tectonic coupling (Avouac and Burov, 1996). In-eastic flexural model is used to for competent parts of crust and mantle, channel flow model is used for ductile domains. Both models are coupled via boundary conditions. The boundaries between competent and ductile domains are not predefined but are computed as function of bending stress that conrols brittle-ductile yielding in the lithosphere. Diffusion erosion and flat deposition are imposed at surface. In these experiments, initial topography and isostatic crustal root geometry correspond to that of a 3 km high and 200 km wide Gaussian mount. Bottom. Setup of fully coupled thermo-mechanical collision-subduction model (Burov et al., 2001; Toussaint et al., 2004b). In this model, topography is not predefined and deformation is solved from full set of equilibrium equations. The assumed rheology is brittle-elastic-ductile, with quartz-rich crust and olivine-rich mantle (Table 1)
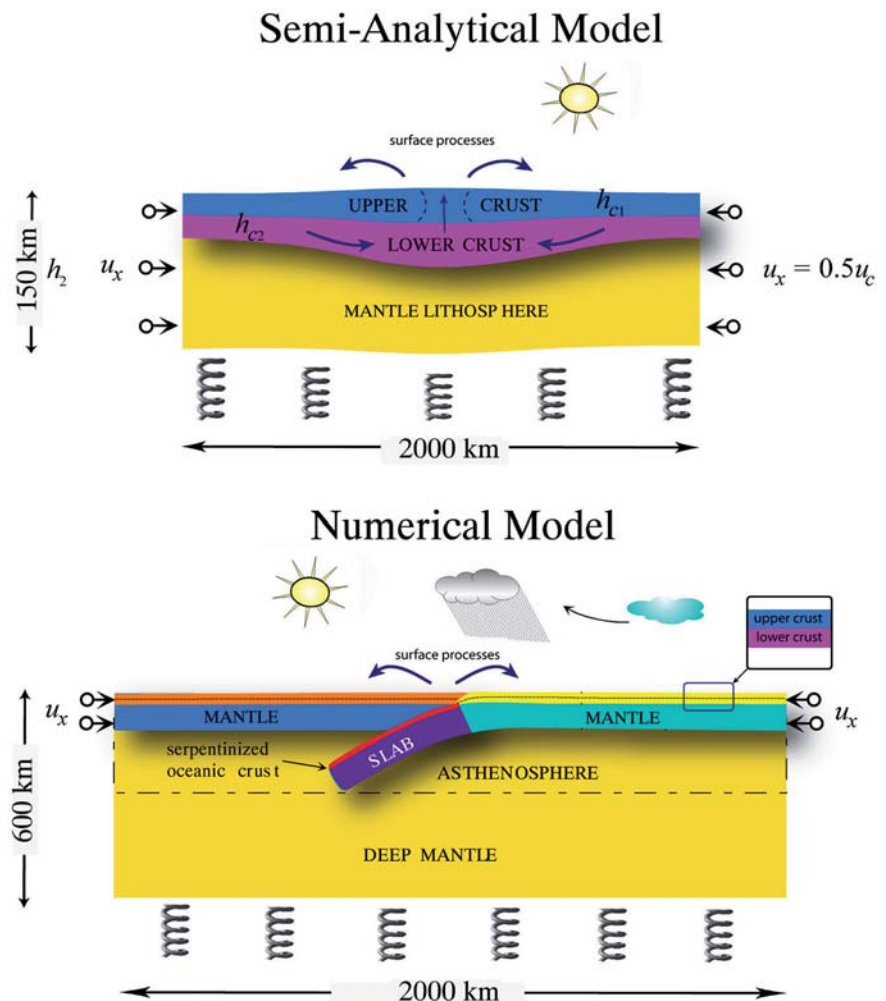
layers are considered in the computation of the flexural response of the lithosphere. The geometry and thickness of the mechanical layers depend on the lithological layering and on the stress field. Since both evolve during the numerical experiment, the mechanical structure is re-computed at each numerical step. Vertical deflections (*w*) of the competent portions of the crust and mantle lithosphere due to change in the stress applied at their boundaries are treated as instantaneous deflections of flexible layers [Appendix A]. Deformation of the ductile crust, driven by the deflection of the competent layers that bound the low viscosity lower crustal channel, is modelled as a flow of a non-Newtonian fluid in a channel of variable thickness. No horizontal flow at the axis of symmetry of the range (*x* = 0) is allowed. Away from the mountain range, where the channel has a nearly constant thickness, the flow is computed according to the thin channel approximation [Appendix B]. Since the conditions for this approximation are not satisfied in the thickened region, we use a semi-analytical solution for the ascending flow fed by remote channel source [Appendix C]. The distance al at which the channel flow approximation is replaced by a formulation for the ascending flow, equals to 1 to 2 thicknesses of the channel, depending on the integrated strength of the upper crust [Appendixes B and C]. Since the common brittle-elastic-dutile rheology profiles imply decoupling between the mantle and crust [Fig. 2a], in

particular where the crust is thick, deformation of the crust is expected to be relatively insensitive to what happens in the mantle. Shortening of the mantle lithosphere is therefore neglected. Naturally, this assumption will not directly apply if partial coupling of mantle and crustal lithosphere occurs (e.g., Ter Voorde et al., 1998; Gaspar-Escribano et al., 2003). For this reason, in the next sections, we present a less constrained fully numerical model, in which the conditions on the crust-mantle interface are not pre-described.

The various equations define the mechanical structure of the lithosphere, flexure of the competent layers, ductile flow in the ductile crust, erosion and sedimentation at the surface are solved at each numerical iteration as depicted in the following flow-chart:

see Box 1, Eq. 13

B.C. and I.C. refer to boundary and initial conditions, respectively. Notation (*k*) implies that related value is used on k-th numerical step. Notation (*k*–1) implies that the value is taken as a predictor from the previous time step, etc. All variables are defined in Table 1. The following continuity conditions are satisfied at the interfaces between the competent layers and the ductile crustal channel:

see Box 1, Eq. 14

Box 1.
Eq. 13 + 14

Input			Output	

$$
\begin{cases}
\text{I. } u_{k-1}, v_{k-1}, T_{c\,(k-1)}, w_{k-1}, h_{k-1} \\
\qquad + B.C.\&I.C._k \qquad \rightarrow \quad (A1, 12, 14) \quad \rightarrow \quad T \\[4pt]
\text{II. } T, \dot{\varepsilon}, A, H^*, n, T_{c(k-1)} \quad \rightarrow \qquad (6\text{–}11) \qquad\qquad \sigma^f, h_{c1}, h_{c2}, h_m \\[4pt]
\text{III. } \sigma^f, h_{c1}, h_{c2}, h_m, h_{k-1}, \\
\qquad p_{k-1}^-, p_{k-1}^+ + B.C._k \quad \rightarrow \qquad (A1) \qquad \rightarrow \quad w_k, T_{c(k)}, \sigma(\varepsilon), y_{ij(k)} \\[4pt]
\text{IV. } w_k, \sigma(\varepsilon), y_{ij(k)}, \tilde{h}_{k-1}, \sigma^f, \\
\qquad \dot{\varepsilon}, h_{k-1}, T_{ck} + B.C._k \quad \rightarrow \quad (B5, B6, C3) \;\rightarrow\; u_k, v_k, \tilde{h}_k, h_k, T_{ck+1}, \tau_{xy}, \delta T_1 \\[4pt]
\text{V. } h_k, (\text{i.e., } I.C._k) \qquad\qquad \rightarrow \qquad (3\text{–}4) \qquad \rightarrow \quad h_{k+1}, \delta T_2
\end{cases}
\qquad (13)
$$

continuity of vertical velocity	$v_{c1}^- = v_{c2}^+;\; v_{c2}^- = v_m^+$	
continuity of normal stress	$\sigma_{yy_{c1}}^- = \sigma_{yy_{c2}}^+;\; \sigma_{yy_{c2}}^- = \sigma_{yy_m}^+$	
continuity of horizontal velocity	$u_{c1}^- = u_{c2}^+;\; u_{c2}^- = u_m^+$	(14)
continuity of the tangential stress	$\sigma_{xy_{c1}}^- = \sigma_{xy_{c2}}^+;\; \sigma_{xy_{c2}}^- = \sigma_{xy_m}^+$	
kinematic condition	$\dfrac{\partial \tilde{h}}{\partial t} = v_{c2}^+;\; \dfrac{\partial w}{\partial t} = v_{c2}^-$	

Superscripts "+" and "−" refer to the values on the upper and lower interfaces of the corresponding layers, respectively. The subscripts c_1, c_2, and m refer to the strong crust ("upper"), ductile crust ("lower") and mantle lithosphere, respectively. Power-law rheology results in self-lubrication and concentration of the flow in the narrow zones of highest temperature, that is near the Moho. For this reason, there is little difference between the assumption of no-slip and free slip boundary for the bottom of the ductile crust.

The spatial resolution used for calculations is $dx = 2$ km, $dy = 0.5$ km. The requirement of stability of integration of the diffusion equations (3), (4) ($dt < 0.5dx^2/k$) implies a maximum time step of < 2000 years for $k = 10^3$ m²/y and of 20 years for $k = 10^5$ m²/y. It is less than the relaxation time for the lowest viscosity value (~ 50 years for $= 10^{19}$ Pa s). We thus chose a time step of 20 years in all semi-analytical computations.

5.2 Unconstrained Fully Coupled Numerical Model

To fully demonstrate the importance of interactions between the surface processes, ductile crustal flow and major thrust faults, and also to verify earlier ideas on evolution of collision belts, we used fully coupled (mechanical behavior - surface processes - heat transport) numerical models, which combine brittle-elastic-ductile rheology and account for large strains, fault localization, and erosion/sedimentation mechanisms (Fig. 4, bottom).

We have extended the Paro(a)voz code (Polyakov et al., 1993, Appendix D) based on the FLAC (Fast Langrangian Analysis of Continua) algorithm (Cundall, 1989). This "2.5 D" explicit time-marching, large-strain Lagrangian algorithm locally solves Newtonian equations of motion in continuum mechanics approximation and updates them in large-strain mode. The particular advantage of this code refers to the fact that it operates with full stress approximation which allows for simple and accurate computation of total pressure, P, as a trace of the full stress tensor. The solution of these equations is coupled with those of constitutive and heat-transfer equations. Parovoz v9 is thus a fully thermally coupled code that also handles explicit elastic-ductile-plastic rheologies, free-surface boundary conditions, full metamorphic changes, and surface processes (erosion and sedimentation). The Lagrangian numerical mesh, which periodically becomes distorted and thus needs remeshing, is doubled by a denser passive marker grid allowing to interpolate grid

values, specifically stresses, with minimal losses during remeshing.

We test continental collision assuming accommonly referred initial scenario (Fig. 4, bottom), in which (1) the rapidly subducting oceanic slab first entrains a very small part of a cold continental "slab" (there is no continental subduction at the beginning), and (2) the initial convergence rate equals to or is smaller than the rate of the preceding oceanic subduction (two-sided initial closing rate of 2×6 mm/y during 50 My for Alpine collision test (Burov et al., 2001) or 2×3 cm/y during the first 5–10 My for the India-Asia collision test (Toussaint et al., 2004b). The rate chosen for the India-Asia collision test is smaller than the average historical convergence rate between India and Asia (2×4 to 2×5 cm/y during the first 10 My. (Patriat and Achache, 1984).

For continental collision models, we use commonly inferred crustal structure and rheology parameters derived from rock mechanics (Table 1; Burov et al., 2001). The thermo-mechanical part of the model that computes, among other parameters, the upper free surface, is coupled with the surface process model based on the diffusion equation (4a). On each type step the geometry of the free surface is updated with account for erosion and deposition. The surface areas affected by sediment deposition change their material properties according to those prescribed for sedimentary matter (Table 1). In the experiments shown below, we used linear diffusion with a diffusion coefficient that has been varied from 0 to 2000 m²/y (Burov et al., 2001). The initial geotherm was derived from the common half-space model (e.g., Parsons and Sclater, 1977) as discussed in the section "Thermal mode" and Appendix D.

The universal controlling variable parameter of all continental experiments is the initial geotherm (Fig. 2a), or thermotectonic age (Turcotte and Schubert, 1982), identified with the Moho temperature Tm. The geotherm or age defines major mechanical properties of the system, e.g., the rheological strength profile (Fig. 2a). By varying the geotherm, we can account for the whole possible range of lithospheres, from very old, cold, and strong plates to very young, hot, and weak ones. The second major variable parameter is the composition of the lower crust, which, together with the geotherm, controls the degree of crust-mantle coupling. We considered both weak (quartz dominated) and strong (diabase) lower-crustal rheology and also weak (wet olivine) mantle rheology (Table 1). Although we mainly applied a convergence rate of 2 × 3 cm/y, we also tested smaller convergence rates (two times smaller, four times smaller, etc.).

6   Experiments

6.1 Semi-Analytical Model

Avouac and Burov (1996) have conducted series of experiments, in which a 2-D section of a continental lithosphere, loaded with some initial range (resembling an averaged cross-section of Tien Shan), is submitted to horizontal shortening (Fig. 4, top) in pure shear mode. Our goal was to validate the idea of the coupled (erosion-tectonics) regime and to check whether it can allow for stable localized mountain growth. Here we were only addressing the problem of the growth and maintenance of a mountain range once it has reached some mature geometry.

We thus consider a 2000-km-long lithospheric plate initially loaded by a topographic irregularity. Here we do not pose the question how this topography was formed, but in later sections we show fully numerical experiments, in which the mountain range grows from initially flat surface. We chose a 300–400-km-wide "Gaussian" mountain (a Gaussian curve with variance 100 km, that is about 200 km wide). The model range has a maximum elevation of 3000 m and is initially regionally compensated. The thermal profile used to compute the rheological profile corresponds approximately to the age of 400 My. The initial geometry of the Moho was computed from the flexural re-

sponse of the competent cores of the crust and upper mantle and neglecting viscous flow in the lower crust (Burov et al., 1990). In this computation, the possibility of the internal deformation of the mountain range or of its crustal root was neglected. The model is then submitted to horizontal shortening at rates from about 1 mm/y to several cm/y. These rates largely span the range of most natural large-scale examples of active intracontinental mountain range. Each experiment modelled 15–20 My of evolution with time steps of 20 years. The geometries of the different interfaces (topography, upper-crust-lower crust, Moho, basement-sediment in the foreland) were computed for each time step. We also computed the rate of uplift of the topography, dh/dt, the rate of tectonic uplift or subsidence, du/dt, the rate of denudation or sedimentation, de/dt, (Fig. 5), stress, strain and velocity field. The relief of the range, Δh, was defined as the difference between the elevation at the crest $h(0)$ and in the lowlands at 500 km from the range axis, $h(500)$.

In the case where there are no initial topographic or rheological irregularities, the medium has homogeneous properties and therefore thickens homogeneously (Fig. 5b). There are no horizontal or vertical gradients of strain so that no mountain can form. If the medium is initially loaded with a mountain range, the flexural stresses (300–700 MPa; Fig. 5a) can be 3–7 times higher than the excess pressure associated with the weight of the range itself (~100 MPa). Horizontal
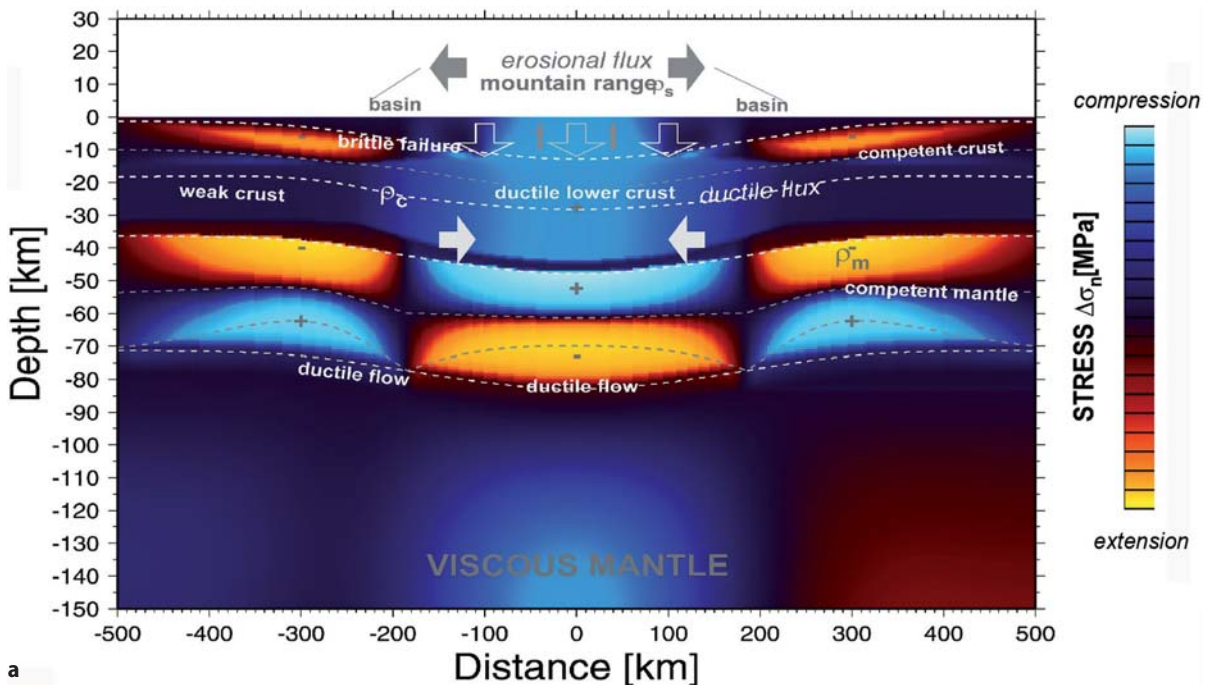
Fig. 5a. Example of normalized stress distribution in a semi-analytical experiment in which stable growth of the mountain belt was achieved (total shortening rate 44 mm/y; strain rate 0.7×10^{-15} sec^{-1} erosion coefficient 7500 m^2/y

shortening of the lithosphere tend therefore to be absorbed preferentially by strain localized in the weak zone beneath the range. In all experiments the system evolves very rapidly during the first 1–2 million years because the initial geometry is out of dynamic equilibrium. After the initial reorganization, some kind of dynamic equilibrium is reached, in which the viscous forces due to flow in the lower crust also participate in the support of the surface load.

6.1.1   Case 1: No Surface Processes: "Subsurface Collapse"

In the absence of surface processes the lower crust is extruded from under the high topography (Fig. 5b). The crustal root and the topography spread out laterally. Horizontal shortening leads to general thickening of the medium but the tectonic uplift below the range is smaller than below the lowlands so that the relief of the range, Δh, decays with time. The system thus evolves towards a regime of homogeneous deformation with a uniformly thick crust. In the particular case of a 400-km-wide and 3-km-high range it takes about 15 My for the topography to be reduced by a factor of 2. If the medium is submitted to horizontal shortening, the decay of the topography is even more rapid due to in-elastic yielding. These experiments actually show that assuming a common rheology of the crust without intrinsic strain softening and with no particular assumptions for mantle dynamics, a range should collapse in the long term, as a result of subsurface deformation, even the lithosphere undergoes intensive horizontal shortening. We dubbed "subsurface collapse" this regime in which the range decays by lateral extrusion of the lower crustal root.

6.1.2   Case 2: No Shortening: "Erosional Collapse"

If erosion is intense (with values of k of the order of 10^4 m^2/y) while shortening is slow, the topography of the range vanishes rapidly. In this case, isostatic readjustment compensates for only a fraction of denudation and the elevation in the lowland increases as a result of overall crustal thickening (Fig. 5b). Although the gravitational collapse of the crustal root also contributes to the decay of the range, we dubbed this regime "erosional", or "surface" collapse. The time constant associated with the decay of the relief in this regime depends on the mass diffusivity. For $k = 10^4$ m^2/y, denudation rates are of the order of 1 mm/y at the beginning of the experiment and the initial topography was halved in the first 5 My. For $k = 10^3$ m^2/y the range topography is halved after about 15 My. Once the crust and Moho topographies have been smoothed by surface processes and subsurface deformation, the system evolves towards the regime of homogeneous thickening.

6.1.3   Case 3: Dynamically Coupled Shortening and Erosion: "Mountain Growth"

In this set of experiments, we started from the conditions leading to the "subsurface collapse" (significant shortening rates), and then gradually increased the intensity of erosion. In the experiments where erosion was not sufficiently active, the range was unable to grow and decayed due to subsurface collapse. Yet, at some critical value of k, a regime of dynamical coupling was reached, in which the relief of the range was growing in a stable and localized manner (Fig. 5b, bottom). Similarly, in the other set of experiments, we started from the state of the "erosional collapse", kept the rate of erosion constant, and gradually increased the rate of shortening. At low shortening rates, erosion could still erase the topography faster then it was growing, but at some critical value of the shortening rate, a coupled regime was reached (Figs. 5a, 5b). In the coupled regime, the lower crust was flowing towards the crustal root (inward flow) and the resulting material in-flux exceeded the amount of material removed from the range by surface processes. Tectonic uplift below the range then could exceed denudation (Fig. 5) so that the elevation of the crest was increasing with time. We dubbed this regime "mountain growth". The distribution of deformation in this regime remains heterogeneous in the long term. High strains in the lower and upper crust are localized below the range allowing for crustal thickening (Fig. 5a). The crust in the lowland also thickens owing to sedimentation but at a smaller rate than beneath the range. Figure 5b shows that the rate of growth of the elevation at the crest, dh/dt ($x=0$), varies as a function of time allowing for mountain growth. It can be seen that "mountain growth" is not monotonous and seems to be very sensitive, in terms of surface denudation and uplift rate, to small changes in parameters. However, it was also found that the coupled regime can be self-maintaining in a quite broad parameter range, i.e., erosion automatically accelerates or decelerates to compensate eventual variations in the tectonic uplift rate (Fig. 5c). Figure 5c shows that the feedback between the surface and subsurface processes can maintain the mountain growth regime even for large deviations of k_s and $\partial \varepsilon_{xx}/\partial t$ from the equilibrium state. These deviations may cause temporary oscillations in the mountain growth rate (curves 2 and 3 in Figure 5c) that are progressively damped as the system finds a new stable regime. These experiments suggest that orogenic systems may be quite resistant to climatic changes or variations in tectonic rates, yet they may very rapidly

"subsurface" collapse (compression)
$u_x = 6.3$ mm/y ($\varepsilon_{xx} = 10^{-16}$ s^{-1}) + rapid erosion ($k_s = 10000$ m^2/y)

topography

crustal root

"erosional" collapse (no compression)
$u_x = 0.0063$ mm/y ($\varepsilon_{xx} = 10^{-19}$ s^{-1}) + rapid erosion ($k_s = 10000$ m^2/y)

topography

crustal root

localized stable growth (compression)
$u_x = 44$ mm/y ($\varepsilon_{xx} = 0.7 \times 10^{-15}$ s^{-1}) + erosion ($k_s = 7500$ m^2/y)

topography

crustal root

du = subsurface tectonic uplift rate

dh at 5 My
dh at 10 My

dh = surface uplift rate

de

dh

de

de = erosion rate

process rates: dh, de, du [mm/y]

distance x [km]

b

◀ **Fig. 5b.** Results of representative semi-analytical experiments: topography and crustal root evolution within first 10 My, shown with interval of 1 My. Top, right: Gravity, or subsurface, collapse of topography and crustal root (total shortening rate 2×6.3 mm/y; strain rate 10^{-16} s^{-1} erosion coefficient 10000 m^2/y). Top, left: erosional collapse (total shortening rate 2× 0.006.3 mm/y; strain rate 10^{-19} s^{-1} erosion coefficient 10000 m^2/y). Bottom, left: Stable localised growth of the topography in case of coupling between tectonic and surface processes observed for total shortening rate 44 mm/y; strain rate $0.7×10^{-15}$ s^{-1} erosion coefficient 7500 m^2/y. Bottom, right: distribution of residual surface uplift rate, dh, tectonic uplift rate, du, and erosion-deposition rate de for the case of localised growth shown at bottom, left. Note that topography growth in a localized manner for at least 10 My and the perfect anti-symmetry between the uplift and erosion rate that may yield very stable steady surface uplift rate

collapse if the limits of the stability range are exceeded (curves 3,4 in Fig. 5c). We did not further explore the dynamical behavior of the system in the coupled regime but we suspect a possibility of chaotic behaviors, hinted, for example, by complex oscillations in case 3 (Fig. 5c). Such chaotic behaviours are specific for feedback-controlled systems in case of delays or other changes in the feedback loop. This may refer, for example, to the delays in the reaction of the crustal flow

to the changes in the surface loads; to a partial loss of the sedimentary matter from the system (long-distance fluvial network or out of plain transport); to climatic changes etc.

Figure 6 shows the range of values for the mass diffusivity and for the shortening rate that can allow for the dynamical coupling and thus for mountain growth. As a convention, a given experiment is defined to be in the "mountain growth" regime if the relief of the range increases at 5 My, which means that elevation at the crest ($x = 0$) increases more rapidly than the elevation in the lowland ($x = 500$ km):

$$dh/dt\ (x=0\,\text{km}) > dh/dt\ (x=500\,\text{km})\ \text{at}\ t=5\,\text{My} \qquad (15)$$

As discussed above, higher strain rates lead to reduction of the effective viscosity (μ_{eff}) of the non-Newtonian lower crust so that a more rapid erosion is needed to allow the feedback effect due to surface processes. Indeed, μ_{eff} is proportional to $\dot{\varepsilon}^{1/(n-1)}$. Taking into account that n varies between 3 and 4, this provides a half-order decrease of the viscosity at one-order increase of the strain rate from 10^{-15} to 10^{-14} s^{-1}. Consequently, the erosion rate must be several times higher or slower to compensate 1 order increase or decrease in the tectonic strain rate.

Fig. 5c. Tests of stability of the coupled "mountain growth" regime. Shown are the topography uplift rate at the axis ($x = 0$) of the range, for various deviations of the coefficient of erosion, k, and of the horizontal tectonic strain rates, $\partial\varepsilon_{xx}/\partial t$, from the values of the most stable reference case "1", which corresponds to the mountain growth experiment from Fig. 5b (bottom). Feedback between the surface and subsurface processes maintains the mountain growth regime even for large deviations of ks and $\partial\varepsilon_{xx}/\partial t$ (curves 2,3) from the equilibrium state (1). Cases 4 and 5 refer to very strong misbalance between the denudation and tectonic uplift rates, for which the system starts to collapse. These experiments suggest that the orogenic systems may be quite resistant to climatic changes or variations in tectonic rates, yet they rapidly collapse if the limits of the stability are exceeded

Fig. 5d. Influence of erosion law on steady-state topography shapes: 0 **a**, 1 **b**, and 2nd **c** order diffusion applied for the settings of the "mountain growth" experiment of Fig. 5b (bottom). The asymmetry in **c** arrives from small white noise (1%) that was introduced in the initial topography to test the robustness of the final topographies. In case of highly non-linear erosion, the symmetry of the system is extremely sensitive even to small perturbations

6.1.4   Coupled Regime and Graded Geometries

In the coupled regime the topography of the range can be seen to develop into a nearly parabolic graded geometry (Fig. 5b). This graded form is attained after 2–3 My and reflects some dynamic equilibrium with the topographic rate of uplift being nearly constant over the range. Rates of denudation and of tectonic uplift can be seen to be also relatively constant over the range domain. Geometries for which the denudation rate is constant over the range are nearly parabolic since they are defined by

$$de/dt = k\, d^2h/dx^2 = \text{const.} \qquad (16)$$

Integration of this expression yields a parabolic expression for $h = x^2(de/dt)/2k + C_1x + C_0$, with C_1 and C_0 being constants to be defined from particular boundary conditions. The graded geometries obtained in the experiments slightly deviate from parabolic curves because they do not exactly correspond to uniform de-

nudation over the range (h is also function of du/dt, etc.). This simple consideration does however suggest that the overall shape of graded geometries is primarily controlled by the erosion law. We then made computations assuming nonlinear diffusion laws, in order to test whether the setting of the coupled regime might depend on the erosion law. We considered nonlinear erosion laws, in which the increase of transport capacity downslope is modelled by a 1st order or 2nd order nonlinear diffusion (Eq. 4). For a given shortening rate, experiments that yield similar erosion rates over the range lead to the same evolution ("erosional collapse", "subsurface collapse", or "mountain growth") whatever is the erosion law. It thus appears that the emergence of the coupled regime does not depend on a particular erosion law but rather on the intensity of erosion relative to the effective viscosity of the lower crust. By contrast, the graded geometries obtained in the mountain growth regime strongly depend on the erosion law (Fig. 5d). The first order diffusion law leads to more realistic, than parabolic, "triangular" ranges whereas the 2nd order diffusion leads to plateau-like
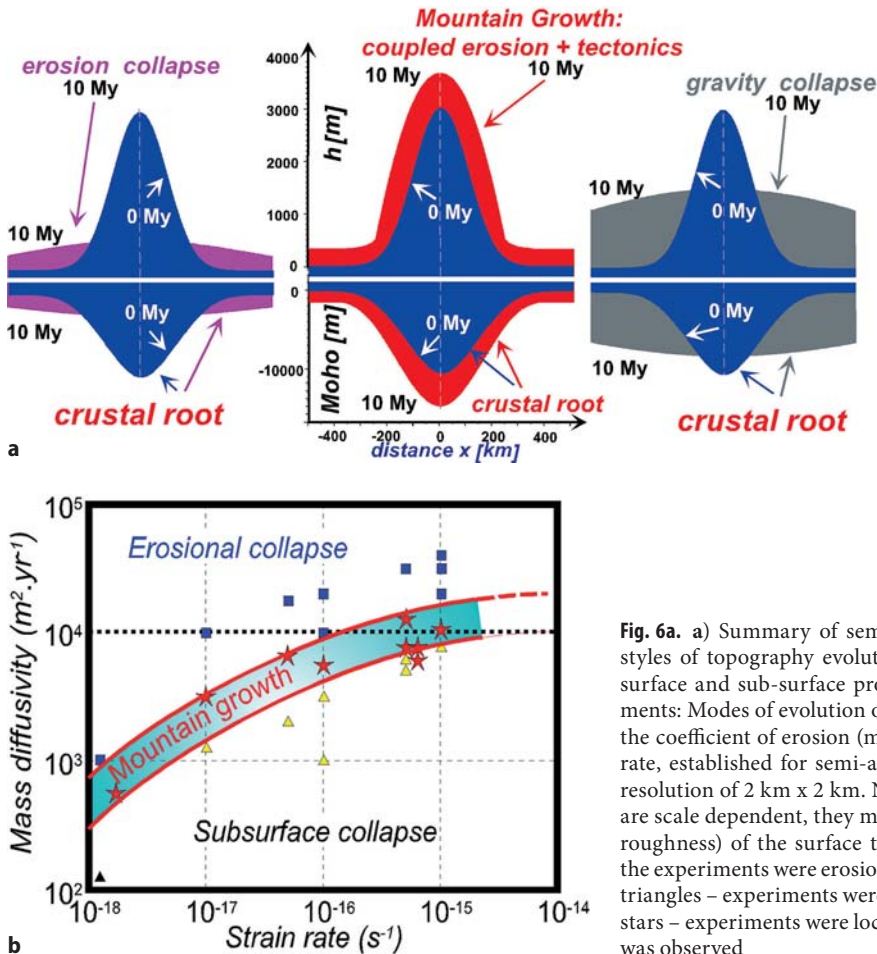
Fig. 6a. a) Summary of semi-analytical experiments: 3 major styles of topography evolution in terms of coupling between surface and sub-surface processes. **b)** Semi-analytical experiments: Modes of evolution of mountain ranges as a function of the coefficient of erosion (mass diffusivity) and tectonic strain rate, established for semi-analytical experiments with spatial resolution of 2 km x 2 km. Note that the coefficients of erosion are scale dependent, they may vary with varying resolution (or roughness) of the surface topography. Squares correspond to the experiments were erosional (surface) collapse was observed, triangles – experiments were subsurface collapse was observed, stars – experiments were localized stable growth of topography was observed

geometries. It appears that the graded geometry of a range may reflect the macroscopic characteristics of erosion. It might therefore be possible to infer empirical macroscopic laws of erosion from the topographic profiles across mountain belts provided that they are in a graded form.

6.1.5 Sensitivity to the Rheology and Structure of the Lower Crust

The above shown experiments have been conducted assuming a quartz rheology for the entire crust (= weak lower crust), which is particularly favorable for channel flow in the lower crust. We also conducted additional experiments assuming more basic lower crustal compositions (diabase, quartz-diorite). It appears that even with a relatively strong lower crust the coupled regime allowing for mountain growth can settle (Avouac and Burov, 1996). The effect of a less viscous lower crust is that the domain of values of the shortening rates and mass diffusivity for which the coupled regime can settle is simply shifted: at a given shortening rate lower rates of erosion are required to allow for the growth of the initial mountain. The domain defining the "mountain growth" regime in Fig. 6 is thus shifted towards smaller mass diffusivities when a stronger lower crust is considered. The graded shape obtained in this regime does not differ from that obtained with a quartz rheology. However, if the lower crust was strong enough to be fully coupled to the upper mantle, the dynamic equilibrium needed for mountain growth would not be established. Estimates of the yield strength of the lower crust near the Moho boundary for thermal ages from 0 to 2000 My. and for Moho depths from 0 to 80 km, made by Burov and Diament (1995), suggest that in most cases a crust thicker than about 40–50 km implies a low viscosity channel in the lower crust. However, if the lithosphere is very old or thin (> 1000 My), the coupled regime between erosion and horizontal flow in the lower crust will not develop.

6.1.6 Comparison with Observations

We compared our semi-analytical models with the Tien Shan range (Fig. 1a) because in this area, the rates of deformation and erosion have been well estimated from previous studies (Avouac et al., 1993: Metivier and Gaudemer, 1997), and because this range has a relatively simple 2-D geometry. The Tien Shan is the largest and most active mountain range in central Asia. It extends for nearly 2500 km between the Kyzil Kum and Gobi deserts, with some peaks rising to more than 7000 m. The high level of seismicity (Molnar and

Deng, 1984) and deformation of Holocene alluvial formations (Avouac et al., 1993) would indicate a rate of shortening of the order of 1 cm/y. In fact, the shortening rate is thought to increase from a few mm/y east of 90°E to about 2 cm/y west of 76°E (Avouac et al., 1993). Clockwise rotation of the Tarim Basin (at the south of Tien Shan) with respect to Dzungaria and Kazakhstan (at the north) would be responsible for this westward increase of shortening rate as well as of the increase of the width of the range (Chen et al., 1991; Avouac et al., 1993). The gravity studies by Burov (1990) and Burov et al. (1990) also suggest westward decrease of the integrated strength of the lithosphere. The westward increase of the topographic load and strain rate could be responsible for this mechanical weakening. The geological record suggests a rather smooth morphology with no great elevation differences and low elevations in the Early Tertiary and that the range was reactivated in the middle Tertiary, probably as a result of the India-Asia collision (e.g., Tapponnier and Molnar, 1979; Molnar and Tapponnier, 1981; Hendrix et al., 1992; 1994). Fission track ages from detrital apatite from the northern and southern Tien Shan would place the reactivation at about 20 My (Hendrix et al., 1994; Sobel and Dumitru, 1995). Such an age is consistent with the middle Miocene influx of clastic material and more rapid subsidence in the forelands (Hendrix et al., 1992; Métivier and Gaudemer, 1997) and with a regional Oligocene unconformity (Windley et al., 1990). The present difference of elevation of about 3000 m between the range and the lowlands would therefore indicate a mean rate of uplift of the topography, during the Cenozoic orogeny, of the order of 0.1–0.2 mm/y. The foreland basins have collected most of the material removed by erosion in the mountain. Sedimentary isopachs indicate that $1.5 \pm 0.5 \times 10^6$ km^3 of material would have been eroded during the Cenozoic orogeny (Métivier and Gaudemer, 1997), implying erosion rates of 0.2–0.5 mm/y on average. The tectonic uplift would thus have been of 0.3–0.7 mm/y on average. On the assumption that the range is approximately in local isostatic equilibrium (Burov et al., 1990; Ma, 1987), crustal thickening below the range has absorbed 1.2 to 4×10^6 km^3 (Métivier and Gaudemer, 1997). Crustal thickening would thus have accommodated 50 to 75% of the crustal shortening during the Cenozoic orogeny, with the remaining 25 to 50% having been fed back to the lowlands by surface processes. If we now place approximately the Tien Shan on the plot in Fig. 5 the 1 to 2 cm/y shortening corresponds to a basic strain rate of $\varepsilon_{xx} = 1.5$–3×10^{-16} s^{-1} and the 0.2–0.5 mm/y denudation rate implies a mass diffusivity of a few 10^3 to 10^4 m^2/y. These values actually place the Tien Shan in the "mountain growth" regime (Figs. 5b, 6). We therefore conclude that the localized growth of a range like the Tien Shan indeed could re-
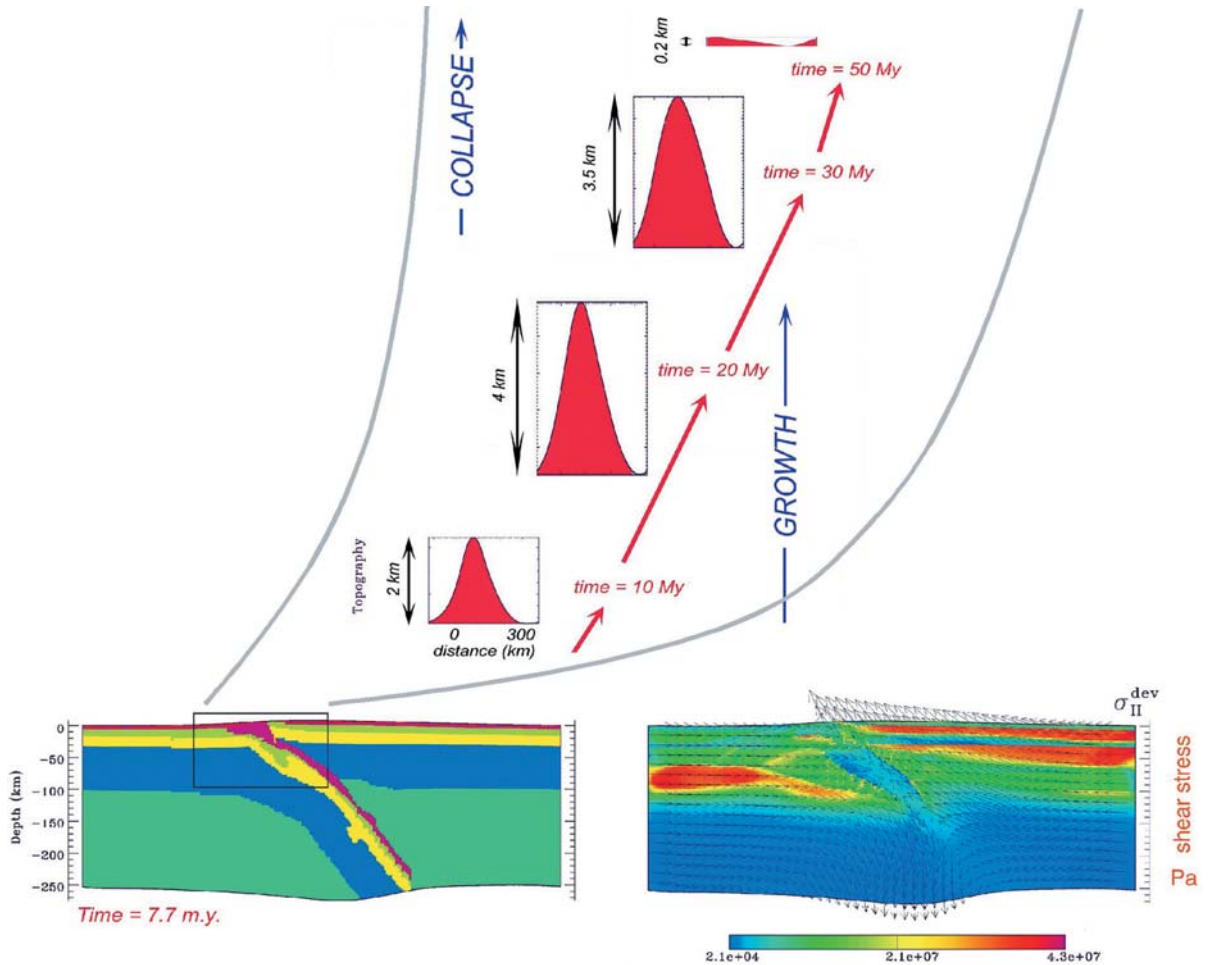
Fig. 7. Coupled numerical model of Alpine collision, with surface topography controlled by dynamic erosion. This model demonstrates that erosion-tectonics feedback help the mountain belt to remain as a localized growing feature for about 30 My. Note that final gravity collapse at 50 My results from erosion-tectonic misbalance after important amounts of shortening. Bottom, left: material phase field evolution at 7.7 My. Bottom, right: shear stress field. The numerical code (Parovoz) solves Newtonian force balance equations (large strain mode) coupled with brittle-ductile-elastic constitutive equations for main material phases, heat transfer equations and surface process equations. Colour code: purple – sediment/subduction channel; salad green – upper crust; yellow – lower crust; blue – lithosphere mantle; green – asthenosphere

sult from the coupling between surface processes and horizontal strains. We do not dispute the possibility for a complex mantle dynamics beneath the Tien Shan as has been inferred by various geophysical investigations (Vinnik and Saipbekova, 1984; Vinnik et al., 2006; Makeyeva et al., 1992; Roecker et al., 1993), but we contend that this mantle dynamics has not necessarily been the major driving mechanism of the Cenozoic Tien Shan orogeny.

6.2 Numerical Experiments

Fully numerical thermo-mechanical models were used to test more realistic scenarios of continental conver-

gence (Fig. 4 bottom), in which one of the continental plates under-thrusts the other (simple shear mode, or continental "subduction"), the raising topography undergoes internal deformations, and the major thrust faults play an active role in localization of the deformation and in the evolution of the range. Also, in the numerical experiments, there is no pre-defined initial topography, which forms and evolves in time as a result of deformation and coupling between tectonic deformation and erosion processes. We show the tests for two contrasting cases: slow convergence and slow erosion (Western Alps, 6 mm/y, $k = 500–1000$ m^2/y) and very fast convergence and fast erosion (India - Himalaya collision, 6 cm/y during the first stage of continent-continent subduction, up to 15 cm/y at the preceding

stage of oceanic subduction, k = 3000–10000 m²/y). The particular interest of testing the model for the conditions of the India-Himalaya-Tibet collision refers to the fact that this zone of both intensive convergence (Patriat and Achache, 1984) and erosion (e.g., Hurtrez et al., 1999) belongs to the same geodynamic framework of India-Eurasia collision as the Tien Shan range considered in the semi-analytical experiments discussed in the previous sections (Fig. 1a).

For the Alps, characterized by slow convergence and erosion rates (around 6 mm/y (Schmidt et al., 1997), k=500–1000 m²/y according to Fig. 6), we have studied a scenario in which the lower plate has already subducted to a 100-km depth below the upper plate (Burov et al., 2001). This assumption was needed to enable the continental subduction since, in the Alps, low convergence rates make model initialization of the subduction process very difficult without a perfect knowledge

of the initial configuration (Toussaint et al., 2004a). The numerical experiments (Fig. 7) confirm the idea that surface processes (k=500 m²/y), which selectively remove the most rapidly growing topography, result in dynamic tectonically-coupled unloading of the lithosphere below the thrust belt, whereas the deposition of the eroded matter in the foreland basins results in additional subsidence. As a result, a strong feedback between tectonic and surface processes can be established and regulate the processes of mountain building during a very long period of time (in the experiments, 50 My): the erosion-sedimentation prevents the mountain from reaching gravitationally unstable geometries. The "Alpine" experiments demonstrate that the feedback between surface and tectonic processes may allow the mountains to survive over very large time spans (50 My). This feedback favors localized crustal shortening and stabilizes topography and
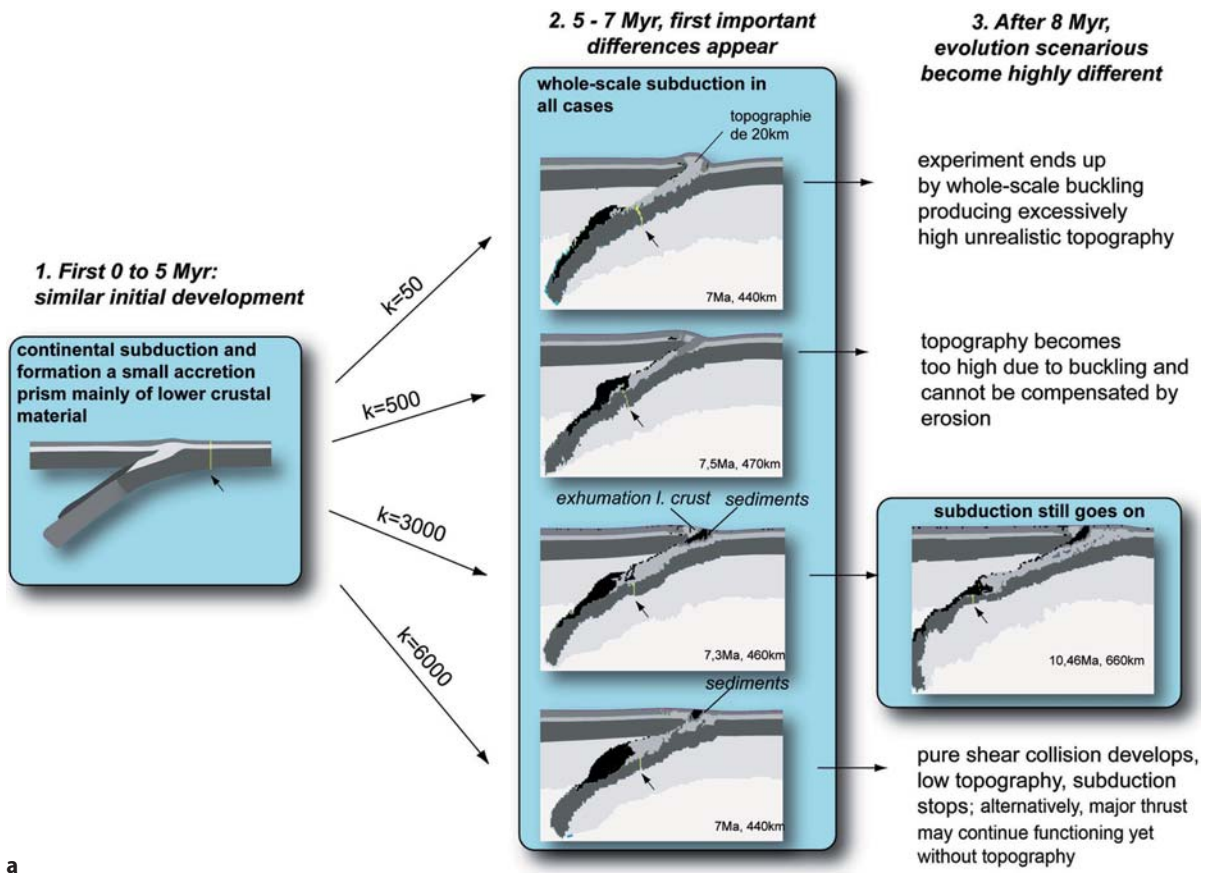
Fig. 8a. Coupled numerical models of India-Eurasia type of collision as function of the coefficient of erosion. These experiments were performed in collaboration with G. Toussaint using numerical setup (Fig. 4, bottom) identical to (Toussaint et al., 2004b). The numerical method is identical to that of (Burov et al., 2001 and Toussaint et al., 2004a,b; see also the experiment shown in Fig. 7). Sub-vertical stripes associated with little arrows point to the position of the passive marker initially positioned across the middle of the foreland basin. Displacement of this marker indicates the amount of subduction. Δx is amount of shortening. Different brittle-elastic-ductile rheologies are used for sediment, upper crust, lower crust, mantle lithosphere and the asthenosphere (Table 1b)

Topography evolution

Fig. 8b. Smoothed surface profiles generated in the experiments of Fig. 8a (India-Eurasia type of collision). *k* is coefficient of erosion. Topography is unrealistically high for small *k* = 50 m²/y , and too low for high *k* > 1000 m²/y; the range 500 m²/y < *k* < 3000 m²/y corresponds to localized mountain growth. Note complex behavior of the topography in case of *k* = 3000 m²/y: The mountain range and the major thrust tend to migrate towards the subducting plate

thrust faults in time. Indeed even though a slow convergence scenario is not favorable for continental subduction, the model shows that once it is initialised, the tectonically coupled surface processes help to keep the major thrust working. Otherwise, in the absence of a strong feedback between surface and subsurface processes, the major thrust fault is soon blocked, the upper plate couples with the lower plate, and the system evolution turns from simple shear subduction to pure shear collision (Toussaint et al., 2004a; Cloetingh et al., 2004). However, topography cannot infinitely grow even in the "feedback" mode: as soon as the range grows to some critical size, it cannot be sup-

ported anymore due to the limited strength of the constituting rocks, and ends up by gravitational collapse. This has happened in the Alpine experiment towards 50 My of convergence (Fig. 7).

Our experiments on the fast "Indian-Asia" collision were based on the results of Toussaint et al. (2004b). The model and the entire setup (Figure 4, bottom) are identical to those described in detail in Toussaint et al. (2004b). For this reason, we refer the interested reader to this study (see also Appendix D and description of the numerical model in the previous sections). Toussaint et al. (2004b) tested the possibility of subduction of the Indian plate beneath the Himalaya and Tibet at

early stages of collision (first 15 My). This study used by default the "stable" values of the coefficient of erosion (3000 ± 1000 m^2/y) derived from the semi-analytical model of (Avouac and Burov, 1996) for a shortening rate of 6 cm/y. The coefficient of erosion was only slightly varied in a way to keep the topography in reasonable limits, yet, Toussaint et al. (2004b) did not test the sensitivities of the Himalayan orogeny to large variations in the erosion rate. Our new experiments fill this gap by testing the stability of the same model for a large range of k, from 50 m^2/y to 11,000 m^2/y. These experiments (Fig. 8) demonstrate that, depending on the intensity of the surface processes, horizontal compression of continental lithosphere can lead either to strain localization below a growing range and continental subduction; or to distributed thickening or buckling/folding (Fig. 8a). The experiments suggest that homogeneous thickening occurs when erosion is either too strong ($k > 1000$ m^2/y), in that case any topographic irregularity is rapidly erased by surface processes (Fig. 8b), or when erosion is too weak ($k < 50$ m^2/y). In case of small k, surface elevations are unrealistically high (Fig. 8b), which leads to vertical over-loading and failure of the lithosphere and to an increase of the frictional force along the major thrust fault. As a consequence, the thrust fault is locked up leading to coupling between the upper and lower plate; this results in overall buckling of the region whereas the crustal root below the range starts to spread out laterally with formation of a flat "pancake-shaped" topography. On the contrary, in case

of a dynamic balance between surface and subsurface processes ($k = 2000 - 3000$ m^2/y, close to the predictions of the semi-analytical model, Fig. 6), erosion/sedimentation resulted in long-term localization of the major thrust fault that kept active during 10 My. At the same time, in the experiments with $k = 500$–1000 m^2/y (moderate feedback between surface and subsurface processes), the major thrust fault and topography were almost stationary (Fig. 8a). In case of a stronger feedback ($k = 2000$–5000 m^2/y) the range and the thrust fault migrated horizontally in the direction of the lower plate ("India"). This basically happened when both the mountain range and the foreland basin reached some critical size. In this case, the "initial" range and major thrust fault were abandoned after about 500 km of subduction, and a new thrust fault, foreland basin and range were formed "to the south" (i.e., towards the subducting plate) of the initial location. The numerical experiments confirm our previous idea that intercontinental orogenies could arise from coupling between surface/climatic and tectonic processes, without specific help of other sources of strain localization. Given the differences in the problem setting, the results of the numerical experiments are in good agreement with the semi-analytical predictions (Fig. 6) that predict mountain growth for k on the order of 3000–10,000 m^2/y for strain rates on the order of 0.5×10^{-16} s^{-1} – 10^{-15} s^{-1}. The numerical experiments, however, predict somewhat smaller values of k than the semi-analytical experiments. This can be explained by the difference in the convergence mode
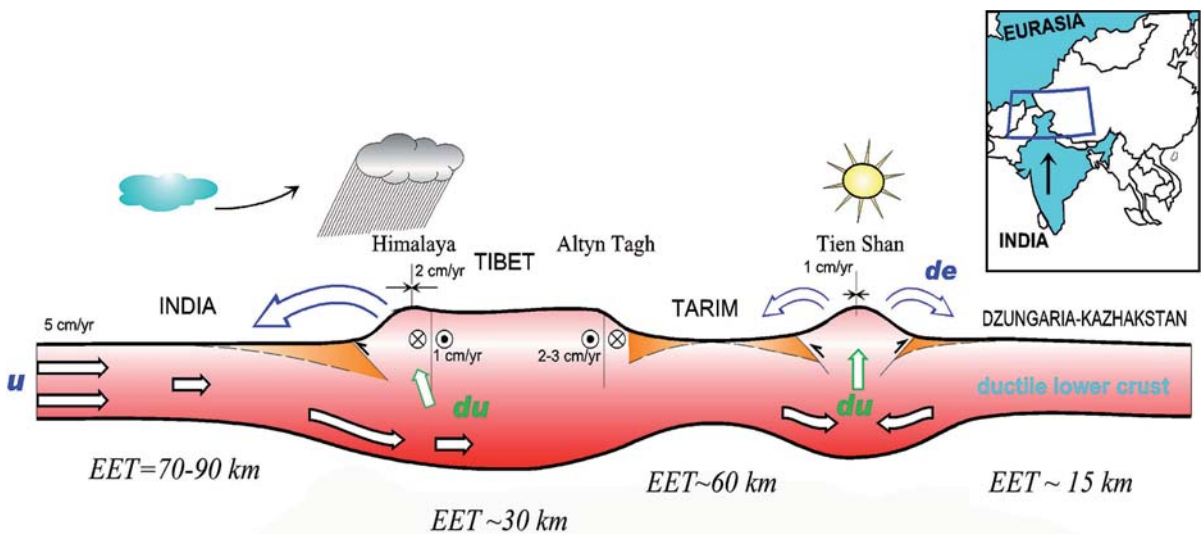
Fig. 9. Conceptual model for erosionally-controlled India - Eurasia collision derived from the numerical experiments. Asymmetry in climatic conditions to the south of the Himalaya with respect to Tibet to the north may explain the asymmetric development of the Himalayan-Tibetan region (Avouac and Burov, 1996). On the contrary, similar dry climatic conditions to the north and south of the Tien Shan range favour the development of its highly symmetric topography even if the colliding plates (Tarim block and Kazakh shield) have extremely contrasting mechanical properties (Burov et al., 1990; Vinnik et al., 2006)

attained in the numerical experiments (simple shear subduction) and in the analytical models (pure shear). For the same convergence rate, subduction resulted in smaller tectonic uplift rates than pure shear collision. Consequently, "stable" erosion rates and k values are smaller for subduction than for collision.

7   Conclusions

It appears that deformation of continents is highly sensitive to surface processes and, consequently, to climate. The surface processes may be a dominating factor of orogenic evolution that largely controls the evolution and shapes of the surface topography, major thrust faults, and foreland basins. For example, similar dry climatic conditions to the north and south of the Tien Shan range favor the development of its highly symmetric topography despite the fact that the colliding plates have extremely contrasting, asymmetric mechanical properties (in the Tarim block, the equivalent elastic thickness, EET = 60 km, whereas in the Kazakh shield, EET = 15 km (Burov et al., 1990)).

Although there is no perfect model for surface processes, the combination of modified diffusion and fluvial transport models provides satisfactory results for most large-scale tectonic applications.

In this study, we investigated the interactions between the surface and subsurface processes for three representative cases:

1. Very fast convergence rate, such as the India-Himalaya-Tibet collision.
2. Intermediate rate convergence settings (Tien Shan).
3. Very slow convergence settings (Western Alps).

In case of slow Alpine collision, we have shown that the persistence of once created topography may be insured by coupling between the surface and tectonic processes. Surface processes basically help to initialize and maintain continental subduction for a certain amount of time (5–7 My, maximum 10 My). They can stabilize, or "freeze" dynamic topography and the major thrust faults for as long as 50 My.

The way Central Asia has absorbed indentation of India may somehow reflect the sensitivity of the tectonic deformation to surface processes (Fig. 9) as asymmetry in climatic conditions to the south of the Himalaya with respect to Tibet to the north may explain the asymmetric development of the Himalaya-Tibetan region (Avouac and Burov, 1996). Interestingly, the mechanically asymmetric Tien Shan range situated north of Tibet, between the strong Tarim block and weak Kazakh shield, and characterized by similar climatic conditions at both sides of the range, is highly symmetric (Fig. 9). Previous numerical models of continental indentation that were based on continuum mechanics, but neglected surface processes, predicted a broad zone of crustal thickening, resulting from nearly homogeneous straining, that would propagate away from the indentor. In fact, crustal straining in Central Asia has been very heterogeneous and has proceeded very differently from the predictions of these models: a long-lived zone of localized crustal shortening has been maintained, in particular along the Himalaya, at the front of the indentor, and the Tien Shan, well north of the indentor; broad zones of thickened crust have resulted from sedimentation rather than from horizontal shortening (in particular in the Tarim basin, and to some extent in some Tibetan basins such as the Tsaïdam (Métivier and Gaudemer, 1997). Present kinematics of active deformation in Central Asia corroborates a highly heterogeneous distribution of strain. The 5cm/y convergence between India and stable Eurasia is absorbed by lateral extrusion of Tibet and crustal thickening, with crustal thickening accounting for about 3cm/y of shortening. About 2 cm/y would be absorbed in the Himalayas and 1cm/y in the Tien Shan. The indentation of India into Eurasia has thus induced localized strain below two relatively narrow zones of active orogenic processes while minor deformation has been distributed elsewhere. Our point is that, as in our numerical experiments, surface processes might be partly responsible for this highly heterogeneous distribution of deformation that has been maintained over several millions or tens of millions of years (Fig. 9). First active thrusting along the Himalaya and in the Tien Shan may have been sustained during most of the Cenozoic thanks to continuous erosion. Second, the broad zone of thickened crust in Central Asia has resulted in part from the redistribution of the sediments eroded from the localized growing reliefs. Moreover, it should be observed that the Tien Shan experiences a relatively arid intracontinental climate while the Himalayas is exposed to a very erosive monsoonal climate. This disparity may explain why the Himalaya absorbs twice as much horizontal shortening as the Tien Shan. In addition, the nearly equivalent climatic conditions on the northern and southern flanks of the Tien Shan might have favored the development of a nearly symmetrical range. By contrast the much more erosive climatic conditions on the southern than on the northern flank of the Himalaya may have favored the development of systematically south vergent structures. While the Indian upper crust would have been delaminated and brought to the surface of erosion by north dipping thrust faults, the Indian lower crust would have flowed below Tibet. Surface processes might therefore have facilitated injection of Indian lower crust below Tibet. This would explain crustal thickening of Tibet with minor hori-

zontal shortening in the upper crust, and minor sedimentation.

We thus suspect that climatic zonation in Asia has exerted some control on the spatial distribution of the intracontinental strain induced by the India-Asia collision. The interpretation of intracontinental deformation should not be thought of only in terms of boundary conditions induced by global plate kinematics but also in terms of global climate. Climate might therefore be considered as a forcing factor of continental tectonics.

To summarize, we suggest three major modes of evolution of thrust belts and adjacent forelands (Fig. 6):

1. Erosional collapse (erosion rates are higher than the tectonic uplift rates. Consequently, the topography cannot grow).
2. Localized persistent growth mode. Rigid feedback between the surface processes and tectonic uplift/subsidence that may favor continental subduction at initial stages of collision.
3. Gravity collapse (or "plateau mode", when erosion rates are insufficient to compensate tectonic uplift rates. This may produce a plateaux in case of high convergence rate).

It is noteworthy (Fig. 5c) that while in the "localized growth regime", the system has a very important reserve of stability and may readapt to eventual changes in tectonic or climatic conditions. However, if the limits of stability are exceeded, the system will collapse in very rapid, catastrophic manner.

We conclude that surface processes must be taken into account in the interpretation and modelling of long-term deformation of continental lithosphere. Conversely, the mechanical response of the lithosphere must be accounted for when large-scale topographic features are interpreted and modelled in terms of geomorphologic processes. The models of surface processes are most realistic if treated in two dimensions in a horizontal plane, while most of the current mechanical models are two dimensional in the vertical cross-section. Hence, at least for this reason, a next generation of 3D tectonically realistic thermomechanical models is needed to account for dynamic feedbacks between tectonic and surface processes. With that, new explanations of evolution of tectonically active systems and surface topography can be provided.

Acknowledgements

References

Ahnert, F., (1970) Functional relationships between denudation, relief and uplift in large mid-latitude drainage basins, Am. J. Sci., 268, 243–263.

Ashmore, P. E., (1982) Laboratory modelling of gravel braided stream morphology, Earth Surf. Processes Landforms, 7, 201–225.

Andrews, D. J., R.C. Bucknam, (1987)Fitting degradation of shoreline scarps by a nonlinear diffusion model, J. Geophys. Res., 92, 12857–12867.

Avouac, J.P., (1993) Analysis of scarp profiles: evaluation of errors in morphologic dating, J. Geophys. Res., 98, 6745-6754.

Avouac, J.-P., Tapponnier, P., Bai, M., You, H., G. Wang, Active thrusting and folding along the northern Tien Shan and late Cenozoic rotation of the Tarim relative to Dzungaria and Kazakhstan, J. Geophys. Res., 98, 6755–6804, 1993.

Avouac, J.-P., P. Tapponnier, (1993) Kinematic model of active deformation in Central Asia, Geophysical Research Letters, 20, 895–898.

Avouac, J. P., E. B. Burov, (1996) Erosion as a driving mechanism of intracontinental mountain growth, J. Geophys. Res., 101(B8), 17,747 –17,769.

Basile, C., P. Allemand, (2002) Erosion and flexural uplift along transform faults, Geophys. J. Int. 151, 646–653

Batchelor, G.K., (1967) An introduction to fluid dynamics, Cambridge University Press, p.615 Beaumont, C., (1981) Foreland basins, R. Astr. Soc. Geophys. J., 65, 389–416.

Beaumont, C., Fullsack, P., and J. Hamilton, Erosional control of active compressional orogens, Thrust Tectonics, Ed. K.R. McClay, Chapman & Hall, London, 1–31, 1992.

Beaumont, C., Fullsack, P., and J. Hamilton, Styles of crustal deformation in compressional orogens caused by subduction of the underlying lithosphere, submitted to: Proceedings of 5th International Symposium on Seismic Reflection Probing of the Continents and their Margins, eds.: R. Clowes and A. Green, 1994.

Beaumont, C., H. Kooi, and S. Willett, Coupled tectonic-surface process models with applications to rifted margins and collisional orogens, in Geomorphology and Global Tectonics, edited by M. A. Summerfield, pp. 29–55, John Wiley, New York, 2000.

Bonnet, S., and A. Crave, (2003) Landscape response to climate change: Insights from experimental modeling and implications for tectonic versus climatic uplift of topography, Geology, 31, 123–126.

Braun, J., and M. Sambridge, Modelling landscape evolution on geological time scales: A new method based on irregular spatial discretization, Basin Res., 9, 27– 52, 1997.

Beekman, F., (1994) Tectonic modelling of thick-skinned compressional intraplate deformation, PhD thesis, Free University, Amsterdam.

Bird, P., and A. J. Gratz, (1990) A theory for buckling of the mantle lithosphere and Moho during compressive detachments in continents, Tectonophysics, 177, 325–336.

Bird, P., (1991) Lateral extrusion of lower crust from under high topography in the isostatic limit, J. Geophys. Res., 96, 10275–10286.

Brace, W.F., and D.L. Kohlstedt, Limits on lithospheric stress imposed by laboratory experiments. J. Geophys. Res., 85, 6248–6252, 1980.

Byerlee, J. D., (1978) Friction of rocks. Pure Appl. Geophys., 116, 615–626.

Burbank, D.W., Causes of recent Himalayan uplift deduced from deposited patterns in the Ganges basin, Nature, 357, 680–683, 1992.

Burbank, D. W., and J. Vergés, (1994) Reconstruction of topography and related depositional systems during active thrusting, J. Geophys. Res., 99, 20,281–20,297.

Burov, E.V., M.G. Kogan, H. Lyon-Caen, and P. Molnar, Gravity anomalies, the deep structure, and dynamic processes beneath the Tien Shan, Earth Planet. Sci. Lett., 96, 367–383, 1990.

Burov, E. B., and Diament, (1992) M., Flexure of the continental lithosphere with multilayered rheology, Geophys. J. Int., 109, 449–468.

Burov, E. B., Lobkovsky, L.I., Cloetingh, S., and Nikishin, A. M., Continental lithosphere folding in Central Asia (part 2), constraints from gravity and topography, Tectonophysics, 226, 73–87, 1993.

Burov, E.B., and S. Cloetingh, (1997) Erosion and rift dynamics: new thermomechanical aspects of post-rift evolution of extensional basins, Earth and Planet Sci. Lett., 150, 7–26.

Burov, E.B. and M Diament, (1995) The effective elastic thickness (Te) of continental lithosphere: What does it really mean? J. Geophys. Res., 100, 3905–3927.

Burov, E.B., Jolivet, L., Le Pourhiet, L., and A. Poliakov, A thermemechanical model of exhumation of HP and UHP methamorphic rocks in Alpine mountain belts, Tectonophysics, 113–136, 2001.

Burov, E., A.B. Watts, The long-term strength of continental lithosphere: "jelly-sandwich" or "crème-brûlé"?, GSA Today, 16, 1, doi: 10.1130/1052–5173(2006)016<4:TLTSOC, 2006.

Carson, M.A., and M.J. Kirkby, (1972) Hillslope Form and Processes, Cambridge University Press, 475p.

Carter, N.L., and M.C. Tsenn, (1987) Flow properties of continental lithosphere, Tectonophysics, 36, 27–63.

Castelltort, S., and G. Simpson, (2006) Growing mountain ranges and quenched river networks, CRAS.

Chen, Y., Cogne, J.P., Courtillot, V., Avouac, J.P., Tapponnier, P., Buffetaut, E., Wang., G., Bai., M., You, H., Li, M., and C. Wei, Paleomagnetic study of Mesozoic continental sediments along the northern Tien Shan (China) and heterogeneous strain in Central Asia, J. Geophys. Res., 96, 4065–4082, 1991.

Chéry, J., Vilotte, J. P., and M. Daignieres, (1991) Thermomechanical evolution of a thinned continental lithosphere under compression: Implications for Pyrenees, J. Geophys. Res., 96, 4385–4412.

Chorley R.J., S.A. Schumm, and D.E. Sugden, (1984) Hillsopes in Geomorpholgy, 255–339, Methuen, London.

Cloetingh, S., Burov, E., Matenco L., Toussaint, G., and G. Bertotti, Thermo-mechanical constraints for the continental collision mode in the SE Carpathians (Romania), Earth and Planet Sci. Letters, 218(1–2), pp. 57–76, 2004.

Copeland P. and T.M. Harrison, (1990) Episodic rapid uplift in the Himalya revealed by 40Ar/39Ar analysis of detrital K-feldspar and muscovite, Bengal fan, Geology, 18, 354–357.

Crave, A., and P. Davy, A stochastic "precipiton" model for simulating erosion/sedimentation dynamics, Comput. Geosci., 27, 815– 827, 2001.

Crave, A., D. Lague, P. Davy, J. Kermarrec, D. Sokoutis, L. Bodet, and R. Compagnon, Analogue modelling of relief dynamics, Phys. Chem. Earth, Part A, 25(6–7), 549–553, 2000.

Culling, W.E.H., (1960) Analytical theory of erosion, Journal of Geology, 68, 336–333.

Culling, W.E.H., (1965) Theory of erosion on soil-covered slopes, Journal of Geology, 73, 230–254.

Cundall, P.A., (1989) Numerical experiments on localization in frictional material: Ingenieur-Archiv, v. 59, p. 148–159.

Davies, G. F., (1994) Thermomechanical erosion of the lithosphere by mantle plumes, J. Geophys. Res., 99, 15709–15722.

Davy, P., and A. Crave, (2000)Upscaling local-scale transport processes in largescale relief dynamics, Phys. Chem. Earth, Part A, 25(6–7), 533–541.

Densmore, A. L., R. S. Anderson, B. G. McAdoo, and M. A. Ellis, Hillslope evolution by bedrock landslides, Science, 275, 369– 372, 1997.

Densmore, A. L., M. A. Ellis, and R. S. Anderson, Landsliding and the evolution of normal fault-bounded mountain ranges, J. Geophys. Res., 103(B7), 15,203– 15,219, 1998.

Ellis, S., Fullsack, P., and C. Beaumont; Oblique convergence of the crust driven by basal forcing: implications for length-scales of deformation and strain partitioning in orogens, Geophys. J. Int., 120, 24–44, 1995.

England, P.C., and D.P. McKenzie, (1983) A thin viscous sheet model for continental deformation, Geophys. J. R. Astron. Soc., 73, 523–5323.

England, P., and S. W. Richardson, The influence of erosion upon the mineral facies of rocks from different metamorphic environments, J. Geol. Soc. Lond., 134, 201–213, 1977.

Flint, J. J., Experimental development of headward growth of channel networks, Geol. Soc. Am. Bull., 84, 1087– 1094, 1973.

Flint, J.-J., Stream gradient as a function of order magnitude, and discharge, Water Resour. Res., 10(5), 969–973, 1974.

Fleitout, L., and C. Froidevaux, Tectonics and topography for a lithosphere containing density heterogeneities, Tectonics, 1, 21–56, 1982.

Flemings, P. B., and T.E. Jordan, A synthetic stratigraphic model of foreland basin development, J. Geophys. Res., 94, 3851–3866, 1989.

Flemings, P. B., and T.E. Jordan, Stratigraphic modelling of foreland basins: interpreting thrust deformation and lithosphere rheology, Geology, 18, 430–434, 1990.

Fletcher, C.A.J., Computational techniques for fluid dynamics 2, Springer-Verlag, Berlin Heidelberg, 552 pp., 1988

Fournier, F., Climat et Erosion: la relation entre l'érosion du sol par l'eau et les précipitations atmosphériques, Presse Universitaire de France, Paris, 201 pp, 1960.

Gaspar-Escribano, J.M., Ter Voorde, M., Roca, E. and Cloetingh, S., Mechanical (de-)coupling of the lithosphere in the Valencia Through (NW Mediterranean): What does it mean ? Earth and Planet Sci. Lett., 210, 291–303, 2003

Garcia-Castellanos, D., Vergés, J., Gaspar-Escribano, J., and S. Cloetingh, Interplay between tectonics, climate, and fluvial transport during the Cenozoic evolution of the Ebro Basin (NE Iberia), J. Geophys. Res., VOL. 108, NO. B7, 2347, doi:10.1029/2002JB002073, 2003

Garcia-Castellanos, D., Interplay between lithospheric flexure and river transport in foreland basins, Basin Res., 14, 89–104, 2002.

Garcia-Castellanos, D., M. Fernàndez, and M. Torne, Modeling the evolution of the Guadalquivir foreland basin (southern Spain), Tectonics, 21(3), 1018, doi::10.1029/2001TC001339, 2002.

Gossman, H, Slope modelling with changing boundary conditions - effects of climate and lithology, Z. Geomoph. N.F., Suppl. Bd. 25, 72–88, 1976.

Govers, G., Evaluation of transporting capacity formulae for overland flow, in Overland Flow: Hydraulics and Erosion Mechanics, edited by A. J. Parsons and A. D. Abrahams, pp. 243 – 273, UCL Press, London, 1992a.

Govers, G., Relationship between discharge, velocity and flow area for rills eroding loose, non-layered materials, Earth Surf. Processes Landforms, 17, 515–528, 1992b.

Gratton, J., Crustal shortening, root spreading, isostasy, and the growth of orogenic belts: a dimensional analysis, J. Geophys. Res., 94, 15627-15634, 1989.

Gregory, K.M., and C. Chase, Tectonic and climatic significance of a late Eocene low-relief, high-level geomorphic surface, Colorado, J. Geophys. Res., 99, 20141–20160, 1994.

Hamilton, J.M, Kim, J., and F. Waleffe, Regeneration mechanisms of near-wall turbulence structures, J. Fluid. Mech., 287, 317–348, 1995.

Hanks, T.C., Buckham, R.C., LaJoie, K.R., and R.E. Wallace, Modification of wave-cut and fault-controlled landforms, J. Geophys. Res., 89, 5771-5790, 1984.

Hansen, E.B., and M.A. Kelmanson, An integral equation justification of the boundary conditions of the driven-cavity problem, Computers & Fluids, 23, 1, 225–240, 1994.

Hairsine, P. B., and C. W. Rose, Modeling water erosion due to overland flow using physical principles, 1, Sheet flow, Water Resour. Res., 28(1), 237–243, 1992.

Hancock, G., and G. Willgoose, Use of a landscape simulator in the validation of the SIBERIA catchment evolution model: Declining equilibrium landforms, Water Resour. Res., 37(7), 1981– 1992, 2001.

Hasbargen, L. E., and C. Paola, Landscape instability in an experimental drainage basin, Geology, 28(12), 1067– 1070, 2000.

Hendrix, M.S., Graham., S.A., Caroll, A.R., Sobel, E.R., McKnight, C.L., Schulein, B.J., and Z. Wang, Sedimentary record and climatic implications of recurrent deformation in the Tien Shan: Evidence from Mesozoic strata of the north Tarim, south Junggar, and Turpan basins, northwest China, Geol. Soc. of Am. Bull., 104, 53–79, 1992.

Hendrix, M.S., T.A., Dumitru and S.A; Graham, Late Oligocene-early Miocene unroofing in the Chinese Tian Shan: An early effect of the India Asia collision, Geology, 487–490, 1994.

Hirano, Simulation of developmental process of interfluvial slopes with reference to graded form, J. Geol, 83, 113–123, 1975.

Howard, A. D., Long profile development of bedrock channels: Interaction of weathering, mass wasting, bed erosion and sediment transport, in Rivers Over Rock: Fluvial Processes in Bedrock Channels, Geophys. Monogr. Ser., vol. 107, edited by K. J. Tinkler and E. E. Wohl, pp. 297– 319, AGU, Washington, D.C., 1998.

Howard, A. D., W. E. Dietrich, and M. A. Seidl, Modeling fluvial erosion on regional to continental scales, J. Geophys. Res., 99(B7), 13,971 – 13,986, 1994.

Huppert, H.E., The propagation of two dimensional and axisymmetric gravity currents over a rigid horizontal surface, J. Fluid. Mech., 121, 43–58, 1982.

Hurtrez, J.-E., F. Lucazeau, J. Lave´, and J.-P. Avouac, Investigation of the relationships between basin morphology, tectonic uplift, and denudation from the study of an active fold belt in the Siwalik Hills, central Nepal, J. Geophys. Res., 104(B6), 12,779– 12,796, 1999.

Kaufman, P.S., and L.H. Royden, Lower crustal flow in an extensional setting: Constraints from the Halloran Hills region, eastern Mojave Desert, California, J. Geophys. Res., 99, 15723–15739, 1994.

King, G.C.P., R.S. Stein a,d J.B. Rundle, The growth of geological structures by repeated earthquakes, 1. Conceptual framework, J. Geophys. Res., 93, 13307–13318, 1988.

King, G., and Ellis, The origin of large local uplift in extensional regions, Nature, 348, 689–693, 1990.

Kirby, S.H., Rheology of the lithosphere. Rev. Geophys., 21, 1458 –1487, 1983.

Kirby, S.H., and A.K. Kronenberg, Rheology of the lithosphere: Selected topics, Rev. of Geophys., 25, 1219–1244, 1987.

Kirkby, M. J., Hillslope process-response models based on the continuity equation, Spec. Publ. Inst. Br. Geogr., 3, 15– 30, 1971.

Kirkby, M.J. A two-dimensional model for slope and stream evolution, in Abrahams, A.D. ed., Hillslope Processes: Boston, Allen and Unwin., 203–224, 1986

Kirkby, M., Leeder, M., and N. White, The erosion of actively extending tilt-blocks: a coupled for topography and sediment budgets, application to the B&R, 13 pp., 1993.

Koch, D.M., and D. L. Koch, Numerical and theoretical solutions for a drop spreading below a free fluid surface, J. Fluid Mech., 287, 251–278, 1995.

Kohlstedt, D. L., Evans, B., and Mackwell; S. J., Strength of the lithosphere: Constraints imposed by laboratory experiments: Journal of Geophysical Research, 100, 17,587–17,602, 1995.

Kooi, H., and C. Beaumont, Escarpment evolution on high-elevation rifted margins: Insights derived from a surface processes model that combines diffusion, advection and reaction, J. Geophys. Res., 99, 12191–12209, 1994.

Kooi, H., and C. Beaumont, Large-scale geomorphology: Classical concepts reconciled and integrated with contemporary ideas via a surface processes model, J. Geophys. Res., 101(B2), 3361– 3386, 1996.

Kruse, S., M. McNutt, J. Phipps-Morgan, and L. Royden, Lithospheric extension near lake Mead, Nevada: A model for ductile flow in the lower crust, J. Geophys. Res., 96(3), 4435– 4456, 1991.

Kusznir, N.J.; and D.H. Matthews, Deep seismic reflections and the deformational mechanics of the continental lithosphere, J. petrol., Spec. Lithosphere Issue, 63–87, 1988.

Kusznir, N.J., The distribution of stress with depth in the lithosphere: thermo-rheological and geodynamic constraints, Phil. Trans. R. Soc. Lond., A337, 95–110, 1991.

Lague, D., P. Davy, and A. Crave, Estimating uplift rate and erodibility from the area– slope relationship: Examples from Brittany (France) and numerical modelling, Phys. Chem. Earth, Part A, 25(6– 7), 543– 548, 2000.

Lague, D., A. Crave, and Ph. Davy, Laboratory experiments simulating the geomorphic response to tectonic uplift, J. Geophys. Res., VOL. 108, NO. B1, 2008, doi:10.1029/ 2002JB001785, 2003

Lavé, J., and J. P. Avouac, Fluvial incision and tectonic uplift across the

Himalayas of central Nepal, J. Geophys. Res., 106(B11), 26,561– 26,591, 2001.

Leeder, M.R., Denudation, vertical crustal movements and sedimentary basin infill, Geologische Rundschau, Stuttgart, 80, 2, 441–458, 1991.

Le Pourhiet L, Burov E, Moretti I., Rifting through a stack of in-homogeneous thrusts (the dipping pie concept), Tectonics, 23 (4): TC4005, doi:10.1029/2003TC001584, 2004

Lobkovsky, L.I., Geodynamics of Spreading and Subduction zones, and the two-level plate tectonics, Nauka, Moscow, 251 pp., 1988.

Lobkovsky, L.I. and V.I. Kerchman, A two-level concept of plate tectonics: application to geodynamics. Tectonophysics, 199, 343–374, 1991.

Luke, J.C., Mathematical models for landform evolution, J. Geophys. Res., 77, 2460–2464, 1972.

Luke, J.C., Special Solutions for Nonlinear Erosion Problems, J. Geophys. Res., 79, 4035–4040, 1974.

Ma, X., Lithospheric dynamic Atlas of China, China Carto-graphic Publishing House, Beijing, China, 1987.

Makeyeva, L.I., L.P. Vinnik and S.W. Roecker, Shear-wave split-ting and small scale convection in the continental upper mantle, Nature, 358, 144–147, 1992.

Masek, J. G., Isacks, B. L., and E. J. Fielding, Rift flank uplift in Tibet: Evidence for a viscous lower crust, Tectonics, 13, 659–667, 1994a.

Masek, J. G., Isacks, B. L., Gubbels, T.L., and E. J. Fielding, Ero-sion and tectonics at the margins of continental plateaus, J. Geophys. Res., 99, 13941–13956, 1994b.

Metivier, F., and Y. Gaudemer, Mass transfer between eastern Tien Shan and adjacent basins (central Asia): constraints on regional tectonics and topography, Geophys. J. Int., 128, 1–17, 1997.

Molnar, P., Climate change, flooding in arid environments, and erosion rates, Geology, 29(12), 1071–1074, 2001.

Molnar, P. and Q. Deng, Faulting associated with large earth-quakes and the average rate of deformation in central and eastern Asia, J. Geophys. Res., 89, 6203–6228, 1984

Molnar, P., and H. Lyon-Caen, Some simple physical aspects of the support, structure, and evolution of mountain belts, in: Processes in continental lithospheric deformation, Geol. Soc. Am. Spec., Rap. 218, 179–207, 1988

Molnar P., and Tapponnier, A possible dependence of the tec-tonic strength on the age of the crust in Asia, Earth Planet. Sci. Lett., 52, 107–114, 1981.

Molnar, P., and P. England, Late Cenozoic uplift of mountain ranges and global climate change: chicken or egg, Nature, 346, 29–34, 1990.

Mizutani, T., Laboratory experiment and digital simulation of multiple fillcut terrace formation, Geomorphology, 24, 353–361, 1998.

Nash, D.B., Morphologic dating of degraded normal fault scarps, J. Geol., 88, 353–360, 1980.

Newman, W.I., Nonlinear diffusion: Self-similarity and travel-ling-waves, PAGEOPH, 121, 3, 417–441, 1983.

Newman, W.I., and D.L. Turcotte, Cascade model for fluvial geomorphology, Geophys. J. Int., 100, 433–439, 1990.

Parson, B., and J. Sclater, An analysis of the variation of ocean floor bathymetry and heat flow with age, J. Geophys. Res., 93, 8051–8063, 1977.

Patriat, P., and J. Achache, India-Eurasia collision chronology has implications for crustal shortening and driving mecha-nism of plates, Nature, 311, 615–621, 1984.

Pelletier, J.D., Persistent drainage migration in a numerical landscape evolution model. Geophys. Res. Lett., 31, doi:10.1029/2004GL020802, 2004.

Persson, K.S., Garcia-Castellanos D., and D. Sokoutis , River transport effects on compressional belts: First results from

an integrated analogue-numerical model, J. Geophys. Res., VOL. 109, B01409, doi:10.1029/2002JB002274, 2004

Pinet, P., and M. Souriau, Continental erosion and large-scale relief, Tectonics, 7, 3, 563–582, 1988.

Ranalli, G., Rheology of the Earth: Chapman & Hall, Sec. Edi-tion., London, 413 pp, 1995.

Roecker, S.W., Sabitova, T.M., Vinnik, L.P., Burmakov, Y.A., Golvanov, M.I., Mamatkanova, R., and L. Minirova, Three dimensional elastic wave velocity structure of the western and central Tien Shan, J. Geophys., Res., 98, 15779–15795, 1993.

Roering, J. J., J. W. Kirchner, L. S. Sklar, and W. E. Dietrich, Hillslope evolution by nonlinear creep and landsliding: An experimental study, Geology, 29(2), 143–146, 2001.

Schmid, S. M., Pfiffner, O. A., Schönborg, G., Froitzheim, N., and Kissling, E., Integrated cross-sections and tectonic evo-lution of the Alps along the Eastern Traverse. In: Deep struc-tures of the Swiss Alps, O. A. Pfiffner, P. Lehner, P. Heitzmann, S. Mueller and A. Steck (Editors), Birkhäuser, Basel, pp. 289–304, 1997.

Schorghofer, N., and D. H. Rothman, Acausal relations between topographic slope and drainage area, Geophys. Res. Lett., 29(13), 1633, doi:10.1029/2002GL015144, 2002.

Schumm, S. A., M. P. Mosley, and W. E. Weaver, Experimental Fluvial Geomorphology, John Wiley, New York, 1987.

Seidl, M. A., and W. E. Dietrich, The problem of channel ero-sion into bedrock, Catena Suppl., 23, 101–124, 1992.

Sheperd, R. G., and S. A. Schumm, Experimental study of river incision, Geol. Soc. Am. Bull., 85, 257–268, 1974.

Simpson G., and F. Schlunegger, Topographic evolution and morphology of surfaces evolving in response to coupled flu-vial and hillslope sediment transport, J. Geophys. Res., VOL. 108, NO. B6, 2300, doi:10.1029/2002JB002162, 2003

Sklar, L., and W. E. Dietrich, River longitudinal profiles and bedrock incision models: Stream power and the influence of sediment supply, in Rivers Over Rock: Fluvial Processes in Bedrock Channels, Geophys. Monogr. Ser., vol. 107, edited by K. J. Tinkler and E. E. Wohl, pp. 237–260, AGU, Wash-ington, D.C., 1998.

Sklar, L. S., and W. E. Dietrich, Sediment and rock strength controls on river incision into bedrock, Geology, 29(12), 1087–1090, 2001.

Smith, C. E., Modeling high sinuosity meanders in a small flume, Geomorphology, 25, 19–30, 1998.

Smith, T. R., and F. P. Bretherton, Stability and the conserva-tion of mass in drainage basin evolution, Water Resour. Res., 8(6), 1506–1529, 1972.

Snyder, N. P., Bedrock channel response to tectonic, climatic, and eustatic forcing, Ph.D thesis, Dep. of Earth, Atmos., and Planet. Sci., Mass. Inst. of Technol., Cambridge, Mass., 2001.

Snyder, N. P., K. X. Whipple, G. E. Tucker, and D. J. Merritts, Landscape response to tectonic forcing: DEM analysis of stream profiles in the Mendocino triple junction region, northern California, Geol. Soc. Am. Bull., 112, 1250–1263, 2000.

Simpson, G., Role of river incision in enhancing deformation. Geology 32 (2004), 341–344.

Sobel E. and T. A. Dumitru, Exhumation of the margins of the western Tarim basin during the Himalayan orogeny, Tec-tonics, in press, 1995

Stein, R.S., G.C.P. King and J.B. Rundle, The growth of geolog-ical structures by repeated earthquakes, 2. Field examples of

continental dip-slip faults, J. Geophys. Res., 93, 13319–13331, 1988.

Summerfield, M.A. and N.J. Hulton, Natural control on fluvial denudation rates in major world drainage basins, J. Geophys. Res., 99, 13871–13883, 1994.

Talbot, C.J., and R.J. Jarvis, Age, budget and dynamics of an active salt extrusion in Iran, J. Struct. Geology, 6, 521–533, 1984.

Tapponnier, P., and P. Molnar, Active faulting and Cenozoic tectonics of the Tien Shan, Mongolia and Baykal regions, J. Geophys. Res., 84, 3425–3459, 1979.

Ter Voorde, M., Van Balen, R.T., Bertotti, G. and Cloetingh, S.A.P.L., The influence of a stratified rheology on the flexural response of the lithosphere to (un)loading by extensional faulting. Geophys. J. Int., 134, 721–735, 1998.

Toussaint, G., Burov, E., and L. Jolivet, Continental plate collision: unstable versus stable slab dynamics, Geology, 32, No. 1, 33–36, 2004a.

Toussaint G., Burov, E., and J.-P. Avouac, Tectonic evolution of a continental collision zone: a thermo mechanical numerical model, Tectonics, 23, TC6003, doi:10.1029/2003TC001604, 2004b.

Tsenn, M.C. , and N.L. Carter, Flow properties of continental lithosphere. Tectonophysics, 136, 27–63, 1987.

Tucker, G. E., and R. L. Bras, Hillslope processes, drainage density, and landscape morphology, Water Resour. Res., 34(10), 2751– 2764, 1998.

Tucker, G. E., and R. L. Bras, A stochastic approach to modeling the role of rainfall variability in drainage basin evolution, Water Resour. Res., 36(7), 1953– 1964, 2000

Turcotte, D.L., and G. Schubert, Geodynamics. Applications of continuum physics to geological problems, J. Wiley & Sons, New York, 450 p., 1982.

Vinnik, L.P. and A.M. Saipbekova, Structure of the lithosphere and asthenosphere of the Tien Shan, Annales Geophysicae, 621–626, 1984.

Vinnik, L.P., I. M. Aleshin, M. K. Kaban, S. G. Kiselev, G. L. Kosarev, S. I. Oreshin, and Ch. Reigber, Crust and Mantle of the Tien Shan from Data of the Receiver Function Tomography, Izvestiya, Physics of the Solid Earth, 42, pp. 639–651, Pleiades Publishing, Inc., 2006.

Vilotte, J.-P., M. Daignières and R. Madariaga, Numerical modeling of intraplate deformation: simple mechanical models of continental collision, J. Geophys. Res., 87, 10709–10728, 1982.

Vogt, P.R., Bermuda and Applachian-Labrador rises, common hotspot processes, Geology, 19, 41–44, 1991.

Wang J.N., B.E. Hobbs, A.Ord, T. Shimamoto, and M. Toriumi, Newtonian dislocation creep in quartzites: Implications for the rheology of the lower crust, Science, 265, 1204–1206,

Westaway, R., Evidence for dynamic coupling of surface processes with isostatic compensation in the lower crust during active extension of western Turkey, J. Geophys. Res., 99, 20203–20223, 1994.

Willett, S. D., Orogeny and orography: The effects of erosion on the structure of mountain belts, J. Geophys. Res., 104(B12), 28,957 – 28,982, 1999.

Windley, B. F., M.B. Allen, C., Zhang, Z.Y., Zhao, and G.R. Wang, Paleozoic accretion and Cenozoic redeformation of the Chinese Tien Shan range, central Asia, Geology, 18, 128–131, 1990.

Appendix A
Model of Flexural Deformation of the Competent Cores of the Brittle-Elasto-Ductile Crust and Upper Mantle

The vertical displacements of the competent layers in the crust and mantle in response to redistribution of surface and subsurface loads (Fig. 4, top) can be described by plate equilibrium equations in assumption of nonlinear rheology (Burov and Diament, 1995). We assume that the reaction of the competent layers is instantaneous (response time $dt \sim \mu_{min}/E < 10^3$ years, where μ_{min} is the minimum of effective viscosities of the lower crust and asthenosphere)

$$\frac{\partial}{\partial x}\left(\frac{\partial}{\partial x}\left(\frac{E}{12(1-v^2)}\,\widetilde{T}_e^3(\phi)\,\frac{\partial^2 w(x,t)}{\partial x^2}\right)\right.$$

$$\left.+ \widetilde{T}_x(\phi)\,\frac{\partial w(x,t)}{\partial x}\right) + p_-(\phi)\,w(x,t) - p_+(x,t) = 0$$

$$\widetilde{T}_e(\phi) = \left(\frac{\widetilde{M}_x(\phi)}{L}\left(\frac{\partial^2 w(x,t)}{\partial x^2}\right)^{-1}\right)^{1/3}$$

$$\widetilde{M}_x(\phi) = -\sum_{i=1}^{n}\sum_{j=1}^{m_i}\int_{y_{ij}^-(\phi)}^{y_{ij}^+(\phi)}\sigma_{xx}^{(j)}(\phi)\,y_i^*(\phi)\,dy \qquad (A.1)$$

$$\widetilde{T}_x(\phi) = -\sum_{i=1}^{n}\sum_{j=1}^{m_i}\int_{y_{ij}^-(\phi)}^{y_{ij}^+(\phi)}\sigma_{xx}^{(j)}(\phi)\,dy$$

$$\sigma_{xx}^{(j)}(\phi) = sign(\varepsilon_{xx})\,\mathbf{min}\left(|\sigma^f|,\,\sigma_{xx}^{e(j)}(\phi)\right)$$

$$\sigma_{xx}^{e(j)}(\phi) = y_i^*(\phi)\,\frac{\partial^2 w(x,t)}{\partial x^2}\,E_i(1-v_i^2)^{-1}$$

where $w = w(x,t)$ is the vertical plate deflection (related to the regional isostatic contribution to tectonic uplift du_{is} as $du_{is} = w(x,t) - w(x,t-dt)$), $\phi \equiv \{x,y,w,w',w'',t\}$, y is downward positive, $y_i^* = y - y_{ni}(x)$, y_{ni} is the depth to the ith neutral (i.e., stress-free, $\sigma_{xx}|_{y_i^*=0}$) plane; $y_i^-(x) = y_i^-$, $y_i^+(x) = y_i^+$ are the respective depths to the lower and upper low-strength interfaces (see Fig. A). σ^f is defined from Eqs. (10–11). n is the number of mechanically decoupled competent layers; m_i is the number of "welded" (continuous σ_{xx}) sub-layers in the ith detached layer. p_-w is a restoring stress ($p_- \sim (\rho_m - \rho_{c1})g$) and p^+ is a sum of surface and subsurface loads. The most important contribution to p^+ is from the load of topography, that is, $p^+ \sim \rho g h(x,t)$, where the topographic height $h(x,t)$ is defined as $h(x,t) = h(x,t-dt) + dh(x,t) = h(x,t-dt) + du(x,t) - de(x,t)$, where $du(x,t)$ and $de(x,t)$ are, respectively tectonic uplift/subsidence and denu-

dation/sedimentation at time interval $(t–dt, t)$, counted from sea level. The thickness of the ith competent layer is $y_i^+ – y_i^- = \Delta h_i(x)$. The term w'' in (A.1) is inversely proportional to the radius of plate curvature $R_{xy} \approx –(w'')^{-1}$. Thus, the higher is the local curvature of the plate, the lower is the local integrated strength of the lithosphere. The integrals in (A.1) are defined through the constitutive laws (6–9) and Eq. (10–11) relating the stress σ_{xx} and strain $\varepsilon_{xx} = \varepsilon_{xx}(\phi)$ in a given segment $\{x,y\}$ of plate. The value of the unknown function $\tilde{T}_e(\phi)$ has a meaning of a "momentary" effective elastic thickness of the plate. It holds only for the given solution for plate deflection w. $\tilde{T}_e(\phi)$ varies with changes in plate geometry and boundary conditions. The effective integrated strength of the lithosphere (or $T_e = \tilde{T}_e(\phi)$) and the state of its interiors (brittle, elastic or ductile) depends on differential stresses caused by local deformation, while stresses at each level are constrained by the YSE. The nonlinear Eqs. (A.1) are solved using an iterative approach based on finite difference approximation (block matrix presentation) with linearization by Newton's method [Burov and Diament, 1992]. The procedure starts from calculation of elastic prediction $w_e(x)$ for $w(x)$, that provides predicted $w_e(x)$, $w_e'(x)$, w_e'' used to find subiteratively solutions for $y_{ij}^-(\phi)$, $y_{ij}^+(\phi)$, and $y_{ni}(\phi)$ that satisfy Eqs. (5), (6), (7), (10). This yields corrected solutions for $\tilde{M}_x$ and $\tilde{T}_x$ which are used to obtain $\tilde{T}_e$ for the next iteration. At this stage we use gradual loading technique to avoid numerical oscillations. The accuracy is checked directly on each iteration, through back-substitution of the current solution to Eq. (A.1) and calculation of the discrepancy between the right and left sides of Eq. (A.1). For the boundary conditions on the ends of the plate we use commonly inferred combination of plate-boundary shearing force $Q_x(0)$,

$$\tilde{Q}_x(\phi) = -\sum_{i=1}^{n}\sum_{j=1}^{m_i} \int_{y_{ij}^-(\phi)}^{y_{ij}^+(\phi)} \sigma_{xy}^{(j)}(\phi)dy \qquad (A.2)$$

and plate boundary moment $M_x(0)$ (in the case of broken plate) and $w = 0$, $w' = 0$ (and $h = 0$, $\partial h/\partial x = 0$) at $x \rightarrow \pm\infty$. The starting temperature distribution and yield-stress profiles (see above) are obtained from the solution of the heat transfer problem for the continental lithosphere of Paleozoic thermotectonic age, with average Moho thickness of 50 km, quartz-controlled crust and olivine-controlled upper mantle, assuming typical horizontal strain rates of $\sim 0.1 \div 10 \times 10^{-15}$ s^{-1}. (Burov et al., 1993; 1995). These parameters roughly resemble the Tien Shan and Tarim basin (Fig. 1a).

Burov and Diament (1995) have shown that the flexure of the continental lithosphere older than 200–250 My is predominantly controlled by the mechani-

cal portion of mantle lithosphere (depth interval between T_c and h_2). Therefore, we associate the deflection of Moho with the deflection of the entire lithosphere (analogously to Lobkovsky and Kerchman, 1991; Kaufman and Royden, 1994; Ellis et al., 1995). Indeed, the effective elastic thickness of the lithosphere (T_e) is approximately equal to $\sqrt[3]{T_{ec}^3 + T_{em}^3}$, where T_{ec} is the effective elastic thickness of the crust and T_{em} is the effective elastic thickness of the mantle lithosphere (e.g., Burov and Diament, 1995). $\lim \sqrt[3]{T_{ec}^3 + T_{em}^3} \approx \max(T_{ec}, T_{em})$. T_{ec} cannot exceed h_{c_1}, that is 15–20 km (in practice, $T_{ec} \leq 5$–10 km). T_{em} cannot exceed $h_2 – T_c \sim 60$–70 km. Therefore $T_e \approx T_{em}$ which implies that total plate deflection is controlled by the mechanical portion of the mantle lithosphere.

Appendix B
Model of Flow in the Ductile Crust

As it was already mentioned, our model of flow in the low viscosity parts of the crust is similar to that formulated by Lobkovsky (1988), Lobkovsky and Kerchman (1991) (hereafter referred as L&K), or Bird (1991). However, our formulation can allow computation of different types of flow ("symmetrical", Poiseuille, Couette) in the lower crust (L&K considered Couette flow only). In the numerical experiments shown in this paper we will only consider cases with a mixed Couette/Poiseuille/symmetrical flow, but we first tested the same formulation as L&K. The other important difference with L&K's models is, naturally, the use of realistic erosion laws to simulate redistribution of surface loads, and of the realistic brittle-elastic-ductile rheology for modeling the response of the competent layers in the lithosphere.

Tectonic uplift $du(x,t)$ due to accumulation of the material transported through ductile portions of the lower and upper crust $(dh(x,t) = du(x,t) – de(x,t))$ can be modelled by equations which describe evolution of a thin subhorizontal layer of a viscous medium (of density ρ_{c_2} for the lower crust) that overlies a non-extensible pliable basement supported by Winkler forces (i.e., flexural response of the mantle lithosphere which is, in-turn, supported by hydrostatic reaction of the astenosphere) (Batchelor, 1967; Kusznir and Matthews, 1988; Bird and Gratz, 1990; Lobkovsky and Kerchman, 1991; Kaufman and Royden, 1994).

The normal load, which is the weight of the topography $p_+(x)$ and of the upper crustal layer (thickness h_{c_1} and density ρ_{c_1}) is applied to the surface of the lower crustal layer through the flexible competent upper crustal layer. This internal ductile crustal layer of variable thickness $\Delta h_{c_2} = \Delta h_0(x,0) + \tilde{h}(x) + w(x)$ is regionally compensated by the strength of the underlying competent mantle lithosphere (with density ρ_m).

Variation of the elevation of the upper boundary of the ductile layer ($d\tilde{h}$) with respect to the initial thickness ($\Delta h_0(x,0)$) leads to variation of the normal load applied to the mantle lithosphere. The regional isostatic response of the mantle lithosphere results in deflection (w) of the lower boundary of the lower crustal layer, that is the Moho boundary, which depth is $h_c(x,t) = T_c(x,t) = \Delta h_{c2} + y_{13}$ (see Table 1a). The vertical deflection w (Eq. A.1) of the Moho depends also on vertical undulation of the elastic-to-ductile crust interface y_{13}.

The absolute value of $\tilde{h}$ is not equal to that of the topographic undulation h by two reasons: first, h is effected by erosion; second, $\tilde{h}$ depends not only on the uplift of the upper boundary of the channel, but also on variation of the thickness of the competent crust given by value of $y_{13}(x)$. We can require $\tilde{h}(x,t) - \tilde{h}(x,t-dt) = du - dy_{13}$. Here $dy_{13} = y_{13}(\phi,t) - y_{13}(\phi, t-dt)$ is the relative variation in the position of the lower boundary of the elastic core of the upper crust due to local changes in the level of differential (or deviatoric) stress (Fig. 5a). This flexure- and flow-driven differential stress can weaken material and, in this sense, "erode" the bottom of the strong upper crust. The topographic elevation $h(x,t)$ can be defined as $h(x,t) = h(x,t-dt) + d\tilde{h} - de(t) - dy_{13}$ where dy_{13} would have a meaning of "subsurface or thermomechanical erosion" of the crustal root by local stress.

The equations governing the creeping flow of an incompressible fluid, in Cartesian coordinates, are:

$$-\frac{\partial \sigma_{xx}}{\partial x} + \frac{\partial \tau_{xy}}{\partial y} + F_x = 0; \; -\frac{\partial \sigma_{yy}}{\partial y} + \frac{\partial \tau_{xy}}{\partial x} + F_y = 0$$

$$\sigma_{xx} = -\tau_{xx} + p = -2\mu \frac{\partial u}{\partial x} + p$$

$$\sigma_{xy} = \tau_{xy} = \mu\left(\frac{\partial u}{\partial y} + \frac{\partial v}{\partial x}\right) \qquad \text{(B.1a)}$$

$$\sigma_{yy} = -\tau_{yy} + p = -2\mu \frac{\partial v}{\partial x} + p$$

$$\frac{\partial u}{\partial x} + \frac{\partial v}{\partial y} = 0 \qquad \text{(B.1b)}$$

$$\mu = \frac{\sigma}{2\dot{\varepsilon}}$$
$$\dot{\varepsilon} = \sigma^n A^* \exp(-H^*/RT) \qquad \text{(B.1c)}$$

where μ is the effective viscosity, p is pressure, u and v are the horizontal and vertical components of the velocity $\mathbf{v}$, respectively. F is the body force. $u = \partial\psi/\partial x$ is the horizontal component of velocity of the differential movement in the ductile crust, $v = -\partial\psi/\partial x$ is its vertical component; and $\partial u/\partial y = \dot{\varepsilon}_{c20}$ is a component of shear strain rate due to the differential movement

of the material in the ductile crust (the components of the strain rate tensor are consequently: $\dot{\varepsilon}_{11} = 2\partial u/\partial x$; $\dot{\varepsilon}_{12} = \partial u/\partial y + \partial v/\partial x$; $\dot{\varepsilon}_{22} = 2\partial v/\partial y$).

Within the low viscosity boundary layer of the lower crust, the dominant basic process is simple shear on horizontal planes, so the principal stress axes are dipped approximately $\pi/2$ from x and y (hence, σ_{yy} and σ_{xx} are approximately equal). Then, the horizontal component of quasi-static stress equilibrium equation $div\boldsymbol{\sigma} + \rho g = 0$, where tensor $\boldsymbol{\sigma}$ is $\boldsymbol{\sigma} = \boldsymbol{\tau} - P\mathbf{I}$ ($\mathbf{I}$ is identity matrix), can be locally simplified yielding thin layer approximation (e.g., Lobkovsky, 1988; Bird and Gratz, 1990):

$$\frac{\partial \tau_{xy}}{\partial y} = \frac{\partial p}{\partial x} - F_x = -\frac{\partial \tau_{yy}}{\partial x} \qquad \text{B.2)}$$

A basic effective shear strain-rate can be evaluated as $\dot{\varepsilon}_{xy} = \sigma_{xy}/2\mu_{eff}$, therefore, according to the assumed constitutive relations, horizontal velocity u in the lower crust is:

$$u(\tilde{y}) = \int_0^{\tilde{y}} 2\dot{\varepsilon}_{xy}\partial\tilde{y} + C_1 =$$
$$= \int_0^{\tilde{y}} 2^n A^* \exp(-H^*/RT(y)) \left|\tau_{xy}\right|^{n-1} \tau_{xy}\, \partial\tilde{y} + C_1 \qquad \text{(B.3)}$$

Here $\tilde{y} = y - y_{13}$. $y_{13} = y_{13}(\phi)$ is the upper surface of the channel defined from solution of the system (A.1). C_1 is a constant of integration defined from the velocity boundary conditions. τ_{xy} is defined from vertical integration of Eq. (B.2). The remote conditions $h = 0$, $\partial h/\partial x = 0$, $w = 0$, $\partial w/\partial x = 0$ for the strong layers of the lithosphere (Appendix A) are in accordance with the condition for ductile flow: at $x \to \infty$ $u_{c2}^+ = u_c$; $u_{c2}^- = u_m$; $\partial p/\partial x = 0$, $\partial p/\partial y = \bar{\rho}_c g$; $p = P_0$.

There is also an "inherent" boundary condition, free flow on the far ends of the ductile channel. From the formal point of view, the conservation of mass in the channel is not observed under this condition. However, it is not crucial in the particular case because the channel is long and has flexible walls (in the experiments, 30–50 times longer than its thickness and 10 times longer than total horizontal shortening). Therefore, local perturbations in the flow beneath the mount and basins do not reach the remote end(s) of the channel. In a general case, it is even reasonable to assume that the horizontal tectonic deformation on the ends of the plate is transmitted through the strong parts of the crust, while the low viscosity crust may flow in- or out of the system. In the particular numerical experiments described here, we checked the balance of volume and found the loss of mass to be negligible (< 5% of the entered volume).

In the trans-current channel flow the major perturbation to the stress (pressure) gradients is caused by slopes of crustal interfaces $\alpha \sim \partial \tilde{h}/\partial x$ and $\beta \sim \partial w/\partial x$. These slopes are controlled by flexure, isostatic re-adjustments, surface erosion, and by "erosion" (weakening) of the interfaces by stress and temperature. The later especially concerns the upper crustal interface. In the assumption of small plate defections, the horizontal force associated with variation of the gravitational potential energy due to deflection of Moho (w) is $\rho_{c_2} g \tan(\beta) \sim \rho_{c_2} g \sin(\beta) \sim \rho_{c_2} g \partial w/\partial x$; the vertical component of force is respectively $\sim \rho_{c_2} g \cos(\beta) \sim \rho_{c_2} g (1 - \partial w/\partial x) \sim \rho_{c_2} g$. The horizontal and vertical force components due to slopes of the upper walls of the channel are respectively $\rho_{c_2} g \tan(\alpha) \sim \rho g \sin(\alpha) \sim \rho_{c_2} g d\tilde{h}/dx$ and $\rho_{c_2} g \cos(\beta) \sim \rho_{c_2} g (1 - d\tilde{h}/dx)$. The equation of motion (Poiseuille/Couette flow) for a thin layer in the approximation of lubrication theory will be:

$$\frac{\partial \tau_{xy}}{\partial y} = -\frac{\partial \tau_{yy}}{\partial x} \approx \frac{\partial p}{\partial x} - \rho_{c2} g - \frac{\partial(\tilde{h} + w)}{\partial x}$$

$$\frac{\partial \tau_{yy}}{\partial y} + \frac{\partial \tau_{yx}}{\partial x} - \frac{\partial p}{\partial y} \approx -\rho_{c2} g \left(1 - \frac{\partial(\tilde{h} + w)}{\partial x}\right) \qquad \text{(B.4)}$$

$$\frac{\partial u_{c2}}{\partial x} + \frac{\partial v_{c2}}{\partial y} = 0$$

where pressure p is $p \approx P_0(x) + \bar{\rho}_c g(\tilde{y} + y_{13} + h)$; h is taken to be positive above sea-level; $\bar{\rho}_c$ is averaged crustal density.

In the simplest case of local isostasy, w and $\partial w/\partial x$ are approximately $\bar{\rho}_c/\Delta(\bar{\rho}_c - \rho_m) \sim 4$ times greater than $\tilde{h}$ and $d\tilde{h}/dx$, respectively. The pressure gradient due to Moho depression is $\rho_m g \partial(\tilde{h}+w)/\partial x$. "Correction" by the gradient of the gravitational potential energy density of crust yields $(\rho_m - \bar{\rho}_c) g \partial(\tilde{h}+w)/\partial x$ for the effective pressure gradient in the crust, with w being equal to $\tilde{h}((\rho_m - \bar{\rho}_c)/\rho_m)$. In the case of regional compensation, when the mantle lithosphere is strong, the difference between $\tilde{h}$ and w can be 2–3 times less. To obtain w, we solve the system of Eq. (A.1). Substitution of Eq. (B.3) to Eq. (B.4) gives:

$$\frac{\partial \tau_{xy}}{\partial y} \approx \frac{\partial p}{\partial x} - \rho_{c2} g \frac{\partial(\tilde{h} + w)}{\partial x}$$

$$\frac{\partial p}{\partial y} \approx \rho_{c2} g \left(1 - \frac{\partial(\tilde{h} + w)}{\partial x}\right)$$

$$\frac{\partial u}{\partial y} = 2^n A^* (-H^*/RT) |\tau_{xy}|^{n-1} \tau_{xy} \qquad \text{(B.5)}$$

$$\frac{\partial v}{\partial y} = -\frac{\partial u}{\partial x}$$

The value $1 - \partial(\tilde{h}+w)/\partial x \approx 1$ due to the assumption of small deflections ($w/T_e \ll L/T_e$, $\tilde{h} \sim 0.2$–$0.5w$, where L is the length of the plate). One has to note that strain rates of the lower crustal rocks (assuming quartz-controlled rheology) increase approximately by a factor of 2 for each $\sim 20°C$ of temperature increase with depth [e.g., Bird, 1991]. This results in that the flow is being concentrated near the Moho, and the effective thickness of the transporting channel is much less than Δh_{c_2}.

Depth integration of Eq. (B.5) gives us the longitudinal and vertical components of the basic material velocity in the lower crust. For example, we have:

$$u = \int_0^{h_{c2} - y_{13}} 2^n A^* \exp(-H^*/RT(\tilde{y})) |\tau_{xy}|^{n-1} \tau_{xy} \, \partial \tilde{j}$$

$$v \Big|_0^{h_{c2} - y_{13}} = -\frac{\partial}{\partial x} \int_0^{h_{c2} - y_{13}} u \partial \tilde{y} \approx \frac{\partial(\tilde{h} + w)}{\partial t} \qquad \text{(B.6)}$$

The later equation gives the variation of thickness of the ductile channel in time (equal to the difference between the vertical flow at the top and bottom boundaries). Lobkovsky (1988) (see also Lobkovsky and Kerchman, 1991), Bird (1991) already gave an analytical solution for evolution of the topography dh/dt due to ductile flow in the crustal channel for the case of local isostatic equilibrium (zero strength of the upper crust and mantle). Kaufman and Royden (1994) provide a solution for the case of elastic mantle lithosphere but for Newtonian rheology. In our case, the irregular time-dependent load is applied on the surface, and nonlinear rheology is assumed both for the ductile and competent parts of the lithosphere. Hence, no analytical solution for u and v can be found and we choose to obtain u and v through numerical integration.

The temperature which primarily controls the effective viscosity of the crust, is much lower in the uppermost and middle portions of the upper crust (first 10–15 km in depth). As a result, the effective viscosity of the middle portions of the upper crust is 2–4 orders higher than that of the lower crust (10^{22} to 10^{23} Pa s compared to 10^{18} to 10^{20} Pa s, Eqs. (7, 8)). Therefore, we can consider the reaction of the lower crust to deformation of the upper crust as rapid. The uppermost parts of the upper crust are brittle (Figs. 2 and 5), but in calculation of the flow they can be replaced by some depth-averaged viscosity defined as $\bar{\mu}_{eff} = \bar{\sigma}^d/2\dot{\varepsilon}$ (Beekman, 1994). In spite of some negligence by the underlying principles, this operation does not introduce significant uncertainties to the solution because the thickness of the "brittle" crust is only 1/4 of the thickness of the competent crust. Analogously to the ductile (mostly lower) crust, we can extend the solution of the equations for the horizontal f low to the stronger upper portions of the upper crust. However, due to high-

er viscosity, and much lower thickness of the strong upper crustal layers, one can simply neglect the perturbations of the flow velocity there and assume that $v = v(y \leq y_{13})$, $u = u(y \leq y_{13})$ (y is downward positive). For numerical reasons, we cut the interval of variation of the effective viscosity at 10^{19} to 10^{24} Pa s.

Solution for the channel flow implies that the channel is infinite in both directions. In our case the channel is semi-infinite, because of the condition $u = 0$ at $x = 0$ beneath the axis of the mount. Thin flow approximation thus cannot be satisfied beneath the mount because of the possibility of a sharp change of its thickness. Therefore, we need to modify the solution in the vicinity of $x = 0$. This could be done using a solution for the ascending flow for $x < a_l$. An analytical formulation for the symmetric flow in the crust and definition for the critical distance a_l are given in Appendix C. There we also explain how we combine the solution for the ascending symmetric flow beneath the axis of the mountain range with the asymptotic solution for Poiseuille/Couette flow for domains off the axis. A similar approach can be found in literature dealing with cavity-driven problems (e.g., Hansen and Kelmanson, 1994). However, most authors (Lobkovsky and Kerchman, 1991; Bird and Gratz, 1990) ignore the condition $u = 0$ at $x = 0$ and the possibility of large thickness variations and simply considered a thin infinite channel.

Boundary Conditions

We have chosen simplest boundary conditions corresponding to the flow approximations. Thus, the velocity boundary conditions are assumed on the upper and bottom interfaces of the lower crustal channel. Free flow is the lateral boundary condition. The velocity condition also could be combined with a pre-defined lateral pressure gradient.

A link between the competent parts of the lithosphere and flow in the ductile parts is effectuated through the conditions of continuity of stress and velocity.

The problem of choice of boundary conditions for continental problems has no unique treatment. Most authors apply vertically homogeneous stress, force or velocity on the left and right sides of the model plate, Winkler-type restoring forces as bottom vertical condition, and free surface/normal stress as a upper boundary condition (e.g., England and McKenzie, 1983; Chery et al., 1991; Kusznir, 1991). Other authors use shear traction (velocity/stress) at the bottom of the mantle lithosphere (e.g. Ellis et al., 1995). Even choice between stress and force boundary conditions leads to significantly different results. Yet, the only observation that may provide an idea on the boundary conditions in nature comes from geodetic measurements and kinematic evaluations of surface strain rates and

velocities. The presence of a weak lower crust leads to the possibility of differential velocity, strain partitioning between crust and mantle lithosphere and to possibility of loss of the material from the system due to outflow of the ductile crustal material (e.g. Lobkovsky and Kertchman, 1991; Ellis et al., 1995). Thus the relation between the velocities and strain rates observed at the surface with those on the depth is unclear. It is difficult to give preference to any of the mentioned scenarios. We have thus chosen the simplest one.

Appendix C
Analytical Formulation
for Ascending Crustal Flow

In the general case of non-inertial flow (low Reynolds number), a symmetric flow problem (flow ascending beneath the mount) can be resolved from the solution of the system of classical viscous flow equations (Fletcher, 1988; Hamilton et al., 1995):

$$0 = \rho_{c2} F_x - \frac{dp}{dx} + \frac{\partial}{\partial y}\left(2\mu\left(\left(\frac{\partial u}{\partial y} + \frac{\partial v}{\partial x}\right)\right)\right)$$

$$0 = \rho_{c2} F_y - \frac{dp}{dy} + \frac{\partial}{\partial x}\left(2\mu\left(\left(\frac{\partial u}{\partial y} + \frac{\partial v}{\partial x}\right)\right)\right) \qquad \text{(C.1)}$$

$$\frac{\partial u}{\partial x} + \frac{\partial v}{\partial y} = 0$$

We define $\partial p/\partial x \approx \partial\tilde{p}/\partial x + g(\rho_{c2}\partial w/\partial x + \rho_{c1}\partial(du)/\partial x)$, $du \approx d\tilde{h}$ and $\partial p/\partial y = \partial\tilde{p}/\partial y - g\rho_{c2}$ where $\tilde{p}$ is dynamic, or modified pressure. The flow is naturally assumed to be Couette/Poiselle flow away from the symmetry axis (at a distance a_l). a_l is equal to 1–2 thicknesses of the channel, depending on channel thickness-to-length ratio. In practice a_l is equal to the distance at which the equivalent elastic thickness of the crust (T_{ec}) becomes less than ~5 km due to flexural weakening by elevated topography. For this case, we can neglect the elasticity of the upper surface of the crust and use the condition of the stress-free upper surface. The remote feeding flux q at $x \rightarrow \pm a_l$ is equal to the value of flux obtained from depth integration of the channel source (Couette flow), and free flow is assumed as a lateral boundary condition. The flux q is determined as $q \sim \int u dy$ (per unit length in z direction). This flux feeds the growth of the topography and deeping of the crustal root. Combination of two flow formulations is completed using the depth integrated version of the continuity equation and global continuity equation [Huppert, 1982] :

$$\int \frac{\partial v}{\partial y}\,dy + \frac{\partial}{\partial x}\left(\int u\,dy\right) = 0 = \frac{\partial(\tilde{h}+w)}{\partial t} + \frac{\partial q}{\partial x}$$

$$q\big|_{x=a_l,\,x\le a_l} = q\big|_{x=a_l,\,x\ge a_l}$$

$$\underbrace{\int_o^{a_l(\phi)}(\tilde{h}+w)\,dx}_{\text{ascending flow}} + \underbrace{\int_{a_l(\phi)}^{\infty}(\tilde{h}+w)\,dx}_{\text{channel flow}} = qt^{\theta}, \qquad (C.2)$$

where θ is some non-negative constant, $\theta = 1$ in our case. With that we can combine solutions for horizontal flow far off the mount axis (Couette/Poiseuille flow) with solutions for ascending flow below the mount (e.g., Hansen and Kelmanson, 1994). Assuming a new local coordinate system $x^{\prime} = x$, $y^{\prime} = -y - (h_{c2}+(h_{c2}-y_{13})/2)$, the boundary conditions for the flow ascending near the symmetry axis would be $u = v = 0$; $du/dy^{\prime} = 0$ at $x^{\prime} = 0$, $y^{\prime} = 0$ (beneath the mount axis). Then, we assume that the viscosity (μ) in the ascending flow is constant and equal to $\bar{\mu} = \bar{\mu}(a_l)$ where $\bar{\mu}(a_l)$ is the depth-averaged value of the effective non-linear viscosity defined from the solution for the channel flow (Appendix B) at distance $x = a_l$. Use of constant viscosity is, however, not a serious simplification for the problem as a whole, because a_l is small and thus this simplification applies only to a small fraction of the problem.

Introducing the vorticity function $\xi = \mathrm{rot}\,\mathbf{v} = \partial u/\partial y - \partial v/\partial x = \nabla^2\psi$, assuming laminar flow, we then write Stoke's equations as (Talbot and Jarvis, 1984; Fletcher, 1988; Hamilton et al., 1995):

$$\mu\frac{\partial \xi}{\partial x} = \frac{\partial p}{\partial y}$$

$$\mu\frac{\partial \xi}{\partial y} = -\frac{\partial p}{\partial x} \qquad (C.3)$$

$$\xi = \nabla^2\psi$$

At the upper surface of the fluid, streamline $\psi = 0$, is taken to be stress-free (low T_{ec}, see above) which leads to the following conditions: $p\cos 2\alpha = 2\mu\partial^2\psi/\partial y^{\prime}\partial x$; $p\sin 2\alpha = \mu(\partial^2\psi/\partial x^2 - \partial^2\psi/\partial y^{\prime 2})$. Here α is downward inclination of the surface to the horizontal. Finally, the symmetry of the flow requires $\psi(-x,y^{\prime}) = -\psi(x,y^{\prime})$.

The general solution in dimensionless variables (Talbot and Jarvis, 1984): $X = h_{max}x^{\prime}$; $Y = h(0)y^{\prime}$; $p = (\mu q/\pi h_{max}^2)p^{\prime}$; $\psi = (q/\pi)\psi^{\prime}$, where h_{max} is the maximum height of the free surface, is:

$$\psi = \tan^{-1} X/Y + XY/(X^2+Y^2) +$$
$$+ \sum_{n=0}^{\infty}(-1)^n(n+1)Y^{2n+2}((2n+2)!)^{-1}f^{(2n)}(X) +$$
$$+ \sum_{n=0}^{\infty}(-1)^n(n+1)Y^{2n+3}((2n+3)!)^{-1}\gamma^{(2n)}(X);$$

$$p = K - \lambda Y + 2(Y^2 - X^2)/(X^2+Y^2)^2 + \qquad (C.4)$$
$$+ \sum_{n=0}^{\infty}(-1)^n X^{2n+1}((2n+1)!)^{-1}f^{(2n+1)}(X) - G(X) +$$
$$+ \sum_{n=0}^{\infty}(-1)^n Y^{2n+2}((2n+2)!)^{-1}\gamma^{(2n+1)}(X)$$

$$G(X) = \int_0^x \gamma(s)\,ds$$

f and γ are arbitrary functions of expansion series and $f^{(j)}$, $\gamma^{(j)}$ are their j^{th} derivatives, $\lambda = \pi\rho g h_{max}^3/\mu q$, K is constant. γ and f are determined numerically because the expressions for ψ and p are nonlinear and cannot be solved analytically. The calculation of ψ and p is done on the assumption of small curvature of the free surface which allows linear approximation of γ and f, i.e., as $\gamma = AX$ and $f = BX$. Then the free surface can be searched in the form of a parabolic function , e.g., $\tilde{h} \sim C - DX^2$ (Talbot and Jarvis, 1984).

The assumptions of constant viscosity and stress-free upper surface are questionable. To avoid this problem, we can solve Eqs. (B.1) for the ascending flow analogously to how it was done for the channel flow (Appendix B). The solution to Eq. (B.1) in the case of the ascending flow can be obtained assuming $\mu = \mu(y)$, $\tau_{xy}(x,0) \ne 0$ and $U = u$ and $V = \Phi(y)$ where $\Phi(y)$ is to be determined. Here we simplify Eq. (B.1c) by assuming that the viscosity is only depth dependent, which is a better approximation to the nonlinear law (8) than the assumption of constant viscosity.

The primary boundary conditions are $U(0,y) = 0$ (symmetric flow), $\tau_{xy}(x,y^*) = 0$ (assumption of the existence of a shear-free surface at some depth y^*, e.g., depth of compensation), $\tau_{xy}(x,0) = \tau_e$, $p(x,0) = \bar{\rho}_c g(h+y_{13})$ (shear stress and pressure continuity on the boundary with the overlying competent upper crustal layer of effective thickness y_{13}).

From $U(0,y) = 0$, (B.1a), $v = \Phi(y)$, we get:

$$U = x\partial\Phi(y)/\partial y;$$
$$\sigma_{xx,yy} = \pm 2\mu\partial\Phi(y)/\partial y; \ \tau_{xy} = x\mu\partial^2\Phi(y)/\partial y^2. \qquad (C.5)$$

With the assumption that $y^* \ll a_l$ and from (B.1a) this yields:

$$\partial^2\tau_{xy}/\partial x^2 - \partial^2\tau_{xy}/\partial y^2 + 2\partial^2\sigma_{xx}/\partial x\partial y -$$
$$-\partial Fx/\partial y + \partial Fy/\partial x = 0 \qquad (C.6)$$

which provides the expression for $\Phi(y)$ ($\partial F_x/\partial y$ and $\partial F_y/\partial x \approx 0$):

$$\partial^2(\mu\partial^2\Phi(y)/\partial y^2)\partial y^2 = 0, \text{ or } \partial^2\tau_{yy}/\partial y^2 = 0 \qquad (C.7)$$

With the conditions $\tau_{xy}(x,y^*) = 0$, $\tau_{xy}(x,0) = \tau_e$ and under assumption that $\partial y^*/\partial x$ is small, we can obtain: $\tau_{xy}(x,y) \approx \tau_e(1-y/y^*)$ and $p(x,y) \approx x^2\partial(\mu\partial^2\Phi(y)/\partial y^2)\partial y + C_1(y)$. $C_1(y)$ is to be found from the boundary conditions on p (Davies, 1994).

Since the expressions for stress are defined, the velocities U and V can be obtained from integration of Eqs. (B.1a,b) relating stress components and du/y, dv/y. We have to determine the constants of integration in a way providing continuity with the solution for the channel flow at $x = a_l$. For that we define the boundary conditions at $x = \pm a_l$: $U(\pm a_l, y) = u_l$; $V(\pm a_l, y) = v_l(\pm a_l, y)$ (where u_l and v_l are provided by the solution for channel flow).

As pointed out by Davies (1994), it is impossible to provide an analytical or simplified semi-analytical solution for the case when the viscosity μ is defined exactly through the power law (8).

Appendix D
Numerical Algorithm for the Full Thermo-Mechanical Model

This mixed finite-element volume/finite difference code Parovoz is based on the FLAC technique (Cundall, 1989). It solves simultaneously Newtonian dynamic equations of motion (A1), in a Lagrangian formulation, coupled with visco-elasto-plastic constitutive equations (A2), heat transport equations (A3), and state equation (A4) (see Appendix A, (Burov et al., 2001; Le Pourhiet et al., 2004) for details concerning numerical implementation).

$$\left\langle \rho \frac{\partial \mathbf{v}}{\partial t} \right\rangle - div\boldsymbol{\sigma} - \rho\mathbf{g} = 0 \qquad (D1)$$

$$\frac{D\sigma}{Dt} = F(\sigma, \varepsilon, \mathbf{v}, \nabla\mathbf{v}, \dots T \dots) \qquad (D2)$$

$$\rho C_p\partial T/\partial t + \mathbf{v}\nabla T - k_c div(\nabla T) - H_r - \\ -frac\times\sigma_{II}\partial\varepsilon_{II}/\partial t = 0 \qquad (D3)$$

assuming adiabatic temperature dependency for density and Boussinesq approximation for thermal body forces:

$$\rho = \rho_0 (1 - \alpha\Delta T) \qquad (D4)$$

Here $\mathbf{v}$, $\boldsymbol{\sigma}$, $\mathbf{g}$, k_c are the respective terms for velocity, stress, acceleration due to body forces, and thermal conductivity. The brackets in Eq. (A1) specify conditional use of the related term: in quasi-static mode, the inertia is dumped using inertial mass scaling (Cundall, 1989). The terms t, ρ, C_p, T, H_r, α, $frac\times\sigma_{II}\partial\varepsilon_{II}/\partial t$ designate respectively time, density, specific heat, temperature, internal heat production, thermal expansion coefficient, and shear heating term moderated by experimentally defined *frac* multiplier (*frac* was set to 0 in our experiments). The terms $\partial/\partial t$, $D\sigma/Dt$, F are a time derivative, an objective (Jaumann) stress time derivative, and a functional, respectively. In the Lagrangian framework, the incremental displacements are added to the grid coordinates allowing the mesh to move and deform with the material. This enables solution of large-strain problems locally using small-strain formulation: on each time step the solution is obtained in local coordinates, which are then updated in the large strain mode. Volume / density changes due to phase transitions are accounted via application of equivalent stresses to affected material elements.

Solution of Eq. (A1) provides velocities at mesh points used for computation of element strains and of heat advection $\mathbf{v}\nabla T$. These strains are used in Eq. (A2) to calculate element stresses, and the equivalent forces are used to compute velocities for the next time step.

All rheological terms are implemented explicitly. The rheology model is serial viscous-elastic-plastic (Table 1). The plastic term is given by explicit Mohr-Coulomb plasticity (non-associative with zero dilatency) assuming a linear Navier-Coulomb criterion. We imply internal friction angle ϕ of 30° and maximal cohesion S of 20 Mpa, which fit best the experimental Byerlee's law of rock failure (Byerlee, 1978):

$$\tau = S + \sigma_n \, tg \, \phi \qquad (D5)$$

where τ is the shear stress and σ_n is the normal stress. Linear cohesion softening is used for better localization of plastic deformation ε_p ($S(\varepsilon_p) = S_0 \min (0, 1 - \varepsilon_p/\varepsilon_{p0})$ where ε_{p0} is 0.01).

The ductile-viscous term is represented by nonlinear power law with three sets of material parameters (Table 1) that correspond to the properties of four lithological layers: upper crust (quartz), middle-lower crust (quartz-diorite), mantle, and asthenosphere (olivine):

$$\mu_{\text{eff}} = \left(\frac{\partial\varepsilon}{\partial t}\right)_{II}^{d(1-n)/n} (A^*)^{-1/n} \exp (H/nRT) \qquad (D6)$$

where $\left(\dfrac{\partial\varepsilon}{\partial t}\right)_{II}^{d} = \left(Inv_{II}\left(\dfrac{\partial\varepsilon_{ij}}{\partial t}\right)\right)^{\frac{1}{2}}$

is the effective strain rate and $A^* = \frac{1}{2}A\cdot3^{(n+1)/2}$ is the material constant, H is the activation enthalpy, R is the

gas constant, n is the power law exponent (Table 1b). The elastic parameters (Table 1a) correspond to commonly inferred values from Turcotte and Schubert (1982).

Surface processes are taken into account by diffusing (D7) the topographic elevation h of the free surface along x using conventional Culling erosion model (Culling, 1960) with a diffusion coefficient k.

$$\frac{\partial^2 h}{\partial t^2} = k\frac{\partial^2 h}{\partial x^2} \qquad\qquad (D7)$$

This simple model is well suited to simulate fan deltas, which can be taken as a reasonably good analogue of typical foreland basin deposits. This model is not well adapted to model slope-dependent long-range sedimentation, yet, it accounts for some most important properties of surface processes such as dependency of the erosion/sedimentation rate on the roughness of the relief (surface curvature).

PARA(O)VOZ allows for large displacements and strains in particular owing to an automatic remeshing procedure, which is implemented each time the mesh becomes too destorted to produce accurate results. The remeshing criterion is imposed by a critical angle of grid elements. This angle is set to 10° to reduce frequency of remeshing and thus limit the associated numerical diffusion. The numerical diffusion was effectively constrained by implementation of the passive marker algorithm. This algorithm traces passively moving particles that are evenly distributed in the initial grid. This allows for accurate recovering of stress, phase, and other parameter fields after each remeshing. PARA(O)VOZ has been already tested on a number of geodynamical problems for subduction/collision context (Burov et al., 2001; Toussaint et al., 2004a, 2004b).

On Some Geometric Prism Asymmetries

Federica Lenci · Carlo Doglioni

Abstract. The asymmetry between orogens or accretionary wedges related to geographically opposed subduction zones is marked by volumes of the orogens above sea-level that are about 6–8 times smaller for those belts associated to W-directed subduction zones with respect to the orogens related to E- or NE-directed slabs. The mean slope of wedge topographic surfaces is about 1.9° for W-directed subduction and 4.8° for E-NE-directed subduction respectively. The regional foreland monocline may be >5° along W-directed subduction zones where the fast subsiding and deepest trenches and foredeeps form. Opposingly, along E-NE-directed subduction zones the regional foreland monocline is on average <3°, foredeeps and foreland basins are shallower and slower subsiding. This generates the paradox that smaller accretionary prisms may rather be associated to very deep trenches, and highly elevated orogens may have small foredeep/foreland basins.

As a general rule, apart few exceptions, the subduction hinge migrates away from the upper plate along W-directed subduction zones, whereas it migrates toward the upper plate along E-NE-directed slabs. This opposite behavior can account for the asymmetry on the dip of the regional monocline, and the inclination of the topographic and structural envelops. End members are the Barbados, Apennines, Carpathians, and the Banda arc for the first type, and the Andes, Alps, Zagros, and Himalayas for the second type.

Distinctive characters of the asymmetry are also the single vergence versus double vergence, fast versus slow subsidence rates in the foredeep or foreland basin, shallow rocks versus deep rocks involved by the prism, well-developed backarc basin versus no or poorly developed backarc basin. In the accretionary prisms associated to the W-directed subductions the basal décollement is in general much shallower (<10 km) than along the orogens along E-NE-directed subduction zones (>30 km), thus generating low and high relief, respectively. This global signature points to a rotational tuning of the orogen's asymmetry. However, besides these first-order differences, each orogen is the combination of distinct second-order internal parameters that frequently vary along strike, such as the décollement depth, and the mechanical properties.

1   Introduction

The more we know about subduction zones and processes acting at plate margins, the more complex become the models, and the more each zone seems unique. The aim of this paper is to present data on the morphology (i.e., the geometric features) of the frontal and shallower part of subduction zones, and to verify the possible existence of two hierarchical levels in controlling diversities between subduction zones, one at the global scale, and the second being regional.

The great variety of subduction zones in terms of morphological, structural and evolutionary features is well-known since the first studies on plate interaction at convergent margins (Isacks and Barazangi, 1977). Depth and dip of the subduction, magnitude of subduction-related earthquakes, stress state in the overriding plate, the presence/absence of an active back arc basin, and single/double vergence orogen are some of the variables. The western (Marianas) and the eastern (Peru-Chile) Pacific margins are end-members in such a scenario: a deep, almost vertical old oceanic lithosphere underthrusting a tensional overriding plate with back arc spreading and single vergence wedge at the western margins, vs. a younger shallower oceanic lithosphere, nearly horizontally dipping, below a highly compressional upper plate with a double vergence orogen at the eastern margins. Rocks involved in the orogens are strongly sensitive to the direction of the subduction polarity, being basement rocks more widely outcropping and sourcing the foreland basin or the trench along E- or NE-directed subduction zones (Garzanti et al., 2006).

Attempts at finding a common genetic mechanism have not succeeded to date. The different age and composition of the subducting plate (Hager and O'Connell, 1978; Jarrard, 1986), the slab pull force (Royden and Burchfiel, 1989), and the rates of convergence versus the subduction hinge migration between plates (Was-

chbusch and Beaumont, 1996) are all parameters used to interpret these differences. Cruciani et al. (2005) have shown the absence of correlation between slab dip and age of the subducting lithosphere. The "westward" drift of the lithosphere, i.e., the relative undulated, roughly "eastward" mantle flow is another alternative possible explanation (Nelson and Temple, 1972; Dickinson, 1978; Uyeda and Kanamori, 1979; Doglioni et al., 1999; Crespi et al., 2007).

In the present paper convergent margins are analyzed in terms of geometric configuration of the wedge and the lower plate, considering geographic polarity of the margin and age and composition of the subducting plate. The term "wedge" is therefore used in a broader sense, describing the triangular shape of rocks at the leading edge of the hangingwall plate along a convergent margin, whether oceanic or continental. The few parameters compiled in the paper are mostly related to the frontal part of the prism, in the brittle regime. However, other larger scale values such as the orogen elevation are controlled by the whole rheology of the belt, both brittle and ductile at depth.

The following 12 main subduction zones are analyzed, eight along the circumpacific margins, plus the Banda arc, the Barbados accretionary prism, the Apennines and the Carpathians. The choice was made in order to cover the most important subduction zones worldwide, and it was constrained by the available data along the different prisms.

The measured parameters are: the angle of the wedge upper surface (topographic) envelope (α), the depth of the main décollement (both the depth of the base of the wedge and the depth of the stratigraphic décollement layer in the foreland), the cross-sectional area of the belt, and the dip of the foreland monocline (β). This analysis has been carried out from seismic reflection profiles and from regional geologic balanced cross-sections available in the literature (Fig. 1). Geographic polarity of subduction zone and age and composition of lower plate have been related to inclination of the regional monocline (β), wedge topographic envelope (α), depth of the wedge basal décollement, and cross-sectional area of associated belt. The analysis showed an asymmetry, that depends more on geographic polarity rather than on characteristics of subducting lithosphere. Those margins with a "E-NE" direction of subduction are commonly characterized by higher values of topographic envelope, lower values of dip of the foreland monocline, deeper décollements and higher cross-sectional area of the belt with respect to "western" margins. Another first-order kinematic indicator is the behavior of the subduction hinge that can migrate toward or away from the upper plate (Doglioni et al., 2006).
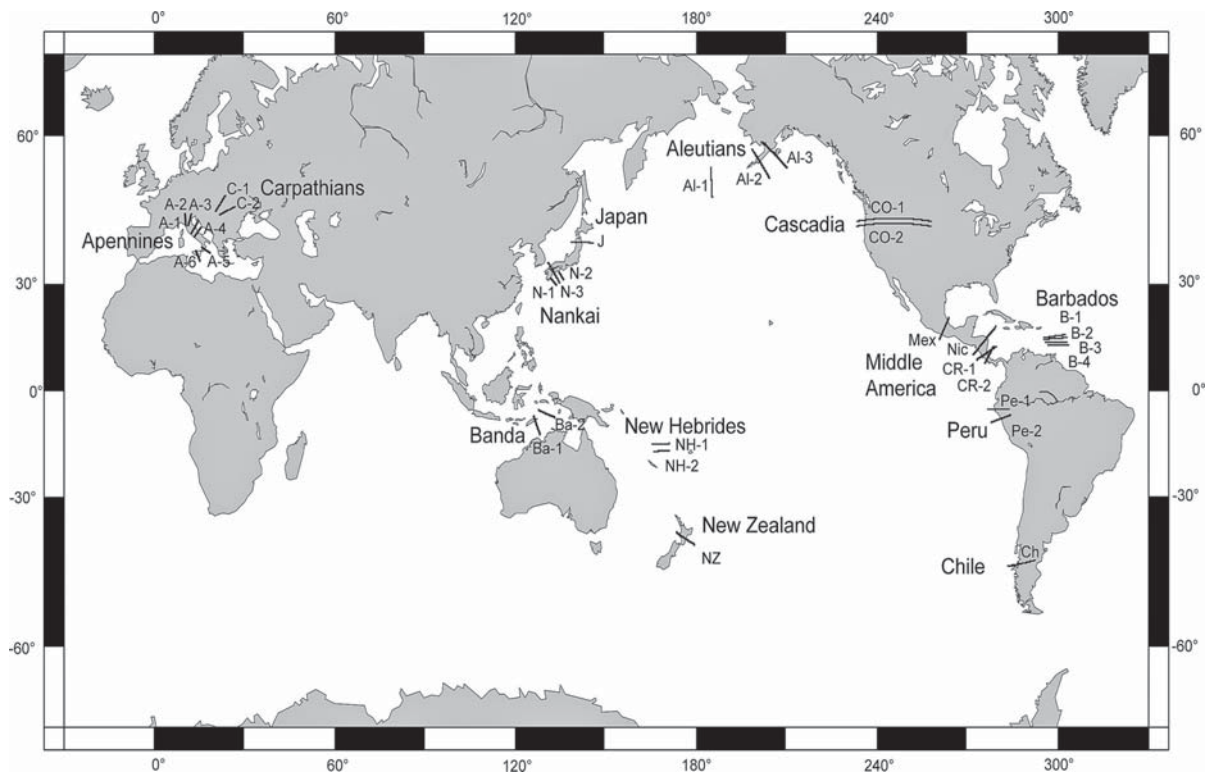

Fig. 1. Studied margins, location and nomenclature of the sections
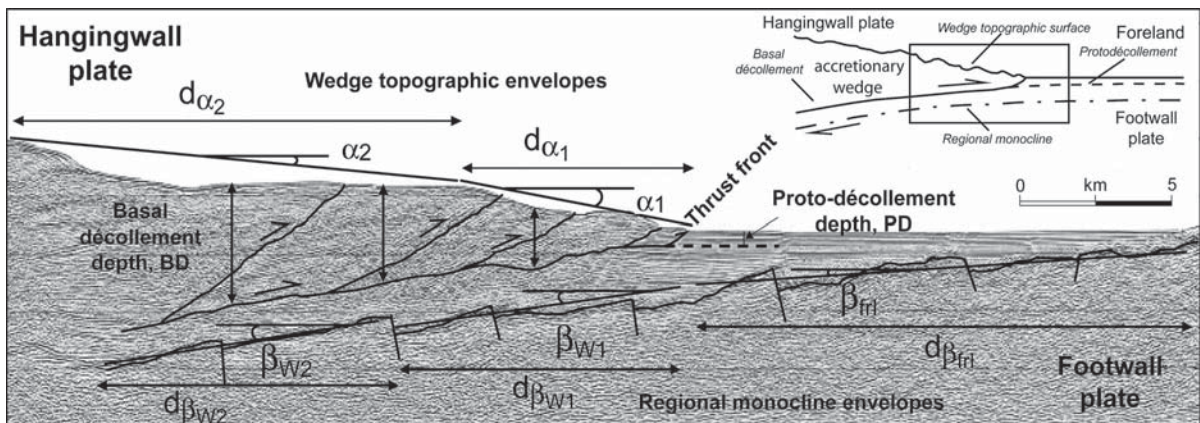
2   The Measured Parameters

In spite of the natural variability, there are elements common to all subduction zones (Chapple, 1978; Davis et al., 1983; Dahlen, 1990). The deformation front of orogens, thrust belts or accretionary prisms, has notoriously a wedge-shape geometry in cross-section (Fig. 2), delimited at its top by a topographic surface and at its base by a basal décollement, which separate the prism from the down-going plate. The lower plate generally shows little deformation, except possibly for a few normal faults due to plate bending. While being underthrust, the lower plate describes a monocline, i.e., foreland or regional monocline. Fluids flow may play an important role in controlling prism development (Bangs et al., 1999; Silver et al., 2000; Roure et al., 2005). Climate and erosion have been shown to affect the orogenic evolution (Willett, 1999; Willett et al., 2001; Avouac, 2003).

The aforementioned elements are described by parameters defined by Davis et al. (1983) in their "Critical Tapered Wedge Model": the envelope of the wedge's topographic surface and of the regional monocline are described by the angles α and β, respectively (Fig. 2). Their sum, the so-called taper angle ($\theta = \alpha + \beta$), is a peculiar quantity for each wedge, since it is a function of the physical properties of the material involved in the deformational process and the orientation of the principal stresses (Dahlen et al., 1984; Davis and Engelder, 1985; Dahlen, 1990).

The importance of the β angle, as one of the descriptive parameters of the geometry of a convergent margin, has also been discussed by Boyer (1995), Mariotti and Doglioni (2000), and Koyi and Vendeville (2003). Boyer (1995) investigated the consequences of changes in foreland basement pre-deformational dip on deformational styles (in terms of thrust spacing and magnitude of shortening), width, and frontal advance of accretionary wedges. Analyzing the Apennines and the Alps, Mariotti and Doglioni (2000) detected two orders of variation of the β angle: a first one at the scale of orogens, being steeper beneath the W-directed Apennines subduction (10–15°) than in the Alps (2–6°), and a second one at the regional scale, moving along strike. Salients and recesses correspond in general to steeper and shallower regional monocline values occurring along pre-existing Mesozoic basins and swells, respectively. Recently Koyi and Vendeville (2003) investigated the effect of décollement dip on geometry and mode of deformation of related wedges, by means of sandbox modeling.

The geometry of the wedge and of the shallower part of the footwall plate have been determined in our analysis (Fig. 2), measuring parameters defined in the literature (α, β, θ) and new parameters (i.e., basal décollement and proto-décollement depths) on seismic reflection profiles and regional balanced geologic sections available in the literature. A further study parameter is the cross-sectional area of the belt associated to the margin, measured on topographic profiles traced along each study section. The basal décollement (BD) is the deepest thrust of the accretionary prism and clearly deepens and thickens moving toward the interior of the belt. The proto-décollement depth (PD) is instead a fixed value that describes the thickness of

Fig. 2. Main elements characterizing the frontal and shallower part of a subduction zone (*top right*) and interpreted seismic reflection line with measured parameters (modified from Scholl et al., 1986). α) angles with respect to an horizontal reference line of the wedge topographic envelopes, α_1 and α_2, and relative horizontal validity interval, d_{α_1} and d_{α_2}. β) angles with respect to an horizontal reference line of the regional monocline envelopes in the stable foreland, β_{frl}, and below the wedge, β_{W_1} and β_{W_2}, and relative horizontal validity interval, $d_{\beta_{frl}}$, $d_{\beta_{W_1}}$ and $d_{\beta_{W_1}}$. Basal décollement depth, BD) wedge thickness measured each 5 km inward the thrust front. Proto-décollement depth, PD) thickness of sediments above the stratigraphic décollement layer in the foreland

the rocks above the basal décollement at the front of the accretionary prism (Fig. 2).

3   Methodology

Seismic reflection profiles and regional geologic balanced cross-sections used in this study are listed in Table 1. Where available, more than one section has been considered for a single margin. Seismic reflection profiles originally in TWT that were depth-converted in this study are: the Apennines section A-5, converted using seismic velocity model in De Voodg et al. (1992), and Catalano et al. (2001); the Barbados sections B-1, B-3, and B-4, converted using seismic velocity model in Bangs et al. (1990); the Banda sections Ba-1 and Ba-2, converted assuming standard velocities. Measured regional geologic balanced cross-sections are: the Carpathians sections C-1 and C-2, and the Apennines sections A-3, A-4 and A-6. All the remaining sections were seismic reflection profiles originally in depth.

The dip of the regional monocline was measured both in the undeformed foreland (β_{frl}) and below the deformed wedge (β_W) (Fig. 2). The α and β_W parameters were studied detecting multiple segmented envelopes on each section, identifying more than one value for both α and β_W angles (i.e., α_i, β_{W_i}) and a related horizontal validity interval, i.e., $d_{\alpha_{W_i}}$ and $d_{\beta_{W_i}}$ (see Fig. 2). Figure 3 shows the geometry of wedges, as drawn by the α_i and β_{W_i} angles and relative validity intervals.

Afterwards, mean values of α and β_W for each section have been calculated as follows (refer to Fig. 2):

$$\alpha_{mean} = \frac{(\alpha_1 \cdot d_{\alpha_1}) + (\alpha_2 \cdot d_{\alpha_2}) + \ldots + (\alpha_n \cdot d_{\alpha_n})}{d_{\alpha_1} + d_{\alpha_2} + \ldots + d_{\alpha_n}} \qquad (1)$$

$$\beta_{W_{mean}} = \frac{(\beta_{W_1} \cdot d_{\beta_{W_1}}) + (\beta_{W_2} \cdot d_{\beta_{W_2}}) + \ldots + (\beta_{W_n} \cdot d_{\beta_{W_n}})}{d_{\beta_{W_1}} + d_{\beta_{W_2}} + \ldots + d_{\beta_{W_n}}} \qquad (2)$$

$$\vartheta_{mean} = \alpha_{mean} + \beta_{W_{mean}} \qquad (3)$$

as reported in Table 1 and Fig. 4.

A further element investigated here is the basal décollement, i.e., the deepest fault plane separating the hangingwall plate from the footwall plate (Fig. 2). The significance of the décollement depth on wedge configuration is that a deeper décollement corresponds to a larger volume of material accreted into the wedge, and therefore, under the same friction conditions (Davis and Engelder, 1985; Mulugeta; 1988; Colletta et al., 1991; Koyi, 1995; Koyi et al., 2000), to a higher topographic elevation (Liu et al., 1992). In general, mass transfer at subduction zones may mechanically oc-

cur in two directions: transfer from the footwall to the hangingwall plate, termed "accretion" (Karig and Sharman III, 1975; Moore et al., 1984; Moore et al., 1995), and transfer from the hangingwall to the footwall plate, defined as "erosion" (von Huene and Lallemand, 1990; von Huene and Scholl, 1991). In the first case the décollement is the deepest thrust involving the footwall plate and whereas in the second case the deformation involves only the hangingwall plate. In this study no distinction has been made on the base of mechanism of mass transfer. The décollement is rather studied as "basal décollement depth, BD", i.e., vertical distance between the fault plane itself and the wedge topographic surface, and as "protodécollement depth, PD", i.e., thickness of the sediment pile above the stratigraphic décollement layer in the stable foreland (see Fig. 2). The BD has been measured every 5 km starting from the thrust front inward. A BD_{mean} value for each study section has been obtained and a normalized value has also been calculated, using the following equations (refer to Fig. 2):

$$BD_{mean} = \frac{BD_1 + BD_2 + \ldots + BD_n}{n} \qquad (4)$$

with n equal to the number of measurements on each study section

$$BD_{normalized} = \frac{BD_{mean}}{\text{distance from the trust front}} \qquad (5)$$

Calculated values are reported in Table 1 and Fig. 4. The operation of normalization has been necessary since the basal décollement strongly depends on the position of the wedge with respect to the subduction hinge: the steeper the monocline, the deeper the décollement, i.e., the BD is strongly related to β. Nevertheless normalizing the BD_{mean} value ensures a value independent from its study length and therefore comparable. Increasing β, α tends to decrease, as well as the volume of the involved rocks since décollements are shallower.

A topographic profile was drawn along each study section and the area of the belt associated with the margin has been measured, i.e., the cross-sectional area above sea level pertaining to the belt (Table 1 and Fig. 4). An inboard edge of 500 km from the trench axis has been used. The length is an arbitrary choice in order to cover most of the double vergent orogens, which are very wide (e.g., Cordillera).

The parameters were measured as far as possible on each section (see Fig. 3). Subsequently, an analysis of average values was performed, in function of the polarity of the subduction zone and composition of the
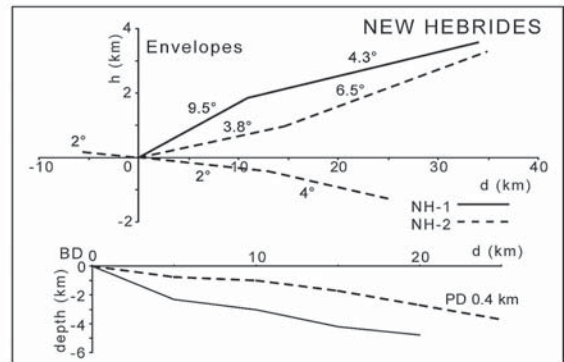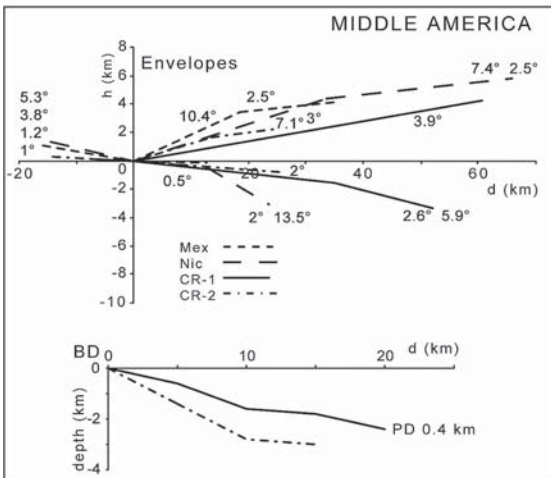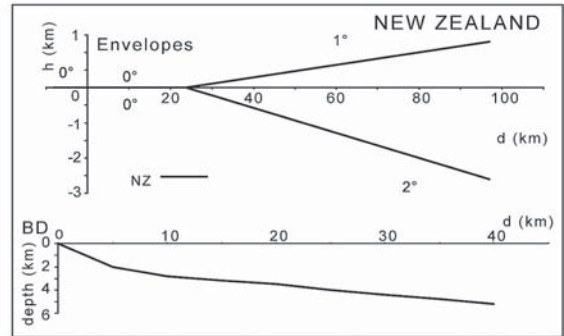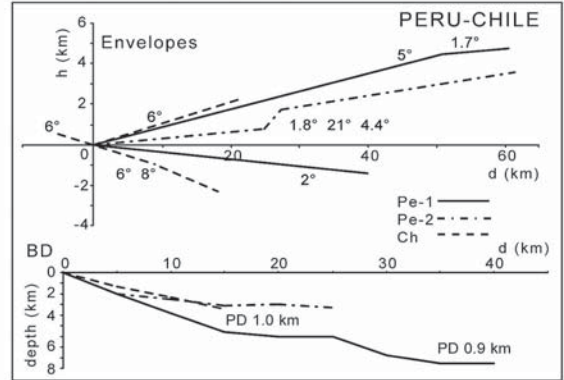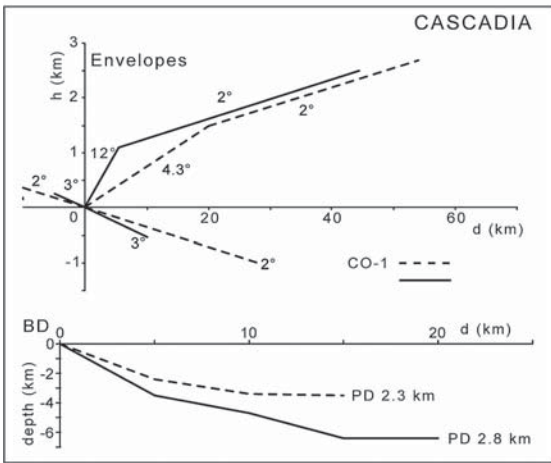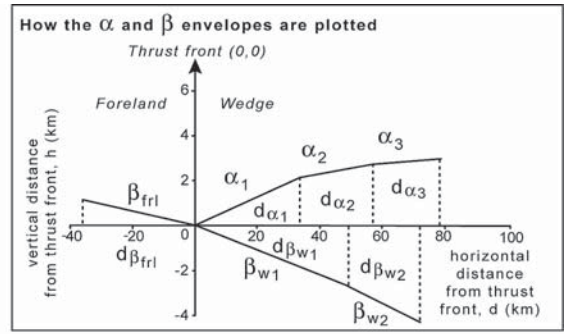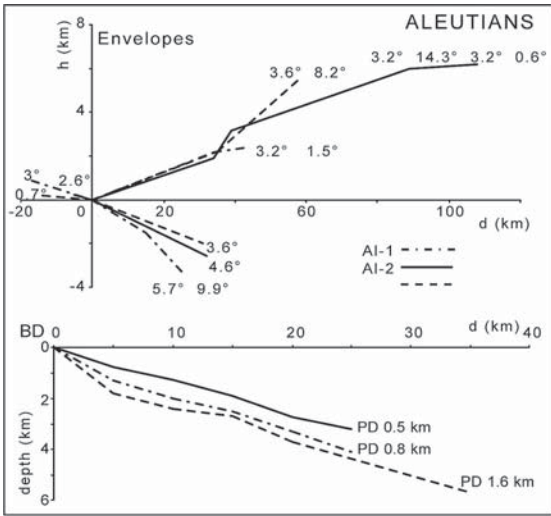
Fig. 3. Raw data for each study section: wedges topographic envelopes and regional monoclines envelopes with measured angles; related basal décollement profiles with proto-décollement depth, where measured. A reference plot for the envelopes is also present (*top right*). Due to different length of sections, plots have different scale and different vertical exaggeration. *BD*, basal décollement, *PD*, proto-décollement
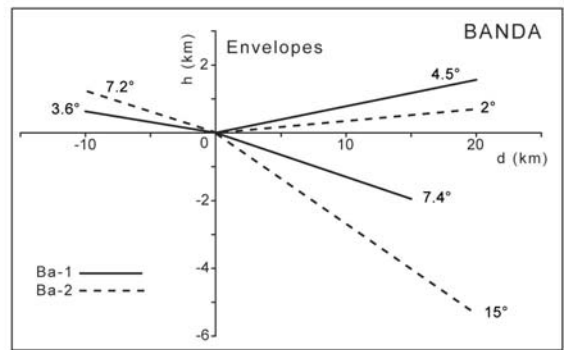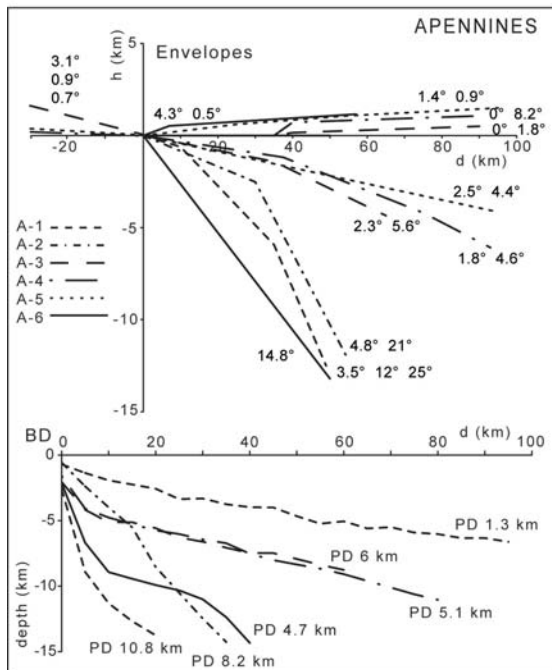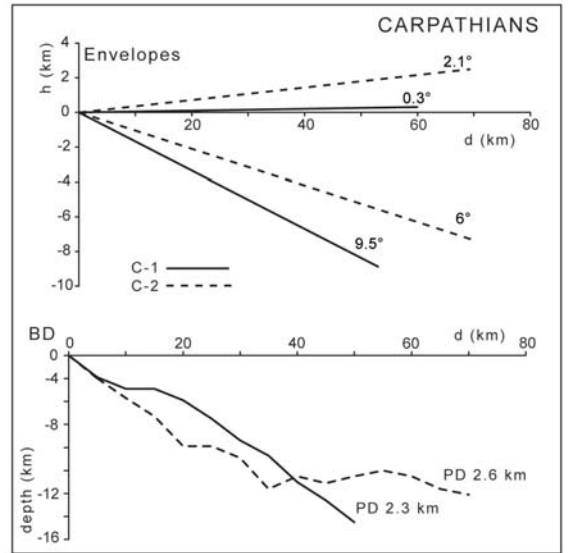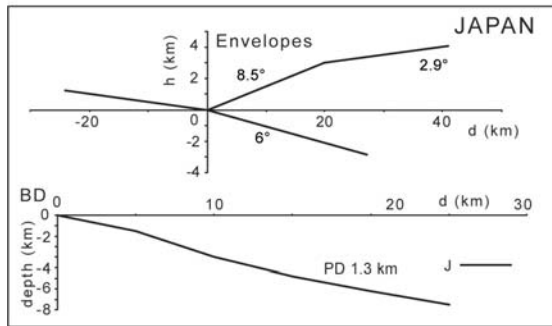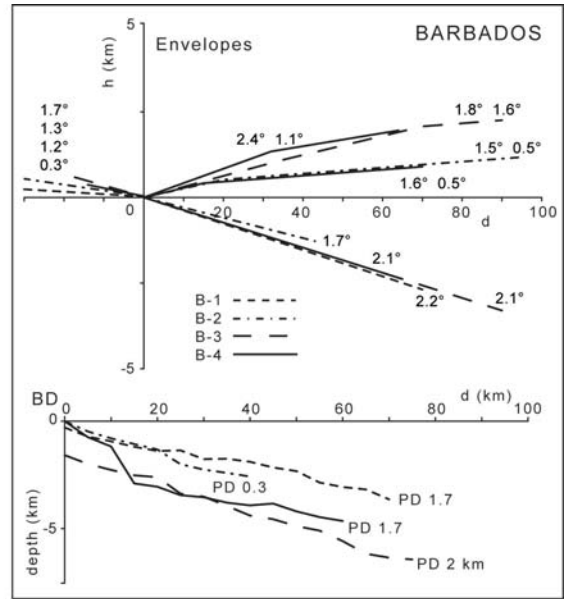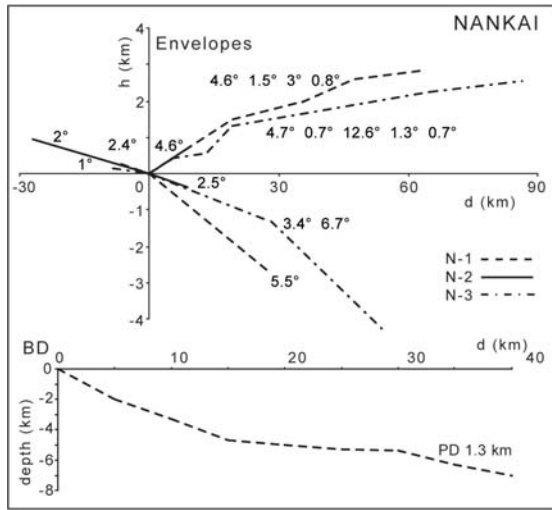
b

Fig. 3. *Continued*
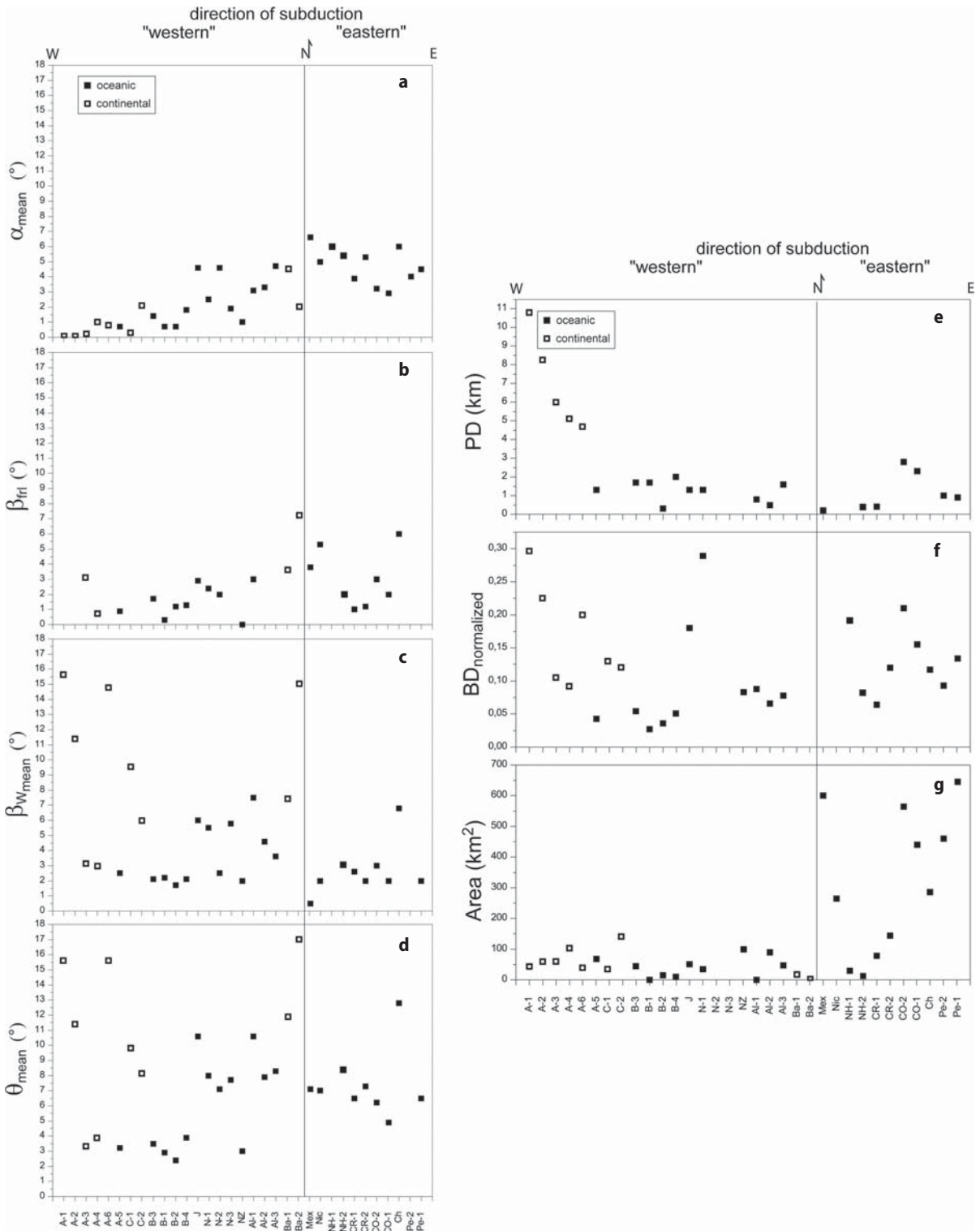
Fig. 4. Results of the analysis for each study section. Sections are distributed along the x axis following their spatial orientation (i.e., azimuth and polarity of related subduction zone), from W to E. Subduction of continental and oceanic crust is also distinguished. See Fig. 1 and Table 1 for sections nomenclature, location and orientation. **a**) Slope of the wedge topographic envelope (α_{mean}, as in Eq. 1). **b**) Dip of the regional monocline in the foreland (β_{frl}). **c**) Dip of the regional monocline below the wedge ($\beta_{W_{mean}}$, as in Eq. 2). **d**) Mean taper angle (θ_{mean}, as in Eq. 3). **e**) Proto-décollement depth (*PD*). **f**) Basal décollement depth normalized to length of section (*BD_{normalized}* as in Eq. 5). **g**) Cross-sectional area of the belt

Table 1. Results

Margin	Section	Source	Reference Position (Lat., Long.)	α_{mean} (°)	β_{frl} (°)	$\beta_{W_{mean}}$ (°)	θ_{mean} (°)	$BD_{normalized}$	PD (km)	Area (km²)	Subducting plate composition	age (Myr)[z]	direction of subduction[aa]	azimuth
Aleutians	Al-1	a)	50.5, 185	3.1	3.0	7.5	10.6	0.088	0.8	0	oceanic	54	NW	-48.002
	Al-2	b)	54, 203	3.3	-	4.6	7.9	0.066	0.5	90	oceanic	46	NW	-39.815
	Al-3	c)	56, 208	4.7	-	3.6	8.3	0.078	1.6	47	oceanic	46	NW	-36.0
Cascadia	CO-1	d)	44.7, 233	2.9	2.0	2.0	4.9	0.155	2.3	440	oceanic	8	E-NE	37.573
	CO-2	d)	44.4, 233	3.2	3.0	3.0	6.2	0.210	2.8	565	oceanic	8	E-NE	35.935
Middle America	Mex	e)	14.8, 260.4	6.6	3.8	0.5	7.1	-	0.2	600	oceanic	15	NE	3.351
	Nic	f)	10.3, 271.6	5.0	5.3	2.0	7.0	-	-	265	oceanic	18	NE	8.701
	CR-1	g)	9, 272.8	3.9	1.0	2.6	6.5	0.064	0.4	78	oceanic	18	NE	10.865
	CR-2	h)	8, 275.6	5.3	1.2	2.0	7.3	0.120	-	144	oceanic	18	NE	11.998
Peru-Chile	Pe-1	i)	-5.6, 276.5	4.5	-	2.0	6.5	0.134	0.9	645	oceanic	45	E	81.022
	Pe-2	j)	-9.5, 277.5	4.0	-	-	-	0.093	1.0	460	oceanic	45	E	80.525
	Ch	k)	-46, 283	6.0	6.0	6.8	12.8	0.117	-	286	oceanic	5	E	78.676
New Zealand	NZ	l)	-38.5, 173	1.0	0.0	2.0	3	0.083	-	100	oceanic	98	NW	-53.897
New Hebrides	NH-1	m)	-15.8, 165	6.0	-	-	-	0.191	-	12	oceanic	52	NE	9.216
	NH-2	m)	-17.8, 165.5	5.4	2.0	3	8.4	0.082	0.4	5	oceanic	52	NE	10.512
Banda	Ba-1	n)	-10, 127	4.5	3.6	7.4	11.9	-	-	17	continental		N-NW	-1.216
	Ba-2	o)	-7.25, 133.8	2.0	7.2	15.0	17.0	-	-	0	continental		N-NW	-0.0030
Nankai	N-1	p)	30.7, 135.3	2.5	2.4	5.5	8.0	0.289	1.3	35	oceanic	21	W-NW	-57.142
	N-2	q)	30.7, 135.3	4.6	2.0	2.5	7.1	-	-	-	oceanic	21	W-NW	-57.142
	N-3	q)	30.7, 135.3	1.9	-	5.8	7.7	-	-	-	oceanic	21	W-NW	-57.142
Japan	J	r)	40, 145.8	4.6	2.9	6.0	10.6	0.180	1.3	51	oceanic	130	W-NW	-65.079
Carpathians	C-1	s)	50, 23.7	0.3	-	9.5	9.8	0.130	-	35	continental		W	-114.202
	C-2	s)	47.8, 27	2.1	-	6.0	8.1	0.120	-	140	continental		W	-112.295

Table 1. *Continued*

Margin	Section	Source	Reference Position (Lat, Long.)	α_{mean} (°)	β_{frl} (°)	β_{Wmean} (°)	θ_{mean} (°)	$BD_{normalized}$	PD (km)	Area (km²)	Subducting plate			
											composition	age (Myr)[z]	direction of subduction[aa]	azimuth
Apennines	A-1	t)	44.8, 10.8	0.0	-	15.6	15.6	0.296	10.8	44	continental		W	-118.263
	A-2	t)	44.6, 11.8	0.0	-	11.4	11.4	0.225	8.2	60	continental		W	-117.839
	A-3	u)	43.5, 14	0.2	3.1	3.1	3.3	0.105	6.0	60	continental		W	-116.76
	A-4	u)	43.1, 14.3	1.0	0.7	2.9	3.9	0.091	5.1	103	continental		W	-116.561
	A-5	v)	42.8, 18	0.7	0.9	2.5	3.2	0.043	1.3	68	oceanic	-	W	-115.092
	A-6	w)	42, 14.8	0.8	-	14.8	15.6	0.200	4.7	40	continental		W	-116.15
Barbados	B-1	x)	16.3, 301.3	0.7	0.3	2.2	2.9	0.027	1.7	0	oceanic	68	W	-104.614
	B-2	y)	15.5, 301.4	0.7	1.2	1.7	2.4	0.036	0.3	15	oceanic	68	W	-104.524
	B-3	x)	14.4, 302.4	1.4	1.7	2.1	3.5	0.054	1.7	45	oceanic	68	W	-104.63
	B-4	x)	13.4, 302.5	1.8	1.3	2.1	3.9	0.051	2.0	10	oceanic	68	W	-104.523

Source: *a*) Scholl et al. (1986). *b*) Bruns and von Huene (1986). *c*) von Huene et al. (1986a). *d*) Snavely et al. (1986). *e*) Collins and Watkins (1986). *f*) Ranero et al. (2000). *g*) Shipley and Buffler (1986). *h*) Kolarsky et al. (1995). *i*) Kulm et al. (1986). *j*) Miller et al. (1986). *k*) Behrman et al. (1994). *l*) Davey and Childs (1986). *m*) Fisher and Greene (1986). *n*) Crostella and Powell (1976). *o*) Schlutter and Fritsch (1985). *p*) Kawamura and Aoki (1986). *q*) Shipboard Scientific Party (2000). *r*) von Huene et al. (1986b). *s*) Roure et al. (1993). *t*) Pieri (1983). *u*) Bally et al. (1986). *v*) Cernobori et al. (1996). *w*) Bello et al. (2000). *x*) Westbrook et al. (1988); Ladd et al. (1990). *y*) Moore et al. (1995). α_{mean}: mean slope of the wedge topographic surface, measured as in equation 1). β_{frl}: dip of the regional monocline in the foreland. β_{Wmean}: mean dip of the regional monocline below the wedge, measured as in equation 2). θ_{mean}: mean taper angle, measured as in equation 3). $BD_{normalized}$: basal décollement depth, measured as in equation 5). *PD*: proto-décollement depth. *Area*: cross-sectional area of the belt above sea level, within 500 km from the trench axis. *Subducting plate*: [z] Jarrard (1986); [aa] Gripp and Gordon (2002)

downgoing plate. Standard errors for calculated mean values have also been computed.

On the basis of direction of subduction as a function of the polarity along the undulated mainstream of plate motions (Doglioni, 1990; Crespi et al., 2007), two classes of subduction zones emerges: the "eastern" (E- or NNE-directed), and the "western" (W-directed) classes. The "eastern" margins include: Cascadia, Middle America, Peru-Chile, and New Hebrides. The "western" margins include: Aleutians, North New Zealand, Nankai, Japan, Barbados, Banda, Apennines, and Carpathians. On the basis of composition of the downgoing plate, the groups are: Aleutians, Cascadia, Middle America, Peru-Chile, New Hebrides, New Zealand, Nankai, Japan, Ionian Apennines (section A-5), and Barbados for the oceanic plates; Banda, Apennines, and Carpathians for the continental plates.

For each group of margins mean values of the parameters have been calculated as follows: *see Box 1* reported in Table 2 and Fig. 5.

Box 1.
Eq. 6 to 12

$$\alpha_{mean}* = \frac{(\alpha_{mean})_{section\ 1} + (\alpha_{mean})_{section\ 2} + \ldots + (\alpha_{mean})_{section\ n}}{number\ of\ sections} \quad (6)$$

$$\beta_{frl}* = \frac{(\beta_{frl})_{section\ 1} + (\beta_{frl})_{section\ 2} + \ldots + (\beta_{frl})_{section\ n}}{number\ of\ sections} \quad (7)$$

$$\beta_{W_{mean}}* = \frac{(\beta_{W_{mean}})_{section\ 1} + (\beta_{W_{mean}})_{section\ 2} + \ldots + (\beta_{W_{mean}})_{section\ n}}{number\ of\ sections} \quad (8)$$

$$\vartheta_{mean}* = \frac{(\vartheta_{mean})_{section\ 1} + (\vartheta_{mean})_{section\ 2} + \ldots + (\vartheta_{mean})_{section\ n}}{number\ of\ sections} \quad (9)$$

$$PD* = \frac{(PD)_{section\ 1} + (PD)_{section\ 2} + \ldots + (PD)_{section\ n}}{number\ of\ sections} \quad (10)$$

$$BD_{normalized}* = \frac{(BD_{normalized})_{section\ 1} + (BD_{normalized})_{section\ 2} + \ldots + (BD_{normalized})_{section\ n}}{number\ of\ sections} \quad (11)$$

$$Area* = \frac{(Area)_{section\ 1} + (Area)_{section\ 2} + \ldots + (Area)_{section\ n}}{number\ of\ sections} \quad (12)$$

Table 2.
Average data and standard errors of study parameters based on direction of subduction ("western" or "eastern") and composition of downgoing plate (oceanic or continental)

	"Western"	"Eastern"	"Continental"	"Oceanic"
$\alpha_{mean}*$ (°)	1.90 ± 0.34	4.80 ± 0.36	2.03 ± 0.68	3.29 ± 0.38
$\beta_{frl}*$ (°)	2.16 ± 0.49	3.04 ± 0.66	3.32 ± 1.09	2.24 ± 0.40
$\beta_{Wmean}*$ (°)	6.10 ± 0.96	2.66 ± 0.57	8.87 ± 1.63	3.29 ± 0.42
$\theta_{mean}*$ (°)	7.99 ± 0.96	7.41 ± 0.74	10.50 ± 1.50	6.58 ± 0.61
$PD*$ (km)	3.15 ± 0.81	1.14 ± 0.38	5.87 ± 1.43	1.26 ± 0.19
$BD_{normalized}*$	0.120 ± 0.020	0.132 ± 0.016	0.160 ± 0.024	0.105 ± 0.016
Area* (km^2)	48 ± 9	317 ± 72	45 ± 13	197 ± 50

$\alpha_{mean}*$: mean slope of wedges topographic surfaces, measured as in equation 6); $\beta_{frl}*$: mean dip of regional monoclines in stable forelands, measured as in equation 7); $\beta_{W_{mean}}*$: mean dip of regional monoclines below wedges, measured as in equation 8); $\theta_{mean}*$: mean taper angles, measured as in equation 9); $PD*$: mean proto-décollements depth, measured as in equation 10); $BD_{normalized}*$: basal décollements depth, measured as in equation 11); $Area*$: cross-sectional area of belts above sea level, measured as in equation 12)

Fig. 5. Results based on geographic polarity of margins and composition of lower plates. **a**) Mean slope of the wedge topographic envelope (α_{mean}*, as in Eq. 6); **b**) mean dip of the regional monocline in the foreland (β_{frl}*, as in Eq. 7); **c**) mean dip of the regional monocline below the wedge ($\beta_{W_{mean}}$*, as in Eq. 8); **d**) mean taper angle (θ_{mean}*, as in Eq. 9); **e**) mean proto-décollement depth (*PD**, as in Eq. 10); **f**) mean basal décollement depth normalized to length of sections (*BD*$_{normalized}$* as in Eq. 11); **g**) mean cross-sectional area of the belt (*Area**, as in Eq. 12)

4   The Data

In Fig. 3 α_i, β_{frl} and β_{W_i} and basal décollement depths are plotted for each study section together with their investigated distance. Data are plotted with respect to the frontal thrust which occupies the (0,0) position both in the envelopes graph and in the BD graph. In the latter the PD value is also reported, where measurable.

Table 1 reports mean values of the parameters for every study section, as calculated by Eqs. 1 to 5. In Fig. 4 results are plotted versus geographic polarity of subduction zone, distinguishing between continental and oceanic downgoing plates.

Table 2 and Fig. 5 show mean values of the parameters for each class of margins, as calculated by Eqs. 6 to 12.

Figure 5a shows that for the investigated margins α_{mean}*, i.e., mean slope of wedge topographic envelopes, is lower in the "western" class than in the "east-

ern" class (1.90±0.34 degrees vs. 4.80±0.36 degrees), and in the "continental" class than in the "oceanic" one (2.03±0.68 degrees vs. 3.29±0.38 degrees).

In general, continental monoclines are steeper than oceanic monoclines (Fig. 5b and 5c). A pronounced difference between the two classes is registered for the dip of regional monocline below the wedge ($\beta_{W_{mean}}$* is 8.87±1.63 degrees for the continental ones vs. 3.29±0.42 degrees for the oceanic ones), while statistically it is weak but higher in case of monoclines in the foreland (β_{frl}* is 3.32±1.09 degrees for the continental ones vs. 2.24±0.40 degrees for the oceanic ones). In the "western" class $\beta_{W_{mean}}$* is steeper than in the "eastern" class: mean value for "western" margins is 6.10±0.96 degrees vs. 2.66±0.57 degrees for "eastern" margins.

Figure 6 shows β_{frl} and $\beta_{W_{mean}}$ values plotted versus age of the subducting oceanic plates. Results seem to suggest that there is no linear dependence between age of the crust and dip of the oceanic regional monocline.

The mean taper angle, θ_{mean}*, is higher in case of continental subducting plates with respect to oceanic subducting plates (Fig. 5d): 10.50±1.50 degrees vs. 6.58±0.61 degrees. Instead, the θ_{mean}* value, the critical taper, is quite similar in case of "western" and "eastern" margins, being respectively 7.99±0.96 degrees and 7.41±0.74 degrees (Fig. 7). This seems to suggest that mechanical laws governing wedges' building do not change significantly with geographic polarity: within the two classes, angles of the envelopes invert their values, without considerably modifying their sum. However, the most evident data from Fig. 7 is that, regardless of the composition of the downgoing plate, β is steeper and α is shallower for W-directed subduction zones, whereas β is shallower and α is steeper for E- or NE-directed sunduction zones. For
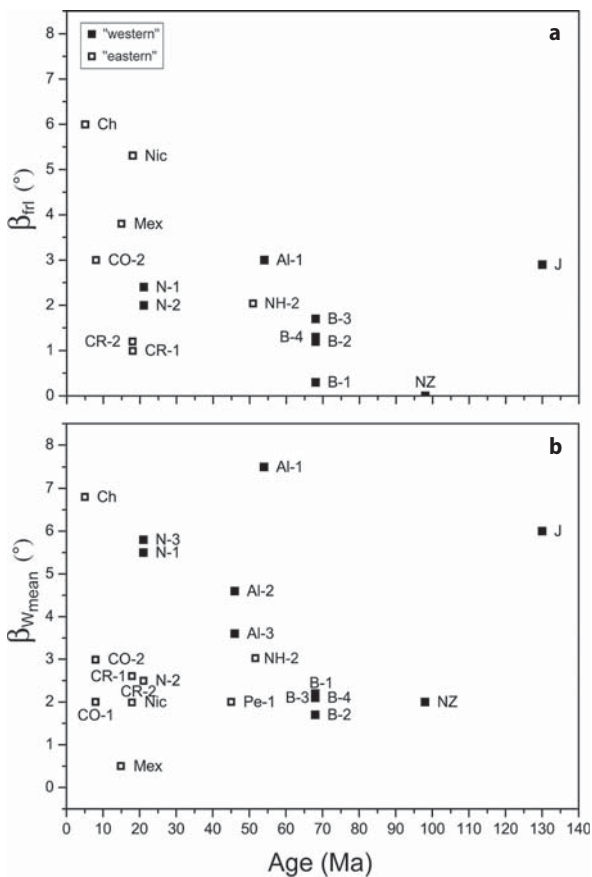
Fig. 6. Dip of the regional monocline for each oceanic section as a function of the age of ocean floor, **a)** in the foreland and **b)** below the wedge. Note the absence of linear dependence between age and dip of the subducting oceanic monocline
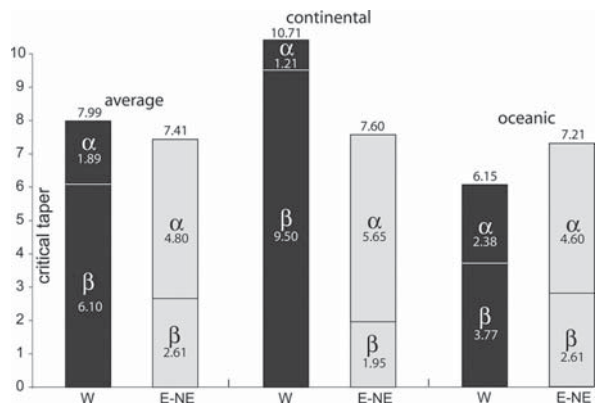
Fig. 7. Average values of the topographic envelope (α), dip of the foreland monocline (β), and critical taper (=α+β) for the two classes of subduction zones, i.e., W-directed and E- or NE-directed. Note that the "western" classes show lower values α and steeper values of β

the "eastern" continental subductions (e.g., Alps, Zagros, Himalayas) we refer to literature data (Mariotti and Doglioni, 2000; Lenci, 2003; Duncan et al., 2003; Mugnier and Huyghe, 2006).

5   Other Parameters Affecting Prism Evolution

Besides the aforementioned analysis, a variety of geometric and kinematic elements determine the bulk structure of an orogen or accretionary prism. They are namely the depth of the basal décollement (e.g., Bigi et al., 2003), the convergence rate, the shortening rate, the subduction rate (Doglioni et al., 2006), the dip of the foreland monocline (Mariotti and Doglioni, 2000), the topographic envelope, the structural envelope, the basal and the internal friction (Dahlen et al., 1984), the foredeep or foreland subsidence rate (Doglioni, 1994), the prism uplift rate, the thrusts spacing (Morellato et al., 2003), the heat flow variability, the thickness and composition of the upper and lower plates, the erosion rate (Willett, 1999), the climate, the sediment supply in the foredeep, and the extension rate, if any. All these parameters are not discussed in detail here but are nevertheless fundamental in orchestrating the orogen evolution and determining the peculiar character of each single belt.

Another crucial parameter, is the behavior of the subduction hinge. The subduction hinge is considered the point where the downgoing footwall plate presents the maximum curvature. It is a transient point that moves during subduction (Royden and Burchfiel,

1989; Waschbusch and Beaumont, 1996; Lallemand et al., 2005; Doglioni et al., 2006). Relative to the upper plate, the hinge can move forward or backward (Fig. 8). The accretionary prism or orogen geometry kinematics are very sensitive to its behavior, and two opposite settings develop. For example, the hinge migrating toward the upper plate occurs with double vergent orogens, higher topography and widely involved deep basement rocks involved, shallow regional monocline and foredeep, no active backarc spreading. The case of subduction hinge migrating away from the upper plate is rather associated with a low topography accretionary prism, mostly composed of shallow rocks, deep trench and backarc basin development.

Apart few exceptions, this distinction seems to apply particularly for E- or NE-directed subduction zones and W-directed subduction zones, respectively. Moreover, the rate of subduction is larger than the convergence rate along W-directed subduction zones, whereas it is smaller along E- or NE-directed subduction zones (Fig. 8). Along W-directed slabs, the subduction rate is the convergence rate plus the slab retreat rate, which tends to equal the backarc extension rate. Along E- or NE-directed slabs, the amount of hinge migration toward the upper plate corresponds to the shortening in the orogen. Moreover, the amount of shortening in the upper plate decreases the subduction rate, and no typical backarc basin forms. With respect to the subduction zones described in this paper, the subduction hinge migrates away from the upper plate along the Barbados, Carpathians, Apennines, Northern New Zealand, Nankai, Aleutians, and all W-directed subduction zones. The Japan subduction,
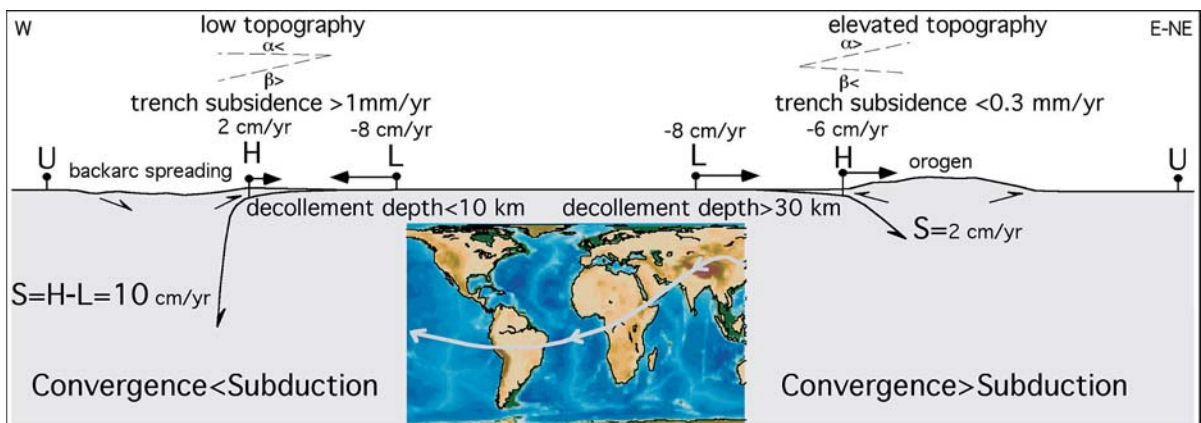
Fig. 8. Simple kinematics of subduction zones, assuming fixed the upper plate U. More frequently along west-directed subduction zones, the subduction hinge H diverges relative to U, whereas it converges along the opposite subduction zones. L, lower plate. The velocities are just an example and are positive when they diverge, being negative in convergent settings relative to U. Note that the subduction S is larger than the convergence along W-directed slabs, whereas S is smaller in the opposite case. The two end-members of hinge behavior are respectively accompanied in average by low and high topography, steep and shallow foreland monocline, fast and slower subsidence rates in the trench or foreland basin, single vs. double vergent orogens, etc., highlighting a worldwide subduction asymmetry along the flow lines of plate motions (Doglioni, 1993) indicated in the insert

although westerly directed, presently shows a sub-duction hinge migrating toward the upper plate, indicating inversion of the system, with no active back-arc extension and shrinking of the basin (Doglioni et al., 2006). The others, the Cascadia, Middle America, Perù, Chile, New Hebrides subduction zones are associated with subduction hinge migrating toward the upper plate (Doglioni et al., 2006). Also in the Himalayas (e.g., Mugnier and Huyghe, 2006) the subduction hinge moves toward the upper plate.

6   Discussion

The décollement's parameters ($PD*$ and $BD_{normalized}*$) are highly influenced by the nature of the downgoing plates (Table 2, Fig. 5e and 5f). It is known that the décollement is shallower in cases of subduction of oceanic lithosphere (Moore et al., 1991), while in continental subduction the depth increases considerably, probably due to the greater thickness of sedimentary cover on continental crust. Lenci et al. (2004) have shown how in the Apennines the accretionary prism involving a shallower section (<3 km) of the Ionian oceanic crust's sedimentary cover determined a smaller volume than the setting to the north, in the central-northern Apennines, where the accretionary prism has a deeper décollement (>10 km) and a consequently larger volume in the prism, in spite of a smaller amount of subduction due to the continental nature of that segment of

the slab. The shallower décollement allows the generation of a salient and the accretionary prism is therefore more advanced with respect to the deeper décollement, where the accretionary prism is thicker, the lithostatic load on the décollement is higher. This generates a recess of the prism (Fig. 9).

This study confirms the above statement and gives a bulk estimate of the differences between the two compositional contexts at least for the 12 considered subduction zones. On the oceanic plates (see Table 2), the sedimentary cover entering subduction zones, i.e., $PD*$, is 1.26±0.19 km thick on average, whereas it reaches 5.87±1.43 km on average on the continental downgoing plates. The dimensionless parameter representing the mean depth of the basal décollement ($BD_{normalized}*$, measured as in Eq. 11) is 0.160±0.024 in the continental plates and 0.105±0.016 in the oceanic ones. This means that at the same distance from the thrust front, the basal décollement might be nearly 1.5 times deeper in the continental wedges than in the oceanic ones with a proto-décollement depth 4.5 times higher in the continental downgoing plates than in the oceanic ones.

Belts on top of "W"-directed subduction zones (Fig. 5g) show the lowest area values (Fig. 10): Area* is 48±9 km² for the "western" margins and 317±72 km² for the "eastern" margins. Moreover, with the exception of sections NH-1 and NH-2 and of section CR-1, all of the "western" sections have a lower cross-sectional area of the belt with respect to "E-NE"-di-
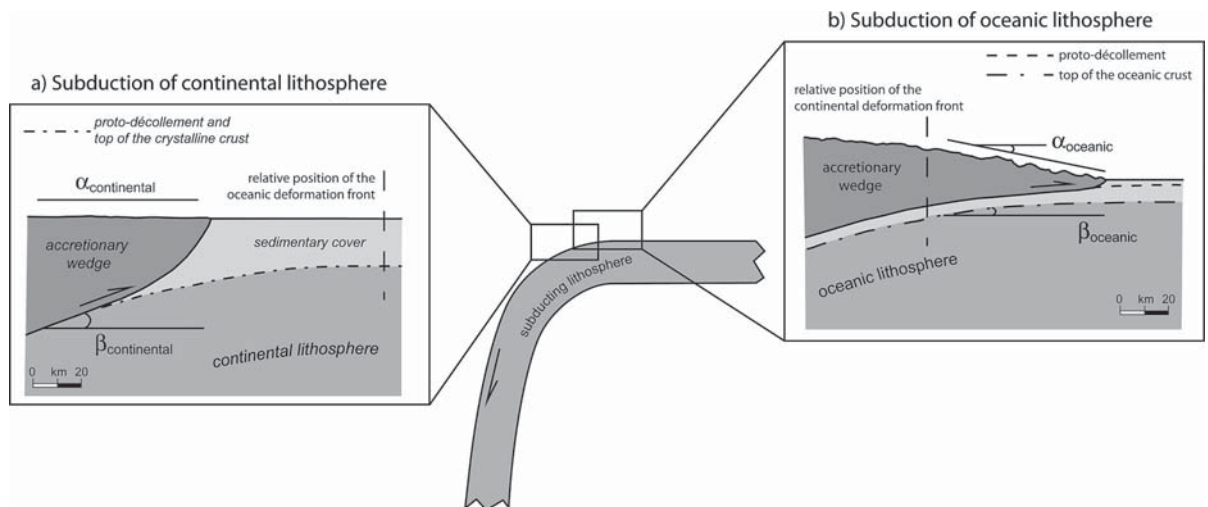
Fig. 9. Schematic diagrams showing difference in dip of the foreland monocline (β) and slope of the wedge topographic envelope (α), starting from the same hypothetical plate curvature, in case of a W-directed subduction zone where **a**) the slab is continental lithosphere, and **b**) oceanic lithosphere. Due to a deeper décollement, wedges developing on top of subducting continental lithosphere (**a**) are less advanced with respect to the oceanic ones (**b**), therefore for the same plate curvature they sit on portion of the foreland monocline, which is more inclined. As a consequence, the frontal portion of a continental wedge may show very little topography, with α values, which are often equal to zero and the envelope to the anticlines may be even negative (as for the Apennines). Note that the continental décollement may coincide with the base of the sedimentary cover, or even involve part of the crystalline crust
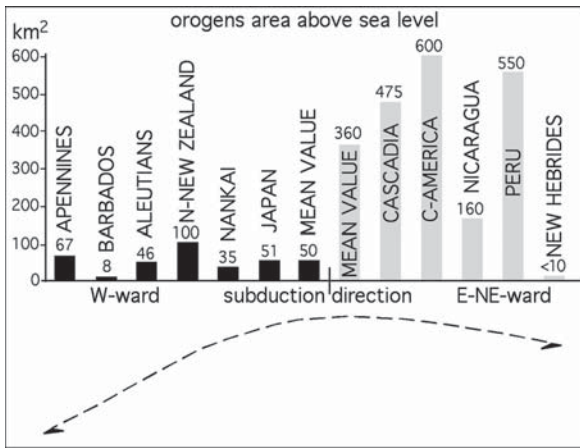
Fig. 10. Average values of the area above sea level of few subduction zones, showing how orogens above E- or NE-directed subduction zones are about 6–8 times larger than the W-directed subduction zones-related accretionary prisms

rected subduction zone sections (see Fig. 4g). As an accepted general rule, the deeper the décollement, the larger the volume of the accretionary wedge. Recall that the depth of the décollement is considered as the thickness of an undeformed crust involved by deformation. During nappe stacking deeper décollement planes generate internally, while the accretion occurs at shallower more external stratigraphic layers.

Shallow décollement in the accretionary prism related to the "western" margins generate smaller volumes of accreted rocks and the topography is then low. The measured depth of the décollement on these prisms (e.g., Apennines, Barbados, Nankai) tends to be shallower than 10 km. The highest topographic elevations, in fact, occur in belts associated with "eastern" margins (Fig. 10), such as the Cascadia, the Middle America, and the Peru-Chile Trenches as well as the Alps, the Zagros and the Himalayas (Harabaglia and Doglioni, 1998). In these belts the décollement and thrust planes affect the whole crust and enter in the upper mantle. Therefore the basal décollement is >30 km and the orogen is highly elevated. This asymmetry points to a worldwide deeper involvement of the lithosphere along E-NE-directed subduction zones.

This analysis seems to suggest that we can interpret the variable geometry of each margin within the two classes, "western" and "eastern", but considering the interplay between parameters together with local characteristics. That is, we have to consider the interplay between dip of the downgoing plate, and thickness of the sedimentary cover (i.e., the availability of material that can be accreted into the wedge) and their effect onto the other parameters. For instance, in the Eastern Aleutians (section Al-3), where the Pacific plate is subducting north-westward, the wedge

shows a higher value of α_{mean} with respect to the average value of the "western" margins: α_{mean} is 4.7 degrees vs. α_{mean}* of 1.90±0.34 degrees for "western" margins or α_{mean}* of 2.38±0.43 for "oceanic western" margins. This is probably due to the proximity of the wedge to the Alaskan continental platform, and the consequent thick sedimentary cover above the subducting plate as shown by the relative PD value: a greater volume of sediments entering the wedge necessarily leads to a thicker wedge, other conditions being equal (such as friction on the décollement plane and material involved). Another apparent outlier is represented by the Central Apennines, where the continental Adriatic lithosphere is subducting westward, as clearly evidenced by tomographic images (Ciaccio et al., 1998; De Gori et al., 2001; Piromallo and Morelli, 2003) and by a few hundreds of kilometers shortening in the passive continental margin sedimentary sequences involved in the accretionary wedge (Bally et al., 1986). In this area (sections A-3 and A-4), the regional monocline has a low dip value. This is probably due to a lower subductibility of the Adriatic plate in this sector, as suggested by Mariotti and Doglioni (2000). The complex crustal history of the Adriatic plate, in fact, led to a high lateral variability in thickness, composition and rheology, and, consequently, in mechanical behavior when involved in mountain building, as also shown by the variation along strike of the measured parameters (see Fig. 3 and Table 1). Moreover, the North New Zealand and Barbados sections are characterized by a lower β_{Wmean} with respect to the mean value of "western" monoclines. On the other hand, the α_{mean} and PD values are included among the average (see Table 1). A possible explanation can be found in the relative position of the wedge with respect to the subduction hinge (Fig. 9): due to a high efficiency décollement the wedge may advance further over the incoming plate, i.e., above a less dipping portion of the monocline. This explains also the high value of the dip of continental monoclines, and the low values of the slope of the related wedge topographic envelope. In continental subduction, in fact, the increased depth to the basal décollement (see Fig. 3, Tables 1 and 2) can result in the accretionary wedge being thicker, but not extending as far out over the incoming continental plate. The measured regional monocline dip in a continental downgoing plate can be higher (Fig. 7) than that of an oceanic plate, due to the different position of the wedge above the plate (Fig. 9), and as a consequence the frontal part of the wedge will be characterized by very low values of the wedge topographic envelope, since the wedge does not develop frontal topography (compare average values in Table 2). The Apennines clearly show this mechanism, with high β_W values and low α angles. The α values become negative (i.e., landward dipping) if we consider the envelope of the growing folds

crests at the front of the wedge such as in the Northern Apennines (Doglioni and Prosser, 1997).

Other outliers are: section N-2, which probably shows anomalous values due to the shortness of the section (compare with sections N-1 and N-3 in Fig. 3); the Chile section (Ch), with high values of β, both in the foreland (β_{frl}) and below the wedge (β_{Wmean}), due to the proximity of the section to the Chile Ridge, so that part of the dip is related to the thermal state of the young oceanic crust; the New Hebrides sections (NH-1, NH-2), of which anomalous values have probably to be related to the complexity and early age of the subduction zone (Pysklywec et al., 2003 and references therein); the Japan section (J), which shows a high α_{mean} value, probably to be connected to a high friction décollement plane (Gutscher et al., 1998), or the inversion of the system. In fact the subduction hinge is now moving toward the upper plate (Doglioni et al., 2006). The ($\alpha+\beta$) value is greater for the continental subducting plate than for the oceanic subducting plate as a general rule, regardless of the polarity of the subduction. This can be explained by the lower density of continental rocks and the consequent deeper décollement accreting rocks, preventing their subduction and increasing the volume of the orogen. Moreover, it seems confirmed that the wedge envelope is lower when it is subaerial than when it is submarine, due to the water load and to the erosion. However, this distinction is beyond the scope of this paper.

7 Conclusions

The thrust belts and orogens in general are the combination of a number of distinct parameters (Fig. 11). However, as a first-order signature, two main types of subduction zones and related orogens can be distinguished (Fig. 8), i.e., 1) those where the subduction hinge migrates away from the upper plate, and 2) those in which the subduction hinge migrates towards the upper plate (Doglioni et al., 2006). The steeper foreland monocline and faster subsidence rates in the trench or foredeep (>1 mm/yr, Doglioni, 1994), the lower topographic envelope, and the smaller cross-sectional area occur where the subduction hinge migrates away from the upper plate. This setting is usually associated to W-directed subduction zones, and since the hinge rolls back from the upper plate, the dip of the slab and the related hinge are more pronounced. An exception is the W-directed Japan subduction where the hinge is migrating toward the upper plate (Doglioni et al., 2006), but the system is inverting and the backarc basin shrinking (Mazzotti et al., 2001). In the opposite E- or NE-directed subduction zones (along the undulated flow of Fig. 8), the hinge migrates systematically towards the upper plate, the slab is generally less in-

clined and shallower. As a consequence, the foreland regional monocline mimics the slab behavior, since it is the uppermost part of it, and it is shallower, less inclined, and the subsidence rate is low (<0.3 mm/yr). The topographic envelope is steeper than in the opposite setting, and the cross-sectional area is very large. If we compare the foreland monocline dip data in Table 1, and consider this value as representative of the dip of the shallow part of the subducting slab, we observe that the "older-heavier-steeper" model holds locally but is not a general rule (Fig. 6). Cruciani et al. (2005) have shown how the slab dip in the first 250 km is not simply correlated to the age of the slab. Other controlling factor may operate in determining the inclination of slabs, such as the thickness of the overriding plate and the "eastward" mantle flow implicit with the recognition of the "westward" drift of the lithosphere (Doglioni et al, 1999; Crespi et al., 2007).

This analysis confirmed that the subducting plate nature is only partly a controlling factor on the morphology of the frontal and shallower part of subduction zones. In particular, along W-directed subduction zones, continental convergent margins are characterized by a lower slope of the wedge topographic envelope, a steeper regional monocline, a deeper décollement (both in terms of sediments entering the wedge and basal wedge detachment) with respect to oceanic convergent margins.

Moreover, this analysis showed an asymmetry of studied convergent margins, which can be described by the "lower α - higher β - shallower décollement - lower area versus higher α - lower β - deeper décollement - higher area" proposition. This asymmetry seems more sensitive to the geographic polarity, i.e., W-directed versus E-NE-directed subduction zones. Alternatively, it can be described by the opposite behavior of the subduction hinge, migrating away or toward the upper plate, rather than to the age of the oceanic lithosphere or the subducting plate nature. Although located closer to the subduction hinge (Fig. 9a), the Apennines continental sections, for example, show a geometry of both wedge and foreland monocline which is comparable to that of the "western" oceanic sections. Further similar examples are: i) the Carpathians (Roure et al., 1993), characterized by a blocked vertical continental slab following the interpretation of Oncescu (1984), ii) the Banda arc, where the Australian continental lithosphere is subducting westward (Tandon et al., 2000), and iii) the Sandwich arc, where, although the westward subducting oceanic lithosphere is of variable age, the arc geometry is laterally uniform and comparable to that of Barbados and western pacific margins.

Subsidence rate in the foredeep is much faster (>1mm/yr) along foredeeps of W-directed subduction zones and the regional monocline is steeper (Doglioni, 1992; 1994). The prism related to these subductions

has shallow depth of the basal décollement and is composed mostly by shallow rocks and sedimentary cover. The structural elevation is instead very elevated along orogens related to E-NE-directed subduction zones where the basal décollement is deeper than the crust and deep rocks are extensively involved in the orogen (Doglioni et al., 1999). The single vergent accretionary prism related to W-directed subduction zones is formed at the expense of the shallow layers of the lower plate (e.g., Apennines, Carpathians, Barbados).

The orogens generated by E- or NE-directed subductions are double vergent since the early stages, and upper plate rocks mostly compose them (e.g. Andes) until the continental collision takes place, extensively involving the rocks of the lower plate (e.g., Alps, Zagros, Himalayas). The convergence/shortening ratio in this type of orogens is higher than 1 and is inversely proportional to the viscosity of the upper plate. The higher the viscosity, the smaller the shortening and faster the subduction rate. The convergence/shortening ratio along W-directed subduction zones is instead generally lower than 1 (Doglioni et al., 2006). The foreland regional monocline is on average steeper along W-directed subduction zones than along the opposite settings (Fig. 7). The topographic envelope is instead less inclined and the critical taper slightly smaller than along orogens related to E- or NE-directed subduction zones (Fig. 8). This asymmetry is particularly highlighted by topography, being W-directed subduction zones characterized by much lower elevation than the opposite settings (Fig. 10).

The present analysis proposes the polarity of the subduction as a plausible key-reading of convergent margins. These asymmetries can be related to the rotational forces controlling plate tectonics and determining a net rotation of the lithosphere roughly westerly directed (Doglioni et al., 2003; Scoppola et al., 2006) along the undulate flow of plate motions (Doglioni, 1990). Therefore the first-order control on orogens and accretionary prisms can be global, determining two end-member classes geographically controlled (Fig. 8), whereas local/regional stratigraphic-rheological characteristics (e.g., Bigi et al., 2003) may cause diversions from the expected theoretical behavior without completely obscuring the geographic tuning (Fig. 11). A possible explanation of this tuning could be provided by the "westward" drift of the lithosphere. The net rotation of the lithosphere relative to the asthenospheric mantle has been suggested by a number of authors, i.e., Rittman (1942), Le Pichon (1968), Bostrom (1971), Nelson and Temple (1972), Dickinson (1978), Uyeda and Kanamori (1979), Doglioni (1990), Gripp and Gordon (2002), Crespi et al. (2007). As a consequence of the delay of the lithosphere with respect to the underlying mantle, a main flow of plate motions should develop: signal and consequence of this main flow should be represented by the asymmetry of subduction zones (Doglioni et al., 1999). Recently, Scoppola et al. (2006) have proposed the occurrence of very low-viscosity intra-asthenospheric layers allowing the tidal drag to be efficient in determining the "westward" lithospheric rotation.

Fig. 11. The orogens are structured by the combination of a number of parameters, the most important listed in the figure
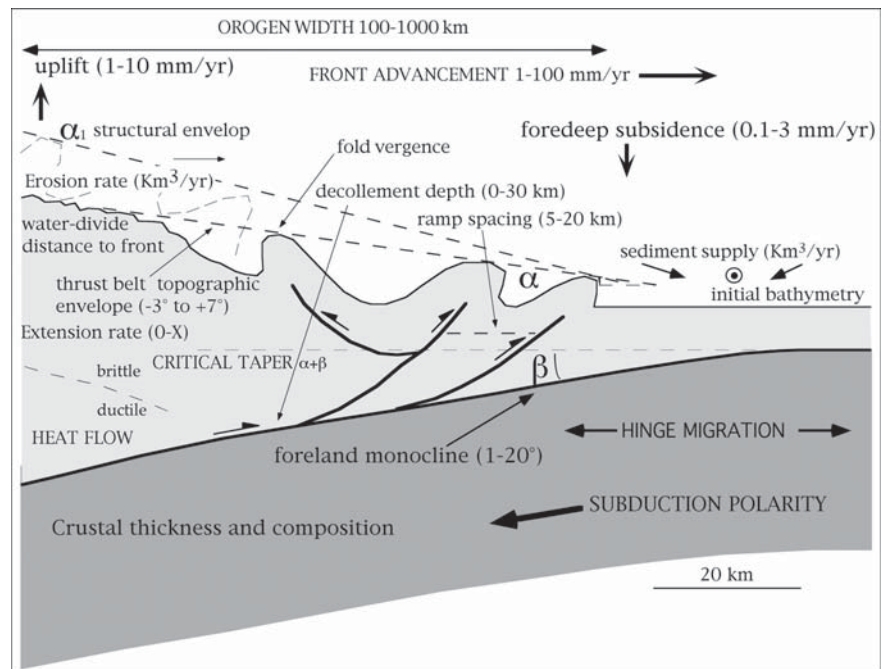
Acknowledgements

References

Avouac J-P (2003) Mountain building, erosion, and the seismic cycle in the Nepal Himalaya. Advances in Geophysics, 46:1-80, DOI: 10.1016/S0065-2687(03)46001-9.

Bally AW, Burbi L, Cooper C, Ghelardoni R (1986) Balanced sections and seismic reflection profiles across the central Apennines. Mem Soc Geol It 35:257–310.

Bangs NL, Shipley TH, Moore JC, Moore G (1999) Fluid accumulations and channeling along the Northern Barbados Ridge décollement thrust: J Geophys Res 104:20,399–20,414.

Bangs NLB, Westbrook GK, Ladd JW, Buhl P (1990) Seismic Velocities From the Barbados Ridge Complex: Indicators of High Pore Fluid Pressures in an Accretionary Complex. J Geophys Res 95:8767–8782.

Behrmann JH, Lewis SD, Cande SC (1994) Tectonics and geology of spreading ridge subduction at the Chile Triple Junction: a synthesis of results from Leg 141 of the Ocean Drilling Program. Geol Rundsch 83:832–852.

Bello M, Franchino A, Merlini S (2000) Structural model of Eastern Sicily. Mem Soc Geol It 55:61–70.

Bigi S, Lenci F, Doglioni C, Moore JC, Carminati E, Scrocca D (2003) Décollement depth vs accretionary prism dimension in the Apennines and the Barbados. Tectonics 22:1010, doi:10.1029/2002TC001410.

Bostrom RC (1971) Westward displacement of the lithosphere. Nature 234:536–538.

Boyer SE (1995) Sedimentary basin taper as a factor controlling the geometry and advance of thrust belt. Amer J Sci 295:1220–1254.

Bruns TR, von Huene R (1986) Aleutian Trench, Shumagin Segment, Seismic Section 104. In: von Huene R (ed), Seismic images of modern convergent margin tectonic structure. AAPG Studies in Geol, 26, Tulsa, OK, United States, pp 14–15.

Catalano R, Doglioni C, Merlini S (2001) On the Mesozoic Ionian basin. Geophys J Int 144:49–64.

Cernobori L, Hirn A, McBride JH, Nicolich R, Petronio L, Romanelli M, STREAMERS/PROFILES Working Groups (1996) Crustal image of the Ionian basin and its Calabrian margins. Tectonophysics 264:175–189.

Chapple WM (1978) Mechanics of thin-skinned fold and thrust belts. Geol Soc Am Bull 89:1189–1198.

Ciaccio MG, Cimini GB, Amato A (1998) Tomographic images of the upper mantle high-velocity anomaly beneath the Northern Apennines. Mem Soc Geol It 52:353–364.

Colletta B, Letouzey J, Pinedo R, Ballard JF, Balé P (1991) Computerized X-ray tomography analysis of sandbox models: examples of thin-skinned thrust systems. Geology 19:1063–1067.

Collins BP, Watkins JS (1986) The Middle American Trench. In: von Huene R (ed), Seismic images of modern convergent margin tectonic structure. AAPG Studies in Geol, vol 26, Tulsa, OK, United States, pp 31–32.

Crespi M, Cuffaro M, Doglioni C, Giannone F, Riguzzi F (2007) Space geodesy validation of the global lithospheric flow. Geophys J Int 168:491–506, doi: 10.1111/j.1365-246X.2006.03226.x.

Crostella AA, Powell DE (1976) Geology and hydrocarbon prospects of the Timor area. Indon Petrol Ass Proc 4:149–171.

Cruciani C, Carminati E, Doglioni C (2005) Slab dip vs. lithosphere age: no direct function. Earth Planet Sci Lett 238:298–310.

Dahlen FA (1990) Critical taper model of fold and thrust belts and accretionary wedge. Earth Planet Sci Lett 19:55–99.

Dahlen FA, Suppe J, Davis D (1984) Mechanics of Fold-and-Thrust belts and Accretionary Wedges: Cohesive Coulomb Theory. J Geophys Res, 89, 10087–10101.

Davey FJ, Childs JR (1986) Convergent Margin off East Coast of North Island, New Zealand, Parts I and II. In: von Huene R (ed), Seismic images of modern convergent margin tectonic structure. AAPG Studies in Geol, vol 26, Tulsa, OK, United States, p 49.

Davis DM, Engelder T (1985) The role of salt in fold-and-thrust belts. Tectonophysics 119:67–88.

Davis DM, Suppe J, Dahlen FA (1983) Mechanics of Fold-and-Thrust Belts and Accretionary Wedges. J Geophys Res 88:1153–1172.

De Gori P, Cimini GB, Chiarabba C, De Natale G, Troise C, Deschamps A (2001) Teleseismic tomography of the Campanian volcanic area and surrounding Apenninic belt. J Volcanol Geothermal Res 109:55–75.

De Voogd B, Truffert C, Chamot-Rooke N, Huchon P, Lallemand S, Le Pichon X (1992) Two-ship deep seismic soundings in the basins of the Eastern Mediterranean Sea (Parsiphaea cruise). Geophys J Int 109:536–552.

Dickinson WR (1978) Plate tectonic evolution of North Pacific rim. J Phys Earth 26, Suppl 51–519.

Doglioni C (1990) The global tectonic pattern. J Geodyn 12:21–38.

Doglioni C (1992) Main differences between thrust belts. Terra Nova 4:152–164.

Doglioni C (1993) Geological evidence for a global tectonic polarity. J Geol Soc London 150:991–1002.

Doglioni C (1994) Foredeeps versus subduction zones. Geology 22:271–274.

Doglioni C, Carminati E, Bonatti E (2003) Rift asymmetry and continental uplift. Tectonics 22: doi:10.1029/2002TC001459.

Doglioni C, Carminati E, Cuffaro M. (2006) Simple kinematics of subduction zones. Int Geol Rev 48:479–493.

Doglioni C, Harabaglia P, Merlini S, Mongelli F, Peccerillo A, Piromallo C (1999) Orogens and slabs vs their direction of subduction. Earth Sci Rev 45:167–208.

Doglioni C, Prosser G. (1997) Fold uplift versus regional subsidence and sedimentation rate. Marine Petrol Geol 14:179–190.

Duncan C, Masek J, Fielding E (2003) How steep are the Himalaya? Characteristics and implications of along-strike topographic variations. Geology 31:75–78.

Fisher MA, Greene HG (1986) The New Hebrides Trench, Lines 1 and 12. In: von Huene R (ed), Seismic images of modern convergent margin tectonic structure. AAPG Studies in Geol, vol 26, Tulsa, OK, United States, pp 43–48.

Garzanti E, Doglioni C, Vezzoli G, Andò S (2007) Orogenic Belts and Orogenic Sediment Provenances. J Geol in press.

Gripp AE, Gordon RG (2002) Young tracks of hotspots and current plate velocities. Geophys J Int, 150:321–361.

Gutscher MA, Kukowski N, Malavieille J, Lallemand S (1998) Material transfer in accretionary wedges from analysis of a systematic series of analog experiments. J Struct Geol 20:407–416.

Hager BH, O'Connell RJ (1978) Subduction zone dips and flow driven by the plates. Tectonophysics 50:111–134.

Harabaglia P, Doglioni C (1998) Topography and gravity across subduction zones. Geophys Res Lett 25:703–706.

Isacks B.L, Barazangi M. (1977) Geometry of Benioff zones: lateral segmentation and downwards bending of the subducted lithosphere. In: Talwani M, Pitman WC (eds), Island Arcs, Deep Sea Trenches and Back Arc Basins, American Geophysical Union, Washington, DC, pp 99–114.

Jarrard RD (1986) Relations among subduction parameters. Rev Geophys 24:217–284.

Karig DE, Sharman III GF (1975) Subduction and accretion in trenches. Geol Soc Am Bull 86, 377–389.

Kawamura T, Aoki Y (1986) The Nankai Trough Margin, record 55-8. In: von Huene R (ed), Seismic images of modern convergent margin tectonic structure. AAPG Studies in Geol, vol 26, Tulsa, OK, United States, pp 55–56.

Kolarsky RA, Mann P, Montero W (1995) Island Arc Response to Shallow Subduction of the Cocos Ridge, Costa Rica. In: Mann P (ed), Geologic and Tectonic Development of the Caribbean Plate Boundary in Southern Central America. Geol Soc Am Spec Paper 295:235–262.

Koyi HA (1995) Mode of internal deformation in sand wedge. J Struct Geol 17:293–300.

Koyi HA, Hessami K, Teixell A. (2000) Epicenter distribution and magnitude of earthquakes in fold-thrust belts: insights from sandbox models. Geophys Res Lett 27:273–276.

Koyi HA, Vendeville BC (2003) The effect of décollement dip on geometry and kinematics of model accretionary wedges. J Struct Geol 25:1445–1450.

Kulm L.D, Miller J, von Huene R (1986) The Peru continental margin, record section 2. In: von Huene R (ed), Seismic images of modern convergent margin tectonic structure. AAPG Studies in Geol, vol 26, Tulsa, OK, United States, pp 39–40.

Ladd JW, Westbrook GK, Buhl P, Bangs N (1990) Wide-aperture seismic profiles across the Barbados Ridge complex. In: Moore JC, Mascle A, et al. (eds), Proc ODP, Sci Results, 110, College Station, TX (Ocean Drilling Program), pp 3–6.

Lallemand S, Heuret A, Boutelier D (2005) On the relationships between slab dip, back-arc stress, upper plate absolute motion and crustal nature in subduction zones. Geochem Geophys Geosyst 6, Q09006, doi:10.1029/2005GC000917.

Lenci F (2003) Monoclinale regionale e orogeni nelle zone di subduzione. PhD Thesis, Università La Sapienza, p 139.

Lenci F, Carminati E, Doglioni C, Scrocca D (2004) Basal Décollement and Subduction Depth vs. Topography in the Apennines-Calabrian arc. Boll Soc Geol It 123:497–502.

Le Pichon X (1968) Sea-floor spreading and continental drift. J Geophys Res 73:3661–3697.

Liu H, McClay KR, Powell D (1992) Physical models of thrust wedge. In: McClay KR (ed), Thrust tectonics, Chapman and Hall, London, pp 71–81.

Mariotti G, Doglioni C (2000) The dip of the foreland monocline in the Alps and Apennines. Earth Planet Sci Lett 181:191–202.

Mazzotti S, Henry P, Le Pichon X (2001) Transient and permanent deformation of central Japan estimated by GPS 2. Strain partitioning and arc-arc collision: Earth Planet Sci Lett 184:455–469.

Miller J, Hussong D, von Huene R (1986) The Peru continental margin, record section 3. In: von Huene R (ed), Seismic images of modern convergent margin tectonic structure. AAPG Studies in Geol, vol 26, Tulsa, OK, United States, pp 41–42.

Moore JC, Bjiu-Duval B, Natland JH, The Leg 78 Shipboard Scientific Party (1984) Offscraping and underthrusting of sediment at the deformation front of the Barbados Ridge; an introduction to the drilling results of Leg78A and explanatory notes. In: Orlofsky S (ed), Deep Sea Drilling Project, Init Rep, 78A, Washington, DC, US Govt. Printing Office, pp 5–22.

Moore JC, Taira A, Moore G (1991) Ocean drilling and accretionary processes. GSA Today, 1:267–270.

Moore GF, Zhao Z, Shipley TH, Bangs N, Moore JC (1995) Structural setting of the Leg 156 area, Northern Barbados Ridge accretionary prism. In: Shipley TH, Ogawa Y, Blum P, et al. (eds), Proc ODP, Init Repts, 156, College Station, TX (Ocean Drilling Program), pp 13–27.

Morellato C, Redini F, Doglioni C (2003) On the number and spacing of faults. Terra Nova 15:315–321, doi: 10.1046/j.1365-3121.2003.00501.x.

Mugnier J-L, Huyghe P (2006) Ganges basin geometry records a pre-15 Ma isostatic rebound of Himalaya. 34:445–448, doi: 10.1130/G22089.1.

Mulugeta G. (1988) Modelling the geometry of Coulomb thrust wedge. J Struct Geol, 10:847–859.

Nelson TH, Temple PG (1972) Mainstream mantle convection, a geologic analysis of plate motion. Am Ass Petrol Geol Bull 56:226–246.

Oncescu MC (1984) Deep structure of the Vrancea region, Romania, inferred from simultaneous inversion for hypocentres and 3-D velocity structure. Ann Geophys 2:22–28.

Pieri M (1983) Three seismic profiles through the Po Plain. In: Bally AW (ed), Seismic expression of structural styles, AAPG Studies in Geol vol 15(3), Tulsa, OK, United States, pp 3.4.1/8–3.4.1/26.

Piromallo C, Morelli A (2003) P-wave tomography of the top 1000 km under the Alpine-Mediterranean mantle. J Geophys Res 108 doi:10.1029/2001JB001690.

Pysklywec RN, Mitrovica JX, Ishii M (2003) Mantle avalanche as a driving force for tectonic reorganization in the southwest Pacific. Earth Planet Sci Lett 209:29–38.

Ranero C, von Huene R, Flueh E, Duarte M, Baca D, McIntosh KD (2000) A cross section of the convergent Pacific margin of Nicaragua. Tectonics 19:335–357.

Rittmann A (1942) Zur thermodynamik der orogenese. Geol Runds 33:485–498.

Roure F, Roca E, Sassi W (1993) The Neogene evolution of the outer Carpathian flysch units (Poland, Ukraine and Romania) kinematics of a foreland/fold-and-thrust belt system. Sediment Geol 86:177–201.

Roure F, Swennen R, Schneider F, Faure JL, Ferket H, Guil-haumou N, Osadetz K, Robion P, Vandeginste V (2005) Incidence and Importance of Tectonics and Natural Fluid Migration on Reservoir Evolution in Foreland Fold-and-Thrust Belts. Oil & Gas Science and Technology Rev IFP, 60:67–106.

Royden LH, Burchfiel BC (1989) Are systematic variation in thrust belt style related to plate boundary processes? (the western Alps versus the Carpathians). Tectonics 8:51–62.

Scoppola B, Boccaletti D, Bevis M, Carminati E, Doglioni C. (2006) The westward drift of the lithosphere: a rotational drag? Bull Geol Soc Am 118:199–209; doi: 10.1130/B25734.1.

Schluter HU, Fritsch J (1985) Geology and tectonics of the Banda Arc between Tanimbar Island and Aru Island (Indonesia) – results of R/V Sonne Cruise SO-16, 1981. Geol Jahrbuch Reihe, E 30, 44.

Scholl DW, McCarthy J, Ryan H (1986) Forearc Margin, Central Aleutian Ridge. In : von Huene R (ed), Seismic images of modern convergent margin tectonic structure. AAPG Studies in Geol, vol 26, Tulsa, OK, United States, pp 10–13.

Shipboard Scientific Party (2000) Leg 190 Preliminary Report: Deformation and fluid flow processes in the Nankai Trough accretionary prism, ODP Prelim Rpt, 190 [Online], available from: http://www-odp.tamu.edu/publications/prelim/190_prel/190PREL.PDF>.

Shipley TH, Buffler RT (1986) Costa Rica continental Margin: Line CR-7. In: von Huene R (ed), Seismic images of modern convergent margin tectonic structure. AAPG Studies in Geol vol 26, Tulsa, OK, United States, pp 33–34.

Silver EA, Kastner M, Fisher AT, Morris JD, McIntosh KD, Saffer DM (2000) Fluid flow paths in the Middle America Trench and Costa Rica margin. Geology, 28:679–682. doi:10.1130/0091-7613.

Snavely PD Jr, von Huene R, Miller J (1986) The Central Oregon Continental Margin, Lines WO76-4 and WO76-5. In: von Huene R (ed), Seismic images of modern convergent margin tectonic structure. AAPG Studies in Geol, vol 26, Tulsa, OK, United States, pp 24–25.

Tandon K, Lorenzo JM, O'Brien GW (2000) Effective Elastic Thickness of the Northern Australian Continental Lithosphere Subducting Beneath the Banda Orogen (Indonesia) Inelastic Failure at the Start of Continental Subduction. Tectonophysics 329:39–60.

Uyeda S, Kanamori H (1979) Back-Arc Opening and the Mode of Subduction. J Geophys Res 84:1049–1061.

von Huene R, Fisher M, Miller J (1986a) The Eastern Aleutian Continental Margin. In: von Huene R (ed), Seismic images of modern convergent margin tectonic structure. AAPG Studies in Geol, vol 26, Tulsa, OK, United States, pp 20–23.

von Huene R, Lallemand S (1990) Tectonic erosion along the Japan and Peru convergent margins. Geol Soc Amer Bull 102:704–720.

von Huene R, Nasu N, Culotta R, Aoki Y (1986b) The Japan Trench: line ORI 78-4. In: von Huene R (ed), Seismic images of modern convergent margin tectonic structure. AAPG Studies in Geol, vol 26, Tulsa, OK, United States, pp 59–60.

von Huene R, Scholl DW (1991) Observations at convergent margins concerning sediment subduction erosion, and the growth of continental crust. Rev Geophys 29:279–316.

Waschbusch P, Beaumont C (1996) Effect of slab retreat on crustal deformation in simple regions of plate convergence. J Geophys Res 101:28133–28148.

Wessel P, Smith WHF (1995) New Version of the Generic Mapping Tools Released. EOS Trans, AGU, 76:329.

Westbrook GK, Ladd JW, Buhl P, Bangs N, Tiley G (1988) Cross section of an accretionary wedge: Barbados Ridge Complex. Geology 16:631–635.

Willett SD (1999) Orogeny and orography: The effects of erosion on the structure of mountain belts. J Geophys Res 104:28957–28981.

Willett SD, Slingerland R, Hovius N (2001) Uplift, shortening and steady state topography in active mountain belts. Am J Sci 301:455–485.

Part II
Exploration of Thrust Belts (1) :
Seismic Imaging and Traps

II

Chapter 3
Understanding Seismic Propagation Through Triangle Zones

Chapter 4
2D Depth Seismic Imaging in the Gaspé Belt, a Structurally Complex Fold Thrust Belt in the Northern Appalachians, Québec, Canada

Seismic imaging remains the main challenge for petroleum exploration in foothills areas. Structural interpretation and subsequent kinematic and basin modelling require also to convert the time sections into the depth domain. Using two case studies in the Polish Carpathians and in the Gaspé Appalachians in Québec, part II of this volume documents the work flow and iterations between the structural and velocity models during seismic processing and depth migration of the profiles.

First described in the Canadian Rockies, frontal triangle zones are common features in many thrust belts. Although they constitute attractive targets for the exploration, they are usually poorly imaged, due to the occurrence of steep or even overturned beds, accounting for rapid vertical and lateral changes in the seismic velocities. Jardin et al. (Chapter 3) describe the results obtained during direct seismic modelling and depth migration in the frontal part of the Polish Carpathians, an area which is also covered by Chapter 20 (part IV).

Bêche et al. (Chapter 4) present the workflow, velocity model and results obtained by depth migration in the Northern Appalachians in Canada, a Paleozoic orogen where post-orogenic erosion accounts for higher average seismic velocities at the surface than in Neogene thrust belts.

Understanding Seismic Propagation through Triangle Zones

Anne Jardin · Rosina Chaker · Piotr Krzywiec

Abstract. Getting a geologically realistic seismic image still remains a great challenge in foothills exploration. When geological structures are complex, seismic sections show distorted images and become difficult to be interpreted. Seismic processing tools, like time and depth migrations, have been developed to deal with this. Furthermore, when lateral velocity variations are strong, depth migration is definitely required. However, for a correct application of this processing, the construction of a detailed depth model describing lateral and vertical velocity variations is essential.

This study aims at showing that, in triangle zones, the structural features can be better retrieved if the seismic wave propagation through the complex subsurface is better understood. This is obtained by application of a workflow combining direct seismic modelling and depth migration processing. The seismic modelling gives a consistent and accurate velocity model used as input in the seismic depth migration. To illustrate the benefits of this approach, we present a synthetic case study based on a schematic model and a real case study from the frontal part of the Polish Carpathians.

1   Introduction

The development of new prospects for oil and gas exploration will rely on our ability to detect reservoirs in complex structural settings (Aamir et al., 2006). In these areas, seismic imaging difficulties are mainly due to highly contrasting velocities, steep structural dips and inverse faults. These limitations lead to erroneous interpretations especially when only time seismic sections are interpreted. To reduce the risks of exploration drilling, seismic modelling is the well-adapted method for assessing the ambiguities of interpretations.

Various modelling techniques exist to simulate the seismic responses through a subsurface model. Kinematic modelling computes seismic reflection traveltimes and simulates seismic ray paths. This is the method most applicable to structural problems and is used to easily compare synthetic and real data by simulating the real seismic acquisition.

In this paper, an advanced seismic modelling and migration processing workflow will be proposed. The objectives of this combined method are, on one hand, to understand the complex ray paths of the seismic waves and, on the other hand, to compute a seismic image representative of the real structures. This approach will be applied on synthetic and real data sets. The synthetic example will aim at understanding the seismic path distortion within a schematic triangle structure and at analysing the variability of the depth migrated images. The real case of the Polish Carpathians will be used to evaluate the efficiency of the combined modelling and migration studies for structural interpretation.

2   Geological and Seismic Characteristics of Triangle Zones

2.1 Geological Settings

Triangle zones are particularly prominent at the foothills margin. It appears in areas where conjugate thrusts are developed as a result of the compressive stress propagation onto the foreland. A schematic model of triangle zone has been proposed (Jones, 1996) illustrating the triangle structures of the Canadian Rocky Mountains (Fig. 1).

A triangle zone or passive roof duplex is composed of a sequence of dipping autochthonous rocks juxtaposed against opposite-dipping strata contained in
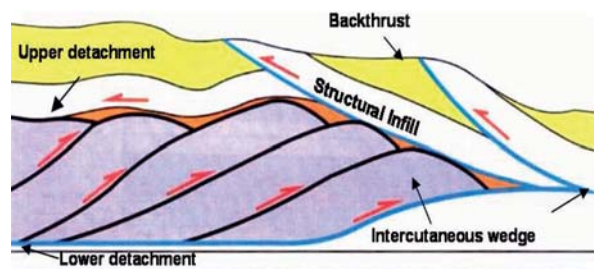
Fig. 1. A schematic model of a "Triangle Zone" or "Passive Roof Duplex" proposed by Jones (1996). The geometrical features are characterized by a sequence of dipping autochthonous layers overlain by rocks dipping in the opposite direction

imbricate thrust structure. These sequences are usually underlain by relatively underformed rocks.

The upper detachment separates the autochthonous rocks on its hanging-wall from the allochthonous rocks in its footwall. The lower detachment is a surface common to the entire thrust and fold belt. It separates allochthonous from autochthonous rocks. The roof and floor of the thrust have opposite vergence and merge at depth to form a frontal tip line that marks the extremity of the intercutaneous wedge. The wedge will continue thickening and advancing into the foreland basin until a critical point along the lower detachment.

2.2 Seismic Imaging Difficulties

In triangle zones, several factors reduce the effectiveness of seismic methods. The topography in the central part of the triangle zone is usually rugged and is associated with near-surface velocity inversions which degrade the quality of the seismic image. These characteristics lead to low signal-to-noise ratio, inadequate penetration of energy through overburden, poor geophone coupling with the surface and wave scattering.

Because of the limited assumptions of time processing, the quality of the time sections is usually deteriorated and seismic interpretation often leads to erroneous structural interpretation. Seismic processing workflow must be selected according to the characteristics of the velocity variations. Therefore, depth migration which takes into account lateral velocity variations is the adapted technique for depth seismic imaging in complex areas. But, in order to deliver a reliable depth image, this processing needs a depth velocity model for accurately focussing the diffracted energy and shifting the events in their true position. Thus, the approach described in the next paragraph will aim at better imaging the triangle zone features by an improvement of both seismic propagation understanding and depth migration processing.

3 Combined Seismic Modelling and Migration Workflow

We propose to apply a combined workflow of two main modelling and migration steps (Fig. 2). Firstly, an initial velocity model is built based on an a priori geological knowledge from regional studies and well data (especially measured depths and sonic velocities) associated with seismic velocity analysis and time section interpretation. This model is then iteratively refined by modelling. IFP has developed a model builder and ray tracer software appropriate to model complex geological features and simulate seismic ray travel paths. The flexibility of this technique allows using both block and smoothed parameterised models through which ray paths and traveltimes are computed for various seismic acquisition patterns. The ray shooting modelling is performed by 2-D and 3-D two-point paraxial ray tracing (Clarke, 1997) which is the kernel of many kinematic applications such as quality control of velocity models, tomography and Kirchhoff migration. A blocky model is made of blocks within which the velocity is constant or variable with a vertical gradient.
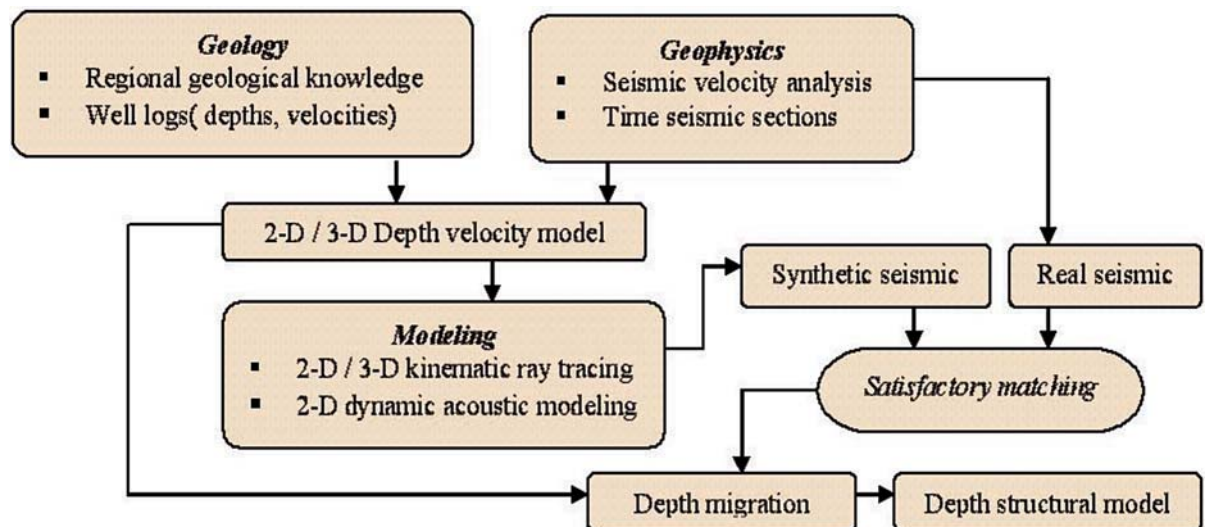
Fig. 2. Combined modelling and migration workflow allowing reliable velocity model building and depth seismic imaging. A priori information from geology and geophysics is used to build an initial depth model iteratively refined by comparison between synthetic and real seismic data

Once the blocky model has been built, a smoothing is introduced in order to replace sharp interfaces with smooth velocity variations.

Secondly, synthetic seismic travel times computed for zero and non-zero offset patterns are compared with picked traveltimes from real shot points and stacked traces. A satisfactory matching ensures a reliable kinematic computation and validates the estimated velocity model. Then this model is introduced in the depth migration processing. In presence of rough topography and complex overburden, innovative migration algorithms using wave equation or Kirchhoff formalisms have been developed by IFP to accurately migrate 2D and 3D seismic data (Duquet et al., 2003), (Rousseau et al.; 2000). Finally the depth seismic image is interpreted to give a depth structural model.

4 Synthetic Model Study

Two models based on the geometrical features of the schematic triangle structure of the figure 1 are built with high and low velocity contrasts within the duplex formation. Each reflector is described by one interface and velocities are assigned to each block (Fig. 3). The constant velocity value (V) and the vertical velocity gradient (K) for each unit of the two models are summarised in Table 1. Smooth versions of these blocky velocity models are computed to overcome the propagation effects related to non realistic abrupt velocity contrasts.

For kinematic ray-tracing modelling, various 2D acquisition patterns were used to model zero-offset sections (Fig. 4) and shot-point gathers (Fig. 5). The sources and receptors are located on the first interface which is used to simulate the curved topography. The green dots shown at this interface indicate a selection of geophone positions. Fig. 6 shows the zero-offset time seismic sections obtained with the two models.

Dynamic modelling is also performed to obtain synthetic traces. These traces will be used to test the sensi-

Table 1. Velocity parameters for the two synthetic blocky models with low (MODEL 1) and high (MODEL 2) velocity contrasts. Structural features of the model are given on Figure 3

Velocity indexes	Depth (km)	Velocity (km/s)		Velocity gradient (s⁻¹)
		Model 1	Model 2	
V0	0	1.5	1.5	0
V1	0.65	3.35	3.35	0.1
V2	3.5	5.88	5.88	0.2
V3	1.9	3.9	6	0
V4	2.3	3.52	4	0.1
V5	2.2	3.52	3.52	0.1
V6	1.98	3.52	5.5	0.1
V7	1.98	3.52	3.52	0.1
V8	2.8	3.52	5.5	0.1
V9	1.5	3.52	3.52	0.1
V10	4.6	5.7	5.7	0.1
V11	1.0	3.52	3.52	0.1
V12	1.26	3.52	3.52	0.1

tivity of depth seismic images to velocity variations by performing pre-stack depth migration (Fig. 7).

4.1 Time Seismic Artefacts

Various effects of complex seismic-ray propagation are detected:

- Shadow zones at the deep interfaces are noticeable on the 2D ray-tracing results (Figs. 4, 5 and 6). The analysis of these results indicates that these reflector discontinuities are generated either by the geometrical features of the triangle zone or the velocity distribution within the duplex units. Figures 4 and 5 show that the rays are distorted when they crossed the ramp or travelled through the duplex. As the

Fig. 3. Synthetic blocky velocity model with velocity values indicated in Table 1

MODEL 1 : Duplex with low velocity contrast

MODEL 2 : Duplex with high velocity contrast
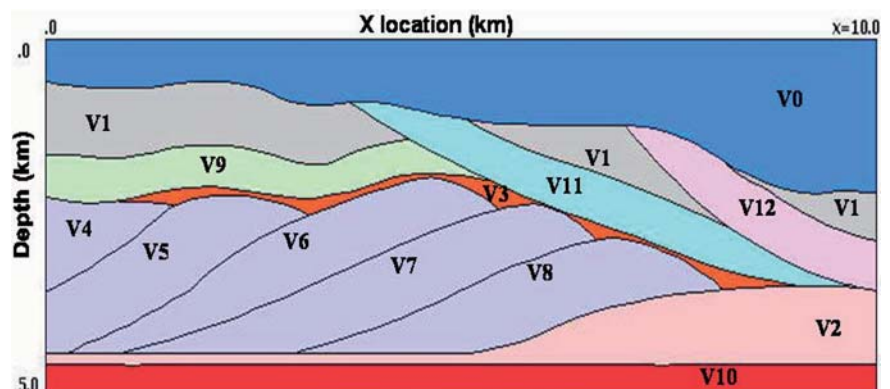
Fig. 4. Zero offset ray tracing modeling for the synthetic models with low (top-MODEL1) and high (bottom-MODEL2) velocity contrasts showing ray path distortion through backthrust and duplex layers and possible shadow zones at the deep and horizontal interface

geological structure is common for both models, the impact of strong variations in the velocity distribution is analyzed on the seismic responses. We can say that this phenomenon of shadow zone extent is more important for the model with the duplex presenting high velocity contrast.

■ Particular attention is paid to the deep horizontal interface. The complicated travel paths of the seismic waves yield pull up effect giving a geometrical deformation of the seismic event (Fig. 6). This may lead to errors in the seismic interpretation because a pull-up could be associated with an anticline. Fig. 6, we do not notice significant kinematic variations on the time zero-offset sections computed with the high or low velocity contrast models, demonstrating that the pull-up effect of the deep reflector is mainly due to the velocity contrast between the dipping layers of the backthrust and the overburden gentle structure. We can conclude that the velocity variations of the duplex do not strongly modify the presence of this effect; they just change the size of the pull-up phenomenon.

4.2 Sensitivity of Depth Migrated Images to Velocity Models

Pre-stack depth migration was applied on synthetic traces to analyze depth-migration failures related to the triangle-zone geometry and velocity model uncertainties. Several depth models used in migration processing were computed by producing increasingly smoothed versions of the exact blocky models. The sensitivity of depth seismic images to these smoothed models could then be assessed. The results of depth imaging using three smoothed velocity models are shown in Fig. 7. To judge how good these depth images are, we pick the deepest reflector and compare its depth to the exact value. From this comparison, it is clear that in the depth image A (top of Fig. 7), all elements of the model are correctly positioned and imaged. The depth images B and C (respectively middle and bottom parts of Fig. 7) show a slight degradation of the image as this deep reflector is not positioned at the true depth. Thus, the degradation of the image with increasing smoothing is gradual. This image degradation is strongest in

Fig. 5. Different shot point tracing modeling through the synthetic models with low (top-MODEL1) and high (middle and bottom-MODEL2) velocity contrasts showing raypath distortion through backthrust and duplex layers

MODEL 1 : Duplex with low velocity contrast

MODEL 2 : Duplex with high velocity contrast
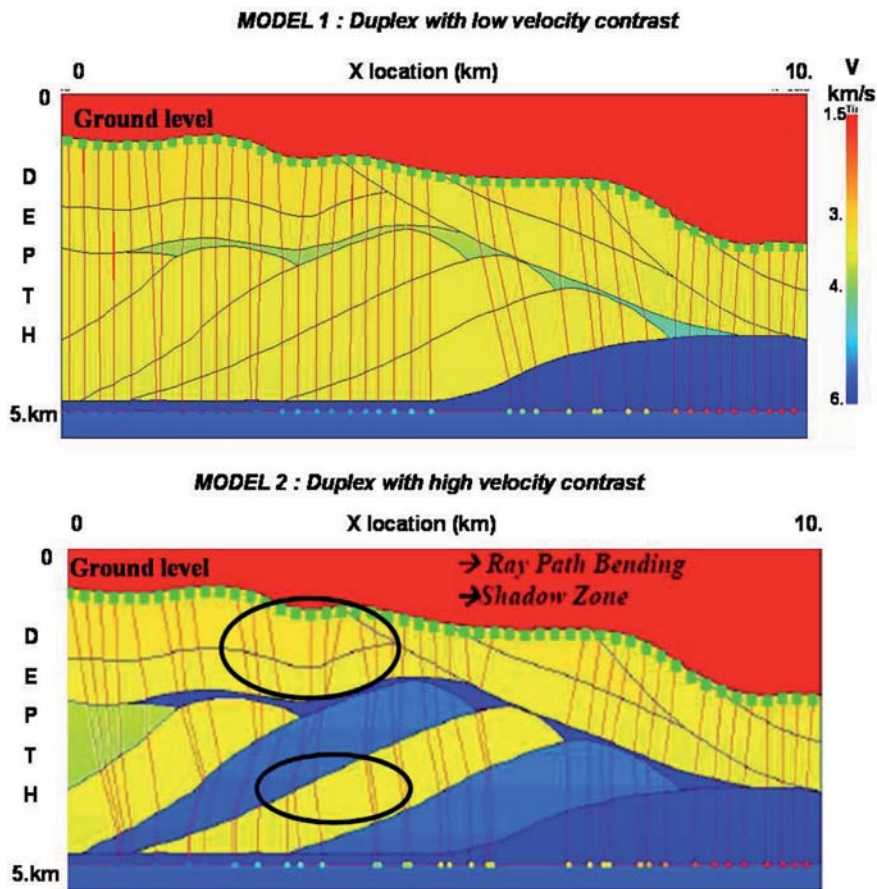
MODEL 2 : Duplex with high velocity contrast
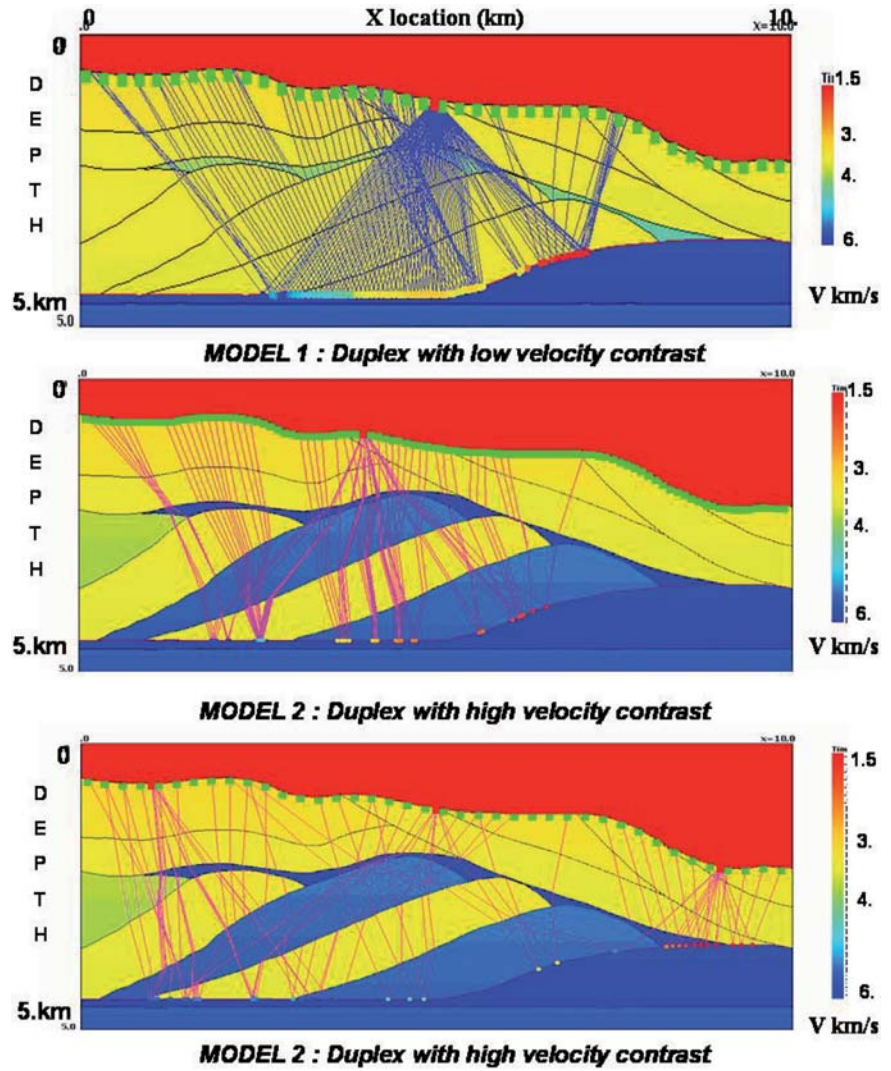
Fig. 6. Synthetic zero offset time sections for the synthetic models with low (top-MODEL1) and high (bottom-MODEL2) velocity contrasts showing pull-up effect and non illuminated or shadow zones at the deepest interfaces

MODEL 1 : Duplex with low velocity contrast

MODEL 2 : Duplex with high velocity contrast
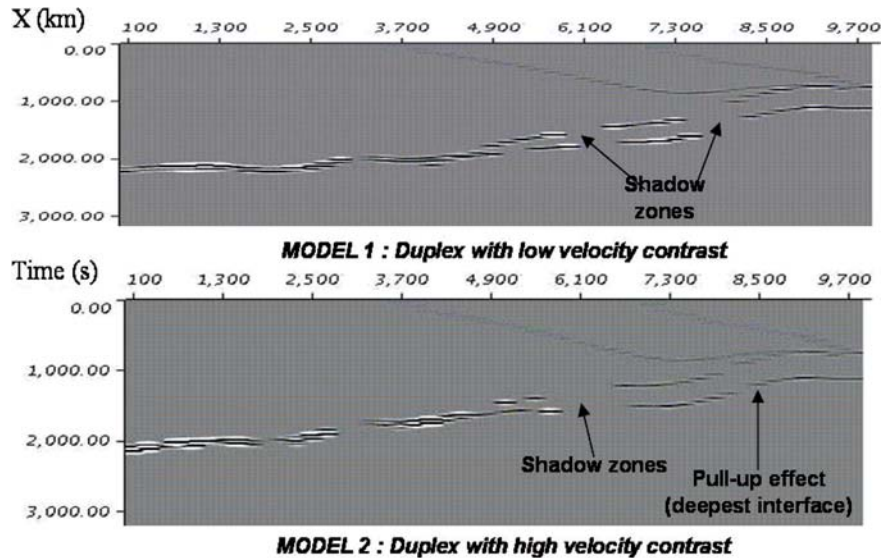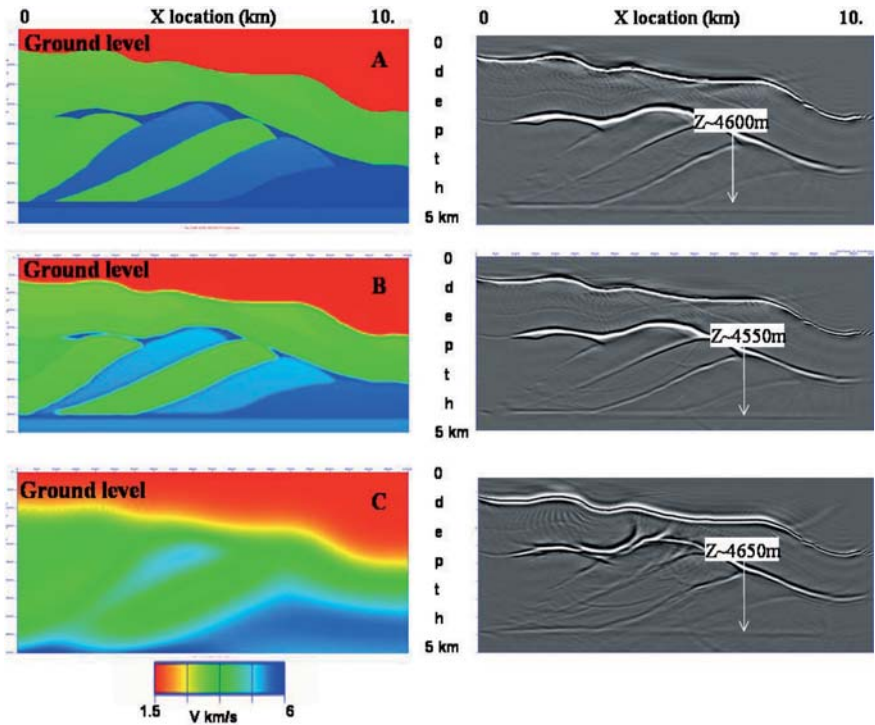
Fig. 7. Sensitivity analysis of depth seismic images to smoothness degrees of depth velocity models introduced in pre-stack depth migration of synthetic seismic traces computed by dynamic modelling. Depth accuracy of the target deep interface has changed with the increase of the smoothing parameters (increase from A to C)
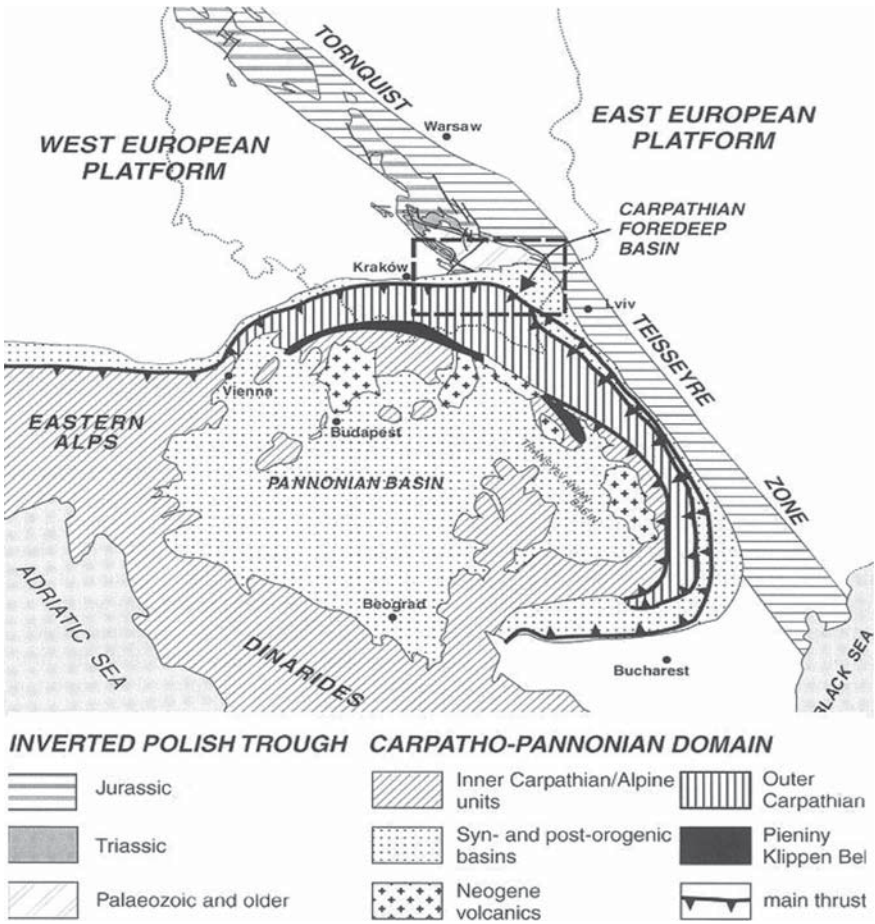
Fig. 8: Geological map and location of the study area in the Polish Carpathian foredeep basin

the deeper complex zone where the smoothing has the largest effect on wave propagation.

If depth migration is performed via a wave-equation algorithm, a blocky representation of the velocity model could be used. However, the Kirckhoff migration, the most often applied algorithm in complex area, requires a smooth velocity model. Thus, we propose to build a first velocity model with a blocky representation that allows the integration of geological information in the velocity model. Then this model is smoothed and its kinematic coherency is checked by ray tracer modelling before performing a depth migration.

5 Polish Carpathians Real Case Study

The geology of the Carpathians is very complex and seismic horizons are highly deformed by tectonics movements, numerous faults and thrusts. The Carpathian foredeep and the Carpathian overthrust belong to the largest petroleum provinces of central Europe (Fig. 8). The Outer Carpathian orogenic belt consists of several imbricated thrust sheets built-up of Cretaceous to lower Miocene Flysch deposits and imbricated Miocene foredeep deposits (Lafargue et al., 1994). The Zglobice and Stebnik units are the most external thrust sheets in the nape pile. The central part of the Zglobice Unit is a passive-roof duplex defining a Miocene triangle zone. Fig. 9 (top) shows the time migrated section of the 2D seismic line 3-02-02K which was acquired across the triangle zone (Krzywiec, 2001), (Krzywiec and et al., 2004). Above the duplex, in the roof of the triangle zone, major synclinal folds are recognised in the Miocene deposits. Some of the inferred tectonic structures are classified as synsedimentary structures that developed during deposition of the post evaporitic Miocene siliciclastic foredeep infill. An important detachment level within the foredeep is defined by the Badenian evaporitic deposits (rock salt, anhydrites, and gypsum). This evaporitic horizon forms an excellent marker for the analysis of seismic reflection data. Beneath the floor thrust of the Zglobice unit, there is a deep buried erosional val-

Fig. 9. The time migrated stack section 3_02_02K (top) and the vertical depth converted stack section with a constant velocity value (3500 m/s) (bottom)

Time migrated stack section

Depth converted stack section
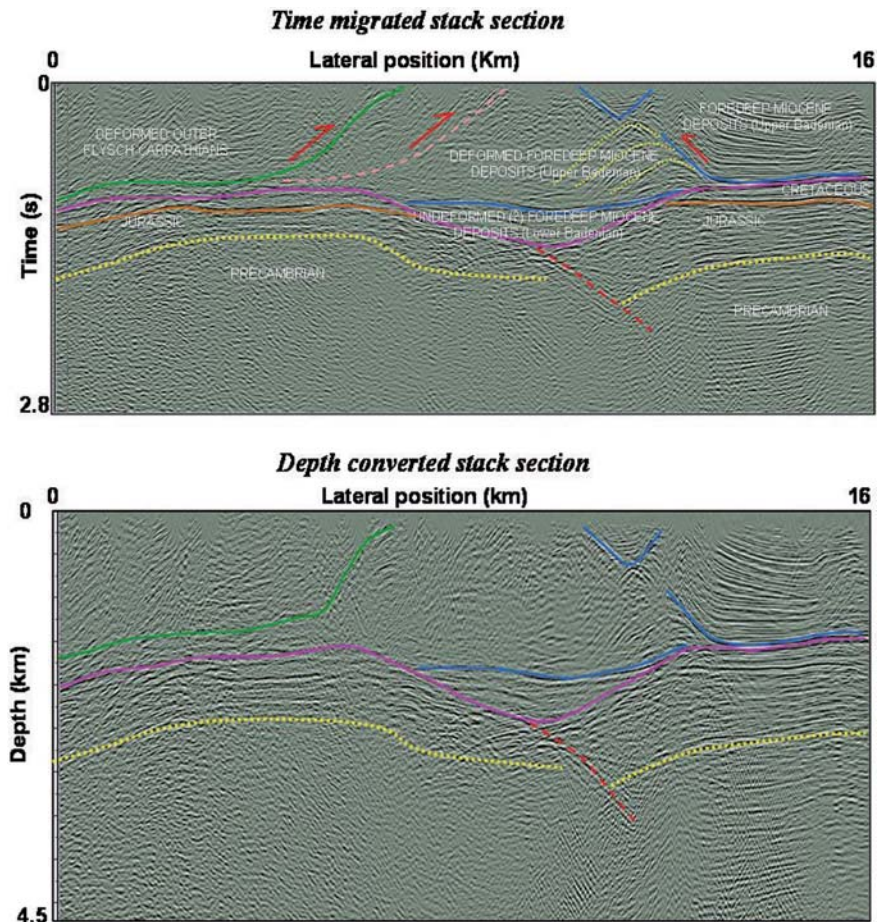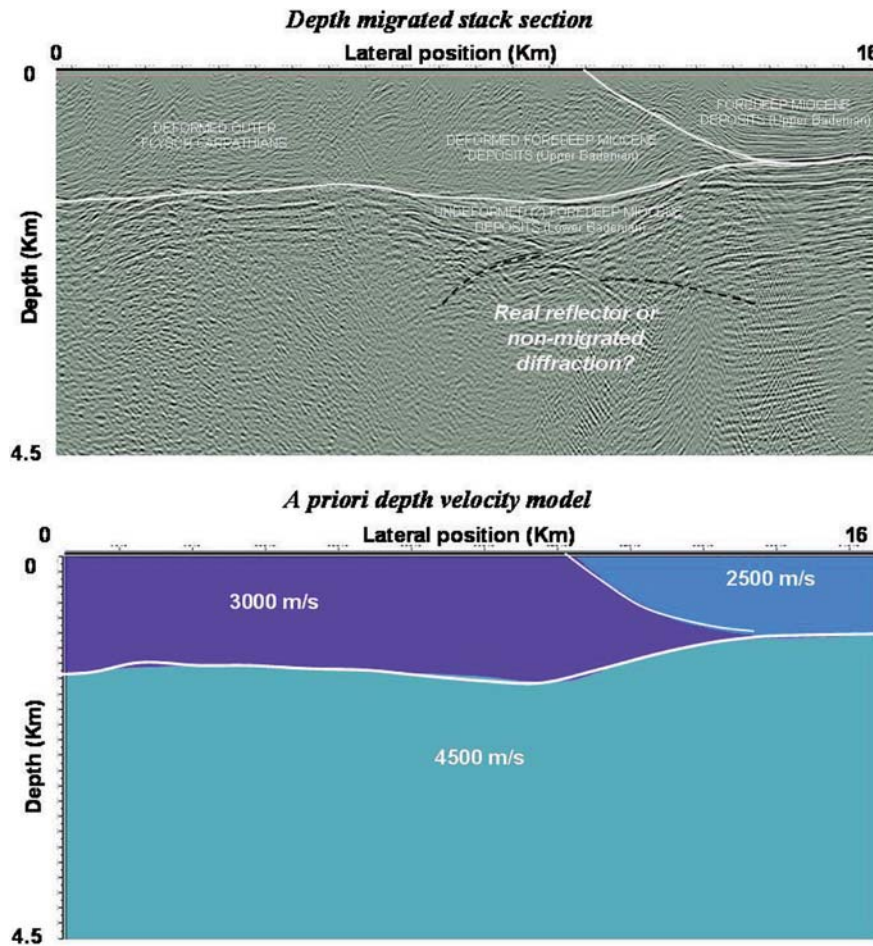
Fig. 10. The depth seismic image (top) obtained by poststack depth migration. Residual hyperbolic events remain visible below the incised valley (Lower Badenian Deposits) and could be interpreted as real reflectors or non-migrated diffractions (top seismic image). The a priori constant velocity model (bottom) used in migration was built from stacking velocity mean values

ley cuts into the Meso-Paleozoic basement. The vertical depth conversion of the time migrated stack using constant velocity values is presented Fig. 9 (bottom). The geometrical features of several geological interfaces have been clearly modified after this operation on the left and right parts of this seismic image.

An initial depth migration of the stack time section (i.e., post-stack depth migration) was performed using a priori velocity model derived from seismic stacking velocity analysis and velocities from projected well logs (Fig. 10). After this processing, several ambiguities in structural interpretation below the triangle structure remain – e.g., real reflected event or non migrated diffraction. Structural model improvement still requires a more accurate velocity model for seismic depth imaging and will be obtained by application of the combined modelling – migration approach.

5.1 Accurate velocity model building

A 2D subsurface model is built based on the interpretation of the seismic stack 3-02-02K depth-convert-ed using the a priori velocity model (Fig. 11). The surfaces selected for modelling are those which delimit the triangle structure: Flysch and Miocene surfaces in the deformed and undeformed Miocene foredeep infill, the evaporitic formation, the incised valley, the fault and the main surfaces that composed its footwall and hangingwall (Cretaceous, Jurassic and Carboniferous, Precambrian formations). Using interval velocity computed from vertical seismic profile measurements, P-velocity values are assigned to the different blocks of the horizontal extent of the 2D depth model (Table 2). The depth of the model is calibrated against the interpreted depth seismic line 3-02-02K. Thus, the 2D model is defined in practice over 16 km is x-direction; 4.6 km is z-direction. Data on CMP elevation and floating datum static corrections written in the trace header do not indicate great variations, implying that we have, in this case, a relatively gentle topography. The datum plane estimated around 200 m is taken into account in the model description.

A kinematic modelling was performed using this initial velocity model. Seismic acquisition parameters used for modelling are derived from real acquisition

Table 2: Layer velocity variations for the geological units of the Polish Carpathians case study

Geological units	Layer velocity variations (m/s)
Carpathians Flysch	3500–3800
Deformed Miocene units	2700–3300
Undeformed Miocene units	2700–3300
Miocene evaporites	3800–4200
Sub-evaporitic lower Badenian siliciclastics (including infill of the erosional valley)	3400–3800
Cretaceous	3700–4600
Jurassic	4500–5000
Carboniferous	5500
Precambrian	5500

parameters. Travel times are calculated by both shot-gather and zero-offset ray-tracing modes through the velocity model for the horizons picked on the 3-02-02K section: Flysch formation limits, interface base of deformed and undeformed Miocene units, incised valley interface base, Cretaceous and Jurassic interface bases. As the zero-offset mode simulates a time stack section, these travel times are superimposed on the 3-02-02k real stack section to check the kinematic coherency between the real and synthetic data (Fig. 12). The aim is to assess the depth velocity model.

Compared to the a priori velocity model (Fig. 10), this second velocity model is more sophisticated and showed velocity variations that could be correlated with structural and geological variations (Fig. 11).

Fig. 11. The depth seismic image (top) obtained by poststack depth migration using a more detailed velocity model (bottom). This model was computed by applying the combined modelling and imaging approach of the figure 2 and contains lateral and vertical gradient variations. A better focussing of the diffraction events below the incised valley is clearly visible due to the velocity model improvement
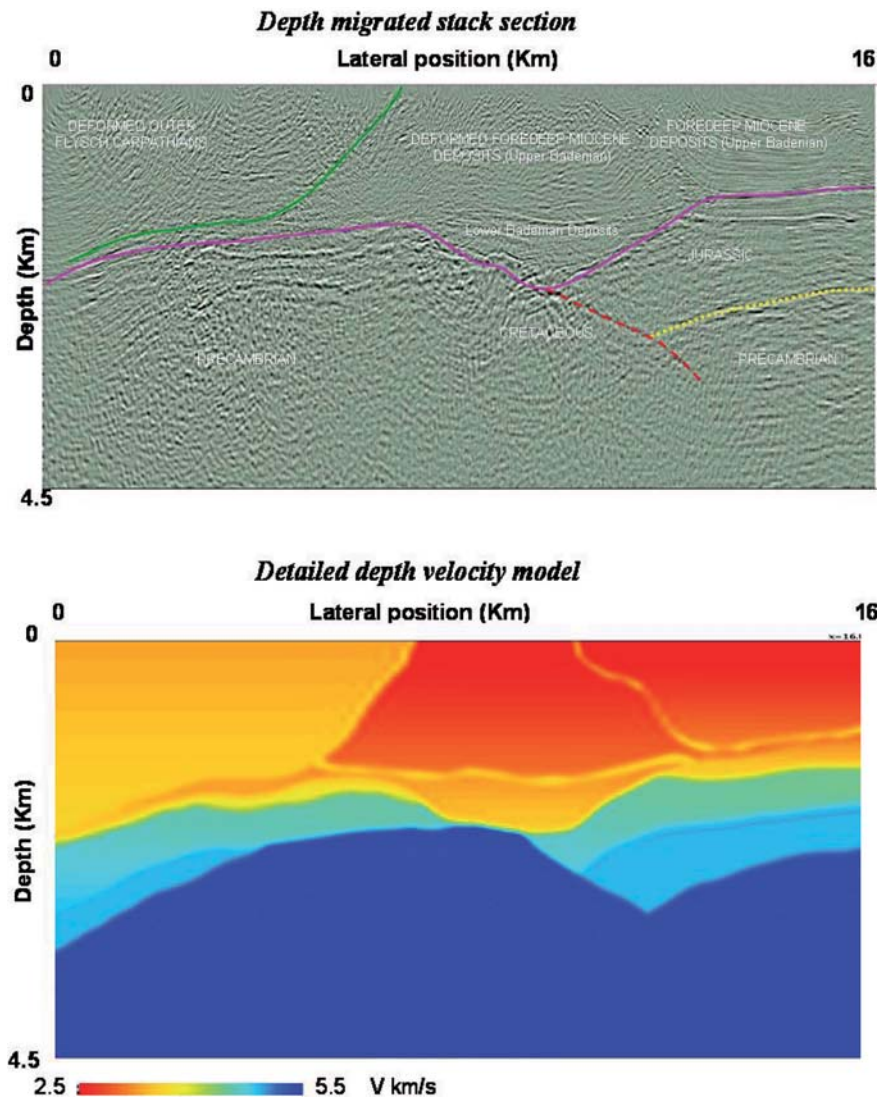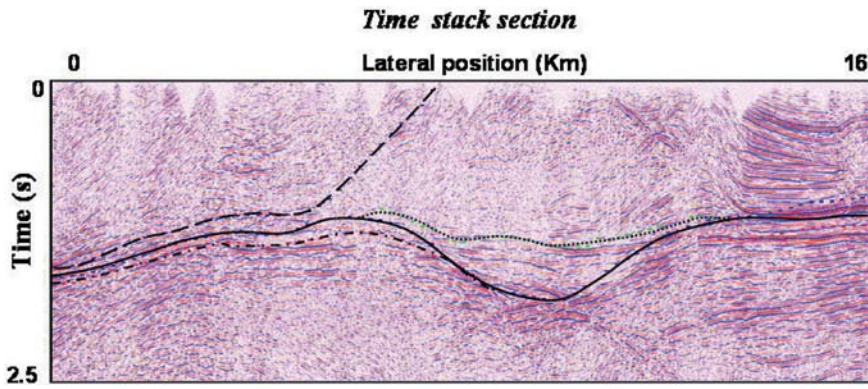
Time stack section

Fig. 12. Comparison of real times from direct interpretation of stack time section and synthetic times (in black curves). Synthetic times were computed by kinematic modelling through the depth velocity model of the figure 10. This analysis is done to check the kinematic consistencies of all the data used in seismic imaging processing

Depth migrated stack section with a priori model

Depth migrated stack section with detailed model
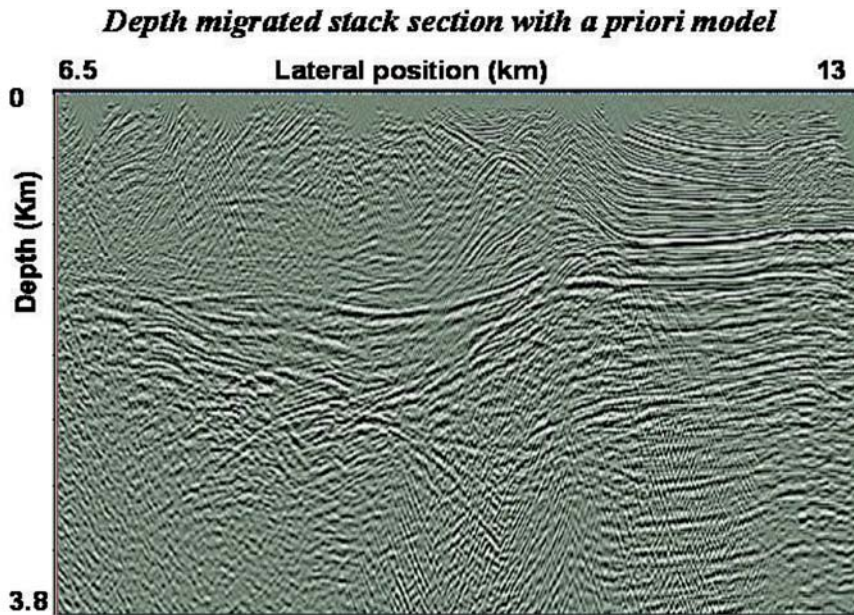
Fig. 13. Comparison of depth images using the a priori velocity model (*top*) and the detailed velocity model (*bottom*). Improvement of diffraction focussing and fault delineation are clearly visible. This is due to the better estimation of velocity variations in the overburden triangle zone
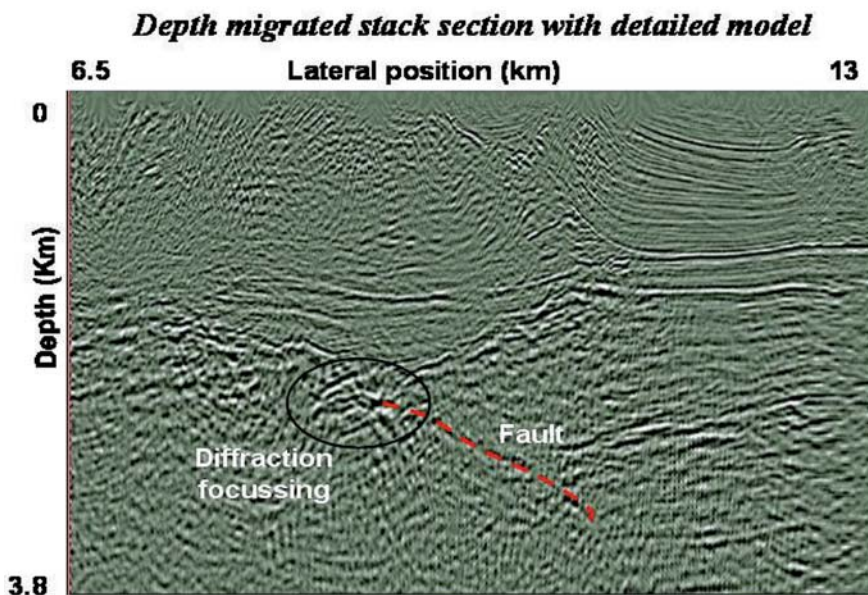
Fig. 14. Comparison of depth (*top*) and time (*bottom*) migrated seismic images. Depth migration has improved the layer delineation (no crossing reflectors) and the geometry of the deformed Miocene deposits (passive roof duplex and backthrust)
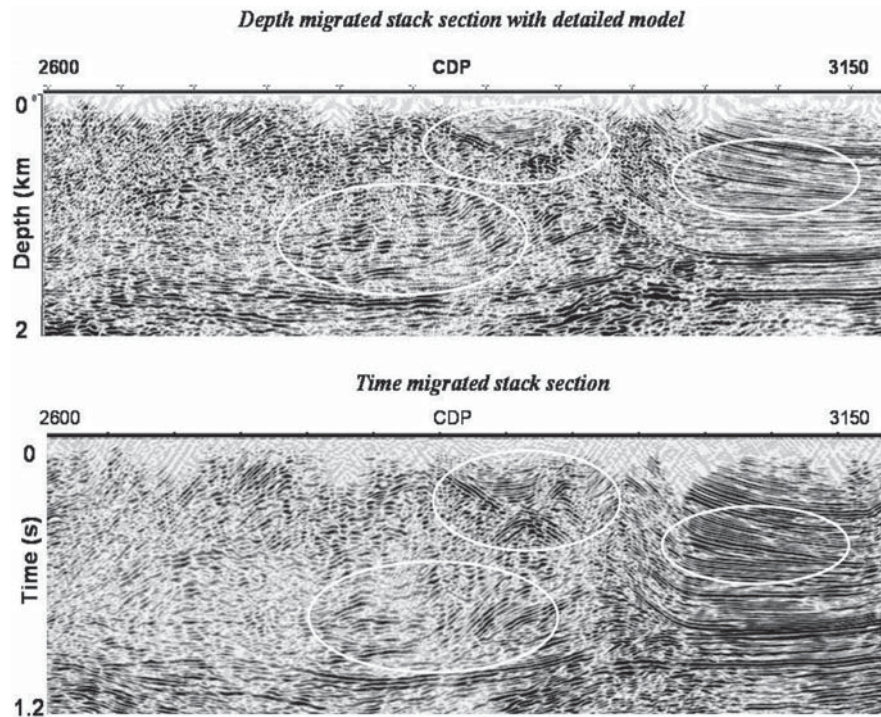
5.2 Depth migration

The blocky velocity model is slightly smoothed before performing the depth migration whatever the algorithms used. The depth seismic images using the two velocity models in the area of the triangle structure are compared (Fig. 13). The seismic event located around 2000-3000 m is better migrated and reflector endings are more visible when the kinematically consistent velocity model has been used. Thus the quality of the seismic image is improved. This will help in reducing the ambiguities in the seismic interpretation, especially those below the core of the triangle zone. To complete this analysis, the time migrated stack section and the depth migrated stack image are compared (Fig. 14). Even if time migration could also give a good diffracted energy focussing, layer termination and local pinch outs are better resolved on depth images. The dips of the geological units are also more accurately and directly estimated. Further improvements can still be obtained by application of an efficient pre-stack depth migration on the pre-processed shot point gathers followed by the stacking of partial angle traces. The checking of seismic event flatness on depth migrated trace gathers ensures the reliability of the velocity data as an additional quality control of depth imaging processing.

6   Conclusion

In fold and thrust belt areas, structural features named "triangle zones" are characterized by complex layer geometry and velocity variations. The poor quality of the seismic image encountered in such geological settings is due to the complex propagation of seismic energy through the overburden structure associated with strong velocity distribution. It results in shadow zones and in geometrically deformed seismic events, which make any interpretation difficult. In order to select the seismic processing parameters like migration velocities and reduce the ambiguities in structural interpretation, it is important to better understand the real seismic wave propagation for these specific seismic events. In this study it was performed using adapted seismic modelling and the application of a combined modelling and migration workflow.

Two examples, a synthetic example based on a schematic triangle zone and a real case from the Polish Carpathians, have been addressed. Velocity models were built and introduced in the seismic modelling software. Using non-zero and zero-offset ray-tracing modelling, seismic interpretation has been carried out to analyse specific seismic travel paths encountered in these areas. We have demonstrated that these events could be generated by complex seismic wave propagation which leads to ambiguities in time seismic in-

terpretation because specific artefacts like pull-up and shadow-zone effects are present.

Based on geophysical and geological framework, a velocity model was built using an interpretative approach. This depth model was next introduced in the seismic modelling software in order to assess its kinematic accuracy. The aim was to compare the synthetic and the real data. When the two agreed to within an acceptable level of accuracy, the depth velocity model has been used for depth migration.

These two case studies illustrated the practical use of ray-tracing modelling to:

- Simulate and understand seismic wave propagation and analyse seismic processing and interpretation difficulties in this complex geological context.
- Check the kinematic accuracy of the velocity model built by an interpretative and iterative approach.

The conclusion is that the combined analysis of real and synthetic gathers computed by adapted seismic modelling can provide the key elements for the determination of the structural origin and of the seismic nature of particular events which can not be clearly interpreted on seismic time sections. In case of complex seismic propagation, their efficient identification will guide the geologist interpreter for properly analysing the picked reflections and the geophysicist processor for applying the adapted imaging processing with appropriate parameters.

Acknowledgements

References

Aamir M., Maas Siddiqui M. (2006), Interpretation and visualisation of thrust sheets in a triangle zone in eastern Potwar, Pakistan, The Leading Edge, 1 : 24 –37.

Clarke R.(1997), Modelling and inversion of 3D complex kinematic data, Ph.D thesis, Université de Pau et des pays de l'Adour.

Duquet, B., Xu S., Lambaré G. (2003), 3D multi arrival Kirchhoff versus wave equation migration, Application to the 3D SEG/EAGE salt Model, The Leading Edge, 10 : 969–972.

Jones P.B. (1996), Triangle zone geometry, terminology and kinematics, Bulletin of Canadian Petroleum Geology, 2 : 139–152.

Krzywiec P. (2001), Contrasting tectonic and sedimentary history of the central and eastern parts of the Polish Carpathian foredeep basin-results of seismic data interpretation, Marine and Petroleum Geology 18: 13–38.

Krzywiec P., Aleksandrowski P., Florek R., Siupik J. (2004), The structure of the Outer Carpathian orogenic front: an example of the Miocen Zglobice unit between Brzesko and Wojnicz – new data, new models, new questions, Przegload Geologiczny, 11 : 1051–1059.

Lafargue E., Ellouz N., Roure F. (1994), Thrust controlled exploration plays in outer Carpathians and their foreland (Poland, Ukraine and Romania), First Break, 2: 69–79.

Rousseau V., Nicoletis L., Svay-Lucas J., Rakotoarisao H. (2000), 3D true-amplitude migration by regularization in the angle domain, 62nd EAGE Conference, Expanded Abstracts.

2D Depth Seismic Imaging in the Gaspé Belt, a Structurally Complex Fold and Thrust Belt in the Northern Appalachians, Québec, Canada

M. Bêche · D. Kirkwood · A. Jardin · E. Desaulniers · D. Saucier · F. Roure

Abstract. The Gaspé Belt is located in the Québec part of the Northern Appalachians. Its present geometry is complicated by the fact that the rocks were deposited on and deformed over previously structured fold and thrust belt. The objective of the recent (2000–2002) seismic survey of the Ministère des Ressources Naturelles et de la Faune du Québec was to obtain new seismic cross sections in this complex fold belt in order to better interpret its structural geometry. The surface geology displays high complexity, with sub-horizontal to sub-vertical bedding, open to tight folds and normal, reverse and strike-slip faults. A depth seismic imaging study was carried out on a 2D cross section through the Gaspé Belt by integrating all available geological data throughout the processing procedure. The challenge of seismic processing was the determination of the velocity model used for depth migration. For this case study, various methods for velocity model determination, from interpretative estimation to advanced travel time inversion, were applied and the combined interpretations of these depth migrated images were used to confirm a recent structural model of Acadian foreland thrust and fold belt in the Gaspé Peninsula.

1　Introduction

Fold and thrust belts are present on the majority of the continents and mark the compression zones of continental accretion. These zones are characterized by complex geological features.

The lateral displacement of broad volumes of rocks along faults juxtapose units that are deformed, folded, fractured and of contrasting petrophysical characteristics. The geometrical and mechanical complexities within the geological units induce lateral and vertical variations of seismic propagation velocities (Gray et al., 2002). From a seismic point of view, fold and thrust belts are also characterized by very heterogeneous conditions at the surface, from rough topography to complex structures at the outcrop. The consequences of these heterogeneities are on the one hand, the presence of blind areas, artefacts and refractions on seismic sections, and on the other hand, discontinuous seismic events. The difficulty in transforming time sections into depth sections is one of the main

causes of failure in petroleum exploration in fold and thrust belts. For example, large anticlinorial features imaged on time sections can in some cases correspond to seismic artefacts (i.e. pull-up effect), that are inexistent once tested by drilling. In fold and thrust belt settings, identification of faults and determination of layer thickness are often difficult due to poor seismic image quality. Seismic processing based on pre-stack depth migration associated with efficient depth velocity model building has been successfully applied to improve knowledge of the subsurface (Muller et al., 2000; Gray et al., 2002). Such processing carries out a more accurate time to depth conversion and a better focus of seismic energy. Depth-migrated images are more suitable because they more accurately restore the geometrical reality of the structures.

The hydrocarbon potential in the Gaspé Peninsula of the Québec Northern Appalachians is mostly restricted to the Late Ordovician to Early Devonian rocks of the Gaspé Belt. Rocks of the Gaspé Belt rest unconformably on the Mid-Ordovician Taconian fold and thrust belt that includes allochthonous Cambro-Ordovician slope and rise deposits of the Laurentian continental margin. Rocks of the Gaspé Belt were in turn deformed by the Mid-Devonian Acadian orogeny. The present geometry of the Gaspé Belt is thus complicated by the fact that the rocks were deposited on and deformed over a previously structured fold and thrust belt type basement. Most of the Silurian-Devonian rock succession in the northeastern part of the Gaspé Peninsula is within the oil and gas window and potential reservoir rock units include clastic rocks as well as fractured limestones (Lavoie and Bourque, 2001). The structural complexity of the Gaspé Belt has led us to develop an innovative method in the processing of more than 300 km of regional geophysical seismic reflection data acquired by the Secteur Énergie of Ministère des Ressources naturelles et Faune du Québec (hereafter referred to as MRNFQ) from 2000 to 2002. Our purpose is to improve depth seismic imaging and the structural interpretation of the Gaspé Belt by integrating seismic and geological data into the processing of seismic profiles.

This paper presents the integrated method used for our case study of the Gaspé Belt. The first step of seismic imaging requires building depth velocity models by using available geological data and advanced travel time inversion. Secondly, the velocity model is introduced in depth migration processing to compute the depth seismic images which in turn are validated for geophysical and geological consistency. The next step is to test and modify the structural framework presented by Kirkwood et al. (2004) for the mid-Devonian Acadian orogeny.

Results presented in this paper were obtained by applying advanced processing on data from line 2001-MRN-10b acquired by the MRNFQ across the central part of the Gaspé Peninsula.

To evaluate the structural improvements provided by the depth seismic images, we will discuss the results obtained for three selected geological areas illustrating the main structural features of the central zone of the Gaspé Belt: the "Lac des Huit-Miles" syncline, the Causapscal anticline, and the "Shickshock Sud" fault. The structural model proposed by Kirkwood et al. (2004) offers a promising geological setting for potential structural traps and new hydrocarbon plays. More detailed imaging and a better description of the main structural features including the faults, will help provide a more accurate evaluation of the petroleum system.

2   Regional Geological Context of the Gaspé Belt

In the Gaspé Peninsula, the Appalachian Orogen is made up of three distinct Paleozoic rock assemblages: the Early Paleozoic rocks of the Taconian Belt to the north, its successor basin, the Gaspé Belt that comprises middle Paleozoic rocks, and the late Paleozoic Maritimes Basin at the southern tip of the peninsula (Figs. 1, 2). The Taconian Belt of the Gaspé Peninsula crops out in the northern part of the peninsula and is divided into two Cambro-Ordovician tectonostratigraphic zones, the Humber and Dunnage zones, defined throughout the Appalachians by Williams (1979) and Williams et al. (1988). The Humber zone contains slope and rise sediments and rift-associated volcanic mafic rocks that have been thrust on the Cambro-Ordovician passive margin sequence during the late Ordovician Taconian Orogeny, and overlain by Upper Ordovician flysch (Sacks et al., 2004; Pincivy et al., 2003; Malo, 2004). It is subdivided in to three tectonic domains, typical of fold and thrust belts: a parautochthonous domain showing imbricate faults, an external thrust sheet domain and an internal thrust sheet domain. Northwest-verging folds and large-scale thrusts dominate the structural style of the Humber Zone, and are associated with the emplacement of the thrust

sheets (St-Julien and Hubert, 1975) during the late Ordovician. The Dunnage Zone comprises ophiolites, melanges, volcanic arc sequences, and marine flysch deposits. In the Gaspé Peninsula, the Dunnage Zone is present only as inliers along major faults or as nappes and slices thrust on top of the internal domain of the Humber Zone (e.g. the Mont Albert Thrust Sheet). The limit between the Humber and the Dunnage zones is known as the Baie Verte - Brompton line (BBL), which follows the Shickshock Sud Fault (SSF) in the northwestern part of the Gaspé Peninsula. Some deformation features within the Dunnage Zone are attributed to Taconian accretionary processes (De Broucker 1987; Tremblay et al.1995), but the major regional deformation is Acadian-related (Malo, 2004).

Post-Taconian rocks of the Gaspé Peninsula occur within the Gaspé Belt, a deformed successor basin (Bourque et al., 1995) that overlies the exposed southern part of the Humber zone. This basin developed following the Taconian orogeny and comprises Upper Ordovician to Middle Devonian clastic and carbonate rocks with some minor mafic volcanic rocks (Bourque et al., 2000). Stratigraphically, the Gaspé Belt is made up of four main broad rock assemblages, from oldest to youngest (Fig. 3):

1. Upper Ordovician-lowermost Silurian deep water fine-grained siliciclastic and carbonate facies of the Honorat and Matapedia groups.
2. Silurian-lowermost Devonian shallow to deep water shelf facies of the Chaleurs Group.
3. Lower Devonian mixed siliciclastic and carbonate fine-grained deep shelf and basin facies of the Upper Gaspé Limestones and Fortin Group.
4. Lower to Middle Devonian nearshore to terrestrial coarse-grained facies of the Gaspé Sandstones.

Three distinctive unconformities limit the sedimentary packages in the Gaspé Belt (Fig. 4). They are:

1. The Taconian unconformity separating the Taconian Belt rocks from the Gaspé Belt rocks.
2. The Salinic unconformity, related to synsedimentary extensional faulting, in the Chaleurs Group;
3. The Acadian unconformity, occurring between Middle or Upper Devonian and Carboniferous rocks (Bourque et al., 2001).

In northeastern and northwestern Gaspé, Silurian strata of the Gaspé Belt unconformably overly rocks of the Taconian Belt (Malo and Bourque, 1993). In north-central Gaspé, the contact between both zones occurs along the Shickshock Sud fault, a regional fault with a long-lived, complex faulting history (see below) (Malo and Kirkwood, 1995).
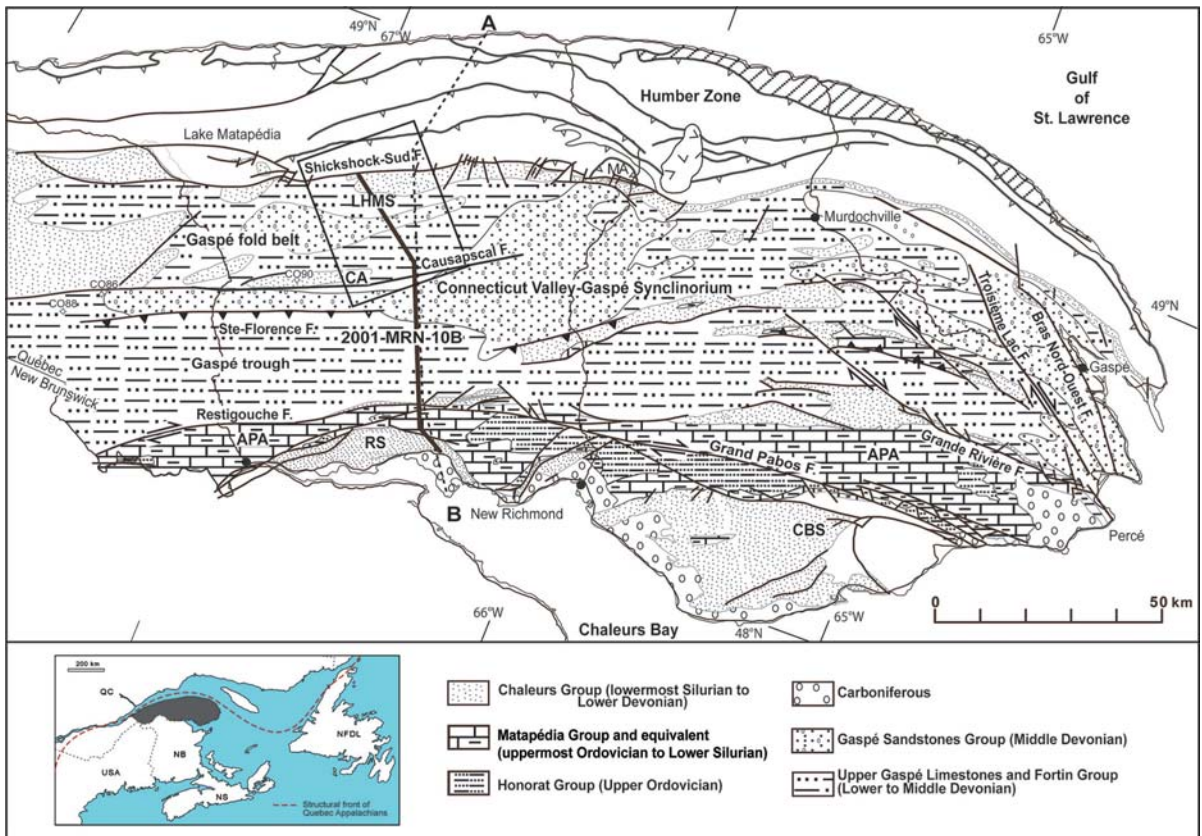
Fig. 1. Simplified geological map of Gaspé Peninsula, northern Appalachians. Modified from Kirkwood et al. (2004). Note location of MRNFQ seismic lines 2001-MRN-10b, VB 04 and VB 06 in central Gaspé, and this study area in the boxed zone. LHMS: "Lac des Huit-Miles" syncline; FA: Faribault anticline; CA: Causapscal anticline; APA: Aroostook-Percé anticlinorium; GA: Gastonguay anticline; RS: Ristigouche syncline; CBS: Chaleurs Bay synclinorium; MA: Mont Albert Thrust Sheet. Transect AB: cross section shown on Fig. 3
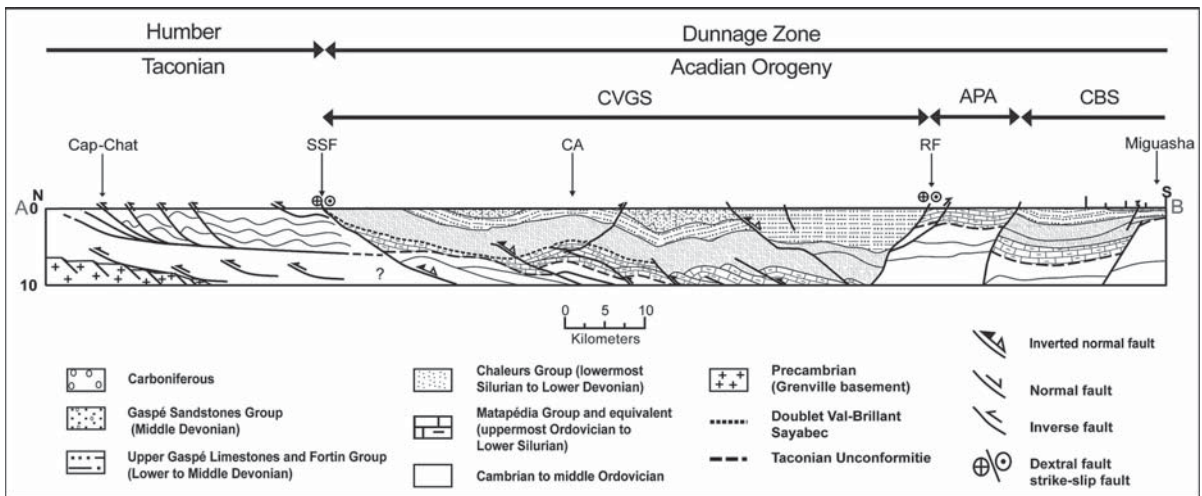
Fig. 2. Simplified cross section of the Gaspé Peninsula, northern Appalachians. Modified from Brisebois and Brun, in Hocq et al. (1994). CVGS: Connecticut Valley-Gaspé synclinorium; APA: Aroostook-Percé anticlinorium; CBS: Chaleurs Bay synclinorium; LF: Logan fault; SSF: Shickshock Sud fault; CA: Causapscal anticline; GPF: Grand-Pabos fault; RGF: Rivière Garin fault; DA: Duval anticline
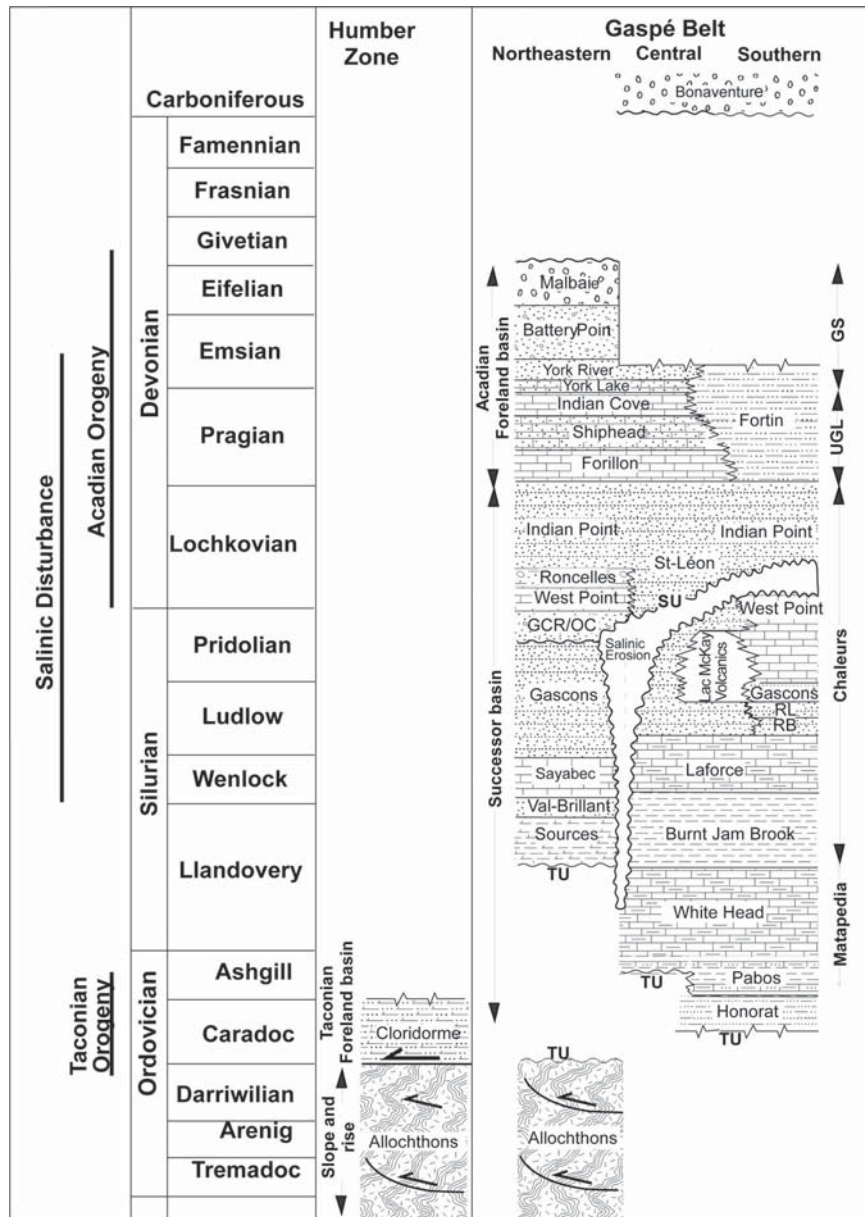
Fig. 3. Generalized stratigraphic columns for folded belts (Humber Zone and Gaspé Belt). From Kirkwood et al. (2004). *GCR/OC*: Griffon Cove River/Owl Cape; *GS*: Gaspé sandstones; *RB*: Ruisseau Bleu; *RL*: Ruisseau Louis; *SU*: Salinic unconformity; *UGL*: Upper Gaspé limestones

Structurally, the Gaspé Belt is divided into three regionally extensive zones (Fig. 1): the Connecticut Valley-Gaspé synclinorium (CVGS), the Aroostook-Percé anticlinorium (APA), and the Chaleurs Bay synclinorium (CBS). The structural style of these zones is for the most part attributed to the Devonian Acadian deformation, although the contribution of a Silurian Salinic Disturbance is increasingly regarded as an important tectonic event in the southern part of the peninsula (Malo, 2001). Regional northeast-trending open and upright folds dominate the Gaspé Belt, with minor reverse faults that parallel the axial trace of folds and major east-northeast- to east-trending dex-

tral strike-slip faults. Major faults either border (e.g. the Shickshock Sud fault) or cut across (e.g. the Grand Pabos and Ste-Florence faults) the three main structural zones. Also, a regional northeast-trending cleavage is well developed throughout the Gaspé Belt.

Conceptions on the tectonic evolution of the Gaspé Peninsula during the Acadian Orogeny have varied from the development of a collisional fold belt dominated by regional synclinoria and anticlinoria bounded by reverse faults (Roksandic and Granger, 1981) to a wrench tectonic scenario (Malo and Béland, 1989) to a two-phase scenario of a fold and thrust belt cut by strike-slip faults (Kirkwood et al., 2004). Malo and

Béland (1989) described a wrench tectonic model to explain folds, strike-slip faults, and cleavage based on their study of the Aroostook-Percé anticlinorium in the southern part of the peninsula. Kirkwood et al. (1995) and Malo and Kirkwood (1995) proposed a two-phase development of the Acadian Orogeny, beginning with a first phase of fold and cleavage development accompanied by vertical extension, followed by a phase of dextral strike-slip deformation with a horizontal extension component. The deformation phases were related to a transition from a pure shortening deformation to a simple shear dominant deformation in an overall transpressive setting. Kirkwood (1999) then showed that this transpressive setting is characterized first by coaxial deformation, represented by folding and axial planar parallel extension, followed by dextral strike-slip shearing and orogen-parallel horizontal extension. Reverse and strike-slip faults are interpreted as probably related to a same crustal décollement level limiting the supracrustal sequence (Dunnage Zone and Gaspé Belt) and the Grenville basement of Laurentia. Finally, based on detailed structural mapping in northeastern Gaspé and new public domain seismic reflection data from the Québec government in western Gaspé, Kirkwood et al. (2004) reviewed the previous model and proposed the development of a fold and thrust belt during the earliest phase of the Acadian Orogeny, followed by strike-slip faulting in Mid Devonian time. The seismic images presented here provide a more accurate representation of the subsurface structural style of the Acadian belt as well as the underlying Taconian basement.

The structures imaged on the seismic profiles indicate that broad open folds mapped at the surface in the Gaspé Belt formed above shallow dipping structures located in the deeper units.

The structural geometry is much more compatible with a compressional fold and thrust belt than with the transpressive tectonic regime that has previously been invoked for the Acadian orogeny.

3 Integrated Seismic and Geological Method

In fold and thrust belt settings, processing results in time seismic sections, which can be far from a correct representation of the geological features and effective depth imaging procedures are required to produce seismic images that are consistent with the real subsurface geometry. The challenge of our work in the Gaspé Belt was to obtain reliable seismic images in this structurally complicated context to better interpret the subsurface structural style of the Mid-Devonian Acadian Gaspé Belt as well as the underlying Taconian basement. The surface geology displays structural complexity, with sub-horizontal to sub-vertical bedding, open to tight fold, a moderate to strong pervasive cleavage and normal, reverse and strike-slip faults.

The rocks also present strong lateral velocity contrasts and seismic data show low signal-to-noise ratio. The proposed depth seismic imaging workflow is divided into three main steps: 1) geological and geophysical data collection and integration, 2) depth seismic imaging applying post- or pre-stack migration processing (Fig. 1), and 3) depth velocity model building using both blocky and smooth parameterizations. The depth velocity model is especially uncertain in complexly structured zones and must be estimated by combining and integrating both geological and geophysical data and techniques.

3.1 Initial Geological and Geophysical Data

All the geological background needed for the depth seismic imaging study was collected before reprocessing of the seismic data, specifically regional geological knowledge, available well data and outcrop studies essential in land exploration. A field survey was carried out along seismic line 2001-MRN-10b, which for the most part follows the NS striking Nouvelle river, from the Chaleurs Bay to the south, to the Lac-des-Huit-Miles syncline to the north.

This field work consisted in the study of available outcrops and regional surface geology, with the aim of having a reference mark (a priori data) which would be of great help in the creation of realistic velocity models. Among other things, fracture systems and schistosity were observed with close attention, as they are of utmost importance in our understanding of wave propagation and resulting seismic images. It is well known that a well-developed vertical cleavage or schistosity masks other geological structures, and is nearly invisible on seismic reflection (no reflection is generated). During this field survey, sampling of different lithologies was conducted, and collected samples were later submitted for petrophysical analysis at the Cergy-Pontoise university labs. These analyses gave rather poor results, as most samples were pervasively cleaved and thus improper for analysis. However, some samples were of sufficient quality to determine a range of magnitude for compressional wave velocity (Vp).

Moreover, using the sparse well data available (three wells :Vérendrye No1 (1972FC090), 1967FC086 and 1969FC088)) have been drilled in a radius of 90 km along the seismic profile, the deepest to a depth of 3800 meters), stratigraphic sections and velocities of some formations were deduced, again helping in the creation of realistic velocity models.

The initial geophysical information results from the analysis of seismic stack sections obtained by standard and advanced time processing. This analysis provides

an identification of shadow zones, an estimation of the structural sensitivity to post stack time migration velocities and an evaluation of the complex propagation of the seismic signal through the complex overburden. Initial information for velocity model building is obtained from stack velocity analysis (i.e. normal moveout and dip moveout corrections).

3.2 Depth Seismic Imaging Techniques

Seismic processing relates to the process of altering the seismic data to suppress noise, enhancing the desired signal (higher signal-to-noise ratio) and migrating seismic events to their appropriate location in space and depth. Processing steps generally include analysis of velocities, static corrections, moveout corrections, stacking and migration. Optimal seismic processing results in depth profiles readily interpretable, showing clear and unambiguous subsurface structures and reflection geometries.

Depth migration can be viewed as a two-step processing procedure. The first step is to focus the diffracted energy, as for any migration processing. The second step is to convert the seismic data from the time domain to the depth domain. Both pre-stack and post-stack depth migration techniques directly provide depth seismic images, but require the construction of a detailed velocity model describing the geometry of the geological layers and the intra-bed velocity variations in the depth domain. Post-stack depth migration can be an adequate processing technique if the conventional stack sections can be reasonably considered to represent a zero-offset section and if coherent seismic reflectors are visible. Post-stack depth migration application is an interpretative processing technique, requiring simple velocity scan analysis and several iterations between seismic interpreters and processors for structural consistency control. Post-stack depth migration allows only a few control points at well locations on velocity variations within the overburden layers. Pre-stack depth migration techniques (hereafter termed PSDM) provide the best seismic images in terms of geometry but present the disadvantage of being dependent on the reliability of the input velocity model.

This processing technique offers more control i.e., coherency checking and flatness control of seismic event on prestacked depth migrated gathers. For the case study presented here, PSDM is carried out by applying an in-house migration software (WaveEquation, developed at Institut Français du Pétrole), based on wavefield propagation for 2D land acquisitions.

Common image gathers computed by pre-stack migration are available both in shot, in offset and in angle domains. In complex structural settings where pre-stack seismic data are unavailable, it is difficult to define immediately a reliable depth velocity model from stacked seismic data only. To cope with this difficulty, an integrated approach has been developed at IFP (Ehinger et al., 2001), which combines pre-stack seismic interpretation and advanced travel time inversion. The travel time inversion software is quite appropriate to resolve the velocity model problem in complex areas: a reliable horizon picking in seismic pre-stack domain is required and geological constraints are taken into account to limit the ambiguities of depth seismic imaging in complex subsurface.

3.3 Depth Velocity Model Building

Due to the flexibility of the IFP travel time inversion software, various types of velocity models adapted to the subsurface complexity can be built. Two main parameterizations of the computed velocity models can be selected depending on the pre-stack time picking difficulties. A blocky velocity model, with simple velocity variations within the main sedimentary unit is built using geological framework, regional structural geology and fieldwork. With this parameterization, structural boundaries are modelled by velocity contrasts. A smooth velocity model is characterized by velocity values not necessarily linked with structural boundaries. This parameterization is very useful to obtain reliable lateral and vertical velocity variations even if faults and sedimentary units can not obviously be detected. This approach is particularly well adapted to complex geological settings.

The integrated method has been applied on line 2001-MRN-10b located in the central part of the Gaspé Belt. Blocky and smooth velocity models were built using surface geology information, pre-stack time migrated sections interpretation and travel time inversion of selected dipping seismic events. These velocity models were then used for PSDM processing.

Flatness control of seismic events on common image gathers, also known as the iso-X method, (Al-Yahya, 1989; Deregowski, 1990; Robein, 2003) ensured the kinematic validity of the input velocity models. The interpretation of the different seismic depth images provides additional information on the structural model and more specifically on the nature of faults within the sedimentary layers and the geometry of deeper thrusts.

Fig. 4. The proposed integrated seismic and geologic workflow in three steps. The first step consists in collecting the initial geologic and geophysical data used during the depth seismic imaging and velocity model building steps. Then both post-stack and pre-stack depth migration processing applications are required to obtain the most realistic depth seismic images. Step three involves depth velocity model building and proposes to compute two types of model parameterizations adapted to the structural objective
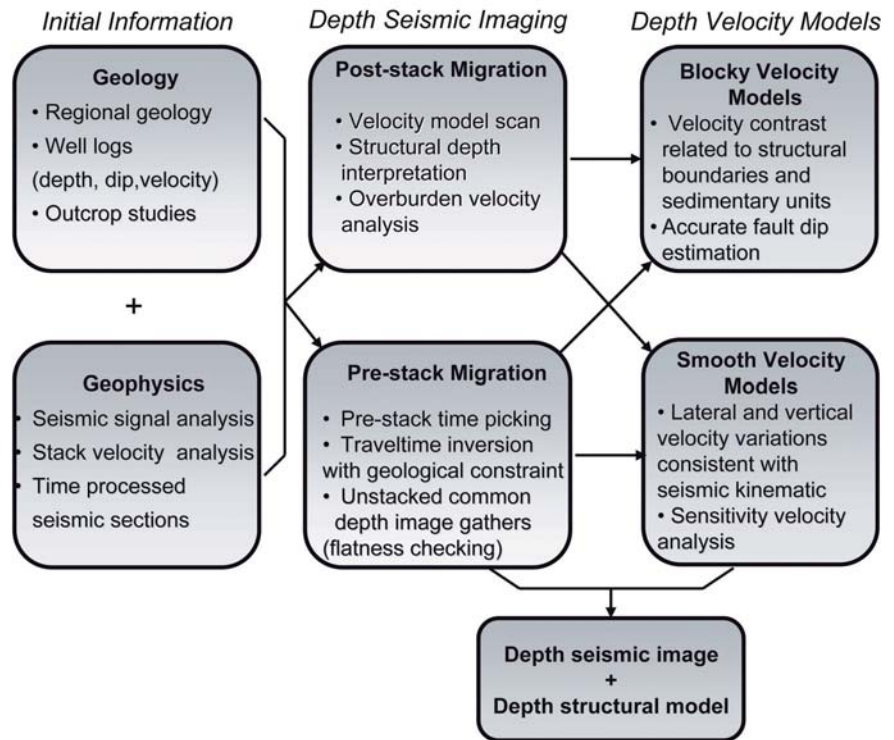
4   The "Lac des Huit-Miles" Syncline

4.1 Geological Setting

The northernmost synclinal structure of the Connecticut Valley - Gaspé synclinorium in northcentral Gaspé Peninsula, the "Lac des Huits-Miles" syncline is a large open syncline 35 km wide that reaches 6.5 km in depth in its core (Fig.5). It comprises Lower Silurian to Devonian rocks of the Chaleurs, Upper Gaspé Limestone and Gaspé Sandstone groups. The syncline is limited to the north by the Shickshock Sud fault and to the south by the Causapscal anticline and the Causapscal fault. Both PostSTM and PSDM provide quality seismic images that can be used to define the broad stratigraphic architecture and regional structure of the syncline. The stratigraphy was extended at depth by tracing major reflections guided by the surface geology. There is no available borehole information in the syncline to help calibrate the stratigraphy at depth. The closest well is located some 50 km to the southwest and did not penetrate the entire stratigraphic sequence.

At the surface along the seismic line, the contact between the Humber Zone to the north and the Gaspé Belt to the south coincides to the Shickshock Sud fault. The fault is a major fault in the Gaspé Peninsula and has a complex history. Field observations and timing relationships within the fault zone provide evidence for thrusting during Ordovician times (Taconian orogeny), normal faulting during the Silurian and Early Devonian times and dextral strike-slip movement during the Middle Devonian Acadian Orogeny (Sacks et al., 2004). At the surface, the Ruisseau Isabelle Mélange crops out within the ~100–500 meters wide Shickshock Sud fault zone and is made up of different lithological components such as black mudstone, green sandstones and serpentinized ultra-mafic blocks (Malo et al., 2001; Sacks et al., 2004). The complex structural features of this mélange are attributed to repeated faulting along the Shickshock Sud fault, and it is reasonable to think that this structural feature extends at depth.

The lithological characteristics and faunal assemblages of this mélange unit have prompted Malo and others (2001) to correlate the unit with similar rocks of the Humber zone (the Rivière Ouelle Formation) thus establishing its affinity to the continental margin.

Deformation fabrics within the mélange are ascribed to the Acadian orogeny (Malo et al., 2001). To the south, the Causapscal fault is interpreted as a backthrust (Desaulniers, 2006), and is one of the major faults related to transpressive deformation during the Acadian orogeny.

At the very base of the syncline, the Chaleurs Group is represented by the Awantjish Formation, a lower deep-water claystone, 30 to 40 meters thick.

In the Northern part of the Gaspé Belt, these deposits are upper Llandoverian in age, and unconformably overlie the Cambrian-Ordovician folded rocks (Bourque et al., 1999). In the area immediately south of the Schickschock Sud fault, in the vicinity of seismic line 2001-MRN-10b rocks of the Awantish Formation rest unconformably over rocks of the Ruisseau Isabelle mélange.

Locally, a thinly bedded fine-grained limestone unit, the Sources Formation, is interlayered with or replaces the Awantjish claystone. The Awantjish Formation is overlain by a lithological assemblage made of two formations, composed of a very distinctive nearshore quartz sandstone of the Val-Brillant Formation, gradually changing to platformal limestones of the Sayabec Formation (Bourque et al., 1999). The Val-Brillant Formation is estimated to be 50 to 90 meters thick, while the Sayabec Formation ranges around 80-150 meters in thickness (Lachambre, 1987). The platformal limestones of the Sayabec Formation are composed of peritidal, reefal, and various subtidal facies, and is considered a good chronological marker (Bourque et al., 2001).

The Sayabec Formation gradually changes to the Saint-Léon Formation, with a minimum thickness of 2200 meters (Brisebois and Morin, 2004). The Saint-Léon Formation is typically fine-grained and is made of sandstone, mudrock, occasional conglomerate, and reef limestones (namely the West Point Formation). Of particular interest, this formation is contemporaneous of the Salinic Disturbance (Ludlovian-Pridolian times), and has recorded the Salinic erosional unconformity that, although it is only locally observed, can be very important, cutting unequally into the Late Ordovician and Silurian sequence, in places indicating almost 1500 m of differential uplift. Conglomerate bodies in the middle part of the St-Léon Formation found in the close-by Faribault anticline and the northeastern part of the peninsula (namely the Griffon Cove River and Owl Capes members) are unequivocally associated with the Salinic unconformity (Lachambre, 1987; Bourque et al., 2001; Brisebois and Morin, 2004).

Conformably overlying the Chaleurs Group, the Upper Gaspé Limestone Group is composed of the Forillon, Shiphead and Indian Cove formations. It reaches up to 500 meters thick in western Gaspé (Lavoie, 1992) and 950 meters in Central Gaspé (Desaulniers, 2006). At its base, the Forillon Formation is a homogeneous succession of shaly dolomitic and siliceous calcilutite or limy mudstone. On some outcrops, patches of high organic matter content give the rock a darker color and a hydrocarbon odor (Brisebois and Morin, 2004). The overlying Shiphead Formation is more heterogeneous and has a higher siliciclastic content, consisting of alternating thin to very thick siliceous

and dolomitic limestone and mudstone beds. In the Causapscal anticlinal, the Shiphead Formation contains basalts, in the form of three or four pillowed lava flows, to 15 m thick each, interstratified within the uppermost mudstone beds. The upper part of the group is the Indian Cove Formation, a homogeneous unit of cherty to siliceous or silty calcilutite, which is also known to locally contain basalt flows and mafic lapilli tuffs. The Upper Gaspé limestones are conformably overlain by the Gaspé Sandstone Group.

The youngest rocks unit in the syncline, the Gaspé Sandstone Group, is composed of the York Lake, York River, and Battery Point formations. The York Lake Formation is made of alternating limestone and feldspathic sandstone layers. On the northern limb of the syncline, the York Lake Formation is composed of two layers of limestone alternating with two layers of sandstone, for a thickness of about 400 meters. On the southern limb of the syncline, thickness of the York Lake increases to up to 1000 meters. The York Lake limestones are quite similar to those of the underlying Indian Cove Formation, although somewhat less siliceous, and like the latter, they contain some basalt flows. The last limestone layer is considered the top of the York Lake Formation, and gives place to the York River Formation, composed of a siltstone-mudstone-sandstone sequence, where feldspathic wackes dominate. It amounts to a total thickness of around 500 meters. The last unit of the syncline is the Battery Point Formation, a felspathic-rich wacke and arenite assemblage, with some mudstone and minor limestone. Some basalt pillow flows are also associated with this unit.

Some of these geological formations represent remarkable stratigraphic and seismic markers. Worth mentioning, the Val-Brillant - Sayabec transition, at the base of the sequence, is very distinctive and shows up as almost continuous on the whole seismic section. This reflector, comprising two couples of high-amplitude reflections, is known as the Val-Brillant - Sayabec Doublet (Desaulniers, 2006). Levels of very distinct reflectors in the St-Leon Formation, interpreted as remarkable sedimentary sequences (see next section), erosional (Salinic?) features, and possible reef build-ups (Morin et al., 2002a), hint at a syntectonic deposition of this formation in a tectonically active environment. Finally, the base of the Upper Gaspé limestones (Forillon Formation) and of the Gaspé sandstones (York Lake Formation), showing both an important lithological change in the sedimentary sequence of the syncline, prove to be very good stratigraphic and seismic markers as well.

5   Structural Interpretation

The depth seismic imaging workflow presented above has been applied to seismic line 2001-MRN-10b. The depth seismic image obtained along the northernmost portion of the line, the "Lac des Huit-Miles" syncline, shows more continuous reflectors and provides detailed information concerning the architecture of sedimentary layers and the geometry of faults and folds affecting the Gaspé Belt and their relationship to deeper structures (Fig. 5). The structural interpretation presented here focusses on three particular zones along the Lac des Huit Miles syncline (Fig. 5):

1. The core of the syncline displaying a fault-related fold in the basal part of the Silurian-Devonian sequence;
2. The zone directly underlying the southern limb of the syncline, where folds have been imaged in the underlying Taconian Belt; and
3. The northern contact of the Gaspé Belt with the Humber Zone, along the Shickshock Sud fault.

5.1 The "Lac des Huit-Miles" Syncline

At the base of the syncline, the Val-Brillant - Sayabec Doublet and overlying reflectors are cut by small sub-vertical faults, interpreted as normal, synsedimentary faults (Desaulniers, 2006) and compatible with available stratigraphic and paleogeographic models (Bourque 2001). The lowermost units of the St-Léon Formation thicken dramatically, from 500 m on the north limb of the syncline to more than 1200 meters in the core of the syncline (Fig. 6).

The drastic transition occurs very rapidly across the axial surface of the syncline and could be related to structural thickening in the hinge of a small-scale anticline located in the core of the regional syncline (Fig. 6). However, a constant thickness of more than 1000 meters for the lowermost units of the St-Léon Formation persists further south along the south limb of the syncline (Fig. 6). On our seismic profiles (Figs. 6, 7 and 8), normal faults affecting the Siluro-Devonian are restricted to the lowermost part of the sedimentary sequence and cannot be followed high-

Fig. 5. PSDM image of the northern part of seismic line 2001-MRN-10b, with the zones of particular interest (top, boxes 1 to 3), and with interpretations (bottom). For.: Forillon; Shp., S.: Shiphead; I. C., I. Cove: Indian Cove; Y.L.: York Lake; RIM: Ruisseau Isabelle Mélange

er up into the sequence. This is in agreement with documented normal faulting during the deposition of the St-Leon Formation (Bourque, 2001). We have interpreted the change in thickness of the lowermost units of the St-Léon Formation as syndepositional thicknening due to movement along a normal fault presently located in the core of the syncline (Desaulniers, 2006). Based on the fact that the normal faults are restricted to pre-Lower Devonian times, the age of the normal faulting event is assigned to the upper Silurian/lowermost Devonian (Ludlovian to Pragian), and is attributed to Salinic extensional tectonics, an event that resulted in block faulting and tilting along normal listric faults in the northeastern part of the Gaspé Belt (Bourque, 2001). Our seismic images however help constrain the timing of the normal faulting event in the Lac des Huit-Miles syncline to the Ludlow-Pridoli since thickening is clearly restricted to the lowermost St-Léon and stratigraphic markers higher up are not displaced.
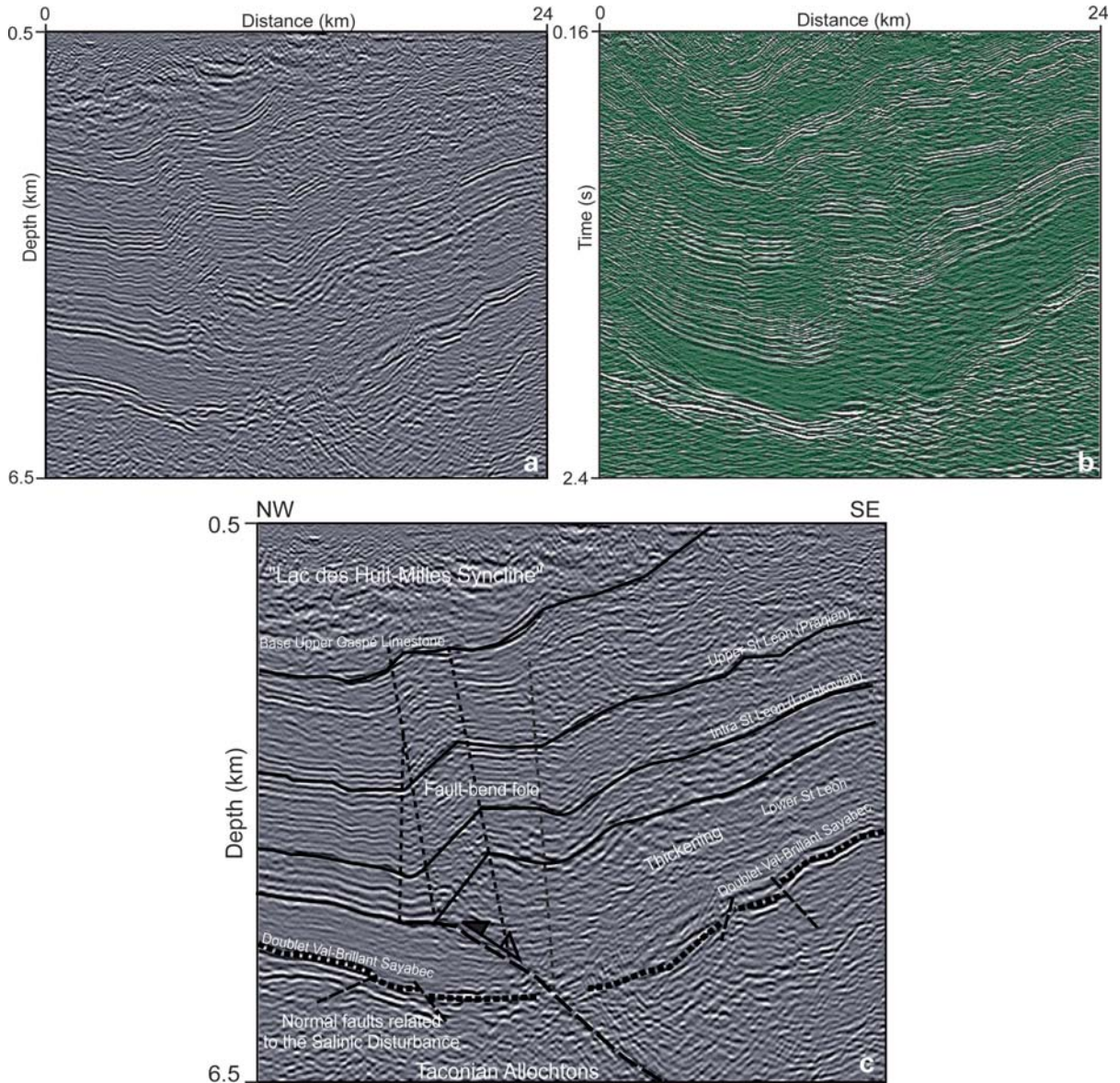
Fig. 6. **a** PSDM and **b** PostSTM images of the "Lac des Huit-Miles" syncline, **c** geological interpretation of a fault-bend fold in the core of the syncline showing a dramatic thickening of the lowermost units of the St-Leon Formation from north (*left*) to south (*right*). The thickening is related to synsedimentary normal faulting during the deposition of the lower St-Léon (Wenlock-Ludlow). The reverse fault is interpreted as the reactivation of a major normal fault. On the Val-Brillant – Sayabec Doublet, normal faults are attributed to the Salinic Disturbance

Of particular interest, Fig. 6 shows a fault-related fold geometry in the core of the syncline.

The seismic section clearly shows a 100-m-scale anticline cored by a 30 to 40 degrees south-dipping reverse fault. The Val-Brillant - Sayabec Doublet is displaced and the lowermost beds of the St-Léon Formation are also discontinuous across the fault. The fold shape of the asymmetrical anticline displays a steep but not overturned north limb. The dip of strata along the north limb decreases and the fault disappears up section. Two axial surfaces can be traced along the steeply dipping north limb of the anticline and extend down to what seems to be a concave-downward bend in the fault surface. These features are typical of either a fault-propagation folding mechanism or a fault-bend folding mechanism (Shaw et al., 2005). Regardless of the fold category, the geometry of the fold clearly indicates that folding occurred due to beds moving upwards along the hanging wall of the fault, although the amount of displacement is difficult to estimate. The fault most probably acted as a reverse fault at some stage during the formation of the syncline, reactivating the normal fault located in the core of the syncline. Timing of the inversion can be constrained to post-Pragian time since stratigraphic markers of the Upper Gaspé Limestones are also folded. Higher up in the stratigraphic sequence, the fault eventually disappears within the St-Léon and the uppermost units are simply folded. At depth, the fault seems to be rooted in the Taconian allochthon underlying the syncline. Thus, this fault could be strictly an Acadian structure that reactivated a Salinic normal fault or alternatively a Taconian thrust ramp reactivated as a normal fault during the Salinic event and then inverted as a thrust fault during the Acadian.

5.2 The Causapscal Anticline

Deep reflectors under the syncline (between 6 to 8 km in depth) are quite different from those of the Silurian and Devonian sequences of the Gaspé Belt and define a large-scale anticline. These structures are in fact located in the Taconian basement beneath the Gaspé Belt sequence, immediately below and slightly to the south of the fault-related fold at the base of the syncline. Below the Lac des Huit-Miles syncline, a major fault cuts through the lowermost units of the Silurian and Devonian sequence of the syncline, and can be followed at depth cutting through rocks of the Taconian Belt. To the south of this major fault, north dipping reflectors hint to the presence of a subsurface anticline located below the Causapscal anticline exposed at the surface. The folding involves the uppermost section of Taconian Belt as well as the overlying Siluro-Devonian sedimentary package. This anticline is limited to

the south by a major fault (Fig. 7). Normal faults cutting through the folded reflectors of the anticline are correlated to the normal faulting event (Salinic Event) responsible for faulting of the Val-Brillant – Sayabec doublet. Also, the core of the anticline displays backthrusts, within which the Causapscal north-dipping fault seems to be rooted. As no synsedimentary deformation can be seen in the anticline, we conclude that the Causapscal backthrust postdated the deposition of its youngest sediments. It is our opinion that the creation of the backthrust is related to the locking of the major reverse fault, and resulted from the ongoing Acadian compressive phase.

5.3 The Northern Contact of the Gaspé Belt Along the Shickshock-Sud Fault

New images resulting from depth migration have clearly imaged the trace of the ShickShock Sud fault in the subsurface, which was positioned slightly to the north and with a steeper dip on previous interpretations based on post-stack time migrated (PostSTM) seismic images (Figs. 8a and b) (Morin and Laliberté, 2002). This fault shows a maximum dip of 30–40° on our depth images (Desaulniers, 2006). The image presented here (Fig. 8c) shows the contact between the Taconian and Acadian belts which at the surface is represented by the vertically dipping Shickshock-Sud fault and in the subsurface by the discontinuity between the syncline and the underlying rocks. The discontinuity could be either an angular unconformity or a major décollement level involving thrusting of the Acadian Belt over the Taconian Belt. On the northern limb of the "Lac des Huit-Miles" syncline, Siluro-Devonian sediments of the syncline rest unconformably either on rocks of the Ruisseau Isabelle Mélange or on rocks of the Taconian Belt, in the hanging wall of the Shickshock Sud fault. Below the syncline, a strong reflector is similar to the Val-Brillant - Sayabec Doublet although reflections above do not seem to correlate well with the expected reflectors of the overlying St-Léon Formation. The repetition of the Val-Brillant - Sayabec Doublet below would imply a cut-off located near the core of the syncline and a major décollement zone with more than 20 km of offset. Alternatively, the reflector could belong to a slice from the Taconian allochthon.

6   Discussion

This study aimed at elaborating an integrated method using a-priori geological information in the seismic imaging workflow. The method has proved successful to image small-scale structures and the detailed archi-
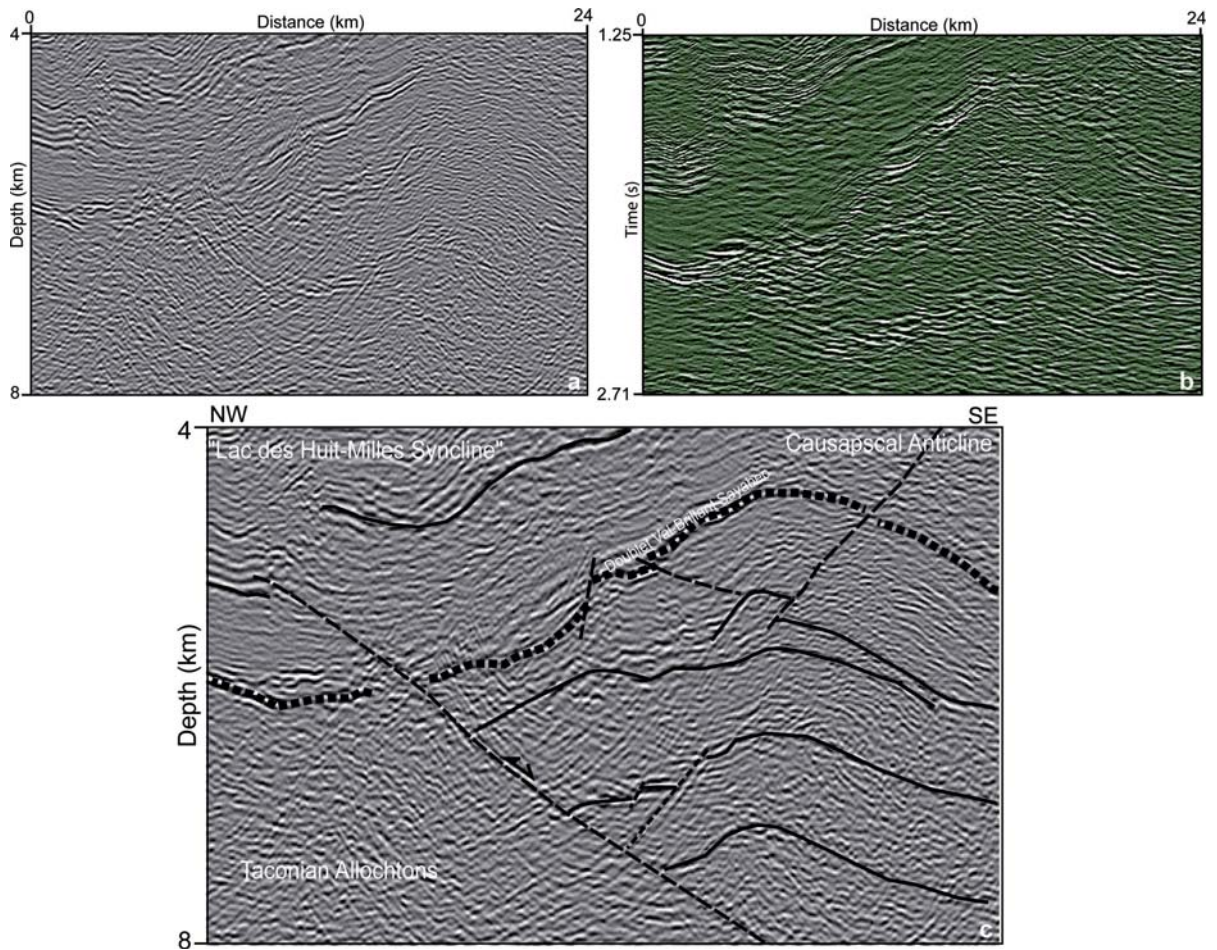
Fig. 7. a PSDM and **b** PostSTM images beneath the "Lac des Huit-Miles" syncline, **c** geological interpretation of a reverse fault rooted beneath the "Lac des Huit-Miles" syncline in the underlying Taconian Belt. The interpretation highlights a system of imbrications involving Taconian- and Acadian-deformed sediments

tecture of the stratigraphic sequence of the Gaspé Belt, as shown by our preliminary results of the processing and interpretation of 2D line 2001-MRN-10b. Poststack time migrated sections are valuable to define the regional structures and broad stratigraphic divisions in complex structural settings (Fig. 9a). However, in order to define smaller-scale exploration targets, velocity models must be built by integrating as much of the surface geology as possible. Travel-time inversions on specific reflectors also help constrain and verify the velocity model. As shown in our case study of the Gaspé Belt, PSDM images provide the geologist with a more detailed representation of the subsurface geology and are a key part of the interpretation process (Fig. 9b).

A great advantage of depth seismic imaging compared to time seismic imaging (Fig. 9) is to provide direct geological interpretation without the need for time to depth conversion. By using this method, we

were able to precisely determine the various thicknesses of the geological units, which can be estimated by simple observation of the depth image. However, to obtain a good depth image, one must build the most realistic and precise velocity model. It is the inherent paradox in any use of the PSDM: optimal processing of the data requires an optimal model of the area, which means that one must know beforehand the answer one is looking for. Which is why taking into account geological data at the beginning of the imaging process is necessary and of paramount importance.

For most stratigraphic plays and plays in simple structural settings, time migrated seismic profiles are more than adequate to image the subsurface. However, for structural plays in more complex settings, depth seismic imaging is recognized as the best representation of the subsurface. In such settings, time imaging often leads to inadequate imaging of steeply dipping strata and faults as well as incorrect estimation of
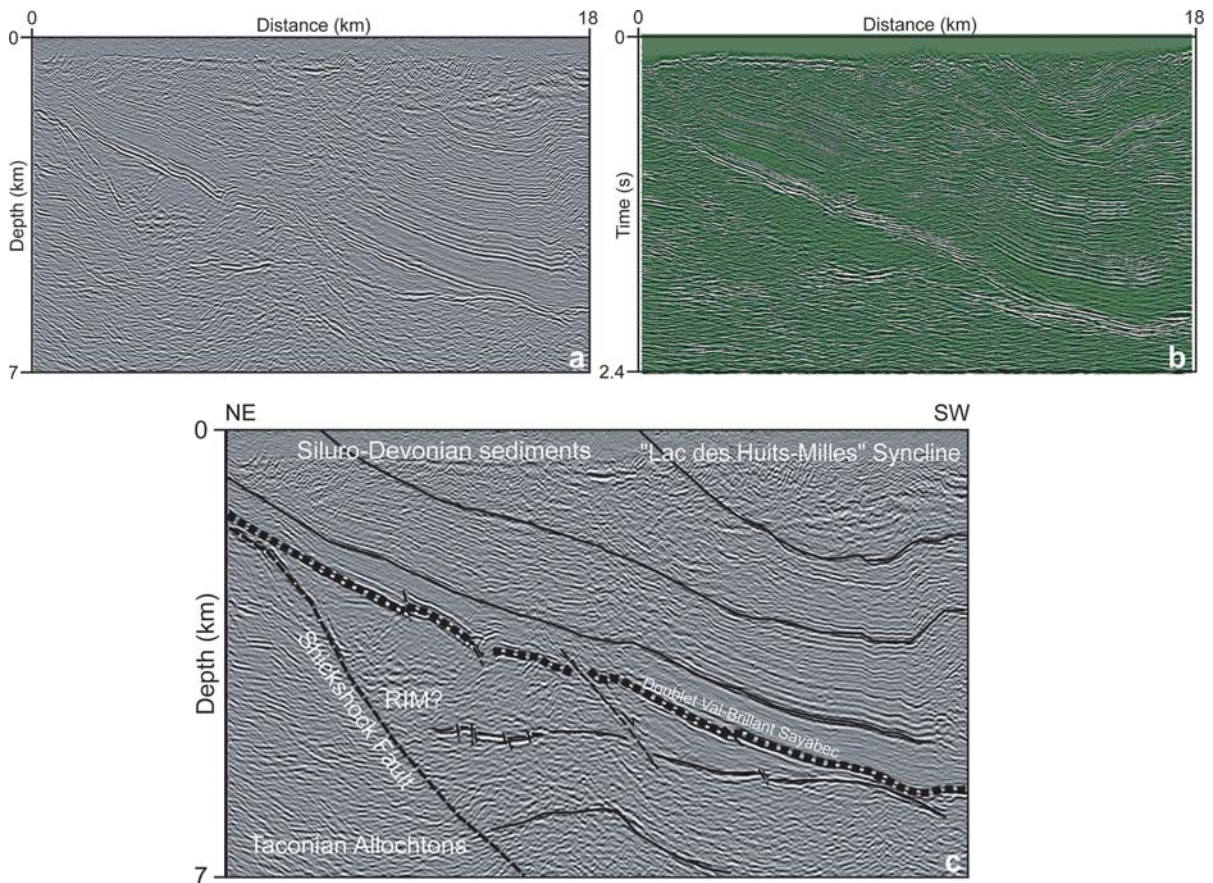
Fig. 8. **a** PSDM and **b** PostSTM images of the northern contact of the "Lac des Huit-Miles" syncline. **c** Geological interpretation of the Shickshock-Sud fault zone, that separates the Taconian Belt and the Dunnage zone. On the Val-Brillant – Sayabec Doublet, normal faults are related to the extensive Salinic Event

depth. Our interpretation of the "Lac des Huit-Miles" syncline defines a thin-skinned structural style compatible with a fold and thrust belt environment. Folds are distorted or only partially imaged on time-migrated seismic sections. In our case study, the northern, steeply dipping limb of the fault-related fold in the core of the "Lac des Huit-Mile" syncline was poorly imaged on the post-stack time section. Previous interpretations were unable to distinguish between a fault and a fold. The more detailed seismic profile helped determine that the fault disappears up section. Our interpretation implies the reactivation of old Taconian structures during the Acadian orogeny, as illustrated by the fault-related fold structure in the core of the syncline.

PSDM profiles image more clearly the lithological contrasts in the sedimentary assemblages of the "Lac des Huit-Miles" syncline, and highlight what seem to be structural imbrications beneath the syncline. Extensional structures (normal faults) can be observed in the bottom-most part of the stratigraphic sequence at the Val-Brillant-Sayabec Doublet level, which we link to the Salinic Disturbance. Timing of normal faulting can be constrained to the Ludlow-Prodoli time period in the northern Gaspé Belt. Under the "Lac des Huit-Miles" syncline, we can observe that Siluro-Devonian sediments of the syncline rest unconformably on the Taconian allochthon, particularly in the northern part of the studied section in the hanging wall of the Shickshock Sud fault. Previous time imaging results were unable to image the subsurface expression contact between the Gaspé Belt and the Taconian Belt. The Shickshock Sud fault is clearly visible on our PSDM images where it shows a maximum dip of 30–40° and can be traced down to 5000 meters with possible extension to lower depths. As inferred by surface geology, the Shickshock Sud fault does represent the limit between the Taconian and Acadian belts at the northern limit of the syncline.

Our structural interpretation of these images provides new evidence in support of the fold and thrust belt model presented by Kirkwood et al. (2004). Struc-
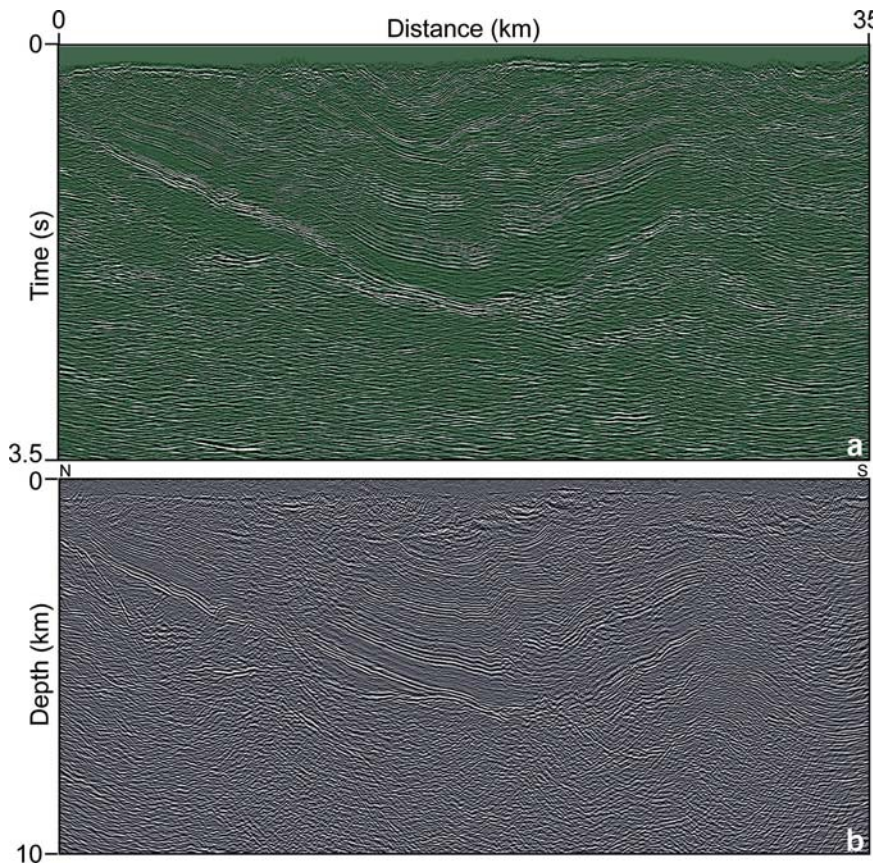
Fig. 9. a PostSTM image and **b** PSDM image on the "Lac des Huit – Miles" Syncline

tural imbrications imaged beneath the core of the syncline show similarities with previous interpretations of Morin and Laliberté (2001) on regional-scale seismic lines (VB 06 and VB04 A-B-C) located ~70 km west of line 2001-MRN-10b. These observations support our interpretation that the structural style described to the Acadian Orogeny is a "fold and thrust belt" style. However, study of the deep Taconian structures remains difficult, mainly because of data provenance. Indeed, the seismic survey was designed for subsurface imaging and not for crustal-scale studies at depth of more than 5000 m. Thus, maximum offsets available on 2001-MRN-10b line are of 3000 meters, too small for optimal crustal studies.

7   Conclusion

Our studies of the "Lac des Huit-Miles" syncline shows that our innovative method is well suited for fold and thrust belt investigation. This study was successful in integrating a-priori geological information in seismic modelling and imaging processes, and has demonstrated the improvements in interpretation of structural style that can be obtained from depth seismic images. On these, correct thickness, dip, and depth of sediment packages and related structures (folds and faults) are directly observed, rather than deduced from time image approximate interpretation. Thus, based on our interpretation of normal faulting in Upper Silurian - Lower Devonian times (Val-Brillant – Sayabec doublet and lower St Léon), we have shown that the "Lac des Huit-Miles" syncline records deformation related to the Salinic Disturbance and that related normal faulting can be constrained to the Ludlow-Prodoli time period in the northern Gaspé Belt. The Shickshock Sud fault appears clearer on our depth image and shows a dip of 30–40° towards SE at depth, supporting the hypothesis of this fault being related to a major Acadian décollement level. Thin-skinned thrusting seems to dominate over the area, with possible reactivation of older faults during the Acadian Orogeny, as exemplified by the reactivation of a Taconian (or older) fault in the underlying rocks below the syncline, which led to the development of a fault-related fold in the syncline.

To validate our interpretations, this study will serve as a starting point to a basin modelling study of the Gaspé Peninsula. Balanced cross-sections of the 2001-MRN-10b line will be constructed. They will be incor-

porated in kinematic modelling, using IFP software (Thrustpack). Petrophysical, log and thermal maturation data will be added to the kinematic modelling and help define the evolution of the Gaspé Belt and evaluate the petroleum potential of the area.

References

Al Yahya, K. M. (1989) Velocity analysis by iterative profile migration: Geophysics, 54, 718–729.

Bourque PA (2001) Sea-level fluctuations, syn-sedimentary tectonics, reef settlement and development, and implications for hydrocarbon exploration in Silurian-Lowermost Devonian Gaspé Belt, Québec Appalachians. Bulletin of Canadian Petroleum Geology, 49, No2: 217–237.

Bourque, P.A., Malo, M. and Kirkwood, D., 2000. Sedimentary history and paleogeography of the shelf at the NW margin of Iapetus during Silurian-Early Devonian time. GSA Bull., 112 : 4–20.

Bourque PA, Malo M and Kirkwood D (2001) Stratigraphy, tectono-sedimentary evolution and paleogeography of the post-Taconian - Pre-Carboniferous Gaspé Belt: an overview. Bulletin of Canadian Petroleum Geology, 49, No 2: 186–201

Brisebois D and Morin C (2004) Stratigraphie du synclinorium de Connecticut Valley - Gaspé de l'Ouest de la Gaspésie. Ministère des Ressources Naturelles report ET 2003-01, 30 pp. Deregowski S (1990), Common-offset Migrations and Velocity analysis. First break, 6: 225–234.

Desaulniers E (2006) Imagerie sismique de la ligne 2002-MRN-10b : Recherche d'une approche géophysique au service de l'interprétation. M. Sc. thesis, Université Laval, Québec, 124 pp

Ehinger A, Broto K, Jardin A and KIMASI project team (2001) 3D Tomographic Velocity Model Deptermination for Two North Sea Case Studies, 63rd Mtg.: Eur. Assn. Geosci. Eng., Session: M-37

Gray S, Cheadle S, Vestrum R, Gittins J, Zhu T, Nanan H (2002) Using advanced seismic imaging tool to see the invisible beneath foothills structures. CSEG recorder: 16–28

Hocq M, Verpaelst P, Chartrand F, Clark T, Lamothe D, Brisebois D, Brun J, Martineau G (1994) Géologie du Québec. Les Publications du Québec

Jardin A, Desaulniers E, Kirkwood D, Roure F, Rodriguez S (2004) Sensitivity analysis of depth images to velocities for structural interpretation in foothills. EAGE Conference, Expended Abstracts, Paris

Kirkwood D, Lavoie M and Marcil J (2004) Structural style and hydrocarbon potential in the Acadian foreland thrust and fold belt, Gaspé Appalachians, Canada. In R. Swennen,

Roure F and Granath J (eds) Deformation, fluid flow, and reservoir appraisal in foreland fold and thrust belts, AAPG Hedberg Series, no. 1: 412– 430

Kirkwood D, Desaulniers E, Laliberté JY, Jardin A and Bêche M (2005) Integrated Geological and Seismic Interpretation of the Gaspé Belt, a Structurally Complex Fold and Thrust Belt in the Northern Appalachians. AAPG Annual Meeting, Calgary

Lachambre G (1987) Le Silurien et le Dévonien basal du Nord de la Gaspésie. Ministère de l'Énergie et des Ressources du Québec report ET84-06, 83 pp

Lavoie D (1992) Carbonate sedimentation in an extensional tectonic regime: the Lower Devonian Upper Gaspé Limestones, Québec Appalachians. Canadian Journal of Earth Sciences, 29: 118–128

Lavoie D, Bourque PA (2001) The history of hydrocarbon exploration in the Silurian-Devonian Gaspé Belt: 100 years of modest success. Bulletin of the Canadian Society of Petroleum Geologists 49, No 2: 180–185

Malo M (2001) The Late Silurian - Early Devonian tectono-sedimentary history of the Gaspé Peninsula: from a transtensional Salinic basin to an Acadian foreland basin. Bulletin of the Canadian Society of Petroleum Geologists 49, No 2: 202–216

Malo M (2004) Paleogeography of the Matapédia basin in the Gaspé Appalachians: initiation of the Gaspé Belt successor basin. Canadian Journal of Earth Sciences, 41: 553–570

Malo M, Béland J (1989) Acadian strike-slip tectonics in the Gaspé Region, Québec Appalachians. Canadian Journal of Earth Sciences, 26: 764–1777

Malo M, Kirkwood D (1995) Faulting and progressive deformation history of the Gaspé belt, northern Appalachians: A review. In: Current Perspectives in Appalachian-Caledonian geology, J. Hibbard, C. van Staal and P. Cawood (eds.), GAC Special Paper 41: 267–282.

Malo M, Cousineau PA, Sacks P E, Riva J F V, Asselin E and Gosselin P (2001) Age and composition of the Ruisseau Isabelle Mélange along the Shickshock Sud fault zone: constraints on the timing of mélanges formation in the Gaspé Appalachians. Canadian Journal of Earth Sciences, 38(1): 21–42

Morin C and Laliberté JY (2002a) The unexpected Silurian–Devonian structural style in western Gaspé, New insight for promising hydrocarbon plays. Canadian Society of Petroleum Geology Diamond Jubilee Convention, Calgary, Program and Abstracts

Morin C and Laliberté JY (2002b), Overview of the very first mega-transect seismic survey throughout the Appalachian Gaspé Belt. Canadian Society of Petroleum Geology Diamond Jubilee Convention, Calgary, Program and Abstracts

Muller J, Ricarte P, Forgues E (2000) An adapted 2D processing sequence for foothills data through synthetic examples. SEG Technical Program Expanded Abstracts: 457–460

Pincivy A, Malo M, Ruffet G, Tremblay A and Sacks PE (2003) Regional metamorphism of the Appalachian Humber Zone of Gaspé Peninsula: 40Ar/39Ar evidence for crustal thickening during the Taconian orogeny. Canadian Journal of Earth Sciences, 40: 301–315

Robein, E. (2003) Velocities, time-imaging and depth imaging in reflection seismics -Principles and methods: EAGE.

Roksandic, M.M., and B. Granger (1981) Structural styles of Anticosti Island, Gaspé Passage, and eastern Gaspé Peninsula inferred from reflection seismic data, In : Field meeting, Anticosti-Gaspé, 1981, P.J. Lespérance (ed.), Vol. II: Stratig-

raphy and paleontology: IUGS Subcommission on Silurian Stratigraphy and Ordovician-Silurian Boundary Working Group, Département de géologie, Université de Montréal, p. 211–221.

Sacks PE, Malo M, Trzcienski Jr, Pincivy A and Gosselin P (2004) Taconian and Acadian transpression between the internal Humber Zone and the Gaspé Belt in the Gaspé Peninsula: tectonic history of the Shickshock Sud fault zone. Canadian Journal of Earth Sciences, 41: 635–653

St-Julien P and Hubert C (1975) Evolution of the Taconian orogen in the Québec Appalachians. American Journal of Science, 275-A: 337–362

Tremblay A and Pinet N (1994) Distribution and characteristics of Taconian and Acadian deformation, southern Québec Appalachians. Geological Society of America Bulletin, 106: 1172–1181

Williams H (1979) Appalachian Orogen in Canada. Canadian Journal of Earth Sciences, 16: 792–807

Williams H (1995) Temporal and spatial divisions. Chapter 2. In Geology of the Appalachian-Caledonian orogen in Canada and Greenland. Edited by H. Williams. Geological Survey of Canada, Geology of Canada, No. 6 (also Geological Society of America, The Geology of North America, Vol. F-1), pp 21–44

Williams H and St-Julien P (1982) The Baie Verte - Brompton Line: Early Paleozoic continent ocean interface in the Canadian Appalachians. In Major structural zones and faults of the northern Appalachians. Edited by P. St-Julien and J. Béland. Geological Association of Canada, Special Paper 24: 177–208

III

Part III
Exploration of Thrust Belts (2) :
Fluid Flow and Hydrocarbon Systems

Recent advances in analytical resolution, integration of stable isotope and fluid inclusion studies with classic petrography and basin modelling, provide a new understanding of paleo-fluid circulations, diagenesis and evolution of petroleum systems in foreland fold-and-thrust belts. Part III illustrates fluid flow reconstructions and hydrocarbon systems in two Alpine orogens, i.e., the Southern Pyrenees in Spain, and the Northern Apennines in Italy, respectively.

Travé et al. (Chapter 5) document the evolution of fluid flow in the Southern Pyrenees with compartmentalization of the hydrologic system in time and space in the foreland fold and thrust belt and progressive exhumation of the internal parts of the belt through the complex interactions between formation, meteoric and evaporites derived fluids.

Picotti et al. (Chapter 6) describe the geochemistry and maturity of the hydrocarbons trapped in Miocene reservoirs of the Northern Apennines, and discuss the timing of the petroleum charge as a function of the burial of the different source rock horizons and tectonic agenda.
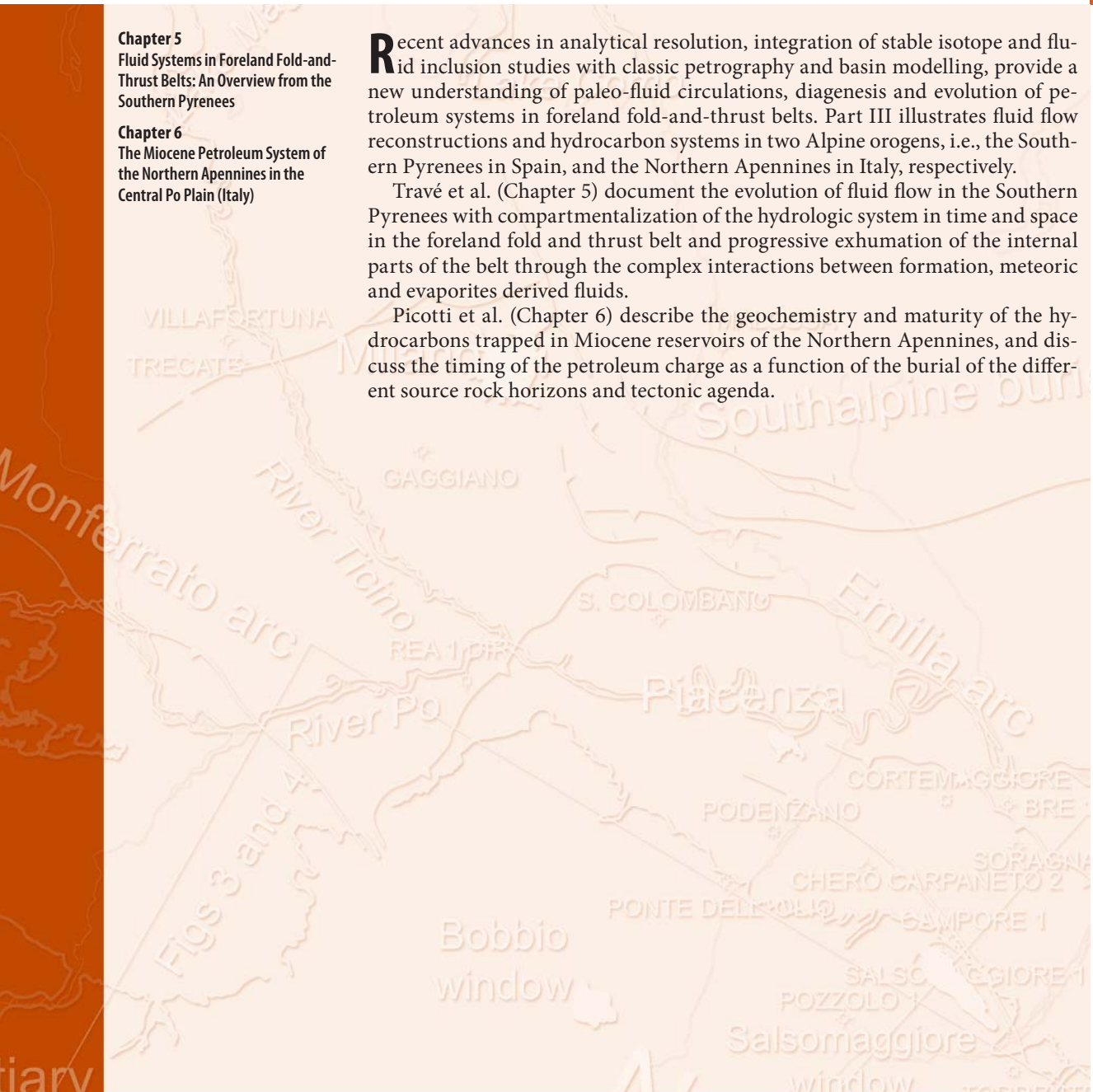
Fluid Systems in Foreland Fold-and-Thrust Belts: An Overview from the Southern Pyrenees

Travé, A. · Labaume, P. · Vergés, J.

Abstract. The analysis of three different regions of the South-Pyrenean fold-and-thrust belt reveals that during the Tertiary compression the hydrological system was compartmentalised in time and space. During the early-middle Eocene, when the thrust front affected marine soft-sediments in the Ainsa basin, the thrust fault zones were dominated by formation fluids derived from Eocene marine waters trapped in the underlying Eocene marls, although influences of meteoric waters were also present. During the middle-late Eocene, when the thrust front emplaced marine rocks over continental red-beds in the eastern Catalan basin (L'Escala thrust), the thrust fault zones were dominated by meteoric fluids. These fluids flowed preferentially along these faults, draining laterally the meteoric fluids and acting as barriers hindering their flowing towards more external parts of the belt. During the Oligocene, the most external part of the fold-and-thrust belt in the eastern Catalan basin developed on top of a salt detachment horizon. The thrust front affected continental materials of late Eocene-Oligocene age. At this moment, the thrusts were conduits for meteoric fluids arriving from the surface and also for evolved meteoric fluids migrating over short distance upwards after being in contact with the underlying evaporitic beds.

Most of the fractures show a similar sequence of microfractures. Microfractures of stage 1 formed when the sediment was poorly lithified. Microfractures of stage 2 represent the main episode of vein formation which developed when a progressive induration of the host sediment occurred. During microfracture stage 3, formed in an extensional regime, the host sediment was more indurated. The repetition of this sequence of microfractures in different fracture generations of the same outcrop indicates that the sediment induration was restricted to the vicinity of the vein. Away from the veins, the sediment remained poorly lithified during the entire deformation cycle. Calcite cement within the host rock precipitated later than the syn-compressive veins, when the sediment was more indurated.

Elemental geochemistry and stable isotopes of the calcite veins indicates that early generation of microfractures is infilled by local fluids (either marine or meteoric), whereas external fluids (meteoric or evolved meteoric) infilled the main compressive stage of microfractures. The hot temperature of these fluids (157ºC to 183ºC in the Atiart-Arro example) indicates their circulation through deep parts of the thrust belt.

The progressive increase of the $^{87}Sr/^{86}Sr$ ratio through time is due to the progressive uplift, exposure and erosion of the internal Pyrenean Axial Zone.

1 Introduction

Geofluids are related to the formation and deformation of the fold-and-thrust belts and sedimentary foreland basins. The geodynamic evolution of the belt - foreland basin system moves geofluids and, in their turn, geofluids condition the geodynamic evolution of the system by controlling the propagation of fractures and faults and the dynamics of fault activity. The fluid sources are likely to change during this coupled evolution, in particular because most foreland basins evolve from marine and largely underfilled to continenta overfilled and largely bypassing (e.g. Allen et al., 1986) (Fig. 1). Fractures and faults may have a major control on fluid distribution and migration pathways, acting as barriers or as conduits. The detailed petrology of the vein filling fractures, coupled with their distribution, geometry and microstructural study, is a key to understanding the coupling between fractures, faults and fluid, in particular 1) the mechanisms and kinematics of fluid-deformation relationships, 2) the fluid flow events and their relative timing, and 3) the synchronism, or not, between fracturation and fluid flow. The geochemical composition of the fracture-filling minerals and their comparison with the geochemistry and mineralogy of their host rocks allow to assess 1) the physico-chemical characteristics of the fluid, and therefore the fluid type and origin, 2) the degree of fluid/rock interaction (high versus low), 3) the type of fluid flow regime (closed versus open), and 4) the fluid pathways (pervasive versus channelized). Finally, the integration of all these data within a specific geological setting constrains the relative timing of fluid flow and the fluid driving force.

The main fluid flow systems in foreland-orogen contexts are driven by tectonics (Oliver, 1986; Burkhard & Kerrich, 1988; Machel & Cavell, 1999) and topography (Garven 1985, 1989, 1995). Structural and microstructural study of faults related to compression indicates
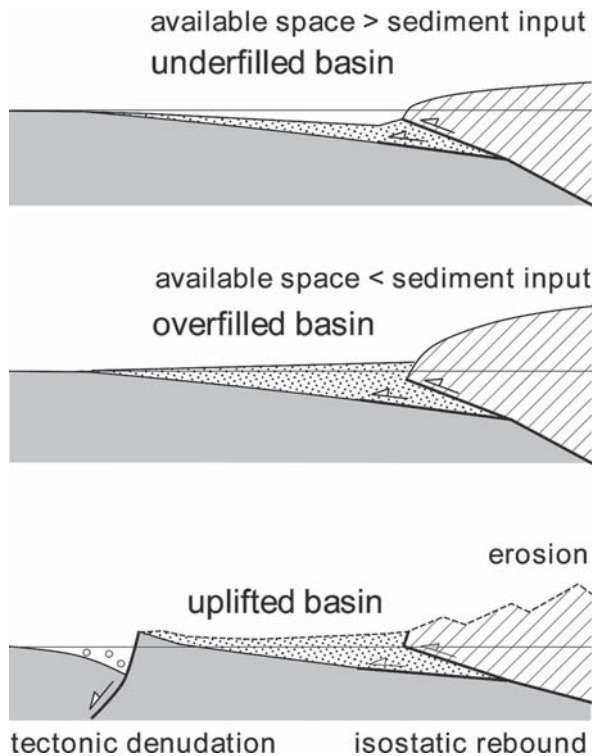
Fig. 1. Evolution of a foreland basin from marine and largely underfilled to continental. overfilled and largely bypassing. Post-orogenic vertical motions are mainly controlled by the interplay between tectonic and surficial denudation with concomitant isostatic rebound

that a high-fluid pressure highly favours thrusting (Roure et al., 1994, 2005) although it is not a prerequisite (Dietrich et al., 1983; Cosgrove, 1993). Orogenic compression may drive fluid migration directly (Oliver, 1986), and significant fluid flow may migrate towards the foreland coevally with thrusting (Ge and Garven, 1992; Qing & Mountjoy, 1992). Bradbury & Woodwell (1987) inferred that each thrust sheet acted as a separate hydrodynamic unit for expulsion of fluids into the foreland. Geochemical studies of calcite cements in compressive fault zones indicate in some cases high fluid-rock interaction and relatively closed palaeohydrogeological regime (Dietrich et al., 1983; Budai, 1985; Kyser & Kerrich, 1990; Muchez et al., 1995; Calvet et al., 1996; Travé et al., 1997, 1998; Ferket et al., 2004) but, in other cases calcite cements indicate low fluid-rock interaction and relatively open palaeohydrogeological regime (Burkhard & Kerrich, 1988; Marquer & Burkhard, 1992). Quantitative modelling of fluid migration in active foreland basins reveals that fluid flow derived from basin sediment compaction is subordinate to that resulting from the rising hinterland topographic relief of the orogen (Ge & Garven, 1992; Bethke & Marshak, 1990; Bitzer et al., 1998).

Ge & Garven (1994) calculated that the total volume of fluid expelled during thrusting is in the order of 1% of the total volume of pore fluid that moved through the section after thrusting (i.e., by topographically-driven flow), and these fluids did not travel more than a few km into the foreland. Low fluxes of tectonically-expelled fluids are also indicated in the Rocky Mountain Foreland Basin (Machel & Cavell, 1999) and in the Variscan foreland because recrystallization and lithification of the host rocks occurred earlier than thrusting (Muchez et al., 1995).

The South-Pyrenean fold-and-thrust belt represents an ideal natural field laboratory for the study of fluid migration during orogenic compression because the evolution of the foreland basin from marine underfilled to continental overfilled and the coupled thrust front propagation are particularly well recorded. The aims of this paper are to compare the type and origin of the synkinematic fluids and the type of palaeohydrogeological regime at different moments of the thrust front propagation. For this, we use data from three areas in three different parts of the belt representative of the main situations of the belt front during the main tectonic events: the Atiart-Arro thrust-fold system in the Ainsa basin, and the L'Escala thrust and El Guix anticline, both located in the eastern Catalan basin (Fig. 2). Data from Atiart-Arro and El Guix are synthesised from detailed works already published separately elsewhere (Atiart-Arro: Travé et al., 1997, 1998; El Guix: Travé et al., 2000), whereas data from L'Escala are new data presented here for the first time. Details of analytical techniques and methods, as well as the detailed petrology in the cases of Atiart-Arro and El Guix, are not presented in this paper and the readers are referred to the previouly published papers.

We will also discuss the place of oil migration in the fluid history from an example in the eastern Catalan basin (Caja et al., 2006), and compare fluid flow in the thrust front with that associated with the emplacement of basement thrust sheets in inner parts of the belt (Grant et al., 1990; Banks et al., 1991; McCaig et al., 1995).

2   South-Pyrenean Fold-and-Thrust Belt

The continental collision of Iberia and Europe produced the formation of the Pyrenean orogen with a partial subduction of the Iberian lithosphere to the north (Choukroune et al., 1989; Roure et al., 1989; Muñoz, 1992; Beaumont et al., 2000). Convergence began during the Campanian and most of compressional deformation ceased during the early Miocene. Two large flexural foreland basins formed on both sides of the growing mountain chain: the Aquitaine retroforeland and the Ebro foreland basins (Fig. 2). After an early

Fig. 2. Structural sketch of the Pyrenean belt and location of the studied outcrops. A: Atiart-Arro (early-middle Eocene); B: L'Escala (middle-late Eocene); C: El Guix (Oligocene); D: outcrop zone of Armanciès Formation marls (lower Eocene); E: outcrop area of Gavarnie basement thrust discussed in the text
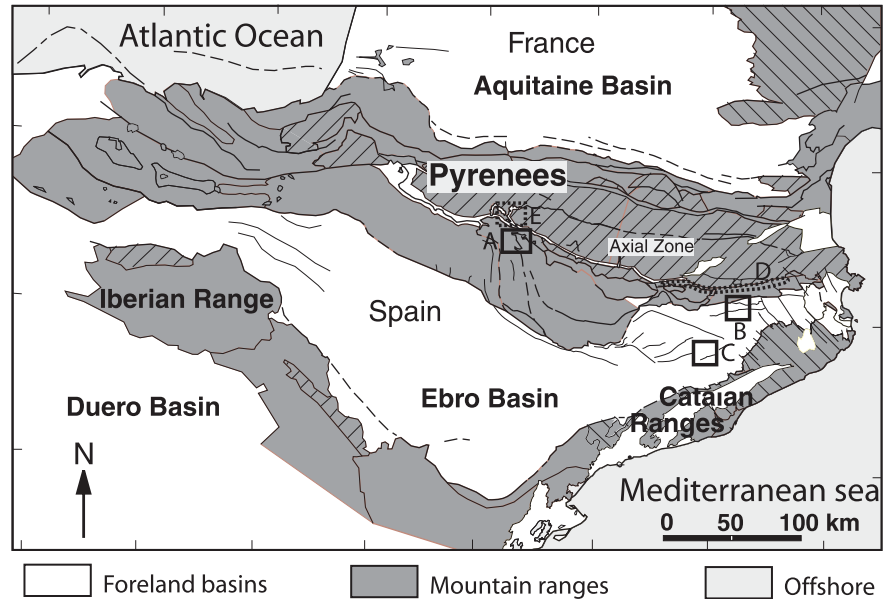
period of low subsidence rate and mainly continental or marine platform sedimentation, the South-Pyrenean foreland basin developed as underfilled and marine during the early-middle Eocene, with turbiditic troughs both in the easternmost and westernmost parts (the eastern Catalan and the Ainsa-Jaca basins, respectively). Subsequently, the basin became overfilled and continental from the middle-late Eocene to the end of shortening during the late Oligocene (Puigdefàbregas et al., 1986, 1992; Vergés et al., 1995, 1998). At the middle-upper Eocene boundary (~37 Ma) the uplift of the Western Pyrenees triggered the end of the marine foreland basin stage and originated an intermountain basin limited by the Pyrenees, the Catalan Coastal Ranges and the Iberian Range (Vergés & Burbank, 1996). An internal fluvial network delivered sediments to the Ebro Basin characterized by a large central lake (e.g., Anadón et al., 1979; Arenas & Pardo 1999). In the eastern Catalan basin, the deposition of the Cardona salts (~37 Ma) coincides with this transition from marine to continental conditions. The end of deformation along the South-Pyrenean thrust front occurred during the late Oligocene as determined by magnetostratigraphy on growth strata (~24.7 Ma) (Meigs et al., 1996). Fission track cooling ages in the Axial Zone of the central Pyrenees, however, reveal that basement uplift in the back of the fold-and-thrust belt ended its major uplift at about 30 Ma (Fitzgerald et al., 1999), and that younger movements occurred around 20 Ma along the southern edge of the Axial Zone (Sinclair et al., 2005; Campani et al., 2005). The Ebro basin infilled up to the late Miocene times when it was captured by Mediterranean rivers and thus ending its endorheic char-

acter (e.g., Coney et al., 1996; García-Castellanos et al., 2003).

During Pyrenean shortening there was a general migration of tectonic activity towards the foreland as well as of the sedimentary depocentres. Three main periods of thrust sheet movements can be differentiated with different rates of motion (e.g. Vergés et al., 2002), namely:

1. An early period during the Late Cretaceous-Paleocene, related to the emplacement of the uppermost thrust sheets, with very low rates of about 0.5 mm/a;
2. A second period, during the early and middle Eocene, which is characterized by fast rates of thrust sheet emplacement in the order of 4.0 to 4.4 mm/a in submarine conditions;
3. During the third period (late Eocene – Oligocene) there was a decrease of the rates of thrust emplacement down to 1.5 to 2.6 mm/a.

The second and third periods largely coincide with the underfilled and overfilled stages of basin evolution, respectively.

The three selected structural domains (Fig. 2) to conduct this geofluid study are representative of the two last stages of the thrust front – foreland basin system migration. The Atiart-Arro fold-and-thrust system represents the submarine stage, during the early-middle Eocene. The L'Escala thrust represents an intermediate stage, during the middle-late Eocene in transitional marine-continental conditions. The El Guix anticline represents the latest stage, during the Oligocene, with continental conditions (Fig. 3).
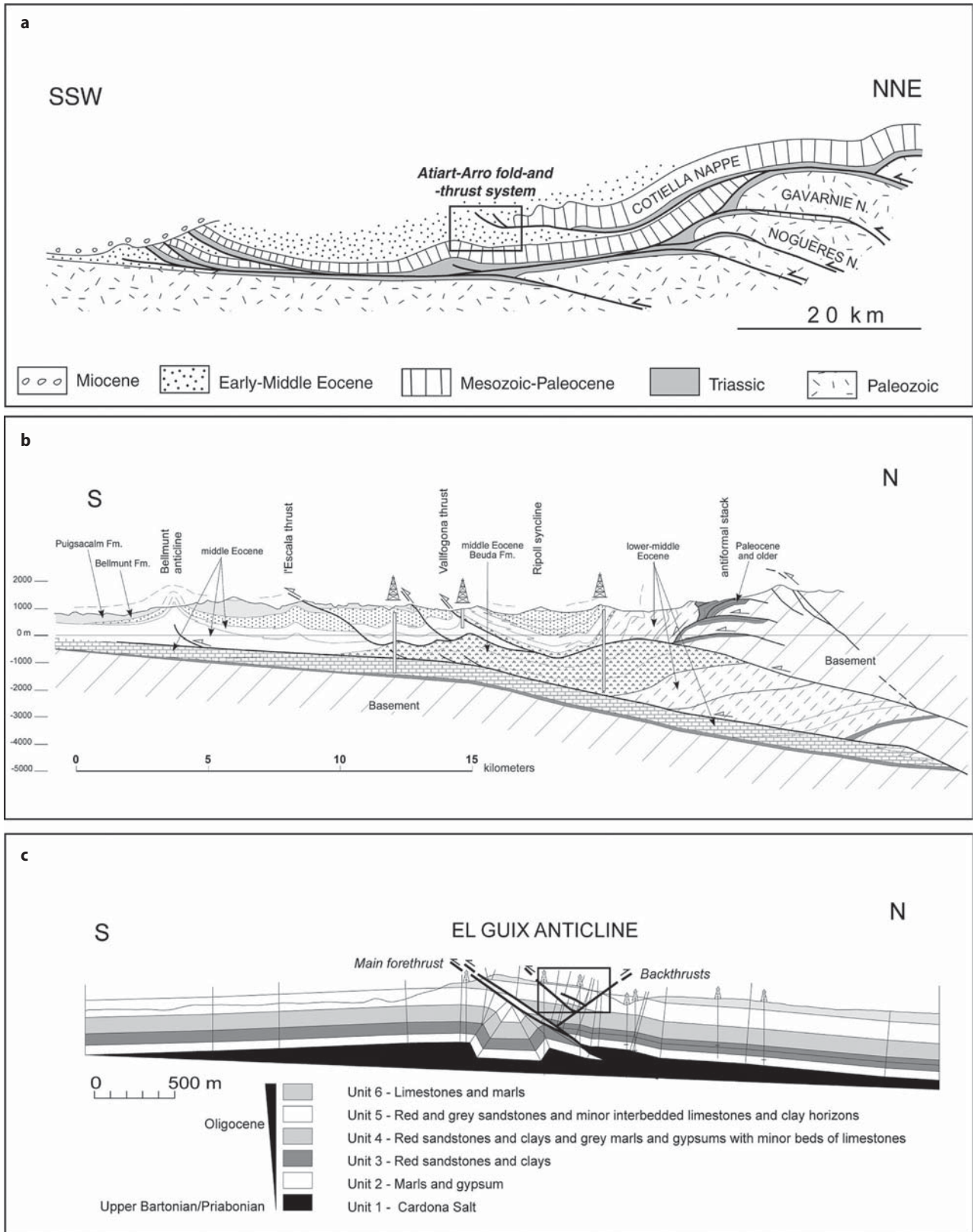
Fig. 3. Cross-sections of the studied areas. **a)** Atiart-Arro fold-and-thrust system (schematic section before erosion of the inner part of the Cotiella nappe). The box corresponds to Fig. 4. **b)** L'Escala thrust. **c)** El Guix anticline. The box corresponds to Fig. 8

3 Early Development of Submarine Thrust Front: Atiart-Arro Fold-and-Thrust System

3.1 Geological Framework

The Atiart-Arro fold-and-thrust system is located in the eastern part of the Ainsa sub-basin, a marine depocentre in the inner part of the central South-Pyrenean basin. The Ainsa sub-basin is mainly filled up by lower and middle Eocene marls with sandstone and conglomerate intercalations forming turbiditic channel-levee complexes, and comprises westward prograding outer-shelf/slope facies intercalations in the eastern part (e.g. Mutti et al., 1988). These deposits rest above Upper Cretaceous-Paleocene shelf carbonates, Permo-Triassic marls and sandstones, and a Paleozoic basement. The northern part of the basin-fill is thrust by the Cotiella Nappe, detached in the Triassic sediments and mainly consisting of Upper Cretaceous-Paleocene carbonates (Fig. 4) (Séguret, 1972). The nappe moved southwards for at least 20 km and was probably rooted in the Paleozoic basement of the Axial Zone of the belt, although this root cannot be precisely identified due to subsequent deformation and erosion (e.g. Martinez-Peña & Casas-Sainz, 2003). The Atiart-Arro fold-and-thrust system is a SW-verging imbricate structure developed in the basin-fill at the front of the nappe. Erosional surfaces and unconformities related to the fold-and-thrust system show that the main movement of the Cotiella Nappe occurred during the early Eo-

cene (Ypresian), and that deformation continued during the middle Eocene (Mutti et al., 1988).

The study of the fluid behaviour was carried out on four hectometric-scale outcrops, corresponding to three thrust-fault zones and one syncline: the Sampert, Atiart, and Los Molinos thrusts, from the NE to the SW (and structurally from top to bottom), and the Arro syncline in the footwall of the Los Molinos thrust (Fig. 4) (Travé et al., 1998). The Atiart and Los Molinos thrusts probably root within the Cotiella thrust, whereas the Samper thrust is a rootless "out-of-the-syncline" thrust. The Arro syncline is asymmetric, with a steeply-dipping eastern limb and a gently-dipping western limb.

The studied mesostructures affect mainly marly lithologies. The thrust fault zones consist in a-few-metres thick intervals where deformation is marked by the association of shear bands in marls and calcite shear veins. Calcite veins are also observed over a few tens of metres in the thrust-fault footwalls, but they are rare or absent in the hangingwalls. The shear bands feature S-C structures related to the development of pressure-solution cleavage. The most intensely strained shear bands have mineral assemblages characterised by the occurrence of dickite, which is absent in the protolith as well as in the less strained domains of fault zones (Buatier et al., 1997). Many calcite veins show a three-stage evolution of their microstructure with 1) diffuse veinlet networks associated with sand disaggregation, 2) crack-seal shear microstructures forming most of the vein volume, and 3) late extensional openings. The geometry of stage 1 and 2 microstructures is coher-

Fig. 4. Detailed cross-section of the Atiart-Arro fold-and-thrust system
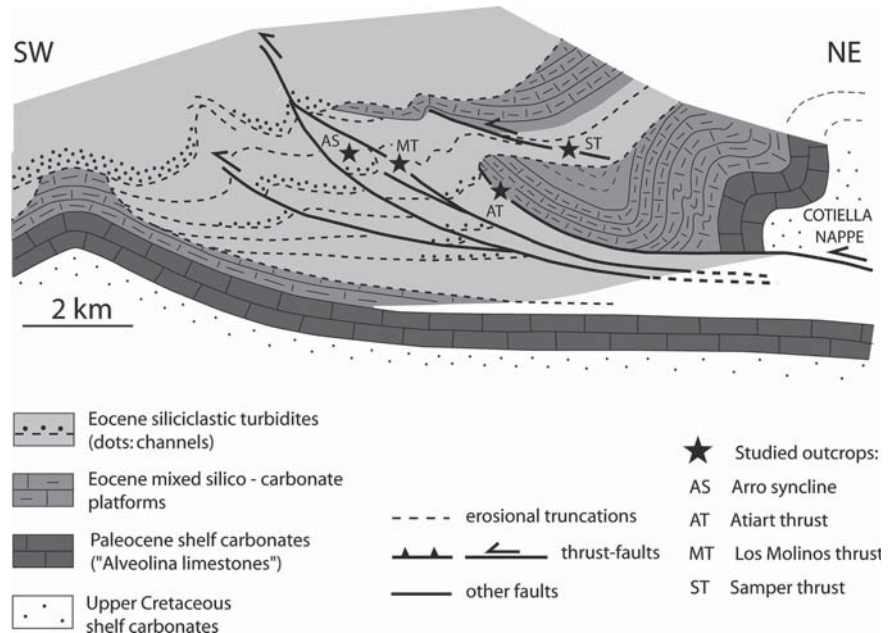
ent with the syn-thrust shearing kinematics and their chronology relates to the progressive induration of the sediment during vein formation, whereas stage 3 corresponds to a syn- or post-shear boudinage of the veins forming tabular bodies more competent than the surrounding marls. The crack-seal microstructures attest the episodic nature of fault slip and calcite precipitation. Similar shear veins are also present in the Arro syncline, with three generations that formed before, during and after folding, respectively. The most-abundant ones are the syn-folding veins, which formed along the bedding planes in relation to bedding-slip in the steep limb of the syncline. In the Arro syncline, as well as in the Samper and Los Molinos thrusts, calcite veins contain minor amounts of celestite. Other petrographic features of the veins are described in Travé et al., (1997).

Macroscopic deformation is weak outside the thrust fault zones and regional cleavage is absent. However, a locality in the western limb of the Arro syncline features oval burrows that attest about 20% of NE-SW horizontal shortening prior to sediment lithification (Travé et al., 1998). Sand disaggregation observed in the earliest stages of shear vein formation also shows that deformation affected initially poorly-lithified sediments.

3.2 δ¹⁸O and δ¹³C of Host Rock and Calcite Veins

The $\delta^{18}O$ and $\delta^{13}C$ values from the host marls range from -8.2‰ to -5.8‰, and from -3.3 ‰ to -0.7‰ PDB, respectively (Fig. 5, Table 1). They are thus lower than those of the Eocene marine carbonates which range from -4‰ to +2‰ and from -0.3‰ to +2.8‰ PDB,

respectively (Shackleton & Kennett, 1975; Veizer & Hoefs, 1976; Hudson & Anderson, 1989), this depletion most probably resulting from burial diagenesis.

Calcite cements from the three microscopic stages of vein development, as well as the pre-, syn- and post-syncline veins at Arro do not show significant differences of isotopic values. On each outcrop, the oxygen isotopic values of the calcite cements in veins are systematically depleted between 1.3 and 2.8‰ PDB in relation to the host marl calcite, probably indicating a higher temperature of the fluid from which the vein calcite precipitated with respect to its adjacent host rock (Marshall, 1992), or a deeper setting of precipitation.

The Atiart and Los Molinos thrusts, which are deep-rooted thrusts, also show depletion in ¹³C of the calcite in veins with respect to the host marl calcite. This is interpreted as an input of an external ¹³C-depleted mineralising fluid channelized through the thrust-fault zones. On the contrary, in the Arro syncline and the Samper thrust, which have no roots towards deeper domains, the similar $\delta^{13}C$ in the calcite from veins and host marls shows that the $\delta^{13}C$ of the mineralising fluid was mainly controlled by that of the host sediment.

The isotopic values of calcite from the dickite-bearing marls in thrust zones range from -9.0‰ to -5.8‰ PDB in $\delta^{18}O$, and from -2.6‰ to -1.5 ‰ PDB in $\delta^{13}C$, respectively, i.e. without significant differences with respect to calcite from the less deformed marls. However, the calcite veinlets inside these dickite-bearing marls show higher $\delta^{18}O$ values (from -7.3‰ to -4.4‰ PDB in $\delta^{18}O$, and from -2.5‰ to -1.6‰ PDB in $\delta^{13}C$), probably resulting from in situ clay-water reactions, i.e. the dickite formation through partial disso-
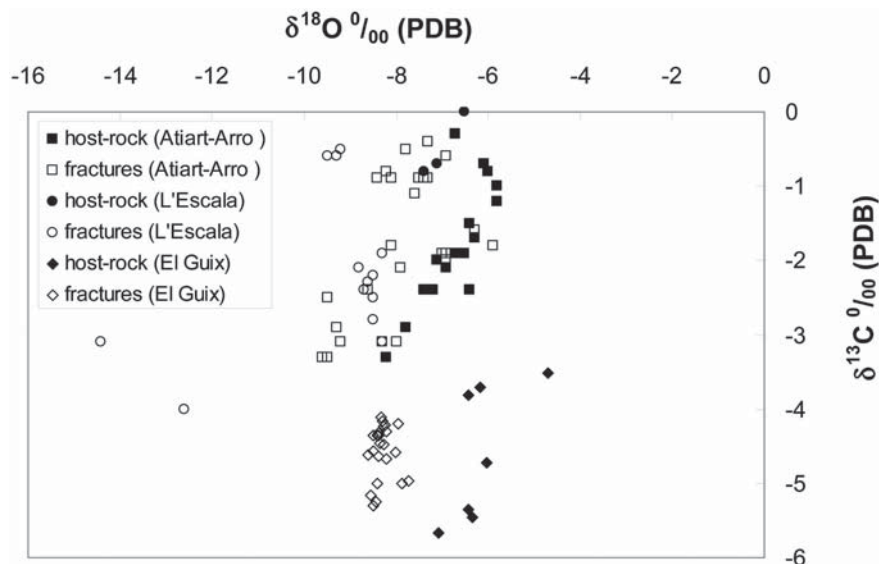

Fig. 5. $\delta^{18}O$ versus $\delta^{13}C$ of calcite cements in the veins and host-rocks

Table 1. $\delta^{18}O$, $\delta^{13}C$ and $^{87}Sr/^{86}Sr$ ratio of calcite cements in the veins and host-rocks. The column dif $\delta^{18}O$ indicates the difference between de $\delta^{18}O$ of the calcite cement in the veins and its adjacent host-rock. For Atiart-Arro and El Guix, G1, G2 and G3 refer to the three stages of microstructure development, respectively

		Structure/microstructure	$\delta^{18}O$	$\delta^{13}C$	dif $\delta^{18}O$	$^{87}Sr/^{86}Sr$
Atiart-Arro	Syncline / Arro	G 2	-7.8	-0.5	1.7	
		G 2	-8.1	-1.8	2.0	
		G 2	-6.9	-0.6	0.8	
		G 2	-7.5	-0.9	1.4	
		Host-rock	-6.1	-0.7		0.707914
		G 2	-8.2	-0.8	1.5	
		G 2	-8.2	-0.8	1.5	
		G 2	-7.3	-0.9	0.6	
		G 2	-8.4	-0.9	1.7	
		Host-rock	-6.7	-0.3		
		Host-rock	-5.8	-1		0.707892
		Host-rock	-5.8	-1.2		
		Host-rock	-5.8	-1.2		
		G 2	-8.1	-0.9	2.3	0.707862
		G 3	-7.6	-1.1	2.6	0.707912
		G 1	-7.3	-0.4	1.5	0.707886
		G 2	-7.4	-0.9	1.4	0.707916
	Thrusts / Los Molinos	G 2	-9.2	-3.1	1.8	0.709173
		Host-rock	-7.4	-2.4		
		G 2	-9.6	-3.3	2.2	
		Host-rock	-6.4	-2.4		
		Host-rock	-6.9	-2.1		
		Host-rock	-6.7	-1.9		
		G 2	-9.5	-3.3	2.3	
		Host-rock	-7.2	-2.4		
		Host-rock	-6.5	-1.9		
	Thrusts / Atiart thrust	Host-rock	-6.4	-1.5		
		G 2	-5.9	-1.8	0.5	0.708153
		G 2	-6.9	-2	0.5	
		G 2	-7	-1.9	0.6	
		G 2	-6.9	-1.9	0.5	
		G 2	-7.9	-2.1	1.5	0.708247
		Host-rock	-7.1	-2		
		Host-rock	-6.3	-1.7		
		Host-rock	-6	-0.8		
		G 2	-6.3	-1.6	0.3	
	Thrusts / Samper	Host-rock	-8.2	-3.3		
		Host-rock	-7.8	-2.9		
		G 2	-9.3	-2.9	1.1	
		G 2	-9.5	-2.5	1.3	
		G 2	-8.3	-3.1	0.5	
		G 2	-9.2	-3.1	1	
		G 2	-8.6	-2.4	0.4	
		G 2	-8	-3.1	0.2	

		Structure/microstructure	$\delta^{18}O$	$\delta^{13}C$	dif $\delta^{18}O$	$^{87}Sr/^{86}Sr$
L'Escala	pre-thrust	pre-thrust diaclase	-8.5	-2.8	1.1	0.708179
		pre-thrust diaclase	-8.3	-1.9	0.9	
	thrust	bed to bed sliding	-8.8	-2.1	1.4	
		thrust fault	-8.3	-3.1	0.9	0.708165
		thrust fault	-8.6	-2.3	1.2	
		thrust fault	-8.5	-2.2	1.1	0.708171
		bed to bed sliding	-8.5	-2.5	1.1	0.708189
		bed to bed sliding	-8.7	-2.4	1.3	
	post-thrust	sinistral fault	-9.5	-0.6	2.1	
		Host-rock	-6.5	0		
		NW-SE diaclase	-12.6	-4	5.2	
		Host-rock	-7.4	-0.8		
		NW-SE diaclase	-14.4	-3.1	7.3	0.70847
		Host-rock	-7.1	-0.7		0.708952
		sinistral fault	-9.2	-0.5	2.5	0.708572
		Host-rock	-6.7	-0.3		
		sinistral fault	-9.3	-0.6	2.6	
El Guix	less deformed area	Host-rock	-6.34	-5.46	-	0.70941
		Host-rock	-6.42	-5.35	-	
		G 2	-7.88	-5.01	1.5	0.70911
		G 2	-7.72	-4.97	1.3	0.70911
		G 2	-8.41	-5.01	2.0	
		G 2	-8.56	-5.16	1.5	
		G 2	-8.49	-5.3	1.4	
		G 2	-8.44	-5.24	1.4	
		Host-rock	-7.07	-5.66	-	
	fore-thrust	G 2	-8.49	-4.57	3.8	0.70887
		G 2	-8.61	-4.61	3.9	
		Host-rock	-4.7	-3.52	-	0.70865
	lower backthrust	G 1	-8.5	-4.36	2.5	
		G 2	-8.2	-4.3	2.2	0.70909
		G 2	-8.42	-4.36	2.4	0.70909
		G 2	-8.37	-4.36	2.4	0.70909
		G 2	-8.38	-4.32	2.4	0.70909
		G 2	-8.34	-4.46	2.3	
		G 2	-8.28	-4.47	2.3	
		Host-rock	-6.02	-4.72		
	upper backthrust	G 2	-8.01	-4.58	1.9	0.70906
		G 3	-8.28	-4.23	2.1	
		G 2	-8.32	-4.11	2.3	0.70906
		Host-rock	-6.16	-3.71		0.70878
		G 2	-8.37	-4.63	2.0	
		G 2	-8.22	-4.67	1.8	
		Host-rock	-6.42	-3.82		
	up.b.foo.	G 2	-8.31	-4.17	1.9	
		G 2	-7.97	-4.2	1.6	
		G 2	-8.25	-4.21	1.8	

lution of illite and drainage of potassium by fluid flow along the shear zones (Buatier et al., 1997). Alteration of rock-fragments and feldspars has been proved to produce an ^{18}O increase in the fluid (Yeh & Savin, 1977; Longstaffe, 1993). In the context of the Atiart-Arro thrust system, the kinematics of dickite formation are inferred to have been promoted by strain and fluid flow (Buatier et al., 1997), rather than by temperature as classically described in diagenetic or hydrothermal environments. Comparing the values of the four outcrops, both the host marl calcite and the calcite cements in veins show a progressive depletion in both ^{18}O and ^{13}C from the Atiart thrust and Arro syncline to Los Molinos thrust and to the Samper thrust (Travé et al., 1997). The structural location and burial history of the four outcrops make it difficult to explain the trend of isotopic depletion by differences in burial of the structures. A possible explanation could be a higher meteoric influence in the structures located closer to the emerged part of the belt (i.e. the Samper thrust).

3.3 $^{87}Sr/^{86}Sr$ Values of Host Rock and Veins

In the Arro syncline, the calcite and celestite veins and the calcite fraction of the host marls, show $^{87}Sr/^{86}Sr$ ratio ranging between 0.70774 and 0.70795, without a significant difference between the pre-, syn- and post-syncline veins (Fig. 6, Table 1). This range of values is consistent with the $^{87}Sr/^{86}Sr$ ratio of the Eocene seawater (Katz et al., 1972; Burke et al., 1982; DePaolo & Ingram, 1985), indicating that the source of strontium to precipitate the calcite and celestite in veins and the calcite cement in the host sediment was the same. The later was controlled by the $^{87}Sr/^{86}Sr$ ratio of the Eocene seawater during the whole evolution of the Arro

syncline. The ^{34}S values of the celestite also indicates precipitation from an Eocene marine water (Travé et al., 1997). Therefore, the vein-forming fluid was probably the interstitial water trapped in the Eocene marine marls derived from the Eocene seawater, or a fluid equilibrated with the Eocene calcitic sediments.

The siliciclastic detrital fraction in the marls has substantially higher $^{87}Sr/^{86}Sr$ ratios (0.71723–0.71894) with respect to the Eocene seawater, giving rise to the more radiogenic $^{87}Sr/^{86}Sr$ ratios in the bulk marl (0.70976–0.70987) than in the calcite fraction. This indicates that this detrital fraction originates from the erosion of Paleozoic rocks outcropping in the paleo-Axial Zone.

In the Atiart and Los Molinos thrust-fault zones, the $^{87}Sr/^{86}Sr$ ratios in vein calcite range from 0.70815 to 0.70927, i.e. more radiogenic than the Eocene seawater values. These relatively high values indicate that the vein calcite in fault zones precipitated from a fluid with a different composition than the fluid present outside the fault zones and, consequently, that these zones acted as fluid conduits during shear deformation. This more radiogenic fluid composition could originate from 1) interaction with the Paleozoic rocks or the Eocene marls existing in deeper settings, 2) in-situ mineralogical transformations of the Eocene marls in the intensely strained sediments (e.g. the illite to dickite transformation), or 3) the weathering by meteoric water of the Paleozoic rocks in the emerged part of the belt. In the case that the source was the Eocene marls, either from deeper settings or from local more deformed part of the thrust-fault zones, the detrital phyllosilicates submitted to higher temperature and/or pressure could have expelled their more radiogenic Sr during dissolution and mineralogical transformations. The three sources are possible and they could have acted alone or simultaneously.
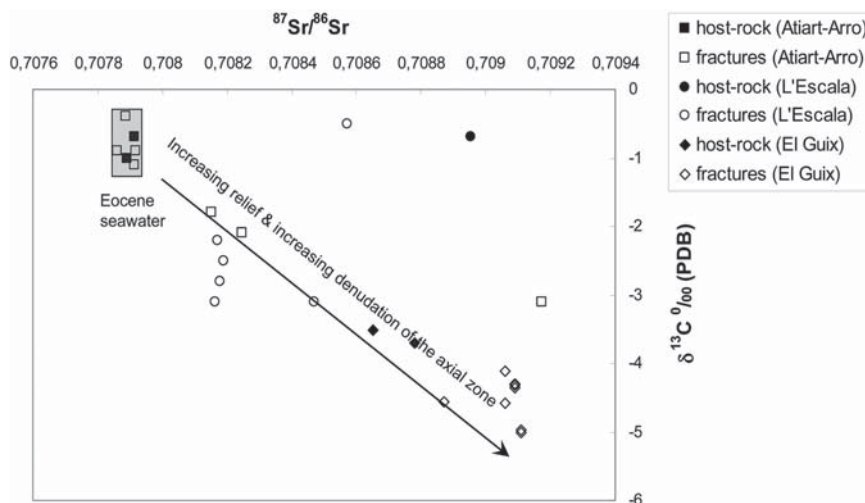

Fig. 6. $^{87}Sr/^{86}Sr$ ratio versus $\delta^{13}C$ values of calcite cements in the veins and host-rocks

3.4 Elemental Geochemistry

The elemental composition of the fluid from which calcite precipitated was determined from the elemental geochemistry of the calcite cements (Travé et al., 1997). The results show that the elemental composition of the fluid from which all types of calcite precipitated had a Mg/Ca ratio between 0.006 and 0.126, a Sr/Ca ratio between 0.012 and 0.39, a Mg/Sr ratio between 0.089 and 4.938, a Ca/Fe ratio between 79 and 8286, and a Mn/Ca ratio between 0.1×10^{-4} and 4×10^{-4}. Most of these values are consistent with formation water and not with unmodified marine waters or oxidizing/reducing meteoric waters. The samples from the Atiart thrust and Arro syncline have higher values of Sr/Ca and lower values of Mg/Sr than the samples from the other two outcrops, reflecting original seawater composition to a certain extent (Travé et al., 1997).

3.5 Fluid Circulation in the Early Development of the Submarine Thrust Front

Syn-kinematic fluid flow in the submarine thrust front during the early-middle Eocene is evidenced macroscopically by the abundance of calcite shear veins within the marls involved in the Atiart-Arro fold-and-thrust system.

Microstructures indicate that deformation affected initially poorly lithified sediment, and the crack-seal mechanism of formation of the shear veins attests the episodic nature of fault-slip and associated fluid flow in fractures. Distribution of the veins suggests that the main source of fluid was dewatering of the poorly permeable marls from the thrust footwalls, probably related to both (i) vertical compaction due to burial under thrust sheets, and (ii) tectonic horizontal shortening. These fluids were drained upwards towards the thrust-fault zones, in which they migrated laterally towards the thrust front due to the anisotropy of the fracture permeability in these zones.

The $^{87}Sr/^{86}Sr$ ratios of the host marl calcite and of the calcite and celestite in the veins away from the thrust-fault zones indicate that the original water trapped interstitially in the marls was Eocene seawater. This is corroborated by the $\delta^{34}S$ in the vein celestite from the Arro syncline, which yielded values ranging from 18.3 to 21.7‰ (CDT) (Travé et al., 1997), consistent with those of the Eocene seawater sulphate (Claypool et al., 1980). The $\delta^{18}O$ and $\delta^{13}C$ values of the same samples reveal a change of the porewater composition from marine to formation-water during the early burial stage. Fluid inclusion microthermometry of the celestite in the Arro syncline veins, indicating ho-

mogenization temperatures ranging between 157 and 183°C and salinities around 7 wt% eq. NaCl (Travé et al., 1998), reveal the presence of a hot, saline ascending fluid restricted to the veins, where it was mixed with the local formation water (Travé et al., 1998). These two types of fluids were drained towards the thrust-fault zones where they acquired a higher $^{87}Sr/^{86}Sr$ ratio, probably related to local fluid-sediment reactions (the dickite formation). The $\delta^{13}C$ depletion in vein calcite from the Atiart and Los Molinos thrusts may result from the input along the thrust zones of ^{13}C-depleted mineralising fluids, whereas the $\delta^{18}O$ depletion in the calcite from the structurally highest/innermost thrust-fault zones suggests also the influence of meteoric water derived from the emerged part of the belt in these structures.

The earliest fluid regime in the Ainsa basin was an intergranular (porous) flow of the local fluid (compactional flow) allowing for a pervasive isotopic and elemental exchange with the marls prior to vein formation. With the onset of compressional deformation, channelized flow along tectonic slip surfaces became dominant, contributing to local sediment dewatering, but also to the input of external fluids along the thrust fault zones. The geochemical data do not record significant evolution of fluid composition during the successive episodes of vein formation along the slip surfaces at a same locality. Such a fluid regime dominated by the dewatering of local sediments is consistent with the submarine context of deformation that affected recently deposited, poorly lithified sediments. This tectonic context suggests that fluids may have been overpressured.

4 Intermediate Development of the Fold-and-Thrust System within a Marine-Continental Transitional Environment: L'Escala Thrust

4.1 Geological Framework

The L'Escala thrust is part of the Alpens-L'Escala antiformal structure within the south-eastern Pyrenean foreland basin (eastern Catalan basin) (Muñoz et al., 1986). The structure is constituted by thrusts and folds affecting the middle and upper Eocene alluvial fan and deltaic syn-tectonic deposits of the Bellmunt and Puigsacalm Formations, respectively (Fig. 7). The folded foreland is limited at the north by the Vallfogona thrust and, at the south, by the Bellmunt anticline from the subhorizontal sediments of the Ebro basin (Fig. 3b).

The L'Escala anticline developed in the hanging-wall of a thrust which places middle-upper Lutetian continental sediments of the Bellmunt Formation over
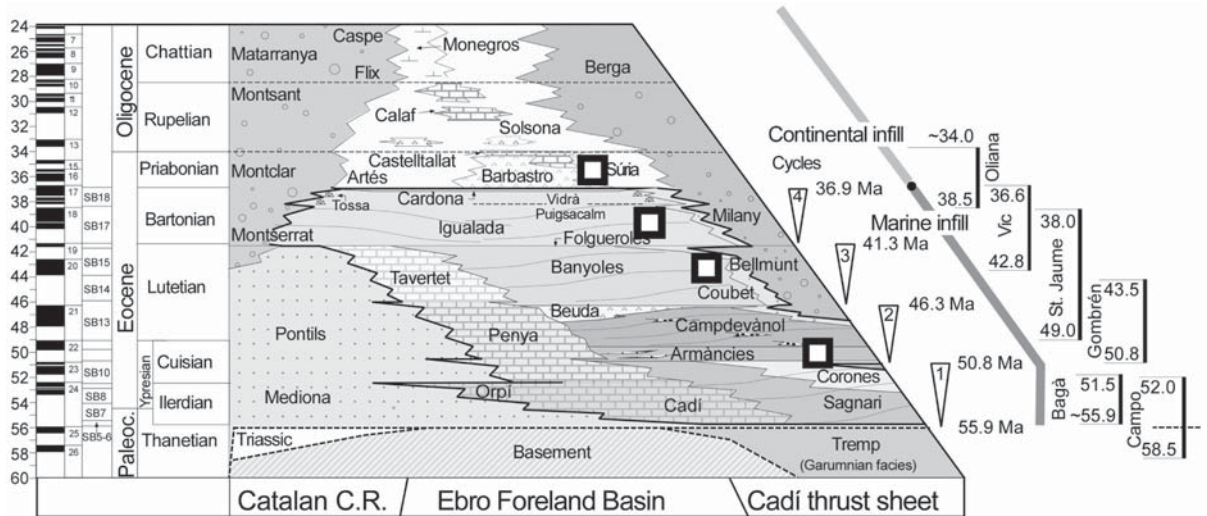
Fig. 7. Stratigraphic framework of the south-eastern Pyrenean foreland basin with location of the El Guix outcrop (upper square), L'Escala outcrop (two intermediate squares), and Armancies Formation (lower square)

lower Bartonian marine sediments of the Puigsacalm Formation (Muñoz et al., 1986).

The Bellmunt Formation is constituted by a clastic succession evolving from fluvio-deltaic to alluvial red deposits prograding from the Pyrenean Axial Zone towards the south margin of the Lutetian basin (Ramos et al., 2002). The limit between the Bellmunt Formation and the Puigsacalm Formation is sharp and corresponds to a marine transgression at a basin scale. The Puigsacalm Formation is constituted by grey microconglomerates and sandstones with glauconite prograding from the east and forming metric-thick sequences interpreted as deltaic systems.

In the studied outcrop, the Bellmunt Formation is formed by decimetric to metric intervals of clays, siltites, sandstones, and conglomerates interpreted as channel and flood plain deposits. The Puigsacalm Formation in the studied outcrop basically consists of calcite cemented sandstones.

The sampled section comprises three different thrust fault zones. The main fault places materials of the Bellmunt Formation on top of the Puigsacalm Formation, and the other two faults affect only the Bellmunt Formation. Three sets of cross-cut calcite-filled fractures have been recognised: 1) extensional pre-thrust fractures (cut and deformed by the thrust plane), 2) thrust-related shear-fractures (thrust faults and associated bed to bed sliding), and 3) post-thrust fractures cutting the thrust planes. The latter consists of: 3a) sinistral strike-slip faults, and 3b) NW-SE extensional fractures. The pre-thrust fractures have only been observed in the Bellmunt Formation. Calcite cements within the thrust faults have been observed in the three thrust faults and calcite cements in the

bedding planes have been only observed in the Bellmunt Formation. Calcite cements in the thrust faults and in the bedding planes precipitated synchronously to thrust activity due to successive shear openings, as indicated by the occurrence of shear bands formed by the crack-seal mechanism. The post-thrust sinistral strike-slip faults and NW-SE fractures have been only observed in the footwall of the lower thrust in the Puigsacalm Formation. The former are filled by calcite cement precipitated synchronously to shear-fault opening, whereas the NW-SE fractures correspond to extensional diaclases, parallel to the compression-related cleavage planes, and filled by calcite cement not affected by pressure-solution related to cleavage formation.

The pre-thrust fractures are diaclases with sharp, straight or undulated walls and are filled by calcite cements constituting veins from 1 cm to 5 cm thick and up to several metres long. These fractures are filled by two generations of cement: a first generation constituted by a non isopachous rim of euhedral calcite crystals and a second generation of anhedral sparry calcite cement from few millimetres up to 2 centimetres thick, with deformed mechanical twin planes and undulating extinction.

The thrust fractures are the thrust faults and the associated stratification planes which moved synchronously to the thrust movement due to bed to bed sliding and are filled by calcite cements constituting veins from 1 to 10 cm thick. The veins within the thrust fractures are constituted by calcite cement, forming different shear bands (up to 6 successive shear bands have been observed in a single fracture) parallels to the fracture wall. Locally, the limits between the shear bands

are stylolitic surfaces. Each shear band is formed by a crack-seal mechanism. The calcite crystals are brownish-greenish, anhedral or subeuhedral, locally elongated, variable in size from 30 μm up to 2 mm, smaller close to the crack-seal border and increasing in size farward. The bigger crystals show abundant mechanical twinning planes and undulating extinction.

The post-thrust fractures include two sets of fractures: the sinistral faults and the NW-SE fractures. The veins filling the sinistral faults are constituted by calcite crystals, with planar or interpenetrated borders. The crystals are transparent and up to 5 mm large and show mechanical twinning planes and undulating extinction. The NW-SE fractures are diaclases. The fracture walls are sharp and straight. The fractures are filled by euhedral sparry transparent calcite crystals up to 5 millimetre large, with planar or interpenetrated borders, abundant deformed mechanical twinning planes and undulating extinction.

4.2 $\delta^{18}O$ and $\delta^{13}C$ of Host Rock and Calcite Veins

The $\delta^{18}O$ of the Puigsacalm Formation host rock range from -7.4 to -6.5‰ PDB and the $\delta^{13}C$ range from -0.8 to 0.0‰ PDB (Fig. 5, Table 1). These values are more depleted in $\delta^{18}O$ and within the same range for $\delta^{13}C$ than the isotopic values of the Eocene marine carbonates (from -4 to +2‰ PDB and from -0.3 and +2.8‰ PDB, respectively). These depleted $\delta^{18}O$ values of the bulk host rock are probably a mixture of depleted $\delta^{18}O$ values of the calcite cement precipitated in the interparticle porosity during relative burial conditions and a more enriched $\delta^{18}O$ values of the marine components. The $\delta^{13}C$ values around 0‰ probably indicate that the main source for C to produce the calcite cements may have been the marine bioclastic components (Discocyclines, Nummulites, echinoderms, bivalvia, bryozoans,..) which form 50% of the Puigsacalm Formation host rock.

The carbonate fraction of the Bellmunt Formation host rock has not been analysed because the texture of the rock did not allow to analyse separately the calcite cement from the abundant Paleozoic, Mesozoic and older Tertiary carbonate clasts.

The $\delta^{18}O$ and the $\delta^{13}C$ values of the calcite cement in the pre-thrust fractures range from -8.5 to -8.3‰ PDB and from -2.8 and -1.9‰ PDB, respectively. The $\delta^{18}O$ and the $\delta^{13}C$ of the calcite cement in fractures related to bed to bed sliding and in the thrust faults are very similar, ranging from -8.8 to -8.3‰ PDB and from -3.1 to -2.1‰ PDB, respectively. The similarity of the $\delta^{18}O$ and $\delta^{13}C$ between the calcite cements within pre-thrust and thrust-related fractures indicates that both precipitated from the same fluid or from differ-

ent fluids with similar composition, which is less probable. Hence, during thrusting, the pre-thrust fractures became open for fluid circulation and for precipitation of calcite cements.

The $\delta^{18}O$ of the calcite cement in the post-thrust strike-slip faults range from -9.5 to -9.2‰ PDB and the $\delta^{13}C$ range from -0.6 to -0.5‰ PDB. These $\delta^{18}O$ values are on average 2-3‰ more depleted than those of the Puigsacalm Formation bulk host rock, whereas the $\delta^{13}C$ values are within the same range as those of the host rock. The similarity between the $\delta^{13}C$ values between the host rock and the calcite cement within the fractures indicates host-rock buffering. The difference in $\delta^{18}O$ between the bulk host rock and the calcite cement within the pre-thrust and thrust-related fractures and post-thrust strike-slip faults, is probably because $\delta^{18}O$ of the bulk host rock is a mixture between a lower $\delta^{18}O$ of the interparticle calcite cement and a $\delta^{18}O$ closer to 0‰ of the marine bioclastic components, whereas the $\delta^{18}O$ of the calcite cements within the fractures reflect only the composition of the calcite cement which has a non marine origin, either precipitated from meteoric or from formation waters.

The $\delta^{18}O$ of the calcite cement in the post-thrust NW-SE fractures range from -14.4 to -12.6‰ PDB and the $\delta^{13}C$ range from -4.0 to -3.1‰ PDB. The $\delta^{18}O$ of the calcite cement in the post-thrust NW-SE fractures is in average 6-7‰ more depleted than the Puigsacalm Formation host rock, and the $\delta^{13}C$ is in average 3-4‰ more depleted than the host rock. The very low $\delta^{18}O$ values suggest a relatively hot fluid. The depleted $\delta^{13}C$ values indicate that this external fluid was probably, in origin, a meteoric fluid enriched in ^{12}C probably due to the ingress of isotopically light soil-CO_2 (Cerling, 1984; Cerling et al., 1989). This fluid did not interact with the Puigsacalm Formation host rock.

4.3 $^{87}Sr/^{86}Sr$ Values of Host Rock and Calcite Veins

The $^{87}Sr/^{86}Sr$ ratio of the Puigsacalm Formation bulk host rock is 0.70895. In the calcite cements, values are 0.70818 in the pre-thrust fractures, 0.70816 to 0.70817 in the thrust fault zones, 0.70819 in the bedding-parallel veins, 0.70857 in the post-thrust strike-slip faults, and 0.70847 in the post-thrust NW-SE fractures (Fig. 6, Table 1).

The $^{87}Sr/^{86}Sr$ ratio of the Bartonian sea (age of the Puigsacalm Formation) was 0.7077–0.7078 (DePaolo & Ingram, 1985; Hess et al., 1986; Koepnick et al., 1985; Mead & Hodell, 1995; Palmer & Elderfield, 1985) and, therefore, all the studied cements are non marine in origin.

The $^{87}Sr/^{86}Sr$ ratio of the Puigsacalm Formation bulk host rock (0.70895) reflects the mixture of the

bioclastic Eocene marine components and the silici-
clastic fraction derived from an external source, prob-
ably the interaction of fluids with Paleozoic rocks.

The $^{87}Sr/^{86}Sr$ ratio homogeneity of calcite cements
in the pre-thrust fractures, thrust fault zones and bed-
ding-parallel veins, indicates a common origin for
the fluid, as already suggested by the oxygen and car-
bon isotopic values. This radiogenic fluid composition
could originate from 1) interaction with the Paleozo-
ic rocks or the Paleozoic siliciclastic components of
the Puigsacalm Formation host rock existing in deep-
er settings, 2) in-situ mineralogical transformations of
the Paleozoic siliciclastic components of the host rock,
or 3) the weathering by meteoric water of the Paleozo-
ic rocks in the emerged part of the belt.

The calcite cements in the post-thrust strike-slip
faults and in the post-thrust NW-SE fractures show
$^{87}Sr/^{86}Sr$ values closer to the Puigsacalm Formation
host rock values than the cements in the former frac-
tures indicating a higher contribution either of the Pa-
leozoic rocks or of the Paleozoic siliciclastic compo-
nents of the host rock. In the case of the post-thrust
strike-slip faults, the similar $\delta^{13}C$ values are more in
agreement with a high contribution of the Paleozo-
ic siliciclastic components of the host rock, whereas
in case of the post-thrust NW-SE fractures the low-
er $\delta^{18}O$ and lower $\delta^{13}C$ of the calcite cement better ac-
count for an origin of the $^{87}Sr/^{86}Sr$ values by miner-
alogical transformations of the underlying Paleozoic
rocks, at higher temperature.

4.4 Elemental Geochemistry

The calcite veins filling the pre-thrust and thrust-re-
lated fractures show a similar range of values charac-
terised by low Fe (between 405 and 2770 ppm), low Sr
values (from below the detection limit up to 1735 ppm
of Sr), Mn content from 370 up to 1815 ppm, and Mg
content between 645 and 7945 ppm.

The calcite veins filling the post-thrust strike-slip
faults are characterised by a very high Fe content (be-
tween 2915 and 9105 ppm), between 365 and 1260 ppm
of Mn, between 885 and 5715 ppm of Mg and from be-
low the detection limit up to 1515 ppm of Sr.

The calcite veins filling the post-thrust NW-SE frac-
tures are characterised by very high Sr content (from
655 and 3535 ppm), between 345 and 1185 ppm of Mn,
between 400 and 3195 ppm of Fe, and from below the
detection limit up to 1795 ppm of Mg.

The calcite cement filling the porosity within the
Puigsacalm Formation host rock has a composition
similar to the post-thrust strike-slip faults, with Mn
content between 265 and 705 ppm, Fe content between
2595 and 6900 ppm, Mg content between 1230 and

3605 ppm and from below the detection limit up to
445 ppm of Sr.

The cement in the pre-thrust and thrust-related
fractures precipitated from a fluid consistent with a
meteoric water composition.

The cement in the Puigsacalm Formation host rock
and in the post-thrust strike-slip faults precipitated
from a fluid consistent with a formation water compo-
sition, probably because a deeper burial location of the
structure after the thrust emplacement.

The cement in the NW-SE fractures precipitated
from a fluid consistent either with a meteoric modified
to a formation water composition.

4.5 Fluid Circulation During the Intermediate Development of the Fold-and-Thrust System within a Marine-Continental Transition Environment

The different stages of vein formations, characterised
by different geochemical signatures, attest the evolu-
tion of the fluid system during the tectonic history.

4.5.1   Prior to the Main Tectonic Shortening

No evidences of fluid circulation exist during the de-
velopment of the pre-thrust fractures because no pre-
cipitation of cement took place. Precipitation of calcite
cements within these fractures did not occurred until
the main tectonic shortening.

4.5.2   The Main Thrust Event

Compressive deformation and thrust emplacement
occurred while sedimentation was still active in the
basin. The veins related to the main tectonic shorten-
ing occur either in the thrust faults or related to bed-
ding slip during flexural folding. The concentration of
veins inside and in the few tens of metres below and
above the thrust faults and their absence far from the
thrust faults indicates that these zones were zones of
preferential fluid flow during compressive deforma-
tion. As it also occurred in the Ainsa area, the crack-
seal mechanism of formation of the calcite shear veins
indicates synchronicity between vein formation and
fault movement within the thrust-related fractures
and attests the episodic nature of fault-slip and asso-
ciated fluid flow.

A meteoric fluid, with relatively low Fe, low Sr and
high Mg content, $\delta^{18}O$ ranging from -8.8 to -8.3‰
PDB and $\delta^{13}C$ ranging from -3.1 to -2.1‰ PDB, and
$^{87}Sr/^{86}Sr$ ranging from 0.70816 to 0.70819, circulated

through the thrust-related fractures as well as through the pre-thrust fractures during thrust development. This fluid had no or very low interaction with the host rock. The identical chemical composition of the calcite cement filling the three main thrust faults, the bedding planes and the previously formed fractures indicates that they belonged to the same interconnected fluid system and therefore, the presence of a widespread distributed homogeneous fluid.

The meteoric fluids, derived from the emerged part of the belt and arriving to the thrust fault zones, flowed preferentially along these zones, in a drainage pattern dominated by higher fracture permeability parallel to the thrust faults. Due to this lateral drainage, the thrust fault zones probably acted as barriers hindering their flowing towards more external parts of the belt.

The differences in the $^{87}Sr/^{86}Sr$ ratio and $\delta^{13}C$ between the calcite cement in the pre-thrust and thrust-related fractures and the Puigsacalm Formation host rock indicates that the geochemistry of cement was poorly controlled by that of the host rock and, therefore, that the fluid was not buffered by the host rock and an open palaeohydrological system during the main thrust event.

4.5.3   The Post-Thrust Strike-Slip Event

Calcite shear veins precipitated synchronously to strike-slip fault activity following thrusting. The elemental geochemistry of the calcite cements in these faults is consistent with precipitation from a fluid with a formation water composition. The calcite cements precipitated from this fluid are characterised by very high Fe content, $\delta^{18}O$ ranging from -9.5 to -9.2‰ PDB, $\delta^{13}C$ ranging from -0.6 to -0.5‰ PDB and $^{87}Sr/^{86}Sr$ of 0.70857. These $^{87}Sr/^{86}Sr$ ratio and $\delta^{13}C$ values are closer to the Puigsacalm Formation bulk host rock values than the calcite cements in all the other fractures indicating the higher intensity of fluid-rock interaction. A high interaction between the fluid and the host rock seems to be restricted, in the studied section, at this episode of the geodynamic evolution, and cementation of the Puigsacalm Formation host rock probably occurred at this time. The $\delta^{18}O$ values of the Puigsacalm Formation bulk host rock probably indicate a mixture between the marine contribution of the bioclastic components and a more depleted contribution of the calcite cement precipitated during burial conditions. The $\delta^{13}C$ values indicate that the main source for carbon to produce the calcite cements may have been the marine bioclastic components which form 50% of the host rock. The $^{87}Sr/^{86}Sr$ ratio indicates the non marine origin of the fluid trapped in the sediment, and the great influence of the siliciclastic components of the host rock. The $^{87}Sr/^{86}Sr$ anomaly in the calcite ce-

ment in the fault probably results from local clay mineral reactions.

4.5.4   The Late Extensional Tectonic Phase

The post-thrust NW-SE extensional fractures are the latest observed features, formed by the opening of the pre-existing cleavage planes. They thus post-date the compressional deformation.

The calcite cements in these NW-SE fractures, with relatively low Mg and Fe and relatively high Sr content, low $\delta^{18}O$ values ranging from -14.4 to -12.6‰ PDB, $\delta^{13}C$ ranging from -4.0 to -3.1‰ PDB and $^{87}Sr/^{86}Sr$ ratio of 0.70847, are interpreted as precipitated from a hot meteoric fluid. This fluid had no or very low interaction with the carbonate fraction of the Puigsacalm Formation host rock, whereas the $^{87}Sr/^{86}Sr$ ratio indicates contribution of the Palaeozoic rocks. The high temperature during calcite precipitation indicates a deep-circulating fluid.

Thus, at this stage, the paleohydrogeological system remained open to external meteoric fluids arriving from more internal and emerged parts of the belt, but with rather long circulation in relatively deep structures.

The extensional character of these fractures is interpreted as a stage of compressive stress relaxation associated with tectonic uplift and relief formation.

5   Late Development of Continental Thrust and Fold system: El Guix Anticline

5.1 Geological Framework

The El Guix anticline corresponds to the southernmost structure of the south-eastern Pyrenean foreland basin, detached above the Priabonian Cardona salt separating the non-deformed strata from the folded and thrusted strata. Compressional activity in the area represents the latest stages of the Alpine compressional tectonics (Sans & Vergés, 1995).

The El Guix anticline is a double structure composed of two anticlines (Fig. 3c). The sampled section displays two sets of linked fractures rooted at different depths and affecting different lithologies. Structurally, it is located in the northern anticline in which a major north-directed thrust (backthrust) merges with several south-directed thrusts (forethrusts) (Fig. 8). Shortening across the anticline is approximately 21%, consisting of 16% of layer-parallel shortening prior to folding and thrusting, and only 5% during folding and thrusting (Sans et al., 2003).

The deformed sedimentary pile is made up of fine-grained, fluvio-lacustrine deposits, consisting of clays,
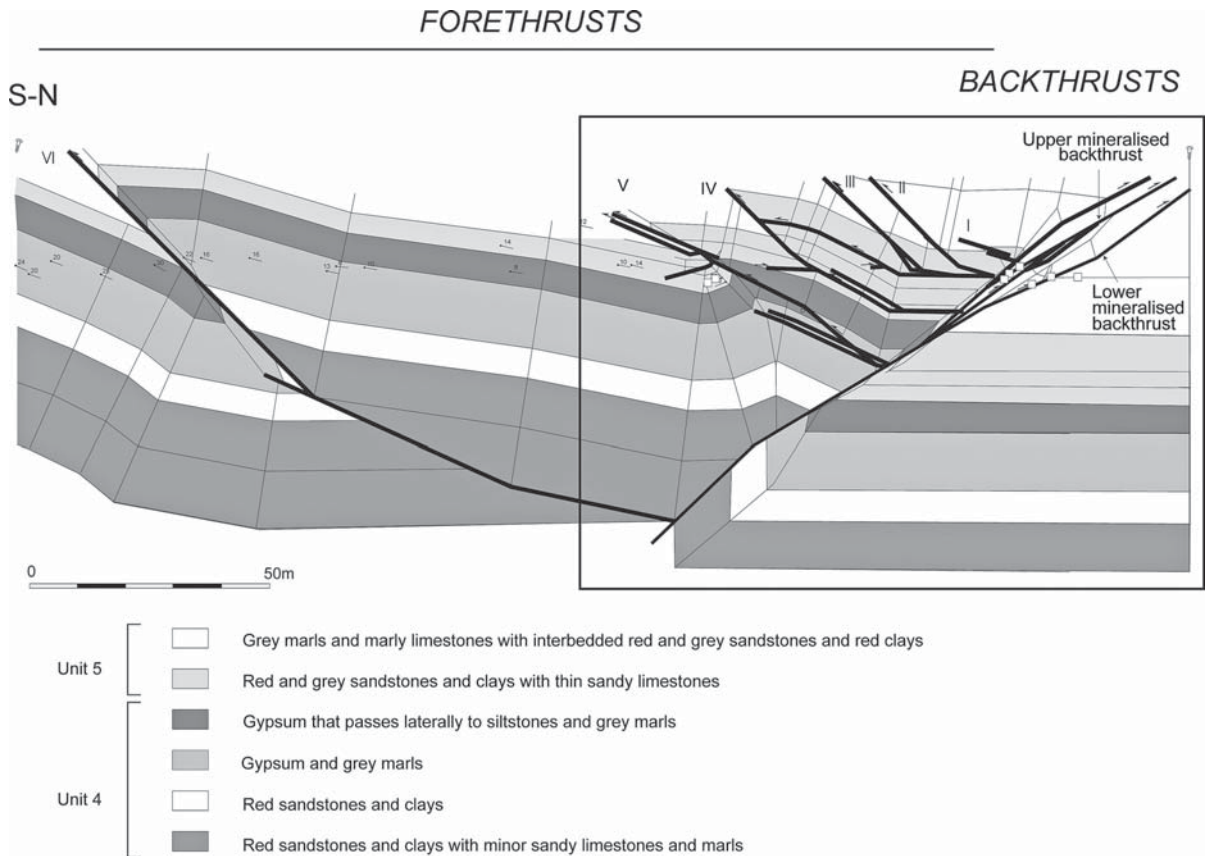
Fig. 8. Detail of the sampled structures in the El Guix area

sandstones and limestones of late Eocene-Oligocene age, overlying the evaporite sequence. These rocks are located approximately 300 metres above the detachment horizon. During thrusting, the maximum burial determined by vitrinite reflectance was 2 km, indicating that the folding and thrusting occurred at depth (Vergés et al., 1998), which is consistent with the pre-growth nature of the deformed rocks.

The backthrust is an intensely deformed, 2 m thick zone, which has an offset of 30 m, formed by an array of four north-directed faults. Only two of them present calcite veins, and they henceforth are refered as lower and upper mineralised backthrust. The footwall of the upper mineralised backthrust presents minor fractures filled with calcite veins. The sediments located between the main forethrust and the backthrust array are deformed by a set of south-directed thrusts (forethrusts) which branch in layer parallel detachments and, at a deeper level, merge with the backthrust (Fig. 8). Forethrusts I to IV only cut sandstone beds, whereas forethrusts V and VI cut sandstone beds and a lower gypsum horizon. None of these forethrusts is mineralised and their slip ranges from half a metre to a few metres. The footwall of forethrust V presents

a set of cross-cutting south and north-directed minor faults with an offset of several centimetres. These minor faults are filled with calcite veins.

Less deformed areas of the anticline also present small fractures filled with calcite. We studied fractures located about 20 m to the north of the backthrust array affecting subhorizontal beds of grey marls and fine sandstones, and 200 m above the other samples affecting horizontal lacustrine limestones in the hanging-wall of the backthrust array.

In the El Guix anticline, calcite veins are mostly found where the host rocks are clays and limestones, and are almost absent in the fractures affecting sandstones. The calcite veins range from millimetres to centimetres in thickness and show slickensides.

The evolution pattern of the calcite-sealed fractures consists of three stages (Fig. 9) which reflect an evolution of the microstructures very similar to that observed at Atiart-Arro. In each fracture, deformation started with a network of discontinuous micro-fractures (stage 1), slightly oblique to the sedimentary lamination and associated with a ductile deformation of the host sediment. Later, crack-seal shear veins, locally affected by micro-stylolitic surfaces, record the
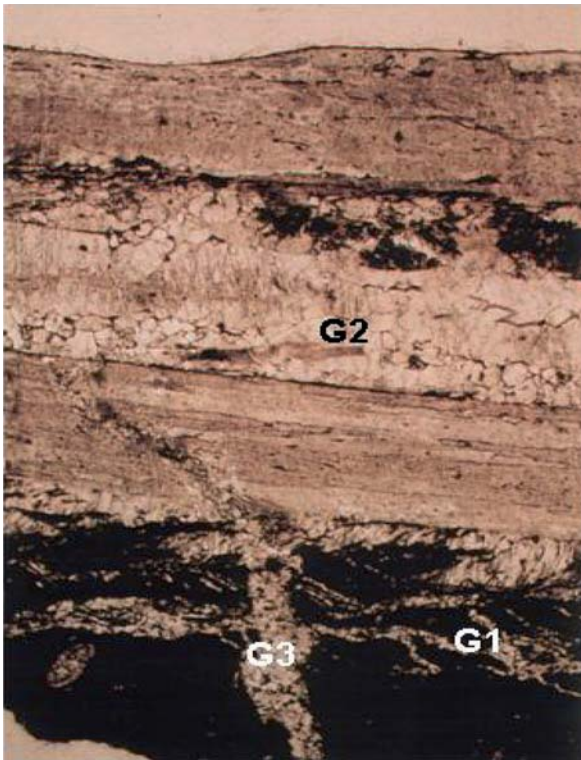
Fig. 9. Petrology of the veins showing the three microfracture stages

main thrust activity (stage 2). Finally, extensional fractures, cross-cut at a large angle the microfractures of stage 2 (stage 3).

The cement filling microfracture stage 3 also fills the vuggy porosity affecting the calcite cement filling microfracture stage 2 and the intergranular porosity of the host rock.

Further petrographic features of the veins are described in Travé et al. (2000).

5.2 δ^{18}O and δ^{13}C Values of Host Rock and Calcite Veins

The δ^{18}O values of the host rock (lacustrine limestones and carbonate fraction in the marls) range from -7.1‰ to -4.7‰ PDB, and the δ^{13}C values vary between -5.7‰ and -3.5‰ PDB (Fig. 5, Table 1), which are consistent with freshwater limestones and meteoric calcite cements (Veizer, 1992).

The oxygen and carbon isotopic composition of the calcite cements filling the different fractures (from –8.6 to -7.7‰ PDB and from -5.3 to -4.1‰ PDB, respectively) plot within a much narrower range of values than the isotopic composition of the host rocks adjacent to the fractures.

The calcite veins filling the upper mineralised backthrust have more negative isotopic values than the values of their adjacent host rock by 1.8 to 2.3‰ for δ^{18}O values and 0.4 to 0.9 ‰ for δ^{13}C. The calcite veins filling small fractures in the upper mineralised backthrust footwall have δ^{18}O values between 1.6 and 1.9‰ and δ^{13}C values 0.4‰ more negative than the values of their adjacent host rock. The calcite veins filling the lower mineralised backthrust have δ^{18}O values between 2.2 and 2.5‰ more negative and δ^{13}C values between 0.3 and 0.4 more positive than the values of their adjacent host rock. The calcite veins filling minor faults in the forethrust footwall have δ^{18}O values between 3.8 and 3.9‰ and δ^{13}C values 1.1‰ more negative than the values of their adjacent host rock. The calcite veins filling small fractures in the less deformed areas have δ^{18}O values between 1.3 and 2.0‰ more negative than the values of their adjacent host rock and δ^{13}C values between 0.4 and 0.5‰ more positive than their adjacent host rock (Fig. 5, Table 1).

The oxygen isotopic compositions of all the calcite veins in the El Guix anticline are consistent with precipitation from a meteoric or an evolved meteoric fluid (Hudson, 1977; Marshall, 1992). The carbon isotopic compositions of the calcite veins with values within the same range of values as the calcite fraction of the host rocks indicate that the carbon for these veins proceeded from homogenising C derived from the host rock.

The values of the calcite cements in microfracture stages 1, 2, and 3 are all within the same range, between -8.6‰ and -7.7‰ PDB for δ^{18}O and between -5.3‰ to -4.1‰ PDB for δ^{13}C, indicating a common fluid responsible for calcite precipitation during the different stages.

5.3 ^{87}Sr/^{86}Sr Values of Host Rock and Calcite Veins

The calcite fractions of the host rock have a ^{87}Sr/^{86}Sr ratio ranging from 0.70865 to 0.70941 (Fig. 6, Table 1). The calcite veins in the different fractures have a ^{87}Sr/^{86}Sr ratio varying from 0.70887 to 0.70911. The halite and gypsum samples from the underlying Cardona Salt Formation have values ranging from 0.70793 to 0.70797, which are slightly higher than the late Eocene-early Oligocene marine signal ranging from 0.7077 to 0.7079 (Hess et al., 1986; Hess et al., 1989; Denison et al., 1993).

Although the host rocks adjacent to the different fractures have a different ^{87}Sr/^{86}Sr ratio, the calcite veins in the diverse fractures plot within a narrow range of values, averaging those of the host rocks, as has been already obseved for the stable isotope values. An ^{87}Sr/^{86}Sr versus δ^{13}C plot gives a well defined

correlation of the 7 values (r=0.91), with the two extreme values determined by the calcite fraction of the host rocks and the intermediate values defined by the calcite veins in the fractures. This correlation indicates that the $^{87}Sr/^{86}Sr$ isotopic composition of the calcite veins in the fractures was sourced within the adjacent host rocks. Influences from the underlying Cardona Salt Formation are not reflected by the $^{87}Sr/^{86}Sr$ ratio of the calcite veins in the fractures.

5.4 Elemental Geochemistry

The elemental composition of the fluid from which calcite precipitated was determined from the elemental geochemistry of the calcite cements (Travé et al., 2000). The results show that most of the mineralising fluids for the analysed calcite veins have Mg/Ca molar ratios lower than 0.2, which is consistent with a formation water composition. Only three samples from the small fractures in the upper mineralised backthrust footwall have a Mg/Ca molar ratio higher than 0.2, which is consistent with a meteoric water composition. The Sr/Ca molar ratio of the mineralising fluid for calcite veins in the small fractures in the upper mineralised backthrust footwall, in the lower mineralised backthrust, and in the minor faults in the forethrust footwall is higher than 0.007, which is consistent with a formation water composition. The Sr content in the upper mineralised backthrust and in the small fractures in the less deformed areas is always below the detection limit. Most of the mineralising fluids for calcite veins in the upper mineralised backthrust have a Ca/Fe molar ratio higher than 1000, consistent with a meteoric water composition. By contrast, most of the mineralising fluids for calcite veins in the small fractures in the upper mineralised backthrust footwall, in the lower mineralised backthrust, in the minor faults in the forethrust footwall and in the small fractures in the less deformed areas have a Ca/Fe molar ratio lower than 1000, consistent with a formation water composition. Most of the mineralising fluids for calcite veins in all the studied samples have a Mn/Ca molar ratio higher than 0.0002, consistent with a meteoric water composition. The presence of Na is restricted to the upper mineralised backthrust, the small fractures in the upper mineralised backthrust footwall and the lower mineralised backthrust, indicating that only the backthrust array allowed precipitation from a fluid derived from the underlying Cardona Salt Formation.

To sum up, the fluid precipitating the calcite veins in the upper mineralised backthrust was basically consistent with a meteoric origin, whereas the fluid precipitating the calcite veins in the other fractures was basically consistent with a formation water origin. However, the presence of Na in all the fractures of the backthrust array including the upper mineralised backthrust indicates that these fractures also served as a pathway for a fluid which has been in contact with the underlying evaporites.

Differences between the three microfracture stages are not evident in the Mg/Ca, Ca/Fe and Mn/Ca molar ratios of the precipitating fluids. However, the presence of Sr and Na only in microfracture stage 2 indicates that during this stage the topographycally-driven fluid flow, arrived deeper, at the underlying Cardona Salt Formation.

The intergranular porosity of the host rock was filled during precipitation of cement in microfracture stage 3.

5.5 Fluid Circulation During the Late Development of Continental Fold-and-Thrust System

In the El Guix area, meteoric fluids, with high Fe/Mn and Fe/Mg ratios, without Na and Sr, enriched with ^{13}C and with low $^{87}Sr/^{86}Sr$ with respect to their host rock were widely distributed in the structure throughout all its evolution, within a relatively open palaeohydrological system. Evolved meteoric fluids, with lower Fe/Mn and Fe/Mg ratios, with Na and Sr, depleted in ^{13}C and with high $^{87}Sr/^{86}Sr$ with respect to their host rock were only present during thrust faults development within a relatively closed palaeohydrological system. The underlying evaporites acted as the lower boundary of the aquifer.

6   Discussion and Conclusions

In this section we summarize the existing links between fluid history and tectonic evolution in the South-Pyrenean foreland basin during the Tertiary. These relationships show a mutual interaction, also detected in other foreland basins, which are working together during the forwards propagation of tectonic stresses through the sedimentary basin. The understanding of the role of fluids before, during and after thrusting as well as the role of the thrust faults as conduits or seals for fluid migration are key questions to be addressed. Understanding this interaction may help to clarify and better explore the migration of hydrocarbons in fold-and-thrust belts and foreland basins.

Timing of Thrusting, Fluid Migration, Thermal History and Relationships With Hydrocarbons

Fluid migration has been detected through the entire Tertiary evolution of the South-Pyrenean thrust front

as revealed by the three analysed examples (Atiart-Arro, L'Escala and El Guix) with different ages of deformation (Table 2).

In Atiart-Arro and El Guix sites, a similar sequence of microstructures, formed during the main compressive event, has been recognised. Microfracture stage 1 is characterised by sediment disaggregation showing that vein formation began in poorly lithified sediment. Microfracture stage 2 corresponds to the main episode of shear vein formation indicating a change in the deformation mechanism due to progressive induration of the host sediment. Microfracture stage 3 indicates a decrease of intensity of compressive deformation and could correspond to local extensional rebound in the veins that form tabular bodies more competent than the host-sediment host sediment.

Because veins of different generations in a same outcrop show a similar chronology of microfractures, we conclude that sediment induration was restricted to the vicinity of the vein, probably due to cement precipitation in the vein, and that the sediment away from the veins remained poorly lithified during the whole deformation sequence.

In both areas, Atiart-Arro and El Guix, geochemical characteristics of the calcite cements in the three microfracture stages are similar, and the main episode of bulk host-rock cementation by calcite occurred after compressive deformation. This occurred because in this foreland basin the front of deformation advanced within the soft sediment early after its deposition.

Differently, in the L'Escala site, the sequence of microfractures coeval with thrusting has not been recognised. In this outcrop, the analysed structures correspond to pre-thrusting fractures, probably developed coevally to the first shortening events characterised by intense spread layer-parallel shortening (Casas et al., 1996; Sans et al., 2003), syn-thrusting fractures, and post-thrusting fractures. As occurred in the other two areas, the main episode of bulk host-rock cementation by calcite occurred after the main compressive deformation, i.e., synchronously to the development of the post-thrust strike-slip faults.

The sequence of calcite veins in the Atiart-Arro fold-and-thrust system developed under submarine thrusting during early-middle Eocene times. The sequence of calcite veins in the L'Escala thrust precipitated during middle-late Eocene times under transitional marine-continental conditions. And finally, the calcite veins filling the fractures at the El Guix anticline precipitated during early Oligocene times under continental conditions (Fig. 10). These continental conditions were established in the entire basin at the Priabonian (late Eocene), when the uplift of the western Pyrenees closed up the foreland connection to the Atlantic (e.g., Vergés et al., 1995; Serra-Kiel et al., 2003a, b).

A good correlation for the $^{87}Sr/^{86}Sr$ values of the calcite veins in the Arro fold (Atiart-Arro fold-and-thrust system) with the Eocene marine waters is observed (Fig. 6). However, the samples from L'Escala

Table 2. Evolution pattern of the structures, microstructures, fluids, hydrologic regime, and fluid type. The "*" indicate the main thrusting event. The arrows indicate chronology

	Evolution pattern				
	Structures	**Fractures**	**Fluids**	**Hydrologic system**	**Fluid type**
Atiart-Arro	3 thrusts faults 1 footwall syncline	3 stages of microfractures in syn-thrust shear veins	local and deep derived hot fluids (in the syncline) + larger distance* (in the thrusts)	closed (in the syncline) and more open* (in the thrusts)	Seawater to formation water (in the syncline) and Deep derived + meteoric + local transformations* (in the thrusts)
L'Escala	pre-thrust diaclases 3 thrust faults post-thrust sinistral faults post-thrust NW-SE diaclases	3 stages of macrofractures (pre, syn and post-thrust)	no fluid recorded ⇩ larger distance* ⇩ local ⇩ larger distance	open* ⇩ closed ⇩ open	Meteoric* ⇩ Evolved meteoric ⇩ Hot meteoric or deeply derived
El Guix	forethrusts backthrusts	3 stages of microfractures in syn-thrust shear veins	local ⇩ larger distance* ⇩ local	closed ⇩ open* ⇩ closed	Meteoric ⇩ Evolved meteoric* ⇩ Meteoric
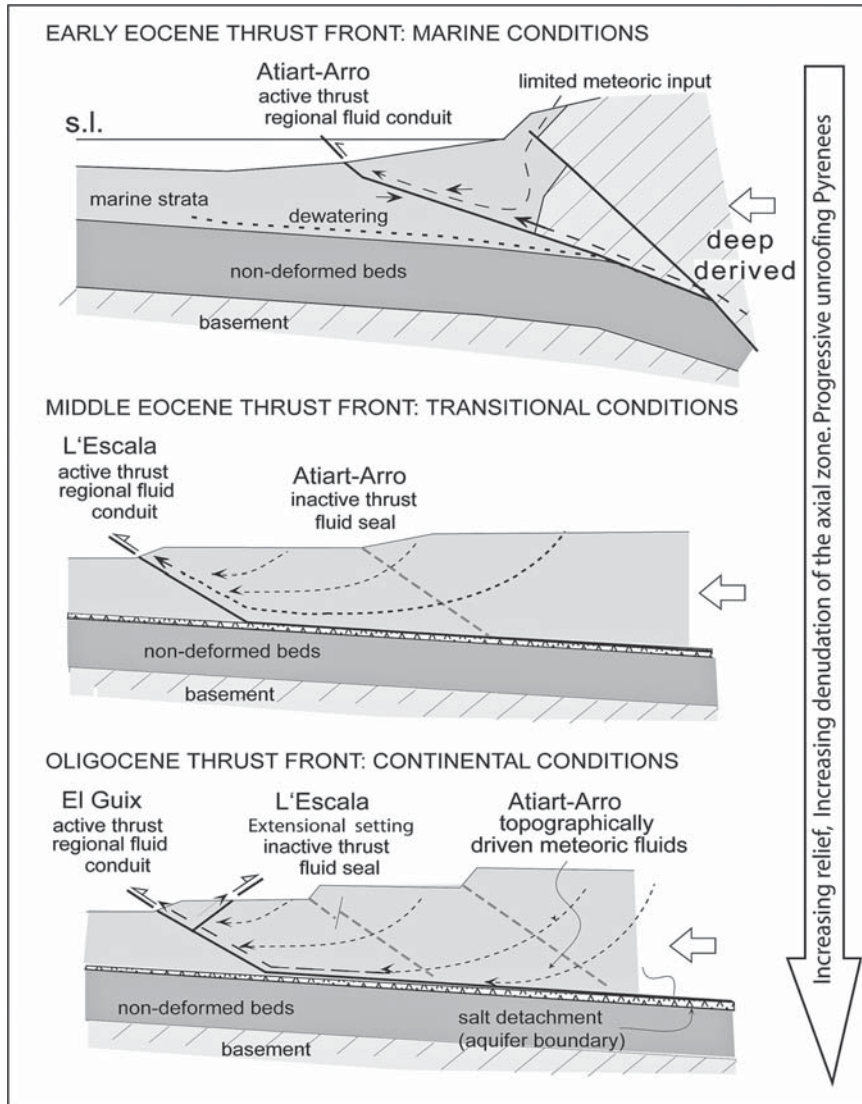
Fig. 10. Model of fluid flow pattern during the geodynamic evolution of the Southern Pyrenean fold-and-thrust belt. The different studied areas are drawn in the different sections although they did not develope at the same time or within the same section. They should be regarded as "type" outcrops

and El Guix show a progressive more radiogenic $^{87}Sr/^{86}Sr$ ratio and more depleted $\delta^{13}C$ values.

The $^{87}Sr/^{86}Sr$ ratios in lake water and in non marine carbonates reflect the ages and Rb/Sr ratios of the rocks exposed to weathering in the drainage basin in which carbonates were deposited (Neat et al., 1979). Thus, these $^{87}Sr/^{86}Sr$ ratios may increase by exposure of crystalline basement rocks to weathering (Brass, 1976), and the stratigraphic variations of the $^{87}Sr/^{86}Sr$ ratios of non marine carbonate rocks can be used to detect changes in the geology or hydrology of the drainage basin (Neat et al., 1979). Similarly, the $^{87}Sr/^{86}Sr$ ratios of calcite cements have been attributed to reflect the isotopic composition of Sr release into the pore fluid by different Rb-bearing rocks and minerals (Stanley & Faure, 1979). On the other hand, the homogeneity of $^{87}Sr/^{86}Sr$ ratios of calcite cements in a lithological

unit is a reflection of the rate of flow of formation water through the lithologic unit or aquifer. Relatively rapid water flow tends to make $^{87}Sr/^{86}Sr$ ratios homogeneous, whereas stagnant conditions caused by low permeability or a low hydrostatic gradient permit local variations to develop in the isotopic composition of Sr of calcite cements (Stanley & Faure, 1979).

The progressive increase in the $^{87}Sr/^{86}Sr$ ratio observed in the studied samples (Fig. 6), from the Arro-Atiart thrust system to L'Escala thrust and, finally, to the El Guix anticline, is interpreted to have been produced by a progressive increase of exposure of crystalline basement rocks to weathering and progressive erosion of the Axial Zone of the belt. An increase of the basement clasts, reaching up to about 70% at the top of a middle Eocene succession, has been observed from the lower Lutetian to middle Bartonian succes-

sion of the Ripoll syncline, in the northern part of the eastern Catalan basin (Ramos et al., 2002).

All the host rock samples of the three studied regions show a great overlap of the $\delta^{18}O$ values, around -6.5‰ PDB (from -8.2 to -4.7‰) (Fig. 5). The calcite cements within the fractures in the three studied regions also show a great overlap of the $\delta^{18}O$ values, around -8.5‰ PDB (from -9.6 to -5.9‰). Systematically, the calcite veins of each locality show a shift around -2 ‰ (always lower than -3.9‰) of the $\delta^{18}O$ values with respect to their adjacent host rock. Conversely, the host rock samples of the three studied regions show distinct $\delta^{13}C$ values (from -5.7 to -3.5‰ at El Guix, from -3.3 to -0.7‰ at Atiart-Arro and from -0.8 to 0‰ at L'Escala). The $\delta^{13}C$ values of the calcite cements within the fractures in the three studied regions are all comprised from -5.3 to -0.4‰. In Atiart-Arro and L'Escala regions they show a major overlap of the values, whereas at El Guix the calcite cements show more depleted $\delta^{13}C$ values than in the former areas (Figs. 5 and 6). In all the cases the maximum difference between the calcite cement in the fracture and their adjacent host rock is lower than 2.3‰ for $\delta^{13}C$.

In the three studied regions, calcite cement within the host rock precipitated later than in the syn-compressive veins, in a more evolved stage of the deformation history, when the sediment was more indurated. That means that in the earlier stage of deformation the fractures permeability was higher than the host rock permeability even when the porosity within the host rock was still important. In the Atiart-Arro and L'Escala outcrops the $\delta^{18}O$ and $\delta^{13}C$ values of the host rock probably is a mixture of the marine components and the calcite cements precipitated after the main compressive event, with more negative $\delta^{18}O$ values. The lower $\delta^{13}C$ values of the El Guix (both host rocks and calcites cements in veins) could be indicative of the increase of meteoric waters involved in the system, as also deduced from the $^{87}Sr/^{86}Sr$ ratios. This progressive depletion of the $\delta^{13}C$ values of host rock and calcite cements have also been observed in the Atiart-Arro region when comparing the four different outcrops, with possible higher meteoric influences in the structures located closer to the emerged parts of the belt (Travé et al., 1998).

Hot temperature of fluids moving through the fractures during thrusting seems to be coherent with two additional results. In the Atiart-Arro example, microthermometry of fluid inclusions give temperatures between 157ºC and 183ºC (Travé et al., 1998), which are too high for the constrained burial depth between a few hundred of metres and 3 km (Travé et al., 1998). Temperatures between 120ºC and 145ºC have also been reported in calcite veins from the lower Eocene Armancies carbonates (Caja et al., 2006) located in the northern flank of the Ripoll syncline (Fig. 2),

which developed coeval to Bellmunt Formation deposition, and which were buried about 3 km (Vergés et al., 1998). So, with a geothermal gradient of 30ºC km-1, that is slightly high for foreland basins, the observed temperatures for the fluids are higher than the ones resulting from only burial depths.

So, we interpret that the thrust-fault zones acted as drains for the fluids derived from both the emerged part of the belt (meteoric fluids) and deeper settings of the thrust systems (footwall dewatering and hot ascending fluids).

This fault control on the fluid system was related to the architecture of the fold-and thrust belt, itself controlled by the organisation of the stratigraphy. Indeed, the main sole thrust of the wedge is located within evaporites (salt or gypsum) horizons, either in the Triassic (Ainsa), the middle Eocene (l'Escala) or the upper Eocene (El Guix), according to the distribution of the various depocentres (Séguret, 1972; Vergés et al.1992). These evaporite detachment levels were barriers for deep fluids migrating from the underlying basement, whereas thrusts within the wedge may have drained laterally deep fluids originating from the hinterland thrust basement units forming the Axial Zone. Thus, the hot and high radiogenic fluids that arrived at the thrust front most probably correspond to originally meteoric fluids involved in topographically-driven flow between the Axial Zone relief and the thrust front, and that could interact at depth with the Axial Zone thrust basement before migrating upward through the frontal thrusts.

Other than the thrust fault zones, the only stratigraphic level potentially capable to drain the fluids at a regional scale is the Paleocene to middle Eocene limestone unit below the detritic basin-fill (cf. Fig. 3A for Ainsa, and Fig. 7 for L'Escala and El Guix). These limestones are sealed upward by marly or evaporite horizons and may have drained deep fluids toward the foreland, preventing them to go further upward in the tectonic wedge. Nevertheless, in the Ainsa area, these limestones are also present in the Cotiella nappe, where they could drain meteoric fluids toward the frontal thrusts in the detritic basin-fill (Fig. 3A). By contrasts, the detritic units, which constitute the main part of the wedge and its foreland are constituted by lenticular bodies of sandstones and conglomerates embedded within marly units. These bodies may have acted as local drains, but could not compete with the thrust faults for long-distance circulation within the wedge.

The close interaction between thrusting and fluids can be used to decipher the timing of fluid migration. As in many fold-and-thrust belts, the thrust system propagates towards the foreland involving younger undeformed strata. We suggest that the thrusts are not only the primary conduits for fluids moving from up-

	Factors controlling the fluid dynamics			
	Type of structure	Type of microstructure	Existence of high relief	Type of host rocks
Atiart-Arro	***	***	*	*
L'Escala	***	-	**	-
El Guix	***	***	***	*

Table 3.
Factors controlling the fluid dynamics in the three studied areas

lifted internal areas of the belt to buried external regions of the foreland, but also that the fluids also migrate through time along the propagating thrust system, carrying hot fluids from deeper areas of the thrust system.

Different structures, mesostructures and microstructures were embedded by fluids of different origin and composition (i.e., dewatering of connate waters, different degree of interaction with meteoric waters, hot ascending fluids, fluids having interacted with salts, etc.), showing an important coupling of thrust geometry and fluid composition. Specifically, the evolution of the nature of the fluids and of their interactions with the host rocks are consistent with the evolution of the South-Pyrenean thrust front from deep submarine (Atiart-Arro) to mixed shallow marine - continental (L'Escala), and eventually to intra-mountainous continental (El Guix), coevally to the increase of relief forming and Palaeozoic rock exhumation and erosion in the Axial Zone of the belt (Table 3). The type of structure/microstructure and the existence or not of a high relief seems to be the main factors controlling the fluid dynamics (Table 3), whereas the host rock type do not seem to have played a specific role.

Evidences of oil seep or hydrocarbon bearing fluid inclusions have not been observed in the three studied regions, however an interesting point in the Southern Pyrenean belt is in the northern flank of the Ripoll syncline where the lower part of the Armancies Formation is a good hydrocarbon source rock and presents many oil shows along more than 100 km of E-W trending outcrops. A recent study of the calcite cements filling fractures in the Armancies Formation reveals the presence of two main generations of cements (Caja et al., 2006). The first is attributed to the syn-thrusting event whereas the second, which presents oil inclusions, evidences hydrocarbon migration through the Armancies Formation coeval with this late calcite cement precipitation. The petrological and geochemical characters of this second generation of calcite cements allow us to correlate them to the post-thrusting calcite cements filling the late extensional fractures at L'Escala, and ascribed to a late shortening or post-shortening event. The Armancies Formation went into the oil window under burial of about 3 km during deposition of Bellmunt redbeds (Vergés et al., 1998), and was subsequently incorporated into the hanging-wall of the Vallfogona thrust during deposition of the upper part of the Bellmunt redbeds. Consequently, oil generation probably spanned a short period of time before significant thrusting took place and oil migration probably occurred soon after its generation and on limited distance, most of the oil shows being located in the same Armancies formation.

The frontal thrusts studied in this paper were connected to basement thrusts in the inner part of the belt. In the central Pyrenees, the major Gavarnie basement thrust deformed and uplifted the inner part of the Cotiella thrust sheet from the middle Eocene. In the Pic de Port Vieux-Plan de Larri area where the Gavarnie thrust places Palaeozoic strata (Silurian to Devonian sediments) above Permo-Triassic redbeds (Fig. 2), an hypersaline Sr-rich brine was pumped by fault activity from the underlying redbeds (Grant et al., 1990; Banks et al., 1991; McCaig et al., 1995). The flow pattern was highly organised and unidirectional, parallel to the limestone mylonites in the thrust zone. Fluid extraction from the footwall was over short (metric) distances, but flow along the mylonite was rapid and at a kilometre-scale, veins also attesting episodic upward escape of fluid from the fault zone into the hanging-wall (McCaig et al., 1995). By contrast, no evidences were found for a significant input of either surface or metamorphic fluids during thrusting. Synchronously, in the Pineta thrust complex that affected the Upper Cretaceous-Paleocene cover in the hangingwall of the Gavarnie thrust, the fluid flow system was dominated by two fluids, an external fluid resulting from metamorphic devolatilisation reactions in the underlying silicate rocks (Permo-Triassic slates or Hercynian granodiorites), and a descending connate fluid from the overlying carbonates, both transported at least several kilometres (Bradbury & Woodwell, 1987; Rye & Bradbury, 1988).

These works and our results thus show that thrust fault zones are likely to focus long distance transport of fluids pumped from the surrounding rocks and displaced from the basement to the foreland basin.

Acknowledgements

References

Allen, P.A., Homewood, P., Williams, G.D. (1986) Foreland Basins: an introduction. In: Allen, P.A., Homewood, P. (eds.) Foreland Basins. Special Publications of the International Association of Sedimentologists 8: 3–12.

Anadón, P., Colombo, F., Esteban, M., Marzo, M., Robles, S., Santanach, P., Solé Sugrañes, L. (1979) Evolución tectonoestratigráfica de los Catalánides. Acta Geol. Hispánica 14: 242–270.

Arenas, C., Pardo, G. (1999) Latest Oligocene-Late Miocene lacustrine systems of the north-central part of the Ebro Basin (Spain): sedimentary facies model and palaeogeographic synthesis. Palaeogeography, Palaeoclimatology, Palaeoecology 151: 127–148.

Banks, D.A., Davies, G.R., Yardley, B.W.D., McCaig, A.M., Grant, N.T. (1991) The chemistry of brines from an Alpine thrust system in the Central Pyrenees: an application of fluid inclusion analysis to the study of fluid behaviour in orogenesis. Geochim. Cosmochim. Acta 55: 1021–1030.

Bartrina, M.T., Cabrera, L., Jurado, M.J., Guimerà, J., Roca, E. (1992) Evolution of the central Catalan margin of the Valencia through (Western Mediterranean). Tectonophysics 203: 219–247.

Beaumont, C., Muñoz, J. A., Hamilton, J., Fullsack, P. (2000) Factors controlling the Alpine evolution of the central Pyrenees inferred from a comparison of observations and geodynamical models. Journal of Geophysical Research 105: 8121–8145.

Bethke, C.M., Marshak, S. (1990) Brine migrations across North America — the plate tectonics of groundwater. Annual Review of Earth and Planetary Sciences 18: 287–315.

Bitzer, K., Travé, A., Carmona, J.M., Calvet, F. (1998) Fluid flow in foreland basins during emplacement of thrust sheets: modelling the south-Pyrenean Ainsa basin. Bull. Soc. Géol. France 5: 627–634.

Bradbury, H.J., Woodwell, G.R. (1987) Ancient fluid flow within foreland terrains. In: Goff, J.C., Williams, B.P.J. (eds.). Fluid flow in sedimentary bsins and aquifers. Geological Society Special Publication 34: 87–102.

Brass, G.W. (1976) The variation of the marine ^{87}Sr/^{86}Sr ratio during Phanerozoic time: interpretation using flux model. Geochimica et Cosmochimica Acta 40: 721–730.

Buatier, M., Travé, A., Labaume, P. Potdevin, J.L. (1997) Dickite related to fluid-sediment interaction and deformation in Pyrenean thrust-fault zones. Eur. J. Mineral. 9: 875–888.

Budai, J.M. (1985) Evidence for rapid fluid migration during deformation, Madison Group, Wyoming and Utah Overthrust Belt. In: Longman, M.W., Shanley, K.W., Lindsay, R. F., Eby, D.E. (eds.). Rocky Mountain Carbonate Reservoirs –

A Core Workshop. Soc. Econ. Paleont. Miner. Core Workshop, 7: 377–407, Tulsa.

Burke, W.H., Denison, R.E., Hetherington, E.A., Koepink, R.B., Nelson, H.F., Orro, J.B. (1982) Variation of sea-water ^{87}Sr/^{86}Sr throughout Phanerozoic time. Geology 10: 516–519.

Burkhard, M., Kerrich, R. 1988. Fluid regimes in the deformation of the Helvetic nappes, Switzerland, as inferred from stable isotope data. Contrib. Miner. Petrol, 99: 416–429.

Caja, M.A., Permanyer, A., Marfil, R., Al-Aasm, I.S., Martín-Crespo, T. (2006) Fluid flow record from fracture-fill calcite in the Eocene limestones from the South-Pyrenean Basin (NE Spain) and its relationship to oil shows. Journal of geochemical exploration 89: 27–32.

Campani M., Jolivet M., Labaume P., Brunel M., Monié P., Arnaud N., 2005. Denudation kinematics of an orogenic prism: integrated thermochronology and tectonic study in the W-Central Pyrenees (France-Spain). Joint Earth Science Meeting « Thrust Belts and Foreland Basins », Société Géologique de France – Sociedad Geologica de Espana, 14–16 décembre 2005, Rueil-Malmaison.

Calvet, F., Travé, A., Roca, E., Soler, A., Labaume, P. (1996) Fracturación y migración de fluidos durante la evolución tectónica neógena en el Sector Central de las Cadenas Costero Catalanas. Geogaceta 20: 1715–1718.

Casas, J. M., Durney, D., Ferret, J., Muñoz, J. A. (1996) Determinación de la deformación finita en la vertiente sur del Pirineo oriental a lo largo de la transversal del río Ter. Geogaceta 20: 803–805.

Cerling, T.E. (1984) The stable isotopic composition of modern soil carbonate and its relationship to climate. Earth planet. Sci. Lett. 71: 229–240.

Cerling, T.E., Quade, J., Wang, Y. Bowman, J.R. (1989) Carbon isotopes in soils and palaeosols as ecology and palaeoecology indicators. Nature 341: 138–139.

Choukroune, P., and ECORS team (1989) The ECORS Pyrenean deep seismic profile reflection data and the overall structure of an orogenic belt. Tectonics 8: 23–39.

Claypool, G.E., Holser, W.T., Kaplan, I.R., Sakai, H., Zak, I. (1980) The age curves of sulfur and oxygen isotopes in marine sulfate and their mutual interpretation. Chem. Geol. 28: 199–260.

Coney, P. J., Muñoz, J. A., McClay, K. R., Evenchick, C. A. (1996) Syntectonic burial and post-tectonic exhumation of the southern Pyrenees foreland fold-thrust belt. Journal Geological Society, London 153: 9–16.

Cosgrove, J. W. (1993) The interplay between fluids, folds and thrusts during deformation of a sedimentary succession. Journal of Structural Geology 15: 491–500.

Denison, R.E., Koepnick, R.B., Fletcher, A., Dahl, D.A., Baker, M.C. (1993) Re-evaluation of early Oligocene, Eocene, and Paleocene seawater strontium isotope ratios using outcrop samples from the U.S. Gulf Coast. Paleoceanography 8: 101–126.

DePaolo, D. J., Ingram, B.L. (1985) High-resolution stratigraphy with strontium isotopes. Science 227: 938–941.

Dietrich, D., McKenzie, J.A., Song, H. (1983) Origin of Calcite in syntectonic veins as determined from carbon-isotope ratios. Geology 11: 547–551.

Ferket H., Swennen R., Ortuño-Arzate S., Cacas M.C., Roure F., 2004. Hydrofracturing in the Laramide foreland fold-and-thrust belt of Eastern mexico. In Swennen R., Roure F., Granath J., eds., Deformation, fluid flow and reservoir appraisal in foreland fold-and-thrust belts, AAPG Hedberg Series, Memoir, 1, 133–156.

Fitzgerald, P. G., Muñoz, J. A., Coney, P. J., Baldwin, S. L. (1999) Asymmetric exhumation across the Pyrenean orogen: implications for the tectonic evolution of a collisional orogen: Earth And Planetary Science Letters 173: 157–170.

García-Castellanos, D., Vergés, J., Gaspar-Escribano, J., Cloetingh, S. (2003) Interplay between tectonics, climate, and fluvial transport during the Cenozoic evolution of the Ebro Basin (NE Iberia): Journal of Geophysical Research 108: B7, 2347, doi: 10.1029/2002JB002073.

Garven, G. (1985) The role of regional fluid flow in the genesis of the Pine Point deposit, Western Canada sedimentary basin. Economic Geology 80: 307–324.

Garven, G. (1989) A hydrogeologic model for the formation of the giant oil sands deposits of the Western Canada Sedimentary Basin. Ameriacan Journal of Science 289: 105–166.

Garven, G. (1995) Continental scale groundwater flow and geologic processes. Annual Review of Earth and Planetary Sciences 23: 89–117.

Ge, S., Garven, G. (1992) Hydromechanical modeling of tectonically driven groundwater flow with application to the Arkoma foreland basin. J. Geophys. Res. 97, B6: 9119–9144.

Ge, S., Garven, G. (1994) A theoretical model for thrust-induced deep groundwater expulsion with application to the Canadian Rocky Mountains. J. Geophys. Res. 99, B7: 13851–13868.

Grant, N.T., Banks, D.A., McCaig, A.M., Yardley, B.W.D. (1990) Chemistry, source, and behavior of fluids involved in Alpine thrusting of the Central Pyrenees. J. Geophys. Res. 95: 9123–9131.

Hess, J., Stott, L.D., Bender, M.L., Kennett, J.P., Schilling, J.-G. (1989). The Oligocene marine microfossil record: age assessments using strontium isotopes. Paleoceanography 4: 655–679.

Hess, J.; Bender, M.L.; Schilling, J.G. (1986) Evolution of the ratio of strontium-87 to strontium-86 in seawater from Cretaceous to present. Science 231: 979–984.

Hubbert, M. K., Rubey, W. W. (1959) Role of fluid pressure in the mechanics of overthrust faulting. Geological Society of America Bulletin 70: 115–205.

Hudson, J.D. (1977) Stable isotopes and limestone lithification. J. Geol. Soc. London 133: 637–660.

Hudson, J. D., Anderson, T. F. (1989) Ocean temperatures and isotopic compositions through time. Transactions of the Royal Society of Edinburgh 80: 183–192.

Juez-Larré, J., Andriessen, P.A.M. (2006) Tectonothermal evolution of the northeastern margin of Iberian since the break-up of Pangea to present, revealed by low-temperature fission-track and (U-Th)/He thermochronology. A case history of the Catalan Coastal Ranges. Earth and Planetary Science Letters 243: 159–180.

Katz, A., Sass, E., Starinsky, A., Holland, H.D. (1972) Strontium behaviour in the aragonite–calcite transformation: an experimental study at 40–98°C. Geochim. Cosmochim. Acta 36: 481–496.

Koepnick, R.B.; Denison, R.E.; Burke, W.H.; Hetherington, E. A.; Nelson, H.F.; Otto, J.B.; Waite, L.E. (1985) Construction of the seawater ^{87}Sr/^{86}Sr curve for the Cenozoic and Cretaceous: Supporting data. Chem. Geol., Isot. Geosci. Sect., 58: 55–81.

Kyser, T.K., Kerrich, R. (1990) Geometry of fluids in tectonically active crustal regions. In: Nesbitt, B.E (ed.). Short Course on Fluids in Tectonically Active Regimes of the Continental Crust. Mineralogical Association of Canada, 18: 133–230, Vancouver.

Longstaffe, F.J. (1993) Meteoric water and sandstone diagenesis in the Western Canada Sedimentary Basin. In: Horbury, A.D., Robinson, A.G. (eds.). Diagenesis and basin development. American Association of Petroleum Geologists. Studies in Geology, 36: 49–68.

Machel, H.G., Cavell, P.A. (1999) Low-flux, tectonically-induced squeegee fluid flow ("hot flash") into the Rocky Mountain Foreland Basin. Bulletin of Canadian Petroleum Geology 47: 510–533.

Marquer, D., Burkhard, M. (1992) Fluid circulation, progressive deformation and mass-transfer processes in the upper crust: the example of basement-cover relationships in the External Crystalline Massifs, Switzerland. Journal of Structural Geology 14: 1047–1057.

Marshall, J. D. (1992) Climatic and oceanographic isotopic signals from the carbonate rock record and their preservation. Geological Magazine 129: 143–160.

Martínez-Peña, B., Casas Sainz, A. M. (2003) Cretaceous-Tertiary tectonic inversion of the Cotiella Basin (southern Pyrenees, Spain): International Journal of Earth Sciences (Geol Rundsch), 92: 99–113.

McCaig, A.M., Wayne, J.M., Marshall, J.D., Banks, D., Henderson, I. (1995) Isotopic and fluid inclusion studies of fluid movement along the Gavarnie thrust, Central Pyrenees: reaction fronts in carbonate mylonites. Am. J. Sci. 295: 309–343.

Mead, G.A., Hodell, D.A. (1995) Controls on the ^{87}Sr/^{86}Sr composition of seawater from the middle Eocene to Oligocene: Hole 689B, Maud Rise, Antarctica. Paleoceanography 10: 327–346.

Meigs, A. J., Vergés, J. Burbank, D. W. (1996) Ten-million-year history of a thrust sheet: Geological Society of America Bulletin 108: 1608–1625.

Muchez, P., Slobodnik, M., Viaene, W. A., Keppens, E. (1995) Geochemical constraints on the origin and migration of palaeofluids at the northern margin of the Variscan foreland, soutern Belgium. Sedimentary Geology 96: 191–200.

Muñoz, J. A. (1992) Evolution of a continental collision belt: ECORS-Pyrenees crustal balanced section, in McClay, K. R. (ed.) Thrust Tectonics: London, Chapman & Hall, p. 235–246.

Muñoz, J. A., Martínez, A., Vergés, J. (1986) Thrust sequence in the Spanish eastern Pyrenees. Journal of Structural Geology 8: 399–405.

Mutti, E., Séguret, M. and Sgavetti, M. (1988) Sedimentation and deformation in the Tertiary sequences of the southern Pyrenees: AAPG Mediterranean Basins Conference, p. 169.

Neat, P. L., Faure, G., Pegram, W.J. (1979) The isotopic composition of strontium in non-marine carbonate rocks : The Flagstaff Formation of Utah. Sedimentology 26: 271–282.

Oliver, J. (1986) Fluids expelled tectonically from orogenic belts: their role in hydrocarbon migration and other geologic phenomena. Geology 14: 99–102.

Palmer, M.R.; Elderfield, H. (1985) Sr isotope composition of sea water over the past 75 Myr. Nature, 314: 526–528.

Puigdefàbregas, C., Muñoz, J. A. Marzo, M. (1986) Thrust belt development in the Eastern Pyrenees and related depositional sequences in the southern foreland basin, in Allen, P. A. Homewood, P. (eds.), Foreland basins, Special Public. of the International Association of Sedimentologists 8: 229–246.

Puigdefàbregas, C., Muñoz, J. A., Vergés, J. (1992) Thrusting and Foreland Basin Evolution in the Southern Pyrenees, in

McClay, K. R. (ed.), Thrust Tectonics, Chapman & Hall, p. 247–254.

Qing, H., Mountjoy, E.(1992) Large-scale fluid flow in the Middle Devonian Presqu'ile barrier, Western Canada Sedimentary Basin. Geology 20: 903–906.

Ramos, E., Busquets, P., Vergés, J. (2002) Interplay between longitudinal fluvial and transverse alluvial fan systems and growing thrusts in a piggyback basin (SE Pyrenees). In Marzo, M., Muñoz, J. A., Vergés, J. (eds.) Sedimentary Geology on Growth Strata, Sedimentary Geology 146: 105–131.

Roure, F., Choukroune, P., Berastegui, X., Muñoz, J. A., Villien, A. M., Thereon, P., Bareyt, M., Séguret, M., Cámara, P., Déramond, J. (1989) ECORS deep seismic data and balanced cross sections: Geometric constraints on the evolution of the Pyrenees: Tectonics 8: 41–50.

Roure, F., Carnevali, J.O., Gou, Y. and Subieta, T. (1994) Geometry and Kinematics of the North Monagas thrust Belt (Venezuela). Marine and Petroleum Geology 11: 347–362.

Roure, F., Swennen, R., Schneider, F., Faure, J.L., Ferket, H., Guilhaumou, N., Osadetz, K., Robion, P., Vandeginste, V. (2005) Incidence and importance of tectonics and natural fluid migration on reservoir evolution in foreland fold-and-thrust belts. Oil & Gas Science and Technology – Rev. IFP 60: 67–106.

Rye, D.M., Bradbury, H.J. (1988) Fluid flow in the crust: an example from a Pyrenean thrust ramp. American Journal of Science 288: 197–235.

Sans, M., Vergés, J. (1995) Fold development related to contractional salt tectonics: southeastern Pyrenean thrust front, Spain, in Jackson, M. P. A. Roberts, D. G. Snelson, S. (eds.), AAPG Memoir 65 on Salt Tectonics: a global perspective, Chapter 18: 369–378.

Sans, M., Vergés, J., Gomis, E., Parés, J.M., Schiatarella, M., Travé, A., Calvet, F., Santanach, P., Doulcet, A. (2003) Layer parallel shortening in salt-detached folds: constraint on cross-section restoration. Tectonophysics 372: 85–104.

Séguret, M. (1972) Etude tectonique des nappes et séries décollées de la partie centrale du versant sud des Pyrénées, Série géologie structurale, n°2, Montpellier, Publications de l' Université des Sciences et Techniques du Languedoc (Ustela).

Serra-Kiel, J., Travé, A., Mató, E., Saula, E., Ferràndez, C., Busquets, P., Tosquella, J., Vergés, J. (2003a) Marine and transitional Middle/Upper Eocene Units of the Southeastern Pyrenean Foreland Basin (NE Spain). Geologica Acta 1: 177–200.

Serra-Kiel, J., Mató, E., Saula, E., Travé, A., Ferràndez, C., Àlvarez-Pérez, G., Busquets, P., Samsó, J.M., Tosquella, J., Frnaquès, J., Romero, J., Barnolas, A. (2003b) An inventory of the Marine and Transitional Middle/Upper Eocene Deposits of the Southeastern Pyrenean Foreland Basin (NE Spain). Geologica Acta 1: 201–232.

Shackleton, N. J., Kennett, J. P. (1975) Paleo-temperature history of the Cenozoic and the initiation of Antarctic glaciation: oxygen and carbon isotope analyses in DSDP Sites 277, 279 and 281. Initial Reports of the Deep Sea Drilling Project, 29: 743–755.

Sinclair, H.D., Gibson, M., Naylor, M., Morris, R.G. (2005) Asymmetric growth of the Pyrenees revealed through measurement and modelling of orogenic fluxes. American Journal of Science 305: 369–406.

Stanley, K.O., Faure, G. (1979) Isotopic composition and source of strontium in sandstone cements: The High Sequence of Wyoming and Nebraska. J. Sed. Petr. 49: 45–54.

Travé, A., Labaume, P., Calvet, F., Soler, A. (1997) Sediment dewatering and pore fluid migration along thrust faults in a foreland basin inferred from isotopic and elemental geochemical analyses (Eocene south-Pyrenees, Spain). Tectonophysics 282: 375–398.

Travé, A., Labaume, P., Calvet, F., Soler, A., Tritlla, J., Buatier, M., Potdevin, J.L., Séguret, M., Raynaud, S., Briqueu, L. (1998) Fluid migration during Eocene thrust emplacement in the south Pyrenean foreland basin (Spain): an integrated structural, mineralogical and geochemical approach. In: Mascle, A., Puigdefàbregas, C., Luterbacher, H.P., Fernàndez, M. (eds.), Cenozoic Foreland Basins of Western Europe. Geol. Soc. London, Spec. Publ. 134: 163–188.

Travé, A., Calvet, F., Sans, M., Vergés, J., Thirlwall, M. (2000) Fluid history related to the Alpine compression at the margin of the south-Pyrenean Foreland basin: the El Guix anticline. Tectonophysics 321: 73–102.

Veizer, J. (1992) Depositional and diagenetic history of limestones: stable and radiogenic isotopes. In: Clauer, N., Chaudhuri, S. (eds.), Isotopic Signatures and Sedimentary Records. Lecture Notes in Earth Sciences 43: 13–48. Springer, Berlin.

Veizer, J., Hoefs, J. (1976) The nature of O^{18}/O^{16} and C^{13}/C^{12} secular trends in sedimentary carbonate rocks. Geochimica et Cosmochimica Acta 40: 1387–1395.

Vergés, J., Muñoz, J.A., Martinez, A. (1992) South Pyrenean fold-and-thrust belt : Role of foreland evaporitic levels in thrust geometry, in McClay, K.R. (ed.), Thrust Tectonics, London, Chapman et al., p. 255–264.

Vergés, J., Millán, H., Roca, E., Muñoz, J. A., Marzo, M., Cirés, J., den Bezemer, T., Zoetemeijer, R., Cloetingh, S. (1995) Eastern Pyrenees and related foreland basins: Pre-, syn- and post-collisional crustal-scale cross-sections. In Cloetingh, S., Durand, B., Puigdefàbregas, C. (eds.) Marine and Petroleum Geology 12: 903–916.

Vergés, J., Burbank, D. W. (1996) Eocene-Oligocene Thrusting and Basin Configuration in the Eastern and Central Pyrenees (Spain), in Friend, P. F. Dabrio, C. J. (eds.), Tertiary Basins of Spain. The Stratigraphic Record of Crustal Kinematics, Cambridge University Press. World and Regional Geology 6: 120–133.

Vergés, J., Marzo, M., Santaeulària, T., Serra-Kiel, J., Burbank, D. W., Muñoz, J. A., Giménez-Montsant, J. (1998) Quantified vertical motions and tectonic evolution of the SE Pyrenean foreland basin., In Mascle, A., Puigdefàbregas, C., Luterbacher, H. P., Fernàndez, M. (eds.), Cenozoic Foreland Basins of Western Europe, London, Geological Society Special Publications 134: 107–134.

Vergés, J., Fernàndez, M. Martínez, A. (2002) The Pyrenean orogen: pre-, syn-, and post-collisional evolution, in Rosenbaum, J. G. Lister, G. S. (eds.), Reconstruction of the evolution of the Alpine-Himalayan Orogen, Journal of Virtual Explorer 8: 55–84.

Yeh, H.W., Savin, S.M. (1977) Mechanisms of burial metamorphism of argillaceous sediments: 3. O-isotope evidence. Geological Society of America Bulletin 88: 1321–1330.

The Miocene Petroleum System of the Northern Apennines in the Central Po Plain (Italy)

Vincenzo Picotti · Rossella Capozzi · Giuseppe Bertozzi · Fausto Mosca · Andrea Sitta · Maria Tornaghi

Abstract. We describe the Miocene petroleum system in the context of the geology of the Northern Apennines as a system fed by multiple sources including some potential for deep oil accumulation. The presence of sources deeper than the Miocene reservoir is required by the high thermal maturity of the oils, the thermogenic nature of methane and the high ion content, in the reservoir brines, deriving from decaying organic matter. This is in contrast with the lower thermal maturity measured in the Miocene reservoir coupled with its low organic matter content. A Miocene secondary source, however, is required by the presence of a Tertiary organic marker in the oil. The deeper sources charged reservoirs of different age, geometry and sediment provenance, mostly as a function of stepwise migration of the foredeep and the overlying Ligurian units toward the foreland, which provided rapid overburden. The porosity of the reservoir was preserved in the anticlines mostly because of up-dip migration into early formed structures in the foredeep units. Therefore, the structural evolution of the area, especially the time interval between deposition and deformation of the foredeep units, is crucial for the definition of the quality of the reservoirs. Finally, the Quaternary reactivation of the thrust sheets in the foothills changed the geometry of the reservoirs, inducing new accumulations and/or dismigration from deeper and older traps.

1 Introduction

The petroleum exploration and production history of the Northern Apennines and the facing Po Plain go back to the end of the XIX century (around 1870), when natural oil seepages were exploited in the foothills close to Parma. The first wells producing oil and thermogenic gas from a Miocene reservoir in the same area of the central Po plain between Parma and Piacenza were drilled around 1923–1925. In 1932 82% of the oil production of Italy came from the Vallezza oil field (Parma) (Scicli, 1972; AGIP, 1984). Research, however, was expanded after 1950, when biogenic gas from various pools of Pliocene and Pleistocene reservoirs were discovered around the Po river delta and some tens years after with the discovery of deep reservoirs in the western Po Plain, sourced by Triassic rocks

(Errico et al., 1979). At the end of the last century, the wells drilled in the Po Plain province were more than 2600.

Today the Po Plain is a mature area from the exploration point of view, however, in the foothills of the Northern Apennines and the adjacent Po Plain, the so-called Miocene petroleum province, some open problems exist. They are mainly due to scarce quality of the available aged seismic lines, and to the occurrence of surface lithologies, such as highly deformed Ligurian units (see Pini, 1999 and Zattin et al., 2002), which makes it difficult to reconstruct the geological structures. These difficulties could be partially overcome using surface geological data that, however, are difficult to obtain in a densely vegetated, poorly outcropping, area.

Most important to define is the source rock that charged the Miocene reservoirs. Riva et al. (1986) provided geochemical data documenting an origin from siliciclastic formations and the presence of a Tertiary geochemical marker for these oils; therefore these authors suggested that the Miocene deep-water clastics of the Apennine foredeep succession represent a source – reservoir system. Whereas such a source could account for the occurrence of the gas in the Miocene reservoirs, volumetrically the most abundant hydrocarbons, two important arguments make it difficult to accept this for the oil: first, the occurrence of the oil in the central portion of the Po Plain, although the foredeep basins were originally much wider, and, in the present deformed state, build the backbone of the Northern Apennines; second, the low TOC content and the type III kerogen, highly diluted within the foredeep succession, makes it difficult to infer a high oil generation potential for the Miocene units.

A last problem, still open to discussion is the prediction of porosity in the foredeep units, that is highly variable and for which no published models are available. In our paper we address these problems in order to better define the petroleum system and eventually to open new perspectives for the evaluation of the residual reserves in this province. For this purpose we discuss the structures and the geochemistry of fluids (brines, oil and gas) stored in some Miocene reser-

voir. As many aspects of the study case have been already treated by previous authors, we concentrate on our data and discuss them in the frame of the open problems presented above.

2   Geological Background

The Northern Apennines are a fold-and-thrust belt evolving during the Tertiary as a response to the subduction of the Adriatic plate under the European lithosphere. The flexuring of the lithosphere brought about the evolution of subsiding foreland basins and thick foredeep successions, which developed since the Oligocene and which were progressively incorporated within the thrust belt. The evolution of the pronounced foredeep and the stretching of the back-arc area (Ligurian – Provençal and Tyrrhenian basins, Late Oligocene to Early Miocene and Late Miocene to Pliocene respectively) have been interpreted as the result of the retreat of the Adriatic slab (Elter et al., 1975; Malinverno and Ryan, 1986). The residual oceanic accretionary wedge, the so-called Ligurian unit, encroached onto

the foredeep and travelled toward the foreland from the Oligocene to the Early Pliocene as a surface nappe, overthrusting, as a rule, the youngest foredeep turbidites (Zattin et al., 2002).

The central Po Plain (Fig. 1) includes also, along its northern side, the front of the Southern Alps, which are of a fold-and-thrust belt of Middle to Late Miocene age. This belt developed during the post-collisional history of the Alps as a retro-wedge with southern vergence (Bertotti et al., 1998), that however was deactivated during the Messinian (see discussion in Willet et al., 2006), and finally tilted to the south and included into the foreland of the Northern Apennines.

The front of the Apennines, covered by Plio-Pleistocene sediments, presently lies below the Po Plain where it forms three arcuate thrust systems, from west to east: the Monferrato, the Emilia and the Ferrara arcs (Fig. 1). The growth of the three arcuate belts was strongly diachronous: the Monferrato arc started in the Early Miocene, the Emilia arc in the Tortonian and the Ferrara arc in the Messinian (Castellarin and Vai, 1986). The eastward progression of deformation is related to the counterclockwise rotation of the
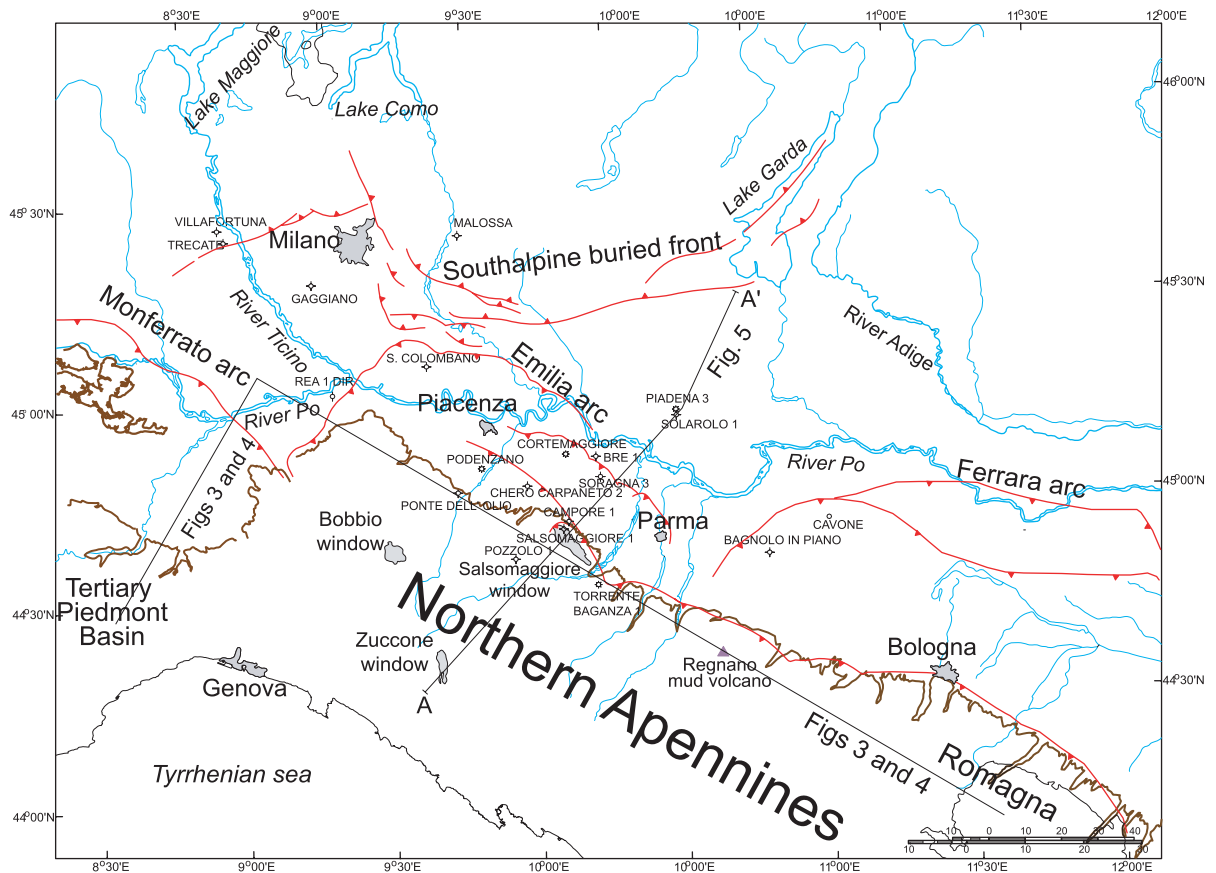
Fig. 1. Simplified structural sketch map of the Northern Apennines and adjacent Po Plain, with location of the wells quoted in the text and tracks of the cross-sections

Apennine orogen (LePichon et al., 1971), apparently due to the along-strike increasing importance of the slab retreat toward the southeast. The youngest arcuate system is apparently inactive, since all the structures are sealed by Middle to Upper Pleistocene deposits. Within the Emilia arc, a few structures are still active, namely the San Colombano thrust, that forms an isolated hill within the Po Plain (in the sector of the Emilia arc close to the San Colombano well, Fig. 1). The Monferrato arc is an active thrust system, especially in its western part, where it interacts with the fluvial network (e.g. Carraro et al., 1995).

In the Northern Apennines, the mountain front does not coincide with the tip of the orogenic wedge, and, even in the presence of some neotectonic activity in the foothills (Bernini and Papani, 1987), there is no clear correlation between this major geomorphic feature and any large-scale tectonic structure.

Our study area extending along the foothills and the adjacent Po Plain west of Parma (Fig. 1), belongs to the structure of the Emilia arc. It comprises the front of the Ligurian nappe, the underlying Tertiary foredeep deposits, outcropping in a half-window (the Salsomaggiore structure), and the Plio-Pleistocene deposits, progressively less deformed and covering the most external thrusts below the Po Plain.

3 Stratigraphy of the Petroleum System

3.1 Looking for a Source: The Organic-Rich Deposits of the Central Po Plain

In this paragraph we will briefly recall the main characteristics of the sediments that potentially could be the source rocks of the oils of the Miocene province. We do not intend to provide an exhaustive review, and the reader is referred to the cited literature for the adopted stratigraphic nomenclature.

The oldest proven source rock is the Upper Anisian to Ladinian interval of the northwestern Po Plain. It consists of two formations: the older is the Upper Anisian and the Lower Ladinian Besano Shale (=Grenzbitumenzone of Swiss authors, e.g. Bernasconi and Riva, 1993), a reduced succession (around 15 m) of interbedded black shales and organic-rich dolostones, deposited in a small intraplatform basin (Riva and Bernasconi, 1993; Bernasconi, 1994). Its organic content is very high (ranging 1 to 15% TOC), but its paleogeographic distribution is limited to the western Southalpine foothills, and very probably does not reach the subsurface of the Po Plain. The younger formation is the Upper Ladinian Meride Limestone, again an intraplatform succession of limestones, dolomites and thin black shales, but much thicker (250 to 600 m) even though poorer in organic carbon, averag-

ing around 1% TOC. Its distribution is wider in the Po Plain, where it has been documented to be the source of the oil of the Villafortuna-Trecate and Gaggiano fields (Riva et al., 1986; Mattavelli and Novelli, 1990); however, to the south, it is limited by facies changes toward continental clastics, drilled in the Rea 1 dir well (Fig.1) and eventually by emerged land, below the present-day Apennines (Fig. 2). The potential of these Middle Triassic successions to generate the oils of the Northern Apennines is therefore nil, as confirmed by geochemical data (Riva et al., 1986).

The other important source rock in the region is part of the Upper Triassic succession. It consists of two formations: the older Zorzino Limestone, never drilled in the subsurface of the Po Plain, consists of a thick interval of organic-rich carbonates, also deposited in fault-bounded intraplatform basins, created by rifting associated with the onset of the stretching of the Adriatic margin (Bertotti et al., 1993). This interval could be the source of the Cavone oil that has been generally referred to an anoxic carbonate source rock (Riva et al., 1986). The younger formation is overlying the Riva di Solto Shale (Thery et al., 1989; Stefani and Burchell, 1990; 1993) , a thick (locally more than 1 km) succession of prevailing shales with an average 1% of TOC that is much more widespread and is considered to be the source of the oil of the Malossa field (Riva et al., 1986; Mattavelli and Novelli, 1990). Together with the overlying Zu limestone (again interbedded with organic-rich shales), they probably were extending toward the south below the Northern Apennines (Fig. 2), where coeval and similar, although thinner, succession outcrop again (Upper Triassic of the Tuscan nappe system of the Apennines).

The last potential source rock of the Mesozoic are two well-known intervals of black shales, representing the two Oceanic Anoxic Events (OAE) of the late early Aptian (OAE 1a, the so-called Selli level) and the Late Cenomanian (OAE 2, the Bonarelli level) (e.g. Jenkyns 1980; Erba, 2004, and references therein). They consist of decimetre-thick black shales, intercalated within a pelagic succession of limestones and marlstones. Although they have a limited thickness, these intervals could have some minor petroleum potential, mainly because their widespread distribution in the Tethyan basins and their richness of organic carbon (2 to 13%, Jenkyns, 1980). In the literature we find, however, no evidence that this interval was a source rock for oil accumulation in Italy (Riva et al., 1986; Mattavelli and Novelli, 1990).

Finally, Tertiary successions have been considered as possible source rocks for the oils of the Miocene system (Cortemaggiore group). These include the sediments of the foredeep succession (Marnoso-arenacea Formation) or their foreland ramp counterparts (Gallare Marls). This hypothesis is based on the occurrence
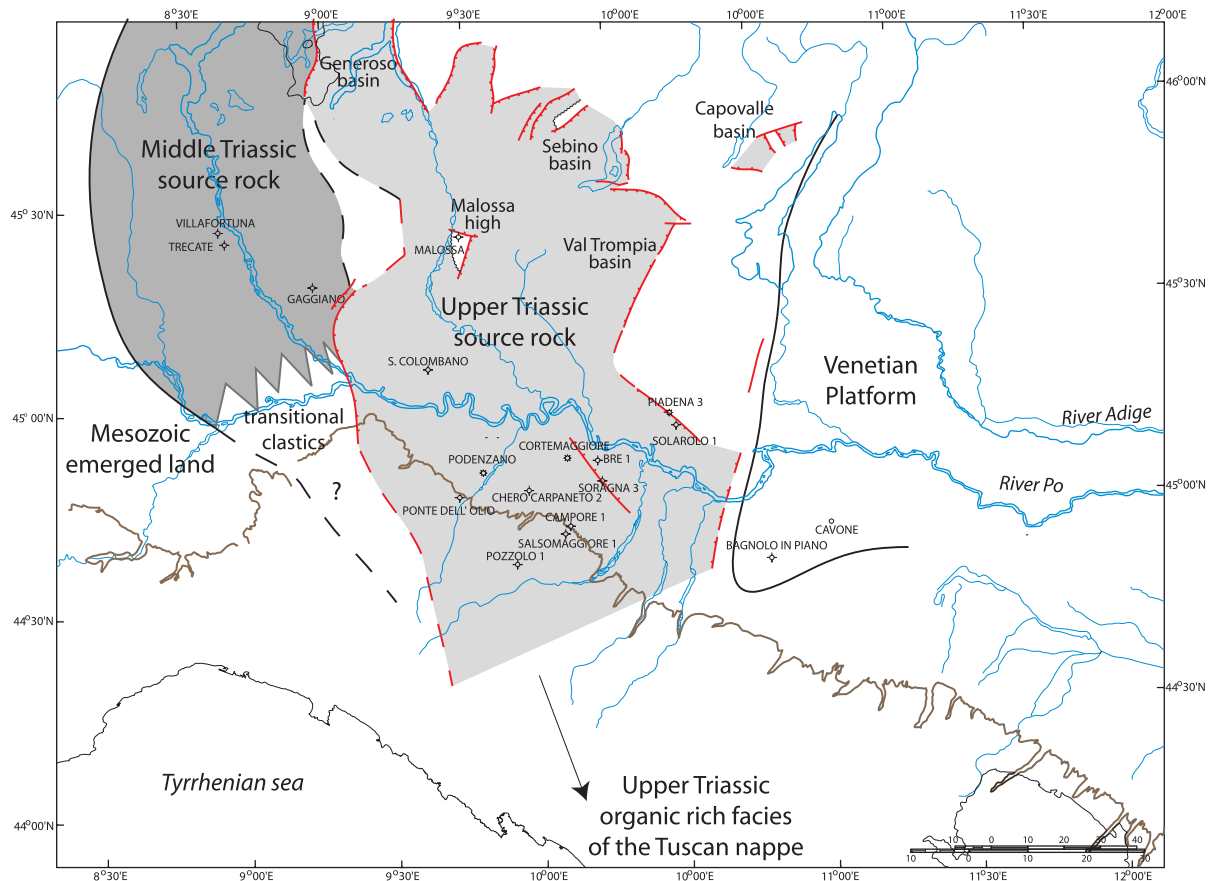
Fig. 2. Distribution of Triassic organic-rich successions in the Southalpine foothills (after Bertotti et al., 1993) and the subsurface of the central Po Plain

in the oils of biomarkers typical of the Tertiary, such as 18α(H)oleanane and sterane X, whereas other geochemical parameters of the Cortemaggiore group oils do not fit well with the rock extracts (Riva et al., 1986). These and other Oligocene and Miocene sediments of the area have been sampled by us for their organic matter content; our results confirm the literature data in most cases. With an average TOC content of less than 0.4% and a terrestrial origin of the kerogen, these successions appear gas prone, but can hardly account for the oil of the Miocene reservoirs.

## 3.2 The Reservoirs: Stratigraphy of the Tertiary Foredeeps

The Miocene petroleum system of the central Po Plain has been referred to a general "Marnoso-arenacea" reservoir (Riva et al., 1986; Mattavelli and Novelli, 1990). This is the name of a formation of the northern Apennines of Romagna that was deposited in the foredeep of the Apennines during the Middle and Late Miocene

(e.g. Gandolfi et al., 1983; Dondi and D'Andrea, 1986; Zattin et al., 2002). There is a discrepancy between the stratigraphy of the original Marnoso- arenacea Formation and the use of the term that has been suggested by Riva et al. (1986) and Mattavelli and Novelli (1990). These authors included in this name all clastic deposits from the Early Miocene to the onset of the Messinian (Late Miocene). During this time period, however, the configuration of the Northern Apennines foredeep was changing, as well as the source of the clastic material, reflecting, the dramatic changes in the paleogeography (Boccaletti et al., 1990). In fact, different basin geometries developed through time as will be briefly described in the following. This stratigraphic uncertainty renders shaky the Riva et al. (1986) oil-rock extracts correlation.

In order to distinguish the different sedimentary formations we constructed a cross correlation along a section crossing the Piedmont Tertiary Basin along dip and the Northern Apennines foothills along strike (Fig. 1 and Figs. 3, 4), with a datum line at the top of the Serravallian.

Fig. 3. Stratigraphic cross-section reconstructed at the top Serravallian, providing local stratigraphic nomenclature (see the track in Fig. 1 and text for different sources)
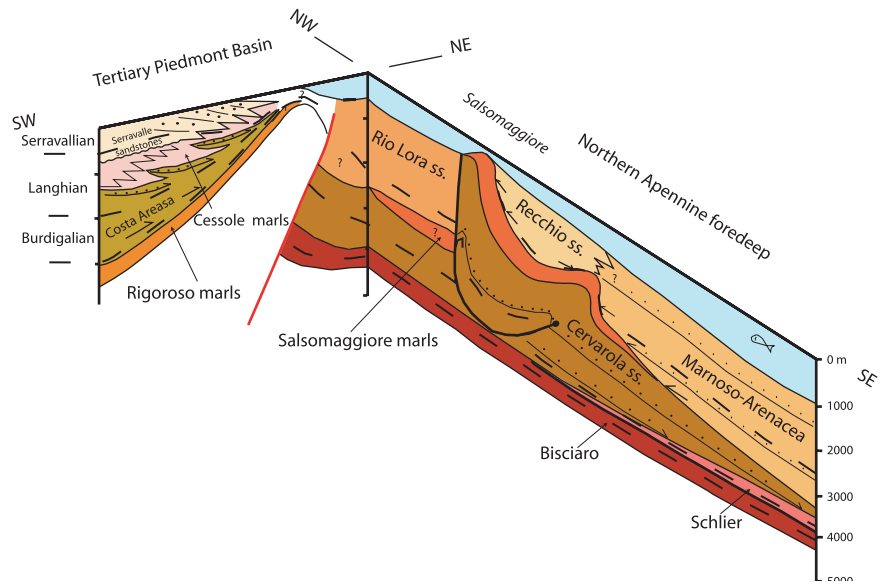

The Burdigalian to Serravallian evolution of the Tertiary Piedmont Basin (TPB), crossed by our section in its eastern sector (Fig. 3), is typical of a thrust top basin, perched above the evolving thrust of the Monferrato arc. Overlying foreland slope marls (Rigoroso Marls), a turbiditic lobe, developing throughout the Burdigalian and early Langhian (Costa Areasa Formation), gradually passes into a prograding slope to platform unit (Cessole Marls) deposited during the Langhian. At the top of this unit, an abrupt unconformity developed, overlain by a coarse-grained unit of deltaic environment: the Serravalle Sandstone that developed throughout the Serravallian (Ghibaudo et al., 1985). The evolution of the TPB was independent from the southeastern area since the Burdigalian, both with respect to sediment provenance, located in the Alpine sector to the south and west (Carrapa, 2002), and its depocenters that were not communicating with the less deformed foredeep to the east.

In the subsurface of the western Po Plain and the westernmost foothills of the Apennines, east of the Monferrato thrust (at its footwall), few data are available on the Middle Miocene, based on only a few wells and small outcrops. A coarse-grained unit has been defined in the Middle Miocene, called Rio Lora sandstone from the name of a small window below the Ligurian unit in the foothills west of Piacenza, with provenance from the Alps to the northwest, as documented by the presence of glaucophane (for the use of marker minerals, see discussion in Gandolfi et al., 1983). Poor data exist on facies characteristics of this unit (scattered data based on cores of the Ponte dell'Olio well), but this sector was during the Serravalian the center of the foredeep, even though we cannot precise its paleobathymetry. To accumulate detritus from a source at

least 150 km to the Nortwest, the most suitable mechanism is gravity-driven transport: this means that a turbiditic origin of the sand-rich intervals of the Rio Lora sandstone is most likely.

The Burdigalian to lower Langhian clastic unit is the Cervarola Sandstone, derived from the Alps, and consisting of lithic arkoses, rich in clasts derived from a shallow metamorphic basement (presumably the Austroalpine) located to the northwest. The geometry of this unit shows a depocenter located close to the present-day foothills in the western portion of the Northern Apennines (Fig. 3): at the Bobbio window (Fig. 1) where about 3000 m are exposed. In the Salsomaggiore well (Fig. 1), the reconstructed thickness is around 1600 m (see next chapter). Moving to the southeast along strike of the Apennines, we found the Cervarola depocenter shifted in a more internal position, close to the present-day water divide. The profile, running along the foothills (Fig. 3), therefore, is oblique with respect to the depocenter axis, and slowly moves from the vicinity of the depocenter in the northwest to the foreland in the southeast. Figure 3 shows the decreasing thickness of the Cervarola Sandstone and the lateral passage to the foreland slope marls of the Schlier unit. At Salsomaggiore, many wells penetrated the uppermost few hundred meters of this unit, drilled more than 70 years ago. As a whole, the Cervarola Sandstone can be described as a succession of interbedded marls (mostly sandy marls) and sandstones, whose cementation strongly varies both vertically and laterally, suggesting a possible carbonate origin of these patchy cements, as it is the case for other outcropping successions in a central basin location (e.g. the Tortonian Marnoso-arenacea, Fontana et al., 1986). The oil-bear-
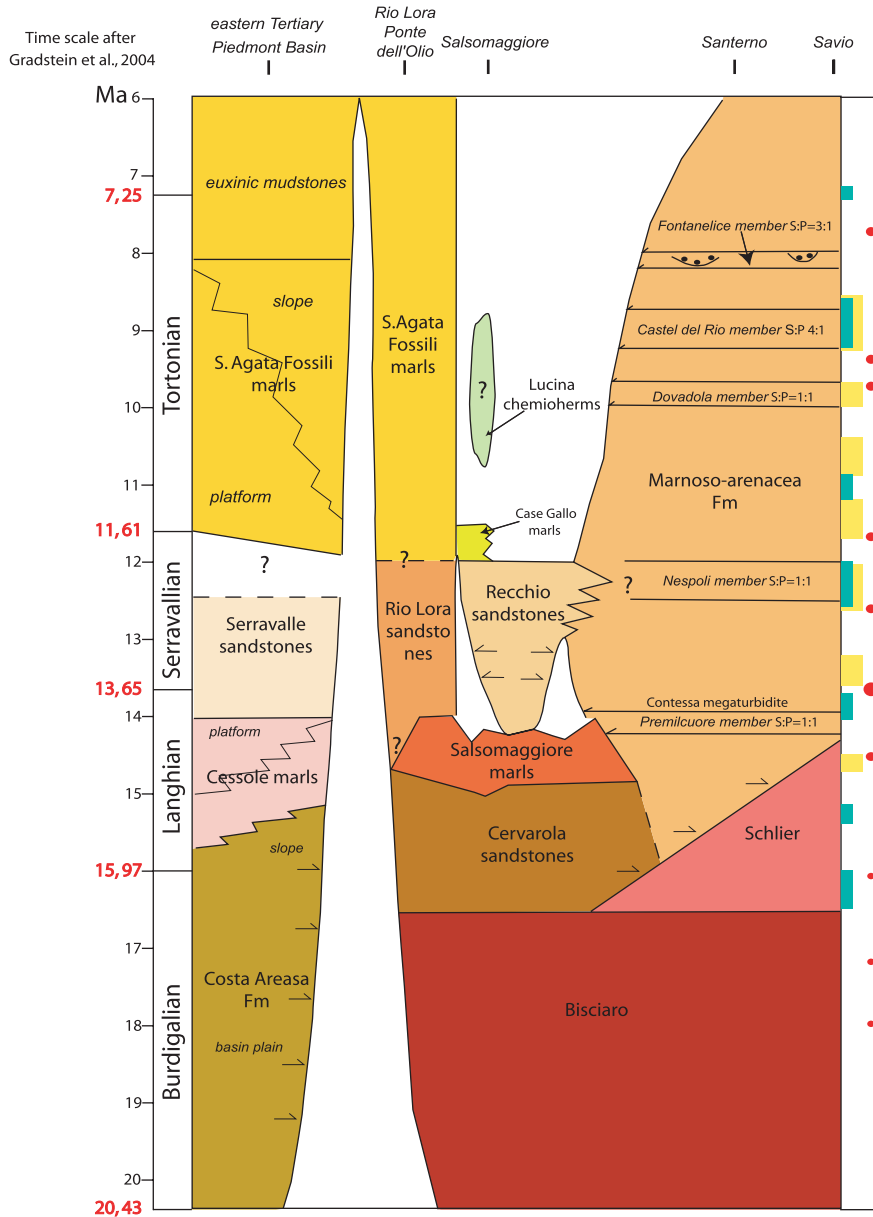
Fig. 4. Chronostratigrapic scheme along the same cross section of Fig. 3, including the Tortonian. Time scale after Gradstein et al., 2004. The lithostratigraphic subdivision of the Marnoso-arenacea Fm is from Antolini et al., (2001); S:P is the sandstone:pelite ratio. To the right, dots represent timing of the δ^{18}O-positive peaks of Abreu and Anderson (1998), proportional to their intensity. The bars indicate the duration of the third-order lowstand system tracts after Haq et al. (1987) and Hentz and Zeng (2003), blue and yellow, respectively

ing beds consist of sand with a high porosity. The correlability of the coarser intervals is good, documenting a lateral continuity of the sand layers that represent more or less 50% of the entire succession.

During the Langhian, a dramatic paleogeographic change took place in the western part of the foredeep, likely related to tectonic activity of the Salsomaggiore structure. It was associated with a change of the clastic transport system, which brought about the local de-activation of the Cervarola turbiditic lobe: the sandstones gradually pass up-section into a succession of marls, with minor interbedded coarser layers: the Salsomaggiore marls (Figs. 3 and 4) that locally acted as a seal for the Cervarola Sandstone. At the end of the

Langhian, a sharp seaward shift of the coastline occurred in the Tertiary Piedmont Basin with the rapid progradation of the deltaic system of the Serravalle Sandstone (Figs 3 and 4). Within the foredeep, a renewed input of coarse-grained clastics is recorded both over the growing Salsomaggiore structure and the undeformed basin to the southeast. Here, another turbiditic lobe developed: the Marnoso-arenacea unit, still supplied from the northwest, but along different transport routes, with the upper Langhian sand-rich Premilcuore member (Fig. 4). Atop the Salsomaggiore anticline, a thickening and coarsening upward succession of interbedded sandstones and marls occurs, the Recchio sandstone. This coarse unit (Figs 3 and 4), be-

ing the reservoir for the fields immediately east of Salsomaggiore, still contains glaucophane like the coeval Rio Lora Sandstone (Spinelli, 1964) but mixed with coarser-grained detritus derived from the north: it possibly represents a laterally confined basin, closed to the west by the growing Salsomaggiore thrust, toward which it shows clear onlap relationships in the field, and to the south by the front of the Ligurian unit.

The late Langhian sharply defined arrival of detritus over most the Northern Apenninic foredeep nicely coincides with a positive peak of the $\delta^{18}O$ (the strongest of the Miocene, Abreu and Anderson, 1998) and with a pronounced lowstand on the curve of Haq et al. (1987) (Fig. 4). This suggests that the deforming foredeep recorded the eustatic sea-level variations, as documented for the Pliocene of the Northern Apennines (Capozzi and Picotti, 2003).

After the Serravallian, the foredeep shifted northward in the central Po Plain: fine-grained deposits occur in the foothills of the westernmost Northern Apennines, whereas coarse-grained successions still were deposited in the Marnoso-arenacea basin to the southeast (Figs. 3 and 4). Upper Miocene equivalents of the Marnoso-arenacea, deposited north of the Salsomaggiore structure, are the reservoirs of the Cortemaggiore field (see Fig. 1) (Pieri, 1992).

4   Tectonic Evolution of the Northern Apenninic Foredeep

The structural evolution of the Northern Apennines will be discussed by means of two cross sections (Fig. 5). Profile AA', running across the foothills and the Po Plain, is based on a re-interpretation of the depth-converted seismic line of Pieri (1987; his line BB'), combined with a cross section across the Northern Apennines north of the water divide, interpreted at depth after a profile of Zanzucchi (1980). Profile BB' is a cross section oriented along strike of the main Apenninic features, crossing the Salsomaggiore culmination. It has been constructed after the map of Zanzucchi (1980), checked on the field and finally compared with an unpublished seismic line running parallel to its western portion.

4.1 Profile AA'. The Tip of the Orogenic Wedge and the Foreland Deformation

Four main features characterize the external front of the Northern Apennines in the area studied: 1) the Ligurian nappe; 2) the Salsomaggiore thrust; 3) the Cortemaggiore thrust; and 4) the Piadena-Brè inverted basin.

1. Ligurian nappe. The northeastward advancing thrusting of the Ligurian allochthonous units over the sediments of the foredeep is reflected by the northeastward younging of sediments underlying the allochthonous units. For this reason, the age of the deposits underlying the Ligurian nappe constrains the timing of this advancement (Zattin et al., 2002). Along our transect three tectonic windows in the Ligurian nappes document this relationship (Fig. 1). The Zuccone window (Fig. 5), close to the watershed, shows an Aquitanian age for the youngest foredeep formation. In the Bobbio window, some ten km west of the cross section (see Figs. 1 and 5), the youngest deposit is Burdigalian in age, whereas the northern Salsomaggiore window shows different ages: to the south of the anticline the Ligurian units overlie Langhian rocks, to the north of the anticline Upper Messinian deposits. This age difference documents the growth of the structure during Serravallian and Tortonian times and confirms the role of structural highs growing in the foredeep and hampering the advancement of the nappe, as discussed by Zattin et al., 2002. In fact, during the Burdigalian, the front of the nappe advanced 3 km/My, abruptly slowing in the Langhian to 0.5 km/My and finally stopping, in the area of the growing thrust, during the Serravallian and Tortonian. Both, emplacement of the Ligurian units and the Tertiary foredeep deposits produced rapid overburden of the underlying sediments. The Zuccone window that rather appears as a horst, is bounded by normal faults, that possibly reactivated ancient thrust contacts. The cross-cutting relationships of these high-angle faults with the deeper low-angle thrusts are not clear, even though their activity should be contemporaneous for the Pliocene and Pleistocene.

2. Salsomaggiore thrust. Close to the northern tip of the Cervarola clastic wedge, this thrust started growing in the Langhian, as suggested by the Salsomaggiore marls (see discussion in Chapt. 3). The anticline grew during the Serravallian as an intrabasinal structure close to the depocenter of the Recchio Sandstone, whereas during the Tortonian it started to create a submarine relief and the top of the structure became eroded. The reconstructed shortening is about 6 km. Again, in this structure a prominent southwest-dipping normal fault now juxtaposes the Ligurian units with the Salsomaggiore thrust. This extensional structure, which shows evidence of Quaternary activity, plays an unclear kinematic role on the regional evolution of the foothill belt that seems to be controlled rather by compression. However, important normal faults active close to the mountain front of the Northern

Apennines have been reported (Bertotti et al., 1997; Capozzi and Picotti, 2002; 2006).

3. Cortemaggiore thrust. This 20-km-long thrust sheet started to grow at the end of the Tortonian, again close to the tip of the Tortonian clastic wedge (the subsurface Marnoso-arenacea; see Fig. 3), as suggested by convergence of the uppermost reflectors of the wedge. The thrust was particularly active forming a submarine structure during the Messinian, the deposits of which are in fact reduced in thickness above the thrust sheet. After formation of the late Messinian unconformity, the eroded thrust top was onlapped by uppermost Messinian sediments that include the Ligurian wedge (Artoni et al., 2004), and finally by a reduced prism of Pliocene sediments, which still shows convergence toward the thrust top. The very rapid emplacement of the Ligurian unit (up to 10 cm /y), after many million years of local inactivity of this nappe in the back of the Salsomaggiore structure, can be explained by gravity emplacement re-establishing the equilibrium of the thickened wedge. The Pleistocene is very thin and only slightly deformed close to the tip of the fault, which is clearly sealed by these deposits. The overall shortening attains 7 km.

4. Piadena – Brè basin. The Messinian depocenter, in the footwall of the Cortemaggiore thrust, is particularly clearly developed over this 22 km-long-basin. The seismic stratigraphy of the basin suggests the possible presence of an Upper Triassic succession with Lombardian facies, i.e. organic-rich deposits (Zorzino Limestone, and/or Argillite di Riva di Solto and Zu Limestone), which are known as good source rocks (see Chapt. 3). The sharp lateral truncation of these reflectors suggests the presence of a basin bounded by faults, which could have been active during the Late Triassic to Early Jurassic rifting period (Bertotti et al., 1993). These normal faults appear to have been reactivated during the Messinian, when this sector was affected by rapid subsidence with the deposition of a thick foredeep wedge (Fig. 3). The sedimentary prism, whose geometry was perturbated by the fault reactivation, is wider than the Serravallian and Tortonian basins, and located more externally in the foreland. North of the basin, the Messinian tends to cover the tip of a northward thickening Miocene wedge of the Southalpine retroforeland, documenting its deactivation. Finally, during the Pliocene, the basin was inverted, as documented by the the growth pattern of the reflectors close to the anticlines of Brè and Piadena (Fig. 5). The depocenter of the Pliocene and Lower Pleistocene clastic wedge was the same as during the Messinian, suggesting that the Messinian was the last step of the encroachment of the Northern Apenninic foredeep onto the foreland.

4.2 Profile BB′. The Quaternary Northwest Verging Reactivation of the External Thrust Sheet

In map view, the Salsomaggiore anticline shows a domal shape, that suggests possible lateral ramps or strain interferences (Fig. 5). In order to highlight its lateral culminations and depressions, we constructed a cross section oriented along strike of the main structures of the Apennines and running along the axis of the Salsomaggiore anticline (section BB′, Fig. 5). The geometry of the eroded portion of the anticline has been reconstructed after projecting about 4 km to the south the unit boundaries along their dip toward the crest of the anticline, mainly using our section AA′ (Fig. 5) and other available dip sections crossing the anticline (Zanzucchi, 1980). The section BB′, has been interpreted into depth mainly after field geology, with the aid of few subsurface informations, such as the stratigraphy of Chero Carpaneto 2 and Salsomaggiore 1 wells, whereas the eastward termination of some Pliocene reflectors (under Bacedasco, see BB′, Fig. 5), come from an unpublished seismic line, running parallel, but few km north of the section BB′.

The bottom of the Pleistocene is clearly deformed and uplifted, defining a wide asymmetric anticline with culmination at Salsomaggiore (at the intersection with section AA′, see section BB″, Fig. 5), a longer limb to the southeast and a vergence to the northwest. The shape of this anticline has not been the same in previous times, such as the Messinian, when the Ligurian units passed over the thrust top (as described in sect. 4.1.). In our reconstruction of the eroded portion of the anticline, in fact, the Ligurian units (floored by a purple line in section BB′) are thicker close to the culmination, pinching-out to disappearance in the vicinity of the creek Recchio, and eventually reappearing toward the river Taro (Fig. 5). This suggest that, during the Messinian, the period of the rapid gravitational emplacement of the Ligurian units, the actual culmination of the Salsomaggiore anticline was located between the Recchio and the Taro channels, whereas the present-day culmination was morphologically less pronounced, providing accommodation for the thick (around 1.5 km) Ligurian wedge.

The shape of the culmination was even different during Serravallian, as suggested by the westward thinning of the Recchio sandstone, which defines another relative culmination during this time: This Serravallian culmination has been explored by the Chero-Carpaneto 2 well, that documents the absence of the units comprised between the Burdigalian (Cervarola Sandstone) and the upper Messinian period, marking the onset of a new subsidence pulse for the
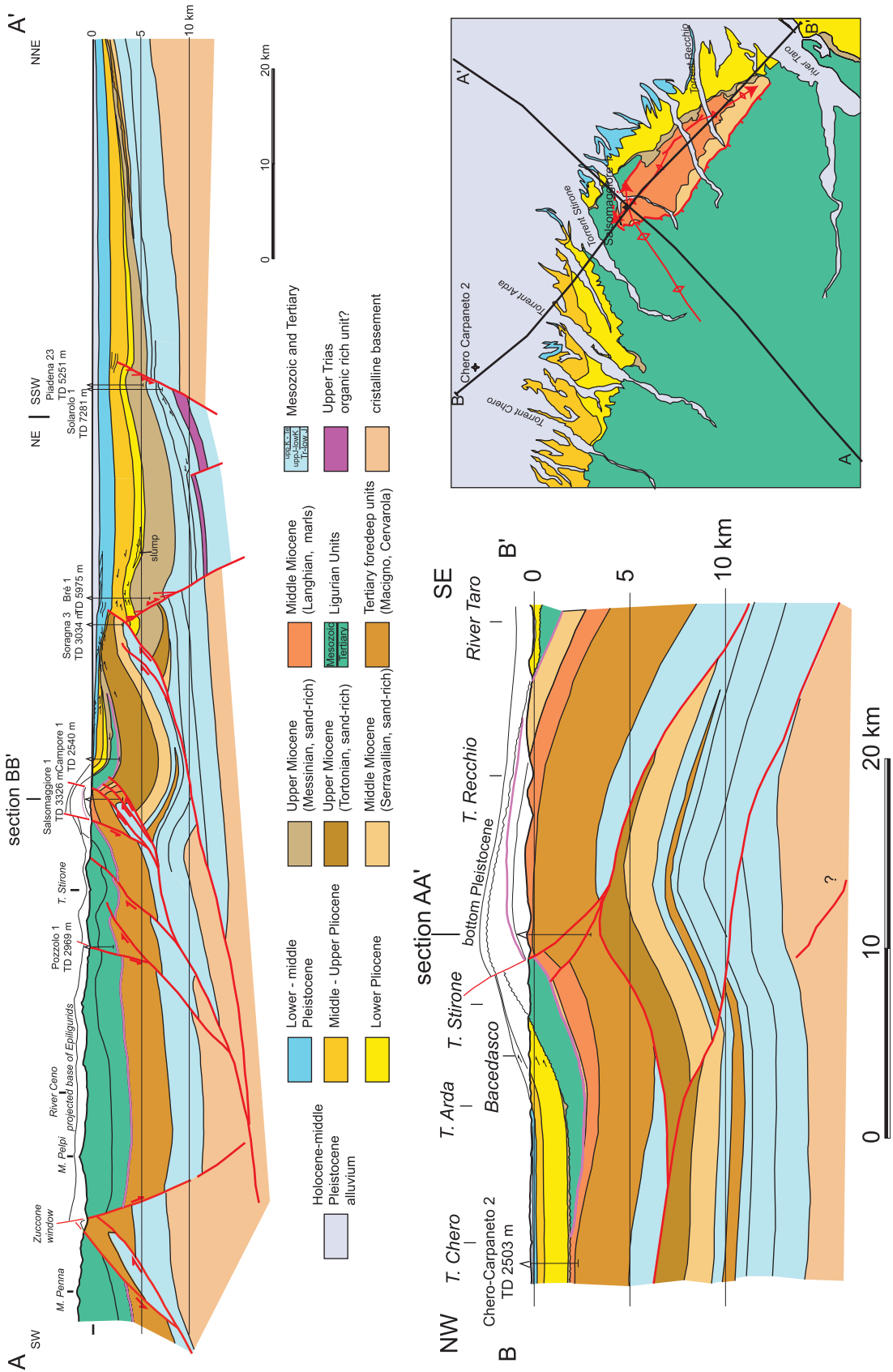
Fig. 5. Cross-sections along dip and strike of the front of the Northern Apennines in the area studied. Deep interpretation after the seismic line of Pieri (1987) in the subsurface of the Po Plain. Apennine surface data after Zanzucchi (1980) and our own field work

western half of the section BB', providing accommodation for the Plio-Quaternary deposits.

The described diachronous culminations are associated to different kinematic behaviour along strike of the hangingwall of the Salsomaggiore thrust. The oldest (Chero Carpaneto: Serravallian to Messinian; Recchio-Taro: ?Tortonian to Messinian) have similar wavelengths of about 10 km and likely represent different asperities of the footwall ramp of the Salsomaggiore thrust. As an alternative, they could be due to the inversion of previous (normal) faults in the hangingwall. This latter phenomenon, indeed difficult to ascertain in this case, is quite common in this sector of the Northen Apennines. The Salsomaggiore culmination, associated with a wider anticline (about 20 km) has been related to the Quaternary activity of the deeper Cortemaggiore thrust, ramping toward the northwest with a shortening of about 2 km. Note that the same Cortemaggiore thrust along the perpendicular section (AA' in Fig 5), practically do not show Pleistocene deformation, if we except some folding. This inferred deep northwest verging ramp, and associated anticline, could explain the observed Quaternary features such as the important local exhumation (up to 2 km eroded) and the high relief of the Salsomaggiore hills, as well as the activity of the main southwest dipping normal fault, located in the upper thrust sheet (described at point ii of sect. 4.1, section AA', Fig. 5). This fault, oriented perpendicular to the axis of the culmination, could play the role of southern boundary of the culmination.

5   Fluid Composition: Origin, Evolution and Migration

At Salsomaggiore, saline waters and hydrocarbons from spontaneous emissions have been described since 193 B.C., and were widely exploited for centuries. We collected samples from seven drilled wells, located around and in the center of the village of Salsomaggiore, at the culmination of the structure (see Figs. 1 and 5) in an area of about 20 km². These wells reached an average depth of about 1000 m. The stratigraphy of the wells indicates various interbedded sand and marly layers yielding hydrocarbons and brines, and minor cemented sandstones, within the Langhian interval. Sandy-marly interbeds, more regularly arranged, occur in the underlying Burdigalian interval. The measured porosity reaches up to 20%, however, the occurrence of hydrocarbons and saline waters is discontinuous, essentially due to the patchy cementation. Sampling was carried out during spring 2004 and samples were analysed for their physical, chemical and isotopic characteristics. All chemical and isotopic analyses have been duplicated and some of the

wells were resampled, to validate the analyses, during the fall of 2004.

The water temperature is very constant among the different wells and in the range of 16–18°C.

5.1 Composition of Brines

The content of major ions in the Salsomaggiore saline water is very high (Table. 1 and Fig. 6), in a range which is quite unique amongst the known cold vents of Italy.

Within connate saline waters the increase of Na and Cl ions becomes significant in the case of water coming from intermediate depth, deeper than 700 m. Ca increases with depth and formation age, likely in association with sulphate reduction due to bacterial activity (White, 1965). The concentration of the different ions depends on membrane-filtering mechanisms that, as described in the literature (e.g. White, 1965; Hanor, 1987), could account for an increase of water salinity with depth to up to 10 times that of seawater. These changes in interstitial water chemistry reflect the interaction with solid phases during burial and with time. When subsurface waters move along steep hydraulic gradients through shales or clays, the matrix can act like a reverse-osmosis membrane, retarding the movement of larger molecules. The main differences between the Salsomaggiore brines and seawater are a huge increase of chloride and calcium (Fig. 6), whereas Mg and SO_4 are depleted or absent, respectively; however, H_2S does not occur. Significant contents of iron and NH_4 occur (see Table. 1) together with iodine (54 mg/L) and bromine (up to 245 mg/L).

The ion content of the Salsomaggiore waters fit the range of values of "membrane-concentrate saline water" and matches a depth of origin between 1000 and 4000 m. A ten mineral phase system, which reacts to a chloride enrichment, is most suitable to explain the interactions between water and solid phases
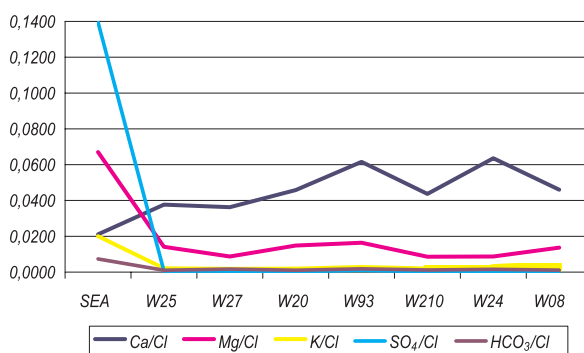

Fig. 6. Major ions content in seawater and in Salsomaggiore brines, normalized to Cl⁻

Table 1. Chemical analyses on the Salsomaggiore brines. Ion content in ppm

Samples	pH	Eh mV	Ca^{2+}	Mg^{2+}	Na$^+$	K$^+$	Cl$^-$	SO$_4^{2-}$	HCO$_3^-$	NH$_4^+$	Fe	Si
Well 25 25/05/04	6.72	-130	2725.4	1021.4	47900	153	72318	43	73.2	126	14.47	2.1
Well 27 25/05/04	7.22	-181	2324.6	559.36	42750	116	64164	38	109.8	108	11.63	2.3
Well 20 25/05/04	6.65	-117	4388.8	1422.7	63100	184	95715	22	97.6	144	13.46	3.3
Well Salsomaggiore 1 22/04/04	6.79	-103	5852	1556.5	60900	269	95006	90	170.8	135	11.53	3.4
Well 210 25/05/04	6.75	-240	4028	790.40	59100	185	92170	22	109.8	153	22.59	2.4
Well 24 22/04/04	7.16	-203	4509	620.16	47950	102	70900	24	109.8	99	10	1
Well 8 22/04/04	6.4	-100	4306	1280	51180	292	93588	8.93	104	200	63.3	8.69
Seawater			400	1272	10560	380	18980	2649	140	0.07	0.02	7

within the Salsomaggiore siliciclastic reservoir (Hanor, 1996). In this case, we assume that the system developed in the absence of CO_2, as normal under subsurface condition. In fact, the δ^2H- and $\delta^{18}O$-values provide evidence that the analysed saline waters never mixed with meteoric water (see next chapter) documenting a system closed to the supply of CO_2 from the surface. In the absence of CO_2, calcite and dolomite interact no longer with the system and the alkalinity does not change. With high chloride content, quartz is mobilized: however, Si in the brines increases slowly, because it is incorporated into other mineral phases. In this system, anorthite partially dissolves and the calcium concentration increases in the solution, whereas K and Na do not increase because they are involved in the precipitation of K-feldspar and albite (Hanor, 1996). This mass transfer between mineral phases can locally increase the porosity of the reservoir, as could be the case for Salsomaggiore.

NH_4, bromine and iodine are likely due to the *in situ* reduction of abundant organic matter, even if we cannot establish the source of this from the water composition. However, most Northern Apenninic brines, derived from Miocene reservoirs as in the Regnano mud volcano system (Capozzi and Picotti, 2002), do not show a similar enrichment. In this case, there was not enough organic matter to generate high amounts of these ions: in fact, in this case, the hydrocarbon composition includes only thermogenic methane with minor retrograde condensate. Therefore, the high NH_4, bromine and iodine concentrations could only be supplied to the brine by the oil that characterizes the Salsomaggiore to Cortemaggiore area.

As sulphate is totally depleted, we would expect the occurrence of bacterially mediated sulphide. However, as sulphide no longer occurs, a possible subsurface equilibrium could have been reached. At the measured values of pH and alkalinity, relatively moderate sulphate reduction process probably occurred in the system and prevented the precipitation of calcium carbonate (Morse, 2003).

The total removal of H_2S can be ascribed to the very high Fe content which can precipitate, in the measured range of pH and Eh, mainly as marcasite (Seeman, 1987).

5.2 Brine Isotopes

Isotopic measurements of brines in sedimentary basin (Fig. 7 and Table. 2) typically show a trend toward ^{18}O enrichment with minor ^2H enrichment (Clayton, 1966, Clark and Fritz, 1997). δ^2H enrichment in basinal brines can be partially explained by dehydration of clay minerals, but can also be generated through exchange with H_2S or hydrocarbons that, in turn, can impart a positive shift in $\delta^{18}O_{H_2O}$. The hyperfiltration mechanism hypothesized to explain the high ion contents in the Salsomaggiore waters, is likely a more suitable mechanism that can account for the enrichment in Cl^-, ^{18}O and ^2H. This interpretation could be supported by a comparison with the Regnano isotopic values that have been correlated to membrane-filtered formation waters (Capozzi and Picotti, 2002). The filtrate water is expected to be depleted in heavier isotopes and, in fact, even if the reservoir of both Salsomaggiore and Regnano water is constituted by Tertiary siliciclastic

sediments, in the Regnano case filtration through the fault zone crossing the topmost Ligurian unit is clearly testified by chloride and isotope depletion.

5.3 Hydrocarbons

The main compositional characteristics of the Salsomaggiore oil indicate some differences from the oil of the northern Cortemaggiore group (Riva et al., 1986), occurring in the subsurface of the adjacent Po Plain. Both Salsomaggiore and Cortemaggiore group oils indicate an oxic environment of deposition of marine/deltaic siliciclastic source rocks and include 18α(H)oleanane that has been reported in source rocks and oils of Tertiary age. The thermal evolutionary stage of Salsomaggiore is late mature and corresponds to Ro >1 as in the Cortemaggiore oil, that comes from a younger, Tortonian reservoir. In contrast, in the Cortemaggiore group, Langhian to Serravallian reservoirs yield oil of less thermal maturity (peak mature Ro = 0.7–0.8) as at Vallezza, S. Giorgio and Podenzano (Riva et al., 1986). The Salsomaggiore reservoir is Burdigalian in age and the thermal maturity of its oil is high, Ro% > 1.1, whereas the Ro% in host rock cuttings is well below 1. This suggests possible oil migration, together with methane, from a deeper source. This hypothesis is strengthened by the occurrence of thermogenic methane with $\delta^{13}C$ values in the range from -40.5 to -45 ppt and δ^2H in the range from -152 to -165 ppt in the Cortemaggiore field (Pieri, 1992). These isotopic values are very similar to those measured in the Regnano mud volcano and are interpreted as signatures of methane migrating from a deep (Mesozoic) source into the Tertiary reservoir, where it was mixed with the saline waters (Capozzi and Picotti, 2002). At Salsomaggiore, a further source of organic matter in the Tertiary siliciclastic system could be supported by the high NH_4, iodine and bromine contents in the saline waters which clearly depends on the decaying proteins of organisms. The Tertiary succes-

Table 2. Hydrogen and oxygen isotope composition of brines of the Salsomaggiore oil field

| Samples	$\delta^{18}O$ (VSMOW)	δ^2H (VSMOW)
W 25 Salsomaggiore	10.57	-9.1
W 27 Salsomaggiore	11.05	-19.7
W 20 Salsomaggiore	11.45	-13.3
W 1 Salsomaggiore	9.14	-9.2
W 210 Salsomaggiore	12.63	-11.7

sions, in fact, with their low TOC content, cannot account for such values.

6 Discussion: An Integrated Model for the Miocene Petroleum System

The kinematic history we reconstructed for the Salsomaggiore structure provides a model to integrate the described characters of hydrocarbons and brines. This model, although valid for the Salsomaggiore structure, bears fundamental insights for the whole Miocene petroleum system.

The data presented above document that the Salsomaggiore petroleum system is comparable to those of Cortemaggiore and Regnano, in agreement with Riva et al. (1986), which in fact grouped these oils in the same "Cortemaggiore group".

The main point of difference with respect to the Riva et al. (1986) interpretation is the deep origin of the hydrocarbons, even if some Miocene contribute is required by the presence of a Tertiary organic marker in the oil. To the best of our knowledge, the foredeep units of the Northern Apennines are devoid of organic-rich intervals. A possibility exists, that the oil leached the organic molecules, markers of the Tertiary, from the reservoir during its residence into the reservoir itself. Whatever the Tertiary contribution, however, the deep origin of the hydrocarbons is docu-
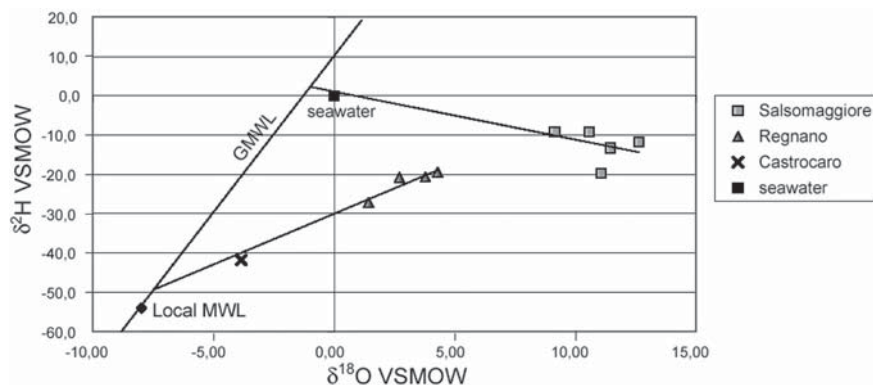
Fig. 7. δ^2H versus $\delta^{18}O$ of the Regnano and Salsomaggire waters. The Salsomaggiore and Regnano isotope composition of brines falls in the field of formation water without meteoric mixing. The more positive isotope values in the Salsomaggiore brines suggest they underwent to hyperfiltration processes. GMWL: Global Meteoric Water Line; Local MWL: Local Meteoric Water Line

mented by the high fractionation and maturity of the oil and the thermogenic imprint of the methane. These deep sources have never been drilled, or documented indirectly in the Northern Apennines, but should be Mesozoic, Upper Triassic (see Fig. 2) and/or (?) Cretaceous. Furthermore, the distribution of the oil of the Cortemaggiore group does not match that of the Miocene foredeep that is elongated along strike of the Apennines. Rather, it matches the distribution of the Upper Triassic source rocks, as illustrated in Fig. 2. As a matter of fact, the brines spontaneously leaking at surface from the Regnano mud volcano to the southeast differ from Salsomaggiore in that they never came into contact with oil, as documented by the low content of NH_4, bromine and iodine.

Within the Miocene province, the stratigraphic age of the reservoirs changes frequently, ranging from the Burdigalian Cervarola Sandstone of Salsomaggiore to the Serravallian Recchio sandstone in Torrente Baganza, to the Tortonian Marnoso-arenacea of Cortemaggiore. In the literature, all these different reservoirs, charged with the same oil of the "Cortemaggiore group", have been treated as the same formation and proposed as a source-reservoir system (Riva et al., 1986). The presence of the same oil in so different reservoirs implies common and deeper, source(s).

The geochemistry of brines of Salsomaggiore documents their origin from formation waters of the Tertiary foredeep units, in this case the Burdigalian Cervarola Sandstone. The formation waters have been trapped in the early formed (Langhian) structure, preventing the late compaction and loss of porosity in the tectonic culmination.

The ?Plio- Quaternary northwest verging reactivation of the Miocene thrust belt produced a domal culmination in the Salsomaggiore anticline, creating new gradients and the migration of oil via water-washing.

7   Conclusions

We described the main elements of the Miocene petroleum system of the central Po in order to reassess the petroleum potential of this province.
The Miocene reservoirs range from Burdigalian to Tortonian. Their locally good porosity is related to their deformation, occurring soon after their deposition and allowing for fluid trapping, preventing complete mechanical compaction that, in contrast, occurred in the intervening structural depressions. Another factor of permeability reduction, i.e. the carbonate cementation, is a process very difficult to predict, both for its patchy nature and late dissolution during brine migration.

The source is suggested to be multiple, likely dominated by Mesozoic (Upper Triassic, ?Cretaceous), in

our cross sections located at depth ranging from 7 to 10 km (Fig. 5). The sand-rich units of the Miocene are rather gas prone, but they have contributed with unknown percentage of normal maturity oil, bearing the Tertiary biomarker recorded by Riva et al. (1986).

Overburden to the source(s) is mainly due to the Tertiary foredeep units, tectonically covered by the Ligurian units. This foreland-ward moving couple brought about the rapid maturation of the source rocks during the Miocene, with hydrocarbons migrating up-dip toward the foreland where they could be trapped in the growing structures.

Finally, natural leakage of oil and brines occur in the Salsomaggiore culmination that is part of a wider Serravallian – Tortonian anticlinal trap deformed during the Quaternary. The recent tectonically induced changes in the geometry of this prominent culmination allowed further migration of oil *via* water-washing. This still active migration process could be too young to have generated important accumulation at the culmination of the structure. Alternatively, the oil could have dismigrated from a deeper trap whose sealing effects could have deteriorated after the recent deformation. This second hypothesis implies the possible presence of deeper accumulations of unspecified potential.

References

Abreu, V.S. and Anderson, J.B., 1998. Glacial eustasy during Cenozoic: sequence stratigraphic implications. AAPG Bull. 82, 1385–1400.
AGIP, 1984. Geologia d'Italia. CEDI, S.Donato Milanese.

Antolini, P., Borsetti A.M., Cremonini G., Pialli G. and Ricci Lucchi F., 2001. Foglio 254 Modigliana. Note illustrative della carta geologica d'Italia alla scala 1:50.000. Istituto poligrafico dello Stato, pp 118.

Artoni, A., Papani G., Rizzini F., Bernini, M., Roveri, M., Gennari, R., Calderoni M., Rossi, M., Rogledi S., Argnani A., 2004. The Salsomaggiore structure (Northwestern Apennine foothills, Italy): a Messinian mountain front shaped by mass-wasting products. Geoacta, 3, 107–127.

Bernasconi, S. M., 1994. Geochemical and microbial controls on dolomite formation in anoxic environments: a case study from the Middle Triassic (Ticino, Swizerland). Contr. Sedim., 109 pp.

Bernasconi, S. M., and Riva, A., 1993. Organic geochemistry and depositional environment of a hydrocarbon source rock: the Middle Triassic Grenzbitumenzone formation, southern Alps, Italy/Switzerland, in: Spencer, A. M., editor, Generation, accumulation and production of Europe's hydrocarbons III: European Association of Petroleum Geologists Special Publication, Springer, Heidelberg, p. 179–190.

Bernini, M. and Papani G., 1987. Alcune considerazioni sulla struttura del margine appenninico emiliano fra lo Stirone e l'Enza (e sue relazioni con il sistema del Taro). Acta Naturalia Ateneo Parmense, 23, 219 – 240.

Bertotti, G., Picotti, V., Bernoulli D, and Castellarin, A., 1993. From rifting to drifting: tectonic evolution of the South-Alpine upper crust from the Triassic to the Early Cretaceous, Sediment. Geol., 86, 53–76.

Bertotti, G., Capozzi, R. and Picotti, V., 1997. Extension controls Quaternary tectonics, geomorphology and sedimentation of the N-Apennines foothills and adjacent Po Plain (Italy). Tectonophysics, 282, 291–301.

Bertotti, G., Picotti, V. and Cloetingh, S., 1998. Lithospheric weakening during "retro-foreland" basin formation: tectonic evolution of the central South Alpine foredeep. Tectonics, 17, 1, 131–142.

Boccaletti, M., Calamita, F., Deiana G., Gelati, R., Massari, F., Moratti, G., and Ricci Lucchi, F., 1990. Migrating foredeep-thrust belt system in the northern Apennines and Southern Alps. Palaeogeogr. Palaeoclimat. Palaeoecol., 77, 3–14

Castellarin, A., and Vai, G.B., 1986. Southalpine versus Po Plain apenninic arcs. In: The Origin of Arcs, F.C. Wezel (ed.), Development in Geotectonics, 21, Elsevier, Amsterdam, 253–280.

Capozzi, R. and Picotti, V., 2002. Fluid migration and origin of a mud volcano in the Northern Apennines (Italy): role of deeply rooted normal faults. Terra Nova, 14, 5, 363–370.

Capozzi, R, and Picotti, V., 2003. Pliocene sequence stratigraphy, climatic trends and sapropel formation in the Northern Apennines (Italy). In: Meyers, P.A., Negri, A. (Eds.), Paleoclimatic and Paleoceanographic Records in Mediterranean Sapropels and Mesozoic Black Shales. Palaeogeogr. Palaeoclim. Palaeoecol. 190, 349–371.

Capozzi, R. and Picotti, V., 2006. Genesis of cold seeps and mud volcanoes of the Northern Apennine foothills. CIESM 2006. Fluid seepages / mud volcanism in the Mediterranean and adjacent domains. CIESM Workshop Monographs n°29, 59–64.

Carrapa, B., 2002. Tectonic evolution of an active orogen as reflected by its sedimentary record, an integrated study of the Tertiary Piedmont Basin (Internal Western Alps, NW Italy). Ph.D. Thesis, ISBN 90–9016220–8, Amsterdam, 177p.

Carraro F., Collo G., Forno M. G., Giardino M.,Maraga F., Perotto A. & Tropeano D. (1995). L'evoluzione del reticolato idrografico del Piemonte centrale in relazione alla mobilità quaternaria. In: Polino R. & Sacchi R. (Eds.), Acc. Naz. Sc., Roma, Scritti e Documenti, 14: 445–461.

Clark, I.D., and Fritz, P., 1997. Environmental Isotopes in Hydrogeology. Lewis Publishers, Boca Raton, New York, pp.328.

Clayton, R.N., Friedman, I., Graff, D.L., Mayeda, T.K., Meents, W.F., and Shimp, N.F., 1966. The origin of saline formation water, 1. Isotopic composition. Journ. of Geophys. Research, 71, 3869–3882.

Dondi, L., and D'Andrea, M.G., 1986. Paleogeografia della Pianura Padana e Veneta dall'Oligocene Superiore al Pleistocene. Giornale di Geologia, 48, 197–225.

Elter, P. and Trevisan, L., 1973. Olistostromes in the tectonic evolution of the Northern Apennines, in: De Jong K.A. and Scholten R. Eds., Gravity and Tectonics, John Wiley and Sons, p. 175–188.

Elter, P., Giglia, G., Tongiorgi, M. and Trevisan, L., 1975. Tensional and compressional areas in the recent (Tortonian to present) evolution of the Northern Apennines: Bollettino Geofisica Teorica e Applicata, v.17, p. 3–18.

Erba E., 2004. Calcareous nannofossils and Mesozoic oceanic anoxic events. Marine Micropaleontology, 52, 85–106.

Errico, G., Groppi., G., Savelli, S., and Vaghi, G.C., 1979. Malossa Field, deep discovery in Po Valley, in: Giant Oil and Gas Fields of the Decade: 1968–1978. AAPG Memoir 30, 525–538.

Fontana, D., McBride, E.F. and Kugler, R., 1986. Diagenesis and porosity evolution of submarine-fan and basin-plain sandstones, Marnoso-Arenacea Formation, northern Apennines, Italy. Bulletin of Canadian Petroleum Geology 34, 313–328.

Gandolfi, G., Paganelli, L. and Zuffa, G.G., 1983. Petrology and dispersal pattern in the Marnoso-arenacea Formation (Miocene, Northen Apennines). Journ. Sedim. Petrol., 53, 493–500.

Ghibaudo, G., Clari, P. and Perello, M., 1985 , Litostratigrafia, sedimentologia ed evoluzione tettonico-sedimentaria dei depositi miocenici del margine Sud-Orientale del Bacino Terziario Ligure-Piemontese (Valli Borbera, Scrivia e Lemme). Boll. Soc. Geol. Ital. 104, 349–397.1985.

Gradstein F.M., Ogg J.G., Smith A.G., Bleeker W. and Lourens L., 2004. A new Geologic Time Scale, with special reference to Precambrian and Neogene. Episodes, 27, 2, 83–100.

Hanor, J.S., 1987. Origin and Migration of Subsurface Sedimentary Brines. Society of Economic Paleontologists and Mineralogists Short Course No. 21, pp.1–247.

Hanor, J.S., 1996. Variations in chloride as a driving force in siliciclastic diagenesis. In: Crossey, L.J., Loucks, R., and Totten, M.W. (eds.), Siliciclastic diagenesis and fluid flow: concepts and applications: SEPM Special Publication, n. 55, p. 3–12.

Haq, B.U., Hardenbol, J., and Vail, R., 1987. Chronology of fluctuating sea levels since Triassic, Science 235, 1156–1167.

Hentz T.F. and Zeng H., 2003. High frequency Miocene sequence stratigraphy, offshore Louisiana: Cycle framework and influence on production distribution in a mature shelf province. AAPG Bull. 87, 197–230.

Jenkyns, H. C., 1980. Cretaceous anoxic events: from continents to oceans. J. geol. Soc. London,. 137, 171–188..

LePichon, X., Pautot, G., Auzende, J.-M. and Olivet, J.-L.1971, La Méditerranée Occidentale depuis l'Oligocène: schéma d'évolution. Earth and Planetary Sciences Letters, 13, 142–152.

Malinverno, A. and Ryan, W., 1986. Extension in the Tyrrhenian Sea and shortening in the Apennines as result of arc migration driven by sinking of the lithosphere. Tectonics, 5, 227–245.

Mattavelli, L., and Novelli, L., 1990. Geochemistry and habitat of the oils in Italy. AAPG Bull., 74, 10, 1623–1639.

Morse, J.W., 2003. Formation and diagenesis of carbonate sediments. Treatise in Geochemistry, 7, 67–85.

Pieri M., 1987. Three seismic profiles through the Po Plain. In: Bally A.W. (Ed.) Atlas of seismic stratigraphy, volume 3. AAPG Studies in Geology, n 27, 90–110.

Pieri, M., 1992. Cortemaggiore Field-Italy Po Plain, Northern Apennines. In: Foster, N.H., and Beaumont, E.A., Treatise of Petroleum Geology, Atlas of Oil and Gas Fields, Structural Traps VII: Tulsa, OK, American Association of Petroleum Geologists, p. 99–118.

Pini, G.A., 1999. Tectonosomes and olistostromes in the Argille Scagliose of the Northern Apennines, Italy. Special Paper-Geological Society of America 335, 73 pp.

Riva, A., Salvatori, T., Cavaliere, R., Ricciuto, T., and Novelli, L., 1986. Origin of oils in the Po Basin, Northern Italy. Advances in Organic Geochemistry, 10, 391–400.

Seemann, R., 1987. Mineralparagenesen in Osterreichischen Karsthohlen. Proc. VIII int. Spel. Cong., Bowling Green, 256–259.

Scicli, A., 1972. L'attività estrattiva e le risorse minerarie della Regione Emilia-Romagna. Artioli, Modena, 626 pp.

Spinelli, L., 1964. Studio petrografico e sedimentologico di una formazione clastica elveziana dell'Appennino Parmense: serie del Recchio – Salsomaggiore. Rend. Soc. Miner. Ital., 20, 251–278.

Stefani, M.M., Burchell, M.T., 1990. Upper Triassic (Rhaetic) argillaceous sequences in Northern Italy: Depositional dynamics and source potential. In Huc A.Y. (Ed.) Deposition of organic facies. AAPG Stud. Geol. 30, 93–106.

Stefani, M.M., Burchell, M.T., 1993. A review of the Upper Triassic source rocks of Italy. In: Generation, Accumulation and Production of Europe's Hydrocarbons, Spencer, A.M. (Ed.), Special Publication of EAPG. Springer, 1, 169–178, Berlin.

Thery J.M., Cros P., Bouroullec J., 1989. Relations entre environment et sdimentologie de la mattire organique: le Trias du Nord de l'Italie. Bull. Centre Rech. Expl-Prod Elf-Aquitaine, 13, 23–33.

White, D.E., 1965. Saline waters of sedimentary rocks. In: Fluids in subsurface environments (A. Young and J.E. Galley, eds.), The American Association of Petroleum Geologists Memoir 4, pp. 342–366.

Willett, S., Schlunegger F., and Picotti V., 2006. Messinian climate change and erosional destruction of the central European Alps. Geology, 34, 8, 613–616, doi: 10.1130/G22280.1.

Zanzucchi, G., 1980. I lineamenti geologici dell'Appennino parmense. Note illustrative alla Carta e Sezioni geologiche della Provincia di Parma e Zone limitrofe (1:100.000). Vol. dedicato a Sergio Venzo, Grafiche STEP (ed.), Parma, 201–233.

Zattin, M., Picotti, V., and Zuffa, G.G., 2002. Fission-track reconstruction of the front of the Northern Apennine thrust wedge and overlying Ligurian unit. Am. Jour. of Science, 302, 4, 346–379.

Part IV
Structural Modeling / Restoration

Part IV of the volume reports structural/kinematic modelling at the scale of individual fold structures or at the scale of the entire thrust belt, as well as the use of 2D restorations to derive internal strain.

Mercier et al. (Chapter 7) review the different types of markers (growth strata and collapse-structures, morphology, microtectonics) used as kinematic records of folding, and how they can account for hinge migration, the occurrence of which being a pending question in individual fold kinematics. The authors show that few hinge kinematics can be explicitly established from field observations, and that mobile hinges are extremely scarce in the literature, leading to an overrepresentation of fixed hinge cases.

Moretti et al. (Chapter 8) discuss the various methods used to restore horizon surfaces (simple shear or flexural slip). They show that surface restoration process allows to compute a strain field, and that resulting eigen values, main strain direction and dilatation may in turn allow to predict fracture patterns. They apply their method to a set of thrust sheets located in the southern Sub-Andean Zone in the Neogene Andean Foothills of Bolivia. Because the computed internal strain tensor is highly dependent on the method used for the restoration, they discuss the results expected from each method.

Lingrey (Chapter 9) address the problem of the restoration of fold-thrust belts in a setting of significant wrench deformation where the condition of plane strain does not apply. The paper presents a structural reconstruction for Trinidad and the adjacent Gulf of Paria with a micro-plate kinematic model of the South American-Caribbean plate boundary.

In their paper, Hardebol et al. (Chapter 10) discuss the exhumation pattern and history of the Alberta thrust belt and its distal foreland. They combine 1D conceptual and 2D forward thermo-kinematic modelling for constraining the restoration of the syntectonic sedimentary wedge and also for better resolving burial and exhumation history (i.e., timing, amplitude and wavelength), with constraints derived from organic maturity ranks and fission tracks.

Folds Kinematics in "Fold-and-Thrust Belts" the "Hinge Migration" Question, a Review

Eric Mercier · Silvain Rafini · Riadh Ahmadi

Abstract. In Fold-and-Thrust Belt domains, fold amplification may occur either according to hinge migration process (i.e., hinges move relative to the affected material) or by limb rotation around fixed hinges. The validation of the « excess area law » at all kinematic stages of folding, suggests that they grow by hinge migration rather than by limb rotation, consequently, almost all fold kinematic models use the hinge migration process. We show that at least four independant approaches should a priori allow to demonstrate the occurrence of hinge migration mechanisms in nature: i) growth stratal geometry, ii) specific collapse-structures analysis (flaps), iii) morphological imprints of fold growth, and iv) microtectonic signatures. In practice, we observe that the latter is inoperative. We show, through this bibliographic review, that few hinge kinematics could be explicitly established from field observations, and conclude that, i) both expected kinematic behaviours are encountered and can coexist, ii) mobile hinges are extremely scarce in the literature, such that a paradoxal and theoretically unexpected overrepresentation of fixed hinge cases is observed. We discuss this latter point by reconsidering the efficiency of each approach and, without negating limb rotation existence, we propose explanations based on a methodological bias favouring the underestimation of hinge migration frequency.

1   Introduction

Limb rotation (Fig.1) has long been considered, without much discussion, to be the dominant mechanism allowing fold amplification into surficial tectonic domains, and notably within Fold-and-Thrust Belts. Such behaviour implicates that limbs rotate around hinges, which remain stationary relative to the material affected during folding (Figs. 2 and 3), as what we could call the "classical kinematic model of folding". During the early 80s, Suppe (1983) proposed a new kinematic model which specifies that limb dips are settled during the first stage of folding, while fold growth is permitted by hinge mobility (Fig. 4). According to these new models, refer to as "Fault-Bend Folds", folding results from a surficial accommodation of displacement along deep layer-parallel thrusts (i.e. detachements) and shallow-dipping thrusts (i.e. ramps).
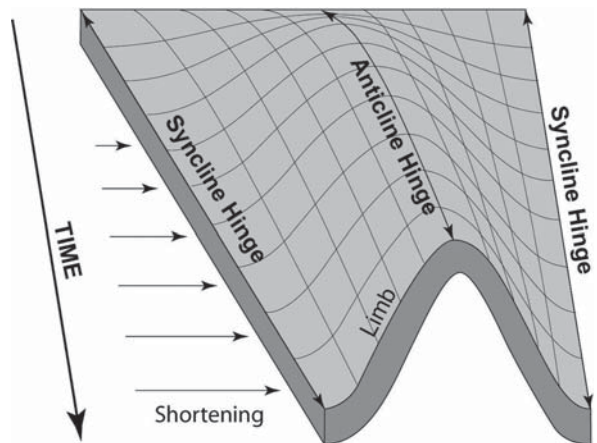

Fig. 1. Classical fold model characterized by limb rotation around fixed hinges. Note that the third dimension in the diagram is time

These models were realized after formalization by De Sitter (1956), Curie et al. (1962) and Dalhstrom (1969) of the cross-section balancing concepts, meaning that Fault-Bend Folds verify the mass-conservation law (i.e., conservation of layer lengths and thickness) at each stage of its kinematic evolution.

Several ramp-related folding models have been subsequently developed in agreement with balancing concepts (e.g. Suppe, 1985; Chester & Chester, 1990; Al Saffar, 1993; Mercier et al., 1997), which all are characterized by i) limb dip acquisition at the initial folding stage, which is compulsorily imposed by the ramp, ii) the mobility (i.e. migration) of some hinges wich is then required during fold growth, and iii) underlaying basal thrust-system corresponding to decollements and ramps.

Beside fault-related folds, authors recognize another major fold-amplification process, the well-known detachment folding, which requires a wide thickness of ductile sediment behaviour (Dahlstrom, 1969; Dahlstrom, 1990; Poblet and McClay, 1996). A widespread assumption before 1990 was that kinematics of such structures correspond to the above-mentioned "classical kinematic model of folding", called the fixed-hinge
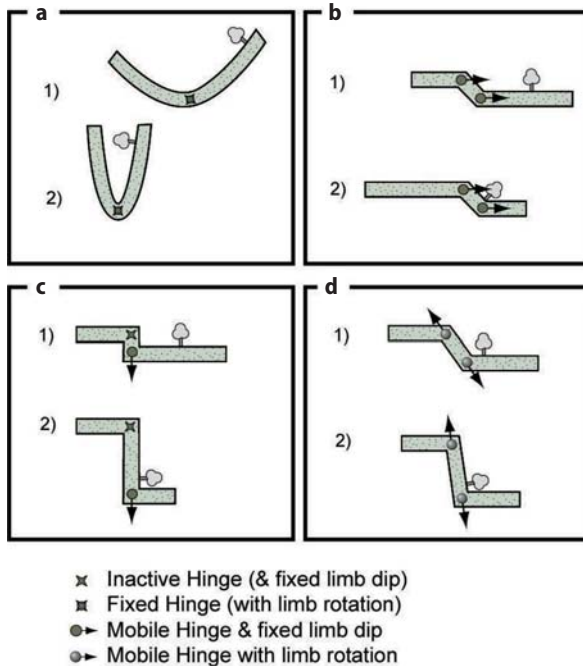
Fig. 2. Different kinematic hinge behaviours during deformation.*Fixed hinge*: hinge is fixed relative to deformed layers, and limbs rotate (**a**). *Inactive hinge*: hinge is fixed relative to deformed layers, and limbs do not rotate (**c**). *Mobile hinge*: hinge is mobile relative to deformed layers, this migration is associated (**d**) or not (**b**, **c**) with limb rotation

ly meaningless and poorly supported by field observation (Fig. 6). After this critical point, some detachment fold kinematic models were formalized. They stipulate that hinge migration behaviours could or not be associated with limb rotation, then allowing the validation of the excess-area law at each kinematic stage (Epard and Groshong, 1995; Poblet and McClay, 1996).

Moreover, hinge migration is a classically admitted growth process for several elementary structures frequently encountered in Fold-and-Thrust Belts contexts, such as the variable-dip thrusts or wedge thrusts (Fig. 7).

At this stage, one could coherently conclude that hinge migration should appear as a dominant behaviour, if not the alone one, involved in folding within Fold and Thrust Belts areas. Such a statement yet has to be discussed considering the following critical aspects:

- On a first hand, field indications supporting hinge migration remain scarcely reported in the literature, meaning that few natural arguments exist although its significance and necessity are theoretically demonstrated (see below);
- On another hand, attempts in developing balanced kinematic models that favour fixed hinges (limb rotation process rather than hinge migration) are poorly validated by field observations (Hardy and Ford, 1997; Allmendinger, 1998; Groshong and Epard, 1994; Homza and Wallace, 1995).

behaviour (Fig. 1). Nevertheless, Dahlstrom (1990) demonstrates that such a kinematic model does not accord with balancing concepts, as the excess-area law can hardly be verified unless a variable detachment depth is allowed during fold growth, which is natural-

So, it appears to be relevant to summarize the available field arguments that tried to support the occurrence of the hinge migration mechanism, and makes an assessment on field investigations which provides
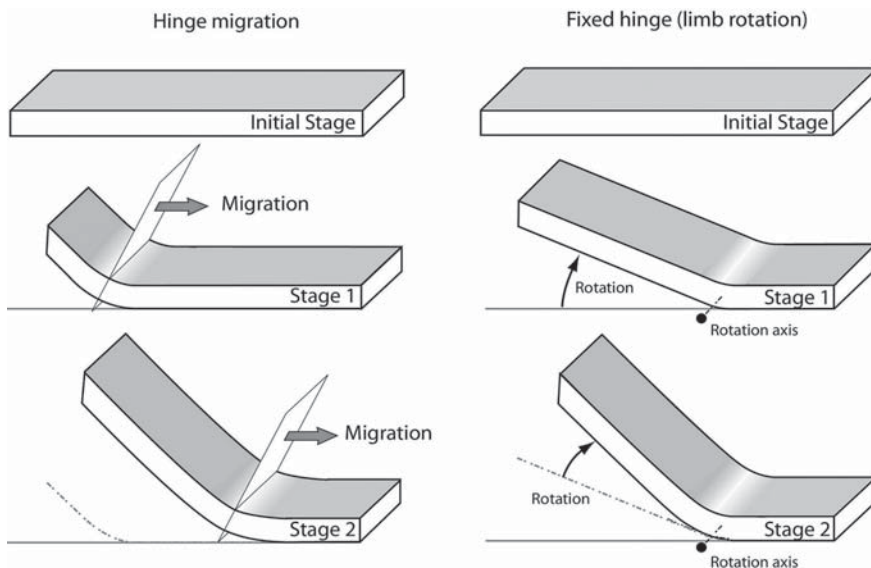

Fig. 3. Comparison between mobile hinge and fixed hinge kinematics. Note that at a finite deformation stage (*Stage 2*) we can not distinguish between the two kinematic processes. It is thus necessary to look specific dynamic markers
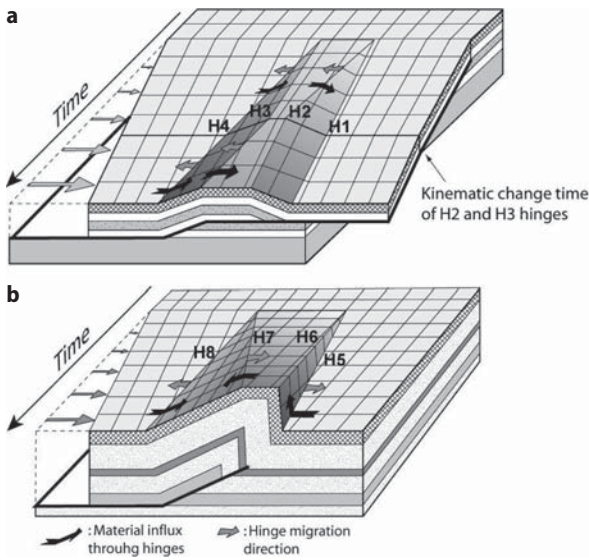
Fig. 4. Kinematic evolution of principal fault-related fold model: **a** Fault-Bend Fold (Suppe, 1983), **b** Fault-Propagation Fold (Suppe and Medwedeff, 1985). Note that some hinge kinematic changes from a certain stage of the evolution of the Fault-Bend Fold. Note that the third dimension in the diagram is time. *H1*: inactive; *H2*: Initially mobile and after becomes inactive; *H3*: Initially inactive and after becomes mobile; *H4*, *H5*, *H7*, and *H8*: mobile; *H6*: inactive when fault dip is near 29°, otherwise is mobile *H5* if fault dip is over 29°, and move in the opposite direction when the fault dip in under 29°
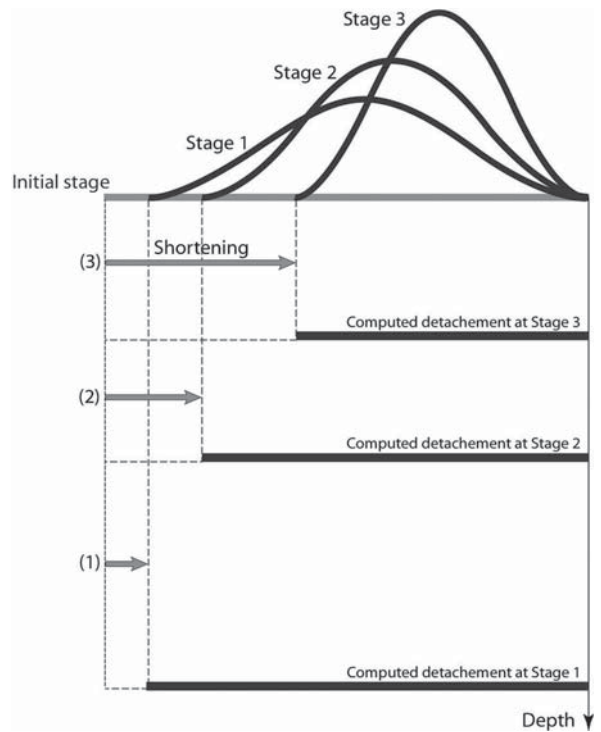
Fig. 6. Application test of the excess area low to fixed hinge detachment fold model. Detachment depth is computed at different deformation stages using the structural relief (*S*) and the shortening rate (*R*): $H = S*/R$ (and $S*=S$)We observe that detachment depth is hugely variable (inspired after Dahlstrum, 1990) which can not fit with geological reality
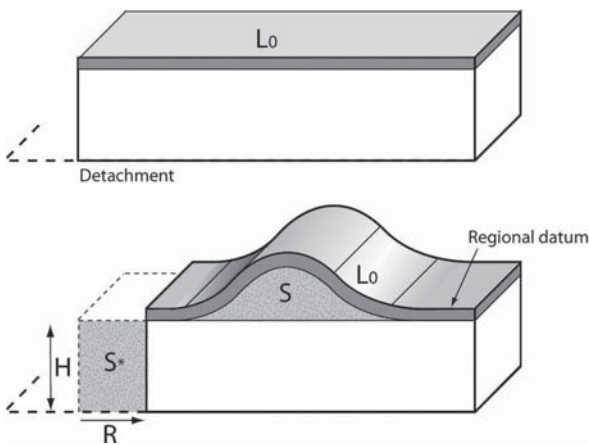
Fig. 5. Excess area law: in standard conditions of balanced cross-section (constant layer thikness, planar deformation, shortening perpendicular to structure) layer length (L_0) still constant, and we have equivalence between structural relief above "regional datum" (*S*) and back-translated surface (*S**): $S* = R \times H$ ((R) = shortening; (H) = detachment layer depth). After several authors, the model is validated if all kinematic stages respect also this law.
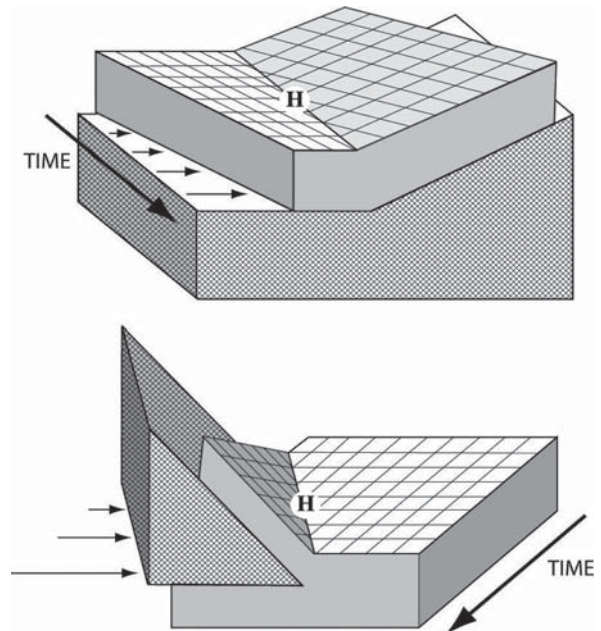
Fig. 7. Kinematics of variable dip thrust sheet, and wedge thrust; in both cases the deformation is associated with hinge migration (*H*). Note that the third dimension in the diagram is time

information about its implication into natural folding phenomena.

However, determining the deformation path of a tectonic structure is a complex issue as the present deformation stage (finite deformation state) does not imply any univocal relationships with the intermediate stages, and consequently does not allow a kinematic reconstitution consisting in a single path (Fig. 3). Such reconstitutions thus need alternative kinematic records to be provided, meaning that: i) pertinent kinematic markers must be determinated, and ii) these markers must be preserved during later deformation stages.

This review proposes to examinate and discusses the different types of markers that were used by authors for supplying folding kinematic records, in order to analyse their contribution relevant to the argumentation about hinge migration occurrence. We'll thus treat successively the following approaches: growth stratal analysis, collapse-structures, morphological signatures, and microtectonic imprints.

2   Growth Strata

When fold grows simultaneously with sedimentation, syntectonic strata development fossilizes fold geometries at successive depositional time, before they get themselves deformed (Riba, 1976; Graham, et al., 1986; Medwedeff, 1989). The alteration of the specific growth strata geometries due to erosion during following deformation stages can partially erase those records. Nevertheless, it is theoretically possible to perform backward iterative analysis integrating erosional processes in order to rebuild previous stages, thus accessing to folding kinematics and hinge behaviour over time evolution.

Authors mainly developed forward modelling, which predict growth strata geometries based on specific postulates concerning the kinematics of fold growth. Furthermore, these models can lead to achievments on folding kinematics through an inverse approach, provided that sedimentary and erosional aspects are quantitatively well constrained.

Two different cases can be considered depending on the relative intensity of deformation processes and sediment accumulation, meaning the ratio between tectonic uplift and sedimentation rate (Storti and Poblet, 1997):

2.1 Case of Tectonic Uplift Faster than Sediment Filling

In this case the fold is exposed to erosion because it does not remain totally covered by syntectonic lay-

ers, and progressive unconformity develops as growth strata gradually onlaps over fold limbs. Storti and Poblet (1997) and Rafini and Mercier (2002) generated forward models allowing determination of specific syncline hinges behaviours based on their final geometries. As a relevant conclusion, the presence of dual curvature within growth stratal architecture (shoulder-like geometry) turns out to be strictly indicative of a hinge migration process, whereas a progressive dip-change fan can only be generated by limb rotation (Fig. 8). Application of this diagnostic tool to natural structures thus theoretically leads to recognition of either hinge migration or limb rotation mechanisms, or a combination, as long as syntectonic formations are well preserved and observable in critical regions of its geometries.

2.1.1   Field Example of Mobile Hinge Behaviour

Located in the area of Sant Llorenç de Morunys (southern Pyrenees), the E–W trending Berga Conglomerates basin (Late-Eocene to Oligocene) overlays the Middle Eocene pre-growth strata which outcrops in the northern part of the basin as a large anticlinal structure. The northern border of the basin displays a progressive unconformity indicating a northward syncline hinge migration (Riba, 1976; Ford et al. 1997; Suppe et al. 1997). Thanks to numerical geometrical forward simulations, Rafini and Mercier (2002) have demonstrated that hinge migration behaviour
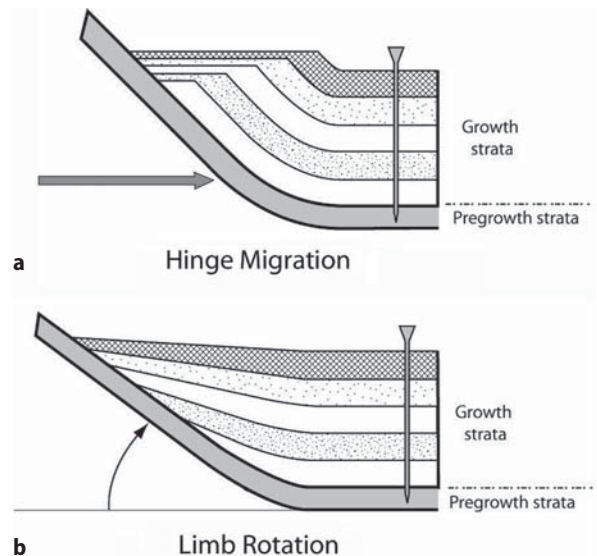
Fig. 8. Numerical model results of growth strata geometry in syncline hinge associated with (**a**) *hinge migration*, or (**b**) *limb rotation*. Model drowns at constant ratio: sedimentation rate/ shortening rate (Rafini and Mercier, 2002, modified). Note the concavity shape in the hinge migration case

leads to growth stratal architecture adequately matching the observed geometry (Fig. 9). This field example hence constitutes an excellent demonstration of hinge migration occurrence. However, it should be pointed out that:

- Nothing allows to link this proven migrating syncline hinge to the fold, as pre-growth strata outcroping north of the basin are crosscut by a major thrust system (Vallfoogona Thrust) that breaks the continuity of the structure, thus preventing its entire reconstruction. Indeed, the structure could also be considered as a wedge thrust system (Fig. 7) for instance (Medwedeff, 1992; McClay, 1992).
- This structure seems to be a singular example of hinge migration-involving growth strata. Indeed, except Ahmadi et al. (2006) who applied Rafini and Mercier's (2002) program on quaternary deformed pediment in southern Tunisia, no other analysis of progressive unconformity concluded to the existence of hinge migration process in folds amplification. We should however advance that this may be provisory since, as an example, several other basins located into the northeastern area of Spain constitute relevant potential targets if one refers to the regional tectono-sedimentary history (Anadon et al., 1986; Colombo and Vergès, 1992).

2.1.2   Field Example of Fixed Hinges Behaviour

Syntectonic basins displaying progressive unconformities as drawn in Fig. 8b appears to be less scarce (Hardy and Poblet, 1994; Vergès et al., 1996; Strorti and Poblet, 1997). Such examples concern basins located downhill of anticlines where authors demonstrated a fixed hinge behaviour with rotation of the limbs. Nevertheless, we should here point out that, as concluded by Rafini and Mercier (2002), relevant geometric arguments allowing to diagnose hinge migration are typically situated in the upper portion of growth strata. Numerical modeling allowed the authors to state that, if the basin undergoes erosional activity during or after deformation, these arguments could, at least partially, vanish such that interpretation of the resulting geometry becomes ambiguous. Indeed, the very criti-

Fig. 9. Sant Llorenç de Morunys growth strata. (**a**) Field data (Ford et al., 1997 modified) and (**b**) model (Rafini et Mercier, 2002 modified)
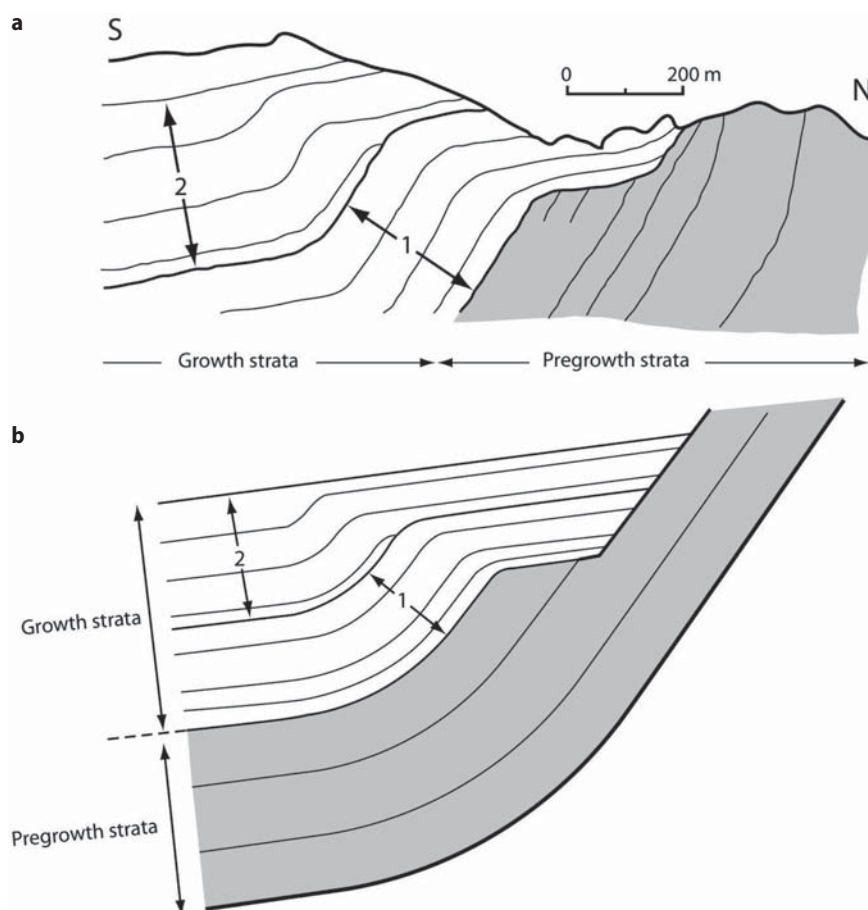
cal feature, and yet required, is the continuous (limb rotation) or discontinuous (hinge migration) variations of limb dips, which specifically occur in the upper portion of the structure (shoulder) in case of hinge migration. Numerical testings including erosional activity revealed that a distinction between these two options can be widely mistaking when the conditions allow only local observations and does not permit to properly localise it into the structure at a wider scale. Consequently, growth strata analysis for such conditions can lead to false conclusions in terms of limb rotation processes. Accordingly, it can be shown that several examples mentioned above could be revised in this way.

2.2 Case of Sedimentation Rate Greater than Tectonic Uplift

In this case the fold does not emerge from the basin, as syntectonic sediments entirely cover the top of the structure. It is thus impossible to identify any progressive unconformity, however, growth strata exhibit diagnostic layer thickness variations as a consequence of tectonic uplift (Fig. 10). Detailed analysis of these thickness variations provides some insights about the kinematics of folding. After Suppe et al. (1992), several authors have proposed theoretical growth stratal geometric models for classical fold types (Fig. 10) (Shaw and Suppe, 1994; Poblet and Hardy, 1995; Hardy and Poblet, 1995; Wickham, 1995; Zapata and Allmendinger, 1996; Salvini et al., 2001; Salvini and Storti, 2002; Bernal and Hardy, 2002; Masaferro, 2002; Grando and McClay, 2004). Some of these authors include geological data (mainly seismic profiles) supporting their theoretical investigations. It emerges from these works that there are several examples in which comparison of natural and theoretical observations (Fig. 10c) concluded in the fixity of all hinges (Poblet and Hardy, 1995; Masaferro, 2002; Grando and McClay, 2004).

Yet, no one of these structures could allow validation of all required observations relative to fault-related folds (Fig. 10a and 10b), rather satisfying analysis could only establish such validation on one of the two fold limbs (Suppe et al., 1992; Shaw and Suppe, 1994; Zapata and Allmendinger, 1996).

3   Flap Structures

When fold grows, it leads to sharp reliefs above the surrounding topographic level, and collapse of the uppermost layers can occur especially if an underlying soft layer is present, thus constituting a preferential landslide detachment layer. Harrison and Falcon (1934) developed a typology of such collapse structures based

on Iranian field examples, in which they notably described the flap structures that consist in a complete overturn of the uppermost layer at a finite deformation stage (Fig. 11a). These authors advanced that flaps could form subsequently to fold growth, similarly as classically interpreted collapse development.

Nevertheless, a recent re-examination of some of these Iranian structures by Sherkati (2004) led to reconsider former conclusions about chronological relationships between folding and flap formation. As claimed by the author, development of flap subsequent to fold growth turns out to be irrealistic, and a rather synchroneous evolution is proposed, therefore associated with a progressive migration of the syncline hinge (Fig. 11b). Such kinematic interpretation of flap devel-
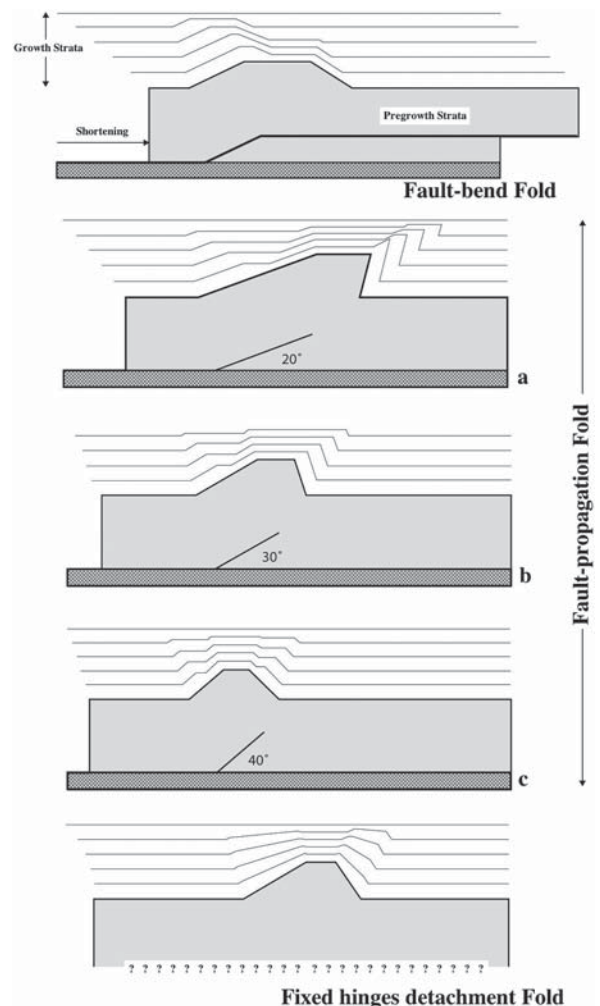
Fig. 10. Growth strata geometry associated to principal fold model (using original (EM) program, developed according to Suppe et al., 1992, et Storti and Poblet's, 1997 concepts). Constant ratio > 1: Sedimentation rate/Tectonic up-lift. **a** Fault-Bend Fold; **b** Fault-Propagation Fold with fault dip respectively (a, b, c) 20°, 30° & 40°: **c** Fixed hinge Detachment Fold
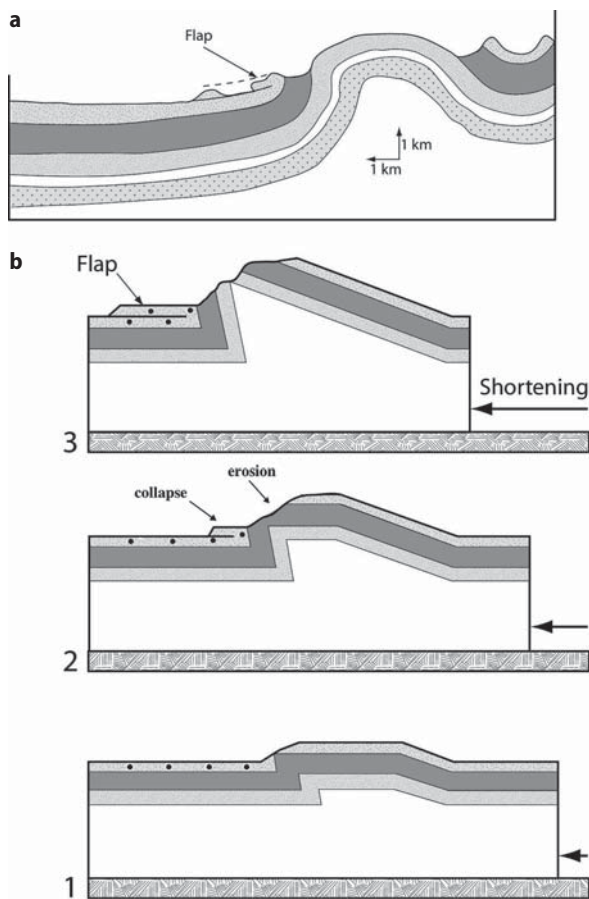
Fig. 11. (a) Example of Flap structure (Harrison and Falcon, 1934), **(b)** kinematic interpretation modified from Mercier et al. (1994)

opment, attesting of hinge migration occurrence, was shared by other works based on observation of natural examples (Mercier et al., 1994; Saint Bezar et al., 1998, 1999).

Nevertheless discussions about flap structures continue. First, the hangingwall mechanics of the flap still is not defined, and second, Storti and Salvini (1999) have proposed another kinematic model prospecting the occurrence of reverse series by the "roll-over fault-propagation fold". Yet, this hypothesis prognoses explicitly the hinge migration process.

4   Morphological Imprints

Reliefs formed after faulting and folding are immediately exposed to erosion, notably as a consequence of the increasing topographic difference with the hydrographic base level. Morphological evolution is controlled by independent factors such as lithology, climate, eustatism and local tectonic activity. In spite of the complexity of these phenomena, numerous attempts of conducting morphological analysis to investigate fault dynamics are available in the literature.

Concerning the dynamics of folds amplification, Medwedeff (1992) and Mueller and Suppe (1997), led pioneer works in order to constrain hinge behaviour from mophological observations, carried out on syncline hinges associated to Wedge Thrust structure (Fig. 7) located in the Wheeler Ridge (California). These authors have demonstrated that terraces and alluvial fans were progressively incorporated into limbs, hence continuously uplifted during fold growth. It should be noticed that such interpretation was recently criticized by Bielecki and Mueller (2002) who proposed to interpret morphological features in terms of solifluction processes.

Following the same approach, Scharer et al. (2005) recently obtained insights about the dynamics of an active detachment fold system from fluvial terraces characterization in southwestern China (Tian Shan basin), which allowed the authors to conclude in a combined hinge migration and limb rotation behaviour.

Specifically, drainage network maturity and river longitudinal profile anomalies constitute relevant arguments for constraining the kinematics of folding. Such approach was developed by Delcaillau et al. (1998, in press), Delcaillau (2001, 2004), Champbel et al. (2002) and Jie et al. (2005), who focused on lateral amplification of several fold systems located in northern India, Taiwan and China. These studies illustrated the effects of a progressive incorporation into limbs of initially horizontal sectors, consistent with a gradual migration of the hinges during fold growth. Recently tilted areas are characterized by juvenile parallel drainage systems with few confluences as well as river longitudinal profiles far from the equilibrium profile.

Ahmadi et al. (2006) also used equilibrium profiles and drainage network maturity criteria to investigate fold kinematics in the Tunisian Atlas quaternary system. As shown by the authors, the base level here remains constant since the early stages of folding as it is not affected by eustatic changes (endoreic salt lake). Moreover, the present erosional surface of the anticline is assimilated to a structural surface (top of a massive limestone thick level) over the entire structure, leading to homogeneous surficial lithologic conditions (Fig. 12). A major consequence of such a peculiar context is that eustatic and lithological influences can be overridden, thus allowing erosional activity to be interpreted as a direct response to tectonic uplift. This study permitted to demonstrate that folds grow laterally exclusively involving hinge migration and demonstrated, as a more important conclusion, that anticlines evolve within outward hinge migration and a continuous incorporation into fold limbs of intially horizontal material from both sides of the hill (Fig.13).
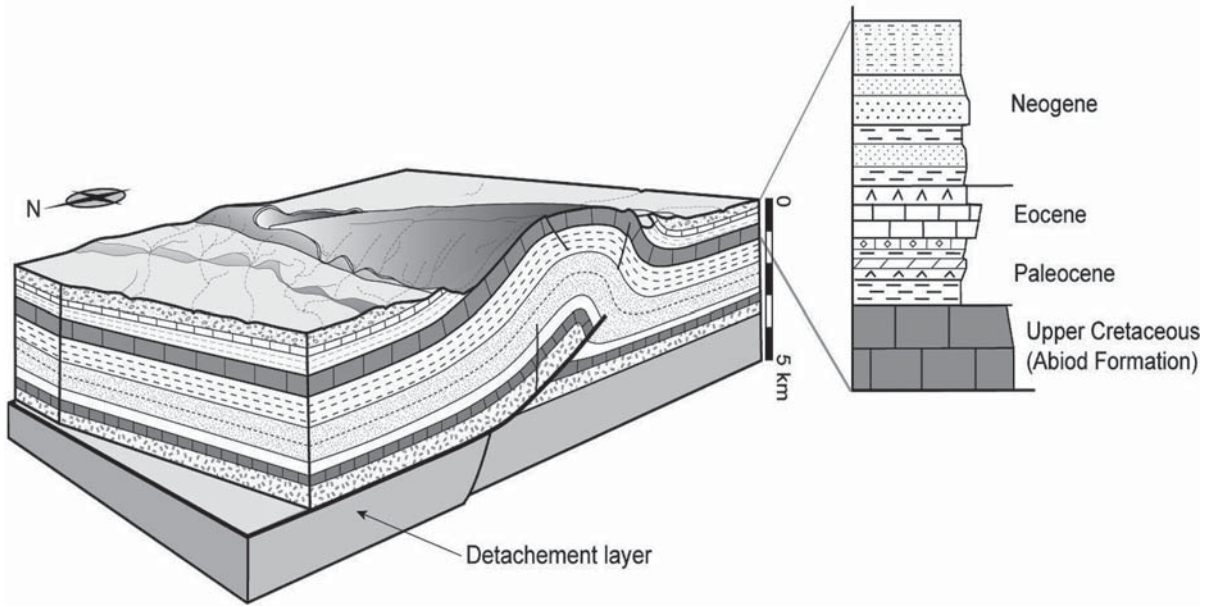
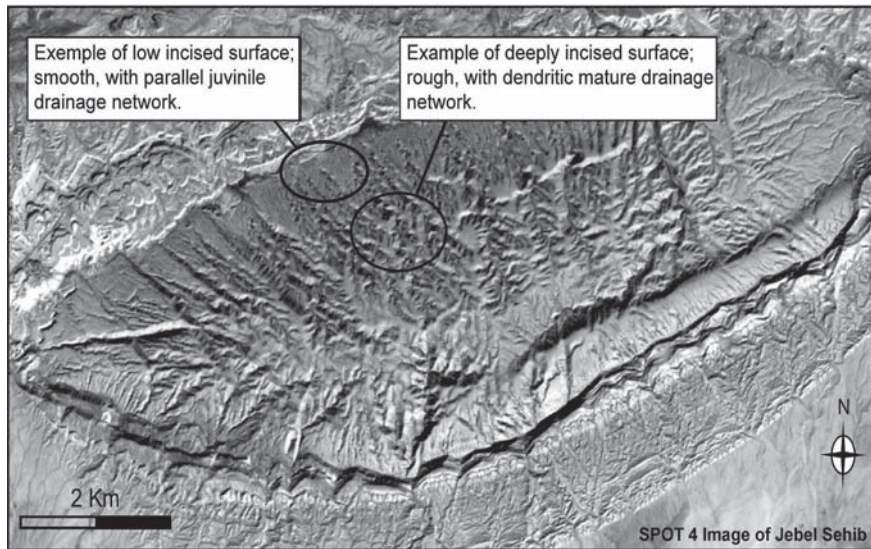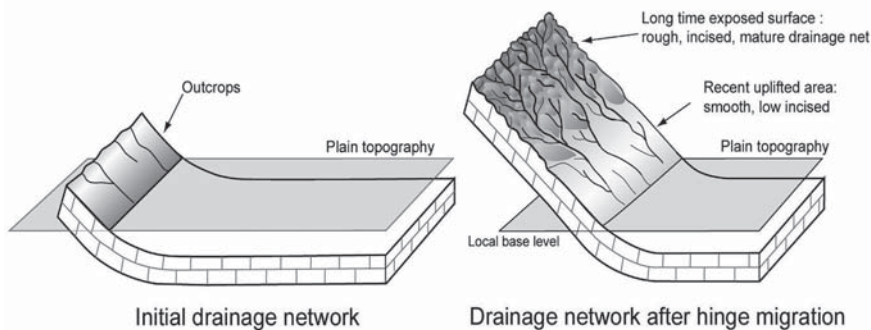**Fig. 12.** Diagram showing the Jebel Sehib deep geometry (cf. Fig. 13)

Fig. 13. Morphological feature in migrating hinge fold model example of Jebel Sehib (inspired from Ahmadi et al. (2006)). Note the differential incision and drainage network maturation in this mobile hinge case: material feed to fold core through back syncline hinge in Fault-propagation fold

Such results are perfectly consistent with predictions of the fault-propagation fold kinematic model (Fig. 4)

5   Microtectonic Signatures

Characterization of a finite deformation stage through micro- and meso-structural analysis of folds in order to constrain their growth mechanisms constitutes the most conventional approach, and certainly the most intuitive. Indeed, classical theoretical kinematic models of folding predict secondary deformation patterns (joints, shearing micro- and meso-faults, styloliths...) consecutive to folds amplification (e.g. Price and Cosgroove, 1990), that were extensively investigated as potential markers of folding intermediate stages. Authors commonly distinguish two ways of accommodating such folding-related internal stresses: flexural flow and flexural slip.

However, according to theoretical models, the accommodation of secondary deformations into fold limbs (simple shearing) does not represent a diagnostic tool, as different types of folds can lead to similar finite deformation patterns (e.g. Saint Bezar et al. 1998; Rafini and Mercier, 2002). On the other hand, hinge deformations (pure shearing) should theoretically provide a particularly relevant kinematic marker of hinge migration occurrence as the entire limb at a given stage is necessarily passed through hinges at former stages and supposedly underwent characteristic deformations, thus bearing precious records of hinge behaviours.

Pioneer microstructural analyses addressing this problem were carried by Beutner et al. (1988) on a Thrust Sheet structure, therefore associated to a flat to ramp to flat system (Fig. 7) in which implication of a hinge migration process is implicit. Targeted pellitic and limestone intercalations allochthone series exhibited three distinct cleavages synchronous with thrusting, as well as numerous microstructures (fracture sets, pressure shadow…). Such field conditions seem well suited to constrain hinge kinematics from microtectonic analysis. Nevertheless, the authors concluded that "The structures described above do not lead uniquely or even necessarily to a kinematic interpretation involving a flat to ramp to flat setting".

The hinge migration, that Beutner et al. (1988) failed to demonstrate from numerous microtectonic markers on a simple elementary structure (flat/ramp system), turns out to be almost impossible to achieve on more complicated folds. Fischer et al. (1992) and Fischer and Anastasio (1994), who studied several folds in the Rocky Mountains as well as in the Appalachian fold belt, exclusively conclude to the occurrence of limb rotation processes. A similar conclusion was also achieved by other works: Hedlund et al. (1994) in

the Rocky Mountains, Mansy et al. (1995) and Lacquement et al. (1997) in the Ardennes, Grelaud et al. (2000) in the Pyrenees, and Guiton et al. (2003) in Morocco.

Finally, Ahmadi et al. (submited) led a similar analysis on a structure that was proven from morphological arguments to evolve with hinge migration. As an achievement, these authors could not demonstrate hinge migration from microtectonic observations although it was unequivocally occurring.

Results mentioned in this chapter highlight the fact that demonstration of a hinge migration occurrence from microtectonic observations could almost never be achieved in the literature. Note that, as generally predicted by folding kinematic models, material formerly situated on hinges is progressively incorporated during fold growth into limbs that keep undergoing significant simple-shearing. Such evolution can possibly generate an overprint of primary hinge deformations, as a consequence of subsequent shearing into
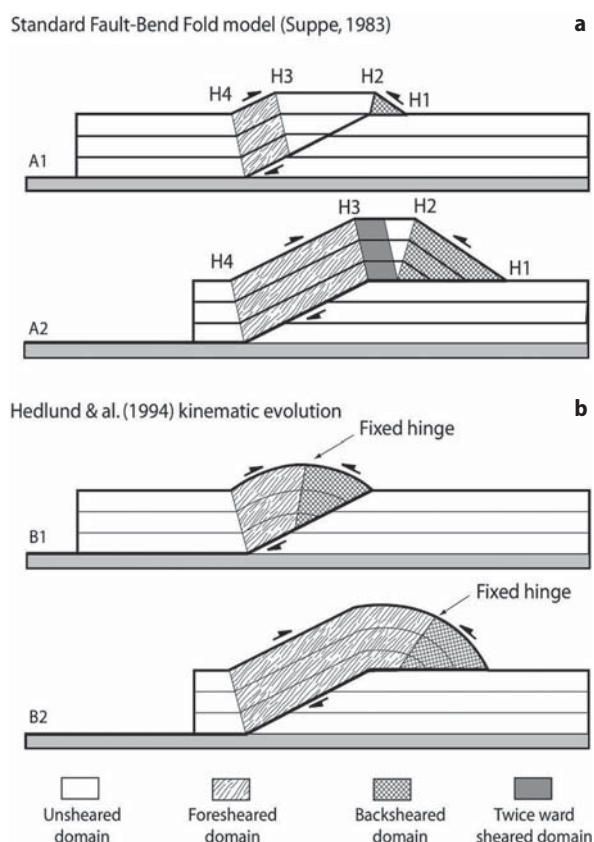
Fig. 14. **a** Internal deformation mechanics relative to Fault-Bend Fold model. **b** Main conclusions of Hedlund et al. (1994) work. According to these authors the observed finite deformation indicates a fixed hinge. Note that this model considers the hinge migration in the back syncline hinge, but did not respect the excess area low at all kinematic stages

limbs, leading to a total vanishing of hinge-migration inherited microtectonic records.

As a sole example, Thorbjornsen and Dunne (1997, Fig. 14a) could observe some evidence of hinge motion related to the development of a thrust-related anticline into sandstone series, localised in the central Appalachian Plateau (West Virginia). They measured mesoscale contraction faults in the inner arcs of the forelimb, which they interpreted to be formed in the hinge and have moved to the forelimb as the hinge migrated. It should be pointed out that the preservation of these structures, although they coexist with a significant layer-parallel simple-shearing into the limb, is certainly to be related to their size (mesoscale), and then to the rheological properties of sandstone formations in which stratigraphical discontinuities are typically less frequent than in carbonaceous rocks, favouring propagation of inner arc contractional faults from microscale to mesoscale.

Considering authors who conclude to fixed hinges, we expect two cases:

- In some cases, fixed hinges are compatible with kinematic models. For instance, Fischer et al. (1992) demonstrated the absence of frontal hinge mobility in the Hossfeldt anticline which has a typical Fault-Propagation fold geometry. According to the kinematics of this fold model (Fig. 4), the frontal hinge has a weakly mobile to stationary behaviour.
- In other cases, authors failed to demonstrate the hinge mobility, concluding to fixed hinge and underlining the inconsistency with the referred model (e.g. Fig. 14).

6   General Discussion and Conclusions

As a first achievement, the review conducted in this paper high lights the fact that both theoretically predicted hinge behaviours - that is, mobile hinges, and fixed hinges associated to limb rotation - do effectively occur, and coexist in Fold and Thrust Belts domains.

Nevertheless, we show that field examples of the second process are overrepresented as compared to the first one. Indeed, even after about fifteen years of worldwide research activities, case studies in which hinge migration could be formally achieved remain very scarce.

Furthermore, the scarcity of hinge migration field examples treated in bibliography can reasonably relate to a lack of relevant markers. As mentioned above, growth strata analysis provides persuasive criteria. Yet, it turns out to be in practice sorely useable considering that i) folds associated with growth strata are infrequent, and ii) when it occurs, the unequivocal interpretation in terms of hinge migration requires de-

tailed geometric observations and a particularly good preservation of the structure which is rarely available. Likewise, flap structures occurrences are exceptional in nature, and preservation conditions allowing their morphological analysis are very demanding so that such structures remain infrequently mentioned in the literature. Moreover, microtectonic features must be potentially present in all hinges. However, our review concludes that although numerous studies were conducted, the microtectonic arguments for kinematic analysis is poorly convenient, and hardly none of these works could lead to an accurate achievement concerning hinge migration occurrences even when the latter was demonstrated from subsidiary approaches.

We mentioned that almost all of fold kinematic models use the hinge migration process. The statistical overrepresentation of fixed hinges behaviour in our inventory thus appears as paradoxal, and needs to be closely explained.

Thus, we propose that there may exist methodological biasings that favour hinges fixity rather than mobility. The growth strata analysis approach illustrates the fact that phenomena such as erosion occurring synchroneously or subsequently to deformation may alter some diagnostic geometric arguments for hinges migration, leading authors to conclude fixed hinge behaviour. Similarly, the lack of specific tectonic arguments for mobile hinges was interpreted by some authors as a demonstration of the fixity of hinges. In fact, it seems clear that authors intuitively consider hinge fixity as a casual process whereas hinge migration needs to be demonstrated. In other words, hinge fixity behaviour is assumed as long as their migration is not proven.

Nevertheless, some studies distinctly establish the occurrence of hinge fixity from explicit arguments, and several works achieved that all hinges remain fixed during fold growth (e.g. Poblet and Hardy, 1995; Mansy et al., 1995; Lacquement et al., 1997; Masaferro et al., 2002; Grando and McClay, 2004). The existence of fixed hinge folds can lead to any of the following conclusions:

- In these cases, validity conditions for the application of the excess area law are not verified. Therefore, either i) deformation is not planar, which is always true for folds related to hallocinetic phenomena. This could explain fixed hinge folds studied by Poblet and Hardy (1995), Masaferro et al. (2002), and Grando and McClay (2004). ii) Shortening is not perpendicular to the structure axis, we known for instance that folds associated to lateral ramps evolve exclusively by limb rotation processes (Frizon de Lamotte et al., 1995).
- The classical expression of the excess area law has to be revised. We here highlight the fact that few

essentially theoretical works, based on modifications of the classical formulation of this law, led to some consensus concerning its application to the fixed-hinges fold models (Hardy and Ford, 1997; Allmendinger, 1998; Groshong and Epard, 1994; Homza and Wallace, 1995; Hardy and Finch 2005).

To summarize, the different methods investigated to get insights about the kinematics of folds appears to be less efficient at demonstrating hinge migration than hinge fixity due to a higher sensitivity of the diagnostic features to preservation conditions (erosion of growth strata, microtectonic overprinting…). The unbalanced sampling of these two hinge behaviours after numerous field studies may thus not be reflecting realistic processes, as suggested by theoretical kinematic modeling. In contrast with broadly used markers as growth strata and microtectonics, the more recent development of the morphological imprints analysis method turns out to be very relevant, and less subject to preservation sensitivity. Nevertheless, such arguments result from a complex dynamics of surficial phenomena that require further research investigations.

Acknowledgements

References

Ahmadi, R., Mercier, E., Ouali, J., Mansy, J.L., Van-Vliet Lanoe, B., Launeau, P. & Rhekiss, F. (2006). The geomorphological hallmarks of hinges migration in fault related folds. A study case in southern tunisian atlas. Journal of Structural Geology. 28, 721–728.

Ahmadi R., Mercier E., Ouali J. Rhekiss F. (Submitted). Relationship between folding and fracture in fault-related fold. Case of Jebel Sehib Tunisian Atlas: a single-step Fault-Propagation Fold.

Allmendinger R.W. (1998). Inverse and forward numerical modelling of tri-shear fault-propagation folds, Tectonics, 17, 640–656.

Al Saffar M. (1993). Geometry of fault-propagation folds: method and application Tectonophysics, 223, 363–380.

Anadon, P. Cabrera, L. Colombo, F. Marzo, M. Riba, O. (1986). Syntectonic intraformational unconformities in alluvial fan deposits, eastern Ebro Basin margins (NE Spain). Foreland basins. Eds. Allen and Homewood. Spec. Publs int. Ass. Sediment. N° 8. 259–271.

Bernal, A Hardy, S. (2002). Syn-tectonic sedimentation associated with three-dimensional fault-bend fold structures: a numerical approach, Journal of Structural Geology, 24, 609–635.

Beutner, E.C. Fisher, D.M Kirkpatrick, J.L. (1988). Kinematics of deformation at a thrust fault ramp from syntectonic fibers in pressure shadows, Geol. Soc. Am. Special paper 222, 77–88.

Bielecki, A. E., Mueller, K. J., (2002). Origin of terraced hill slopes on active folds in the southern San Joaquin Valley, California. Geomorphology, 42, 131–152.

Champel B., van der Beek, P.A., Mugnier J.L., & Leturmy P. (2002). Growth and lateral propagation of fault related folds in the Siwaliks of western Nepal : Rates, mechanisms and geomorphic signature. Journal of Geophysical Research, 107 (B6), 10.1029/2001JB000578.

Chester J. S. & Chester F. M. (1990).- Fault-propagation folds above thrusts with constant dip. Journal of Structural Geology, 12, 903–910.

Colombo F. & Vergès J. (1992). Geometría del margen S.E. de la Cuenca del Ebro: discordancias progresivas en el Grupo Scala Dei. Serra de La Llena (Tarragona) Acta Geologica Hispanica, 27, 33–53.

Curie J.B., Pantnode H.W. & Trump R.P. (1962). Devevelopment of folds in sedimentary strata. Géol. Soc. Am. Bull. 73, 655–674.

Dahlstrom, C. D. A. (1969). Balanced cross-sections, Canadian Journal of Earth Sciences , 6, 743–757.

Dahlstrom C. D. A. (1990). Geometric constraints derived from the law of conservation of volume and applied to evolutionnary models for detachment folding, A. A. P. G. Bull. , 74, 336–344.

Delcaillau B. (2001). Geomorphic response to growing fault-related folds: example from the foothills of central Taiwan. Geodinamica Acta, 14, 265– 287.

Delcaillau B., (2004). Reliefs et Tectonique récente. Vuibert (Ed.), Paris, 262 pp.

Delcaillau B., Deffontaines B., Angelier J., Deramond J., Floissac L., Souquet P. & Chu, H.T., (1998). Morphotectonic evidence from lateral propagation of an active frontal fold; the Pakuashan anticline, foothills of Taiwan. Geomorphology, 24, 263– 290.

Delcaillau B., Carozza J.M. & Laville E. (in press). Recent fold growth and drainage development: The Janauri and Chandigarh anticlines in the Siwalik foothills, northwest India Geomorphology,

De Sitter, L.V. (1956). Structural Geology : New York, McGraw-Hill, 552 p..

Epard J.L. & Groshong R.H. (1995). Kinematic model of detachment folding including limb rotation, fixed hinges and layer-parellel strain, Tectonophysics, 247, 85–103.

Fischer M. P., Woodward M. B. & Mitchell M. M. (1992). The kinematics of break-thrust folds. J. Struct. Geol. ,14, 451–460.

Fisher D. M. & Anastasio D. J. (1994). Kinematic analysis of a large-scale leading edge fold, Lost River Range, Idaho. Journal of Structural Geology , 16, p. 337–354.

Ford M., Williams E.A., Vergés J., & Hardy S., (1997). Progressive evolution of a fault-related fold pair from growth strata geometries, Sant Llorenc̜ de Morunys, SE Pyrenees. Journal of Structural Geology, 19, 413–441.

Frizon de Lamotte D., Guezou J.C. & Averbuch O. (1995). Distinguishing lateral folds in thrust-systems; examples from Corbières (SW France) and Betic Cordilleras (SE Spain) Journal of Structural Geology, 17, 233–244.

Grando G. & McClay K. (2004). Structural evolution of the Frampton growth fold system, Atwater Valley-Southern Green Canyon area, deep water Gulf of Mexico, Marine and Petroleum Geology, 21, 889–910.

Graham, S.A., Tolson, R.B., Decelles, P.G., Ingersoll, R.V., Bargar, E., Caldwell, M., Cavazza, W., Edwards, D.P., Follo, M.F., Handschy, L., Lemke, L., Moxon, I., Rice, R., & Smith, G.A., (1986). Provenance modelling as a technique for analysing source terrane evolution and controls on foreland sedimentation, in Allen, P.A., and Homewood, P., eds., Foreland basins: International Association of Sedimentologists, Special Publication 8, 425–436.

Grelaud S., Buil S., Hardy S. & Frizon de Lamotte, D. (2000). Trishear kinematic model of fault-propagation folding and sequential development of minor structures: the Oupia anticline (NE Pyrenees, France) case study. Bulletin de la Société Géologique de France, 171, 441–449.

Groshong R. H. & Epard J.-L. (1994). The role of strain in area-constant detachment folding. Journal of Structural Geology, 16, 613–618.

Guiton M. L. E., Sassi W., Leroy Y.M. & Gauthier B. D. M. (2003). Mechanical constraints on the chronology of fracture activation in folded Devonian sandstone of the western Moroccan Anti-Atlas. Journal of Structural Geology, 25, 1317–1330.

Hardy S. & Poblet J. (1994). Geometric and numerical model of progressive limb rotation in detachment folds. Geology, 22, 371–374.

Hardy S.& Poblet J. (1995). The velocity description of deformation: Paper 2. Sediment geometries associated with fault-bend and fault-propagation folds. Marine and Petroleum Geology. 12, 165–176.

Hardy S. & Ford M. (1997). Numerical modelling of trishear fault propagation folding. Tectonics, 16, 841–854.

Hardy S. & Finch E. (2005). Discrete-element modelling of detachment folding, Basin Research,17, 507–520.

Harrison J. V. & Falcon N. L. (1934). Collapse structures. Geological magazine, LXXI, 529–534.

Hedlund C. A. Anastasio D. J. & Fisher D.M. (1994). Kinematics of fault-related folding in a duplex, Lost River Range, Idaho, USA., Journal of Structural Geology ,16, p. 571–584.

Homza T.X. & Wallace W.K., (1997). Detachment folds with fixed hinges and variable detachment depth, northeastern Brooks range, Alaska. Journal of Structural Geology, 19, 337–354.

Chen Jie, R. Heermance, D.W. Burbank, K.M. Scharer & Wang C.S. (2005). Lateral Propagation And Growth Of Quaternary Kashi-Atushi Detachment Fold System In The Southwestern Tian Shan - Tarim Foreland, China, international conference on "Theory and Application of Fault-Related Folding in Foreland Basins" Beijing, 59–60.

Lacquement F., Mansy JL, Mercier E., Averbuch O. & Meilliez F. (1997). Mécanismes de plissement disharmonique dans le Paléozoïque Ardennais., Aardk. Medel., 8, 119–122.

Mansy J. L., Meilliez F., Mercier E., Khatir A. & Boulvain F. (1995). Le rôle du plissement disharmonique dans la tectonogenèse de l'allochtone ardennais. Bulletin de la Société géologique de France, 166, 295–302.

Masaferro J.L., Bulnes M., Poblet J.& Eberli G.P.(2002). Episodic folding inferred from syntectonic carbonate sedimentation: the Santaren anticline, Bahamas foreland Sedimentary Geology, 146, 11–24

McClay K. R. (1992). Glossary of thrust tectonics terms. Thrust tectonics , Ed. K. R. McClay. Chapman and Hall (Ed). 419–433.

Medwedeff D. A. (1989). Growth fault bend folding at Southeast Lost Hills, San Joaquin Valley, California. A. A. P. G. Bull., 73, p. 54–67.

Medwedeff D.A. (1992). In: Mitra, S. & Fisher, G.W. (Eds.), Geometry and Kinematics of an Active, Laterally Propagating Wedge Thrust, Wheeler Ridge, California, Structural Geology of Fold and Thrust Belts, John Hopkins Studies in Earth and Space Sciences, vol. 5, 1–28.

Mercier E. (1992). Une évolution possible des chevauchements associés aux plis de propagation : le transport sur le plat (modélisation et exemple. Bulletin de la Société géologique de France, 163, 713–720.

Mercier E., De Putter T., Mansy J. L. & Herbosch A. (1994). L'écaille des Gaux (Ardennes belges): un exemple d'évolution tectono-sédimentaire complexe lors du développement d'un pli de propagation. Geol. Rundsch. 83, 170–179.

Mercier E., Outtani F. & Frizon de Lamotte D. (1997). Late evolution of fault-propagation folds: principles and example. Journal of Structural Geology, 19, 185–193.

Mercier E., Ahmadi R. & Rafini S. (Submitted) Fixed hinges detachment fold: a new kinematic model compatible with the "excess area law" Tectonophysics.

Mueller K. & Suppe J. (1997). Growth of Wheeler Ridge anticline, California: geomorphic evidence for fault-bend folding behaviour during earthquakes. Journal of Structural Geology 19, 383–396.

Poblet J. & Hardy S. (1995). Reverse modelling of detachment folds; application to the Pico del Aguila anticline in the South Central Pyrenees (Spain). Journal of Structural Geology. 17, 1707– 1724.

Poblet J. & McClay K. (1996). Geometry and kynematics of singlelayer detachment folds, A. A. P. G. Bull., 80, 1085– 1109.

Price N. J. & Cosgroves J. W. (1990). Analysis of geological structures. Cambridge University Press 1990. p 366–384.

Rafini S. & Mercier E. (2002). Forward modelling of foreland progressive unconformities. Sedimentary Geology, 146, 75–89.

Riba O. (1976). Tectonogenèse et sédimentation: deux modèles de discordances syntectoniques pyrénéennes. Bull. B. R.G.M. (2ème série, Section 1) 4, 383– 401.

Saint Bezar B., D. Frizon de Lamotte, J.L. Morel & E. Mercier (1998). Kinematics of large scale tip line folds from the High Atlas thrust belt (Morocco). Journal of Structural Geology. 20, 999–1011.

Saint Bezar B., D. Frizon de Lamotte, J.L. Morel & E. Mercier (1999). Kinematics of large scale tip line folds from the High Atlas thrust belt (Morocco) : Reply. Journal of Structural Geology. 21, 691–693

Salvini F., Storti F. & McClay K. (2001). Self-determining numerical modeling of compressional fault-bend folding, Geology , 29: 839–842.

Salvini F. & Storti F.(2002). Three-dimensional architecture of growth strata associated to fault-bend, fault-propagation, and décollement anticlines in non-erosional environments. Sedimentary Geology, 146, 57–73.

Scharer K. M., Jie Chen, Burbank D. W, Weldon, R. J. II & Heermance R. (2005). Late Quaternary Fluvial Terraces Response To The Active Kashi-Atushi Detachment Fold System In The Southwestern Chinese Tian Shan Foreland Basin, international conference on "Theory and Application of Fault-Related Folding in Foreland Basins" Beijing, 143–144.

Shaw J. H. & Suppe J. (1994). Active faulting and growth folding in the eastern Santa Barbara Channel, California, Geol. Soc. Am. Bull. , 106, 607–626.

Sherkati S. (2004). Style tectonique et cinématique du plissement dans le Zagros Iranien : conséquences pétrolières. PhD Thesis, Université de Cergy-Pontoise.

Storti F. & Poblet J. (1997). Growth strata architectures associated to decollement folds and fault-propagation folds. Inferences on fold kinematics. Tectonophysics, 282, 353–373.

Storti F. & Salvini F. (1999). Kinematics of large scale tip line folds from the High Atlas thrust belt (Morocco): Discussion. Journal of Structural Geology. 21, 689–690.

Suppe J. (1983). Geometry and kinematics of fault-bend folding. American J. Sc. , 283, p. 684–721.

Suppe J. (1985). Principles of structural geology. Englewood Cliffs, New Jersey, Prenctice-Hall Inc. 537 p.

Suppe J., Chou T. G. & Hook S. C. (1992). Rates of folding and faulting determined from growth strata. Thrust tectonics Ed. K. R. McClay, Chapman & Hall., 105–121.

Suppe J., Sabat F., Munoz J.A., Poblet J., Roca E.,& Vergés J., (1997). Bed-by-Bed folg growth by kink-band migration: Sant Llorenc̦ de Morunys, Eastern Pyrenees. Journal of Structural Geology, 19, 443–461.

Thorbjornsen K.L. & Dunne W.M. (1997). Origin of a thrust-related fold: geometric vs kinematic tests, Journal of Structural Geology, 19, 303–319.

Vergés, J., Burbank, D.W., & Meigs, A. J., (1996). Unfolding: An inverse approach to fold kinematics. Geology, 24, 175–178.

Wickham J. (1995). Fault displacement-gradient folds and the structure at Lost Hills California (USA), Journal of Structural Geology, 17, 1293–1302.

Zapata T.R. & Allmendinger R.W. (1996). Growth stratal records of instantaneous and progressive limb rotation in the Precordillera thrust belt and Bermejo basin, Argentina. Tectonics, 15, 1065–1083.

The Use of Surface Restoration in Foothills Exploration: Theory and Application to the Sub-Andean Zone of Bolivia

Isabelle Moretti · V. Delos · J. Letouzey · A. Otero · J.C Calvo

Abstract There are various methods to restore horizon surfaces. As in cross-section balancing, either simple shear deformation mode or flexural slip approach can be proposed. The first mode of deformation preserves the distances in a given direction, whereas the second one preserves the length and angles on the surface, i.e. the areas. After a presentation of the methods, we will discuss on a case study the information about the correctness of the geometry as well as the dilatation and internal strain directions that could be deduced from restoration.

The studied area consists on a set of thrust sheets located in the southern Sub-Andean Zone in the Neogene Andean Foothills of Bolivia. The hydrocarbon targets are quite deep and located on the hinge of steep anticlines where the seismic images show a poor resolution. Balancing techniques are therefore crucial for the definition of the target. Because the reservoir, lower Devonian in age, is tight, the quantification of the strain is expected to predict the fractures. Surface restoration process allows to compute a strain field. Results, eigen values, main strain direction and dilatation, will be shown for the top reservoir of one of the structures. Because the computed internal strain tensor is highly dependent on the method used for the restoration, we will describe which results can be expect from each method.

1 Introduction

The peak of the development of balanced cross-section tools in the 90's led to various commercial products (Geosec, Locace, 2D Move; Kliegfield et al., 1986; Moretti & Larrère, 1989). The research continued with the surface unfolding (Gratier & Guillier, 1993; Mallet & Massot, 2001) and we are now close to the emergence of commercial products for true 3D restoration (Moretti et al., 2006a). Considering that the mathematical and computer science problems are now solved for surface restoration, one can focus on the geological questions. There are different algorithms and different ways to use these algorithms. Which property characterizes each one? How to choose the most appropriate

one, not based on software availability but on geological context? The aim of this paper is to answer these questions.

In the following, we will call surface restoration or 2.5D restoration the processes that allow to unfold and unfault a surface corresponding to a horizon. It is a backward process that can be performed using commercial products such as 3D Move or KINE3D-2, among others, although many non-commercial products and prototypes also exist. We will call 2D restoration the cross-section balancing process and 3D restoration the volumic restoration. Geological/physical concepts such as deformation modes are important, but in 3D, there is no way to apply a concept to real data set "by hand". Therefore, algorithms must translate these concepts into mathematical properties. Then, the software tools allow the geologist to apply them. When developing 3D tools, we frequently need to simplify the geological/physical concepts in order to make the tools stable, or easy to use, when not just existing. In this paper we tried to clarify the hypotheses behind some concepts and algorithms and the eventual gaps between them. Commercial software tools usually propose numerous methods, but they do not always specify which method must be applied to a given geological case.

The construction of stratigraphic surfaces and tectonic horizons such as faults, which is required to build the 3D model from the data, is another challenge that we will not describe in detail here. The incorporation of a priori concepts, such as the unfoldability of the horizons, clearly helps to constrain this construction when the data are not numerous nor precise enough. Such an approach has been described amongst others by Galera et al. (2003) and Thibert et al. (2006). This first step is fundamental and definitively helps to construct coherent horizon in a given area. In the current paper however, we will focus on the following step, i.e., we will see how the restoration may, or may not, help defining the horizon geometry, the fault offset and the fracture network.

2   Methods

2.1 Cross-Section Restoration Modes

In 2D restoration, the methods have been rather well established for a couple of years, the basic assumption being the preservation of the areas in a vertical plane (plane strain hypothesis) corrected, or not, by the compaction/decompaction effects. The four main deformation modes are the flexural slip, the simple shear, the ductile flow and the rigid rotation. Figure 1 and Table 1 synthesize the corresponding deformation and the quantities that are preserved for each method.

- With the flexural slip method, the principle is to preserve in a vertical plane layer areas, lengths and thicknesses. If the restored layer is isopach, the preservation of both thickness and length results in the area conservation. If the thickness varies, the strict preservation of bed thickness and bed length may

lead to area changes. In the commercial tool that proposes this method - flexural slip for non-isopach layer - LOCACE, the user may choose to give priority to the preservation of lengths or to the preservation of thicknesses (see Moretti et al., 1989 for details).

- With the simple shear method one preserves the distance in the shear direction (neither the length, nor the thickness), the areas being not preserved. The shear direction can be defined on laboratory measurements for various granular materials, and is usually around 60°. However, it is more difficult for natural rocks moving along pre-existing faults, at the time scale of the geological deformation, because increasing compaction may change their mechanical behavior versus depth; this has been debated by various authors (Verrall, 1981; Gibbs, 1983; White et al., 1986; Faure and Chermette, 1989)

- With the ductile flow, the appropriate method to apply for decollement levels such as shale or salt, only the global area is preserved. It is a simplification of the 3D volume conservation.
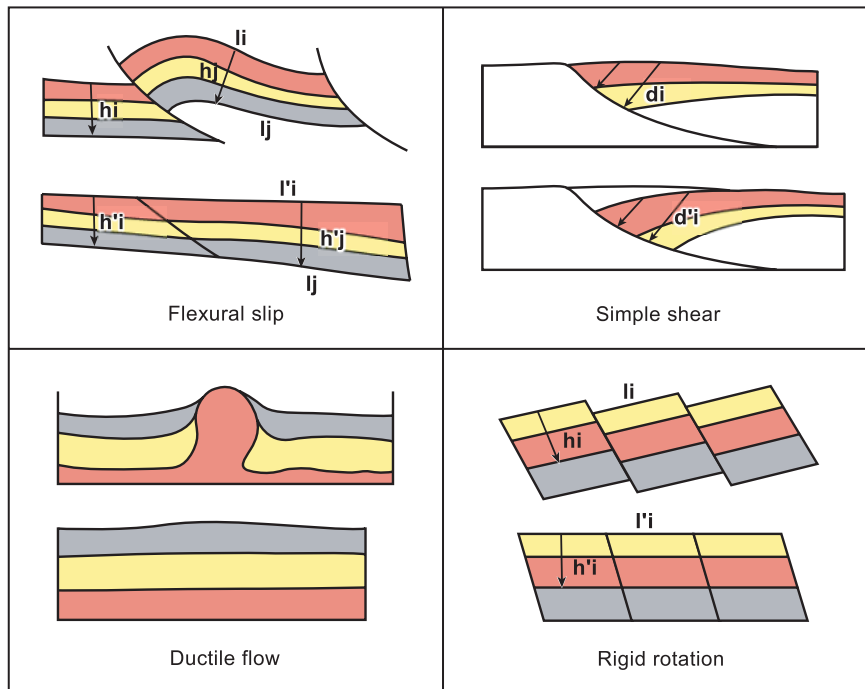
Fig. 1. The four main deformation modes in cross-section restoration: Flexural slip, Simple shear, Ductile flow and Rigid rotation. Characteristic lengths are: h for thickness, l for bed length, and d for distance in the shear direction (simple shear case)

Values	Flecural slip	Simple shear	Ductil flow	Rigid rotation
Global surface	$S = S'$	$S > S'$	$S \neq S'$	$S = S'$
Thickness of the horizon	$H_i = H'_i{}'$	$H_i \neq H'_i{}'$	no coincidence	$H_i = H'_i{}'$
Length of the horizon	$L_i = L_i{}'$	$L_i > L_i{}'$	no coincidence	$L_i = L_i{}'$

Table 1. Conservation of characteristic lengths (thickness H and bed length L) and area (S). Letter refers to initial geometry and prime to the unfolded one

▪ With the rigid rotation, also called domino style (Angelier & Colletta, 1983), within a given faulted block everything is preserved, including bed lengths, thicknesses, areas and even cut-off angles between faults and horizons.

While balancing a cross-section, the geologist often has to use more than one deformation mode. For instance, in compressional areas, a combination of flexural slip for the competent layers and ductile flow for the poorly competent decollement levels is required. At smaller scale, the tryshear concept combines the flexural slip and the simple shear methods. Sometimes, the final geometry of the layers as well as the fault shape and the horizon-fault cut-off help the geologist to choose the right deformation mode: concen-

tric folds require flexural slip deformation when similar folds are compatible with a simple shear mode.

2.2 Unfolding

In 2.5D restoration, one needs to unfold the structures and to erase the fault offsets. The first step to restore a horizon is to have a representation of this horizon through a surface, generally intersected by faults. The representation of a surface can be determinist, i.e. nodes on a triangular or rectangular mesh, or implicit, a continuous equation allowing to represent the surface at any scale. Similarly the unfolding may be based on a discrete or continuous approach, i.e. based on triangle (or square), on node displacements or on a global

Fig. 2. Methods of surface unfolding and main preserved parameters. See the text for the description of each methods. *Green* planes indicate that during the unfolding, the elements remain in the same vertical section
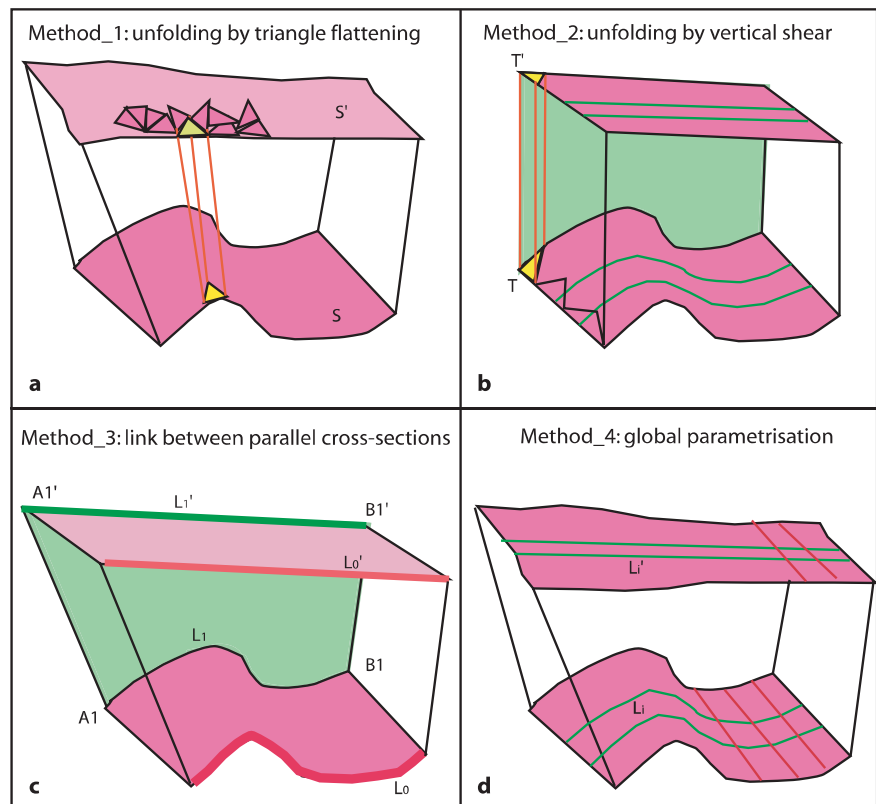
Table 2. Conservation of characteristic lengths (bed length L_i), bed area (S) and triangle area (T). Letter refers to initial geometry and prime to the unfolded one

Values	Method 1	Method 2	Method 3	Method 4
Global surface	S ~ S′	S > S′	S ≠ S′	S = S′
Surface of one triangle	Area T = Area T′	Area T > Area T′	no coincidence	Area T = Area T′
Length of the horizon in a given direction	$L_i \approx L_i'$ if the surface is developable	$L_0 > L_0'$ $L_1 > L_1'$	$L_0 = L_0'$ $L_1 = L_1'$	$L_0 = L_0'$ $L_1 = L_1'$ $L_i = L_i'$

transformation. Figure 2 synthesizes the four existing methods of unfolding and Table 2 lists the preserved characteristic lengths and area.

2.2.1   Method 1 - Triangle Adjustment

In the 90's, 2.5D restoration based on triangulated surfaces was tested (Gratier & Guillier 1993). The principle was to reset each tilted triangle in the same horizontal plane and then to look for the best adjustment between a flattened triangle and the previous ones already located in the final plane geometry. Despite some prototypes are still running (as UNFOLD, Gratier et al., 1999; Rouby et al., 2000), this approach has not been chosen for the development of industrial products since the results happened to be too dependent on the triangulation and on the search for the best fit during the adjustment of the flat triangles. The authors of UNFOLD guarantee that their last developments have allowed them to overcome this limitation in case of unfoldable surfaces.

2.2.2   Method 2 - Flattening-Simple Shear

The flattening is the simplest method. It is available in most geophysical work-stations and can be used on any surface representation. Mathematically it is very simple, being in a 3D space, with z as vertical coordinate, the transformation of a point is given by :

M (x,y,z) = > M'(x,y, Z constante value user defined) [vertical shear]

When picking seismic data, the explorationists use this method as a visualization functionality, not as a true restoration, especially when working with time-scale seismic data. However, the principle of some 2.5D restoration tools is to combine the flattening with a choice of the shear angle, as in 2D restoration, and possible translations.

To apply a simple shear method a reference level is required. In the flattening mode implementation as done in the geophysical software, the reference is the selected horizon. Another possibility is to consider the fault as reference (Sanders et al., 2005). This concept was initially proposed by Verall (1981) among others for the deformation of syntectonic sediment in an extensional context. The reference level is in that case a listric fault and its decollement level (Fig 1). The use of this deformation mode for restoration of competent beds in compressional areas remains highly questionable in 3D as in 2D: the horizon area is not preserved and, when more than one layer are restored, the thicknesses are not preserved.

2.2.3   Method 3 - Extrapolation of Parallel Cross-Sections Restoration

An alternative approach is based on the extension of the cross-section restoration. The horizons and faults are restored in a vertical plane, whereas the surfaces referring to the pre-deformation stage are built by linking the 2D cross-sections. The restoration in the cross-sections could have been done using flexural slip or simple shear deformation modes.

Although the description of this method is easy from an algorithmic point of view, its geological meaning is less clear and seem even contradictory: on one hand, one supposes that the deformation happens along a main direction, on another hand one allows the horizon length to change in the perpendicular direction; as a result the horizon areas are not preserved except if the case is purely cylindrical.

2.2.4   Method 4 - Global Area and Length Preservation

The other 2.5D restorations are now all based on a parameterization of the surfaces (Bennis et al. 1991; Mallet, 2001). They preserve the lengths and the areas of the horizons if the surface is unfoldable. If this is not the case, the algorithm will search the best solution. In KINE3D-2, for instance, the user may choose his preference between preservation of lengths (red and green lines in Fig 2d) and preservation of angle (between the red and green lines) in order to secure a global area conservation. Because the parameterization is not a deterministic approach, the way to implement and use the algorithm may have an incidence on the results (please refer to the book of Mallet (2001) for a description of the algorithm).

Goals of Method 1 and Method 4 are close, but they differ on the chosen mathematical approach. For instance, in the Method 1 and Method 4, the direction of the restoration vectors is not bounded by the hypothesis and can be in any direction. These methods allow to represent real 3D deformation. On the opposite, in Method 3 the direction of the deformation is partially imposed, and totally imposed for Method 2.

2.3 Unfaulting

In addition to the unfolding, to restore the horizons the user needs generally to erase the fault offsets. This process can be done "a posteriori" by zipping the fault lips (rotation, translation and internal deformation could be necessary) or jointly with the unfolding by imposing the continuity of the parameterizations across the fault (Method 4 only). Alternatively

one may accept gaps and overlaps and avoid imposing internal deformation (Rouby et al., 2002). When using a method based on parallel cross-section (Method 3), the contact fault/horizon is constrained on the cross-section and then imposed by construction on the surfaces.

2.4 Nomenclature

The surface unfolding algorithms mix various well-developed geological concepts that are rather clear on cross-section (Fig 1). However, the resulting methods often do not have an obvious structural or geological name and the potential user has to remain careful about which quantities are preserved and which are the boundary conditions for each method. Figure 2 synthesizes the main features of the various methods. In this article we will mainly use the number of methods defined in § 1.2. However, to make it easy, we will refer to "flexural slip" as Method 4 and "simple shear" as Method 2. The designation of "flexural slip" for Method 4 is an analogy since the flexural slip mode in cross-section also preserves the lengths of the hori-zon and the areas. However, there is no thickness preservation here since surface restoration does not take into account the layer thicknesses.

The simple shear deformation mode is known to be a good approximation of the deformation of granular materials such as the poorly consolidated sediments of extensional areas (Verrall, 1981, Gibbs, 1983; White et al., 1986). The ductile lower crust deformation also can be modeled using this approach. In contrast, in the upper crust, the competent layers behave more likely according to the flexural slip mode while the incompetent decollement level such as salt and shale behave as a fluid. This issue has been largely discussed previously (Suppe, 1983; Moretti et al., 1989). However, a 3D restoration based on the flexural slip method can be hard to implement. Despite 2.5D restoration solutions exist, what is the value of the results obtained with the different methods?

3   Case study

The case study is located in the southern part of the Sub-Andean Zone of Bolivia (Figs. 3 to 8)
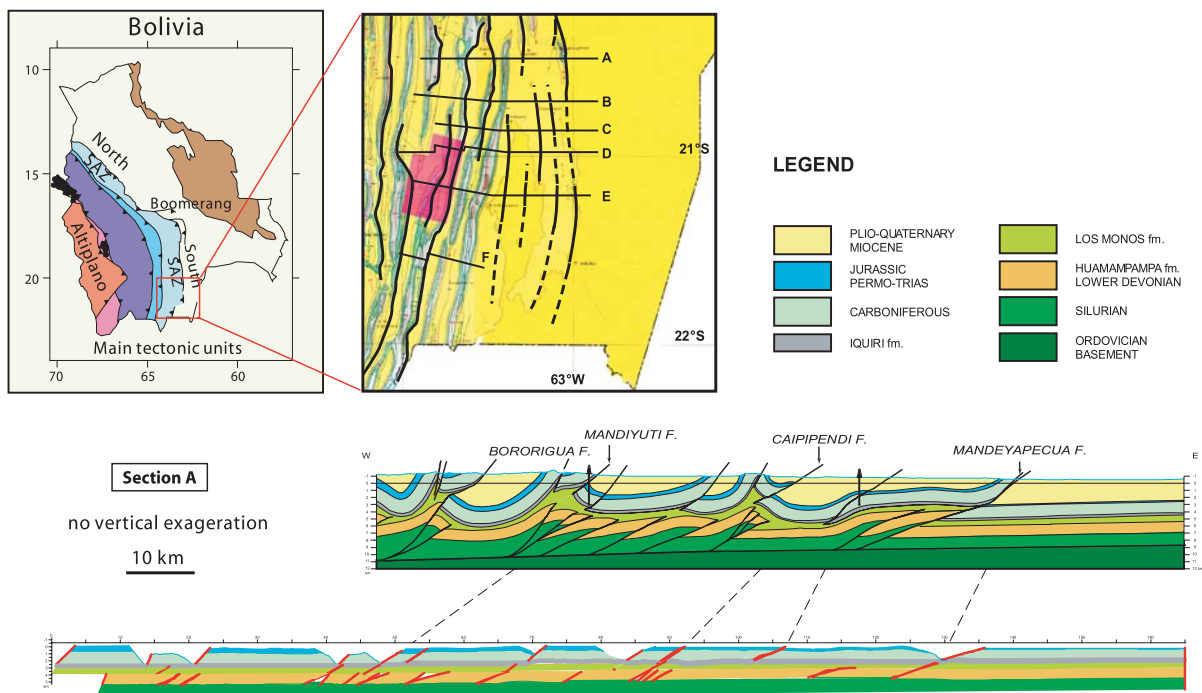
Fig. 3a. Studied area: South Sub-Andean Zone of Bolivia. The exploration is mainly active in the three outcropping thrust anti-clines in the east. On the geological map: the black lines are the main thrusts, dashed when they do not crop out. The east-west bold black lines localize the cross-sections and the pink area indicates where 3D seismic data was available. The legend and the color code are also valid for the other figures. The shown restored cross-section is the northern one. The display is 1x1. The two decollement levels: the Silurian shale (dark green) and the Los Monos Fm (light green) have been restored using a global area conservation approach, whereas all the competent beds have been restored with a flexural slip method that preserves both lengths and thicknesses
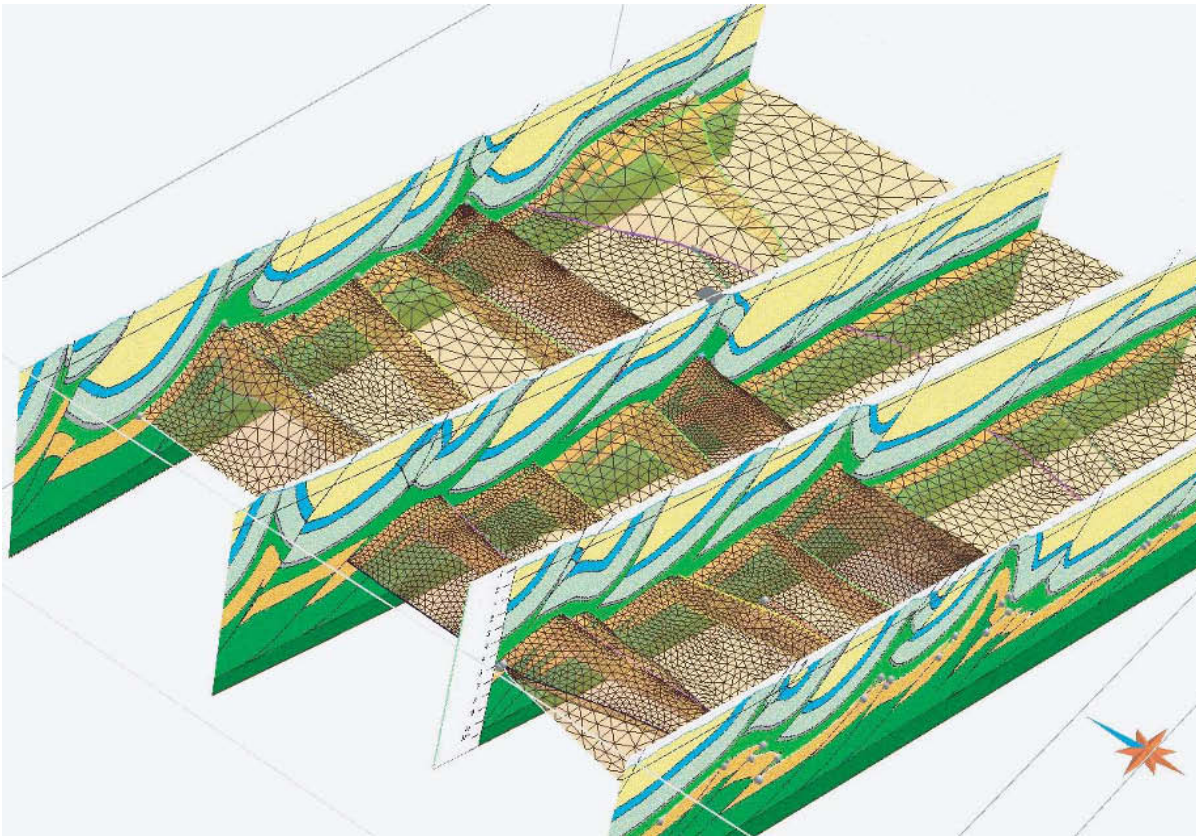
Fig. 3b. The case study: various cross-sections and the top of the reservoir that is studied (Sections A,B,C and D figure 3a). The size of the shown 3D block is about 80 km (E-W) and 65 km (N-S). The quality of the seismic image is poor in the anticlines in such a complex area and the restoration tools, 2D as 2.5D are first used to better define the geometry. In addition, this reservoir is tight (bulk porosity around 1.5%), the reserve estimations and production modeling are based on the fracture network quantification

The Sub-Andean Zone (SAZ) of Bolivia is a Neogene east-verging thrust system that constitutes the eastern border of the Andes. The thrust sheets comprise an approximately 10-km-thick siliciclastic succession with Palaeozoic-Mesozoic platform sediments at the base (green-orange-blue in Fig. 3) overlain by up to 3 km thick Neogene foreland deposits (yellow in Fig. 3).

The studied area is characterized by a thin-skin tectonic style. The main thrusts slip over the Silurian shale (Baby et al., 1992; Moretti et al., 1996; Moretti et al., 2002). Westward, in the Inter-Andean Zone, a "basement" made up of Ordovician and deeper horizons is clearly involved in the thrusts as described by several authors (Kley, 1996; Giraudo and Limachi, 2001).

One key point to constrain the structural style at a smaller scale is to identify the potential decollement levels. The main one is located within the Kirusillas Formation (top dark green in Fig. 3), the second one is the shaly part of the Upper Devonian, namely the Los Monos and Iquiri Fms. (light green in Fig. 3). Other

shale layers in the lower Paleozoic series, for instance within the Icla Formation (part of the orange in Fig. 3) or within the Ordovician series, display also preferential shear deformation in small-scale structures.

In the south SAZ, the main petroleum system consists of the Silurian and Devonian shales as source rocks and all the sandstone units as reservoirs (Moretti et al., 1995). Most hydrocarbon traps are structural traps in anticlines.

The Sub-Andean Zone of Bolivia is a very prolific exploration zone. During the last ten years, the exploration targets have changed. Numerous oil fields have been discovered in the years 70–90 in the Carboniferous and upper Devonian in the foreland and easternmost emerging anticlines. Now, the exploration is more active farther west with deep targets in the lower Devonian (Humampampa, Santa Rosa Sandstones). The existence of this petroleum system was proven since the discovery of the San Alberto gas field (well San Alberto-X9 in 1990 by YPFB), but the deep prospects in the south SAZ have been more systematically targeted within only the past 10 years. In addition

to the cost of the deep wells, moving westward also means steeper anticlines and poor resolution of the seismic images. For the geologists however, the more challenging issues come from the fact that the target is now below an important decollement level, i.e., the middle Devonian shale of the Los Monos Formation.

To better define the prospects below this decollement level, structural concepts are required. Shortening of each anticline can be defined in the upper part of the sedimentary piles based on geological maps and cross-sections. However, the faults below the decollement level are not linked directly to the one above. Seemingly, the offset of an individual fault in the lower Devonian usually does not connect to any specific fault in the Carboniferous and upper sequence. A complete discussion of the geology and exploration issue in the
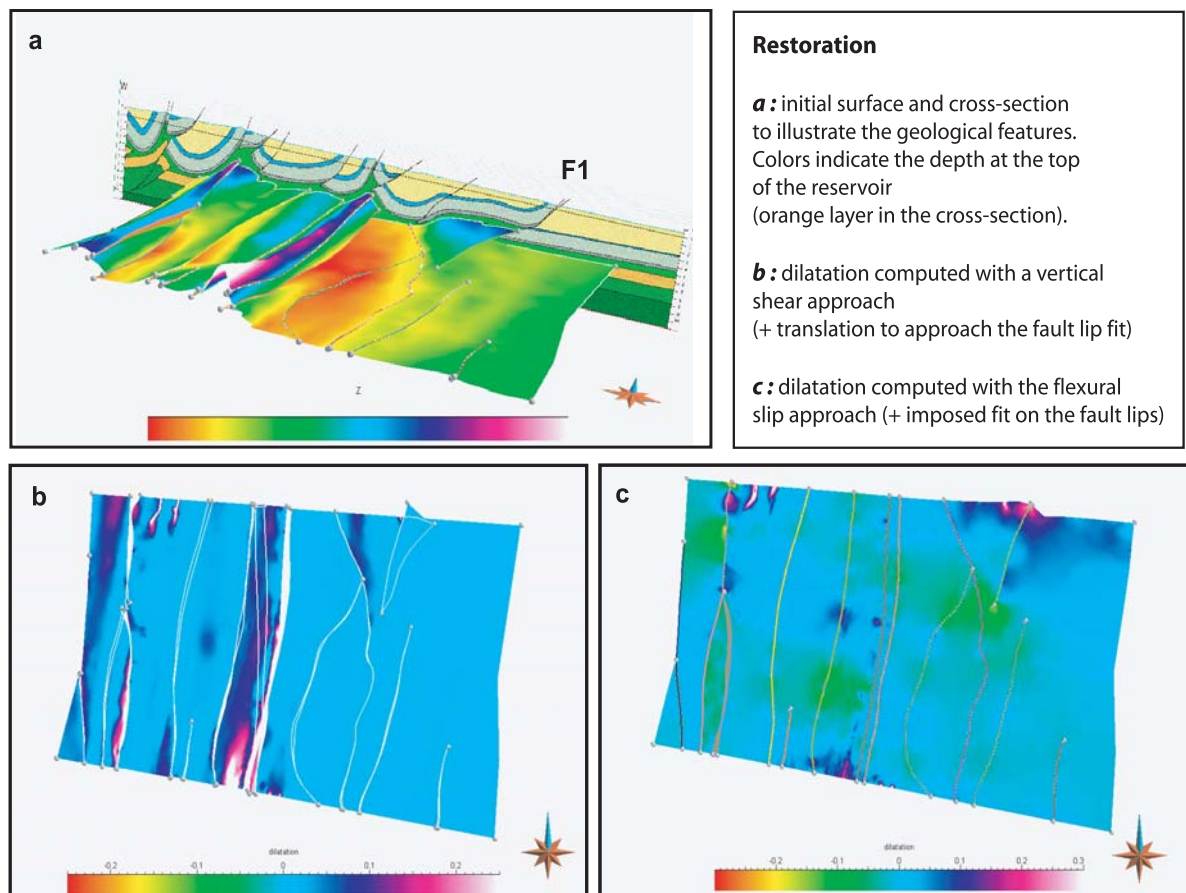
area can be found in Moretti et al. (2006b), the goal of this paper being rather to show how structural concepts plugged in a 3D geomodeler may help to define the prospects and to assess the reservoir quality.

For confidentiality reasons, slight changes have been applied to the original data, i.e., for the reservoir depths and field size shown in Figures 3 to 7.

4   Construction of the 3D Structural Model

The following work-flow has been applied:

1. Construction and restoration of six E-W cross-sections;
2. Construction of the 3D surface model;

Restoration

a : initial surface and cross-section to illustrate the geological features. Colors indicate the depth at the top of the reservoir (orange layer in the cross-section).

b : dilatation computed with a vertical shear approach (+ translation to approach the fault lip fit)

c : dilatation computed with the flexural slip approach (+ imposed fit on the fault lips)

Fig. 4. Comparison of surface restoration using a vertical shear versus flexural approach. Ligth blue shows zones without local area variation during the restoration. With the vertical shear deformation mode, the dilatancy being the ratio between the area of an element of the surface (for instance a triangle) and the map area of this element, increases with the dip. With the flexural slip approach, the area is globally preserved, on a particular point the area could change during restoration in a zone which is not perfectly unfoldable. This property is related to the curvature so in general the hinge of the narrow anticlines present some dilatancy. In addition, in the present case, one has imposed a contact on the fault lips (Fig. 2c), honoring these constrains induce also dilatancy. In the shown example, one sees the high values of dilatancy in the hinge of the highest anticline and near the fault the surface variation induced by the imposed contacts. The influence of this constrain of contact is highlighted in Fig. 4c
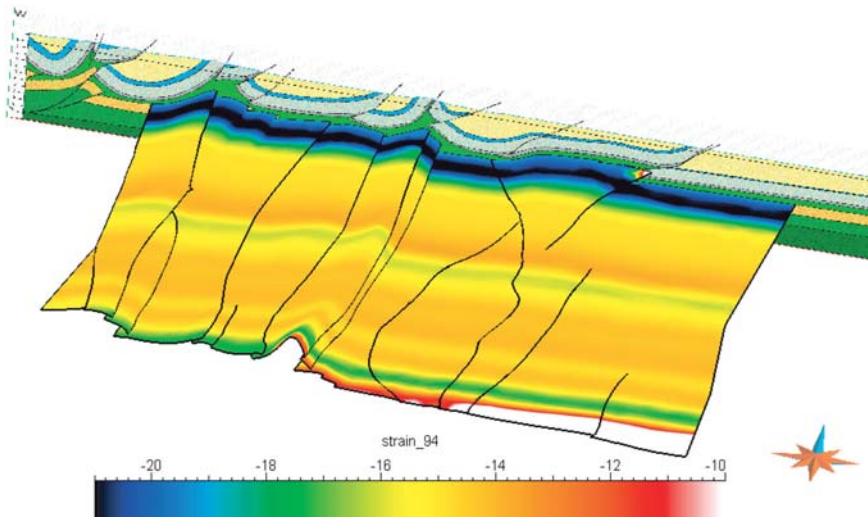
Fig. 5. Static analysis of the current geometry: amount of shortening orthogonal to the structures (N94°). The values are around 15% ± 1% on the studied area except northward where they reach 21%. This abnormally fast increase highlights the error made on the F1 fault offset

3. 2.5D restoration of the reservoir top;
4. Checking of the coherency of the fault offset and on strike shortening, and finalization of a coherent interpretation in 2D and 3D.

Figure 3 shows one of the cross-sections and its restored geometry, whereas Figure 3b shows the top of the reservoir in the 3D model. This restoration helped to refine the geometry of the various sheets and the cut-off angle of the Devonian reservoir below the Los Monos Formation. The existence of numerous tectonic slices in the hinge of anticlines is proven by the well data in large gas fields such as Margarita. The lower part of this interpretation is rather different from a previously published paper (see Fig. 14; Dunn et al., 1995), even if its upper part is the same. Nevertheless, the exact number of faults affecting the Huamampampa Formation remains hypothetical in the structures without wells because seismic images still remain relatively poor in the area (Black and Figeroa, 1999).

The 2D restoration alone is not good enough to preclude any ambiguity. The trend evolution of the fault offset is another important parameter that we used before achieving the 2.5D restoration.

The E-W shortening is about 45 km in the northern part of the studied area (Fig. 3) and decreases slightly to 38 km in the south (cross-section E, map in Fig. 3).

5   Comparison of Flexural Slip / Simple Shear Methods: Geometry and Dilatation

Figure 4 shows the results of two restorations. The first one (Fig 4b) was obtained with a vertical-shear method (method 2) for the unfolding followed by translation of the faulted pieces in order to get an acceptable final geometry (minimization of overlaps and gaps). The second restoration (Fig. 4c) was done with the flexural slip method (Method 4) which preserves the areas. Contacts have been imposed along the fault lips.

5.1 Geometry

Based on the geometry alone, the two flat horizons seem correct. However, the eastern vertical flank of the A1 anticline is poorly restored when using the vertical shear method (Fig. 4b): this flank remains below the main overriding flank of the anticline and cannot be restored to its expected position near the eastern block when using a constant shear angle. The irrelevance of simple shear method to restore high angle thrust units in most cases is well known and this will not be discussed further in this paper. In results obtained for the other thrusts (see Figs. 4 & 5), the fault lip contact is satisfactory since the structures are rather cylindrical, except for the fault which corresponds to the first emerging thrust (F1 - Mandeyapecua Fault). The fault tip is located within the studied area, and there is an increase of the fault offset northward from its southern extremity. When restoring the horizon near fault F1, there is a local overlap with the vertical shear approach that cannot be solved by translating the surface since it would create a gap farther south. Seemingly, when using the flexural slip and imposing a contact on this fault, the resulting unfolded geometry shows a large dilatancy.

In both cases, the geologist would probably conclude that the geometry of the horizon is wrong and would rather go back to correct the initial surface. This problem is due to the excessive northward widening

of the fault offset along F1 in this early interpretation (Fig. 4a).

To summarize this first step, both methods help highlighting large errors in slightly deformed areas (here around F1 in the eastern foreland). The simple shear method (Method 2) is unable to check the coherency of the faulted thrust sheet in highly deformed compressional zones while the global approach (Method 4) may point out this kind of discrepancy.

Construction of the surfaces in a restored stage with the Method 3 is done by linking the restored cross-sections. However, because these surfaces are constructed and not computed by the deformation of the initial surface, they will only reflect the hypotheses concerning the fault contact. Since the restoration process is a heavy method, a quantitative analysis of the current geometry should be sufficient to highlight this problem. Figure 5 illustrates the amount of shortening computed perpendicularly to the structure (N94°). As expected, this shortening is rather constant: from north to south the variation of offset along a fault is compensated by the increase of the fold dip or by the complementary change of offset along another fault. However, northward, the shortening increases quickly to 21% near the A cross-section, thus showing the geometrical inconsistency of the layer. In 3D as in 2D, the quantitative analysis of the geometry of the horizons, called line balancing in 2D, allows to highlight the main inconsistencies very quickly (provided the requisite tools are available through a software, because measuring bed lengths by hand is no longer fashionable...). The main advantage of restoration versus static analysis, in 2D as in 2.5D, is the ability to locate problems related to unconsistent geometries.

5.2 Internal Deformation

The second point to address by the explorationist with a restoration tool, after correcting the geometry, is to describe the internal strain and thereby the fracture density and main strain direction. In 2.5D restoration, internal strain can be represented by dilatation, i.e., the local area variation on the surfaces, which is distinct from the dilatancy used by rock mechanists.

The global area change of the surface is 0.3% in the flexural slip case (initial horizon 6275 km^2, unfolded one 6295 km^2). When doing a pure vertical flattening in the vertical shear case, the area change is around -14%. In the illustrated restoration however (Fig. 4b), translations have been added to the flattening to avoid overlaps in case of thrusting. Therefore, the final area is closer from the initial one, 6100 km^2 (-3%) but with gaps and overlaps. The local changes vary from 0 to 57% in the simple shear case, and can only be positive since a true area is always larger than a map area

and the mean value is 7%. On the other side, for flexural slip the values vary mainly from -10 to 10% and the mean value is 0.2%. In the shown example the highest values are reached at the hinge of the A1 anticline and near the faults, where they may correspond to an error in the cut-off angle.

The dilatation computed for the simple shear approach is mainly controlled by the dips (difference between the true area and the map area of each triangle). It is high in the flanks but low in almost horizontal zones such as the top of the anticline. Therefore, it cannot be interpreted in terms of internal strain during the deformation in the present compressional case.

The dilatation computed for the flexural slip approach is a combination of the influence of the curvature and the fault-horizon intersection geometry. It can be interpreted in terms of internal strain when the geometry is not questionable.

In alternative solutions which, by construction, do not preserve the areas (i.e., methods based on parallel cross-sections restoration such as Method 3), the dilatation does not reflect any geological meaning, except if the deformation is 100% cylindrical. Alternatively, any change of horizon area between two constrained cross-sections will mainly reflect the non-cylindricity of the structures.

As a conclusion, except with the methods preserving the areas, i.e., Method 1 and 4, it is more relevant to use the curvature than the dilatancy to infer any amount of internal strain. However, such a curvature can be directly computed on the current geometry, without requiring any restoration.

6   Dilatation & Extensional Internal Strain

During the restoration, a strain field is computed, which corresponds to a tensor (i.e., eigen vectors can be extracted and provide the principal strain vectors). These vectors are specified in direction and amplitude. They correspond to the derivative of the local transformation that allows to pass from an element of the surface to its initial geometry.

In the Sub-Andean Zone, a large number if not all outcropping faults relate to the current Andean compression, more or less E-W, which started in Miocene times. However, when measuring fracture data in the field, geologists always note that the fracture network records a much longer geological history. In the case of the Sub-Andean zone of Bolivia, the co-existence of pre-existing fractures and fracture corridors with the fractures created during the Andean compression is obvious (see for instance Florez-Nino et al., 2005). Therefore, we must remain cautious when using solely the restoration of the last stage of deformation, even if it is the main one, to obtain a qualitative idea of the

overall deformation and fracture. However, the current strain field is an important parameter for the creation, opening and closure of the fractures and therefore, the modeling of this field is an important issue which constitutes the first step for any reservoir strain quantification.

Joints are supposed to be created by extension. As a result the areas where the deformation is extensional are more likely fractured. When extracting the eigen values of the deformation tensor one may display the positive ones, i.e., the areas where positive surface variation happens. Figure 6 shows this eigen value for three deformation methods (Method 2, Meth-

od 4 with and without imposed fault lip closure). The image has been focused on the A1 anticline at the level of the reservoir beds.

For the simple shear restoration (Method 2), Fig. 6a, the maximum of extension is found in the flank of the anticline, whereas the crest is a minimum.

For the flexural slip with no imposed fault lip contact, Fig. 6b, the maximum of fractures is expected at the crest of the anticline.

For the flexural slip restoration of the full horizon, imposing a contact on the fault lips, Fig 6c, a high probability of fracture at the crest of the anticline is
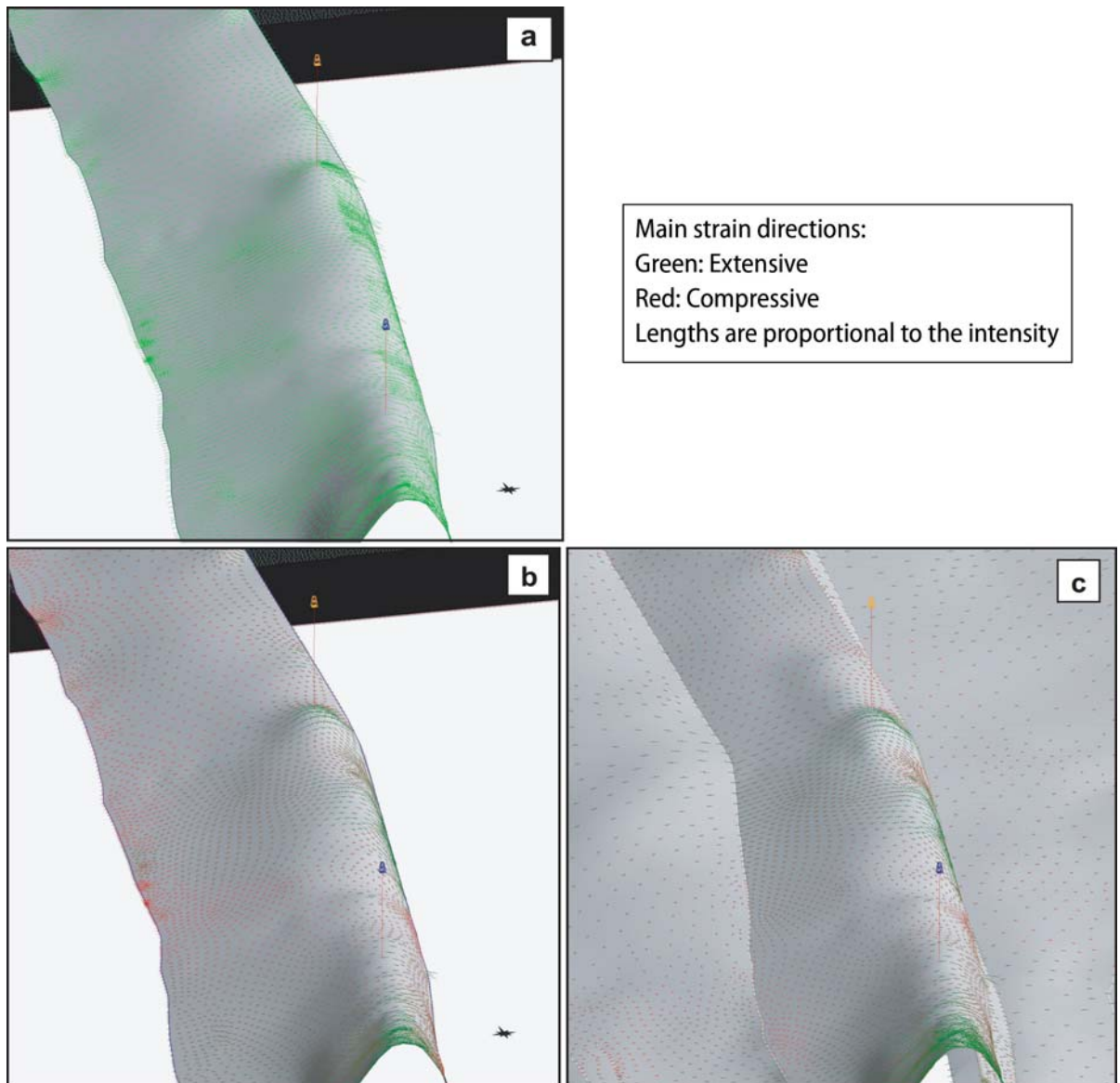
Fig. 6. Comparison of principal strain directions computed with various surface restoration methods (**a**) a vertical shear (**b**) flexural slip approach with no fault lip contact, (**c**) flexural slip with fault lip contacts

also computed. However there are also high values in an east-west corridor between the two wells (dark blue values). High values are also found near the F1 fault, but as discussed in the previous section we consider that it is due to an error on the surface geometry.

High values and therefore high probabilities of fractures are also found in some specific parts of the crest of the anticline, at the impact of the yellow well, for instance. They correspond to small scale structures in comparison of the main thrust sheets, and most likely, they relate to second order decollement levels. As already mentioned, most thrusts root at the top of the main decollement (dark green in Figs. 3 and 5a). A second decollement is shown as the medium green line in the middle of the section, above the reservoir that fills the hinge of the anticline and allows disharmony between the lowest and upper part of the sections. Finally, a third decollement is located a few hundred meters below the reservoir. The activation of this third decollement within the main folds is a common feature in the area and leads to the small-scales structures observed, jointly with small reverse faults not represented here.

As a conclusion, the Method 4 involving global parameterization and surface conservation provides a qualitative tool to predict the fracture density induced by the last deformation stage. The computed values are highly dependent on the geometry (curvature) and boundary conditions (imposed fault lips). In case of uncertainties and errors on the surface geometry, the results will be questionable. With the methods that do not preserve the areas (Method 1 to 3), the results are not always relevant. With the global approach, i.e., Method 4, the errors (horizon geometry and/or horizon-fault intersection) are spread by both the unfolding and the unfaulting. Therefore, the degree of resolution and smoothing of horizon geometry is another important factor, although it will not discussed in this paper.

7   Computed Principal Strain Directions

The processing of the deformation allows the computation of the eigen strain directions. These strains represent only the internal deformation. The displacement/rotation that does not induce any internal strain are not taken into account in this strain tensor. If a structure is 100% unfoldable, and when there is no constrain imposed through the boundary conditions, the internal strain tensor is null and therefore, the eigen vectors of the tensor are theoretically not defined. Practically, the vectors are not exactly null and their values are still computed by the program. They are displayed in Figure 6 for the same three cases of deformation as in Figure 4.

With the simple shear method (Method 3, Fig 6a), the principal strain vectors are all extensional and the principal direction reflects the dip direction. With the flexural slip (Method 4, Fig. 6b and c), one may note that the two arrows are often on the same lengths.

In conclusion, the principal strain directions can be computed. However, they are not interesting for the geologist when the internal strain is too small, because the switch from a direction to another may also be due to numerical noise.

8   Best Prediction

To summarize, (1) the computed strain tensor is likely representative of the geological deformation when the internal strain is not null, and (2) a high density of new fractures or opening of old fractures is expected at places where local extension happens. Figure 7 is derived from the previous results (method 4, without fault lip closure constrain) and shows the main areas of interest. Through a threshold, we keep transparent the part of the structures where the strain tensor is almost null (dilatancy of less than 0.5%). Therefore, the compressional strain has been hidden and an adequate color code has been retained. The lengths of the extensional strain vectors are proportional to their amplitude (see in Fig. 4b for the full image of the dilatance and Fig. 6b for the strain tensor.

There are three patches with maxima:

- the crest of the anticline where this one becomes narrow (around the blue well and southward);
- the structure drilled by the yellow well, south of the first patch;
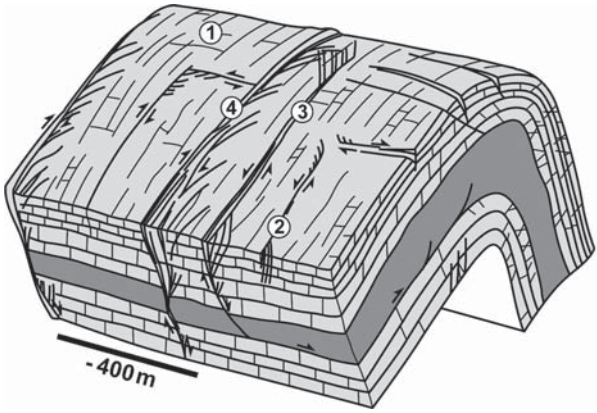- the concave flank of the anticline where it is very steep.

The main direction of fractures found with this model is more or less east-west oriented and corresponds to the last family of fractures, i.e., the ones generated by folding. Other sets of fractures exist, as shown in Figure 8. In addition to pre-existing fractures inherited from the Paleozoic and Mesozoic tectonic phases, other features have created during the Andean compressional phase. In the early stage of compaction, rather large internal deformation happens in the foreland due to the layer parallel shortening. The fractures and joints created during this phase are likely parallel to the compression, i.e., east-west oriented (potentially features number 2 and 4 in Fig. 8). However, this kind of fractures cannot be modeled through a backward surface restoration since they are not linked to large scale geometric changes of the surfaces.

In the studied case, surface restoration may help to improve the surface definition when the geometry
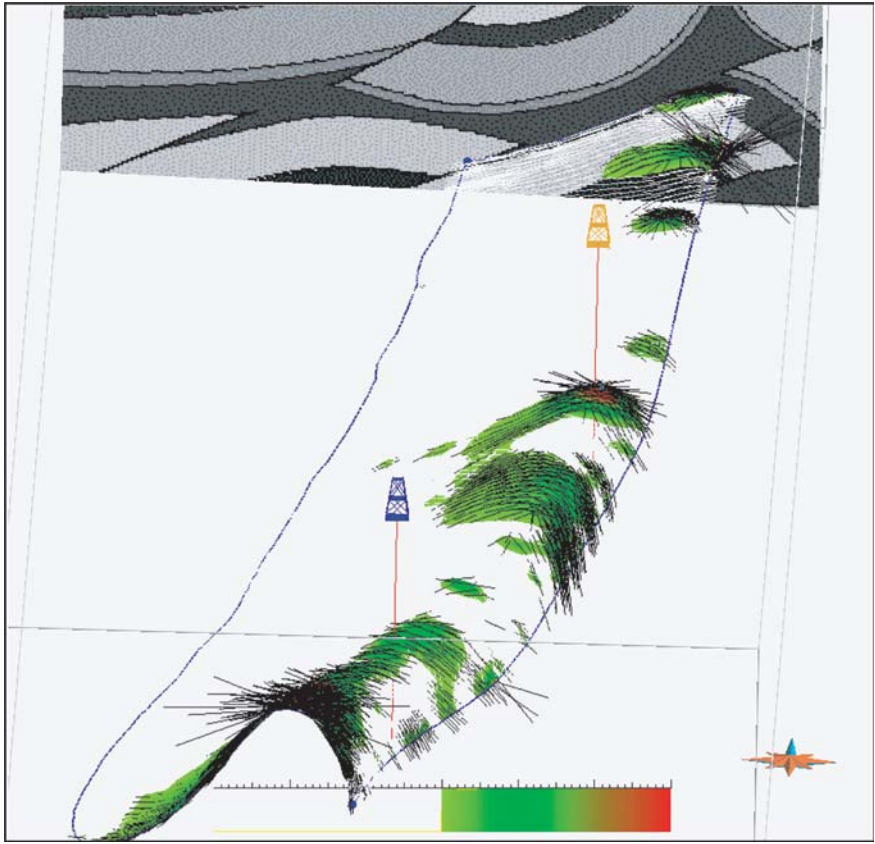
Fig. 7. Prediction for the density and direction of the new fractures developed during the folding of this anticline. The colored background indicates the dilatancy, negative values are transparent. The black lines indicate the direction of the principal strain, length is proportional to intensity

Fig. 8. Conceptual model of fault and fracture systems in the Sub-Andean Zone of Bolivia. Modified from Florez et al., 2005

1. Joints
2. Small Faults
3. Intermediate Faults
4. Fault Zones

is accurate enough. The 2.5D restoration can be used for a realistic estimation of fracture density and fracture direction. However, as highlighted in Figures 4 & 6, the results in terms of density and direction are strongly dependent on the chosen method. In this respect, conclusions derived from the hypothesis of a simple shear deformation mode versus a flexural slip mode are completely different, while the difference is not so drastic when working only on the geometry.

9   Conclusion

Usually, restoration is not the main goal for the structuralist, but it is rather a way to control the consistency of the proposed geometry. On the opposite, specialists in basin modeling or in reservoir characterization need to have an idea of the depositional geometry and of the evolution of the basin versus time. The struc-

Table 3. Comparison of the results obtained with various unfolding methods. Note that in addition to the differences highlighted here, i.e., those due to the unfolding and unfaulting methods, the geometry accuracy impacts the results (see details in the text)

Unfolding	Method 2 Simple-shear	Method 3 Interpolation between parallel cross-section	Method 4 Flexural slip
Forced unfaulting	Area variation: yes Perfect fit on the fault lips: impossible with a constant shear angle Computed dilatation: often meaning less (except in extension for not consolidated material)	Area variation: yes Fit on the fault lip: by construction, induces surface variation Computed dilatation: meaning less Direction of internal strain: no geological meaning	Area variation: small, but exists if the contacts on the fault is not perfect Fit on the fault lip: yes, induces dilatancy and internal strain Computed dilatation could be interpreted in terms of error of the geometry and/or fracture density Direction of internal strain: geological meaning
Search best fit during unfaulting	Area variation: yes No perfect fit on the fault lips	Area variation: yes Fit on the fault lip: by construction Computed dilatation: often meaning less	Area variation: no No perfect fit on the fault lips Computed dilatation could be interpreted in terms of fracture density except near the fault Direction of strain: geological meaning

turalist needs to insure the preservation of the characteristic lengths that have to be controlled (horizon lengths, thickness, fault lips), when the others need a rather rough geometry during the burial as well as indications on the timing of structure growth. The requisite for an adapted restoration tool, 2D as 2.5D, may thus be different, depending on the objectives. For intance, the Method 3 that links parallel cross-sections, may give relevant global geometry, but this approach precludes the consistency of other parameters versus time during the restoration. Area, fault lips geometry, and direction of displacement are imposed, not computed. It is therefore very crucial for the user of the tools to identify the question, the geological context, the uncertainty of the data, and to keep in mind the hypothesis behind each method.

The conclusions reached here on the comparison between the methods are synthesized in Table 3. This table clearly differentiates the hypothesis from the computed results for each method. At the stage of the quality control of a model, the study clearly shows that Method 2 and 3 cannot help. In contrast, a combination of cross-section balancing and surface restoration with Method 4, in the presented case of the Sub-Andean Zone allows a better definition of the geometry of both horizons and faults. The search of a good closure of the fault lip, without large internal deformation, appears as a very good criterion to eliminate unrealistic fault geometries, versus depth and along strike.

When predicting fracture density prediction, we must remain cautious with the meaning of a dilatation computed by Method 3. Method 2 is not applicable in a compressional tectonic setting. In all cases, a 3D restoration will improve the strain tensor definition, as well as a cumulative computation of strain versus time. However, adding erroneous values through time to reach a strain tensor in a thrust fold, which can be done when using the incremental approach of Method 2, will only result in non interpretable conclusions. The quality of predictions is dependent on the quality of the geometry. The SAZ case study is on this topic specific. In many other places, the subsurface data are now good enough to apply these techniques. Here, the initial geometry is well constrained by the restoration, when using the appropriate method. Therefore, it is relevant both in terms of paleogeography and to propose further computation of the fracture density.

KINE3D-1 and 2 are marketed by Paradigm-Earth Decision. Jean-François Lecomte, Alexandre Macris, Renaud Gillet, Renaud Divies and Vincent Martinez have also participated in the development of KINE3D in addition to the two first authors. The 2D restorations have been done with LOCACE™, an IFP software marketed by the BEICIP.

References

Angelier J. and Colletta B., 1983. tension fractures and extensional tectonics, Nature, 301, 49–51.

Baby, P., Herail, G., Salinas, R & Sempere T., 1992. Geometry and kinematic evolution of passive roof duplexes deduced from cross section balancing: example from the foreland thrust system of the southern Bolivian subandean zone. Tectonics, v 11, n°3, 523–536.

Bennis, C., Vezien, J.-M. & Iglesias, G., 1991. Piecewise Surface Flattening for Non-Distorted Texture Mapping, Computer Graphics, 25, N. 4, 237–246.

Black, B. & Figeroa, 1999. Interpretation strategy drives acquisition of 2-D seismic in the sub-Andean Bolivia. The Leding Edge, 1360–1662

Dunn J., K. Hartshorn, Hartshorm, P., 1995. Structural styles and hydrocarbon potential of the Sub Andean Thrust belt of southern Bolivia. in Petroleum basin of south America, AAPG Memoir 62, pp 523–543.

Faure J.L. and Chermette, J.C., 1989. Deformation of tilted blocks, consequence on block geometry and extension measurements. Bull. Soc geol France, 8, IV, N°3,

Florez-Nino J.M., Aydin A., Mavko G., Antonellini M. & Ayaviri A., 2005. Fault and fracture systems in a fold and thrust belt: an example from Bolivia. AAPG Bulletin, V 89, N°4, 471–493.

Galera C., C. Bennis, I. Moretti & J. L. Mallet, 2003. Construction of Coherent 3D geological blocks, Computers & geosciences, 29, 971–984

Gibbs, A., 1983. Balanced cross-section construction from seismic sections in the areas of extenional tectonics. Journal of structural geology, 5, 153–160.

Giraudo R. and Limachi R., 2001. Pre-Silurian control in the genesis of the central and southern Bolivian fold belt. Journal of South American Earth Sciences 14, 665–680.

Gratier J.P. & Guillier, B., 1993. Compatibility Constraints on Folded and Faulted Strata and Calculation of the Total Displacement Using Computational Restoration. Journal of Structural Geology, 15, 391–402

Gratier, J.P., Hopps, T., Sorlien, C., Wright, T., 1999. Recent crustal deformation in Southern California deduced from the restoration of folded and faulted strata. Journal of Geophysical Research 104, 4887–4899.

Kley J., 1996. Transition from basement-involved to thin-skinned thrusting in the Cordillera oriental of southern Bolivia. Tectonics 15(4), 763–775.

Kligfield, R., Geiser P and J. Geiser, 1986. Construction of geological cross-section using micro-computer systems. Geobyte, spring, 60–67.

Mallet, J.-L., 2001. Geomodeling. Oxford University Press.

Mallet J.L. et Massot, J., 2001. Improving balanced restoration using structural Model information. 21th Gocad Meeting proceeding.

Moretti, I. & Larrère, M., 1989. LOCACE: Computer-Aided Construction of Balanced Geological Cross-section. Geobyte, 4, 1-24.

Moretti I, E. Diaz Martinez, G. Montemurro, E. Aguilera & E. Perez., 1995. The Bolivian source rocks: Sub Andean Zone, Madre de Dios, Chaco. Revue de l'IFP. v 50, n°6, 753–777.

Moretti I, Baby P., Mendez E. and Zubieta D., 1996. Hydrocarbon generation in relation to thrusting in the Sub Andean Zone from 18 to 22°S, Bolivia. Marine and Petroleum Geology, v 2, 17–26.

Moretti I, P. Labaume, S. Sheppard, & J. Boulègue, 2002. Compartmentalisation of the migration pathways in the Sub-Andean Zone, Bolivia. Proceeding of Geofluid 2000, Barcellona, Tectonophysics, 348, 5–24.

Moretti, I., F Lepage and M. Guiton, 2006a. 3D Restoration : Geometry and Geomechanics, Oil and Gas technology, v 61, 2, 277–289.

Moretti I. , J. Letouzey, A. Otero, J.C Calvo, 2006b. Structures growing and decollement level role in the Sub Andean Zone of Bolivia. Caipipendi block. Cartagena meeting, Sept 2006, Proceeding.

Muron, P. & Mallet, J.-L., 2003. 3D Balanced Unfolding: the Tetrahedral Approach. Paper presented at the 23rd Gocad Meeting, Nancy (France).

Rouby, D., Xiao, H. & Suppe, J., 2000. 3D Restoration of Complexly Folded and Faulted Surfaces Using Multiple Unfolding Mechanisms. American Association of Petroleum Geologists Bulletin, 84, 805–829.

Rouby, D., Raillard, S., Guillocheau, F., Bouroullec, R. & Nalpas, T., 2002. Kinematics of a Growth Fault/Raft System on the West African Margin Using 3D Restoration. Journal of Structural Geology, 24, 783–796.

Sanders, C., Bonora M., Richards D., Kozlowski E., Sylwan C. and Cohen M., 2005. Kinematic structural restoration and discrete fracture modeling of a thrust trap : a case study from the Tarija Basin, Argentina. Marine and Petroleum Geology 21, 845–855.

Suppe, J. (1983) Geometry and Kinematics of Fault-Bend Folding. American Journal of Science, 283, 684–721.

Thibert, B., Gratier, J.P., Morvan, J.M., 2005, A direct method for modeling and unfolding developable surafces and its applisation to the Ventura Basin (California). Jouranl Of Structural Geology, 27- 303–316.

Verrall, P., (1981) Structural interpretation with application to North Sea problems. Course note n°3, join. Ass. for petroleum Exploration courses (UK).

White, N., Jackson, J. A. & Mc Kenzie, D., 1986. The Relationship Between the Geometry of Normal Faults and That of Sedimentary Layers in Their Hanging Walls. Journal of Structural Geology, 8, 879–909.

Plate Tectonic Setting and Cenozoic Deformation of Trinidad: Foldbelt Restoration in a Region of Significant Strike-Slip

Steven Lingrey

Abstract. The geology of northeastern South America reflects transpressional deformation of a Cretaceous-Paleogene passive margin by the plate boundary interaction with an eastward advancing Caribbean plate. Structural elements affecting Trinidad and the adjacent Gulf of Paria include a complex mix of contraction, extension, and strike-slip. Detached fold-thrust style deformation is predominant, but its coherent expression is complicated and concealed by subsequent right-lateral strike-slip and associated extensional deformation. Pre-Cenozoic extension between North and South America led to a north-facing passive margin for eastern Venezuela and Trinidad. In the early Cenozoic, relative plate motions between North and South America became mildly contractional. In the Trinidad region, deformation and localized uplift of some elements of the passive margin began. Through the Oligocene, the leading edge of the Caribbean plate advanced eastward imposing a transpressional deformation onto the passive margin of eastern Venezuela and Trinidad. In the late Miocene, Caribbean-South American relative motion became fundamentally translational.

The consequences of this evolving plate-tectonic history on Trinidad are three episodes of deformation. First is an ambiguous period of early deformation, some elements of which appear to have activated modest crustal contraction/uplift within the passive margin. Second is a developing period of southeast-vergent, detached and basement-involved fold-thrust contraction corresponding to the diachronous, transpressional east-southeastward advance of the Caribbean plate. The nature of the deformation appears to reflect a strain partitioning with oblique convergence accommodated by the combined motions of an east-west right-lateral strike-slip system on the north and an east-northeast trending, southeast-vergent dip-slip contraction system in the fold-thrust belt to the south. Right-lateral strike-slip offsets are approximately 150–200 km; magnitudes of shortening are on the order of ~120 km in Eastern Venezuela and of ~60 km in Trinidad. Third is a period of distributed right-slip shear across Trinidad and the Gulf of Paria due to a change in relative plate motion to due-eastward translation. Strike-slip systems became predominant and spread southward with right-stepping relays that localized rhombochasm-style extensional basins.

Restoration of Trinidadian fold-thrust contraction is complicated. Transects across present-day foldbelt geography

cross zones of important strike-slip, violating the condition of plane strain. Map-based methods using an interpreted set of micro-plates were used to account for the various regions of contraction, extension, and strike-slip since the Late Oligocene. Two palinspastic maps are interpreted:

a) a 10.5 Ma restoration
b) a 25 Ma restoration.

The 10.5 Ma restoration creates a palinspastic base for better understanding the original shape and distribution of the Trinidadian fold-thrust belt. The 25 Ma restoration creates a palinspastic base for better understanding the original shape and distribution of the passive margin depositional systems. Profile restoration studies in the Eastern Venezuelan foldbelt serve as a quantified analog for proportional strains in the narrower, younger Trinidadian foldbelt. As a check on the map-based restorations, an interpreted cross-section is presented for the eastern Gulf of Paria. This is a paleo-structural profile (mid-Miocene) and is constrained by the 10.5 Ma palinspastic base map. Section-based methods of foldbelt restoration are applied to this section to assess net contractional shortening. The magnitude of shortening determined by the section restoration (61 km) is in agreement with the estimate of shortening made on the basis of strain projection from Eastern Venezuela (56 km).

1 Introduction

Fold-belt restorations typically involve 2D transformations of structural profiles. They rely on an assumption of plain strain. The geology of northeastern South America reflects transpressional deformation of a Cretaceous-Paleogene passive margin by the plate boundary interaction with an eastward advancing Caribbean plate (e.g., Burke et al., 1984; Speed, 1985; Mann et al., 1990; Pindell, 1991). Surface structural elements of the Eastern Venezuelan Mountains show contraction, extension, and strike-slip organized into two coherent domains. A northern, coastal domain contains principally east-striking faults and elongate east-trending basins associated with right-lateral strike-slip (Pérez and Aggarwal, 1981; Schubert, 1984; Vierbuchen,

1984), and a southern, interior domain contains principally east-northeast-striking faults and folds associated with contractional thrust faulting (Bellizzia and Dengo, 1990; Roure et al., 1994). The reasonable interpretation appears to be that the transpressional motion between the Caribbean and South American plates is accommodated by a strain partitioning system; the pure right-slip strain in the coastal domain and the pure dip-slip contractional strain in the interior domain combine to describe the right-lateral transpression (e.g., Avé Lallement, 1997). In such a system, the 2D structural profile restorations of the Eastern Venezuelan Mountains by Parnaud et al. (1995) are sensible measures of the contractional component of the overall transpression.

Fold-belt restoration in Trinidad and the Gulf of Paria is, however, more complicated because of overlapping domains of contraction, extension, and strike-slip (Fig. 1). Detached fold-thrust style deformation is predominant, but its coherent expression is compli-

cated and concealed by subsequent right-lateral strike-slip and associated extensional deformation. Interpretation of fold-thrust structural features in 2D profiles is complicated. Profiles oriented orthogonal to the fold-belt trend intersect significant strike-slip features. In some regions, the fold-belt is buried beneath thick extensional deposits in relay zones between strike-slip faults. Simple 2D profile restoration of the Trinidadian fold-belt is invalid.

Restoration of strike-slip deformation can be handled by 2D map-based transformations. They need not necessarily rely on an assumption of plain strain as regions of contraction and extension can be accommodated by areal gain or loss, respectively. This study presents a structural reconstruction for Trinidad and the adjacent Gulf of Paria as a micro-plate kinematic model of the South American-Caribbean plate boundary. The boundaries of the micro-plates coincide with my interpretation of the major structural faults constituting a network of thrust-fault deformation fronts,
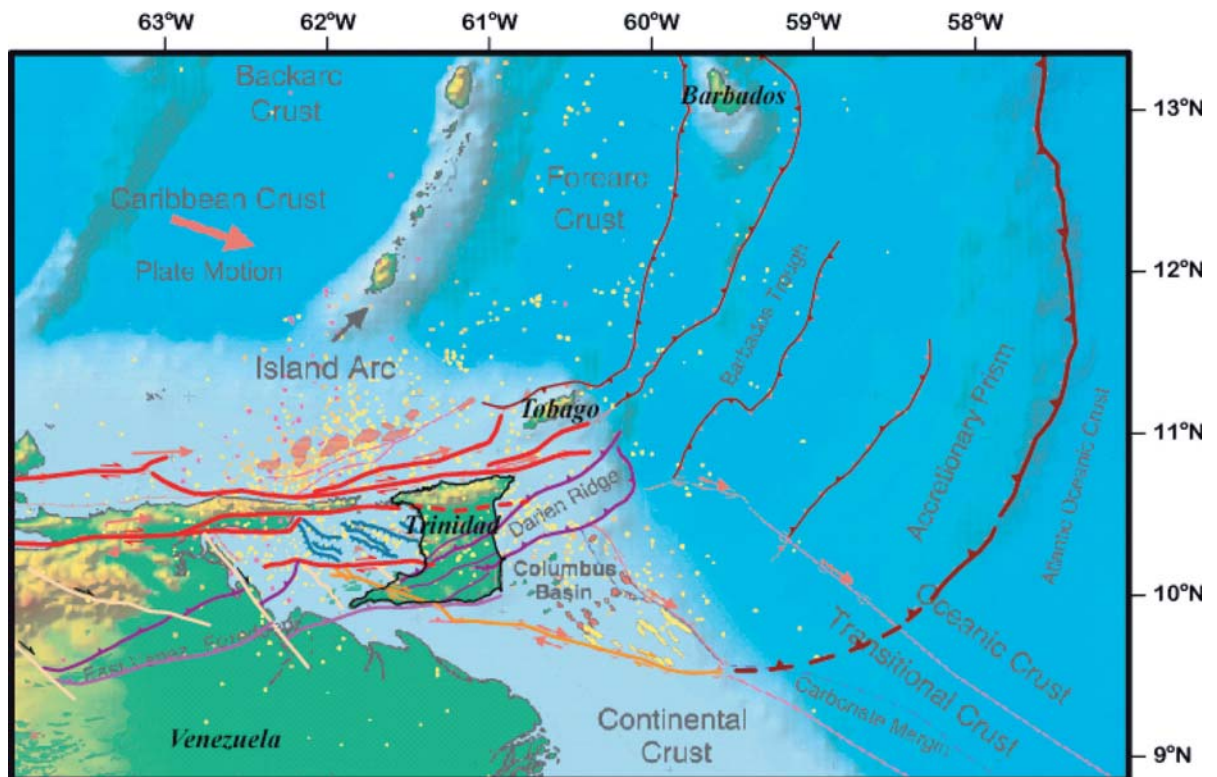
Fig. 1. Regional tectonic setting of Trinidad and adjacent Gulf of Paria showing fault patterns that define the South American-Caribbean plate boundaries. Faults in northeast Venezuela-Gulf of Paria-Trinidad are compiled from (Belizzia et al., 1976; Flinch et al., 1999; Babb and Mann, 1999); offshore fault pattern are as compiled by Klitgord (2002). North-northeast trending contractional faults (burgundy) mark accretionary complex at leading-edge (east) of the Caribbean Plate where Atlantic oceanic crust is consumed by west-dipping subduction zones. East and west-northwest trending faults (red and orange) mark right-shear transform boundary at southern-edge of the Caribbean plate. Current relative plate motion between South American (fixed) and Caribbean plates is due eastward. Earlier (pre-Late Miocene) relative plate motion was east-southeastward and hence transpressive. Contractional strain is recorded in the East Venezuelan and Trinidad fold and thrust belts. Foldbelt in Venezuela is largely intact; foldbelt in Trinidad is, however, cross-cut and deformed by the widely distributed zone of transform-related right shear

linear zones of strike-slip, and extensional fault-blocks. The combined motions of these micro-plates necessarily sum to equal the interpretations of Late Cenozoic relative plate motion between the South American and Caribbean plates.

2 Summary of Cretaceous to Recent Tectonic Evolution

The plate tectonic history of the Trinidad Gulf of Paria/ Trinidad region involves three plates, the South American, the North American, and the Caribbean. Studies of global plate motions (Norton, 1996; Mueller et al., 1999; Pindell and Kennan, 2002; Fig. 2) lead to the definition of four successive tectonic settings:

1. The passive margin setting: NAm-SAm sea-floor spreading from Cretaceous through Early Paleogene (Fig. 3A)
2. The "proto-Caribbean" setting: NAm-SAm incipient subduction proximal to the SAm ocean-continent boundary from mid-Paleogene to Late Paleogene (Fig. 3B),

3. The transpressional setting: Carib-SAm oblique convergence diachronously initiating from west to east from Late Paleogene to Early Neogene (Fig. 3C)
4. The translational setting: Carib-SAm due eastward translation from Late Neogene to present (Fig. 3D).

The latter three plate tectonic settings lead to three distinct episodes of Cenozoic deformation. They are characterized as Episodes 1, 2, and 3.

2.1 Episode 1

An ambiguous period of early deformation inferred from the N-S contraction between the North American and South American plates; most of the deformation is considered to be at the distal edge of the passive margin where a north-vergent accretionary deformation complex is envisioned above subducting oceanic crust (Pindell and Dewey, 1991; Higgs and Pindell, 2001; Pindell and Kennan, 2002; Fig. 3B). While exposed structural features associated with episode 1 in Trinidad are lacking, deformation is implied by un-

Fig. 2. Models of Cenozoic plate motions for the Caribbean and North American plates relative to a fixed South American Plate. In the Paleogene, North American plate motions become mildly southward (contractional), perhaps a source of episode 1 deformation affecting passive margin deposition. In the late Paleogene-Neogene, the east-facing subduction margin of the Caribbean plate advances eastward across the northern margin of South America. Models of Caribbean-South American plate motion indicate transpression prior to 10 Ma and translation after 10 Ma for an east-west oriented plate boundary
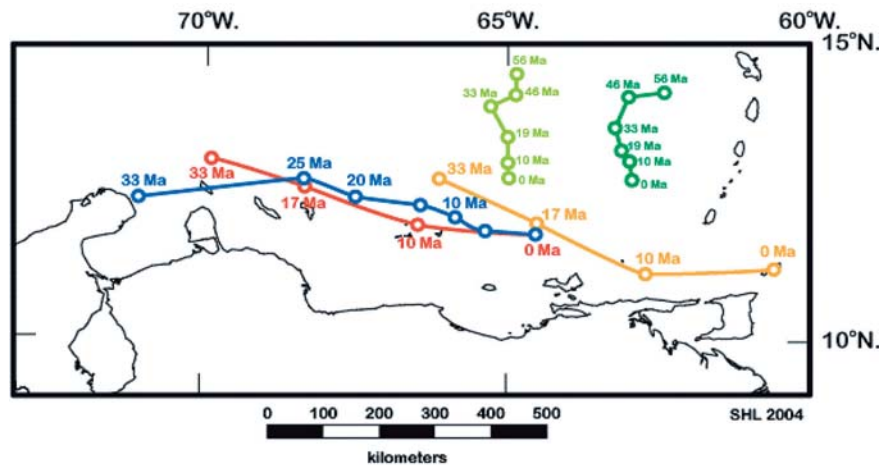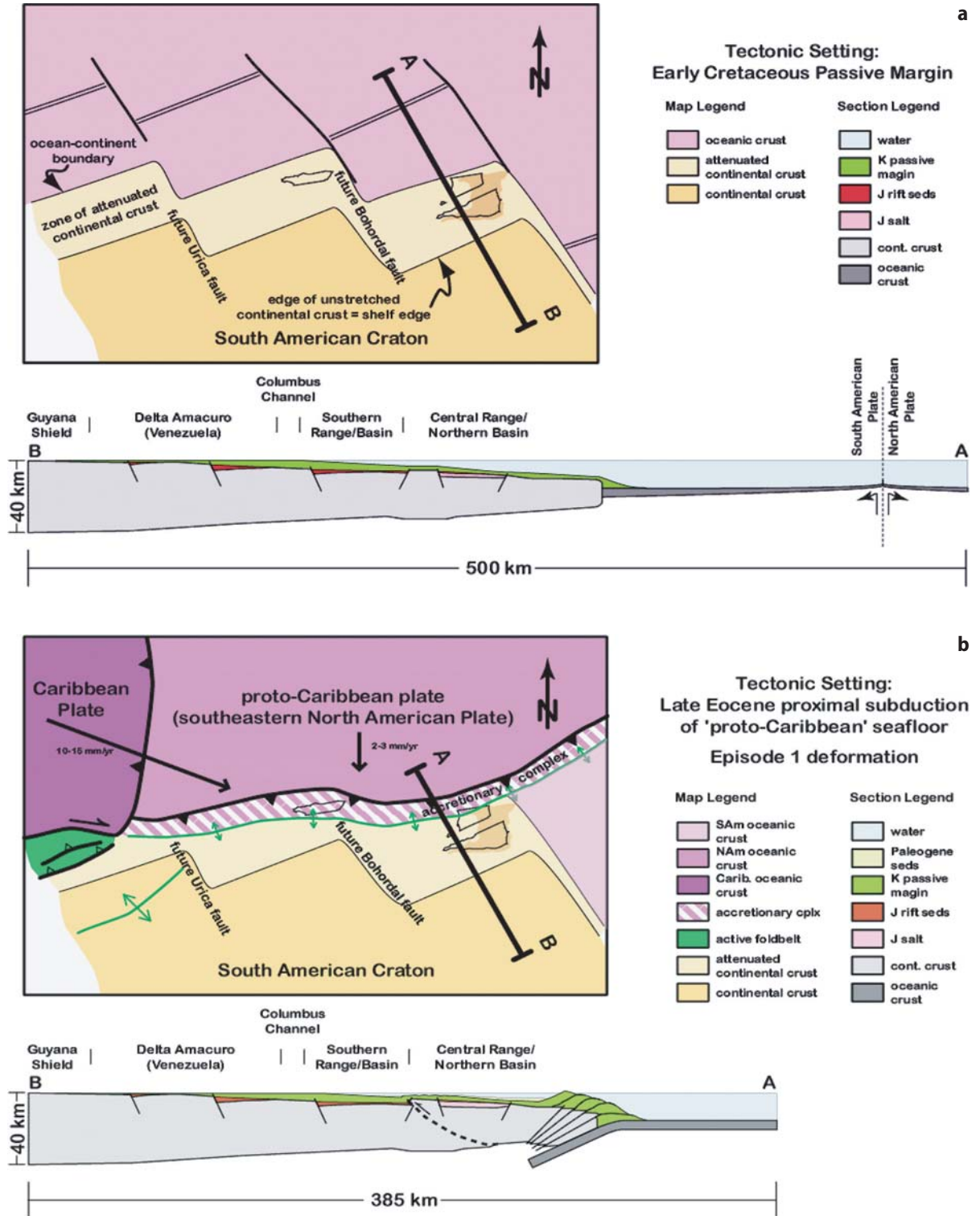
Fig. 3a,b. Idealized tectonic settings for northeastern South America illustrated by tectonic map and crustal cross-section. In all cases, a tectonic map shows inferred locations of major elements of Trinidad geography (Northern Range, Central Range/Northern (Caroni) Basin, Nariva foreland/Southern Range) as black outlines; a brown shadow shows the present-day position of Trinidad. **a**) Early Cretaceous: rifting and sea-floor spreading between North and South America creates a north-facing passive margin. **b**) Late Eocene: Episode 1 deformation shows small magnitude of oceanic subduction (~ 50 km), accretionary contraction at distal edge of South American passive margin, and possible contractional uplift of slope regions of passive margin
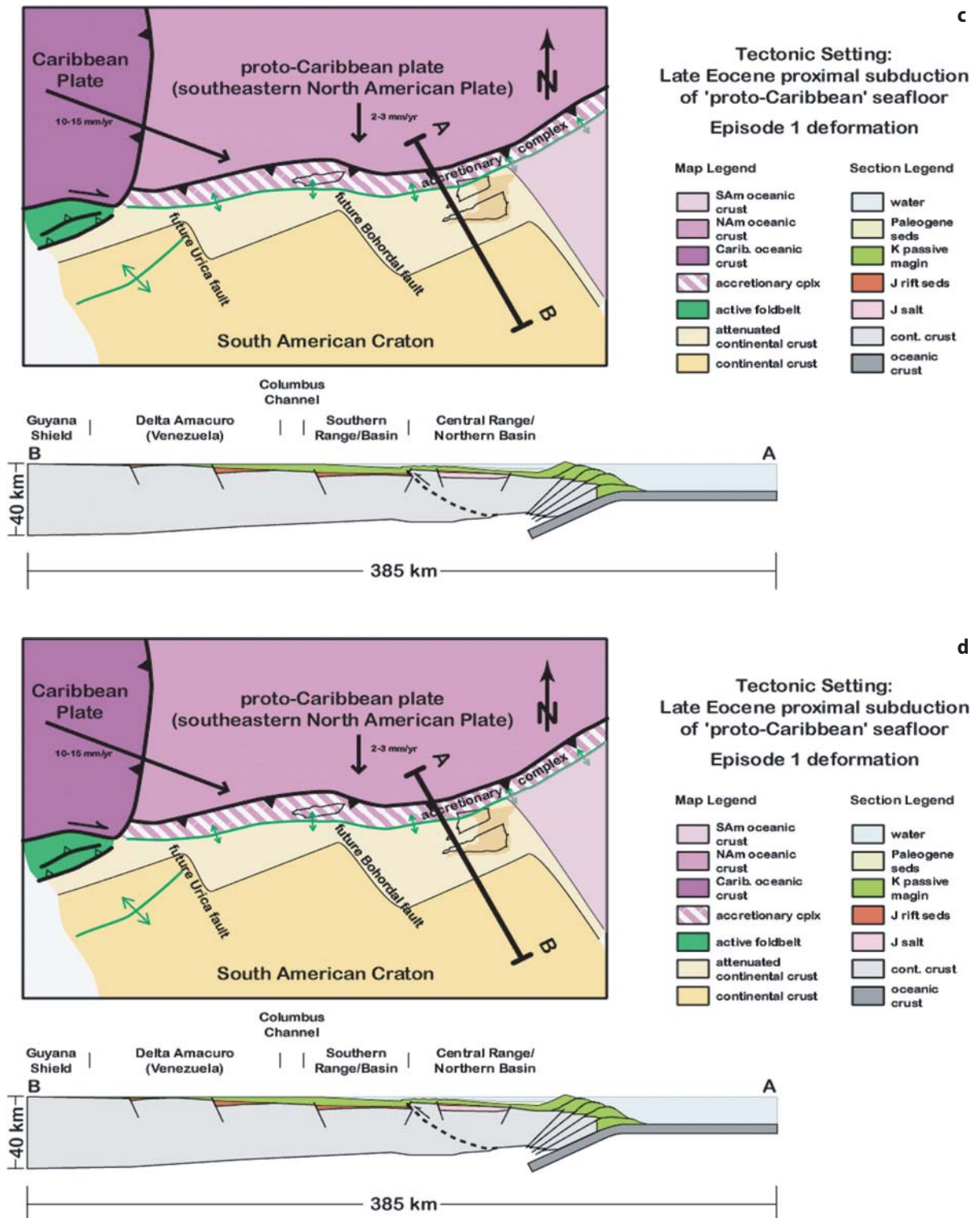
Fig. 3c,d. **c**) Mid-Miocene: Episode 2 deformation accommodates transpression between Caribbean and South American plates. Strain partitioning creates a northern region of strike-slip deformation and a southern region of foreland fold-thrust contraction. The submarine Nariva foredeep basin lies beneath the Southern Basin; the emergent thrust belt hinterland ("Serrania" belt) lies beneath the Central Range/Northern Basin. **d**) Present: Episode 3 deformation develops a broad zone of distributed strike-slip across the northeastern corner of South America. Earlier fold-thrust belt is disrupted

conformity (early Paleogene erosion) and by the presence of unique Eocene lithofacies in the Central Range (Pointe-a-Pierre sandstone, Plaissance olistostromes; Kugler, 1953; Barr and Saunders, 1968; Persad, 1985; Tyson and Ali, 1990; James and Rigby, 1993; Algar and Erikson, 1995). These units indicate disturbance of the formerly quite passive margin slope environment. One hypothesis is that minor elements of this contraction may have activated crustal elements within the passive margin, e.g., mid-Paleogene uplift of the Central Range region (Pindell and Kennan, 2002; Algar and Erikson, 1995). No attempt is made here to reconstruct this deformation.

2.2 Episode 2

A developing period of southeast-vergent, detached and basement-involved fold-thrust contraction corresponding to the diachronous, transpressional eastward advance of the Caribbean plate from late Eocene through middle Miocene (Passalacqua et al, 1995; Avé Lallement, 1997; Pindell and Kennan, 2002; Fig. 3C). The nature of the deformation system is interpreted to reflect a strain partitioning whereby the oblique convergence is accommodated by the combined motions of a northern strike-slip system and a southern dip-slip system (the fold-thrust belt). Three characteristic foldbelt trends are manifest in Eastern Venezuela and are interpreted to extend into Trinidad:

1. The Serranía belt, an interior (hinterland) region that involves significant crystalline basement shortening beneath a widespread exposure of imbricated Lower Cretaceous strata.
2. The Pirital belt, an internal/external region that involves Cretaceous and lesser basement thrusting, but that preserves some syntectonic foredeep deposits.
3. The Furrial belt, an external (foreland) region that is detached above basement and, at its leading edge, is detached above Cretaceous.

These classified belts are equivalent to the Serranía del Interior, Inner Foothills, and Outer Foothills regions of Hung (2005). Magnitudes of contraction are considered to be significant: on the order of ~120 km in Eastern Venezuela (Roure et al., 1994; Parnaud et al., 1995; Hung, 2005) and of ~60 km in Trinidad (this study). It should be noted that Hung (2005) has considered 6 possible subsurface interpretations for a centered transect across the Eastern Venezuela Basin producing a wide range of estimates for late Cenozoic shortening (15–115 km). Greater amounts of inferred basement involvement lessen shortening while greater amounts of inferred Cretaceous imbrication above décollement

increase shortening. Roure (in Roure et al., 1994; Parnaud et al., 1995), in formulating a balanced section for a western transect across the Eastern Venezuelan Basin, interprets both significant imbrication above a décollement and deeper uplift of sub-Cretaceous basement. Roure's interpretation suggests approximately 120 km of detached shortening. It is this interpretation that was chosen. An important characteristic of the East Venezuela foldbelt is the periodic occurrence of northwest trending right-lateral strike-slip faults (Urica, San Francisco, and Bohordal (?) Faults, Munro and Smith, 1984; Rosales, 1972). These tear (?) faults give the thrust trends a sawtooth appearance in mapview as they show right-separation offset of the Serranía, Pirital, and Furrial belts. In this manner, the northeast-trending thrust faults and folds combine with the northwest-trending cross faults to form and overall deformation region that trends east-west, parallel to the northern strike-slip system at the southern edge of the Caribbean plate. The Bohordal Fault is a conjectural fault without surface geologic expression other than the somewhat linear trace of the Venezuelan coast at the Gulf of Paria. Since foldbelt patterns in the subsurface of the Gulf of Paria are interpreted to show a right separation at this location, the fault is included as a Urica-like tear fault. The Los Bajos Fault in southwestern Trinidad (Wilson, 1940; Salvador and Stainforth, 1968) appears to be dominantly an episode 3 structural element, but may have begun as an Urica-like tear fault and hence may show episode 2 offset as well.

2.3 Episode 3

A period of right-slip shear broadly distributed across Trinidad and the Gulf of Paria that corresponds to due eastward translation of the Caribbean plate from Late Miocene to Present (Mueller et al., 1999; Weber et al., 2001; Mann et al., 2001). This motion marks a change in relative plate motion from the earlier east-southeast transpression to dominantly eastward translation. While strain partitioning persists, the dip-slip component becomes very much subsidiary to the strike-slip component. Thick deposits of Upper Miocene and Pliocene sediments accumulate in the northern two-thirds of the Gulf of Paria apparently due to a system of northwest striking normal faults (Babb and Mann, 1999; Flinch et al., 1999). I interpret this region of late subsidence to indicate that a significant component of the right-slip is accommodated on the right-stepping relay transfer between the El Pilar strike-slip zone on the north and the Warm Springs/Central Range strike-slip zones on the south that serves to form a rhombochasm over the northern two-thirds of the Gulf of Paria (similar to Schubert's (1982) interpretation of the Cariaco Basin at the western end of the

El Pilar fault). These kinematics suggest that the latest Cenozoic El Pilar strike-slip motion tips out to the east (i.e., onto the island of Trinidad) and that the Warm Springs strike-slip motion tips out to the west (i.e., into the western Gulf of Paria). Seismicity and GPS studies of contemporary motions in and around the island of Trinidad appear to confirm that no current strike-slip is occurring across the Northern Range-Northern Basin boundary (Russo et al., 1993; Weber et al., 2001). Estimates of crustal extension within the rhombochasm (10–15%) suggest 22–33 km of right-slip on the Warm Springs strike-slip zone. Pindell and Kennan (2002) via estimates of paleogeographic juxtapositions imply approximately 100 km of right-slip, but this seems too large for the observed throws on the large normal faults. The internal foldbelt trends of episode 2 are fragmented and offset by the episode 3 deformation. In the southern Gulf of Paria and the Southern Range of Trinidad, however, the external elements of south-vergent contraction persist through episode 3. At the deformation front (Pedernales passive roof duplex of Flinch et al., 1999; Southern Anticline in Trinidad), tectonic wedging into the Paleogene strata causes north-vergent back-thrusting in the Tertiary section.

3   Map-Based Kinematic Models of Late Cenozoic Deformation

The major structural elements observable in surface geology, or for the Gulf of Paria, in seismic data are compiled onto a tectonic base map (Fig. 4a). In the northern Gulf of Paria, the seismic fault patterns of Flinch et al. (1999) have been used. Normal-, reverse-, and strike-separation faults are present. These faults are classified into several categories and distinguished by various colors. Blue traces are predominantly north to northwest striking normal-separation faults. Red traces are predominantly east-west oriented normal- and strike-separation faults. Orange traces are northwest trending zones of inferred right-lateral strike-slip. Lavender traces are observed to inferred locations of thrust deformation fronts; dark-to-light shading of the lavender traces indicates an interpreted older-to-younger principal age to the time of deformation (older = Late Oligocene/Early Miocene; younger = Late Miocene/Recent). The blue, red, and orange faults record episode 3 deformation. The thrust fault traces darker than the lightest shade (Furrial Deformation Front) record the presently fragmented episode 2 deformation.

In view of the subsequent distortions of episode 2 structural elements by episode 3, a palinspastic mapview model has been interpreted in order to restore the original episode 2 tectonic trends. Restoration of episode 3 deformation is intended to recover the original geometry of the presently segmented and dislocated episode 2 structural elements. A second palinspastic model attempts to account for the contractional (episode 2) deformation. This model incorporates strain patterns interpreted for the Eastern Venezuelan Mountains and projects them onto the restored Trinidadian foldbelt trends.

The method of map-view restoration is planimetric; it is analogous to solutions for relative motion history in plate tectonics (Le Pichon, 1968; McKenzie and Morgan, 1969; Atwater, 1970). I have presumed that a network of large faults accounts for the majority of horizontal motions (strike-slip offsets and heave components of normal and reverse faults) across the region of Trinidad and the Gulf of Paria. If this is correct, then the large faults enclose a set of internally rigid (more or less) tectonic blocks or micro-plates. While smaller than lithospheric plates and in most cases detached within the crust, the horizontal kinematics of these interpreted micro-plates should be amenable to plate tectonic style analysis. Between any three micro-plates, identification of the nature and magnitude of motion across two block boundaries (faults), constrains the motion across the third boundary via vector summation. In general, the area of the micro-plates is held constant. As such, gaps and overlaps between restored micro-plates would represent contraction and extension, respectively. An exception to the fixed area of the micro-plates is made for the fold-thrust terranes. An areal expansion is inferred to partially account for internal strain on fold and fault structures across the modeled micro-plate. Each thrust faulted micro-plate was uniformly stretched so as to close about half of the large fault gap between micro-plates. This is an approximate estimate to correct for: a) erosional removal of the original leading-edge thrust sheet (hanging-wall ramp cut-offs) and b) the internal shortening strain within the thrust sheets (small thrusts and folds). The remaining gap represents an estimate of the breadth of the sub-thrust footwall for each of the fold-thrust belts. This method of application for distributed strain across thrust terrane micro-plates is shown in Fig. 5. Mathematical computation was recorded in Excel spreadsheets and map representation of micro-plate displacements was graphically constructed in Adobe Illustrator.
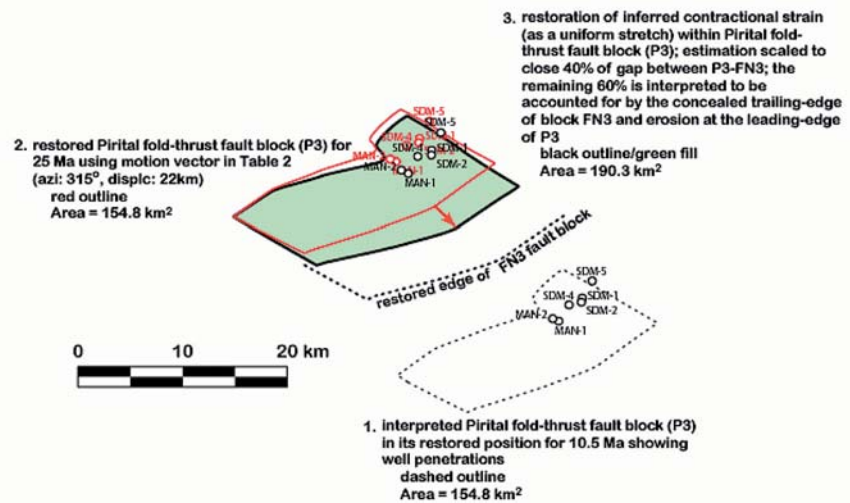
3.1 Episode 3 Inverse Model

A map-based palinspastic restoration has been calculated in order to reconstruct the original distribution of structural elements for 10.5 Ma (time prior to episode 3 deformation). In order to account for the episode 3 deformation, a micro-plate subdivision of the
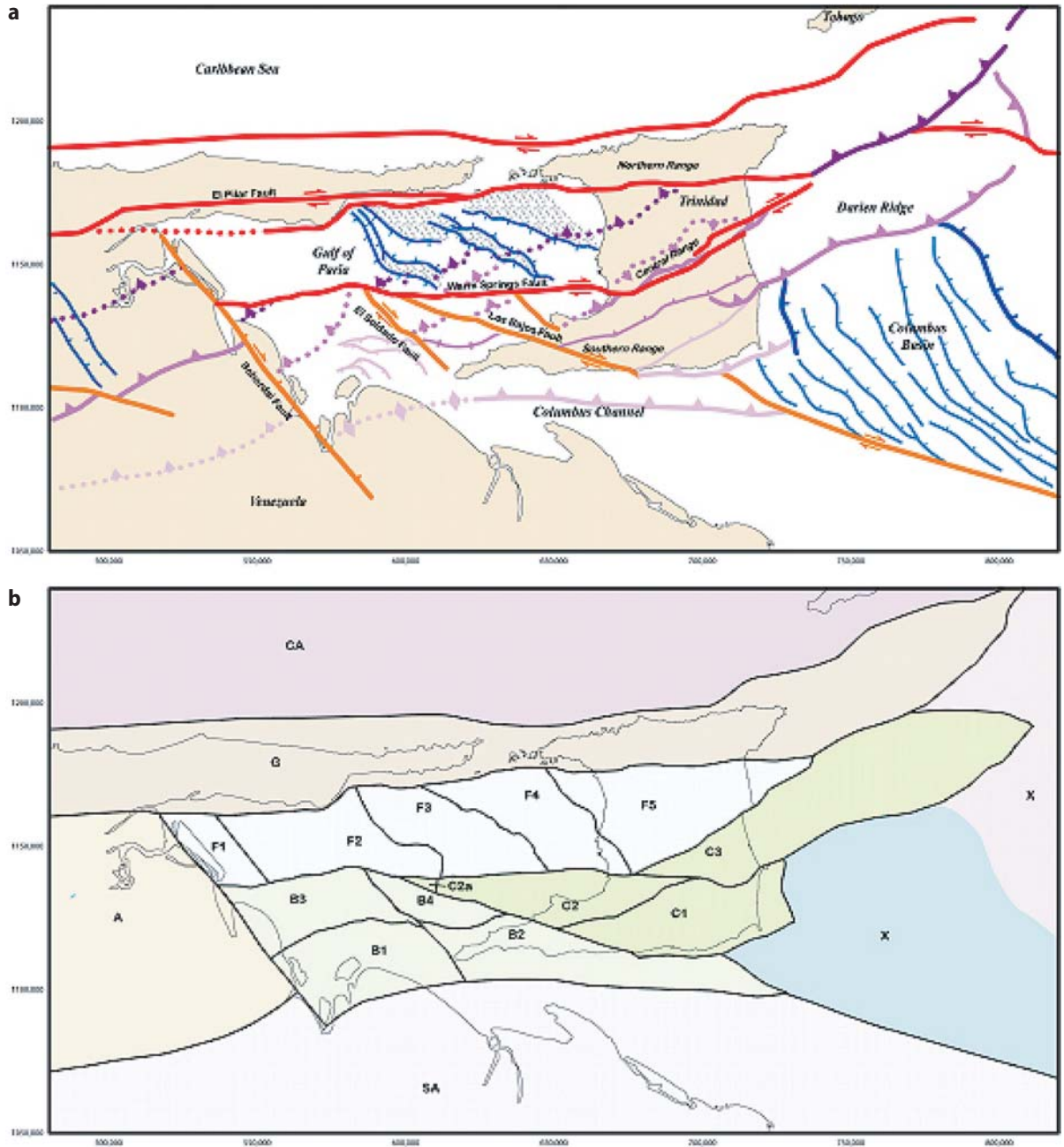
Fig. 4. Distribution of major structural elements of Trinidad and the Gulf of Paria as compiled from surface geology (Kugler, 1959; Bellizzia et al., 1976) and subsurface interpretation (Robertson and Burke, 1989; Flinch et al, 1999.; Babb and Mann, 1999; proprietary seismic interpretation by author in southern Gulf of Paria): **a**) Surface fault traces; faults are color coded by type: *red*, east-trending right-lateral strike-slip faults; *orange*, northwest-trending right-lateral strike-slip faults; *blue*, northwest-trending normal faults (tick marks on downthrown side); *lavender*, east- to northeast-trending thrust faults (barbs on upthrown side, double-barbs on south-vergent tectonic wedges). For the thrust faults, three shades are shown: *light*, currently active thrust front (leading edge of Furrial belt); *medium*, mid- to Late Miocene thrust front (leading edge of Pirital belt); *dark*, latest Oligocene-Early Miocene thrust front (leading edge of Serrania belt). **b**) Micro-plate subdivision for the palispastic restoration of episode 3 deformation: SA (*gray*), cratonic South America; A (*flesh*), fold-thrust belt of the Eastern Venezuelan Mountains; *B1*, *B2*, *B3*, and *B4* (*light green*), fold-thrust belt of Pedernales, southern Gulf of Paria, and Southwest Peninsula of Trinidad (southwest of Los Bajos Fault); C1, C2, *C2a*, and *C3* (*green*), Central and Southern Range fold-thrust belts of Trinidad; *F1, F2, F3, F4*, and *F5* (*light blue*), extensional fault blocks of the northern Gulf of Paria and Northern (Caroni) Basin of Trinidad; G (*brown*), Paria Peninsula of Venezuela and Northern Range of Trinidad; CA (*lavender*), Caribbean plate; x (*blue*), Columbus Basin; x (*pink*) southern parts of the Lesser Antillies accretionary complex. The regions marked by x were ignored by the palinspastic restoration

Fig. 5. Method for the restoration of fault blocks within thrust terranes

Map-view restoration procedure for fault blocks within thrust terranes

3. restoration of inferred contractional strain (as a uniform stretch) within Pirital fold-thrust fault block (P3); estimation scaled to close 40% of gap between P3-FN3; the remaining 60% is interpreted to be accounted for by the concealed trailing-edge of block FN3 and erosion at the leading-edge of P3
black outline/green fill
Area = 190.3 km²

2. restored Pirital fold-thrust fault block (P3) for 25 Ma using motion vector in Table 2 (azi: 315°, displc: 22km)
red outline
Area = 154.8 km²

restored edge of FN3 fault block

0   10   20 km

1. interpreted Pirital fold-thrust fault block (P3) in its restored position for 10.5 Ma showing well penetrations
dashed outline
Area = 154.8 km²

Gulf or Paria/Trinidad region was made using the major fault traces (Fig. 4b). Fifteen micro-plates (A, B1, B2, B3, B4, C1, C2, C2a, C3, F1, F2, F3, F4, F5, G) are defined. The kinematic model assigns a motion vector to each of the micro-plates. Standard vector geometry (as used in global plate tectonics) defines relative motions at the boundaries of all the micro-plates. The model was adjusted to accord with the following constraints:

1. Extension in the northern Gulf of Paria and Caroni basin is 15%,
2. The maximum right-lateral strike-slip offset on the Warm Springs fault is 33 km and occurs where the fault crosses the western Trinidad coastline.,
3. The maximum right-lateral strike-slip offset on the Los Bajos fault is 10.5 km and occurs on the Southwest Peninsula (Tyson, 1989; Wilson, 1940),
4. The El Pilar fault system is interpreted to have 75 km of right-slip (prorated from the total 100 km of post Early Miocene slip; Schubert, 1984; Vierbuchen, 1985), and
5. The Southern Range/Pedernales deformation front is interpreted as dip-slip contraction (motion vector oriented perpendicular to the fault trends) with a magnitude of strain proportional to that interpreted for the Furrial belt in the Eastern Venezuelan Basin (~12% shortening strain from Roure et al., 1994). Modeled motion vectors used for the 10.5 Ma restoration are shown in Table 1. The resultant restoration is shown in Fig. 6.

3.2 Episode 2 Inverse Model

A second map-based palinspastic restoration has been calculated in order to reconstruct the original distribution of structural elements for 25 Ma (time prior to episode 2 deformation). The restoration of the episode 3 deformation permits the more logical connection of the episode 2 deformation fronts as contiguous features defining the fold and thrust belt deformation patterns for the Gulf of Paria/Trinidad region (Fig. 7). These thrust belts are interpreted to be a continuation of the fold-thrust deformation mapped for the Eastern Venezuelan Basin. Three tectonic belts are distinguished:

1. The **Serrania belt** is interpreted to be the hinterland region representing the earliest formed thrust faults showing the greatest shortening, greatest tectonic thickening, and consequently greatest exhumation and erosion (using the restored regional profile of Parnaud et al. (1995) as a guide, the contractional strain is estimated at approximately 48% of total shortening),
2. The **Pirital belt** is interpreted to be a more external region representing younger thrust faults and somewhat lesser shortening, thickening, and erosion (the contractional strain is estimated at approximately 40% of total shortening).
3. The **Furrial belt** is interpreted to be a proximal foreland region with the youngest thrust faults showing small shortening, thickening, and little erosion (Miocene foredeep deposits are by-and-large preserved; the contractional strain is estimated at approximately 12% of total shortening).
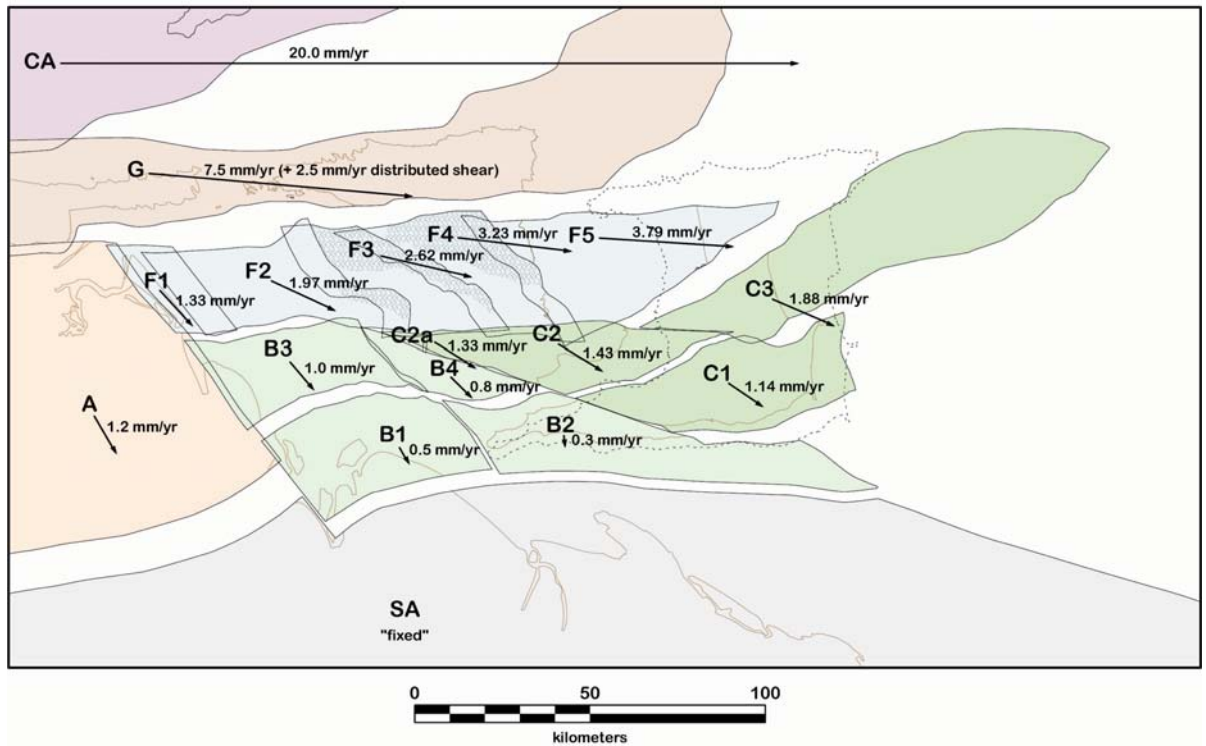
Fig. 6. Palinspastic restoration of episode 3 translations for interpreted micro-plate motions. Magnitude and orientations of the vectors are constrained by: **a**) overall relative plate motion between Caribbean and South American plates, **b**) estimated proportion of Late Miocene and younger strike-slip on the El Pilar fault, **c**) interpreted magnitude of east-northeast extension across northern Gulf of Paria, **d**) interpretation of the 10.5 km right-separation as a result of pure strike-slip motion (Tyson, 1989; Wilson, 1940), and e) interpretation of dip-slip contraction across the present Trinidadian fold-thrust deformation front. Under-constrained micro-plate boundaries were inferred by interpolation or by inference via velocity circuits. The numerical results are recorded in Table 1

On the basis of the restored foldbelt patterns, a micro-plate subdivision for the episode 2 deformation is made (Fig. 7). Sixteen micro-plates (F1, P1, S1, F2, P2, S2, F3, FN3, P3, S3, F4, FN4, FN4a, P4, S4, G) are defined. The kinematic model assumes dip-slip contraction within the foldbelt. Northwest-striking tear faults partition the foldbelt into four domains; from east-to-west, east-northeast striking thrust deformation fronts step northwards across the tear faults, creating the sawtooth aspect to characteristic of the Eastern Venezuelan fold-thrust belt. Carib-SAm plate boundary strike-slip motion is concentrated north and south of micro-plate G. The model was adjusted to accord with the following constraints:

1. The orientation of the dip-slip is presumed to gently fan with the easterly component increasing to the east (the westernmost vectors are aligned parallel to the inferred Bohordal fault and the eastern-

most vectors are parallel to the reconstructed, proto-Los Bajos fault),

2. The magnitude of shortening is estimated by applying a shortening factor calculated from the Parnaud et al. (1995) restoration where the net shortening is

Fig. 7. Interpreted pattern of major fold-thrust belt trends for ▶ Trinidad and the Gulf of Paria prior to episode 3 distortions. The map base is the palinspastic restoration of Figure 5. Three belts are identified and named based on a correlation with the Eastern Venezuelan fold-thrust belt. From northwest (hinterland) to southeast (foreland) they are: a) the Serrania trend – extensive exposure of middle and lower Cretaceous strata; little or no syntectonic deposits, b) the Pirital trend – exposures of upper Cretaceous and Paleogene strata; local preservation of syntectonic deposits, and c) the Furrial trend – principally exposures of syntectonic (Nariva, proximal and Cipero, distal) deposits. Thrust faults are shaded to indicate the sequential age of their formation: dark – Late Oligocene/Early Miocene, medium – Early/Middle Miocene, light – Late Miocene/Present. Orange faults are interpreted locations of right-slip tear faults

Table 1. Interpreted parameters for the geometry of motion vectors, 10.5 Ma to Present. (Map scale: 1cm equals 5km)

Block	Azimuth for = se	Azimuth inv = nw	Rest. ang.	Displc. (km)	Del x (cm) (Azimuth for = se)	Del y (cm) (Azimuth for = se)	Del x (cm) (Azimuth inv = nw)	Del y (cm) (Azimuth inv = nw)
A	150.00	330.00	120.00	12.000	1.200	-2.078	-1.200	2.078
B1	150.00	330.00	120.00	5.000	0.500	-0.866	-0.500	0.866
B2	175.00	355.00	95.00	3.000	0.052	-0.598	-0.052	0.598
B3	140.00	320.00	130.00	10.000	1.286	-1.532	-1.286	1.532
B4	135.00	315.00	135.00	8.000	1.131	-1.131	-1.131	1.131
C1	124.34	304.34	145.66	11.381	1.879	-1.284	1.879	1.284
C2	121.37	301.37	148.63	14.307	2.443	-1.489	-2.443	1.489
C2a	122.21	302.21	147.79	13.328	2.255	-1.421	-2.255	1.421
C3	113.40	293.40	156.60	18.758	3.443	-1.490	3.443	1.490
F1	137.79	317.79	132.21	13.328	1.791	-1.974	-1.791	1.974
F2	115.00	295.00	155.00	19.660	3.564	-1.662	-3.564	1.662
F3	103.02	283.02	166.98	26.160	5.098	-1.179	-5.098	1.179
F4	96.83	276.83	173.17	32.260	6.406	-0.768	-6.406	0.768
F5	93.67	273.67	176.33	37.921	7.569	-0.486	-7.569	0.486
G	95.00	275.00	175.00	75.000	14.943	-1.307	-14.943	1.307

Palinspastic Base at 10.5 Ma for Trinidad and the Gulf of Paria, showing restored Oligo-Miocene Foldbelt trends
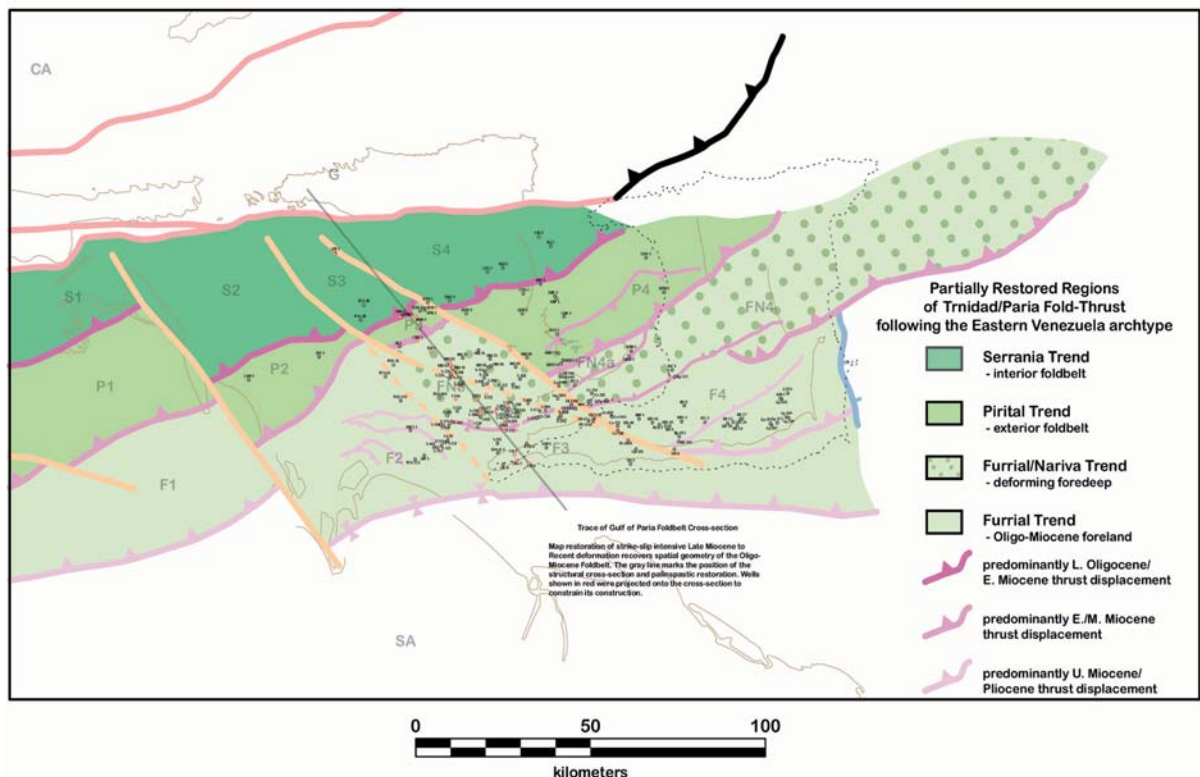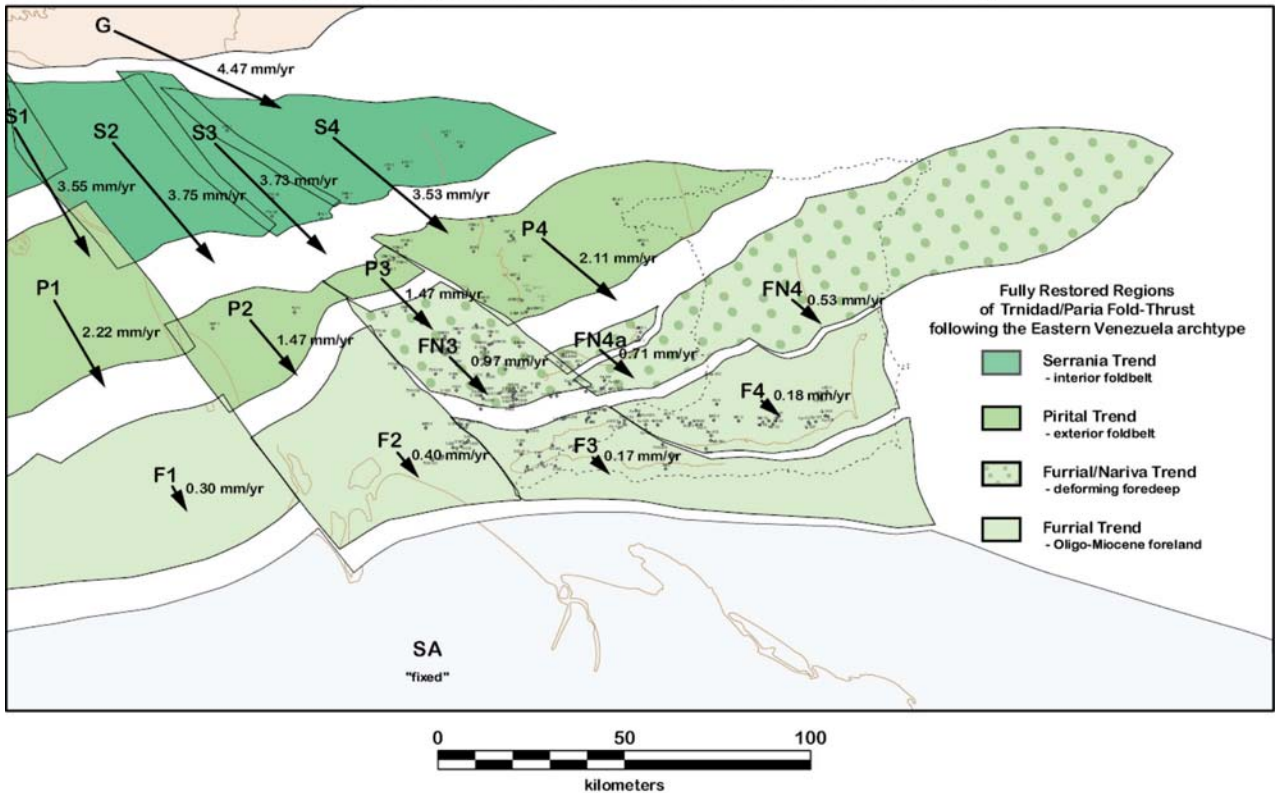
Fig. 8. Palinspastic restoration of episode 2 translations for interpreted fold-thrust trends, segmented by tear faults. Magnitude and orientations of the vectors are constrained by application of longitudinal strain patterns interpreted for the Eastern Venezuelan Mountains on the basis of palinspastic section restoration (Parnaud et al., 1995). The presumed strain was recast as a factor that when multiplied by the dip-direction breadth of the fold-thrust belt segment gives the estimated magnitude of its displacement. The numerical results are recorded in Table 2

proportional to the average width of the thrust belt; separate factors were calculated for the Serrania, Pirital, and Furrial belts).

3. The El Pilar system is interpreted to have its initial 25 km of right-slip. Modeled motion vectors used for the 25 Ma restoration are shown in Table 2. The resultant restoration is shown in Fig. 8.

4   Gulf of Paria Structural Profile

In an attempt to interpret the foldbelt structural geometry, especially that presently concealed beneath Upper Miocene and younger sediments (i.e., those strata presently buried by the 10.5 Ma unconformity), a regional structural profile was constructed for the central Gulf of Paria. Because the episode 3 and episode 2 kinematic axes are not parallel, it is impossible to draw a 2D restorable cross-section across the

current arrangement of contractional structural features. To resolve this difficulty, the structural profile is constructed for the restored foldbelt map for a transect made upon the 10.5 Ma palinspastic base (Fig. 7). The profile extends for 115 km in a NNW-SSE direction. Restored well positions constrain the interpretation of the structural profile. Wells that are located within 5 km of the profile trace have been projected onto the line. A total of twenty-three wells are projected onto the cross-section line. Most wells either extend only a few 100 meters or do not even penetrate the 10.5 Ma unconformity. Eight wells (from south to north: S-189, S-014, S-232, S-113, S-366, NM-02, MAN-2, GPE-1) extend more than 500 meters below the 10.5 Ma unconformity to give some constraint on the structural relief at the top Cretaceous. An estimated topography assumes a coastline position near the interpreted Pirital deformation front (approximate position of the IGA-1 well). To the north, a uniform slope inclined 1.8

Table 2. Interpreted parameters for the geometry of motion vectors, 25–10.5 Ma. (Map scale: 1cm equals 5km; Model.2)

Block	Azimuth for = se	Azimuth inv = nw	Rest. ang.	Displc. (km)	Del x (cm) (Azimuth for = se)	Del y (cm) (Azimuth for = se)	Del x (cm) (Azimuth inv = nw)	Del y (cm) (Azimuth inv = nw)
F0	155.00	335.00	115.00	13.068	1.105	-2.369	-1.105	2.369
P0	155.00	335.00	115.00	55.249	4.670	-10.014	-4.670	10.014
S0	155.00	335.00	115.00	116.959	9.886	-21.200	9.886	21.200
F1	150.00	330.00	120.00	4.500	0.450	-0.779	-0.450	0.779
P1	150.00	330.00	120.00	33.300	3.330	-5.768	-3.330	5.768
S1	150.00	330.00	120.00	53.300	5.330	-9.232	-5.330	9.232
F2	140.00	320.00	130.00	6.000	0.771	-0.919	-0.771	0.919
P2	140.00	320.00	130.00	22.000	2.828	-3.371	-2.828	3.371
S2	140.00	320.00	130.00	56.200	7.225	-8.610	-7.225	8.610
F3	135.00	315.00	135.00	2.500	0.354	-0.354	-0.354	0.354
FN3	135.00	315.00	135.00	14.500	2.051	-2.051	-2.051	2.051
P3	135.00	315.00	135.00	22.000	3.111	-3.111	-3.111	3.111
S3	135.00	315.00	135.00	56.000	7.920	-7.920	-7.920	7.920
F4	130.00	310.00	140.00	2.700	0.414	-0.347	-0.414	0.347
FN4	130.00	310.00	140.00	7.950	1.218	-1.022	-1.218	1.022
FN4a	130.00	310.00	140.00	10.700	1.639	-1.376	-1.639	1.376
P4	130.00	310.00	140.00	31.700	4.857	-4.075	-4.875	4.075
S4	130.00	310.00	140.00	52.950	8.112	-6.807	-8.112	6.807
S1-S4 ave	131.27	311.27	138.73	54.169	7.147	-8.142	-7.147	8.142
G	115.00	295.00	155.00	67.000	12.145	-5.663	-12.145	5.663

degrees to the south is inferred. To the south, a bathyal foredeep basin with seafloor hills above actively growing anticlines is envisioned. As is the usual convention for Trinidad, the southern end is situated on the left of the profile. The final section interpretation and its palinspastic restoration are displayed in Fig. 9.
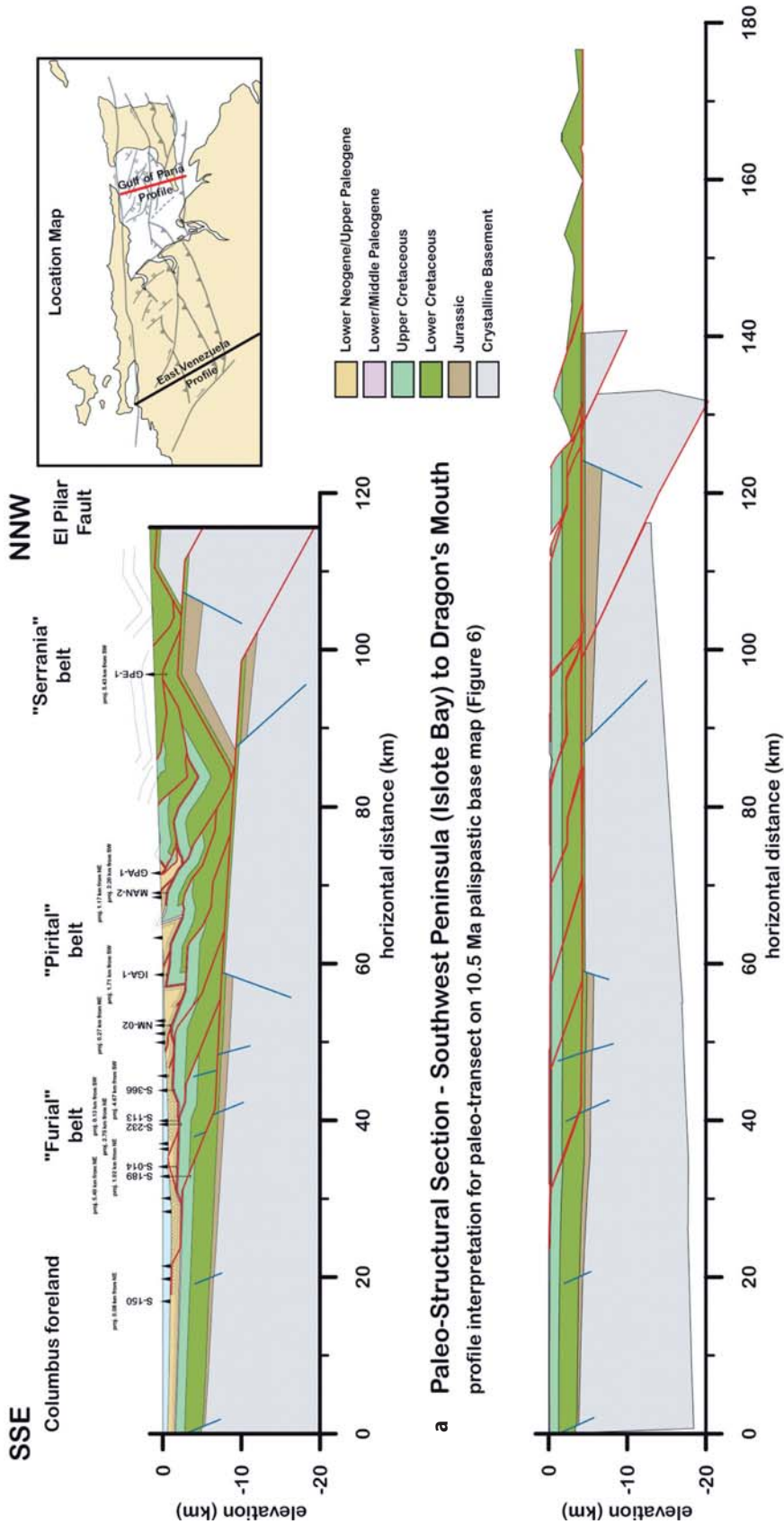
The interpretation of structural geometry of imbricate thrust sheets and thrust-related anticlines is constrained by the well control, the idealized geometry of fault-bend and fault propagation folding of Suppe (1983; Suppe and Medwedeff, 1990), and an inferred base of Cretaceous regional inclined at 2–3 degrees to the north. The passive margin Cretaceous is estimated to be 3575 m thick at the south end of the section. The Cretaceous is presumed to thicken northwards to a maximum of 4500 m near the position of the IGA-1 well. North of this point the Cretaceous possibly thins, but for the purposes of the section construction here, a relatively constant thickness is maintained. As a generalization, the lower two-thirds are considered to be Lower Cretaceous and the upper one-third Upper Cretaceous. The few well penetrations in the region of the northern Gulf of Paria seem to show a uniform ab-

sence of Upper Cretaceous. This is explained here by structural uplift associated with the hinterland of the fold-thrust belt. Perhaps a better alternative would be to presume that the Upper Cretaceous was thin and eroded prior to the post 25 Ma thrust faulting. By analogy with the subsurface fold forms along the Barrackpore-Penal anticlinal trend (onshore structural element in southwestern Trinidad), the fault-related anticlines are considered to be asymmetric fault-propagation folds with upper décollement break-through. Basement-involved structural shortening is restricted to the northern Gulf of Paria.

The restoration of this line is a minimal test of the quality of the interpretation as well as a semi-independent test of the overall shortening within the detached fold-thrust belt. The estimated shortening via application of the foldbelt breadth multiplier scaled to the Eastern Venezuela Basin predicts fold-thrust shortening of 56 km. The palinspastic cross-section restoration estimates the shortening as 61 km. These are viewed as essentially the same result and therefore imply that the use of the Eastern Venezuela Basin short-

Late Miocene Fold Belt Architecture of the Eastern Gulf of Paria

a Paleo-Structural Section - Southwest Peninsula (Islote Bay) to Dragon's Mouth

profile interpretation for paleo-transect on 10.5 Ma palispastic base map (Figure 6)

b Restoration Section - Southwest Peninsula (Islote Bay) to Dragon's Mouth

Fig. 9. Paleo-cross section showing an interpretation of Late Miocene structural geometry for a north-northwest/south-southeast transect. Approximate location of section in the current reference frame is shown in the inset; also shown is the location of the Eastern Venezuelan Mountains profile of Parnaud et al. (1995). The precise location of the section is shown on Fig. 6. Posted wells have been palinspastically relocated (removal of episode 3 dislocations). Section interpretation is 2D-balanced, as shown in the section restoration. Restoration suggests fold-thrust belt shortening of 61 km

ening as a guide to predicting the Trinidadian shortening to be valid.

5   Conclusions

Currently active features associated with the episode 3 deformation dominate the structural expression of geology on the island of Trinidad and the Gulf of Paria. These patterns emphasize east- to east-southeast-trending right-lateral strike-slip across the Trinidadian fold-thrust belt. The strike-slip faults overprint, segment, and disrupt and earlier patterns of dip-slip thrust faulting. Consequently, the thrustbelt deformation in Trinidad is polyphase and its motions cannot be simply analyzed by 2D section restoration oriented orthogonal to surface thrust traces.

Interpretation of the episode 2 thrust belt deformation is aided by a map-based palinspastic restoration that serves to undo the distorting effects of the later strike-slip. Magnitudes of strike-slip are interpreted on the basis of surface geology and estimates of east-west extension in regions of relay transfer. Honoring these constraints, a system of net motion vectors are inferred for a subdivision of the Trinidad/Gulf of Paria transition zone between the Caribbean and South American plates into fourteen microplates. The episode 3 restoration recovers the alignment of thrust deformation fronts defining a hinterland-to-foreland sequence of tectonic belts onto a palinspastic base. The structural and stratigraphic character of these tectonic belts appear to correlate with a similar pattern of tectonic belts observed in the Eastern Venezuelan Mountains that are still extant and unaffected by subsequent structural disruption. Interpreted strain patterns, generalized from restorations in the Eastern Venezuelan Mountains, suggest magnitudes of contraction for the restored Trinidadian tectonic belts. Honoring the constraints of these strain patterns, a system of net motion vectors are inferred for a subdivision of the Trinidadian tectonic belts into fifteen microplates (major thrust sheets). The episode 2 restoration recovers the primary arrangement (less the ambiguous effects of the Paleogene episode 1 deformation) of pre-Miocene passive margin rock units.

The episode 3 restoration provides a basis for interpreting a 2D structural profile of the Trinidadian fold-thrust belt for the Gulf of Paria uncomplicated by cross-cutting strike-slip faults. Assuming that the thrust motions are dominantly dip-slip, balanced section methods of subsurface interpretation and profile restoration give an estimated magnitude of shortening of 61 km. This is reasonably close to the 56 km of shortening along the same transect implied by the net motion vectors inferred for the episode 2 (map-based) restoration. This suggests that the nature and style of deformation in the Trinidadian fold-thrust belt is analogous to that interpreted for the better exposed East Venezuelan fold-thrust belt.

References

Algar, S. and Erikson, J.P., 1995, Correlation of the Jurassic through Oligocene stratigraphic units of Trinidad and northeastern Venezuela: International Geology Review, v. 37, p. 313–334.

Atwater, T., 1970, Implications of plate tectonics for the Cenozoic tectonic evolution of western North America: Geological Society of America Bulletin, v. 81, p. 3,513–3,536.

Avé Lallement, H., 1997, Transpression, displacement partitioning, and exhumation in the Caribbean/South American plate boundary zone: Tectonics, v. 16, p. 272-289.

Babb, S. and Mann, P., 1999, Structural and sedimentary development of a Neogene transpressional plate boundary between the Caribbean and South American plates in Trinidad and Gulf of Paria: in Mann, P. (ed.), Caribbean Basins; Sedimentary Basins of the World, v. 4, p. 495–557.

Barr, K.H. and Saunders, J.B., 1968, An outline of the geology of Trinidad: Transactions of the Fourth Caribbean Geological Conference, p. 1–10.

Bellizzia, A. and Dengo, G., 1990, The Caribbean mountain system, northern South America: in Dengo, G. and Case, J.E. (eds), The Caribbean Region: Geological Society of America, The geology of North America, v. H, p. 167–175.

Bellizzia, A., Pimental, N., Bajo, R., 1976, Mapa geológico structural de Venezuela: Caracas, Minesterio de minas e Hidrocarburos, escala 1:500,000.

Burke, K., Cooper, C., Dewey, J.F., Mann, P., Pindell, J.L., 1984, Caribbean tectonics and relative plate motions: in Bonini, W.E., Hargraves, R.B., and Shagam, R., The Caribbean-South American Plate Boundary and Regional Tectonics: Geological Society of America Memoir 162, p. 31–63.

Flinch, J.F., Rambaran, V., Ali, W., de Lisa, V., Hernandez, G., Rodrigues, K., and Sams, R., 1999, Structure of the Gulf of Paria pull-apart basin (Eastern Venezuela-Trinidad): in Mann, P. (ed.), Caribbean Basins; Sedimentary Basins of the World, v. 4, p. 477–494.

Higgs, R. and Pindell. J., 2001, Cenozoic composite-basin tectonics and sedimentation, Venezuela-Trinidad oil province: (abstract) American Association of Petroleum Geologists Bulletin, v. 85, Issue 13 (Supplement).

Hung, E.J., 2005, Thrust belt interpretation of the Serranía del Interior and Maturín subbasin, eastern Venezuela: Geological Society of America Special Paper 394, p. 251–270.

James, K.H. and Rigby, S.M., 1993, Mesozoic-early Paleogene paleogeography of Venezuela/Trinidad and its implications for Caribbean/South America plate interaction: (abstract) American Association of Petroleum Geologists Bulletin, v. 77, p. 326.

Klitgord, K.D., 2002, Regional tectonics of northeastern South America: ExxonMobil Exploration Company proprietary report.

Kugler, H.G., 1953, Jurassic to recent sedimentary environments in Trinidad: Bulletin de l'Association Suisse des Géologie et Ingénieur du Pétrole, v. 20, p. 27–60.

Kugler, H.G., 1959, Geologic map and sections of Trinidad: The Petroleum Association of Trinidad, Port of Spain, scale 1:250,000.

Le Pichon, X., 1968, Sea-floor spreading and continental drift: Journal of Geophysical Research, v. 73, p. 3,661–3,697.

Mann, P., Schubert, C., Burke, K., 1990, Review of Caribbean neotectonics: in Dengo, G. and Case, J.E. (eds), The Caribbean Region: Geological Society of America, The geology of North America, v. H, p. 307–338.

Mann, P., Weber, J., Wood, L.J., 2001, Tectonic framework for Trinidad and its eastern offshore area: (abstract) American Association of Petroleum Geologists Bulletin, v. 85, Issue 13 (Supplement).

McKenzie, D.P. and Morgan, W.J., 1969, Evolution of triple-junctions: Nature, v. 224, p. 125–133.

Mueller, R.D., et al., 1999, New constraints on the Late Cretaceous/Tertiary plate tectonic evolution of the Caribbean: in Mann, P. (ed.), Caribbean Basins; Sedimentary Basins of the World, v. 4, p. 33–59.

Norton, I., 1996, Relative plate motion model for Venezuela regional study: proprietary Exxon Company report: referenced in part through Goodman, et al., 1998, American Association of Petroleum Geologists 1998 Annual Meeting: AAPG Bulletin 82, p. 1918–1919.

Parnaud, M.J. et al., 1995, Petroleum geology of the central part of the Eastern Venezuelan Basin: in Tankard, A.J, Suarez, R., and Welsink, H.J. (eds.), Petroleum Basins of South America: American Association of Petroleum Geologists Memoir 62, p. 741–756.

Passalacqua, H., Fernandez, F., Gou, Y., Roure, F., 1995, Crustal architecture and strain partitioning in the eastern Venezuelan Ranges: in Tankard, A.J, Suarez, R., and Welsink, H.J. (eds.), Petroleum Basins of South America: American Association of Petroleum Geologists Memoir 62, p. 667–679.

Pérez, O. and Aggarwal, Y.P., 1981, Present-day tectonics of the southeastern Caribbean and northeastern Venezuela: Journal of Geophysical Research, v. 86, p. 10,791–10,804.

Persad, K.M, 1985, Outline of the geology of Trinidad: Fourth Latin American Geological Congress, Port of Spain, p. 738–758.

Pindell, J.L., 1991, Geological rationale for hydrocarbon exploration in the Caribbean and adjacent regions: Journal of Petroleum Geology, v. 14, p. 237–257.

Pindell, J.L. and Dewey, J.F., 1991, Cenozoic transpressional model for the tectonic and basinal development of Venezuela and Trinidad: (abstract) American Association of Petroleum Geologists Bulletin, v. 75, p. 654.

Pindell, J. and Kennan, L., 2002, Palinspastic paleogeographic evolution of Eastern Venezuela and Trinidad: (abstract) in 16th Caribbean Geological Conference, p. 99.

Rosales, H., 1972, La falla de San Francisco en el oriente de Venezuela: in Congreso Geologico Venezolano, 4th, Memoria, v. 4, p. 2,322–2,336.

Roure, F., et al., 1995, Geometry and kinematics of the North Monogas thrust belt (Venezuela): Marine Petroleum Geology, v. 11, p. 347–362.

Russo, R.M., Speed, R.C., Okal, E.A., Shepherd, J.B., Rowley, K.C., 1993, Seismicity and tectonics of the southeastern Caribbbean: Journal of Geophysical Research, v. 98, p. 14,299–14,319.

Salvador, A. and Stainforth, R.M., 1968, Clues in Venezuela to the geology of Trinidad and vice versa: Transactions of the Fourth Caribbean Geological Conference, p. 31–40.

Schubert, C., 1982, Origin of the Cariaco basin, southern Caribbean Sea: Marine Geology, v. 47, p. 345–360.

Schubert, C., 1984, Basin formation along the Bocono-Moron-El Pilar system, Venezuela: Journal of Geophysical Research, v. 89, p. 5711–5718.

Speed, R.C., 1985, Cenozoic collision of the Lesser Antilles and continental South America and the origin of El Pilar fault: Tectonics, v. 4, p. 41–69.

Suppe, J., 1983, Geometry and kinematics of fault-bend folding: American Journal of Science, v. 283, p. 684–721.

Suppe, J. and Medwedeff, D.A., 1990, Geometry and kinematic of fault-propagation folding: in Jordan, P., Noack, T., Schmid, S., and Bernoulli, D. (eds), The Hans Laubscher volume: Eclogae Geologicae Helvetiae, v. 83, p. 409–454.

Tyson, L., 1989, Structural features associated with the Los Bajos fault and their interpretation in light of current theories of strike-slip tectonics: Transactions of the 12th Caribbean Geological Conference, p. 403–414.

Tyson, L. and Ali, W., 1990, Cretaceous to middle Miocene sediments in Trinidad: in Second geological conference of the Geological Society of Trinidad & Tobago, Fieldtrip Guide, p. 35–46.

Vierbuchen, R.C., 1985, The geology of the El Pilar fault zone and adjacent areas in northeastern Venezuela: in Bonini, W.E., Hargraves, R.B., and Shagam, R. (eds.), The Caribbean-south American plate boundary and regional tectonics: Geological Society of America Memoir 162, p. 189–212.

Weber, J.C., Dixon, T.H., DeMets, C., Ambeh, W.B., Jansma, P., Mattioli, G., Saleh, J., Sella, G., Bilham, R., Perez, O., 2001, GPS estimate of relative motion between the Caribbean and South American plates, and geologic implications for Trinidad and Venezuela: Geology, v. 29, p. 75–78.

Wilson, C.C., 1940, The Los Bajos fault of south Trinidad, B.W.I., American Association of Petroleum Geologists Bulletin, v. 24, p. 2102–2125.

Kinematics of the SE Canadian Fold and Thrust Belt: Implications for the Thermal and Organic Maturation History

N.J. Hardebol · J.P. Callot · J.L. Faure · G. Bertotti · F. Roure

Abstract. The southern Canadian Foreland Fold and Thrust Belt forms a north-eastward tapering contractional belt comprising Mesoproterozoic intracontinental, Palaeozoic continental margin and Mesozoic to lower Tertiary foredeep sequences that record an upper Cretaceous to Palaeocene contractional history. Shortening is accommodated by a few major thrusts (e.g. Lewis thrust and McDonald thrust), estimated at ~115–125 km and accompanied by the development of a presumably thick, currently eroded syntectonic foredeep wedge. The contractional features are overprinted by a second deformation phase of Late Eocene-Oligocene extension with the formation of two pronounced halfgraben systems (i.e. Flathead Valley Graben and Rocky Mountain Trench) and bounding listric normal faults that merge at depth with the pre-existing thrust decollements.

This paper especially aims to elucidate the exhumation pattern and history that have not only affected the deformed Canadian Foreland Belt on the small wavelength of individual thrustsheets, but also on an extended scale involving the undeformed distal foreland.

The construction of three east-west trending regional and simplified structural cross-sections provided structural coherency and allowed for first-order structural balancing and restoration of the deformed and strongly eroded sedimentary wedge. A combination of 1D conceptual and 2D forward kinematic modelling allowed for the restoration of the syntectonic sedimentary wedge and also for better resolving burial and exhumation history (i.e., timing, amplitude and wavelength). The modelling was constrained by organic maturity ranks with a dense regional coverage together with published fission track inferences for necessary constraints on timing. It is shown that the current thermo-chronological dataset allow, for two distinct burial and exhumation scenarios; the first in which overburden and peak temperatures are achieved by purely sedimentary burial and the second with a strong tectonic loading component. It is postulated that FT and organic maturity constraints allows for a more moderate restored thickness of the deformed and eroded sedimentary wedge than previously inferred. This study makes the feasibility and uncertainties more apparent that accompanies the unravelling of the denudation history of a strongly deformed sedimentary wedge and also illustrates the strong bearing of basal decollement geometry effected by inherited basin architecture. The integration of kinematic and exhumation inferences reveal a short-wavelength syn-orogenic exhumation (~4–6 km) limited to the deformed Foreland Belt associated with thrustsheet emplacement during the upper Cretaceous–lower Palaeocene contraction, followed by a second episode of large wavelength exhumation involving the entire former foredeep (i.e., with amplitudes of 2 to 4 km) during the upper Palaeocene-Eocene.

1   Introduction

It is widely recognized that Foreland Fold and Thrust Belts (FFTB) exhibit an intricate interaction between foredeep deposition and structural stacking from sheet emplacement together filling up the accommodation space generated by the flexure (Ford, 2004 and references therein). Thus, in a Foreland Belt setting, both tectonic and sedimentary processes are expected to control the burial, thermal and organic maturation history (e.g. Hacquebard and Donaldson, 1974; England and Bustin, 1985, 1986; Hardebol et al., 2005). Consequently, an integrated forward thermo-kinematic modelling approach is necessary to determine these two burial components and derive at more accurate estimates of the thickness of the eroded sedimentary wedge.

Performing regional scale restorations of the deformed belt and eroded foredeep wedge combined with burial and thermal history modelling provide a necessary basis for subsequent integrated thermo-kinematic and ultimately fluid flow modelling (Faure et al., 2004; Roure et al., 2004, 2005). Thus, this forms a valuable workflow, especially for petroleum system appraisal.

The Canadian Cordillera experienced substantial exhumation that affected not only the deformed Foreland Belt on the wavelength of thrust sheets but extended far into the undeformed distal foreland. Therefore, extensive denudation has severely thinned a presumably originally thick syntectonic sedimentary wedge. While the scarcity of syntectonic sediments hampers kinematic inferences, it also makes a proper restoration of the deformed wedge more relevant for deriving

more accurate burial and exhumation estimates especially for petroleum systems appraisal.

The Canadian Foreland Belt is a well suited study area for this integrated approach since much structural geologic work has already discussed its kinematics (e.g., Bally 1966; Dahlstrom, 1970; Price, 1981, 1994; Fermor and Moffat, 1992; Faure et al., 2004). The presence of many coal rank studies with a paucity of maturity ranks and burial history inferences further enhances its suitability (Hacquebart and Donaldson, 1974; Kalkreuth and McMechan, 1988; Kalkreuth et al., 1989; England and Bustin, 1991). Not only in the foreland, but also in deformed Foreland Belt, organic maturity ranks (OMR) have played a prime role in the inference of the presumed thick sedimentary overburden. Thicknesses of the syntectonic sedimentary wedge have so far been inferred assuming that the maturation history predates tectonism and as such record a pure sedimentary burial (Hacquebard and Donaldson, 1974; Faure et al., 2004; Osadetz et al., 2004; Feinstein et al., 2005; Hardebol et al., 2005).

Recent studies that integrate these maturity rank inferences with fission track constraints and integrated forward thermo-kinematic modelling have demonstrated the occurrence of 8–10 km of erosion on the wavelength of individual thrust sheets. This exhumation of the belt commenced during contractional tectonism associated with thrustsheet emplacement in late Cretaceous-Palaeocene times (e.g., Faure et al., 2004; Osadetz et al., 2004; Feinstein et al., 2005).

Moreover, pronounced exhumation has been documented not only for the deformed belt, but also on a large scale involving the undeformed distal foreland (i.e., the Western Canadian Sedimentary Basin, North of Edmonton (Fort McMurray-Fort St-John), from Edmonton to the Rocky Mountain House, and from Banff to Calgary (Hacquebard, 1977; Willet et al., 1997; Issler et al., 1999; Faure et al., 2004). Superficial sediments in the external Foothills and the adjacent foreland basin have maturity indicators substantially higher than expected from their present depth, suggesting a missing sedimentary load of 2 to 5 km (a.o. Steiner et al., 1972; Hacquebard, 1977; Bustin, 1991; Willet et al., 1997; Faure et al., 2004; Osadetz et al., 2002).

Despite this wealth of knowledge on both the kinematics and maturation ranks and history, the possible linkage and its implication for petroleum systems are addressed only by a few comprehensive studies (Osadetz et al., 1992; Faure et al., 2004). A proper understanding of kinematics is necessary and receives significant attention in this paper, which is focused on the south-easternmost Canadian Cordilleran Foreland Belt (SE British Columbia & SW Alberta). The study will first present new structural and restored profiles to control the structural complexity of the study area. This will be the basis for the forward kinematic modelling, involving both the sedimentary burial of the foredeep and the contractional deformation of the belt (e.g. Faure et al., 2004). The consequences of timing and kinematics of the burial and deformation history on the temperature and maturation history have been tested by 1D conceptual modelling and 2D forward thermo-kinematic modelling.

2   Geological Context

2.1   Tectonic Framework

The Canadian Cordillera of which the Foreland-Fold and thrust Belt (FFTB) forms the eastern portion (Gabrielse and Yorath, 1992), consists of a tectonic collage of amalgamated volcanic, island arc and oceanic terranes and strongly deformed sedimentary sequences deposited and accreted onto the leading edge of the North American Craton during a Late Jurassic to Palaeocene ocean-continent convergence (Monger and Price, 1979; Price, 1981; McMechan and Thompson, 1989; Price, 1994). The Canadian Cordillera can be subdivided into morpho-tectonic belts (Fig. 1) which are from the Pacific ocean eastward:

- The Insular Belt
- The Coastal Plutonic Complex
- The Intermontane Belt composed of several terranes accreted to the paleo-passive margin.
- The Omineca-Purcell crystalline belt, made of deep crustal body exhumed by core complexes.
- The Foreland-Fold and thrust Belt (FFTB) and associated foreland basin.

This study mainly focuses on the southernmost portion of the Canadian FFTB or alternatively referred herein as the Foreland Belt. The area encompasses a north-eastward tapering contractional wedge that records the Late Cretaceous-Palaeocene Laramide Orogenic phase, bounded to the West by the Rocky Mountain Trench, and to the East fading into the undeformed foreland basin (Fig. 2).

The southern Foreland Belt comprises a sequence of Mesoproterozoic intracontinental, Palaeozoic continental margin and Mesozoic to lower Tertiary foredeep sequences. The Mesoproterozoic Belt-Purcell supergroup consists of an up to 10-km-thick sequence of shallow water limestones, siliciclastic shelf and slope related sediments deposited in a basin with its depocenter in the south that fastly rapidly pinches out in the study area (Price and Sears, 2000). The Palaeozoic consists of a predominately carbonate platform-to-basin succession deposited in a persistent passive margin setting. The overlying Mesozoic sequence (i.e. the Upper Jurassic and Lower Cretaceous Fernie formation-
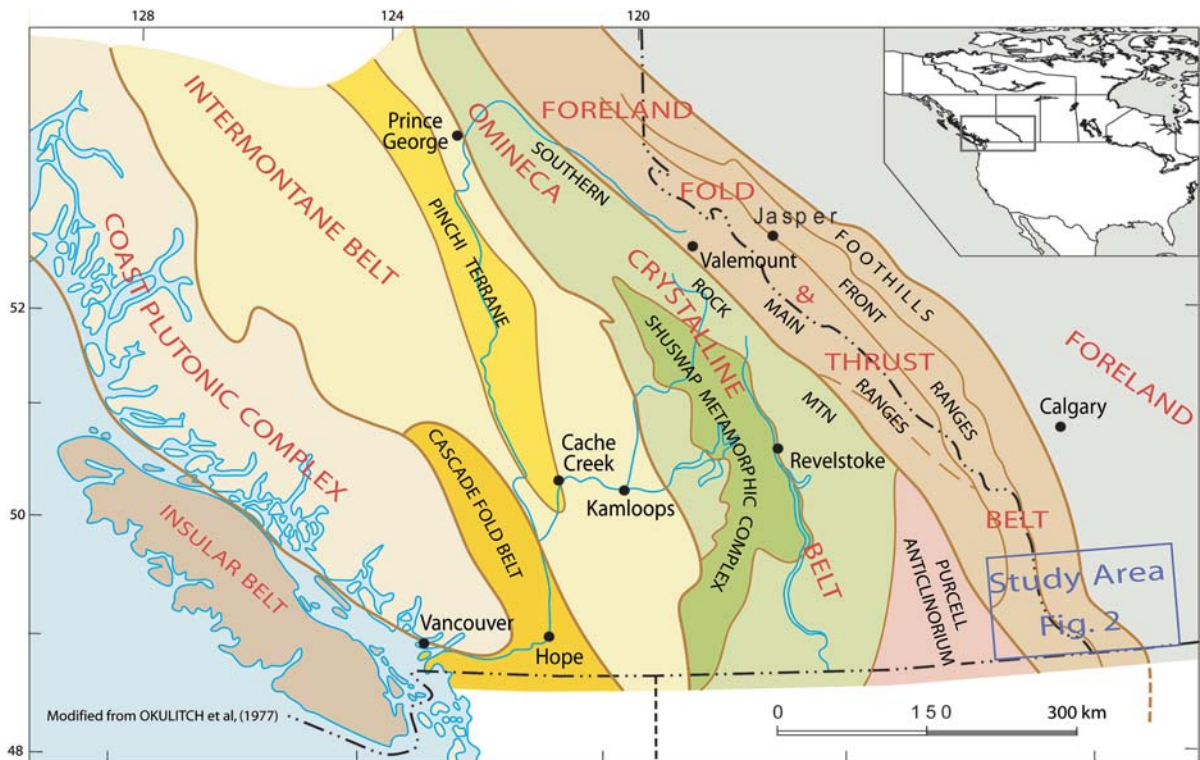
Fig. 1. Overview of the southern Canadian Cordillera outlining its morpho-tectonic subdivision together with the principle lateral continuous fault systems

Kootenay group) mark the onset of the foreland flexure and foreland basin development, a marine transgression following an episode of exposure and continental deposits. They are especially well preserved in the Foothill region.

2.2 Main Structural Elements of the FFTB

A compilation of the main structural elements is outlined in map view (Fig. 2) and is further examined later on with the construction and balancing of 3 E-W regional cross-sections (Fig. 3). The area is partitioned by the Lewis thrust (LT) into a hangingwall block consisting mainly of to Mesoproterozoic and Palaeozoic strata emplaced over a Cretaceous-lower Palaeocene clastic foredeep sequence referred to as the Foothills. The LT hangingwall block features a series of Oligocene extensional features structures.

2.2.1 LT Hangingwall: Clark and MacDonald Ranges and Fernie "Basin"

The LT hangingwall block is dominated by the Lewis thrust sheet (LTS) that forms the most elongated sheet

and accounts for most of the shortening accommodated in the southern FFTB. Its kinematics and structural style are strongly controlled by lateral changes in the basal decollement architecture and yield high lateral variability.

In the Clark Range, the LTS is at the surface and consists of a broadly folded, thin erosional remnant of a formerly much thicker Mesoproterozoic to Mesozoic sedimentary sequence (Osadetz et al., 2004). In the Cate and Sage Creek windows, lower Belt-Purcell strata from the LT hangingwall are found in contact with upper Cretaceous of its footwall block (Figs. 2 and 3) (Price, 1964, 1965; Mudge and Earhart, 1980; Fermor and Moffat, 1992; Sears, 2001). Together with wells that penetrate the footwall, these windows allowed for surface sampling (OMR & FT) for a better appraisal of the exhumation history of a presumably thick LTS and underlying footwall block (Osadetz et al., 2004; Feinstein et al., 2005).

A much more complete, yet broken up, portion of the LTS remains preserved further to the west (i.e., Galton, Lizard and MacDonald Ranges) where Palaeozoic strata remain partly attached to the Mesoproterozoic sequence (Fig. 3b). Only in the Howell Creek structure, fault-bounded upper Cretaceous strata are preserved within the Lewis thrust hangingwall. The
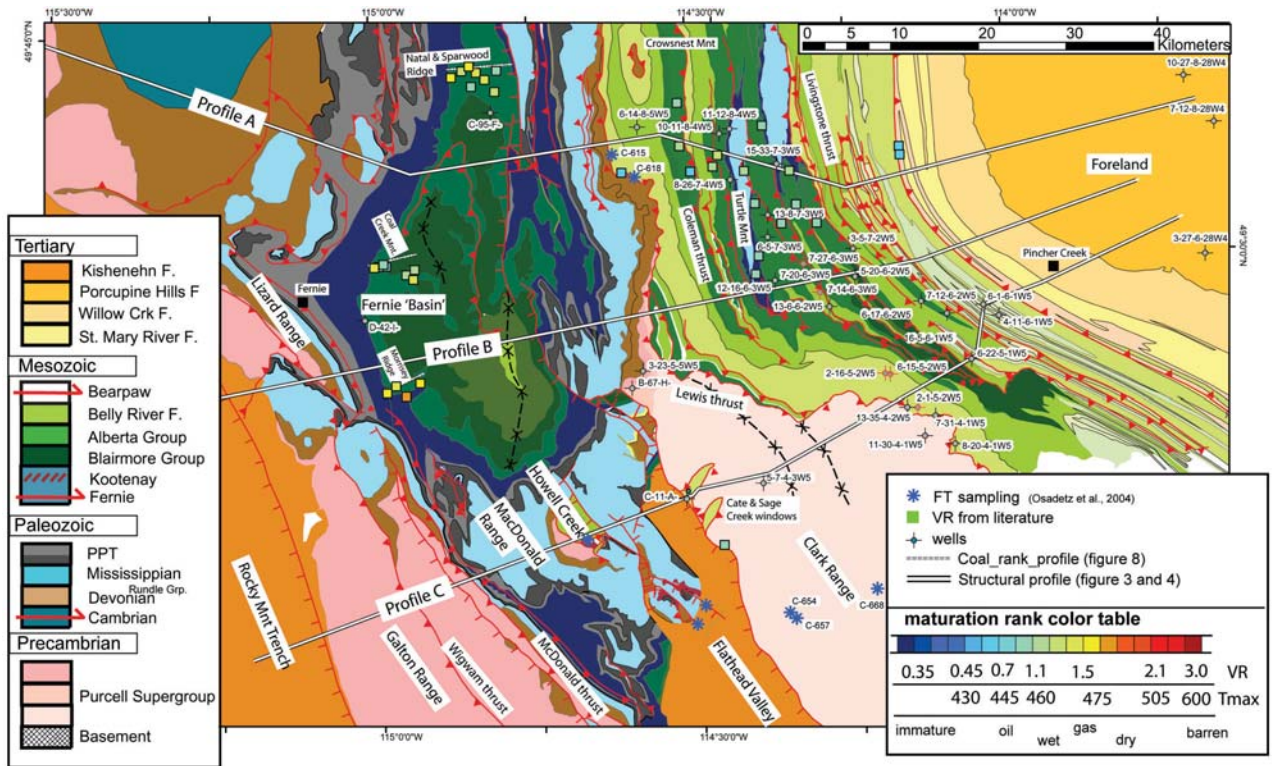
Fig. 2. Structural map of the SE Canadian Cordillera Foreland Belt located SW of Calgary between 49–50° N. The principle structural features in the context of the kinematic history are depicted together with the location of the structural profiles (figure 3), wells, published coal rank measures used for synthetic well modelling (figure 8 and 9) and FT sampling locations as published by Osadetz et al. (2005)

structure indicates that Upper Cretaceous Alberta and Wapiabi formations were still more widely preserved in the LT hangingwall till late Eocene-Oligocene time and in the Howell Creek protected from exhumation by this downfaulted block (Labreque and Shaw, 1973; Osadetz et al, 2004). As such, this fault-bounded preservation will show its value in the context of LTS kinematic and exhumation history.

The Fernie "Basin" represents a synclinal feature in the hangingwall of the LTS containing a remarkably well preserved pile of Jurassic-Cretaceous clastics (Figs. 2 and 3). With the presence of three levels of coal seams, the Fernie "Basin" gained significance in coal exploration and maturity rank estimates. The preservation of the sequence is due to its relative low structural position in comparison to the surrounding lower Palaeozoic sedimentary sequences of the Crowsnest Pass, Clark and MacDonald Range (Figs. 2, 3 and 4). In the Clark Range, the structural much higher position of the Palaeozoic strata results from the inversion of a thick former Belt-Purcell basin infill that is displaced by the LT over a large distance to its current autochthonous position superimposed onto Cretaceous units of the Foothills.

2.2.2   Foothills and Foreland

The Foothills (Fig. 2) make up the eastern portion of the study area, east of the Lewis thrust front and are characterized by closely spaced, easterly verging imbricate thrust slices of a Meso- to Cenozoic clastic, former foredeep succession. The main thrusts that together accounts for most of the deformation in the LT footwall block are, from west to east, the Coleman, Turtle Mountain, Livingstone and Mill Creek thrusts (Figs. 2 and 3). The first three thrusts still carry significant volumes of competent Palaeozoic limestones over quite a distance eastward forming distinct structural culminations as exposed, for instance, in the Turtle Mountains. In the outer-Foothills East of the Livingstone thrust, the Mill Creek thrust together with multiple other faults only carry Meso- and Cenozoic sequences (Figs. 2 and 3; Begin et al., 1996).

The Foothills are bordered to the east by a backthrust which uses the upper Campanian Bearpaw shales as decollement level. As the overlying sequence of Maastrichtian and Palaeocene foredeep clastics is decoupled from the underlying Mesozoic sequence
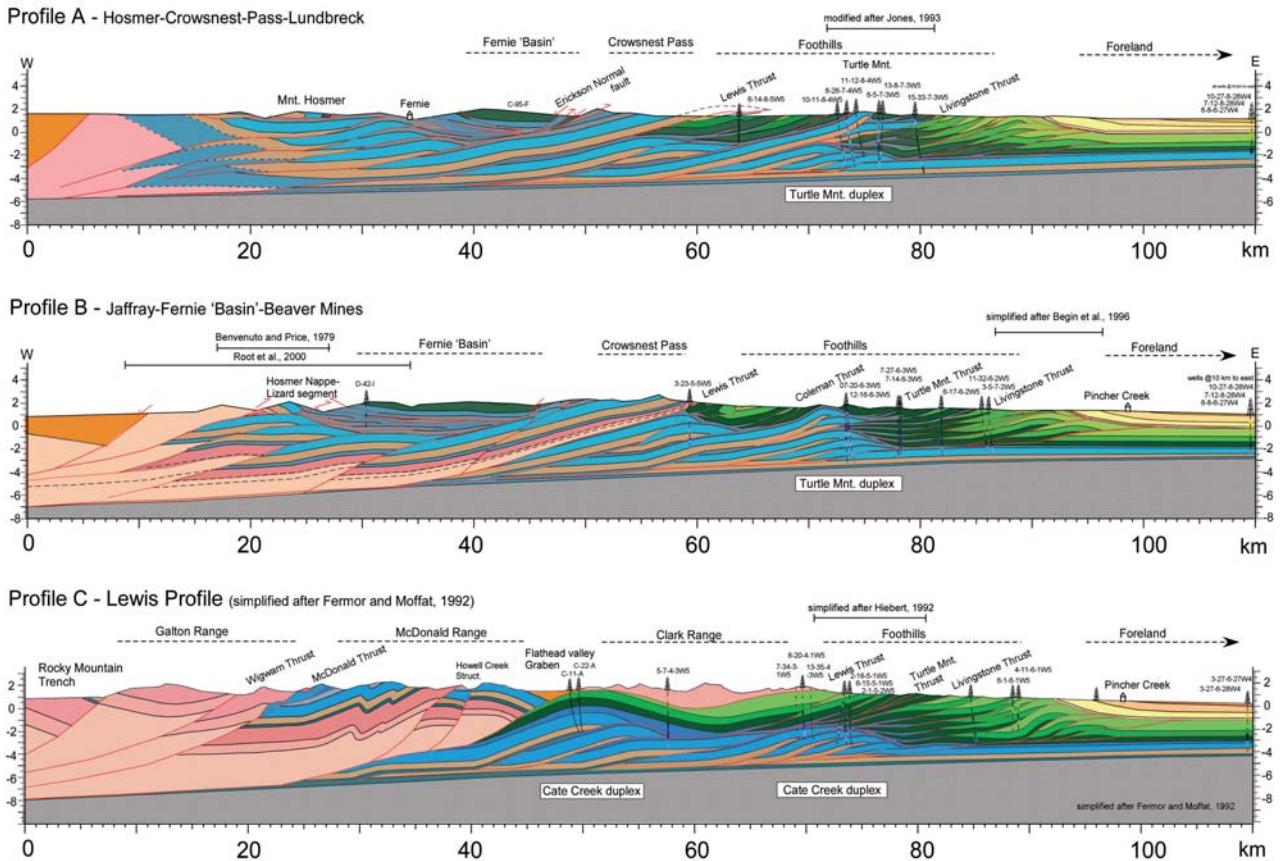
Fig. 3. Three WSW-ENE trending structural profiles across the Foreland Fold and Thrust Belt from the Rocky Mountain Trench in the West to the Foreland in the East (see figure 2 for location). **a** Profile A across Mnt. Hosmer in the West, Fernie 'Basin', Crowsnest Pass, Turtle Mnt. eastward into the distal Foothills and foreland. **b** Profile B across Lizard Range south of Fernie, Fernie 'Basin', crossing the southern tip of Turtle Mnt. culmination near Beaver Mines into the foreland north of Pincher Creek. **c** Profile C across the Galton Range, MacDonald Range, traversing the enigmatic Howell Creek structure and Cate Creek window, Clark Range turning into Foothills and foreland in the East, south of Pincher Creek

they are not involved in the strongly deformed Foreland Belt, only slightly eastward tilted decoupled from the underlying imbricated triangle zone.

2.2.3 Oligocene Extensional Features

The FFTB shows widespread evidence of significant normal faulting overprinting older contractional features. In the study area, the LTS is dissected by the Flathead Normal fault (and its northern continuation, the Erickson normal fault) that forms the eastern border of the late-Oligocene Flathead halfgraben (Figs. 2 and 3). The Flathead normal Fault (FNF) is a listric fault with up to 12 km of net slip that merges at depth with the underlying Lewis thrust (Constenius, 1996; Fermor and Moffat, 1992; McMechan, 1981; Bally et al., 1966). Subsidence along the FNF created an asymmetric graben containing up to 3400 m of nonmarine,

Eocene-Oligocene fault-growth strata which is unconformably overlying Lower Cretaceous strata of the Blairmore Group (Price, 1962; McMechan, 1981; Constenius, 1996; Osadetz, 2004). Coarse erosional products from local surrounding sources also contribute to the understanding of the exhumation history, as pebbles of the Blairmore Group derived from the adjacent Clark range indicate that a 6- to 8- km-thick LTS persisted until Oligocene time before being further eroded to the present-day thin remnant (Osadetz et al., 2004; Constenius, 1996).

Another Tertiary halfgraben system, with a more pronounced physiographic expression is formed by the Rocky Mountain Trench. This depression stretches for 1600 km from south into the US, to the British Columbia-Yukon border in the north where the graben passes into a transtentional fault with large lateral displacement (a.o. Dahlstrom, 1970; Gabrielse and Yorath, 1992).

2.3 Petroleum Systems

The southern Canadian Foreland Belt holds a century of petroleum exploration that exemplifies how geologic advancements in seismic techniques and understanding of structural styles and kinematics allowed for successful exploitation in structural complex areas. After the hydrocarbon first discoveries in the Crowsnest Pass and Turner Valley area (end 19th century), significant gas pool discoveries were made in the Pincher Creek and Waterton area (Fig. 3). These pools are both located in antiformal stacks (i..e., Pincher Creek and Waterton duplexes) comprising Palaeozoic thrustsheets with especially a thick imbricated sequence of porous Devonian (Palliser Formation) and Mississippian limestones of the Rundle Group (Fermor and Moffat, 1992). Furthermore, hydrocarbons have been found in Cretaceous sandstones (Belly River formation) trapped in anticlinal structures in vicinity of the triangle zone. Source rock intervals are best developed in the marine Mississippian (Exshaw formation, type II OM) and Fernie-Kootenay shales and coal seams. Several other source rock intervals have been identified in the dominantly siliciclastic formations, i.e., in the Blairmore group (type III kerogen), and in the Cretaceous Alberta group (type II kerogen) (Creaney and Allen, 1992).

3   Structural Restoration and Kinematics

3.1 Structural Cross-Sections

The construction of three parallel trending transects, only a few tens of kms apart, assists in understanding along-strike structural variability of the Foreland Belt. Achieving structural coherency among apparent disparate structures helped to make simplification while maintaining the key-structural elements and overall structural style.

The profiles are constrained by surface geology (Leech, 1960; Price, 1962, 1965; Norris, 1993a, 1993b; Lebel et al., 1997; Lebel and Hiebert, 2001; Stockmal and Lebel, 2003) detailed structural profiles (i.e., for the Turtle Mountain: Jones, 1993; Fernie Basin: Root et al., 2000; for the Triangle zone and foothills: Norris, 1993a, 1993b; Hiebert and Spratt, 1996; Stockmall et al., 1996; MacKay, 1996;) and well data (see Fig. 2). Profile C is derived from the classic Lewis profile as published by Fermor and Moffat (1992) and previously presented by Bally et al. (1966), Price (1981) and Price and Fermor (1985).

3.1.1   Detachment Levels and Geometry

The southern FFTB is dominated by mostly easterly verging thrust faults that commonly follow bedding-parallel decollements and ramps that generally cut up through the stratigraphic succession in the direction of hangingwall displacement (Bally et al., 1966; Dahlstrom, 1970; Price, 1986). The geometry of the basal decollement forms ultimate control on deformation style and the amount of rock incorporated in the deformed and exhumed wedge. Yet, the decollement's geometry could only be tentatively obtained by applying a combination of structural inferences from exposed hangingwall base geometries, information from wells penetrating into the assumed autochthonous, and some clear seismic basement reflectors (Bally, 1966; Fermor and Moffat, 1992).

The Foreland Belt comprises a supracrustal sedimentary contractional wedge, with a basal detachment from which all principle thrusts branch off and that also decouples the underlying, essentially undeformed North American craton, i.e. the Hudsonian basement (Bally et al., 1966; Price, 1981; Fermor and Moffat, 1992; van der Velden and Cook, 1994, 1996; Fig. 3).

In the northwestern Foreland Belt, between the Rocky Mnt. Trench and the Flathead Valley, the basal decollement resides at the base of the thick and competent Mesoproterozic Belt-Purcell sequence. Successively the Wigwam and Macdonald thrusts branch from this detachment, cutting through the complete Belt-Purcell and overlying Palaeozoic sequence and reach surface under a steep angle. In absence of an appropriate decollement level in the lower Palaeozoic, the Palaeozoic sequence remains attached to the underlying thick Belt-Purcell Group (Fig. 3c). In contrast, to the north, in the Lizard Range and around Mount Hosmer, (Figs. 2 and 3a), the presence of Cambrian shale and Devonian gypsum levels allow for differential displacement within the hangingwall of the LT (Benevuto and Price, 1979).

In fact, as discussed in detail by Price and Sears (2000), the flat-ramp geometries of the Lewis and related thrusts, is strongly controlled by the margins and infill of the already mentioned Mesoproterozoic Belt Purcell Basin in the south and Lower-Palaeozoic basin to the northwest.

This thick Lower-Palaeozoic basin fill, with its basin margin slicing the study areas northwestern corner comprises incompetent shales and argillaceous limestones that allow multiple Palaeozic imbricates (Figs. 2 and 3a – northwestern most portion). The Belt-Purcell basin fill, absent north of the Crowsnest Pass, but rapidly thickening southward (i.e., main depocenter located further south in Montana), controls the basal

decollements position in the Clark Range and the LT lateral hangingwall ramp geometry.

The above exemplifies clearly how the Belt-Purcell and Lower Palaeozoic basin geometry, by controlling the Lewis thrust flat-ramp geometry, have such a strong bearing on the present-day tectonomorphological expression and exhumation history of the Foreland Belt.

East of the Lewis thrust, in the foothills, widely spaced thrusts branch off from the basal decollement just above the crystalline basement, carrying competent Palaeozoic platform carbonates. The Mesozoic rocks are detached from the underlying Palaeozoic at the Jurassic marine shales of the Fernie Group allowing for a different structural style with closer spaced faults. Other stratigraphic intervals in which decollements preferably develop are the Devonian Fairholme-Palliser formations, the Mississippian Exhaw-Banff formations, the Cretaceous Blairmore Group, Alberta and Wapiabi formations and the Bearpaw shales (Fermor and Moffat, 1992; Price, 1986; Begin et al., 1996). Rigorous simplification of the structural profiles has been achieved by reducing the number of decollement levels while preserving consistency. Beside the decollement at the Fernie-Kootenay shales that accommodates most of the differential displacement, other less persistent flats within the Blairmore group are preserved.

3.1.2 Structural Culminations, Duplex and Imbrication Structures

Across the Foreland Belt, the Fernie shales allow for decoupling between Palaeozoic and overlying Mesozoic rocks. Elongated, widely spaced thrust sheets developed in the thick succession of Devonian and Mississippian limestone beds that act as competent and passive beams. The decoupled Palaeozoic tends to form structural culminations in the form of anticlinal stacks (Fig. 3). Smaller-scale imbrications are omitted, yet the duplex envelope is maintained to preserve the total involved rock volume and allow for accurate volume balancing. In the overlying Mesozoic, decoupled by the interjacent Fernie shales, the thrusts are overall closer spaced and shortening is preferentially accommodated by imbrication.

A significant amount of the total shortening is accommodated by a few prominent antiformal stacks, i.e., the Cate Creek, Waterton, and Turtle Mountain duplexes. In the structural transects (Fig. 3), two series of first order antiformal culminations of Palaeozoic limestone stacks can be discerned in the Foothills at first order. The Turtle Mountain culmination (Figs 3a and 3b) is a duplex made of Palaeozoic strata decoupled from the overlying Mesozoic clastics at the Fernie

shale interval which is not involved in the antiformal stack but draped over it. The Waterton duplex (Fig. 3c) to the south, where the Turtle and Livingstone thrusts carry again the two topmost sheets, align well with the Turtle Mountain culmination but is obscured by the LTS reentrant on top. The second system of antiformal stacks involving Palaeozoic strata (Cate Creek duplex) can be found in the westernmost portion of LT footwall (Fig. 3c). It shows again decoupling at the Fernie Shale interval with a detached and broadly folded Mesozoic strata and remnants of the LTS superimposed. Several wells penetrate the structure indicating strong imbrication at the antiform hinge as it is exposed in structural windows along the Cate and Sage Creeks. This culmination has less conceivable counterparts in the two northern transects with some imbrication just underneath the eastern edge of the LTS and penetrated by well 3-23-5-5W5 (Fig. 3b).

Although the structural culminations indisputably entail a strong component of in-sequence thrusting and decoupling between the Palaeozoic and Mesozoic sequences, they nevertheless also exhibit some indications for out-of-sequence and out-of-duplex thrusting. Both the Livingstone and Turtle Mountain thrusts do emplace Palaeozoic over Mesozoic, crosscutting the both the Palaeozoic and Mesozoic sequences and the Fernie shales as former decoupling level. This is especially well illustrated by the Turtle Mountain culmination in Figure 3a.

Our cross-sections depict simplified structural culminations with less imbrication than previously envisioned (e.g., Fermor and Moffat, 1992). Equivalent shortening has been achieved by slightly increasing displacements on the remaining thrusts and with less steep ramp angles. Recent insights suggest that for some structures less imbrication might indeed be the case (pers. comm. P. Fermor and G. Soule). For instance, it turns out that there is actually no small thrust carrying the Palaeozoic beneath the triangle zone (Fig. 3c) as has been depicted in Fermor and Moffat (1992). Also less imbrication at the leading edge of the Waterton structures is envisioned than has been previously presented (pers. comm. P. Fermor and G. Soule).

It is noteworthy that many of the above-described culminations store economically profitable petroleum accumulations (Fermor and Moffat, 1992). Especially the Waterton and Pincher Creek duplexes have been successfully penetrated by many operating wells.

3.2 Cross-Section Balancing

The Foreland Belt can be vertically subdivided into three structural entities:

1. The undeformed Hudsonian basement.
2. The Mesoproterozoic basin fill and overlying Palaeozoic detached from the basement.
3. The Meso-Cenozoic deformed wedge decoupled at the Fernie shale interval.

The omission of more detailed complexity, such as small-scale imbrication, multiple smaller decollement intervals and more complex flat-ramp geometries (Fermor, 1999; Price and Sears, 2000), will not significantly affect the first-order shortening estimates. Since the Foreland Belt lacks clear signs of transpression it can be assumed that the net displacement direction is approximately perpendicular to the strike of the thrust belt and shortening estimates can be legitimately made along the ENE-WSW trending profiles.

The three structural cross-sections have been restored using Locace® (developed by IFP qnd commercialized by Beicip-Franlab; Morretti and Larrere, 1989) with the triangle zone footwall block as pin point. Further, the Rocky Mountain Trench (RMT) is generally considered to mark the eastern limit of transpressional features of large lateral offset. As such, it provides a reference marker to compare total shortening estimates across the Foreland Fold and Thrust Belt. Despite the fact that the three cross-sections embrace high structural variety only a few tens of km apart, this study illustrates well that structural coherency can be achieved and comparable sedimentary cover shortening of 115-125 km can be obtained (Fig. 4). The corresponding shortening in the basement is perhaps achieved in the internal Omineca Belt along crustal branching faults like the Monashee decollement (e.g., Brown et al., 1992).

With the definition of another marker point, where the Lewis thrust climbs into the Devonian, the magnitude of the contraction achieved by Mesoproterozoic and lower Palaeozoic basin inversion can be derived. Notwithstanding lateral differences in LT hangingwall architecture, consistent displacement in order of 85–100 km can be obtained for all three restored cross-sections. Seismic reflection studies (van der Velden and Cook, 1994, 1996) indicate that the LTS counterpart block is possibly located underneath the Rocky Mountain Trench. This would set an upper limit of ~80 km to the displacement accommodated by the LTS and also confines the restored lengths of the overlying Palaeozoic and Mesozoic structural units. Presuming in-sequence displacement, the restored length of the Palaeozoic imbrications in the LTS footwall should not extend west of this proposed counterpart block. Price and Sears (2000) noted the inconsistency between the shortening estimates of Fermor and Moffat (1992) of ~140 km from structural balancing and 115 km (van der Velden and Cook, 1994) from LTS footwall ramp geometry outlined by seismic reflectors. Our study in-

dicates reduced shortening estimates that may support the proposed position of the footwall ramp as the counterpart block of the LT hangingwall Belt-Purcell strata as found in the Clark Range.

3.3 The Eroded Thickness Profile

The combination of structural balancing, inferred kinematics and resulting exhumation also aided the restoration of the currently severely denudated Mesozoic and overlying Tertiary foredeep wedge.

The conservation of a small patch of uppermost Alberta (i.e., upper Cretaceous Wapiabi formation) in a down-faulted fault block of the Howell Creek structure, forms the stratigraphically highermost physical indicator in the Lewis thrustsheet of the currently removed wedge (Fig. 4c). Also, the widespread occurrence of lower Alberta Formation in the Fernie "Basin" is noteworthy (Figs. 3 and 4). Furthermore, the coal seams in the Fernie "Basin" allow for an approximation of additional removed overburden from maturation history modelling with an estimation of 2 to 4 km of Belly River strata (discussed further on). About 2 km of Belly River in the footwall of the Lewis thrust (Osadetz et al., 2004) forms the only physical proof of Belly River in vicinity of the LTS (Fig. 4c).

The good conservation of Cretaceous strata in the LTS in the Fernie 'Basin' results from a major change in the basal decollement architecture that has been earlier mentioned (Figs. 3 and 4). It is underlain by the Mesoproterozoic Belt-Purcell Basin sequence at its southeastern edge (Clark Range) and affected by the southeastern tip of an inverted lower Palaeozoic miogeosyncline at the Fernies Basins northwestern edge (Price and Sears, 2000). As such, the Fernie 'Basin' illustrates the inherited effect of the basal decollement architecture on the present-day erosional profile.

The LT deformation front marks another feature that expresses the tight coupling between the denudation pattern and decollement and basement structure. The profound change in the orientation of the present-day Lewis thrust front can be observed with a sharp swing from north-south in the north to northwest-southeast toward the south of the study area (Fig. 2). This deflection is not purely an erosional feature but reflects a deep seated change in the orientation of the Foreland Belt itself that also affects the trend of the Foothills thrusts (Begin et al., 1996). This change in orientation, often referred to as the ‚Crowsnest Deflection‘ (Dahlstrom, 1970), results from a huge lateral step in the LT basal decollement geometry as it cut from South to North from the Belt-Purcell basin-fill into the Palaeozoic sequence (Price and Sears, 2000; Fig. 3).
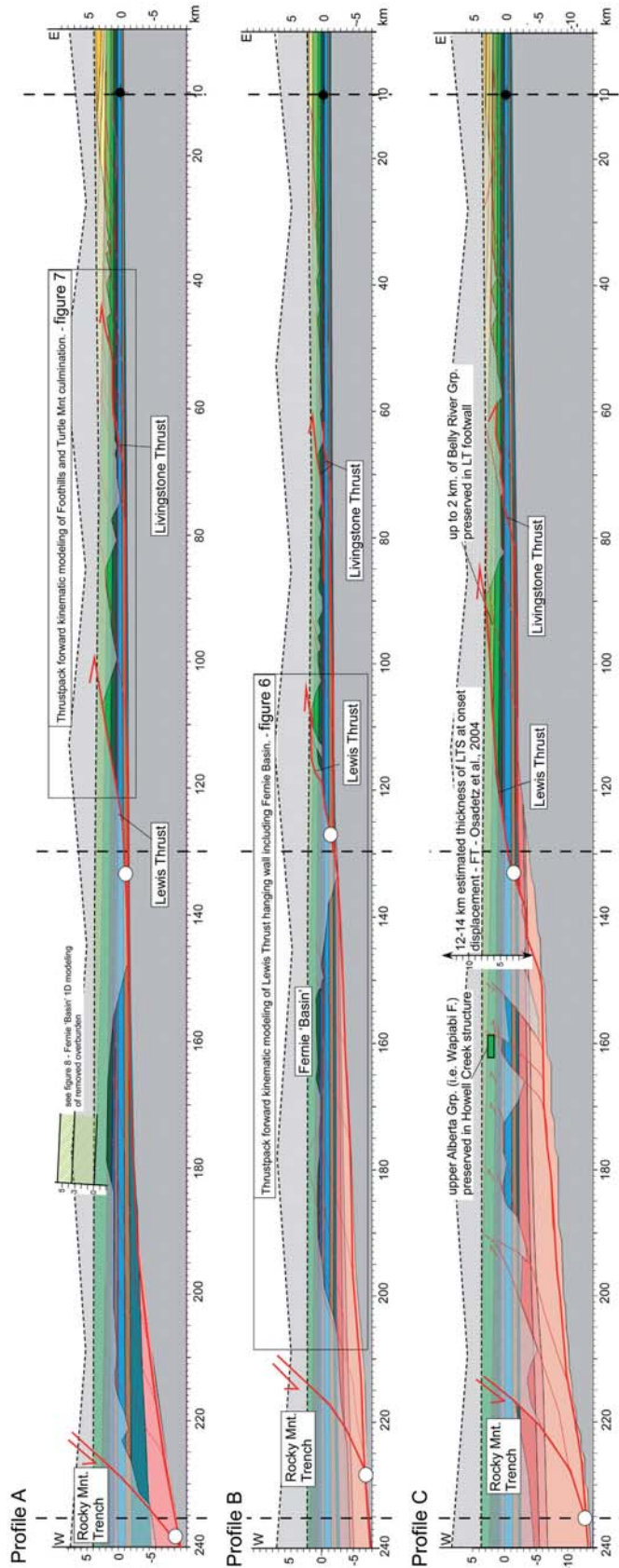
Fig. 4. Balanced structural cross-sections. Fault blocks are restored to their original position prior to displacement. Superimposed is an inferred syntectonic sedimentary foredeep wedge that is currently severely denudated as outlined by the eroded thickness profile (grey latticed overlay)

The thickness of the eroded strata in the least deformed easternmost extent of the structural profiles (in the foreland, east of triangle zone) are inferred from coalification ranks that require an additional overburden of 3–4 km (Hacquebard, 1977; England, 1986; Bustin 1991). Recent fission track studies from the Lewis thrust sheet (Osadetz et al., 2004; Feinstein et al., 2005) have inferred a 12–14 km thickness of the Lewis thrust sheet at onset of displacement (Fig. 4). OMR from the Fernie basin result in estimates of Campanian Belly River overburden on the order of 3–4 km (further on in this study; Osadetz et al., 2004; Feinstein et al., 2005).

The three resulting erosion profiles indicate two components of denudation:

1. A highly irregular component controlled by fault block exhumation
2. Regional exhumation that has completely removed the Tertiary former foredeep wedge (Fig. 4 – greyish masks).

3.4 Forward Kinematics

The main thrusts in the Omineca and Foreland Belt entail a Cretaceous to Palaeocene contractional history. A more detailed sequence (Fig. 5) has been adopted for subsequent Thrustpack forward kinematic modelling (Faure et al., 2004).

At a large scale, from the Omineca Belt and Purcell Anticlinorium to the Foreland, an in-sequence foreland-ward migration of thrust activity can be envisioned (Fig. 5). Thrusting in the Foreland Belt started in the Galton and McDonald Ranges, probably in Campanian time, shifting eastward through Maastrichtian and Palaeocene times. The presence of Belly River in the footwall of the LTS being overridden by this sheet over a distance of at least 20 km, indicate that the last stage of the LTS displacement history postdate the Campanian (70 Ma). However, it constrains neither the onset of displacement along the LT nor its cessation. Thrust fault overprint relationships across the belt indicate significant time overlaps of thrust displacement, not only of small splays but also for the main thrusts. With an eastward growth of the Canadian Cordilleran deforming wedge, subsequently involving the Foreland Belt and Foothills, the main thrusts may have formed in-sequence but are not really abandoned with the formation of new ones (Price, 2001) (Fig. 5).

The eastward encroachment of the active deforming belt and related foredeep reach their culmination in the uppermost Palaeocene. As the subsequent forward kinematic modelling illustrates the contractional phase results in minor exhumation only.

The onset of normal fault activity (Fig. 5) is relatively well constrained from associated half-graben infill (McMechan, 1981; Constenius, 1996). These features might mark the cessation of contraction in the Foreland Belt if they express a large decrease in regional stresses in the Cordillera from plate-margin reorganization (Constenius, 1996). In contrast, when the normal faulting is driven by gravitational collapse of a crustal over-thickened high relief Cordillera interior in Eocene time, then this local extension might well coincide with ongoing contraction in the more distal Foothills (Vanderhaege, 2002, 2004).

Forward 2D kinematic modelling performed with Thrustpack, a tool developed by IFP (Sassi and Rudkiewicz, 1999), allow for further refinement of the kinematic scenarios.

Two forward kinematic models have been performed:

1. In the LT hangingwall focussing especially on the burial history of the Fernie 'Basin' (Fig. 6);
2. The second is done on the Foothills with special attention for the Turtle Mountain culmination (Fig. 7). Slices from the balanced profiles (Fig. 4) form the initial stage and subsequent stages are obtained by assigning fault block displacement, subsidence and erosion (Roure and Sassi, 1995; Sassi and Rudkiewicz, 1999; Faure et al., 2004; Deville and Sassi, 2006).

Figure 6 outlines the progressive burial and exhumation of the Fernie 'Basin' and deformation of surrounding fault blocks. It shows that its burial, uplift and exhumation history results from an intricate mixture of sedimentation and fault block displacement. Its uplift history is strongly controlled by the imbrication of the underlying, pinching out Belt-Purcell basin-infill and also by profound decoupling at the Fernie shale interval (Figs. 6b and 6c). Structural stacking, or alternatively an ancient triangle zone along the Fernie 'Basin' western flank, determines the interplay between tectonic and sedimentary burial. Subsequent normal faulting along its eastern flank preserve the Fernie 'Basin' from denudation (Fig. 6d).

The second model addresses the forward kinematics in the Foothill zone (Fig. 7), that especially elucidated the implications of presumed strong foredeep subsidence for the growth and preservation of the encroaching deformational prism. A high amount of foredeep subsidence and basement flexure is required to accommodate the sedimentary overburden estimated from coalification studies in the Foreland. This entails a larger wavelength basement flexure by which also most of the thickened deformational prism remains conserved during contraction. This persistent mix of tectonic and sedimentary overburden in the
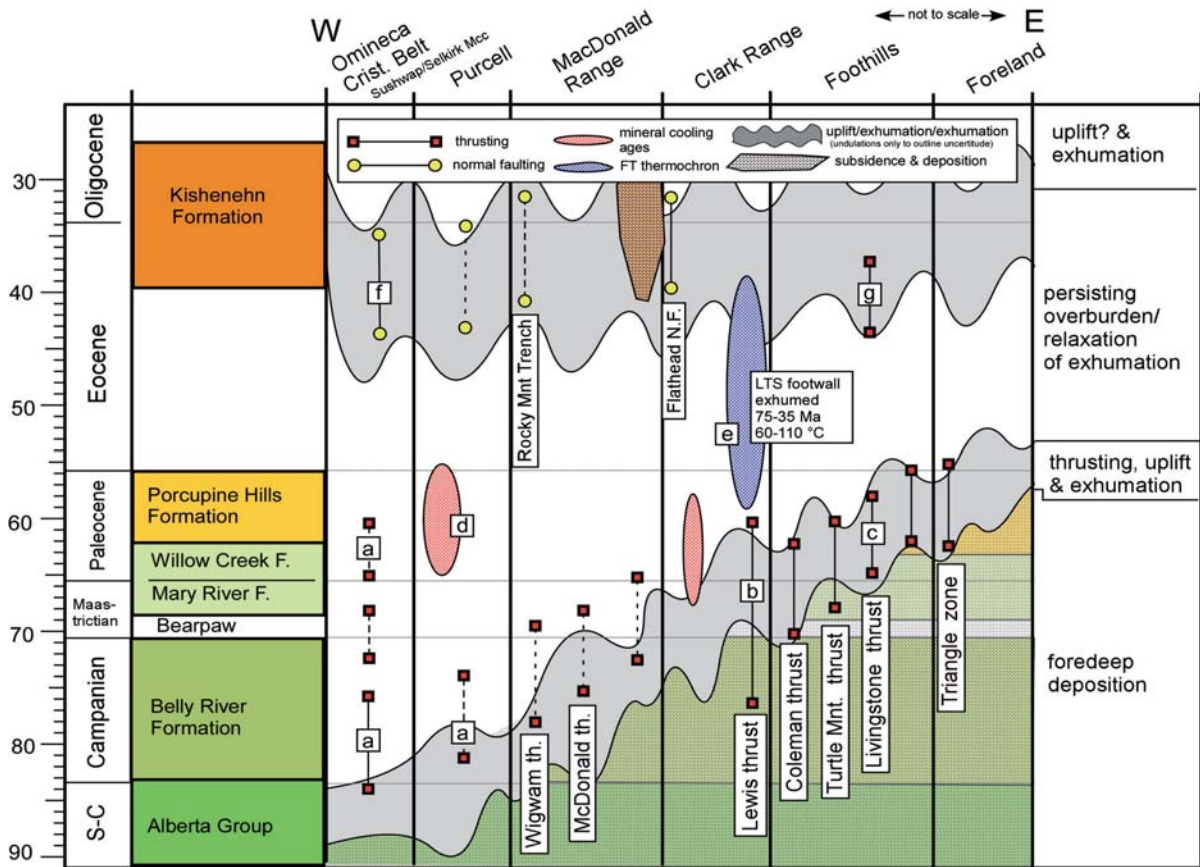
Fig. 5. Applied time chart for forward-kinematic modelling of Upper Cretaceous (Santonian-Campanian) to Paleogene (Oligocene) outlining temporal relationship between the main events (i.e. subsidence and deposition, faulting, intrusion, uplift and exhumation). For certain features literature constraints are provided: **a** Thrustsheet associated with polydeformed sillimanite-orthoclase paragneisses indicate post-80 Ma ductile shearing (Parrish et al., 1988; Carr et al., 1992) comes with cessation of shortening at ~58 Ma; **b** Fermor and Moffat (1992) and Sears et al. (2001) indicate that movement on LTS (northernmost Montana) ended at ~59 Ma – porphyritic dykes; **c** Fermor and Moffat (1992); (d) cooling curves suggest rapid uplift and erosion of the Purcell Anticlinorium between 65–55 Ma (Archibald et al., 1984); **e** FT T-t modelling for Lewis thrust hangingwall cooling 110–60 °C between 75–35 Ma; **f** Cooling ages suggest tectonic unroofing of the Sushwap Metamorphic Core Complex (Vanderhaeghe and Teyssier, 1997; Vanderhaeghe et al., 2003). In addition, Eocene strata and plutons (with K-Ar Eocene ages) have been involved in listric normal faulting (Archibald et al., 1984; Parrish, 1988); **g** Forward kinematic modelling with Thrustpack® indicates late stage out-of-sequence displacement along the Livingstone thrust also involves the Turtle Mts. thrust of about ~10 km which indicates significant exhumation of the Foothills

Belt and adjacent Foreland got perceivably exhumed in Late Eocene-Oligocene time in combination with recorded extensional faulting.

This scenario further postulates a late stage reactivation along the Livingstone thrusts, carrying the roof thrustsheet of the Turtle Mountain culmination. The structure indicates a strong component of out-of-sequence and out-of-duplex displacement that might well resemble another more profound example recognized in Moose Mountain culmination (located further north – Banff-Calgary transect; Faure et al., 2004; pers. comm.). Contrary to preceding displacement (Figs. 7b and 7c), the reactivated Livingstone thrust (Fig. 7d) cuts through the Fernie shales (i.e., former

decoupling level) and carries the complete overlying pile. As the thick pile of imbricated foredeep sediments have presumably been preserved during the main contractional phase, displacement along the Livingstone thrust likely coincides with significant regional erosion of the deformed wedge.

In conclusion, this forward kinematic modelling outlines the Foreland Belt burial history as mixture of structural stacking and sedimentary overburden that persisted until a late Eocene-Oligocene exhumation episode. Evidently, this will have a strong bearing on alternative burial, thermal and maturation history inferences as will be discussed in more detail below.
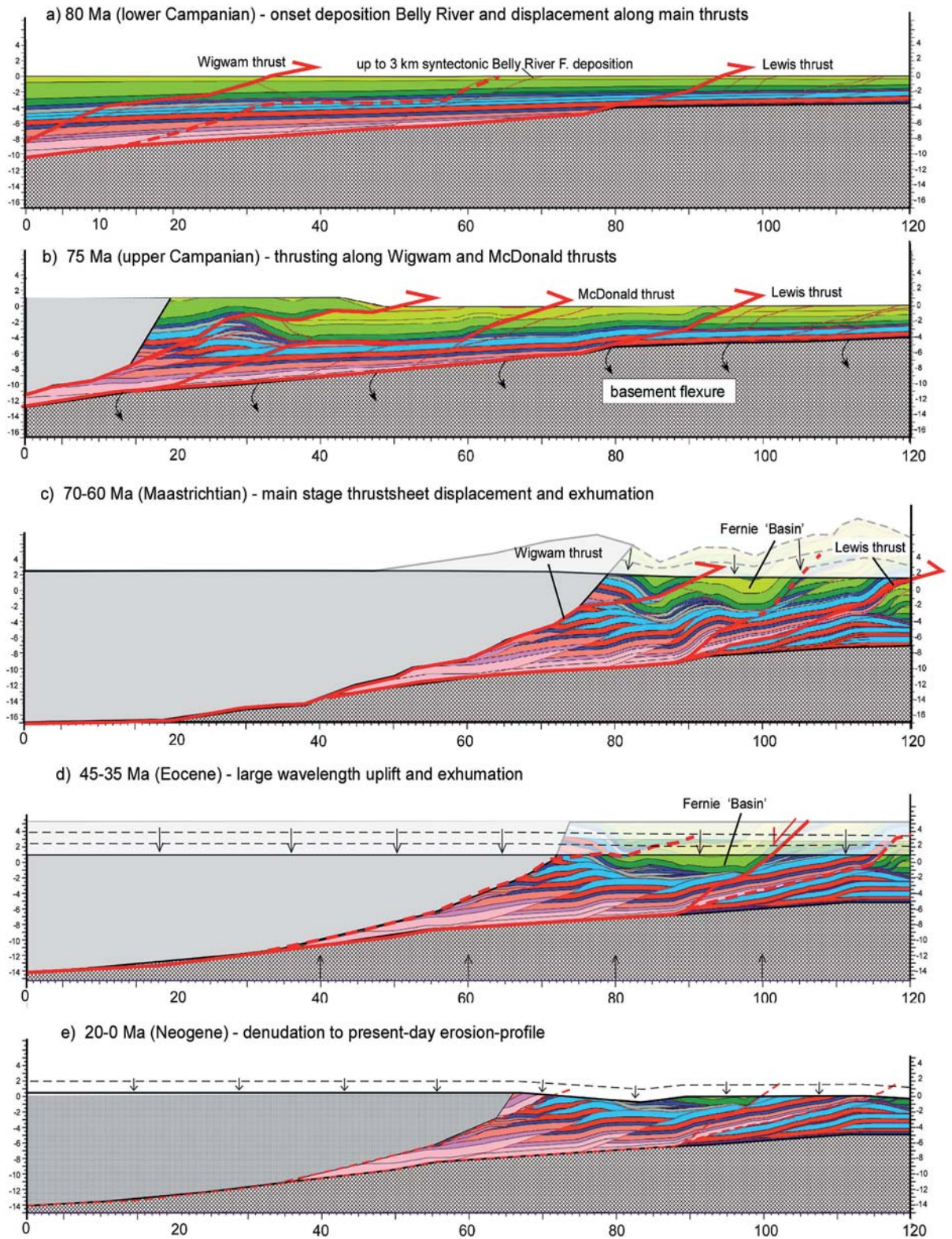
Fig. 6. Forward kinematic Thrustpack modelling outlining the evolution of the Lewis Thrust sheet hangingwall with especially the Fernie Basin

Fig. 7. Forward kinematic Thrustpack modelling outlining the evolution of Foothills with especially the Turtle Mts. culmination
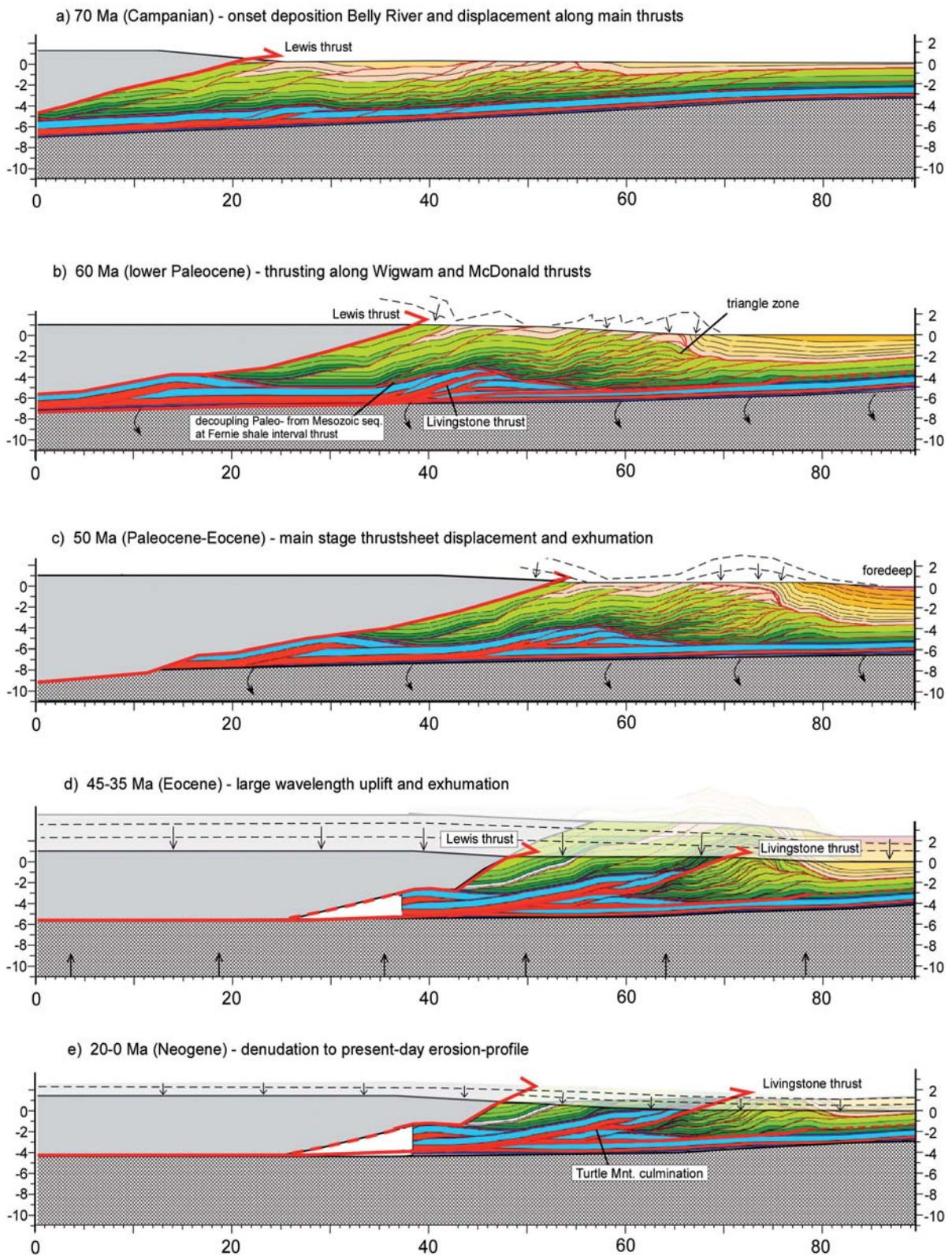
4   Inferences on Thermal and Maturation History

4.1 Organic Maturation

Vitrinite Reflectance (VR) and Tmax values from rock-pyrolyses are often adopted as indicators for the maturation history of organic matter. They result from a composite effect of time and temperature, and to much less extent pressure (Teichmüller, 1986; Tissot, 1987; Sweeney and Burnham, 1990; Roure, 2004). An interesting feature of organic maturity ranks (OMR), is that once a specific rank has been attained it can not be reversed (Green et al., 2002). The use of OMR in the context of thermo-chronometry is limited by the fact that the finite maturity rank only gives an integrated effect of time and temperature. While OMR data is oftentimes interpreted to result from peak-temperatures, the ranks in reality record the total effect over time possibly incorporating multiple thermal events. As a consequence, the reliance on maturity ranks alone for resolving the thermal history remains unsatisfactory without the integration of alternative thermochronological constraints like Fission Track analyses (FT). The integration of a dense regional coverage of Vitrinite Reflectance (VR) with FT Temperature-time (T-t) modelling for accurate constraints on timing (e.g., Osadetz et al., 2004) better constrain the temperature and exhumation history and enhances petroleum system predictions.

Numerous burial history and paleogeothermal studies from coal moisture content, vitrinite reflectance ranks and fission track studies have been performed in the undeformed Cordilleran foreland basin and have demonstrated the erosion of a 2-5 km (even up to 8 km) from the present day topography (Steiner et al., 1972; Hacquebart, 1977; England and Bustin, 1986; Bustin, 1991; Kalkreuth and McMechan, 1988, Kalkreuth et al., 1989; Willet et al., 1997; Faure et al., 2004). Some studies discuss the maturation and implications for burial and thermal history in the disturbed Foreland Belt (e.g., Hacquebard and Donaldson, 1974; Pierson and Grieve, 1985; Langenberg and Kalkreuth, 1991; Osadetz et al., 1992; Langenberg et al., 1998; Faure et al., 2004; Feinstein et al., 2005).
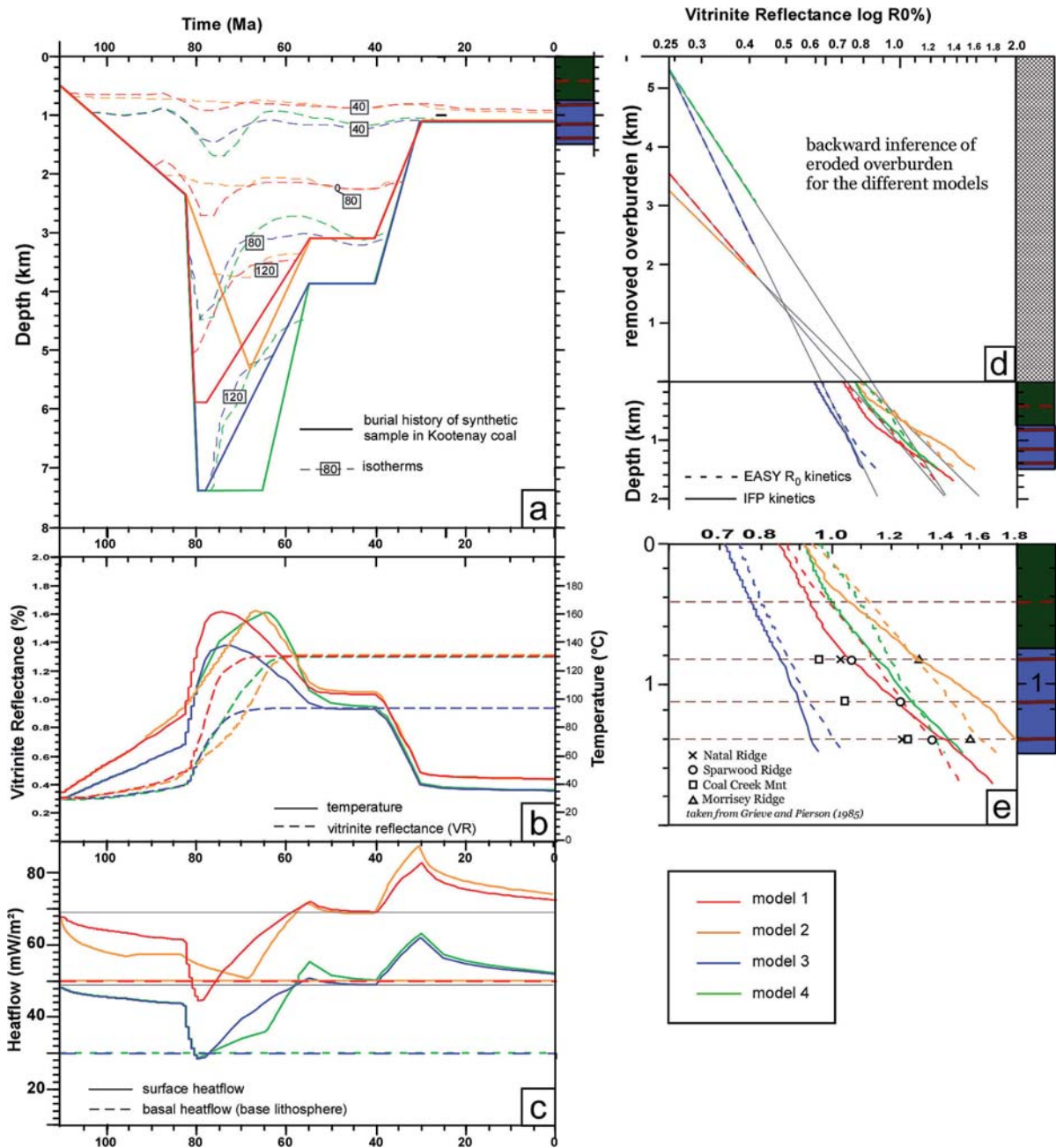
4.2 1D Modelling

1D modelling has been conceivably applied in the foreland basin but its application in the deformed belt itself including the intricate interference of tectonic loading with sedimentation and erosion is less perceptible (e.g., Nurkowski, 1984; Osadetz et al.,1992; Langenberg et al., 1998). While classical 1D burial and thermal history models do not allow for accurate thermal model-

ling of thrust sheet displacement, they remain a useful tool to quantify the subsidence and thermal evolution of the autochthon. Other studies on kinematic modelling accounting for thermal and maturation inferences have shown that 1D modelling is a legitimate approach for a first insight, while extended 2D modelling is required to account for thrustsheet emplacement in structural complex areas (Faure et al., 2004; Deville and Sassi, 2006; Lampe et al., 2006). The workflow of integrated thermo-kinematic modelling developed at IFP for the appraisal of burial, thermal and maturation history of foothills reservoirs (Roure and Sassi, 1995; Roure et al., 2004, 2005), 2D forward kinematic models (i.e., Thrustpack; Sassi and Rudkiewicz, 1999, 2000), involving incremental thrust emplacement with coeval erosion and sedimentation enhances the value of 1D well modelling (i.e., Genex®). An extension to Genex® can account for tectonic burial from duplications by thrustsheets, although emplacement occurs instantaneously. Nevertheless, Genex® software has proven useful for testing multiple and simplified scenarios that embrace a wide range of possible burial and thermal histories also within the deformed Foreland Belt (Faure et al., 2004).

With the conceptual 1D modelling presented below, the premise that organic maturity ranks result from peak temperatures reached prior to thrusting from pure sedimentary burial will be reassessed (Hacquebard and Donaldson, 1974; Hacquebart, 1977; England and Bustin, 1985). Two case studies have been performed of which a set of conceptual 1D forward (i.e. burial) history scenarios are being presented. The first study concentrates on the Fernie 'Basin' (Fig. 8) and aims to test a variety of pure sedimentary burial histories for the Belly River overburden of the LT hangingwall block. The second study (i.e. Clark Range) focuses on the thermal and maturation history of the LT footwall block, especially aiming to test the effect of tectonic burial from a thick overriding LTS.

It should be emphasized that this modelling consists of conceptual models to test the sensitivity of type, magnitude and timing of burial for thermal and maturation histories and does not aim for realistic well modelling. As such, the simplified instantaneous thrustsheet emplacement of Genex® is permissible, if we maintain reasonably thermal histories (i.e. FT constrained) at the contact between hanging- and footwall block and accounting transitory heat advection (Ungerer et al., 1990).

Furthermore, the modelling does address the effects of varied geothermal gradients that are in our modelling especially controlled by heat flow from the base and perturbations due to vast vertical movements. The modelling tests thermal perturbations in the sedimentary cover by defining a fixed basal heat flow and by superimposing a burial and exhumation

Fig. 8. 1D burial and exhumation history modelling for the Fernie 'Basin'. Four different burial-exhumation scenarios are proposed and thermal and maturation history implications being tested. Modelling output is compared with measured VR ranks and coalification gradients. **a** Four burial and thermal histories for synthetic sample in the middle Kootenay coal seam. **b** Thermal and vitrinite reflectance history. **c** Imposed basal and derived surface heatflow histories. **d** Calculated coalification gradients combined with grey extrapolated trend lines for testing validity by backward inference of imposed overburden. **e** Calculated coalification gradients plotted against measured gradients from coalification profiles for four locations in the Fernie 'Basin'

history. The fixed basal heat flow (i.e. constant mantle heat flow and heat production in the crust) is imposed to achieve appropriate initial and finite thermal conditions and a maturation history that meet the observations. Evidently, basal heat flow sources from litho-

spheric scale geodynamics and crustal heat production might vary significantly. Yet, this conceptual model is bounded to the supracrustal cover, and regional tectonic implications will only briefly be addressed. Superficial geothermal gradients are also potentially af-

fected by variable conductivities of the sediments and fluid flow, but fall beyond the scope of this conceptual modelling (Majorowicz et al., 1990). The overburden estimates made within this conceptual modelling are limited by simplified thermal parameterization of the preserved and removed sedimentary overburden (i.e., uniform; conductivity: 3.0 W/m/K; capacity: 2.8 MJ/m^3/K), yet suit its purpose.

4.2.1   Fernie "Basin"

For the first case-study, comprising the Fernie Basin (Fig. 8), a conceptual well is constructed to test possible scenarios that fit with the VR from three different coal seams over a depth interval of ~600 m at four different localities within the basin (Pearson and Grieve 1985). Four different scenarios are being tested, imposing variations of the amount of Belly River overburden, duration and timing of maximum burial phase, and variable basal heat flow (Table 1).

In model 1 and 2 a time-invariant basal heat flow of 50 mW/m^2 is applied that implies a superficial steady-state thermal gradient of ~37 °C/km. For model 3 and 4, a fixed 30 mW/m^2 is imposed resulting in an initial steady-state thermal gradient of ~27 °C/km for the sedimentary cover.

The thermal consequences of the different burial scenarios are outlined by the isotherm evolution (Fig. 8a) and temperature for the Kootenay coal seams (Fig. 8b) and surface heat flow history (Fig. 8c). Despite of simplified thermal boundary conditions, the burial history leads to a complex, non-steady-state thermal evolution depicted by warping of the isotherms (Fig. 8a) and jigsaw surface heat flow curves (Figs. 8b and 8c) . The surface heat flow drops result from rapid subsidence and burial, while the peaks result from fast removal of the sedimentary overburden. As a consequence, peak-temperatures can be reached under perturbed, non-steady-state thermal conditions with the most profound thermal gradient drops for models 1 and 3 with a change from ~37 to ~22 °C/km and

~27 to 17 °C/km, respectively (Fig. 8a; Table 1). Except of model 3, all models achieve peak temperatures of ~160°C, during maximum burial and under the perturbed thermal conditions. For model 3, the limited time interval between the rapid burial and exhumation did not allow for further heat-up by removal of the thermal perturbation.

Notwithstanding the various imposed burial histories and basal heat flow input, the models produce finite VR ranks and coalification that match the observed values taken from Grieve and Pierson (1985) for four transects in the Fernie 'Basin' gradients (Figs. 8d and 8e). Both a 3.5 km of Belly River overburden with 50 mW/m^2 basal heat flow (model 1 and 2) and 5 km of Belly River overburden with 30 mW/m^2 basal heat flow (model 4) fit the observed VR values of 1.0–1.4% for the Kootenay coal seams. Only in model 3 does the 5.5 km of Belly River sediment overburden achieve limited VR ranks of 1.0% due to isotherm down warping and insufficient time for erasing the perturbation before getting exhumed.

Figure 8d presents predicted coalification gradients (i.e., log(%R_0)/km; Bustin and England, 1986; Bustin, 1991) for the four different models applying both the EASYR¬o (Sweeney and Burnham, 1990) and IFP kinetic laws (Ungerer, 1990) for organic maturation. In Figure 8e the same calculated gradients are plotted against measures from three Fernie 'Basin' Kootenay coal seams (Grieve and Pierson, 1985) and show how the different model runs cover the samples' scatter.

We have further tried to envision the effect of the presumed vast burial by Campanian Belly River sediments (Osadetz et al., 2004) for accurate estimation of this thickness itself (Fig. 8d). An often applied tool for restoring the original overburden from measured coalification gradients in the preserved strata, is by extrapolation of the gradients and taking the intersect with zero-depth VR rank of 0.25% (Bustin and England, 1986). Backward usage, by constructing trendlines from the applied overburden values and comparing them to the modelled gradients (Fig. 8d), give an indication of the uncertainty involved in the esti-

		Model 1	Model 2	Model 3	Model 4
Input	Basal heatflow (mW/m2)	50	50	30	30
	Thickness (km) removed overburden	3.5	3.25	5.5	5.5
	VR rank	1.4	1.4	1.0	1.4
Output	Thermal grad. (C/km) steady state	~37	~37	~27	~27
	Thermal grad. (C/km) during peak T.	~22	~34	~17	~22
	Coalification gradient log%RoR/km (with EASY kinetics)	~0.14	~0.17	~0.09	~0.11

Table 1.
Input and output parameters of the 1D modelling for the four alternative models concerning the Fernie "Basin" (Fig. 8)

mation of overburden by extrapolation of measured coalification gradients. The effect of vast sedimentary burial and resulting non-steady-state thermal gradients combined with realistic kinetic laws for organic maturation (Sweeney and Burnham, 1990; Ungerer, 1990) produce non-linear $\log(\%R_0)$/km coalification gradients (Fig. 8d) that hamper this simple method for inferring overburden in geologic complex areas.

Alternatively to the above-presented coalifaction gradients with depth, do bedding-parallel coalification trends do allow to discriminate between syn- and post-deformational coalification (i.e. 'Hilt's law'; Hacquebard and Donaldson, 1974; Grieve, 1987). Pierson and Grieve (1985) successfully applied this tool in a regional VR study for the Fernie Basin showing a southward increasing trend in significance of post-folding coalification. This trend, with 25–40% of post-folding coalification in the north (Natal and Sparwood Ridge), to 75% south of Morrisey ridge, might result from a southward increasing effect of tectonic burial by thrustsheet stacking. In the northwest the stacking onto the syncline is possibly minor due to an assumed triangle zone at Mt. Hosmer (P. Fermor, pers. com.) while to the south the effect of the Wigwam and McDonald thrust sheets have stronger bearing.

Although our range of input parameters cover the measured VR scatter, especially basal heatflow variations across the Fernie 'Basin', presumably marking a single thermotectonic entity, seems an implausible explanation. Instead, lateral variations in tectonic and sedimentary burial and exhumation and subsequent thermal variations in supracrustal cover appear a better explanation.

4.2.2   Clark Range

The second case study concentrates on the Clark Range with well control from 07-02-004-01W5 5, Shell Waterton 2#, 07-34-003-01W5, Shell Waterton 7# and C-011-A/082-G-07 for which Tmax values are provided, and from the Sage Creek No. 2 well with VR ranks after Feinstein et al. (2005). Figure 9 outlines the conceptual well modelling involving three structural units. The middle unit, on which the modelling is focused, comprises the Alberta (middle green) and Blairmore (dark green) groups initially overlain by, a later displaced, pile of Campanian Belly River sediments (light green) (Osadetz et al., 2004; Feinstein et al., 2005). The unit is underlain by multiple thrustsheet stacks simplified to one footwall block. This central structural unit is being overthrusted by an initially thick LTS, of which at present only a ~500-m-thin upper-Proterozoic Belt-Purcell erosional remnant is preserved (Figs. 9a and b – upper panel). VR values around 0.8% and comparable Tmax values of ~450°C document a relatively

low maturity rank, generally considered to result solely from pre-thrusting sedimentary burial from Belly River (light green) overburden. Osadetz et al. (2004) provide additional constraints with FT T-t modelling (i.e., Clark Range samples #657 & #668; Fig. 2) that indicate temperatures of 100°C at the base of displaced LTS over the 65–40 Ma time interval. Furthermore, corrected bottom-hole logging temperatures provide present-day geothermal gradient estimates of slightly less than 20°C/km (Osadetz et al., 2004). Multiple explanations can account for this low geothermal gradient (e.g., fluid flow in sedimentary cover or deeper rooted reduced heat flow), yet in this modelling we can only achieve this by imposing a low basal heatflow of 15 mW/m^2 without arguing for any factual regional implication.

Multiple conceptual scenarios have been tested of which two end-members are further discussed (Figs. 9a and 9b). Figure 9a shows a scenario in which peak temperatures are achieved by sedimentary burial of 5 km of Belly River (light green) prior to the displacement of the LTS. The 1D-integrated burial-temperature modelling indicates that peak temperatures cannot be reached by simply imposing 5 km of Belly River overburden. The extremely low thermal gradient, that is further perturbed by vast burial, does prevent the LT footwall block to reach the necessary temperatures of ~120°C for achieving VR of 0.8%. Only in combination with a higher initial geothermal gradient (i.e., imposed in model by increasing basal heat flow to 30 mW/m^2), can the measured VR values be obtained by sedimentary burial alone, prior to onset of thrusting. To prevent subsequent contribution from the tectonic load, i.e., the emplaced LTS, the LTS requires quick exhumation together with a reduction of basal heatflow to the inferred current value (Fig. 9a). To achieve the required temperature at the base of the LTS in accordance with FT T-t modelling (Osadetz et al., 2004), all of the Mesozoic sediments (5–8 km) require fast lower Palaeocene removal.

The alternative scenario (Fig. 9b) achieves the recorded maturity ranks of the middle unit by applying a 2 km of Belly River sedimentary load combined with a tectonic load from the LTS, comprising a 5 km overburden including the Blairmore Grp (dark green), preserved for 20 Ma before it gets subsequently exhumed as well (Fig. 9b – upper panel).

The modelling shows that maturity ranks of 0.8% can be easily reached with both end-member models of (1) pure sedimentary burial and (2) tectonic loading. In fact, the real problem for the maturation history in the LT footwall block is not to reach VR values of 0.8% but to prevent the overburden from the LTS to achieve much higher ranks. FT constraints from the base of the LTS suggest temperatures below 110°C for Late Cretaceous-Palaeocene time, indicating footwall
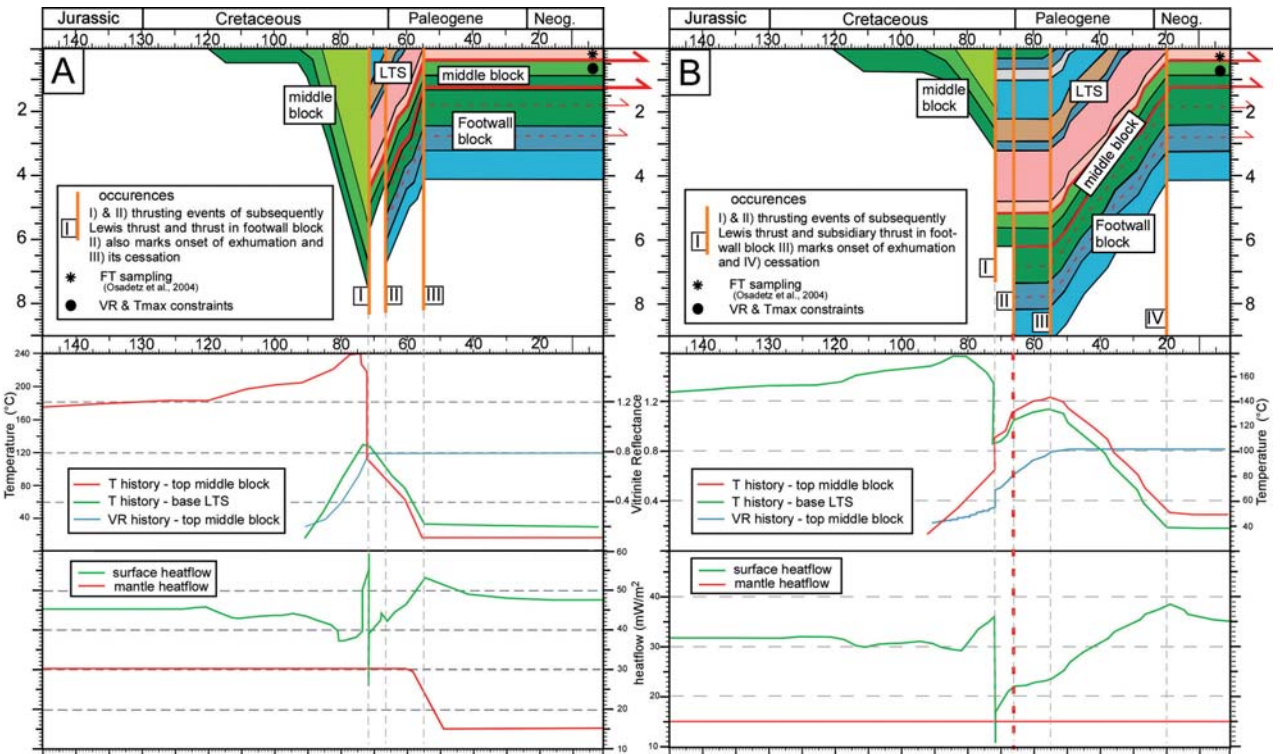
Fig. 9. Conceptual well modelling testing two end-member burial history scenarios for the Lewis thrust footwall block (i.e. Clark Range) with **a** pure sedimentary burial and **b** a combination of sedimentary burial and structural stacking are being tested. The two underlying panels outline the thermal, vitrinite and thermal history as a result of by the sedimentary and tectonic burial, respectively

temperatures in the order of 120–130 °C (Osadetz et al., 2004). Alternative constraints on the exhumation of the LTS (i.e., Blairmore erosional products in adjacent Eocene Flathead Valley graben) indicate a persistent LTS overburden of 5–6 km at least for the Palaeocene. As such, the second model (Fig. 9b) seems to be in better accordance with these observations.

5   Discussion: Implications for Regional Tectonics

In combining inferences from the above-discussed conceptual 1D burial and exhumation history modelling with forward kinematic modelling, different uplift histories can be conceived for various regions across the Foreland Belt. Forward kinematic modelling has shown that (Fig. 6) sedimentary burial can dominate the Fernie 'Basin' in Campanian time coeval with structural stacking along its western flank and in its footwall block. The 3.5 km of Belly River overburden, inferred from the 1D modelling (Fig. 8) can account for the measured maturity ranks. As such, this 'Basin' located within the LTS can be regarded as a piggy-back basin with coeval syntectonic deposition and displacement along the underlying Lewis thrust.

On the contrary, in the Clark Range, where the same decollement transports a much thicker Belt-Purcell Basin fill, upthrusting of the thick LTS gives much less room for synchronous Belly River deposition. Here, tectonic burial appears as governing factor for the maturation history of the LT footwall block and Belly River overburden plays a less significant role (Fig. 9b). For the Clark Range, Belly River thicknesses in the LT hangingwall block have conceivably not surpassed the thickness of 2 km still present in its footwall and also inferred for the Foothills.

Therefore, extrapolation of overburden and exhumation inferences across the different structures can only be made attentive to kinematic variations due to changes in geometry of the basal decollement.

For the internal Foreland Belt, the combination of numerous vitrinite reflectance studies providing a dense regional coverage in conjunction with FT studies for better constraints on timing have shown to be valuable (Osadetz et al., 2004). Yet combined inferences of both the restored overburden and paleothermal gradient can not be independently made with the current dataset and especially require additional FT studies. Imposing 5 km of Belly River overburden as proposed by Osadetz et al. (2004) and Feinstein et al.

(2005) onto LTS while maintaining the FT T-t constraint at the base of the sheet inevitably implies extremely low geothermal gradients of about 10°C/km that can be achieved by strong superficial geothermal perturbation affected by this burial. Alternatively, a more moderate Campanian burial history (i.e., Belly River Deposition) might be proposed for the internal Foreland Belt (i.e., Fernie 'Basin', Clark and McDonald Ranges) with strong syntectonic thickness variations for the Belly River (0–3.5 km). With a reduced thickness of LTS of ~10 instead of ~13 km at onset of displacement, the temperatures and maturation history in the LT hangingwall and footwall block (this study; Osadetz et al., 2004) can be maintained with a more realistic geothermal gradient.

The integration of inferences from structural balancing with the kinematic and 1D burial-exhumation modelling allowed for the first-order restoration of the deformed sedimentary wedge including the syntectonic foredeep sequence (Fig. 4). Despite uncertainties in lateral thickness variations of the inferred syntectonic Belly River overburden, eroded thickness estimates can still be envisioned along profile. The eroded thickness profiles exhibit an irregular pattern showing spatial variability in the amount of exhumation from individual upthrusted sheets.

The geometry of the basal decollement ultimately controls the thickness of the deformed wedge and thereby the eroded thickness. As such, the geometry of the basal decollement influences a larger wavelength exhumation signal encompassing multiple thrustsheets. In the Clark range, the thick LTS allowed for ~10–12 km of denudation down to the Mesoproterozoic Belt Purcell Group, while the Palaeozoic strata are still well preserved northward with a shallower basal decollement in the Cambrian. This strong bearing of basal decollement geometry from inherited basin architecture on the derived erosion profile legitimates the combination of renewed structural restoration work with conceptual 1D modelling of the burial and exhumation history as conducted in this paper.

Figure 10 depicts the local and large wavelength denudation signals and combines it with higher temperature thermochronology from mineral cooling ages in the Omineca-Purcell crystalline belt to the West (Parrish et al., 1988; Parrish, 1995; Vanderhaeghe and Teyssier, 1997; Vanderhaeghe et al., 2003). The FT data (Osadetz et al., 2004; Feinstein et al., 2005) in affinity of the LTS clearly reveals multiple exhumation phases. Strong fault-controlled denudation occurred in the upper Cretaceous to early Palaeocene to depths of 4–6 km. Eocene to present-day exhumation appears to have a much wider wavelength also involving the exhumation of the foreland.

The estimated total amount of removed overburden for the undeformed foreland, is derived mainly from

OMR inferences with some FT studies in the Williston basin to the north (Issler et al., 1999; Osadetz et al., 1992, 2002). Yet these studies do not allow for distinguishing multiple exhumation events.

Nevertheless, a major Neogene erosion event is evidenced from geomorphical markers, i.e., erosional peneplains present in the denudated foreland. The Cypress Hills, located eastward in the distal foreland (Fig. 10), are capped by Oligocene conglomerates that provide evidence for 450 to 1500 m of eroded strata formed from the Oligocene to the present (Bustin, 1991; Dawson et al., 1994).

40Ar/39Ar and U/Pb thermochronology in the inner complexes confirm this multiphase exhumation history commencing in early Palaeocene and lasting until Oligocene time. The formation of core complexes in the Omineca-Purcell crystalline belt have been recognized to play an important role in the Tertiary Cordillera evolution and places the large wavelength exhumation history in a geodynamic context (Vanderhaeghe and Teyssier, 1997; Liu, 2001; Vanderhaeghe et al., 2003).

Supported by thermo-kinematic modelling, three episodes of exhumation become apparent (Fig. 10). The first episode involves short wavelength exhumation associated with upper Cretaceous to lower Palaeocene thrust tectonics limited to the Foreland Belt. The second episode during Eocene-Oligocene times is accompanied by the formation of the Flathead and Rocky Mountain graben systems with cooling of the Flathead Footwall block constrained from FT T-t modelling to range from ~100 to ~50°C (Osadetz et al., 2004). It also involves the exhumation of the Core Complexes (Archibald, 1984; Parrish, 1988; Vanderhaeghe and Teyssier, 1997; Vanderhaeghe et al., 2003) together with significant erosion of the foreland over a distance of 1000 km with a regional trend of 4 km in the Foreland Belt waning to 1–2 km in the plains. The remaining exhumation of up to 2 km occurred in Neogene time. The Oligo-Eocene large wavelength exhumation history, as it is accompanied by normal fault activity and linked to profound core complexes unroofing, conceivably entails crustal and astenosphere-lithosphere dynamics. This might be linked to changes in plate tectonic configuration and overall lithosphere evolution (Monger et al., 1994; Liu, 2001; Vanderhaeghe et al., 2003).

6 Conclusions

A coherent picture of the structural complexity of the Foreland Fold and Thrust Belt is acquired with the construction of three east-west trending regional and simplified structural cross-sections. In conjunction with 1D conceptual modelling and forward kinemat-
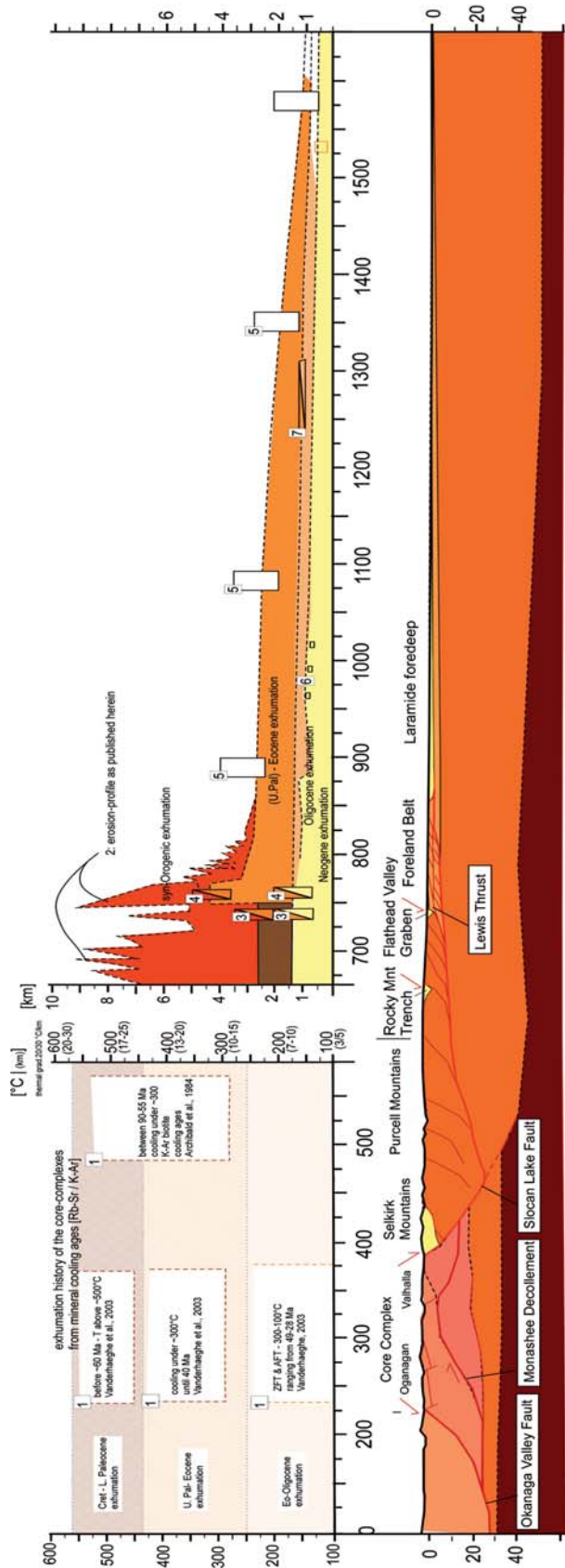
Fig. 10. Outline of a multiphase exhumation history along an extended crustal-scale profile. The exhumation history in the Intermontane Belt with the Oganagan, Valhalla and Sushwap Core complex are recorded by mineral cooling ages [1] (Vanderhaeghe et al., 2003; Parrish et al., 1988; Archibald et al., 1984). The erosion profile and exhumation history in the Foreland Belt is derived from the restored profiles as presented herein [2] together with FT T-t modelling after Osadetz et al. (2004) with [3 – sample 690, [4] – sample 668. The large wavelength exhumation pattern is constrained by OMR-studies [5] (e.g. Bustin et al., 1991) and erosional remnants like the Peigan Kipp [6] and Cypress Hills [7] from Dawson et al., 1994

ic modelling, it allows for first-order structural balancing and restoration of the deformed sedimentary wedge. The restoration provided consistent shortening estimates for the three transects on the order of 115–125 km of which most is accommodated by a few major thrusts, i.e., especially the Lewis and Livingstone thrusts. It also reveals the strong bearing of the basal decollement geometry, affected by inherited basin architecture, on the derived erosion profile and exhumation pattern prospects, especially well illustrated by the Lewis thrust sheet. Furthermore, the contemplation of the displacement and exhumation history, as performed in this study, illustrates the feasibility, limitations and uncertainties involved in the restoration of a strongly deformed sedimentary wedge.

Our results allow for a more moderate restored thickness of the deformed and eroded sedimentary wedge with maximum 3.5 km of Belly River overburden than previously envisioned. The eroded thickness profiles show short wavelength syn-orogenic exhumation (~4–6 km) from by thrustsheet emplacement (late Cretaceous–late Palaeocene) that is limited to the deformed Foreland Belt. A second episode (late Palaeocene-Eocene) of large wavelength exhumation involves the entire former foredeep with estimates of 3–5 km for the deformed belt waning to 1–3 km for the foreland.

The thermal proxies used in this study for constraining the burial and exhumation history are evidently affected by superficial thermal perturbations from vast sedimentary burial, sedimentary blanketing, solid block advection caused by thrust sheet displacement and also fluid flow circulations (Bustin, 1991; Osadetz et al., 1992). The conceptual 1D modelling also aimed for some sensitivity analyses providing estimates of the uncertainties involved as presented in Figure 10 by the numbered boxes. This study shows that the current thermo-chronological dataset cannot entirely discriminate between two burial and exhumation history scenarios: either with purely sedimentary burial or, alternatively, a strong component from structural stacking. For the LTS, we can not elusively discriminate between two thermo-kinematic scenarios:

1. Delayed LTS displacement preceded by deep Campanian burial or
2. Synchronous LTS displacement with a more moderate Campanian Belly River burial and tectonic overburden preserved by a delayed exhumation.

However, strategic FT sampling for constraining t-T pathways combined with OMR for a dense regional coverage in conjunction with integrated forward thermo-kinematic modelling could still provide further refinement in timing and wavelengths of the exhumation of the Intermontane Belt to Foreland Basin.

Especially thermo-chronological constraints that provide paleo-geothermal inferences can improve future overburden and exhumation studies in combination with extended 2D thermo-kinematic modelling. Realistic modelling with Thrustpack can also be applied to specific data controlled structures (Sassi and Rudkiewicz, 1999; Faure et al., 2004). Alternatively, conceptual, numerical thermo-kinematic modelling aids for a more generalized understanding of a footwall block's thermal history with heat advection from an overriding thrustsheet and a multi-phase exhumation history (ter Voorde et al., 2004).

Future work will also be devoted to thermodynamics on an extended crustal and mantle-lithospheric scale. Geodynamic modelling can provide a more quantitative understanding of the driving mechanisms and could link lithospheric thermal perturbations with upper crustal kinematics and associated uplift history. The Foreland Belt marks the transition zone of the Canadian Cordillera with the stable North American Craton in the East (Cook, 1995; Cook et al., 1992). Not only significant thinning of the thermal lithosphere as revealed by seismic sounding studies and surface heatflow, but also variations in compositional layering and rheological stratification have a potential effect on the strain style, localization and coupling with the superficial thermo-kinematic history of the Foreland Belt and adjacent Foreland.

Acknowledgments

References

Archibald, D.A., Krogh, T.E., Armstrong, R.L. and Farrar, E. (1984) Geochronology and tectonic implications of magma-

tism and metamorphism, southern Kootenay Arc and neighbouring regions, southeastern British Columbia. Part II: Mid-Cretaceous to Eocene. Can. J. Earth Sci. 21: 567–583.

Bally, A.W., Gordy, P.L., Stewart, G.A. (1966) Structure, seismic data and orogenic evolution of the southern Canadian Rockies. Bull. Can. Petr. Geol. 14: 337–381.

Beaumont, C. (1981) Foreland Basins. Geophysical Journal of the Royal Astronomical Society 65: 291–329.

Begin, N.J. and Lawton, D.C. and Spratt D.A. (1996) Seismic interpretation of the Rocky Mountain thrust front near the Crowsnest deflection, southern Alberta. Bulletin of Canadian Petroleum Geology Bulletin of Canadian Petroleum Geology 44: 1–13.

Benvenuto, G.L., Price, R.A. (1979) Structural evolution of the Hosmer thrust sheet southeastern British Columbia. Bull. Can. Petr. Geol. 27: 360–394.

Bustin, R. (1991) Organic maturity in the western Canada sedimentary basin, International Journal of Coal. Geology 19: 319–358.

Brown, R.L., Carr, S., Coleman, V., Johnson, B., Cook, F., Varsek, J. (1992) The Monashee decollement of the southern Canadian Cordillera: a crustal-scale shear zone linking the Rocky Mountain Foreland belt to lower crust beneath accreted terranes. In: Thrust Tectonics. K. McClay (Ed.) Chapman & Hall, London, pp 357–364.

Carr, S. (1992) Tectonic Setting and U-Pb Geochronology of the Early Tertiary Ladybird Leucogranite Suite, THor-Odin-Pinnacles Area, Southern Omineca Belt, British Columbia. Tectonics 11: 258–278.

Constenius, K.N. (1996) Late Paleogene extensional collapse of the Cordilleran foreland fold and thrust belt, Geological Society of America Bulletin 108: 20–39.

Creaney S, Allan J, (1992) Petroleum systems in the foreland basin of western Canada. In Leckie DA, Macqueen RW (ed). Foreland Basins and Fold Belts AAPG Memoir 55, pp. 279–308

Dahlstrom, C.D.A. (1970) Structural Geology in the eastern margin of the Canadian Rocky Mountains. Bull. Can. Petr. Geol. 18: 332–406.

Dawson, F.M., Evans, C.G., Marsh, R., Richardson, R. (1994) Chapter 24 - Uppermost Cretaceous and Tertiary Strata of the Western Canada Sedimentary Basin. In: Mossop G, Shetsen I (compilers) Geological Atlas of the Western Canada Sedimentary Basin. Canadian Society of Petroleum Geologists and Alberta Research Council, Calgary and Edmonton, p. 387–406.

Deville, E. and Sassi, W. (2006) Contrasting thermal evolution of thrust systems: An analytical and modelling approach in the fron of the western Alps. AAPG Bull. 90: 887–907.

England, T.D.J, Bustin RM (1985) Effect of thrust faulting on organic maturation in the southeastern Canadian Cordillera, Advances in Organic Geochemistry 10: 609–616

England, T.D.J., Bustin R.M. (1986) Thermal Maturation of the western Canadian sedimentary basin south of the Red Deer River: I) Alberta Plains. Bull. Can. Petr. Geol. 34: 71–90

Faure, J.L., Osadetz, K., Benaouali, N., Schneider, F., Roure, F. (2004) Kinematic and petroleum modelling of the Alberta foothills. Rev. Inst. Fr. Petrol. 59: 81–108

Feinstein, S., Kohn, B., Osadetz, K., Price, R. (2005) Thermochronometric reconstruction of the pre-thrust paleogeothermal gradient and thickness of the Lewis thrust sheet, Southeastern Canadian Foreland Belt. Geology <<in prep.>>

Fermor, P. (1999) Aspects of the three-dimensional structure of the Alberta Foothills and Front Ranges. GSA Bulletin 111: 317–346.

Ford, D. (2004) Depositional wedge Tops: interaction between low basal friction external orogenic wedges and flexural foreland basins. Basin Research 16: 361–375.

Fermor, P.R., Moffat, I.W. (1992) Tectonics and structure of the Western Canada Foreland Basin. In Macqueen, R.W., Leckie, D.A. (eds.) Foreland Basins and Fold Belts. AAPG Memoir 55: 81–105

Gabrielse, H. and Yorath C.J. (1992) Geology of the Cordilleran Orogen in Canada; Geological Survey of Canada, The Geology of Canada Number 4, 847 p

Green, P.F., Duddy, I.R., Hegarty, K.A. (2002) Quantifying exhumation from apatite fission track analysis and vitrinite reflectance data: precision, accuracy and latest results from the Atlantic margin of NW Europe. In: Doré, A. G., Cartwright, J., Stoker, M. S., Turner, J. P. and White, N. Exhumation of the North Atlantic Margin: Timing, mechanisms and Implications for Petroleum Exploration. Geological Society Special Publication 196: 331–354.

Grieve, D. (1987) Coal rank distribution, Flathead coalfield, southeastern British Columbia (82G/2.82G/7), Geological fieldwork, 1986: British Columbia Ministry of Energy, Mines and Petroleum Resources Paper 1987-1, 361–364.

Hacquebard, P.A., Donaldson, J.R. (1974) Rank Studies of Coals in the Rocky Mountains and Inner Foothills Belt Canada. Geological Society of America Special Paper 153: 75–94.

Hacquebard, P.A. (1977) Rank of coal as an index of organic metamorphism for oil and gas in Alberta. In: The Origin and Migration of Petroleum in the Western Canada Sedimentary Basin, Alberta - A geochemical and maturation study. G. Deroo, T.G. Powell B. Tissot and R.G. McCrossan (eds.). Geol. Surv. Can. Bull. 262: 11–22

Hacquebard, P.A. and Cameron, A.R. (1989) Distribution and coalification patterns in Canadian bituminous and anthracite coals. Int. J. Coal Geol. 13: 207–260.

Hardebol, N.J., Faure, J.L., Callot, J.P., Bertotti, G., Roure, F. (2005) Global Controls, Coupled Kinematic and Thermal Modelling of the Lewis Transect, Southwest Alberta, Canada. AAPG 2005 Annual Convention, Program with Abstracts.

Issler, D.R., Willett, S.D., Beaumont, C., Donelick, R.A., Grist, A.M. (1999) Paleotemperature history of two transects across the Western Canada Sedimentary Basin: Constraints from apatite fission track analyses. Bull. Can. Petrol. Geol. 47: 475–486

Jones, P.B. (1993) Structural geology of the modern Frank Slide and ancient Bluff Mountain Slide, Crowsnest, Alberta. Bull. Can. Petr. Geol. 41: 232–243.

Kalkreuth, W., Langenberg, W., McMechan, M. (1989) Regional coalification pattern of Lower Cretaceous coal-bearing strata, Rocky Mountain Foothills and foreland, Canada - implications for future exploration. Int. J. Coal Geology 1:, 261–302.

Kalkreuth, W.M., McMechan, M. (1988) Burial History and Thermal Maturity, Rocky Mountain Front Ranges, Foothills, and Foreland, East-Central British Columbia and Adjacent Alberta, Canada. AAPG Bull. 72.11: 1395–1410.

Labrecque, J.E., Shaw, E.W. (1973) Restoration of Basin and Range faulting across the Howell Creek Window and Flathead valley of southeastern British Columbia, Bulletin of Canadian Petroleum Geology 21: 117–122

Lampe, L., Kornpihl, K., Sciamanna, S., Zapata, T., Zamora, G., Varadé, R. (2006) Petroleum systems modelling in tectonically complex areas – A 2D migration study from the Neuquen Basin, Argentina. J. Geoch. Expl. 89: 201–204.

Langenberg, C.W., Kalkreuth, W., Holmes, K. (1998) Components of syn- and post-deformational coalification in the Mountain Park area west central Alberta. Bull. Can. Petr. Geol. 46.4: 564–575.

Langenberg, W., Kalkreuth, W. (1991) Tectonic controls on regional coalification and vitirinite-reflectance anisotropy of Lower Cretaceous coals in the Alberta Foothills, Canada. Bull. Soc. geol. France 162: 375–383.

Leech, G.B. (1960) Geologic Map Fernie - preliminary (West Half - 82G) Geological Survey of Canada, map 35–1961.

Lebel, D., Hiebert, S.N., Spratt, D.A. (1997) Pincher Creek (82H/5), Alberta Geology, Geological Survey of Canada, Open File map 3543, scale 1:50.0000.

Lebel, D., Hiebert, S.N. (2001) Geologic Map Beaver Mines (82G/8- East Half), Alberta, Geological Survey of Canada, Open File map 4024, scale 1:50.0000.

Liu, M. (2001) Cenozoic extension and magmatism in the North American Cordillera: the role of gravitational collapse. Tectonophysics 342, 407–433.

MacKay, P.A. (1996) The Highwood Structure: a tectonic wedge at the foreland edge of the Southern Canadian Cordillera. Bull. Can. Petr. Geol. 44: 215–232.

Majorowicz, J.Q., Jones, F.W., Ertman, M.E., Osadetz, K.G., Stasiuk, L.D. (1990) The Relationship between Thermal Maturation Gradients, Geothermal Gradients and Estimates of the Thickness of the Eroded Foreland Section, Southern ALberta Plains, Canada. Marine and Petroleum Geology 7: 138–152.

McMechan, M.E. and Thompson, R.I. (1989) Structural style and history of the Rocky Mountain Fold and Thrust Belt. In: Western Canada Sedimentary Basin, A Case History. B.D. Ricketts (ed.) Can. Soc. PEtr. Geol. P. 47–76.

McMechan, R.D., (1981) Stratigraphy, sedimentology, structure and tectonic implications of the Oligocene Kishenehn Formation, Flathead Valley graben, southeastern British Columbia. PhD thesis, Queens University, Kingston.

Morretti, I., Larrere, M. (1989) Computer-Aided Construction of Balanced Geological Cross-Sections. Geobyte 16–24.

Monger, J.W.H., Price, R.E. (1979) Geodynamic evolution of the Canadian Cordillera - progress and problems. Can. J. Earth Sci.16: 770–791.

Monger, J.W.H., Clowes, R.M., Cowan, D.S., Potter, C.J., Price, R.A., and Yorath, C.J. (1994) Continent-ocean transitions in western North America between latitudes 46 and 56 degrees: Transects B1, B2, B3, pp. 357–397. In Phanerozoic Evolution of the North American Continent-Ocean Transitions, Edited by Speed, R.C., Geological Society of America, DNAG, Continent-Ocean Transect volume.

Mudge, M.R. and Earthart, R.L. (1980) The Lewis Thrust Fault and Related Structures in the Disturbed Belt, Northwestern Montana. Geological Survey Prof. Pqper 1174, U.S. Dep. Of the Int, U.S. Gov. Printing Office.

Norris, D.K. (1993a) Geology and structure cross-sections, Blairmore (West Half), Alberta, Geological Survey of Canada, Map 1829A, scale 1:50.0000.

Norris, D.K. (1993b) Geology and structure cross-sections, Beaver Mines (West Half), Alberta, Geological Survey of Canada, Map 1838A, scale 1:50.0000.

Nurkowski, JR (1984) Coal quality, coal rank variation and its relation to reconstructed overburden, Upper Cretaceous

and Tertiary Plains coals, Alberta, Canada. AAPG Bull. 68: 285–295.

Osadetz, K.G., Kohn, B.P., Feinstein, S., and Price, R.A. (2004) Foreland belt thermal history using apatite fission-track thermochronology: Implications for Lewis thrust and Flathead fault in the southern Canadian Cordilleran petroleum province. IN: Swennen, R., Roure, F., and Granath, J.W. (eds.), Deformation, fluid flow, and reservoir appraisal in foreland fold and thrust belts, AAPG Hedberg Series, No. 1, American Association of Petroleum Geologists, Tulsa, USA, 21–48.

Osadetz, K.G., Kohn, B.P., Feinstein, S., O'Sullivan, P.B. (2002) Thermal history of Canadian Williston basin from apatite fission-track thermochronology - implications for petroleum systems and geodynamic history. Tectonophysics 349: 221–249.

Osadetz, K.G., Jones, F.W., Majorowicz, J.A., Pearson, D.E., Stasiuk, L.D. (1992) Thermal history of the cordilleran foreland basin in western Canada: A review. In Leckie DA, Roger W. Macqueen RW (eds) Foreland Basins and Fold Belts. AAPG Memoir 55. pp 259–278.

Parrish, R.R. (1995) Thermal evolution of the southeastern Canadian Cordillera. Can. J. Earth Sci. 32: 1618–1642.

Parrish RR, Carr SD, Parkinson DL (1988) Eocene extensional tectonics and geochronology of the southern Omineca Belt, British Columbia and Washington. Tectonics 7: 181–212

Pearson, D.E., Grieve, D.A. (1985) Rank variation, coalification pattern and coal quality in the Crowsnest coalfield, British Columbia. Can. Inst. of Mining and Metallurgy Bull. 78 no. 881: 39–46

Price, R.A. (2001) An evaluation of models for the kinematic evolution of thrust and fold belts: structural analysis of a transverse fault zone in the Front Ranges of the Canadian Rockies north of Banff, Alberta. Journal of Structural Geology 23: 1079–1088

Price, R.A., Sears, J.W. (2000) A preliminary palinspastic map of the Mesoproterozoic Belt/Purcell Supergroup, Canada and U.S.A.: Implications for the tectonic setting and structural evolution of the Purcell anticlinorium and the Sullivan deposit. In Lydon JW, Höy T, Slack JF, Knapp M (eds) The geological environment of the Sullivan deposit, British Columbia. Geological Association of Canada, Mineral Deposits Division, MDD Special Volume No. 1, pp. 61–81

Price, R.A. (1994) Chapter 2 - Cordilleran tectonics and the evolution of the Western Canada Sedimentary Basin. In Mossop G, Shetsen I (compilers) Geological Atlas of the Western Canada Sedimentary Basin. Canadian Society of Petroleum Geologists and Alberta Research Council, Calgary and Edmonton. pp. 13–24.

Price, R. (1986) The southeastern Canadian Cordillera: thrust faulting, tectonic wedging, and delamination of the lithosphere. Journal of Structural Geology 8: 239–254.

Price, R.A., Fermor, P.R. (1985) Structure Section of the Cordilleran Foreland Thrust and Fold Belt West of Calgary Alberta. Geological Survey of Canada, Paper 84–14.

Price, R.A. (1981) The cordilleran Thrust and Fold Belt in the southern Canadian Rocky Mountains. In: McClay KR, Price NJ (eds), Thrust and nappe tectonics, Geological Society of London, special Publication no. 9, pp. 427–448.

Price, R.A. (1965) Geologic Map Flathead Area (Alberta and Britsh Columbia Geological Survey of Canada, Memoir 336, 221 p.

Price, R.A. (1964) The Precambrian Purcell System in the Rocky Mountains of Southern Alberta and British Columbia. Bulletin of Canadian Petroleum Geology 12: 399–426.

Price, R.A. (1962) Geologic Map Fernie - east half (Alberta and Brithish Columbia). Geological Survey of Canada, Paper 61–64.

Price, R.A. (1961) Geologic Map Fernie - preliminary (East Half - 82G) Geological Survey of Canada, map 35–1961.

Root, K.G., Boettcher, D., Gordy, P. (2000) The MacDonald (Bourgeau) Thrust in the southernmost Canadian Rocky Mountain Belt: an application of the "Princess and the Pea" concept for determining the displacement on a major thrust fault: GeoCanada 2000, Program with Abstracts.

Roure, F., Swennen, R., Schneider, F., Faure J.L., Ferket, H., Guilhaumou, N., Osadetz, K., Robion Ph., Vendeginste, V. (2005) Incidence and importance of Tectonics and natural fluid migration on reservoir evolution in foreland fold and thrust belts. In Brosse E. et al., eds., Oil and Gas Science and Technology, Oil and Gas Science and Technology, IFP Rev. 60: 67–106.

Roure, F., Nazaj, S., Mushka, K., Fili, I., Cadet, J.P., Bonneau M. (2004) Kinematic evolution and petroleum systems: an appraisal of the Outer Albanides. In McKlay (ed.), Thrust Tectonics and Hydrocarbon Systems, AAPG Mem. 82: 474–493.

Roure, F., Sassi, W. (1995) Kinematic of Deformation and Petroleum System Appraisal in Neogene Foreland-Fold and thrust Belts. Petroleum Geosciences 1: 253–269

Sassi, W., Rudkiewicz, J.L. (1999) Thrustpack version 6.2: 2D Integrated Maturiy Studies in Thrust Areas. IFP Report 45: 372.

Sears, J.W. (2001) Emplacement and denudation history of the Lewis-Eldorado-Hoadley thrust slab in the northern Montana Cordillera, USA: Implications for steady-state orogenic processes. Am. J. Sc. 301: 359–373.

Steiner, J., William, G.D., Dickie, G.J., (1972) Coal deposits of the Alberta Plain. In: G.B. Melon, J.W. Kramers and E.J. Seagel (eds.), Proceedings, First Geological Conference on Western Canadian Coal, Edmonton, Research Council of Alberta, Information series n°60, 85–96.

Stockmal, G. (2001) Structural style and evolution of the triangle zone and external Foothills, southwestern Alberta: Implications for thin-skinned thrust-and-fold belt mechanics. Bull. Can. Petr. Geol. DOI: 10.2113/49.4.472 49.4, 472–496.

Stockmal, G.S., Lebel, D. (2003) Geology Blairmore (East Half – 82G/9E), Alberta, Geological Survey of Canada, Open File 1653, scale 1:50.0000

Sweeney, J.J., Burnham, A.K. (1990) Applications of a Simple Model of Vitrinite Reflectance Based on Chemical Kinetics. AAPG Bulletin 74: 1559–1570.

Teichmüller, M. (1986) Organic petrology of source rocks, history and state of the art, Advances in Organic Geochemistry 10: 581–599.

Ter Voorde, M., De Bruijne, C., Cloetingh, S. and Andriessen, P. (2004) Thermal consequences of thrust faulting: simultaneous versus successive fault activation and exhumation. EPSL 223: 397–415.

Tissot, B. (1987) Thermal history of sedimentary basins, maturation indices, and kinetics of oil and gas generation. AAPG Bull. 71: 1445–1466.

Ungerer, P.,Burrus, J., Doligez, B., Chénet, P.Y. Bessis, F. (1990) Basin evaluation by integrated two-dimensional modelling of heat transfer, fluid flow, hydrocarbon generaton and migration, AAPG Bull 74.3, 309–335.

Vanderhaeghe, O., Teyssier, C. (1997) Formation of the Suswap metamorphic core complex during late-orogenic collapse of the Canadian Cordillera: Role of ductile thinnning and partial melting of the mid- ot lower crust.. Geodinamica Acta (Paris) 10: 41–58.

Vanderhaeghe O, Teyssier C, McDougall I, Dunlap WJ (2003) Cooling and exhumation of the Suswap Metamorphic Core Complex constrained by 40Ar/39Ar thermochronology. GSA Bull. 115: 200–216.

Van der Velden, A and Cook, F.A. (1994) Displacement of the Lewis thrust sheet in southwestern Canada: New evidence from seismic reflection data. Geology 22, 819–822.

Van der Velden and A.J. Cook, F.A. (1996) Structure and tectonic development of the southern Rocky Mopuntain trench. Tectonics 15: 517–544.

Willett, S.D., Issler, D.R., Beaumont, C. Donelick, R.A., Grist, A.M. (1997) Inverse modelling of annealing of fission track in apatite: application to the thermal history of the Peace River Arch, Western Canada Sedimentary Basin. Am. J. Sci., 297, 970–1011.

Part V
Zagros/Makran Thrust Belts

Part V of the volume is dedicated to the understanding of the building, structural evolution and active tectonics of the Zagros and Makran thrust belts, as well as to the history and role of early salt diapirism on the deformation of the Zagros detached cover.

Ahmadhadi et al. (Chapter 11) demonstrate that in the Central Zagros basement faults were reactivated during a Lower Miocene early stage of collisional stress build-up. This early basement fault reactivation presumably produced an early phase of large-scale flexure/forced-folding in the cover which strongly controlled intra-basin architecture and facies changes in the Lower Neogene and likely played a significant role during the early stage of fracturing within the Asmari Formation before the main Mio-Pliocene phase of cover folding.

On the basis of field work, seismic profile interpretation and well data aiming at reconstructing the history of subsidence, temperature and maturity of source-rocks in the Izeh Zone and in Northern Fars, Rudkiewicz et al. (Chapter12) report a coupled structural, thermal and geochemical basin modelling undertaken to handle compositional generation, maturity and expulsion of hydrocarbons in these areas. Important result are that generation and expulsion behaviour of Jurassic and Albian source-rocks considerably varies within the Izeh Zone and that thickness of the Late Cretaceous–Eocene sediments and the first vertical movements at regional scale in the inner part of the belt considerably influenced the maturation expulsion, migration and entrapment of petroleum from these source-rocks.

Mouthereau et al. (Chapter 13) synthesize structural, seismotectonics and microtectonics studies, as well as results of recent mechanical modelling of the topography and stratigraphic constraints on the timing of Plio-Pleistocene folding and Zagros basin evolution, in order to examine which mechanical behaviour better explains the development of the Zagros Folded Belt at both local and regional scales. They argue that an overall thick-skinned deformation has followed the initial margin inversion during the late Neogene, probably coeval with buckling of the detached sedimentary strata. Their interpretation disagrees with the classical view of thin-skinned propagation of the Zagros Folded Belt.

Oveisi et al. (Chapter 14) report a geomorphic analysis in the Mand anticline at the south-western-most front of the Zagros wedge. They show that the Mand anticline is a very active structure, which would absorb 35 to 50% of the 8 mm/yr convergence across the entire Zagros, with the Late Pleistocene shortening rate being inferred to be 3 to 4 mm/yr perpendicular to the anticline. This result is consistent with a classical forward-propagating deformation sequence during at least the Late Pleistocene.

Jahani et al. (Chapter 15) describe the morphology and the present activity of the salt diapirs of the eastern Zagros and discuss the chronology of salt movements as well as their relationships with the regional geodynamic context. They show that nearly all the diapirs were already active prior to Zagros folding either

as emergent diapirs forming islands in the Paleogene to Neogene sea or as buried domes initiated at least by the Permian. These diapirs first helped localizing subsequent deformation, then were reactivated by salt-cored detachment folding which allowed salt movement along faults in the whole eastern Fars Zagros Fold-Thrust Belt.

As a complementary approach to chapter 15, Callot et al. (Chapter 16) address the timing of salt diapirism, the influence of salt distribution and structures on fold propagation, the mechanisms of rapid salt extrusion, and the localisation of salt diapirs relative to fault and folds in the Fars domain by means of analogue sandbox experiments. Their main results are that the driving mechanism of Hormuz halokinesis during the Zagros folding and erosion is the squeezing of pre-existing salt diapirs, which also influenced the location of thrusts and strike-slip faults. Depending on the diapir wall attitude and its thickness relative to the sedimentary column thickness, the diapirs are either shortened and localize sharp overturned folds, or else act as preferentially oriented ramps, part of the diapir being incorporated in the fold. During fold growth and active shortening, erosion or rejuvenation of the diapir allows upward salt extrusion.

Ellouz et al. (Chapter 17) present an update of the onshore geology of the Makran accretionary prism based on new field data in the Pakistani area combined with interpretations of remote-sensing satellite data and interpretation of reprocessed seismic lines. The results are synthesized in the form of two synthetic geological transects, with an updated stratigraphic chart based on the new dating. The results reveal strong along-dip and along-strike changes in tectonic style through time, which are related to changes in velocity rates and direction of convergence due to re-organization along plate boundaries, location and rates of sedimentation over the growing prism, involvement of oceanic ridges in the subduction zone, and/or activity of secondary décollement levels within the accretionary prism.

In their companion paper, Ellouz et al. (Chapter 18) complement onshore field investigations of Chapter 17 and report the results of the 2004 CHAMAK research cruise which surveyed most of the accretionary complex off Pakistan. Analysis of new bathymetric and seismic data as well as drill cores shows that the frontal part of the Makran accretionary prism is less two-dimensional than previously expected, and that the along-strike tectonic variations reflect lateral variations in sediment deposition as well as underthrusting of a series of basement highs and kinematic complexity in the vicinity to the Ar-Eu-India triple junction.

Early Reactivation of Basement Faults in Central Zagros (SW Iran): Evidence from Pre-folding Fracture Populations in Asmari Formation and Lower Tertiary Paleogeography

Faram Ahmadhadi · Olivier Lacombe · Jean-Marc Daniel

Abstract . Early reactivation of basement faults and related development of flexures/forced-folds in the Central Zagros are discussed based on fracture populations observed in outcrops and aerial photographs/satellite images and paleogeographic maps. The presence of pre-folding joint sets slightly oblique to anticline axes and observed even within synclines or the occurrence of N-S (and E-W) trending fracture sets near N-S trending basement faults and strongly oblique to cover folds are not compatible with simple fold-related fracture models in this region. These early fractures are proposed to have formed within the cover above deep-seated basement faults in response to the formation of flexures/forced folds whose geometries and orientations may be different from the present-day folds in the Central Zagros. This early stage of intraplate reactivation of the NW-SE and N-S trending basement faults likely marks the onset of collisional deformation and stress build-up in the Zagros basin. This reactivation led to facies variations and development of different sub-basins in the Central Zagros during the sedimentation of the Oligocene-Miocene Asmari Formation. The evaporitic series of the Kalhur Member within the Asmari Formation resulted from the development during Aquitanian times of a long and narrow restricted lagoon environment, between two main basement faults (i.e., DEF and MFF), and provide one of the main key constraints on the beginning of deformation in the region. Finally, based on observed fracture populations and proposed geodynamic evolution in the Central Zagros basin, it is suggested that partitioning of N-S Arabia-Eurasia convergence into a belt-perpendicular NE-SW shortening and a belt-parallel right-lateral strike-slip motion (as currently along the Main Recent Fault) in the Central Zagros may have started as early as Oligocene (?)-Lower Miocene times.

Keywords. Zagros, Asmari, tectonics, fold, fracture, basement
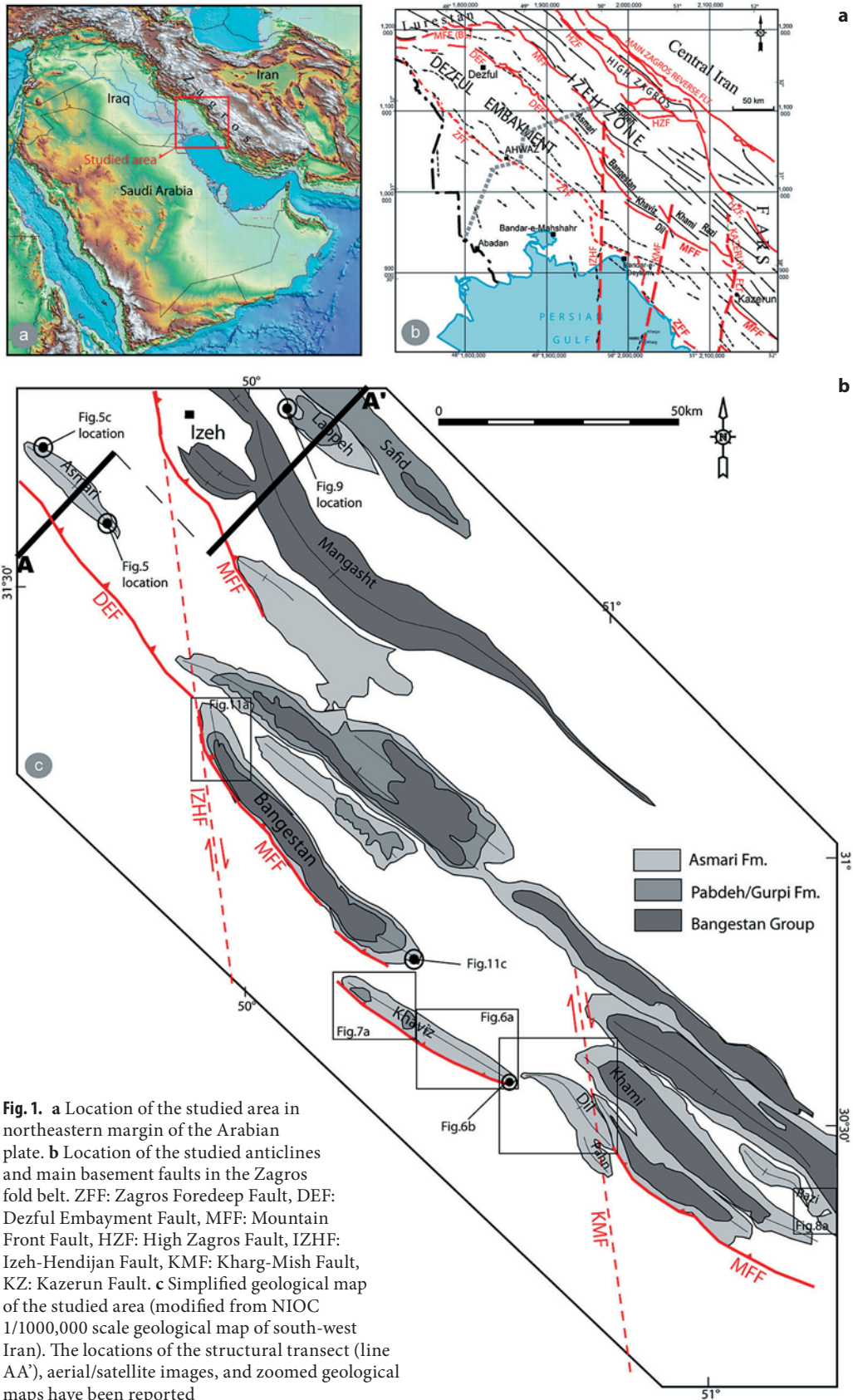
1 Introduction

Reactivation of basement faults occurs during orogenic evolution of collided passive margins, and this structural process is known to exert a strong control on the evolution of orogens (Dewey et al., 1986). Basement fault reactivation may induce localization of thrusts and folds in the developing shallow thrust wedge, reversal of extensional faults and development of crystalline thrust sheets, out-of-sequence thrusting and refolding of shallow nappes, development of accommodation structures such as lateral ramps, and development of basement uplifts (Wiltschko and Eastman, 1983; Glen, 1985; Cooper and Williams, 1989; Roure et al., 1990; Narr and Suppe, 1994; Butler et al., 1997).

A number of regional studies have demonstrated the compressional reactivation of preexisting structures within both the cover and the basement of foreland thrust belts worldwide (e.g., Alps: Roure et al., 1990; Lacombe and Mouthereau, 2002; Urals: Brown et al., 1999; Andes: Winslow, 1981; Kley et al., 1999; Cristallini and Ramos, 2000; Rockies: Dechesne and Mountjoy, 1992; Taiwan: Mouthereau et al., 2002; Lacombe et al., 2003; see also Letouzey, 1990; Mitra and Mount, 1998). Moreover, reactivation of intraplate basement faults and structural inversion of sedimentary basins have also been documented in the foreland far from the orogens (e.g., Tapponnier et al., 1986; Ziegler, 1987; Ziegler et al., 1995; Lacombe and Mouthereau, 1999; Marschak et al., 2000).

The Zagros belt results from the still active collision of the Arabian plate with the continental blocks of Central Iran (e.g. Stocklin, 1968; Jackson and McKenzie, 1984) (Fig.1). The Main Zagros Thrust (MZT) is considered as the suture, currently inactive, between the Arabian and Central Iran plates. GPS studies suggest that about one third of the active Arabia–Eurasia shortening (ca. 7 mm yr-1) is taken up in central Zagros (Vernant et al., 2004). Folding (and thrusting) of the Zagros sedimentary cover occurred mainly during the Mio-Pliocene by the end of deposition of the syntectonic upper Agha Jari Formation, about 7–3 Ma ago (Falcon, 1960; Stoneley, 1981; Berberian and King, 1981; Homke et al., 2004), while the Arabia-Eurasia continental collision culminated. The timing of the onset of this continental collision is, however, poorly constrained (estimates range from Late Cretaceous to Pliocene times, e.g., Berberian and King, 1981; Alavi, 1994; Agard et al., 2005; Sherkati et al., 2006) and has remained a matter of debate.

In the Zagros foredeep, although the geometry of the deformed cover is relatively well-known thanks to

Fig. 1. **a** Location of the studied area in northeastern margin of the Arabian plate. **b** Location of the studied anticlines and main basement faults in the Zagros fold belt. ZFF: Zagros Foredeep Fault, DEF: Dezful Embayment Fault, MFF: Mountain Front Fault, HZF: High Zagros Fault, IZHF: Izeh-Hendijan Fault, KMF: Kharg-Mish Fault, KZ: Kazerun Fault. **c** Simplified geological map of the studied area (modified from NIOC 1/1000,000 scale geological map of south-west Iran). The locations of the structural transect (line AA'), aerial/satellite images, and zoomed geological maps have been reported

few seismic reflection lines, drilled-wells and excellent quality exposures (Fig. 2), information on the underlying basement is poor. The depth to basement can be estimated at 10–12 km on the basis of the results of aeromagnetic surveys (Morris, 1977) and from balanced cross-section (Blanc et al., 2003; McQuarrie, 2004; Sherkati et al., 2006). However, there is no clear image of basement fault pattern and defining their role in the structural evolution of the Zagros fold belt remains difficult. Reactivated basement normal faults inherited from the Tethyan rifting at a depth between 10 and 20 km have been thought for a long time to be responsible for the major earthquakes along the Zagros belt (Berberian, 1981, 1995; Jackson, 1980; Jackson et al, 1981; Jackson and McKenzie, 1984). Moreover, basement structures likely played a role in the deformation of the Zagros by localizing some topographic steps and major (often active) thrust faults in the cover (Berberian, 1995; Letouzey et al., 2002; Mouthereau et al., 2006). Recent balanced cross-sections in the Zagros emphasize that the basement is involved in shortening (Fig. 2) (Blanc et al., 2003; Letouzey and Sherkati, 2004; Sherkati et al., 2006). The generalized involvement of the basement in shortening is thought either to have followed (Molinaro et al., 2005; Lacombe et al., 2006) or to have been roughly coeval with (Mouthereau et al., this issue) folding of the sedimentary cover which occurred in late Miocene-Pliocene times. Oveisi et al. (this issue) provide evidence that both the sedimentary cover and the basement are currently deforming coevally but in a decoupled way at the Central Zagros front. In the Fars, Mouthereau et al. (2006) documented localized basement fault reactivation as early as during the middle Miocene.

Our aim in this paper is to demonstrate that in the Central Zagros basement faults were reactivated during a (late Oligocene ?)-Lower Miocene early stage of collisional stress build-up and that this early basement fault reactivation (1) strongly controlled the paleogeography in the Paleogene and Lower Neogene, (2), presumably produced a phase of early large-scale flexure/forced-folding in the cover and (3) likely played a significant role during the early stage of fracturing within the Asmari Formation before the main Mio-Pliocene phase of cover folding (Stocklin, 1968; Berberian, 1981). For these purposes, we have looked at the fracture populations observed in the Asmari Formation cropping out in several anticlines in the Izeh Zone and Dezful Embayment and have carefully examined facies variations in the central part of the Zagros fold belt from Paleocene to Lower Miocene. Finally, the implications for the timing of the onset of collisional deformation and stress build-up in the Zagros belt are discussed.

2 Geological Setting and Tectonic Evolution of the Zagros Fold Belt

2.1 Main Lithological Units

The Zagros fold belt is located along the north-eastern margin of the Arabian plate (Fig. 1a). It forms a 200–300 km-wide series of remarkable folds extending for about 1200 km from eastern Turkey to the Strait of Hormuz. The sedimentary column in the Zagros is estimated to be up to 12 km (James and Wynd, 1965; Falcon, 1974; Huber, 1977) and comprises the Cenozoic foreland sequence and the underlying Paleozoic-Mesozoic deposits of the Arabian margin and platform. The sedimentary column, ranging from Cambrian to Plio-Quaternary, is embedded between two main detachment levels (mobile group), namely the Hormuz Salt Formation (Infra-Cambrian) at the base and the Gachsaran Formation (Lower Miocene) at the top (Lees, 1950; Falcon, 1969; Colman-Sadd, 1978). Since

Fig. 2. Regional transect through the studied area showing regional deformation style in the Izeh zone and the north of Dezful Embayment (line AA' in Fig. 1c). Important basement features, Mountain Front Fault (MFF), Dezful Embayment Fault (DEF), and dextral strike-slip Izeh-Hendijan Fault (IZHF) are seen in this transect (modified from Sherkati et al., 2006)
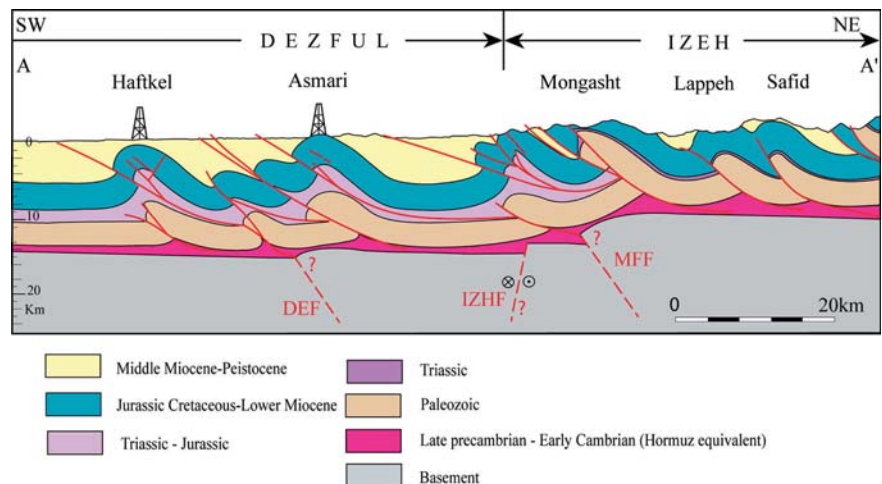
the main stratigraphic units exposed in the studied area correspond to the Cretaceous to Pliocene-Quaternary time interval during which the main tectonic movements took place, we briefly describe hereafter the lithological series of this period (Fig. 3a). The Lower Cretaceous shows almost uniform carbonate platform sediments including the Khami and lower part of the Bangestan Group. The Upper Cretaceous is characterized by the neritic carbonate series of the Sarvak and Ilam formations, and terminates with the basinal facies (deep water marls and shales) of the Gurpi Formation. The Tertiary sedimentary series are less uniform and show a variety of facies from neritic to deep basinal (Pabdeh Formation) to shallow marine carbonates of the Jahrum and Asmari formations (Fig. 3b-c) during the Lower Tertiary. Spanning the Middle Miocene to Pliocene are the Gachsaran evaporites, the marls of the Mishan Formation, then the deltaic/estuarine shales and sandstones of the Agha-Jari Formation which reflect a first-order basin-scale regressive sequence and which marks the progressive infilling of the Zagros foreland basin. The Tertiary sedimentary history ended with deposition of the diachronous coarse fluvial conglomerates of the Pleistocene Bakhtiary Formation.

2.2 Geodynamics and Deformation, Previous Work

The present morphology of the Zagros is the result of the structural evolution and depositional history of the northern part of the Arabian plate including a platform phase during the Paleozoic; a Tethyan rifting phase in the Permian-Triassic; a passive continental margin phase (with sea-floor spreading to the northeast) in the Jurassic-Early Cretaceous; subduction to the north-east and ophiolite-radiolarite obduction in the Late Cretaceous; and collision-shortening during the Neogene (Falcon, 1974; Berberian and King, 1981; Berberian et al., 1982; Berberian, 1983).

From a geodynamic point of view, different models for the evolution of the Zagros mountain system in southern Iran have been proposed (e.g., Falcon, 1967; Stocklin, 1968; Wells, 1969; Ricou, 1970; Nowroozi, 1972; Haynes and McQuillan, 1974; Alavi, 1980, 1994, 2004; Berberian and King, 1981; Jackson et al., 1981; Ni and Barazangi, 1986). In almost all of them, northward movement of the Arabian plate relative to the Central Iran during Tertiary times resulted in thrust faulting and overfolding in the Imbricated Belt adjoining the trench zone and gentler folding in the Simply Folded Belt to the southwest. Despite this, the beginning of compression in the Zagros fold belt is poorly dated. The initial Arabian-Central Iran continental collision is considered to be Late Creta-

ceous (Hayenes and McQuillan, 1974; Berberian and King, 1981; Alavi, 1994), Eocene-Oligocene (Hooper, 1994), Oligocene-Miocene (Berberian et al., 1982) or late Miocene in age (Stoneley, 1981; McQuarrie et al., 2003). Berberian and King (1981) proposed that folding in the Zagros foldbelt started around 5 Ma and coincides with the second phase of extension in the Red Sea and Gulf of Aden. Based on the unconformity between the Agha-Jari and Bakhtyari formations, Falcon (1961) suggested that the deformation was initiated in the Early Pliocene. On the basis of several unconformities at different stratigraphic levels, Hessami et al. (2001) proposed that deformation has occurred by pulses since the end of the Eocene, and reached the front of the folded belt during an end-Pliocene phase. All these estimations are based on ages of unconformities and sediment formations mostly defined by James and Wynd (1965). Documented Holocene anticline growth (Mann and Vita-Finzi, 1988; Vita-Finzi, 2001; Oveisi et al., this issue) and recent seismicity (Jackson and McKenzie, 1984) indicate that deformation in the Zagros belt is still active, especially at deep crustal levels. Homke et al. (2004) defined the beginning of the deformation in part of the Zagros foreland basin (Push-e Kush Arc) at 8.1 to 7.2 Ma based on magnetostratigraphical study of Miocene-Pliocene sediments. Allen et al. (2004) stated that extrapolating present-day deformation rates for 3–7 million years produces displacements that equal or exceed the total deformation on many of fault systems that are currently active in the Arabia-Eurasia collision zone including the Zagros Simple Folded Zone. This age range is much shorter than the overall age of the collision which began in the early Miocene (16–23 Ma) or even earlier (Hempton, 1987; Yilmaz, 1993; Robertson, 2000) with an early Miocene flexure before folding (Sherkati et al., 2006). Agard et al. (2005) documented several major tectonic events that took place at the end of the Cretaceous, during the Late Eocene, and from the Mid-Miocene onwards (ca. <20–15 Ma) and concluded that collision must have started before ca. 23–25 Ma in the northern Zagros.

2.3 Basement Fault Pattern in the Studied Area

There is no published information about basement depth available from seismic refraction or reflection and without such knowledge it is difficult to have a clear image of basement faults patterns and their role in geodynamic evolution of the Zagros fold belt. Two dominant tectonic trends, respectively N-S and NW-SE, exist in the Arabian Shield (e.g., Stern, 1985). Moreover, there is evidence for the continuation of several structures known in the Arabian Shield northwards into the Zagros Basin, before these structures
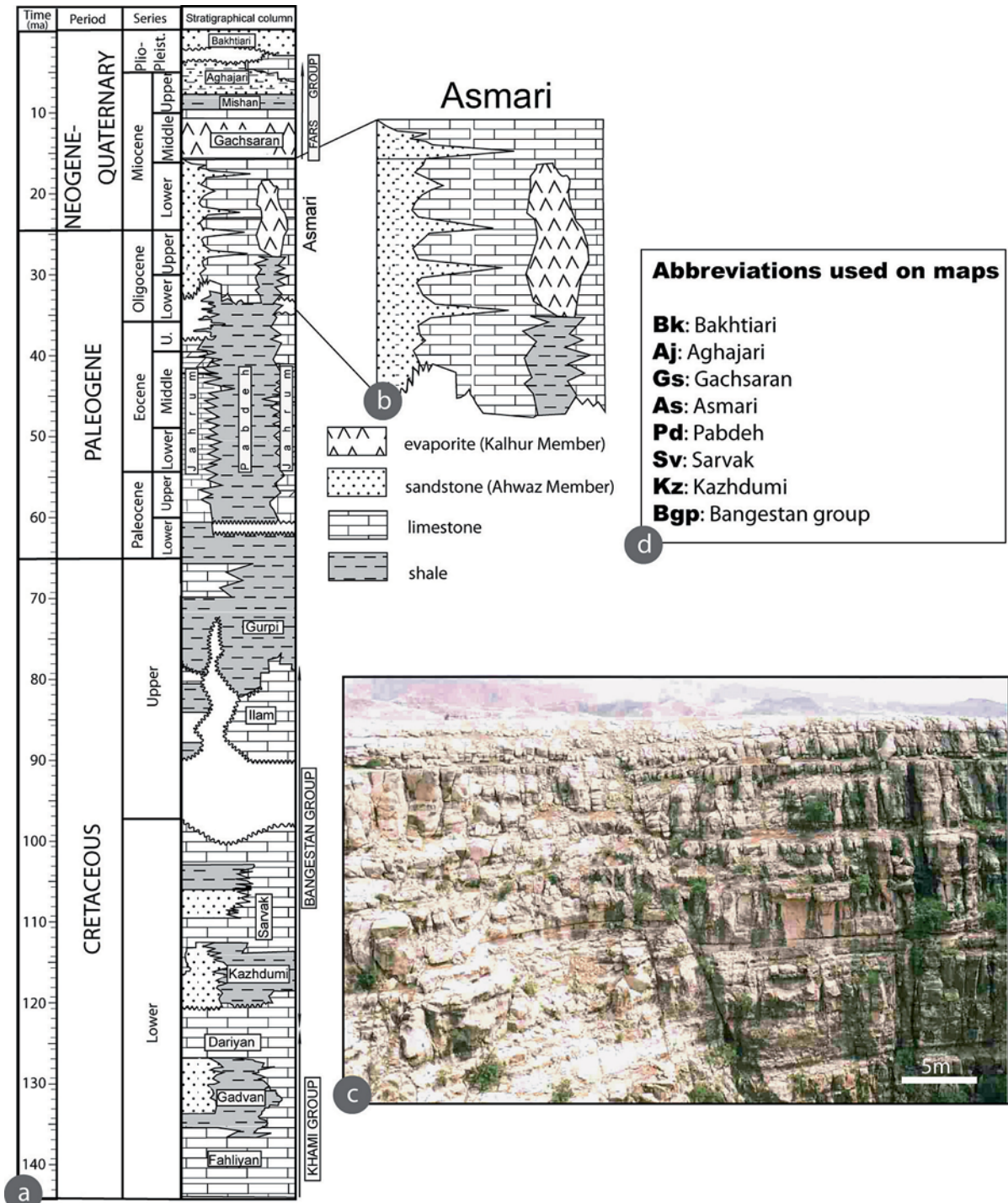
Fig. 3. a Lithostratigraphical chart showing the main stratigraphical units in the Central Zagros from Cretaceous to Pleistocene times. **b** Detail of the Asmari Formation. **c** Main exposed carbonate lithology of the Asmari Fm (e.g., Asmari anticline). **d** Abbreviations used in the following geological maps

were reactivated during the Cenozoic Zagros orogeny (Berberian, 1995; Talbot and Alavi, 1996; Hessami et al., 2001, Bahroudi and Talbot, 2003). In the Zagros belt, the approximate location and geometry of the basement Faults, despite the lack of detailed deep crustal knowledge, have been defined using a geodetic survey, more or less precise epicenter/hypocenter locations, as well as topographic and morphotectonic analyses (Berberian, 1995). The first group of basement faults includes the High Zagros Fault (HZF), the Mountain Front Fault (MFF), the Dezful Embayment fault (DEF), and the Zagros Foredeep Fault (ZFF) (Fig. 1b). Fault plane solutions for earthquakes along these faults indicate that they all dip about 60° NE (Bahroudi and Talbot, 2003), suggesting that they now act as reverse faults although they may have been activated as normal faults during the Permo-Triassic opening of Neo-Tethys (e.g., Jackson, 1980; Berberian, 1995).

Another group of basement faults are N-S trending faults which developed during the latest Proterozoic and early Cambrian in the Arabian basement (Beydoun, 1991). During the Mesozoic, and especially in the Triassic and Late Cretaceous, the N-S uplifts and basins related to this group of basement faults were intermittently reactivated (Edgell, 1992; Sherkati and Letouzey, 2004). These faults are steep to vertical and currently undergo right-lateral strike-slip motion (Baker et al., 1993; Berberian, 1995; Sepehr, 2001; Hessami et al., 2001). Some of these faults, located in the studied area, are the Izeh-Hendijan Fault (IZHF), the Kharg-Mish Fault (KMF), and the Kazerun Fault (KZ) (Fig. 1b). The Balarud Fault (BR) is an E-W left-lateral shear zone northwest of the Dezful Embayment.

The main morphotectonic regions in the Zagros fold belt are bordered by these major deep-seated basement faults (Fig. 1b). Figure 1c provides a simplified geological sketch map of the studied area.

3 Evidence for Pre-Folding Development of Joint/Vein Sets in the Asmari Formation

Fractures in folded sedimentary rocks are usually interpreted as the result of folding (Stearns, 1968; Stewarts and Wynn, 2000). Among different groups of so-called fold-related fractures, axial joints are supposed to be the result of local extension in the outer arc of the folds. Furthermore, based on consistent relations of the fractures with bedding attitude, even in the noses of folds, they are supposed to be in direct relation with fold geometry (Stearns and Friedman, 1972; Nelson, 2001). Fig. 4a shows, schematically, this symmetrical relationship between fold geometry and fold-related fracture pattern in map view; Fig. 4b presents the fracture pattern which can be expected to develop in a sedimentary cover undergoing flexure/forced-folding above dip-slip basement faults (Ameen, 1988; Cosgrove and Ameen, 2000).

The Asmari Formation (Fig. 3b-c) is one of the main reservoir rocks in SW Iran. This formation crops out along the Zagros fold belt where it forms the famous whaleback anticlines and is well-known as a carbonate fractured reservoir. Many studies dealing with the fracture pattern of the Asmari carbonates have been carried out and are still in progress. While McQuillan (1973, 1974, and 1985) stated that some fracture orientations bear no relation to the folds, Gholipour (1998) believes that the fractures within Asmari Formation are associated with vertical and axial growth of concentric folding (see also, Wennberg et al., 2006). The relative chronology of different fracture sets with folding in the Zagros is therefore still controversial.

In order to define the regional fracture pattern and its chronological relationship with folding, a careful analysis of fracture sets was carried out. To this pur-
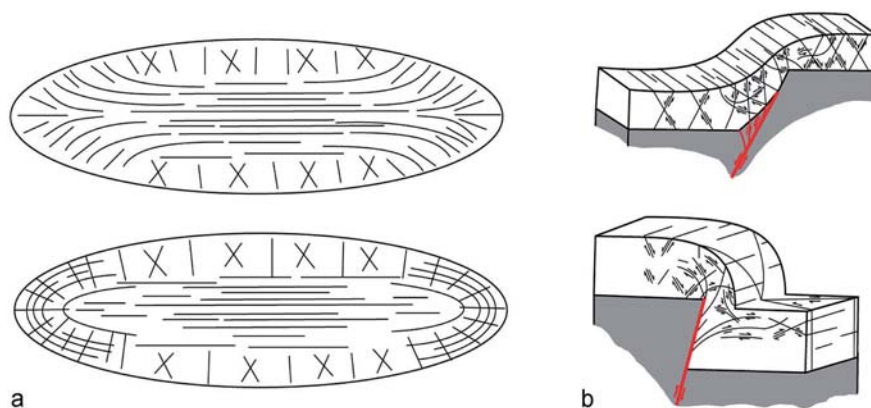
Fig. 4. Possible patterns of fold-related fracture sets. **a** Conceptual fracture models of Stearns (1968, 1978) in cylindrical and pericline parts of a simple buckle fold, in map view. Note the change in strike of fold-related fractures with changing bedding attitude in the pericline. **b** Fracture pattern in the cover above dip-slip normal (up) and reverse (down) basement faults (after Ameen, 1988, 1990)

a   b

pose, the orientations of sets of joints, veins and shear fractures/faults were measured in several anticlines located in the Izeh zone and in the northern part of the Dezful Embayment (Fig. 1c), within the uppermost part of the Asmari Formation which displays a lithology dominated by mudstones to wackestones (Fig. 3). Rather than focusing on fold-fracture relationships in a single anticline, data collection was thus organized to cover a large area in order to be able to differentiate regional fracture trends from fold-related fractures and local complexity. This allowed the relationships between fracture sets and regional structural trends to be discussed although all sets were not observed in all anticlines, especially those located away from underlying N-S basement faults.

At the outcrop scale, the most represented fractures are rectilinear with quite a regular spacing and a significant length (3 to a few tens of meters). These fractures can be confidently classified as joints because they do not show any evidence of offset across the fracture plane (mode-I opening); they are generally perpendicular to major bedding surfaces, and fracture walls often show plumose structures/hackle marks. These joints are frequently associated with parallel-mineralized veins. In contrast, some fractures were determined to have had a shearing mode of deformation where evidence of tail cracks or extensional jogs could be observed in the field.

It is, however, out of the scope of this paper to describe all the fracture sets identified in the investigated area and their relative chronology, which is reported in detail elsewhere (Ahmadhadi et al., submitted). In this paper, we only focus on the fracture sets which illustrate pre-folding extensional fracture development. In the following, members of a fracture set share both a common range of strike and dip orientation and a common deformation mode. For most of the joint sets, common orientation could be identified only after removal of bedding dip by stereographic rotation. Commonality of fracture orientation after removal of bedding dip, where the fractures are subparallel and bed perpendicular, is taken as supportive of a pre-folding origin (Hancock, 1985). Fracture strikes either perpendicular or parallel to bedding strike are not affected by rotation of bedding to remove the dip and may be interpreted as occurring during any stage of fold growth. When the pre-folding origin of a fracture set is consistently deduced from several anticlines, a regional significance of this pre-folding fracture set can be confidently derived.

Most joint sets described hereinafter are either pseudo-axial (i.e., sub-parallel to fold axes) or oblique to fold axes; most of them were reactivated (re-opened and/or sheared) during later fold development.

3.1 Early N040–050° (and N020–030°) Joint/Vein Sets

Among the different fracture sets observed in the investigated anticlines, an early set of N040–050° trending joints has been identified in numerous outcrops. A good example of this set is provided by the Asmari anticline (location Fig.1c) where a population of straight, regularly-spaced N040–050° fracture sets is observed on the crest and near the SE termination of this anticline (Fig. 5 a and b). These fractures often display plumose structures (e.g., in the Safid anticline) and/or occur as parallel-mineralized vein systems (e.g., Bangestan anticline); the attitude of these fractures with respect to bedding in fold flanks indicates that they predate folding and should be interpreted in their unfolded attitude. The strike of this joint set is often slightly oblique to present-day fold axes or to the local bedding strike (e.g., in Asmari, Khaviz, and Bangestan anticlines). Development of this joint set could be synchronous with the formation of stylolitic peaks parallel to this direction (Ahmadhadi, 2006).

The aerial photograph of Fig. 5 (a, b), taken near the top of the Asmari anticline confirms that the N040–050° fracture set is not strictly perpendicular to the fold axis. It corresponds to a very regular pattern of systematic joints without any directional perturbation. At the same location, lineaments in form of N140° trending fracture swarms (Fig. 5a), slightly oblique to the fold axis, are identified (see Sect. 3.2). As some of these fractures abut on fractures belonging to the regular N040–050° fracture set, the latter developed first. Such a chronology is further compatible with the fact that the N040–050° fracture set forms a very regular fracture pattern compared to the N140° set. Finally, a minor N-S set is observed. It corresponds to relatively short rectilinear fractures which generally abut on the two previous fracture families (see Sect. 3.3).

A second minor group of fractures comprises N20° to N30° joints (e.g., in Asmari, Khaviz, Bangestan). In Bangestan anticlines, they postdate the development of the 040–050° joint set, but show conflicting chronological relationships with N140° fractures. They likely reflect a slight evolution of the compressional trend from N40°–50° to N20°–30°, also marked by the change in trends of stylolitic peaks (Ahmadhadi, 2006).

3.2 Pseudo-Axial N140° Joint/Vein Sets

The Khaviz anticline (Figs. 6 and 7, location Fig.1c) is remarkably rectilinear with a mean axial trend of about 110–120° and dip of the flanks of about 30°. The NE flank is more gently inclined than the SW flank. Fracture measurements were performed in the field
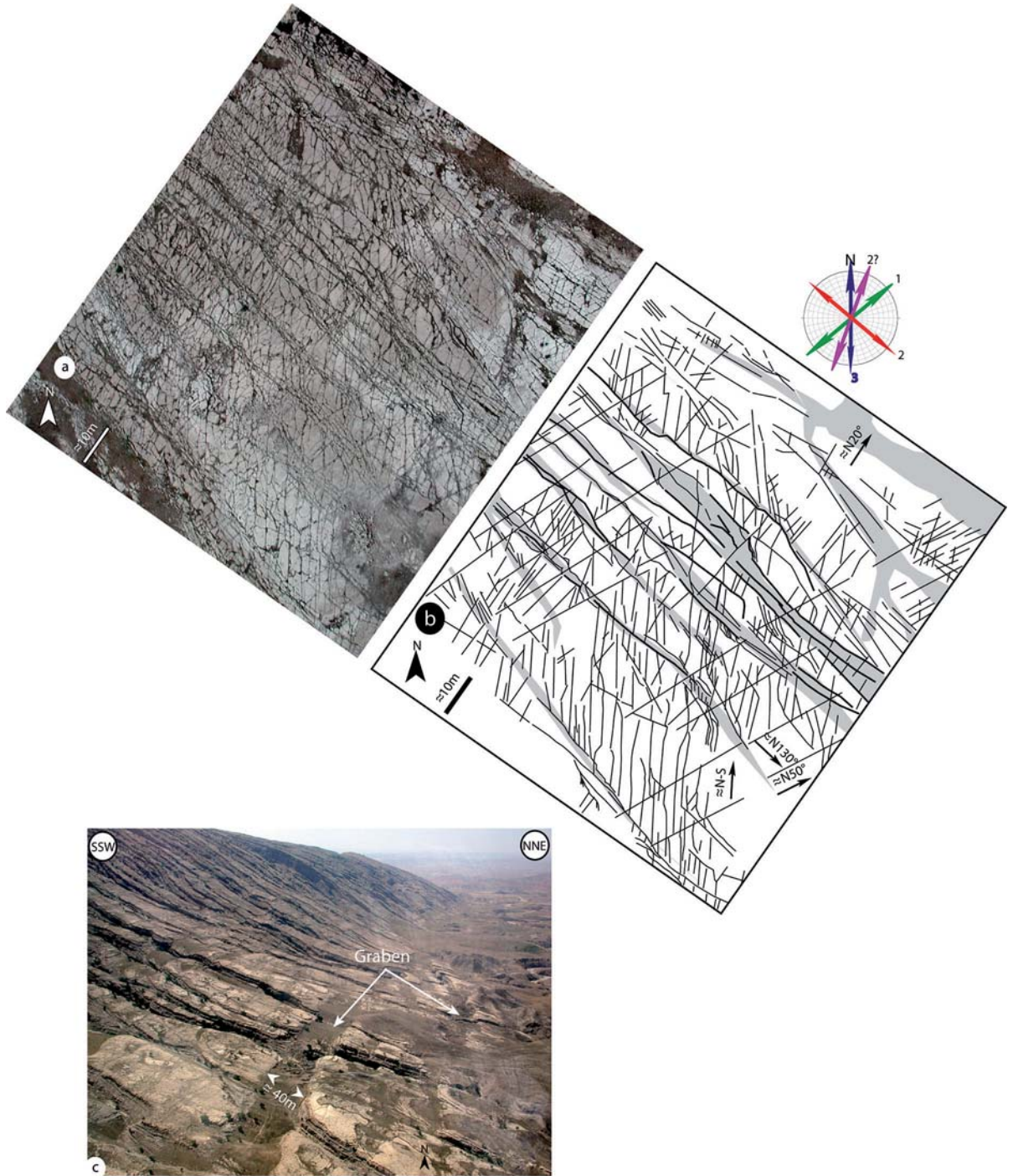
Fig. 5. Main fracture sets observed on the southern plunge of the Asmari anticline (see Fig. 1c for location): **a** aerial photographs and **b** Interpretation. The regular, non-disturbed fracture network with an azimuth of about N50° is considered as the first fracture set; N130-140° trending fractures formed a series of fracture swarms almost parallel to the fold axis; N-S fracture sets abut on the previous sets. **c** A series of ESE-WNW grabens near the NW termination of the fold on its northern flank

around the SE nose of the anticline (Fig. 6). It is noteworthy that the directions of large-scale lineaments observed on the satellite image from the NW part of the anticline (Fig. 7) are roughly similar to those of the small-scale fracture sets (Fig. 6b). This suggests again that the scale of observation has little influence on the identification and statistical measurements of these fracture sets.

As shown in Fig. 6a, a group of fractures which are perpendicular to bedding and have a mean strike of 130°–150° are observed around the SE nose of the anticline where the fold axis swings into an orientation of 120–130°. In most sites, these fractures mimic axial fractures, but are in fact slighty oblique to the local fold hinge : their strike always deviates clockwise from the anticline axis and in most sites this deviation ranges from 10° to 20°. In addition, the strike of these fractures in the pericline is not consistent with that predicted for axial, fold-related fractures (Figs.4a and 6). These characteristics support that the 130°–150° bed-perpendicular fractures rather predate folding. Unfor-

tunately, the low bedding dip precludes unambiguous demonstration that these fractures have been actually folded (unfolding would have revealed a better commonality of fracture orientation than with the current bedding attitude, hence a pre-folding origin). Larger deviations of the trend of this joint set relative to the anticline axis can be seen in the stations K3, K9, and K10. These stations are located almost along an arbitrary N-S trending line, although no N-S fault was observed on the measurement location or on the geological map. After unfolding, the fractures (red on Fig.6a) become vertical, with a 155–170° trend. In these three sites, the strong obliquity of fracture strike with fold axis further confirms that these fractures are not fold-related (see Sect. 5).

Fault slip-data were additionally collected in the NE flank of the Khaviz anticline (Fig.7). An important point at the first glance is that most of the fault-plane strikes slightly obliquely to the local bedding strike (N130°–N°140° vs. N110–120°) although the local fold axis is very rectilinear nearby the measurement site. Special attention was paid to the geometrical attitude of these faults with respect to tilted beds;
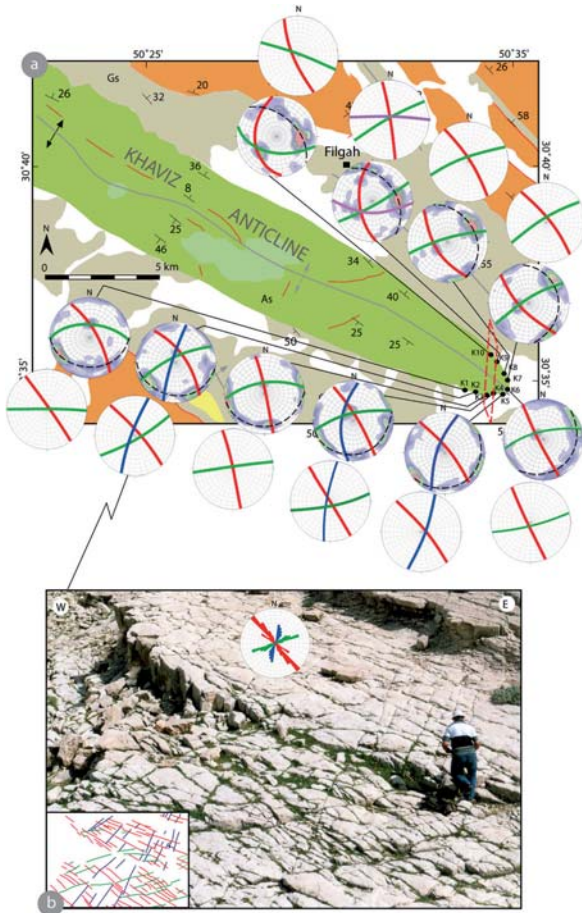
Fig. 6. a Geological map of the eastern part of the Khaviz anticline (see Fig. 1c for location) and fracture orientations around its NE termination. Diagrams: Schmidt lower hemisphere projection. Red, green, blue, purple: N140°, N050°, N-S-N020° and E-W trending fracture sets, respectively. Dashed lines are bedding planes. Fractures on diagrams with white background have been unfolded. The N140° fracture is persistently observed around anticline termination regardless of bedding attitude. The neraly N-S fracture trend, observed in the sites K3, K9, and K10, is likely related to an underlying N-S trending fault zone, indicated by a dashed line. b Main fracture sets observed in site K2
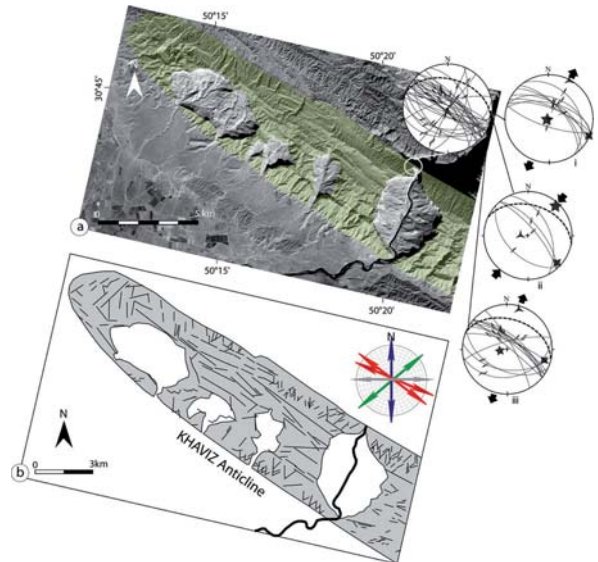
Fig. 7. a SPOT 5 satellite image on the western part of the Khaviz anticline. b Main sets of fractures observed on satellite image. Large photo-scale lineament show almost the same trends as those which were observed on the SE nose of this anticline at the outcrop scale. Fault slip data: Wulff lower hemisphere projection; five, four, and three corner stars correspond to the maximum (σ1), intermediate (σ2) and minimum (σ3) principal stress axes, respectively; Convergent/divergent solid arrows show the direction of compression and extension, respectively. Dashed lines are bedding planes

within a heterogeneous fault population, this geometrical reasoning allows separation of data subsets based on their age relative to fold development, even though no direct cross-cutting relationships between faults or superimposition of striations on fault planes are observed. These faults were further interpreted in terms of stress regimes using the method developed by Angelier (1990).

Among the data set, three populations of faults were identified and separated on the basis of their kinematics and their chronology relative to folding. The first set consists of steeply dipping normal faults with dip-slip slickenside lineations. The stress tensor computed from this set does not display a vertical σ1 axis; rather, the σ1 axis is perpendicular to bedding, while the other stress axes lie within the bedding plane. In such a case, the fault system has to be interpreted after back tilting to its initial position. After unfolding, the dip-slip normal faults indicate a pre-folding horizontal N30° extension (Fig. 7, diagram i), roughly consistent with the pre-folding N140° joint set identified in the SE nose of the anticline. Most of the remaining faults can be separated into a set of reverse faults and a set of oblique-slip normal faults, respectively related to a N40° compression and a N20° extension, both postdating folding (Fig. 7, diagrams ii and iii). The geometry of some of the post-folding faults suggests that they could result from the reactivation of the earlier normal faults despite the absence of evidence of superimposed striations on fault planes. The reverse faults likely mark the compressional state of stress responsible for folding. The significance of the late post-folding normal faults in terms of extension at fold hinge could seem questionable since the site of measurements is apparently located away from this hinge; however, since only the uppermost part of the fold is visible (most

part remains buried) and taking into account the low dip of the flank, it is likely that at the scale of the fold, the site is still located in its outer rim, so we conclude that this normal fault set and the related N020° extension presumably reflects extension at the fold hinge.

The Razi anticline (Fig. 8, location Fig. 1c) is located in the northern part of the Mountain Front Fault (MFF) at about 56 km south-eastward of the Khaviz anticline. Fracture orientations were collected along a valley cutting the anticline axis and both flanks were accessible to measurements. This anticline has a quite gentle geometry and the structural dip is even less than 10°. Among fracture data, a group of fractures striking N130°–N140° and N040°–050° are consistently observed (Fig. 8a), as in the Khaviz anticline. The N140° fractures are everywhere perpendicular to the bedding plane. Furthermore, two of the measurement stations (R1 and R2, Fig. 8a) where this fracture group is observed are located in a gentle syncline next to the Razi anticline, in the concave-upward part of which fold-related axis-parallel extensional fractures are unlikely. These observations demonstrate that, as in the Khaviz anticline, the N140° fracture set (and probably the N040°–050° as well) predated folding (or were created at a very early stage of folding).

On the NE flank and near the NW termination of the Asmari anticline where the structural dip is low, some grabens can be observed (Fig. 5c). These grabens are trending ESE-WNW, oblique to the fold axis. Therefore, they presumably predated folding that led to the present-day Asmari anticline structure. Although likely, offset of the normal faults bounding these grabens due to bedding-parallel slip during folding, which could have unambiguously demonstrated that these grabens developed before folding, could unfortunately not be observed. However, offsets of early outcrop-
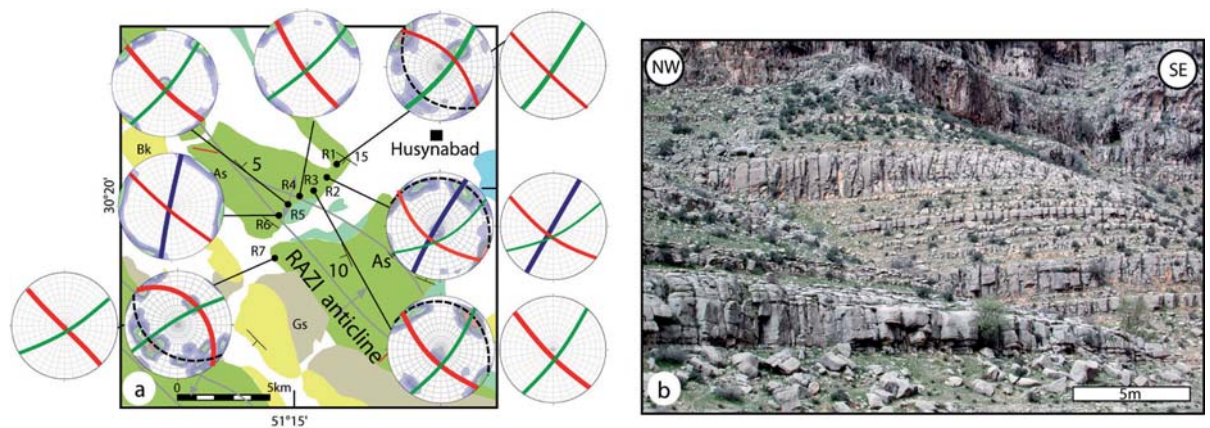
Fig. 8. **a** Geological map of the Razi anticline (see Fig. 1c for location) and fracture orientations on both flanks and fold crest. Note that the prominent joint sets are observed in the adjacent syncline (sites R1 and R2). **b** Intensive fracturing within horizontal beds in the Razi anticline. Colour code for fracture sets: same key as in Fig. 6. Fractures on diagrams with white background have been unfolded
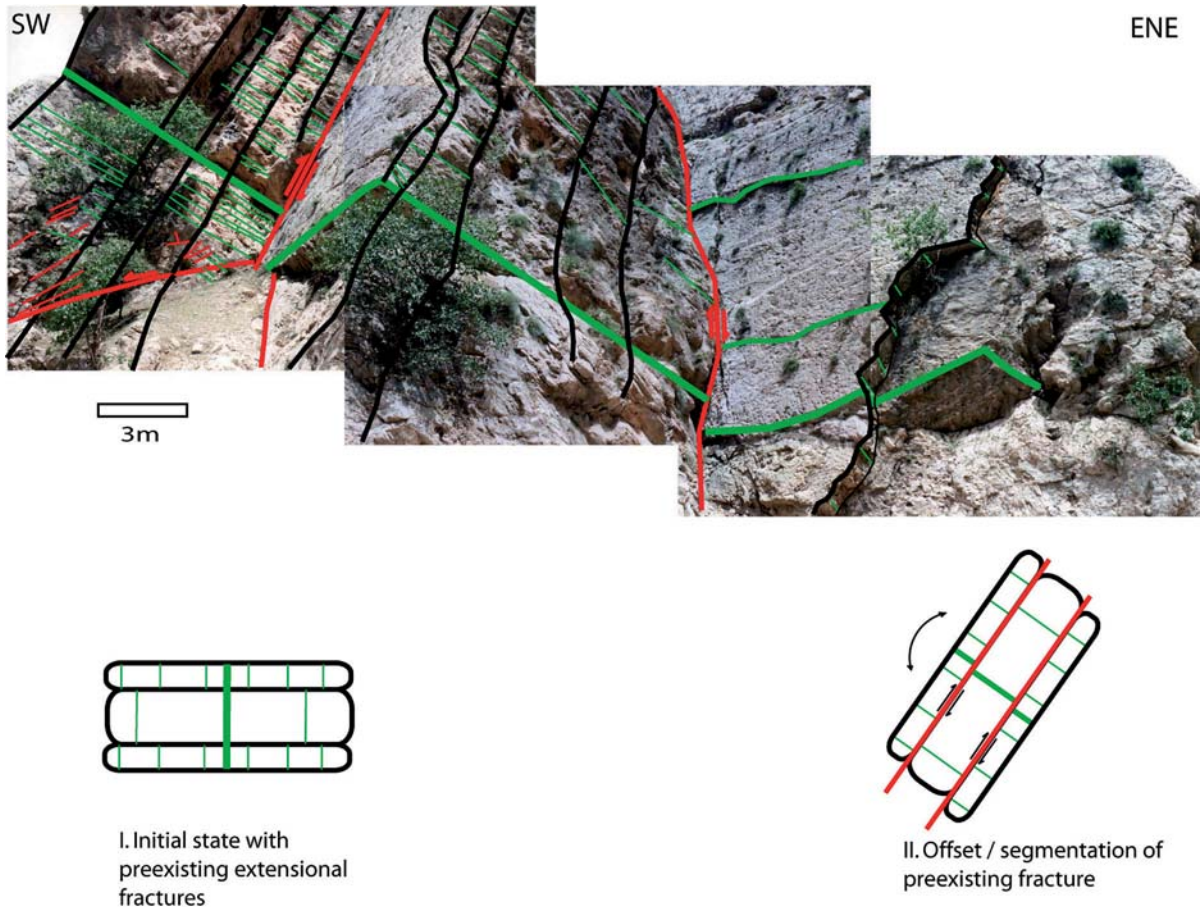
Fig. 9. Offset and segmentation of a large extensional N130°-140° trending fractures within Asmari carbonate beds by bedding-parallel slip in the SW limb of the Lappeh anticline (see Fig. 1c for location). This observation supports extensional fracture development before layer tilting (folding)

scale N130–140° trending extensional fractures (and even normal faults) by bedding-parallel slip have been observed in other outcrops (e.g., the Lappeh anticline, location Fig. 1c), which supports that early extensional fractures and normal faults formed in response to pre-folding extensional state of stress (Fig. 9).

As for the normal faults, the N140° trending joints and veins of this set were reopened and/or sheared during later folding (Ahmadhadi et al., submitted).

3.3 N-S (and Perpendicular E-W) Trending Joint/Vein Sets Oblique to Fold Axes

Another group of fractures which show no symmetrical relationship with fold geometry in the studied area include N-S fractures. These N-S fractures are commonly found associated with perpendicular E-W joints and mineralized veins (Fig. 10), the interpretation of which is still enigmatic (Ahmadhadi, 2006),

so the reason of this association will not be dealt with hereinafter. It was mentioned previously that in the nose of the Khaviz anticline, nearly N-S trending fractures oblique to the fold axis were observed. The NW termination of the Khami anticline and the NE flank of the Dil anticline are two other examples in which N-S and E-W trending joint sets perpendicular to bedding bear no symmetrical relationship with fold geometry (Fig. 10). This strongly suggests that these sets are not fold-related and that they have to be interpreted as pre-folding joint sets. Their abutting relationships on the N050° and N140° sets further confirm that all three sets are likely pre-folding.

In the Asmari anticline the N-S set has been observed next to N-S trending faults in the eastern part of the fold (Fig. 5), which are likely underlain by a N-S trending basement fault. More generally, the sites where the N-S trending fractures were measured in these anticlines more or less coincide with the location of an underlying basement fault (Fig. 10).

In the very same way, interpretation of Spot images of the NW termination of the Bangestan anticline (Fig. 11) also shows N-S and E-W trending lineaments (i.e., large-scale fractures) which are strongly oblique to the fold axis. These fracture sets developed in the vicinity of the nearby underlying N-S trending Izeh fault (Fig. 11).

In summary, outcrop investigation and lineament interpretation on satellite photos indicate that N-S (and sometimes associated E-W) trending fracture sets predominantly occur in the outcrops located near N-S trending basement faults (e.g., IZHF and KMF, Fig. 1b and c); this suggests that the development of these fracture sets is not fold-related but is rather controlled by the reactivation of these N-S basement faults.

4   Paleogeographic Evidence for a Basement Fault Control on Sub-Basin Geometries and Lateral Facies Variations During Oligocene-Lower Miocene Times

The main objective of this section of the paper is to study whether the basement faults affected basin architecture and facies distribution during lower Tertiary times. Such information can be used to date the inception of deformation in the foredeep and therefore to test models where fracturing predates folding. With this aim, we examined paleofacies evolution in the region located between the Bala-Rud (BR) Fault to the north-west and the Kazerun Fault to the east (Fig. 1b)
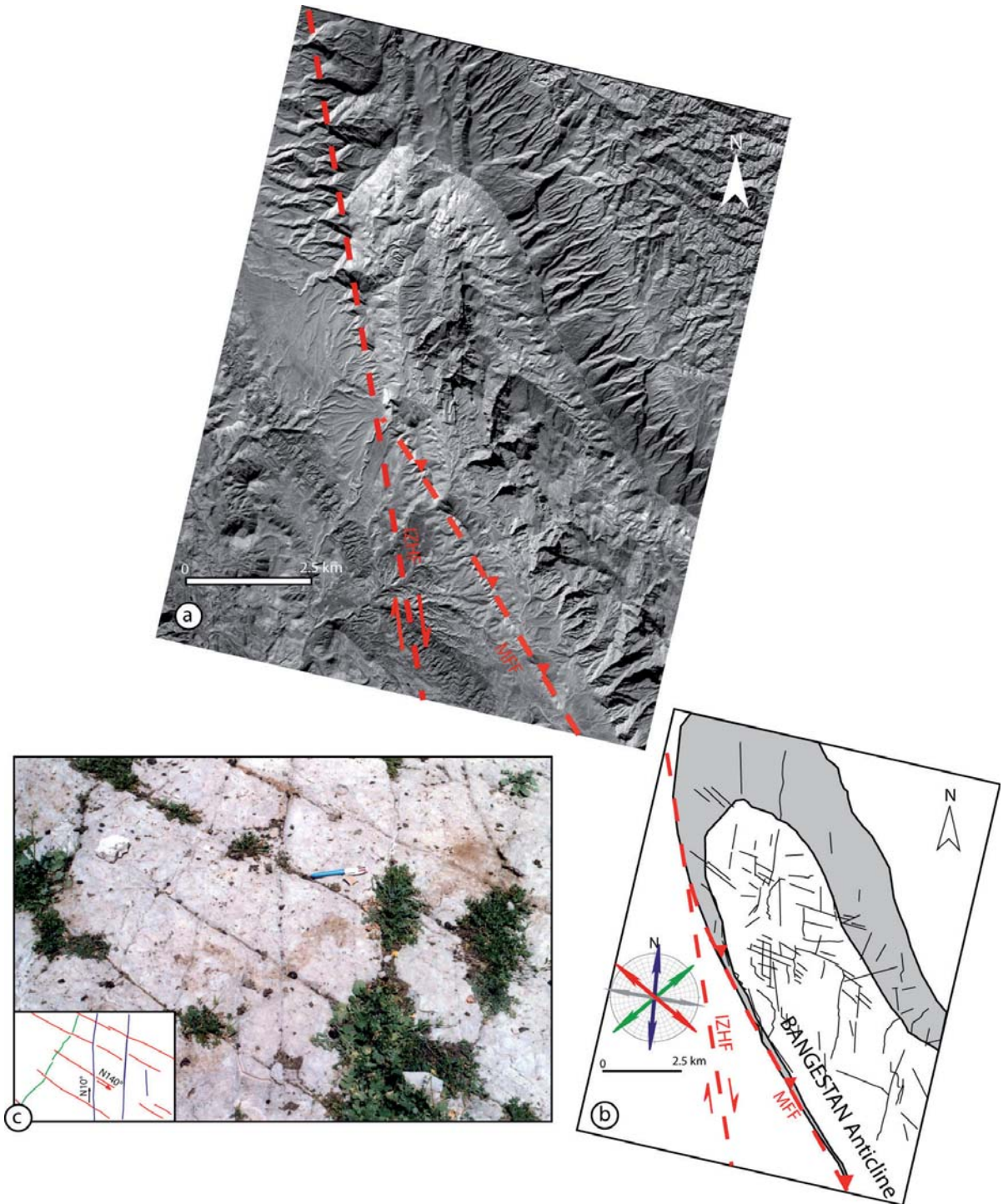
Fig. 11. **a** SPOT 5 satellite image on the SE termination of the Bangestan anticline (see Fig. 1c for location) and **b** interpretation of large-scale fractures on the NW termination of the Bangestan anticline close to a N-S trending basement fault (IZHF). Note that the main interpreted lineaments strike N-S and E-W, i.e., oblique to the local structural trend. **c** Main joint sets observed in the field in the SE nose of the Bangestan anticline

during the Lower Tertiary. Our study is mainly based on both previous works (James and Wynd, 1965; Berberian and King, 1981; Motiei, 1993) and a new analysis of well data from the Dezful Embayment. We especially focus on Oligocene to Lower Miocene paleofacies, which is the period of the Asmari sedimentation.

The Zagros basin with marine carbonate platform sedimentation became established in the early Jurassic and continued until Miocene times with the greatest subsidence being located in the northeast, possibly along several faults (Berberian and King, 1981). During the Palaeocene and Eocene the Pabdeh (neritic to basinal marls and argillaceous limestones) and the Jahrum (massive shallow marine carbonates) Formations were deposited in the middle and on both sides of the Zagros basinal axis, respectively (Fig. 12a). This basin was gradually narrowed and in Lower Oligocene times the Lower Asmari Formation, including carbonates, deeper marine marls, and sandy limestone (Ahwaz Member) were deposited (Fig. 12b). Different intra-basins and facies including clastic facies (Ahwaz/Ghar sandstone Member), carbonates and evaporites (Kalhur Member) were well developed during the Upper Oligocene-Early Miocene time (Fig. 12b to d). The important feature at this time is the rough co-
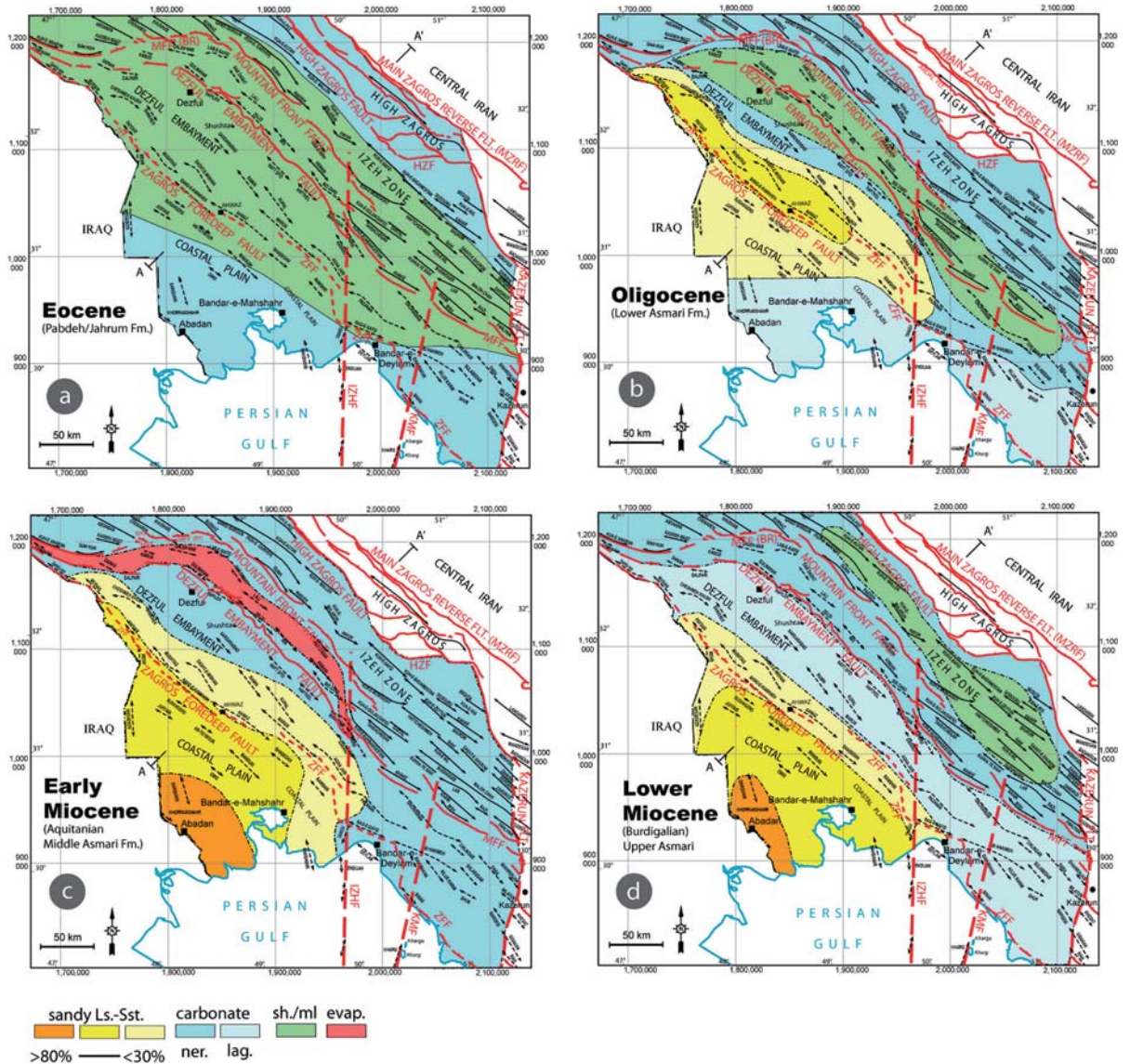
Fig. 12. Paleogeographical maps in the Central Zagros based on previous work (James and Wynd, 1965; Berberian and King, 1981; Motiei, 1993) and information from unpublished paleologs of drilled wells and surface sections in the Central Zagros: **a** Eocene; **b** Oligocene; **c** Lower Miocene (Aquitanian); **d** Lower Miocene (Burdigalian); see text for details

incidence of these intra-basins with the main NW-SE trending basement faults (i.e. MFF and DEF). Just in the center of the basin, basinal facies (marls and shales) changed to an evaporitic facies (Fig. 1c). No intermediate facies variation and transition from marls and shales to evaporites has been reported in the literature. This narrow basin is limited to the north and northeast by the MFF and BF and to the south and to the east by the DEF and IZHF, respectively. Farther south, the Ahwaz/Ghar Member delta front, indicated by more than 30% of the sand content of the Asmari carbonate, formed just and parallel to the south of the ZFF. This sand content gradually increases southward (Fig. 12c and d). During Burdigalian times, the Upper Asmari carbonates covered the entire basin with a hemipelagic facies toward the northern part of the Mountain Front Fault (Fig. 12d).

The present-day approximate coincidence of facies changes and the elongated shape of the confined, evaporitic sub-basin with basement faults is noteworthy. However, one has to take into account the influence of Mio-Pliocene deformation on the distribution of paleofacies in the Oligocene-Lower Miocene times. The amount of shortening estimated on the basis of balanced cross-sections in the Central Zagros, including the High Zagros and extending to the southwest of the Dezful Embayment, was reported to be about 50 km (Sherkati et al., 2006). Shortening in the Dezful Embayment is lower than in the High Zagros and the Izeh zone where a large amount of shortening is accommodated by imbricated thrust nappes. This means that the amount of southwest-ward differential displacement of the cover above the basement, somewhere between MFF and DEF can be considered negligible for our concerns. Nevertheless, there is always some discrepancies concerning the (projected) location of basement faults in the present-day cover but in any case, this intra-basin could not be displaced from the Izeh zone, northeast of the MFF, into the Dezful Embayment.

As a result, we conclude that during lower Tertiary times, both the geographic distribution of the facies and the location of the basement faults appear remarkably consistent. During Eocene times, the Pabdeh basin covered a wide area from the south of the High Zagros fault toward the Zagros Foredeep Fault (Fig. 12a). The depocenter of this basin gradually narrowed and migrated toward somewhere between the MFF to the north and the ZFF to the south following the progradation of the carbonate platform and clastic facies of the Lower Asmari Formation during the Lower Oligocene (Rupelian) (Fig. 12b). The development of a long narrow evaporitic intra-basin (Kalhur Member) during the latest Oligocene-early Lower Miocene (Chattian-Aquitanian, Fig. 12c) likely indicate an abrupt facies change (both laterally and ver-

tically), which seems to be difficult to interpret simply by eustasy or any sedimentological process alone, without any tectonic control. Rather, the localization of this intra-basin somewhere between the MFF which borders its northern margin and the DEF which borders its southern margin (Fig. 12c) and also an abrupt facies change from marls to evaporites, suggests a direct relation between this restricted lagoon intra-basin and deep-seated basement faults. So, even though an eustatic control cannot be ruled out, we suggest that the genesis of this sub-basin has been, at least partly, tectonically controlled.

If the above-mentioned basement faults were reactivated during lower Tertiary times with a component of vertical motion, causing large wavelength flexure or forced-folds in the overlying cover and therefore local topographic uplifts, they should have influenced accommodation space for the sedimentation especially for those areas located above them. To test this idea, a simplified transect based on the thickness variations of the main lithostratigraphical units (formations) with definite time lines (top and bottom) and data accessibility in the region was built (Fig. 13). The direction of this transect was chosen to cut the main NW-SE trending basement faults in the studied area (Fig. 1b). The Sarvak formation does not seem to be affected by the NW-SE trending basement faults (Fig. 13a). This formation shows almost a uniform variation in their thickness between ZFF and MFF, while the important fluctuations appear within Pabdeh/Jahrum and Asmari formations (Fig. 13b). Both thickness and main facies variations coincide with the location of the main basement faults; this strongly suggests that these faults were reactivated during Pabdeh/Jahrum and Asmari deposition.

5 Discussion: Early Fracture Development in the Asmari Formation Related to Flexure/Forced-Folding above Reactivated Basement Faults

Based on the field observations in the Central Zagros (Sect. 3), some prominent fracture sets cannot be interpreted by a conventional fold-related fracture model, and therefore explained by a single episode of fracturing during the Mio-Pliocene cover folding. There are several lines of evidence supporting that they are not fold-related fracture sets: (i) most of identified fracture sets are made of joints/veins lying perpendicular to bedding whatever their position in the fold (Figs.6 and 8) (ii) the N140° trending joints and normal faults (Figs.5 to 8), which mimic axial fractures, are in fact slightly oblique to the anticline axes and are sometimes observed in the adjacent synclines (e.g., Razi anticline); (iii) these N140°–160° fracture sets display a relatively consistent trend even in the nose of anticlines
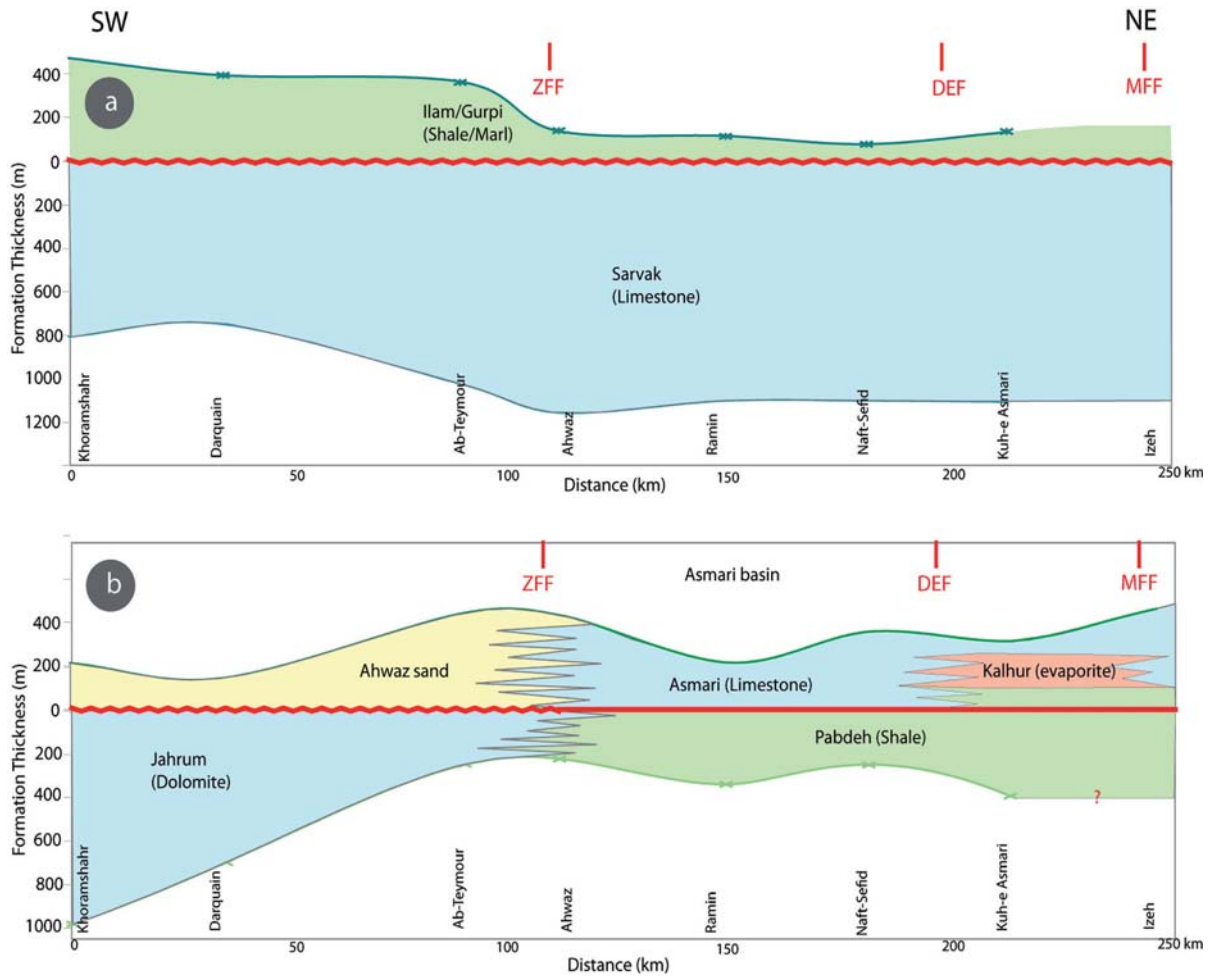
Fig. 13. Simplified transect perpendicular to the general trends of the folds in the Central Zagros (see transect location on Fig. 1b, and text for details). The Sarvak Formation does not show any thickness variations across NW-SE-trending basement faults **a**, while important fluctuations appear within the Pabdeh/Jahrum and Asmari Formations (Paleogene to Lower Miocene) **b**

(e.g., the Khaviz anticline), in contrast with common predictions of axial, fold-related fractures; (iv) the N-S trending outcrop-scale fractures and photo-scale lineaments are strongly oblique to the general fold axial trend in the sites close to N-S trending underlying basement faults (e.g., Dil, Khami, and Bangestan anticlines). On the other hand, the orientations of the main fracture group (~N140°–160°), despite the lack of their direct relations with the folds, are nearly similar in the Khaviz, Razi, Asmari and Bangestan anticlines (Figs.5 to 8, 11) and in the other anticlines investigated within the Central Zagros (Ahmadhadi et al., submitted). These observations strengthen the idea that this prominent fracture group developed under an extensional stress field (either local or regional) which affected the Asmari Formation before the main Mio-Pliocene phase of cover folding (Ahmadhadi et al., 2005).

We have suggested that basin architecture and facies variations and distribution during the Asmari sedimentation could have been controlled by the reactivation of deep-seated basement faults. We propose that at that time, the reactivation of the N140° and N-S basement faults included a component of vertical motion, which caused large wavelength flexure or forced-folds in the overlying cover (Fig. 14). Flexures/forced-folds could have induced an extensional state of stress above NW-SE trending basement faults (e.g. MFF, ZFF) within the uppermost part of the sedimentary cover (e.g. the Asmari limestones, which were likely rapidly lithified after deposition). The observed N-S trending fracture set (e.g., Khaviz anticline) and the location of measurement sites containing this fracture group near underlying N-S trending basement faults (e.g. IZHF and KMF) suggest that they should have also initiat-
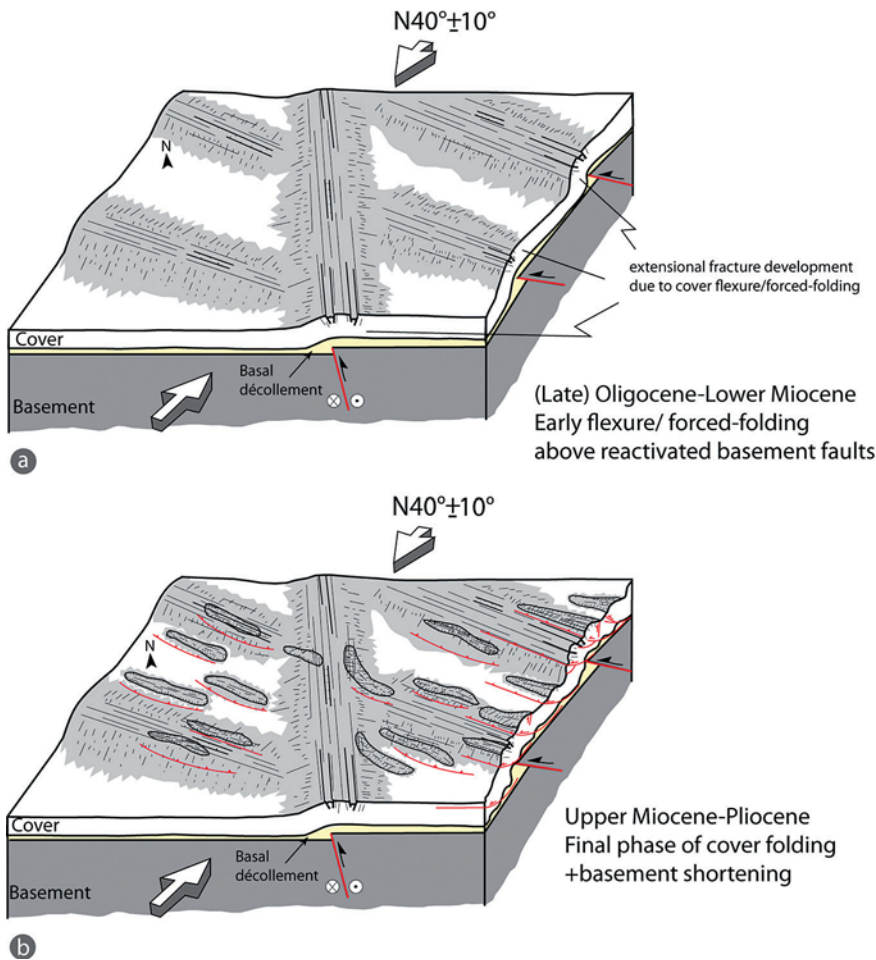
Fig. 14. Proposed model of early fracture development in the Central Zagros related to the reactivation of deep-seated main basement faults **a** followed by superimposition of Mio-Pliocene folds **b**

ed quite early and presumably synchronously with the reactivation of the NW-SE trending basement faults (Fig. 14). Edgell (1992) stated that the reactivation of N-S trending basement faults occurred since the latest Cretaceous. Our observations in the Asmari Formation suggest that this reactivation probably continued in the Lower Tertiary and that the N-S trending fractures are likely related to the reactivation of these transverse basement faults. This is in agreement with recently documented movements along the MFF and N-S trending faults during deposition of Gachsaran Fm (Abdollahiz et al., 2006).

However, as suggested by Fig. 4b, extensional fractures similar to those identified in the Central Zagros may develop whatever the type of vertical motion along basement faults, and it is generally difficult to distinguish between a normal and a reverse movement along basement faults if only extensional fractures are observed in the overlying cover. So one may question whether early extensional fractures were caused by flexure/forced-folding above either compressionally or extensionally reactivated basement faults (Fig. 4b).

One should also consider the possibility that these extensional fractures developed in the cover in response to forebulge development and extensional stresses related to Arabian plate flexure.

The possibility of creating extensional fractures in the cover (and also to extensionally reactivate NW-SE pre-existing basement faults) in response to plate flexure/forebulge development in the Central Zagros during Lower Miocene times has been investigated through a preliminary numerical modelling of bending stresses based of subsidence curves (Ahmadhadi, 2006). It is out of the scope of this paper to discuss this modeling in detail. First results suggest that bending stresses related to the Arabian plate flexure may have been high enough to cause development of early extensional fractures within the Asmari Fm., but that the area which underwent significant bending stresses appears smaller than the region where early extensional fractures were actually recognized in the field.

The earliest N040–050° regional joint set suggests that the Zagros basin was loaded by a N040–050° directed far-field compression during lower Miocene
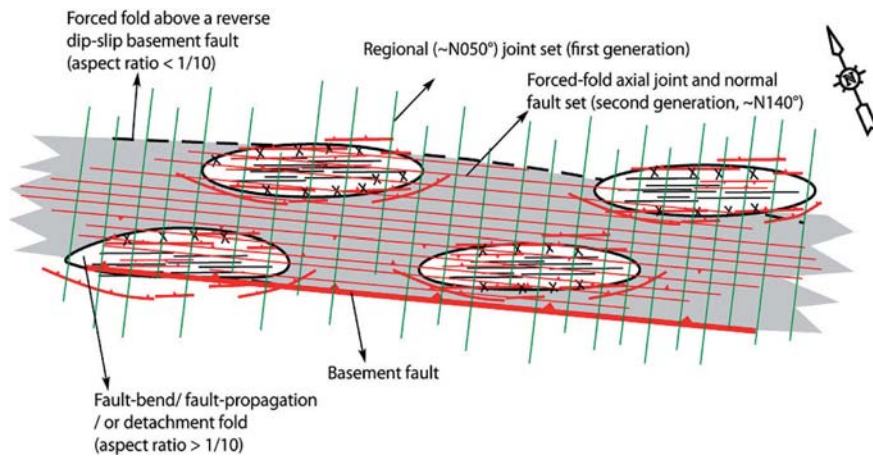
Fig. 15. Schematic model in map view of the superimposition of the Mio-Pliocene folds on an earlier large-scale forced-fold above a reactivated NW-SE-trending basement fault in the Central Zagros. This model makes it possible to explain the directional persistency of the fracture sets around the nose of an anticline and the presence of axis-parallel joint set in an adjacent syncline

times. So, as an alternate interpretation to plate flexure, we propose that the early extensional fractures developed locally above flexure/forced-folds related to the compressional reactivation of basement faults. In response to the N040–050° compression, and despite our limited knowledge on their geometry, the N140 and N-S-trending basement faults were likely reactivated with a component of vertical motion: a dip-slip component of reverse motion along N140° trending faults and an oblique-slip component of motion (reverse, right-lateral) along N-S-trending faults (Fig. 14).

Based on the previous discussion on the Asmari intra-basins, we propose that large-scale forced-folding above reactivated NW-SE trending basement faults may be a possible explanation for the development of NW-SE trending joints and normal faults during the first stage deformation in the Zagros. As explained before, paleogeography, facies variations and intra-basin development also support the onset of cover deformation in the form of large wavelength forced-folds before the whale-back anticlines developed during Mio-Pliocene shortening. One of the major differences in the geometry of early forced-folds and Mio-Pliocene buckle folds is their aspect ratio (half wavelength to axial length ratio) (Fig. 15). As the forcing members that generate the forced-folds generally result from long linear steps in the basement, the resulting folds frequently have a long aspect ratio and are, although not always, asymmetric (Sattarzadeh et al., 2000). The amount of aspect ratio in buckle folds has been proposed in the range of 1/5 to 1/10 (Sattarzadeh et al., 2000). So, we can expect to find evidence of early episodes of fracture development above basement faults around the terminations of some present folds in the Zagros and even in adjacent synclines despite the differential shortening of cover and basement (Figs. 14 and 15), in agreement with field observations.

6   Implications for the Onset of Compressional Deformation and Stress Build-up in the Zagros Belt

6.1 Basement Fault Reactivation in the Foreland of the Zagros Orogen and Far-Field Arabia-Eurasia Orogenic Stresses

Our analysis of the early fracture pattern and basin architecture at the time of deposition of the Asmari limestones therefore supports the occurrence of early compressional reactivation of basement faults within the Zagros basin. Such intraplate compressional deformations basically require that the build-up of intraplate compressional stresses, which likely result from a (far-field) stress transmission from the plate boundary, leads to sufficient stress magnitudes to overcome the local strength of the crust and cause reactivation of pre-existing weaknesses. Frictional resistance is generally less than shear rupture strength under the same confining pressure (e.g., Etheridge, 1986), so the stress necessary to initiate sliding on favorably oriented pre-existing faults is less than that needed to initiate new faults in intact rocks. In addition, depending on the nature of fractured rocks, preexisting fractures may become overpressured during compression, thereby decreasing the effective normal stress holding the opposite walls of the faults together (Sibson, 1993). Preexisting N140° and N-S basement faults therefore acted as crustal weaknesses when the Arabian crust underwent later shortening.

Such an intraplate stress build-up requires an efficient transmission of orogenic stresses, which largely depends on the amount of coupling between the orogen and the foreland (Ziegler et al., 1998). Reactivation of the N140° and N-S striking pre-existing basement faults within the Arabian foreland indicates that

the far-field stress transmission from the Arabia-Central Iran plate boundary, and therefore mechanical coupling between the Arabian and Eurasian plates were already efficient at that time. However, the transmission of stress through the pre-fractured Arabian crystalline basement was likely heterogeneous and complex, so the deformation front propagated in an irregular fashion through the basement and the cover. This is in agreement with the distinction made by Lacombe and Mouthereau (1999, 2002) between the front of the shallow thrust cover wedge, the reactivation front (the outermost inverted structure) and even the deformation front (the outermost microstructures related to orogenic stresses).

The timing of cover folding relative to basement shortening needs careful consideration since it reflects the sequence of deformation at the front of the orogen. It is of considerable importance when addressing the question of whether shortening in the basement occurred first and was transmitted to the cover, or the cover detached first because of low friction basal horizons, and deep-seated thrusting occurred second. The answer to this question is a key to understand how orogenic wedges reached a state of equilibrium. We provide herein evidence of an early involvement of the basement in shortening in Central Zagros through reactivation of inherited basement faults, before any significant involvement of the cover in the orogenic wedge. Folding/wedging of the cover occurred later, mainly during the Mio-Pliocene, together with a generalized involvement of the basement in collisional shortening.

6.2 Timing of Early Fractures and Reactivation of Basement Faults in the Central Zagros

Although the relative age of small-scale fractures can sometimes be established using for instance abutting relationships, their absolute age is generally more difficult to ascertain. Deformation in the Zagros belt including folding and fracturing is the consequence of the Arabia-Eurasia continental collision. The age for initiation of this collision has been estimated from ~64 Ma (Beberian and King, 1981), using the end of ophiolite obduction, to ~5 Ma (Philip et al., 1989), using the angular unconformity between Bakhtiary conglomerates and the underlying Agha-Jari Formation (Falcon, 1974). None of these approaches provides a date for the first time Arabian and Eurasian continental crusts came into contact in response to convergence (Allen et al., 2004). Deformation and syn-tectonic sedimentation took place on the northern side of the Arabian plate in the Early Miocene (~16–23 Ma) (Robertson, 2000; Sherkati et al., 2006), related to the overthrusting of allochthonous nappes originating on the Eurasian side of the Neo-Tethys (Allen et al., 2004). Other studies in the same region put the initial collision-related deformation in the Oligocene (Yilmaz, 1993), or even in the Middle Eocene (~ 40 Ma) (Hempton, 1987).

North-south Arabia-Eurasia convergence across the northwest Zagros is achieved through a combination (partitioning) of NE-SW shortening and right-lateral strike-slip faulting on the Main Recent Fault (MRF) in the NW Zagros (Fig. 1b) (Talebian and Jackson, 2004). Talebian and Jackson (2002) reported an offset of about 50–70 km along the right-lateral strike-slip MRF based on a restoration of the drainage patterns and geological markers. Then they proposed an age of about 3–5 Myr for the initiation of the MRF. This represents an average velocity of about 15 mm/yr along this fault. There are at the present day no other major, northwest-southeast-trending seismically active right-lateral strike-slip faults within this part of the Zagros belt that could help partition the overall convergence in this way (Allen et al., 2004). Furthermore, based on recent GPS measurements of convergence between the Central Iranian block and the Arabian plate (Vernant et al., 2004), the Central Zagros accommodates about 4–7 ± 2 mm/yr of north-south shortening. The maximum slip rate along the MRF would be of 4 ± 2.5 mm/yr if the fault achieves complete partitioning of this shortening. This is not in agreement with a Pliocene (3–5 Ma) initiation of the MRF (Talebian and Jackson, 2002) and with a cumulative lateral slip of 50–70 km along that fault, which leads to a long-term slip rate of 10–17 mm/yr (Talebian and Jackson, 2002). If the cumulative right-lateral offset on the MRF is correct, and if the age of the Bakhtiari Formation, which is essential from establishing the age of the MRF, is not underestimated, it is possible that horizontal slip may have occurred along precursor faults to the MRF or in the vicinity of the future MRF between the Late Cretaceous (using the age of the Ophiolite body as an offset marker (Talebian and Jackson, 2002) and the Pliocene, during dominantly transpressive deformation in the High Zagros. Agard et al. (2005) already suggested occurrence of belt-parallel strike-slip movement within the Crushed zone much before the Plio-Quaternary right-lateral movement along the MRF reported by Talebian and Jackson (2002).

Based on the evidence of facies changes, forced folding above basement faults in the Central Zagros strongly affected the Asmari basin during Aquitanian times (Lower Miocene) and possibly continued up to the final stage of deformation in the Upper Miocene – Pliocene times. Fig. 16 shows a tentative scenario of the geodynamic evolution of the Central Zagros basin. The geodynamic evolution of the basin during the lower Tertiary, at least in the Central Zagros, is not clear. Most parts of the Paleocene sediments, based on pale-
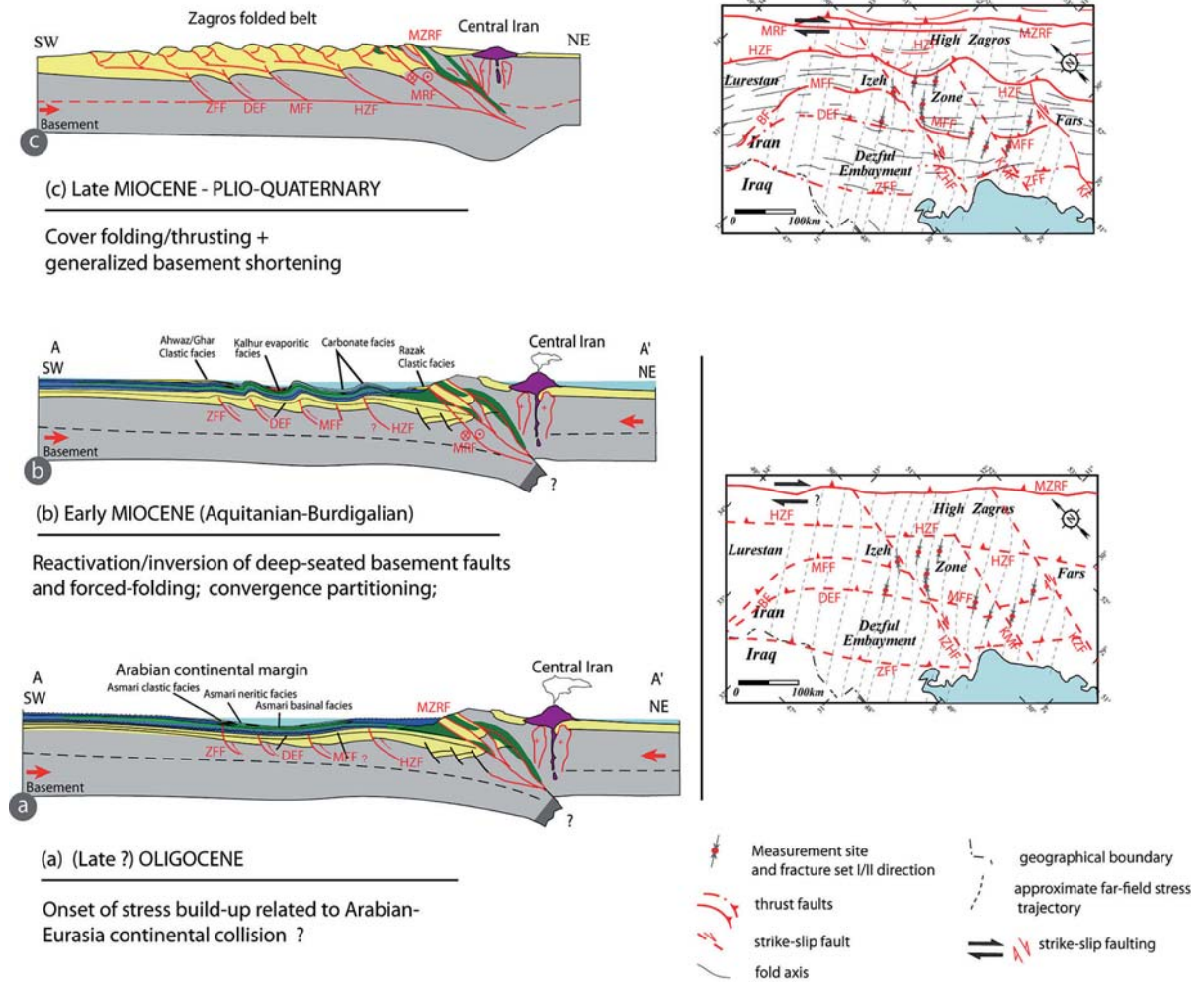
Fig. 16 Proposed lower Tertiary geodynamic evolution of the Central Zagros basin, on lithospheric cross-sections (left) and in map view (right) during **a** (late?) Oligocene; **b** Early Miocene (Aquitanian-Burdigalian); **c** Upper Miocene-Plio-Quaternary. This model suggests early involvement of the basement in shortening before any significant involvement of the cover in the orogenic wedge. The main episode of cover deformation and the generalized involvement of the basement in collisional shortening occurred later, during the Upper Miocene-Pliocene times

olog data in the Dezful Embayment, have been eroded and this unconformity sometimes reaches Maastrichtian formations in this region. Documented emergent zones near N-S basement fault (e.g., IZHF) during the latest Cretaceous and even Paleocene times suggest that these N-S-trending basement fault may have been reactivated. Progressive basin restriction and sedimentary flux progradation toward the depocenter of the previous Pabdeh basin, and the emergence of the Eocene carbonate platform (Jahrum/Shahbazan carbonates) in the southern part of the basin (Fig. 12b) during Eocene-Oligocene times, suggests that the NW-SE-trending basement faults were presumably reactivated by a far-field stress resulting from Arabia-Eurasia continental collision. During Early Miocene (Aquitanian) times, significant changes in the basin architecture and facies distribution occurred. At this time, early reactivation of basement faults (e.g., MFF, DEF) led to forced-folding (Fig. 16) which at least partly controlled the formation of the Kalhur evaporitic intrabasin which is located between the Mountain Front Fault (MFF) and the Dezful Embayment Fault (DEF).

The present study clearly emphasizes the overall importance of basement tectonics in the early structural evolution of the foreland of the Zagros collisional orogen. We propose a sequence of deformation in which the basement is involved early in the shortening, i.e., through Oligocene-Lower Miocene localized inversion of pre-existing basement faults in response to early intraplate stress build-up. During this time the cover was loaded by a N040°–050° compression, but did not suffer any important deformation, ex-

cept forced-folds or large-scale flexures above reactivated basement faults which induced local extensional states of stress. During the Mio-Pliocene paroxysm of deformation, the cover was involved in the orogenic wedge, while generalized involvement of the basement in shortening gave birth to the main morphotectonical regions in the Zagros fold belt (Figs. 16 and 1b).

6.3 Geodynamic Implications

The group of NW-SE-trending fractures are thought to have formed during the early stage of forced-folding above the main Zagros basement faults, and within the Asmari Formation during its deposition. Taking into account the earliest N050° regional joint set (Ahmadhadi et al., submitted) and also the second group which formed above forced folds, it is suggested that collisional stress build-up could have started, at least, as early as the Aquitanian (~23 Ma) and maybe earlier (Oligocene).

The first stage of basement fault reactivation may have started as early as the Oligocene, during the deposition of the Asmari Formation. This early basement fault reactivation may, together with the regional early N050° joint set, mark the onset of compressional stress build-up related to the Arabia-Central Iran continental collision (Fig. 16a). Then, amplification of basement fault movements during the Upper Oligocene to Lower Miocene (Chattian- Early Aquitanian, ~ 27–23 Ma) led to different isolated intra-basins in the studied area and initiated a series of fractures, parallel to general trends of these intra-basins and basement faults (Fig. 16b). In agreement with Allen et al. (2004) and Agard et al. (2005), we propose that 22–30 Ma (Chattian-Aquitanian) is a likely minimum age for initial plate collision, and that partitioning of the N-S Arabia-Eurasia convergence into belt-perpendicular shortening and belt-parallel strike-slip faulting in the NW Zagros happened long before what has been estimated for the initiation of the MRF.

Conclusions

The majority of fracture sets observed in the Asmari Fm in the Central Zagros are not compatible with conventional fold/fracture models. We proposed herein that they have been initiated before the main Mio-Pliocene shortening episode. Intra-basin architecture and facies changes during Lower Tertiary times suggest that large-scale forced-folds or flexures above compressionally reactivated basement faults controlled the Asmari sub-basins. The timing of reactivation of the main basement faults was estimated early Aquitanian in age, possibly before (late Oligocene). The non-com-

patibility between fracture populations in the Central Zagros folds and classical fold-related fracture models arises from the differences between the geometry and orientation of early large-scale and likely gentle forced-folds above reactivated basement faults and the superimposed Mio-Pliocene smaller-scale folds. This study emphasizes that early basement block movements may have an impact on fracture development in the cover rocks. However, the transmission of orogenic stress through the fractured crystalline basement of the Zagros was probably heterogeneous and complex, so the deformation front likely propagated in an irregular fashion through the basement and the cover leading to a complex chronology of fracture development in the cover. Such a complexity should be taken into account in further studies of folded and fractured reservoirs.

Finally, from a geodynamic point of view, it comes from our study that partitioning of the Arabia-Eurasia N-S-trending convergence and initiation of belt-parallel strike-slip movements (as currently along the Main Recent Fault) probably occurred as early as 22–30 Ma (Chattian-Aquitanian), which is likely to be the minimum age for the onset of Arabia-Eurasia plate collision in the Central Zagros.

Acknowledgement

References

Abdollahie, F. I., A. Braathen, M. Mokhtari and S. A. Alavi (2006), Interaction of the Zagros Fold-Thrust Belt and the Arabian-type, deep-seated folds in the Abadan Plain and the 4 Dezful Embayment,SW Iran, Petroleum Geoscience, 12(4), 347–362.

Agard, P., Omrani, J., Jolivet, L., and Mouthereau F., 2005, Convergence history across Zagros (Iran): constraints from collisional and earlier deformation, Int. J. Earth Sc., 94, 401–419, doi 10.1007/S00531-005-0481-4

Ahmadhadi, F., Daniel, J.M., Lacombe, O. and Mouthereau F., 2005, Fracture development within Asmari carbonates in the Central Zagros fold belt, SW Iran: An insight into the

role of basement faults on Lower Tertiary facies changes and possible forced-folding. Vein Earth Science Meeting SGF-SGE, Thrust belts and foreland basins, O. Lacombe, J. Lavé and F. Roure convenors, Rueil-Malmaison, Décembre 2005, Abstract volume, p 17–21

Ahmadhadi F., 2006, Fracture development in the Asmari Fm., SW Iran: typology, timing and relation to folding and Arabia-Eurasia collisional tectonics ; Insights from field studies and mechanical models. Unpublished PhD thesis, Université P. et M. Curie, Paris, France, 300p

Ahmadhadi F., Daniel J .M. and Lacombe O., Evidence for pre-folding joint development in the Oligo-Miocene Asmari Formation in the Central Zagros Fold Belt, Iran. Submitted

Alavi, M., 1980, Tectonostratigraphical evolution of the Zagro-sides of Iran, Geology, vol.8, p.144–149.

Alavi, M., 1994, Tectonics of the Zagros Orogenic belt of Iran: new data and interpretations. Tectonophysics, 229, 211–238.

Alavi, M., 2004, Regional stratigraphy of the Zagros fold-thrust belt of Iran and its proforeland evolution, American Journal of Science, vol.304, p.1–20.

Allen, M., Jackson, J., and Walker, R., 2004, Late Cenozoic reorganization of the Arabian-Eurasian collision and comparison of short-term and long-term deformation rates, Tectonics, vol. 23, TC2008, doi:10.1029/2003TC001530

Ameen, M. S., 1988, Folding of layered cover due to dip-slip basement faulting, Ph.D. thesis, University of London.

Ameen, M. S., 1990, Macrofaulting in the Purbeck-Isle of Wight monocline, proceeding of the geologists' Association, 101, 31–46.

Baker C., Jackson, J., and Priestley, K., 1993, Earthquakes on the Kazerun line in the Zagros Mountains of Iran: strike-slip faulting within a fold-thrust belt, Geophys. J. Int., vol.115, p.41–61.

Berberian, M., and Tchalenko, J., 1976a, Earthquakes of the southern Zagros (Iran): Bushehr region, Geol. Surv. Iran, vol.39, p.343–370.

Berberian, M., 1981, Active faulting and tectonics of Iran, In: H. K. Gupta and F. M. Delaney (Editors), Zagros-Hindu Kush-Himalaya Geodynamic evolution, Am. Geophys. Union, Geodyn. Ser., vol.3, p.33–69.

Berberian, M., 1995, Master blind thrust faults hidden under the Zagros folds: active basement tectonics and surface morphotectonics, Tectonophysics, vol. 241, p.193–224.

Berberian, M. and King, G.C.P., 1981, Paleogeography and tectonic evolution of Iran, Canadian Journal of Earth Science, vol. 18, 210–265.

Berberian, F., Muir, I. D., Pankhurst, R. J. and Berberian, M., 1982, Late Cretaceous and early Miocene Andean-type plutonic activity in northern Makran and Central Iran, J. Geol. Soc. London, 139(5): 605–614.

Beydoun, Z. R., 1991, Arabian plate hydrocarbon, Geology and Potential – A Plate tectonic approach, AAPG, Studies in Geology 33, 77 p.

Blanc, E. J. P., M. B. Allen, S. Inger, and H. Hassani, 2003, Structural styles in the Zagros simple folded zone, Iran. J. Geol Soc. London, 160, 401–412.

Brown D., Alvarez-Marron J., Perez-Estaun A. Puchkov V. and Ayala C., 1999, Basement influence on foreland thrust and fold belt development : an example from the southern Urals, Tectonophysics, 308, 459–472

Butler R.W.H., Holdsworth R.E. and Lloyd G.E., 1997, The role of basement reactivation in continental deformation. J. Geol. Soc. London, 154, 69–72

Colman-Sadd, S. P., 1978, Fold Development in Zagros Simply Folded Belt, Southwest Iran, The American Association of Petroleum Geologists Bulletin, V. 62, No.6, pp. 984–1003.

Cooper, M., 1992, The analysis of fracture systems in subsurface thrust structures from the foothills of the Canadian Rockies, in McClay, K. R., ed., Thrust tectonics, London, Chapman and Hall, p.391–405.

Cooper M.A. and Williams G.D., 1989, Inversion tectonics, Geol. Soc. London Spec. Publ., 44, 375pp

Cosgrove, J. W., and Ameen, M. S. (eds.), 2000, Forced Folds and Fractures. Geological Society, London, Special Publications, 169, © The Geological Society of London.

Cristallini E.O. and Ramos V.A., 2000, Thick-skinned and thin-skinned thrusting in the La Ramada fold and thrust belt : crustal evolution of the High Andes of San Juan, Argentina (32°SL), Tectonophysics, 317, 205–235

Dechesne R.G. and Mountjoy E.W., 1992, Multiple thrust detachment at deep levels of the southern Canadian Rocky Mountain Main Range, Alberta and British Columbia, in Mitra S. and Fisher G.W.eds; Structural Geology of Fold and Thrust belts, John Hopkins University Press, 225–238

De Sitter, L. U., 1956: Structural geology, New York, McGraw-Hill, 552p.

Dewey J.F., Hempton M.R., Kidd W.S.F., Saroglu F. and Sengor A.M.C., 1986, Shortening of continental lithosphere : the neotectonics of eastern Anatolia - a young collision zone. In Coward M.P. and Ries A.C. eds, Collision Tectonics, Geol. Soc. London Spec. Publ., 19, 3–36

Etheridge M.A., 1986, On the reactivation of extensional fault systems. Royal Soc. of London Philosophical Transactions, ser.A., 317, 179–194

Edgell, H. S., 1992, Basement tectonic of Saudi Arabia as related to oil field structures, In: Rickard et al. (eds.), Basement tectonic 9, Kluwer Academic Publishers, Dordrecht, p. 169–193.

Falcon, N.L., 1961, Major earth-flexing in the Zagros Mountains of southwest Iran., J. Geol. Soc. London, 117(4): 468: 367–376.

Falcon, N., 1967, The geology of the north-east margin of the Arabian basement shield, Adv. Sci., v.24, p.31–42.

Falcon, N.L., 1969, Problems of relationship between surface structures and deep displacements illustrated by the Zagros range, In: Time and place in orogeny: Geol. Soc. London, Spec. Publ. vol.3, p.9–22.

Falcon, N. L., 1974, Southern Iran: Zagros mountains, In: A. M. Spencer (Editor), Mesozoic-Cenozoic Organic belts, data for orogenic studies, Geol. Soc. London, Spec. Pub. 4, 199–211.

Gholipour, A. M., 1998, Patterns and Structural Positions of Productive Fractures in the Asmari Reservoirs, Southwest Iran, The Journal of Canadian Petroleum Technology, vol. 37, no. 1, 44–50.

Glen R.A., 1985, Basement control on the deformation of cover basins : an example from the Cobar district in the Lachlan fold belt, Australia, Journal of Structural Geology, 7, 301–315

Hancock, P. L., 1985, Brittle microtectonics: principles and practice, Journal of Structural Geology, 7, 437–457.

Harris, J. F., Taylor, G. L., and Walper, J.L., 1960, Relation of deformational fractures in sedimentary rocks to regional and local structures, American Association of Petroleum Geologist Bulletin, v.44, p.1853–1873.

Haynes, S. J., and McQuillan, H., 1974, Evolution of the Zagros suture zone, southern Iran, Geological Society of America Bulletin, vol.85, p.739–744.

Hempton, M. R., 1987, Constraints on Arabian plate motion and extensional history of the Red Sea, Tectonics, 6, 687–705.

Hessami, K., Koyi, H.A., Talbot, C.J., Tabasi, H., and Shabanian, E., 2001, Progressive unconformities within an evolving foreland fold-thrust belt, Zagros Mountains: J. the Geol. Soc. London, v. 158, p. 969–981.

Homke, S., J. Verges, M. Garces, H. Emami and R. Karpuz, 2004, Magnetostratigraphy of Miocene-Pliocene Zagros foreland deposits in the front of the Push-e Kush Arc (Lurestan Province, Iran), Earth and Planetary Science Letters, 225(3–4), p. 397–410.

Hooper, R. J., Baron, I. R., Agah, S., Hatcher, R. D., Jr., 1994, The Cenomanian to recent development of the Southern Tethyan Margin in Iran, in: M.I. Al-Husseini (Ed.), Middle East Petroleum Geosciences GEO, vol. II, pp. 505–516.

Huber, H., 1977, Geological map of Iran with explanatory note, Natl. Iran. Oil Co. Explor. Prod. Affairs, Tehran.

Jackson, J. A., 1980, Reactivation of basement faults and crustal shortening in orogenic belts, Nature, vol.283, p.343–346.

Jackson, J. A. and McKenzie, D., 1984, Active tectonics of the Alpine-Himalayan Belt between western Turkey and Pakistan, Geophys. J. R. astr. Soc., vol.77, p.185–264.

Jackson, J. A., Fitch, Ti., and McKenzie, D. P., 1981, Active thrusting and evolution of the Zagros fold belt. In: K. McClay and N. Price Editors, Geol. Soc. London, Spec. Publ., 9: 371–379.

James, G. S., and Wynd, J. G., 1965, Stratigraphic nomenclature of Iranian Oil Consortium Agreement area, American Association of Petroleum Geologists Bulletin, 49(12), 2182–2245.

Lacombe O. and Mouthereau F., 1999. Qu'est-ce que le front des orogènes ? l'exemple de l'orogène pyrénéen. C. R. Acad. Sc., t. 329 , II, 12, 889–896

Lacombe O., Mouthereau F., Angelier J., Chu H.T. and Lee J.C., 2003, Frontal belt curvature and oblique ramp development at an obliquely collided irregular margin : geometry and kinematics of the NW Taiwan fold-thrust belt. Tectonics, 22, 3, 1025,10.1029/2002TC001436

Lacombe O. and Mouthereau F., 2002. Basement-involved shortening and deep detachment tectonics in forelands of orogens : insights from recent collision belts (Taiwan, western Alps, Pyrenees). Tectonics, 21, 4, 10.1029/2001TC901018

Lacombe O., Mouthereau F., Kargar S. and Meyer B., 2006, Late Cenozoic and modern stress fields in the western Fars (Iran) :implications for the tectonic and kinematic evolution of Central Zagros. Tectonics, 25, TC1003, doi:10.1029/ 2005TC001831

Lees, G.M., 1950, Some structural and stratigraphical aspects of the oil fields of the Middle East: 18th Int. Geol. Cong., Great Britain, Proc., pt. 6, p. 26–33.

Letouzey J., 1990, Fault reactivation, inversion and fold-thrust belt. In Petroleum and Tectonics in Mobile belts, J. Letouzey ed., Technip, Paris, 101–128

Letouzey J. and Sherkati S., 2004, Salt movement, tectonic events, and structural style in the Central Zagros Dold and Thrust Belt (Iran), In "Salt sediments interactions and hydrocarbon prospectivity", 24th ann. GCSSEP Foundation, Bob F. Perkins research Conf.

McQuarrie, N., 2004, Crustal scale geometry of the Zagros fold-thrust belt, Iran: Journal of Structural Geology, p.519–535.

Mann, C. D., and Vita-Finzi, C., 1988, Holocene serial folding in the Zagros, in: M. Audley-Charles, A. Hallam (Eds.), Gondwana and Tethys, Geol. Soc. London, Spec. Publ., vol. 37, pp. 51–59.

Marshak S., Karlstrom K. and Timmons J.M., 2000, Inversion of Proterozoic extensional faults : an explanation for the pattern of Laramide and Ancestral Rockies intracratonic deformation, United States, Geology, 28, 8, 735–738

Mitra S. and Mount V.S., 1998, Foreland basement-involved structures. American Association of Petroleum Geologists Bulletin, 82, 70–109

McQuarrie, N., Stock J.M., Verdel C. and Wernicke B.P., 2003, Cenozoic evolution of Neotethys and implications for the causes of plate motions; Geophys. Res. Letters, 30, 20, 2036, doi:10.1029/2003GL017992

McQuarrie, N., 2004, Crustal scale geometry of the Zagros fold-thrust belt, Iran, Journal of Structural Geology, 26, 519–535.

McQuillan, H., 1973, Small-Scale Fracture Density in Asmari Formation of Southwest Iran and its Relation to Bed Thickness and Structural Setting, American Association of Petroleum Geologists Bulletin, vol. 57, no. 12, 2367–2385.

McQuillan, H., 1974, Fracture Patterns on Kuh-e Asmari Anticline, Southwest Iran, American Association of Petroleum Geologists Bulletin, vol. 58, no. 2, 236–246.

McQuillan, H., 1985, Carbonate Petroleum Reservoirs, (Roehl & Choquette), Springer-Verlag, New York, Inc.

Morris P., 1977, Basement structure as suggested by aeromagnetic surveys in southwest ran, paper presented at Second Geological Symposium of Iran, Iranian Pet. Inst., Oil Serv. Co. Iran, Tehran

Motiei, H., 1993, Stratigraphy of the Zagros, Geological Society of Iran Publications (in Persian).

Mouthereau F., Deffontaines B., Lacombe O. and Angelier J., 2002. Variations along the strike of the Taiwan thrust belt : Basement control on structural style, wedge geometry and kinematics. In Byrne T.B., and Liu C.-S., eds, Geology and Geophysics of an Arc-Continent Collision, Taiwan, Republic of China, Boulder, Colorado, Geol. Soc. Am. Spec. Pap., 358, chapter 3, 35–58

Mouthereau F., Lacombe O. and Meyer B., 2006, The Zagros fold belt (Fars, Iran): constraints from topography and critical wedge modelling, Geophys. J. Int., 165(1), 336–356, doi: 10.1111/j.1365–246X.2006.02855.x

Mouthereau F., Lacombe O., Tensi J., Bellahsen N., Kargar S., Amrouch K., Mechanical constraints on the development of the Zagros fold belt (Fars), this issue.

Narr W. and Suppe J., 1994, Kinematics of basement-involved compressive structures, American Journal of Science, 294, 802–860

Nelson, R.A., 2001, Geological analysis of naturally fractured Reservoirs, Second Edition, Gulf Professional Publishing.

Ni, J., and M. Barazangi, 1986, Seismotectonics of the Zagros continental collision zone and a comparison with the Himalayas, Journal of Geophysical Research, vol. 91, part B8, 8205–8218.

Nowroozi, A., 1972, Focal mechanism of earthquakes in Iran, Turkey, West Pakistan and Afghanistan and plate tectonics of the Middle East, Bull. Seismol. Soc. Am., vol.62, no.3, p.823–850.

Oveisi B., Lavé J. and Van der Beek P., Active folding and deformation rate at the central Zagros front (Iran), this issue

Price, N. J., 1966, Fault and joint development in brittle and semi-brittle rock, New York, Pergamon Press, 176p.

Price, N. J., and J. W. Cosgrove, 1990, Analysis of geological fractures, Cambridge University Press, Cambridge.

Price, R. A., 1967, The tectonic significance of mesoscopic sub-fabrics in the Southern Rocky Mountains of Alberta and British Columbia, Canadian Journal of Earth Sciences, v.4, p.39–70.

Ricou, L. E., 1970, Comments on radiolarites and ophiolite nappes in the Iranian Zagros mountains, Geological Magazine, v.107, p.479–480.

Robertson, A. H. F., 2000, Mesozoic-Tertiary tectonicsedimentary evolution of a south Tethyan oceanic basin and its margins in southern Turkey, in Tectonics and Magmatism in Turkey and the Surrounding Area, edited by E. Bozkurt, J. A. Winchester, and J. D. A. Piper, Geol. Soc. London, Spec. Publ., 173, 97–138.

Roure F., Howell D.G., Guellec S. and Casero P.,1990. Shallow structures induced by deep-seated thrusting. Petroleum and Tectonics in Mobile belts, J. Letouzey ed., Technip, Paris, 15–30

Sattarzadeh, Y., J. W. Cosgrove, and C. Vita-Finzi, 2000, The interplay of faulting and folding during the evolution of the Zagros deformation belt, In: Cosgrove, J. W., & Ameen, M. S., (eds.), Forced folds and fractures, Geol. Soc. London, Spec. Publ., 169, 187–196.

Sherkati, S., and Letouzey, J., 2004, Variation of structural style and basin evolution in the central Zagros (Izeh zone and Dezful Embaymy), Iran: Marine and Petroleum Geology, v. 21, p. 535–554.

Sherkati, S., Letouzey, J., and Frizon de Lamotte, D., 2006, The central Zagros fold-thrust belt (Iran): New insights from seismic data, field observation and sandbox modelling, Tectonics, 25, TC4007, doi:10.1029/2004TC001766

Sibson R.H., 1993, Load-strengthening vs load-weakening faults, Journal of Structural Geology, 15, 123–128

Stearns, D. W., 1968, Certain aspects of fracture in naturally deformed rocks, in Riecker, R. E., ed., NSF advanced science seminar in rock mechanics, Bedford, Massachusetts, Air Force Cambridge Research Laboratory, p.97–116.

Stearns, D. W.,1978, Faulting and forced folding in the rocky mountains foreland, Geological Society of America Bulletin, 151, 1–37.

Stearns, D. W., and M. Friedman, 1972, Reservoirs in fractured rock, AAPG Memoir 16, 82–100.

Stewarts, S. A., and Wynn, T. J., 2000, Mapping spatial variation in rock properties in relationship to scale-dependent structure using spectral curvature, Geology, v.28, p.691–694.

Stöklin, J., 1968, Structural history and tectonics of Iran; a review, American Association of Petroleum Geologists Bulletin, vol.59, no.7, p.869–872.

Stoneley, R., 1981, The geology of the Kuh-e Dalneshin area of southern Iran, and its bearing on the evolution of southern Tethys, J. Geol. Soc. London, vol.138, p.509–526.

Talebian, T., and J. Jackson, 2002, Offset on the Main Recent Fault of NW Iran and implications for the late Cenozoic tectonics of the Arabia-Eurasia collision zone, Geophys. J. Int. v. 150, p. 422–439.

Talebian, M., and Jackson, J. A., 2004, A reappraisal of earthquake focal mechanism and active shortening in the Zagros mountains of Iran, Geophys. J. Int., vol.156, p.506–526.

Tapponnier P., Peltzer G. and Armijo R., 1986. On the mechanics of the collision between India and Asia. Geol. Soc. Spec. Publ. London, 19, 115–157

Tatar, M., Hatzfeld, D., and Ghafory-Ashtiany, M., 2004, Tectonics of the Central Zagros (Iran) deduced from microearthquake seimicity, Geophy. J. Int., vol.156, p.255–266.

Tatar, M., Hatzfeld, D., Martinod, J., Walpersdorf, A., Ghafori-Ashtiany, M. and Chéry, J., 2002, The present day deformation of the Central Zagros (Iran), Geophys. Res. Lett., vol.29, 33-1 to 33-4, doi: 10.1029/2002GL015159.

Vernant, P., F. Nilforoushan, D. Hatzfeld, M. R. Abbassi, C. Vigny, F. Masson, H. Nankali, J. Martinod, A. Ashtiani, R. Bayer, F. Tavakoli, and J. Chéry, 2004, Present day crustal deformation and plate kinematics in the Middle East constrained by GPS measurements in Iran and northern Oman, Geophys. J. Int., v. 157, p. 381–398.

Vita-Finzi, C., 2001, Neotectonics at the Arabian plate margins, Journal of Structural Geology 23, 521–530.

Wells, A. J., 1969, The crush zone of the Iranian Zagros mountains, and its implications, Geological magazine, v.106, p.358–394.

Wennberg, O.P., Svånå, T., Azizzadeh, M., Aqrawi, A. M. M., Brockbank, P., Lyslo, K. B. and Ogilvie, S., 2006, Fracture intensity vs. mechanical stratigraphy in platform topcarbonates: the Aquitanian of the Asmari Formation, Khaviz Anticline, Zagros, SW Iran, Petroleum Geoscience, 12, p. 235–245

Wiltschko. D and Eastman D., 1983, Role of basement warps and faults in localizing thrust fault ramps, Geol. Soc. Am. Mem., 158, 177–190

Winslow, M.A., 1981, Mechanisms for basement shortening in the Andean foreland fold belt of southern South America, Thrust and Nappe Tectonics, J. Geol. Soc. London, 513–528

Yilmaz, Y., 1993, New evidence and model on the evolution of the southeast Anatolian orogen, Geological Society of America Bulletin, 105, 251 – 271.

Ziegler P.A., 1987 Late Cretaceous and Cenozoic intraplate compressional deformations in the Alpine foreland - a geodynamic model, Tectonophysics, 137, 389–420

Ziegler P.A., Cloetingh S. and van Wees J.D., 1995, Dynamics of intraplate compressional deformation : the Alpine foreland and other examples.Tectonophysics, 252, 7–59

Ziegler P.A., Van Wees J.D. and Cloetingh S., 1998, Mechanical controls on collision-related compressional intraplate deformation, Tectonophysics, 300, 103–129

Evolution of Maturity in Northern Fars and in the Izeh Zone (Iranian Zagros) and Link with Hydrocarbon Prospectivity

Jean Luc Rudkiewicz · Shahram Sherkati · Jean Letouzey

Abstract Paleozoic and Mesozoic reservoirs (Permo-Triassic, Neocomian and Cenomanian carbonates) could be considered as potential targets for hydrocarbon exploration in Northern Fars and in the Izeh Zone of Central Zagros. A regional study has been carried out to reconstruct the history of subsidence, temperature and maturity of source-rocks through geological times in that area. The relationship between the structural evolution of the fold-and-thrust belt and the thermal history of the source-rocks is recognized as a critical parameter for hydrocarbon exploration, together with the extension of the source-rocks, which might be present at various stratigraphic levels along regional transects crossing the study area.

This study is based on integration of field work, seismic profile interpretation and well data. Coupled structural, thermal and geochemical modelling was undertaken to handle compositional generation and expulsion.

Probable Early Paleozoic source-rock matured everywhere in the Izeh Zone in Jurassic time and expulsion of liquid hydrocarbon mostly occurred during the Cretaceous period, hence long before Zagros folding. It is suggested that the presence of paleo-structures and of Triassic evaporites, acting as top seal, are among the main factors for a successful Permo-Triassic gas exploration in the study area. Generation and expulsion behaviour of Jurassic and Albian source-rocks considerably varies within the Izeh Zone. Thickness of the Late Cretaceous–Eocene sediments and the first vertical movements at regional scale in the inner part of the belt considerably influenced the maturation expulsion, migration and entrapment of petroleum from these source-rocks. An accurate timing of structural formation and the source-rock distribution are therefore crucial factors for trap assessment in Mesozoic reservoirs.

1   Introduction

1.1 Objective

The Zagros fold belt and its foreland are one of the most prolific petroleum provinces in the world. Among the hydrocarbon provinces of Iran, the Dezful Embayment (Fig. 1) has been the most studied, from a stratigraphic point of view (James and Wynd, 1965; Setudehnia, 1978; Motiei, 1995), structural style (Falcon, 1967 and 1974; Colman-Sadd, 1978; Sherkati and Letouzey, 2004) and petroleum system analysis (Murris, 1980; Bordenave and Burwood, 1990 and 1995; Bordenave and Huc, 1995). However, when moving away from the Dezful Embayment, where the main hydrocarbon discoveries are located (Fig. 2), the information is more limited. This information includes, however, extensive field work carried out by OSCO's geologists in the 60s and 70s, and the result of a few wells, among which we can cite Kuh-e Bangestan, Kuh-e Rig, Shurom, Dudrou and Mokhtar. Therefore, this paper intends to discuss the timing of maturity and source-rock expulsion in Northern Fars and in the Izeh Zone of Central Zagros (Fig. 1).

Permo-Triassic carbonates (Middle to Late Permian Dalan and Early Triassic Kangan Fms.) and Mesozoic limestone reservoirs (Jurassic Surmeh Fm., Neocomian Khami Group and Cenomanian Sarvak Fm.) are potential targets for hydrocarbon exploration in Northern Fars and in the Izeh Zone.

The prospectivity assessment of the Izeh Zone and of Northern Fars depends upon the distribution of generating and expelling source-rocks, the existence of reservoir and cap rocks and the existence of traps at the time of oil and gas expulsion. Our assessment will not discuss in detail the occurrence of source-rock and their facies distribution. Our main aim is to define the areas where burial and temperature history might have made possible generation and expulsion. The work is based upon structural cross-sections in Northern Fars and synthetic wells located in the Izeh Zone (Fig. 1). Regional structural and geochemical modelling was undertaken to reconstruct the history of temperature and maturity of source-rocks through geological times. Through modelling, most constraints issued from geological history could be taken into account (Tissot and Welte, 1984; Burrus et al., 1991; Rudkiewicz et al., 2000).

The present study is based on the integration of field work, seismic profile interpretation and well data. We will first review the various petroleum systems in the study area and then we will describe the modelling techniques used and the implications of temperature,
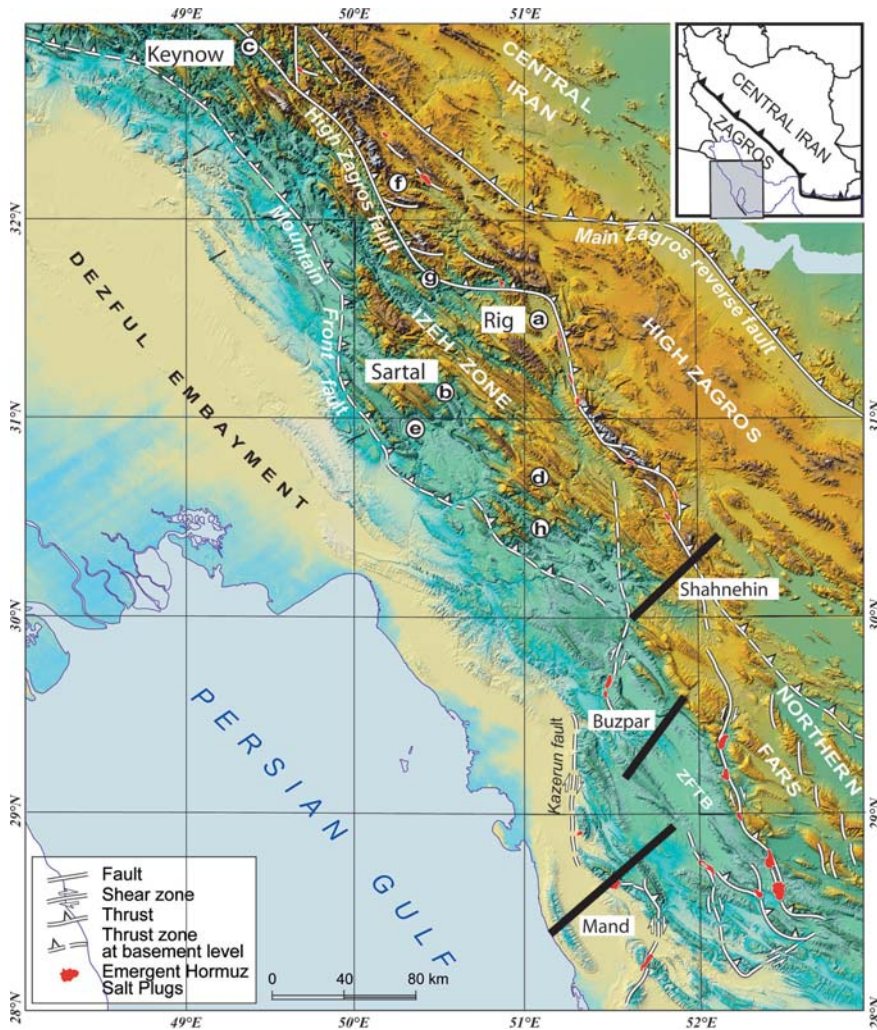
Fig. 1. Location map of the Dezful Embayment, the Izeh Zone, Northern Fars and the High Zagros area. The *bold black* lines in Northern Fars represent the location of 2D modelling transects, whereas the circles named "*a*" to "*h*" represent synthetic 1D wells located in selected deepest preserved synclines in the Izeh Zone. Altitude is colour coded from SRTM data

maturity and expulsion modelling on the prospectivity of the area. The commercial software Genex (Beicip-Franlab, 1995) and the IFP in-house tool Thrustpack (Sassi, 2005) were used to handle temperature, maturity and compositional generation and expulsion modelling through geological times.

1.2 Rapid Review of the Regional Geology

Numerous studies have reviewed the structural evolution of the Central Zagros fold belt (Ricou, 1974; Hessami et al., 2001; Sherkati, 2004). In short, the Zagros is a collisional belt between the Iranian block and the Arabian shield, whose convergence started at the beginning of the Late Cretaceous (Ricou, 1974; Berberian and King, 1981), accelerated during the Late Miocene and Pliocene (Stöcklin, 1968) and continued up to the present day (Glennie, 2000; Sella et al., 2002; Bordenave and Hegre, 2005). The converging plates

deformed paleozoic sediments, mesozoic rocks deposited during the past tethyan evolution (Dercourt et al., 1993) and synfolding Cenozoic sediments (Homke et al., 2004; Verges et al., 2005).

Within the structural division of Zagros (Stöcklin, 1974; Alavi, 1994), the area under study is limited from the foreland (Dezful Embayment) by the Mountain Front Thrust Fault to the SW and towards the hinterland by the High Zagros Fault to the NE (Fig. 1). The Izeh Zone is located NW of the transverse Kazerun fault. The part of Northern Fars studied in this paper is located SE of the Kazerun fault (Fig. 1). Within this area, the structural complexity is essentially related to the interplay between subsidence, faulting, folding, sedimentation and erosion processes. This is a common feature of many foreland and fold-and-thrust belts orogens (e.g. Roure et al., 1993). In addition, the structural complexity of the Zagros has been recognised as resulting from the mechanical behaviour of a sedimentary sequence where several detachment lev-

Fig. 2. Location map oil and gas fields in the Central Zagros (NIOC, 1993). Oil fields are represented in *dark blue* and gas fields in *yellow*
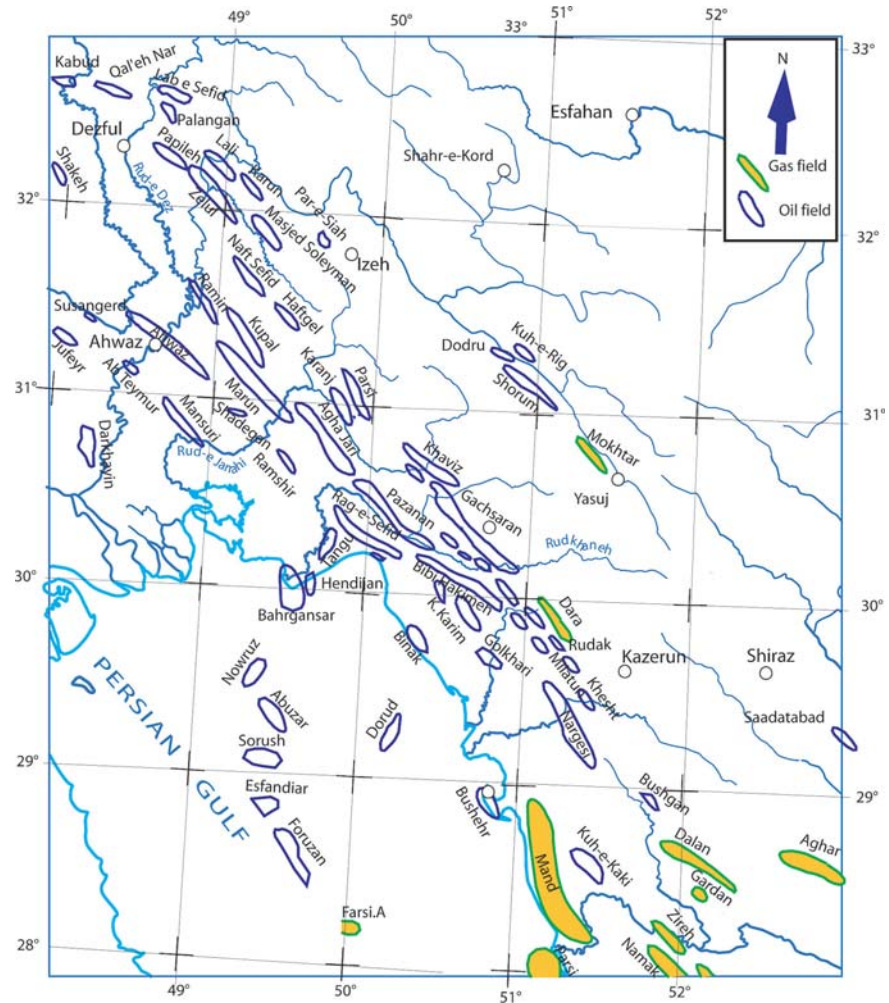
els, locally changing, are at work (O'Brien, 1950; Mc Quillan, 1974; Favre, 1975; Collman-Sadd, 1978; Motiei, 1995; Sherkati, 2004). Within the Izeh Zone and Northern Fars, the main detachment levels are located in the Late Proterozoic/Lower Paleozoic (Hormuz salt), in the Triassic (where the evaporitic Dashtak Fm. is present), in Mesozoic (where Kazhdumi or Pabdeh Fms. are in shaly organic-rich facies) and in Cenozoic (Gachsaran Fm.) (Sherkati and Letouzey, 2004; Bosold et al., 2005).

1.3 Petroleum Systems

Two main petroleum systems exist in the Zagros Fold belt, a Paleozoic Petroleum System (Bordenave, 2002a) and the Middle Cretaceous to Early Miocene Petroleum System (Bordenave, 2002b). They are linked to the existence of effective source-rocks and effective top seals. Nevertheless, because of stratigraphic complexity, lateral variations induce changes from the well-known situation in the Dezful Embayment towards the Izeh Zone and Northern Fars (Fig. 2).

The Paleozoic sourced system caused the accumulation of huge amounts of gas in the Permian Deh Ram Group. These accumulations were conditioned to the existence of thick enough evaporites in the Triassic Dashtak Fm. to form an efficient cap rock. The source for hydrocarbons in the Permian carbonates is usually attributed to the Llandoverian shales, because of its occurrence 600 km away from Izeh Zone. 150 km north of Bandar Abbas, at Kuh-e Gahkum and at Kuh-e Faraghan, Silurian shales are 40 m thick, having TOC values up to 4.1% although being over mature (Bordenave and Burwood, 1990). This level extends from the Arabian Platform where it forms the base of the Qusaiba Fm. (Mc Gillivray and Husseini, 1982) to Northern Africa (Chaouche, 1992; Lünning et al., 2000).

However, in the paleozoic outcrops at the base of the High Zagros Thrust in the Izeh Zone, no Silurian sediments were found, because this interval was eroded, as the result of the Hercynian orogeny. It is known
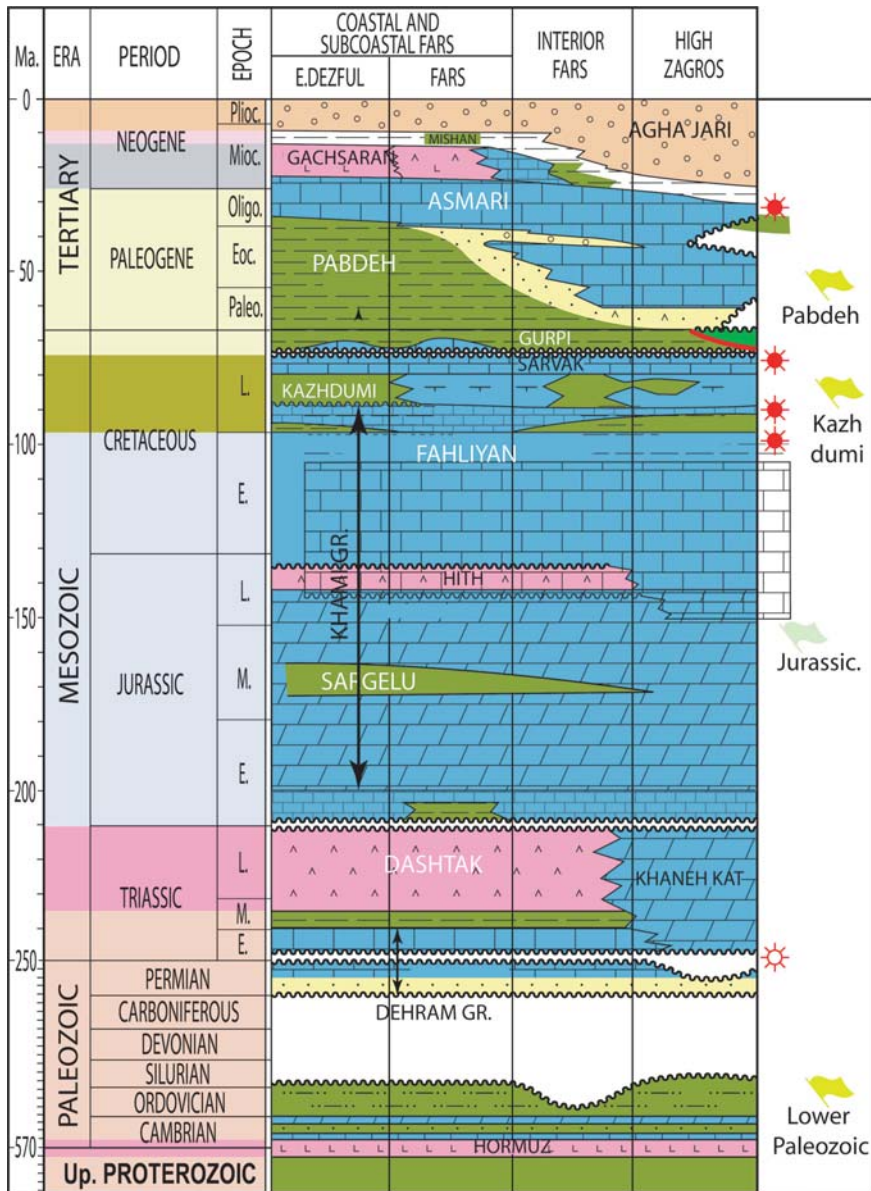
Fig. 3. Simplified stratigraphic chart, indicating the petroleum systems. Source-rocks are indicated with *green* shadowing, reservoirs with *blue* shadowing and seals with *pink* shadowing (modified after Bordenave and Burwood, 1995)

from the description of the facies variation of the Dalan Fm. that a well-individualized high existed north of Kuh-e Dena. This high was associated to the deposition of siliciclastics originated from the Late Proterozoic to Early Cambrian Mila Fm., and to the development of reefoid facies in the Lower part of the Dalan Fm. (Szabo and Kheradpir, 1978). Moreover, the high was marked by the deposition of stacked paleo-soils time-equivalent of the deposition of the Nar Member of the Dalan Fm. in Fars (Insalaco et al., 2006).

The Kuh-e Surmeh outcrop in Central Fars and several deep wells drilled in Fars and offshore showed that this high extended to the south, separating an eastern Silurian basin extending from Kuh-e Gahkum to

Oman from a western basin assumed to extend from Saudi Arabia to the Dezful Embayment (Bordenave, 2002a).

In addition to the Llandoverian possible source-rocks, we have to mention the existence of dark shale attributed to the Cambrian lacustrine to deltaic Mila Fm.. This shale sampled in the Izeh Zone near Kuh-e-Sefid (N 32°58, E49°37), showed TOC values up to 11% and Tmax values in the range of 450°C.

From these considerations, it is probable that the Llandoverian source-rocks do not exist in the part of the study area located in Northern Fars, while they are more likely to exist in the Izeh Zone. Not being sure of the distribution of the Llandoverian shales, we will use

the term "Early Paleozoic shale" for modelling purpose, whatever its stratigraphic age may be.

The second petroleum system is related to the Tethyan history of the Zagros. During the Mesozoic period, the Izeh Zone and Northern Fars underwent an episode of continuous deposition and more than 3 km of sediments accumulated on the margin of the Arabian plate. Several major source-rock layers were deposited in depressions when euxinic conditions prevailed as the result of water layering. Their distribution is reasonably established (Bordenave and Burwood, 1990 and 1995; Bordenave 2002b). Source-rocks were described in the Middle Jurassic (Sargelu Fm.), Valanginian (base of the Garau Fm.), Albian (Kazhdumi Fm.), and Middle Eocene (part of the Pabdeh Fm.). In addition, prolific Hanifa-Tuwaiq Mountain source-rocks extended during the Late Jurassic in Saudi Arabia and in the Arabo-Persian Gulf (Carrigan et al., 1994).

Jurassic and Early Cretaceous source-rocks accumulated in the Mesopotamian depression (Murris, 1980), and their facies changed abruptly toward the NE along a well-marked shelf edge into high-energy platform facies (Murris, 1980; Bordenave and Huc, 1995). The shelf edge passed between Kuh-e Mungasht and Kuh-e Bangestan. At Kuh-e Bangestan-1, nearly 300 m of Sargelu source-rocks showed TOC values averaging 4% with Tmax values around 442°C, while a few hundred meters of Garau facies were described at the base of the Fahliyan Fm.. It is assumed from this information that the Sargelu and the Garau source-rocks exist in the SW part of the Izeh Zone, but are replaced by shallow carbonates in its NE part and in Northern Fars.

Two source-rock layers, the Kazhdumi and the Pabdeh are assumed to charge the prolific fields of the Dezful embayment (Bordenave and Burwood, 1990 and 1995). The Kazhdumi source-rocks were deposited in a silled intrashelf depression that corresponded almost exactly to the present-day Dezful Embayment. However, the organic-rich Kazhdumi facies was assumed to extend eastwards into the Kuh-e Rig to Shiraz area (Bordenave and Hegre, 2005). This extension would explain the oil accumulation in the Sarvak and in the Fahliyan/Dariyan carbonates of the fields located in the Kuh-e Rig area, in Saadat Abad and Sarvestan, south of Shiraz (Fig. 2), and oil seepages described north of Shiraz. As part of this study, a sample of Kazhdumi with TOC of 5% and a Tmax of 440°C recently collected in the Dashtak anticline (N 30°30, E52°30) confirms the extension of the Kazhdumi source-rock in the Shiraz area. However, the Kazhdumi was deposited in an oxic organic-lean facies at Sabspushan-1 well, south of Shiraz and in the Jahrum area as shown in several outcrops (Bordenave and Burwood, 1995). Organic-rich Pabdeh was deposited in a NW-SE elongated trough, parallel to the Zagros suture, extending from Lurestan to Fars (Bordenave and Hegre, 2005). However, in most of the Izeh Zone and Northern Fars, the Pabdeh is immature.

All source-rocks consist of Type II to type IIS kerogen (Bordenave and Burwood, 1990).

The potential reservoirs of this second petroleum system are the Jurassic and Early Cretaceous carbonates of the Khami Group (Surmeh, Fahliyan and Dariyan Fms.) and the carbonates of the Middle to Late Cretaceous Bangestan Group (Sarvak and Ilam Fms.). The Miocene Asmari Fm. that is well developed in Dezful Embayment is not considered as a potential reservoir in the Izeh Zone and in Northern Fars, because it is either outcropping or at shallow depth.

Top seals are more problematic, as the Mesozoic evaporites of the Hith/Gotnia Fm. laterally disappear when moving to Northern Fars (Bordenave and Huc, 1995). However, the Mokhtar-1 well drilled in the Yasuj area showed that thick organic-rich Kazhdumi could be, in addition of its classical role of source-rocks, considered as an efficient seal (Bosold et al., 2005). Within the Bangestan Group, lateral facies changes or high stand shales could possibly form cap-rocks (Taati Qorayem, 2005).

2 Methodology and Modelling Results

Once the structural cross-sections were interpreted and balanced (Sherkati and Letouzey, 2004), an assessment of the petroleum system could be done. The technique used here is basin modelling through maturity and expulsion modelling. Basin modelling puts figures and physical/chemical equations on geological assumptions to reconstruct a basin and its history (Ungerer et al., 1990). It can calculate, for example, if a given source-rock is mature, if oil, condensate and/or gas were expelled from it. However, the results depend upon the validity of the initial assumptions. Nevertheless, basin modelling is an effective way of checking assumptions. It can be used to check what might happen according to the organic richness of the Kazhdumi Fm. with, for instance, average TOC values being 0.5%, 1%, 2% or 5%.

In a thrust and foreland system like the Zagros Fold belt, our basin modelling aims at answering the following questions:

- What is the maturity of possible source-rocks in a given formation, here Lower Paleozoic, Jurassic or Cretaceous ?
- At what geological times did it reach maturity? After or before the formation of the structural traps linked to the Zagros orogeny?
- Did the kerogen-bearing formations expel any hydrocarbon to nearby structures?

■ What is the nature of expelled hydrocarbons: heavy-oil, oil, condensate, wet-gas or dry-gas?

2.1 Thermal Modelling

The first step in maturity modelling consists in temperature modelling (Tissot and Welte, 1984; Doligez et al, 1985). In order to reconstruct the temperature through time, the standard procedure is to collect present-day temperatures in wells and to deduce from this data the boundary conditions that have to be applied to compute present-day temperatures from coupled conductive/convective heat transfer. These boundary conditions are crustal heat flux and surface temperatures. Then, in order to compute the temperatures in the past, where no direct measurements are possible, the boundary conditions are extrapolated to the past. A cross-check with paleo-thermometers, such as vitrinite reflectance, Tmax from Rock Eval or transformation ratio of organic matter is needed to be sure that the basal heat flow can be confidently extrapolated (Durand et al., 1985).

Such a standard work has been performed on a representative set of 57 wells in Central Zagros. Present-

day temperature data is not easily available and a map of thermal gradient (Motiei, 1985) was used as substitute for temperature information. The crustal heat flux coming into the basin was calibrated on this temperature data (Fig. 4, after Gabalda, 2004). It shows that Izeh Zone and Northern Fars are significantly cooler than the Dezful Embayment. Though hard temperature control points are scarce in the area, the present-day heat flow trend probably reflects the deep crustal heterogeneity of the lithosphere and its ancient passive margin signature.

Present day heat flows have been kept constant through geological times, even though this is known as been an oversimplification, due to the past geodynamic structure of the thrust belt. An analysis of the variation of subsidence through time shows the relative stability of the north-eastern part of the Arabian Platform, and seems to justify the use of constant heat flow, at least during the Jurassic, Cretaceous, and Paleogene (Bordenave and Hegre, 2005). Classically, Tethyan rifting was associated, during the Permian and Triassic, with elevated heat flows, followed by post rift decay. However, the crustal stretching factor that could be used as a constraint on the paleo heat flow is impossible to derive, because the whole passive margin
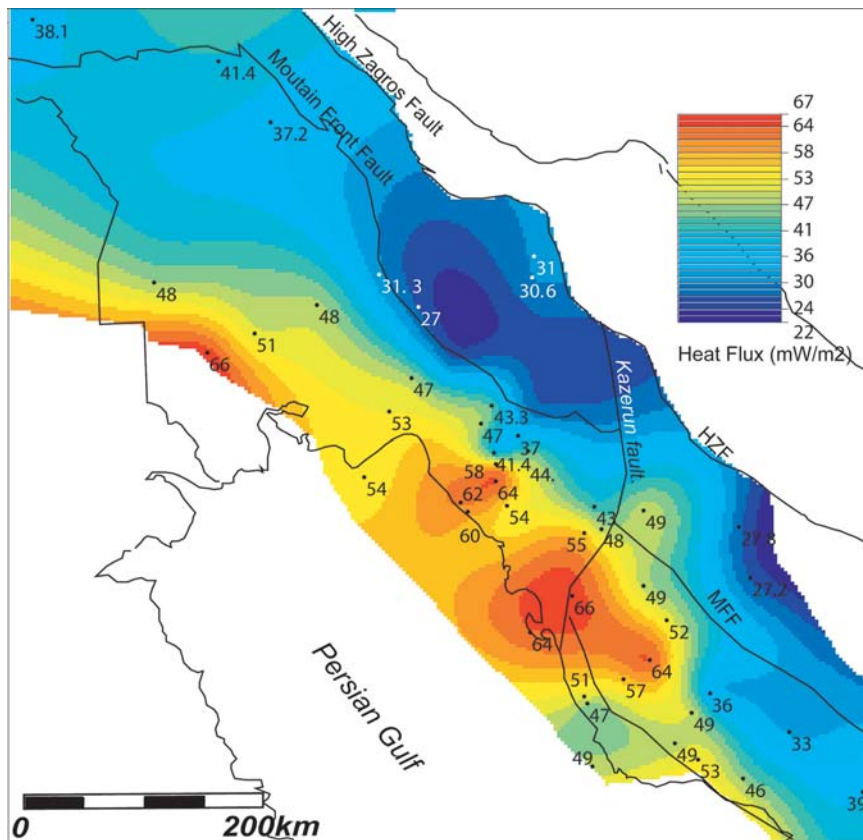
Fig. 4. Regional heat flow map. Heat flow was deduced from temperature data available at regional scale through present-day thermal calibration (Gabalda, 2004, unpublished report). Posted values show the calibration points from which the map has been interpolated. Original gradient data has been published by Motiei (1995). Note the rapid decrease of heat flow in the Izeh Zone and Northern Fars, as compared to those of the Dezful embayment. Heat flow in the Izeh Zone is only controlled by temperature data coming from the Rig and Shurom wells. *HZF*: High Zagros fault, *MFF*: Mountain front fault

setting has been overprinted by the Arabian-Iranian collision. So the heat flow was kept constant through time, which results only in a possible shift of paleomaturity during the Triassic and perhaps the Early Jurassic times, long before structural traps linked to the Zagros orogeny existed.

2.2 Structural Modelling in Northern Fars

Several successive episodes of sedimentation/erosion should be considered in the studied area (Stöcklin, 1968 and 1974; Berberian and King, 1981; Alavi, 1994; Sharland et al., 2001):

1. A long Paleozoic and probably Precambrian history, with several stratigraphic gaps due to the various collisional events, among which a mild Acadian phase was followed by a strong Hercynian phase that caused up to one thousand meters of erosion on N-S oriented blocks, and the deposition of Permian on significant angular unconformity (Szabo and Kheradpir, 1978; Berberian and King, 1981; McGillivray and Hussaini, 1992).
2. A passive margin set up during the Mesozoic and part of the Cenozoic, where sediments compact mostly vertically, as the basin grows through filling up accommodation space;
3. A multiphase collision margin set up mostly since the Neogene, but starting as early as the Coniacian, when the former NeoTethys was closing up and the Zagros thrust belt was building. Then movements of sediments were both vertical, through synstructural deposits and horizontal, through thrust movements.

For structural modelling purpose, we have only considered the last compressional event. Two different modelling tools were used to reconstruct the maturity/expulsion history of the source-rocks during the two episodes. The 1D tool Genex (Beicip, 1995) has been used to account for the first stages, until the onset of horizontal deformation of sediments, and then in order to reconstruct the structural history of the collision system, we have used the Thrustpack software to get access to 2D results on cross-sections. Fig. 1 shows the location of the modelled cross-sections in Northern Fars.

Thrustpack is a 2D software that has been developed for forward kinematic reconstruction of fold-and-thrust belts. Taking into account synflexural or synkinematic sedimentation and erosion, it provides geometric constraints to reconstruct the burial history of potential source-rocks and the simultaneous or delayed formation of structural anticlinal traps (Sassi, 2005). A balanced cross-section is the starting point from which the geometry through time is reconstructed (Fig. 5; for balanced sections see Sherkati et al., 2006). Then, depending upon the geological history of the thrust belt, stages of deformation are selected, for which it is decided to move the different modules of the balanced cross-section, with deformation rates suited to the global tectonic history of the area. Through trial and error, a scenario of deformation steps with thrust movements and flexural uplift or subsidence together with syntectonic deposition or erosions is reconstructed. The final step of deformation should lead as close as possible to the present day geometry.

Table 1 lists the stages of deformation that have been selected to account for the thrusting history in the Zagros fold belt. There is an arbitrary part in the selection of deformation ages for all events that happened after the deposition of Asmari Formation. Most age-dating information available comes from James and Wind (1965) which attributed the Gachsaran Fm. as to the Early Miocene, the Mishan Fm. to the Early to Middle Miocene, the Agha Jari is indicated as being Late Miocene to Pliocene and the Bakhtiari to be Late Pliocene in age. However, these authors underlined the lack of diagnostic fossils in the later formation. The absolute ages corresponding to the Miocene and younger stages are taken from Haq and Van Eysinga (1998).
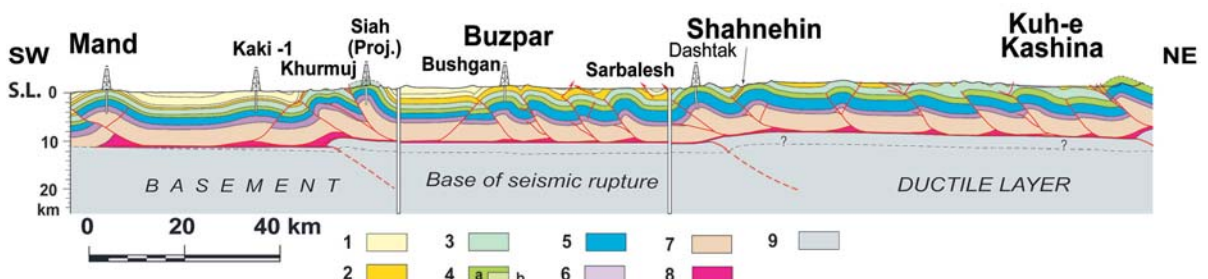
Fig. 5. Balanced structural cross-section used to perform maturity and expulsion modelling (simplified after Sherkati and Letouzey, 2004) Formation legend: *1. Mishan, Agha Jari and Bakhtiari Fms, 2. Gachsaran Fm, 3 Pabdeh, Gurpi and Asmari Fms, 4. Kazhdumi (a) and Sarvak (b) Fms, 5. Early Cretaceous to Early Jurassic interval, 6. Triassic, 7. Paleozoic, 8. Hormuz salt, 9 Basement*

Table 1. Stages of deformation used in the structural modelling

Stage	Geological age	Starting age in Ma	Ending age in Ma
Present day	Pleistocene	1.62	0
Bakhtiari	Pliocene	5	1.62
Upper Miocene	Miocene	7	5
Agha Jari	Miocene	9	7
Mishan	Miocene	11.2	9
Gachsaran	Miocene	16.6	11.2
Asmari	Miocene	23.7	16.6

The deformation rates need to account for the total shortening of the sections. They were taken in order to be always lower than the plate tectonic convergence rates. No hard constraint on the deformation stages is available. However, the global assumption that the Zagros flexure was progressing through times from the foreland to the hinterland was accounted for through differences in thickness in the Mishan Fm. from external to internal areas (Hessami et al., 2001). It is also assumed that the movements of thrusts started earlier in the internal part of the fold belt, probably during Early Miocene times, and later in the most external.

Other geological assumptions have been used to build a most probable scenario of deformation events:

1. Some structures are developed on faults with large offset for Paleozoic to Cenozoic layers, like Buzpar. Others like Serbalesh (Fig. 6) show less offset in Paleozoic and Mesozoic formations, but exhibit rather a buckling type of deformation. Therefore, we have assumed that the deformation started as early as Mishan times for the structures with large offset, and only later, for structures with less offset.
2. We assumed in this present work that all structures began to grow as soon as shortening started. This assumption is supported by the fact that the lower detachment level in Northern Fars is a low-friction level (Hormuz salt). An alternate assumption, not documented here, would have been to propagate the deformation from hinterland to foreland through Miocene and Neogene times, the most internal structures being the first to form, the most external being the later.
3. Because of observations on seismic sections and because of recent seismicity (Berberian, 1995), we have assumed that the crust gets involved in the deformation. Hormuz salt moves at the same time and accommodates the deformations.
4. Erosion of the section, and specifically of anticlines, occurs whenever their altitude gets several hundreds of meters higher than the surrounding layers.

Erosion also occurs when the average elevation gets higher than the present-day altitude of the section.

5. The thickness and facies of synflexural formations deposited during Middle Miocene to Pleistocene (Mishan, Agha Jari and equivalent) and eroded away at present has been selected to fit Tmax values observed in the field for both the Kazhdumi and Pabdeh source-rocks. In the internal areas little direct indications about the thickness of sediment of Middle and Upper Miocene or Pliocene equivalent of Mishan/Agha Jari or Bakhtiari do exist. The only assumption is to use a thickness equivalent to the one observed in the external thrust areas, because rare Tmax values around 430–440°C indicate early mature state of the source-rocks and a shallow paleo burial of the anticlines.

Fig. 6 shows the reconstructed geometry through time for the Buzpar-Serbalesh transect. The scenario of deformation resulting from this reconstruction is only one of several possible solutions. Care has been taken to fit the present-day maximal burial depth in each of the synclines adjacent to the anticlines, because most of the maturity and expulsion of hydrocarbons will preferentially happen there. The hydrocarbons expelled from the source-rocks will then migrate laterally into the adjacent anticlines, if expulsion is younger than the formation of the Buzpar and the Sarbalesh Zagros folds. Due to the deformation algorithms used in Thrustpack, the geometry in the anticlinal areas is sometimes difficult to match. But here also, we have tried to reach at least a partial overlap of computed and observed shapes.

One can see that to compute the present-day geometry, there is no need to have faults cutting through Jurassic and Cretaceous layers up to the surface; faults would affect the Paleozoic formations and then die out laterally into the Triassic evaporitic Dashtak, as shown by seismic sections in this area. This is especially visible at the anticline of Sarbalesh (Fig. 6). Other faults in this section act as quasi kink axis in Jurassic to Miocene formations, with no large throw.

2.3 Hydrocarbon Generation and Expulsion in Northern Fars

In order to perform maturity and expulsion modelling, source-rocks were assumed to exist in Early Paleozoic, Jurassic and Cretaceous formations everywhere in the Northern Fars-Izeh Zone. Their effective occurrence remains to be discussed. As an example, the Kazhdumi Fm. becomes organic-lean when nearing Kazerun fault (Bordenave and Huc, 1995).

Once the structural history has been reconstructed and the thermal history calibrated, the transforma-

Fig. 6. Kinematic reconstruction of the Buzpar cross-section. Four deformation stages are represented in the upper part of the figure, note the horizontal shortening and the early movements of Paleozoic layers. The lowest sketch shows the total amount of expelled oil (represented by the C15+ saturated fraction) since the deposition of three assumed source-rocks. It shows that the Kazhdumi source-rock, if present, would not have expelled any hydrocarbons (see text)
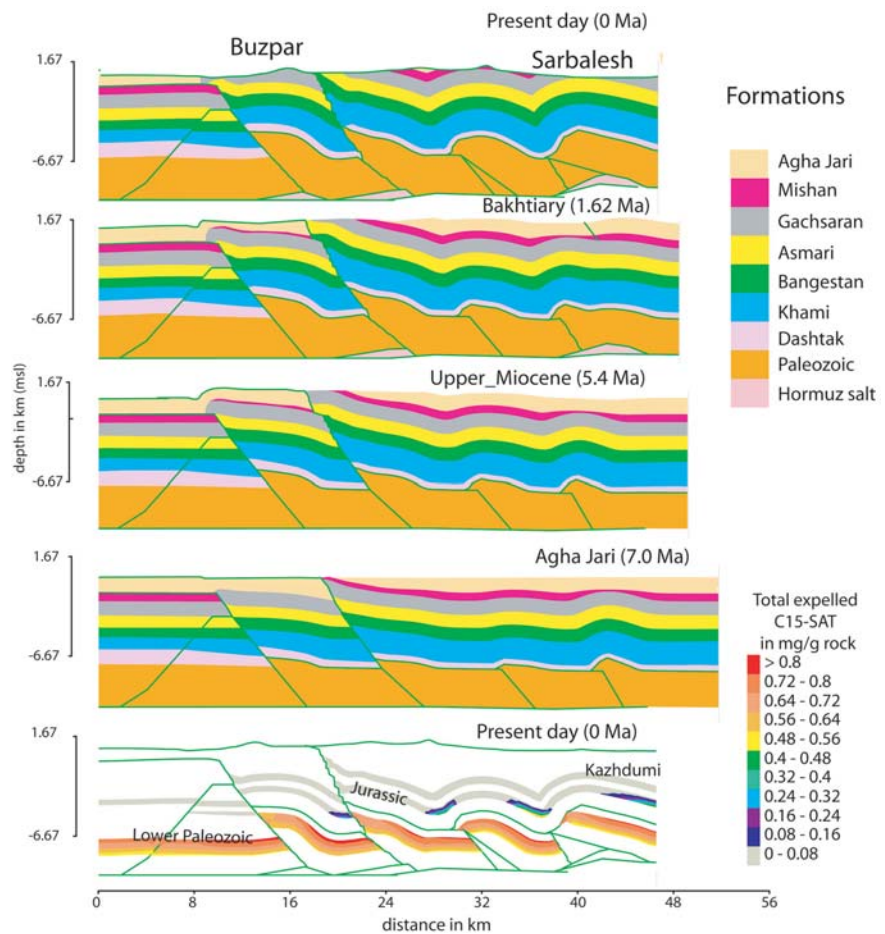
tion ratio of the kerogen can be deduced and the genesis and expulsion of hydrocarbons can be assessed. We have used a kinetic description of cracking (Vandenbroucke et al., 1999) that is able to model the genesis of hydrocarbons with a full range of chemical composition, in order to explain the development of heavy oil, oil, condensate, gas and even CO_2. The kinetics for the hypothetical Lower Paleozoic kerogen were taken from Abu Ali et al. (1999) who measured compositional kinetics from a immature Silurian sample in northwestern Saudi Arabia.

The maturity history of the following formations that may include potential source-rock intervals at least somewhere in the Zagros Fold belt was computed with the following base-case assumptions:

- Pabdeh, with Type II kerogen and TOC of 2%;
- Kazhdumi, with Type II or Type II-S kerogen and TOC of 2%;
- Jurassic (Sargelu Fm.) with 2% TOC, although the Sargelu Fm. is likely to be in shallow platform limestone facies and is not expected to include any source-rocks;

- Early Paleozoic ("Silurian") with Type II kerogen and 2% TOC (although no Llandoverian hot shales are expected in an area that has been a regional high extending from Kuh-e Dena and Kuh-e Surmeh, already observed at the end of the Ordovician, and that has been uplifted during the Hercynian phase, as shown by the deep wells drilled in Fars (Bordenave, 2002a).

Because the history of the folding started during the Early Miocene, we have not modelled the pre Miocene history with the 2D tool. The starting point of the deformation is set arbitrary at 23.7 Ma, corresponding to the beginning of the Middle Asmari deposition, according to the James and Wynd (1965) terminology (Table 1).

Two types of result can be used to discuss the prospectivity of the area: the transformation ratio of the various source-rocks and the expulsion rates computed for the different components.

In the Sarbalesh-Buzpar section, the basal sketch of Fig. 6 shows that Kazhdumi Fm., if it has been present in the section, would not have expelled any hydro-
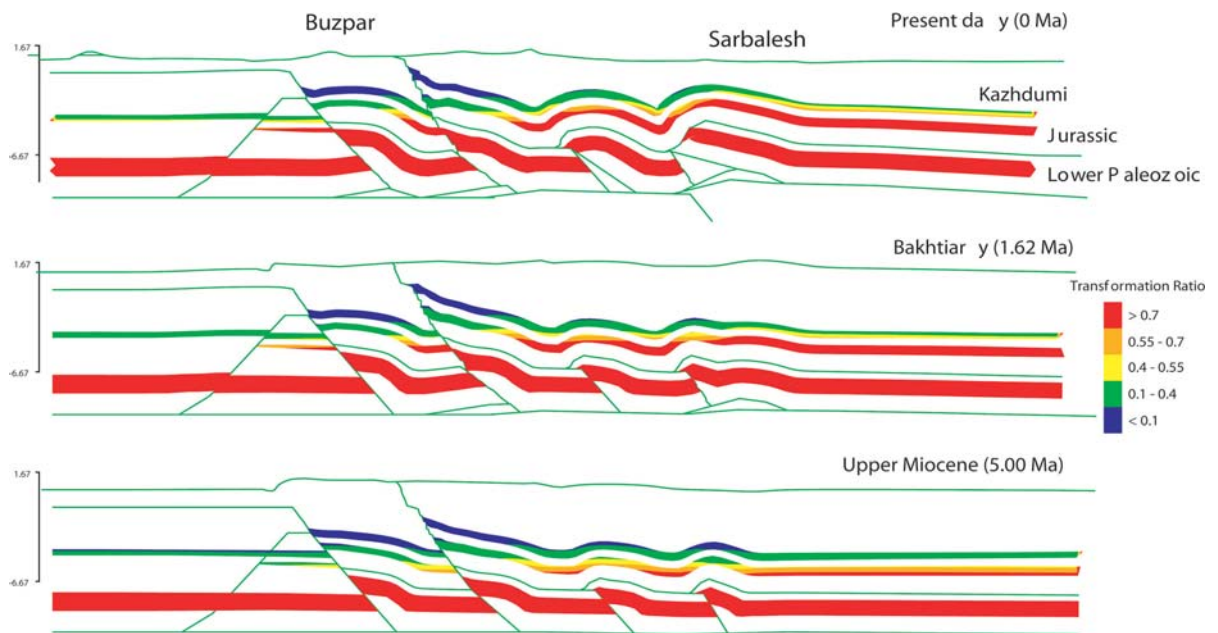
Fig. 7. Computed source-rock maturity on the Buzpar section. Source-rocks in Jurassic and Kazhdumi were assumed to contain standard Type II kerogens, Early Paleozoic kinetic parameters were derived from analysis of a Silurian sample from Saudi Arabia (Abu Ali et al., 1999)

carbon, due to low maturity, whatever the TOC of the formation could be. If present, Sargelu source-rocks would have only expelled oil in the deepest synclines. When comparing to the maturity profile through time on the same section (Fig. 7), the Sargelu Fm. would have been already at the peak oil window in the Late Miocene and within the gas window today. We have to keep in mind that the maturity of source-rocks is not sufficient to evaluate the time of hydrocarbon expulsion, as the time of expulsion also depends on the source-rock richness. Namely, the time shift between maturation and expulsion peaks increases for lean source-rocks.

 Fig. 7 shows the change of maturity on the Sarbalesh-Buzpar section through geological times. These results show when and where hydrocarbons were generated from potential source-rocks. There, any Early Paleozoic source would be over mature before the Miocene. Jurassic source would become mature during Agha-Jari time of deposition in the shallowest locations of the synclines and Kazhdumi would get early maturity with ongoing flexural sedimentation during the Late Miocene.

In the section Shahnehin, north of the previous section (Fig. 8) we have also included hypothetical Jurassic and Kazhdumi source. As previously indicated in our discussion on the extent of the organic-rich Kazhdumi facies, a sample of Kazhdumi with TOC of 5% and Tmax of 440°C was collected in Dashtak anticline (N 30°3, E52°30) showing that the source-rock fa-

cies extends from the Dezful Embayment north-eastwards. The maturity history is similar to the previous section, though the maturity of Kazhdumi is just beginning in the anticlines. In the synclines, both Jurassic and Kazhdumi would be in the oil or condensate window. These results are consistent with the presence of oil in the Sarvak and of shows of oil and gas in the Fahliyan carbonates, as encountered in the structure of Sarvestan, south east of Shiraz, in the same structural zone.

In Fig. 9, the evolution of oil expulsion is modelled for the most external cross-section that starts near the shoreline at the Mand anticline. Three possible source-rocks have been considered: Pabdeh, Kazhdumi and Early Paleozoic. Even if we know that the Kazhdumi and the Pabdeh Fms. are probably not in source-rock facies in the area (Bordenave and Hegre, 2005), we have included them in the modelling in order to test their possible behaviour. A source-rock included in the Early Paleozoic would have been already over mature at the time of Asmari deposition. Any Kazhdumi and Pabdeh organic layer would have been still immature at the time of Mishan deposition. Maturity and expulsion rates would increase with the flexural sedimentation of the Agha Jari and Bakhtiari Fms., until the present day, when Kazhdumi is early mature in anticlines, but is mature in synclines. Pabdeh Fm. would have been early mature in synclines and not mature in anticlines. The results show that the origin of the hydrocarbons in Mand is probably more com-
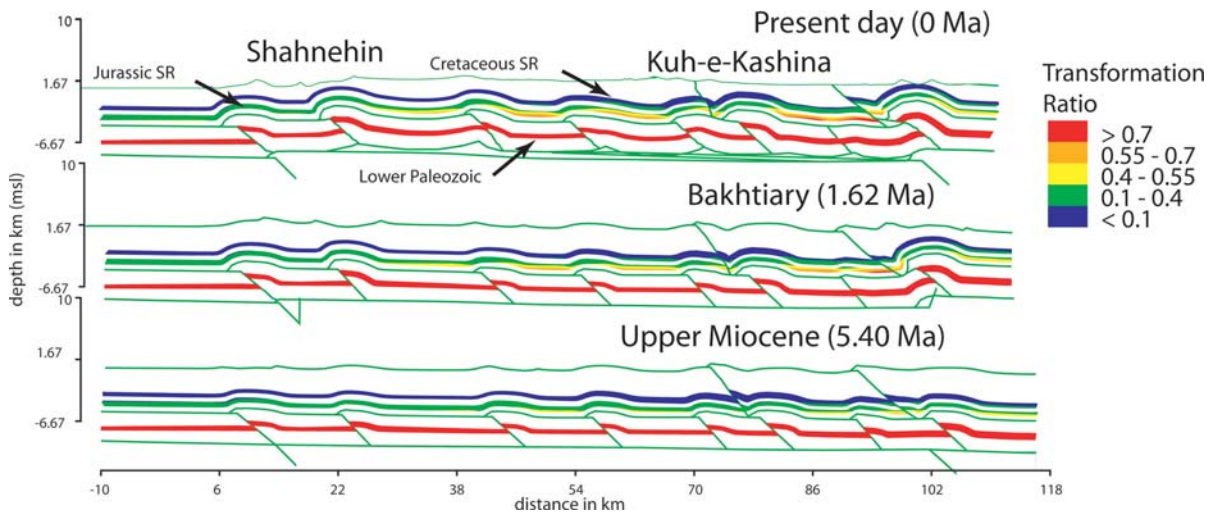
Fig. 8. Computed transformation ratios for various source-rocks on the Shahnehin section in the High Zagros. Note that any source located within the Early Paleozoic would be mature before the Late Miocene; i.e., before the major trap formation. Any source potential in Jurassic layers reached the onset of the peak of the oil zone (transformation ratio above 50%) only in deepest synclinal positions. Any potential younger source-rocks (Kazhdumi or Pabdeh) remained immature

plex that presented by Mamariani et al. (2000). The results could explain the presence of gas in the Permian carbonates in Kuh-e-Mand and also in similar structures, like Dalan, south of the section. So far, the presence of heavy oil in Kuh-e-Mand and oil and gas in the Bangestan carbonates in the nearby Kuh-e Kaki could be possibly explained by early mature Cenozoic source, although no such source-rocks are observed on the wells of Mand. However, lateral migration from the Jurassic Hanifa-Tuwaiq Mountain source-rocks well developed in the Arabo-Persian Gulf would also explain the origin of the heavy oil discovered in the Asmari and in the Sarvak of Kuh-e Mand (Bordenave, personal communication).

Fig. 9 also shows expulsion rates through time for two hypothetical sources located either in the Kazhdumi or in the Paleozoic. The picture for the Lower Paleozoic source shows the expulsion rate in the syncline north of Khurmuj, whose burial is slightly different from the syncline immediately adjacent to Kuh-e-Mand. It can be seen that most of the expulsion occurs prior to the trap formation, hence during the passive margin state of the basin. There is just a small hint of expulsion at the onset of syntectonic burial. Eventually, the risk of non hydrocarbon gases in Permo-Triassic reservoirs can also be checked through modelling. Studies in Northern Germany (Kroos et al., 1995) have shown that there might be a significant contribution of nitrogen from deeply buried Type III source-rock. A nitrogen supply could be expected, provided the organic matter of Lower Paleozoic is rich in C-N chemical bonds. Such a scenario could be tested, where extremely deep paleozoic source-rock and high crustal heat flow might lead to nitrogen generation at the time of trap formation and thus decrease the prospectivity of an area.

2.4 Discussion on Hydrocarbon Prospectivity in the Izeh Zone

When looking at the 2D sections in Northern Fars, it appears that the hydrocarbon expulsion is mostly controlled by the situation from possible sources in the deepest buried synclines. Source-rocks located in anticlinal position always have lower maturity and expulsion. Structural cross-sections through the Izeh Zone have been constructed by Sherkati et al. (2006). From those sections, synthetic wells in deepest synclinal position were therefore constructed to analyze the maturation and expulsion history of hydrocarbons in the Izeh Zone. Synthetic wells constructed from structurally balanced cross-sections are better suited than real wells drilled on anticlines. However, the 1D modelling is aimed at describing the source-rock history, hence the primary migration at the location of the synthetic well. Implicitly, when extrapolating the computed 1D compositions to represent the hydrocarbons accumulated in structures, it assumes that secondary migration is then mostly in lateral direction from the synclines to the highest points and towards the reservoir level.

A total of eight synthetic wells has been constructed and modelled. In this paper, the results of only three of those are discussed (Rig, Sartal and Keynow, see Fig. 1 for location and Figs. 10 and 11 for the results).
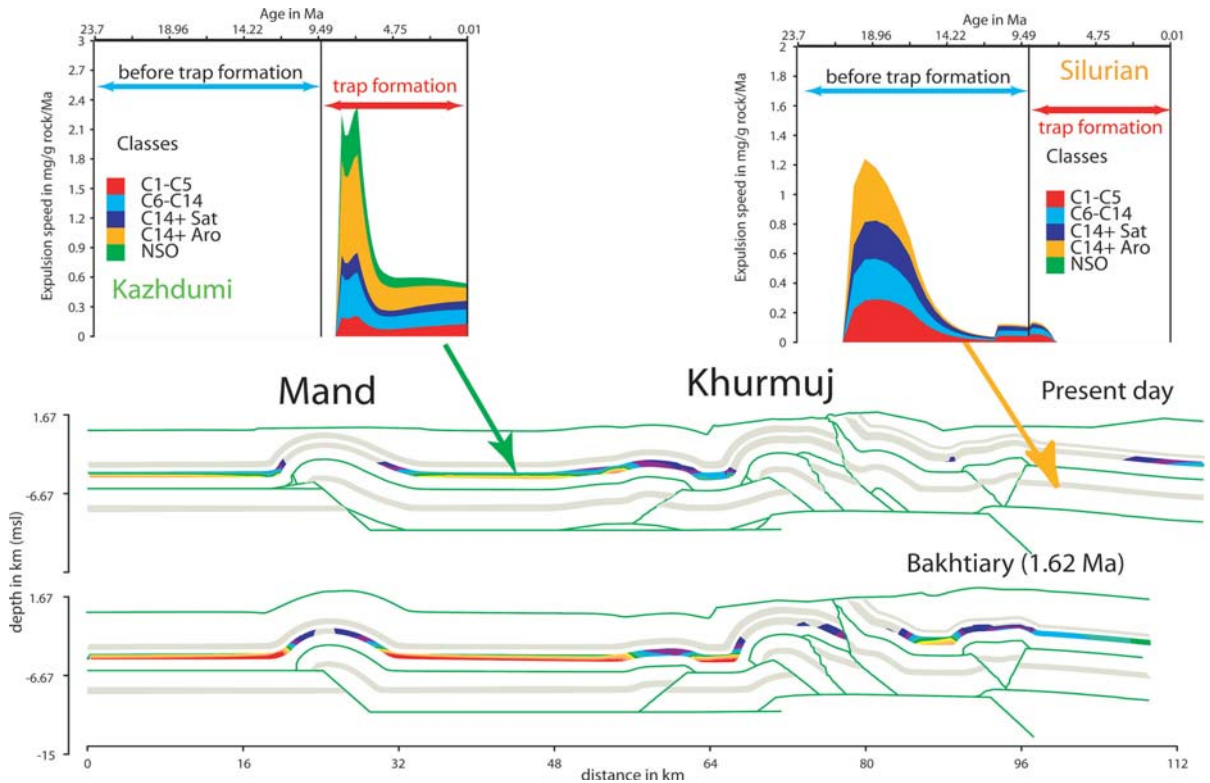
Fig. 9. Computation of the expelled amounts of hydrocarbons in the most external part of Zagros, in the Mand-Khurmuj area section. The two lower sections represent the oil expulsion rates at two time-steps in the basin history, at Bakhtiari times and at present day. Three possible sources have been taken into consideration (Early Palaeozoic, Cretaceous Kazhdumi and Pabdeh-Gurpi of Middle Eocene). The upper pictures represent the expulsion rates through time for two points located in the deepest possible positions. It can be seen that the Early Palaeozoic source-rocks did no longer expel any oil after the formation of the trap, because most of its charge was released during Late Jurassic/Cretaceous times. On the contrary, any potential source-rocks located within the Cretaceous interval would have reached the expulsion peak during the time of trap formation

The lithofacies of the wells have been selected according to the regional facies distribution. Crustal heat flow values are depicted in Fig. 4. Again, as in Northern Fars, we will assume that source-rock facies might be present in various formations and look for the consequence on hydrocarbon charge to structures. Kerogen parameters for all sources were equivalent to those used in Northern Fars.

The synthetic well in the Rig syncline (Fig. 10) shows that Mid Cretaceous shales (Kazhdumi Fm.) entered the oil window in the last 20 Ma, whereas any source-rocks located in the Jurassic would be currently in the condensate window. Any Paleozoic source would be in the gas window since at least 30 Ma. The comparison of maturity windows with the expulsion timing of hydrocarbons (Fig. 11) shows that Kazhdumi shales reached the peak of oil expulsion during folding and formation of the Zagros structures, similar to what was found in the Dezful Embayment (Bordenave and Hegre, 2005). This could explain the occurrence of hydrocarbons trapped in the structure of Rig, where oil is present in the carbonates of the Dariyan

and the Sarvak Fms., in Shurom (oil-bearing Sarvak), in Dodrou, where oil was discovered in the Fahliyan, and in the Mokhtar well, where gas has been encountered in the Daryian and the Fahliyan Fms. capped by a thick repeated section of Kazhdumi. By contrast, when looking at deeper source-rocks, peaks of oil expulsion happened before the Zagros folding, except perhaps for a small remnant expulsion of condensate and gas for any Jurassic source potential. The peak of expulsion of any Paleozoic source would happen during the Late Jurassic to Cretaceous times.

Hydrocarbons expulsion rates in the Sartal syncline show that any potential source existing in the Jurassic layers, likely to be the Sargelu Fm., would be currently at the end of the oil window. Expulsion would be maximum around 16 Ma, contemporaneous with the Zagros folding and the trap formation. This modelling fits with the presence of oil in Early Cretaceous (Fahliyan) reservoirs in the nearby structure of Dodrou. Further east in the Izeh Zone, the maturity of Jurassic source is sensitive to the thickness of Pabdeh-Gurpi Fms.. When the thickness exceeds 1400 m; i.e., in the
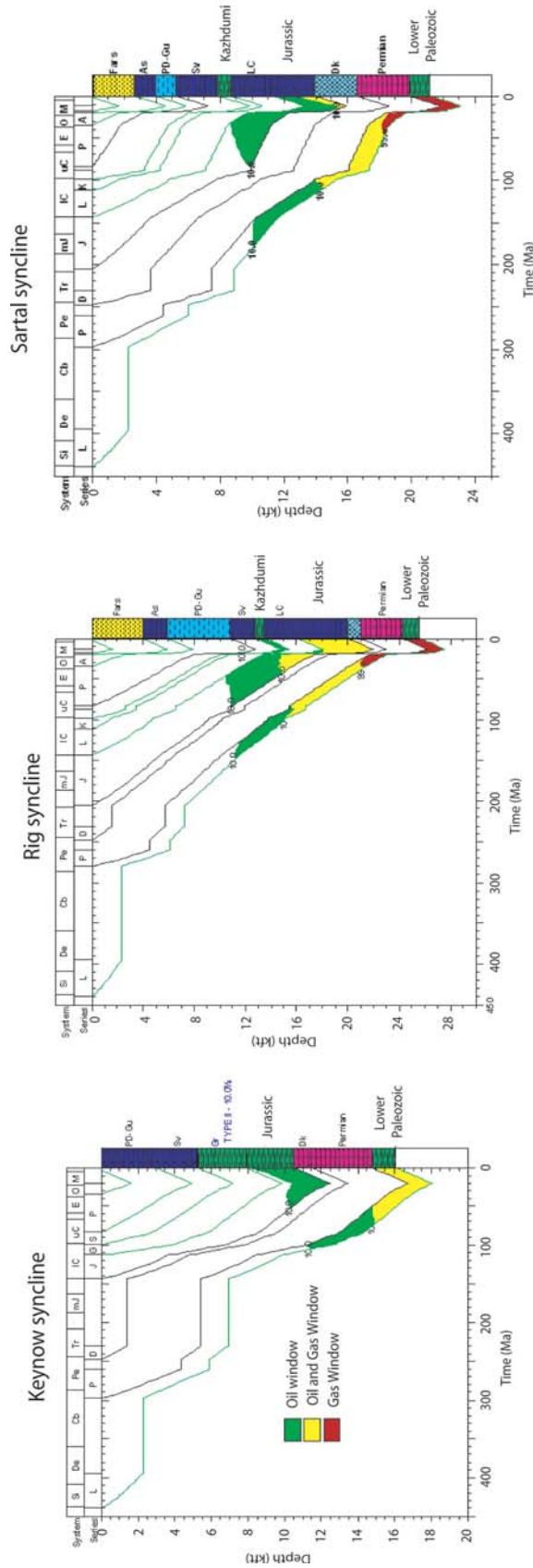
Fig. 10. Burial history and maturity windows fort three synthetic wells located in the Izeh Zone (see Fig. 1 for location). - Early Paleozoic source-rocks matured everywhere well before the Zagros folding. - Early Jurassic source-rocks, if existing, would have expelled oil during the formation of the Keynow and Sartal anticlines. In the same area, Kazhdumi source-rocks would not be mature. - In the Rig syncline, Mid Cretaceous Kazhdumi source-rocks reached the expulsion window at the time of the formation of the Rig anticline
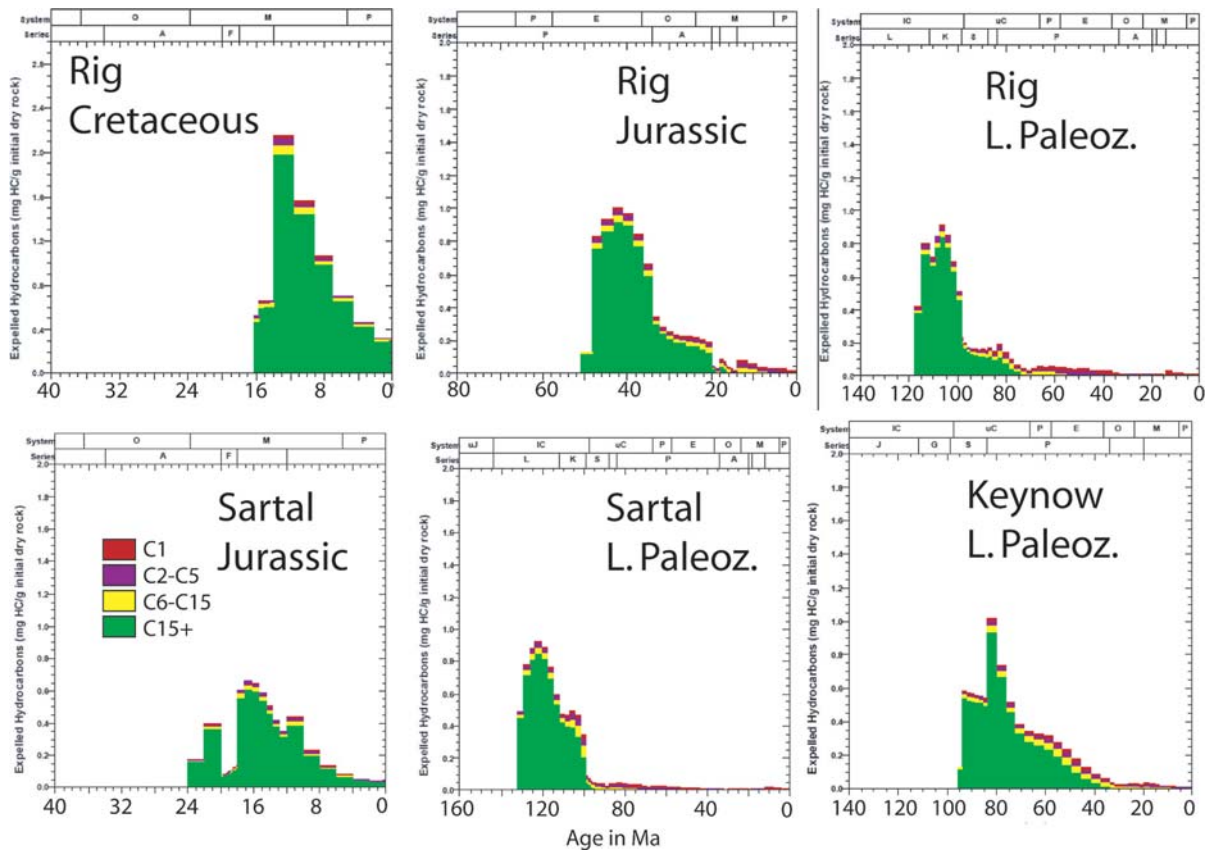
Fig. 11. Expulsion rates for the various source-rocks assumed to exist in the Izeh Zone. Geological time is indicated on the horizontal axis, expulsion rates on the vertical axis, split into the different hydrocarbon components. For comparison, the Zagros folding starts approximately 15 Ma ago (Note that the horizontal time axis of is not equal in the different graphs)

north-eastern part of the Izeh Zone, most of the Jurassic charge is pre-folding, whereas when Pabdeh-Gurpi is thinner, the peak of oil expulsion is postponed until Middle Miocene, and becomes available for Zagros traps. The maturity history of Early Paleozoic source-rocks, whether Cambrian, Ordovician or even Silurian would be similar in the area of Izeh and Northern Fars (Figs. 9 and 11). Peak expulsion happened during the Late Jurassic to Cretaceous times, oil and gas migrated in available traps, regional highs and early formed salt-related structures. Therefore, only small pulses of dry gas expulsion are expected since the time of Zagros thrust belt building. We have to note that the temporary increase of heat flow due to Tethyan rifting during the Permo-Triassic would not make the expulsion peak younger.

3   Conclusion

The relationship between the evolution of the fold and the thrust belt and the thermal history of the source-

rocks is recognised as an important parameter for hydrocarbon exploration, together with the distribution of source-rocks, which are present in various structural settings along a regional transect crossing the belt.

3.1 The Early Paleozoic Permo-Triassic System

Whether in the Izeh Zone or in Northern Fars, any source within the Early Paleozoic (either of Cambrian, Ordovician or Silurian age) clearly generated and expelled liquid hydrocarbons during the Late Jurassic, Cretaceous and perhaps the Early Cenozoic. These hydrocarbons migrated to then existing traps and formed pre-Zagros oil and gas fields. These pre-Zagros fields accumulated in wide very low-relief regional highs and in salt-related domes and N-S elongated structures. The migration path and the location of the pre-Zagros accumulations could be derived from a set of regional isopachs/cumulative isopach maps (Bordenave and Hegre, 2005). Later, when the Zagros Folds were forming, either previously trapped hydrocar-

bons were remigrating to folds located in the close vicinity of the pre-Zagros accumulations, or previously trapped hydrocarbons dysmigrated to surface through faults and were lost. The gas accumulated at present day in the Permo-triassic reservoirs of Zagros folds could have two distinct origins. On one hand, it could then be issued from oil of pre-Zagros fields secondary cracked to gas and remigrated to nearby Zagros folds. On the other hand, it would result from the ultimate stage of kerogen cracking that generates only gas (Vandenbroucke et al., 1999), that occurs with the syntectonic burial. This latter solution is more straightforward and seems therefore more probable.

Exploration for gas in Permian reservoirs in the Izeh Zone and Northern Fars would also be conditioned to the existence of Triassic evaporitic top seal (see its extent in Szabo and Kheradpir, 1978), to efficiently prevent dysmigration.

3.2 The Mesozoic Petroleum System

The modelling of generation and expulsion of hydrocarbons from the Mesozoic source-rocks shows contrasted results for the various sources.

Pabdeh/Gurpi source-rocks became early mature very recently in some of the deepest synclines of the Dezful embayment, in particular at its north-eastern part (Bordenave and Burwood, 1990; Bordenave, 2002b). The contribution of this source-rock to the charge to any structure is assumed to be marginal in the Izeh Zone and in Northern Fars.

The distribution of the Kazhdumi source-rock is an important parameter for oil exploration. The Kazhdumi is well known in the Dezful Embayment. It was recently proven to extend in the Yasuj and in the Shiraz areas. By contrast, it does not exist at Sabspushan-1,

south of Shiraz, nor in the Jahrum area, where it is thin, organic-lean and oxic. In deep synclines, the Kazhdumi source-rocks are mature and have expelled oil-prone hydrocarbons during the formation of structural traps. Hence, expelled hydrocarbons have charged the existing traps through vertical and lateral migration (Bordenave and Hegre, 2005). The result of our modelling is not very sensitive to less-controlled parameters, such as the estimated thickness of the eroded synflexural sediments, the timing of deformation. However, expulsion was delayed or even not happened for source-rock having TOC values lower than 1%. It can be concluded that the prospective Zagros folds for the Sarvak or in the Dariyan and Fahliyan reservoirs are directly associated to the existence of source-rocks facies in the Kazhdumi Fm..

The Jurassic source-rock (Sargelu) is present in the Dezful embayment and in the NW of the Izeh Zone (Bangestan-1 well), but probably does not extend NE of the shelf edge that limited the Mesopotamian Depression. Almost everywhere in the deepest parts of the synclines in the Dezful embayment, in the fold belt and in the Northern Fars, Jurassic source-rocks currently reached the condensate or gas window. By contrast, in the Izeh Zone, its generation and expulsion behaviour greatly varies and several domains could be distinguished, depending upon the thickness of the first flexural sediments (Fig. 13). The timing of generation and expulsion of oil- or gas-prone products depends upon thermal history and burial of Jurassic rocks. With a "cold" thermal heat flow of 50 mW/m^2, and thick flexural deposits, there is a higher chance of trapping liquid products in Zagros structures than with thin flexural deposits. Accordingly, a "warm" heat flow of 58 mW/m^2 , as it exists towards the Dezful embayment would be more in favour of the generation of condensate or gas during the Zagros Folding.
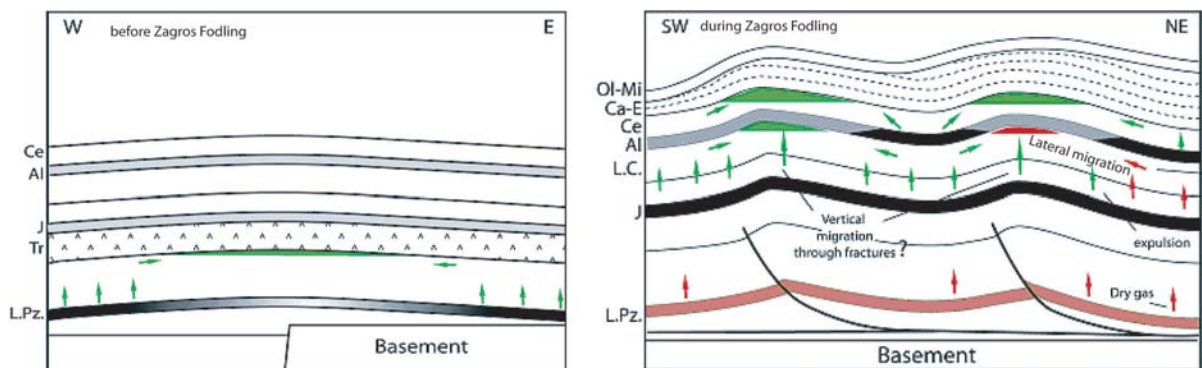
Fig. 12. Conceptual model for expulsion and migration of different types of hydrocarbon from potential source-rocks during the Zagros folding in the Izeh Zone and Northern Fars. Gas represented in red, and oil in green. Generated hydrocarbons from probable Paleozoic source-rocks before Zagros folding (left) would be trapped in large regional paleohighs, or in salt-related structures associated with Hercynian N-S oriented deep-seated basement faults. Dry gas, oil or condensate from Jurassic source might be trapped in Zagros structures, provided the existence of effective seals is effective (right sketch)
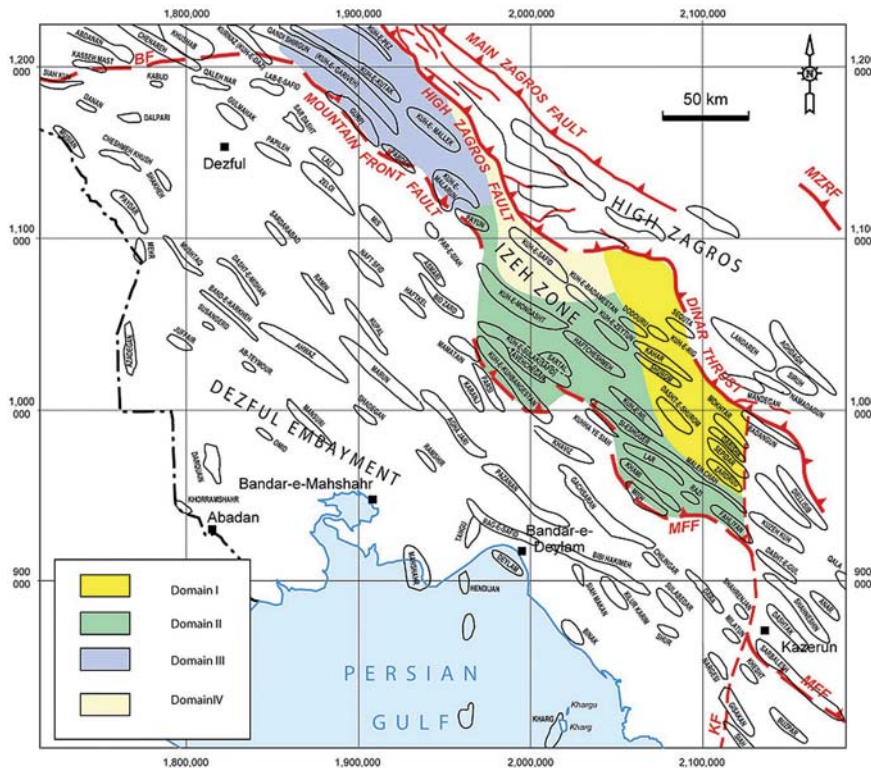
Fig. 13. Map of the timing of expulsion from possible Jurassic source-rock in Izeh Zone.
- Domain I & IV: Pre-folding oil expulsion, fair prospectivity where Jurassic is present, poor prospectivity where it is absent.
- Domain II: Contemporaneous oil expulsion and Zagros folding, good prospectivity where Jurassic source is present. - Domain III: Absence of expulsion area because of shallow burial: poor prospectivity

Similarly, if Jurassic source-rocks are shallow, as could be the case in the High Zagros, there is a better probability of having oil charged into the Zagros structures. If Jurassic source was buried deeply before the Zagros Folding, the oil charge might be lost. Nevertheless, the charge of mesozoic traps from Jurassic source-rocks would be rather different of the entrapment mechanism envisaged in the Paleozoic System (Fig. 12).

As a result of modelling using the 1D Genex program for the pre-folding period and the Thrustpack program for the Zagros folding period, this study gives information on the timing of maturation of potential source-rocks. Three transects located in the SE of the Kazerun fault, and three wells located in the Izeh Zone were used for this purpose. The relative timing of the generation and expulsion from the various source-rocks as compared to the formation of any specific trap is a crucial factor for assessment of the numerous prospects yet undrilled in the study area. The presence of effective top seal has not been addressed in this paper. In addition, more effort is necessary to better know the distribution of the source-rocks in the Izeh Zone and in Northern Fars.

Acknowledgments

References

Abu-Ali M.a, Rudkiewicz J.l, Mcgillivray J.g, and Behar F. (1999) Paleozoic Petroleum System of Central Saudi Arabia. GeoArabia, vol 4. (3). 321–336

Alavi. M. (1994) Tectonics of the Zagros orogenic belt of Iran: new data and interpretations. Tectonophysics. 229, 211–238

Beicip-Franlab (1995) Genex Single Well (User Guide), Beicip-Franlab, 464 pp.

Berberian, M. and King, G.C.P., 1981. Towards a paleogeography and tectonic evolution of Iran, Can. J. Earth Sci, 18(2), 210–265.

Berberian M. 1995 Master blind thrust faults hidden under the Zagros folds: active basement tectonics and surface morphotectonics. Tectonophysics, 241, p. 193–224.

Bordenave, M.L. and Burwood, R., 1990. Source rock distribution and maturation in the Zagros belt; provenance of the Asmari and Bangestan reservoir oil accumulations. Org. Geochem., 16, 369–387.

Bordenave, M.L. and Burwood, R., 1995. The Albian Kazhdumi Formation of the Dezful Embayment, Iran: one of the most efficient petroleum generating systems. In: Katz, B.J., (Ed).

Petroleum Source Rocks. Springer Verlag, Heidelberg, 183–207.

Bordenave, M.L. and Huc, A.Y., 1995. The Cretaceous source rocks in the Zagros Foothills of Iran: an example of a large size intra-cratonic basin. Rev. Inst. Fr. Petrol 50, 527–753.

Bordenave, M.L., 2002a. The Middle Cretaceous to Early Miocene Petroleum System in the Zagros Domain of Iran, and its prospect evaluation. 6pp. AAPG Convention, Houston (extended abstract) available at www.aapg.org/datasystems/abstract/13annual/42471.pdf.

Bordenave, M.L., 2002b. Gas prospective areas in the Zagros Domain of Iran and in the Gulf Iranian Waters. AAPG Convention, Houston, Extended abstract, 6 pp. available at www.aapg.org/datasystems/abstract/13annual/42471.pdf.

Bordenave, M.L. and J.A. Hegre, 2005. The influence of tectonics on the entrapment of oil in the Dezful Embayment, Zagros Foldbelt, Iran. J. Petrol. Geology, 28(4), 339–368.

Bosold, A., Schwarzhans, W., Julapour, A., Ashrafzadeh, A.R., and Ehsani, S.M., 2005. The structural geology of the High Central Zagros revisited (Iran). Petroleum Geoscience, 11, 225–238

Burrus J., Kuhfuss A., Doligez B. & Ungerer P., (1991) - Are numerical models useful in reconstructing the migration of hydrocarbons? A discussion based on the Northern Viking Graben. From England W. A. & Fleet, A. J. (eds), Petroleum Migration Geological Society, Special Publication 59,. 89–109.

Carrigan W.J., Cole G.A., Colling E.L. Jones P.J., 1994, Geochemistry of the Upper Jurassic Tuwaiq Mountain and Hanifa Formation Petroleum Source Rocks of Eastern Saudi Arabia., in B. Katz (edt) Petroleum Source Rocks, Springer Verlag, p. 67–87.

Chaouche A. (1992) Genèse et mise en place des hydrocarbures dans les bassins de l'Erg Oriental (Sahara Algérien). Thèse Université de Bordeaux, France, 347 pp. better to cite Lüning (2000) which covers the full area from Morocco to Saudi Arabia and Iran

Colman-Sadd S.P. (1978) Fold Development in Zagros Simply Folded Belt, Southwest Iran, AAPG Bull., v 62, n° 6, pp. 984–1003.

Dercourt, J., Ricou, L.E. & Vrielynck, B. (eds) (1993) Atlas Tethys Palaeoenvironmental Maps. Gauthier-Villars, Paris, 307 p.

Doligez B., Bessis F., Burrus J., Ungerer P., Chénet P.Y. (1985) Integrated numerical simulation of the sedimentation, heat transfer, hydrocarbon formation and fluid migration in a sedimentary basin: the Themis model, in Thermal modelling in sedimentary basins, Ed J. Burrus, Technip.

Durand B., Alpern B., Pittion J.L., Pradier B. (1985) Reflectance of vitrinite as a control of thermal history of sediments, in Thermal modelling in sedimentary basins, Ed J. Burrus, Technip.

Glennie, K.W., 2000. Cretaceous tectonic evolution of Arabia's eastern plate margin: a tale of two oceans. Middle East Models of Jurassic/Cretaceous Carbonate Systems. SEPM Special Publ. 69,9–20.

Insalaco E. , Virgone A., Courme B., Gaillot J., Kamali M. , Moallemi A., Lotfpour M. and Monibi S. (2006) Upper Dalan Member and Kangan Formation between the Zagros Mountains and offshore Fars, Iran: depositional system, biostratigraphy and stratigraphic architecture GeoArabia Volume 11, v 2, p. 75–176.

Falcon N.L. (1967) The geology of the northeast margin of the Arabian Basement shield. Advancement Science 14, pp. 1–12.

Falcon N.L. 1974 Southern Iran: Zagros Mountains, In A.Spencer (editors) Mesozoic-Cenozoic orogenic belts. Geol. Soc. London special Publ. , 4, p. 199–211.

Gabalda S. (2004) Analyse régionale du régime thermique du Zagros Iranien. Rapport de DEA. Univ. PM Curie, Ecole des Mines de Paris, Ecole des Pétroles et Moteurs. Unpublished report, 48 pp.

Haq B.U. and Van Eysinga F.V.B. (1998): Geological Time Table. Fifth revised, enlarged and updated edition. Elsevier.

Hessami K., Koyi H.A., Talbot C.J., Tabasi H., Shabanian E. 2001 Progressive unconformity within an evolving foreland thrust-belt, Zagros Mountains, J. Geol. Soc. London, 158, p. 969–981.

Homke, S., Verges, J., Garces, M., Emami, H. and Karpuz, R., 2004. Magnetostratigraphy of Miocene-Pliocene Zagros foreland deposits in the front of the Push-e Kush Arc (Lurestan Province, Iran). Earth and Planetary Science Letters, 225, 397–410

James, G.A. & Wynd, J.G. (1965) Stratigraphic nomenclature of Iranian Oil Consortium Agreement Area. Bull. Amer. Assoc. Petrol. Geol., 49, 2182–2245.

Krooss-B-M; Littke-R; Mueller-B; Frielingsdorf-J; Schwochau-K; Idiz-E-F (1995) Generation of nitrogen and methane from sedimentary organic matter: implications on the dynamics of natural gas accumulations. In: Processes of natural gas formation. Rice-Dudley-D (editor); Schoell-Martin (editor) Chemical Geology. 126; 3-4, pp. 291–318. Elsevier. Amsterdam, Netherlands. 1995.

Lüning S., Craig J., Loydell D.K., Torch P., Fitches B., Lower Silurian `hot shales' in North Africa and Arabia: regional distribution and depositional model. Earth-Science Reviews (49)(1–4) (2000) 121–200.

Mamariani M., Kamali M., Angajivand M. (2000) Source Rock Assessment and Geochemical Process Involved in the Formation of Heavy Oil (Kuh-e-Mund, Southwest Iran). Geo 2000 Abstracts, GeoArabia, v5,n° 19.

Mcgillivray, J.G. and Husseini, M.I., 1992. The PaleozoicPetroleum geology of Central Arabia. AAPG Bull., 76, 1473–1490.

McQuillan H. 1974 Fracture Pattern on Kuh-e-Asmari anticline, Southwest Iran, AAPG Bull., v58, n°2, pp 236–246.

Motiei, H., 1995, Petroleum geology of Zagros: Publ. Geol. Survey of Iran (in Farsi), 589 p.

Murris, R.J. (1980) Middle East: stratigraphic evolution and oil habitat. AAPG Bull., 64, pp. 597–618.

NIOC (1993) Oil and Gas General Information Map of the Islamic Republic of Iran.

O'Brien C.A.E. 1950 Tectonic problems of the oil field belt of southwest Iran. 1st Internat. Geol. Cong. Proc., London, 6, pp. 45–48.

Ricou, L. E., 1974 L'évolution géologique de la région de Neyriz (Zagros iranien) et l'évolution structurale des zagrides, Thèse, Université d'Orsay, France.

Roure F., Roca E. and Sassi W. (1993). The Neogene evolution of the outer Carpathian flysh units (Poland, Ukraine and Romania): kinematics of a foreland/fold-and-thrust belt system. Sedimentary Geology, 86, pp. 177–201.

Rudkiewicz J.L., Penteado H.L, Vear A., Vandenbroucke M., Brigaud F., Wendebourg J, Düppenbecker S. (2000) Integrated basin modelling helps to decipher petroleum sys-

tems. In R. Melo and B.J. Katz Eds, Petroleum systems of South Atlantic Margin, AAPG Memoir 73, p27–40.

Sassi W. (2005) Modèles cinématiques et géoméaniques pour l'interprétation structurale et pétrolière des bassins sédimentaires. Mémoire d'Habilitation à Diriger des Recherches, Univ. Montpellier, 317 pp.

Sella G.F., Dixon T.H., Mao A. 2002 A model for recent plate velocities from space geodesy. Journal of Geophysical Research, 107, pp. 11–1, 11–30.

Setudehnia A, 1978 The Mesozoic sequence in south-west Iran and adjacent areas. Journal of Pet. Geol., 1 (1), p3–42.

Sherkati. S., Letouzey, J. (2004). Variation of structural style and basin evolution in the central Zagros (Izeh Zone and Dezful Embayment), Iran. Marine and Petroleum Geology, 21, 535–554.

Sherkati S (2004) Style tectonique et cinématique du plissement dans le Zagros Iranien (Zone d'Izeh) : Conséquences pétrolières. Thèse de l'Université de Cergy-Pontoise, 224 pp.

Sherkati S. , Letouzey J., Frizon de Lamotte D. (2006) The Central Zagros fold-thrust belt(Iran) New insights from seismic data, field observation and sandbox modeling. TECTONICS, VOL. 25, TC4007, doi:10.1029/2004TC001766

Stöcklin, J., 1968, Structural history and tectonics of Iran: a review: AAPG Bull., v. 52, p.1229–1258.

Stöcklin, J., 1974. Possible ancient continental margins in Iran. In: BURK, C.A. and DRAKE, C.L., (Eds). The Geology of Continental Margins, Springer-Verlag. New York, pp. 873–887.

Szabo, F. and Kheradpir, A., 1978. Permian and Triassic stratigraphy, South-West Iran. Journ. Petrol. Geol, 1, 57–82

Taati Qorayem F. (2005) Stratigraphie séquentielle des systèmes carbonatés dans un contexte tectonique actif : le groupe de Bangestan (Albien-Turonien) dans le Zagros (Iran). Thèse de l'Université Bordeaux 3. 266, p 20

Tissot B.P. et Welte D.H. (1984) Petroleum formation and occurrence. Springer Verlag, Berlin

Ungerer P., Burrus J., Doligez B., Chenet P.Y. and Bessis F. (1990) Basin evaluation by integrated 2D modelling of heat transfer, fluid flow, hydrocarbon generation and migration. Bull. Am. Assoc. Pet. Geol. 74, 309–335.

Vandenbroucke M, Behar F., Rudkiewicz J.L., (1999) Kinetic modelling of petroleum formation and cracking implications form the high pressure/high temperature Elgin Field (UK, North Sea) Org. Geochem. 30, pp 1105–1125.

Verges, J., Homke, S., Garces, M., Karpuz, R., Sharp, I., Serrakiel, J., Emami, H. and Goodarzi, M., 2005.Timing of Onset and Destruction of the Foreland Basin in Lurestan, Iran: New Magneto-telluric Data. AAPG Convention, Paris, September 11–14, (Abstract).

Mechanical Constraints on the Development of the Zagros Folded Belt (Fars)

F. Mouthereau · O. Lacombe · J. Tensi · N. Bellahsen · S. Kargar · K. Amrouch

Abstract. We synthesize available structural, seismotectonics and microtectonics studies, mechanical modelling of the topography as well as stratigraphic constraints on the timing of Plio-Pleistocene folding and Zagros basin evolution in order to examine which mechanical behaviour would explain the development of the Zagros Folded Belt at both local and regional scale.

At the local scale we focus on the mechanism of cover folding and internal deformation of cover rocks. At the regional scale we focus on crustal rheology that led to the observed regional topography. Recent mechanical constraints derived from a critical wedge modelling of the regional topography together with available structural studies and seismotectonic studies confirm that the basement is necessarily involved in the deformation. Additionally, crustal rheology should involve a sufficiently strong lower crust to maintain the topography.

Stratigraphic data on the basin scale suggests that the deformation in the Zagros Folded Belt initiated by inversion of the inherited N-S and NW-SE-trending marginal structures in the early Miocene. At 5–3 Ma, the intraplate stresses have increased sufficiently in response to ongoing convergence to exceed the brittle strength of the pre-fractured basement and then to produce the initiation of the Zagros uplift. This event occurred simultaneously with the rapid development of cover folding until the Bakhtyari conglomerates were deposited unconformably on these structures as the fold growth decreased. The Hormuz salts at the base of the pile allowed the upper sedimentary cover to be decoupled from the basement but there is no evidence of independent development through time. This is confirmed by the kinematical consistency of the Mio-Pliocene small-scale faulting in the cover and seismogenic faulting reflecting the internal deformation of basement and cover, despite the occurrence of the thick Hormuz salt layer. Buckling of the cover rocks, rather than thin-skinned propagation of the Zagros Folded Belt, is proposed to be a more reliable mechanism to account for stratigraphic data, field observations, structural studies, microtectonic data and mechanical modelling.

We finally conclude that the overall thick-skinned deformation that followed the initial margin inversion was probably coeval with cover folding (buckling). The way basement and cover deform is thus remarkably different; the basement is pre-fractured so it shortens preferentially by faulting. In contrast, the folding (buckling) of the sedimentary cover developed with the assistance of plastic-viscous processes.

1 Introduction

The Zagros Mountains form a broad orogenic domain in Iran, approximately 2000 km long and 100–200 km wide in front of the Turkish-Iranian plateau (Fig. 1). The mountain range results from the accommodation of the convergence between the rifted continental margin of the Arabian plate and the Iranian continental block, which followed the closure of the neo-Tethys ocean during the Tertiary [Stocklin, 1968; Berberian and King, 1981; Koop and Stoneley, 1982]. The present-day convergence between Arabia and Eurasia is ~3 cm/yr and about 7 mm/yr is currently accommodated across the Zagros collision belt [Vernant et al., 2004].

The collision suture zone is outlined by the Main Zagros Thrust that separates the Sanandaj-Sirjan domain to the North from the Imbricate Zone and the Zagros Folded Belt (ZFB) to the South. The Sanandaj-Sirjan belt is a broad tectono-metamorphic belt which represents the former active margin of the Iranian microplate (Fig. 2). To the South, the Imbricate Zone and the Zagros Folded Belt, separated by the High Zagros Fault, form a large folded domain within the rifted Arabian continental margin. The Imbricate Zone is mainly composed of folded Mesozoic strata (Fig. 2) but locally along the Main Zagros Thrust, ophiolitic rocks, remnants of the obducted ocean or one of its derivatives (e.g., back-arc or fore-arc oceans) are preserved [Stoneley, 1990; Ziegler, 2001].

In this paper we focus on the Central Fars province of the ZFB (Fig. 2). This area is located between the Dezful-Izeh domain to the northwest recently documented by several studies [e.g. Blanc et al., 2003; Sherkati and Letouzey, 2004], and the Bandar-Abbas province at the southeastern extremity of the Fars area investigated by Molinaro et al. [2005]. The Central Fars is a 200 km-wide arcuate folded belt, which results from folding of a thick pile of sedimentary rocks up to 12 km in thickness [Stocklin, 1968] including Paleozoic, Meso-Cenozoic strata and Neogene syno-
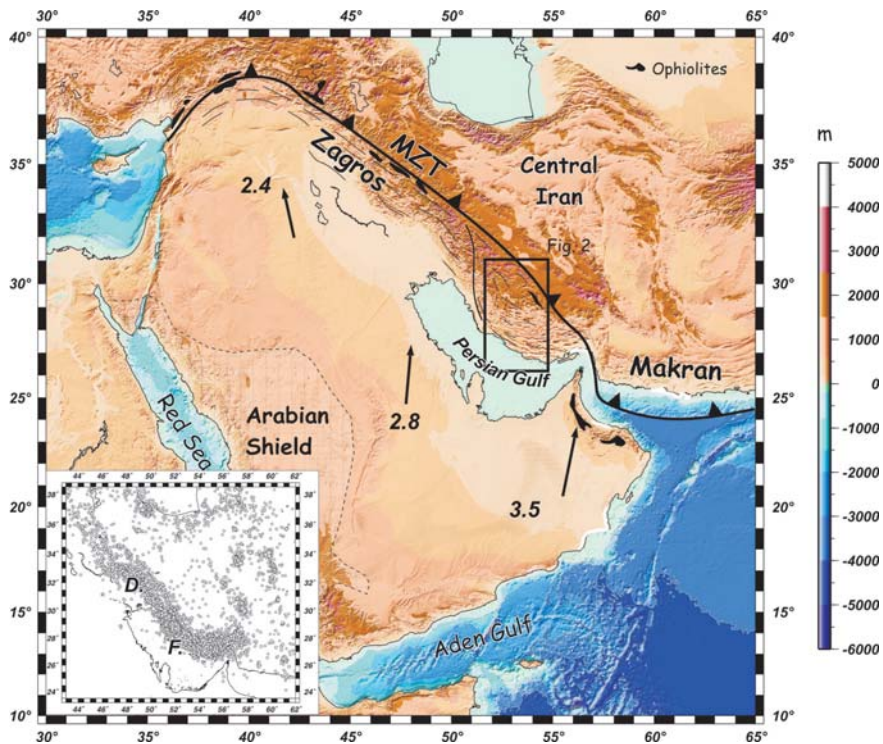
Fig. 1. Geodynamic framework of the Zagros Folded Belt. *Black arrows* show the present-day convergence between the Arabian plate and stable Eurasia deduced from current global plate motion Nuvel 1A [De Mets et al., 1994]. It predicts a present-day convergence of ~3±0.5 cm/yr oriented N-S on average at the front of the Zagros Mountains. The *grey rectangle* indicates the study area of the Fars province. The *inset* shows the distribution of earthquakes (2.4 <mb <7.4) in the Zagros collision belt with focal depths lower than 35 km issued from ISC and CMT catalogs (1965-2003). Many of the earthquakes in the Zagros correspond to events occurring in the basement. Inset : D. for Dezful and F. for Fars areas

rogenic deposits (Fig. 3). The deformation in the Fars area is characterized by periodic folding with axial lengths sometimes greater than 200 km (Fig. 2).

The exceptional geomorphic expression of folding is linked to the presence, within the folded pile, of the competent carbonates of the Asmari Formation, Oligo-Miocene in age, which is one of the main oil reservoirs in the Zagros. The Fars domain of the ZFB is limited to the West by a main structural, topographic and paleogeographic boundary: the Kazerun fault [Motiei, 1993; Sepher and Cosgrove, 2005] (Fig 1). It is a major N-S trending active right-lateral strike-slip fault inherited from the Late Proterozoic fault system of the Pan-African basement [Talbot and Alavi, 1996].

Cover folding is generally thought to be explained by the occurrence of a thick (up to 2 km) incompetent layer of salt at the base of the cover within the Eo-Cambrian series of the Hormuz Formation (Fig. 3). This basal décollement allows decoupling of the sedimentary cover from the underlying Precambrian series and crystalline basement. In addition to this main décollement, second-order shallower detachment levels lying in the sedimentary pile present in other parts of the Zagros Folded Belt [Sherkati and Letouzey, 2004; Molinaro et al., 2005a] may also have been potentially active during folding in our study area. One of the major issues that should be addressed is the mechanisms of folding that produce such a large folded belt. Indeed, no consensus exists so far on whether folding is simply thrust-related folding accommodating shortening in a

brittle cover [McQuarrie, 2004; Sherkati and Letouzey, 2004; Molinaro et al., 2005] or a consequence of buckling of the sedimentary rocks [e.g. Schmalholz et al., 2002; Mouthereau et al., 2006]. In the first type of models, it is the accommodation of deformation associated with cover thrusting which produces folding. In contrast, for the second type of models, folding is caused by mechanical instabilities within the competent cover overlying an incompetent layer. In this case, if faulting occurs it is not the cause but rather the consequence of folding. It is obvious that the mechanical implications of both models in terms of rocks rheology and mechanics of the folded belt are very different.

A second controversy concerns the recent uplift of the ZFB. If the timing of the Zagros uplift is relatively well constrained by a regional unconformity, two different mechanisms have been proposed to explain it: crustal shortening [Mouthereau et al., 2006] or thermal anomaly [Molinaro et al., 2005b]. Whatever the uplift mechanism, seismotectonic studies [Berberian, 1995; Talebian and Jackson, 2004; Tatar et al., 2004] together with subsurface data and cross-section balancing [Blanc et al., 2003; Sherkati and Letouzey, 2004] have suggested that basement-involved shortening may be essential to explain the anatomy of the Zagros folded belt.

Our objective in this paper is to examine which type of mechanical behaviour would better explain particular features observed in the Zagros folded belt at both local and regional scales. On the local scale we

Fig. 2. Simplified geological map of the Fars province of the Zagros Folded Belt (based on the National Iranian Oil Company [1977]. The Imbricate Zone to the North of the High Zagros Fault is clearly distinguished from the Zagros Folded Belt to the South by the lack of Oligo-Miocene deposits. The *heavy black solid line* displays the location of geological section of Fig. 4
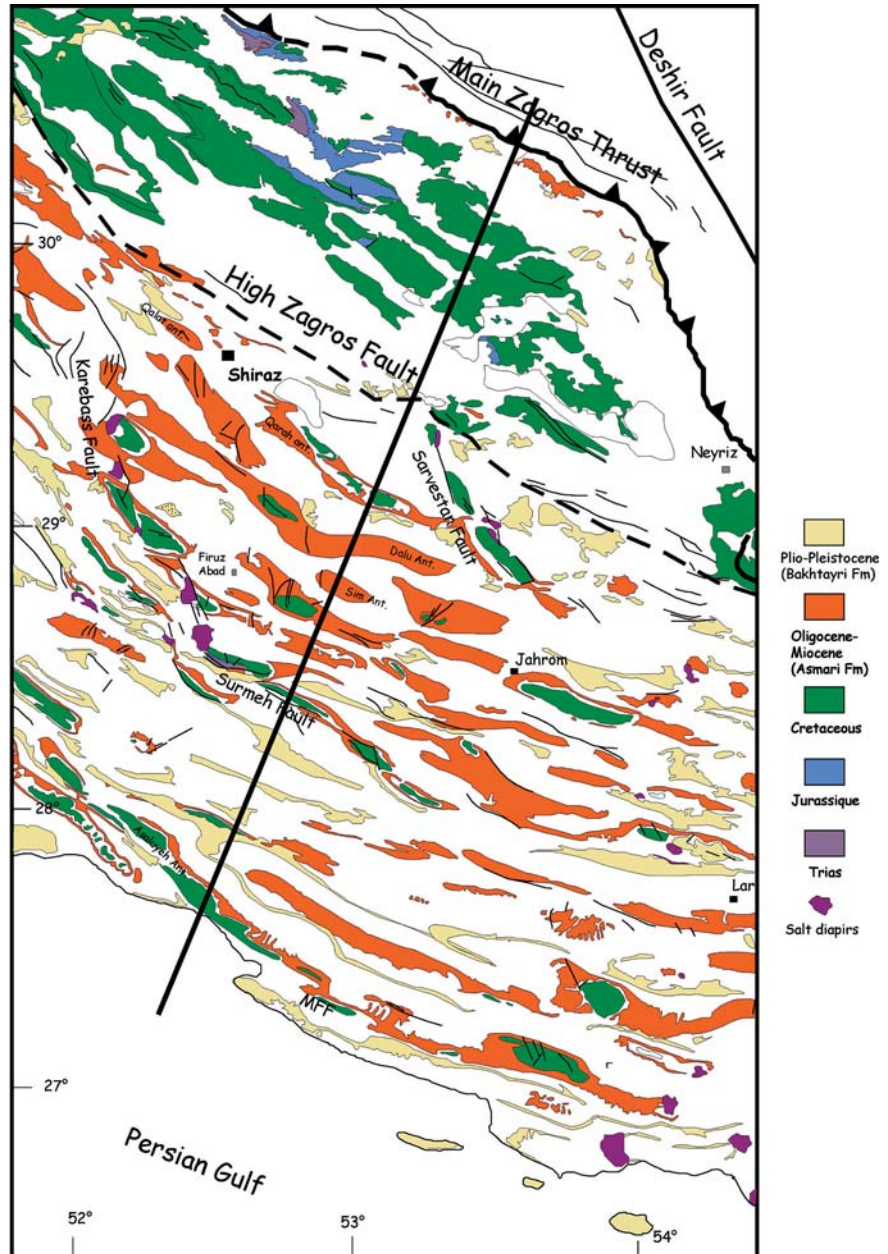

focus on the mechanics of cover folding and how internal deformation is accommodated in cover rocks. On the regional scale we focus on crustal rheology. To this aim, we synthesize available structural studies to constrain the first-order geometry of folds and the location of major basement thrust faults. These data are used to build a crustal-scale section of the Central Fars. Recent modelling of critical wedges [Mouthereau et al., 2006] as well as recently published seismotectonics and microtectonics studies [Lacombe et al., 2006] including recent results on calcite twinning [Amrouch et al., 2005] are combined together with new field observations to constrain the mechanics and the timing of deformation that prevailed in both the sedimentary cover and the basement.

2 From Rifting to Collision of the Arabian Margin: Stratigraphy of the Zagros Basin

We first introduce the Zagros collision belt in the framework of the opening then the closure of the Neo-Tethys. To this purpose, we summarize hereinafter the
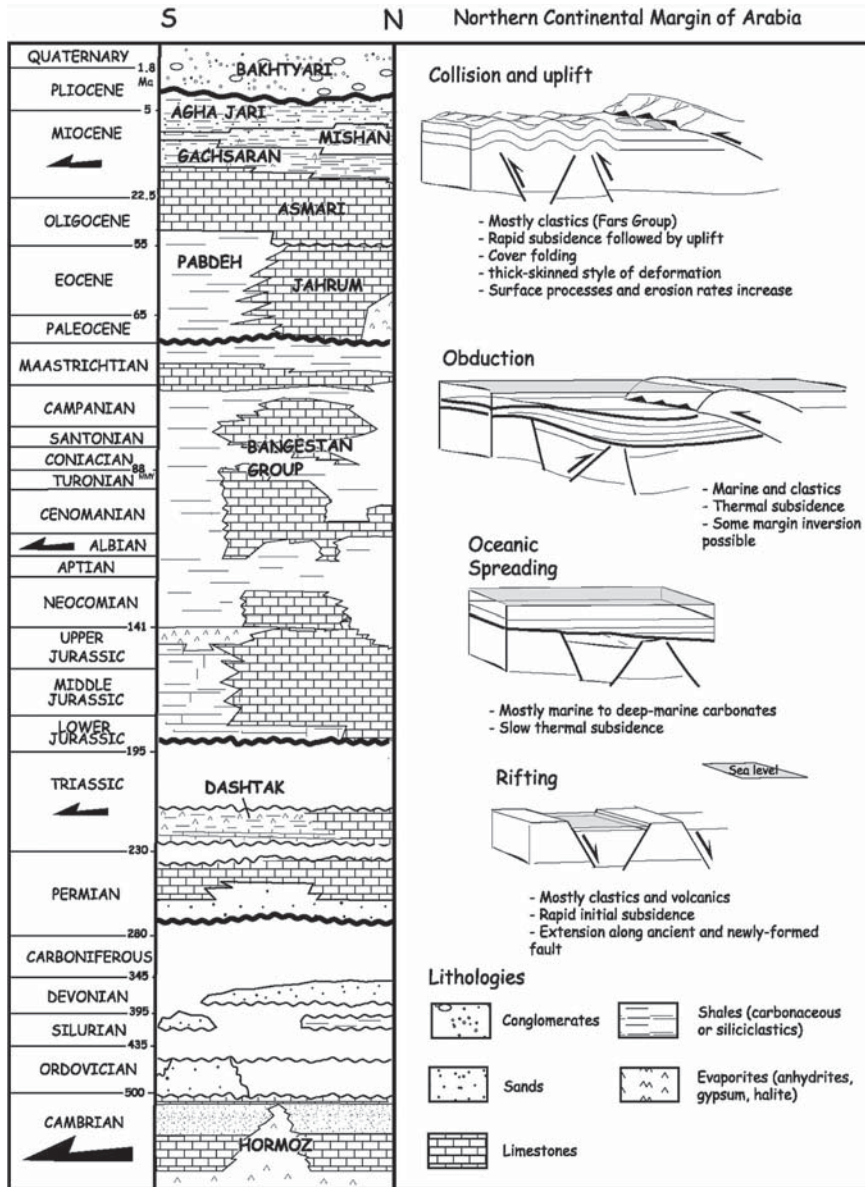
Fig. 3. Simplified chronostratigraphic chart and lithologies encountered in the Central Fars folded belt after [Motiei, 1993]. *Sketches on the right* show the main tectonic events reported on the Arabian continental margin. The basal décollement (*black arrow*) of the folded cover lies within the Eo-Cambrian salts of the Hormuz formation. *Other black arrows* refer to second-order detachment levels encountered in other parts of the Zagros belt

main tectonic events recorded on the Arabian continental margin in the ZFB since the Paleozoic.

Following the Hercynian orogeny, by the end of the Paleozoic, the Arabian lithosphere was stretched (Fig. 3). This episode is recorded in the Zagros basin by a main unconformity at the base of mid-Permian carbonates together with the occurrence of Permian clastics and volcanics in the High Zagros [Koop and Stoneley, 1982]. Extension affected the Zagros crystalline basement and produced a series of NW-trending grabens parallel to the current orientation of the Zagros Belt [Sepher and Cosgrove, 2004]. This fracture pattern is superimposed on an older Precambrian set of fractures in the basement trending N-S oblique to the

Zagros main trend [Talbot and Alavi, 1996]. The Neo-Tethyan rifting initiated at the Trias-Jurassic boundary. A major unconformity at the base of the Jurassic series records this transition. Since this time, the Arabian continental passive margin developed with a different sedimentological pattern than in Central Iran which has drifted away. During the Upper Cretaceous (Campanian), isopachs reveal the presence of a narrow trough located to the south of the present position of the MZT [Koop and Stoneley, 1982]. From the Upper Cretaceous-Paleocene limit until the Eocene the conditions of deposition changed dramatically and subsidence clearly increased to the NW, especially in the Dezful-Izeh domain of the ZFB [Koop and Stoneley,

1982; Sherkati and Letouzey, 2004]. The early Neogene period is characterized by deposition of the carbonates of the Asmari Formation on the Arabian continental margin and of the Qom Formation on the Iranian plateau. Biostratigraphic constraints yield an age ranging from upper Oligocene to lower Miocene for both formations (Chattian-Aquitanian boundary) [Schuster and Wielandt, 1999]. Post-Asmari clastics, known as the Fars Group including the Gashsaran, Mishan and Agha Jari Formations (Early Miocene to Pliocene), have a total thickness of up to 3000 m in the Fars area [Koop and Stoneley, 1982] indicating a rapid tectonically-controlled subsidence. This Group forms a progradational synorogenic sequence in the subsident Zagros foreland basin fed by the products of the erosion of the hinterland that was thickening and uplifting. This stage is considered by several authors as being controlled by the final closure of the Neo-tethyan ocean [Elmore and Farrand, 1981; McQuarrie et al., 2003; Agard et al., 2005] leading to the development of the Zagros orogeny.

The presence of local angular unconformities and disconformities within the folded belt indicates that the Arabian continental margin was probably deforming earlier than generally thought. For instance, Hessami et al. [2001] suggested that folding in the ZFB started at the end of the Eocene and then propagated in-sequence southwards in thin-skinned style. Sherkati and Letouzey [2004] suggested from isopach maps in the NW Zagros that compressive deformation might have been initiated in the upper Eocene-Oligocene times.

Ahmadhadi et al. [this issue] also report an early Miocene reactivation and inversion of NW trending inherited Tethyan normal faults in the Zagros foreland. This emphasizes that the Arabian continental margin underwent compression, inversion and basement-involved shortening during the early stage of the collision.

The last period of sedimentation is characterized by the deposition of alluvial conglomerates of the Bakhtyari Formation throughout the ZFB whose base is dated at 3 Ma in the Northeastern part of the ZFB [Homke et al., 2004]. As continental deposits, the Bakhtyari Formation is probably diachronous both along-strike and across-strike of the Zagros Folded Belt. Regarding the Fars Group whose first-order sedimentary characteristics support ongoing foreland basin evolution, the unconformable deposition of conglomerates on top of previously folded strata suggests that the main phase of shortening in the ZFB occurred before 3 Ma. It is worth noting that such changes in the type of deposition suggest modifications in the efficiency of erosion driven by global cooling well documented at that time [e.g., Molnar and England, 1990] or/and by uplift related to Zagros collision.

# 3 Mechanical Modelling of the Topography: a Critical Wedge Approach

3.1 Thin-Skinned versus Thick-Skinned Model: a Short Review

The presence of a thick and weak salt-bearing formation (i.e., the Hormuz Formation) has led for years to interpret the style of cover folding as resulting from fault-related folding that developed in a thin-skinned style, in agreement with the critical wedge model described by Davis and Engelder [1985]. These authors applied the theory of Coulomb wedges to thin-skinned frictional wedges overlying a ductile decollement. Such salt-based wedges are characterized by low topographic slopes and the absence of clear vergence of folding. The lack of clear fold vergence (Fig. 4) and the observations of low topographic slopes < 0.5° (Fig. 5) seem to support this model. Sand-box experiments involving silicone putty as analogous to viscous properties of salt décollement provided additional constraints on the way the spatial distribution of salt controls the shape of the Zagros Folded Belt and the sequence of deformation [Jackson et al., 1990; Weijermars et al., 1993; Costa and Vendeville, 2002; Bahroudi and Koyi, 2003]. Ongoing cover folding is further supported today by GPS surveys across the ZFB [Walpersdorf et al., in press] and is consistent with quaternary folding at the Mountain Front evidenced through dated tilted marine terraces [Oveisi et al., this issue].

On the other hand, seismotectonic studies over the last 20 years have provided several lines of evidence that the Precambrian basement is shortening and thickening [Jackson, 1980; Berberian and King, 1981; Ni and Barazangi, 1986; Berberian, 1995]. Active basement-involved shortening was confirmed by new accurate estimates of the depths of earthquakes [Talebian and Jackson, 2004; Tatar et al., 2004]. Furthermore, balanced cross-sections have shown that different topographic elevations of the base of the Paleozoic and Mesozoic Formations required basement involvement [Blanc et al., 2003; Sherkati and Letouzey, 2004; Molinaro et al., 2005a].

It consequently appears that the Zagros Folded Belt is actively deforming by superimposed thin-skinned and thick-skinned styles. In order to examine the relative involvement of both thin-skinned and thick-skinned deformation to explain the origin of the present topographic slope, a critical wedge modelling has been recently carried out [Mouthereau et al., 2006]. The main results are summarized hereafter. This work aimed at comparing the observed topographic slopes with that derived from modelling of 1) a shallow brittle wedge of sedimentary cover detached above a salt
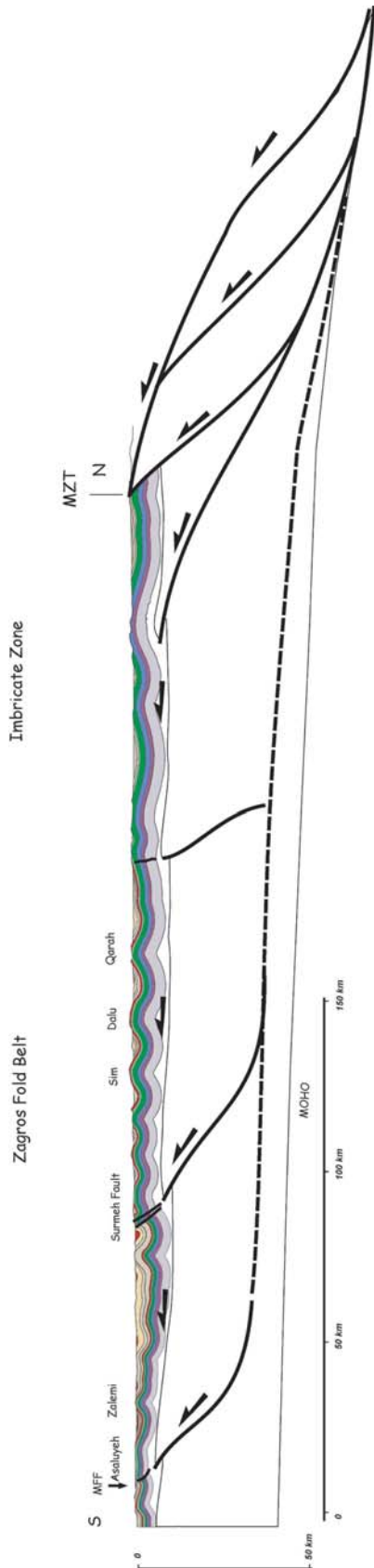
◀ **Fig. 4.** Crustal-scale geological section across the Zagros Folded Belt in the Central Fars. This section attempts at accounting for 1) faulting in the basement especially along the MFF and the Surmeh Fault, 2) decoupling between cover folding and seismogenic basement-involved deformation, 3) lack of evidence for fault-related folds features in the cover as well as 4) the variations in sedimentary rock thicknesses. Note the decrease of fold wavelengths from the Imbricate Zone toward the Surmeh Fault

décollement; 2) a thick brittle wedge of upper crystalline basement decoupled above a ductile lower crust.

3.2 Mechanical Modelling of the ZFB as a Thin-Skinned Critical Wedge

In this model the strength of sedimentary rocks is limited by a Coulomb failure criterion. The convenience of this simple model is that it can be directly compared with structural constraints in existing cross-sections, which assumes fault-related fold geometries, or with other models of salt-based fold-thrust belts. When the state of stress within the wedge attains a critical value, a critical taper is achieved, which is defined by the sum of the dip of its base β (taken positive toward the hinterland) and the dip α of its upper topographic slope (taken positive toward the foreland). The equation that provides the relationship between the wedge taper angle $\alpha+\beta$ and the basal shear stress τ_b and internal friction angle ϕ in the thrust wedge (after [Davis and Engelder], 1985]) is given by

$$\alpha + \beta = \frac{\beta + \left(\dfrac{\tau_b}{\rho_{sed}\, g H}\right)}{1 + (1-\lambda)\left(\dfrac{2}{[1/\sin(\phi)]-1}\right)} \tag{1}$$

where α is the topographic slope of the wedge (positive toward the foreland), β is the slope of the basement (positive toward the hinterland), λ is the pore fluid pressure ratio within the wedge, τ_b is the yield stress of the salt, ϕ is the angle of internal friction (between 30° and 40°), ρ_{sed} is the average volumetric mass of the wedge and H is the thickness of the wedge.

The forces in the salt resisting the advancement of the wedge are believed to be accommodated by simple shear. To constrain the value of the décollement dip β (basement top) we assumed that the top of the basement is parallel to the Moho discontinuity. The dip of the Moho ranges between 0.6° and 1° based on seismological constraints [Hatzfeld et al., 2003] and inversion of gravity data [Snyder and Barazangi, 1986], respectively. Taking into account the slope of the basement

Fig. 5. a Topography (SRTM data) and main structural features and **b** topography derived from SRTM data and topographic slopes estimated along sections 1, 2 and 3 located in a. The folded sedimentary cover is decoupled from the basement above the Hormuz Salt Formation. The present-day and long-term deformation within the basement is attested along the MFF and the Surmeh Fault in agreement with the position of the main basement faults presented by several works [Berberian, 1995; Talebian and Jackson, 2004]. Focal mechanisms reveal that the basement is deforming and thickening along distributed faults probably inherited from Permo-Triassic rifting. Fault plane solutions (4.6 <Mw < 6.7) [from Talebian and Jackson, 2004] are shown with focal spheres in light gray. Focal mechanisms of small earthquakes (1.7 < ML < 4.1) determined from local network [Tatar et al., 2004] are shown with black focal spheres
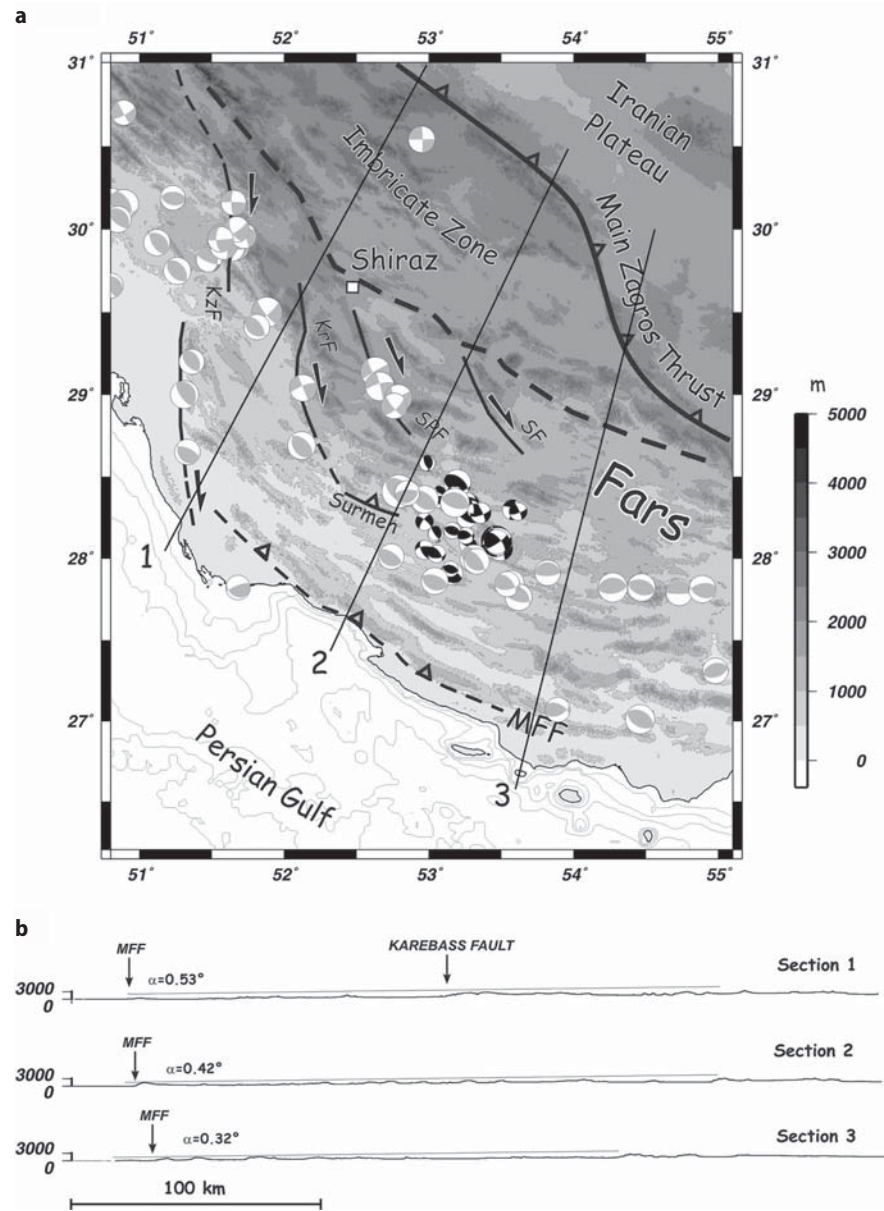
derived from restored sections [McQuarrie, 2004] we finally adopted a value of 0.5°.

The "steepest" topography or the highest topographic slope (~ -0.33°) is obtained for the highest basal shear stress (443 kPa) and the lowest angle of internal friction (30°) (Fig. 6a). The lowest topographic slope (~ -0.39°) is obtained for a lower basal shear stress (11 kPa) and a higher internal friction (40°). It is clear, despite relatively important variations between each model, that the predicted topography is essentially flat. This result reveals that the sedimentary cover and the underlying salts are both remarkably thick in the Zagros. As a result, the ratio $\tau_b / \rho_{sed}gH$ in Eqn (1) is very small of the order of 10^{-3}. This illustrates that

when a thick layer of salt (relatively to its overburden) forms the basal décollement it is generally too weak and cannot support the growth of significant topography. We concluded that the observed topographic slopes across the ZFB can not be reproduced by a salt-based wedge model.

3.3 Mechanical Modelling of the ZFB as a Thick-Skinned Critical Wedge

An alternative is to consider that the Zagros topography results from the thickening of the brittle basement, in agreement with current seismogenic activity,
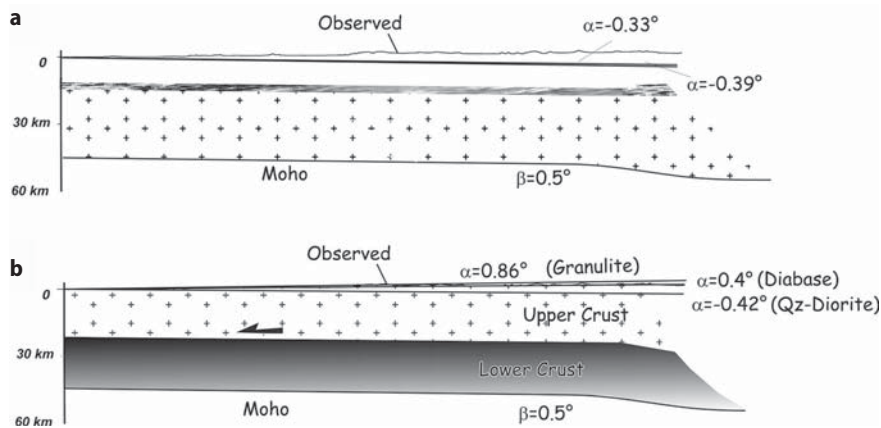
Fig. 6. a Topographic slopes modelled by a thin-skinned wedge of brittle materials overlying a ductile décollement. **b** Topographic slopes modelled by a thick-skinned critical wedge of brittle upper crust sliding over a ductile (non-Newtonian) lower crust for which different rock types are used [after Mouthereau et al., 2006]

that is decoupled above a viscous lower crust. Studies of receiver functions revealed a crustal thickness of 45 km and a ~25 km-thick lower crust [Hatzfeld et al., 2003]. This is consistent with the deepest small earthquakes, observed at 18 km by Tatar et al. [2004] and the depth distribution of major and moderate earthquakes shown by Maggi et al. [2000]. At such depths, temperature-activated ductile deformation in the crust predominated and dislocation creep of minerals occurs. The deviatoric yielding stresses in the lower ductile crust thus follow a power law that is dependent on temperature and strain rates. In order to cover a wide range of viscosities, different rock types such as quartzite for weak lower crust and mafic composition like diabase, quartz-diorite or granulite for stronger lower crust were tested. A cold crustal geothermal gradient of 10–15°C/km was assumed in agreement with temperatures required, at Moho depth, to produce continental subduction.

Assuming a quartz-diorite rheology, a negative value of -0.42° (taper angle of 0.08°) is obtained for α (Fig. 6b). In this case, similarly with the salt-based wedge hypothesis, the lower crust is too weak and cannot maintain the observed topography. In contrast, when stronger rheologies (diabase or granulite) are used, positive topographic slopes of 0.4° and 0.86°, respectively (equivalent to tapers of 0.9° and 1.36°), are obtained in agreement with the observed topography.

In contrast to the thin-skinned hypothesis, we demonstrate that the shortening of the basement above a viscous lower crust is able to reproduce the observed topography. We note that rock composition in the lower crust should necessarily comprise sufficiently strong (mafic) materials. We conclude that although thin-skinned deformation obviously occurs, basement-involved shortening is responsible for the present-day topography.

After having demonstrated that basement-involved shortening is the only viable mechanism to account

for the current regional topography, we now examine both geological observations and constraints from the topography, which support long-lived basement tectonics.

4   Evidence for Long-Lived Faulting in the Basement

### 4.1   Topographic Steps Related to Basement Faulting

Despite the apparent continuity of structures, morphology and surface geology, two locally important topographic steps and structural features are recognized: the Mountain Front Fault (MFF) and the Surmeh Fault, 100 km apart (Fig. 5). Using wavelengths analysis of the topography, these faults clearly affect the overall topography over distance comprised between 40 km and 100 km [Mouthereau et al., 2006].

In the following, we have used the nomenclature defined by Berberian [1995] for major faults. The MFF [Berberian, 1995] is also called the Mountain Front Flexure by Falcon [1961] or the Zagros Frontal Fault by Sepher and Cosgrove [2004]. These latter authors named the Surmeh Fault, the Mountain Front Fault.

The Mountain Front Fault is not directly observable in the field. Its topographic expression is however clearly depicted along the coastline of the Persian Gulf as it is formed by a girdle of en-échelon folds over more than 200 km (Fig. 7). Topographic profiles show a clear topographic step, across the MFF, which is outlined by the uplift of the local base level up to 700 m (e.g., Asaluyeh anticline, profile 1 of Fig. 7). The second topographic offset is about 500 m and occurs across the faulted Surmeh Anticline, one of the few folds of the ZFB where Paleozoic strata are exposed.

Fig. 7. *Top*: Landsat 7 (TM) image of the southern Central Fars province. Large-scale folds bordering the Persian Gulf and related to the Mountain Front Fault (including the Asaluyeh anticline) are well depicted. Topographic profiles across these folds are shown *below*. All topographic profiles are plotted with a common reference frame, i.e. their fold axes
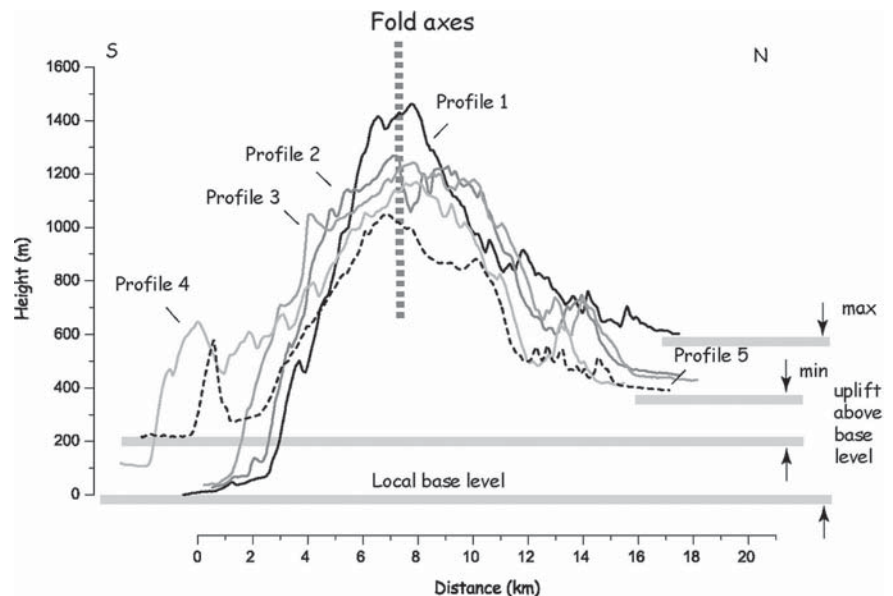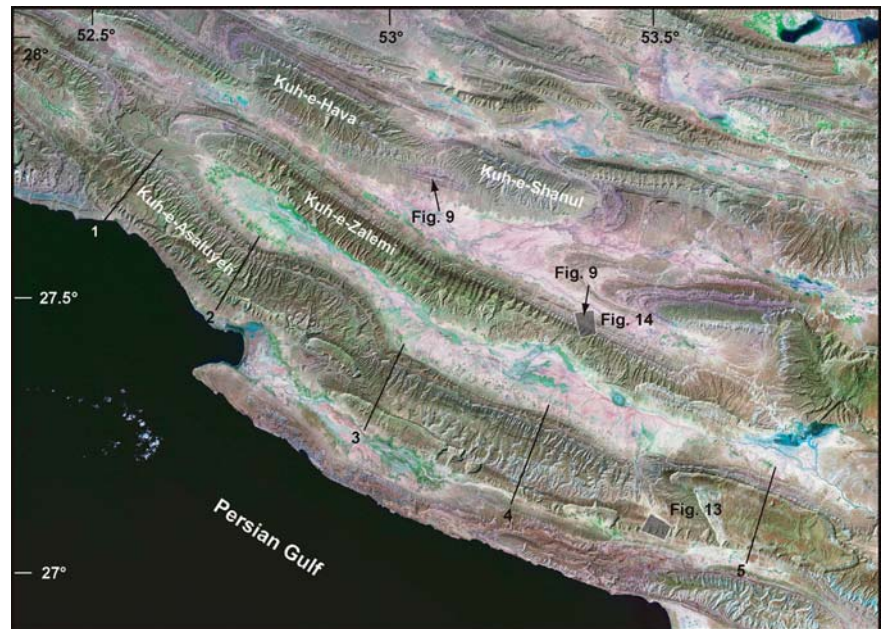
4.2 Current State of Stress in the Basement

Most of the thrust earthquakes in the Zagros Folded Belt occur between the coast of the Persian Gulf and the Surmeh thrust zone (Fig. 5). In this context, the present-day activity of the Mountain Front and Surmeh faults has been demonstrated by extensive seismotectonic analyses by Berberian [1995]. For instance, recent destructive earthquakes like the Ghir (1972, $M_S=6.9$) and the Lar (1966, $M_S=6.2$) earthquakes [Berberian, 1995] aligned along the trace of the Surmeh topographic step and form the Surmeh-Ghir thrust

zone. The Surmeh-Ghir thrust zone is connected with the Karebass Fault, a major right-lateral transverse fault rooted into the basement (Fig. 5). For the MFF, Berberian [1995] has suggested that the location of the Asaluyeh anticline coincides exactly with the trace of a major seismic trend along which large-to-moderate earthquakes occur on buried, high-angle basement reverse fault segments.

The present-day stress regimes in the Fars have been recently derived from available focal mechanisms of earthquakes [Lacombe et al., 2006]. The inversion process applied to a set of moderate earthquakes [Talebian and Jackson, 2004] and microearthquakes [Ta-

tar et al., 2004] led to subhorizontal σ1 axis trending N209°(±15) and N206°(±5) respectively. Noticeably, the value of the Φ=(σ2-σ3/σ1-σ3) ratio in both cases is low (<0.3) suggesting σ2/σ3 stress permutations. Such a regime and the absence of clear structural relationships between strike-slip/reverse mechanisms and major strike-slip/reverse (Surmeh-Ghir) faults shows that basement deformation depicted by microearthquakes at the local scale is rather distributed and occurred under both reverse faults and right-lateral strike-slip faults.

The computed N020–030° compressional trend is in good agreement with the pattern and kinematics of active faults in the western Fars [Baker et al., 1993; Berberian, 1995]. It is also consistent with current geodetic (cover) and seismic (basement) strain shortening axes which are coaxial and oriented N010° on average [Masson et al., 2005].

4.3 Long-Lived Basement Thrusting: Constraints from Middle Miocene Basin Geometry

The Mishan Fm is a well-defined transgressive interval within the Fars Group outlined by the deposition of limestones, silts and bioclastics throughout the Zagros foreland basin. In the Zagros basin, the isopachs of the Mishan Formation provide further constraints on the paleo-topography at the time of deposition, i.e. in Middle to Upper Miocene times (Fig. 8).

The base of the Mishan Fm varies from about 600 m depth at the latitude of Firuz Abad and attains about 900 m southward. A large depocenter developed in the Coastal Fars area between the MFF and the Surmeh Fault and a large portion of the northern Fars domain, roughly limited by the Sabz-Pushan and the Karebass strike-slip faults, is uplifted. Since the subsidence is more pronounced in the depression located in the hangingwall of the Karebass-Surmeh fault, we infer the possibility that basement-involved deformation locally affected the Zagros basin during the Middle Miocene. On average, the isopachs south of Shiraz suggest that the overall subsidence in the basin was controlled regionally by plate flexure and locally by basement thrust loading.

At the southern border of the Zagros basin, in the forelimb of the Asaluyeh anticline, the Gashsaran Formation and the base of the Mishan Formation are missing above the Asmari Limestones [Mouthereau et al., 2006]. This field observation is correlated with isopach maps of the Neogene strata showing at larger scale that the Mishan are continuously thinning toward the MFF. Furthermore, it is also across this anticline that the morphological step is the largest suggesting long-lived basement thrusting along the
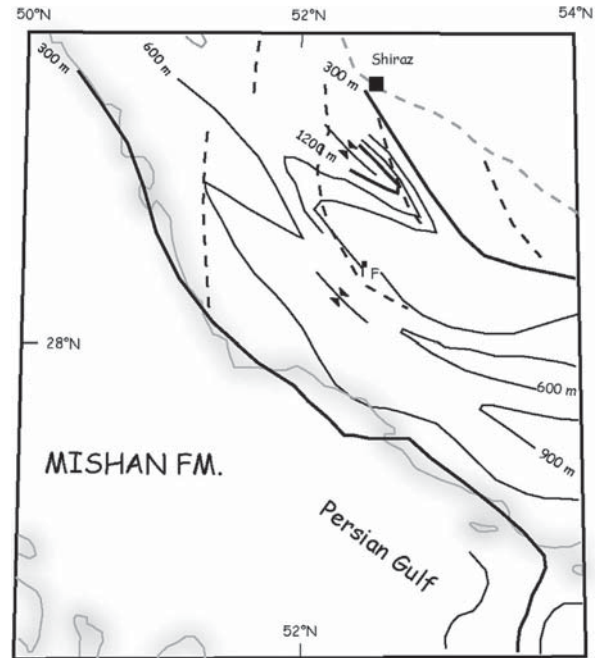
Fig. 8. Isopach maps of the Mishan Formation. Equidistance is 300 m. Main depocenters are shown by *converging arrows*. F: Firuz Abad. *Black dashed lines* correspond to major active transverse structures, e.g., the *one passing* close to Firuz Abad depicts the position of the Karebass-Surmeh Fault

MFF (Fig. 7). We suggest that this stratigraphic hiatus was locally uplifted above sea-level during the upper Miocene. This might be a consequence of basement involvement along the buried MFF, but alternative possibilities such as forebulge uplift or local amplification due to cover folding should be also envisaged.

Whatever the style of deformation, this would suggest that the deformation had already reached the current location of the Mountain Front Fault by Middle-Miocene times.

In summary, it appears that basement-involved deformation occurs mainly by faulting and initiated at least in the Middle Miocene during an early phase of margin inversion.

5   The Main Phase of Cover Folding: Evidence from Unconformities within the Agha Jari and Bakhtyari Formations

We have seen that basement-involved shortening along the Surmeh-Karebass faults segment or the MFF initiated in the Middle Miocene prior to the main phase of cover folding.

On the other hand, GPS studies [Walpersdorf et al., in press] and dated tilted marine terraces [Oveisi et al., this issue] indicate that cover folding is currently ac-

tive with a significant accommodation of shortening across the MFF. According to field observations, the existence of intraformational unconformities within the Agha Jari Formation has been recognized for years in the Dezful or Lorestan areas [e.g. Hessami et al., 2001; Homke et al., 2004]. This places strong constraints on the timing of the initiation of folding in the cover and the rate at which these folds developed. However, no evidence of such unconformities has been described in the Central Fars so far.

During our field investigations in the Central Fars, numerous unconformities or disconformities have been reported within the Agha Jari Fm. However, many of them are not progressive unconformities but rather correspond to unconformities of limited extension, typically of several tens of meters, probably not related to tectonics (Fig. 9). On the other hand, when synclinal sections were available, several progressive intraformational unconformities were observed that are clearly correlated with fold growth.

The first example of folds that clearly display progressive intraformational unconformities within the Upper Agha Jari Formation is found to the North of Shiraz in the vicinity of the Qalat anticline (Fig. 10).

The total thickness of the Agha Jari Formation and Bakhtyari Formation reaches 700 m and form cliffs on both limbs of the Qalat fold. The older strata, i.e. the Upper Agha Jari Fm, show progressive unconformities revealing coeval fold activity to the north. The Bakhtyari strata do not display progressive unconformities but are rather onlapping the underlying folded strata of the Upper Agha Jari Fm toward the crest of the fold.

Another observation of progressive unconformities is found in association with the growth of the Karbasi anticline about 200 km southeast (Fig. 11). Despite the large distance between both folds several similarities are found. For instance, the cliff formed by the Bakhtyari conglomerates displays no evidence of intraformational unconformity. In contrast, the lower and older strata belonging to the Agha Jari Fm show progressive unconformities that can be related to the development of the Karbasi anticline.

Though more observations and stratigraphic constraints are required to draw an accurate image of the sequence of folding, we suggest that the upper Agha Jari strata are synfolding whereas the overlying Bakhtyari conglomerates are mainly post-folding.
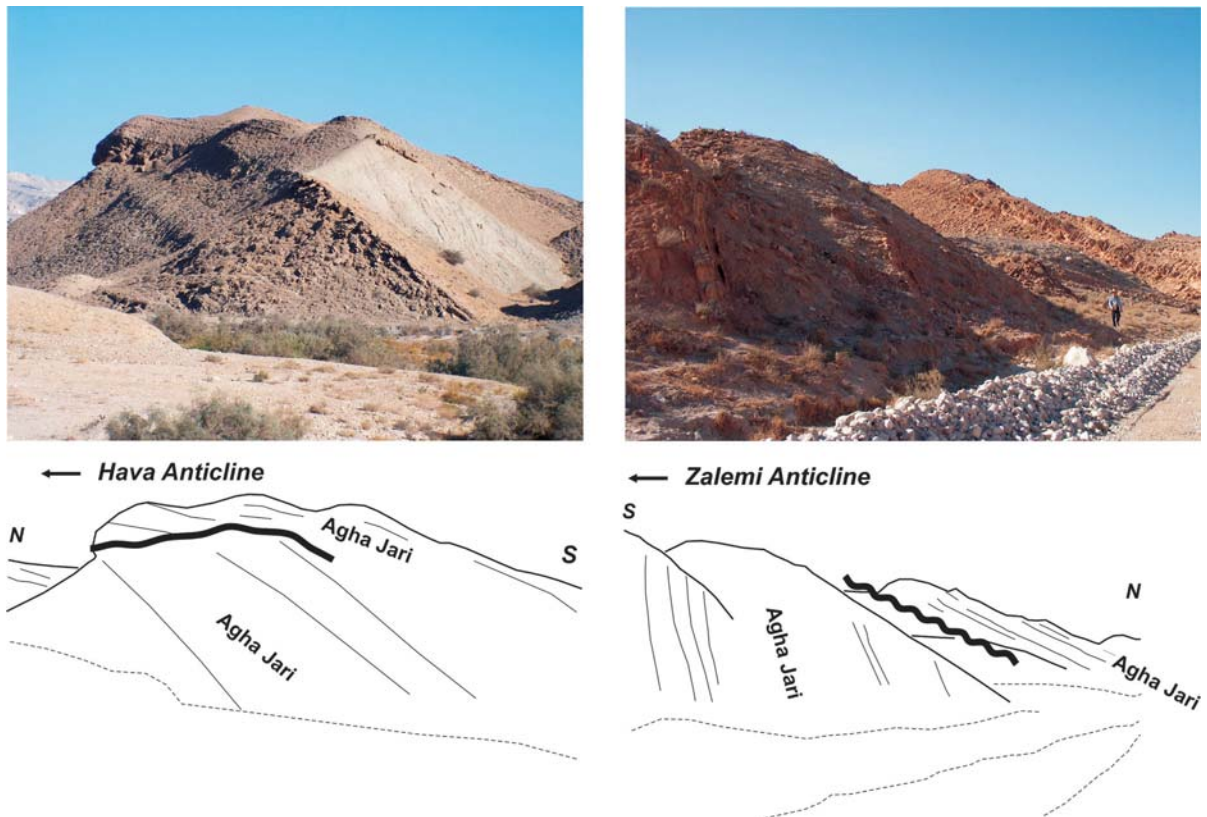

Fig. 9. Examples of intraformational unconformities within the Agha Jari Formation of two fold limbs located in the Southern Central Fars (see Fig. 7 for location). These unconformities are not progressive and of local extent. They are probably not related to fold activity but rather to sedimentary processes in the ancient alluvial plain

Fig. 10. Intraformational unconformities within the upper Agha Jari strata North of the Qalat anticline (see Fig. 2 for location). The upper alluvial conglomeratic beds of the Bakhtyari Fm onlap the older strata of the Agha Jari thus suggesting a slowing down of fold uplift relatively to sedimentation rates
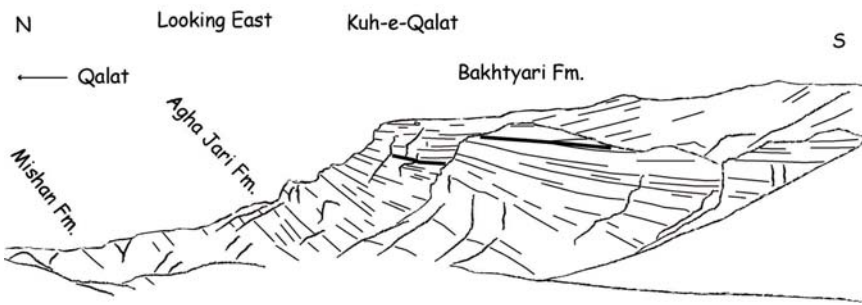
Fig. 11. Intraformational unconformities within the upper Agha Jari strata to the South of the Karbasi anticline (see Fig. 2 for location). The cliff shows the upper alluvial conglomeratic beds of the Bakhtyari Fm. They clearly onlap the older strata of the Agha Jari again suggesting a slowing down of fold uplift relatively to the sedimentation rates
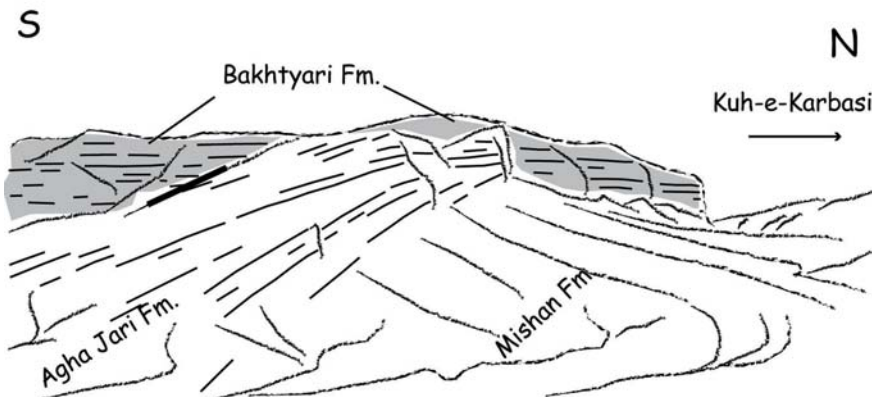
The same chronology has been proposed in the Dezful area [e.g. Homke et al., 2004]. In the Coastal Fars, this inference is supported by the observation that the youngest conglomerates usually unconformably overlie folded strata. The duration of synfolding unconformities ca. 2–2.5 Ma. is approximated by the age of the top of the folded strata, i.e. Upper Agha Jari Fm, and the age of the base of the Bakhtyari Fm provided by Homke et al. [2004] in the Dezful-Izeh area.

This indicates that the folds growth was initially rapid in association with limb rotation. The lack of evidence for diachronous folding further suggests that folding rather occurred coevally across the strike of the belt. Moreover, the geometry (onlaps) of the Bakhtyari conglomerates with respect to underlying folded Agha Jari Formation reveals that the rate of fold uplift decreased with respect to the rate of deposition of the Bakhtyari conglomerates in the Zagros foreland. This provides constraints on the overall mechanism which produced rapid fold development coevally across the Zagros Folded Belt.

6   Long-Term Rheology of Folded Cover Rocks: Insights from Folding Geometry and Mesoscale to Microscale Tectonic Studies

Figure 4 shows a schematic 300-km-long cross-section of the Zagros Fold Belt including the Imbricate Zone. This section has been constructed using structural constraints from NIOC geological maps [National Iranian Oil Company, 1977], structural dips at surface, variations in layers thickness within the Meso-Cenozoic strata based on well data [Motiei, 1993]. The lack of faults at the surface except where active basement thrusts are reported (e.g. MFF, Surmeh, Karebass, Sabz-Pushan fault zone) makes dubious a systematic involvement of thrusting to explain folds in the sedimentary cover. We do not exclude however, when shortening increased and fold limbs rotated, that faulting occurred due to deformation in the fold hinges, but this is not supported by any field observations in our study area.

6.1   Distribution of Fold Wavelengths and Topographic Signature of Folding

Figure 12 shows the distribution of fold wavelengths for 149 folds measured between two successive synclines, in the Eastern and Western Fars areas. A monomodal distribution of the fold widths clearly appears on the graph showing a dominant wavelength of cover folding between 10 and 20 km representing 70% of the measured folds. One important parameter that mechanically controls the observed dominant wave-

length of folding is the thickness of the deformed competent units. Despite some scatter, the Gaussian distribution of fold widths would suggest that a single main competent level is involved. It is worth noting that the presence of intermediate detachment layers described in the Dezful and Bandar-Abbas areas [Sherkati and Letouzey, 2004; Molinaro et al., 2005] is weakly supported by field observations in the Central Fars. Though probably not exhaustive, field observations carried out in the Central Fars only reported the possible involvement of intermediate detachments close to the MFF (Figure 13). Inversely, when well-known incompetent layers such as the Gashsaran Fm can be observed at the surface, they are not involved in the compressional deformation (Figure 14). If other potential detachment like the evaporitic Dashtak Fm (Trias) present only in the Coastal Fars accommodates folding it would lead to lower dominant wavelengths of folds, which are not observed. It thus comes that intermediate detachment layers are of second-order importance to explain the wavelength of folding. Indeed, they only affect the superficial folding style at a scale lower than the dominant wavelength of folding.

As a consequence this would not change our main conclusion that folding is mechanically explained to a first-order by one single detachment level.

A simple relation might exist between the depth to which crustal deformation occurs and the wavelength of its topographic expression; the thicker the deformed unit the larger the wavelengths of deformation. The analysis of wavelengths in the topography can be also qualitatively used as a proxy to distinguish different
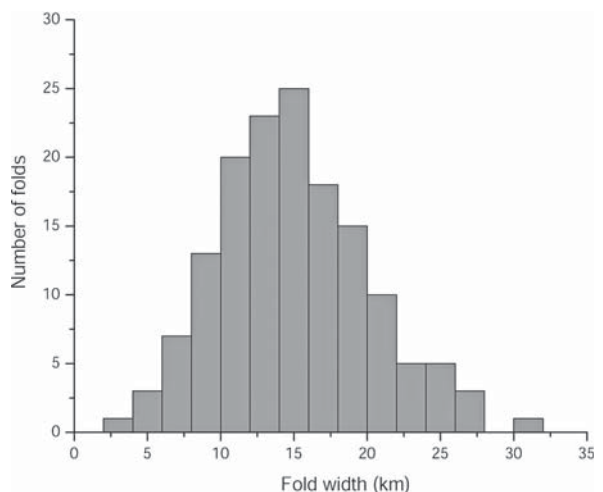
Fig. 12. Distribution of fold widths measured for 149 anticlines in the Fars (see text for explanation). Fold widths have been estimated as the distance between two adjacent synclines independently from the stratigraphy of the folded strata. 101 folds (70% of the measured folds) have wavelengths between 10 and 20 km
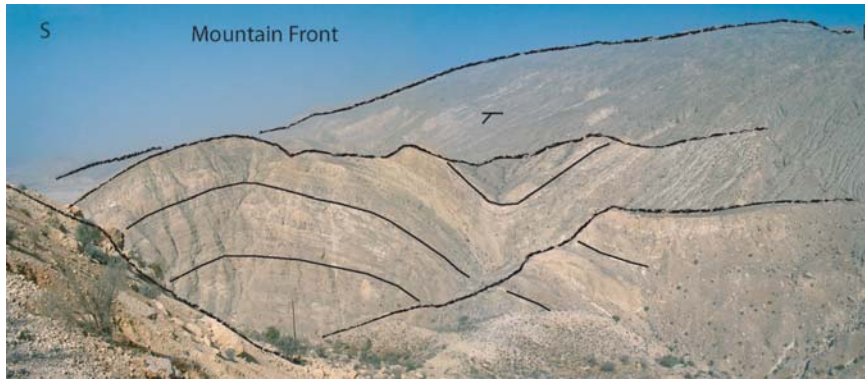
Fig. 13. Example of smaller scale folding in the southern limb of one of the larger scale folds in relation to the Mountain Front Fault (see location on Fig. 7). Such features are atypical in the Central Fars domain and mostly observed along the Mountain Front

Fig. 14. Northern limb of the Zalemi anticline (see location on Fig. 7). Note the normal stratigraphic succession in the Fars Group (Mishan Fm is not visible on this photograph) above the Asmari carbonates. Like many other examples over the Central Fars, the incompetent layers of the Gashsaran Fm (mainly gypsum with marls) do not act as an intermediate detachment

levels of deformation [Mouthereau et al., 2006]. Figure 15 shows 2-D analysis of topographic wavelengths along the strike of the Fars folded belt along three topographic sections. High-pass and low-pass filters were applied to the 3' x 3' gridded SRTM topography.

For example, when wavelengths larger than 40 km, i.e. the maximum wavelength of cover folding (Fig. 15), are removed, the remaining topography of folds shows amplitude reaching 1000 m. These are found 1) close to major active basement fault zones, e.g., the sharp increase of the elevation near the Gulf corresponds to the position of the MFF (Sects 2 and 3), 500 to 1000 m are correlated with the position of active transpressive strike-slip faults such as Kazerun (KzF), Karebass (KrF), Sabz-Pushan (SPF) or Sarvestan (SF) faults; 2) for folds flanked by more deeply incised synclinal valleys or 3) for folds whose development is perturbed by the ascent of salt diapirs, especially in the southern-eastern part of the ZFB (Sect 3). Despite such local perturbations, the deformation associated with folding is remarkably homogeneous in amplitudes and wavelengths and is consequently not visible on the residual topography. This topographic pattern again suggests, in addition to the distribution of fold widths, that the mechanism of folding is primarily controlled by the thickness of the competent cover. Independently from mechanical assumptions, similar conclusions are also

supported by balanced cross-sections [McQuarrie, 2004; Sherkati and Letouzey, 2004]. The quasi-sinusoidal shape of the short-wavelength component of the topography related to folding appears simply superimposed onto larger wavelengths, i.e. larger than 40 km, which reflects basement-involved thickening (Fig. 16).

6.2 Mechanical Behaviour of the Cover Sequence: Constraints from Mesoscale Faulting and Microscale Calcite Twinning

Field observation of folding has revealed that mesoscale faulting is often associated with shear calcite fibers in the few carbonaceous beds of the Fars Group or in the Asmari Formation and gypsum fibers in local evaporite facies from Gachsaran Formation and Agha Jari Formation. In addition, pervasive pressure solution accompanied faulting as evidenced by widespread stylolitization. Hydraulic breccia in some sites indicates that local high fluid pressures assisted faulting. Moreover, analysis of calcite twin strain (Fig. 17) has been carriedout for limestones of the Pabdeh-Gurpi, Asmari-Jahrom, Gachsaran and Mishan Formations [Dissez, 2004; Amrouch, 2005]. The twin shapes reveal that the deformation occurred at temperature lower than 150–200°C and that internal strain did not
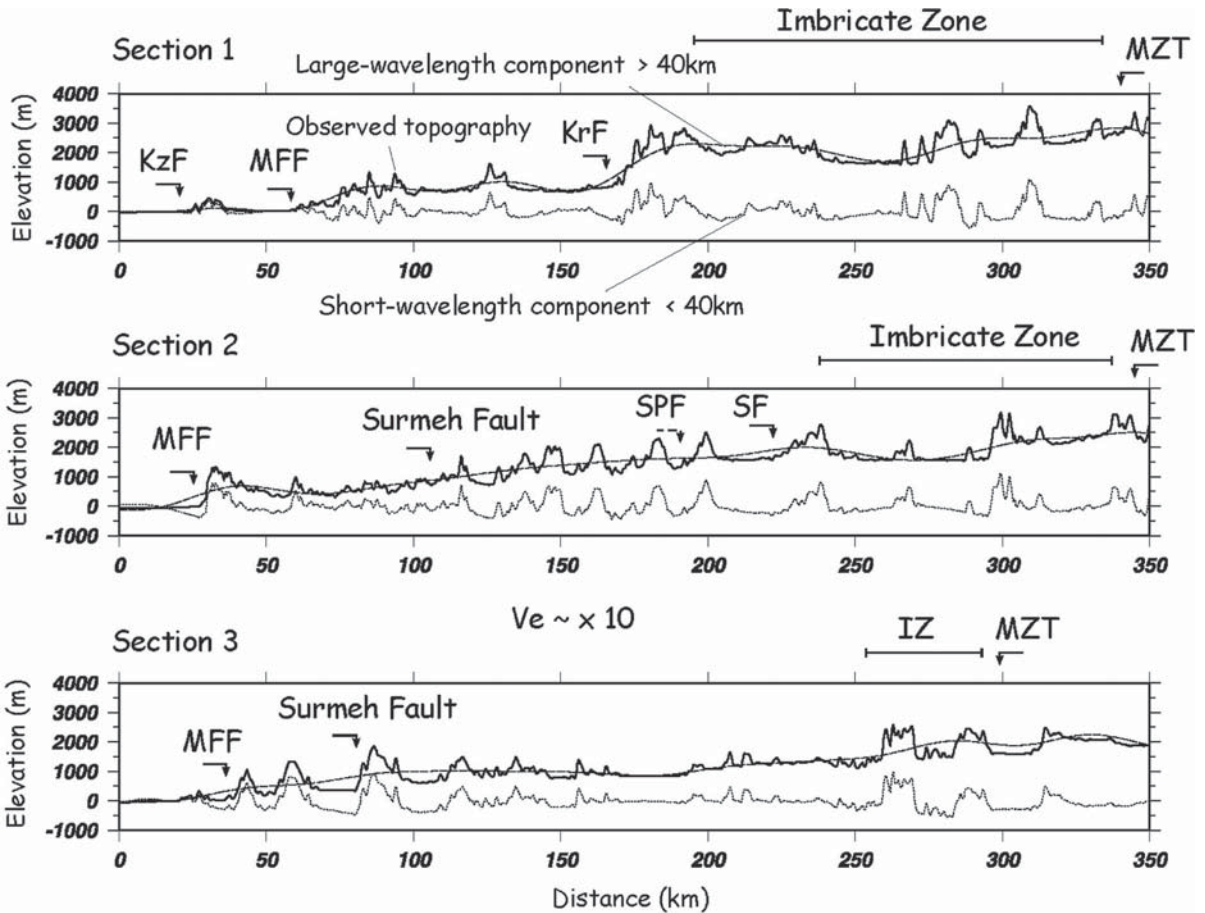
Fig. 15. Wavelength analysis of the topography along transects 1, 2 and 3 (whose location is also presented in Fig. 5). The profiles show the observed topography (*solid lines*) and the filtered topography for both large- and short-wavelength components of the topography (*dashed and dotted lines, respectively*). The main fault zones are the MFF (Mountain Front Fault), SPF (Sabz-Pushan Fault), KzF (Kazerun Fault), KrF (Karebass Fault), SF (Sarvestan fault) and Surmeh (Surmeh Fault). In the northern part of the Fars, the MZT (Main Zagros Thrust) and the Imbricate Zone are also shown

exceed 3–4%. This suggests that even at low depths, viscous-plastic processes were active in cover rocks and has assisted the fold growth.

The reconstructed paleostress orientations from the inversion of calcite twins show a homogeneous mean N020° compression throughout the folded belt and the

Fig. 16. Schematic representation of the way the different wavelengths of deformation including basement-involved shortening and cover folding interact

southern part of the Iranian plateau [Amrouch et al., 2005]. This result is consistent with the compressional stress orientations obtained from the inversion of fault slip data and present-day compression derived from the inversion of focal mechanisms of earthquakes [Lacombe et al., 2006].

Noticeably, all computed stress tensors show a low $\Phi = (\sigma_2 - \sigma_3 / \sigma_1 - \sigma_3)$ ratio suggesting that σ_2 and σ_3 are comparable, accounting for the coeval occurrence of reverse and strike-slip faulting in the cover and the basement. These results suggest that the Hormuz layer, although acting as a major cover-basement décollement and as a mechanical boundary for the upward propagation of most earthquakes, poorly decouples the states of stress within the cover and the basement.

In addition, due to the existence of a constant critical resolved shear stress (CRSS) for twinning, differential stress magnitudes related to a given stress tensor can further be estimated. For a given palaeostress

Fig. 17. Photograph illustrating examples of calcite twins formed in vesicles of this shallow-water bioclastic carbonate within the Gashsaran Formation (Meymand fold, northern Central Fars)

orientation, the (σ1-σ3) values correspond to the peak differential stresses attained during the tectonic history of the rock mass.

To a first-order, differential stress values corresponding to the post-folding N020° compression are low and lie within a nearly similar range (45 ± 15 MPa) in the southern Iranian plateau and across the ZFB [Amrouch et al., 2005]. These differential stress values across the ZFB unexpectedly differ from previously reported stress values in fold belts, which are much higher (e.g., 90–150 MPa in the Idaho-Wyoming thrust belt [Craddock and Van der Pluijm, 1999]) and show a strong decay across both the fold belt and the undeformed foreland (e.g., from 100 to 20 MPa in the Sevier-Appalachian forelands: [Van der Pluijm et al. 1997]).

These low and homogeneous stress values highlight major differences in the mechanics of the ZFB compared to other fold belts. The fact that the sedimentary cover sequence is currently aseismic would support that a significant part of the convergence is accommodated by internal ductile mechanisms in the rocks' mass including pression-solution or plastic strain.

The relatively narrow range of variation of differential stress magnitudes across the ZFB agrees with the homogeneously distributed shortening in the folded cover, where no deformation gradient toward the backstop is observed (Fig. 4).

6.3 Mechanical Implications of Cover Buckling

Large-scale critical wedge modelling together with consistency of internal cover plastic (calcite veins) deformation with seismogenic basement stress regime

suggest that the cover rocks in the Zagros Folded Belt do not simply behave to first-order as a brittle medium.

Moreover, the sequence of folding has suggested a rapid development of folding coevally across the strike of the belt with no clear evidence of southward propagation. Hereafter, we focus on the possibility that most characteristics of cover folding in the ZFB be explained by buckling.

Several analytical and numerical models have already considered folding in the Zagros Folded Belt as a case example for studying mechanisms of buckling [Biot, 1961; Schmalholz et al., 2002; Turcotte and Schubert, 2002]. The theory of buckling predicts that a single competent layer with random perturbations overlying a weaker matrix will develop into a regular fold train when subjected to layer-parallel shortening [e.g, Biot, 1961; Zhang et al., 1996]. The fold train results from the process of selection and amplification of initial perturbations that is dependent on the competency contrasts between matrix and layer.

Practically, only the perturbations with maximum growth rates will transform into finite folds.

Moreover, the initiation of fold growth is exponential when the dominant wavelength is selected and then gradually slows down. At least three observations may support such development in the Zagros Folded Belt:

1. The rapid growth of folds in probably less than 3 Ma while the collision-related compressive deformation on the Arabian continental margin likely started in Middle Miocene times (ca. 20 Ma);
2. Tolds probably initiated coevally across the ZFB;

3. Progressive onlaps of Bakhtyari conglomerates onto older growth strata suggest a slowing down of fold growth (relatively to the rate of deposition).

The thick Paleozoic and Mesozoic carbonates can be treated as a single competent layer overlying a homogeneous and finite viscous matrix lying in the Cambrian salts. It has been noticed for years that the pure elastic solution for buckling dominant wavelengths given by

$$\lambda_b = 2\pi H \sqrt{E/\sigma}$$

often requires unrealistic high layer-parallel stress σ to fit observed buckling wavelengths. However, it has been proposed that folding wavelengths averaged to values of ~20 km in the ZFB may be roughly approximated by a brittle-elastic solution [Mouthereau et al., 2006]. Indeed, the observed wavelengths can be reproduced assuming a layer-parallel stress that must be at least 300 MPa and a low value of Young's modulus E of 10^9 Pa as suggested by recent mechanical experiments on Miocene carbonates [Amrouch, 2005]. The result is however largely dependent on the effective elastic thickness H we chose for the competent layer. A value of less than 2 km, i.e., representing only a quarter of the value of the unfolded layer, i.e. the thickness of the sedimentary cover, is compatible with fold curvature-1 ($> 10^{-5}$ m) and brittle yielding in a brittle/elastic layer. If this mechanism may account for the failure of the thin-skinned critical wedge model and the sequence of folding, it however fails to reproduce the internal pression-solution processes observed and supported by the poor seismogenic potential of the cover sequence.

On the other hand, a pure viscous solution for buckling dominant wavelengths given by

$$\lambda_b = 2\pi H 6^{-1/3} \sqrt[3]{\eta_l/\eta_m}$$

is limited by viscosity contrasts between layer and matrix of less than two orders of magnitudes [Schmalholz et al., 2002]. The viscosity of the Hormuz evaporites has typical viscosities (Newtonian) of salts between 10^{17} and 10^{18} Pa s. In that case, fold wavelengths may be reproduced using a viscous layer of $H=2$ km with viscosity η_l of 10^{19} Pa s.

There are several limitations to both models. First they assume infinitesimal deformation which is only applicable at the initial stages of folding. Second, they are small-scale models that neglect the effects of gravity. Finally, they implicitly consider that the weak viscous matrix is infinitely thicker than the competent layer, which is obviously not the case in the Zagros; e.g. Fig. 4 shows average ratios of the matrix thickness to layer thickness between 0.1 (1:8) and 0.3 (2:7) maximum. A better fit of the observed wavelengths of

folding in the Zagros has been obtained for a more realistic solution involving buckling of a viscous (non-Newtonian)-elastic layer resting on a homogeneous Newtonian matrix with finite thickness [Schmalholz et al., 2002].

Figure 4 shows that from the Imbricate Zone toward the Surmeh Fault, fold wavelengths progressively decrease from 35 km to 11 km as fold amplitudes increase (e.g., Dalu and Sim anticlines in Fig. 2). Then toward the MFF, fold wavelengths increase again from 11 km close to the Surmeh Fault up to 17 km on average. We suggest that folding might have initially developed with homogeneous and relatively lower amplitude/wavelength ratio. Such wavelengths are currently preserved in the Imbricate Zone or close to the MFF. A possible control by basement-involved deformation cannot be excluded. Then as shortening increased, wavelength of folds reduced, limbs rotated, as exemplified by intraformational unconformities, and fold amplitude increased leading to higher amplitude/wavelength ratios. This is especially the case where the southward propagation is limited by the presence of topographic high like the Surmeh Fault.

Conclusions

The aim of the paper was to discuss which type of mechanical behaviour better explains the development of the Zagros folded belt in terms of cover folding, internal deformation of cover rocks and on the regional scale the crustal rheology that led to the observed regional topography.

The available structural studies combined with seismotectonic constraints demonstrate that the basement is necessarily currently involved in collisional deformation. Additional mechanical constraints derived from a critical wedge modelling of the regional topography confirm this result. The basic assumptions in Coulomb critical wedge models and the present day stress regimes together suggest that the state of stress within the upper crust of the Arabian continental margin has everywhere reached the brittle strength of the crust in agreement with Byerlee's law. However, the lack of seismogenic strain derived from the summation of seismic tensors [Jackson et al., 1995] suggests that aseismic deformation is likely to occur in the (lower ?) crust.

In agreement with the failure of a thin-skinned critical wedge model for the Fars, the distribution of deformation in the cover rocks does not display a gradient of deformation increasing rearward (i.e., toward the MZT) as it is usually observed for typical thin-skinned thrust wedges.

The thickness distribution of the Mishan Formation suggests that the Arabian continental margin was

inverted as early as the Middle Miocene in response to continent-continent collision. Margin inversion occurred by the reactivation of NW-SE-trending Tethyan normal faults (e.g., Surmeh Fault, Mountain Front Fault) and Panafrican inherited N-S fault trend (Karebass, Sabz-Pushan, Sarvestan transcurrent faults). During this episode, the sedimentary cover suffered little shortening near active basement faults and deformation was localized along the main basement faults, i.e., the Surmeh Fault and the MFF. This episode is probably a consequence of the intraplate stress build up in the margin following the initiation of the collision.

By the Pliocene-Pleistocene period, cover folding developed rapidly in a few million years all over the ZFB in agreement with the field observations of growth strata associated with folds uplift. At this point, the foreland basin transformed into an orogenic belt controlled by the propagation of a brittle upper crustal wedge. Reverse movements along already inverted basement structures (MFF and Surmeh Fault) increased and faulting was generalized within the upper brittle crust, leading to the current seismic activity in the ZFB. At the same time, the growth of folds rapidly diminished as suggested by the observations that youngest syn-orogenic strata (Bakhtyari Fm) often onlap older synfolding strata (upper Agha Jari Fm).

Observations in the field of the internal deformation of rocks reveal that the rheology of the sedimentary cover during folding was dominated by viscous-plastic and local brittle behaviours. Numerous characteristics of cover folding suggest that folds developed mainly as buckle folds. A mechanical model involving a viscous (non-Newtonian)-elastic layer representing the thick cover (~10 km) resting on a homogeneous Newtonian matrix represented by the Hormuz salt satisfactory reproduces the observed distribution of folds widths.

We conclude that the distributed thick-skinned deformation that followed the initial margin inversion occurred coevally with the main phase of cover folding. The way they deform however is different; the basement is pre-fractured so it shortens preferentially by faulting. In contrast, the folding of the thick sedimentary cover developed by buckling over an incompetent layer of salt with the assistance of plastic-viscous processes.

Acknowledgments

References

Agard, P., J. Omrani, L. Jolivet, and F. Mouthereau, Convergence history across Zagros (Iran): constraints from collisional and earlier deformation, Intern. Journ. of Earth Sciences, doi:10.1007/s00531-005-0481-4, 2005.

Ahmadhadi, F., O. Lacombe, and J.-M. Daniel, Early reactivation of basement faults in Central Zagros (SW Iran): evidence from pre-folding fracture patterns in Asmari Formation and Lower Tertiary paleogeography, this issue.

Amrouch, K., Quantification des orientations et des magnitudes les paléocontraintes tertiaires dans la chaîne plissée du Zagros par l'analyse des macles de la calcite, Master thesis, Université P. et M. Curie (Paris 6), Paris, France, 2005.

Amrouch, K., O. Lacombe, F. Mouthereau, and L. Dissez, Quantification of orientations and magnitudes of the late Cenozoic paleostresses in the Zagros folded belt from calcite twin analysis, in Thust Belts and Foreland Basins, International Meeting, Rueil-Malmaison, 31–35, 2005.

Bahroudi, A., and H.A. Koyi, Effect of spatial distribution of Hormuz salt on deformation style in the Zagros fold and thrust belt: an analogue modelling approach, Journ. of Geolog. Soc. of London, 160, 1–15, 2003.

Baker, C., J.A. Jackson, and K. Priestley, Earthquakes on the Kazerun Line in the Zagros mountains of Iran: Strike-slip faulting within a fold-and-thrust belt, Geophys. Journ. Intern., 115, 41 – 61, 1993.

Berberian, M., Master "blind" thrust faults hidden under the Zagros folds: active basement tectonics and surface tectonics surface morphotectonics, Tectonophysics, 241, 193–224, 1995.

Berberian, M., and G.C.P. King, Towards a paleogeography and tectonic evolution of Iran, Canadian Journal of Earth Sciences = Journal Canadien des Sciences de la Terre, 18, 210–265, 1981.

Biot, M.A., Theory of folding of stratified viscoelastic media and its implications in tectonics and orogenesis, Geological Society of America Bulletin, 72, 1595–1620, 1961.

Blanc, E.J.-P., M.B. Allen, S. Inger, and H. Hassani, Structural styles in the Zagros simple folded zone, Iran, Journal of the Geological Society of London, 160, 401–412, 2003.

Craddock, J.P., and B.A. van der Pluijm, Sevier-Laramide deformation of the continental interior from calcite twinning analysis, west-central North America, Tectonophysics, 305, 275–286, 1999.

Costa, E., and B.C. Vendeville, Experimental insights on the geometry and kinematics of fold-and-thrust belts above weak, viscous evaporitic décollement, Journ. of Struct. Geol., 24, 1729–1739, 2002.

Davis, D.M., and T. Engelder Role of Salt in Fold-and-Thrust Belts, Tectonophysics, 119,6788, 1985.

De Mets, C., R.G. Gordon, D.F. Argus, and S. Stein, Effects of recent revision to the geomagnetic reversal time scale on estimates of current plate motions, Geophysical Research Letters, 2191–2194, 1994.

Elmore, R.D., and W.R. Farrand, Asphalt-bearing sediment in synorogenic Miocene-Pliocene molasse, Zagros Mountains, Iran, American Association of Petroleum Geologists Bulletin, 65, 1160–1165, 1981.

Falcon, N.L., Major earth-flexuring in the Zagros Mountains of south-west Iran, Quarterly Journ. of the Geol. Soc. of London, 177, 367–376, 1961.

Hatzfeld, D., M. Tatar, K. Priestley, and M. Ghafori-Ashtiany, Seismological constraints on the crustal structure beneath the Zagros Mountain Belt (Iran), Geophys. Journ.l Intern., 403–410, 2003.

Hessami, K., H.A. Koyi, C.J. Talbot, H. Tabasi, and E. Shabanian, Progressive unconformities within an evolving foreland fold-thrust belt, Zagros Mountains, Journ. of the Geol; Soc., 158, 969–981, 2001.

Homke, S., J. Verges, G. Garces, H. Emamia, and R. Karpuzc, Magnetostratigraphy of Miocene–Pliocene Zagros foreland deposits in the front of the Push-e Kush Arc (Lurestan Province, Iran), Earth and Planetary Science Letters, 225, 397–410, 2004.

Jackson, J., J. Haines, and W. Holt, The accommodation of Arabia-Eurasia plate convergence in Iran, Journ. of Geophys. Research, 100, 15,205–15,219, 1995.

Jackson, J.A., Reactivation of basement faults and crustal shortening in orogenic belts,Nature, 283, 343–346, 1980.

Jackson, M.P.A., R.R. Cornelius, C.H. Craig, A. Gansser, J. Stöcklin, and C.J. Talbot, Salt diapirs of the Great Kavir, central Iran, in Geological Society of America Memoir, vol. 177, pp. 139, The Geological Society of America, Boulder, 1990.

Koop, W., and R. Stoneley, Subsidence history of the middle East Zagros basin, Permian to Recent, Philosophical Transation of the Royal Society of London, 305, 149–168, 1982.

Lacombe, O., F. Mouthereau, S. Kargar, and B. Meyer, Late Cenozoic and modern stress fields in the western Fars (Iran): Implications for the tectonic and kinematic evolution of central Zagros, Tectonics, 25, doi:10.1029/2005TC001831, 2006, 2006.

Maggi, A., J.A. Jackson, K. Priestley, and C. Baker, A re-assessment of focal depth distributions in southern Iran, the Tien Shan and northern India: do earthquakes really occur in the continental mantle ?, Geophysical Journal International, 143, 629–661, 2000.

McQuarrie, N., Crustal scale geometry of the Zagros fold-thrust belt, Iran, Journ. of Struct. Geol., 519–535, 2004.

McQuarrie, N., J.M. Stock, C. Verdel, and B.P. Wernicke, Cenozoic evolution of Neotethys and implications for the causes of plate motions, Geophysical Research Letters, 30, doi:10.1029/2003GL017992, 2003.

Molinaro, M., P. Leturmy, J.-C. Guezou, D. Frizon de Lamotte, and S.A. Eshraghi, The structure and kinematics of the south-eastern Zagros fold-thrust belt; Iran: from thin-skinned to thick-skinned tectonics, Tectonics, 24, doi:10.1029/2004TC001633, 2005a.

Molinaro, M., H. Zeyen, and X. Laurencin, Lithospheric structure underneath the SE Zagros Mountains, Iran: recent slab break-off?, Terra Nova, 25, 1–6, 2005b.

Molnar, P., and P. England, Late Cenozoic uplift of mountain ranges and global climate change: chicken or egg ?, Nature, 346, 29–34, 1990.

Motiei, H., Geology of Iran : Stratigraphy of Zagros, 536 pp., Geological Survey of Iran, 1993.

Mouthereau, F., O. Lacombe, and B. Meyer, The Zagros Folded Belt (Fars, Iran): Constraints from Topography and Critical Wedge Modelling, Geophys. Journ. Intern., 165, 336–356, 2006.

Ni, J., and M. Barazangi, Seismotectonics of the Zagros continental collision zone and a comparison with the Himilayas, Journal of Geophysical Research, 91, 8205–8218, 1986.

National Iranian Oil Company, N.I.O.C., Geological map of Iran, sheet 5, South-central Iran, Tehran, 1977.

Oveisi, B., J. Lavé, and P. Van der Beek, Active folding and deformation rate at the central Zagros front (Iran), this issue.

Schmalholz, S.M., Y. Podladchikov, and J.P. Burg, Control of folding by gravity and matrix thickness: implications for large-scale folding, Journ. of Geophys. Research, 107, 10.1029/2001JB000355, 2002.

Schuster, F., and U. Wieland, Oligocene and Early Miocene coral faunas from Iran: palaeoecology and palaeobiogeography, Intern. Journ.l of Earth Sciences, 88, 571–581, 1999.

Sepher, M., and J.W. Cosgrove, Structural framework of the Zagros Fold-Thrust Belt, Iran, Marine and Petroleum Geology, 21, 829–843, 2004.

Sherkati, S., and J. Letouzey, Variation of structural style and basin evolution in the central Zagros (Izeh zone and Dezful Embayment), Iran, Marine and Petroleum Geology, 21, 535–554, 2004.

Snyder, D.B., and M. Barazangi, Deep crustal structure and flexure of the Arabian plate beneath the Zagros collisional mountain belt as inferred from gravity observations, Tectonics, 5, 361–373, 1986.

Stocklin, J., Structural history and tectonics of Iran; a review, American Association of Petroleum Geologists Bulletin, 52, 1229–1258, 1968.

Stoneley, R., The Arabian continental margin in Iran during the Late Cretaceous, in The Geology and Tectonics of the Oman Region, edited by A.H.F. Robertson, M.P. Searle and A.C. Ries, pp. 787–795, 1990.

Talbot, C.J., and M. Alavi, The past of a future syntaxis across the Zagros, in Alsop, in Salt Tectonics, vol. 100, edited by G.I. Alsop, D.J. Blundell. and I. Davison, pp. 89–109, Geological Society of America Special Paper, 1996.

Talebian, M., and J.A. Jackson, A reappraisal of earthquake focal mechanisms and active shortening in the Zagros mountains of Iran, Geophys. Journ. Intern., 156, 506–526, 2004.

Tatar, M., D. Hatzfeld, and M. Ghafori-Ashtiany, Tectonics of the Central Zagros (Iran) deduced from microearthquakes seismicity, Geophysical Journal International, 255266, 2004.

Turcotte, D.L., and G. Schubert, Geodynamics: Applications of Continuum Mechanics to Geological Problems, Cambridge University Press, 2002.

Van der Pluijm, B.A., J.P. Craddock, B.R. Graham, and J.H. Harris, Paleostress in Cratonic North America: Implications for Deformation of Continental Interiors, Science, 277, 794–796, 1997.

Vernant, P., F. Nilforoushan, D. Hatzfeld, M.R. Abbassi, C. Vigny, F. Masson, H. Nankali, J. Martinod, A. Ashtiani, R. Bayer, F. Tavakoli, and J. Chéry, Present-day crustal deformation and plate kinematics in the Middle East constrained by GPS measurements in Iran and northern Oman, Geophysical Journal International, 157, 381–398, 2004.

Walpersdorf, A., D. Hatzfeld, H. Nankali, F. Tavakoli, F. Nilforoushan, M. Tatar, P. Vernant, J. Chéry, and F. Masson, Difference in the GPS deformation pattern of North and Central Zagros (Iran), Geophysical Journ. Intern., in press.

Weijermars, R., J.A. Jackson, and B. Vendeville, Rheological and tectonic modeling of salt provinces, Tectonophysics, 217, 143–174, 1993.

Williams, C.A., C. Connors, F.A. Dahlen, E.J. Price, and J. Suppe, Effect of the brittle-ductile transition on the topography of compressive mountain belts on Earth and Venus, Journal of Geophysical Research, 99, 19,947–19,974, 1994.

Zhang, Y., B.E. Hobbs, A. Ord, and H.B. Mühlhaus, Computer simulation of single-layer buckling, Journal of Structural Geology, 18, 643–655, 1996.

Ziegler, M.A., Late Permian to Holocene Paleofacies Evolution of the Arabian Plate and its Hydrocarbon Occurrences, GeoArabia, 6, 445–503, 2001.

Rates and Processes of Active Folding Evidenced by Pleistocene Terraces at the Central Zagros Front (Iran)

Behnam Oveisi · Jérôme Lavé · Peter van der Beek

Abstract. The Zagros fold belt results from active collision of the Arabian plate with central Iran, and is characterized by the development of a spectacular >200 km-wide fold-train in its sedimentary cover. Although the architecture of this accretionary prism has been extensively studied because of its important implications for hydrocarbon exploration, aspects such as the kinematics of individual folds and the sequence of fold development remain to be investigated in detail. It is commonly believed that the ongoing deformation through the Zagros belt has led to the south-westward migration of the front of the fold belt. In the south-western Fars province (central Zagros), the most frontal structure is delineated by the Mand anticline, a well-exposed detachment fold on the shore of the Persian Gulf. This near-symmetrical anticline involves relatively competent Phanerozoic sedimentary rocks above a regional décollement in Hormuz salt. In order to document the geometry and kinematics of this fold, we have constructed several balanced cross-sections on the basis of a recently published section constrained by seismic data (Letouzey and Sherkati, 2004). Several solutions to the length versus area restoration problem common to detachment folds are then proposed: fault-related folding, detachment folding with internal deformation, and detachment folding accompanied by the flexure of the flanking synclines below the regional stratigraphic level. On the western limb of the anticline, fluvio-marine terraces, tilted by 1.7 to 4.5°, provide an additional constraint on fold kinematics and suggest that surface deformation is most compatible with a detachment fold, probably associated with synclinal flexure. Applying such a model, as well as new 14C ages for the marine terrace deposits, we calculate tilting rates of 0.04 to 0.05°/kyr, which would be produced by a Late Pleistocene shortening rate (perpendicular to the structure) of 3 to 4 mm/yr. Although this preliminary estimate suffers from relatively large uncertainties, mostly due to the absence of independent dating of the terraces and independent constraints on the folding model, we conclude that shortening across the Mand anticline could absorb 20 to 35% of the 8 mm/yr convergence across the entire Zagros. This result is consistent with a normal forward-propagating deformation sequence in a thin-skinned tectonic regime. It also implies that the sedimentary cover of the frontal Zagros is fully decoupled from the basement, most probably at the level of the Hormuz salt, in contrast to recent models that suggested active deformation of the sedimentary cover to be controlled by thrust faults in the basement.

1 Introduction

The Zagros fold belt (Fig. 1) results from the collision of the Arabian plate with the central Iran micro-continent. Tectonic convergence is still ongoing in the area and recent deformation of this intracontinental mountain belt is accompanied by intense seismicity (e.g., Ni and Barazangi, 1986; Berberian, 1995; Talebian and Jackson, 2004). The Arabian passive margin sequence is commonly believed to be decoupled from its basement at the level of lower Cambrian salt and to be deformed by thin-skinned tectonics. Despite the spectacular deformation of this sedimentary sequence, most of the seismicity occurs within the underlying basement, mainly through high-angle reverse faulting (Jackson and Fitch, 1981; Berberian, 1995). This rather unique seismotectonic setting has prompted scenarios in which the Zagros convergence is accommodated by distributed basement shortening in conjunction with, but decoupled from, folding of the sedimentary cover (Jackson and Fitch, 1981; Ni and Barazangi, 1986; Berberian, 1995). The role of the basement faults remains, however, a matter of debate and it has recently been proposed that basement deformation is currently controlling the deformation of the sedimentary cover: a thick-skinned tectonic style would thus have succeeded initial thin-skinned tectonics (Molinaro et al., 2005; Sherkati et al., 2005).

The Zagros orogen is known for the spectacular fold structures that affect its thick sedimentary cover (e.g., Farhoudi, 1978; Letouzey et al., 1995) with widely distributed resistant limestone anticlines displaying the large-scale "whale backs" that characterize the morphology of the region. Many of these anticlines have long been considered as archetypal detachment folds, which formed in response to the ongoing deformation above the basal detachment level of the lower Cambrian Hormuz Salt (e.g., Colman-Sadd, 1978), even if recent studies have proposed alternative structural interpretations (e.g. Sherkati and Letouzey, 2004;
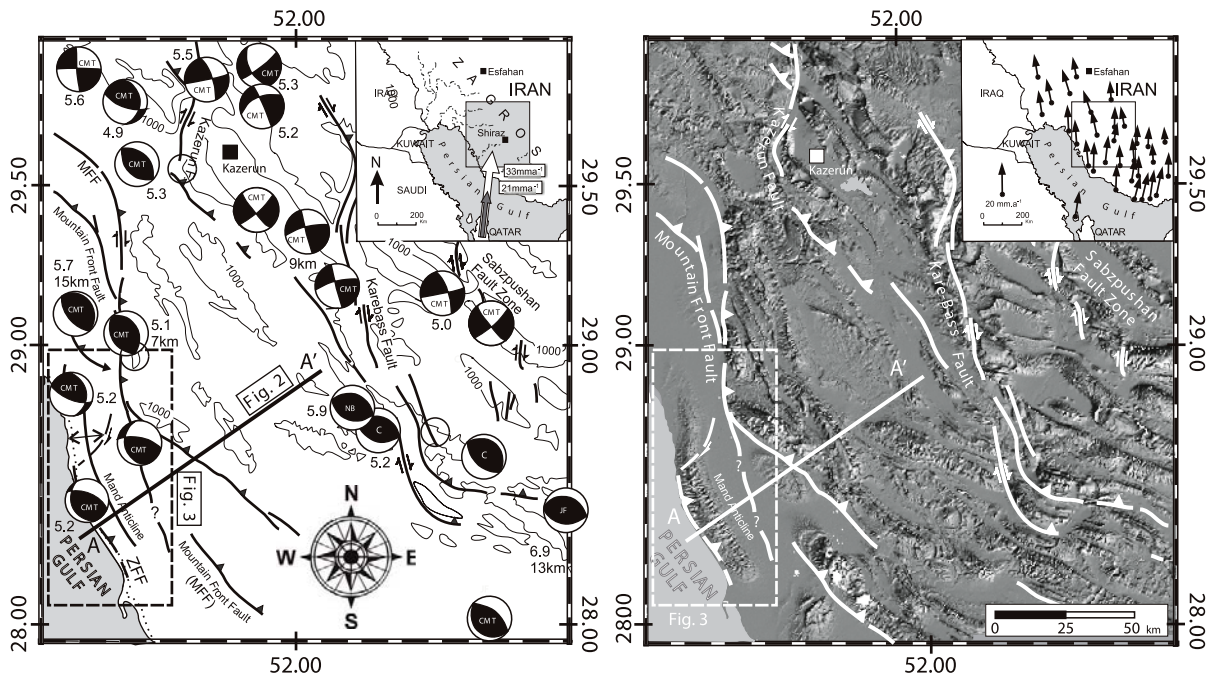
Fig. 1. Seismotectonic (*left panel*) and topographic (*right panel*) map of the Western Fars, central Zagros, showing main surface faults. *Inset in left panel shows* location within Persian Gulf area, as well as Arabia-Eurasia shortening rates from DeMets et al. (1994) and Sella et al. (2002); *inset in right panel shows* GPS velocities (mm/yr) in central Zagros with respect to stable Eurasia (Hessami et al., 2006). Focal mechanism solutions for large earthquakes are from Chandra (1984) (C); Harvard Centroid-moment database (CMT); Jackson and Fitch (1981) (JF); Ni and Barazangi (1986) (NB). Topographic contours with 1000-m interval indicated in left panel. Line shows balanced cross-section of Fig. 2; box shows location of Fig. 3

Mouthereau et al., 2006). The geometry and surface structure of such detachment folds are considered to be controlled by the existence of a major low-viscosity basal layer that permits efficient detachment and material migration (e.g. Mitra, 2002). Various two-dimensional geometric and kinematic models have been proposed to describe detachment folding (e.g., Dahlstrom, 1990; Epard and Groshong, 1995; Poblet and McClay, 1996; Mitra, 2002), which is typically manifested by symmetric or asymmetric folds with cores filled by the basal incompetent unit.

Although the architecture and kinematics of deformation of the sedimentary cover in the Zagros fold belt have important implications for seismic hazard assessment and hydrocarbon exploration, they remain relatively unknown. Some general sections of the Zagros fold belt have been proposed in recent papers (Blanc et al., 2003; McQuarrie, 2004; Sherkati and Letouzey, 2004); however, aspects such as the kinematics of individual folds, the sequence of fold and thrust development, the relationship between fold and fault deformation and the evolution from symmetric detachment folds to asymmetric fault-related folds remain to be investigated.

Here, we focus on a well-exposed map-scale detachment fold (the Mand anticline) occurring along the

shore of the Persian Gulf at the central Zagros front (Fig. 1). This detachment fold presents near-symmetrically folded Cenozoic strata, formed in the relatively competent rock cover above a regional décollement in Hormuz salt. In order to unravel the recent evolution of this most frontal part of the central Zagros wedge, we first review some aspects of Zagros tectonics and geology that are relevant to our study. We then detail the surface geometry and various possible constructions at depth of the Mand detachment fold, including depth-to-detachment and shortening calculations. In order to evaluate Late Quaternary rates of deformation at the front of the Zagros belt, we surveyed tilted marine and fluvial terraces on the SW frontal limb of the Mand anticline. These warped and tilted geomorphic markers provide new insights on recent fold detachment kinematics and on tectonic uplift, tilting and shortening rates.

2   Geological and Seismotectonic Setting

The Zagros orogen is bordered to the SW by the Persian Gulf, which represents the foredeep basin at its front. To the NE, the Zagros is bordered by the Main Zagros Thrust (MZT), considered by many as the su-

ture of the Neo-Tethys Ocean. Classically, two main structural zones in the Fars arc of the Zagros are distinguished on the basis of distinct topographies and outcropping units: the High Zagros Belt (HZB) to the NE, and the Zagros Simple Fold Belt (ZSFB) to the SW. The High Zagros Fault (HZF) separates these two structural domains. It is generally considered that deformation in the HZB initiated before deformation in the ZSFB, according to a classical forward-propagating sequence scenario (e.g., Hessami et al., 2001; Alavi, 2004).

Sedimentation on the Arabian and Zagros platform since the pre-Cambrian has led to deposition of a 5–15 km-thick sedimentary sequence of passive margin to flexural basin series (Stocklin, 1968; Falcon, 1969; Colman-Sadd, 1978), interrupted by several sedimentary hiatuses (e.g., Alavi, 2004). During Paleozoic times, clastics and carbonates were deposited, partly in association with the opening of the Neo-Tethys. Subsequently, Upper Triassic to Lower Cretaceous carbonates and minor evaporites were deposited on the stable, shallow shelf of the Arabian platform. The emplacement of ophiolites during Late Cretaceous time along the margins of the Arabian plate indicates an initial episode of convergence at that time, the extent and nature of which remain controversial (e.g., Beydoun, 1991). Campanian flysch and radiolaritic nappes accumulated in a flexural basin formed by loading of the continental crust, whereas the Late Eocene to Early Miocene is marked by the deposition of several limestone formations (e.g., Jahrom and Asmari Formations). Tertiary island-arc-type volcanism in Iran indicates that subduction of oceanic crust continued until Miocene times (e.g., Colman-Sadd, 1978), when it was followed by the main phase of continental collision in the Zagros. Finally, a major regional angular unconformity between the Agha Jari/Lahbari Fms and the upper Bakhtiari conglomerates is associated with renewed erosion and tectonic activity of the Zagros fold-and-thrust belt: this event is generally dated as Late Pliocene, but could be largely diachronous from NE to SW, accompanying the propagation of the deformation front (Hessami et al., 2001).

Active deformation of the Zagros orogen results from approximately N-S directed collision between Arabia and Continental Eurasia at a rate of 25–30 mm/yr (DeMets et al. 1994; Sella et al. 2002). Seismicity (Berberian, 1995; Talebian and Jackson, 2004) and GPS (Tatar et al., 2002) data suggest that present-day convergence across the Zagros is concentrated in the ZSFB, which constitutes the foreland fold-and-thrust belt of the system. From a recent GPS survey, Tatar et al. (2002) proposed a present-day shortening rate of 8–10 mm/yr for the Zagros, which would accommodate about 40–45% of the total ~21 mm/yr convergence between Arabia and Eurasia (Vernant et al.,

2004). Total shortening since ~5 Ma in the ZSFB is estimated to range between 50 and 80 km (Blanc et al., 2003; McQuarrie, 2004). The stratigraphic succession of rock series with highly variable mechanical properties strongly controls deformation in the ZSFB (e.g., Sherkati and Letouzey, 2004). At the base of the sedimentary cover, Lower Cambrian (Berberian, 1995) incompetent Hormuz series directly overlie the crystalline basement as a basal detachment level and play an important role in guiding the deformation. Talbot and Alavi (1996) suggested a taper angle of ~1° in the Zagros, resulting from very low basal traction in the Hormuz Salt horizon. Reliable waveform modelling shows that large earthquakes in the Zagros often nucleate in the upper crust at depths of 8 to 15 km in the crystalline basement (Jackson and McKenzie, 1984; Ni and Barazangi, 1986; Maggi et al., 2000; Talebian & Jackson, 2004). A recent study of micro-earthquakes in the central Zagros (Tatar et al., 2004) suggests that much of the seismicity is restricted to the upper part of the basement between ~11 km (base of the sedimentary cover), and ~15 km (base of the seismogenic layer). The absence of seismogenic behaviour in the sedimentary cover could partly explain why, according to seismic moment summations, only 5% of the deformation in the Zagros is seismically expressed (Jackson et al., 1995; Masson et al., 2005).

Along its southern front, the Zagros is bounded from its foredeep basin by the Mountain Front Fault (MFF), but local topographic expressions, both onshore and offshore, attest to active folding southwest of this major tectonic boundary; hence, the existence of a more frontal fault, the Zagros Foredeep fault (ZFF), has been proposed by Berberian (1995) (cf. Fig. 1). The Mand anticline, which will be discussed in detail in the present work, is one of these active structures in front of the MFF. It is singular in several aspects: it represents the westernmost frontal structure of the Fars arc; its general orientation is NNW-SSE to N-S, in contrast with the NW-SE orientation of most folds in the Fars arc; and it is located in the azimuth of the Kazerun Fault, which is one of the major N-S strike slip faults in the Zagros orogen and which corresponds to an inferred boundary between the Fars arc, with Hormuz salt at the base of the sedimentary sequence, and the Dezful embayment where this thick incompetent unit is considered absent or much thinner. The absence of both basal Hormuz salt and of major detachment folds like the Mand anticline further west is probably not coincidental, given the strong control that weak basal layers have on detachment fold development.
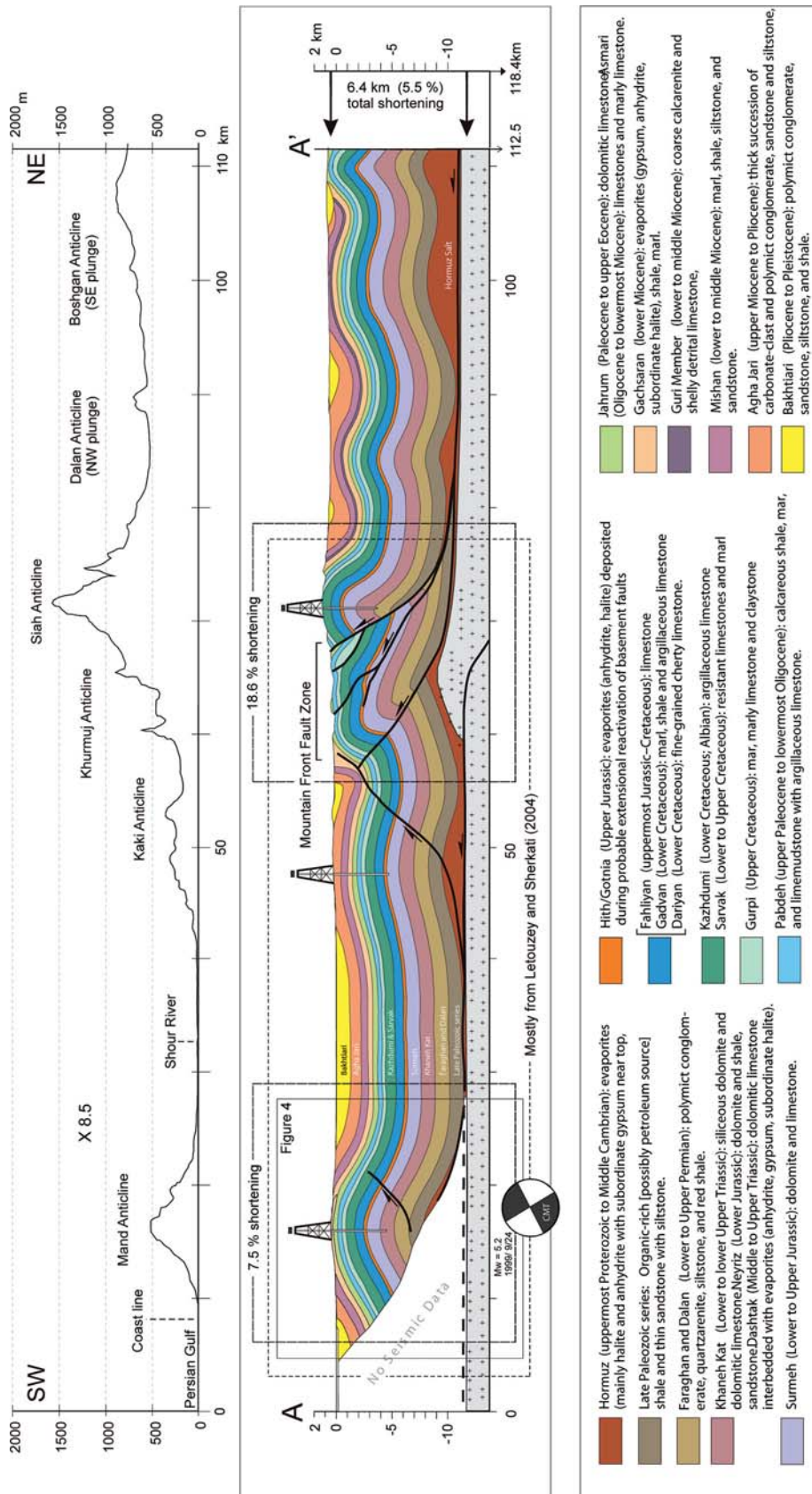
Fig. 2. Balanced cross section of the frontal Zagros between the Persian Gulf and the hangingwall of the Mountain Front Fault (MFF); modified from Letouzey and Sherkati (2004). Box shows location of detailed cross-sections across Mand anticline shown in Fig. 4

2.1 Regional Balanced Cross-Section

In order to estimate the finite deformation of the sedimentary cover and constrain the depth to basement, we have constructed a balanced section across the frontal part of the central Zagros (Fig. 2). In the Mand region, Letouzey and Sherkati (2004; see also Sherkati et al., 2006) have previously proposed a detailed balanced cross-section based on both surface data and unpublished seismic reflection and well data provided by the National Iranian Oil Company (NIOC). Outcrops and borehole data provided them in particular a good thickness control on Permian to recent sedimentary units. Balanced cross-sections rely on the assumption that no material moves into, or out of, the plane of the section. In the study area, this assumption may not be valid, as there may be a considerable regional component of oblique slip relative to fold orientation (e.g., Fig. 1). In constructing the section of Fig. 2, we have used the cross-section of Letouzey and Sherkati (2004), complementing it to the north-east according to structural data and following the sinuous bed method, which supposes constant bed thickness for the competent layers during shortening (Dahlstrom, 1969). Although balanced cross-section solutions are non-unique, and the deepest units are poorly imaged by the seismic lines, the surface structures appear to project through a detached fold over the MFF ramp, where the master fault-cored folds converge on a décollement level in the Hormuz Salt. The balanced sections indicate different degrees of fold asymmetry close to the ZFF, where the Mand detachment anticline is distinctly symmetrical, and over the MFF ramp, where a system of master fault-cored folds has developed with a clear foreland-ward vergence, possibly due to thick-skinned deformation (Fig. 2).

In constructing cross sections across the Zagros fold belt, two major problems have to be faced. First, the projection of concentric detachment folds to depth generally produces severe space incompatibilities that require disharmonic folding of the ductile layers above a basal detachment (Mitra, 2003), and lead to different line length versus area restorations. In the cross-section of Fig. 2, the space problem is generally solved by inferring the presence of thrust faults in the Paleozoic to early Cretaceous competent rocks in the cores of the anticlines, linked to a decreasing ratio of fault offset to layer folding up-sequence. Second, topographic steps accompanied by the progressive north-eastward thinning of the Mio-Pliocene units filling the synclines require that the depth of the base of the sedimentary sequence decreases to the north-east. Because the base of the crust plunges gently (1–2°) to the north-east (Paul et al., 2006), a space problem occurs between the top of the basement and the base of the

sedimentary cover. McQuarrie (2004) has proposed to fill this void with locally more than 5 km of deformed Hormuz salt, but Mouthereau et al. (2006) have shown that such thicknesses of weak salt cannot mechanically sustain the load of the overlying units over geological timescales; the salt would be rapidly squeezed out. Other authors (e.g., Sherkati and Letouzey, 2004; Molinaro et al., 2005; Mouthereau et al., 2006) have invoked thick-skinned tectonics, with a number of basement thrusts controlling a south-west plunge of the top of basement of 1–2°, i.e., slightly more than the topography. In the cross-section of Fig. 2, the south-western part of which was derived from Letouzey and Sherkati (2004), the void between folded strata and the crystalline basement has been filled both by basement imbrications (i.e., thick-skinned deformation) and local thickening of Hormuz evaporites in the core of anticlines. Our balanced cross-section indicates 6.4 km of total horizontal shortening across the most frontal folds that occur along the ZFF and MFF.

3   The Mand Detachment Fold

3.1 Structure

The Mand fold is a doubly-plunging detachment anticline with a curvilinear convex-to-the-south hinge, wide crest and quasi-homoclinal fore- and back-limbs. It extends ~100 km along strike (Fig. 3). The topographically expressed width of the fold is laterally constant at ~16 km, but its amplitude shows a gradient, decreasing toward the northwest along the fold axis. Along the anticline, the near-symmetrical dip panels on each side of the fold obscure any structural vergence and no outcropping fore- or back-thrusts (relative to the south-west directed transport of the belt) are associated with the fold. In contrast to the tightly folded anticlines associated with the MFF ramp, the Mand anticline is an open fold (cf. Fig. 2). At the surface, the fold exhibits limbs dominated by gentle bedding dips between 10–27°, and presents a high wavelength/amplitude ratio ($\delta \approx 8.3$ in its central part). According to seismic and well data (Letouzey and Sherkati, 2004), the flanks of the anticline are buried below 1-2 km of Plio-Pleistocene sediments of the Lahbari and Bakhtiari Formations. The entire width of the anticline may therefore reach 20 to 25 km. The geophysical data and reference cross-section (Fig. 2) provide a tight control on the thickness of sedimentary units involved in the fold, and helped us to derive several sections across the Mand anticline in order to describe its spatial geometry and evolution, as well as to investigate the deformational style (Fig. 4). These balanced cross-sections were constructed orthogonally to the structure, in order to maximize access to structures
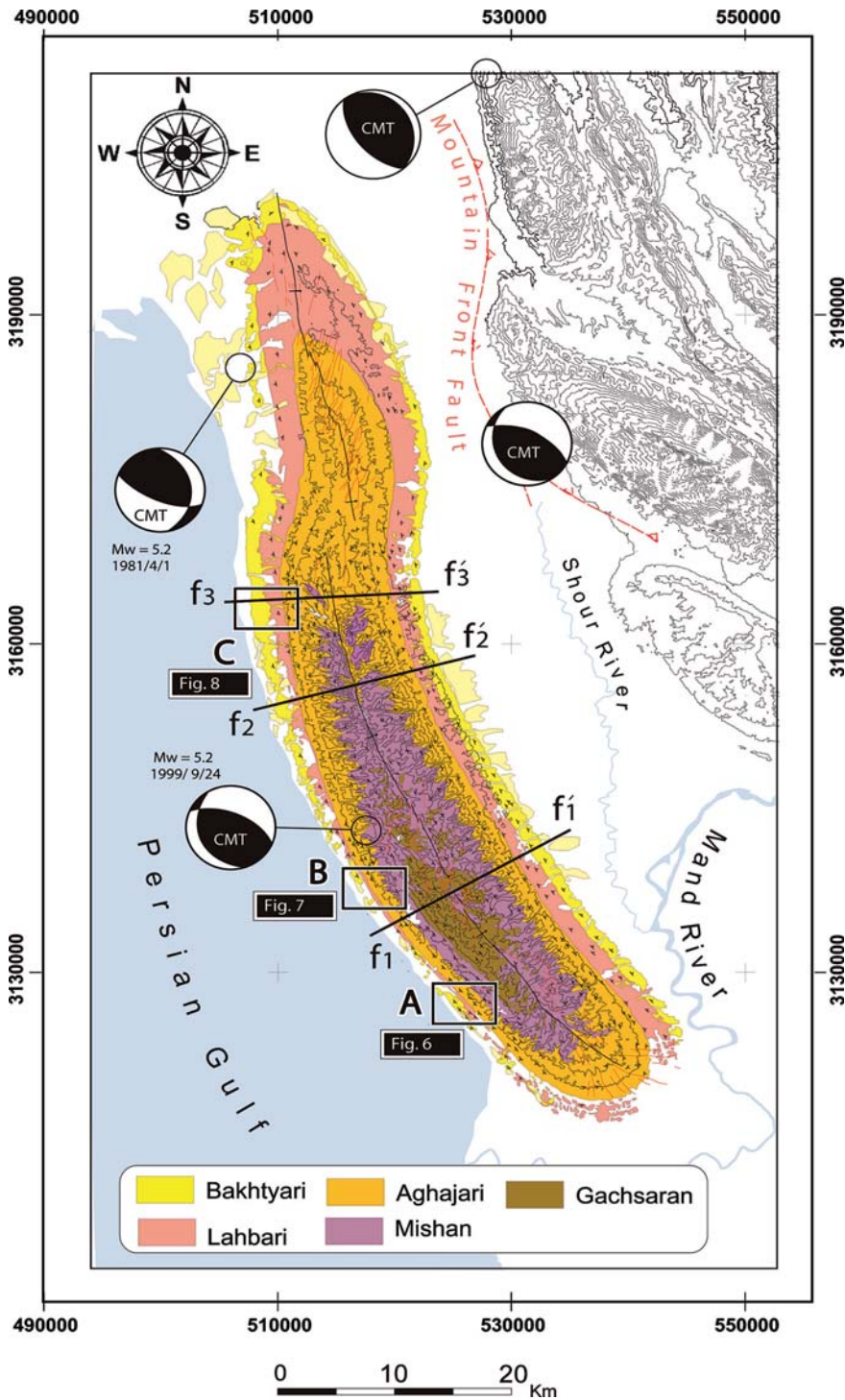
Fig. 3. Geologic map of the Mand anticline with elevation contour lines every 100 m. Focal mechanism solutions for large earthquakes from the Harvard CMT database. Profiles f1-f1', f2-f2' and f3-f3' are shown in Fig. 4. Boxes show locations of surveyed terrace sites (Figs. 6-8)

and bedding exposures. Structural and sedimentological data were mapped in the field and using 1:100,000-scale geologic maps (National Iranian Oil Company, 1976; 1977), Landsat and SPOT satellite images, and a 90-m-resolution digital elevation model (SRTM).

3.2 Fold Solution and Finite Shortening

Detachment folds (Jamison, 1987; Mitra, 2003) form in sedimentary units characterized by significant thickness and competency contrasts, in which the basal lay-

er is commonly an incompetent or low viscosity unit such as shale or salt, and is overlain by thick competent units such as carbonates and sandstones. Under subsequent shortening, fold growth is generally considered to occur by two competing mechanisms: limb lengthening by migration of beds through hinges and limb rotation between fixed hinges by internal deformation. Despite numerous structural studies of detachment folds, the kinematic development of these structures, and their related balancing, remains controversial (De Sitter, 1964; Dahlstrom, 1990; Poblet and McClay, 1996; Poblet et al., 1997; Mitra, 2003). The key questions relate to the relative importance of hinge migration and limb rotation, the amount of internal bed thickening, as well as the nature of deformation of the basal incompetent unit. Fixed hinge models, for example, propose that a detachment fold develops a long wavelength early in its evolution and subsequently evolves primarily by limb rotation and fold tightening (De Sitter, 1964), whereas wavelength is constant in models with mostly hinge migration. In both models, the wavelength/amplitude ratio is considered to be high in the early stages of fold development and to subsequently decrease during fold evolution. These models suffer, however, from an unequal line length versus area restoration and thus require an increase in detachment depth with progressive fold evolution, a solution considered as kinematically and geologically inadmissible (Dahlstrom, 1990). Several alternative solutions have been proposed to solve the balancing problem. First, most of the shortening could be absorbed by internal deformation in the core of gentle folds, with an increasing degree of internal deformation toward the base in order to solve the line lengths versus area restoration at depth (Epard and Groshong, 1995). Internal strain would be accommodated by secondary faulting in competent units, whereas bed thickening could characterize the incompetent stratigraphic units. On the other hand, Mitra (2002; 2003) has proposed that the balancing problem could be reduced by considering that synclinal flexures flanking detachment anticlines could be deflected below the regional position of the considered stratigraphic level.). In this model, affected by variable limb dip and -length, limb rotation is accompanied by hinge migration through the synclinal and/or anticlinal hinges, and at depth by the migration of the basal ductile unit from the base of the syncline toward the anticline core. Synclinal sinking is, however, not commonly recognized, probably because the downward deflection is usually small and occurs over a very broad region (Mitra, 2002; 2003).

In the case of the Mand anticline, the cross-section proposed by Letouzey and Sherkati (2004) (Fig. 2) is unconstrained on its south-western limb due to ab-
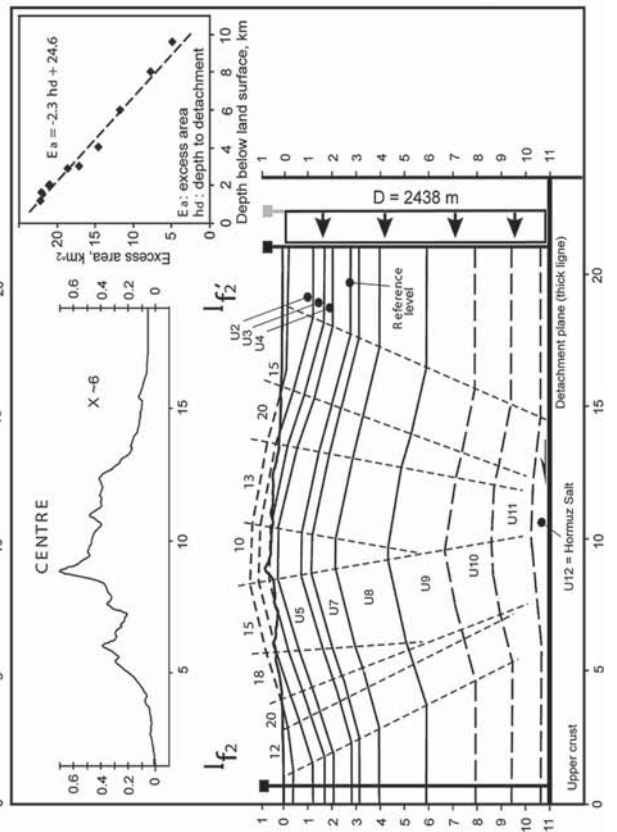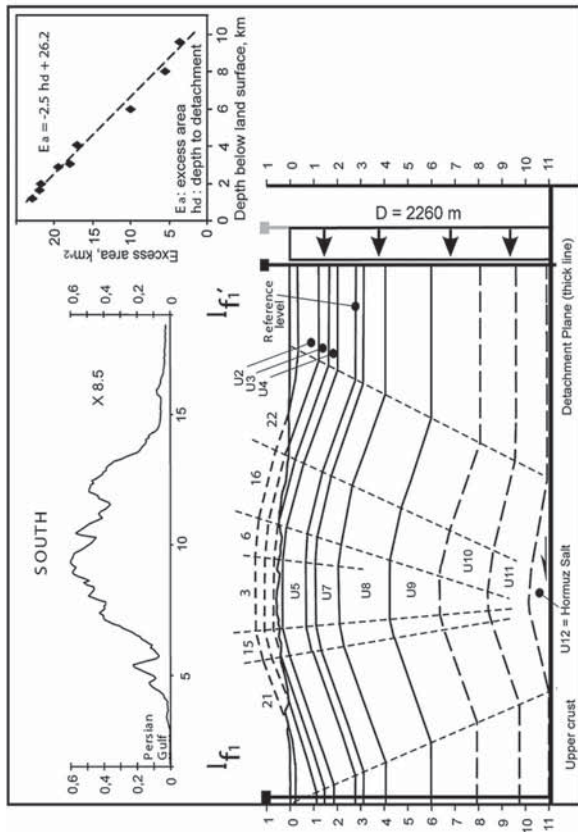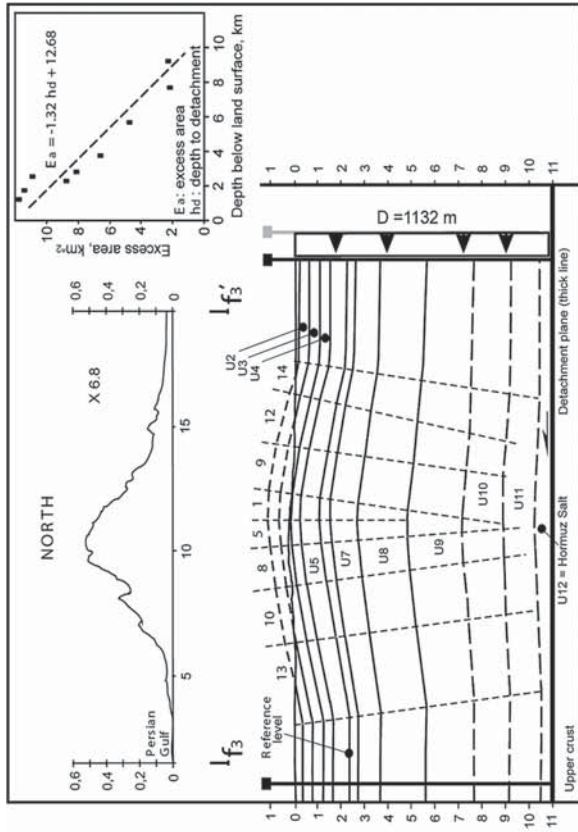
sence of seismic data, and permits several alternative balanced fold solutions.

3.2.1 Case 1: Folding above a SW-Vergent Fault

Sherkati et al. (2006) propose that the Mand detachment fold has evolved towards a fault-bend or fault-propagation fold. The propagation of a forward verging blind fault, with a mean dip of ~30° and associated to a steep (~45°) back-thrust, would have produced a vertical offset of the sedimentary units of several kilometres. Such fault offset would solve the line length versus area problem, but would require more than 2 km offset even for the uppermost sedimentary units close to the surface. There is, however, no topographic indication in the bathymetry of the Persian Gulf for such active faulting. Slip motion on the fault could have been transferred to a more frontal structure, but again the bathymetry does not indicate such a feature.

3.2.2 Case 2: Fold Detachment with Internal Deformation

The stratigraphy of the ZSFB contains several incompetent evaporite and shale intervals that may act as décollement levels (e.g., Sherkati and Letouzey, 2004). The Mand anticline may thicken by internal accommodation strains of such incompetent material (e.g., through homogeneous strain, second order folding, or second order conjugate faulting). Here, we apply the excess area restoration technique (Epard and Groshong, 1993) to evaluate horizontal shortening for different depth levels beneath a reference level. Assuming constant rock density during folding, the excess area is equal to the shortening times the depth to the detachment. Therefore, the slope of the statistical best fit line on diagrams of excess-area (E_a) versus depth to detachment (h_d) indicates total horizontal shortening if area is conserved. We adopt a depth of 11 km to the basal detachment level (Hormuz Salt) and evaluate excess area at different stratigraphic levels for three cross-sections across the Mand anticline (Fig. 4). We take the top of the Asmari Fm (U6 in Fig. 4) as our reference level, in order to avoid complications due to possible secondary detachments in the overlying incompetent Gahsaran unit. A simple cylindrical fold construction leads to E_a-h_d curves that do not project to $E_a = 0$ at $h_d = 11$ km (i.e., the base of the detachment level). In order to produce a more strongly decreasing gradient in excess area with depth, internal deformation and thickening of the units has to be included. The best-fit line on the resulting E_a-h_d curve for the central part of the Mand anticline ($E_a = -2.31h_d + 24.541$; $r^2 = 0.975$ with the detachment level fixed at 8.7 km be-

neath the reference level), for instance, is close to the mean total shortening of 2.4 km that can be inferred from the excess area of each unit individually.
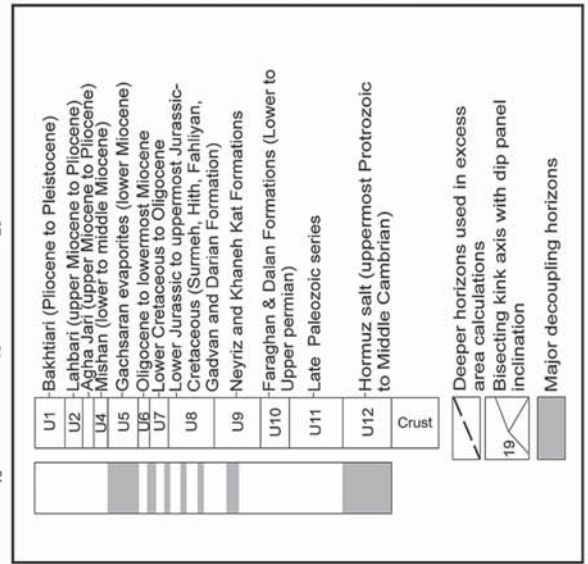
3.2.3 Case 3: Detachment Fold Accompanied by Synclinal Flexures

The cumulative thickness of the Mishan, Agha Jari and Lahbari Formations reaches 1.4 km according to their outcrop pattern in the Mand anticline (Figs. 3 and 4). If we consider the ages determined by magnetostratigraphy further north-west in Lurestan (Homke et al., 2004), i.e. ~12 Ma for the Gachsaran/Mishan transition, and 3–4 Ma for the Lahbari/Bahktiari transition, a regional sedimentation rate of ~0.17 mm/yr can be computed for this period as a response to regional subsidence, which results from the loading of the Arabian platform by the Zagros wedge. On the basis of seismic line data (Letouzey and Sherkati, 2004), the post-Gachsaran sediment thickness in the syncline north-east of the Mand fold is slightly larger than 3 km. In consequence, sedimentation rates would have been >0.4 mm/yr for the last 4 Myr in the syncline between the Mand and Kaki anticlines. This noticeable change in sedimentation rates, even though poorly constrained in time, may suggest that this syncline has been depressed below the regional base-level and that this local effect has greatly enhanced the sedimentation rates. Note that, due to the proximity of the coastline, sea-level can be considered as the regional base-level in this area. Such syncline depression would be accompanied at depth by Hormuz salt migration from the syncline base toward Mand and Kaki anticlinal cores. The difficulty to estimate independently and precisely the regional subsidence rate prevents, however, to properly estimate this flexure.

3.3 Fold Solution and Incremental Deformation at the Surface

The currently available geological and geophysical data do not permit a clear discrimination of the fold solutions to describe the evolution of the Mand anticline.

◀ **Fig. 4.** Fold solutions for the Mand anticline at depth for a detachment fold with bed thickening. The cross-sections are constructed using surface bedding dip, a constant detachment depth and a plot of the relationship between the excess area and depth to the reference horizon (upper right inset diagrams). The compatibility of the restoration is set by adjusting the slope of the excess area versus depth diagram and its intercept with the x-axis that must equal the depth to the detachment. Locations of cross-sections shown in Fig. 3

Additional kinematic information can be gained, however, from surface deformation, in particular if this information can be documented for different time steps. As shown schematically in Fig. 5, different end-member fold models produce distinct incremental deformation patterns, which will be recorded by initially horizontal passive geomorphic marker such as terraces. Fault-bend and fault-propagation folds will lead to uniform uplift above fault segments of constant dip; geomorphic markers will record some tilting where crossing axial surfaces. However, such steeply dipping panels will present a short wavelength and the dip is expected to be similar, i.e. terraces will be parallel, whatever their age (Fig. 5a). In contrast, limb rotation in a detachment fold will produce progressive terrace tilting, long and gently dipping panels and maximum uplift at the anticlinal crest (Fig. 5b). Detachment fold models with hinge migration produce profiles that are composites of the above two cases: progressive tilting of the markers along the limbs, but also steep parallel tilting at the synclinal and anticlinal hinges, with a marked asymmetry of the terrace uplift between the frontal fixed hinge and the backward migrating hinge (Fig. 5c). Finally, adding synclinal flexure to the detachment model will be recorded at the surface by progressive tilting of the marker, but also a transition from uplift to subsidence of the marker somewhere between the anticlinal and synclinal axes (Fig. 5d).
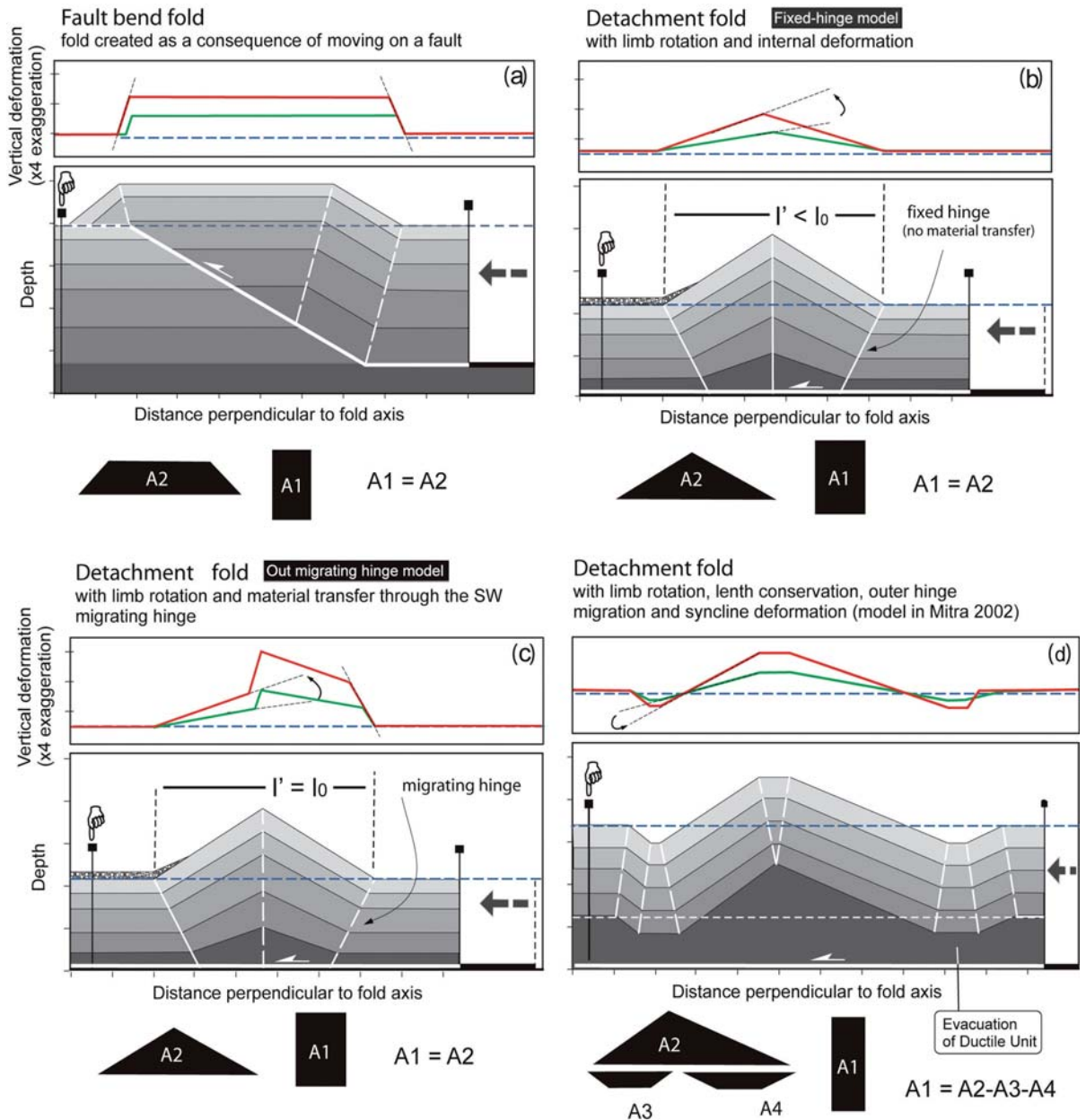
4 Recent Deformation of Mand Anticline

4.1 Tilted Marine and Fluvial Terraces

Geomorphic evidence for active tectonics has been reported from several locations within the Zagros belt along the MFF (Bachmanov et al., 2004) and along the south-eastern coast of the Zagros (Vita-Finzi, 1982). Around the Mand anticline, numerous discordant Bakhtiari units have been mapped: these units correspond to warped and tilted marine and fluvial terraces. Such terraces are particularly useful features since they can provide information on rates of rock uplift and hence rates of folding.

The terraces in the study area were first recognized on Corona and SPOT images, and then surveyed in detail in the field. They usually correspond to inverted topography: gravels or re-cemented shell-rich marine facies have preserved the underlying unconsolidated marly, silty or sandy Agha Jari/Labhari units from erosion; they consequently appear as isolated remnants at the top of small steep hills within a badland eroded landscape (cf. Fig. 9). We chose terrace treads to be surveyed on the basis of their preservation, in order to ensure continuity of the studied terrace level, such that the correlation of the close disconnected treads does

Fig. 5. Different fold models and associated surface deformation (obtained by producing incremental deformation in the different fold models): (**a**) fault-bend fold, (**b**) detachment fold with limb rotation and internal deformation, (**c**) detachment fold with limb rotation and material transfer through the NE axial surface, (**d**) detachment fold with limb rotation, length conservation, migration of the outer hinges and synclinal flexure. Lower panels show finite deformation after an amount of shortening equal to A1 divided by the depth to detachment; fixed and migrating hinges are presented by solid and dashed white lines, respectively. Upper panels show incremental deformation as would be recorded by two marker surfaces with different ages. Method of area balancing for shortening calculations is also indicated for each model

not suffer any ambiguity. The precise locations and elevations of the terraces were measured using kinematic GPS and, where access was too difficult, with a laser distance meter from a GPS-referenced point in order to project all the points in the same geographic projection. The terrace elevations were measured with an accuracy of a few centimeters for the GPS survey and with an accuracy of 0.2–2 m for the distance meter, depending on the ranging distance (between 10 and 250 m). Where possible, we measured the elevation of the top of the terrace gravels or fill material, and also of the unconformity at the base of the terrace or strath

level. Along the western limb of Mand anticline, we surveyed three distinct areas (cf. Fig. 3).

Southern site (site A): In the southern part of the fold, extensive marine terraces have been preserved and display impressive tilted tabular surfaces in the landscape. These marine terraces are constituted by 3–5 m of beach deposits, consisting of a partially to fully cemented sandy matrix with numerous shells (bivalves, oysters, clams…). Two main terrace remnants have been identified at site A, separated by an erosional depression along an ephemeral stream or wadi (Fig. 6). Along the shore of the Persian Gulf, they occur 6–9 meters above present-day sea level and are covered by aeolian sand deposits and meter-high dunes. Inland, their remnants are well exposed up to 1 km from the shoreline and at elevations up to 90 m above sea level. These marine terraces present remarkably linear profiles sloping at 9% to the SW (Fig. 9a). Generally, such marine terraces form in the tidal part of the shoreline, at or a few meters below average sea level, and with an angle of the order of 1%. Assuming such an initial geometry provides a tilt perpendicular to the fold axis of the order of 8.0±0.4% (~4.5°) since terrace formation.

The extensive marine terraces of the southern part disappear a few kilometers north of site A, after a progressive north-westward facies variation from cemented shell strata to cemented fossil dunes in the most inland part. Further north, the general elevation of the preserved tabular unconformable surfaces is lower and their slope more subdued. In addition, sedimentary units above the unconformity are mostly of fluvial- or fan-type deposits. Along most of the Mand anticline, these surfaces are best preserved in a ~500 m-wide coastal strip, where they are often partly covered by modern sand dunes. Sporadically, small remnants of these surfaces are preserved and display elongated and small "mesetas" that can be tracked up to 3 km landward, at the foot of the rugged relief carved
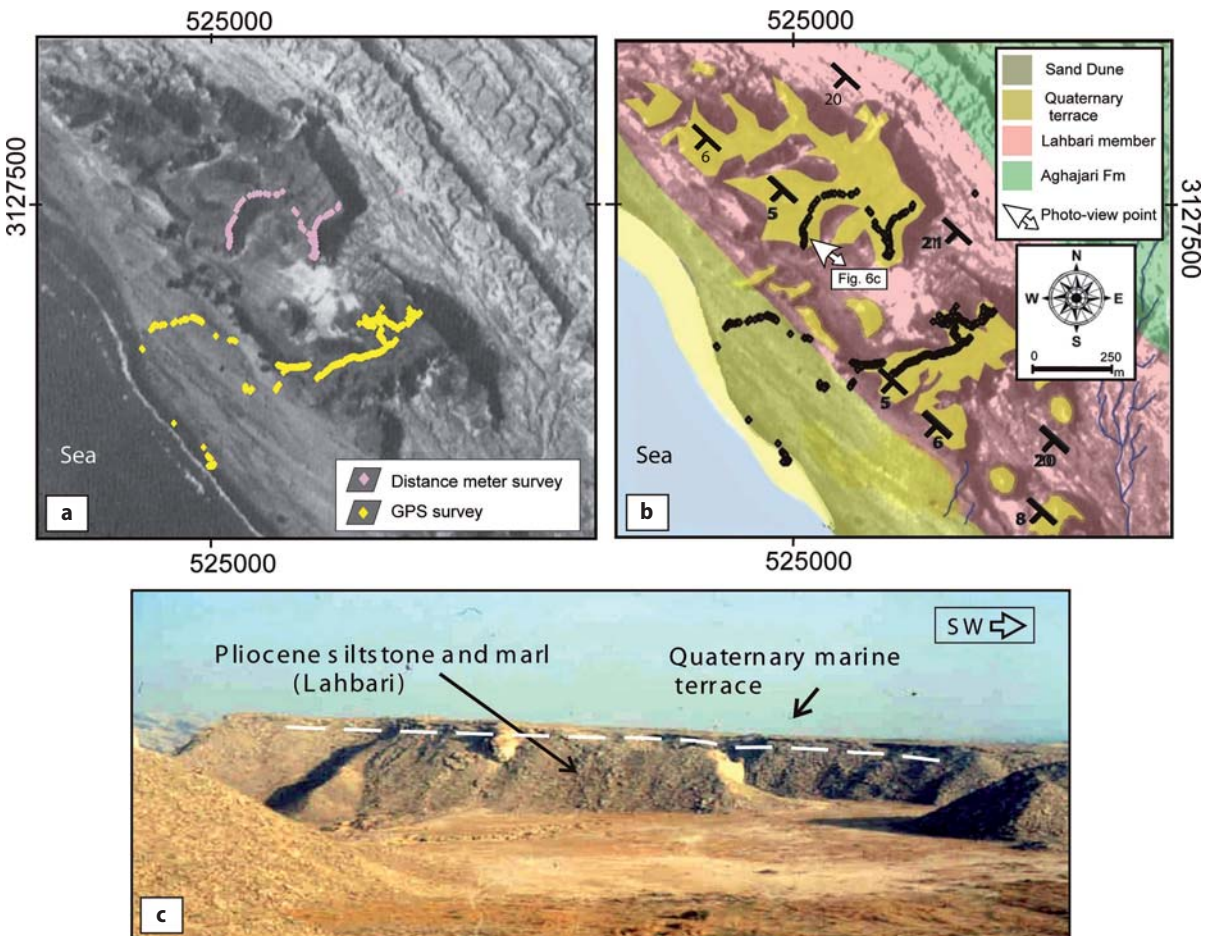
Fig. 6. (**a**) Corona satellite image and (**b**) geomorphologic map of the surveyed marine terrace site A in the southern part of Mand anticline (location indicated on Fig. 3). Survey data points for the construction of Fig. 9a are indicated. (**c**) Field photo of tilted marine terrace, looking SW across the erosional depression created by a wadi (photo viewpoint shown in b). The ~4.5° tilt of the terrace, as well as the angular discordance with the underlying Lakhbari Formation, is clearly visible
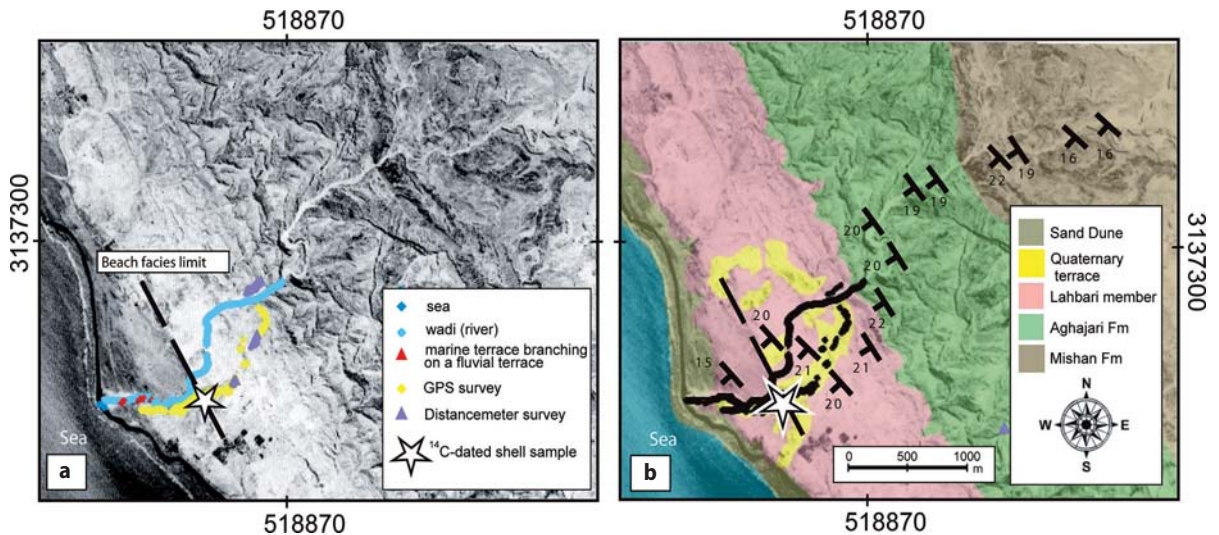
Fig. 7. (**a**) Corona satellite image and (**b**) geomorphologic map of surveyed fluvio-marine terraces at site B in the south-central part of Mand anticline (location in Fig. 3). Survey data points for the construction of Fig. 9b are indicated

into the Agha Jari sandstone units. These surfaces represent isolated remnants of paleo-fan deposits emplaced onto a pediment zone, which developed southwest of the main fold relief in the non-cohesive and easily erodable silty Lahbari units.

Central site (site B): In the south-central part of the anticline, an almost continuous tread of fluvial (or fan) terrace remnants were surveyed up to 1.5 km NE from the shoreline (Fig. 7). They form well-preserved flat and inclined surfaces, with straths that lie below 3 to 4 m of gravels. Toward the Persian Gulf coast, the base of the terrace gravels is replaced by a 2 m-thick sandy beach facies, including a basal layer rich in marine shells (Fig. 9b). The regional slope of the strath does not change, however, at the transition between fluvial and beach facies. As observed in site A, both the terrace strath and tread are nearly linear in profile, sloping at 4.1% to the WSW (Fig. 9b). We hypothesize that the strath terrace has been carved and the gravels facies of the terrace transported and deposited by a similar wadi to the one that currently runs through the site. The latter has a contributing area of 11 km2 and its gradient reaches 1.2%. The original geometry of this wadi during deposition of the terrace material is difficult to estimate, but the ~3% difference of slope between the terrace and the modern wadi is most probably due to tectonic deformation. Since terrace formation, the planar geometry of the wadi has radically changed, however: it was building a narrow fan whereas it is slightly entrenched in its pediment today and locally displays meanders. Such geometric changes, like potential gradient changes, may affect the reconstruction of the initial terrace geometry and the inferred deformation profile (Lavé and Avouac,

2000). We suspect that during the fluvial/fan deposition, the wadi was braiding and straighter than today. In addition, on the basis of the tilt recorded by the beach facies, which is supposed to be deposited near-horizontally, we suspect that the regional gradient of the fan was closer to the 1.2% gradient of the present wadi than to the 1.6% gradient of the modern pediment (Fig. 9b). Assuming such an initial slope provides a tilt perpendicular to the fold axis of the order of $2,9^{+0.2}_{-0.4}$ % (~1.7°) since terrace formation.

Northern site (site C): In the northern part of the anticline, larger outcropping surfaces of the Lahbari Formation have permitted the development of a larger pediment and locally the preservation of an almost continuous tread of fluvial (or fan) terrace remnants up to 3.5 km from the shoreline (Fig. 8). As in site B, they form well-preserved flat and inclined surfaces, with straths lying below 4 to 5 m of gravels. Toward the Persian Gulf, the base of the terrace gravels is replaced by a 4 m-thick sandy beach facies, including several layers rich in marine shells (Figs. 8 and 9c). As in site B, the regional slope of the strath level does not change at the transition between the fluvial and the beach facies. However, the top of the terrace is covered by a 20 m-thick series of finer gavels (Fig. 10c). The strath level and the terrace top are close to linear in profile, sloping at 5.1% to the west, whereas the upper surface of the overlying fine gravel deposits close to the shoreline displays a more subdued slope of 1.8%. Considering again that the wadi, which has probably carved the strath terrace and transported and deposited the gravels of the terrace, is comparable to the present-day wadi, its contributing area is 6 km2, and its modern gradient reaches 1.1%. As for site B, and again
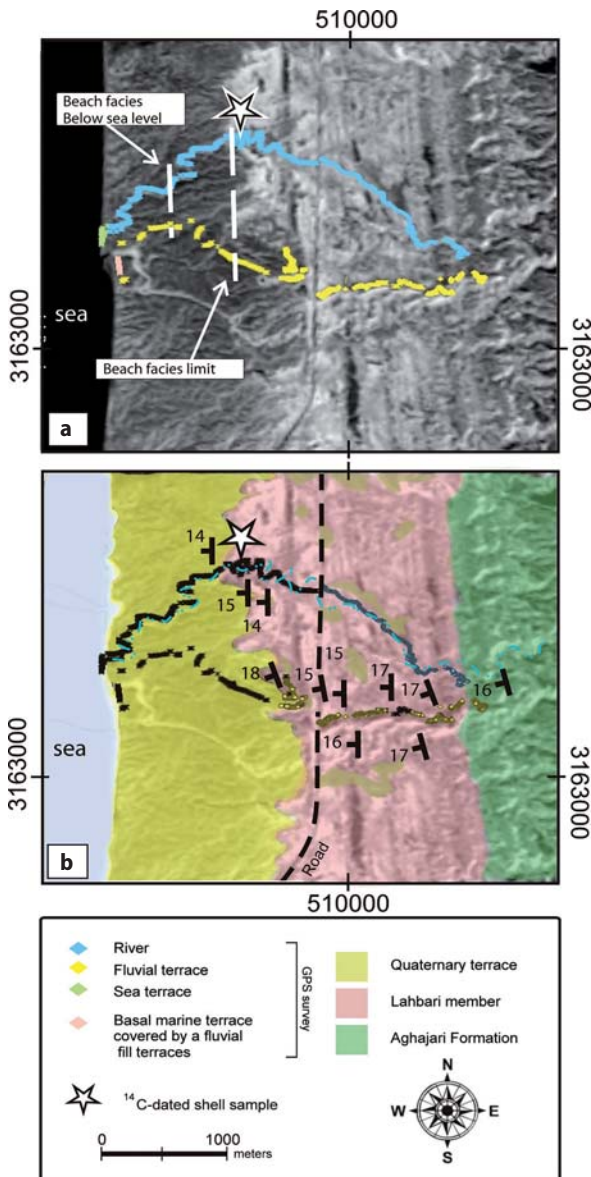
Fig. 8. (**a**) Corona satellite image and (**b**) geomorphologic map of surveyed fluvio-marine terraces at site C in the central-north part of Mand anticline (location in Fig. 3). Survey data points for the construction of Fig. 9c are indicated

on the basis of the tilt recorded by the beach facies, we will assume that the initial slope of the fan/terrace deposit was closer to this 1.1% of the present wadi than to the 1.8% gradient of the modern pediment (Fig. 9c). Using this as the initial slope provides a westward tilt of the order of $4^{+0.2}_{-0.4}$% (~2.3°) since terrace formation.

The general pattern displayed by these three sites is remarkably consistent: whatever their nature, the surveyed surfaces record a regional tilt perpendicular to the local fold axis. Except for uncertainties of the order of 5–10 m that result from a small curvature of the

modern terrace and wadi profiles close to the Agha Jari relief in site B, these terraces appear to have been affected by large-scale tilting and seem exempt of secondary folding, faulting and other small-scale deformation features. The terraces do, however, record different degrees of tilting that result from differences in either terrace ages or local fold maturity. Because sites A and B are only 15 km apart and are associated with a similar amplitude of the main Mand anticline (cf. Fig. 4), we strongly suspect that terrace A has been affected by a 3 times larger tilting than terrace B because it is older and has thus recorded more deformation. In any case, the set of surveyed terrace levels clearly indicates persistent active folding of the Mand anticline.

In addition, stereographic observations on couples of Corona images indicate that the Bakhtiari and terrace surfaces on the Eastern limb of the anticline are also widely affected by tilting, without evidence for short scale folding or faulting, suggesting that the fold deforms, at least in part, by limb rotation on its eastern flank.

4.2 Terrace Dating and Rates of Tilting

Whole shells as well as shell fragments have been sampled from the beach deposits in the terraces of Sites B and C (see location of samples in Figs. 7 and 8). Three bivalve fragments of apparently non-recrystallized calcite have been dated by Accelerator Mass Spectrometer (AMS) ^{14}C (Table 1). They all provided ^{14}C ages between 28 and 37 kyr B.P., which correspond after a rough calibration (van der Plicht et al., 2004) to ages ranging between 30 and 44 kyr B.P. (Table 1).

Numerous 14C ages in this range have been encountered around the Persian Gulf (Vita-Finzi, 1982; Haghipour and Fontugne, 1993; Uchupi et al., 1999), but several studies (Page et al., 1979; Fontugne et al., 1997) have cast doubt on the validity of such ages because of potential partial recrystallization of bivalve shells. The main problem concerning these ages is that it is not obvious that the shallow and relatively

**Table 1.** AMS ^{14}C ages of bivalves sampled in marine terraces or beach facies.

Sample	Lab. no.	^{14}C Age (yr)	Calibrated age § (kyr BP)
ZA-2002-16 *	Poz-11984	37200 ± 600	~41 (39 – 44)
ZA-2002-7a *	Poz-12063	28200 ± 200	~32 (30 – 35)
ZA-2002-7b #	001406	34350 ± 270	~39 (36 – 41)

* ^{14}C dating in the Poznań Radiocarbon Laboratory, Poland.

\# Laboratoire de Mesures Carbone 14 UMS 2572, CEN Saclay, France.

§ Calibration range given by various calibration curves presented in van der Plicht et al. (2004), after having applied a reservoir correction of ~400 yr
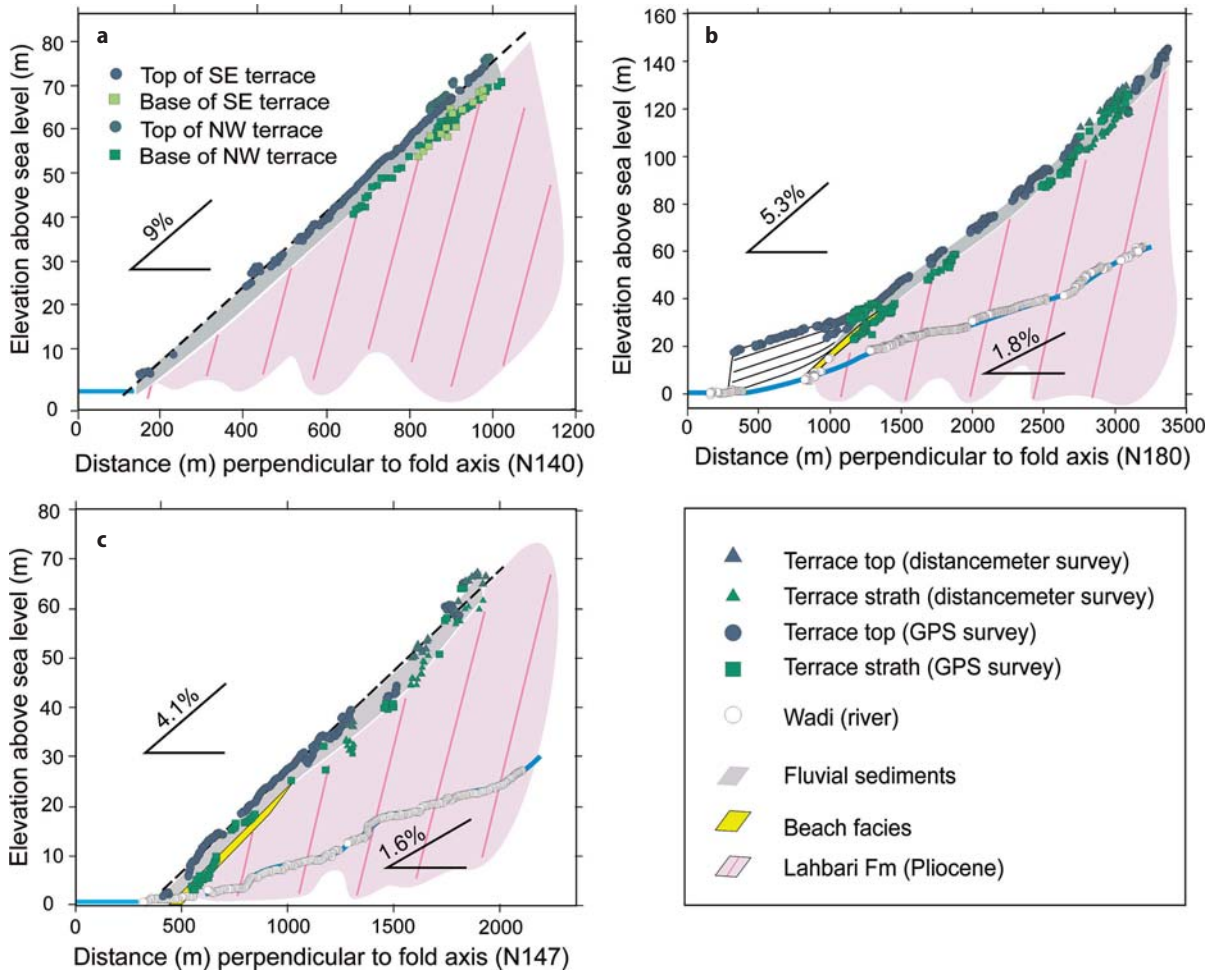
Fig. 9. Topographic profiles of the surveyed tilted terraces at sites A, B and C, along with present-day wadi profiles for sites B and C. Slopes of best-fit straight lines through terrace and wadi data are indicated

restricted Persian Gulf was under marine influence during global sealevel lowstands. The global sea level curve (e.g., Lambeck and Chappell, 2001; Thompson and Goldstein, 2006) indicates that sea level was 70–80 m below present during this period, with, however, secondary sea-level rises up to -50 to -60 m at 45, 48 and 52 kyr (Chappell, 2002) or at 31.5 and 48 kyr (Thompson and Goldstein, 2006). A detailed postglacial shoreline reconstruction of the Persian Gulf, based on a glacio-eustatic model (Lambeck, 1996), predicts the central Gulf to be flooded for mean sea levels higher than -60 m. The bathymetry of the Persian Gulf in front of the Mand anticline displays a progressive drop down to a depth of 60 m, but this lowest point is located at ~40 km SW of the Mand anticline coast. However, a sonar survey of recent sediments in the Persian Gulf (Uchupi et al., 1999), indicates that Late Pleistocene/early Holocene (since ~25 kyr) sedimentation may amount to more than 10 or 20 m off the

Fars coast, in particular along the present study area, where the Gulf receives sediment input from the two major Fars rivers, the Rud e Mand and Rud e Dalaki (Fig. 1). It is therefore possible that a very shallow sea extended up to the Mand anticline during the short-duration secondary highstands between 31.5 and 48 kyr, and would have left some beach deposits. This period was probably also marked by wetter conditions than today; more efficient rivers could thus have been draining and eroding the anticline, forming large pediments topped by several meters of gravel deposits overlying the Pleistocene Lahbari units.

Marine deposits in site A extend much more prominently than in the other sites. For this reason, we expect them to correspond to a major and long duration high stand associated with a major interglacial period. Marine terraces of Kish island, 300 km SE, correlate for example with high stands of marine isotopes stages (MIS) 5e and 7 (Preusser et al., 2003). More generally,

numerous U/Th ages of corals topping marine terraces around the Makran and Persian Gulf (Reyss et al., 1998) indicate generally well-developed and distributed terraces formed during the penultimate interglacial (MIS 5e; 120–125 kyr, Thompson and Goldstein, 2006). If marine terrace A would also have formed at this time, the tilting rate in A would reach 0.038°/kyr, a value comparable to tilting rates ranging between 0.035 and 0.054°/kyr in site B. Although additional dating of the terraces by an independent method would be welcome, this consistency with the attribution of the marine terraces around site A to the penultimate interglacial at 120 kyr B.P. provides us with some confidence in the ^{14}C shell dating. It should be noted, for example, that associating terrace B to MIS 5e, and terrace A to MIS 7, would provide much less consistent tilting rates of 0.014°/kyr and 0.022°/kyr respectively, and would not explain their different sedimentological nature.

4.3   Folding Model and Shortening Rate

The terrace deformation profiles in the three sites provide several first-order observations to unravel the fold kinematics. Firstly, the observed wide-scale tilting precludes uplift above a shallow fault ramp, or would at least require a ramp that progressively flattens upward while transferring slip toward a more frontal structure, which is not observed. Tri-shear models (e.g., Erslev, 1991) could produce progressive tilting of the frontal limb but would be associated with significant bed thickening, in contrast with the constant layer thickness observed on both limbs. On the basis of the fold symmetry, terrace tilting, and increasing tilt with terrace age, it seems that only limb rotation associated to a detachment fold can account for the observed pattern of terrace deformation.

If we consider a simple sinusoidal fold model (Fig. 10), which fits observed surface bedding dips relatively well, the observed bedding of 21°, 16° and 11° along sections f1 (sites A/B), f2, and f3 (site C; cf Figs. 2 and 4), respectively, can be linked to a cosine amplitude of 1.4, 1.1 and 0.9 km, respectively with, im-

portantly, roughly similar wavelengths. Whereas the structural data are not precise enough to detect a possible decrease of the wavelength by fold tightening between sections f3 and f1, these observations do suggest that the Mand detachment fold geometry can be modelled by a simple cosine shape during the different stages of its evolution. In the following, we will therefore assume such a simplified geometry to interpret terrace tilting in terms of shortening across the fold.

The increasing tilt of the terraces with age can be simply related to the evolution of fold amplitude and, with less resolution, to the evolution of fold wavelength. For a high wavelength/ amplitude ratio, the difference of shortening accounting for the different terrace tilting between a model with fixed hinges and constant limb length, and a model with migrating hinges and constant wavelength, was found to be smaller than 3%. Hereafter, we will therefore only present and discuss the results obtained for a fixed-hinge model, i.e., a model where the upper Agha Jari surface is modelled by a cosine curve in the range $(-\pi/2; \pi/2)$, with its wavelength decreasing with increasing shortening and an initial and constant length of 12 km. Accordingly, in the south-central part of the Mand anticline, a tilting of 4.5° (or 8%) and 1.7° (2.9%) as recorded by the terraces at sites A and B, respectively, would have been produced by shortening of the order of 320 m and 125 m, respectively (Table 2). For site C, despite a somewhat larger tilt (~2.3°) (or 4%) than in site B, we find a very comparable shortening value of 130 m. This result arises from the decreasing sensitivity of limb rotation to shortening during fold tightening.

As discussed in Sect. 3.2, one of the main problems with obtaining shortening estimates from detachment folds is related to the incompatibility between line-length versus area restoration. The two previously detailed cases can be examined in terms of present shortening rate:

Case 1: The restoration paradox is solved by bed thickening: the total shortening represents the sum of the shortening absorbed by limb rotation and the shortening absorbed by bed thickening (Fig. 10c). This latter component represents 54 to 65% of the total shortening (Table 2) for limb angles of 21° and 15°, re-

Table 2. Shortening rate calculations according to the considered fold model

	Marker Tilt (%)	Age (kyr)	Sinusoidal Fold model				Shortening using area conservation (m)	Shortening rate (mm/yr) including internal deformtion	Shortening rate (mm/yr) with adjacent syncline model
			Present amplitude (m)	Amplitude change since terrace formation (m)	Length shortening (m)	Shortening rate (mm/yr)			
Site A	8 ± 0.5	120 ± 5	1420	330	320 ± 20	2.7 ± 0.15	750	6.3	3.3
Site B	$2.9^{+0.2}_{-0.4}$	40 ± 5	1420	120	124^{+8}_{-16}	$3.1^{+0.4}_{-0.5}$	270	6.8	3.9
Site C	$4.0^{+0.2}_{-0.7}$	40 ± 5	1100	160	130^{+7}_{-19}	$3.2^{+0.4}_{-0.6}$	370	9.3	4.0
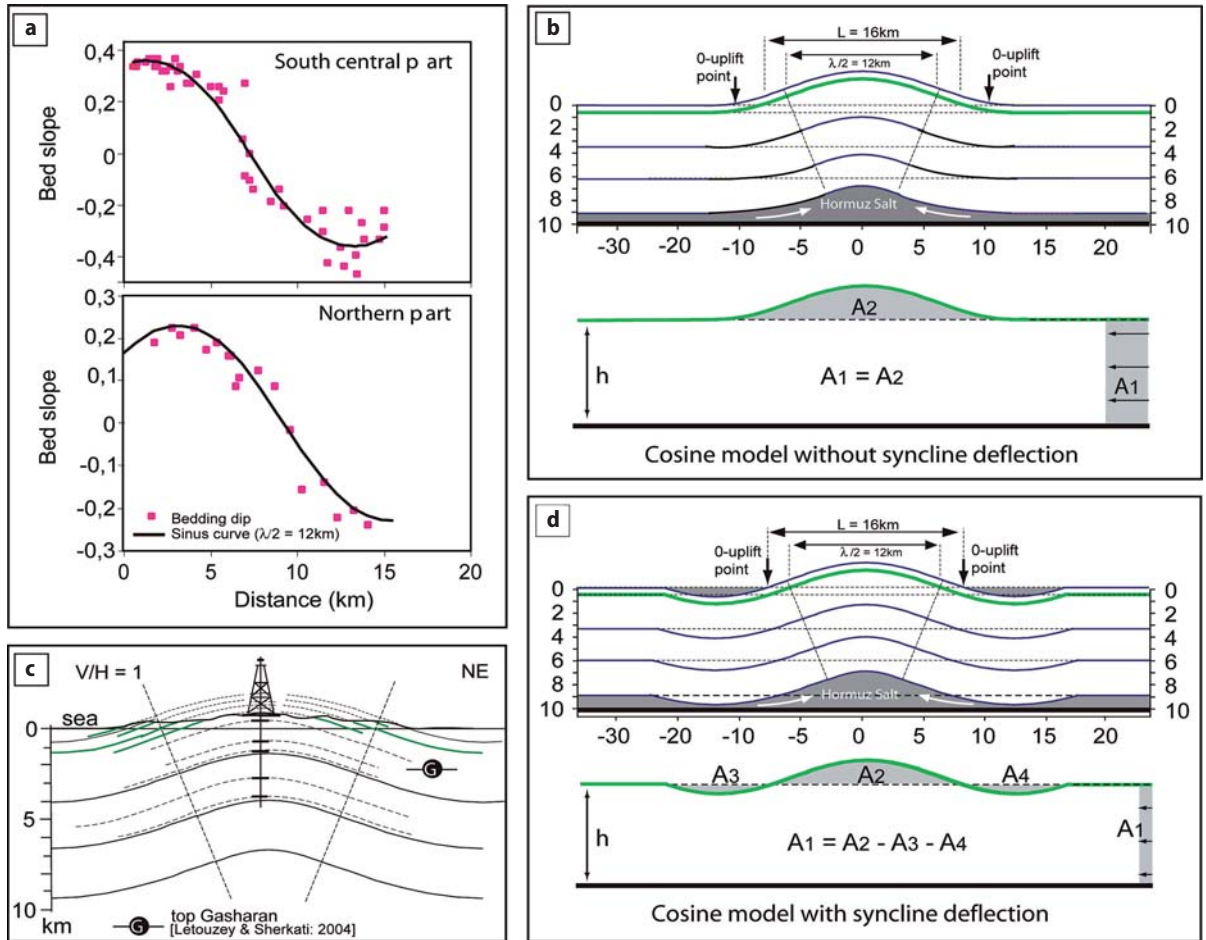
Fig. 10. Cosine model applied to upper folded units of the Mand anticline. (**a**) Bedding dips (from geologic maps and field survey) along the central and northern profiles (f2-f2' and f3-f3' in Fig. 3) follow a sinusoidal curve centred at the anticline axis. (**b**) Fold geometry approximated by a cosine model with a crest to through amplitude of ~3 km and a wavelength (λ) of 24 km. Models without (**c**) or including (**d**) flexure of the flanking synclines yield a distinct area conservation but also distinct locations of the no-uplift point between the anticlinal and synclinal axes

spectively (in terms of instantaneous shortening rate, a limb angle of ~30° is required to annihilate the bed thickening component). With such a model, the total shortening rate across the Mand anticline in site C could reach up to 9 mm/yr and be 35 to 50% larger than in sites A and B.

Case 2: the restoration paradox is solved by synclinal flexure below a regional level (Fig. 10d). In this case the additional flexure of the syncline increases the shortening absorbed by limb rotation by only 25%, and provides total shortening rates ranging between 3 and 4 mm/yr for all three sites (Table 2).

Not only do the above two models predict distinct shortening rates, they also display another different feature at the surface: the location of the pivoting point, or point of no uplift during folding. For a similar fold wavelength and amplitude between the anticlinal crest and the flanking depocenters (wheth-

er these are flat or synclinal), the point of no uplift will be closer to the anticlinal axis in the synclinal flexure model (compare Figs. 10 c and d). In the case of the Mand anticline, its topographically expressed width of ~16 km is much shorter than the estimated anticline wavelength of ~24 km. The external parts of the anticline (~4 km on both sides), which have no topographic expression, may therefore be subsiding and affected by a sedimentation at more rapid rates than the local uplift. Long-term regional subsidence and sedimentation rates probably range between 0.2 and 0.3 mm/yr, assuming 2–2.5 km of regional sedimentation (Fig. 10b; Letouzey and Sherkati, 2004) since the end of the Gachsaran sequence at ~12 Ma (Homke et al., 2004). Considering the above cosine model and tilting rates, such a sedimentation rate would imply the pivoting point to be ~9.5 km away from the anticlinal axis and not ~7 km, as observed from the 0 elevation

of terrace A (note that we implicitly assume here that this terrace has formed during the MIS 5e and that sea level at that time was close to the present-day sea level). Consequently, much higher local sedimentation rates are required, a hypothesis that is compatible with active subsidence of the synclines flanking the Mand anticline.

The above values and estimates of shortening, as well as the preceding argument supporting syncline flexure, are clearly model dependent and no definitive conclusion about fold kinematics and total shortening can be reached without detailed seismic data that would image the upper structures in the frontal syncline. The representation of the fold by a cosine shape probably represents an oversimplification, and the flanking synclines could be much broader than the anticline, as suggested by the cross-section of Fig. 2. However, as in the cosine model, the associated flexure absorbs a reduced amount of shortening and will not significantly affect the shortening estimates. Finally, it should be noted that the above argument about the location of the pivoting point depends on the inferred fold uplift rate, i.e., on terrace dating. If our ^{14}C ages are minimum ages and terraces are older than assumed here, the local uplift to regional subsidence ratio would consequently decrease, and the pivoting point would be located closer to the anticlinal axis.

5   Discussion

Several recent morphotectonic studies have described and quantified different fold kinematics and associated deformation at the surface, as recorded by geomorphic markers (e.g., Lavé and Avouac, 2000; Benedetti *et al.*, 2000; Thompson et al., 2002; Ishiyama et al., 2004; Gold et al., 2006). The present study on the Mand anticline is, however, to our knowledge one of the first to document the recent growth of a detachment fold. The progressive tilting of the coastal marine and fluvio-marine terraces along the Mand anticline highlights that this detachment fold primarily deforms by limb rotation, in contrast to many other fold models where deformation occurs by hinge migration in association with dominant fault motion at depth, like fault-bend folding or fault-propagation folding. Whereas these fold types are favoured by a homogeneous sedimentary sequence but with strong mechanical anisotropy permitting bedding slip, the Zagros sedimentary sequence is characterized by major mechanical stratification, with an upward sequence of basal ductile units, followed by competent units, and upper incompetent units. As proposed by Mitra (2002), such a setting favours the development of detachment folds like the Mand anticline. Although large uncertainties remain concerning its exact geometry at depth, as well as

the original thickness of the basal Hormuz salt, the terrace data suggest that this ductile layer was sufficiently thick to permit ≥500 m flexure of the synclines flanking the Mand anticline and salt migration from the synclines towards the core of the anticline.

We are not able to provide strong evidence in favour of active flexure in the synclines, but several lines of evidence discard the alternative model characterized by dominant bed thickening. Firstly, clear evidence of thickening has not been observed; the anticlinal crest, in contrast, displays numerous extensional fractures. Secondly, the location of the no uplift points in profile indicates that either the anticline is narrower than imaged on seismic sections (Letouzey and Sherkati, 2004), or that the synclines are actively subsiding. Thirdly (but this argument is weaker) the shortening rates computed in sites A, B and C would present more dispersion in the case where bed thickening is accounted for and, in addition, the geological shortening rate in C would be higher than the total present-day shortening absorbed across the Zagros according to GPS data. In the absence of alternative models to describe fold detachment and solve their restoration paradox, the active synclinal flexure model represents our currently preferred model. Consequently, a total shortening of ~1 km, instead of 2.4 km as inferred from our initial fold construction (Fig. 4) that included bed thickening, and a shortening rate of 3–4 mm/yr are expected across the Mand anticline, which represents the regionally most frontal structure of the Zagros. If such a rate has persisted since fold inception, the Mand anticline would have begun to form only 300 kyr ago.

Despite the relatively rapid rates of deformation inferred for the Mand anticline, present-day seismicity associated with this structure is minimal, with only two M_w=5.2 earthquakes occurring below the Mand fold during the last 30 years (cf. Figs. 1 and 3). The Himalayan frontal fold-and-thrust belt is also characterized by the absence of recent seismicity, which has been attributed to the mechanical locking of the basal detachment (Lavé and Avouac, 2000) in between two major earthquakes. In the Zagros, in contrast, recent GPS results (Walpersdorf et al., 2006), as well as the distributed seismicity that occurs mostly in the basement (Tatar et al., 2004), indicate that the Mand anticline, like most of the Zagros sedimentary cover, deforms mostly aseismically. Focal mechanism solutions of the two M_w=5.2 events below the Mand fold present nodal planes that are sub-parallel to the surface structure of the fold (cf. Fig. 3). In the absence of reported centroid depths, we can infer three potential mechanisms:

1. An event occurring on a basement fault, i.e., below 10 km; such a fault could have controlled the initiation of the detachment fold;

2. An event produced on a propagating fault in the lower part of the sedimentary cover; the detachment fold could be evolving toward an asymmetric fault-propagation fold in the future, as observed in mature folds in the internal Zagros (McQuarrie, 2004);

3. A seismic event associated to secondary faults that control thickening of the competent Palaeozoic to Mesozoic units in the core of the fold. The geologic cross-section below the Mand anticline does not require basement involvement, as opposed to the folds further north-east (Letouzey and Sherkati, 2004) and the two latter solutions could eventually be preferred. In any case, significant involvement of the basement seems precluded by the structural data that clearly indicate the symmetry of the fold, as well as by the seismic data (Letouzey and Sherkati, 2004).

Because of the symmetric shape of the fold, and because of the absence of an obvious strike slip fault that could partition oblique motion within the fold, we suggest that shortening is mostly perpendicular to the local fold axis. If so, this local shortening direction is oriented at 40° to 60° from the regional compression direction as indicated by seismicity (Gillard and Wyss, 1995). As a consequence, shortening across the Mand anticline represents 35 to 50% of the strain in the Zagros in absolute value, but absorbs only ~20 to 35% of the 8 mm/yr of the SSW-NNE convergence across the Zagros. On the other hand, the obliquity of the shortening directions in the sedimentary cover with respect to the basement, suggests that shortening and horizontal stress transfer in the sedimentary cover of the frontal Zagros are fully decoupled from the basement, most probably at the level of the Hormuz salt. This conclusion contradicts recent suggestions (e.g., Molinaro et al., 2005; Sherkati et al., 2005; Mouthereau et al., 2006) that, in the Eastern Fars and northwest Zagros, deformation was initiated in the sedimentary cover, starting as early as Late Miocene at the northwest Zagros front (Homke et al., 2004), and that more recent deformation has been dominated by thick-skinned tectonics and by the transfer of basement faulting upward to the sedimentary cover (Molinaro et al., 2005). The rate and style of deformation of the Mand anticline suggest that such a tectonic model and chronology does not apply for the western Fars. The recent activity of the Mand anticline suggests, instead, that a forward-propagating deformation sequence in a thin-skinned tectonic regime is still an on-going process. This process does not preclude, however, simultaneous seismic, and possibly aseismic, deformation in the basement.

6   Conclusion

This study illustrates that combined structural and geomorphic investigations may concur to provide tight constraints on fold geometry and recent kinematics in the extensive and spectacular Zagros fold belt. Building balanced cross-sections of detachment folds requires solving a number of problems, in particular the length versus area restoration issue. Despite extensive structural and geophysical constraints, ambiguities on the fold solution for the Mand anticline still remain. The recent surface deformation, as recorded by dated fluvio-marine terraces on its western limb, helps to precise the fold kinematics and consequently the fold solution: first, progressive tilting of the geomorphic markers excludes deformation related to a fault with a kilometer-scale offset close to the surface; second, the location of the no-uplift point between the external hinge of the anticline and its axis indicates that flanking synclines could be affected by active subsidence. We therefore suspect that the Mand detachment fold is accompanied by the migration of Hormuz salt from below the synclinal flexures toward the core of the anticline. This preliminary conclusion suffers, however, from large uncertainties because of the controversial nature of the ^{14}C ages of marine terrace deposits in the Persian Gulf region (Page et al., 1979; Fontugne et al., 1997), and independent dating of the terraces would be welcome. Moreover, because of the limited extent of the deformed geomorphic markers, the fold solution is probably non-unique. Additional geophysical data would add constraints to the fold model; detailed and high quality seismic data across the fold, the flanking synclines and, more importantly, in the Persian Gulf would permit to test our model by imaging the predicted absence of a major WSW-vergent fault close to the surface, the absence of important bed thickening, and the flexure of synclines below the regional level. They would also bring essential information on the existence of growth strata in the flanking synclines and on the timing of fold inception. Additional work is also required (and has started) on several detachment structures at different stages of their development, in order to unravel the complete kinematic history of detachment folds in Zagros, and how they evolve at the surface from a subdued, wide and symmetrical anticline to a tight, faulted and asymmetric fold.

Notwithstanding these uncertainties, our geomorphic analysis unambiguously shows that the Mand anticline is a very active structure on the south-westernmost front of the Zagros wedge. The Late Pleistocene shortening rate is inferred to be 3 to 4 mm/yr perpendicular to the anticline, which would absorb 35 to 50% of the 8 mm/yr (Vernant et. al., 2004) convergence across the entire Zagros. This result is consis-

tent with a normal forward-propagating deformation sequence in a thin-skinned tectonic regime during at least the Late Pleistocene, with south-westward migration of the front of the wedge. Comparing the rate and direction of shortening across the Mand anticline, as well as recent GPS data (Walpersdorf et al., 2006), with the distribution of seismicity (Talebian and Jackson, 2004; Tatar et al., 2004), also suggests that the sedimentary cover of the frontal Zagros is fully decoupled from the basement, most probably at the level of the Hormuz salt. This conclusion has important implications for the modalities of stress transfer at the scale of the western Fars province in Zagros. It contradicts, in particular, recent models in which basement deformation currently controls the location of the deformation in the sedimentary cover through slip transfer along steep crustal faults.

Acknowledgements

References

Alavi, M. (2004) Regional stratigraphy of the Zagros fold-thrust belt of Iran and its proforeland evolution, American Journal of Science, 304, 1–20.

Bachmanov, D. M. , V. G. Trifonov , Kh. T. Hessami , A. I. Kozhurin , T. P. Ivanova , E. A. Rogozhin , M. C. Hademi, and F. H. Jamali (2004) Active faults in the Zagros and central Iran, Tectonophysics, 380, 221–241.

Benedetti, L., Tapponnier, P., and King, G. (2000) Growth folding and active thrusting in the Montello region, Veneto, northern Italy. Journal of Geophysical Research, 105, 739–766.

Berberian, M. (1995) Master blind thrust faults hidden under the Zagros folds: active basement tectonics and surface morphotectonics, Tectonophysics, 241,193–224.

Blanc, E. J.-P., M. B. Allen, S. Inger, and H. Hassani (2003), Structural styles in the Zagros simple folded zone, Iran, Journal of the Geological Society, London, 160, 401 – 412.

Chandra, U (1984) Focal mechanism solutions for earthquakes in Iran, Physics of the Earth and Planetary Interiors, 34, 9–16.

Chappell, J. (2002) Sea level changes forced ice breakouts in the Last Glacial cycle: new results from coral terraces, Quaternary Science Reviews, 21, 1229–1240.

Colman-Sadd, S.P. (1978) Fold development in Zagros simply folded belt, southwest Iran, American Association of Petroleum Geologists Bulletin, 62, 984–1003.

Dahlstrom, C.D.A. (1969) Balanced cross sections. Canadian Journal of Earth Sciences, 6, 743–757.

Dahlstrom, C.D.A. (1990) Geometric constraints derived from the law of conservation of volume and applied to evolutionary models of detachment folding. American Association of Petroleum Geologists Bulletin, 74, 336–344.

DeMets, C., R. G. Gordon, D. F. Argus, and S. Stein (1994) Effects of recent revisions to the geomagnetic time scale on estimates of current plate motions, Geophysical Research Letters, 21, 2191 – 2194.

De Sitter, L.U. (1964) Structural Geology (2nd edition), McGraw-Hill, New York, 551 pp.

Epard, J.-L., Groshong, R.H. (1993) Excess area and depth to detachment, American Association of Petroleum Geologists Bulletin, 77, 1291–1302.

Epard, J.-L., Groshong, R.H. (1995) Kinematic model of detachment folding including limb rotation, fixed hinges, and layer-parallel strain, Tectonophysics, 247, 85–103.

Erslev, E.A. (1991) Trishear fault-propagation folding: Geology, 19, 617–620.

Falcon, N. (1969) Problems of the relationship between surface structure and deep displacements illustrated by the Zagros Range, in Time and Place in Orogeny, Geological Society (London) Special Publication, 3, 9 – 22,.

Farhoudi, G. (1978) A comparison of Zagros Mountains geology to Island Arcs, Journal of Geology, 86, 323–334.

Fontugne, M., Reyss, J.L., Hatte, C., Pirazzoli, P.A., Haghipour, A. (1997) Global sea level changes as indicated by 14C and 230Th/234U dating of marine terraces in the Persian Gulf and along the Makran Coast (Iran). In: Earth Processes in Global Change—Climate of the Past. Proceedings of the Lanzarote-Fuerteventura UNESCOIUGS Meeting, 1–6 June 1995, Universidad de Gran Canaria, Las Palmas, pp. 81–88, 1997.

Gillard, D. and Wyss, M. (1995) Comparison of strain and stress tensor orientation: application to Iran and southern California, Journal of Geophysical Research, 100, 22197–22213.

Gold, R. D., E. Cowgill, X.-F. Wang and X.-H. Chen (2006) Application of trishear fault-propagation folding to active reverse faults: examples from the Dalong Fault, Gansu Province, NW China, Journal of Structural Geology, 28, 200–219.

Haghipour, A., and Fontugne, M. (1993) Quaternary uplift of Qeshm Island (Iran). Comptes Rendus de l'Académie des Sciences, Paris, 317, 419–424.

Hessami, K., Koyi, H.A., Talbot, C.J., Tabasi, H., and Shabanian, E. (2001) Progressive unconformities within an evolving foreland fold–thrust belt, Zagros Mountains, Journal of the Geological Society, London, 158, 969–981.

Hessami H., Nilforoushan F., and Talbot C. J. (2006), Active deformation within the Zagros Mountains deduced from GPS measurements, Journal of the Geological Society, London, 163, 143–148.

Homke, S., J. Vergés, M. Garcés, H. Emami and R. Karpuz (2004) Magnetostratigraphy of Miocene–Pliocene Zagros foreland deposits in the front of the Push-e Kush Arc (Lurestan Province, Iran), Earth and Planetary Science Letters, 225, 397–410.

Ishiyama T., K. Mueller, M. Togo, A. Okada, K. Takemura (2004) Geomorphology, kinematic history, and earthquake

behavior of the active Kuwana wedge thrust anticline, central Japan, Journal of Geophysical Research, 109, B12408, doi: 10.1029/2003JB002547.

Jackson, J. A., and T. Fitch (1981) Basement faulting and the focal depths of the larger earthquakes in the Zagros mountains (Iran), Geophysical Journal of the Royal Astronomical Society, 64, 561 – 586.

Jackson, J. A., Fitch, T. J. and McKenzie, D. P. (1981) Active thrusting and the evolution of the Zagros fold belt, in: McClay, K. R. and Price, N. J. (eds.), Thrust and Nappe Tectonics, Geological Society (London) Special Publication, 9, 371–379.

Jackson, J.A. and McKenzie, D. (1984) Active tectonics of the Alpine-Himalayan Belt between western Turkey and Pakistan, Geophysical Journal of the Royal Astronomical Society, 77, 185–264.

Jackson, J., Haines, J., & Holt, W. (1995) The accommodation of Arabia-Eurasia plate convergence in Iran, Journal of Geophysical Research, 100, 15,205–15219.

Jamison, W. R. (1987) Geometric analysis of fold development in overthrust terranes, Journal of Structural Geology, 9, 207 – 219.

Lambeck, K. (1996) Shoreline reconstructions for the Persian Gulf since the last glacial maximum, Earth and Planetary Science Letters, 142, 43–57.

Lambeck, K., and Chappell, J. (2001) Sea level change through the last glacial cycle, Science, 292, 679–686.

Lavé, J., Avouac, J.P. (2000) Active folding of fluvial terraces across the Siwaliks Hills, Himalayas of central Nepal. Journal of Geophysical Research, 105, 5735–5770.

Letouzey, J., Colletta, B., Vially, R. & Chermette, J.C. (1995), Evolution of salt related structures in compressional setting. In Jackson, M.P.A., Roberts, D.G., and Snelson, S., eds., Salt Tectonics: Global Perspective. American Association of Petroleum Geologists Memoir, 65, 41–60.

Letouzey J. and S.Sherkati (2004), Salt Movement, Tectonic Events, and Structural Style in the Central Zagros Fold and Thrust Belt (Iran), 24th Annual GCSSEPM Foundation Bob F. Perkins Research Conference, Salt-Sediments interactions and Hydrocarbon Prospectivity, Concepts, Applications and Case Studies for the 21st Century: Houston, Texas, Society of Economic Paleontologists and Mineralogists.

Maggi, A., J. Jackson, K. Priestley, and C. Baker (2000) A re-assessment of focal depth distributions in southern Iran, the Tien Shan and northern India: Do earthquakes really occur in the continental mantle? Geophysical Journal International, 143, 629 – 661.

Masson, F., J. Chéry, D. Hatzfeld, J. Martinod, P. Vernant, F. Tavakoli and M. Ghafory-Ashtiani (2005) Seismic versus aseismic deformation in Iran inferred from earthquakes and geodetic data, Geophysical Journal International, 160, 217–226.

McQuarrie, N. (2004) Crustal-scale geometry of the Zagros fold-thrust belt, Iran, Journal of Structural Geology, 26, 519–535.

Mitra, S. (2002) Structural models of faulted detachment folds, American Association of Petroleum Geologists Bulletin, 86, 1673–1694.

Mitra, S. (2003) A unified kinematic model for the evolution of detachment folds, Journal of Structural Geology, 25, 1659–1673.

Molinaro, M., P. Leturmy, J.-C. Guezou, D. Frizon de Lamotte, and S. A. Eshraghi (2005) The structure and kinematics of the southeastern Zagros fold-thrust belt, Iran: From thin-skinned to thick-skinned tectonics, Tectonics, 24, TC3007, doi: 10.1029/2004TC001633.

Mouthereau, F., Lacombe, O., and Meyer, B. (2006), The Zagros folded belt (Fars, Iran): constraints from topography and critical wedge modelling, Geophysical Journal International, 165, 336–356.

National Iranian Oil Company (1976), Geological Map of Iran, 1,100.000 series, Sheet 20860 W (Mand South).

National Iranian Oil Company (1977), Geological Map of Iran, 1,100.000 series, Sheet 20855 W (Mand North).

Ni, J. and Barazangi, M. (1986) Seismotectonics of the Zagros continental collision zone and a comparison with the Himalayas, Journal of Geophysical Research, 91, 8205–8218.

Page, W.D., Alt, J.N., Cluff, L.S., Plafker, G. (1979) Evidence for the recurrence of large-magnitude earthquakes along the Makran coast of Iran and Pakistan. Tectonophysics, 52, 533–547.

Paul, A., Kaviani, A., Hatzfeld, D., Vergne, J., Mokhtari, M. (2006) Seismological evidence for crustal-scale thrusting in the Zagros mountain belt (Iran) Geophysical Journal International, in press.

Poblet, J. & McClay, K. (1996), Geometry and kinematics of single-layer detachment folds, American Association of Petroleum Geologists Bulletin, 80, 1085–1109.

Poblet, J., McClay, K., Storti, F., Muñoz, J.A. (1997) Geometries of syntectonic sediments associated with single-layer detachment folds, Journal of Structural Geology, 19, 369–381.

Preusser, F., Radtke, U., Fontugne, M., Haghipour, A., Hilgers, A., Kasper, H.U., Nazari, H., Pirazzoli, P.A. (2003) ESR dating of raised coral reefs from Kish Island, Persian Gulf. Quaternary Science Reviews, 22, 1317–1322.

Reyss, J.L., Pirazzoli, P.A., Haghipour, A., Hatte, C., Fontugne, M. (1998), Quaternary marine terraces and tectonic uplift rates on the south coast of Iran. In: Stewart, I.S., Vita-Finzi, C. (Eds.), Coastal Tectonics. Geological Society (London) Special Publication, 146, 225–237.

Sella, G.F., Dixon, T.H. and Mao, A. (2002), REVEL: a model for recent plate velocities from space geodesy, Journal of Geophysical Research, 107, 2081, doi:10.1029/2000JB000033.

Sherkati. S., and Letouzey, J. (2004) Variation of structural style and basin evolution in the central Zagros (Izeh zone and Dezful Embayment), Iran. Marine and Petroleum Geology, 21, 535–554.

Sherkati, S., Molinaro, M., Frizon de Lamotte, D. and Letouzey, J., (2005) Detachment folding in the Central and Eastern Zagros fold belt (Iran). Journal of structural Geology, 27, 1680–1696.

Sherkati. S., J. Letouzey, and D. Frizon de Lamotte (2006), The Central Zagros fold-thrust belt (Iran): New insights from seismic data, field observation and sandbox modelling, Tectonics, 25, doi:10.1029/2004TC001766.

Stocklin, J. (1968), Structural history and tectonics of Iran: A review, American Association of Petroleum Geologists Bulletin, 52, 1229–1258.

Talebian, M, & Jackson, J. (2004), A reappraisal of earthquake focal mechanisms and active shortening in the Zagros mountains of Iran. Geophysical Journal International, 156, 506–526.

Talbot, C.J., and Alavi, M. (1996), The past of a future syntaxis across the Zagros, In: Salt Tectonics (Ed. By G.I. Alsop, D.J. Blundell & I.Davison), Geological Society (London) Special Publication, 100, 89–109.

Tatar, M., Hatzfeld D., Martinod J., Walpersdorf A., Ghafori-Ashtiany M., and Chery J. (2002), The present-day deforma-

tion of the central Zagros from GPS measurements: Geophysical Research Letters, 29, 1927, doi: 10.1029/2002GL015427.

Tatar, M., Hatzfeld D., and Ghafory-Ashtiany M. (2004) Tectonics of the Central Zagros (Iran) deduced from micro-earthquake seismicity. Geophysical Journal International, 156, 255–266.

Thompson W. G., and S. L. Goldstein (2006), A radiometric calibration of the SPECMAP timescale, Quaternary Science Reviews, in press.

Thompson, S., Weldon, R., Rubin, C., Abdrakhmatov, K., Molnar, P., Berger, G. (2002), Late Quaternary slip rates across the central Tien Shan, Kyrgyzstan, central Asia. Journal of Geophysical Research, 107, 2203, doi: 10.1029/2001JB000596.

Uchupi, E., S.A. Swift, and D.A. Ross (1999), Late Quaternary stratigraphy, Paleoclimate and neotectonism of the Persian Gulf region, Marine Geology, 160, 1–23.

van der Plicht, J., Beck, J.W., Bard, E., Baillie, M.G.L., Blackwell, P.G., Buck, C.E., Friedrich, M., Guilderson, T.P., Hughen, K.A., Kromer, B., McCormac, F.G., Bronk Ramsey, C., Reimer, P.J., Reimer, R.W., Remmele, S., Richards, D.A., Southon, J.R., Stuiver, M., and Weyhenmeyer, C.E. (2004) NOTCAL04 comparison-calibration 14C records 26–50 cal kyr BP. Radiocarbon, 46, 1225–1238.

Vernant, P., F. Nilforoushan, D. Hatzfeld, M.R. Abbassi, C. Vigny, F. Masson, H. Nankali, J. Martinod, A. Ashtiani, R. Bayer, F. Tavakoli, J. Chéry, (2004) Present day crustal deformation and plate kinematics in the Middle East constrained by GPS measurements in Iran and northern Oman, Geophysical Journal International, 157, 381–398.

Vita-Finzi, C., Recent coastal deformation near the Strait of Hormuz, Proc. R. Soc. Lond., A 382, 441–457, 1982.

Walpersdorf, A., Hatzfeld, D., Nankali, H., Tavakoli, F., Nilforoushan, F., Tatar, M., Vernant, P., Chery, J., and Masson, F. (2006), Difference in the GPS deformation pattern of North and Central Zagros (Iran), Geophysical Journal International, in press.

The Salt Diapirs of the Eastern Fars Province (Zagros, Iran): A Brief Outline of their Past and Present

Salman Jahani · Jean-Paul Callot · Dominique Frizon de Lamotte · Jean Letouzey · Pascale Leturmy

Abstract The salt diapirs of the eastern Fars (Zagros, Iran) have been reexamined in light of their relationships to the regional geodynamic history. The present-day surface morphology of salt diapirs can be divided into six types, which we suggest represent different stages in a long and complex history: type A are buried diapirs, type B high relief active diapirs, type C with salt fountain and glacier, type D similar to type C but with more erosion and without fountain, type E as dead diapirs and empty crater, and type F linear diapirs generally emerging along faults. We show that nearly all the diapirs of the study area were already active prior to Zagros folding either as emergent diapirs forming islands in the Paleogene to Neogene sea or as buried domes initiated at least by the Permian. They have been reactivated by subsequent tectonic events. At the initiation of Zagros folding, the abundance of emergent diapirs close to the present Persian Gulf coast line weakened the entire sedimentary cover and facilitated the preferential localization of the deformation in a narrow zone. Then, salt-cored detachment folding in the whole eastern Fars Zagros Fold-Thrust Belt reactivated the preexisting domes and allowed salt movement along faults.

Keywords. Zagros (Iran), Hormuz Salt, Salt plugs, Diapir morphology

1 Introduction

The emergent salt diapirs of the Fars Province (Iran) are one of the geological wonders of the world (Fürst, 1976; Kent, 1979). They are distributed in the southeastern part of the Zagros fold-thrust belt (Fig. 1). The name of the Hormuz series was taken from the Iranian Hormuz island, cored by a salt diapir, which also gives its name to the opening strait of the Persian Gulf. The Hormuz series consists of a colored mélange of salt, anhydrite, black dolomite, shale, red siltstone and sandstone, as well as some metamorphic and volcanic blocks which are interpreted either as fragments of the basement (Lee, 1931; Player, 1969; Kent, 1979; Ala, 1974) or as syn-Hormuz deposits, brought to the surface by the diapirs.

The Hormuz and equivalent series were deposited in an evaporite basin during the late Precambri-an-early Cambrian (Motiei, 2001). Coeval salt basins crop out in a large domain including the eastern Zagros, Persian Gulf, Oman, Qatar, Central Iran, Pakistan, and northwest India (Stocklin, 1968; Talbot and Alavi, 1996; Edgell, 1996; Al-Husseini, 2000; Konert et al, 2001; Jeroen et al., 2003). Hormuz salt is supposed to be absent along the north-south trending Arabian arches, inherited from Pan African structures. Its initial thickness remains highly speculative: 1000 m for Kent (1979), 900-1500 m for Player (1969), 1500 m for Huber (1975), and 2000-4000 m for Verrall (1978). In the Fars domain of the eastern Zagros, this basal formation is covered by 7 to 9 km of sedimentary rocks. The Hormuz series penetrates this overburden as diapirs that feed spectacular salt glaciers moving by plastic flow along the ground surface (Kent, 1979; Talbot, 1998).

Most of the previous work in eastern Fars was related to hydrocarbon exploration and resulted in an abundance of geological reports and geological maps. Among the different authors who contributed to the present knowledge on salt diapirs, we wish to emphasize the following contributions:

- Harrison (1930, 1931) described the age of emergence for some diapirs. He pointed out that the older diapir (Darbast or Shamil) emerged during the late Cretaceous. He also noted that some salt diapirs formed islands in the Miocene sea.
- Kent (1958; 1976; 1987) proposed that both static loading and late folding were responsible for diapirs breaching to the surface. He described several salt diapirs and made quite a complete list of those which reached the surface before the Zagros orogeny.
- Player (1969) described facies changes related to salt movements at depth, times of movements, and structural adjustments related to them. He proposed that salt movement possibly began during the Triassic and at least by the Cenomanian. He mentioned evidence suggesting that a lot of salt diapirs existed as emergent structures or as buried structures doming the overlying strata before the Zagros orogeny.
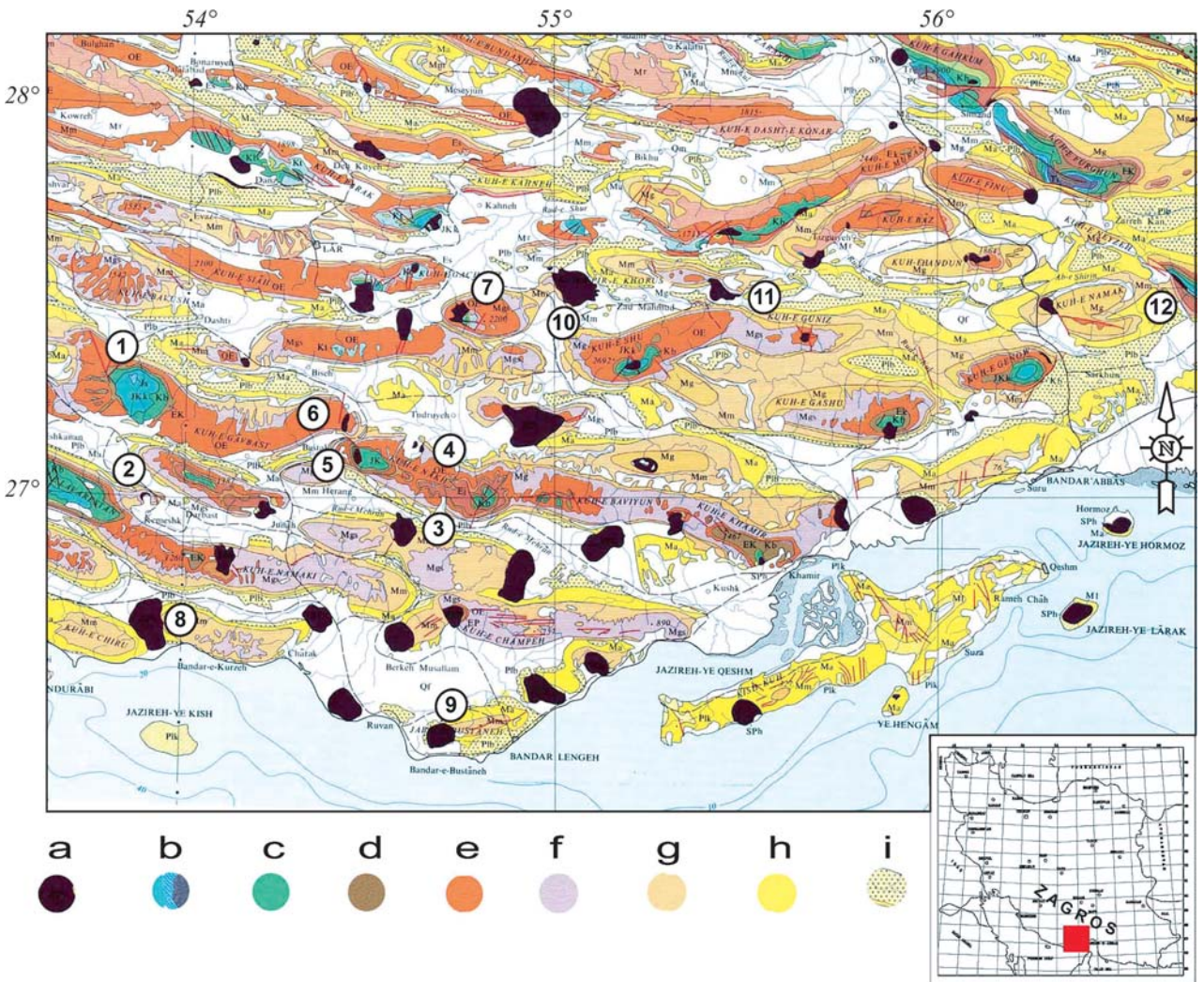
Fig. 1. Geological map of the eastern Fars, Iran, (from NIOC, 1:1000000, 1969). (a) Hormuz salt diapirs, Infracambrian to early Cambrian; (b) late Triassic -Jurassic - early Cretaceous; (c) middle Cretaceous; (d) late Cretaceous; (e) Paleocene – Eocene – Oligocene; (f) early-middle Miocene; (g) late Miocene; (h) late Miocene – early Pliocene; (i) late Pliocene-Quaternary. Location of fifteen salt diapirs and salt dome which are described in the text and Fig.s as follow: (1) Gavbast, (2) Kameshk, (3) Herang, (4) Zangard, (5) Bastak I (6) Bastak II, (7) Shur, (8) Kalat, (9) Bostaneh, (10) Chah-Banu, (11) Shamilo, (12) Darbast, (13) Chah-Ghaib, (14) Champeh, (15) South Park

- Motiei (1995) showed that salt movement sometimes started as early as the Permian in the Persian Gulf.
- Talbot and Alavi (1996) made a first attempt to classify the present morphology of the salt diapirs. Along the Kazerun and Mangarak fault zones, they recognized nine different types of Hormuz extrusions from pre-eruptive structures to thrust-decapitated diapirs through different types of salt domes and fountains. They attributed inception of the salt structures to local manifestations of Jurassic and Cretaceous subduction of the Neo-Tethys before the Zagros orogeny.

- Focusing on salt movements in the Persian Gulf, Edgell (1996) showed that diapiric structures have grown continuously since the late Jurassic and sometimes, as in Bahrain, since the Permian.
- Letouzey and Sherkati (2004) showed that, in the central Zagros, Hormuz salt doming existed before the Neogene Zagros orogeny. The driving mechanism of Hormuz rising and extrusion was squeezing of pre-existing salt domes during Zagros folding. They suggested that thrust fault and tear fault locations in this region are controlled by the presence of pre-existing salt domes, as studied by analogue modeling by Callot et al. (this volume).

The purpose of this preliminary paper is, on the one hand, to describe the morphology and present activity of salt diapirs of the eastern Zagros, based both on published data and field studies and, on the other hand, to discuss the age(s) of salt movements as well as their relationships with the regional geodynamic context. This work is based on a general survey of the whole eastern Fars where the salt diapirs are exposed, with a particular emphasis on the diapirs that we consider representative.

2   Geological and Tectono-Stratigraphic Setting

Located in the middle part of the Alpine-Himalayan orogenic belt, the Zagros is a 1800 km long mountain range extending NW-SE from the Taurus Mountains in NE Turkey (Scott, 1981) to the strait of Hormuz in Iran (Falcon, 1969; Stöcklin 1968; Haynes and McQuilan 1974; Alavi, 1994). The belt is bounded to the NE by the Main Zagros Thrust fault (MZT) and to the SW by the Persian Gulf, which represents its present-day active foreland basin. The Zagros deformation front, defined by topography, follows the northeastern shoreline of the Gulf (Fig. 1). The Zagros fold-thrust belt is divided into three tectonic zones from the NE to the SW: the High Zagros, the Zagros Simply Folded Belt, and the Zagros Foredeep Zone (Stöcklin 1968; Falcon, 1967; 1974). The Simply Folded Zagros is subdivided according to its tectonic and sedimentary evolution into three domains; Lorestan, Izeh, and Fars areas (Motiei, 1994; 1995). The study area is located in the central and eastern part of the Fars province (Fig. 1).

The Zagros fold-thrust belt is the result of a complex geodynamic history in which the following main stages are generally recognized: platform phase during the Paleozoic, rifting during the Permian and Triassic, passive continental margin of the Neo-Tethys ocean in the Jurassic- early Cretaceous, ophiolite emplacement (obduction) dated as late Cretaceous, and finally, collision and crustal shortening since the Neogene (Falcon, 1969; Ricou et al., 1977; Berberian and King, 1981; Agard, 2005; Sherkati et al., 2006). As already indicated above, salt rise began at least since the Permian and continued up to the present.

Above the Pan African basement, the stratigraphic sequence of the Zagros has been formally established by James and Wynd (1965) and recently revisited by Alavi (2004). Seismic evidence from the western Fars shows that pre-Hormuz sediments exist at least in parts of the Zagros (Letouzey and Sherkati, 2004). During the early Paleozoic, shallow-marine and fluvial sandstone, siltstone, and shale were deposited on the low-relief erosion surface formed either on the Precambrian basement or on the Hormuz basins, where they exist. A large Silurian-Carboniferous sedimentary gap (Fig. 2) is apparently the effect of epirogenic movements during Variscan orogeny, which led to a regional regression and general emergence of the region, known as the "Hercynian unconformity". During the Permian, a regional shallow marine transgression with basal coastal clastics (Faraghan formation) covered the entire region (Berberian and King, 1981).

The late Permian and early Triassic periods were characterized in the Zagros by marine carbonate sedimentation (Koop and Stoneley, 1982; Setudehnia, 1978). During the middle-late Triassic, the Zagros was occupied by an evaporitic platform (Murris, 1980). Towards the High Zagros in the northern tip of the basin, the evaporites were replaced by dolomite, suggesting a connection with the Neo-Tethys, which opened at that time (Setudehnia, 1978; Szabo and Kheradpir, 1978; Murris, 1980).

During Jurassic to middle Cretaceous times, sediments were deposited in a steadily subsiding basin (Berberian and King, 1981) in which subsidence was controlled by vertical movements and flexures along major basement faults. A lateral facies change from platform sediments in the SE Zagros to a predominantly basinal facies in the NW is the significant characteristic of this time interval (Setudehnia, 1978). Contractional deformation of this long and very wide margin began on the north-eastern edge of Arabian plate during early Coniacian-late Santonian times (Ricou, 1971; Falcon 1974). Thick Campanian-Maastrichtian sediments (deep water marls, shales, marly limestones, and turbidites) were deposited in front of the ophiolitic nappes. The thickness and facies of late Cretaceous and Paleogene sediments are considerably affected by progressive deformation following the ophiolite obduction (Koop and Stoneley, 1982; Sherkati and Letouzey, 2004).

Continental collision probably began in the Oligocene at the northern promontory of the Arabian plate (Yilmaz, 1993) and propagated southeastwards into the Lower Miocene (Sherkati et al., 2006), creating the Bitlis-Zagros suture zone (Ricou, 1971). Growth strata in the Upper Aghajari formation (late Miocene-Pliocene) are attributed to the main phase of folding (Berberian and King, 1981; Homke et al., 2004; Sherkati et al., 2005). But there is evidence of precursor tectonic movements during the deposition of the Asmari and Gachsaran formation (Sherkati et al., 2005) (Fig. 2). The Bakhtiari conglomerate (Plio-Pleistocene) was deposited after the main phase of folding but is often affected by recent to ongoing deformation. Recent kinematic scenarios proposed for the Zagros fold-and-thrust belt (Molinaro et al., 2005; Sherkati et al., 2006) suggest a two-step evolution with a mainly thin-skinned phase during the Miocene followed by a basement-involved phase since the Pliocene. The total shortening
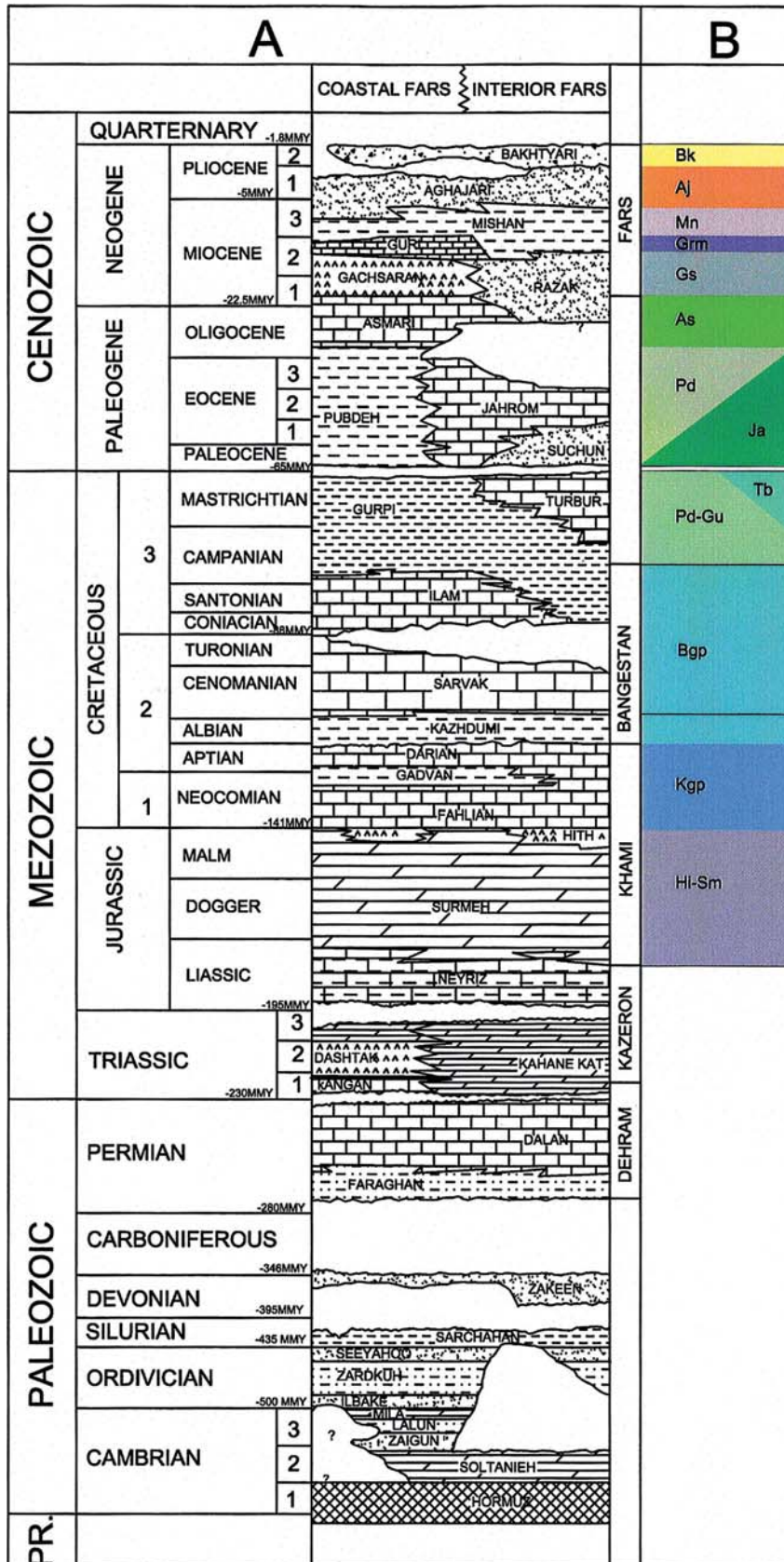
Fig. 2. A: Simplified litostratigraphic column in the Fars domain, Iran, showing the lateral changes of lithology and facies along the Fars basin, compiled and modified from James and Wynd (1965), Bydoun et al (1992) and Motiei (2001); B: Color scale for the geological map of the Figs. 5,6, and 9

amounts to about 50 km (Blanc et al., 2003; Molinaro et al., 2005; Sherkati et al., 2005; 2006).

The whole Zagros belt has been uplifted towards the end of Pliocene time (James and Wynd, 1965; Stocklin, 1968), likely as a consequence of slab break-off (Molinaro et al., 2005a). Convergence is still active at the present in a roughly N-S direction at a rate of approximately 25–30 mm.yr-1 at the eastern edge of the Arabian plate (Sella et al., 2002; Hessami et al., 2002; Vernant et al., 2004).

3   Present and Past Salt Activity in the Eastern Fars

Salt diapirs in the eastern Fars present a large variety of shapes, from high relief, actively upward moving diapirs, to entirely eroded and dead structures. In addition, they have different sizes at outcrop scale, ranging from craters a few km wide to diapirs and glaciers more than 15 km wide. These different morphologies are controlled by various factors, for example, the time of emergence, the rate of salt dissolution, which is controlled by the rate of erosion, the bulk rate of salt emission from the source layer, and eventually by the tectonic activity. Table 1 lists all the parameters of the observed salt plugs.

Estimating the age of the initiation of salt flow and the duration of salt diapirism are difficult tasks (Kent, 1958), because of narrow or alluvium covered exposures of the dome boundaries. In addition, old country rocks are not exposed or show limited contacts with salt around many diapirs. Consequently, the periods of salt activity are not known at all for all diapirs. Early to late Paleozoic salt movements can not be excluded. First, Omanese salt diapirs as well as the Darang diapir show compelling seismic evidence for early Paleozoic diapirism (Jeroen et al., 2003; Letouzey and Sherkati, 2004). Second, the Permian rifting event only affected the distal parts of the Arabian passive margin now accreted to the crushed zone, thus did not play a major role in the southern Fars and Persian Gulf diapir evolution. The ascent of the salt during the Mesozoic through a thick sedimentary cover unaffected by the rifting is unlikely, thus suggesting that the diapirs should have been close to the surface during the Permian- early Triassic. The Hercynian erosive event may have then triggered the salt ascent by removing part of the sedimentary load.

It is important to distinguish two different aspects of salt mobility. The salt diapirs can either reach the surface or only dome up the overlying strata without reaching the surface. Doming is shown by facies anomalies, thinning and gaps of sedimentary units in local areas situated above the rising dome. The age of emergence of a salt diapir can be determined using two kinds of evidence that are often associated with the presence of recycled Hormuz debris and the development of unconformity-bound growth sequences. The presence of recycled material is an indisputable argument, which has long been used by previous workers (see review in Kent, 1958). To our knowledge, halokinetic-sequences flanking salt diapirs have not been described so far in Iran. They are successive packages of thinned and rotated strata bounded by local unconformities, and result from progressive onlaps and shallow "drape folding" over the flanks of the rising diapirs (Rowan et al., 2003). The presence of recycled debris within these growth strata confirms that they cannot be interpreted as the result of deep drag folding formed at depth in shear zones flanking the rising diapir (see Rowan et al., (2003) for a complete discussion). Such a process is also mechanically unlikely according to numerical modeling (Schultz-Ela, 2003).

3.1 Morphology of Salt Diapirs

We have categorized the surface morphology of salt diapirs in the eastern Fars into 6 types, namely A, B, C, D, E, and F. The type A comprises generally circular domes above buried Hormuz salt (Figs. 3A and A`). Type B diapirs exposed with a high relief at the surface, indicates that the salt diapir is active and that salt extrusion is more important than salt dissolution (Figs. 3B and B`). It also indicates a recent emergence because lateral salt flow has not yet started to form glaciers. Type C salt diapirs have large salt glaciers and a fountain (summit dome) above the vent, which can be situated in the center or near the margin of the exposed Hormuz (Figs. 3C and C`). Owing to this lateral spreading, their elevation is generally less than in type B. Type D diapirs show a crater filled to the rim by salt with irregular surface. The walls of the crater are generally made of steep to overturned Neogene beds typically with thinning growth strata. This type represents once-active diapirs, which previously formed islands in the Neogene sea equivalent to the ones in the present Persian Gulf (Figs. 3D and D`). In type E diapirs, the diapirs are dead and the salt is completely eroded, resulting in empty craters filled only by insoluble remnant of the Hormuz series (Figs. 3E and E`). Finally, Type F describes irregular, often linear bodies of salt and associated Hormuz series coring thrust or strike-slip faults (Figs. 3F and F`).

The spatial distribution of these different types of salt diapirs is shown in Fig. 4. Most salt diapirs (37%) are of type D and are situated mainly close to the Persian Gulf. Types B and C with 22% and 8.8%, respectively, are located primarily in the northwestern part of the area. Types A and E, with 8.8% and 14.7%, respectively, are scattered throughout the whole area.

Table 1. List of the studied diapirs (western and southern parts of the eastern Fars area). The diapirs of the northeastern zone will be the subject of future work

No.	Diapir	Present day geometry						Growth strata characteristics				
		Activity at the present	Structural Location	Profile	Shape	Age of the surrounding rocks	Thining & facies change	Age of Growth strata	Age of reworked material	Observed oldest movement	Evidence	Reference
1	Kalat	Active	Periclinal	Shield	C	Bk-Ag				M-L Miocene - Pliocene	Interbedded conglomerate	Kent (1958) , this study
2	Namaki (Darbast or jebel Turanjeh)	Active	Core	Dome	B	Mn-Gs-As-Pb	*	Mn?	*	L Oligocene-Miocene	Fossil of Corals in As	This study
3	Gazeh	Active	Periclinal	Dome	B	Gs-As-Ja_Pb	*	*	*			This study
4	Kameshk	Inactive	Sincline	Hole	E	Mn-Gs-As	As & Mn	As and Mn	L_As and Mn	E Oligocene-Miocene	Interbedded conglomerate and facies Anomalies	Kent (1958) and R.A. Player, this study
5	Charak (Baverdin)	Inactive	Periclinal	Shield	D	Bk-Ag-Mn		U Mn	U Mn	L miocen-Pliocene	Recycled Hz debris transgressionacross dead plug)	R.E. Player & De Bockh, Kent 1958, this study
6	Mughu	Inactive	in plain	Shield	D	Recent Alluvial Ag-Mn	*	Allouvial Ag & Gap (Kz,Sv,Il,Gu) mn	*	L miocene-Pliocene		This study
7	Bostaneh (Khaneh Surkh)	Inactive	Periclinal	Shield	D					M-L Cretaceous & L Miocene-Pliocene	Well data and interbedded conglomerate	De Bockh (Kent 1958), this study
8	Chah-e-Muslam	Inactive	Periclinal	Shield	D	Bk-Ag-Mn				E-M Miocene	Attenuated sequences and Recycled Hz debris	R.E. Player, this study
9	Champeh	Active?	Periclinal	Shield	D	Mn-Gs-As-Pb-Gu?-Il?		As	Gs (Champeh)	Eocene-Oligocene-Miocene-Pliocene	Conglomerates & probable Recycled Hz debris & facies anomaly	R.E. Player & De Bockh (Kent 1958) , this study
10	Herang(Chahberkeh)	Inactive	Periclinal	Hole	E	Mn-Gs		Grm-Gs	Mn-Gs (Chehl)	E-M Miocene	Recycled Hz debris	R.E. Player (1969), this study
11	Bastak 1	Active	Periclinal	Dome	B	As-Ja-Pb-Gu-Il-Sv-Dr-Gd-Fa-Sm-Nz-Dashtak	*	*	*	Triassic? Cenomanian	Facies change	R.E. Player (1969), this study
12	Bastak 2	Active	Periclinal	Dome	B	Mn-Gs-As-Pb	*	*	*	-		This study
13	Zangard	Inactive	N Flank	Hole	E	Mn-Gs-As-Ja-Sa?		Mn-Gs-As	Mn -Grm	Oligocene- M Miocene		This study
14	Paskhand	Active	Periclinal	Dome	B	Grm-Gs-As	shallow water in Grm time	Gs(Chehl) & Grm	Grm-Mol-uper As	Oligocene-Miocene		This study
15	Moallem	Inactive	Periclinal	Shield	D	Bk-Ag-Mn-		Mn?		M-L Miocene	Attenuated sequences and Recycled Hz debris	R.E. Player (1969), this study

Table 1. *Continued*

No.	Diapir	Present day geometry								Growth strata characteristics		
		Activity at the present	Structural Location	Profile	Shape	Age of the surrounding rocks	Thining & facies change	Age of Growth strata	Age of reworked material	Observed oldest movement	Evidence	Reference
16	Homairan (Breke-Suflin)	Inactive	Core	Shield	D	Mn		Mn?		M-L Miocene	Recycled Hz debris	R.E. Player (1969), this study
17	Zendan	Inactive	Periclinal	Shield	D	Bk-Ag-Mn		Mn	Bk-Ag-Mn	M-L Miocene-Pliocene	Attenuated sequences and Recycled Hz debris	R.E. Player (1969), this study
18	Do-Ao	Active?	Sincline	Dome	D	Ag		*		-		This study
19	Mijun	Active	Periclinal	Dome	D	Mn-Gs-As-Pb-Gu		Mn-Gs-As?		Oligocene	Recycled Hz debris	G.A. James (Shepherd unpub. report) & R.A Player, this study
20	Ilcheh	Inactive	Core	Hole	E	Mn		Gs-Guri		M Miocene	Recycled Hz debris	Harrison (Kent, 1958), M.F. Shepherd (unpub.), R.A. Player, (1969) this study
21	Bam	Active	Core	Shield	D	Mn-Gs-As_Ja		*	*	Oligo- Miocene	Recycled Hz debris	R.E. Player (1969), this study
22	Shu	Active	Core	Hole	B	As_Ja-Bgp-Kgp		Creta-As	*	L Cretaceous & M Miocene		This study
23	Chah banu (Hormuz)	Inactive	in plain	Shield	E	Bk-Mn-Gs		Gs		Miocene	Recycled Hz debris	Kent 1969 (unpub.) & Shaw and Harrison (Kent 1958), this study
24	Shur (Chahel)	Very active	Periclinal	Dome	B	As_Ja-Tb-Gu-Bgp	*	U.Gs-Gur-Gap(Pd)	*	-	Well data	This study
25	Burkh	Active	N Flank	Shield -Fountain	C	As_Ja-Tb	*	*	*	-		This study
26	Gach	Active	S Flank	Shield -Fountain	C	Sa-Tb-Gu-Bgp-Dr-Gd-Fa	*	*	*	-		This study
27	Nisf-i-Rah	Active	Core	Dome	B	Sa-Tb-Gu-Bgp-Dr-Gd-Fa	*	*	*	-		This study
28	Kurdeh	Active	S Flank		B	Bk-Sa-Tb-Gu-Bgp-Kgp	*	*	*	M Miocene	Interbedded conglomerate	Harrison (fram Kent 1958), this study
29	Qaleh shur	Inactive	Periclinal	Shield	E	As_Ja-Tb-Bgp-Kgp		*		M Miocene		This study
30	Chah-Ghaib (Na-mak, East Mazyjan)	Active	Periclinal	Shield -Fountain	C	Bk-Ag-Mn-Gs-As_Ja	*	*	*	-		This study

Table 1. *Continued*

No.	Diapir	Present day geometry								Growth strata characteristics		
		Activity at the present	Structural Location	Profile	Shape	Age of the surrounding rocks	Thining & facies change	Age of Growth strata	Age of reworked material	Observed oldest movement	Evidence	Reference
31	Deh Kuyeh	Active	S Flank	Shield glacier	C	As_Ja	*	*	*	-		This study
32	Mazyjan (Gach)- no visited	Active	S Flank		B	As_Ja-Sa-Tb				-		This study
33	south Parak	Active?	N Flank		F	Bk	*	*	*			This study
34	Parak	Active	S Flank	Dome	B	Bgp				L Miocene-Pliocene	Doming	R.E. Player, this study
35	Bnaru (no visited	?	N Flank		D	Bk				-		This study
36	West Gach (no visited)		Periclinal		B	Bk				-		This study
37	Shamilo	Active	Periclinal	Shield glacier	D	Grm-Gs-As_ja	*	Gs?		L-M Miocene	Recycled Hz debris	M.F. Shepherd(unpub.), this study
38	Harmadan	Active	Core		D	As_ja-Sa-Tb-Bgp		Gs?		Jurassic?-Cretaceous-Paleocene-Eocene-Oligocene	Recycled Hz debris	De Bockh(unpub.)& R.A. Player &H. McQuillan, this study
39	Pol	Active	Periclinal	Dome	B	Bk-Ag-Mn-Gs-As-Pd_Gu		Gs		Miocene-pliocene	Interbedded conglemerate & Recycled Hs debris	De Bockh(Kent 1958)& R.A. Player), this study
40	Gachin (Suru)	Inactive	S Flank	Shield	D	Bk	*	*	*	L Cretaceous & M Miocene	Recycled Hz debris attenuated sequence; Interbedded conglomerate	M.F. Shepherd(unpub.)& R.A.Player, this study; De Bockh(Kent 1958)
41	Anguru (Gasho)	Active	S Flank	Dome glacier	B	Mn-Gs-As_Ja-Pd_ Gu-Bgp-Kgp	*	*	*	Senonian & Eocene	Doming producing local laterites and facies anomalies; Recycled Hz materials	R.E. Player (1969), this study; A. Gollestaneh, unpublished
42	Khamir	Inactive	S Flank	Hole	E	Tb-Gu-Il-Sv	*	*	*	Senonian & Oligocene	Local conglomerate and unconformity; Recycled Hz debris	R.E. Player (1969), this study; G.A. James(unpub.)
43	Gavbast Dome	-	Periclinal	Dome	A	-	Gu-Pb-Ja-As			L Cretaceous-E Miocene	Recycled Hz debris	This study

List of abbreviations: *Bk*: Bakhtiari, *Ag*: AghaJari, *Mn*: Mishan, *Gr*: Guri, *Gs*: Gachsaran, *As*: Asmari, *Ja*: Jahrom, *Tb*: Tarbu, *Pb*: Pbdeh, *Gu*: Gurpi, *Il*: Ilan, *Sv*: Sarvak, *Kz*: Kazhdumi, *Bgp*: Bangestan, *Kgp*: Upper Khami, *Dr*: Darian, *Gd*, Gadvan, *Fa*: Falian, *Sm*: Surmeh, *Nz*: Neyriz, *Hz*: Hormuz

The location of some diapirs of type F (8.8%) corresponds approximately to the Mountain Front fault and the particular northeastern zone.

The recent activity of salt diapirs can be deduced from the morphology (Fig. 4). The buried domes, Type A, could become emergent if the salt source is feeding the diapirs at the present or if the overburden is eroded enough to expose the salt. Types B and C correspond to active diapirs; the only difference is in the elevation of diapirs and the presence or absence of salt glaciers. The morphology of type D could be intermediate between type C and E. Type E is no longer active, and type F can correspond to active as well as inactive structures.

If salt ascent is reactivated within type D or E diapirs, where salt dissolution counterbalances salt ascent, they may evolve into Type B or C diapirs (for instance, the Kalat diapir along the Persian Gulf coast, Fig. 4). Type B diapirs themselves could develop lateral glaciers, shortly after their emergence, and progressively form Type C diapirs. Eventually, all could degrade to Type E after depletion of the source layer and erosion of the diapirs.

3.2 Emergent and Buried Domes

Unlike those in the Persian Gulf, most of salt diapirs located in the eastern Fars have already emerged (Edgell, 1996). For the purpose of a brief review of the different types of diapirs, we will present successively:

1. The Gavbast circular structure.
2. Three salt diapirs, namely Kameshk, Zangard, and Herang, which reached the surface before folding.
3. Three salt diapirs, namely Bastak I, Bastak II, and Shur, whose age of extrusion is unambiguous.

The Gavbast dome structure (type A) is located at the junction of three anticlines, the Gavbast anticline to the east and Varavey and Bayram anticlines to the west (Fig. 1). It is a huge rounded dome with a 16 km diameter and 1800 meters elevation above the adjacent plains. It marks a large geometric anomaly within this linear anticline (Fig. 5A). The oldest rocks cropping out on the dome are middle-late Jurassic in age (Fig. 5B). The Gavbast dome structure shows thinning and rotation of the late Cretaceous to early Miocene beds (as shown for the Cretaceous strata (Fig. 5C) and anomaly facies. These suggest that the Gavbast dome is similar to the circular domal structures observed in the Persian Gulf and which correspond to buried salt diapirs (Edgell, 1996). The present-day morphology of the dome suggests that the Neogene Zagros shortening has reactivated the salt ascent (see Vendeville and Nielsen, 1995; Callot et al., this volume). The like-

ly destiny of Gavbast dome structure is to emerge after erosion of the overlying rocks driven by continued folding and faulting. This example is important as it gives an image of what was the situation in the northern part of the studied area before folding, as (1) the dome does not present any major tectonic structures and (2) the geometrical evidence for salt movement are older than the folding.

The morphology of the emergent salt diapirs Kameshk, Zangard and Herang (type E) is nearly the same (Fig. 6). All of them are rounded with diameters of 3.6, 6.3, and 7.5 km, respectively, and are now nearly completely eroded. The Kameshk and Zangard diapirs are merely empty craters with a few remains of Hormuz insoluble blocks, which were formerly brought up with salt. These two salt diapirs crop out within upper Oligocene to upper Miocene strata (Asmari, Mishan and Gachsaran formations) that contain recycled material and growth strata. In the Kameshk salt diapir, lateral variations of sedimentary facies and well-rounded pebbles recycled from Hormuz debris are observed in Oligo-Miocene strata (Fig. 7A). Rounded rock fragments suggest a nearly flat dome near the surface in a high energy environment or an earlier derivation of the pebbles (Kent, 1958). The Zangard salt diapir shows increasing recycled Hormuz debris during the Oligocene-middle Miocene, suggesting higher rate salt growing during the middle Miocene (Fig. 7B). The Herang salt diapir shows recycled angular Hormuz debris in lower Miocene strata. The debris shapes suggest a similar rapid transport from the source, and thus a rapidly growing diapir (Fig. 7C). Generally growth strata around the Kameshk Zangard and Herang salt diapirs show thinning in the late Oligocene-early Miocene, Oligo-Miocene and early-middle Miocene respectively (Figs. 8 A, B and C). The main phase of activity of the Kameshk and Zangard salt diapirs was during the middle Miocene, as shown by the large amount of reworked material, which can represent the larger part of these deposits. The presence of both growth strata and recycled debris in the surrounding rocks shows that diapirs formed permanent islands or near-surface bulges, at least in the Paleogene-Neogene Sea, prior to Zagros folding. Consequently, they depict a situation in the southern part of the studied area in Miocene time comparable to the present-day Persian Gulf.

The Bastak I, II and Shur salt diapirs (type B) are three emerged salt diapirs with different morphology and high elevation compared to the previous group. The Bastak I salt diapir is located in the western nose of the Nakh anticline and is encompassed huge cliffs. It presents an ellipsoid shape with a N-S trending 3.6km long great axis (Fig. 9A). Another salt diapir, Bastak II or north Bastak, is located 4.5km to the NW of Bastak I. The two diapirs are connected by a
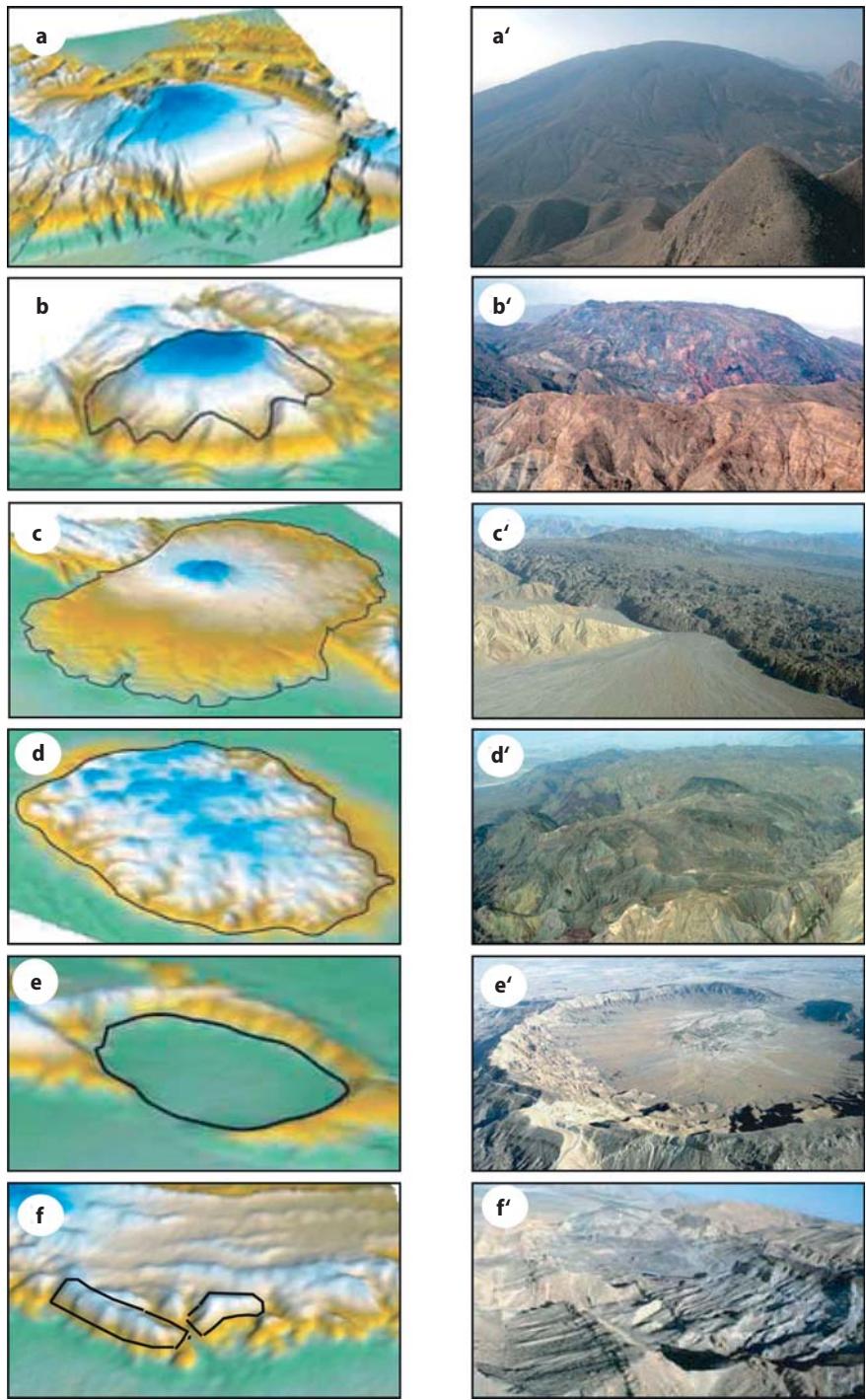
Fig. 3. Digital elevations and related photographs of the 6 surface morphology types of salt diapirs in eastern Fars (see also Fig. 1). **a** and **a'**: Type A comprises circular domes above buried Hormuz salt showing a circular structure, Gavbast dome; **b** and **b'**: Type B indicates that the salt diapir is active and salt extrusion is more important than salt dissolution, Shur salt diapir; **c** and **c'**: Type C salt diapir with a fountain above the deep feeder and salt glaciers extending laterally, with less elevation than type B, Chah-Ghaib salt diapir; **d** and **d'**: Type D is similar to type C but with a corrugated eroded flat top rather than a fountain, Champeh salt diapir; **e** and **e'**: Type E salt was completely eroded and presents only an empty crater with some blocks of insoluble Hormuz rocks, Kamesh salt diapir; **f** and **f'**: Type F describes salt diapirs which are often found along thrust faults, South Parak salt diapir. the scale of digital elevation Fig.s are 1/5

strike-slip fault showing nearly 700 m of right-lateral offset. The two diapirs may join at depth before reaching the parent salt bed (Player, 1969). Surrounding strata include Upper Triassic to Quaternary sequences (Figs. 9A and B). Paleontological data show that much of late Jurassic-Lower Cretaceous rock units are lacking (Player, 1969), suggesting that the salt dome was an active structure during this period. No recycled Hormuz debris nor growth strata exist north and northwest of Bastak I or east and north of Bastak II, suggesting they were buried structures before the Zagros folding. Post-folding late Pliocene rocks consisting almost exclusively of recycled Hormuz debris crop out on their southern flanks, supporting the recent emer-
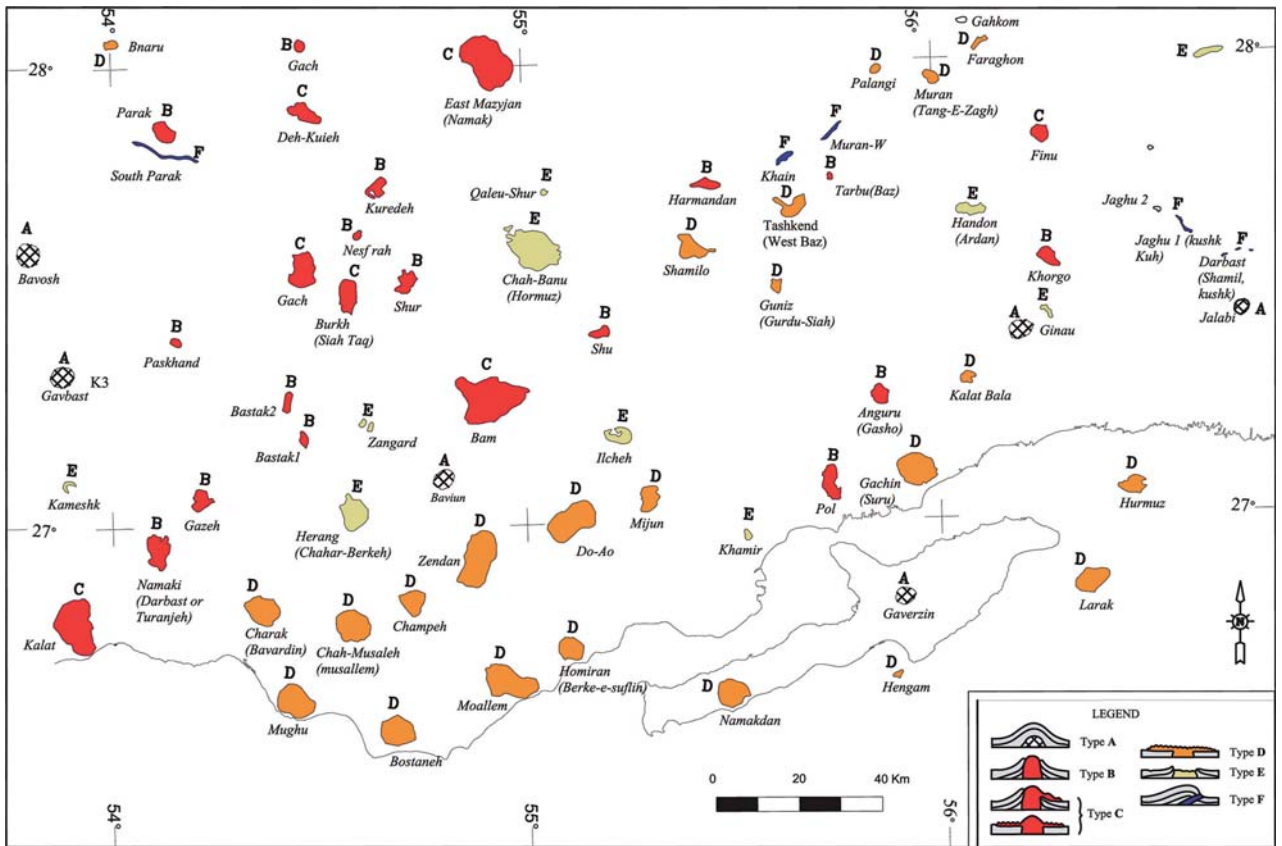
Fig. 4. Distribution of different type of salt diapirs in the eastern Fars. The map shows three region. The legend shows schematic profiles of salt diapir types *A*, *B*, *C*, *D*, *E*, and *F* (see Fig. 3). Salt diapirs with *red* and *orange* colors are showing activity at the present (type *B*, *C*, and *D* with lowest activity), whereas yellow color type *E* is not active. Note that the majority of salt diapirs close to Persian Gulf is of type *D*

gence of the domes (Player, 1969). The Shur or Che-hal salt diapir is located in the eastern plunge of Che-hal anticline. The diapir, which stands nearly 1600 m above the adjacent plains, is one of the highest diapirs in the Fars area. It has a nearly rounded shape with a 3.7 km diameter (Fig. 9C). The salt diapir is confined within middle Cretaceous to lower Miocene country rocks, but without apparent growth strata (Fig. 9D). These three salt diapirs could illustrate the future of the Gavbast salt dome, with emergence being triggered either by strike-slip faulting (Bastak) or by folding-induced upward movement of salt and erosion of overburden (Shur).

3.3 Past Activity of Salt Diapirs

In accordance with the majority of our predecessors (Harrison, 1930, 1931; Kent, 1958, 1976, 1979; Player, 1969; Motiei, 1995; Talbot and Alavi, 1996; Edgell, 1996; Letouzey and Sherkati, 2004; Sherkati and Letouzey, 2004), we believe that all, or almost all, salt

diapirs of the eastern Fars were active before the Zagros orogeny. Their activity before the Zagros orogeny is indicated by gaps in the sedimentary sequence. For example, the Bustaneh salt diapir shows growth strata in the upper Miocene-Pliocene surrounding rocks but also shows a long local gap from the Aptian to the early Eocene (unpublished well data from NIOC, see location of diapirs, Figs. 1 and 12). This old huge salt diapir could correspond to the present-day Gavbast dome.

The salt diapirs can be divided into two general groups (Fig. 10). The first group of salt diapirs emerged as islands early, mainly before the Neogene, as shown by deposition of recycled Hormuz debris in middle Tertiary layers as well as the development of passive drape (flap) folding and thinning growth strata around salt diapirs (Fig. 11). Almost all diapirs located along the coast line belong to this category, but this kind of diapir is sometimes encountered within the belt. The second group of salt diapirs did not emerge before the Zagros orogeny but likely had dome shapes equivalent to the one observed at Gavbast (Fig. 5). The presence of sedimentary thinning, anomaly facies and/or hia-
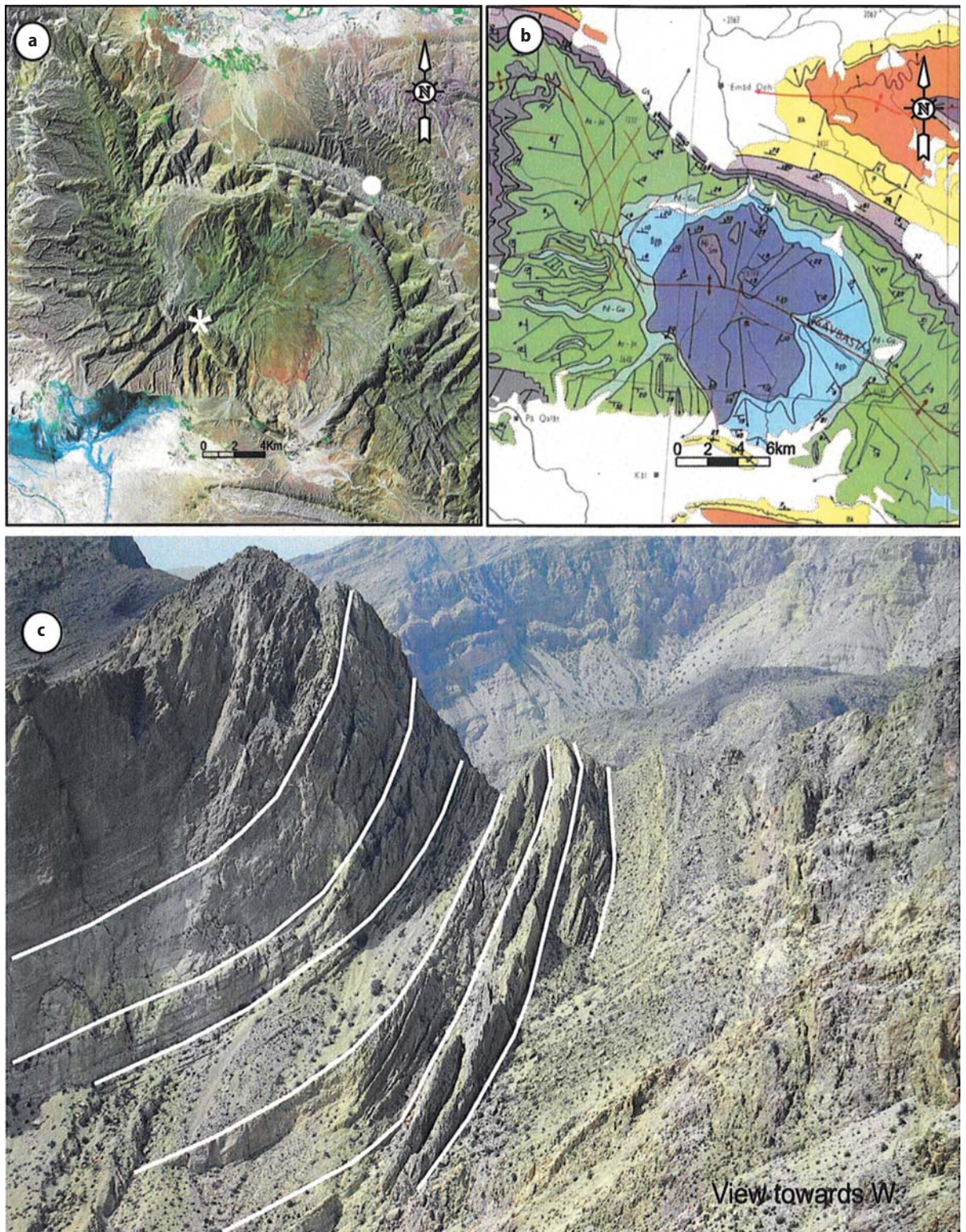
Fig. 5. The Gavbast salt dome structure (see Fig. 1 for location): (**a**) Landsat image showing a rounded dome 16 km in diameter and 1800 meters in elevation above the adjacent plains. (**b**) Geological map showing that the oldest exposed rocks are middle-late Jurassic and surrounding rocks are Cretaceous-Eocene in age (after unpublished 1:250,000 geological maps, NIOC). (**c**) Gavbast dome structure was active during late Cretaceous as shown by the Pabdeh-Gurpi strata thinning. (*) Location of the Photograph C
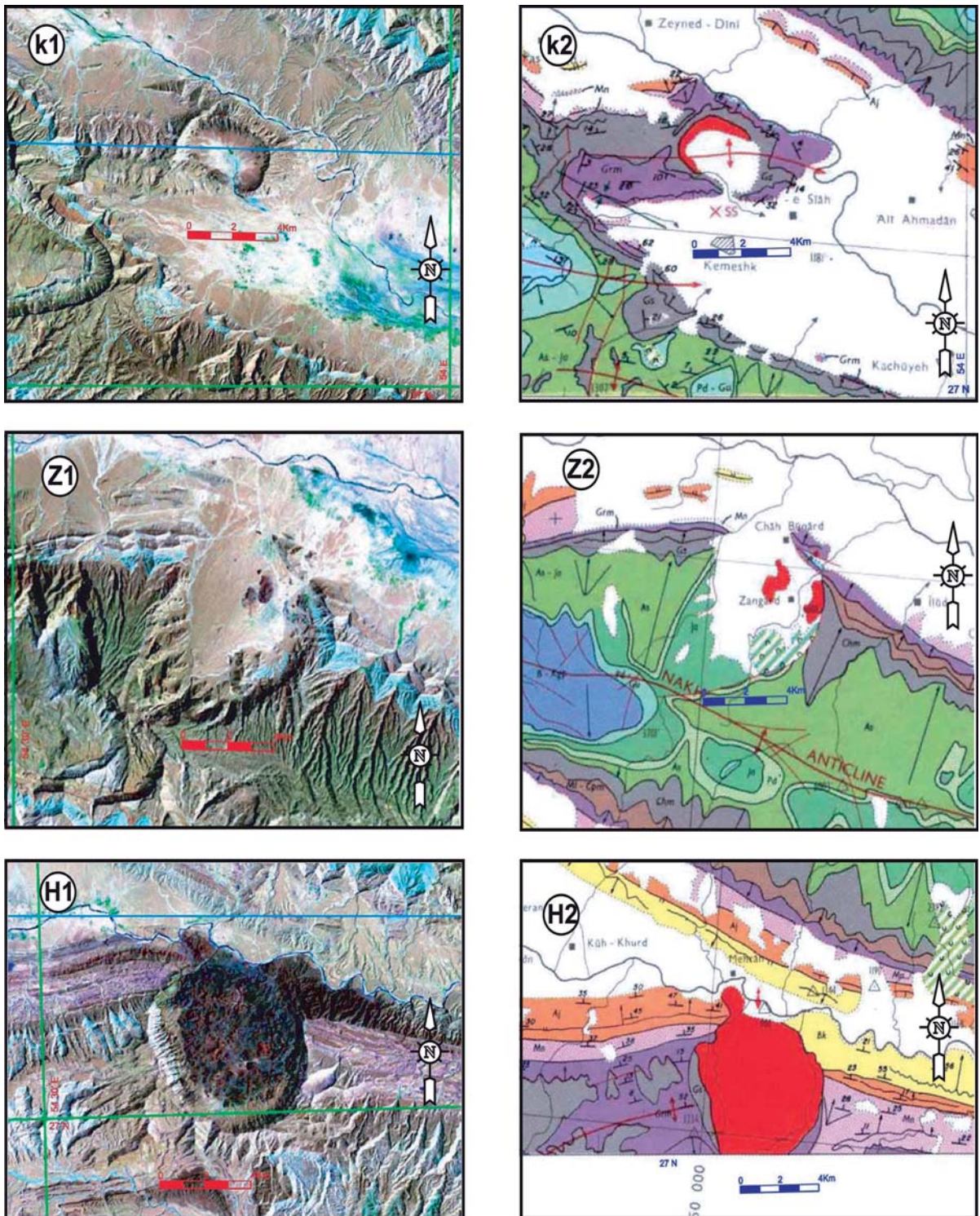
Fig. 6. Landsat images and geological maps of the emergent salt diapirs Kameshk, Zangard and Herang. they are presently inactive. The Kameshk and Zangard diapirs are empty craters with a few insoluble blocks brought to surface by the salt. The Kameshk (*K1* and *K2*) salt diapir is located along a small anticline splaying from the larger Dehnow anticline. Rock outcroppings consist in late Oligocene to late Miocene shallow water carbonates and evaporites. The Zangard salt diapir (*Z1*, *Z2*) is located on the northern flank of the Nakh anticline, and is surrounded by Miocene rocks. The Herang salt diapir (*H1*, *H2*) is located in the saddle between the Herang and Buneh-kuh anticlines. It is in a topographical crater surrounded by Mio-Pliocene rocks (*K2*, *Z2*, *H2*; after unpublished 1:250,000 geological maps, NIOC)

Fig. 7. Recycled Hormuz debris from the Kameshk, Zangard and Herang salt diapirs. (**a**) Well rounded pebbles of recycled Hormuz debris in Oligo-Miocene strata of the Kameshk salt diapir. (**b**) Recycled Hormuz debris in lower and middle Miocene strata of the Zangard salt diapir, showing mature grains of mixed sizes. (**c**) Recycled Hormuz debris in lower Miocene strata of the Herang salt diapir showing immature grains
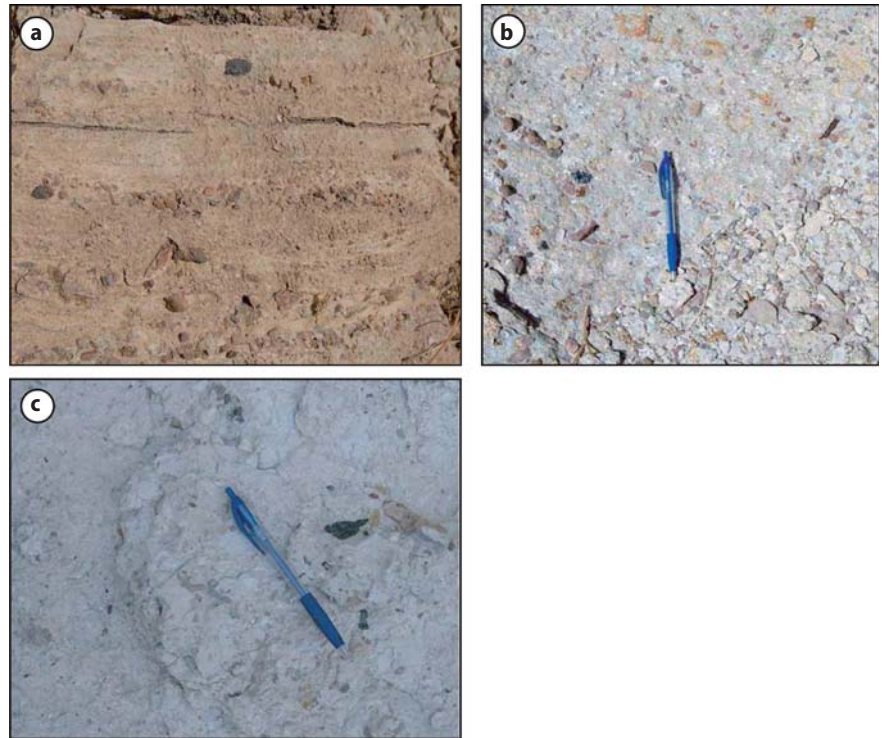
tuses towards the tops of the domes allows us to decipher the history of dome growth (Fig. 5C). The reactivation of salt extrusion during the Zagros orogeny in some cases buried the dome boundaries under extrusive salt, hiding the sedimentary record of the dome growth history.

4   Discussion and Conclusions

The Hormuz and equivalent series were deposited during the late Proterozoic- early Cambrian in a large evaporite basin including the eastern Zagros, eastern Persian Gulf, Oman, Qatar, Central Iran, northwest India, and Pakistani Salt Range (Player 1969; Falcon, 1967; Stocklin, 1968; Talbot and Alavi, 1996; Edgell, 1996; Al-Husseini, 2000; Konert et al., 2001; Jeroen et al., 2003). The area where the diapir density is at a maximum possibly corresponds to a part of the Hormuz basin where the salt layer was originally particularly thick (Player, 1969). This thick salt basin corresponds to the south-eastern Fars and northern part of Persian Gulf. The present-day regular distribution of salt diapirs was interpreted as related to basement faults located below the diapirs. As the diapirs have been transported laterally during the Zagros shortening, even if the basement is faulted, there will be not spatial relationship today. We rather believe that the regular pattern of diapir distribution relates to the ear-

ly development of salt plugs and ridges during the Palaeozoic corresponding to the development of polygonal mini-basins at that time.

In the Central Zagros (including the western Fars), emergent salt diapirs are mainly associated with faults, either strike-slip (tear and wrench faults) or thrust faults, which cut through the whole sedimentary column (Talbot and Alavi, 1996; Hesami et al., 2001; Bahroudi and Koyi, 2003; Sherkati and Letouzey, 2005; Sepehr and Cosgrove, 2005). There are a few instances of salt emergence prior to Zagros folding, such as the Khormoj diapir, which has been emergent from the Neocomian to present-day (Player, 1969). However, most of the diapirs in this area may have formed buried domes. The present-day salt diapirs are interpreted as previously buried domes squeezed during the compression or else brought to the surface by strike-slip fault and pull-apart structures (Talbot and Alavi, 1996) or thrusting (Letouzey and Sherkati, 2004). In comparison, in the south-eastern Hormuz basin (eastern Fars onshore) (Fig. 12), surface geology shows that most, if not all, diapirs were either buried active domes or emergent islands before the Zagros folding. Most of the emergent diapirs are not clearly related to the activity of a fault at the surface. However, a link between deep old basement normal faults and early diapir emplacement is likely, although a present-day geographical association of deep faults and diapir may not correspond to a past relationship. It is worth noting
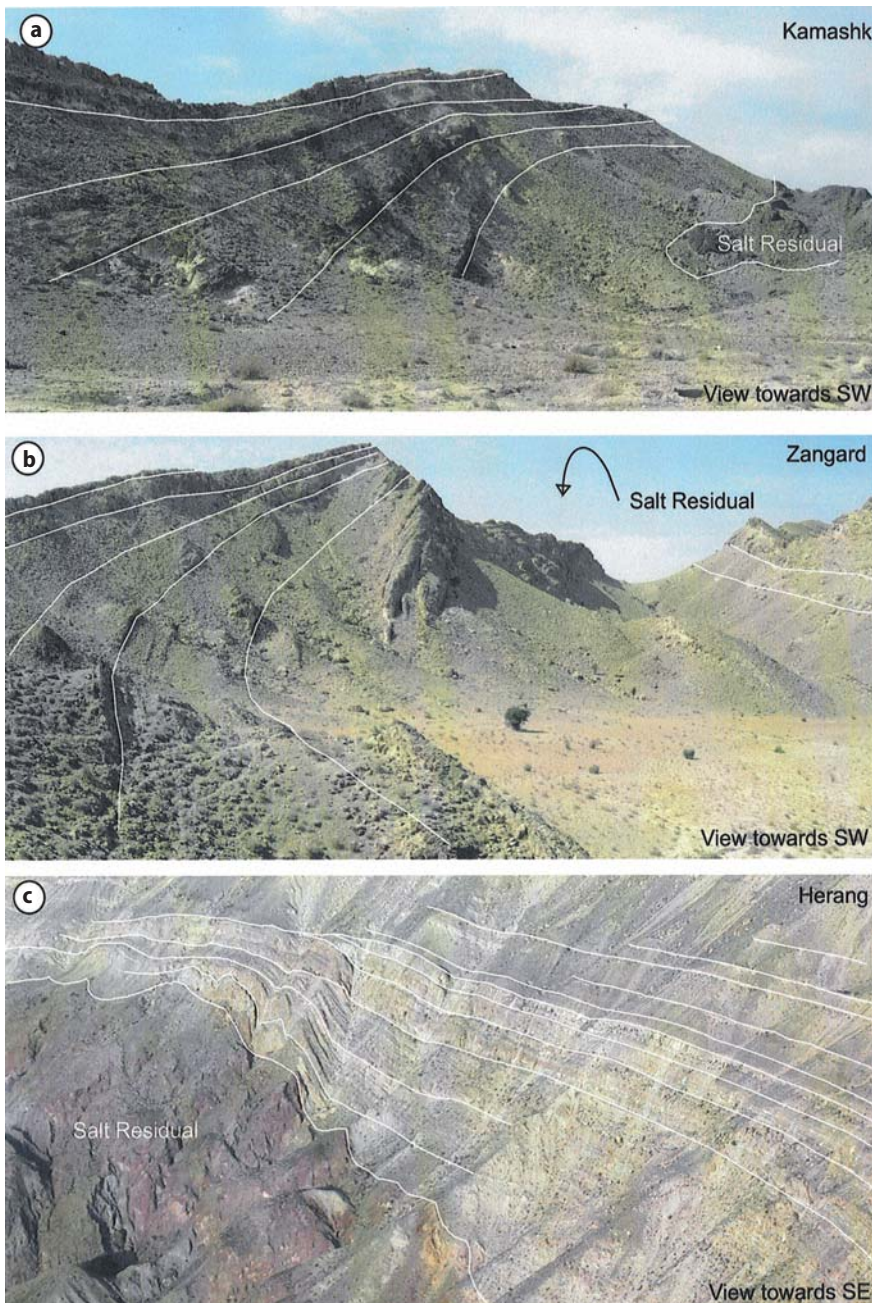
Fig. 8. (a) Photographs of the salt diapirs, Kameshk (**a**), Zangard (**b**) and Herang (**c**), are showing growth strata of the late Oligocene-early Miocene, Oligo-Miocene and early-middle Miocene respectively. In photograph B, location of salt diapir is in behind

that present-day active blind faults are thrust faults (see review in Talebian and Jackson, 2004) rather than strike-slip faults as previously postulated by many authors (see discussion in Edgell, 1996; Talbot and Alavi, 1996).

The present-day distribution of salt diapir types is not random. Instead, three regions can be described: the Zagros Front area, the north-western region and finally the north-eastern region (Fig. 4 and 12). We will present firstly the two first ones, which are quite

homogeneous and then the third, which appears as more complex.

4.1 The Zagros Front Area and North West Region

All the diapirs located at the front of the Zagros belt appear to be of D type, i.e., emergent island before the Zagros folding, whereas in the north-western part, we observe mainly active dome with high relief, associ-

Fig. 9. Landsat images and geological maps of the Bastak I, II and Shur emergent salt diapirs (see location in Fig. 1), with high elevation compared to others. (**a**) Landsat image showing the Bastak I salt diapir in the western plunge of the Nakh anticline and the Bastak II salt diapir in the eastern plunge of the Gavbast anticline. The two diapirs are joined by a right lateral strike-slip fault. (**b**) Corresponding geological map with late Cretaceous to middle Tertiary rocks surrounding the diapirs. (**c**) Landsat image showing the Shur salt diapir in the western plunge of the Chehel anticline. (**d**) Corresponding geological map, showing rocks of middle Cretaceous to early Miocene age (unpublished 1:250,000 geological maps, NIOC)
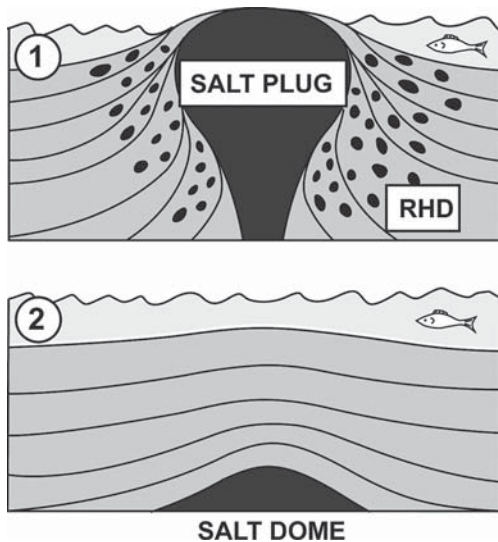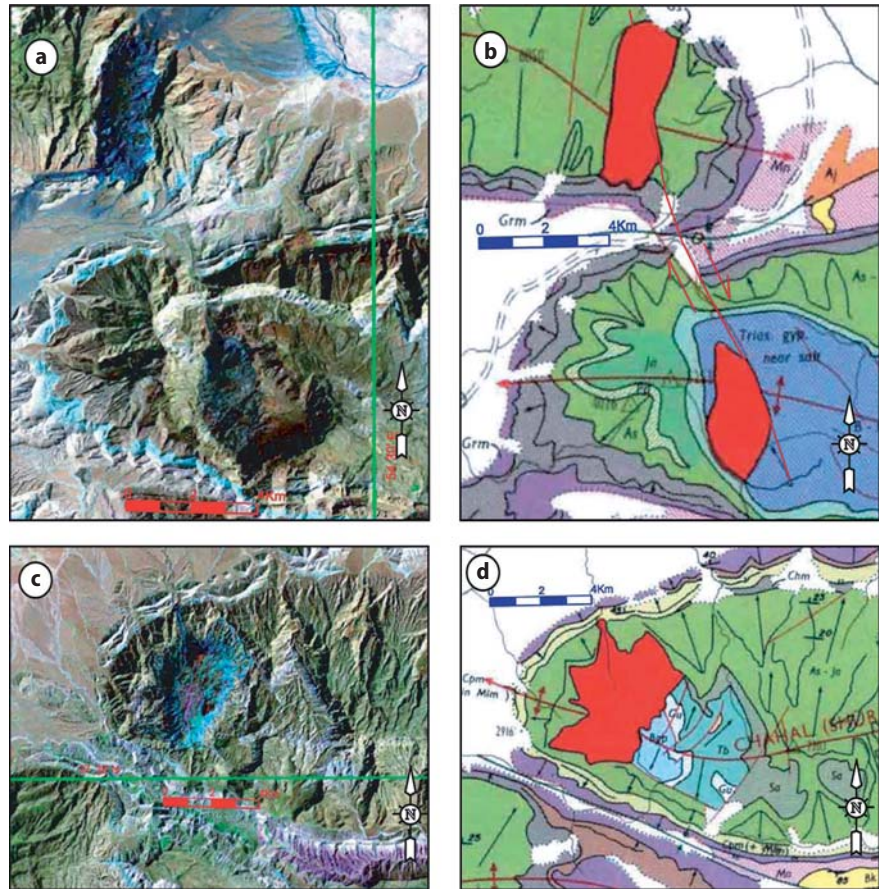
Fig. 10. Schematic sections illustrating salt geometry before the Zagros folding in the eastern Fars. Profile (*1*) shows a salt diapir forming an island with steep growth strata and recycled Hormuz pebbles around the diapir. Profile (*2*) shows a salt dome which is buried and revealed by lateral sedimentary facies variation and thickness changes above the dome

ated to buried actively growing structures. This pattern likely result from the geometry of the inherited Arabian passive margin, and the post-obduction, precollision tectonics movements along this margin. Such movements are suggested by reworked clastic material coming from the north within Paleocene-early Eocene sediments (Sachun Formation, Fig. 2). As Palaeocene- early Eocene sediments prograded from the north, their differential load may have expelled salt southward, away from the suture zone. Moreover, the plate flexuring due to the prograding nappes and sediment allowed the development of an up-dip basin migration, i.e., southward, of the salt in response to the regional tilt. As a result, the thickened salt in the south may have promoted more vigorous rise of the southern diapirs. In contrast, diapirs in the north grew slower as buried diapirs because they were supplied by thinner salt layer. These northern diapirs where then rejuvenated by Neogene Zagros shortening and today include some of the most active salt diapirs in the fold belt, embedded in the high relief structure. However, it is necessary to mention that erosion rainwater along
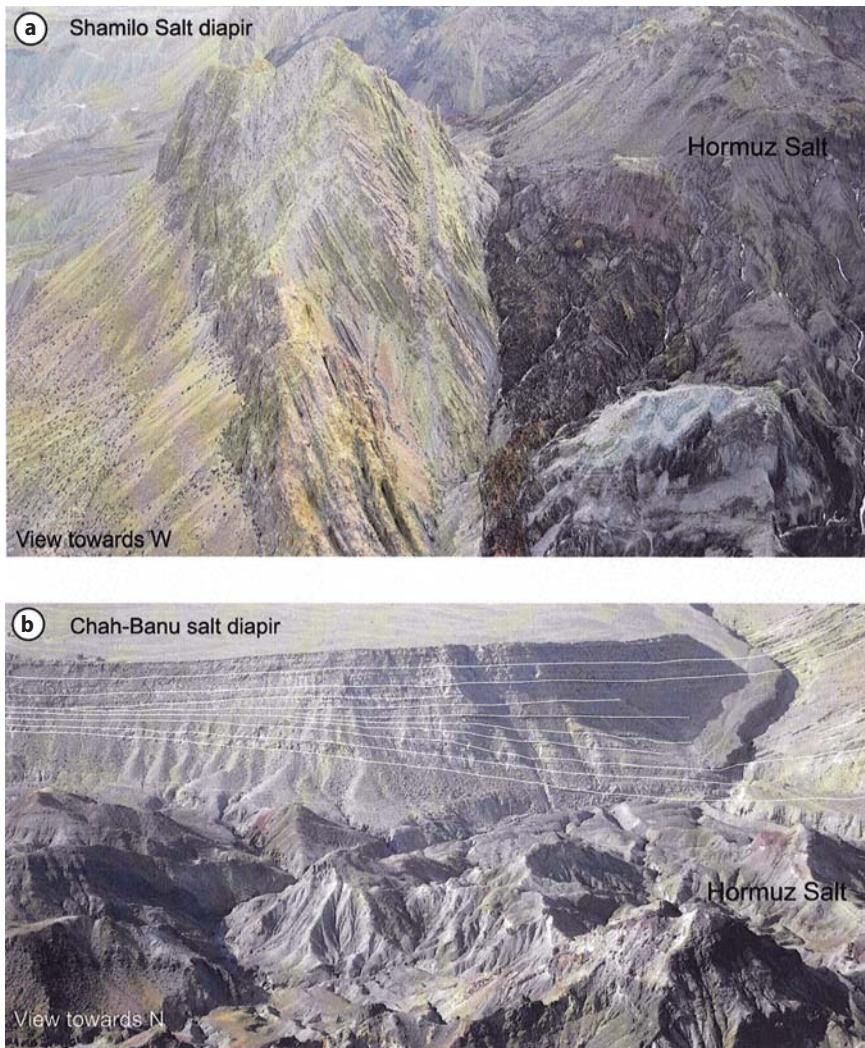
Fig. 11. Photographs showing: (**a**) growth strata with steep or overturned bedding around the Shamilo salt diapir; (**b**) low-dip growth strata adjacent to the Chah-Banu salt diapir

the shore line is more active than within the northern part and reduce the relief of the salt domes.

4.2 The North-Eastern Region

In the north-eastern part the pattern is more diffused with occurrence of several types simultaneously. This region is particular for several reasons. It is not only the location of the regional bending between the Minab fault and the main trend of the southern Fars (Molinaro et al., 2004), but it also shows several fold trends contrasting with the regular fold pattern of the southern Fars. This is interpreted as the consequence of the interaction between the cover fold belt and underlying basement faults with different orientations (Molinaro et al., 2005). Finally, this region shows several active thrusts, associated with diapirs, a pattern similar to

what is observed in the central Zagros where diapirs act as thrust initiators (see Callot et al., this volume). The spatial distribution of diapirs appears also irregular and linked to the tectonics, contrarily to what is observed in the southern Fars.

During the Zagros folding, the domain punctuated by closely spaced diapirs can be considered as an already weakened domain, whereas the northern and western Zagros and the Persian Gulf, where the diapir density is lower, acted as relatively stiff domains. Thus the N-S shortening of the Zagros foreland has been concentrated in the diapir-intruded southern Fars since the early stages of the deformation. This shortening reactivated the buried domes ascent (see Callot et al., this volume) in the northern part of the thick salt basin. Weakening related to the presence of salt bodies thus arises at the scale of the salt diapir itself, but also at the scale of the entire thrust belt. In the Za-

Fig. 12. Age of activity of salt diapirs in eastern Fars determined from growth strata, recycled Hormuz debris and/or facies anomalies. *Light gray* denotes the last reactivation during the Zagros folding (younger than early Miocene). *Dark gray* shows the last reactivity before the Zagros folding (before early Miocene). Bold lines with no pattern indicate salt diapirs with no thinning evidence and cross-bedded pattern shows buried domes. Abbreviation: *Tr*: Triassic; *J*: Jurassic; *K1*, *K2*, *K3*: early, middle, late Cretaceous respectively; *Pa*: Paleocene; *Eo*: Eocene; *Ol*: Oligocene; *M1*, *M2*, *M3*: early, middle, late Miocene; *Pl*: Pliocene

gros fold-belt, late activation of basement faults allows to localize late-stage of deformation, although the initial deformation was largely distributed within the intruded domain.

References

Agard, P., Omrani J., Jolivet L. and Mouthereau, F., (2005). Convergence history across Zagros (Iran): Constraints from collisional an earlier deformation, Int. J. Earth Sci., 94, 401 – 419.

Ala, M. A., 1974. Salt diapirism in southern Iran. Am. Ass. Petrol. Geol. Bull. 58, 758–770.

Alavi, M. 1994. Tectonics of the Zagros Orogenic Belt of Iran: New Data and Interpretation. Tectonophys. 229, 211–238.

Alavi, M. 2004. Regional Stratigraphy of the Zagros fold-thrust belt of Iran and its proforeland evolution. Am. J. Sci. 304, 1–20.

Al-Husseini, M.I., 2000. Origin of the Arabian Plate Structures: Amar collision and Najd rift. GeoArabia 5, 527–542.

Bahroudi, A and Koyi, H.A., 2003. Effect of spatial distribution of Hormuz salt on deformation style in the Zagros fold and thrust belt: an analogue modeling approach. J. Geol. Soc. London, 160, 719–733.

Berberian, M., King, G.C.P., 1981. Towards a paleogeography and tectonic evolution of Iran. Can. J. Earth Sci. 18, 210–265.

Beydoun, Z.R., 1991. Arabian plate hydrocarbon geology and potential- a plate tectonic approach. Am. Assoc. Petrol. Geol. Bull. 33, p. 77.

Blanc, E. J. P., Allen, M. B., Inger, S., Hassani, H., 2003. Structural styles in the Zagros simple folded zone, Iran. J. Geol. Soc. London 160, 401–412.

Callot, JP, Jahani, S., and Letouzey, J., 2006. The role of pre-existing diapirs in fold and thrust belt development (this volume).

Edgell, H. S., 1996. Salt Tectonics in the Persian Gulf basin. In: Alsop, G. L., D. L. Blundell, I. Davison, (Eds), Salt Tectonics, Geol. Soc. London Spec. Pub. 100, 129–151.

Falcon, N. L., 1967. The geology of the northeast margin of the Arabian Basement shield. Advanc. Sci. 24, 1–12.

Falcon, N. L., 1969. Problems of the relationship between surface and deep displacements illustrated by the Zagros range. In: Kent, P., Satterhwaite, G. E. and Spencer, A. M., (Eds), Time and place in orogeny. Geol. Soc. London, Spec. Pub., 3, 9–22.

Falcon, N., 1974. Southern Iran: Zagros Mountains, In A. Spencer (Editor), Mesozoic-Cenozoic Orogenic belts. Geol. Soc. London, Spec. Pub. 4, 199–211.

Furst, M., 1976. Tektonik und Diapirismus der ostlichen Zagrosketten. Geol. Ges. 127, 183–225.

Harrison, J.V., 1930. The geology of some salt diapirs in Laristan, Quar. Jour. Geol. Soc. London 86, 463–522.

Harrison, H., 1931. Salt domes in Persia. J. Inst. Petrol. Technologists 17 (91), 300–320, 9 figs.

Haynes, S. J., McQuillan, H., 1974. Evolution of the Zagros suture zone, Southern Iran. Geol. Soc. Am. Bull. 85, 739–744.

Hessami, K., 2002. Tectonic history and present day deformation in the Zagros fold thrust belt. Uppsala University, Ph.D. thesis.

Hesami, K., Koyi, H. A., Talbot, C.J., 2001. The significant of strike-slip faulting in the basement of Zagros fold and thrust belt. J. Petrol. Geol. 24 (1), 5–28.

Homke, S., Verges, J., Garces, G., Emamia, H. and Karpuzc, R., 2004. Magnetostratigraphy of Miocene-Pliocene Zagros foreland deposits in the front of the Push-e Kush Arc (Lurestan Province, Iran), Earth Planet. Sci. Lett., 225, 397–410.

Huber, H. 1975. Geological map of Iran 1:1000, 000 scale NIOC, Exploration and Production.

James, G. A. and Wynd, J. G., 1965. Stratigraphic nomenclature of Iranian oil consortium agreement area. Am. Ass. Petrol. Geol. Bull. 49, 2182–2245.

Jeroen, M.P., J.B. Filbrandt, J.P. Grotzinger, M.J. Newall, M.W. Shuster, and A. Al-Siyabi, 2003, Surface-piercing salt domes of interior North Oman, and their significance for the Ara carbonate 'stringer' hydrocarbon play: GeoArabia, v. 8, no. 2, p.231–270.

Kent, P.E., 1958. Recent studies of south Persian salt diapirs: Am. Assoc. Petrol. Geol. Bull. 42, 2951–2972.

Kent, P.E., 1970, The salt diapirs of the Persian Gulf region. Leic. Liter. Phil. Soc. Trans., 64, 55–58.

Kent, P.E., and Hedberg, H.D. 1976. Salt diapirism in southern Iran: a Discussion. Am. Ass. Petrol. Geol. Bull. 60, 458.

Kent, P.E., 1979. The emergent Hormuz salt diapirs of southern Iran, J. Petrol. Geol. 2, 117 144.

Kent, P. E., 1987. Island salt diapirs in the Middle East and their tectonic implications. In: Dynamical Geology of salt and related structures (Edited by Leiche, I. and O, Brien, J. J.), 3–37. Academic Press. NY.

Konert, G., Afifi, A. M., Al-Hajri, S. A., De Groot, K., Al Naim, A. A., and Droste, H. J., 2001. Palaeozoic stratigraphy and hydrocarbon habitat of the Arabian plate. In Downey, M. W., Threet, J. C., and Morgan, W. A. (Ed), Petroleum provinces of the twenty-first century. Am. Ass. Petrol. Geol. Memoir, 74, 483–515.

Koop, W.J., and Stoneley, R. 1982. Subsidence history of the Middle East Zagros Basin, Permian to Recent. Phil. Trans. R. Acad. Soc., London. A 305, 149 168.

Lee, G.M. 1931. Salt: Some depositional and Deformational Problems. Symposium on salt domes. J. Inst. Petrol. Tech., 259–280.

Letouzey, J. and Sherkati, S. 2004. Salt Movement, Tectonic Events, and Structural Style in the Central Zagros Fold and Thrust Belt (Iran), In Salt sediments interactions and hydrocarbon prospectivity, 24th Ann.GCSSEP Foundation, Bob F. Perkins research Conf.

McQuillan, H., 1974. Fracture patterns on Kuh-e-Asmari anticline, Southwest Iran. Am. Ass. Petrol. Geol., 58, No. 2, P. 236–246.

Molinaro, M, Guezou,J. C., Leturmy, P., Eshraghi, S. A. and Frizon de Lamotte, D., 2004. The origin of changes in structural style across the Bandar Abbas syntaxis, SE Zagros (Iran). Marine Petrol. Geol., V. 21, 6, 735–752.

Molinaro, M, Zeyen, H., Laurencin, X. 2005. Lithospheric structure underneath the SE Zagros Mountains, Iran: recent slab break-off? Terra Nova, February, 17, 1, 1–6.

Molinaro, M., Leturmy, P., Guezou, J. C., and Frizon de Lamotte, D., 2005b. The structure and kinematics of the southeastern Zagros fold -thrust belt, Iran: from thin-skinned to thick-skinned tectonics. Tectonics, 24, TC3007, doi:10.1029/2004TC001633, 2005

Motiei, H., 1994. Stratigraphy of Zagros. Publi. Geol. Survey of Iran (in Farsi), 536p.

Motiei, H., 1995. Petroleum geology of Zagros. 1 and 2, Geol. Survey of Iran Publications (In Farsi).

Motiei, H., 2001. Simplified Table of rock unit in south west Iran (a map unpublished, KEPS Company).

Murris, R. J., 1980. Middle East: Stratigraphic evolution and oil habitat. Am. Ass. Petrol. Geol. Bull., 64, 597–618.

Player, R.A., 1969. Salt diapirs study. National Iranian Oil Company. Exploration Division, report NO. 1146, (unpublished).

Rowan, M.G., Lawton, T.F., Giles, K.A. and Ratliff, R.A., 2003. Near-salt deformation in La Popa basin, Mexico, and the northern Gulf of Mexico: A general model for passive diapirism. Am. Ass. Petrol. Geol. Bull., 87, 5, 733–756.

Ricou, L. E. 1971. Le croissant ophiolitique périarabe: Une ceinture de nappes mises en place au Crétacé supérieur, Rev. Geogr. Phys. Geol. Dyn.,13, 327 – 350.

Ricou, L., J. Braud, and J. H. Brunn 1977. Le Zagros, Mem. Soc. Geol. Fr., 8, 33 – 52.

Sella, G.F., Dixon, T.H. and Mao, A., 2002. A model for recent plate velocities from space geodesy. J. Geophys. Res., 107, 11–1 – 11–30.

Sepehr, M. and Cosgrove, J.W., 2005. Role of the Kazerun fault zone, in the formation and deformation of the Zagros fold thrust belt, Iran. Tectonics, 24.

Setudenia, A. 1978. Mesozoic sequence in south west Iran and adjacent area J. Petr. Geol. 3–34.

Schultz-Ela, D.D. 2003. Origin of drag folds bordering salt diapirs, Am. Ass. Petrol. Geol. Bull., 87, 5, 757–780.

Scott, B., 1981. The Eurasian-Arabian and African continental margin from Iran to Greece. J. Geol. Soc., London, 138, 719–733.

Sherkati. S., and Letouzey, J. 2004. Variation of structural style and basin evolution in the central Zagros (Izeh zone and Dezful Embayment), Iran. Marine Petrol. Geol., 21, 535–554.

Sherkati, S., Molinaro, M., Frizon de Lamotte, D. and Letouzey, J., 2005. Detachment folding in the Central and eastern Zagros fold-belt (Iran): salt mobility, multiple detachments and final basement control. J Struct. Geol. 27, 1680–1696.

Sherkati, S., Letouzey, J. and Frizon de Lamotte, D., 2006. The Central Zagros fold-thrust belt (Iran): New insights from seismic data, field observation and sandbox modeling. Tectonics, 25, 4, doi:10:1029/2004TC001766.

Stöcklin, J., 1968. Structural history and tectonics of Iran: A review. Am. Ass. Petr. Geol Bull., 52 1229–1258.

Szabo, F. and Kheradpir, A., 1978. Permian and Triassic stratigraphy, Zagros basin, south-west Iran. J. Petrol. Geol. 1, 57–82.

Talebian, M. and Jackson, J., 2004. A reappraisal of earthquake focal mechanisms and active shortening in the Zagros mountains of Iran. Geophys. J. Int., 156, 506–526.

Talbot, C., and J.M. Alavi, 1996, The past of a future syntaxis across the Zagros: in G.L. Alsop, D.L. Blundell, and I. Davison, eds., Salt Tectonics, Geol. Soc., London, Spec. Pub., 100, 129–151.

Talbot, C.J., 1998, Extrusions of Hormuz salt in Iran. Geol. Soc. Spec. Pub., 143, 315–334.

Vendeville, B.C. and K.T. Nilsen, 1995. Episodic growth of salt diapirs driven by horizontal shortening. In Travis, C.J. et al eds., Salt Sediment and Hydrocarbons. GCSSEPM Foundation 16th Annual Research conference Salt, Sediment and Hydrocarbons. December 3–6, p285–295.

Verrall, P., 1978. The significance of thickness variations in the Gachsaran formation. NIOC Exploration report 182.

Vernant, P.h., Nilforoushan, F., Hatzfeld, D., Abbassi, M.R., Vigny, C., Masson, F., Nankali, H., Martinod, J. Ashtiani,A., Bayer, R., Tavakoli, F. and Chéry, J., 2004. Present-day crustal deformation and plate kinematics in the Middle East constrained by GPS measurements in Iran and northern Oman. Geophys. J. Int. 157, 381–398.

Yilmaz, Y., 1993. New evidence and model on the evolution of the southeast Anatolian region. Geol. Soc. Am., Bull. 105, 251–271.

The Role of Pre-Existing Diapirs in Fold and Thrust Belt Development

JP. Callot · S. Jahani · J. Letouzey

Abstract. Evidence of salt movement prior to the main Zagros folding event lead us to question:

1. The role of pre-existing salt structures on the Zagros fold and thrust belt development;
2. The possible mechanisms accounting for rapid salt extrusion;
3. The relative location of emergent diapirs and tectonic structures;
4. the decoupling between salt plug distribution and basement fault location.

We based our interpretations on analogue sand box experiments compared to geological observations. We argue that the driving mechanism of Hormuz halokinesis during the Zagros folding and erosion is the squeezing of pre-existing salt diapirs, which also influenced the location of thrusts and strike slip faults. Emergent diapirs occurred above pre-existing domes along these faults, or at the plunging axes of the fold crests. Depending on the diapir wall attitude and its thickness relative to the sedimentary column thickness, the diapirs are either shortened and localise sharp overturned folds, or else act as preferentially oriented ramps, part of the diapir being incorporated in the fold. During fold growth, erosion or rejuvenation of the diapir growth by shortening allows for the salt extrusion.

Keywords. Zagros, Iran, Salt, Diapirs, Folding, Sand Box Modeling.

1 Introduction

The Iranian Zagros fold and thrust belt (ZFTB) results from closure of the Neo-Tethys oceanic domain and the convergence between Arabia and Eurasia (Takin, 1972; Haynes and McQuillan, 1974; Stocklin, 1974; Ricou et al., 1977; Stampfli et al., 2001; Agard et al. 2005, among many others). In the ZFTB, the Arabian passive margin sequence has been decoupled from its basement and deformed by large-scale folding and thrusting since the Miocene. Although the Zagros has long been recognised as a major petroleum province, the architecture and kinematics of deformation in Za-

gros are still debated, particularly the role of the Hormuz Eocambrian basal salt layer and salt diapir.

The two major salt formations in the Persian gulf and the ZFTB are the deep seated Hormuz series, and the Oligo-Miocene Gasharan Formation. They are both present in the Zagros folded zone and in foreland Persian Gulf (Fig. 1). The Hormuz series in the Zagros outcrop only as allochtonous salt plugs. Approximately 160 Hormuz salt diapirs have extruded in the Zagros mountains and their foreland (Player, 1969; Kent, 1958, 1979, 1987; Edgell, 1996; Talbot 1998; Bahroudi and Koyi 2003). Within the Persian gulf, circular structures are thought to be draped over deep pillows of Hormuz salt (Edgell, 1996). About 20 of the islands in the Southern Gulf owe their existence to Hormuz extrusion (Kent 1987, Fig. 2).

Recent papers proposed general across-strike cross-sections of the ZFTB (Blanc et al., 2003; McQuarrie, 2004; Sherkati and Letouzey, 2004; Molinaro et al 2004; Mouthereau et al., 2006; Sherkati et al., 2006). However, few recent papers addressed the kinematics of fold-and-thrust development, the coupling between the cover and basement, and the role of the successive decollement levels (Molinaro et al., 2003; 2004; Sherkati et al., 2004, 2005, 2006). Most authors emphasize the role of the Hormuz series on fold propagation, basal decollement, disharmony (Bahroudi and Koyi 2003) and fold propagation style (e.g. Sherkati et al., 2005), or the role of basement fold or pull-apart zone on diapirism (Kent 1958; Edgell 1996; Talbot and Alavi 1996). But the Hormuz salt layer was only examined as decollement layer (e.g. Bahroudi and Koyi, 2003; Mouthereau et al., 2006), and the importance of the pre-deformation geometry of the basal salt layer and associated deformation of the adjacent sedimentary cover, although discussed in several paper (e.g. Kent, 1979; Mottei, 1995; Talbot and Alavi, 1996), is still poorly if not integrated into the kinematic model for the ZFTB development. There is some evidence that Hormuz salt diapirism started before the Neogene Zagros folding. Stratigraphic thinning peripheral to circular structures are thought to be draped over deep pillows of salt (Edgell, 1996; Letouzey and Sherkati 2004). Around some Hormuz plugs, in the south-
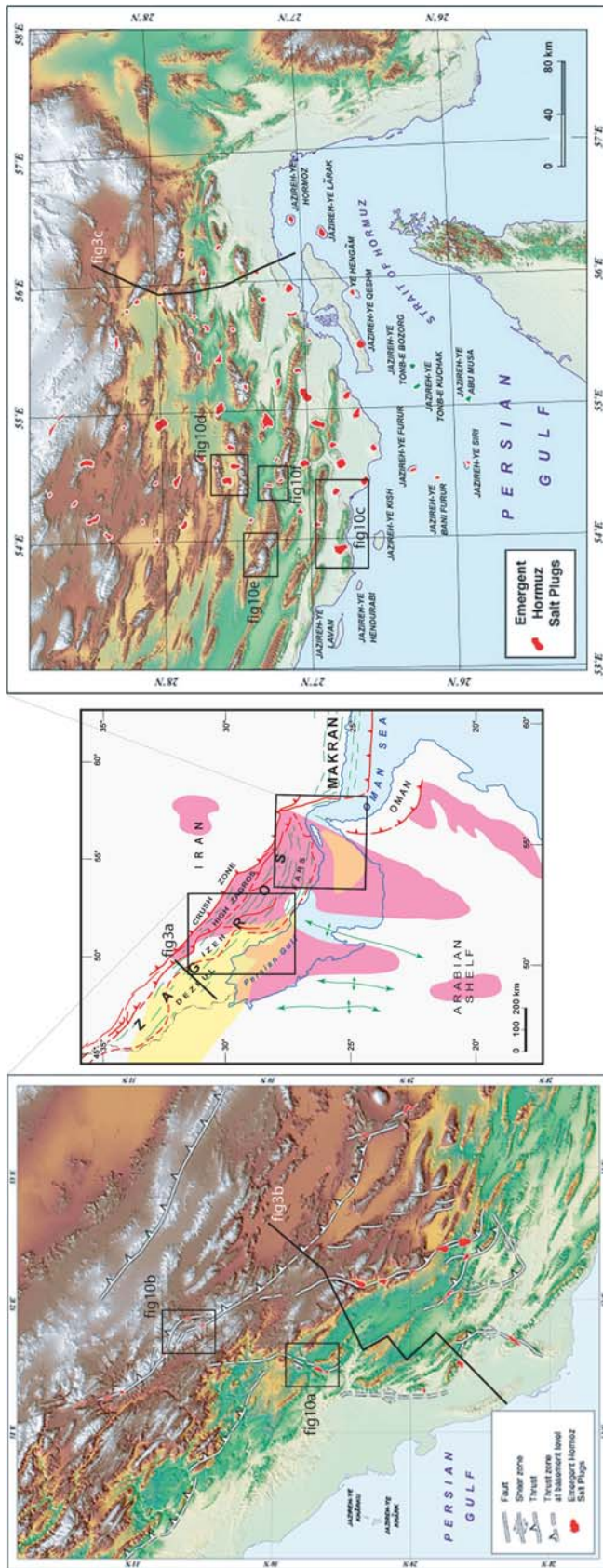
Fig 1. Geological setting of the Zagros fault and thrust belt (ZFTB). A) Pink: Distribution of late Precambrian early Cambrian Hormuz salt plugs based on the distribution of emergent salt plugs; Yellow: Distribution of the Gachsaran salt. B: Central Zagros topographic map (location of the zones in A) with location of the Hormuz salt plugs. Notice that most of the salt plugs are along thrust faults or tear faults related to the Zagros folding event. C): Southern Fars Topographic map (location of the zones in A) with the main tectonic lineaments and the emergent salt domes, which are here mainly associated to the plunging axes of folds or to the eroded fold cores. Lines show the location of the cross section of Fig. 3, and boxes the locations of the pictures of Fig. 10

Fig. 2. Geologic map of the central Fars province showing the relationship between salt plugs in red and the fold and thrust belt (green lines mark the anticlinal axes)

ern Fars region, there is clear evidence of pre-orogenic emergence, provided by interbedded Hormuz detritus in rocks dating from Cretaceous to Miocene (Player, 1969; Kent, 1987).

Letouzey and Sherkati (2004) studied the role of pre-existing diapirs on fold and fault propagation in the central Zagros provinces (Izeh zone, High Zagros an northern Fars). They show that the emergence of Hormuz salt plugs is closely associated with major thrusts parallel to the fold trend in the High Zagros. Plugs also occur as pull-apart structures as described by Talbot and Alavi (1996), or else along tear faults as push-up structures, along the north-south trending strike-slip faults. Faults and related salt plugs are clearly related to the Zagros folding event, even if they are sometimes located above reactivated paleostructures. The analysis of the deformation of sandbox models using X-ray tomography suggests that the initiation of thrust and wrench faults is influenced by pre-existing salt domes which represent weak zones in the sedimentary section. The squeezing of pre-existing salt domes was proposed to be the driving mechanism of Hormuz halokinesis and current extrusion in the central Zagros.

Preliminary studies in the Fars region of the Zagros fold and thrust belt have been completed with surface and subsurface studies in the southern Fars province (see Jahani et al., this volume), and new sand box models. Contrary to the Central Zagros provinces, where emergent diapirs are closely associated with emergent thrusts or strike slip faults, within the Southern Fars province, most of the salt plugs are located within, or at, the plunging axis of folds (Fig. 2). The purpose of this paper is to discuss the timing of salt diapirism, the influence of salt distribution and structures on fold propagation; the mechanisms of rapid salt extrusion, and thus the localisation of salt diapirs relative to fault and folds in the Fars domain.

2   Geological Setting: The Fars Domain

2.1 Geological Setting

2.1.1   Zagros Evolution

The ZFTB of Iran is the result of the opening and closure of the Neo-Tethys ocean along the north-eastern border of the Arabian plate (Stocklin 1968; Ricou et al., 1977; Berberian and King, 1981; Alavi, 1994; Agard et al. 2005, Fig. 1). The ZFTB is composed of a thick sedimentary sequence which covers a Precambrian basement, formed during the Pan-African orogeny (Al-Husseini, 2000). The total thickness of the sedimentary column deposited above the Eocambrian Hormuz salt

before the Neogene Zagros folding can reach over 8 to 10 km (Alavi, 2004; Sherkati & Letouzey, 2004).

During the late Precambrian, a thick Pre-Hormuz sequence of terrigenous clastics, carbonate sediments, known in Oman, accumulated over a large area, and probably exist below the Hormuz basal detachment in some parts of the Zagros region (Letouzey and Sherkati, 2004). The Hormuz series generally consists of salt, anhydrite, with some allochtonous blocs of dark dolomite, sandstone, siltstone, marls and volcanics. These Eocambrian salt and evaporites formation were deposited in several subsiding basins in the Gulf region, in Oman, Central Iran, Pakistan and northwest India, in latest Proterozoic-Lower Palaeozoic times (Fig. 1; Kent 1958; Stoecklin, 1968b; Edgell, 1996; Talbot and Alavi, 1996; Al-Husseini, 2000; Konert et al., 2001; Jeroen et al., 2003). The extent of the salt in the ZFTB and Persian gulf is deduced from emergent diapirs. This distribution only reflects areas where the depositional salt thickness is large enough to develop salt ridges, pillows and diapirs. It is not clear how far it extends into the central Zagros Dezful region where the lower decollement could have occurred within the lower Paleozoic shales or evaporites. The Hormuz salt is believed to be absent along north-south-trending Arabian arches, inherited from Panafrican structures such as the Quatar Arch which extend to the North up to the Fars domain in the Zagros and Deyzful embayment region (Barhoudi and Koyi, 2003; Letouzey and Sherkati, 2004). Figure 1 shows that most of Hormuz salt extrusions occurred in the Zagros folded zone, with a few islands offshore in the Southern Persian Gulf (Kent, 1979).

Deposition of the Hormuz salt was followed during the Palaeozoic by platform type successions of shallow marine, lagoonal and mostly clastic continental deposits which contain important sedimentary gaps, reaching an average thickness of 2 to 4.5 km. A major regional unconformity ("Hercynian unconformity") was observed below the Permian (Stocklin, 1968). A Permian-Lower Triassic-rifting event initiated the opening of the Neo-Tethys ocean along what is now called the "Crushed Zone" or "Imbricated Zone" to the North of the Zagros platform (Stocklin, 1968; Szabo and Kheradpir 1978; Berberian and King, 1981). The onset of drifting probably occurred in Early or Middle Triassic time. In the Zagros basin, the deposition of shallow marine sediments continued from Permian to Miocene times.

The closure of the Neo-Tethys basin was marked by several tectonic events on the Zagros platform. The first was the Early Coniacian-Late Santonian obduction of ophiolites onto the continental crust (Ricou, 1971; Falcon, 1974; Berberian and King, 1981; Berberian, 1995), which changed the basin architecture. The second event was a pronounced reactivation of deep

seated pre-existing N-S faults along former Pan-African basement trends (Koop and Stoneley, 1982). Compressive stress in the Zagros margin continued until the Eocene-Oligocene continent-continent collision and the Miocene Zagros folding event, which began at the end of the Lower Miocene, with thin skinned decollement and south-westerly propagation of the foreland depocentres (Sherkati and Letouzey, 2004; Agard et al., 2005; Sherkati et al., 2006).

The Neogene development of the Zagros belt compartmentalised the evolving foreland basin into sub-basins with different sedimentary and tectonic signatures (Bahroudi and Koyi, 2003). During late Miocene and Pliocene times, regression of the sea and the creation of mountainous relief by folding and thrusting resulted in a continental environment. Large amount of clastic material and red beds were deposited in adjacent synclines (Berberian and King, 1981). The Early to Middle Miocene Gachsaran salt formation was deposited in foreland depression south of the Mountain Front Fault zone (Fig. 1). Finally Pliocene- Pleistocene conglomerates unconformably overlie older formations. Total sedimentary thickness reached 7 to 10 km.

2.1.2   Salt Distribution and Tectonics

In the Eastern Fars and High Zagros areas, the Hormuz salt series played the role of a low friction, basal decollement level (see Barhoudi and Koyi, 2003). It influenced fold style by development of large, box-fold anticlines cored with salt (Colman-Sadd, 1978; Letouzey and Sherkati, 2005; Molinaro et al., 2005). In the Fars province, folding developed first through the development of large detachment anticlines, locally followed by out-of-sequence thrusting due to activation of major basement faults (e.g. Molinaro et al., 2004). Northeast of the Dezful, folding and thrusting developed with a high taper wedge (high friction due to the absence of Hormuz salt in the Izeh Zone, north of the Deyzful embayment, Fig. 3). In the High Zagros emergence of Hormuz evaporite plugs is closely associated with major thrusts parallel to the fold trend, such as the Dinar thrust (Sherkati and Letouzey, 2005). Between the Fars and the central Zagros, the Kazerun and Mangarak fault zones consist of en-echelon segments of steep, right-lateral, strike-slip faults. These en-echelon faults are clearly contemporaneous with folding: anticlines are bent, and die out, or are offset by fault segments (Talbot and Alavi, 1996; Barhoudi and Koyi, 2003). Due to the Hormuz salt distribution they act as oblique, right-lateral ramps, transferring the local Northwest-Southeast shortening across the ZFTB (Bahroudi and Koyi, 2003; Sepehr and Cosgrove 2006). The salt plugs are located as discontin-

uous masses along thrusts and these North-South trending tear fault systems (Talbot and Alavi, 1996; Sherkati and Letouzey, 2004).

Contrary to the Northern Fars and central Zagros where most of the emergent salt diapirs are clearly associated with thrust and strike-slip faults (Talbot and Alavi, 1996; Sherkati and Letouzey, 2004), in the southern Fars (Fig. 2), most of the diapirs occurred in association with the anticlines: either at the nose or in the core of the fold. Few of them occurred along thrust faults, and some occurred along the flank of the anticlines.

2.2 Evidence of Pre-Zagros Salt Diapirism

The age of diapirism in the Hormuz series in the ZFTB have been a subject of interest for many years (Harrisson, 1930; Kent, 1958; Player, 1969; Ala, 1974; Eliassi et al., 1977; Kent, 1979; Gansser, 1992; Talbot and Alavi 1996; Edgell, 1996). Harrisson (1930) and Kent (1958; 1979) showed that most of the salt intrusions in the Fars region occurred during the Neogene Zagros folding. However, based on reworked Hormuz material and unconformities in the vicinity of salt plugs, Players (1969) and Kent (1958) introduced the concept of pre-folding and thrusting salt movements (see also Jahani et al., this volume). They also note that Hormuz salt movements occurred in the southern Fars provinces since the late Cretaceous for numerous plugs, probably as early as Permian for some of them (Mottei, 1995a, b). For many plugs, no final conclusion on the date of inception of movement is justified because of limited availability of seismic lines and also the limited age range of the sediments which are in contact with salt plugs in outcrop. Talbot and Alavi (1996) attributed initiation of the salt structures to local manifestations of Jurassic and Cretaceous subduction of the Neo-Tethys before the Zagros folding event. Discontinuous growth of domes prior the ZFTB development was described by Edgell (1996) and Letouzey and Sherkati (2004), who describe a strong, local unconformity related to growth of salt domes. The Darang structure (Fig. 4a) is a good illustration of the early salt movement. This large circular dome is located in the external part of the ZFTB, close to the Persian Gulf. The available seismic lines show an increase in the structural closure with depth, a pattern characteristic of progressive growth of the dome, the growth history of which started in the early Paleozoic and is still active. Similar pattern was observed on seismic images in the Southern Persian Gulf salt basin. The salt domes of the Omanese salt province also present an early beginning of rise during the Paleozoic (Fig. 4b, Peters et al., 2003). The activity of the salt plugs was rejuvenated during the Mesozoic and early Tertiary.
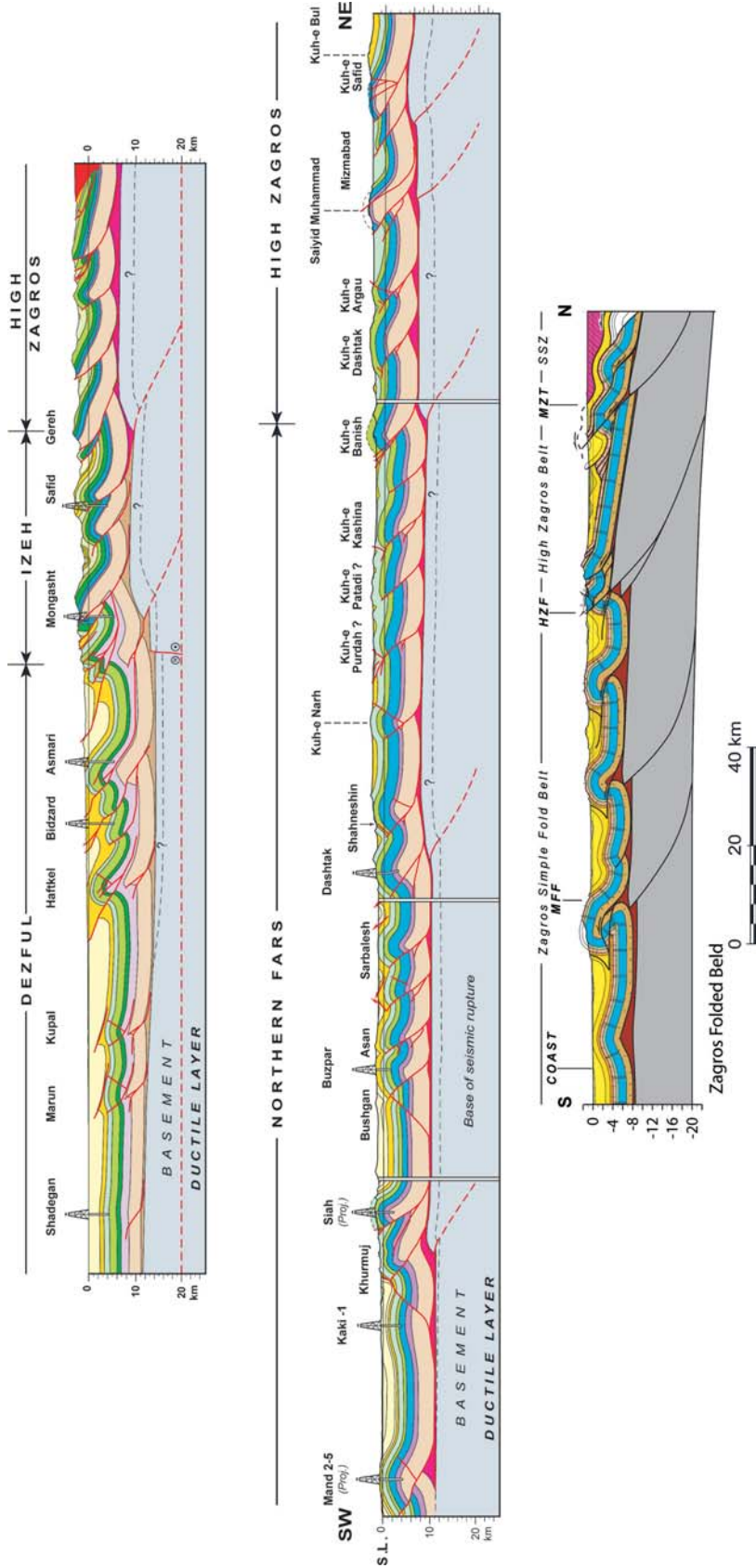
Fig 3 Structural style in the Dezfull and Izeh zone (upper and middle sections, Sherkati and Letouzey, 2004) and the Eastern Fars (lower section, Molinaro et al., 2005). The consequence of the low basal friction due to the action of the Hormuz salt as a basal decollement level, is the symmetry of numerous anticlines in Zagros, and also the vergence of the folds, which is either forward or backward relative to the fold propagation. Large competency contrasts and intermediate decollement levels within the sedimentary pile result in a complex internal geometry in the Zagros folds. The total thickness of the sedimentary column deposited above the Hormuz salt before the Neogene Zagros folding can reach over 10 km
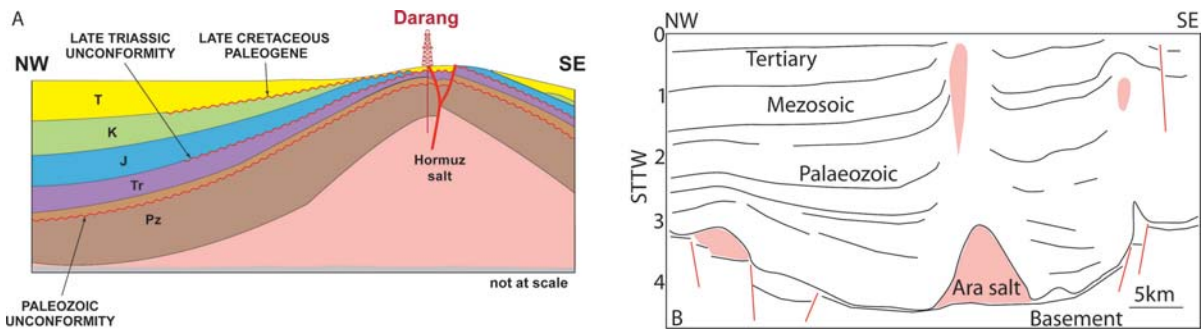
Fig. 4 Evidence of pre-Zagros salt diapirism. The Darang structure is located in front of the Zagros folded belt in the Northern Fars region, close to the Persian Gulf. The Darang well penetrated fifteen hundred meters of Hormuz salt series. The seismic line crossing the structure shows an increase in the structural closure with depth, characteristic of discontinuous growth. Similar features are typically found offshore in the Persian Gulf (Edgell, 1996). The main pulse of structural growth was during the Late Cretaceous. Pre-Hormuz deep horizons are not visible on the seismic line, but this structure is located in the Kazerun fault zone, which is considered as a reactivated basement structure

Concerning the mechanisms of salt extrusion, O'Brien (1950) referred to the local predominance of igneous material in salt plugs and developed a theory of inception of plug movements by igneous activity. This theory was rejected by subsequent authors who have demonstrated that there is no special relationship between salt plug extrusion and igneous intrusion (Kent, 1958). Kent and most of the authors before the 1990's believed that the Hormuz salt rose from great depth under the influence of mainly buoyancy forces. However, the relationship between these deep seated basement faults and the present distribution of salt plugs was reached by several workers (Harrison, 1930; Ala, 1974; Furst, 1990; McQuillan, 1991; Edgell, 1996). Understanding the significant role of extensional faulting in triggering salt diapirism, Jackson and Vendeville (1994), lead Kent (1979), Edgell (1996) and Talbot and Alavi (1996) to suggest the probability of rapid salt extrusion in the Southwest of Iran due to the local pull-apart structures which have been created as a result of the intersection of basement wrench faults and ZFTB thrust fault trends. Players (1969), Kent (1979) and Jahani et al., (this volume) show that some of the Hormuz diapirs reached the surface before the Zagros folding event, whereas others are still buried at depth.

2.3 Objectives

Salt layers are recognised as high efficiency decollement levels in several fold and thrust belts (Davis and Engelder, 1985; Letouzey et al., 1995): for instance, the Potwar (e.g. Grelaud et al., 2003), the Jura Mountains (Guellec et al., 1990; Philippe et al., 1997); the Zagros (e.g. Barhoudi and Koyi, 2003; Sherkati and Letouzey, 2004; Sherkati et al., 2006), the Albanides (Velaj et al.,

1999). This effect has been largely studied and modelled, using both analogue (e.g. Letouzey et al., 1995; Bahroudi and Koyi, 2003; Sherkati et al., 2005) and numerical models (e.g. Simpson, 2005; Stockmal et al., 2005). Nevertheless, few studies emphasized the role played by the inherited salt structures in the localization and development of compressive structures (such as the Dinar thrust, see Letouzey and Sherkati, 2004), although it is clear from both seismic and field evidence of that thrust faults are not evenly distributed with respect to the pre-existing salt structures (Velaj et al., 1999; Jackson et al., 2003).

The main purpose of the present study is to document the effect of pre-existing salt diapirs in a given stratigraphic column on the development of compressive structures during shortening. The geometry of the diapirs, the brittle-to-ductile thickness ratio in the section and the velocity of shortening are the main parameters considered. Such a study more generally questions the mechanisms of salt extrusion in compressive setting. The studied mechanism of Hormuz halokinesis and extrusion in the Southern Fars Province is the squeezing of pre-existing salt domes. Local pull-apart and wrench fault deflection probably also allowed for rapid rising of the evaporites (Talbot and Alavi, 1996; Letouzey and Sherkati, 2004).

3 Analogue Experiments

3.1 Experimental Design

The models were scaled for length, viscosity and time, following the basic principles, discussed by Hubbert (1937) and Ramberg (1981), applied at basin scale (the upper 7 km of the crust). The length ratio between models and natural examples is 10^{-5} (1 cm in the mod-

el represented 1km in nature), the viscosity ratio was 2×10^{-15} (based on a viscosity of 10^{19} Pa s as a maximum value for evaporites), and the time ratio was 4×10^{-10}. It is important to keep in mind that the role of some geological parameters (e.g. temperature gradient, erosion, among others) could not be taken into account.

In the experiments, sedimentary brittle rocks were simulated with sand, which has a low/negligible cohesion, an angle of internal friction of 30°, and a density ranging from 1400 to 1600kg/m³. The ductile behaviour of weak layers within the brittle upper crust were simulated by layers of silicone putty (PDMS). The latter behaves nearly as a Newtonian fluid, with a density close to 1g·cm⁻³ and a viscosity of 2.5×10^4 Pa s at room temperature and strain rates below 3×10^{-3} s⁻¹. All models were shortened either at 4 (model 1572) or 1.7 cm·h⁻¹ from one end (model 1572, 1585, and 1597), which are rather high velocities except for one model which was deformed at 0.4 cm·h⁻¹ (model 1645). The thickness of the basal silicon layer was chosen to be 1.2 cm, whereas the brittle overburden thickness is either 4.5 for thick models or 2.5 cm for thin models. We choose to model axisymmetric diapir to really study the diapir shape effect along a 2D section and avoid 3D strain distribution. All experiment parameters are listed in Tables 1 and 2, together with Fig. 5 which shows the distribution in the horizontal plane of the diapirs.

Our experiments were analyzed by X-ray computerized tomography, a non-destructive technique that generated cross-sectional images through the models (Hounsfield 1973; Mandl 1988; Richard et al., 1989; Colletta et al., 1991). The analysis and interpretation of the experiments were carried out by means of:

1. Images representing vertical sections of the model, perpendicular to the longitudinal sidewalls of the box (i.e. parallel to the direction of shortening)
2. Images representing horizontal sections through the model and line-drawings.
3. Surface pictures at different stages of the deformation
4. 3D reconstruction of fault zones, as well as of several surfaces within the models, at different stages of deformation. For the analysis of surface pictures, a square grid of coloured sand markers was finely traced onto the uppermost surface.

3.2 Results

Considering the geological model, several parameters are tested through analogue experiments:

1. The kinematic boundary conditions, which can either be transpressive of purely compressive;
2. The overall regional strain rate, models being strained at either fast (i.e. 1.7 cm·h⁻¹) or slow speed (i.e. 0.4 cm·h⁻¹);
3. The mechanical stratification, which results from the relative thickness of the mobile ductile silicone layer and the brittle sedimentary overburden of sand layers. In the present study, we choose to consider only the basal decollement level. The role

Table 1. Experimental parameters

Experiment	Width	Length	Silicon thick.	Sand thick.	Duration	Shortening vel.	Shortening	Strike Slip vel.	Strike slip disp.
1210	38.2	78	1.4	1.4+2	6h40	4/3	5.7 (15%)	-	-
1212	41	65	1.3	1.3+2	6h50	3	12.0 (28%)	3	12 (18°)
1572	39	78	1.0 cm	3.6 cm	5h15	1.7	9.0 (23%)	-	-
1585	39	78	0.8	3.2	6h10	1.7	8.2 (21%)	-	-
1597	39	78	1.2	1.8	6h40	1.5	10.0 (26%)	-	-
1645	39	78	1.2	1.8	23h25	0.5/0.4	10.8 (28%)	-	-

Experiment	Diapir nbr	Diapir width	Diapir height	Sand thick. above dome	Spacing	Spacing line	Lines shift
1210	3	10/10/4.5	init. 0		20	-	-
1212	5	6	init. 0		20/25	15	10
1572	4/4	2.5/1.5	1.5/2.5		10	10	5
1585	4/4	3.8/2.5	1/1.7		10	10	5/-5
1597	4/4	5.4/3.3	0.9/1.4		10	10	5
1645	4/4	6.6/3.7	0.9/1.4		10	10	5

Table 2.
Geometric parameters for the diapir distribution
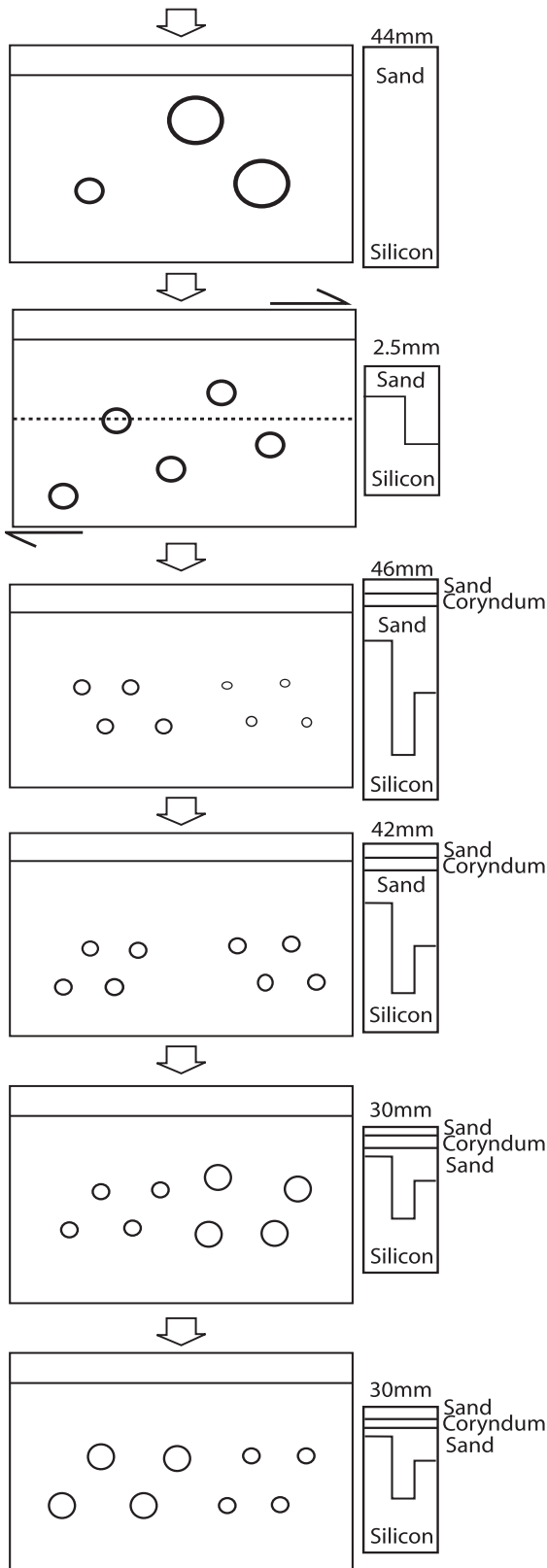
Fig. 5 Geometry of the different models in plan view, with a synthetic sedimentary column (total thickness in mm)

of the sedimentary layers which can potentially decouple the stratigraphic section has already been tested by Sherkati et al. (2006);

4. The diapir shape, which results from the interaction between sedimentation, erosion and basement and regional tectonics, and salt mobility, before the episode of shortening. The chosen shapes are the pillow, cone, finger like, and box.

Neither sedimentation nor erosion are taken into account, although the loading/unloading effect of the sediment supply or removal could affect drastically the total resistance of the section and its evolution during shortening. For sake of clarity, all cross-sections of the model were shortened from the left end side.

3.2.1 Model with Variable Boundary Conditions

The models presented in Fig. 6 are designed to study the evolution of pre-existing domes during compression, and their relation with the thrusts, depending on the obliquity of shortening to the distribution of domes. Horizontal and vertical images within the model at the initial stage show the three or five circular buried silicone domes (model 1210 and 1212, respectively). These two-layered models were shortened horizontally at a rate of 4 cm·h^{-1}, with either 90° or 45° obliquity of shortening. In both cases, during shortening, pre-existing domes initiated the main active faults, are horizontally squeezed, the shortening forcing the silicone mainly upward through the overburden layer, as shown previously by Letouzey et al. (1995), and Vendeville and Nilsen (1995). It is clearly visible on surface view of the models during the shortening that the location of pre-existing domes influences fault propagations (Letouzey and Sherkati, 2004). The obliquity does not influence the first-order deformation pattern, although the oblique shortening results in transpression along the faults initiated at the dome location, which in turn accommodates a greater amount of shortening by the formation of flower-like structures.

3.2.2 Model with Variable Diapir Shapes and Sedimentary Cover

Thickness of the sedimentary cover with respect to the thickness of both the feeding silicon layer and the pre-existing diapir strongly influences the pattern of deformation and structural style. Here are described models which were strained at a medium rate, i.e. 1.4 cm·h^{-1}.

The thick sedimentary cover prevents any significant evolution of the six pre-existing diapirs (Fig. 6, model 1572 and 1585), and react as if there was no di-
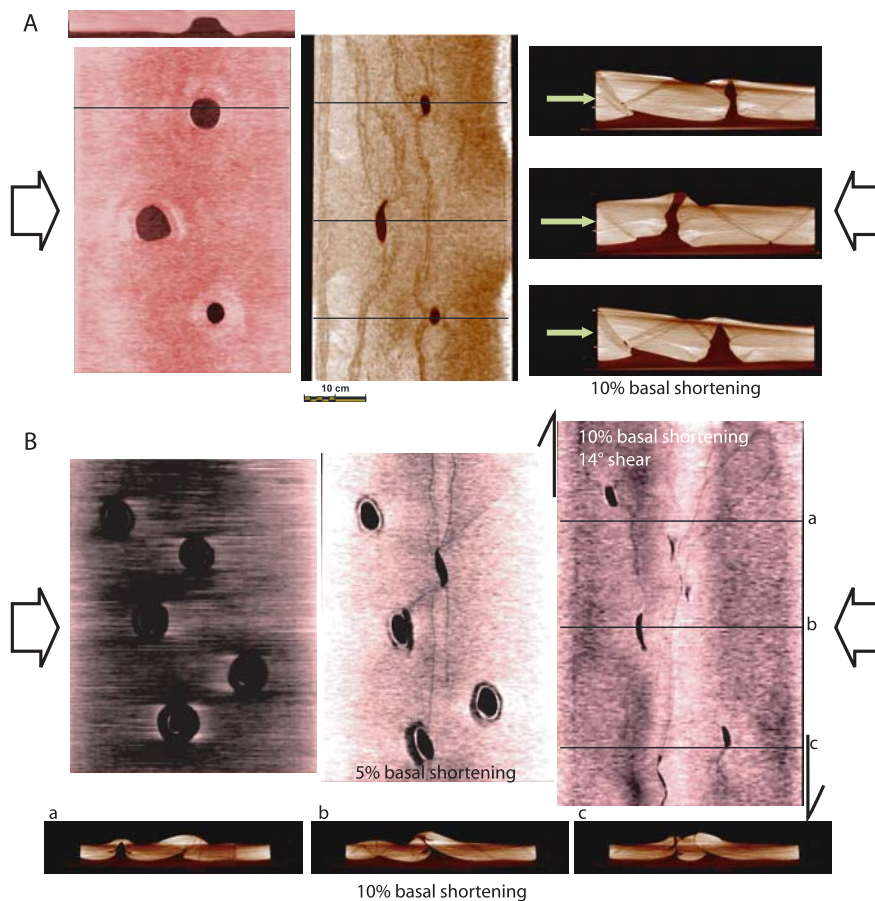
A

10 cm

10% basal shortening

B

10% basal shortening
14° shear

a

b

c

5% basal shortening

a   b   c

10% basal shortening

apiric body at depth. The structural style shows classic large-scale fault propagation folds formed with minor buckling effect. Nevertheless, the diapir body appears to localise the initial thrust faults at depth, which later on propagate toward the surface within the purely brittle cover, and laterally toward adjacent domes. The belt is eventually composed of large box-like anticlines located on top of low-angle thrust faults.

By contrast, the structural style in the case of thin sedimentary covers is much more dominated by the buckling of the sand layer on top of the basal silicon layer, followed by focused fault propagation folding on top of the diapiric body (model 1597, Fig. 7). Similarly to the thick cover models, the early thrust faults initiate at the diapirs. Here it is even possible to observe symmetrical pop-up structures. Thin sedimentary covers favour a progressive remobilisation of the silicone diapir during the shortening and a rejuvenation of its ascent up to the surface, where it eventually spreads. Here the absence of erosion increases the contrast between the model with a thick, and hence strong, sedimentary cover which controls the overall deformation pattern, and the thin, hence weak, sedimentary cover, whose deformation pattern is controlled by the weak silicone body at depth.

In both cases, diapiric bodies nucleate the thrusts faults. Here the shape of the pre-existing dome plays a major role. Finger and box-like diapirs nucleate the thrust fault along their base, where it cuts through the diapir, and a part of the diapir is passively transported in the core of the fold, allowing for the possible remobilisation of the silicon if erosion was to follow. Diapirs with low-angle walls, i.e. pillow and cones, are directly used as preferred ramps and thus only moderately remobilised; they act as thrust soles rather than a transported plug (figures 7 and 8). With thin sedimentary covers, the ramps are much steeper due to the shortening of the diapirs and associated wall rotations. This limits the ability of the ramps to accommodate large displacements and force the development of small sharp folds on top of the diapirs.

3.2.3 Influence of the Velocity of the Folding

The model strained at low velocity, i.e. 0.4 cm·h⁻¹, reveal a somewhat different structural style (Figs. 9a and b, model 1645), although the first-order geometry is preserved. Following initial buckling of the sedimentary section above the silicon, the diapiric bodies initi-

Diapir shape (axisymmetric)

Cylinder ▭ 2cm   Pillow ⌒ 2cm   Cone △ 2cm   Finger 3.5cm
3cm   5cm   2cm   1.5cm

Experiment 1572   Experiment 1585   Experiment 1572

23% shortening   21% shortening   23% shortening
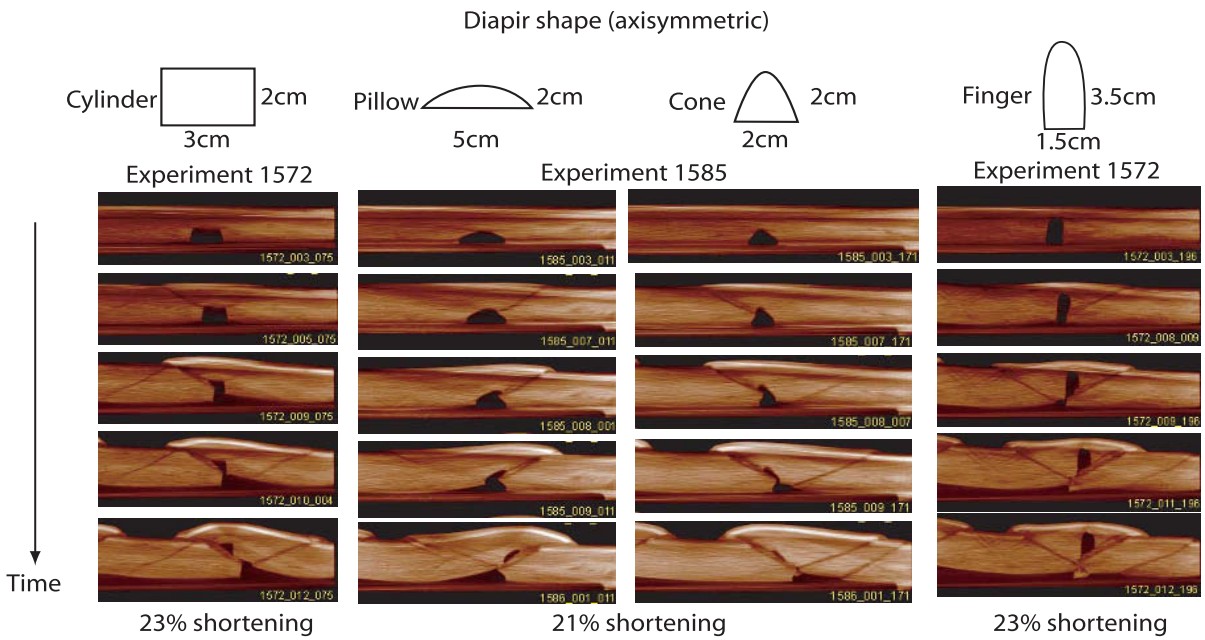
Fig. 7. Models with thick sedimentary cover (5 cm-thick sand-pack), showing evolution of diapirs of variable geometry (4 boxes and 4 fingers, model n°1572, 4 pillows and 4 cones, model n°1585) during shortening at a velocity of 1.4 cm·h⁻¹. Moving wall at the left-end side of the section.

Fig. 8: Models with thin sedimentary cover (3 cm-thick sand-pack, model n°1597), showing evolution of axisymmetric diapirs during shortening at a velocity of 1.4 cm·h⁻¹. The small picture illustrates a local pop-up geometry. Moving wall at the left-end side of the section

Diapir shape (axisymmetric)

Cone △ 2.5cm   Pillow ⌒ 1.5cm
2cm   5cm

Model n°1597

26% shortening

Diapir shape (axisymmetric)

Cone   2.5cm

2cm

Pillow   1.5cm

5cm

Model 1645

28% shortening

A model n°1597

B model n°1645
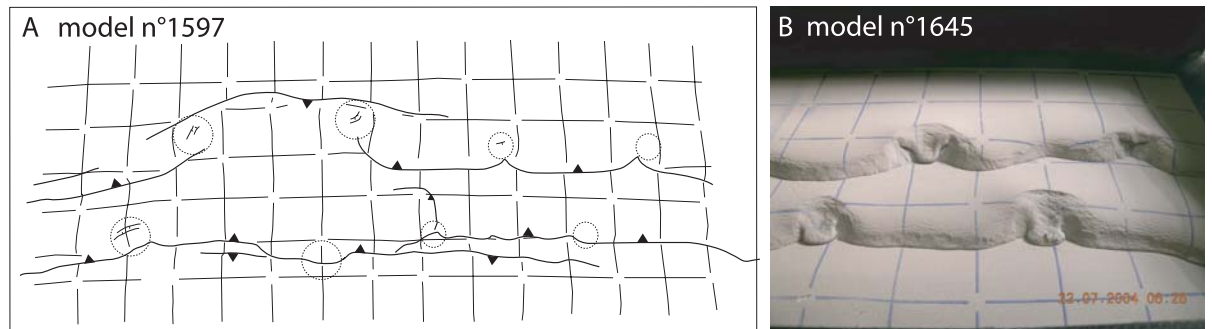
Fig. 10. a Topographic map of the late stage of evolution of the model 1597 with a thin sedimentary cover; **b** Oblique surface picture of the late stage of silicon plug emergence at the apparent termination of fold, model 1645 with thin sedimentary cover

ate and localise the shortening structures. Diapirs are progressively squeezed and extruded with displacement of silicon both upward (i.e. toward the surface) and downward (i.e. toward the basal layer). These further preclude the use of the diapir walls as a ramps due to the increase of their wall angles. Moreover, rather

than a thrust, diapirs evolve into sharp folds with vertical limbs thinning toward the diapirs, a ‚lift off fold'. Ultimately, the folds are overturned and the squeezed diapirs eventually act as thrust faults. In this case of thin sedimentary covers, the steep attitude of the faults limit the displacements along the thrusts, and extru-

sion of silicon occurs on top of the sharp overturned folds (Fig. 10). Both at high and low velocity, diapirs finally localised sharp narrow folds, where shortening and silicone extrusion are concentrated, separating areas where classic, large fault-propagation-fold develops (Figs. 9 and 10). This creates an arcuate cartographic pattern where emergent diapirs are preferentially located either at the apparent fold termination, or else, within the core of the folds for thick covers.

4   Discussion and Conclusions: Evolution of a Thrust-Diapir System

4.1 Kinematic Evolution and Scaling of Material

The shortening velocities applied here are quite high considering the classic velocities obtained from growing fold, i.e. few mm per year. The present-day shortening accommodated within the ZFTB ranges from 4 to 14 mm·yr^{-1} (Masson et al., 2005). Particularly in the central ZFTB, the average velocity reaches 0.7 cm·yr^{-1}, which would correspond to a shortening velocity of ~0.4 cm·h^{-1} using our scaling relationship. As we model no more than 3 to 4 folds across-strike, the chosen velocity of 1.4 cm·h^{-1} is far too high with regard to the natural example. Nevertheless, the velocity increase, which is expressed as an increase of the resistance of the silicone layer, compensates for its low density. Considering the density ratio between salt (ρ~2.2) and classic sedimentary rocks (ρ~2.3–2.8), the density ratio use in the model should be 0.84. The analogue material densities for silicone are 0.99 and for dried Fontainebleau sand sieved onto the model is roughly 1.7, giving thus a density ratio of 0.58. This shows that the analogue for salt is much more buoyant than is salt in the real case. Such mis-scaling is partly compensated by high velocities that limit the buoyancy of silicon.

4.2 Diapir Shape

The diapir observed in the ZFTB and in the Persian Gulf at the present day show an elongate pattern suggesting original non-symmetric shapes, the long axis of which were oblique to the structural grain of the Zagros (Rönnlund and Koyi, 1988). Nevertheless, several lines of evidence suggest that the inception of salt movement could have been as early as Palaeozoic, and most probably linked to the tectonic activity of inherited Pan-African and Arabian trends. A second main phase of diapir building would have been during the regional hercynian erosion, then during the Tethyan rifting during the Triassic. This later phase is restrict-

ed to the Northwestern border of the Iranian margin. We propose that the main salt structures formed during both growth phases would be ridges and salt wall, similarly to what is observed in the North Germany salt basin. Such a salt wall would then develop plug-like instabilities at their crest, which then form the present-day observed salt plugs, a pattern which is strongly suggested from the Oman and Persian Gulf salt domes. Thus, although the spatial distribution of plugs suggest the original tectonic control on the salt structures and their elongation, the main salt plugs formed during the Mesozoic to Early Tertiary would present rather axisymmetric shapes.

The diapir shape plays a fundamental role in controlling the structural style. As demonstrated by our experiments, the diapir first localises the incipient thrust. Its shape then controls the temporal evolution of the diapirs: diapir with high steep walls (finger and box, model 1572, Figs. 7) will be shortened horizontally and expanded vertically, and the incipient thrust will pass by them, developing a shot-cut at the base of the diapir. A large part of the diapir is then incorporated into the developing fold and passively transported above the thrust. By contrast, diapirs with low-angle walls (cones and pillow, models 1585 and 1597, Figs. 7 and 8) act as preferably oriented ramps and localise the thrust plane. In such cases, most of the diapir is incorporated into the footwall of the thrust and is no longer strained. Only a few percent of the diapir volume will be incorporated into the hanging wall as a sole plane for the thrust. Slow shortening favours horizontal shortening of the diapir and steepening of its walls. This allows for a transition from the end members fates of low-angle conical diapirs to high-angle finger-like structures. Conical and pillow diapirs act as favourably oriented ramps (Figs. 7 and 8), whereas finger-like diapirs are thrust off from their roots and incorporated within the fold.

4.3 Mechanisms of Extrusion

In the NW Fars and Izeh zone, salt extrusion appears to be mainly controlled by the activity of major tectonic structures expressed in the Zagros folding, particularly strike-slip fault zones such as the Kazerun lineament or thrust fault such as the Dinar thrust (Talbot and Alavi, 1996; Sherkati et al., 2005, Figs. 11a and b). In such setting, salt is either located at the thrust soles, or else pumped into pull-apart structures (Fig. 11a). By contrast, in the Southern Fars domain, the extrusion of rounded salt plugs, which is a first-order pattern of the recent ZFTB evolution, appears to correlate primarily to the main folded structures. The salt diapirs are mostly located either at the fold periclines (Fig. 11c) or in their core (Fig. 11d), and extrude salt glaciers in
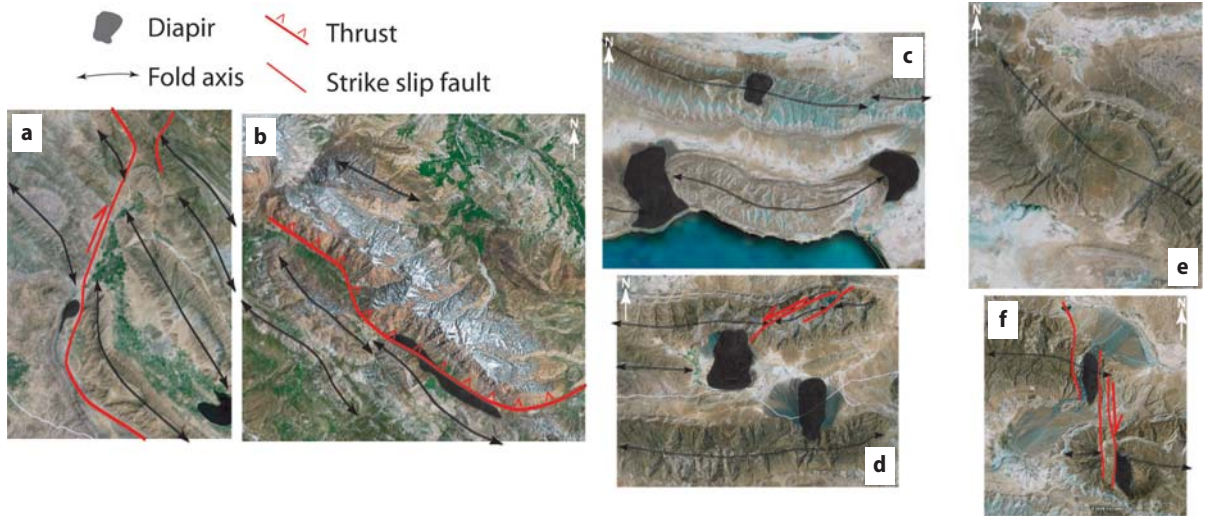
Fig. 11. a The Kazerun strike slip fault with an associated emergent salt plug; **b** The Dina thrust with associated emergent plug; **c** the Charak anticline (Fars area); **d** the Kuh e Gash (north) and Kuh e Bush anticline, with emergent salt plugs and glacier; **e** the Gavbast anticline with growing buried plug; **f** The tectonically controlled plugs of the east Gavbast and Bastak anticline
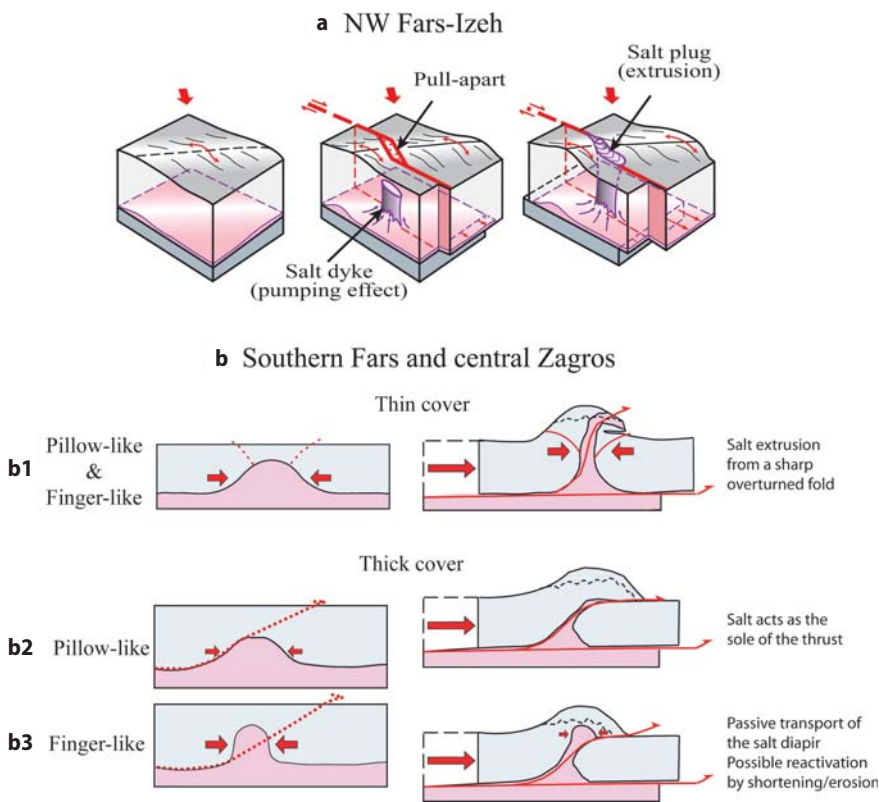
Fig. 12. a Mechanisms of salt extrusion: (**a**) Extrusion along tectonic structures in the Dezful and Izeh zones, after Sherkati et al., 2005; (**b**): Extrusion due to (1) shortening of slightly buried diapir (B1); (2) Thrust fault emplacement, with (B3) or without (B2) diapir incorporation in the hanging wall (see text for explanations)

a direction controlled by the overall vergence of the fold. Several still buried plugs are still rising as shown by the local dome shape of the fold, superimposed on the general fold trend (Fig. 11e, see Jahani et al., this

volume), with, in some cases, salt extrusion beginning along thrust faults with erosional surfaces (Fig. 11f).

The experiments shown here illustrate the fundamental role of the diapir's past on its future evolution

during shortening, as the diapir localises both short-ening and incipient thrust planes. The mode of extru-sion depends first on the size of the pre-tectonic dia-piric bodies, particularly on their initial height with regard to the total sedimentary section, and secondly to the attitude of its wall.

Tall diapirs drastically weaken the sedimenta-ry column, and localise the shortening, thus increas-ing their wall dips and height before the main thrust faults form. Thus such diapirs may never act as prefer-entially oriented thrust planes. Instead, they will an-chor a high angle sharp fold completely cored by salt (Fig. 12b1). Due to the general fold belt vergence, these tight folds will be progressively overturned, encourag-ing the lateral extrusion of a salt glacier (Figs. 11c and 11d). In such configurations, the salt plug appears to be located at the apparent termination of the fold, al-though this termination does not correspond to a real pericline (Figs. 10 and 11c), a feature which is compa-rable to the present distribution of Hormuz salt plug in the Fars Province (Fig. 2).

Small diapirs, with respect to the total sedimenta-ry column thickness, do not modify the strength of the section which then develop classic fault bend folds. These are cored by the detached and passively trans-ported diapirs. The initial wall dip, i.e. low-angle wall of a pillow or high-angle wall of a finger-like diapir, controls whether the thrust fault is rooted either at the top or else the base of the diapir (Figs. 12b2 and b3). In the former case, the salt will drape the thrust plane. In the latter case, a large salt core is transported, and its ascent and extrusion may be reactivated as a response to shortening, leading to doming of the fold (figure 11e), and facilitated by erosion (Fig. 11d).

Acknowledgements

References

Al-Husseini, M.I., 2000. Origin of the Arabian plate structures; Amar collision and Nadj rift. GeoArabia, 5, 527–542.

Agard, P., Omrani, J. Jolivet L. Mouthereau F. (2005) Conver-gence history across Zagros (Iran) : Constraints from colli-sional and earlier deformation. Int. J. Earth Sci. (Geol. Rundsch) 94, 401–419.

Ala, M.A. 1974, Salt Diapirism in Southern Iran: AAPG Bull., v. 58, p. 1758–1770.

Alavi, M.A., 1994, .Tectonics of the Zagros orogenic belt of Iran; New data and interpretations. Tectonophys., 229, 211–238.

Bahroudi, A., and H. Koyi, 2003, Effect of spatial distribution of Hormuz salt on deformation style in the Zagros fold and thrust belt: an analogue modeling approach: J. Geol. Soc., London, v. 160, p. 1–15.

Berberian, M. and King, G.C.P., 1981. Towards a paleogeogra-phy and tectonic evolution of Iran, Can. J. Earth Sci, 18(2), 210–265.Blanc, E.J.-P., Allen, M.B., Inger, S. and Hassani, H., 2003. Structural styles in the Zagros simple folded zone, Iran, J. Geol. Soc. London, 160, 401–412.

Blanc, E. J. P., M. B. Allen, S. Inger, and H. Hassani (2003), Structural styles in the Zagros simple folded zone, Iran. J. Geol Soc. London, 160, 401–412.

Bonini, M. (2003), Detachment folding, fold amplification, and diapirism in thrust wedge experiments, Tectonics, 22,1065,

Colletta, B., J. Letouzey, R. Pinedo, J.F. Ballard, and P. Bale, 1991, Computerized X-ray tomography analysis of sand box models: examples of thin-skinned thrust system: Geology, v. 19, p. 1063–1067.

Colman-Sadd, S.P. (1978), Fold Development In Zagros Simply Folded Belt, Southwest Iran. Am. Ass. Petrol. Geol. Bull, 62, 984 1003.

Davis, D.M., adn Engelder, T., 1985. The role of salt in fold and thrust belts. Tectonophys., 119, 67–88.

Edgell, H. S., 1996, Salt Tectonics in the Persian Gulf basin: in G.L. Alsop, D. L. Blundell, and I. Davison, eds., Salt Tecton-ics, Geol. Soc. Spec. Publ., 100, p. 129–151.

Eliassi, J., A.E. Sobhani, A. Behzad, H. Moinvaziri, and A. Mei-sami, 1977, Geology of Hormuz Island: Second Symposium on Geology of Iran., Iran Oil Association, p. 31–72.

Falcon, N., 1974, Southern Iran: Zagros mountains: in A. Spen-cer, ed., Mesozoic-Cenozoic Orogenic Belts: Geol. Soc. Spec. Publ., 4, p. 199–211.

Gansser, A., 1992, The enigma of the Persian dome inclusions: Eclogae Geologica Helveticae, 85, p 825–846.

Guellec, S. Mugnier, J.L., Tardy, M., and Roure, F., 1990. Neo-gene evolution of the western alpine foreland in he light of ECORS data and balanced cross-section. Mem. Soc. Geol. France 156, 165–184.

Harrison, J.V., 1930, The geology of some salt plugs in Laristan: Quar. Jour. Geol. Soc., London, v. 86, p. 463–522.

Homke, S., Verges, J., Garces, G., Emamia, H. and Karpuzc, R., 2004. Magnetostratigraphy of Miocene-Pliocene Zagros foreland deposits in the front of the Push-e Kush Arc (Lures-tan Province, Iran), Earth Planet. Sci. Lett., 225, 397–410.

Hounsfield, G. N. 1973. Computerized transverse axial scan-ning (tomography). British J. Rad., 46, 1016–1022.

Hubbert, M. K. 1937. Theory of scale models as applied to the study of geologic structures. Geol. Soc. Am. Bull., 48, 1459–1520.

Jackson, M.P.A., and B.C. Vendeville, 1994, Regional extension as a geologic trigger for diapirism: Geol. Soc. Am. Bull., v. 106, p. 57–73.

Jackson, M.P.A., Warin, O.N., Woad, G.M., Hudec, M.R., 2003. Neoproterozoic allochtonous salt tectonics during the Lufil-ian orogeny in the Katangan Copperbelt, central Africa. Geol. Soc. Am. Bull., 115 314–330.

Jeroen, M.P., J.B. Filbrandt, J.P. Grotzinger, M.J. Newall, M.W. Shuster, and A. Al-Siyabi, 2003, Surface-piercing salt domes of interior North Oman, and their significance for the Ara carbonate 'stringer' hydrocarbon play: GeoArabia, v. 8, no. 2, p.231–270.

Kent, P.E. 1958, Recent studies of south Persian salt plugs: Am. Ass. Petrol. Geol. Bull., v. 42, p. 2951–2972.

Kent, P.E., 1979, The emergent Hormuz salt plugs of southern Iran: Jour. of Petroleum Geology, v. 2, p. 117 144.

Kent, P. E. (1986). Island salt plugs in the Middle East and their tectonic implications. In I. Leiche and J. J. O, Brien (Eds) "Dynamical Geology of salt and related structures", Academic Press, New York, 3–37.

Konert, G., A.M. Afifi, S.A. Al-Hajiri, K. de Groot, A.A. Al Naim, and H.J. Droste, 2001, Paleozoic stratigraphy and hydrocarbon habitat of the Arabian Plate: in M.W. Downey, J.C. Three, and W.A. Morgan, eds., Petroleum Provinces of the Twenty-first Century, Am. Ass. Petrol. Geol. Mem. 74, p.483–515.

Koop, W.J., and R. Stoneley, 1982, Subsidence history of the Middle East Zagros Basin, Permian to Recent: Phil. Trans. R. Soc., London, A 305, p. 149 168.

Letouzey, J., B. Colletta, R. Vially, and J.C. Chermette, 1995, Evolution of salt related structures in compressional setting: in M.P.A. Jackson, D.G. Roberts, and S. Snelson, eds., Salt Tectonics: A Global Perspective, Am. Ass. Petrol. Geol. Mem. 65, p. 41–60.

Letouzey, J., S. Sherkati, J.M. Mengus, H. Motiei, M. Ehsani, M. Ahmadnia, and J.L. Rudkiewicz, 2002, A regional structural interpretation of the Zagros mountain belt in northern Fars and High Zagros (SW Iran): AAPG Annual Meeting 2002 (abstract).

Letouzey J. and S.Sherkati (2004), Salt Movement, Tectonic Events, and Structural Style in the Central Zagros Fold and Thrust Belt (Iran), In Salt sediments interactions and hydrocarbon prospectivity, 24th Ann.GCSSEP Foundation, Bob F. Perkins research Conf. CD.

Masson, F., Chéry, J., Hatzfeld, D., Martinod, J., Vernant, P., Tavakoli, F., Ghafory-Ashtiani, M., 2005. Seismic versus aseismic deformation in Iran inferred from earthquakes and geodetic data. Geophys. J. Int., 160, 217–226.

Mandl, G. 1988. Mechanisms of Tectonic Faulting. Elsevier, Amsterdam.

McQuarrie, N., 2004. Crustal scale geometry of the Zagros fold-thrust belt, Iran, J. Struct. Geol., 26, 519–535.

McQuillan, H., 1991, The role of basement tectonics in the control of sedimentary facies, structural pattern and salt plug emplacements in the Zagros fold belt of south-west Iran: J. South. Asian Earth Sci. 5, p. 453–463.

Molinaro, M., Leturmy, P., Guezou, J.-C., Frizon de Lamotte, D. and Eshraghi, S.A., 2005. The structure and kinematics of the south-eastern Zagros foldthrust belt; Iran: from thin-skinned to thick-skinned tectonics. Tectonics, 24, TC3007, doi:10.1029/2004TC001633.

Molinaro, M., Guezou, J.C., Leturmy, P., Eshraghi, S.A. & Frizon de Lamotte, D., 2004. The origin of changes in structural style across the Bandar Abbas syntaxis, SE Zagros (Iran), Mar. Petrol. Geol., 21, 735– 752.

Motiei, H., 1995a, Petroleum geology of Zagros: Publ. Geol. Survey of Iran (in Farsi), 589 p.

Motiei, H., 1995b, Stratigraphy of Zagros: Publ. Geol. Survey of Iran (in Farsi), 536 p.

Mouthereau, F., O. Lacombe O., Meyer B., 2006. The Zagros folded belt (Fars, Iran): constraints from topography and critical wedge modelling, Geophys. J. Int., in press

O'Brien, C.A.E., 1957. Salt diapirism in South Persia, Geologie en Mijnbouw, 337–376.

Philippe, Y., Colletta, B., Deville, E., Mascle, A., 1997. The Jura fold-and-thrust belt: Overall structural and mechanical as-

pects. Kinematic model deduced from mass balancing and regional implications. In Ziegler, W. (ed.) Perithys Memoir 2, Paris, Editions du Museum d'histoire naturelle.

Player, R. A. 1969. Salt plug study. Iranian Oil Operating Companies. Geological and Exploration Division Report No 1146.(unpublished).

Player, R. A. 1969. Salt plugs of southern Iran. Theses. London British Library.

Ramberg, H. 1981. Gravity, Deformation and the Earth's Crust. Academic Press, New York.

Richard, P. & Cobbold, P.R. 1989. Structures en fleur positives et décrochements crustaux: modélisation analogique et interprétation mécanique. C. R. Acad. Sci. Paris, Série II, 308, 553–560.

Ricou, L. E. 1971, Le croissant ophiolitique péri-arabe. Une ceinture de nappes mises en place au Crétacé supérieur. Rev. Géogr. Phys. Géol. Dyn., 13,327–350.

Ricou, L.E., Braud, J.J., and Brunn, J.H., 1977, The Zagros. Mem. Soc. Geol. France, 8, 33–52.

Rönnlund, P., and Koyi, H., 1988. Fry spacing and deformed and undeformed modeled and natural salt domes. Geology, 16, 465–468.

Sans, M. and Vergés, J. 1995. Fold development related to continental salt tectonic: Southeastern Pyrenean thrust front, Spain. In M. P. A. Jackson, D. G. Roberts and S. Snelson, eds., Salt tectonics: a global prospective. Am. Ass. Petrol. Geol. Mem. 65, 369–378.

Sans, M., and H. Koyi, 2001, Modeling the role of erosion in diapir development in contractional settings: Geol. Soc. Am. Mem. 193, p. 111–122.

Sepehr, M. & Cosgrove, J.W., 2004. Structural framework of the Zagros Fold-Thrust Belt, Iran, Mar. Petrol. Geol., 21, 829–843.

Sepehr, M. and J.W. Cosgrove 2005. Role of the Kazerun Fault Zone in the formation and deformation of the Zagros Fold-Thrust Belt, Iran, Tectonics, 24,

Sherkati, S., and Letouzey, J., 2004, Variation of structural style and basin evolution in the central Zagros (Izeh zone and Deyzful Embayment), Iran: Marine and Petroleum Geology ,v.21, p. 535–554.

Sherkati, S., Molinaro, M., Frizon de Lamotte, D. and Letouzey, J., (2005) Detachment folding in the Central and Eastern Zagros fold belt (Iran). J. Struct. Geol., .

Sherkati, S. J. Letouzey, D. Frizon de Lamotte .(2006).The Central Zagros fold-thrust belt (Iran): New insights from seismic data, field observation and sandbox modeling .Tectonics, in press.

Simpson, G., 2005. Interactions between fold-and-thrust belts deformation, foreland flexure and surface mass transport. Thrust Belt and Foreland basins, SGF-SGE Joint Meeting, Rueil Malmaison, 345.

Stampfli, G.M. and G.D. Borel, (2004), The TRANSMED transects in space and time: constraints on the paleotectonic evolution of the Mediterranean domain. In Cavazza, W., Roure, F., Spakman, W., Stampfli, G.M. and Ziegler, P.A. (eds), The TRANSMED Atlas, The Mediterranean region from crust to Mantle. Springer.

Stockmal, G., Beaumont, C., Nguyen, M., Lee, B., 2005. Coupling between surface processes and thin skinned structural style: Insights from dynamical numerical modelling. Thrust Belt and Foreland basins, SGF-SGE Joint Meeting, Rueil Malmaison, 360.

Stoecklin, J., 1968, Structural history and tectonics of Iran: a review: Am. Ass. Petrol. Geol. Bull., v. 52, p.1229–1258.

Stoecklin, J., 1968. Salt deposits in the Middle East., Geol Soc Am. Spec. Pub., 88, 157–181.

Stoecklin, J., 1974, Possible ancient continental margins in Iran. In Burk, C.A. and Drake, C.L. (eds), The geology of continental margins, 873–887, Springer Verlag, New-York.

Szabo, F. and A. Kheradpir (1978), Permian and Triassic stratigraphy, Zagros basin, South-West Iran. J. Petrol. Geol., 57–82.

Talbot, C., and J.M. Alavi, 1996, The past of a future syntaxis across the Zagros: in G.L. Alsop, D.L. Blundell, and I. Davison, eds., Salt Tectonics, Geol. Soc., London, Spec. Pub., 100, p. 129–151.

Talbot, C.J., 1998, Extrusions of Hormuz in Iran. Geol. Soc. Spec. Publ., 143, 315–334.

Takin, M., 1972, Iranian geology and continental drift in the Middle East. Nature, 235, 147–150.

Velaj, T., Davison, I., Serjani, A. and Alsop, I., 1999. Thrust tectonics and the role of evaporites in the Ionian zone of the Albanides. Am. As. Petrol. Geol. Bull., 83, 1408–1425.

Vendeville, B.C., and M.P.A. Jackson, 1992, The rise of diapirs during thin skinned extension: Marine Petrol. Geol., v. 9, p. 331–353.

Vendeville, B.C., and K.T. Nilsen, 1995, Episodic growth of salt diapirs driven by horizontal shortening. GCSSEPM 16th Bob F. Perkins Research Conference, p. 285–295.

Waltham, D., 1997, Why does salt start to move?: Tectonophys., v. 282, p. 117–128.

Impact of Sedimentation on Convergent Margin Tectonics: Example of the Makran Accretionary Prism (Pakistan)

N. Ellouz-Zimmermann · E. Deville · C. Müller · S. Lallemant · A.B. Subhani · A.R. Tabreez

Abstract. This paper discusses the geodynamic evolution of the Makran accretionary prism from a new field investigation in the Pakistani area and from the interpretation of reprocessed seismic lines in the offshore area. The field reconnaissance has provided new structural data about the general structure of the prism and a rejuvenated stratigraphic chart based on new datings. This work outlines that the sediment input in the Makran originated from various origins during Cenozoic times: (1) direct influx from the Indus River conveying eroded series from the Indian shield or Himalayas, (2) strong erosion of the growing inner prism. En-échelon elongated anticlines which are cross-cut by strike-slip faults developed along the eastern Makran Range. Recent out-of-sequence thrust propagation has been evidenced in the onshore area in relation to recent erosion. A large un-deformed platform responsible for a huge trap for sedimentation developed during Miocene and Pliocene times between the emerged part of the Makran and the offshore active compressive front. The internal architecture of the prism is also strongly influenced by the propagation of the deformation within secondary décollement levels. These upper detachments are hosted within the Miocene slope-to-basin prograding wedges, upon which a recent normal growth fault system developed in the near offshore area, at the same time when compression occurred at the front of the prism.

1   Introduction

The main challenge in oil exploration of convergent fold-and-thrust belts and accretionary prisms is to identify the chronology of the deformation and to predict the location of the traps having the maximum of duration and preservation. In many natural examples (Assam, Colombian fold-and-thrust-belts, Sinu, Makran accretionary prisms,...), the location of buried anticlines below un-deformed series coincides with high sedimentation rates, while shortening processes were active. The scope of our project was to investigate the Makran accretionary prism in Pakistan and the nearby triple junction, through structural and sedimentological studies, as well as fluid dynamics evaluation. The triple junction joins the Arabian,

Eurasian and Indian plates and corresponds to the connection between a subduction zone (Makran accretionary prism), a transform fault system (Chaman-Ornachnal) and finally, an intra-oceanic transtensional feature (Murray Ridge) bordering to the East the stretched continental Indian crust.

In the Makran accretionary prism, the transition between the emerged part of the Makran and the offshore compression front is expressed by a wide un-deformed platform, representing a huge sedimentary trap during Mio-Pliocene times. This large sediment input could have various origins through time:

1. Direct influx from Indus River conveying eroded series from Indian shield or Himalayas.
2. Strong erosion of the inner parts of the growing accretionary prism. Both the spatial distribution of loading and the type of sediment transfer (diffuse or locally concentrated as in deltas) play a major role in the structural evolution.

In order to assess the consequences of the migration of the Indus paleo-delta since Miocene time on the tectonic structure of the Makran accretionary complex, we conducted an onshore field survey in early 2001 along the coastline and two transects. The study of the structural style, as well as depositional environment was the main objective of this survey. A secondary objective was to locate and identify the origin of the shale mobilization in the cores of large anticlines and/or expulsion in mud volcanoes, linked with fluid overpressures at depth, which are supposed to be the main driving processes for mud volcanoes. In this paper, we present an update of the Makran onshore geology based on our field data combined with interpretations of remote-sensing satellite data (Landsat 7) and interpretation of three reprocessed seismic lines. The results are synthesized as an updated stratigraphic chart based on the new ages obtained during our field survey and two synthetic geological transects. In a companion paper (Ellouz et al., this issue), we focus our attention on the offshore area by presenting striking results of our 2004 research cruise CHAMAK, initially planned in 2001.

2 Geodynamic Setting and Tectonic Evolution

Present-day architecture of the Makran accretionary prism results from the subduction of the Arabian sea ocean floor, composed of Arabian and Indian oceanic and stretched continental crusts, beneath the Afghan block microplates, now accreted on the Eurasian continent (Fig. 1).

Subduction started during Late Cretaceous times, as testified by the initiation of the Chagai volcanic arc (Arthuron et al., 1982; Dyskstra et Birnie, 1979). The northward subduction of the oceanic parts of the Arabian and Indian plates took place after a period of reorganisation and collision of the various micro-blocks with Eurasia, forming the overriding so-called Eurasian-Afghan plate (Farah and Dejong, 1984; Iqbal and Shah, 1989).

The age of the basement below the North Arabian Sea remains uncertain due to the lack of magnetic anomalies. From the paleogeographic reconstructions Miles and Roest, 1993; Miles et al., 1998; Sharland et al., 2001; Royer et al., 2002), the oceanic crust is inferred to be of Cretaceous age, or possibly Jurassic to the East taking into account the Late Jurassic anomalies along the Eastern African margin (Gnos et al. 1997, Roeser et al. 1996).

The progressive closure of the gap between Eurasian-Afghan and Indian plates, as well as the tectonic involvement of the sediments deposited in the trench, resulted in the migration of the front toward the South and the Southwest, and consequently, the migration to the South of the paleo-Indus delta and fan (i.e. the main sediment supply during Paleogene and Miocene times; Hunting Survey 1956, Coumes and Kolla 1984, Clift et al. 2001, Clift et al. 2002).
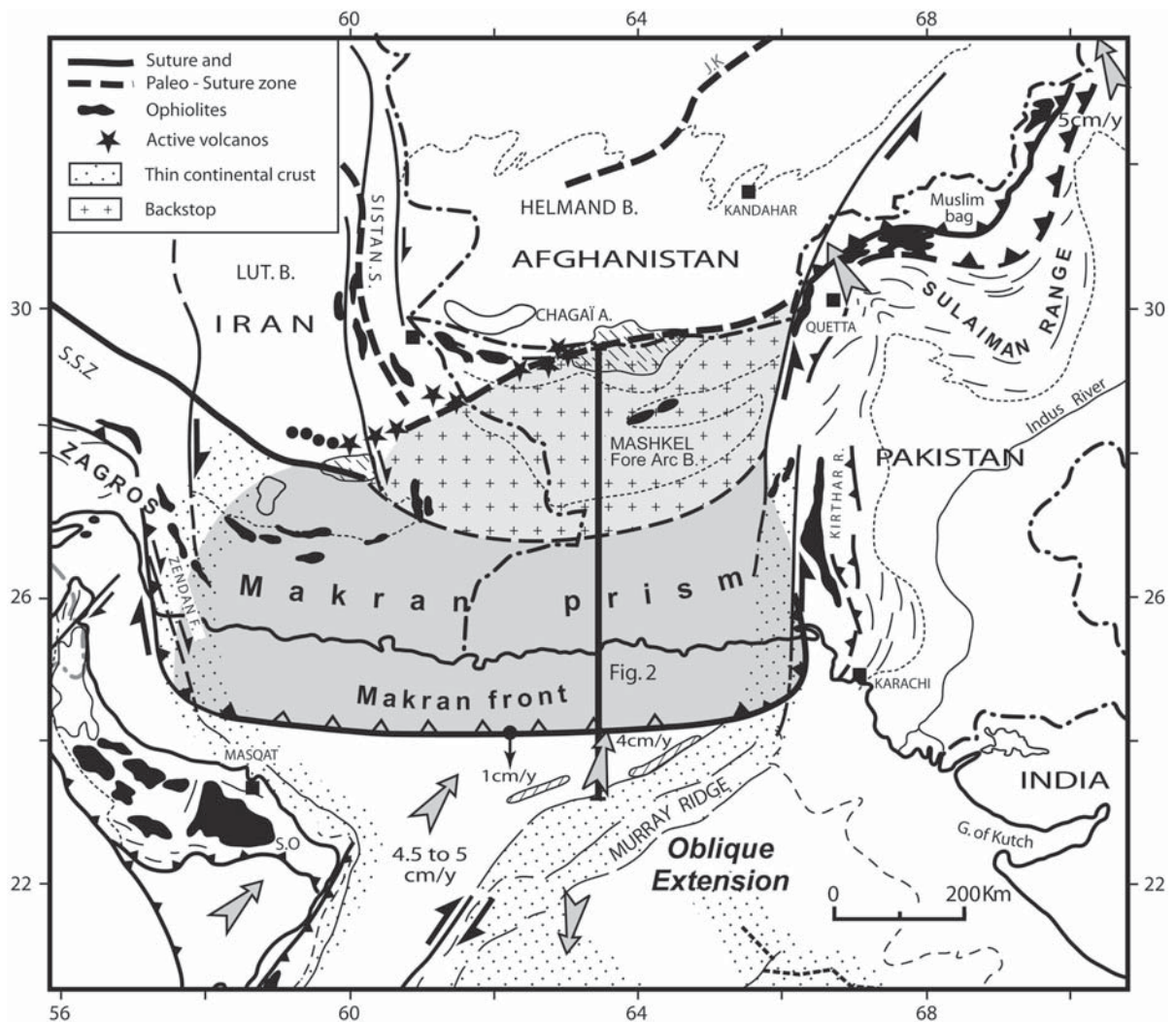
Fig. 1. Present-day tectonic plate setting around the Makran accretionary prism

The last stage, covering Neogene times, is related to the oblique convergence between Afghan and Indian plates, which is accommodated along the left-lateral Chaman-Ornachnal transform zone (Lawrence and Yeats 1979, White 1979, Lawrence et al. 1981, White 1982, Kazmi 1984, Patriat and Achache 1984, Scotese et al. 1988, Minshull et al. 1992, Kazmi and Jan 1997, Fournier et al. 2001). During this period, the Sulaiman and Kirthar ranges developed (Jadoon 1995, Ellouz et al. 1994, 1995) creating a NS topographic high, which induced the de-localization of the Indus River farther to the East (Coumes and Kolla 1984, Critelli 1990, Garzantie et al. 1996, Qayyum et al. 1997).

Convergence between Eurasian accreted microplates and Arabian-Indian plates has been permanent since Upper Cretaceous (White 1982, Schlich 1982, Farah et al. 1984, Byrne and Sykes 1992, Edwards et al. 2000, Fruehn, McCall 2002), but it has changed in rates and direction. The main variation in the convergence rates and vectors occurred during Oligocene time (Fournier et al. 2001, Leroy et al. 2004) and is related to the opening of the Aden Gulf. African plate dislocation resulted 1) in the northward motion of the Arabian plate, and later to a major compressive event in the Zagros, 2) in a rotation of the subducting plates, 3) in the oblique extension along the Murray Ridge, and as a result 4) in an along-strike variation of subduction velocity during Miocene times, due to the collision in western Zagros.

The present-day architecture, at a crustal scale, shown in Fig. 2, (Platt et al. 1985, Fruehn et al. 1997, Kopp et al. 1999; Fig. 2, adapted from Byrne and Sykes 1992, Bijwaard et al. 1998) of the onshore area of the prism suggests a progressive strong slowing-down, or even a stop, of the deformation in some areas since Pliocene, which could have effected an apparent discontinuity in the convergence (either in velocity or direction) processes. This is expressed by the development of a large nearly un-deformed platform, running along the Makran actively rising coastline. In fact,, the deformation front shifted progressively through time to the south, as well as the platform developed between the two zones where compression processes were very active, the inner and the frontal parts of the prism.

3   Existing Data

The field and analytical work have been based on the geological maps published by the Hunting Survey Corporation (1956), and on some small-scale maps extracted from published papers (Lawrence et al. 1981, Arthuron et al. 1982, Legett and Platt 1984, Harms et al., 1984).

Only few exploration wells were drilled in the coastal Range (Fig. 3). They stopped within the Middle Miocene (poorly dated according to field reports from DGCP). On the continental shelf of the Pakistani Makran, few wells have been drilled a long time ago. There are only few calibration constraints from these wells, as the oldest formation reached has been dated either Pliocene or Latest Miocene (questionably). We did not have access to data of the two recent wells of Pasni and Gwadar drilled by the Ocean Energy company, located on the shelf edge. Thanks to DGCP, we had an overview on the scattered seismic information on the Coastal Range, and on some recent offshore seismic lines.

A structural interpretation is proposed in Figs. 4 a & b, which synthesizes the field observation and the interpretation of remote sensing images over the whole Makran Range.

We also reprocessed the CEPM (1977) Indus NW-SE offshore seismic profiles available in the front of the accretionary prism. The offshore frontal zone, presented here, has been interpreted from these reprocessed lines. Over the shelf, a couple of already published seismic profiles (White 1982, Harms et al.,1982; Min-
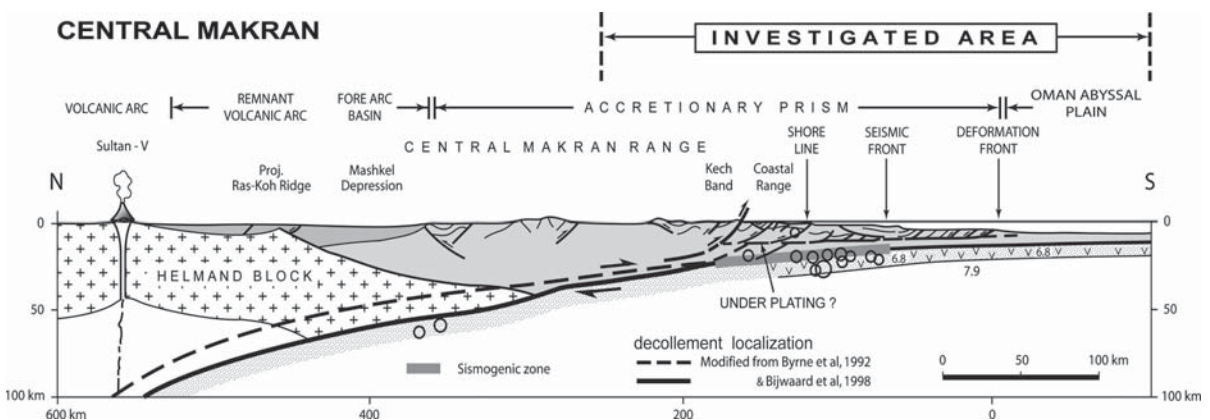
Fig. 2. Crustal section over Pakistani Makran

Fig. 3. Main tectonic units of the Pakistani Makran; location of the existing data, and of the cross-sections and seismic profiles analyzed
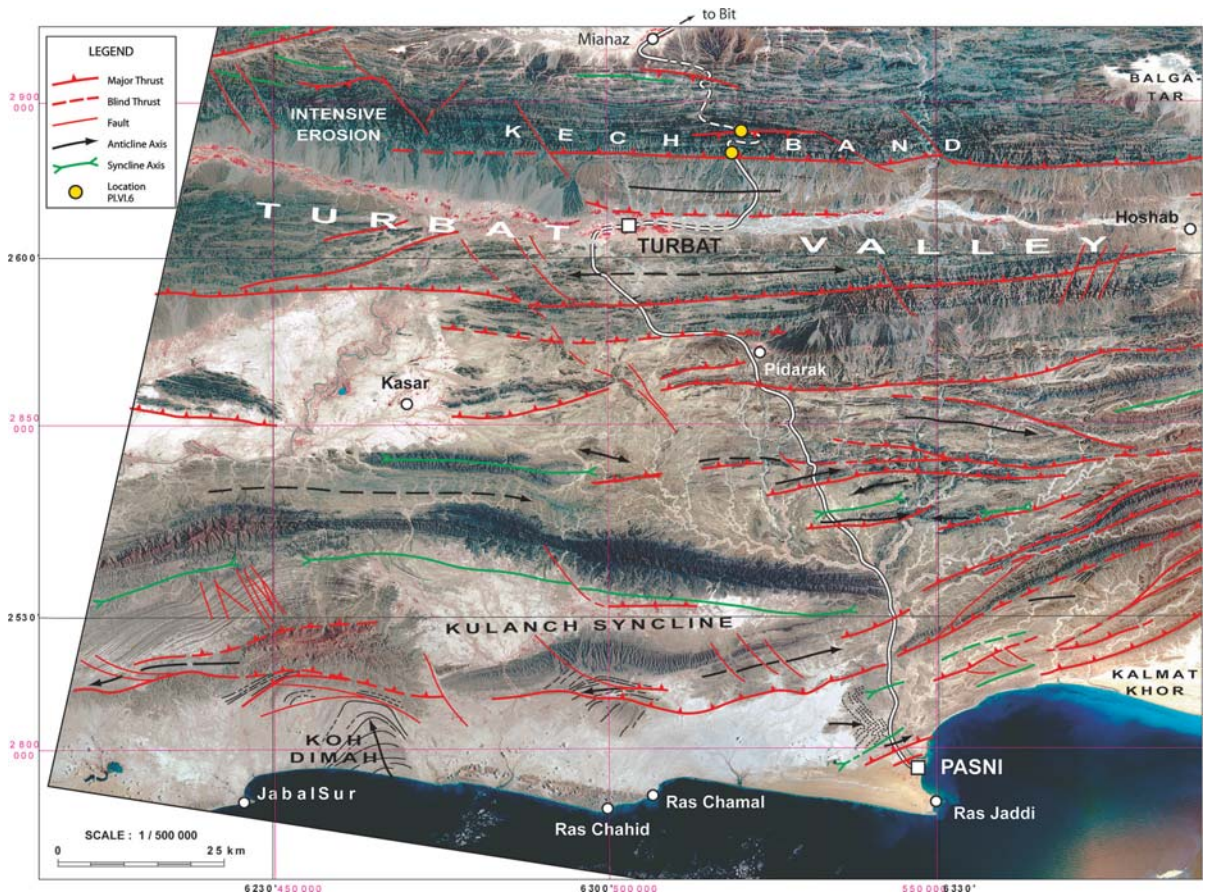
Fig. 4a. Structural scheme based on remote sensing interpretation and field observation. Central part of the Pakistani Makran, where pure convergence mechanisms are inferred

shull et al. 1992, Kopp et al., 2000) have been also re-interpreted. This study benefited also from field data interpretations in the Coastal Range, and in offshore Pakistani Makran, published in Harms et al. (1982), Legett and Platt (1984), Platt et al. (1985), Minshull et al. (1992), Weidicke et al., (2001) and Gaedicke et al., (2002).

4   Regional Investigation and New Data

From the Kech Band, north of Turbat valley (Fig. 3) to the Coastal Range to the South, a field reconnaissance has been carried out with the logistic support of the Geological Survey of Pakistan.

South of Maschkel Basin, the main structural units of the Makran prism have been investigated. From North to South, the involved sedimentary series become more recent: Paleogene-Early Miocene in Kech Band, up to Early Pleistocene in the external part of the Coastal Range. The Pliocene and Pleistocene series developed mainly offshore, on the platform and in the

frontal part of the prism. During the field reconnaissance, it has not been possible to sample the Paleogene series in the eastern part of the Kech Band.

In order to calibrate, as much as possible the stratigraphy, an extensive sampling has been done, from which numerous nanoplankton dating allowed to refine the stratigraphic chart of this area and to compare with the adjacent Indian margin. Finally, we propose a chronology of the deformation and the maximum erosion phases, deduced from reworking through time.

4.1 Stratigraphy of the Pakistani Makran Area

The presented results are based on the investigation of calcareous nanofossils from 240 samples. They were taken in the accretionary prism along the coastal and central Ranges and within depressions (up to Kech the Band toward the North). The formation names we used are the same formations which were introduced on the Geological map of Pakistan (1956) in which the age determinations were based on foraminifers or sim-
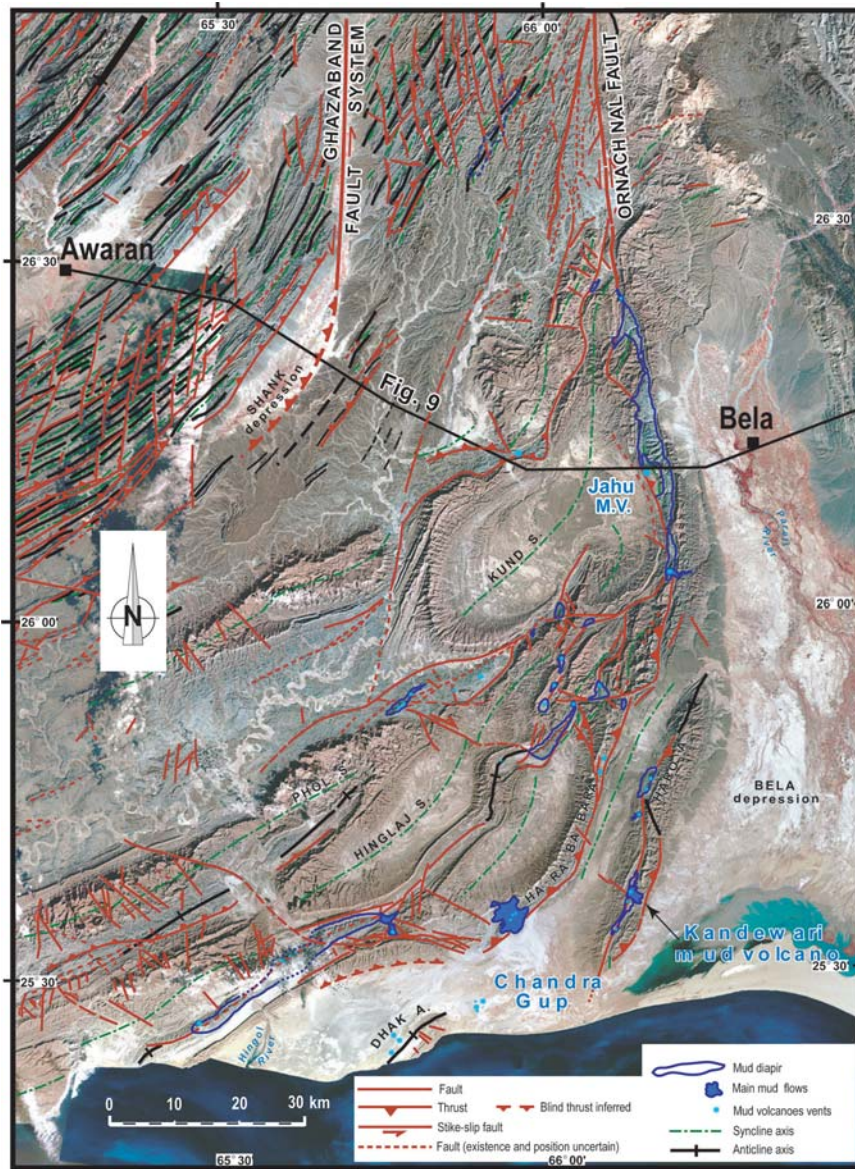
Fig. 4b. Structural scheme based on remote sensing interpretation and field observation. Eastern part of the Pakistani Makran, where dominance of the oblique–slip convergence prevailed, generating transform faults which migrated southward through time as the tectonic prism progressed (Ghazaband fault is older than Ornachnal fault)

ply deduced from the stratigraphic position within the series. These ages were generally older than those deduced from calcareous nanofossils (this study, see Appendix). Formerly, biostratigraphic schemes were also given by Harms et al., (1984) and Raza et al. (1991).

A new regional stratigraphic chart is shown in Fig. 5, sample location and age datings are detailed in the Appendix. Field pictures of the different formations from Middle Miocene to Pliocene are shown in Figs. 6 a to f.

- The Hoshab formation ranging in age from Late Oligocene (Zones NP 24–25) to Early Miocene (zones NN1–3) is the oldest dated series in the Makran prism. This formation is exposed in the

Mand area, along and close to the road from Hoshab to Panjgur (Fig. 3). The dating is not very precise in Early Miocene, because index fossils are extremely rare. Nevertheless, it is possible that the lowermost part of the Miocene is marked by a hiatus. The Hoshab formation, composed of calcareous mudstones with intercalation of sandstones, was deposited as a turbidite system in a relatively deep marine environment.

- The Panjgur formation, Middle Miocene in age (NN5–6), has a wide distribution in the coastal area and in the central prism. The nannofossils are generally rare to few, and become common only within few samples, only the more resistant species being preserved.
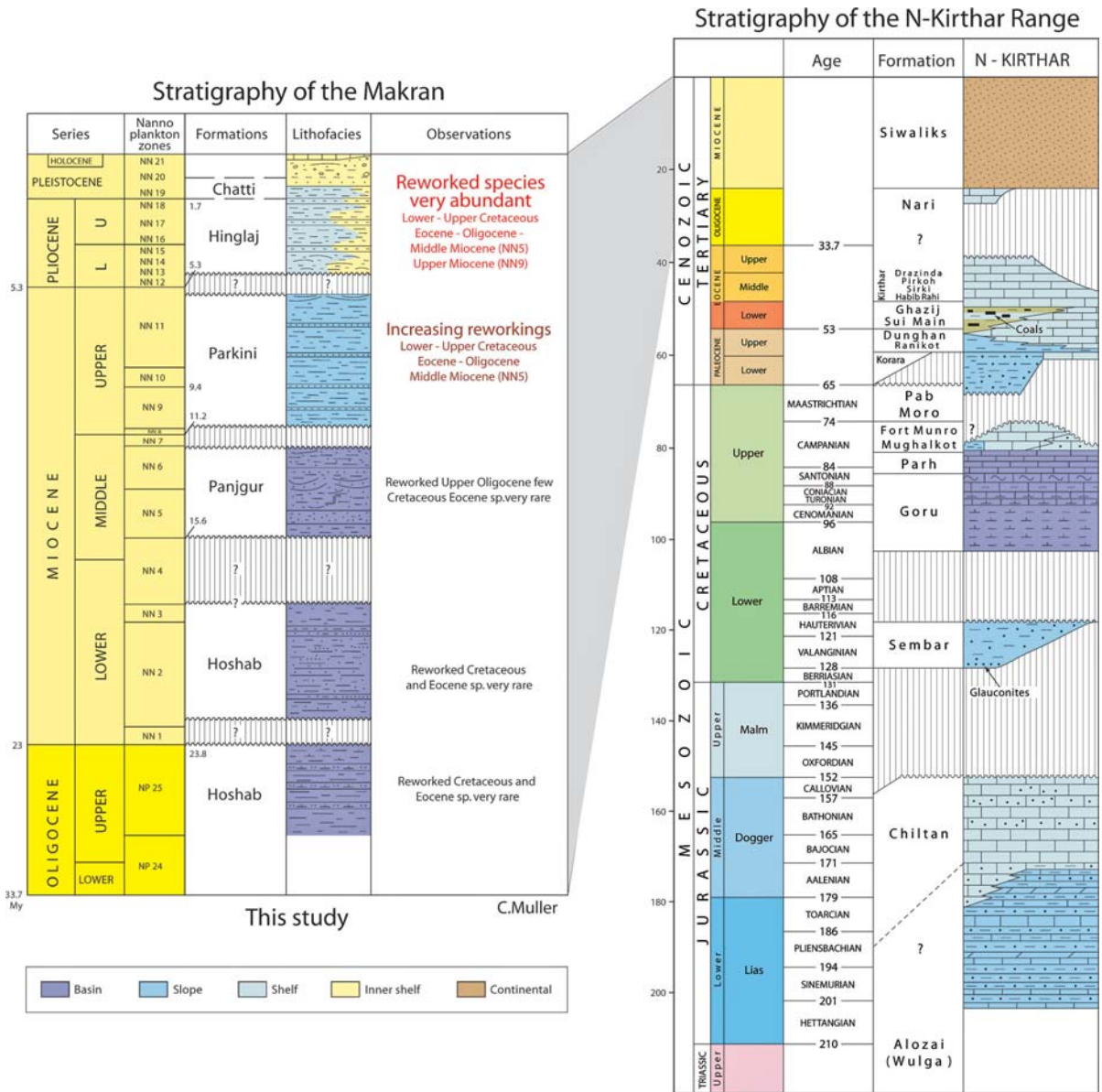
Fig. 5. Regional stratigraphic chart and correlation with the North Kirthar Range: based on new nanofossil dating for the Makran (details in Appendix)

It consists in turbidites deposited in deep environment, with slightly greenish micaceous sandstones (Fig. 6a). The intercalated mudstones often show a rather strong schistosity. The series is characterized by numerous channels with mud pebbles at the base. The Middle Miocene sandstones are characterized by current ripples (Fig. 6b), flute casts and Zoophycos-Ichnofacies tracks (Fig. 6c), indicating deepwater depositional setting, as previously outlined by Harms et al. (1984). There are few reworked species from the Upper Oligocene indicating that,

at this time, erosion took place from uplifted inner parts of the prism.

- The Parkini formation, has a wide distribution along the coastal range, well exposed along the road from Pasni to Turbat. The formation is generally rich in nanofossils representing a complete Upper Miocene series (Zones NN9 to NN11). It consists of mainly light-grey fine grained and less consolidated mudstones, with very fine-grained thin sandstones beds. The rare small and smooth channels which occur within the upper part of the formation, indicate a decreasing water depth. Reworked species
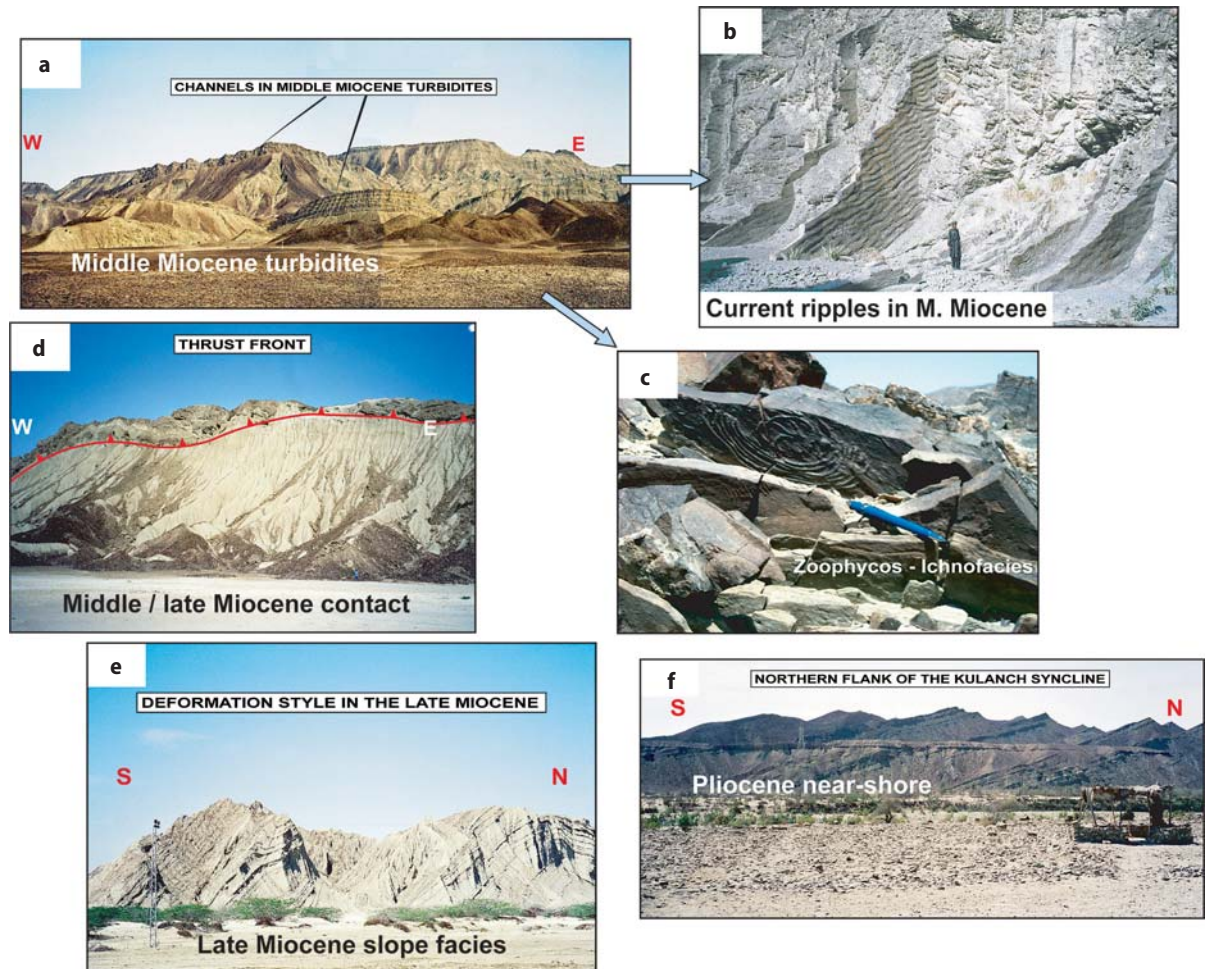
Fig. 6. Field illustrations (location in Fig. 4a) from **a** Middle Miocene basin turbidite, Panjgur fm in north coastal range close to Pidarak, **b** current ripples in Middle Miocene, and **c** Zoophycos-ichnofacies in Middle Miocene turbidites, indicating deep-water depositional setting both b& c from Panjgur fm and located in the Kech band (north of Turbat), **d** Mid- Miocene (above the thrust) to Late Miocene contact close to Talar Syncline, **e** Late Miocene facies (Parkini fm) and deformation in coastal range close to Pasni, **f** Pliocene nearshore sandstones in the Talar syncline

from the Cretaceous, Paleogene and Middle Miocene (NN5) become frequent. The Cretaceous and Paleogene reworkings most probably were transported from the Kirthar Range (from East), where the same associations have been recognized from the Sembar series, whereas the Neogene species clearly originated from the previously uplifted Inner Miocene Makran prism. The sediments were deposited on an upper slope to outer shelf domain (Fig. 6 d & e).

- The Pliocene Hinglaj formation is composed of light-grey mudstones and fine-grained sandstones. It is well exposed in the eastern part of Makran (Fig. 6f). The sediments are very rich in reworked species from the Cretaceous to Upper Miocene, but autochthonous fossils are rare to few, probably due to dilution by reworking. Index fossils, like Discoasters,

are missing due to deposition in a shallow environment, thus a precise dating is not possible.

- The Chatti formation from Lower Pleistocene (Zone NN 19) is exposed along the coastal road in the East of Makran. The series consists of siltstones and fine-grained sandstones. Nanofossils are common, indicating a middle-outer shelf environment.

4.2 Sedimentary Sources

The eastern Makran chart given in Fig. 5 is compared with the one of the Kirthar Range (Ellouz et al. 1994, Ellouz et al. 2002, Müller 2002). Taking into account the relative motion between Indian and Arabian plates, with an average velocity of 1 cm/a from the end of Early Miocene to Present (after the opening of the Aden

gulf), and 5 cm/a (before this time), the North Kirthar and Makran areas were approximately at the same latitude during Early Miocene time, (20 Ma ago).

This study shows that, before Middle Miocene, there is no evidence of any Cretaceous reworking from the Indian Plate. This could also be due to the scarcity of fossils. During late Miocene time, the input from two different areas has been identified:

1. Abundant reworking from Cretaceous to Eocene shows an important transport coming from the east, indicating a "Paleo-Kirthar" origin.
2. At the same time, the occurrence of Middle Miocene species (NN5) outlines the beginning of the erosion of the Miocene part of the Makran prism, since marine sediments of this age are unknown in the Pakistan Ranges bordering the prism to the East (Kirthar, Sulaiman Ranges) where only continental series were deposited.

During Pliocene time, the prism was growing and propagating southward, accreting more recent sediments which have been then uplifted and eroded. This process is evidenced by the appearance of Late Miocene reworked marine species and an increase of the reworking in Pliocene sequences.

The north-south distribution of the depositional facies and the evolution of the prism along dip are shown in Fig. 7. It also shows the appearance of younger décollement levels, gradually appearing above the basal one with the migration of the prograding wedges to the south.

5   Regional Sross-Sections

Two regional sections have been analyzed during a field trip in February 2001: one is located in the area of frontal convergence (N-S section from Turbat to Pasni), whereas the second one is covering the eastern Makran and the transform zone (E-W section from Awaran to Bela and Pab Range). The major units of the Makran prism are outcropping and were observed from Bit (in the Kech Band, Fig. 4a) toward the south and the east. On the offshore frontal part of the prism, scattered seismic data acquired by CEPM in 1977 (INDUS profiles), have been also reprocessed and analyzed. The N-S section have been extrapolated to the offshore shelf area on the base of a modified seismic interpretation of the Gwadar profile (Harms et al., 1988).
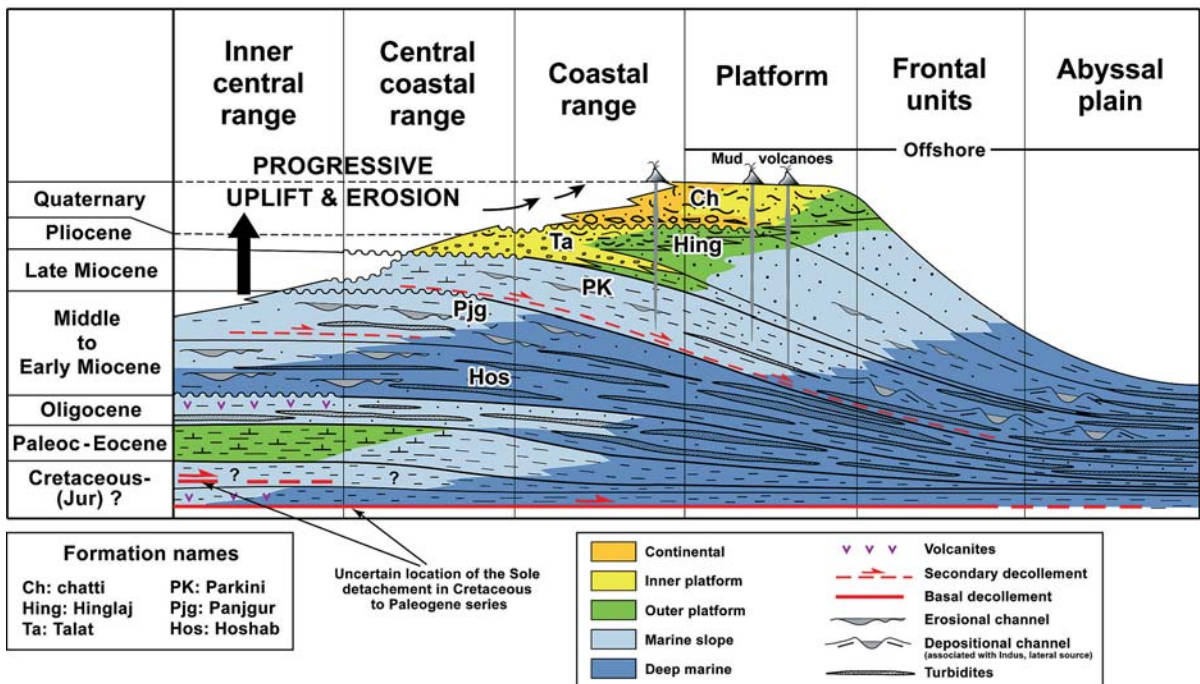
Fig. 7. Tectonostratigraphic chart along the frontal part of the prism (not corrected from the deformation)

Figures 4 a and b present regional views and structural interpretation of the central (4a) and lateral eastern (4b) parts of the prism, which cover the two section areas.

5.1 N-S regional Cross-Section from Turbat to Pasni

The section runs from the Kech Band (Fig. 8), north of Kech-Turbat valley, to the southern offshore platform, which is located onshore 100 to 150 km north of the offshore deformation front. Since only few onshore anticlines have been investigated by seismic acquisitions along the Coastal Range, and poorly calibrated by old wells (Fig. 3), we also based our along-strike interpretation and correlation on detailed remote-sensing studies.

In the coastal Makran Range, to the south, deformation is characterized by elongated southward verging E-W anticlines. The deformation propagates along a basal detachment level close to the top of the oceanic crust, and probably located within Cretaceous to Paleogene deep marine series in the western part of the prism. Along the coastline the large synclines (such as the Kulanch syncline) are still preserved, between zones where the highly deformed Late Miocene Parkini formation is outcropping. Strong disharmony and propagation on secondary décollement levels within the Late Miocene turbidites, is particularly well exposed onshore by the development of imbricate fold-and-thrust system clearly expressed on satellite images (Fig. 4a). Close to the coastline, structures are locally overturned along backthrust faults, which rooted within this shallow detachment. It is therefore difficult to estimate correctly the initial thickness of the Parkini sequence.

5.2 E-W Regional Cross-Section from Bela to Awaran

Laterally, to the east, the thickness of the Late Miocene formations is increasing and the basal detachment jumps to younger levels. Figure 9 details the structural style, from Turbat-Kech valley (West) to Awaran and running over the Bela depression up to the Pab Range (East). At the surface, from west to east, it joins successively an "imbricate fold-and-thrust" zone to larger folds and thrusts close to the transform fault system in the east.

The change in structural style along the section outlines the total decoupling between the large wavelength anticlines in the Lower-Middle Miocene sequences and the near-surface imbrications, in which the whole latest Middle-late Miocene series are intensively folded and repeated several times locally. This easternmost part of the prism has been strongly controlled by the transpressive left-lateral transform movements related to the long-way northward migration of the Indian plate with respect to Asia, since Paleogene time.

Two major strike-slip N-S fault systems develop within the Makran prism, the Ghazaband and the Ornachnal faults (Fig. 9). The Ghazaband fault, which ends southward in the eastern coastal range, was active during the Late Miocene, while the Ornachnal Fault is still active and joins the offshore triple junction. Consequently, deformation has adapted to strain-partitioning processes here. Onshore, close to the Bela depression, the development of "en échelon" folds, often associated with mud volcanism processes (Delisle et al. 2001, Wiedicke et al. 2001), suggested an overpressure regime at depth. These structures have extended offshore, as expressed on seismic data and by the emergence of the new offshore Malan Island in 1999 (fig 3). Not far south of this area, offshore, the northern flank of the Murray Ridge is starting to be underthrust below the prism (Fig. 10). The connection with the Indian plate now subducting or colliding obliquely below the Bela depression area, is illustrated on the section (Fig. 11).

5.3 Schematic General Cross-Section for the Makran Accretionary Prism

A conceptual general cross-section is proposed for the central Makran in the Fig. 13. It is based on the field observation, remote sensing interpretation and results from the two sections analyzed above. These sections are characterized by:

- A basal décollement level located within Paleogene (minimum age attested by the field analyze along the Kech Band) or probably hosted more deeply in older series (Cretaceous, which is supposed to be the age of the first deep marine deposits on the oceanic crust, in this part of the Makran). This sole detachment deepens progressively from 6–8 km at the deformation front (from seismic interpretation, Figs. 11 & 12) down to 11–12 km depth onshore in front of the central Makran Range (north of the Turbat Valley, deduced from section interpretation and restoration).
- A tectonic style strongly depending on the lithological nature of the sediment succession, which is controlled either by the regional or local depositional environment. Before late Miocene, the paleo-depositional model looked probably similar to the present-day one, illustrated on the offshore seismic line 11 (Fig. 11). When the amount of massive sand-
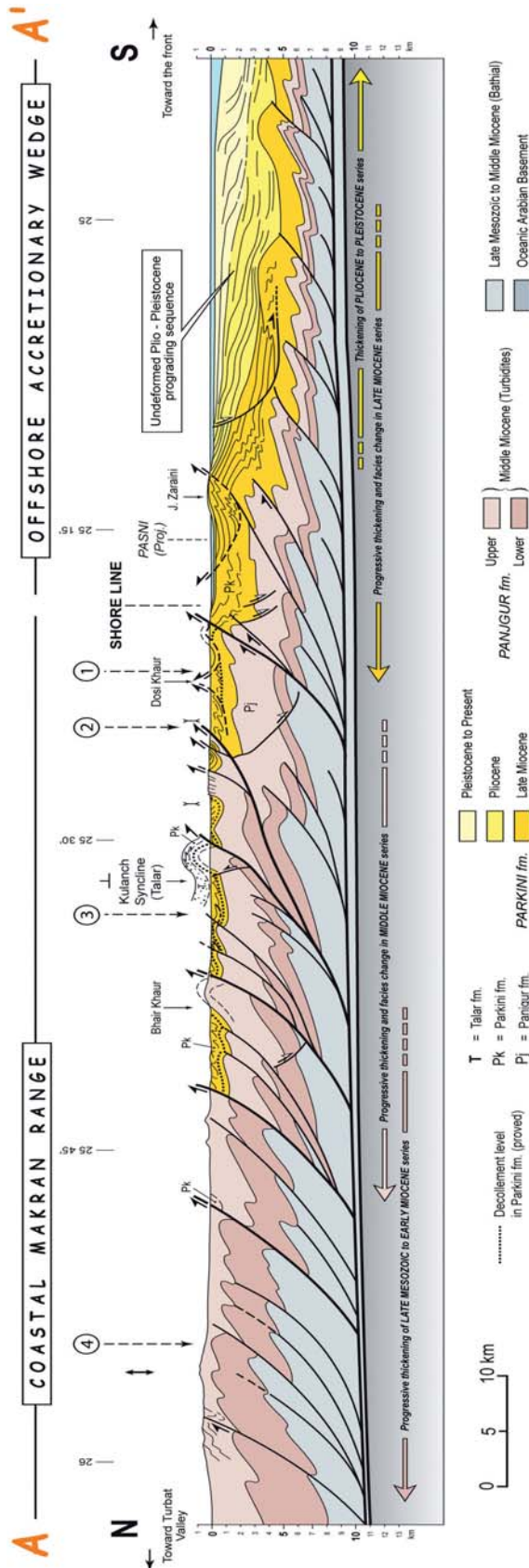
Fig. 8. North-South cross-section from Turbat to Pasni: the age of the basal detachment is unknown, but probably located in Paleogene or older bathial series; note (1) the tectonic progression of the prism while sedimentary wedges are prograding over the already deformed Miocene series; (2) the strong disharmony at the base of Parkini slope fm, level locally used as a secondary décollement.; (3) normal faults which are progressively younger to the south
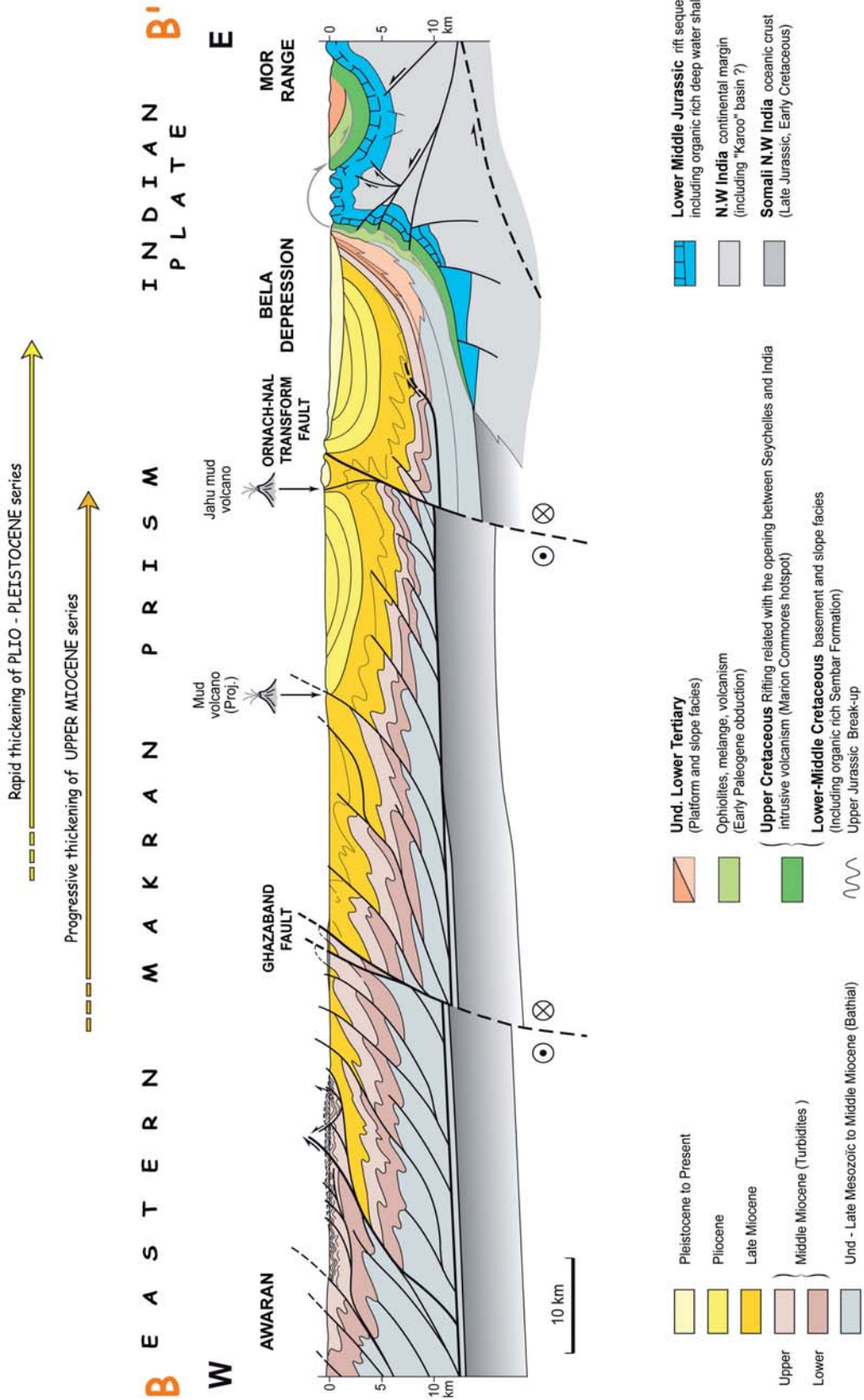
Fig. 9. West-East cross-section from Awaran to Bela and Pab Range: Note the strong disharmony within the late Miocene series (Parkini fm) which is found in the cores of the main anticlines and occasionally is extruded from mud volcanoes; the huge depocenter along the Bela depression where a great part of sand sedimentation was trapped since Pliocene, and the late offset of the prism along the transform faults
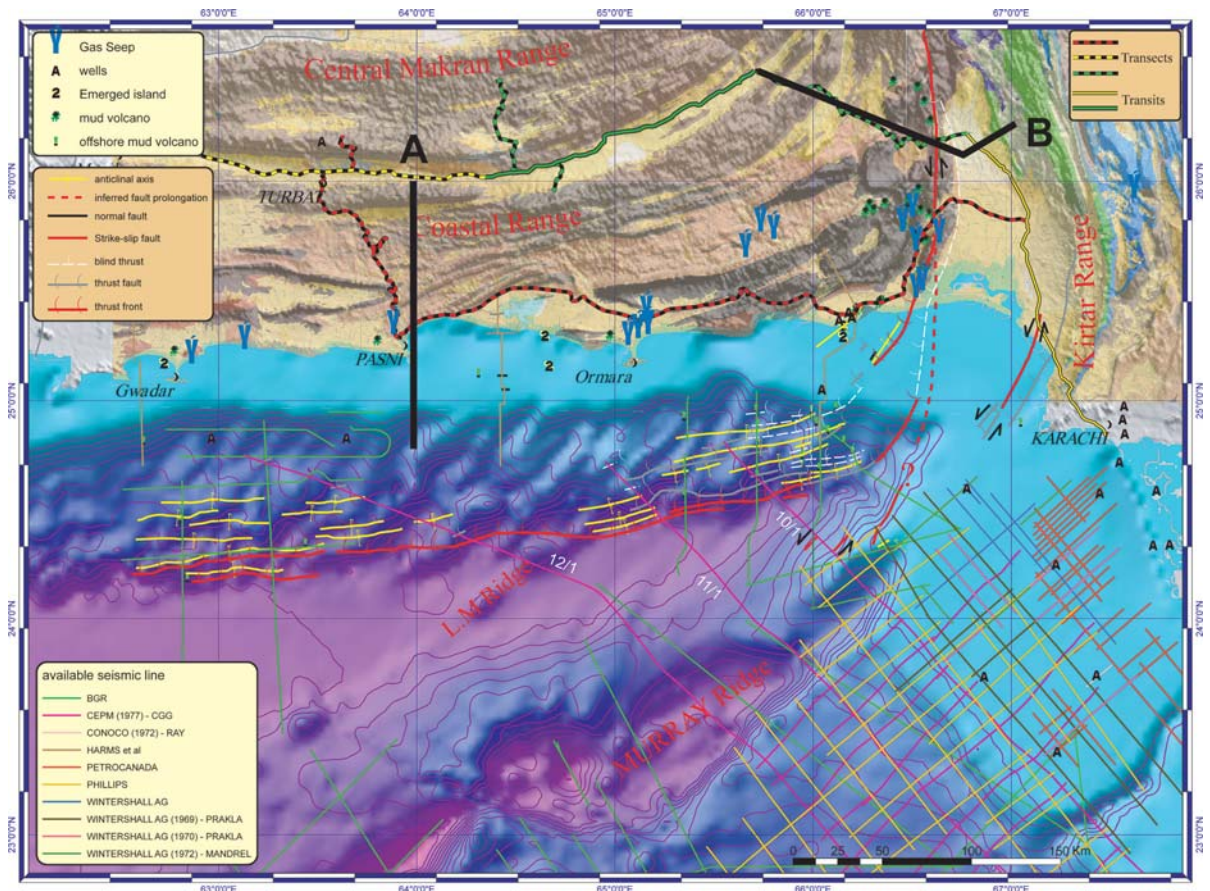
Fig. 10. Structural sketch of the Pakistani Makran

stone deposited in channels was important, large anticlines developed above thrusts or back-thrusts deeply rooted (which is the dominant style in the central Range). When pro-delta silts and shale series were involved within deformation, the tectonic processes where isoclinal folding dominated (Fig. 8).

- The occurrence of a secondary décollement level within the slope series, linked with sedimentary progradation. At, or close to the coastal shelf area, the Late Miocene slope series (Parkini formation) have disharmonic behaviour with respect to the older ones, inducing a local disconnection between surface and deeper structures. These very fine-grained series show commonly a disorganization of the initial stratigraphic layering. Liquefaction processes are observed in several localities notably along the coastal range. Combined with deep gas discharge, solid particles issued from the Parkini mobile formation are commonly expelled by mud volcanoes (Fig. 13).
- The role of the transform system in the structural evolution of the "en échelon" elongated anticlines

along the eastern Makran Range, which are cross-cut by strike-slip deep-rooted faults.
- The development of out-of sequence thrusts between Coastal and Central Makran Ranges in Pakistan. The asymmetry of the Kech-Turbat Valley, south of the Kech Band, characterizes the present-day activity along an out-of sequence thrust fault (Fig. 4a).

6 A View from Analogue Modelling of the Coeval Extension Processes in a Pure Convergent System

The Makran coastal range is characterized by folding and thrusting processes, expressed by a huge and rapid uplift of the coastline. The coeval southward migration of the coastline can be evidenced even at an historic scale as shown by archeological observations on Ichthyophage paleo-villages founded some ten kilometres north of the present-day coastline location (R. Besanval archeological team, personal communication). The active rising-up of Ormara and Gwadar tombo-

Fig. 11. Interpretation of the NW-SE reprocessed CEPM seismic Line: INDUS 12
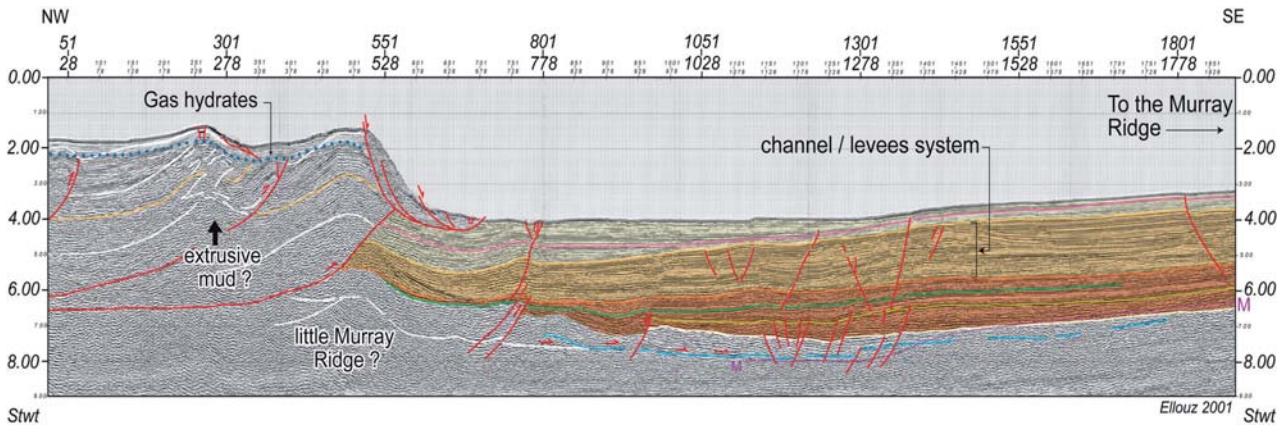
Fig. 12. Interpretation of the NW-SE reprocessed CEPM seismic Line: INDUS 11
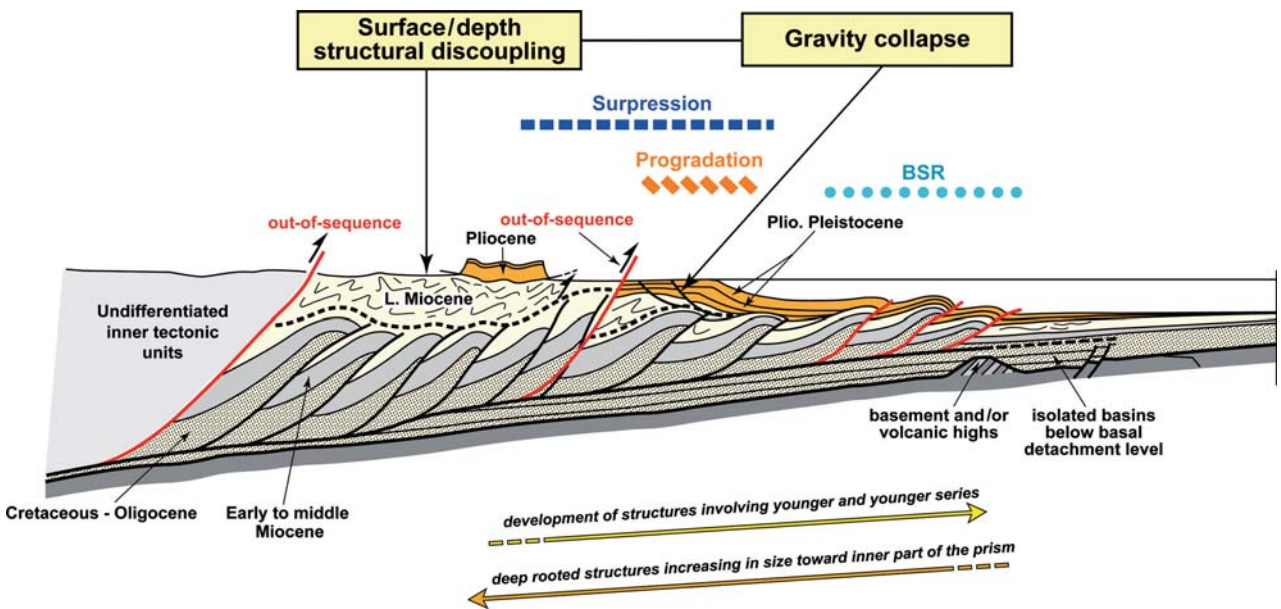
Fig. 13. Regional schematic cross-section over the central Makran prism

los outlines the tectonic shortening at depth, resulting in a passive uplift of the Pleistocene piggy-back levels. Normal faulting is also present, and is expressed, either by small offset normal faults or by large, deeply rooted growth faults developed by gravity sliding over detachments probably associated to local overpressure conditions at depth (Fig. 13). This normal faulting activity has been described also in the Iran part of the Makran (Grando & Mclay 2006). Along the coastal ranges, shale tectonics is very active and is associated with the local development of mud volcanoes. These mud volcanoes are located along the anticlines or the main faults, relating pressure instability at depth. The impact of high sedimentary rates in these areas through time play a major role in these processes.

6.1 Control of the Boundary Conditions from the Sedimentary Input in the Pakistani Makran

Before Pliocene time, the main sedimentary input was driven either by the Indus River (mainly the growing Himalayas) or by the Indian basement. The trench associated with the subduction was progressively filled with these erosion products. The major part of the sediments was at that time conveyed by the paleo-Indus River and deposited in the available space (i.e. the subduction trench and a narrow ocean between Afghan and Indian plates).
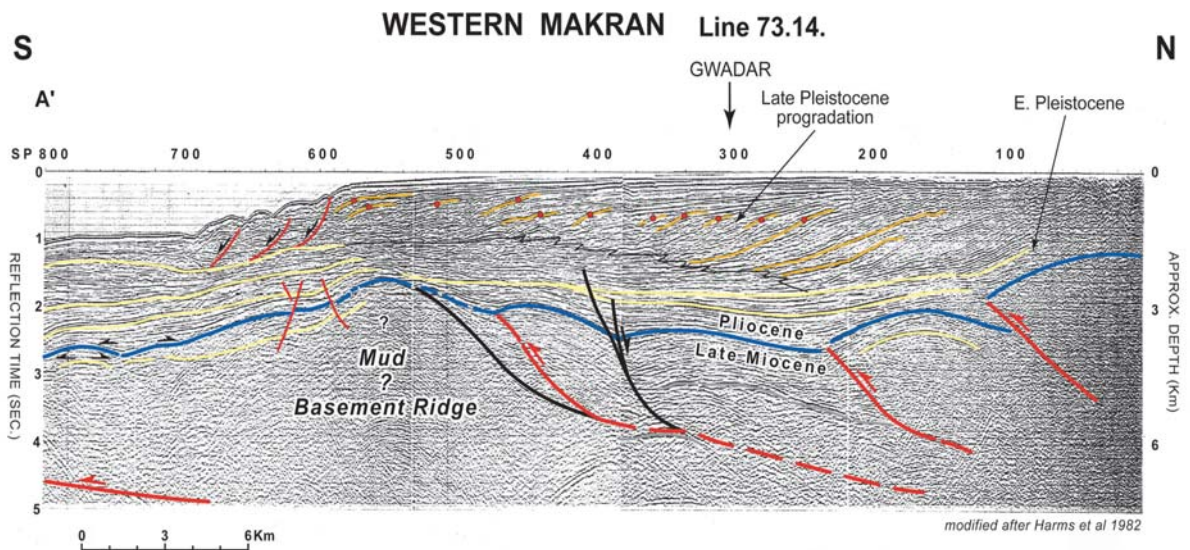
Fig. 14. Interpretation of the reprocessed N-S seismic profile re-interpreted from Harms et al. (1988) along the platform south of Gwadar

From Late Miocene time to Present, and related to the rising topography of the Kirthar and Sulaiman Ranges to the east, the Indus delta and fan system have been deviated south of Karachi, whereas now the main offshore sedimentation develops on the Indian Plate, south of a prominent offshore structure, the Murray Ridge. The growing Makran prism is located north of the Murray Ridge. Since late Miocene, most of the sediment input is derived from the erosion of the prism and is delivered from the north either from small non-permanent rivers, or through a diffuse distribution.

In Fig. 14, the huge late Pleistocene progradation over previously deformed thrusts induced a delocalization of the compressive deformation, which resulted in the migration of the front to the south and the development of out-of-sequence thrusts along the coastal range and the Turbat Valley.

6.2 Analogue Modelling: Application to the Makran

In order to identify and to understand the parameters, which guide the dynamics of the propagation and the locking mechanisms of the deformation, several analogue models have been conducted. X-ray tomography analysis have been used to analyse the 3D deformation through time.

We tested several boundary conditions simulating the 3D architecture in a 60x40 cm experimental box, classically using sand powder and silicone putty as respective analogues of brittle and ductile (décollement) layers.

6.2.1 Phase 1

Boundary conditions of the experiment (3 upper sections of Fig. 15) are characterized by a 2° dipping basement, silicon-putty level (basal décollement) distributed all over the basement (2cm close to the backstop to 1 cm thick along the distal edge), a sand wedge simulating a progradation over 1/5 of the model (from 3 cm thick close to the backstop, to 1cm thick along the distal edge), a continuous 2 cm/hour rate of compression applied during the whole experiment.

Resulting from the compression applied to the backstop, a thrust front developed in the middle of the model at the slope failure, where sand/silicone ratio is close to one. Normal faulting has been observed close to the backstop (partly due to a border effect) and even in the middle of the progradation A. These faults are interpreted as a gravity accommodation due to the sedimentary loading imposed in the upper part of the model (representing an along-dip strong variation of the sand/silicone ratio, and in the nature representing a huge sedimentary deposition as deltaic progradation).

6.2.2 Phase 2

A second silicon-putty level has been deposited from the mid-slope, over the primary thrust front to the distal edge, on half part of the model defining two domains in the model: one with one décollement (Fig. 15, left side), and a second with two décollements (Fig. 15,
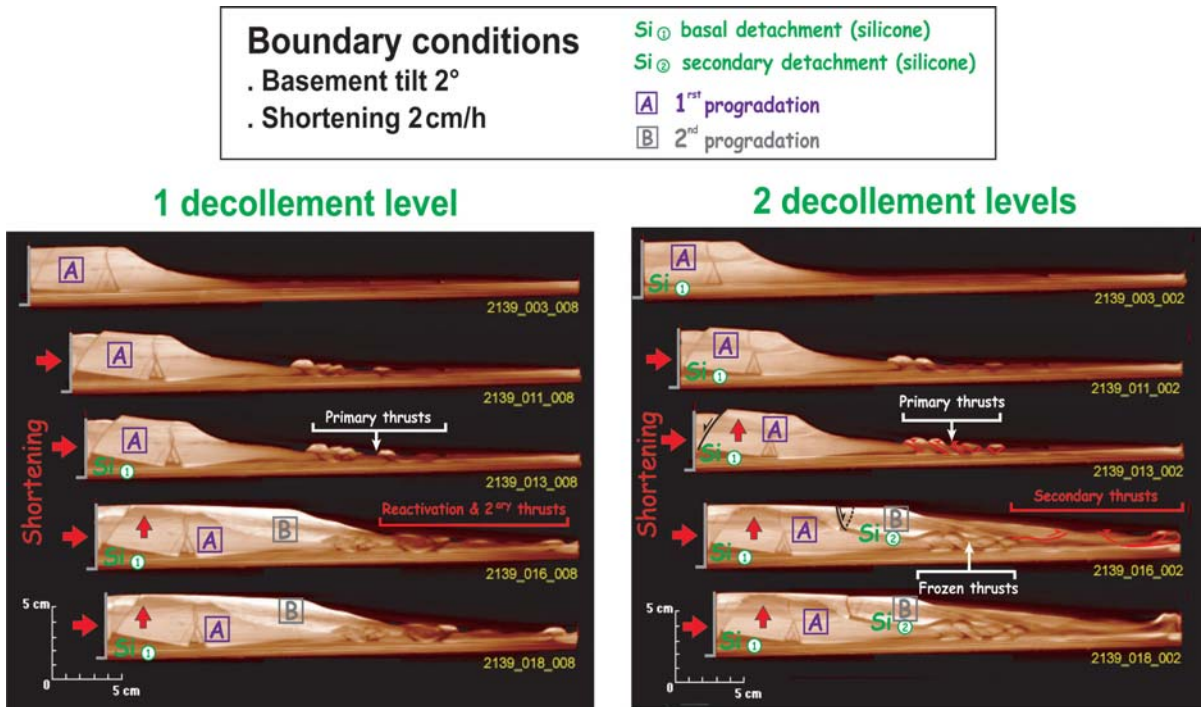
Fig. 15. Evolution of the analogue sand/silicone model of an accretionary prism, developed on a 2° tilted basement, with anisopach sedimentary loading, simulating a prograding wedge during compression of 2 cm/h). Two experimental parts are shown: **a** with one basal décollement level; **b** with two décollement levels. Stage 1 (three sections above) have the same boundary conditions, during Stage 2 a secondary décollement was introduced between the progradation A & B

right side). This step was followed by the deposition of a second prograding wedge all over the model (2 lower sections of Fig. 15).

In the one décollement domain of the model, the thrust propagation is a forward continuous process. Primary thrusts have been deformed before new ones developed progressively away from the backstop, up to the distal edge. The primary normal faults were only slightly rejuvenated.

In the two-decollement domain of the model, the primary thrusts became inactive while deformation propagated differently on the basal and upper detachments. On the upper detachment, a new thrust front was created which involved the upper sand sequence. At the surface, other gravity normal faults started developing (rooted on the silicone up-dip border). The resulting shortening linked to compression applied to the backstop is homogeneous all over the model, but in the upper part of the two decollement part of the model, the total shortening accommodated also the gravity displacement.

We may summarize in four points the main results of the two decollement model as follows: (1) the partial or total "freezing" of the early front due to sedimentary loading, (2) the development of a new compressive front associated to décollement in the basal layer,

(3) the coeval development of normal faults rooted on the upper décollement and, (4) a compressive surface-front disconnected from the deep one.

In the two-décollement model we note a strong disharmony between the deep and surface structures and a relation between the occurrence of the secondary décollement and the development of a second gravity normal fault zone (Fig 15b). From the analysis of this experiment, the normal faulting process becomes active as soon as a critical downdip angle is reached at the top of the upper silicone level (secondary décollement). Analogue modelling evidences the role of a secondary décollement level on both style and propagation of the deformation.

7   Growth Model of the Central Makran Accretionary Prism (Pakistan)

The oldest sediments incorporated in the inner prism are Late Cretaceous/Paleogene in age. The central Makran Range (onshore) is mainly composed of a huge thickness of Late Cretaceous to Oligocene series, intensively deformed and eroded. The sedimentary depositional pattern has been driven by the Paleo-
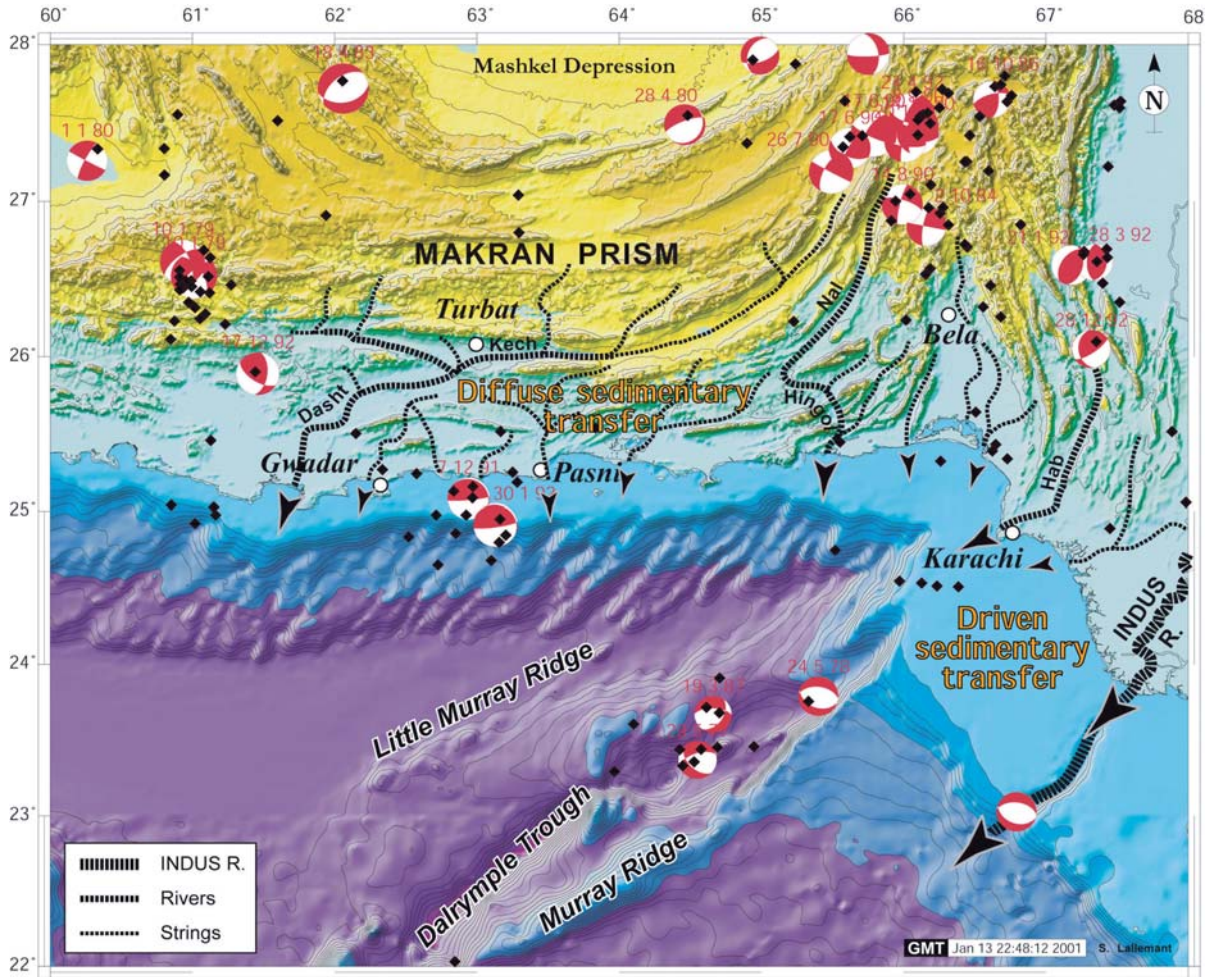
Fig. 16. Hydrographic net and recent sediment input pattern in the Makran area

Indus input through time, since Paleogene. As in the onshore part where similar variations are registered from east to west in Mio-Pliocene series of the offshore part of the prism, the sedimentary nature and thickness varies from east (channel-levees) to west (distal sands and mudstones) in Middle to Late Miocene sequences, suggesting that sedimentary transfer (channel pattern) and deposits (sedimentary lobes) have a rough east-west spatial distribution. This distribution style seems to be more complex since Late Miocene times, where the later deposits originated mainly from the erosion products of the prism (Fig. 16), as shown by the marine Late Miocene fauna found in the Pliocene levels.

7.1 Along- Strike Variation of the Tectonic Style

The western Pakistani part of the prism (central section, Fig. 4a), close to the Iran border, was developed in a frontal convergence setting, accommodating the low-angle subduction of the Cretaceous oceanic crust. Laterally to the East, oblique convergence prevailed. All over the prism, we observed strong lateral variations through time, of the sedimentary filling and of the deformation style. The periodicity, the orientation and the nature of the structures are guided by this sedimentary thickness variation, and by the related depth to décollement levels (Cretaceous, and intra-Miocene) as well. As the sedimentary pile is increasing eastward, the basal detachment jumps to younger levels (Fig. 9).

7.2 Along-Dip Variations of the Tectonic Style

Three types of variation have been identified respectively related to:

1. Heterogeneities in the basement (Fig. 11 & 12). Subduction of some oblique ridges, such as the volca-

nic Little Murray Ridge or the Murray Ridge -the later considered partly as stretched continental Indian crust, Fig. 3- (Gaedicke et al., 2002, Burgath et a., 2002), acted as rigid blocks and generated an uplift of the frontal units due to stacking of tectonic sheets (Figs. 3 & 12).

2. The development of out-of sequence thrusting, when deformation was temporarily blocked at the front, (Figs. 8 & 13), either because of basement highs or also to strong sedimentary rates which could make the propagation of the deformation difficult.

3. The disharmony and/or propagation of the deformation along secondary décollement within the accretionary wedge. Coupled observations coming from field and analogue experiments, led to establish some refinements in the evolution of the Makran prism. From the Inner to Outer zones of the central Makran accretionary prism, a conceptual growth model is proposed for the frontal convergence domain (Fig. 17).

At Present time, three domains can be distinguished from the inner domains toward the tectonic front:

- A wide uplifted zone where tectonic thickening occurred, composed of folds, thrusts and backthrusts, and at places out-of-sequence thrusting activity;
- A prograding domain, with minor deformation. In this area, the high sedimentary rates induced a rapid loading and progradation of the shelf edge. The resulting overpressure at depth induced the development of many mud volcanoes. Due to the resulting gravity instability, growth faults developed, which are mainly rooted within the Upper Miocene Parkini formation;
- An active deformation front, propagating toward the foreland abyssal plain, which transports passively the overlying accreted units as well as piggy-back basins, on the basal décollement.

Through time, the same organization type has been recognized from field and seismic data interpretation. However, the location of individual domains has been shifted laterally from one evolutionary stage to the another one. For example, former growth faults developed straight above an ancient (now inactive) deformation front, were subsequently transported passively until they were ultimately deformed and uplifted. Since
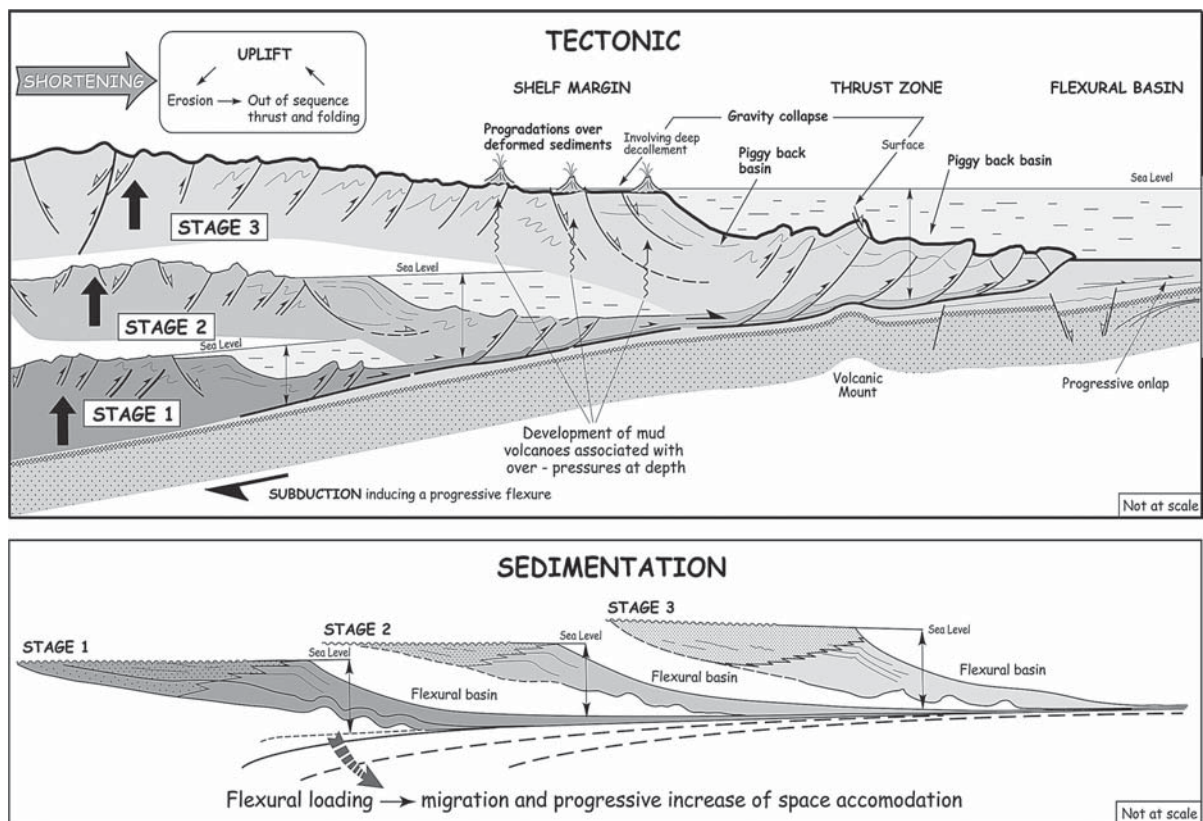
Fig. 17. Conceptual growth model of the Makran prism

Eocene time, a continuous migration of the deformation zones and the related sedimentary wedges above previously deformed units is observed (Fig. 17).

Conclusions

The convergence processes in the Pakistani Makran can be considered as continuously active since the initiation of the subduction (late Cretaceous). The Makran prism has been initiated at least since Early Paleogene time for the internal part of the prism, and then deformation propagated to the south and southwest. We still do not know exactly in which formation the basal décollement is hosted. It could be localized within Cretaceous in the eastern part of the prism or in the western part, close to the Iran border in older formation even in Jurassic. In the southern central range(central part of the prism) deformation was probably mainly active since Middle Miocene times as expressed by the first marine reworking deposited in late Miocene sequences. In the onshore outermost part of the prism (Coastal Range), the first clear evidence of deformation is marked by the strong amount of reworked material (nanofossils) since late Miocene time, in Pliocene series.

The eastern part of the prism, which is obliquely converging with the Pab-Kirthar Ranges is cross-cut by a transform system along which the Indian plate motion to the north is accommodated. These deeply rooted transform faults migrated through times: Chaman fault, was active during Paleogene, Ghazaband fault was active during Miocene, and Ornachnal fault was active in Plio-Pleistocene times. The present-day offshore deformation is characterized also by oblique-slip faults which post-date the thrust emplacement, and occasionally induces deep fluids and mud mobilization. Along the easternmost part of the frontal belt, onshore of the Bela depression, the marine Pleistocene up to the continental Holocene series, locally highly dipping, shows that deformation is still very active.

The strong along-dip and along-strike changes in tectonic style have been related through time to:

1. external factors linked to geodynamics as changes in velocity rates and direction of convergence due to re-organization along plate boundaries. The main changes are linked with the opening of the Aden Gulf, which results in the rapid northward and clockwise rotation of the Arabian plate since the end of the Paleogene. From that time displacement velocity between the Indian plate and Arabian one (both subducted) changed inducing the development of the transtensional Murray Ridge system.

2. internal factors linked respectively to: location and rates of sedimentation over the growing prism, the involvement of oceanic ridges in the subduction zone, and the activity of secondary décollement levels within the accretionary prism. The Paleo-Indus conveyed sediments from Himalayas up to Middle Miocene times directly at the front of the growing prism. Since Late Miocene time, massive sedimentation from the PaleoIndus River were deposited south of a morphological barrier (Murray Ridge), and the prism was mainly filled by the erosion products from the prism. The sedimentary pattern (amount and location of the depocenters) is a very important factor, which has blocked locally the propagation of the deformation, and induced a reorganization of the deformation sites (i.e. jump into younger décollement) generating notably the development of out-of-sequence thrusts. The internal architecture of the prism is also strongly influenced by the propagation of the deformation within secondary décollement levels (hosted in the slope and/or basin shale prograding wedges) which generated growth faulting.

References

Arthuron R.S., Farah A. & Ahmed W. , 1982. The late Cretaceous-Cenozoic history of western Baluchistan, Pakistan-

the northern margin of the Makran subduction complex. In: J.K. Legett, (eds) Trench-Forearc geology, Special Publication Geological Society of London, n° 10, pp 373–385.

Bannert D., Cheemaa A., Ahmed A., and Schaffer U., 1992. The structural development of the Western Fold Belt, Pakistan. Geologisches Jahrbuch B80, pp. 3–60.

Biswas S.K. & Thomas J., 1990. The Deccan Traps and Indian Ocean volcanism. In: Plummer Ph.S. (ed.), First Indian Ocean Petroleum Seminar Proceeding UN Seminary Seychelles, pp. 187–209.

Byrne D.E. and Sykes L.R., 1992. Great thrust Earthquakes and aseismic slip along the plate boundary of the Makran subduction zone. Journal of Geophysical Research, v. 97, n° B1, pp. 449–478.

Burgarth K. P., von rad U., Van Der LiInden W. Block M. Khan A.A., Roeser H. A. & Weiss W. 2002. Basalt and peridotite recovered from Murray Ridge: are they of supra-subduction type?. In: The tectonic and Climatic Evolution of the Arabian sea region. Ed: Clift P. , Kroon D. Gaedicke C. & Craig J. Geological Society of London N° 195.

Clift P.D., Shimizu N., Layne G.D., Blustajn J.S., Gaedicke C., Sschluter H.-U., Clarck M.K. & Amjad S., 2001. Development of the Indus Fan and its significance for the erosional history of the Western Himalaya and Karakoram. Geological Society of America, v. 113, no. 8, pp1039–1051, August 2001.

Clift P. D., Carter A., Krol M. Kirby E. 2002. Constraints on India-Eurasia collision in the Ararbian sea region taken from the Indus Group, Ladakh Himalaya, India. In: The tectonic and Climatic Evolution of the Arabian sea region. Ed: Clift P. , Kroon D. Gaedicke C. & Craig J. Geological Society of London N° 195.

Clift P. 2002. A brief history of the Indus River. In: The tectonic and Climatic Evolution of the Arabian sea region. Ed: Clift P., Kroon D. Gaedicke C. & Craig J. Geological Society of London N° 195.

Coumes F. Kolla V., 1984. Indus fan: seismic structure, channel migration and sediment-thikness in the upper fan. In: Haq B.U. and Milliman J.D. (eds.), Marine geology and oceanography of Arabian Sea and coastal Pakistan, pp. 101–110.

Crame J.A., 1984. Neogene and quaternary mollusca from the Makran coast, Pakistan. . In: Haq B.U. and Milliman J.D. (eds.), Marine geology and oceanography of Arabian Sea and coastal Pakistan, pp. 45–64.

Critelli S., De rosa R. & Platt J.P. 1990. Sandstone detrital modes in the Makran accretionary wedge. Southwest pakistan; implications for tectonic setting and long-distance turbidite transportation. Sedimentary Geology, v. 187, pp. 241–260.

Delisle G., von Rad U., Andruleit H., von Daniels C.H., Tabrez A.R. & Inam A., 2001. Active mud volcanoes on - and offshore eastern Makran, Pakistan. Int J. Earth Sciences (Geol Rundsch), v. 91, pp 93–100.

Demmets C., Gordon R.G., Argus D.F., & Stein S., 1990. Current plate motions. Geophys. J. v. 101, v. 2, pp. 425–478.

Dykstraj J.D. & Birnie R.W., 1979. Reconnaissance geologic maping in Chagai hills, Baluchistan, Pakistan, by computer processing of landsat data. AAPG bulletin, v. 63, n° 9, pp. 1490–1503.

Edwards R.A., Minshull T.A. & White R.S., 2000. Extension across the Indian-Arabian plate boundary: the Murray Ridge. Geophysical Journal Internationnal, v. 142, pp. 461–477.

Ellouz N., Letouzey J., Müller C. Lafargue E., Mallick A., Jaswal T., & Maqsood T. 1994. Tectonic style and Petroleum system of the Sulaiman and N. Kirthar Ranges. IFP Internal report.

Ellouz N, Benard F., Letouzey J., Muller C., Roure F., Malik A., Jaswal T., Maqsood T., 1995. Tectonic style of the Sulaiman Range (Pakistan), a view from analog modeling. AAPG international conference and exhibition, abstracts. AAPG Bulletin. v. 79, n° 8, pp. 1210–1211.

Ellouz et al. 2002. The Makran accretionary Prism- a regional report . IFP Internal report.

Farah A. & Dejong K.A., (eds), 1979. Geodynamics of Pakistan, Geological Survey of Pakistan, Quetta, 361 pages.

Farah A., Lawrence R.D. & Dejong K.A., 1984. An overview of the tectonics of Pakistan. . In: Haq B.U. and Milliman J.D. (eds.), Marine geology and oceanography of Arabian Sea and coastal Pakistan, pp. 161–176.

Fruehn J., White R.S. & Minshull T.A., 1997. Internal deformation and compaction of the Makran accretionary wedge. Terra nova, v. 9, pp. 101–104.

Fournier M., Patriat P. & Leroy S., 2001. Reapraisal of the Arabia-India-Somalia triple junction kinematics. Earth and planetary science letters, v. 189, pp.103–114.

Gaedicke C., Schluter H.U., Roeser H.A., Prexl A., Schreckenberger B., Meyer H., Reichert C., Clift P. & Amjad S.. New insight into the continent - ocean boundary of the Indian Plate, Northern Arabian sea. Tectonophysics, article in press.

Gaedicke C. Prexl A. Schlüter H. U., Meyer H. Roeser H. & Clift P. 2002. Seismic stratigraphy and cprrelation of Major regional uncomformities in the norther Arabian Sea. In: The tectonic and Climatic Evolution of the Arabian sea region. Ed: Clift, Kroon D. Gaedicke C. & Craig J. Geological Society of London n° 195.

Garzantie E., Critelli S. & Ingersoll R.V., 1996. Paleogeographic And Paleotectonic Evolution Of The Himalayan Range as reflected by detrital modes of tertiary sandstones and modern sands (Indus transect, India and Pakistan. Geological society of america bulletin, v. 108, n°6, pp. 631–642.

Gnos E., Immenhauser A. & Peters TJ., 1997. Late cretaceous/early Tertiary convergence between the Indian and Arabian plates recorded in ophiolites and related sediments. Tectonophysics, v. 271, pp.1–19.

Gordon R.G. & Demets C., 1989. Present-day motion along the Owen Fracture Zone and Dalrymple Trough in the Arabian sea. Journal of Geophysical Research, v. 94, pp. 5560–5570.

Grando G., & McClay. Morphotectonic domains and structural styles in the Makran accretionary prism, offshore Iran.. Sedimentary Geology in press,

Harms J.C., Cappel H.N., & Francis D.C., 1984. The Makran coast of Pakistan: it's stratigraphy and hydrocarbon potential. In: Haq B.U. and Milliman J.D. (eds.), Marine geology and oceanography of Arabian Sea and coastal Pakistan, pp. 3–26.

Iqbal M.W.A. & Shah S.M.I.,1980. A guide to the stratigraphy of Pakistan. Records of the geological survey of Pakistan, v. 53.

Jacob K.H. & Quittemeyer R.L., 1979. The Makran region of Pakistan and Iran: Trench-arc system with active plate subduction. In: Farah A. and DeJong K. A. (eds), Geodynamics of Pakistan, pp.305–317.

Kazmi A.H.,1984. Geology of the Indus fan. . In: Haq B.U. and Milliman J.D. (eds.), Marine geology and oceanography of Arabian Sea and coastal Pakistan, pp. 71–84.

Kazmi A.H. & Jan M.Q. 1997. Geology and tectonics of Pakistan. Graphic publishers (eds.).

Kazmi A.H. & Rana R.A. 1982. Tectonic Map of Pakistan. Geological survey of Pakistan, Quetta. Scale 1: 2000000.

Kolla V. & Coumes F., 1990. Extension of structural and tectonic trends from the Indian subcontinent into the Eastern Arabian Sea. Marine and petroleum Geology, v. 7, pp.188–196.

Kopp C., Fruehn J., Flueh E.R., Reichert C., Kukowski N., Bialas J. & Klaeschen D., 1999. Structure of the Makran subduction zone from wide - angle and reflection seismic data. Tectonophysics, v. 329, pp. 171–191.

Kukowski N., Schillhorn , E., Flueh E.R. & Huhn K., 2000. Newly identified strike-slip plate boundary in the northeastern Arabian Sea. Geology, v. 28,n° 4, pp. 355–358, April 2000.

Laughton A.S., Mattews D.H. & Fischer R.L., 1971. The structure of the Indian ocean. In: The Sea. A. Maxwell (eds): New York (John Wiley & Sons, Inc.) v.4, n° 2, pp.543–586.

Lawrence R.D., & Yeats R.S., 1979. Geological reconnaissance of the Chaman fault in Pakistan. In: Farah A. and DeJong K. A. (eds), Geodynamics of Pakistan, pp. 351–357.

Lawrence R.D., Khan S.H., Dejong K.A., Farah A. & Yeats R.S., 1981. Thrust and strike slip fault interaction along the Chaman transform zone, Pakistan. In:Thrust and Nappe tectonics. The Geological Society of London, pp. 363–370.

Legett J.K. & Platt J., 1984. Structural features of the Makran forearc on Landsat imagery. . In: Haq B.U. and Milliman J.D. (eds.), Marine geology and oceanography of Arabian Sea and coastal Pakistan, pp. 33–44.

Leroy S, Gente P, Fournier M, D'Acremont E, Patriat P, Beslier M-O, Bellahsen N, Maia M, Blais A, Perrot J, Al-Kathiri A, Merkouriev S, Fleury J-M, Ruellan P-Y, Lepvrier C, Huchon P (2004) From rifting to spreading in the eastern Gulf of Aden: a geophysical survey of a young oceanic basin from margin to margin. Terra Nova, v. 16, n° 4, pp. 185–192.

MCcall G. J. H. 2002. A summary of the geology of the Iranian border. In: The tectonic and Climatic Evolution of the Arabian sea region. Ed: Clift P. , Kroon D. Gaedicke C. & Craig J. Geological Society of London n° 195,

Miles P.R., Munschy M. & Segoufin J., 1998. Structure and early evolution of the Arabian sea and east Somali basin. Geophysical Journal International, v.134, pp. 876–888, 1998.

Miles P.R. & Roest W.R., 1993. Earliest seafloor spreading magnetic anomalies in the north Arabian Sea and the ocean-continent transition, Geophysical Journal International, v. 115, pp. 1025–1031.

Minshull T.A., White R.S., Barton P.J. & Collier J.S., 1992. Deformation at plate boundaries around the Gulf of Oman. Marine Geology, v. 104, pp. 265–277.

Müller C., 2002. Nannoplankton biostratigraphy of the Kirthar and Sulaiman ranges, Pakistan. Cour. Forsch.-Inst. Senckenberg, v. 237: pp. 15–24.

Pascoe E.H., 1964. A manual of the geology of India and Burma, v. III (ed3), pp. 1345–2130.

Patriat P. & Achache J. 1984. India-Eurasia collision chronology and its implications for crustal shortening and driving mechanisms of plates. Nature, v. 311, pp 615–621.

Platt J.P., Legett J.K., Yong J., Raza H. & Alam S., 1985. Large scale sediment underplating in the Makran accretionnary prism, southwest Pakistan. Geology, v.13, n° 7, pp.507–511.

Platt J.P. & Legett J.K., 1986. Stratal extension in thrust footwalls, Makran accretionary prism: implications for thrust tectonics. The American Association of petroleum geologists bulletin V. 70, NO.2, pp. 191–203.

PowelL C.McA., 1979. A speculative tectonic history of Pakistan and surroundings: some constraints from the Indian ocean. In: Farah A. and DeJong K. A. (eds), Geodynamics of Pakistan, pp. 5–24.

Qayyum M., Lawrence R.D. & Niem A., 1997. Molasse-delta-flysch continuum of the Himalayan orogeny and closure of the Paleogene Katawaz remnant ocean, Pakistan. International geology review, v. 39, pp. 861–875.

Qayyum M., Niem A.R. & Lawrence R.D. 1994. Closure of the Neo-Tethys and evolution of newly discovered delta in §Tertiary Katawaz Basin, Pakistan. Geological society of America, abstracts, v.26, pp.A–242.

Qhueshri M.J., Tariq M.A. & Abid Q.Z., 1993. Geological map of Pakistan (1:10000000). Geological Survey Pakistan, Quetta.

Roeser H.A. & Scientific party, 1997. MAKRAN I: The Makran accretionary wedge off Pakistan – tectonic evolution and fluid migration (part 1). Cruise Report, BGR, Archive No 116 643

Royer JY, Chaubey AK, Dyment J, Bhattacharya GC, Srinivas K, Yatheesh V and Ramprasad T, (2002) Paleogene plate tectonic evolution of the Arabian and eastern Somali Basin. In: Clift PD, Gaedicke C, Craig J (eds). The tectonic & climatic evolution of the Arabian Sea region. Geological Society of London, pp 71–85.

Schlich R., 1982. The Indian Ocean: aseismic ridges, spreading centers and basins. In: Nairn A.E. and Stehli F.G. (eds.), The ocean basins and margins, v. 6. The Indian ocean. Plenum, New York, N.Y., pp. 51–147.

Scotese Cahagan L.M. & Larson R.L., 1988. Plate tectonic reconstructions of the Cretaceous and Cenozoic ocean basins. Tectonophysics, v. 155, pp. 27–48.

Searle R.C., 1990. Imaging the seafloor, new views of plate tectonics. Geophysical Journal International, v.101, n° 1, pp.265–.

Searle M.P., Windley B.F., Coward M.P., Cooper D.J.W., Rex A. J., Rex D., Tingdong LI, Xuchang Xiao, Jan M.Q., Thakur V. C. & Kumar S., 1987. The closing of Tethys and the tectonics of the Himalaya. Geological Society of America bulletin, v. 98, pp. 678–701.

Sharland P.R., Archer R., Casey D.M., Davies R.B., Hall. S.H., Heward A.P., Horbury A.D. & Simmons M.D., 2001. Gulf PetroLink, Bahrain (eds.), Arabian plate sequence stratigraphy, GeoArabia Special Publication 2.

Smewing J. D. Warbuton J. daley, T. CopestakeP. & Ul Haq N. 2002. Sequence stratigraphy of the Soutern Kirthar Foldbelt and Middle Indus basin, Pakistan. In: The tectonic and In: Climatic Evolution of the Arabian sea region. Ed: Clift P. , Kroon D. Gaedicke C. & Craig J. Geological Society of London n° 195.

Smith W & Sandwell D., 1997. Measured and Estimated Seafloor Topography, 1:31270000 Chart, v. 4.2, World data center for Marine Geology and Geophysics, Boulder.

Treloar P.J. & Izatt C.N., 1993. Tectonics of the Himalayan collision between the Indian Plate and the Afghan Block: a synthesis. In: Treloar P.J. and Searle M.P. (eds.), Geological Society Special Publication n° 74, pp. 69–87.

Wiedicke M., Neben S. & Speiss V., 2001. Mud volcanoes at the front of the Makran accretionary complex, Pakistan. Mar. Geol., v. 172, pp. 57–73.

White R. S., 1979. Deformation of the Makran continental margin. In: Farah A. and DeJong K. A. (eds), Geodynamics of Pakistan, pp. 295–304.

White R.S., 1982. Deformation of the Makran accretionary sediment prism in the Gulf of Oman (North-West Indian Ocean). In: Trench-Forearc geology, sedimentation and tectonics on modern and ancient active plate margins, conference. Special publication- geological society of london, v. 10, pp.357–372.

Whitmarsh R.B., 1974 . Some aspects of plate tectonics in the Arabian sea : Initial Reports of the Deep Sea Drilling Project, v. 23, pp . 527–555.

Appendix 1
Main New Biostratigraphic Dating (Nanofossils Determination).

Samples 4-3-1 (Haro anticline: 25° 30' 41.5" N; 66° 05' 4.4" W): Pseudoemiliania lacunosa, Gephyrocapsa oceanica and Helicosphaera carteri (Pleistocene age, zone NN 19).

Samples B10-3 (26° 11' 21.5" N; 66° 11' 55.3" W), B10-4 (26° 11' 11.3" N; 66°11' 38.7" W), B10-5 (26° 11' 16.1" N; 66° 11' 07" W) and B10-7 (26°10' 21.6" N; 66° 11' 4.8" W; Hinglaj formation): Gephyrocapsa sp. and Pseudoemiliania lacunosa (late Pliocene to late early Pliocene, zone NN 18-NN 15).

Samples B10-6 (26° 10' 31.9" N, 66°11' 2.1" W), B10-8 (66° 11' 2.1" N, 66° 11' 2.1" W), B-10-9 (26° 9' 43.3" N; 26° 9' 43.3" W) and B11-3 (25°28'37" N; 64° 22' 26" W; Parkini formation): Discoaster quinqueramus (Upper Miocene,zone NN 11).

Samples B11-8 (25° 30' 48" N; 64° 04' 07" W), B10-9 (25° 30' 07" N; 63° 58' 50" W; Parkini formation): abundance of nannofossils of late Miocene age (zone NN 11).

Samples B12-2 (26° 16' 56" N; 65° 46' 31.2" W; Parkini formation): abundance of nannofossils of late Miocene age (zone NN 10).

Samples B12-3 (26°16' 56" N; 65° 46' 31.2" W; Panjgur formation): abundance of nannofossils of early middle Miocene age (zone NN 5).

Sample B12-4 (26°18' 34" N; 65° 42' 31.8' W; Panjgur formation): Sphenolithus abies, Sphenolithus heteromorphus, Cyclicargolithus abisectus, C. floridanus, Coccolithus pelagicus, Discoaster deflandrei and Discoaster exilis (early middle Miocene, zone NN5).

Samples 22-1 (26° 28' 01" N; 26° 28' 01" W) to 22-7 (26° 27' 18.9' N; 65° 19' 39" W; Panjgur formation): Sphenolithus heteromorphus, Cyclicargolithus abisectus, C. floridanus, Coccolithus pelagicus, Discoaster deflandrei (early middle Miocene age, zone NN 5).

Sample A11-10 (25° 30' 07" N; 63° 58' 50" W; lower Parkini formation): Reticulofenestra pseudoumbilica, Discoaster hamatus, D. calcaris, D. pentaradiatus, Catinaster coalitus (zone NN 9).

Samples A12-1 (26° 24' 31.9" N; 65° 34' 45.2" W) to A12-6 (25° 20' 24" N; 63° 25' 21" W; Parkini Formation): Coccolithus pelagicus, Helicosphaera carteri, Sphenolithus abies, Reticulofenestra pseudoumbilica, Discoaster brouweri, D. quinqueramus, and D. pentaradiatus (Upper Miocene, zone NN 11).

Sample A12-7-1 (25° 24' 45" N; 63° 25' 32" W): Discoaster calcaris and Discoaster bollii (late Miocene, zone NN 10).

Sample A12-8 (25° 24' 45" N; 63° 25' 32" W): Discoaster hamatus, Discoaster calcaris, D. neohammatus, D. bollii and D. brouweri (Upper Miocene, zone NN 9).

Samples 13-1 (25° 44' 27" N; 63° 22' 58" W): Discoaster brouweri, D. pentaradiatus, D. calcaris. Other species include: Cyclococcolithus rotula, C. macintyrei, Sphenolithus abies, Reticulofenestra pseudoumbilica, Helicosphaera carteri, Coccolithus palagicus (Upper Miocene, zone NN 10).

Sample 13-2 (25° 30' 14.8" N; 63° 23' 39.2" W; Talar syncline): Catinaster coalitus, Discoaster hamatus, D. bollii, D. calcaris, Cyclococcolithus macintyrei, and large sized Reticulofenestra pseudoumbilica (late Miocene, zone NN 9).

Sample 13-4 (25° 30' 14.8" N; 63° 23' 39.2" W): few nannofossils indicating a probable middle Miocene age (zone NN 5).

Samples 18-1 (25° 53' 02" N; 63° 03' 57" W) to 18-5 (25° 55' 03" N; 63° 02' 34" W; Panjgur formation): Sphenolithus heteromorphus, Helicosphaera carteri, Cyclicargolithus abisectus, Coccolithus pelagicus (middle Miocene, zone NN 5).

Samples 15-3 (26° 15' 23" N; 62° 12' 47.1" W) and 15-4 (26° 14' 32.5" N; 62° 12' 42.7" W; calcareous siltstones and marls overlying a greenish tuffaceous series in the Mand area) : Cyclicargolithus abisectus, C. floridanus, Coccolithus pelagicus, Sphenolithus predistentus, S. ciperoensis, S. dissimilis, Discoaster deflandrei and Dictyococcites dictyodus (late Oligocene age, zone NP 24-25).

Sample 17-13-3 (25° 53' 01" N; 63° 03' 50" W): Discoaster calcaris (late Miocene).

Samples 17-16 (26° 6' 30.2" N; 63° 12' 1.4" W) and 17-17 (26° 6' 30.1" N; 63° 12' 1.3" W; Panjgur formation) : Sphenolithus heteromorphus (middle Miocene, zone NN 5).

Samples 19-1 (26° 27' 21" N; 63° 57' 07" W) to 19-8 (26° 23' 57" N; 63° 59' 26.5" W; Hoshab formation) Sphenolithus predistentus, S. ciperoensis, S. moriformis, S. conicus, S. dissimilis, Cyclicargolithus abisectus, C. floridanus, Coccolithus pelagicus, and Discoaster deflandrei. No species younger than late Oligocene (NP 25).

Samples 20-8 (26° 07' 08" N; 64° 00' 59" W) to 20-10 (26° 06' 30" N; 64° 01' 02" W; Panjgur formation) : Sphenolithus heteromorphus were observed

together with reworked species from the Oligocene. They might belong to the early middle Miocene.

Sample 21-1 (25° 57' 39.5" N; 64° 13' 42.2" W) : Sphenolithus heteromorphus (early middle Miocene).

Sample 21-4 (25°58' 5.1" N; 64° 13' 55.1" W): Discoaster deflandrei, D. druggii, Sphenolithus belemnos, S. abies, Coccolithus pelagicus, and Cyclicargolithus abisectus (Miocene age, zone NN 3).

Samples 21-5 (26° 03' 26" N; 64° 01' 41" W) to 21-7 (26°05'12" N; 64° 01' 35" W): Sphenolithus heteromorphus (early middle Miocene).

Samples B21-1 (25° 57' 39.5" N; 64° 13' 42.2" W) to B21-4-2 (25° 58' 5.1" N; 64° 13' 55.1" W; Panjgur formation): abundance of nannofossils of early middle Miocene age (zone NN 5).

Offshore Frontal Part of the Makran Accretionary Prism: The Chamak Survey (Pakistan)

Ellouz-Zimmermann N. · Lallemant S.J. · Castilla R. · Mouchot N. · Leturmy P. · Battani A. · Buret C. · Cherel L. · Desaubliaux G. · Deville E. · Ferrand J. · Lügcke A. · Mahieux G. · Mascle G. · Mühr P. · Pierson-Wickmann A.-C. · Robion P. · Schmitz J. · Danish M. · Hasany S. · Shahzad A. · Tabreez A.

Abstract. The Makran accretionary prism developed in the north-western part of the Indian Ocean as a consequence of the subduction of the Arabian Sea since Late Cretaceous times. It extends from southern Iran to the Baluchistan region of Pakistan where it joins the Chaman-Ornach-Nal left-lateral strike-slip fault systems to the north and the Owen Fracture Zone-Murray Ridge transtensional (right-lateral) system to the south in a complex triple junction near the city of Karachi. In September to October of 2004, we surveyed most of the accretionary complex off Pakistan with R/V Marion Dufresne. We achieved a nearly continuous bathymetric mapping of the prism and the subduction trench from 62°30′E to the triple junction near 65°30′E together with nearly 1000 km of seismic reflection (13 lines) and we took 18 piston cores in different geological settings. One of the main results is that the frontal part of the Makran accretionary prism is less two-dimensional than previously expected. We interpret the along-strike tectonic variation as a consequence of lateral variations in sediment deposition as well as a consequence of the underthrusting of a series of basement highs and finally of the vicinity to the triple junction.

1   Introduction

The Arabian Sea, possibly one of the oldest parts of the Indian Ocean, is now underthrusting beneath the Afghan block, currently at the southern edge of the Eurasian plate. This subduction occurs between two major collision systems of the Zagros (Iran) and the Himalaya (Pakistan-Tibet). The subduction of this Arabian Sea lithosphere, composed of Arabian and Indian oceanic and transitional crusts (Miles et al., 1998), started at the end of the Cretaceous and resulted in the development of the oblique Chagaï volcanic arc along the Pakistan and Afghanistan borders. The subduction system stops at a triple junction between the three Arabian-Eurasian-Indian plates located near Karachi city (Pakistan). This junction corresponds to the intersection between the Makran subduction zone (Arabia/Eurasia motion), the Chaman-Ornach-Nal left-lateral transform fault system (India/Eurasia motion), and finally the Murray transtensional Ridge as a part of the Owen Fracture Zone right-lateral system (India/

Arabia motion). The Makran accretionary prism results from the northward motion of the oceanic crust (White and Klitgord, 1976; White, 1983; Minshull et al., 1992), with an average speed of 3 cm/year at present. Large historic earthquakes, such as the magnitude 8.2 recorded in November 1945 (Pacheco and Sykes, 1992; Byrne et al., 1992), are clearly related to the shallow dipping inter-plate mega-thrust. The coseismic motion might be related to the episodic uplift of small mud volcanoes rising up above the sea-level, confirming an overpressure regime imposed at depth.

Our specific interest on the Makran prism was driven by the following facts:

1. Over 60% of the accretionary prism is presently emerged, allowing a detailed structural study onshore as described in a companion paper (Ellouz et al., this issue).
2. The frontal part, located offshore, is where the most recent processes can be analysed, and seems to be more or less linear as far as it joins the transform fault systems.
3. The sedimentation rates vary presently along strike and have been varying through geologic times.
4. Numerous fluid and gas seepages are described both onshore and offshore, outlining high fluid pressures at depth and suggesting fluid circulation linked to both the high sedimentation rates and the overpressure due to horizontal deformation.

2   Geodynamic Setting

2.1 Present-Day Plate Kinematic Setting

The present-day geodynamic setting of the Makran area corresponds to a northward subduction of the Arabian Sea beneath the Iranian and Afghan continental blocks resulting in large interplate thrusting earthquakes (Byrne and Sykes, 1992). Although they exhibit widespread seismicity, the overriding blocks can be considered as the southern edge of the large Eurasian plate. The western part of the downgoing Arabian Sea lithosphere belongs to the Arabian plate

whereas the eastern part is part of the Indian plate. The present-day plate boundary between the Arabian and Indian plates is running along the mostly strike-slip Owen Fracture Zone (Quittmeyer and Kafka, 1984; Gordon and DeMets; 1989, Fournier et al., 2001). The plate boundary shows a nearly east-west bend along the Murray Ridge associated with extensional earthquakes before intersecting the subduction boundary west of Karachi city (Fig. 1a). This point corresponds to a triple junction with a connection to the north with the boundary between Eurasian and Indian plates that is mostly left-lateral strike-slip along two prominent faults: the Ornach-Nal fault system to the south-east and the Chaman fault to the north-west (Quittmeyer and Kafka, 1984). According to traditional plate motion modelling, such as NUVEL-1a (DeMets et al., 1994), the Arabian plate is moving at about 30 mm/yr toward the north (Figs. 1a & b). Although these traditional global models are in quite good agreement with the motions obtained from space geodesy (DeMets et al., 1994), the more recent instantaneous global models based on space geodesy (Sella et al., 2002) show a significant difference in relation to NUVEL 1a in the velocities of the African and Arabian plates. This nearly 30% difference has been confirmed when switching to ITRF2000 reference frame for both the African plate (Calais et al., 2003) and the Arabian plate (Vigny et al., 2006). These authors conclude that the two

plates have slowed down during the last 3 Ma. In this paper, we favour the Vigny et al. (2006) model because it provides a better agreement with the observed deformation in the Murray Ridge area. We are not following Kukowski et al. (2000) who propose a new Ormara microplate between India and Eurasia, neither are we using the Reilinger et al. (2006) model who introduce a Lut block moving independently from Eurasia. Figure 1a summarises the linear velocities along the three plate boundaries according to the three main models quoted above.

2.2 Plate Kinematics Since Late Cretaceous Times

The present configuration of the subduction zone results from a long lasting geodynamic evolution involving several major plate reorganisations since the breakup of this part of the Gondwana at 157 Ma (Cochran, 1988). The evolution of the plate motions in the studied area has been recorded in the Indian Ocean floor and can be divided in two main stages with respect to the Indian continent motion. In a first sequence ranging from Late Cretaceous (Albian) to the Middle Eocene, the Indian plate is moving northwards at relatively fast velocities (Norton and Sclater, 1979), both in terms of absolute motion and the motion relative to Eurasia (10 to 15 cm/yr from west to east) (Patriat
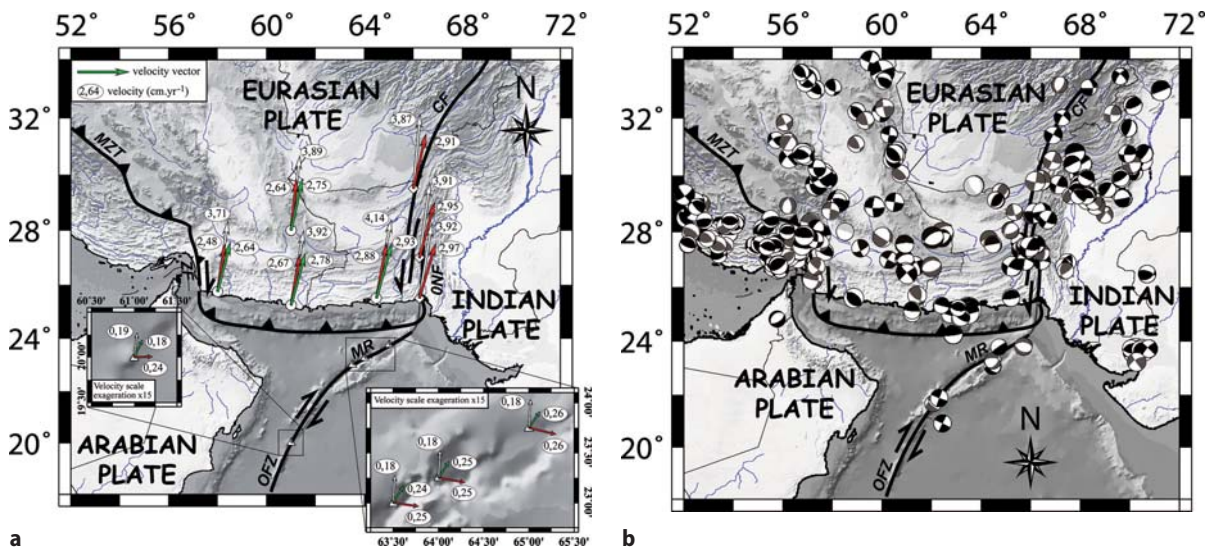
Fig. 1. Present-day plate tectonics setting **a** Relative velocities of the Arabian plate with respect to the neighbouring Eurasian and Arabian plates. The arrows are the linear velocities computed from three recent models: the white arrows according to the "classical" Nuvel-1A model (DeMets et al., 1994) whereas red arrows correspond to the space geodesy model REVEL1 (Sella et al., 2002) and green arrows to a recent GPS based model from Vigny et al. (2006). White circles are Eurasian plate motion relative to fixed Arabia and white diamonds are Indian plate motion relative to fixed Eurasia; **b** Map of the major earthquakes focal mechanisms over the studied area. Hypocentres are represented in 4 depth intervals: 0-30 kms; 30-60 kms; 60-100 kms and >100 km. The earthquakes focal mechanisms are respectively represented by black shaded; dark grey shaded; light grey shaded and very light grey shaded compressive quadrants. Data are compiled from Quittmeyer, R. and Kafka, A., 1984; Laane and Chen, (1983); Jacob et al., (1979); Byrne and Sykes, (1992) and from the Harvard CMT database

and Achache, 1984). After a significant increase in velocity between chron 28 (approx. 61 Ma) and chron 22 (49 Ma), the motion changed suddenly between chron 20 (43 Ma) and chron 18 (39 Ma) to a slower and more northeastward one. This major change in the Indian Ocean spreading pattern is usually related to the onset of the collision between Indian and Eurasian continents (Patriat and Achache, 1984). More precisely, Patriat and Achache (1984) suggested that the change occurred in two stages: from chron 22 to chron 20, the relative motion slowed down along the same direction corresponding to the final closure of the Neotethys. From chron 20 to chron 18, a complete reorganisation of the mid-ocean ridge system accommodated the incipient collision with a major change in the spreading direction. The Indian-African plate boundary had a slightly more complex history. The spreading prior to the chron 28 (83 to 59 Ma) resulted in the Mascarene and Laxmi basins (Bhattacharya et al., 1994; Chaubey et al., 1998; Bernard and Munschy, 2000). The velocity increase of the Indian plate at chron 28 coincides with the jump of the spreading centre to a new location between the Seychelles-Mascarene Plateau and the Laxmi Ridge producing the Arabian Basin to the north and the Eastern Somali Basin to the south. The spreading centres in a complex pattern of propagating rifts, the spreading rate decreasing from 7 cm/yr at chron 22 to less than 2 cm/yr at chron 20 (Chaubey et al., 2002). After 43 Ma, the spreading centre had the present-day configuration of the Carlsberg ridge with a 2 cm/yr rate. The last major change occurred at about 17.6 Ma (chron 5d) as the Sheba ridge started to produce oceanic crust in the Gulf of Aden when the Arabian plate started to drift northeastwards with respect to the African plate (Leroy et al., 2004). As stated above, the present-day plate boundary between India and Arabia is located along the Owen Fracture Zone (Matthews, 1966; Sykes, 1968; Quittmeyer and Kafka, 1984; Fournier et al., 2001) north of a complex triple junction (Fournier et al., 2001) and the whole seafloor underthrusting the Makran margin belongs to the Arabian plate. This plate boundary has probably been active since the onset of spreading in the Gulf of Aden in the Early Miocene (17.6 Ma according to Leroy et al., 2004). An open question remains regarding the India/Africa plate boundary before that time. The simplest interpretation would be to use the same prominent sea-floor topography of the Chain Ridge and Owen Fracture Zone as the main transform system. Several data sets however suggest that the pre-Oligocene transform system was multiple with a large strike-slip fault zone located westward, closer to the southern coast of Oman (Mountain and Prell, 1989 and 1990; Barton et al., 1990; Minshull et al., 1992). For example, the depth to basement in the Oman basin, sediment correlations from seismic profiles on the

Owen Ridge, unidentified magnetic lineations and the contrast in crustal thicknesses, all suggest that the Oman margin was a transform margin in the Late Cretaceous time to Early Tertiary times. As shown by Mountain and Prell (1989) and summarised in Minshull et al. (1992), choosing one hypothesis or the other results in dramatic differences in the age of the subducting Arabian Sea basin.

2.3 Sedimentary Inputs Through Time

Another important factor determining the tectonic regime of an active margin is the amount of sediments entering into the trench system (von Huene and Scholl, 1991; Le Pichon et al., 1992). In the present-day situation, most of the Himalaya-derived oceanic sediments are trapped in the Indus fan and have very little involvement in the Makran accretionary processes due to the presence of the Murray Ridge bathymetric high. According to Qayyum et al. (1997), the deposition of thick Himalaya-derived detrital sequences in the modern Indus fan did not start until the Early Miocene (Fig. 2). These authors propose relating the thick Eocene-Oligocene turbidites from the onshore Makran accretionary prism to the oceanic fan of a fluviatile system known in Pakistan and Afghanistan as the Katawaz formation. Despite an apparent continuity of the accretionary processes in the Makran prism, the geological history is clearly divided into two stages. During the early times of the collision zone, the Makran prism grew by accreting the sedimentary products of the Himalayan collision zone through the shortening of a Palaeo-Indus deep sea fan more or less parallel to the paleo-trench. On the other hand, since the Miocene, the accretionary complex is mostly recycling sediments coming from the erosion of the older prism and conveyed to the modern trench through a series of river and canyon systems.

3   Regional Investigation and New Data

3.1 Pre-Existing Data

Prior to our CHAMAK survey, some scattered swath bathymetric data were acquired with hydrosweep multibeam system during cruises SO90, 122, 123, 124 and 130 of the German R/V Sonne (Kukowski et al., 2001). During the same SO123 ('MAMUT') cruise in 1997, wide-angle seismic data were acquired (Kopp et al., 2000) completing the older seismic reflection data set from the Cambridge group (White, 1976; White and Louden, 1983; Minshull et al., 1992). Thanks to a previous visit to DGCP, some of us had an overview of the scattered seismic information on the Coastal Range,
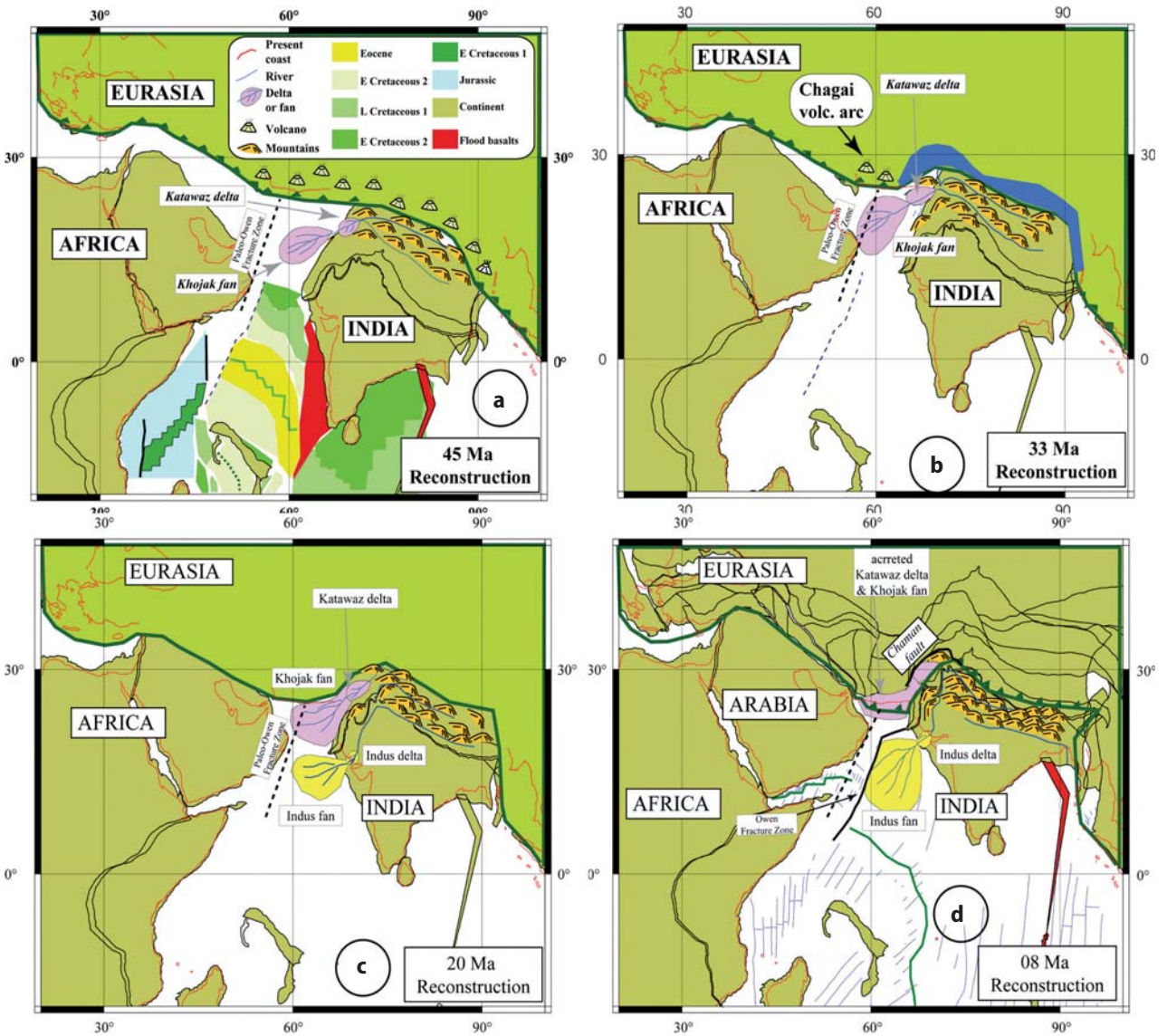
Fig. 2. Plate kinematics in a fixed Eurasia reference frame and sedimentary inputs in the Arabian Sea since Eocene times. Reconstructions have been made using the ODSN interactive facilities which are based on databases from Hay et al. (1999) (http://www.odsn.de/odsn/services/paleomap/paleomap.html) and the Sedimentary bodies is slightly modified from Qayyum et al., (1994). **a** Middle Eocene (45 Ma), onset of the Himalayan collision whose drainage results in the Khojak delta and the Katawaz fan. **b** Eocene-Oligocene (33Ma). The previous delta & fan system is now mature. **c** Lower Miocene (20 Ma). Due to the onset of deformation in the western edge of the Indian continent, a new drainage system appears and results in the modern Indus delta and deep-sea fan system. **d** Upper Miocene (8 Ma). The system of the Owen Fracture and now active Murray Ridge is isolating the Indus fan from the Makran Trench, The old Khojak-Katawaz system is undergoing shortening in the Makran accretionary complex

and of some recent deeper offshore seismic lines. Over the shelf, a couple of already published seismic profiles (Harms et al., 1984) have been re-interpreted. This study benefited from the interpretation of reprocessed CEPM (1977) Indus NW-SE seismic lines (see Ellouz et al., this issue),

On the other hand, the calibration of the seismic reflectors is difficult because only few exploration wells were drilled in the Pakistani Makran continental shelf off the coastal Range. Most of these wells are very old and reached only the Pliocene or the Miocene strata at the oldest, with rather poor constraints on the stratigraphic levels. Unfortunately, we had no access to the Pasni and Gwadar recent wells drilled by Ocean Energy company, both located on the shelf edge.

3.2 New Data from CHAMAK Cruise

CHAMAK Survey was a part of an integrated project which started in 2000 as a collaboration with the Geological Survey of Pakistan (GSP) and National Oceanographic Institute of Pakistan (NOI). The first step was a field reconnaissance in the Makran accretionary prism carried out with the logistical support of the Geological Survey of Pakistan, in February-March 2001. The main results of this field work are presented in a companion paper (Ellouz et al., this issue). CHAMAK cruise was initially planned to start in October 2001. For political and safety reasons, the cruise has been delayed and finally was achieved in September and October 2004. We benefited from the participation and administrative support from the Pakistani navy. The offshore survey was conducted onboard R/V. "Marion Dufresne" operated by IPEV (Institut Polaire Paul Emile Victor) and was devoted to the mapping of the external part of the Makran prism offshore Pakistan. During the cruise, we covered a 65,000 sq. km area with the multibeam echosounder Sea-Falcon. We combined these data with the existing hydrosweep resulting in a nearly continuous complete mapping of the continental slope between 62°30' – 65°30'E & 23°–25°N (Fig. 3).

During the second part of the cruise, around 1000 km of multichannel seismic lines have also been acquired along 13 profiles. The seismic sources were produced by an array of 4 TI sleeve guns (total volume of about 110 cu in) and recorded by two short streamers (respectively a 100 m long 6-channel streamer and a 180 m-long 18-channel one) allowing us to investigate the sediments down to 2.5 s (two way time) with a relatively high spatial resolution on the seabed.

In order to constrain the present-day sedimentary pattern, 27 long cores (half of them with the Calypso giant core) were acquired along the different units of the prism, as well as in the abyssal plain and in the northern flank of the Murray Ridge. When possible these cores were also sampled for fluids, water and gas, sometimes in-situ with the "Goldorak" piston core from A. Lügcke (BGR).

Following the CHAMAK data acquisition cruise, along the Pakistani active margin, several studies were undertaken as parts of an integral project in the aim of understanding the construction of the Makran accretionary prism. Among all the activities, the processing and interpretation of multichannel seismic-reflection lines, the 3.5 kHz profiles and the morphotectonic analysis of the multibeam bathymetry data, as well as the sedimentology, organic matter and gas analysis from the cores, represent the main lines of investigation.

The purpose of this paper is to present a preliminary interpretation of some of the seismic lines and the results from the analysis of the multibeam bathymetric data, illustrating the various structural styles along the recent prism, as well as the main mechanisms involved.

4   Morphology of the Recent Prism

The swath bathymetry data acquired during CHAMAK survey allow us to obtain a good definition and image of the sea-floor morphology and the 3D geometry of the submerged part of the prism, which was poorly documented east of Pasni. In the frontal part of the Makran tectonic wedge, thrust faulting is responsible for the formation of accretionary ridges developed with more or less steep flanks and variable length (White and Louden, 1983; Flueh et al., 1997; Fruehn et al., 1997; Kukowski et al., 2000). At a regional scale, the front of the prism looks rather two-dimensional with an along-strike steepening of the average bathymetric slope toward the east. Focusing on the frontal part of the prism, it appeared that not only the bathymetry profile is shallowing to the east but also the size, the length, and the distance between each thrust is diminishing dramatically.

South of the deformation front, the sediments are deposited in a flat and smooth trench, which is disturbed by some prominent SW-NE trending bathymetric highs more or less buried, like the Little Murray Ridge close to 63°45'E; 24°10'N. The bathymetry shallows drastically on the flank of the northern Murray Ridge where "fossil" meandering channels are identified, marking the southward migration of the distal course of the submarine part of the Indus River (Fig. 3). Southward, the depths increase rapidly in several elongated basins, down to about 4500 m in the Dalrymple trough, representing the southernmost part of the transtensional boundary between the Arabian and Indian plates (Quittmeyer and Kafka, 1984; Edwards, 2000; Fournier et al., 2001).

East of 63°45'N, the accretionary ridges seem to be more sinuous and more prominent than in the area investigated during the 1997 MAMUT survey (Kukowski, 2000) located west of 63°45'N. Consequently, the distance between each ridge is not constant along N-S dip profiles and locally great variations can be observed. Sinuosity is particularly spectacular for the frontal accretionary ridge and results in an indented shape of the prism deformation front (Fig. 3). Moreover the slope of the seaward flank of the frontal ridge is dependant on the distance between two ridges (Fig. 4a), for example becoming steeper where wavelength decreases (Fig. 4b).
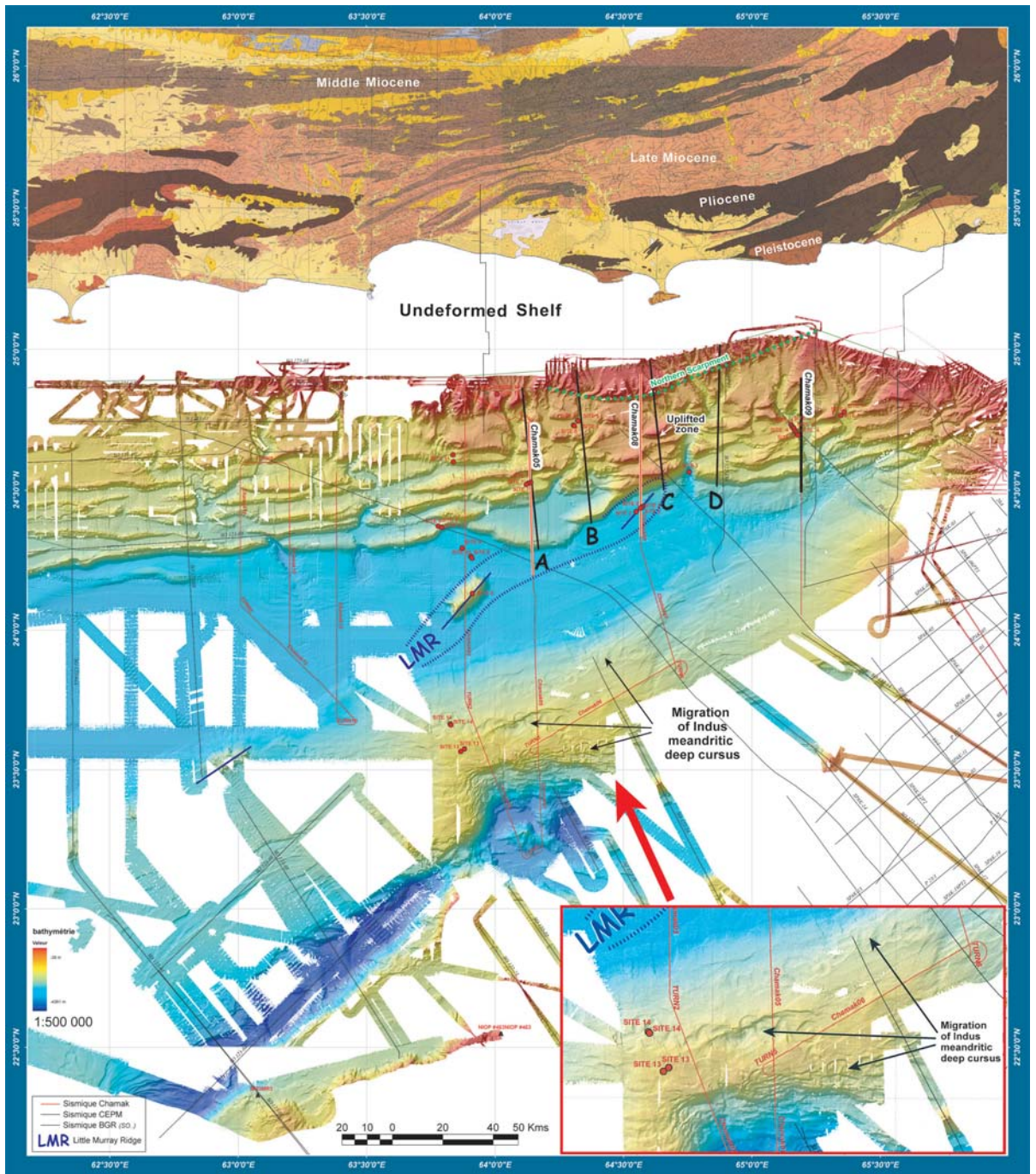
Fig. 3. Composite bathymetry map of the Makran prism using mostly Sea-Falcon multibeam data acquired during Chamak survey combined with the existing hydrosweep data (Kukowski et al., cruise report). The 13 seismic reflection profiles acquired during the cruise are located as well as the cores

The entire offshore wedge is cut by a dense dendritic canyon network (Fig. 3) which is sometimes directly connected to the north with streams or small rivers as Hab, Nal-Hingol or Dasht rivers, from east to west. One of the most striking morphological characteristics of the Makran accretionary wedge is the amount of sediment removal by erosion. Many circular and linear slump scars can be distinguished along the entire prism. The first ones are frequently clustered and generally cut a large portion of the ridges while the linear ones affect only the top of them. Major erosion and sediment transfer processes are expressed in

Figs. 4. Close-up of the bathymetry at two different sites located at the deformation front of the Makran accretionary wedge. **a** Close-up of the seismic CH05 profile (reference profile); **b** Close-up of the seismic CH05 profile (subducted basement high)

a

b
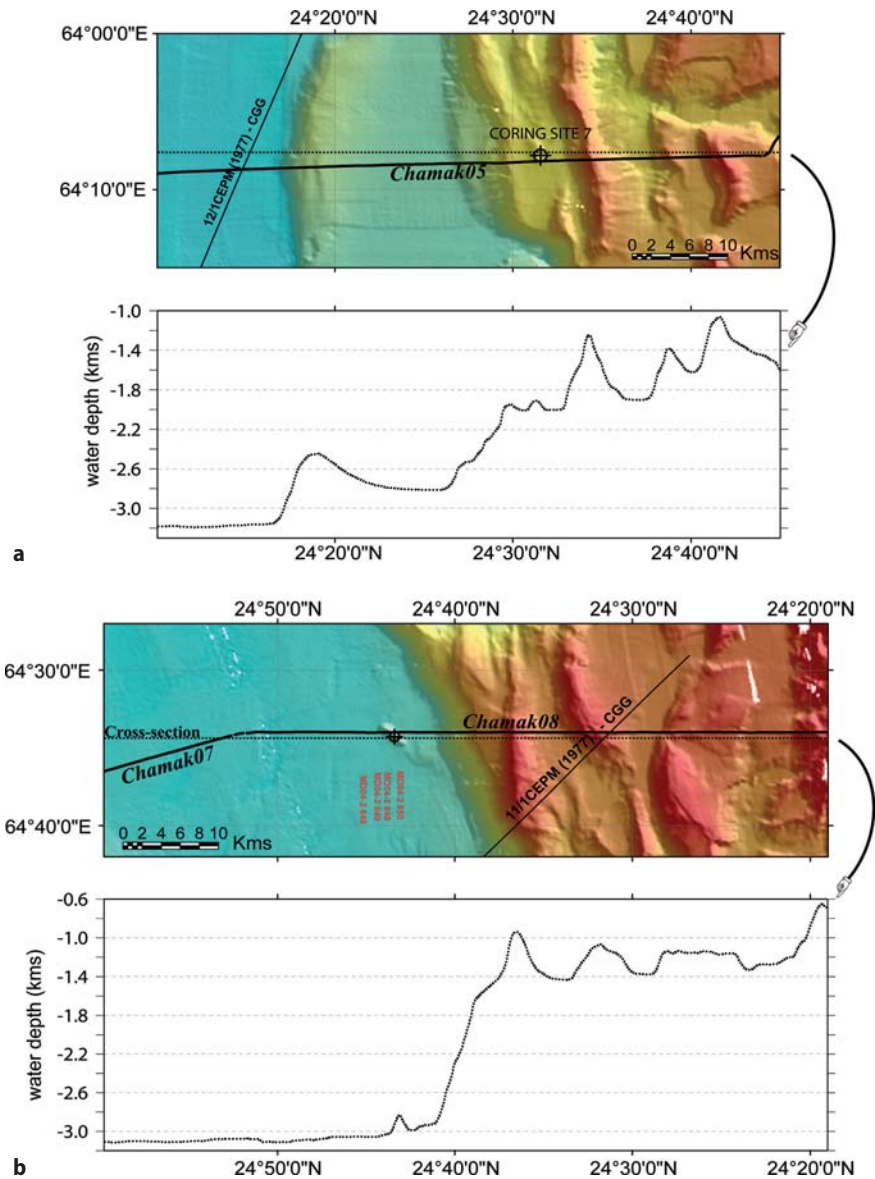
the bathymetry as these large sinuous canyons often are associated with circular slump scars. They consist in small canyons and gullies in the upper slope which rapidly coalesce into large canyons downslope. They flow through the prism down to the trench where they incise into the abyssal plain sea floor. These canyons usually cut perpendicular to the ridges but sometimes, when relief is too high, turn and run parallel to the ridges for several kilometres. The associated debris flows have no obvious morphological expression at the sea floor, either because of the substantial hemipelagic sedimentation (Prins et al., 2000) or because of a complete remobilisation of the sediment packets transferred to a wider area.

5 Deformation Style of the External Central (and Eastern) Makran

Multi-channel seismic reflection lines acquired during the Chamak cruise, image the frontal part of the Makran accretionary prism, from the upper slope-break to the abyssal plain. Seismic data show how shortening of ocean floor sediments from the continental slope, is achieved through imbricate thrust faults, forming an E-W oriented ridge network, to the front up to the easternmost salient close to the Bela depression. The tectonic style is governed dominantly by a forward propagation of the deformation, expressed by off-scrapping of the sediment deposited in the fore-

land basin with a variable thickness. At a large scale a classical large submarine fold and thrust belt develops progressively to the south through time. The connection with the emerged part of the prism is expressed as a wide shelf, where surface deformation is not expressed by compressive structures.

5.1 Nature of the Incoming Sequences

On the north-south trending seismic lines (Fig. 5, locations in Fig. 3), one can see a shallow-dipping regional unconformity, marked by the onlap terminations of the overlying sequence. In a companion paper (Fig. 11 and 12 of Ellouz et al., this issue), this unconformity has been interpreted as the result of intense shortening and erosion of the Makran prism during the Late Miocene times. This tectonic pulse was marked by the increase of reworkings (including Middle Miocene) species found in the Upper Miocene and Pliocene deposits. Schlüter et al. (2002) proposed assigning an Upper Miocene age to this surface interpreted as a major unconformity known at a regional scale and controlled by drilling in Iran. The northward tilting of this surface results both from the flexure of the downgoing elastic lithosphere entering the subduction zone and from the Murray Ridge system deformation, explaining the common tilt observed at the top of the basement highs reflector and at the regional unconformity. Between the unconformity and the basement, the sedimentary units (variable in thickness, locally more than two stwt) have been recorded. They are composed of sub-parallel and continuous reflectors at the base, hosting the basal décollement, and channel-levees system at the top. Above the unconformity, a sedimentary sequence is composed of packages of high amplitude and highly continuous reflectors (hemipelagic sediments?, where the décollement develops at the front) and medium to high amplitude and poor continuity reflectors (distal turbiditic facies?). This sequence shows little flexure and can be recognized to the north as deformed by the imbricate thrusts described above. A lateral facies variation of the supposed distal turbidite sequences is inferred from the presence of channel-like geometries deformed inside the folds on the imbricate thrusts sheets.

5.2 Mechanisms of Deformation

As in other parts of the prism, the imbricate system accounts for the significant structural relief (~ 2 sec.

TWT visible in this section) created as a consequence of the off-scraped sediments from the oceanic crust.

The continuity and parallelism at the sea floor change along strike. The western part of the prism (west of 65°5'W) shows mostly continuous E-W directed structures. Nevertheless, despite the apparent two-dimensional aspect at a large scale, the seismic data show a slightly different configuration at smaller scale. Lateral changes concern the wavelength and the amplitude of the anticlinal ridges (Fig. 6a), as well as the vergence which can even vary within a short distance along strike. Such a rapid change can be seen in the frontal thrust between lines CH10 and CH11 (Figs. 5 and 6b).

East of longitude 63°5'W, sea floor ridges show cuspate geometries reflecting an important variation in the tectonic style. The wavelength of these structures varies not only along strike but also along dip (N-S). From a "high standing" plateau (CH08) to a more classical wedge geometry (CH09), lateral variation on the overall geometry of the prism reflecting different internal structure, outline the great impact of the deep structures on the development of the prism.

These lateral variations in morphology are induced by the highly variable deformation mechanisms active in the Makran accretionary prism. The frontal thrust can be interpreted either as a deep blind thrust (seismic line CH09 in Fig. 5) or as an emerging fault (seismic line CH11 in Fig. 5), even as a triangle zone as interpreted in the profile CH 10 (Fig. 5). Folding associated with this frontal thrust shows an up-section decrease of the vertical throw, which indicates the progressive upward propagation of the fault plane (similar to a fault propagation fold system). At the same time folding associated to limbs tilting are shown by piggy-back basins (Fig. 6b). As a consequence of flat and ramp thrust system, the back limb generally rotates, as recorded locally in some of the piggy-back basins sedimentation. However, it is sometimes difficult to tell whether back limb have rotated progressively or not, due to the lack of syntectonic deposits in some of the piggy-back basins.

The upper part of the margin is constituted by a large platform running along the coastline, in which episodic and minor deformation is expressed, either as regional uplift due to deformation propagation at depth, or as out-of-sequence faulting or to normal faulting mainly driven by gravity gliding like in the western Makran off Iran (Grando and Mc Clay, 2006). Mud volcanoes and gas seepages are quite common in the shelf (Schlüter et al., 2002, Delisle et al. 2001, Ellouz et al. this issue), as a typical consequence of overpressure at depth.
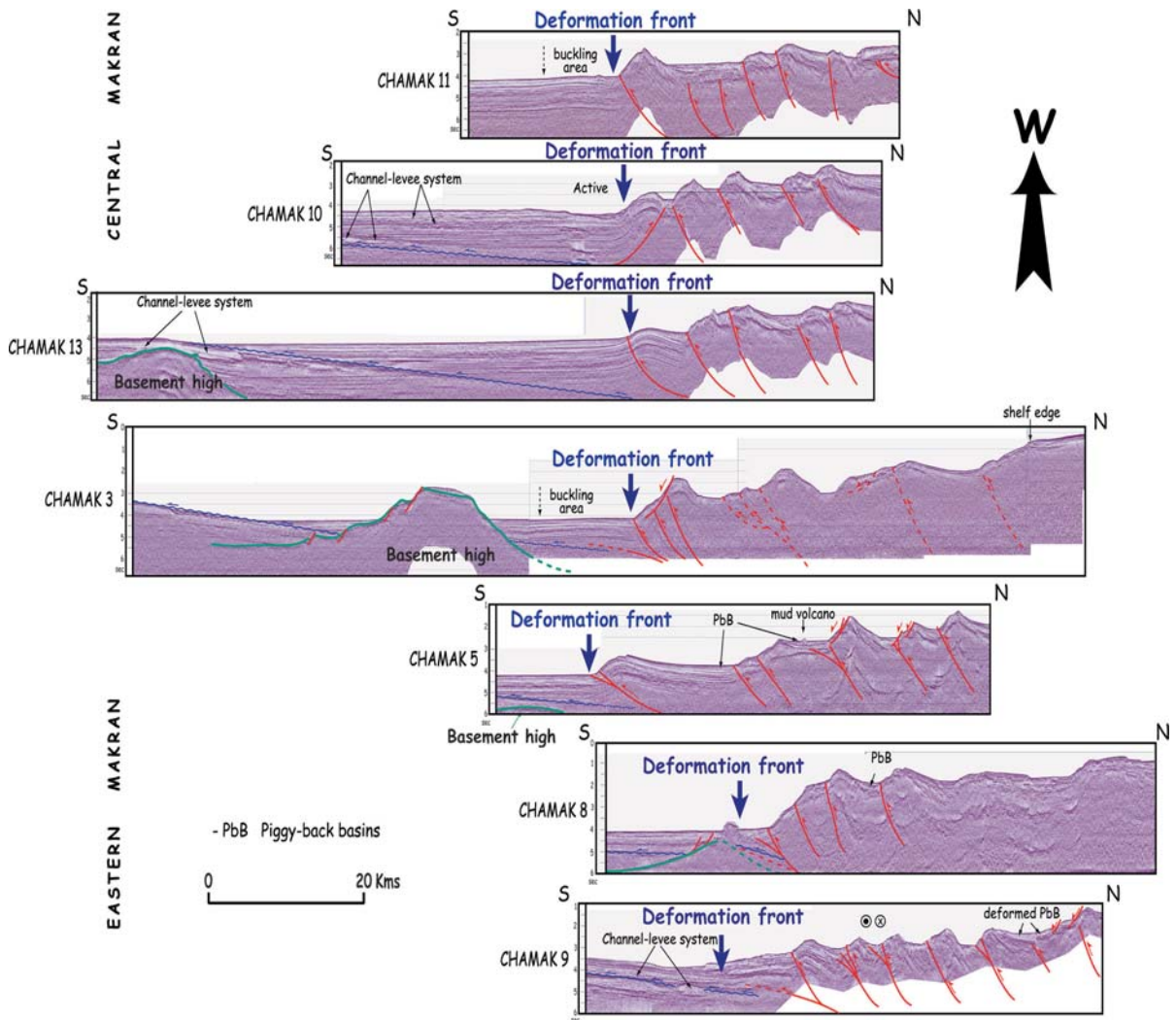
Fig. 5. Display of the seven N-S trending seismic reflection profiles obtained during the CHAMAK cruise. See location on the bathymetric map in Fig. 3

5.3 Piggy-Back Filling

On seismic line CH10 (Fig. 6a), at the foot of the deformation front, an active channel can be recognized (on both seismic and bathymetry data) showing an onlap dominated infill over an erosive surface. The deformation front shows a high degree of lateral variation. In this section an asymmetric fold is observed that can be modelled as a structure of dominant landward (northward) vergence. This unusual tectonic style is well documented for Cascadia (Gutscher et al., 2000; Smit et al., 2003). The imbricate system observed north of the front allows for the formation of several piggy-back basins. To the south, these basins are small and of lim-

ited depth. On the other hand, to the north, two wide basins are present showing a history of multiple deformation pulses with several onlap surfaces indicating their progressive tilting.

Piggy-back basins have developed north of most of the ridges showing a sedimentation recording multiple stages of deformation. An analysis of the reflector geometry in the piggy-back basins of seismic line CH11, allows an identification of a polyphase evolution (Fig. 6b). First, the oldest filling sequences usually terminate southwards as onlaps against pre-growth reflectors with a significant fanning of the growth-strata. Contrasting with these deep layers, the overlying sequences are dominated by pinch-out against growth strata. They are in general associated with sub-parallel
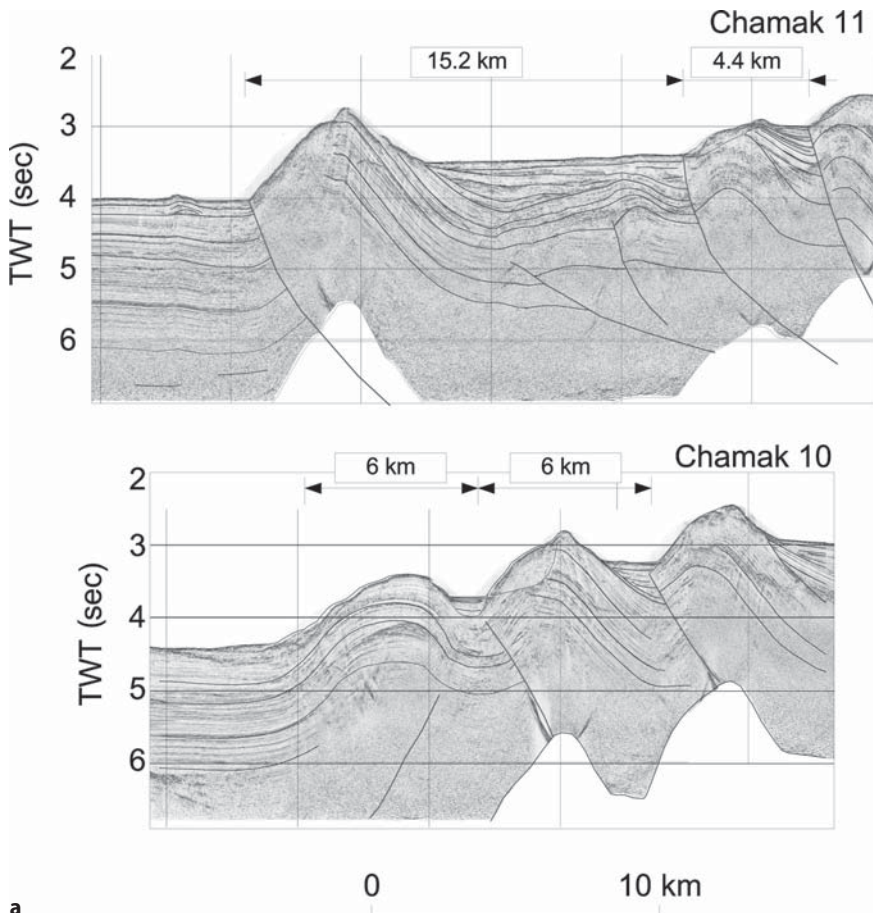
Fig. 6. Detailed seismic interpretation illustrating different mechanisms in the piggyback basins at the rear of the frontal imbricate thrusts; **a** Comparison between profiles CH10 and CH11 concerning the spacing between the main thrust imbricates along the frontal part of the prism; **b** Detail of a piggyback basin on seismic profile CH11 illustrating the geometric relationships between sedimentary reflectors. The nature of reflector terminations allow to identify at least 3 different episodes reflecting changes on the sedimentary/tectonic dynamics
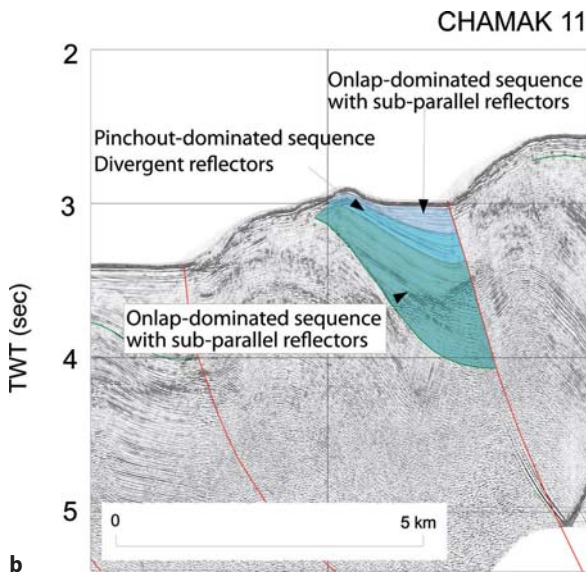
reflectors. This can be interpreted as a period during which sedimentation has been more active than the tectonics, indicating periods of either enhanced tectonic pulses or a slowing of sedimentation rates. The uppermost layer is more similar to the lower piggyback infill with onlaps and fanning corresponding either to a faster deformation rate either to a slower sedimentation rate or any combination.

6   Parameters Affecting the Along–Strike Morphologic and Tectonic Variations

The wavelength between two tectonic sheets is not constant along dip and along strike. The frontal thrusts implies overlap of series from 1.5 s TWT thick in the east of the prism, to 3 s TWT to the west. The bathymetric profiles are changing from east to west locally and can show dramatic variations. Two major parameters seem to guide the deformation style variation: underthrusting of basement ridges and the sedimentation processes. The facies distribution could also be another parameter involved.

6.1 Basement Heterogeneities and Morphological Signature of an Oblique Ridge Subduction

The nature and morphology of the basement through time is still poorly known. Nevertheless, some ridges of various amplitude have been mapped. The most prominent one joins the Owen Fracture Zone to the triple junction, the so-called SW-NE Murray Ridge. Some smaller ridges, with the same orientation are entering the frontal deformation zone and nearly parallel to it (i.e. the "Little Murray Ridge", White, 1983).

Along-strike variations of the tectonic style are illustrated on the two N-S profiles CHAMAK 5 (Fig. 7) and CHAMAK 8 (Fig. 8), which are located in the central part of the Pakistani Makran, where the deformation front's shape reflects a non-cylindrical deformation along strike. On profile 5 (Figs. 3 & 7), the deformation front is characterized by the development of a single thrust more than 20 km off the previous frontal sheet, rooted on more shallow detachment level than the level implied in the inner thrusts.

South of the Makran accretionary prism front, an alignment of sea-mounts following a rough NE-SW direction enters progressively into the subduction zone. An abnormally elevated zone along the Makran prism leads straight to one of these seamounts, suggesting that the ridge has been partly subducted and has resulted in a significant uplift of the prism (Fig. 9, profile C).

The geometry of the front is very different on CHAMAK 8 (Fig. 8), where the frontal part is formed by the stacking of several thrust sheets, resulting in a drastic sharpening of the surface geometry profile. The nature of the seamount at the front is complex. It is clearly related to an old basement high corresponding originally to a horst structure which has probably been reactivated very recently by the seaward migration of the compressional front. This strong heterogeneity in the subducted plate may be related to the blocking of the deformation which will not propagate southward until a critical stability profile will be reached.

A morphological analysis of the prism surface has been performed in order to characterize the morphological effects of the subducted ridge along several morphological sections perpendicular (N-S, dip) or parallel (E-W, along-strike) to the prism. Dip sections allow us to compare the bathymetric level of the piggy-back basins. The two western profiles A and B (Fig. 9) are located out of the so-called "uplifted zone" and there flat areas corresponding to piggy-back basins level are approximately at the same depth. In Fig. 9, one section crosses the uplifted zone (profile C) while the other is out of this zone. All flat areas corresponding to piggy-back basins are shifted and an offset of 400–500 m can be measured.

This offset is also observed along the northern escarpment but rapidly disappears north of it. The area of the prism uplifted due to subduction of the LMR is 40–50 km long (N-S direction) and is 20–30 km wide (E-W direction).

6.2 Sedimentation Rates and Location of the Depocentres

We have observed above that the wavelength between two tectonic units is neither constant along dip nor along strike. Along the frontal part, the thickness of the sedimentary sequence above the regional unconformity involved in the thrusting, varies from 1.5 s TWT to the east to 3 s to the west. It is clear that at present the distribution of eroded products is not two-dimensional over the offshore domain. In the eastern side, presenting a more condensed deformation along dip, the dominant process is the progradation of the shelf to the south. Then, most part of the sedimentary input is trapped in the Upper Margin with a few sediments deposited in the piggy-back basins. Due to a strong water flow, probably the lightest part of the sediment could be transferred to the abyssal plain very dynamically through a ‚canyon network' in a probably steady-state process. Some catastrophic events could sometimes allow the transfer of heavier material to the abyssal plain, expressed as turbidite systems, which can be deposited far from the canyon mouth.

To the west, sedimentation is more regular and evenly distributed between the shelf, the piggy-back basins and the abyssal plain. The sedimentary sequence filling the foreland basin is thickening from the CH 09 to CH 11 toward the Iranian border and gets much thicker offshore Iran (Grando and McClay, 2006).

Fig. 7. Interpretation of the seismic profile Chamak number 5 (CH05)

Fig. 8. Interpretation of the seismic profile Chamak number 8 (CH08)
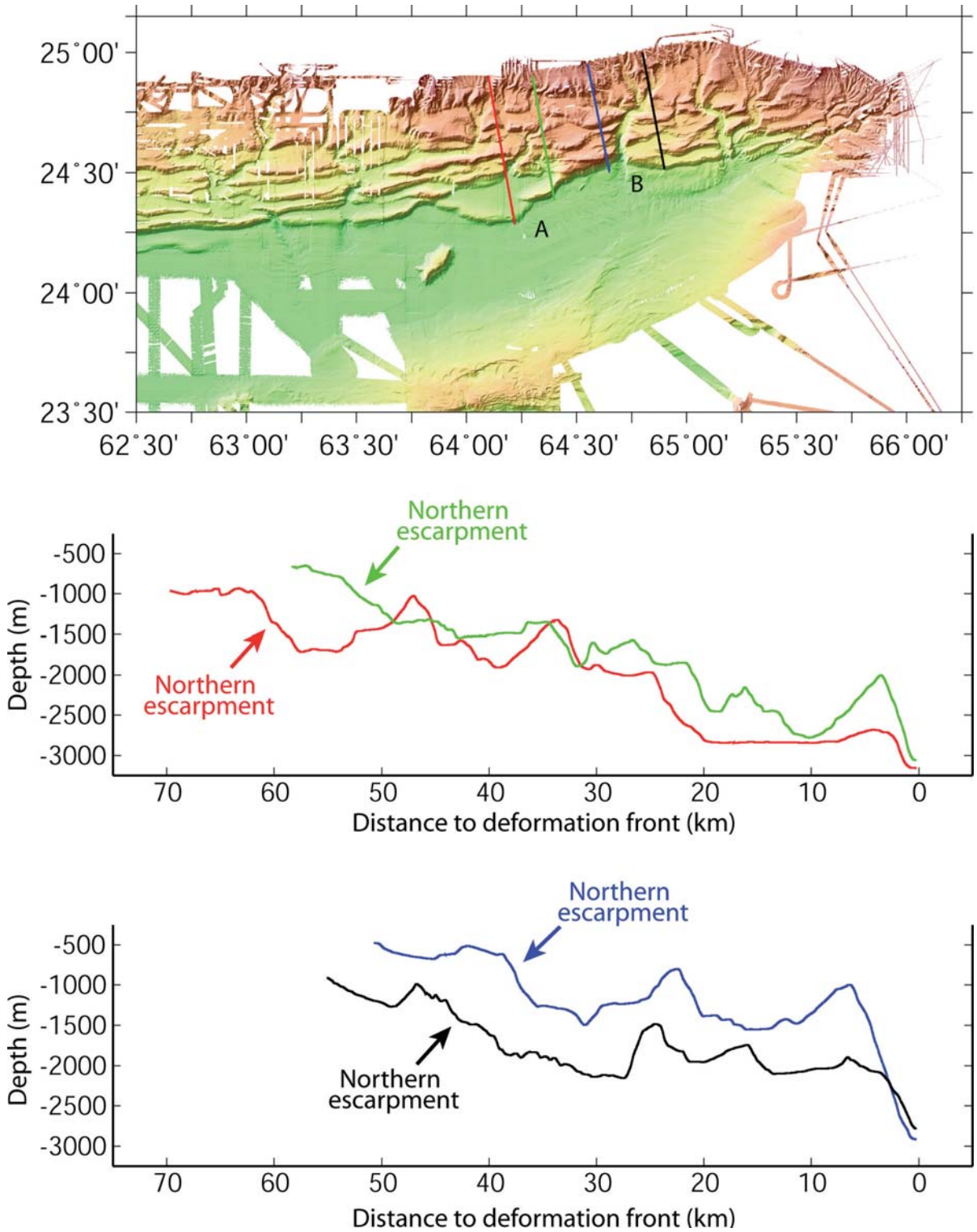
Fig. 9. Bathymetry variation profiles related to the subduction of an oblique ridge

6.3 Change in the Deformation Front in the Vicinity of the Triple Junction

The precise location of the triple junction between Arabian, Indian and Eurasian plates is not well identified. It joins (1) the southernmost part of the India/ Eurasia transform system, which is represented by N-S trending series of left-lateral strike-slip crustal faults, which developed progressively toward the Southwest, since Oligocene times. The Chaman, Ghazaband and Ornachnal faults have been connected at each stage to the paleo-subduction front. In the present-day situation it is probable that the triple junction lies below the offshore extension of the Bela Depression.

The Plio-quaternary sediment thickness increases significantly toward the east. In fact, all the erosion products from the prism and Inner Baluchi Ranges (along Chaman and Ornachnal system and Mor Range) are drained up to the Bela depression, and then deposited over the eastern termination of the subduction front. In this situation, due to extremely high sedimentation rates in the extreme Eastern offshore part, the deformation is less well expressed at surface except if shallower décollement levels have been locally used, or alternatively as mud volcanoes or normal compensation faults. The triple junction is not visible at the sea floor because of deep accommodation of this active convergence (early collision?), it cannot emerge and is migrating through time to the south-east. Further complexity arises from intra-plate deformation within the Indian Plate, expressed as a series of E-W trending "en échelon" fold and fault systems, joining the Kirthar Ranges and the offshore Karachi.

Conclusions

Our survey confirms the previous first-order interpretation of a sea-floor morphology tectonically controlled by the offscraping of the Makran into large thrust packets involving the Makran units deposited in the trench. We also confirm that the anticlinal ridges are suffering a much stronger erosion than most of the other accretionary prisms, probably caused by a rapid uplift related to the shortening of thick units. Despite an apparent linearity of the accretionary system at a broad scale, the preliminary results of our survey indicate a significant local non-linearity of the deformation front. The variation in tectonic style along strike is linked to two interacting factors: 1) architecture of the subducting plate where oblique ridges, the Little Murray Ridge and some seamounts parallel to the Murray Ridge (s.s.) have been identified, and

2) variation along strike of the sedimentation rates, due to a change in the location of the sediment supply source - i.e. Indus (draining Himalayan erosion products), or sediment directly derived from erosion of the prism itself since Late Miocene times. The new dating and determination of paleoenvironments from a previous study conducted onshore Makran (Ellouz et al. this issue) identified a dramatic change of the main sedimentary supply at the end of Miocene times.

The structural interpretation first outlines the strong variation in architecture of the frontal part of the prism along strike, linked with the geometry of the subducted plate, depth to the décollement and sedimentary rates variation. The connection between the onshore part and the highly deformed offshore part of the prism is expressed by a large shelf platform, showing little internal deformation but bounded to the south by a major fault (northern escarpment).

Acknowledgements

References

Barton PJ, Owen TRE, White RS (1990) The deep structure of the east Oman continental margin: preliminary results and interpretation. Tectonophysics 173(1–4):319–331.

Bernard A, Munschy M (2000) Le bassin des Mascareignes et le bassin de Laxmi (océan Indien occidental) se sont-ils formés à l'axe d'un même centre d'expansion ?: Were the Mascarene and Laxmi Basins (western Indian Ocean) formed at the same spreading centre? Comptes Rendus de l'Académie des Sciences - Series IIA - Earth and Planetary Science 330(11):777–783.

Bhattacharya GC, Chaubey AK, Murty GPS, Srinivas K, Sarma KVLNS, Subrahmanyam V, Krishna, KS (1994) Evidence for seafloor spreading in the Laxmi Basin, northeastern Arabian Sea. Earth and Planetary Science Letters 125(1–4):211–220.

Byrne DE, Sykes LR, Davis DM (1992) Great thrust earthquakes and aseismic slip along the plate boundary of the Makran subduction zone. 97(B1):449–478.

Calais E, DeMets C, Nocquet J-M (2003) Evidence for a post-3.16-Ma change in Nubia-Eurasia-North America plate motions? Earth and Planetary Science Letters 216(1–2):81–92.

Chaubey AK, Dyment J, Bhattacharya GC, Royer JY, Srinivas K, Yatheesh V (2002) Paleogene magnetic isochrons and palaeo-propagators in the Arabian and Eastern Somali basins, NW Indian Ocean. In: Clift PD, Gaedicke C, Craig J (eds). The tectonic & climatic evolution of the Arabian Sea region. Geological Society of London, pp 71–85.

Chaubey AK, Bhattacharya GC, Murty GPS, Srinivas K, Ramprasad T, Gopala Rao T (1998) Early Tertiary seafloor spreading magnetic anomalies and paleo-propagators in the northern Arabian Sea. Earth and Planetary Science Letters 154:41–52.

Cochran JR (1988) Somali basin, chain ridge, and origin of the northern Somali basin gravity and geoid low. Journal of Geophysical Research 93(10):11985–12008.

Delisle G., von Rad U., Andruleit H., von Daniels C.H., Tabrez A.R. & Inam A., 2001. Active mud volcanoes on - and offshore eastern Makran, Pakistan. Int J. Earth Sciences (Geol Rundsch), v. 91, pp 93–100.

DeMets C, Gordon RG, Argus DF, Stein S (1994) Effect of recent revisions to the geomagnetic reversal time scale on estimates of current plate motions. Geophysical Research Letters 21(20):2191–2194.

Edwards RA, Minshull TA, White RS (2000) Extension across the Indian-Arabian plate boundary: the Murray Ridge. Geophysical Journal International 142(2):461–477.

Ellouz N., Deville E., Müller C., Lallemant S., Subhani A. and Tabreez A. (2007) Tectonic evolution versus sedimentary budget along the Makran accretionary prism (Pakistan), this issue.

Flueh ER, Kukowski N, Reichert C, cruise participants (1997) F.S. SONNE Cruise Report SO 123, MAMUT, Kiel. GEO-MAR Rep 62.

Fournier M, Patriat P, Leroy S (2001) Reapraisal of the Arabia-India-Somalia triple junction kinematics. Earth and planetary science letters 189:103–114.

Fruehn J, White RS, Minshull TA (1997). Internal deformation and compaction of the Makran accretionary wedge. Terra Nova 9: 101–104.

Gordon RG, DeMets C (1989) Present-day motion along the Owen fracture zone and Dalrymple trough in the Arabian Sea. Journal of Geophysical Research 94:5560–5570.

Grando G., McClay K. (2006), Morphotectonics domains and structural styles in the Makran accretionary prism, offshore Iran. Sedimentary Geology (in press).

Gutscher MA., Klaeschen D., Flueh E., Malavieille J. (2001), Non-Coulomb wedges, wrong-way thrusting, and natural hazards in Cascadia. Geology, 29, 5: 379–382.

Harms JC, Cappel HN, Francis DC (1984) The Makran coast of Pakistan: it's stratigraphy and hydrocarbon potential. In: Haq BU, Milliman JD (eds). Marine geology and oceanography of Arabian Sea and coastal Pakistan, pp 3–26.

Hay, W.W., DeConto, R., Wold, C.N., Wilson, K.M., Voigt, S., Schulz, M., Wold-Rossby, A., Dullo, W.-C., Ronov, A.B., Balukhovsky, A.N. and E. Soeding (1999): ALTERNATIVE GLOBAL CRETACEOUS PALEOGEOGRAPHY, in Barrera, E. and Johnson, C. (eds.), The Evolution of Cretaceous Ocean/Climate Systems, Geological Society of America Special Paper 332, pp. 1–47.

Jacob KH, Quittmeyer RL (1979) The Makran region of Pakistan and Iran: Trench-arc system with active plate subduction. In: Farah A, DeJong,KA (eds). Geodynamics of Pakistan, Quetta. Geological Survey of Pakistan, pp 305–317.

Kopp C., Fruehn J., Flueh E.R., Reichert C., Kukowski N., Bialas J., Klaeschen D. (2000),.Structure of the Makran subduction zone from wide-angle and reflection seismic data. Tectonophysics 329,1,:171–191.

Kukowski N, Schillhorn E, Flueh ER, Huhn K (2000) Newly identified strike-slip plate boundary in the northeastern Arabian Sea. Geology 28(4):355–358.

Laane JL, Chen W-P 1989 The Makran earthquake of 1983 April 18: A possible analogue to the Puget Sound earthquake of 1965? Geophysical Journal International 98(1):1–9.

Pichon X, Henry P, Lallemant SJ (1993) Accretion and erosion in subduction zones: the role of fluids. Annual Review of Earth and Planetary Sciences 21:307–332.

Leroy S, Gente P, Fournier M, D'Acremont E, Patriat P, Beslier M-O, Bellahsen N, Maia M, Blais A, Perrot J, Al-Kathiri A, Merkouriev S, Fleury J-M, Ruellan P-Y, Lepvrier C, Huchon P (2004) From rifting to spreading in the eastern Gulf of Aden: a geophysical survey of a young oceanic basin from margin to margin. Terra Nova 16(4):185–192.

Matthews DH (1966) The Owen fracture zone and the northern end of the Carlsberg Ridge. Philosophical Transactions of the Royal Society of London 259:172–186.

Minshull TA, White RS, Barton PJ, Collier JS (1992) Deformation at plate boundaries around the Gulf of Oman. Mar. Geol. 104: 265–277.

Mountain GS, Prell WL (1990) A multiphase plate tectonic history of the southeast continental margin of Oman. Geological society special publications 49:725–743.

Mountain GS, Prell WL (1989) Geophysical reconnaissance survey for ODP Leg 117 in the northwest Indian Ocean. In: Stewart NJ (ed). Proceedings of the Ocean Drilling Program, Initial Reports, 117. Ocean Drilling Program, College Station, TX, pp 51–64.

Norton IO, Sclater JG (1979) A model for the evolution of the Indian Ocean and the breakup of Gondwanaland. Journal of Geophysical Research 84(12):6803–6830.

Patriat P, Achache J (1984) India-Eurasia collision chronology and its implications for crustal shortening and driving mechanisms of plates. Nature 311:615–621.

Prins MA, Postma G, Weltje GJ (2000) Controls on terrigenous sediment supply to the Arabian Sea during the Late Quaternary: the Makran continental slope. Marine Geology 169(3–4):351–371.

Qayyum M, Lawrence RA, Niem AR (1997) Molasse-Delta-Flysch continuum of the Himalayan orogeny and closure of the Paleogene Katawaz remnant ocean, Pakistan. International Geology Review 39:861–875.

Quittmeyer RC, Kafka AL (1984) Constraints on plate motions in southern Pakistan and the northern Arabian Sea from the focal mechanisms of small earthquakes. Journal of Geophysical Research 89(4):2444–2458.

Schlüter H.U., Prexl A., Gaedicke Ch., Roeser H., Reichert Ch., Meyer H., von Daniels C. (2002) The Makran accretionary wedge: sediment thicknesses and ages and the origin of mud volcanoes. Marine Geology 185 (2002) 219–232.

Sella GF, Dixon TH, Mao A (2002) REVEL: a model for recent plate velocities from space geodesy. Journal of Geophysical Research 107(B4):2081.

Smit JHW, Brun JP, Sokoutis D (2003), Deformation of brittle-ductile thrust wedges in experiments and nature, Journal of Geophysical Research 108, B10, 2480, doi:10.1029/2002JB002190.

Sykes LR (1968) Seismological evidence for transform faults, seafloor spreading, and continental drift. In: Phinney RA (ed). The History of the Earth's Crust. Princeton University Press. Princeton, NJ, pp 120–150.

Vigny C, Huchon P, Ruegg J-C, Khanbari K, Asfaw LM (2006) Confirmation of Arabia plate slow motion by new GPS data in Yemen. 111:B02402.

Von Huene R, Scholl DW (1991) Observations at convergent margins concerning sediment subduction, subduction erosion, and the growth of continental crust, Reviews of Geophysics 29(3):279–316.

White RS, Klitgord KD, (1976) Sediment deformation and plate tectonics in the Gulf of Oman. Earth Plan. Sci. Lett. 32: 199–209.

White RS, (1982) Deformation of the Makran accretionary sediment prism in the Gulf of Oman (north-west Indian Ocean). In: Leggett, J.K. (Ed.), Trench and Fore-Arc Geology: Sedimentation and Tectonics on Modern and Ancient Active Plate Margins, pp. 357–372.

White RS, Louden KE, (1983) The Makran Continental Margin: Structure of a Thickly Sedimented Convergent Plate Boundary.Studies in Continental Margin Geology, Watkins and, J.S., Drake, C.L. (Eds.). Mem. Am. Ass. Petrol. Geol. 34: 499–518.

White RS, (1983) The Little Murray Ridge. Seismic Expression of Structural Styles, Bally, A. (Ed.), AAPG Stud. Geol. 15: 1.3.19–1.3.23.

Whitmarsh RB (1974) Some aspects of plate tectonics in the Arabian Sea, in Leg XXXIII. In: Whitmarsh RB, Weser OE, Ross DA et al. (eds). Initial Reports of the Deep Sea Drilling Project, 23, US Government Printing Office, Washington DC, pp 527–535.

Part VI
Carpathian Thrust Belt

Part VI is focused on Carpathian case studies, with one paper dealing with the interactions between the Southern Carpathians and Moesia in Romania, the three others discussing the frontal triangle architecture, reservoir quality and petroleum systems in the Carpathian foreland in Poland.

Tarapoanca et al. (Chapter 19) document the complex interactions between Moesia and the Carpathians, and the role of pre-existing structures inherited from the former passive margin and Cretaceous orogen during subsequent transcurrent deformation and Neogene lateral escape of the arc.

Krzywiec and Vergés (Chapter 20) compare the triangle zone development in front of the Polish Outer Carpathians and Southern Pyrénées thrust front, respectively, in relation with the occurrence and distribution of evaporite horizons in adjacent foredeeps.

Lesniak et al. (Chapter 21) discuss the distribution, sedimentology, diagenesis and reservoir potential of Miocene sandstone horizons in the Carpathian foredeep in southeastern Poland.

Matyasik et al. (Chapter 22) describe a petroleum occurrence in Devonian carbonate reservoirs of the Carpathian foreland in Poland, and discuss the related petroleum system on the basis of new analytical results.
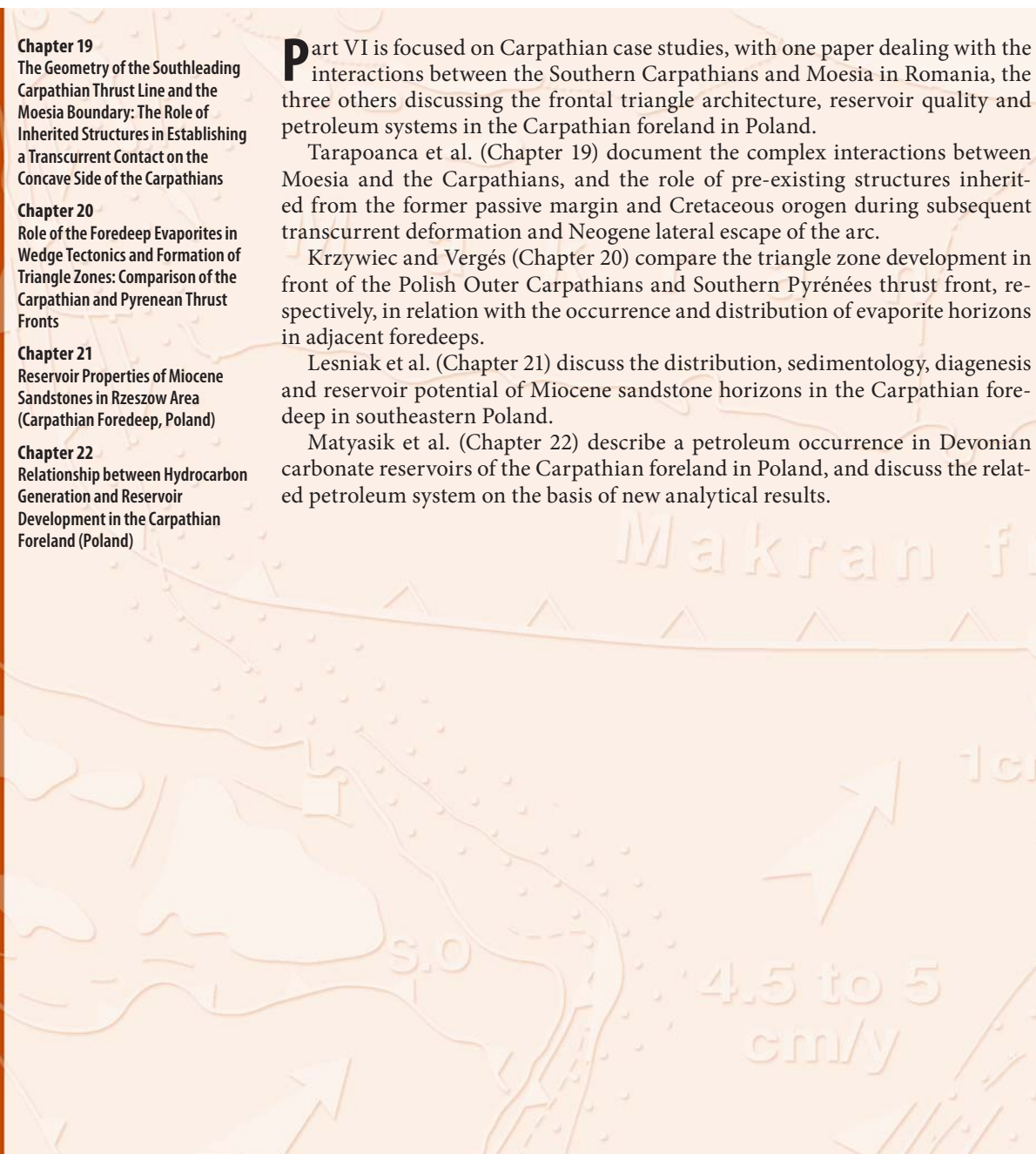
The Geometry of the South Leading Carpathian Thrust Line and the Moesia Boundary: The Role of Inherited Structures in Establishing a Transcurent Contact on the Concave Side of the Carpathians

Mihai Tarapoanca · Dorina Tambrea · Victor Avram · Bogdan Popescu

Abstract The NW-most corner of Moesia offers the possibility to unravel the structural architecture as well as the kinematic characteristics of a highly-bent contact between an orogenic nappe pile and its foreland plate. The major fault system, dominantly transcurent that accommodated during the Tertiary the displacement and rotation of the Latest Cretaceous Carpathian orogenic wedge around the Moesian corner had originated from a passive margin stage when W-E to WNW-ESE extensional faulting predated the formation of the Late Jurassic Severin oceanic crust. In the NW-most Moesia, these old structures are cut by an E-W-trending major normal fault system which accommodated the Late Oligocene (?) - Burdigalian dextral movements of the Carpathian units along the Timok lineament. Structural evidence shows that this initially rather straight N-S dextral transfer fault evolved into a curved anastomozed system parallel to the present-day shape of the orogen not earlier than the Middle Miocene. This was at the time when the Carpathian units commenced to rotate around the Moesian corner along the original Timok and one of the major E-W-trending normal faults. Farther ENE- to E-wards displacement of the Carpathian units along the northern margin of the Moesian plate induced an oblique inversion of the Mid-Tertiary extensional basin by peeling-off E-SE-wards its sedimentary fill. Overall, the inversion created a duplex-style system that changes E-wards to a major plan-view wedge bounded by a NW-SE dextral tear fault passing gradually to the thin-skinned Subcarpathian nappe. In this contribution we stress the role of inherited structural weaknesses within the foreland plate in the creation of a transcurent contact.

Keywords. Transcurent fault, Thrust belt, Plate boundary, Carpathians, Moesia, Timok Fault

1 Introduction

One of the most arcuate segments of the Alpine chain is represented by the South Carpathians where the strike of the orogen changes from E–W to N–S and then again E–W to the Balkans (Fig. 1). The present-day structure of the Carpathian system is the result of a long-lasting evolution that included periods of:

a) lithospheric stretching and break-up;

b) plate convergence and collision;

c) orogen-parallel extension and core-complex formation;

d) rotation and wrenching;

e) basin opening and inversion (e.g. Sandulescu, 1984).

Following the Mid-Cretaceous subduction of the entire Severin oceanic crust which had separated during at least Late Jurassic-Early Cretaceous two pieces of lithosphere derived from the European margin (Dacia and Moesia), the ongoing contraction led eventually to the overthrusting of the Supragetic/Getic/Severin nappe assemblage onto the distal Moesia (exposed presently as the Danubian Autochthonous unit). It also generated duplex formation inside the latter by Late Cretaceous times (e.g. Sandulescu, 1984; Iancu et al., 2005). The further Tertiary kinematics is rather complex, however the overall picture of mechanisms of the tectonic transport of the Carpathian units towards the present-day position around the Moesia corner is generally accepted (e.g. Ratschbacher et al., 1993; Schmid et al., 1998).

The present-day South Carpathians are flanked by a deep foreland basin that has been deformed in response to the progressive movement of orogenic slices around the Moesian western corner. This foreland basin differs significantly from typical foredeeps because the flexural loading of the foreland lithosphere played only a subordinate role in its subsidence (Rabagia and Matenco, 1999; Tarapoanca, 2004).

In this contribution we focus on the South Carpathians Thrust Belt / Moesia boundary and especially on the NW corner of Moesia (Fig. 1), aiming to describe new details concerning the geometry of the contact as well as the tectonic evolution. Our study is mainly based upon the interpretation of new seismic lines acquired mid-2005 across the northern part of the Timok lineament and inside the neighboring basin. They are supplemented by re-interpreted information from older surveys and wells previously drilled within a concession currently explored by Rompetrol. The subsurface data were particularly useful as the contact between the South Carpathians and Moesia is
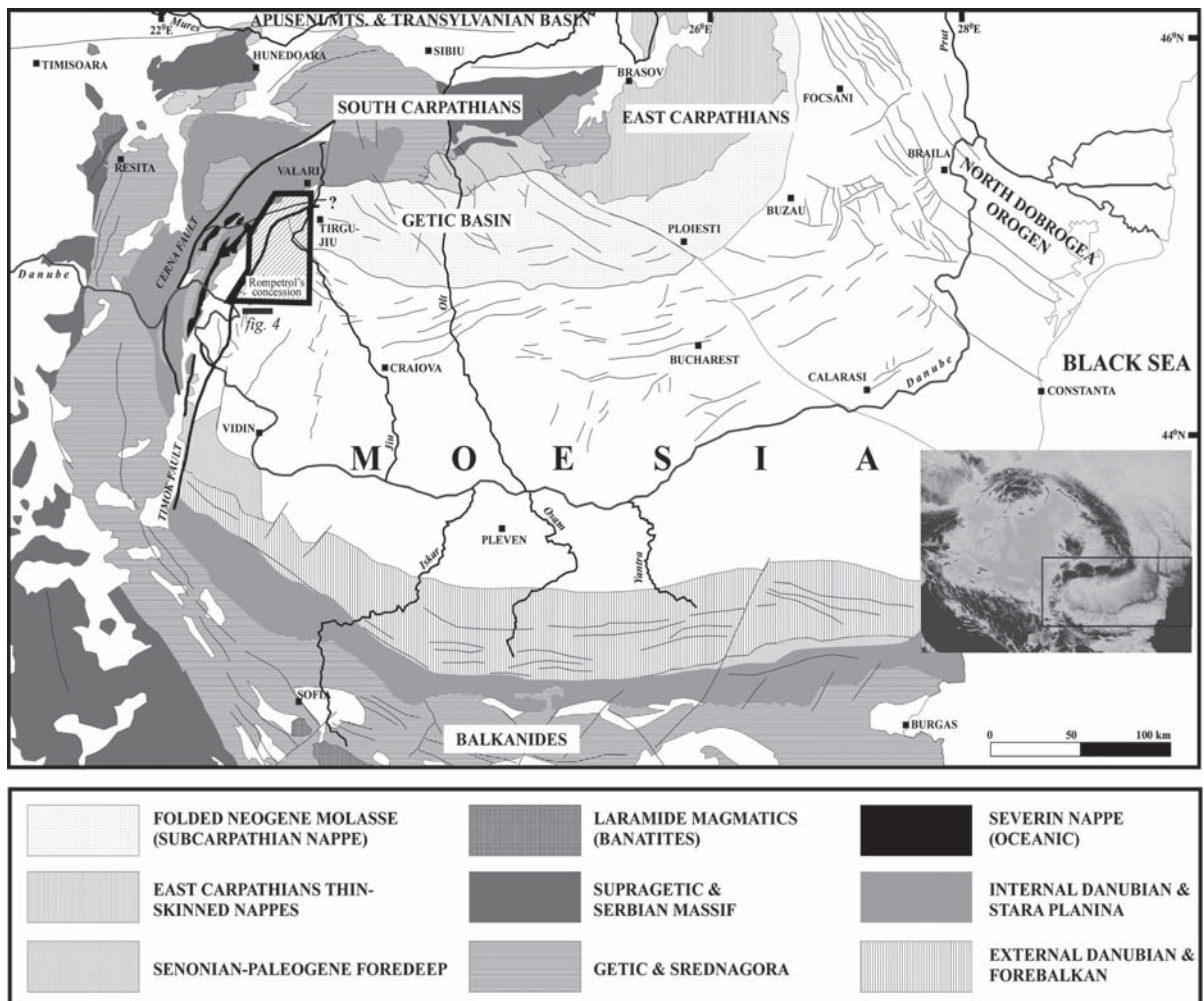
Fig. 1. Major structural units of the Carpato-Balkan thrust belt (modified from Sandulescu, 1988; Tari et al., 1997 and Iancu et al., 2005). The structures from Getic Basin are schematically drawn after Rabagia and Matenco (1999) and those from Moesia (north of Danube River) are taken from Tarapoanca (2004). The Pliocene fill over Moesia and Carpathians was ignored. The thick E-W black line in the westernmost part of Moesia represents the location of the interpreted seismic line shown in Fig. 4. The inset map only shows the topography of the East Alpine-Dinarides-Carpathians realm. The location of our study (NW Moesia) is indicated by the outline of the Rompetrol's concession

hidden by the Neogene sedimentary fill which onlaps onto a Getic klippe to the south and directly onto the Danubian Autochthonous to the north (Fig. 1).

We shall argue that the geometry of the contact between the orogen and foreland is largely controlled by an extensional fault system formed presumably prior to the creation of the oceanic lithosphere (Severin domain). The integration into a regional tectonic framework of the architecture of this older system will result in our sense in a significant advancement to the knowledge of the relationship between the South Carpathians and Moesia. We have devoted particular attention to the impact of the transcurent displacement of the orogenic units upon the Moesian foreland, particularly the opening of an extensional basin during the Late

Oligocene (?) – Burdigalian (hereinafter named Mid-Tertiary). Eventually, the structural setting of the NW Moesian basin is briefly discussed from the standpoint of petroleum systems aiming to shed light on further exploration options.

2   Disruption of the Cretaceous Carpathian Areas: Synthesis of the Tertiary Tectonics

We shall describe in this section the main deformation stages taking place in both the westernmost Moesian realm and the Carpathian nappe pile after they became welded together in Late Cretaceous times. Significant advances in the understanding of many

Fig. 2. Schematic reconstructions of the Carpathians / Moesia major events postdating the Latest Cretaceous collision. The figures are largely based upon Fig. 9 of Fugenschuh and Schmid (2005) with additional information on Moesia from Tarapoanca (2004) and present contribution
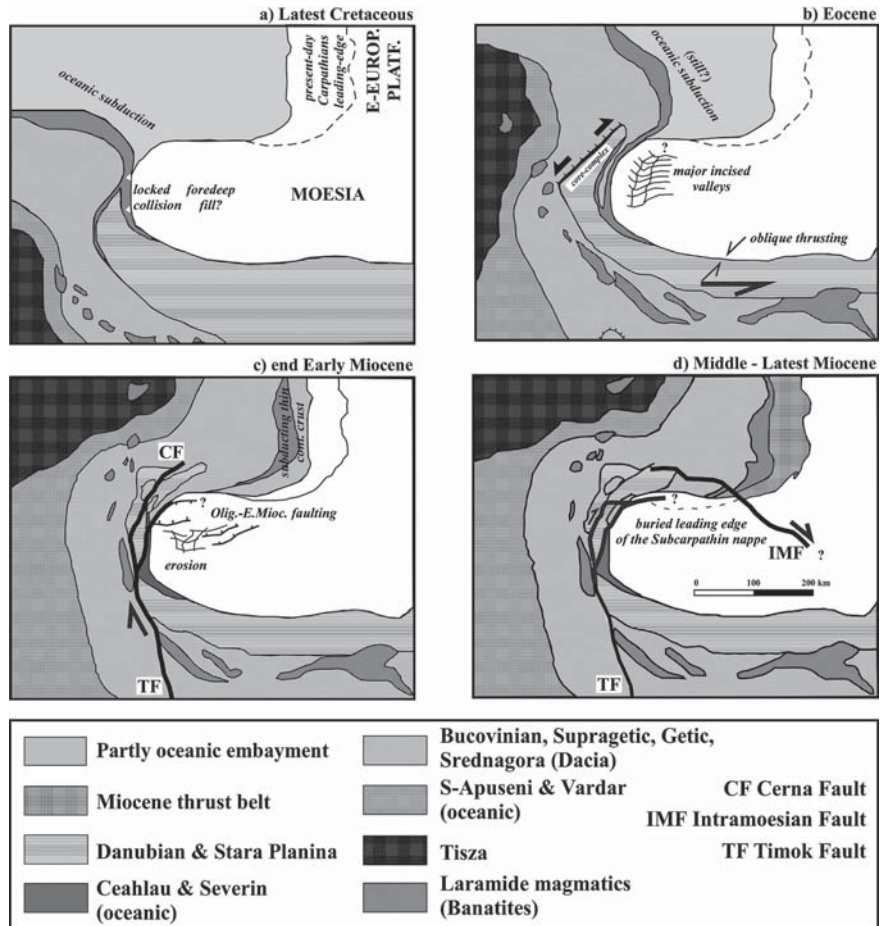
of the peculiarities of this curved orogenic boundary were published in the last decade and derive mainly from structural and fission-tracks studies carried out in the South Carpathians by, e.g., Ratschbacher et al. (1993), Schmid et al. (1998), Matenco and Schmid (1999), Rabagia and Matenco (1999), Willingshofer et al. (2001), subsequently integrated at orogenic scale by Fugenschuh and Schmid (2005). Their regional picture is employed as the main source for the next overview of the Tertiary evolution.

Palinspastic restoration of the Tertiary convergence brings the Carpathian units next to the westernmost part of Moesia by the Latest Cretaceous, facing to the north an oceanic embayment which was completely subducted during the Paleogene (Fig 2a). Remnants of the associated Latest Cretaceous-Paleocene foredeep are found exposed to the SW and N (Fig. 1) as well as in the subsurface of the Getic Basin, while in westernmost Moesia they were largely removed by the subsequent erosion. This erosion which created deep canyons (Paraschiv, 1997; Tarapoanca, 2004) was presumably mostly Eocene in age and coeval, possibly genetically-related, with an orogen-parallel extension

leading to core-complex formation in the Carpathians (Fig. 2b) and with the sinistral shortening in the E-W segment of the Balkanides (Doglioni et al., 1996).

The tectonic transport of the Carpathians around the Moesian corner during the Oligocene was mostly accommodated by dextral wrenching of some 35 km along the Cerna Fault (Berza and Draganescu, 1988, Fig. 2c). The movement continued during the Early Miocene when the accommodating structure became the more externally Timok Fault. The Timok Fault took over some 65 km of dextral displacement (cf. Moser, 2001 in Fugenschuh and Schmid, 2005). Contemporaneously to the transcurrent movements of the orogenic slices, normal faulting and basin opening occurred in the northern Moesian margin (Rabagia and Matenco, 1999) when still some erosion was probably active on the distal, southern Moesia (Tarapoanca, 2004). Moreover, the orogenic nappe pile itself seems to be severely affected by normal faulting as well (Matenco and Schmid, 1999; Fugenschuh and Schmid, 2005).

Starting with the Middle Miocene, the transport of the Carpathian units has further changed to a more ENE-to-E-wards orientation (Hippolyte et al., 1999),

with several E-W and NW-SE dextral faults cutting through the nappe pile and the foredeep fill (Matenco et al., 1997; Rabagia and Matenco, 1999; Matenco and Schmid, 1999). Overall, the Getic Basin or the "Getic Depression" as known in older Romanian literature (i.e., the early foredeep fill of the South Carpathians) has undergone oblique shortening culminating with the emplacement of the Subcarpathian Nappe (Fig. 2d).

3   Geometry of the Orogen / Foreland Boundary and Overview of the Basin Structure

The structural pattern of the NW-most Moesia, as shown in Fig. 3, mainly resulted from the interpretation of several hundreds of kilometers of 2D seismic lines including 250 line km acquired in the summer of 2005. The most striking feature is represented by the sizeable difference in elevations of the base Tertia-ry (Fig. 3a) across the Timok Fault that ranges from several hundreds of milliseconds to more than 2 seconds TWT (corresponding to around 2.5–3 km!). The Timok Fault system is parallel to the present concave bend of the South Carpathians and marks the western limit of a basin that hosts several kilometers-thick sediments mostly of Neogene age. In our study area, the basin floor represented by the regional erosional unconformity that is developed on top of the dominantly carbonatic (Upper Jurassic - Cretaceous) Moesian platform, deepens from around 1.3 s (~ 1.5 km) in the south to more than 5 s (~ 6.5 km) in the NE.

To the east of the Timok Fault, two roughly perpendicular, normal fault systems are mapped:

1. The E-W-oriented one that has the largest offsets at the basin bottom (Fig. 3a) and is mostly Mid-Tertiary in age;
2. The N-S to NE-SW older system (Fig. 3b) that originates presumably from the Permo-Triassic rift-
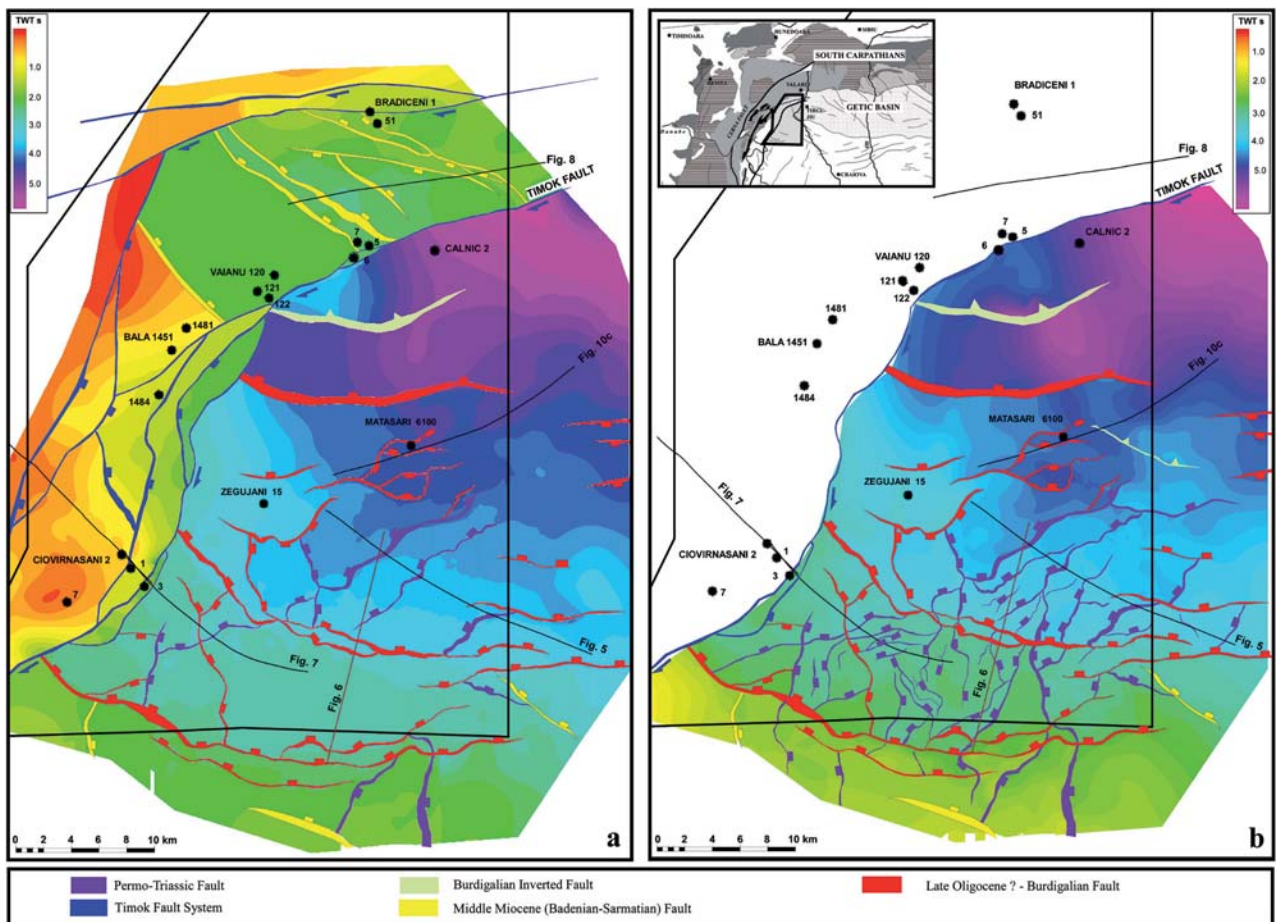
Fig. 3. Structural maps (TWT) of the top of the Moesian platform – base Tertiary unconformity (**a**) and base syn-rift (Paleozoic?) horizon (**b**). Note that the color bar in a. is different from that in b. The location of the seismic lines used in some figures is also shown. Maps location is shown in Fig. 1

ing associated to a passive margin stage. Some of these old faults were slightly rejuvenated during the younger faulting stage (compare Fig. 3b with 3a). The map at the base of the old syn-rift horizon (Fig. 3b) shows basins sometimes as deep as 1 s (over 1 km).

The superposition of these orthogonal extensional events unsurprisingly led to a highly complicated structural style of the NW Moesia (e.g. Fig. 3b). The detailed structural pattern and formation mechanisms are to be discussed below, with the older system addressed first.

3.1 Western Moesia as a Mesozoic Faulted Passive Margin

The Timok Fault has been for some time proposed as a transcurent, loose boundary between the South Carpathian Cretaceous nappe pile and Moesia (e.g. Sandulescu, 1984, 1988). So far, this boundary has been generally seen as separating (Fig. 1) a piece of the basically undeformed continental lower plate (Moesia) from an assemblage that contains remnants of the upper plate (Supragetic/Getic nappes and Balkanides equivalents), a suture (Severin domain, made up of fragments of oceanic lithosphere and overlying Uppermost Jurassic – Lower Cretaceous flysch sediments) and the so-called Danubian Autochthonous. The last is nothing but the distal underthrust margin of Moe-

sia duplicated in the aftermath of Cretaceous collision (e.g. Sandulescu, 1984; Iancu et al., 2005).

Although any creation of oceanic lithosphere implies previous stretching (rifting) of the continental lithosphere, in this case, Moesia had long time "appeared" as lying far from the ancient locus of the rifting. The closest rift that pre-dated the "Severin" spreading was seen located a few hundreds of kilometers to the SE (central-southern Moesia, Tari et al., 1997) and only the wrenching seemed to be responsible for bringing the South Carpathian nappe pile next to the unstretched Moesia (e.g. Ratschbacher et al., 1993). However, very recently, Matresu and Dinu (2004) identified a series of N-S trending extensional basins (Fig. 4) in the westernmost part of Moesia, developing on a quite limited length of around 25 km. A system of E-dipping normal faults bounds half-graben basins which are capped by an erosional unconformity. Although deep well evidence is scarce enough, Matresu and Dinu (2004) tentatively assigned the syn-rift fill of those basins to a Lower Paleozoic age.

Alternatively, we propose in this paper that the age of the E-W extension is most likely Permian (?) - Triassic as similar to that previously proposed for most of the central Moesia (Tari et al., 1997; Rabagia and Tarapoanca, 1999), supported also by the quite widespread coevally bimodal volcanism (e.g. Paraschiv, 1979). We thus consider the N-S trending extensional basins in the western Moesia as resulting from a regional rifting event that pre-dated the onset of spreading and creation of the Severin oceanic crust.
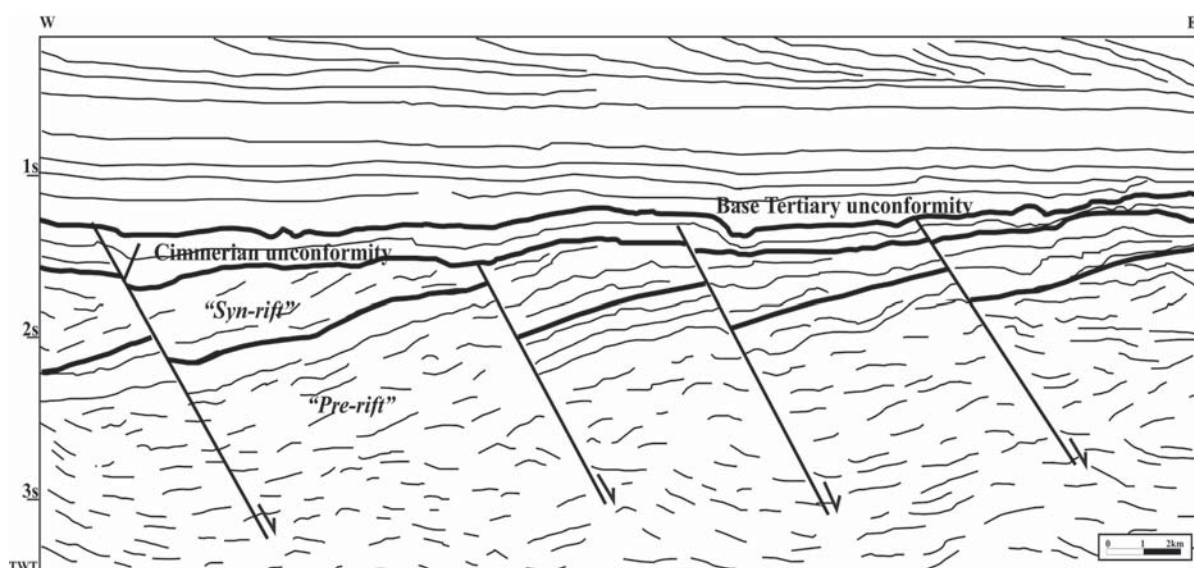
Fig. 4. E-W interpreted seismic line in westernmost Moesia (modified after Matresu and Dinu, 2004). Note that the normal faults bounding the half-grabens are slightly reactivated as proved by the offset of the Cimmerian unconformity. Line location is shown in Fig. 1

Accordingly, the regional unconformity that develops in those basins (Fig. 4) should be mostly Lower Jurassic in age being similar to the Cimmerian unconformity of Tari et al. (1997) and supported by the large well database of Moesia (e.g. Paraschiv, 1979). It may represent in fact either a break-up unconformity related to the onset of "Severin" spreading or the expression of a partial inversion and uplift due to slow stretching-related rift migration as proposed for the mid-Norwegian margin by van Wijk and Cloetingh (2002) in an attempt to model the occurrence of local contraction in the context of overall extension.

Significant for unraveling the configuration of the western Moesian passive margin, we have identified the extension farther north of these N-S basins, however in a more complex structural style. They are represented in Fig. 3b by the N-S normal fault system that progressively changes the orientation to NE-SW, which is subsequently truncated by a younger E-W system. Some of these old faults were slightly reactivated in the Mid-Tertiary, as shown in Figs. 4, 5 and 6. Although there are no wells that penetrated the base Tertiary unconformity in our study area from the NW Moesia, the structural style imaged by the seismic lines (Figs. 5 and 6) looks very similar to those shown elsewhere in Moesia. Transfer zones make the transition between E- and W-dipping normal faults (Fig. 3b) giving a general configuration of basins and ranges. It thus appears that the more oriented towards an E-W direction, the more prone to be reactivated were these ancient faults during the later N-S extension.

3.2 Timok Fault System and the Edge of the Cretaceous Orogenic Pile

In contrasts to the parallel, outcropping dextral Cerna Fault, which was active mainly during the Oligocene times (Berza and Draganescu, 1988; Ratschbacher et al., 1993), the Timok Fault had a longer tectonic activity. Outcropping only to the south of Danube River, the Timok Fault becomes progressively buried towards north by the Upper Miocene - Pliocene sediments (Fig. 7). It shows up as an impressive flower structure separating the uplifted outer part of the Getic/Severin nappe welded to the Danubian Autochthonous from the deep basin formed onto the Moesian lithospheric plate in the Mid-Tertiary. All the Cretaceous thrust sheets die out at the base Tertiary erosional unconformity. An erosional remnant overlying the base Tertiary unconformity, possibly Badenian in age, correlated also with the thickening of the Sarmatian sequence within the basin witnesses a stage of significant vertical differential movements across the Timok Fault during this time span.

On the map (Fig. 3a), the Timok Fault system has a curved shape, parallel to the belt curvature. However, despite the apparent continuity of the "present-day" Timok Fault, we will show in 3.4 that the curved shape of this system of faults resulted progressively not earlier than the Middle Miocene (Badenian - Sarmatian) by the merging of the original Timok with the northernmost extensional fault into an anastomosed dextral shear zone. Also then, the northern NW-trending faults bounded by the Timok Fault and another roughly E-W strike-slip (Figs. 3a and 8) were formed.

All along the curved contact between the South Carpathians and Moesia (to the north of Danube River), the Timok lineament clearly separates remnants of the Latest Cretaceous orogenic wedge from the Tertiary basin, as further indicated by the seismic line from Fig. 8. The high-amplitude W-wards dipping reflectors are interpreted as the top of the Danubian Autochthonous based upon the correlation with a perpendicular seismic line and farther north, with the outcropping units. To the easternmost part of the line, a thrust of the Getic crystalline is proposed, which would represent the southern prolongation of the Valari klippe (shown in Fig. 1). We believe that the thick reflectors package between the base Tertiary unconformity and Danubian Autochthonous is essentially a deformed pile of Late Cretaceous flysch. Apparently, two other

Fig. 5. NW-SE oriented seismic line (a. uninterpreted and b. interpreted) in the NW Moesia (location in Fig. 3). The magenta-colored faults are supposedly related to the Permian - Triassic extension (note the tilted block configuration eroded beneath the Cimmerian unconformity and compare with figure 4). A few of them were reactivated in Mid-Tertiary times (dark blue faults) when a new, orthogonal fault system was formed (light blue faults). The Cimmerian unconformity is believed to underlie a Middle Jurassic dominantly shaly (source-prone) sequence followed by an Upper Jurassic - Cretaceous dominantly carbonate platform as elsewhere in western-central Moesia. The base Tertiary unconformity is covered by a sedimentary sequence mostly Early Miocene (Burdigalian) in age. The Burdigalian salt layer is well constrained in a well (Matasari 6100 – the deepest from our study region, see Fig. 3, disposing also of a checkshot) and readily correlable due to its high amplitude and continuity at regional scale. Generally, in the Getic basin (and all along the Carpathian foredeep) the Burdigalian salt (up to several tens of meters-thick, thicker only in diapirs risen in the SE Carpathians bend area) follows an Uppermost Oligocene – Lowermost Burdigalian pelitic sequence. As the syn-rift sequence becomes increasingly thicker towards north (center of the basin), we suppose that the early syn-rift may be represented by Oligocene sediments (also reported all along the northern margin of the basin and also inside the basin farther to the east). Note the low-angle thrust initiated during the Middle Miocene (Badenian) as proved by the age of the piggy-back basin fill. F1, F2, and F3 denote faults which are mapped in Fig. 10d

NW

SE

2s

3s

4s

TWT

a

0   2   4km

NW

SE

2s

3s

4s

TWT

F1

Top Burdigalian

Earliest Badenian

Base Tertiary uncf.

F3

Burdigalian salt

F2

Oligocene?

Cimmerian uncf.

Base syn-rift
Paleozoic?

b
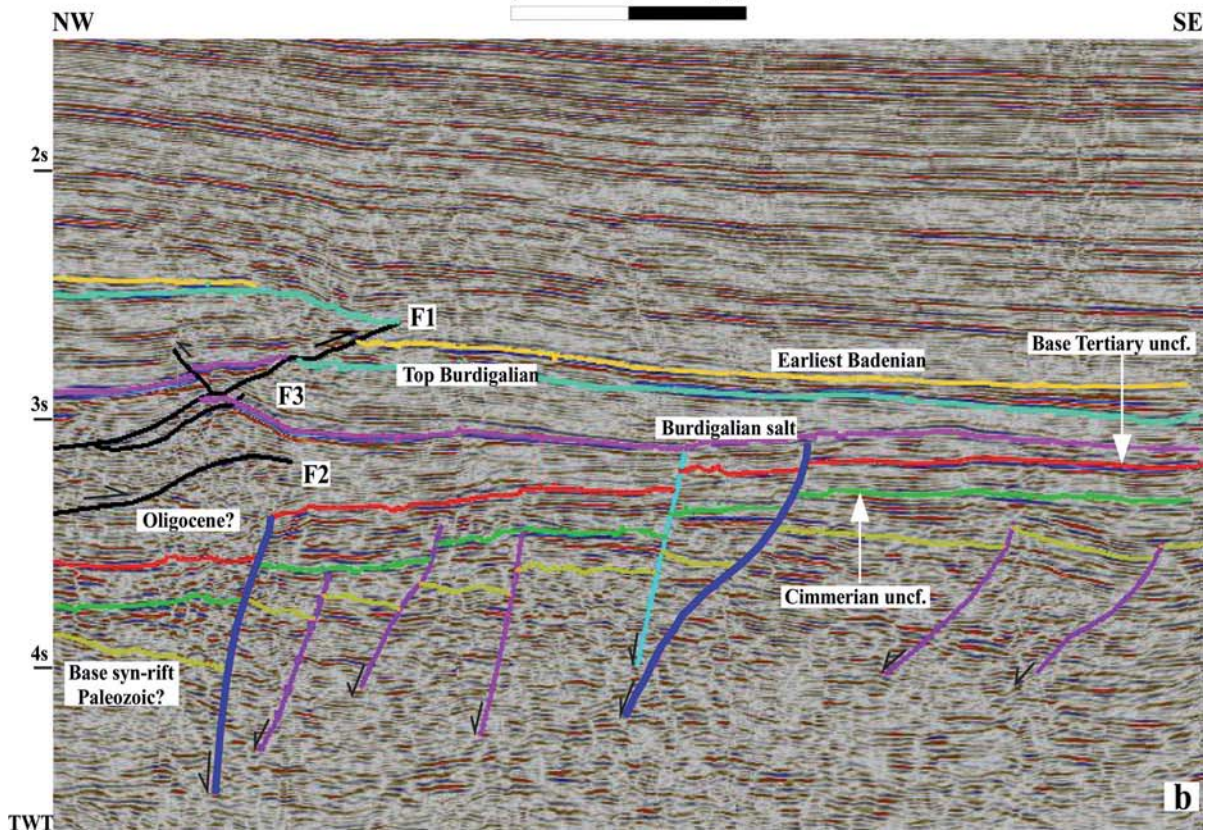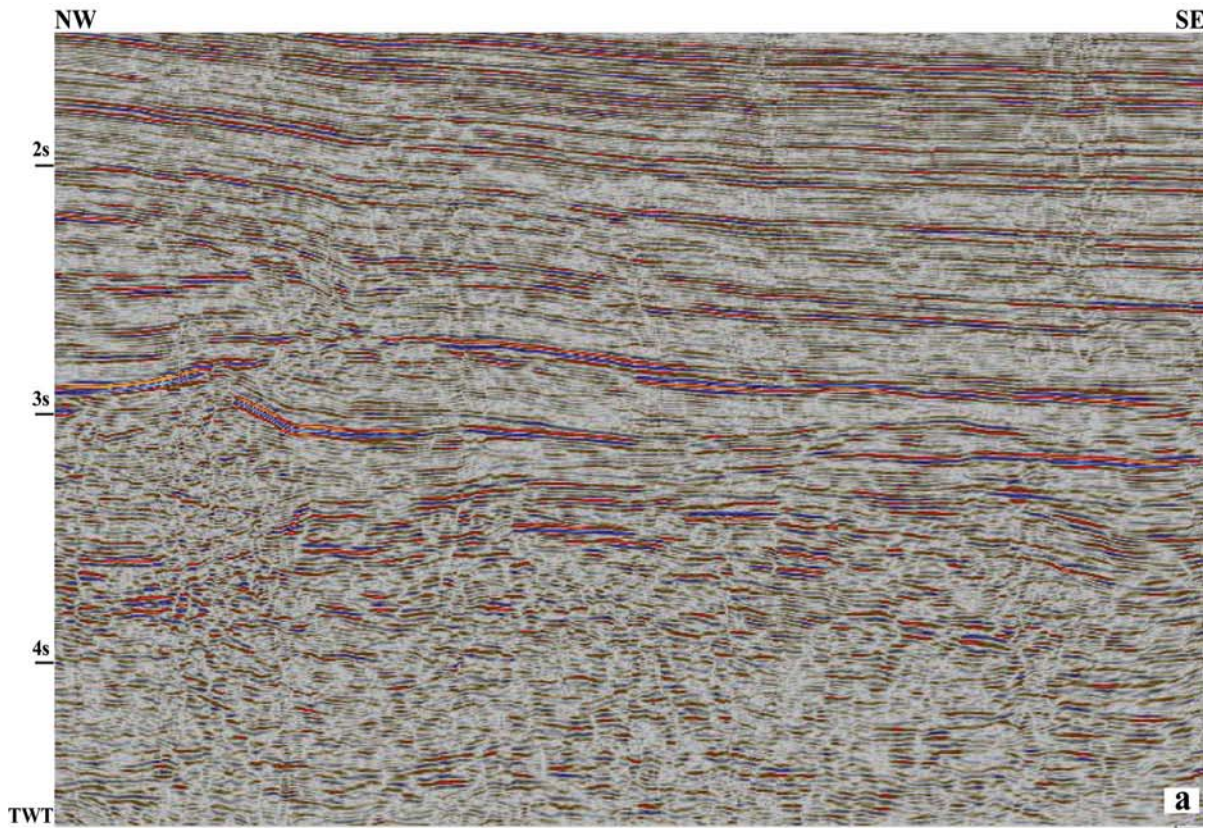
thrust sheets underlie the Getic klippe, which we tentatively assign to the Severin nappe and to a duplex inside the Danubian Autochthonous. Nevertheless, the along-arc correlation of the tectonic units is not straightforward made, as they appear highly disrupted and eroded due to the Eocene core-complex formation (Schmid et al., 1998) prior to the onset of wrenching.

We consider that Timok Fault originates from the ancient Permian - Triassic rifting event that pre-dated the creation of the Severin oceanic crust. Giving the roughly N-S orientation of this fault system (Fig. 3b), it is likely to consider that one of them acted as a significant weakness crustal zone that favored the localization of the strike-slip deformation. Moreover, such a fault system (Figs. 4, 5 and 6) would explain why the Triassic deposits that can be found on Moesia (e.g. Paraschiv, 1979; Tari et al., 1997) and the most external part of the Danubian Autochthonous (Fig. 7) are missing on the distal part of the latter where the metamorphic basement is overlain by Jurassic formations only (e.g. Iancu et al., 2005).

3.3 Mid-Tertiary Structural Style: (Another) Basin Opening

A major extensional event took place during the very beginning of the Early Miocene and probably since the Late Oligocene when the E-W-trending normal faults shown in Figs 3a and b were initiated. Steep and generally N-dipping (Fig. 6), these normal faults have sometimes vertical offsets more than 1 s (over 1 km). Crosscutting the ancient rifted passive margin, they are also part of a system with several transfer zones. Many of the Mid-Tertiary faults seem to have cut preferentially through the transfer zones of the older system. Although within the basinal part of the sector from our study area no well has penetrated the entire Early Miocene section, a minimum thickness of 1.5 km is derived from the deepest one (Matasari 6100, Fig. 3). This E-W normal fault system was also identified farther east to our study area beneath the present-day Getic Basin where the Mid-Tertiary basin subsequently underwent inversion (Rabagia and Matenco, 1999). Also, in the region lying approximately between the Jiu and Olt rivers (Figs. 1 and 2c), ENE-WSW normal faults dying-out at the top platform erosional unconformity were assigned to the same Mid-Tertiary rifting event by Tarapoanca (2004).

The western extent of the Mid-Tertiary rifting is clearly stopped by the Timok Fault as shown in Fig. 3a. On the western side of the Timok Fault there are either basically no corresponding Mid-Tertiary sediments or at least thin (much thinner than in the basin) coarse sequences as the few wells propose ambiguous dating due to the lack of fauna. However, to the north of the present Timok system, the Oligocene and Early Miocene sequences were reported (Vaianu and Cilnic wells, Fig. 3), with thicknesses in the order of tens to a few hundreds of meters. Based upon the structural and thickness pattern of the Mid-Tertiary sequence in the neighboring basin, we propose that the Timok Fault functioned during the Early Miocene (and possibly since the Late Oligocene) as a major transfer fault accommodating to the east the displacement of the Carpathian units via a N to NNE-directed extension (Fig. 9). Furthermore, it appears that not only the foreland but also the orogenic pile was then affected by significant faulting, as described by Matenco and Schmid (1999) and Fugenschuh and Schmid (2005). We can thus infer that from the Oligocene to Early Miocene the tectonic transport of the Carpathian units was progressively transferred from the inner to outer accommodating structures, that is, from wrenching along the Cerna Fault to along the Timok Fault.

Within a larger regional framework, the Mid-Tertiary displacement of the Carpathian units was coeval to the north with shortening in the Pienides (Sandulescu, 1984, 1988) and retro-foredeep formation on the Transylvanian northern margin (e.g. Huismans et al., 1997). This would imply a contemporaneously pure dextral strike-slip to oblique shortening in the East Carpathian evolving wedge (as speculated by Matenco, 1997) in contrast to a pure frontal shortening, postulated for a long time (e.g. Sandulescu, 1984, 1988).

3.4 Middle Miocene Onwards: Basin Inversion

The Middle Miocene marks the onset of compression within the Getic Basin (Fig. 1) with a climax in the Middle Sarmatian given by the emplacement of the Subcarpathian Nappe (e.g. Sandulescu, 1984, 1988). This onset is indicated by the deposition of Badenian evaporites in piggy-back basins over large parts of Getic Basin (Rabagia and Matenco, 1999). The inversion of the former basin should be seen as the effect of oblique compression exerted on the northern margin of Moesian lithosphere by the ENE to E-wards displacement of the Carpathian units (Fig. 2d).

Although the Subcapathian Nappe was apparently mapped (e.g. Dicea, 1995; Rosu, 2005; Figs. 10a, b), the definition of its western termination in the vicinity of Jiu valley (Fig. 1) is still a matter of debate. For a long time it was considered as continuing west of Jiu valley more or less parallel to the South Carpathian bend (e.g. Paraschiv, 1979; Sandulescu, 1984, 1988), but recently it was interpreted as terminating towards the NW in a wide and deep-rooted strike-slip zone which displaces also the northern extensional margin (Matenco et al., 1997; Rabagia and Matenco, 1999).
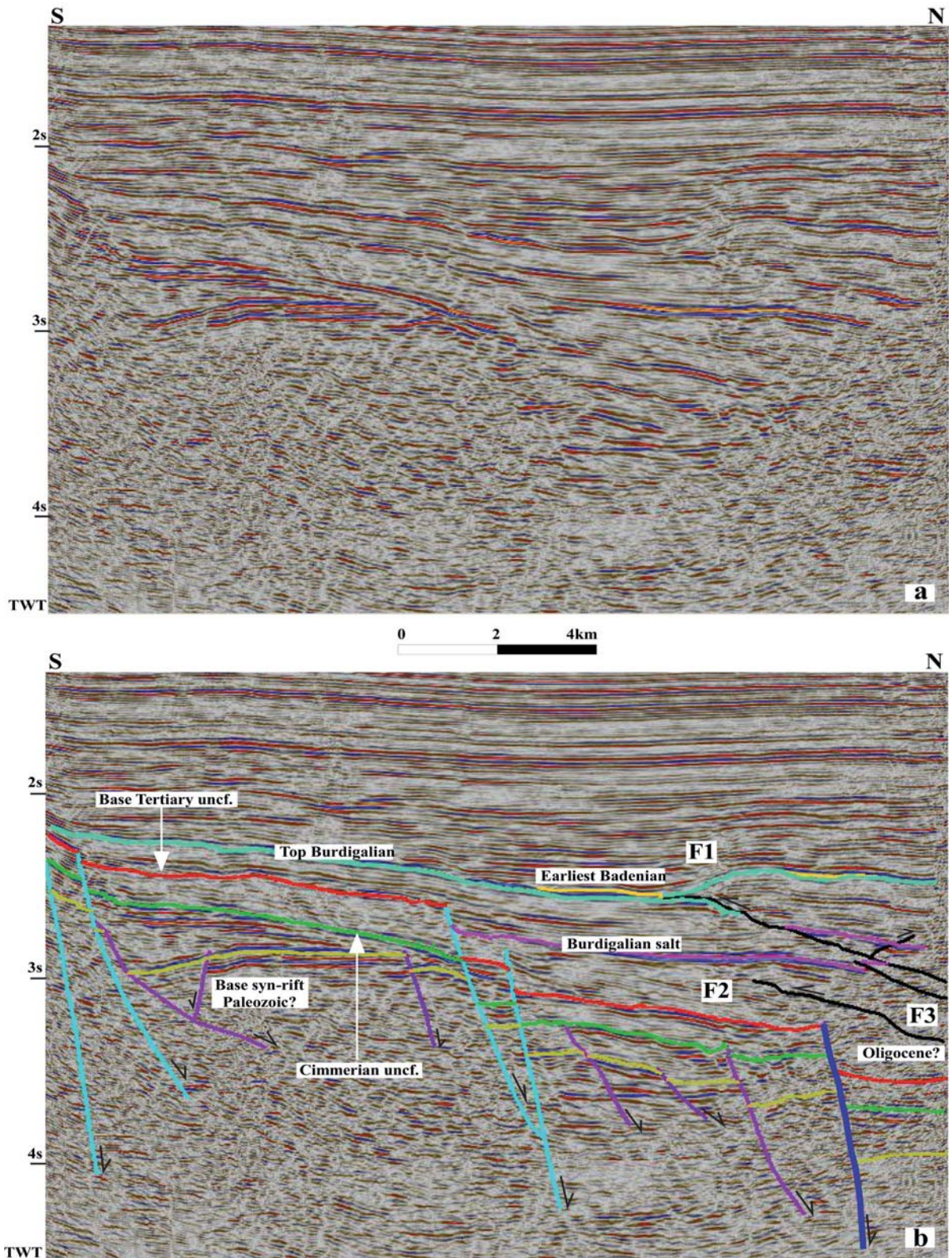
Fig. 6. N-S oriented seismic line (**a** uninterpreted and **b** interpreted) in the NW Moesia (location in Fig. 3). Note the magnitude of the Mid-Tertiary normal faulting (light blue faults). Also note the conspicuous faulted and tilted block eroded under the Cimmerian unconformity. Other symbols as in Fig. 5
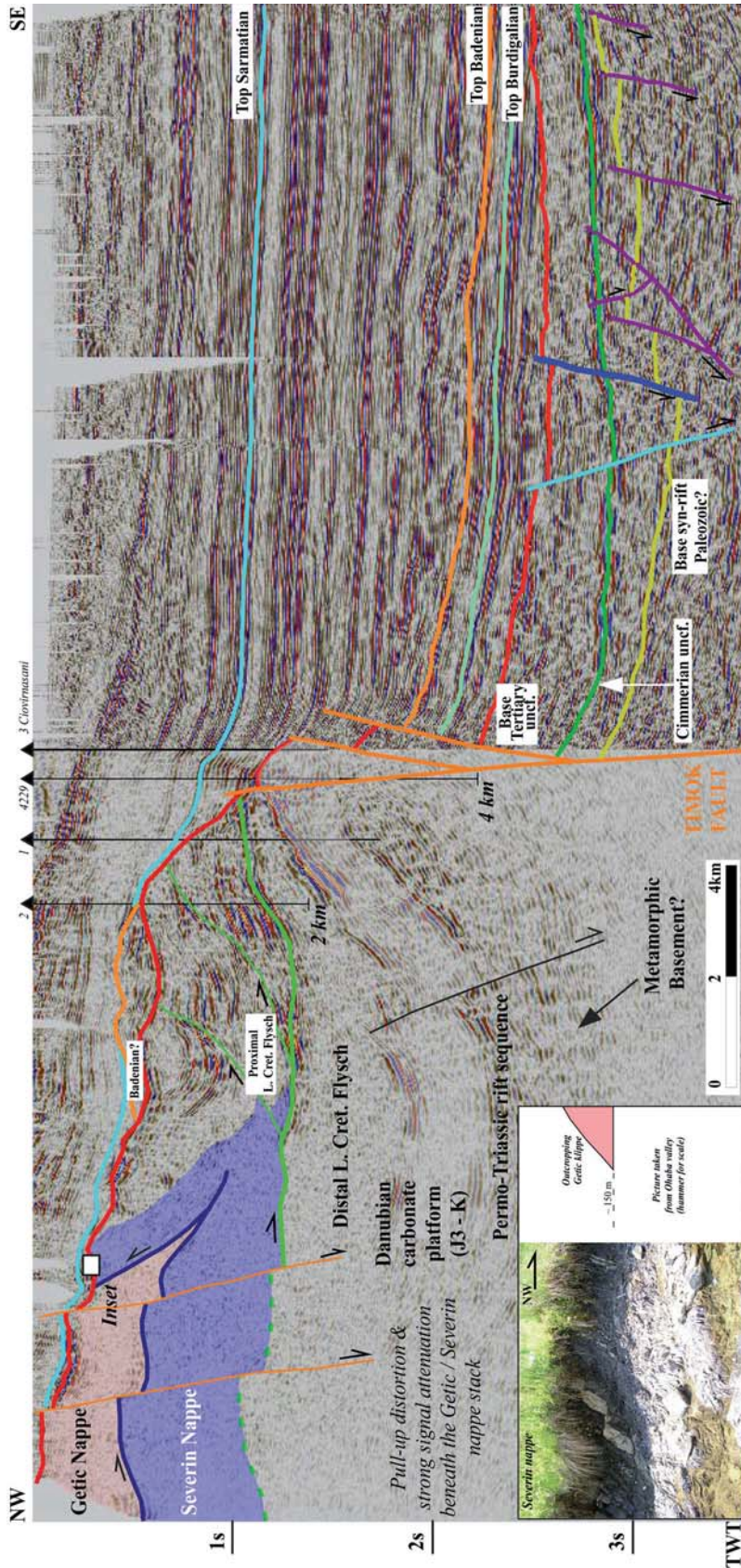
Fig. 7. NW-SE oriented seismic line across the outermost South Carpathians nappe pile, Timok Fault and the deep Moesia (location in Fig. 3). The overthrust sequence labeled as "proximal L. Cret. flysch" onlaps onto a sliver of Severin nappe forming a triangle zone, which can be also observed in outcrops (note the picture taken from a valley at ~ 1 km north from the seismic line). This sequence is made up of predominantly coarse-to-medium grained sediments which were tentatively assigned to either Early Miocene or Eocene age (e.g. Motas, 1981) as no concluding fauna had been recovered. We re-interpret it as a Late Cretaceous proximal sequence thrust over its distal equivalent which is a microfauna-bearing finer sequence. Other fault colors as in Fig. 5. Note also the impressive vertical offset across the Timok Fault. Significant movements along the Timok Fault took place mainly during the Early Miocene and Middle Miocene (Sarmatian) indicated by the thickening of these sequences E-wards, inside the basin. The position of the top Badenian reflector is also constrained through correlation with the well Zegujani 15 (located in Fig. 3)
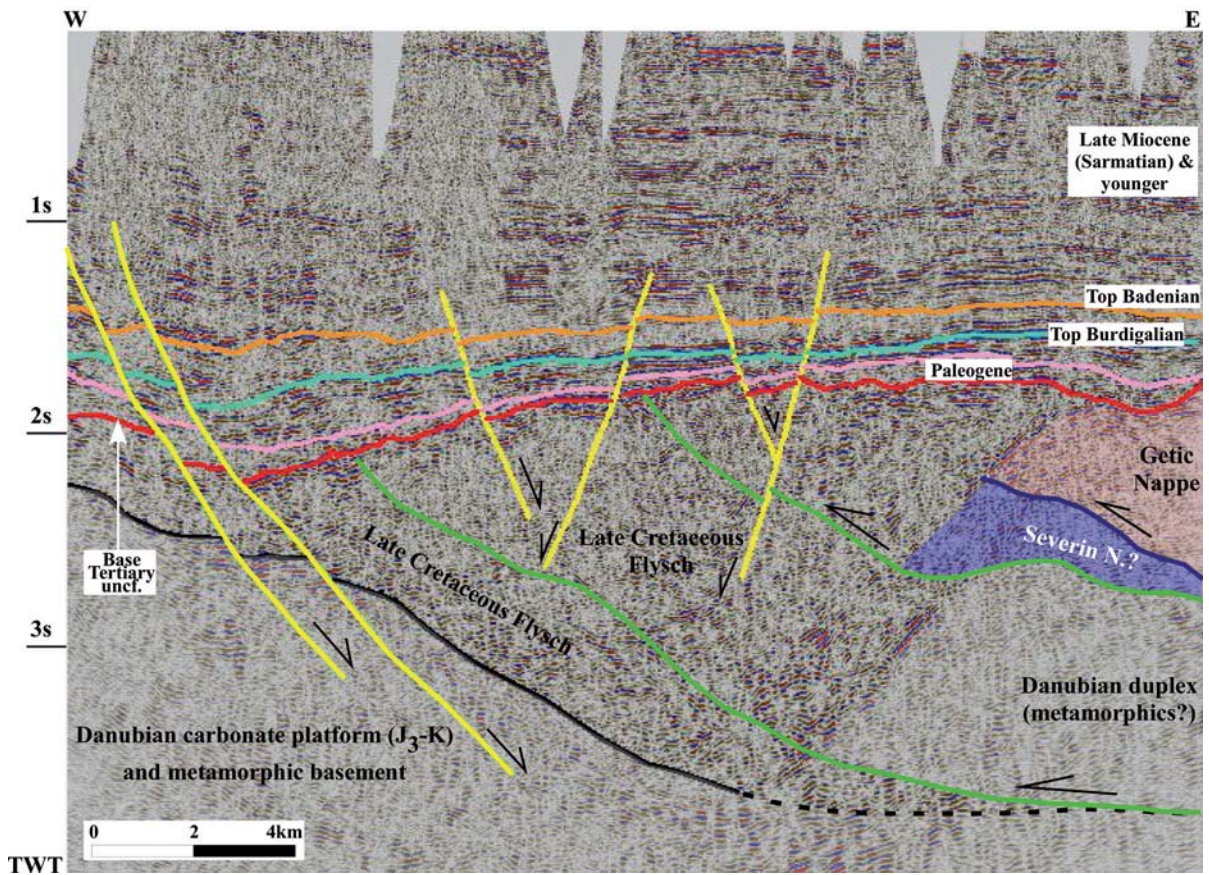
Fig. 8. E-W oriented seismic line, north of the Timok Fault (location in Fig. 3). This line is acquired across the basin margin and images structural units belonging to the Carpathian orogenic pile, similar to those from the western part of line 7. Thrust colors as in Fig. 7. Yellow faults are related to the Middle-to-Late Miocene transtension

This paper brings new information that differs from the previous cited interpretations. Still supporting the strike-slip model, Fig. 10c shows indeed a major tear
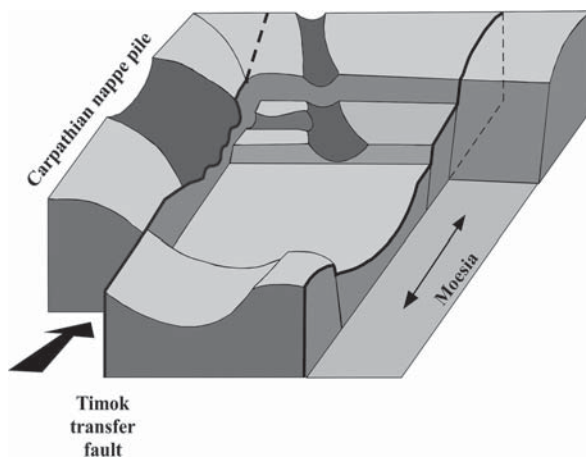
Fig. 9. Sketch of the kinematics of the basin opening during Mid-Tertiary

fault that represents the westernmost continuation of the Subcarpathian Nappe. However, in our interpretation, it is only a thin-skinned structural feature similarly to the nappe itself. To the NW, this strike-slip fault connects an E-W former normal fault whereas to the SE, it progressively changes the dip until passing into the Subcarpathian leading thrust.

In premiere, we found evidence of inverted structures as well as of a thin-skinned thrust fault system to the west of the edge of the Subcarpathian Nappe (Figs. 3a and 10d, respectively). Thrust faults involving mostly the Early Miocene (Burdigalian) sediments are also shown in the seismic lines from Figs. 5 and 6. Except for the westernmost one, these thrusts have roughly NE-SW orientation (Fig. 10d). The shortening along the main thrust (the uppermost one, F1) increases from null to almost 1 km towards the NE. There, the structural style becomes more complicated with another thrust (this one WNW-ESE oriented, F4) found beneath, which confers a duplex-type shape (Fig. 10d).

The previously described Timok Fault system (Figs. 3 and 7) appears as being strongly active dur-
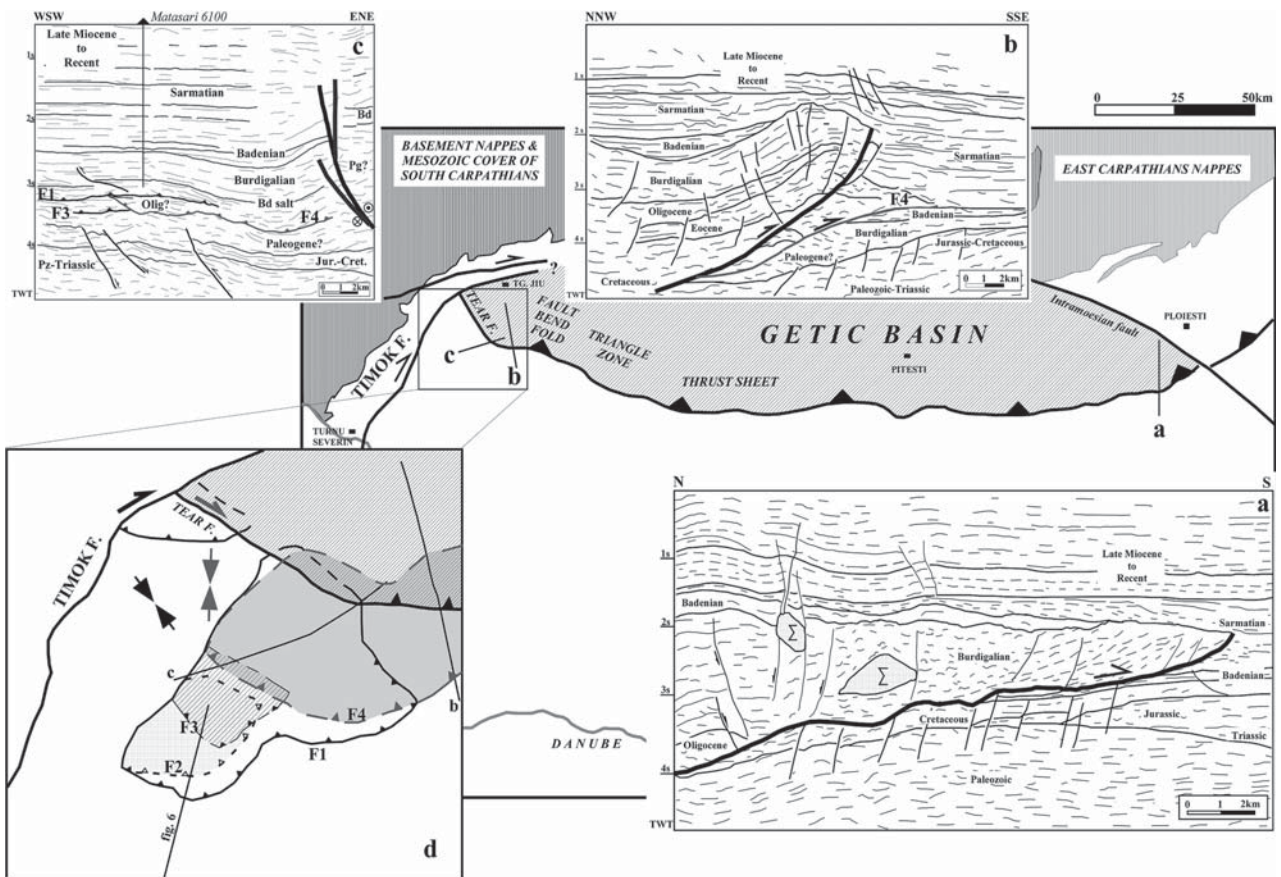
Fig. 10. The structural style of the Subcarpathian Nappe (**a** and **b** are interpreted seismic lines modified from Dicea, 1995 and Rosu, 2005, respectively). Although originally the *line a* was described as imaging the westernmost part of the external thrust sheet of the East Carpathians (Dicea, 1995), in fact it lies to the west of the Intramoesian fault (Tarapoanca, 2004), which is the structural limit between the South and East Carpathians foredeeps. The seismic line shown in **c** evidences a steep shear zone that is interpreted as a dextral tear fault which connects to the leading edge of the Subcarpathian Nappe separating a western domain of relatively minor contraction from an eastern highly shortened one. The subhorizontal thrust planes (barbed thick lines) shown in **c** are faults intersected at small angle by the seismic profile. Also shown in **c** is the deepest well from our study area (bottomed at ~ 5 km). Note in **a** that contraction continued after the Sarmatian main phase of the emplacement of the Subcarpathian Nappe. The map from **d** shows thrust planes mostly organized in a duplex-style to the west of the Subcarpathian Nappe (dashed where covered)

ing the Middle Miocene, particularly during the Sarmatian, indicated by the dramatic change in thickness and elevation of the corresponding sediments across the fault compartments (thin or outcropping to the west and north, over 1.5 km-thick within the basin). Some normal faulting also took place to the southernmost part of the study area (Fig. 3).

We conclude that during the Middle Miocene, the displacement of the Carpathian units took place both along the Timok Fault (formerly acting as a transfer fault) and the northern extensional margin (Fig. 3), thus resulting in a curved anastomozed system. Particularly the movements along the latter, roughly E-W oriented, determined the oblique shortening of the basin fill (Fig. 10d). This is also supported by the continuity of the outcropping ENE-WSW dextral strike-

slip system towards the west (fig. 3; for a more detailed view, see the maps published in Matenco and Schmid, 1999 or Iancu et al., 2005). Between the two overstepping strike-slip faults from the north, a series of NW-SE transtensional faults were formed during Middle-to-Late Miocene (Figs. 3a and 8).

The oblique shortening of the basin fill is initiated in the westernmost part of the Getic Basin and created first the NE-SW-oriented thrust faults shown in Fig. 10d (also Figs. 5 and 6). The inversion of a former extensional fault also took place at that time (Fig. 3a). The onset of shortening should be at the very beginning of the Middle Miocene giving the age of deformed sediments and piggy-back sequence. It may be even earlier, however, it is more difficult to ascertain

an age for the innermost thrust shown in Fig. 10d, given the limited seismic coverage there.

The deeper, WNW-ESE thrust seems to be formed when the NW-SE strike-slip (tear) fault (shown in Figs. 10c and d) was initiated in response to the farther transport of the Carpathian units. Once the NW-SE strike-slip fault cut through the entire basin fill, it took over all the oblique shortening and left the initial thrusts inactive, thus explaining the major difference in elevations between the structures shown in Figs. 10b and c relative to the ones from Figs. 5 or 6.

As a whole, most of the Mid-Tertiary infill of the Getic Basin was peeled-off to the E-SE as a wedge, with the leading line behaving as a tear fault in the west and changing laterally to a frontal thin-skinned thrust. This orientation may have resulted from the original configuration of the extensional basin, that is, the former relay-ramps or other transferring structures may have exerted a certain control.

It appears that when the Carpathian units started rotating along the Timok Fault system in Middle Miocene times, the old orogenic pile became decoupled from western Moesia, thus leading to accelerated subsidence of the latter. Moreover, this would explain why the westernmost extremity of Moesia records quite minor contractional deformation whereas thrusting proceeded along the belt culminating eventually with the emplacement of the Subcarpathian Nappe by late Middle Miocene (Middle Sarmatian, cf. Sandulescu, 1988; Dicea, 1995; Matenco et al., 1997).

We also speculate that some of the former Mid-Tertiary normal faults inside the Getic Basin farther east, particularly those flanking its northern margin, may have been reactivated in this way during the E-wards displacement of the Carpathian units, thus leading to a highly complex structural style of the inversion, as shown by Rabagia and Matenco (1999).

sia NW-most boundary is essentially extensional, with minor contractional deformations taking place at their junction, whereas the Caribbean plate has exerted strong transpression upon the NW corner of the South American plate, leading even to the extrusion and N-wards transport of the Maracaibo triangular continental block (e.g. Pindell., 1991).

We speculate that these contrasting behaviors are mainly related to the presence (and absence, respectively) of weak lineaments within the convex-shaped plate, favorably oriented to the future stresses in the sense of facilitating the tectonic transport of the moving plate. In the case of the Carpathians / Moesia couple, one of the extensional structures inherited from its passive margin stage was likely employed during the future tectonic transport of the Carpathian units and evolved into a major wrench zone.

Furthermore, if one compares the two tectonic plate configurations in terms of shortening within their foredeeps, a similarity concerning the E-wards migration of the contractional deformations could be derived (e.g. Pindell, 1991 and references therein for the Caribbean setting). However, it appears that the time span characteristic of the contractional deformations migration in the Getic Basin is shorter than its counterpart. As shown previously for Carpathians / Moesia, contraction started in the NW-most corner to the end of Early Miocene – beginning of Middle Miocene (Badenian), reached the climax E-wards in the latest Middle Miocene (Sarmatian) and moved to the E-most part in Pliocene, although more diffuse then (Matenco et al., 1997; Hippolyte et al., 1999). In turn, in the Caribbean setting the contraction within the foredeep has started since the Eocene (cf. Pindell, 1991). These comparisons could be of help in directing exploration strategies as both foredeeps host important hydrocarbon reserves.

4 Curved Plate Boundaries: Carpathians / Moesia vs Caribbean / South America

At this point of the discussion, we feel it is worth making a brief analogy of the South Carpathians / Moesia corner with another highly curved tectonic setting which is still developing, namely the Caribbean / South America plates. This was suggested to the first author by H. Doost (personal communication, 2004) and also referred to by Hippolyte et al. (1999). This comparison is useful in picturing how different the foreland plates can deform although the tectonic transport of the upper plates takes place in a rather similar way.

In both cases, there is a plate that dextrally moves and rotates around the corner of another one. The major difference is that the South Carpathians / Moe-

5 The Potential of the Western Moesian Passive Margin Petroleum Systems

The passive margins flanking both modern and ancient oceans are generally prone for generating hydrocarbons from source rocks deposited during syn- to post-rift stages. We have thus integrated the structural pattern of the Moesian passive margin described previously into a regional framework aiming to open new perspectives on the petroleum systems.

Most of the reconstructions of the Mesozoic plate setting in the Carpathian realm (e.g. Sandulescu, 1984; Csontos and Varos, 2004) placed the Severin oceanic crust (and its northern equivalents, Ceahlau and Magura +/- Valais) between the fixed Moesia / East European platform and another continental plate that drifted away towards WSW (Fig. 11a). Alternatively,
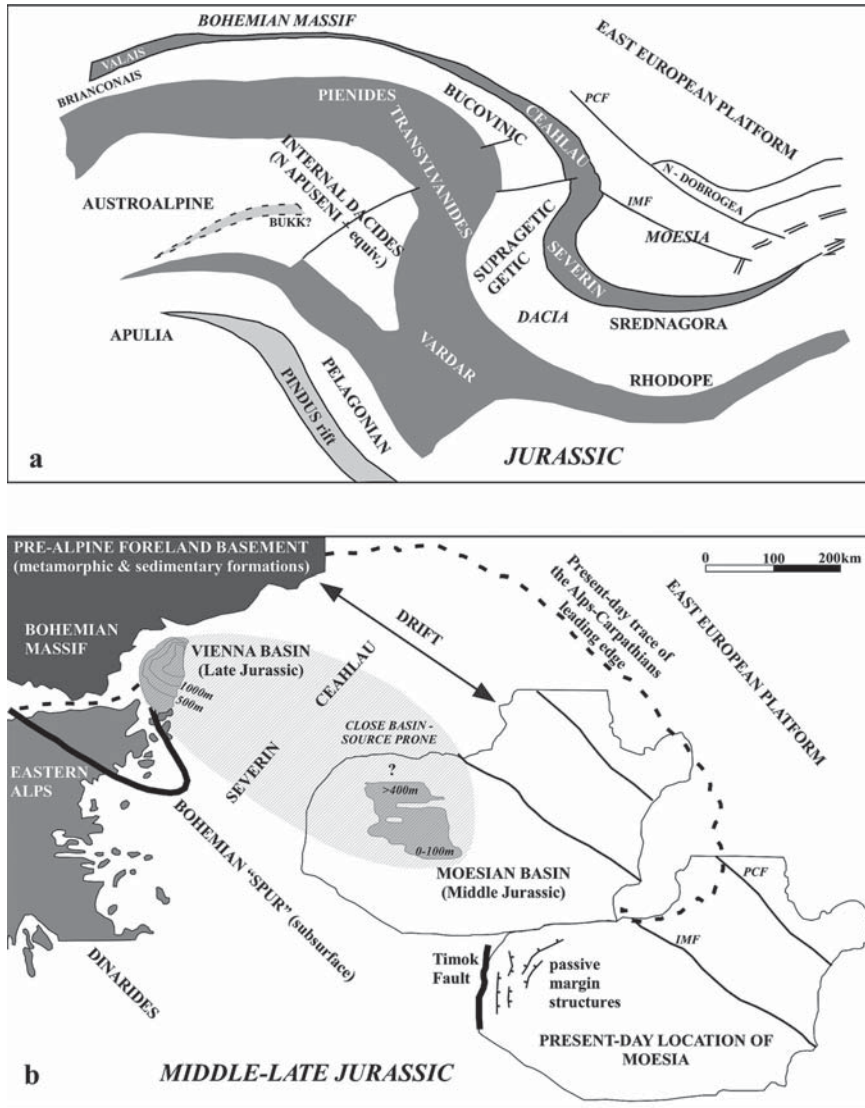
Fig. 11. Plate tectonic models of the Carpathian-Moesian realm prior to the creation of the Severin (and equivalents) oceanic crust (a. from Sandulescu, 1984; b. modified from Tari, 2005). There is no relationship between the gray fills from a. and b. Note that an approximate scale is provided only in b. In b., the thickness maps of the Middle Jurassic (Moesia) and Late Jurassic (Vienna basin) source formations are schematically shown (Tari, 2005 and references therein) as well as the sketch of the rifted passive margin presented in this contribution. We have no intention to discuss the role of the major faults of the foreland plate (IMF Intramoesian fault; PCF Peceneaga-Camena fault) in the Tari's model. Instead, we aim to integrate the Moesian passive margin setting into a larger framework and to provoke further discussions and research on this topic

Tari (2005) proposed that Moesia represents in fact a conjugate plate of the Bohemian segment from the European margin (Fig. 11b). In his model, Moesia is the plate drifted away for over 600 km towards SE during the Middle – Late Jurassic. Very important from the standpoint of hydrocarbon generation, the Middle and Late Jurassic formations known as regional source rocks in western Moesia and the Vienna basin (Tari, 2005 and references therein), appear in this model as deposited within a restricted basin that predated the onset of spreading.

The N-S changing to NE-SW basin structure of the western Moesia, outlined above, seems to sustain Tari's proposed model. These basins appear as remnants of a passive margin that could function indeed in a restricted environment for a while. Although there are no wells that drilled the passive margin sequence pres-

ently buried beneath Tertiary sediments, the faulted tilted blocks (e.g. Fig. 5) and their possible syn-to-post rift source-prone fill represents a new attractive potential petroleum system of the NW-most Moesian area. In fact, our findings could extend farther NW the Middle Jurassic-sourced petroleum system located in central-western Moesia (Popescu, 1995).

The hydrocarbon potential of this area is further strengthened by the expected wide distribution of the Late Oligocene shale sequence (Figs. 5 and 6) buried at the oil window depths. This is the proved main source formation all over the Carpathian nappes and foredeep including most of the Getic Basin (Popescu, 1995).

A third, rather highly speculative petroleum system, might be represented in the NW-most Moesia by the pre-rift Silurian shales (e.g. Paraschiv and Baltes, 1983; Popescu, 1995). Although if present, these source

rocks are expected to be over cooked within the Tertiary basin area, they might have generated hydrocarbons migrated and preserved upwards in traps from the passive margin setting.

Finally, a prolific petroleum system is represented by the biogenic gas in dominantly stratigraphic traps of the Neogene clastics widespread in the post-Badenian sequences of the entire Carpathian foreland area from Romania to Austria.

6   Conclusions

The information provided by the recent seismic surveys and wells drilled in the NW-most Moesian corner sheds more light upon the structural setting and kinematic evolution of the highly-bent contact zone between the South Carpathians and their foreland plate. This contact is essentially transcurent being represented by the Timok dextral lineament which accommodated during the Mid-Tertiary onwards the displacement and rotation of the Carpathian orogenic units around the Moesian corner. The Timok Fault clearly cuts the South Carpathians structural assemblage from the Moesian foreland plate; north of the Danube River, no proof of Carpathian nappes was found to the east of this bounding lineament.

Two extensional stages overlapped in the NW part of Moesia leading to a complex structural setting made up of orthogonal normal fault systems. The oldest is roughly N-S oriented and originates from the (presumably) Permian - Triassic rifting that predated the creation of the oceanic crust at the western and northern margins of the Moesian realm. After the Latest Cretaceous welding of the Carpathian orogen to Moesia, some of those faults acted as a structural weakness prone to be reactivated in a transcurent manner and became the defined Timok Fault system in the Mid-Tertiary. Genetically related to the N-wards translation of the Carpathian units, the more recent E-W oriented fault system was formed in Late Oligocene – Early Miocene driving the opening of a second extensional basin along the northern margin of Moesia.

The tectonic regime changed to transpression not earlier than the Middle Miocene once the Carpathian units started to rotate around the Moesian corner. Structural evidence shows that only then, the former rather straight Timok Fault merged with one of the northern E-W extensional faults leading to a curved dextral strike-slip system. A duplex thrust system had been formed inside the basin until most of the transpression has been taken over by a NW-SE dextral fault which becomes laterally the thin-skinned Subcarpathian Nappe.

As a whole, the Mid-Tertiary basin has been inverted by progressively peeling-off towards E-SE its sedimentary fill. The thin-skinned character of the inversion and the significant down-throwing of the eastern compartment of the Timok Fault system suggest that by the Middle Miocene the former orogenic pile became fully decoupled from the Moesian foreland plate.

New paths are open for hydrocarbon exploration giving the detailed structural picture highlighted in this contribution. Two main petroleum systems can be envisaged: one is related to the Mesozoic passive margin stage with hydrocarbons possibly sourced from syn- to post-rift Mid-Jurassic sequences and trapped in the rift shoulders; the second is related to the Late Oligocene shales (as in the whole Carpathian foredeep) which could produce hydrocarbons migrated towards either the Mid-Tertiary extensional traps or into those created during the Middle Miocene inversion. The biogenic gas accumulated in stratigraphic traps deserves more explorationists' attention these days when smaller fields could be commercial.

References

Berza T, Draganescu A (1988) The Cerna-Jiu fault system (South Carpathians, Romania), a major Tertiary transcurent lineament. DSS Inst. Geol. Geofiz. 72–73: 43–57

Csontos L, Voros A (2004) Mesozoic plate tectonic reconstruction of the Carpathian region. Paleogeogr. Paleoclim. Paleoecol. 210: 1–56

Dicea O (1995) The structure and hydrocarbon geology of the Romanian East Carpathians border from seismic data. Petrol. Geosci. 1: 135–143

Doglioni C, Busatta C, Bolis G, Marianini L, Zanella M (1996) Structural evolution of the eastern Balkans (Bulgaria). Marine Petrol. Geol. 13: 225–251

Fugenschuh B, Schmid S (2005) Age and significance of core complex formation in a very curved orogen: evidence from fission track studies in the South Carpathians (Romania). Tectonophysics 404: 33–53

Hippolyte J-C, Badescu D, Constantin P (1999) Evolution of the transport direction of the Carpathian belt during its collision with the east European platform. Tectonics 18: 1120–1138

Huismans R, Bertotti G, Ciulavu D, Sanders CAE, Cloetingh S, Dinu C (1997) Structural evolution of the Transylvanian Basin (Romania): a sedimentary basin in the bend zone of the Carpathians. Tectonophysics 272: 249–268

Iancu V, Berza T, Seghedi A, Gheuca I, Hann H-P (2005) Alpine polyphase tectono-metamorphic evolution of the South Carpathians: a new overview. Tectonophysics 410: 337–365

Matenco L (1997) Tectonic evolution of the Outer Romanian Carpathians: constraints from kinematic analysis and flexural modeling. Ph.D. thesis, Vrije Universiteit Amsterdam, 160p

Matenco L, Schmid S (1999) Exumation of the Danubian nappes system (South Carpathians) during the early Tertiary: inferences from kinematic and paleostress analysis at the Getic/Danubian nappes contact. Tectonophysics 314: 401–422

Matenco L, Bertotti G, Dinu C, Cloetingh S (1997) Tertiary tectonic evolution of the external South Carpathians and the adjacent Moesian platform (Romania). Tectonics 16: 896–911

Matresu J, Dinu C (2004) Paleozoic extensional basins in the western part of the Moesian platform. In: Dinu C, Mocanu V (eds) Geology, tectonics and hydrocarbon potential of the Romanian Moesian platform. BGF special volume 3, pp 63–70

Motas C (1981) Nouvelles donnees sur les rapports structuraux entre les Carpathes Meridionales et la Depression Getique. (Proceedings of the 12th Congress of the Carpathian-Balkan Geological Association, Bucharest, Romania)

Paraschiv D (1979) The Moesian platform and its hydrocarbon fields (in Romanian with summary in English). Romanian Academy, Bucharest, 196p

Paraschiv D (1997) The pre-Parathethys buried denudational surface in Romanian territory. Rev. Roumaine Geograph. 41: 21–32

Paraschiv D, Baltes N (1983) The relathionship between phytometamorphism and the oil and gas-bearing potential of the Bibesti-Bulbuceni area (in Romanian with summary in English). St. Cerc. Geol. Geofiz. Geograf., Serie Geol. 28: 54–59

Pindell JL (1991) Geologic rationale for hydrocarbon exploration in the Caribbean and adjacent regions. J. Petrol. Geol. 14: 237–257

Popescu BM (1995) Romania's petroleum systems and their remaining potential. Petrol. Geosci. 1: 337–350

Rabagia T, Matenco L (1999) Tertiary tectonic and sedimentological evolution of the South Carpathians foredeep: tectonic versus eustatic control. Marine Petrol. Geol. 16: 719–740

Rabagia T, Tarapoanca M (1999) Tectonic evolution of the Romanian part of the Moesian platform: an integrated model.

In: Matenco L, Ioane D, Seghedi A (eds) Dobrogea – the interface between the Carpathians and the Trans-European Suture Zone. Europrobe TESZ/PANCARDI/GeoRift Abs. Vol., Romanian J. of Tectonics and Reg. Geol. 7 suppl. 1, p. 58

Ratschbacher L, Linzer HG, Moser F, Strusievicz RO, Bedelean H, Har N, Mogos PA (1993) Cretaceous to Miocene thrusting and wrenching along the central South Carpathians due to a cornel effect during collision and orocline formation. Tectonics 12: 855–873

Rosu V (2005) The contribution of the Tertiary tectonic events to the geological structure and formation of hydrocarbon fields in Getic Depression, the sector between Olt and Jiu valleys (in Romanian). Ph.D. thesis, Bucharest University, 240p

Sandulescu M (1984) Geotectonics of Romania (in Romanian). Tehnica, Bucharest, 450p

Sandulescu M (1988) Cenozoic tectonic history of the Carpathians. In: Royden LH, Horvath F (eds) The Pannonian basin. A study in basin evolution. AAPG Memoir 45, pp 17–25

Schmid S, Berza T, Diaconescu V, Froitzheim N, Fugenschuh B (1998) Orogen parallel extension in the Southern Carpathians. Tectonophysics 297: 209–228

Tarapoanca M (2004) Architecture, 3D geometry and tectonic evolution of the Carpathians foreland basin. Ph.D. thesis, Vrije Universiteit Amsterdam, 120p

Tari G (2005) The divergent continental margins of the Jurassic proto-Pannonian Basin: implications for the petroleum systems of the Vienna Basin and the Moesian Platform. In: Transactions GCSSEPM Foundation 25th Annual Res. Conf., pp 955–986

Tari G, Dicea O, Faulkerson J, Georgiev G, Popov S, Stefanescu M, Weir G (1997) Cimmerian and Alpine stratigraphy and structural evolution of the Moesian platform (Romania/Bulgaria). In: Robinson AG (ed) Regional and petroleum geology of the Black Sea and surrounding regions. AAPG Memoir 68, pp 63–90

Van Wijk JW, Cloetingh SAPL (2002) Basin migration caused by slow lithospheric extension. Earth Planet. Sci. Lett. 198: 275–288

Willingshofer E, Andriessen P, Cloetingh S, Neubauer F (2001) Detrital fission track thermochronology of Upper Cretaceous syn-orogenic sediments in the South Carpathians (Romania): inference on the tectonic evolution of a collisional hinterland. Basin Res. 13: 379–395

Role of the Foredeep Evaporites in Wedge Tectonics and Formation of Triangle Zones: Comparison of the Carpathian and Pyrenean Thrust Fronts

Piotr Krzywiec · Jaume Vergés

Abstract. Syntectonic evaporitic levels within foredeep basin play an important role during the last stages of development of fold-and-thrust belts. These evaporites easily transmit tectonic stresses acting as preferred detachment levels. Both within the Spanish Pyrenees as well as within the Polish Carpathians syntectonic evaporites developed in their foredeep basins that controlled final stages of thrusting within the orogenic wedges. Within the SE frontal Pyrenees, thick and laterally extent evaporites of the Cardona and Barbastro formations controlled the position of ramps and backthrusts as well as of triangle zones developed within the Ebro basin. Overlap zones of successive evaporitic levels defined the location of anticlines on the hangingwall of thrust ramps, whereas the external pinch outs of the uppermost evaporitic level define the position of backthrusts. Frontal Polish Carpathian orogenic wedge including a zone of deformed Miocene foredeep sediments (the Zgłobice unit) is also characterized by the presence of Middle Miocene foredeep evaporites, that strongly influenced Miocene stages of the Carpathian thrusting. In the Tarnów area, where foredeep evaporites are thinner and consist mainly of anhydrite, a triangle zone developed within the Zgłobice unit between the north-directed frontal thrust of the flysch (pre-Miocene) Outer Carpathians and the south-directed backthrust related to the Miocene anhydritic layer. The tip point of this triangle zone may have been controlled either by location of a zone of rapid thinning of anhydrites above the northern slope of the pre-Miocene erosional paleovalley, or by an overlap zone of two anhydritic units above this slope. The Zgłobice unit in the Wieliczka area is characterized by a system of north-directed tectonic slices carrying thick rock salt interlayered by siliciclastics. The Wieliczka triangle zone might have formed where lateral changes of evaporitic facies occurred at the transition from thick rock salt to thinner anhydrite facies.

Keywords. Syntectonic evaporitic horizons, detachment folding, triangle zones, SE Pyrenees, Polish Carpathians.

1 Introduction

It long has been recognized that rock salt, due to its specific bulk properties, is one of the most important components of sedimentary basins and thrust belts. Evaporites in general, and rock salt in particular, are of key importance for evolution of fold-and-thrust belts, as evaporitic layers often form preferred levels of detachments within the orogenic wedge (e.g. Davis & Engelder, 1985; Cotton & Koyi, 2000; Costa & Vendeville, 2002; Bahroudi & Koyi, 2003; Costa et al., 2004; Sherkati et al., 2005). The majority of the detached fold-and-thrust belts are displaced above pre-shortening evaporites (see compilation in Letouzey et al., 1995). However, some fold-and-thrust belts also used syn-compressive evaporitic levels related to deposition within their foredeep basins, as it is the case for the Spanish Pyrenees and the Polish Carpathians that are discussed in this paper.

The Carpathians and the Pyrenees belong to the same Alpine–Himalayan orogenic belt formed by the closure of the Tethys Ocean (Fig. 1). At present, the frontal part of the S Pyrenees is well exposed, whereas the front of the Polish Carpathians is mostly buried, especially in their central segment described below. The fronts of the Pyrenees and Carpathians share, however, one common but not so frequent scenario in which syntectonic evaporitic deposits played a very important role in folding and thrusting.

Evaporitic units formed within the foredeep basins could have different thickness and lateral extent, frequently they migrate towards the foreland following foreland-directed migration of the orogenic wedge. Foredeep-related evaporites are involved in folding and thrusting usually during the latest stages of shortening. They tend to focus detachment levels which often leads to formation of complex structures, including triangle zones and duplexes (for overview of triangle zones and related nomenclature see e.g. Jones, 1996; MacKay et al., 1996), that could form important targets during exploration for hydrocarbons.

In fold-and-thrust belts detached above evaporites, shortening is usually transferred rather rapidly along the evaporitic levels to the external boundary of the evaporitic basin where evaporites pinch out. Thus, deformed areas usually correspond to the evaporitic depositional extent. At the pinch out, the abrupt increase of internal strength to thrust displacement often pro-
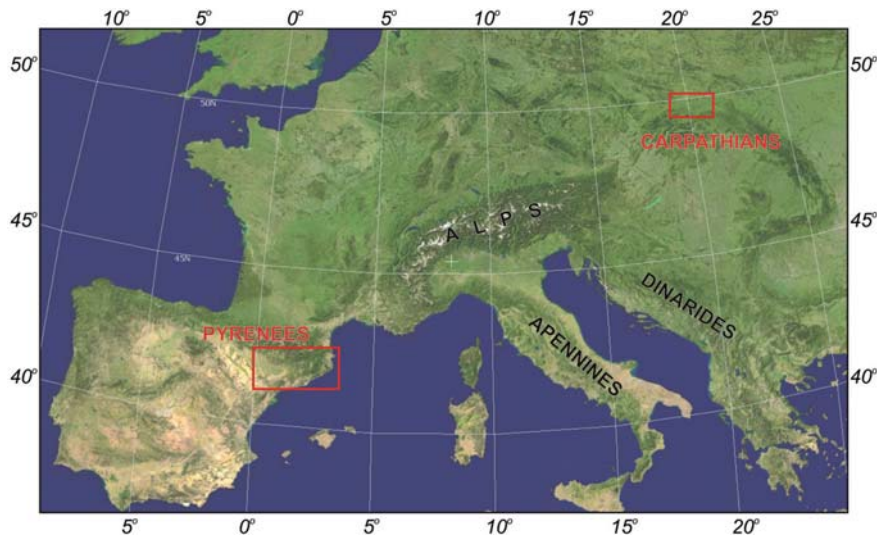
Fig. 1. Location of the Carpathian and Pyrenean orogenic belts. Red rectangles – approximate location of both study areas (cf. Figs. 3 and 6)

duces a backthrust-bounding triangle zone cored by highly deformed rocks.

In this paper we compare the well-exposed SE frontal part of the Spanish Pyrenees with the buried front of the Polish Carpathians. Amongst other parameters, thickness and lateral extent of evaporitic levels are responsible for changes in the tectonic style of studied frontal parts of orogenic belts.

2   The South Pyrenean Frontal Triangle Zone

The South Pyrenean thrust system consists of three major domains:

1. The inner thrust sheets that include thick basement slices that form the core of the orogenic belt.
2. The cover thrust sheets carrying Mesozoic rocks as well as early Paleogene foreland basin deposits.
3. The most external fold-and-thrust structures detached above foredeep evaporites. The age of deformation migrated towards the South starting in the latest Cretaceous in the north and ending around the middle Oligocene in the South (see Vergés et al., 2002, for further details).

The most external SE Pyrenean folds and thrusts developed within the foredeep deposits of the Ebro Basin. Several systems of detached anticlines grew above successive syntectonic foreland evaporitic horizons (e.g. Ramírez and Riba, 1975; Vergés et al., 1992).

The Pyrenean foreland basin is filled by a thick succession of middle Eocene shallows marine marls related to deltas developed along the basin's margins. Above the uppermost shallowing upwards marl unit, about 300 m thick evaporitic succession developed

that recorded marine-continental transition (Fig. 2). The Cardona evaporites recorded the end of marine conditions within the Ebro Basin, when the Atlantic connection became closed. The geometry and extent of this evaporitic unit is well known because numerous wells were drilled and several seismic surveys were completed in this area during potash exploration. Above the flat top of the Cardona evaporites a thick prograding alluvial fan system dominated the infill of the Ebro Basin during the late Eocene and Oligocene times. This system comprised the coarse proximal conglomerates of the Solsona Fm. and the distal Súria Fm. (Ramírez and Riba, 1975; Riba et al., 1983). A thick lacustrine sequence with evaporites (Barbastro Fm.) constituted the infill of the central part of the Ebro Basin.

Whereas the Cardona Fm. was probably related to a relatively rapid depositional event infilling a deep NW-SE trending trough, the Barbastro Fm. was progressively migrating towards the south-west and south in front of the advancing Pyrenean deformation (Vergés and Burbank, 1996).

Three sets of folds display different orientations depending on their position within the foreland basin as well as on their relationship with the most external thrust of the cover thrust sheets (Vergés, 2003), (Fig. 3). NW-SE folds are located to the north of the main Cardona evaporitic basin, NE-SW folds are located above the Cardona salt basin, whereas the most external WNW-ESE folds used the Barbastro evaporites to glide.

The lateral extent of these evaporitic units directly controlled the position and geometry of folds and thrusts during Tertiary shortening. The staircase geometry, with or without superposition, of two evaporitic units is also a very important factor controlling
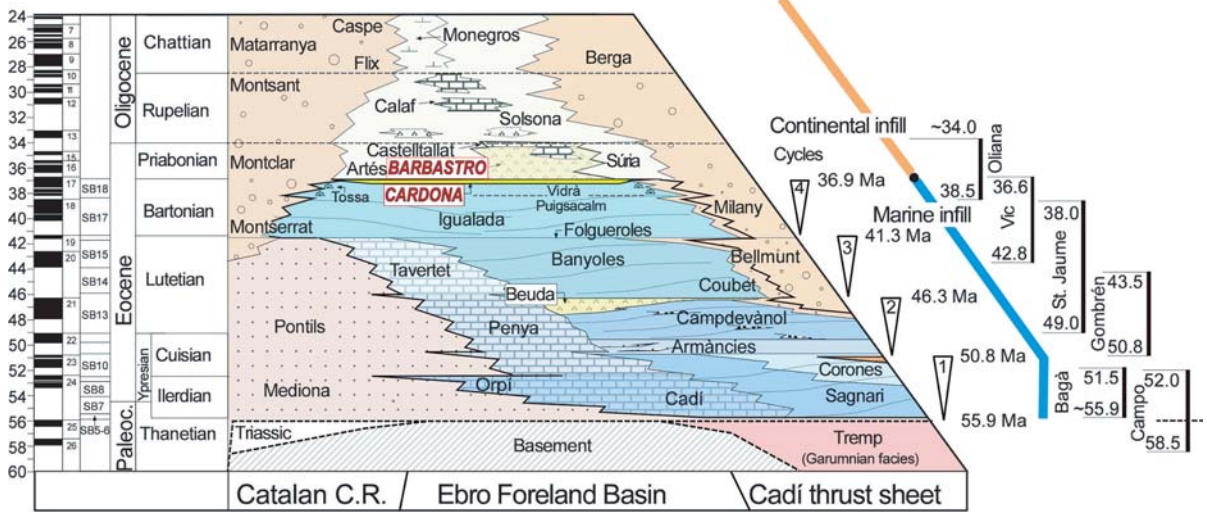
Fig. 2. Stratigraphic panel for the Southern Pyrenees and their foreland basin. Biostratigraphic data combined with magnetostratigraphic information (six sections displayed on the left side of the panel) define the chronostratigraphic framework of the study area (see Vergés et al., 2002 for details). Evaporites of the Cardona and Barbastro formations (shown in red) played an important role in the tectonic evolution of the frontal Pyrenean thrust system

Fig. 3. Structural sketch of the South Pyrenean Triangle Zone developed within the Ebro basin (after Sans, 2003). Red line – location of regional cross-section from Fig. 4
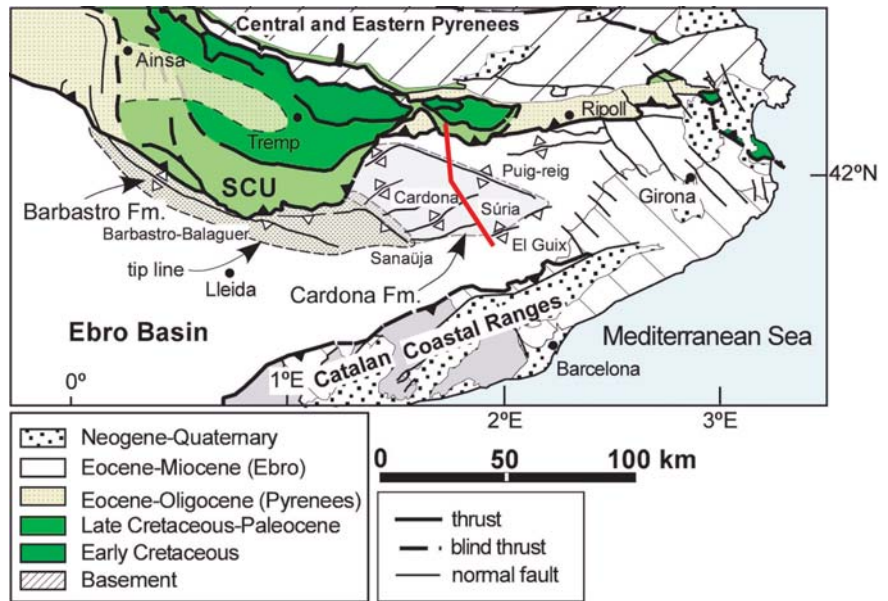
the relationship of two detachment horizons as has been described using field examples from the Pyrenees (Vergés et al., 1992; Sans, 1995; Sans et al., 1996), as well as results of analogue modeling (e.g. Letouzey et al., 1995). When there is a partial superposition of two detachment levels (i.e. in the SE Pyrenees), the detachment climbs up from the lower to the upper evaporites at the pinch out of the lower evaporites. Consequently, single or complex systems of ramps develop together with a hangingwall anticline.

Along the SE depositional limit of the syntectonic foreland evaporites, the increase of strength controlled by the evaporite pinch-out line forced the detachment thrust to continue to develop along the backthrust bounding a triangle zoom (Fig. 4). This is the case of the frontal el Guix and Barbastro anticlines (Fig. 3).

Along the SE Pyrenean thrust belt, various evaporitic detachment levels developed within the Pyrenean foreland basin produced tight anticlines separated by relatively wide and flat synclines that can show salt
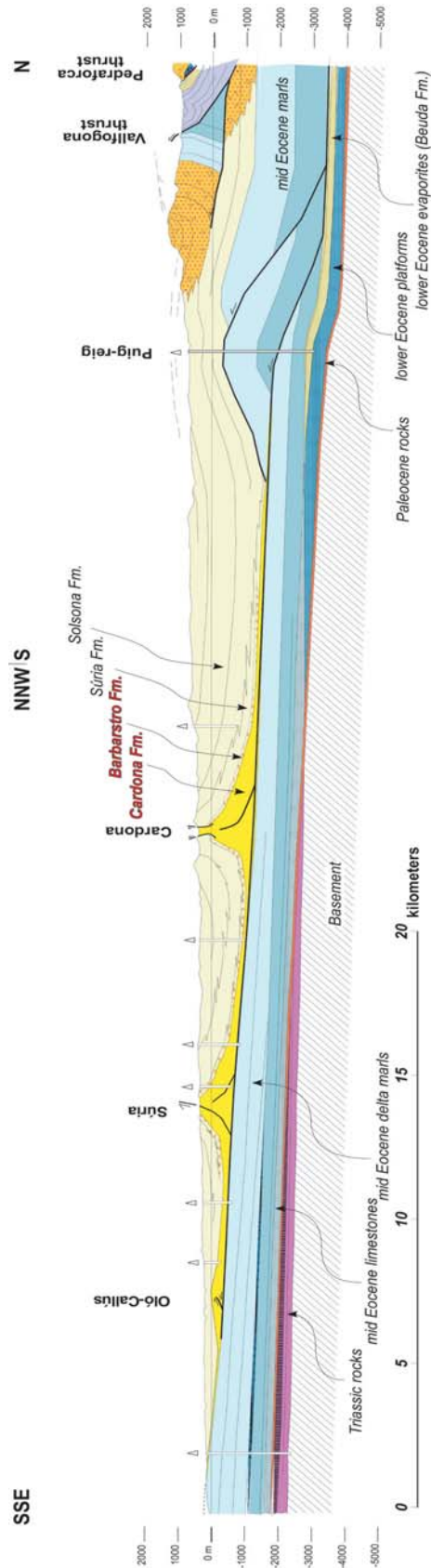
Fig. 4. Balanced geological cross-section across the E Pyrenees detached fold-and-thrust belt (after Vergés et al., 2002). Cardona and Barbastro evaporitic formations that controlled development of the frontal Pyrenean thrust are shown in red

welding (total evacuation of salt beneath the synclines). At the termination of evaporitic basins, an emerging backthrust and a triangle zone formed, bounding the Pyrenean detached fold-and-thrust belt.

3   Wedge Tectonics of the Central Polish Carpathians

The Carpathian orogenic belt consists of three main tectonostratigraphic domains: the Inner Carpathians, the Pieniny Klippen Belt, and the Outer Carpathians that have been deformed during several shortening events since the Late Jurassic (see Picha and Golonka, 2005 for a recent overview of geology of the Carpathian region). The Outer Carpathians, that comprise several thrust sheets (nappes) built predominantly of deep-water flysch sediments, are genetically linked to the Miocene Carpathian foredeep basin that developed in front of the advancing orogenic wedge during final thrusting movements (for summary and further references see Oszczypko, 1998; Oszczypko et al., 2005).

Sedimentary infill of the Polish Carpathian foredeep basin consists of the Eggerian to Sarmatian (approx. upper Chattian – lower Tortonian) sedimentary sequences (Fig. 5) showing a successive northward migration of the basin axis in front of the advancing thrust sheets (nappes). Within this basin, two major segments (domain) could be distinguished:

1. The inner foredeep basin.
2. The outer foredeep basin, with the boundary between them roughly following present-day frontal overthrust of the Carpathian wedge.

The inner foredeep basin is composed of the Lower – Middle Miocene (approx. upper Chattian – Serravalian) mostly terrestrial autochthonous deposits (Fig. 5) that are presently entirely overridden by the Carpathian orogenic wedge. Transition from the inner to the outer domain reflects a major northward shift of the Carpathian wedge and related northward displacement of the foredeep's zone of maximum subsidence.

The outer Carpathian foredeep analyzed in this paper is located to the north from the frontal Carpathian thrust (Fig. 6). It is filled with the Middle Miocene marine deposits, that range from a few hundred meters in thickness in the northern marginal part, up to 3,500 m in the eastern part, in vicinity of the Polish – Ukrainian boundary. Infill of the outer foredeep in front of the Carpathian orogenic wedge consists of the Upper Badenian–Sarmatian (approx. Upper Serravalian – lower Tortonian) succession (Fig. 5). Badenian northward shift of the Carpathian orogenic wedge resulted in a similar shift of the foredeep basin and de-

velopment of a wide depositional zone, i.e., the outer Carpathian foredeep basin. Flooding of the Carpathian foreland led to deposition of the Baranów beds that are 10–20 m thick on average, and are built of muddy shales and sandstones and unconformably overlie Mesozoic rocks of the lower (foreland) plate.

Relatively thin siliciclastic Baranów beds are covered by the Upper Badenian evaporitic succession that belongs to Krzyżanowice and Wieliczka formations (cf. Oszczypko et al., 2005). The Krzyżanowice formation comprises gypsum and anhydrite and associated siliciclastic deposits (mainly claystones) and barren and sulfur-bearing limestones that are commonly considered as having originated due to metasomatosis of sulfates. This formation covers a large part of the outer foredeep basin, only between Kraków and Tarnów it is locally replaced by Wieliczka formation. Thickness of the gypsum and anhydrites of the Krzyżanowice formation is in order of several tens of meters in the marginal part of the basin, up to 10–20 m in more the central part (e.g., in vicinity of the present-day frontal Carpathian thrust analyzed in this paper). The Wieliczka formation consists of rock salt with intercalations of claystones and minor sulfates, with total thickness between 30 and 100 m described in the Wieliczka area (Garlicki, 1979). Two main units are distinguished within this succession: stratiform deposits and boulder deposits. Stratiform deposits consist of layered salt beds with relatively minor fine siliciclastic intercalations. Boulder deposits are formed by blocks of salt of different size (from 1 m3 up to even 100,000 m3) embedded within the siliciclastic, generally clayey succession. First deformations of the evaporitic succession most probably occurred already during late phases of its sedimentation (Kolasa and Ślączka, 1985; Ślączka and Kolasa, 1997). Subsequent tectonic movements related to latest phases of the Carpathian collision and thrusting strongly deformed the entire evaporitic succession of the Wieliczka formation.

Upper Badenian evaporites of the Krzyżanowice and Wieliczka formations are covered by shaly-sandy uppermost Badenian (Chodenice and Grabowiec beds) and Sarmatian siliciclastics (Fig. 5), of generally deltaic origin. Their development was related to increased subsidence within the outer foredeep basin, triggered by an increased rate of overthrusting movements within the Carpathian accretionary wedge and/or increased slab-pull processes within the Carpathian subduction zone. These sediments, that presently form the bulk of the foredeep infill in front of the Carpathian orogenic wedge, were supplied mostly from the south, from eroded Carpathians, with minor sediment supply from the north (Fig. 7; cf. Krzywiec, 2001).

At present, a zone of deformed foredeep deposits (Zgłobice unit; Kotlarczyk, 1985) is located in front
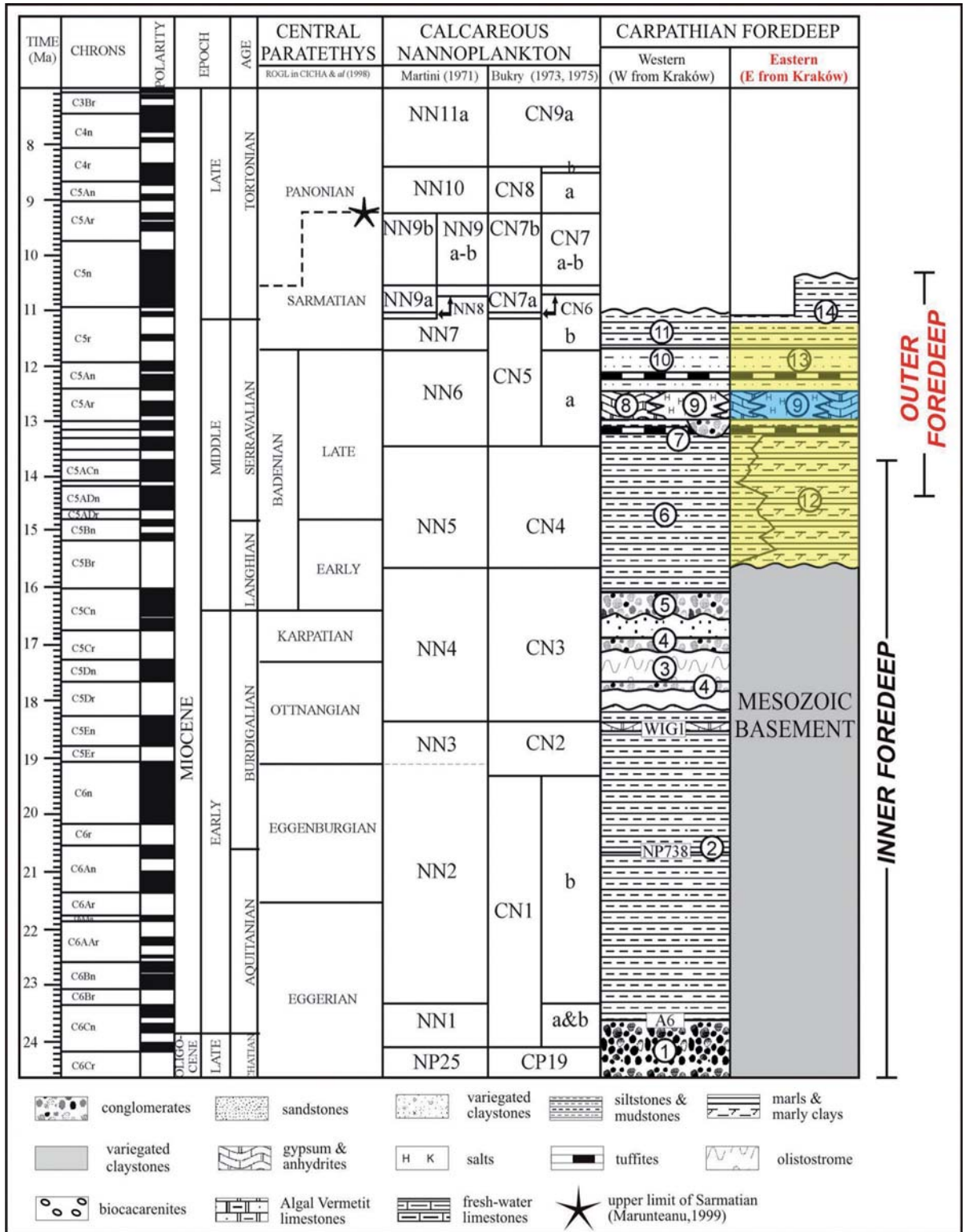
Fig. 5. Stratigraphic table of the Miocene deposits from the Polish Carpathian foredeep basin (after Oszczypko et al., 2005, simplified and supplemented). 1–14: lithostratigraphic unit (see Oszczypko et al. (2005) for detailed explanations). Sediments of the outer fordeep deposited east from Kraków and analyzed in this paper include Baranów beds (12, shown in yellow), evaporitic Wieliczka formation (9, shown in blue), and overlying siliciclastic Chodenice–Grabowiec formations together with the lower part of the Krakowiec beds (13 and 14 respectively, shown in yellow)
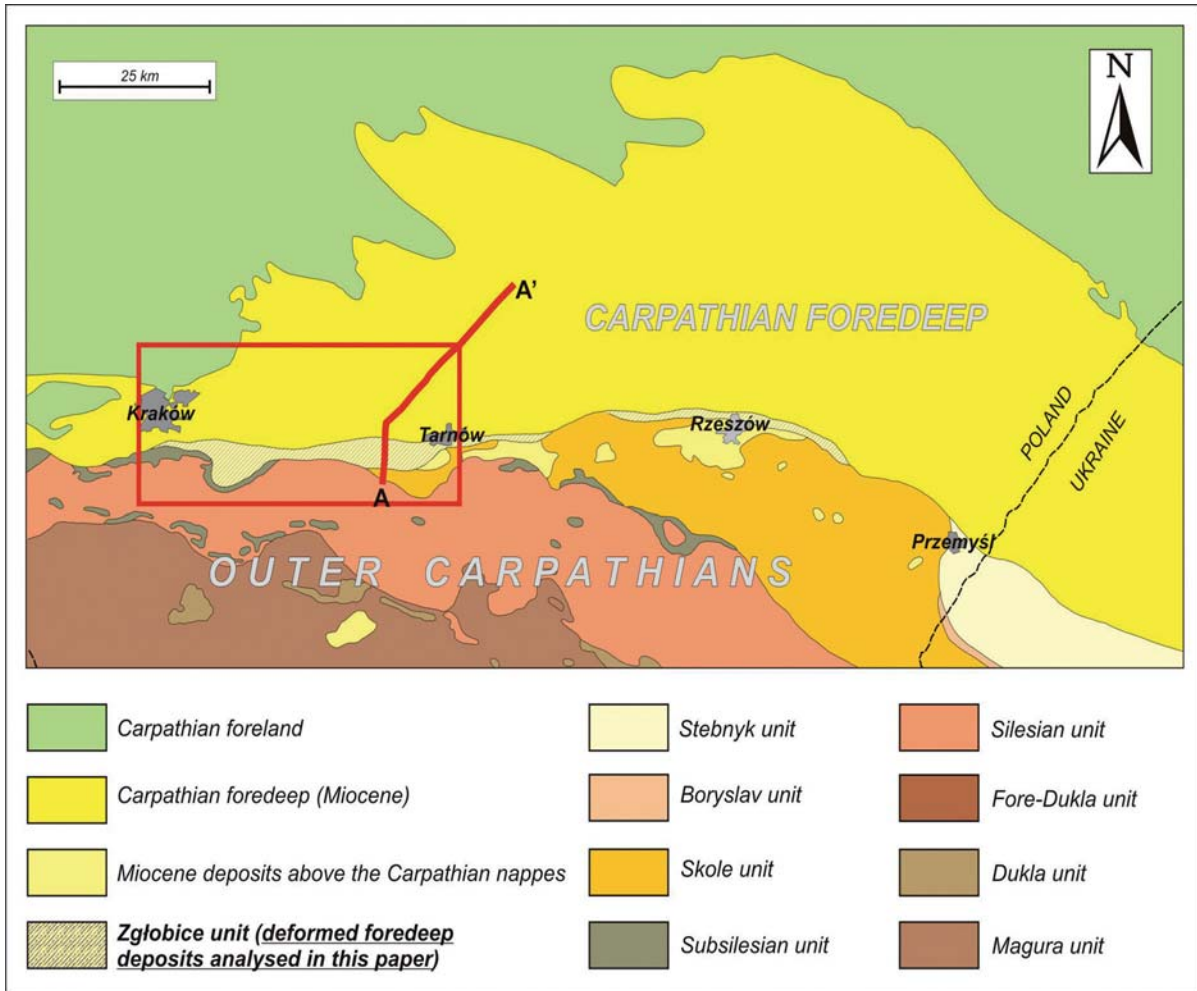
Fig. 6. Generalized geological map of the central and eastern Polish Carpathians. A-A': regional geoseismic cross-section shown on Fig. 7, red rectangle – area shown in Fig. 8
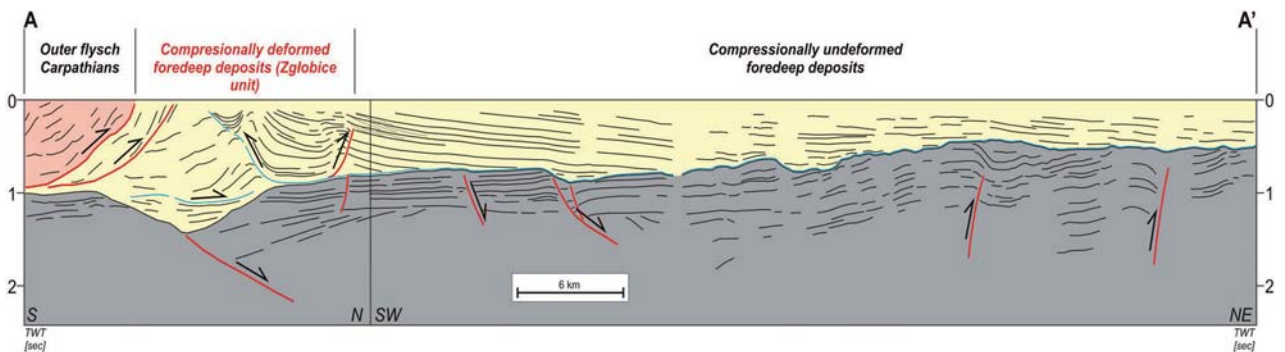
Fig. 7. Regional geoseismic cross-section showing relationship between the Carpathian orogenic wedge and the Carpathian foredeep basin. Blue line – Upper Badenian evaporites (mostly anhydrites). Note overall progradational pattern of the supra-evaporitic uppermost Badenian – Sarmatian foredeep deposits related to regional sediment supply from the south, from the eroded Carpathians. In front of the Outer flysch Carpathians zone of deformed Miocene foredeep deposits developed, including a triangle zone formed directly above the morphological paleovalley cut within the lower plate (cf. Fig. 9)
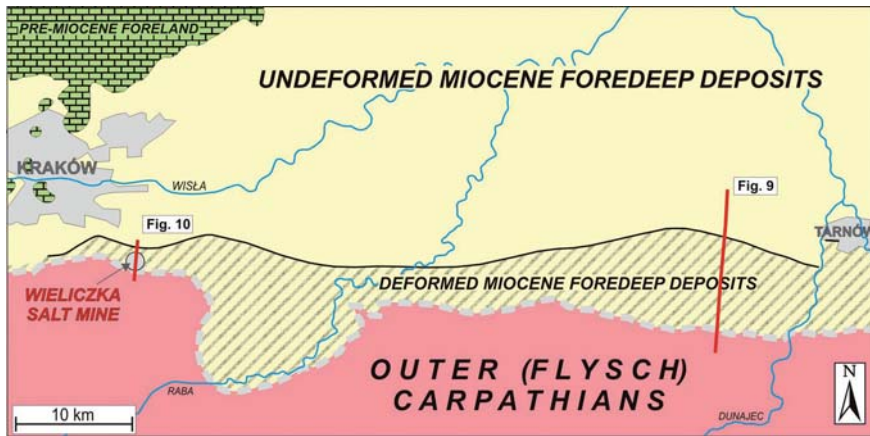
Fig. 8. Geological sketch of the Kraków – Tarnów area showing location of the seismic line from Fig. 9 (red line) and the Wieliczka Salt Mine together with approximate location of conceptual geologicalcross-section from Fig. 10 (red line)
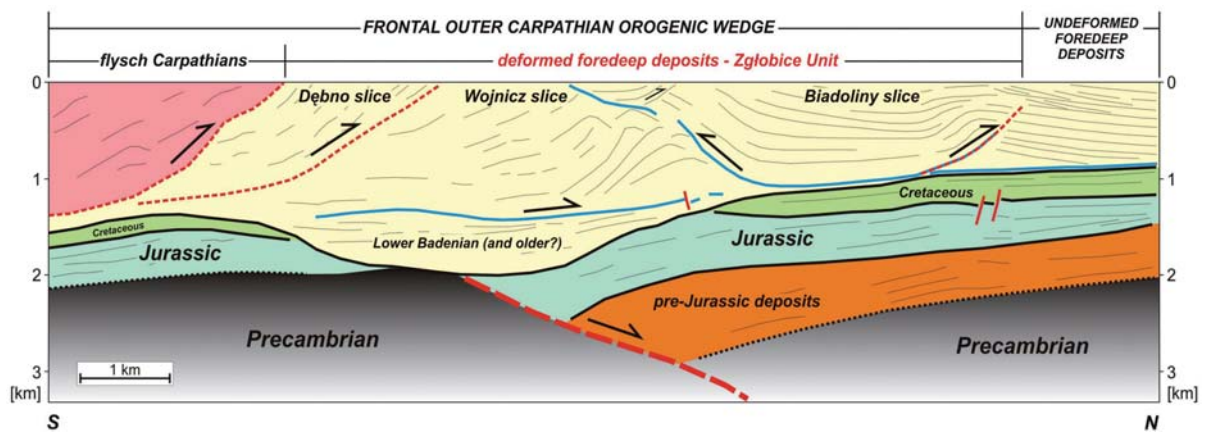
Fig. 9. Geoseismic sketch of the frontal Carpathian orogenic wedge east from Kraków (based on Krzywiec et al., 2004). Location is shown in Fig. 8

of the Outer Carpathian pre-Miocene flysch units (nappes). This Miocene tectonic unit has variable width, up to approx. 10 km in the area located between Kraków and Tarnów (Fig. 8).

Structure and evolution of the frontal Carpathian orogenic wedge have been subject of intense studies for many decades, as this area is related to important economic resources like rock salt and hydrocarbons. Numerous structural models have been proposed for the frontal Carpathians, and almost all of them relied on classical concepts of foreland-verging thrust-and-fold structural models (e.g., Tołwiński, 1956; Poborski & Skoczylas-Ciszewska, 1963; Kirchner & Połtowicz, 1974; Wdowiarz, 1976; Książkiewicz, 1977; Oszczypko & Tomaś, 1985; Połtowicz, 1991; Karnkowski, 2001). Some publications stressed the role of gravitational tectonics in formation of the frontal Carpathian thrust zone (Połtowicz, 1997, 2004). Jones (1997) postulated that in certain parts of the Polish Carpathian front a triangle zone might have developed with some evidence of backthrusting. It is well known that pres-

ence of foredeep evaporites significantly influenced thrust tectonics of the frontal Carpathian orogenic wedge (Połtowicz, 1994).

Within the area between Kraków and Tarnów (Fig. 8) foredeep Miocene deposits are characterized by two different types of compressional deformation. In the more eastern part of this zone, in the vicinity of Tarnów, recently acquired seismic data calibrated by numerous exploratory wells revealed that the front of the Polish Carpathians located within the Miocene Zgłobice unit is related to wedging tectonics. The geometry of the zone of deformed foredeep deposits is shown on the interpreted seismic profile from Fig. 9 (cf. Krzywiec et al., 2004). The Zgłobice unit is located in the footwall of the main N-verging flysch (pre-Miocene) Carpathian thrust sheet and is composed of three tectonic sub-units (slices) built of deformed Miocene foredeep deposits: Dębno, Wojnicz, and Biadoliny slices (Kirchner & Połtowicz, 1974). The southern Dębno slice is north-verging, whereas the northern Biadoliny slice is defined by south-verging backthrust,
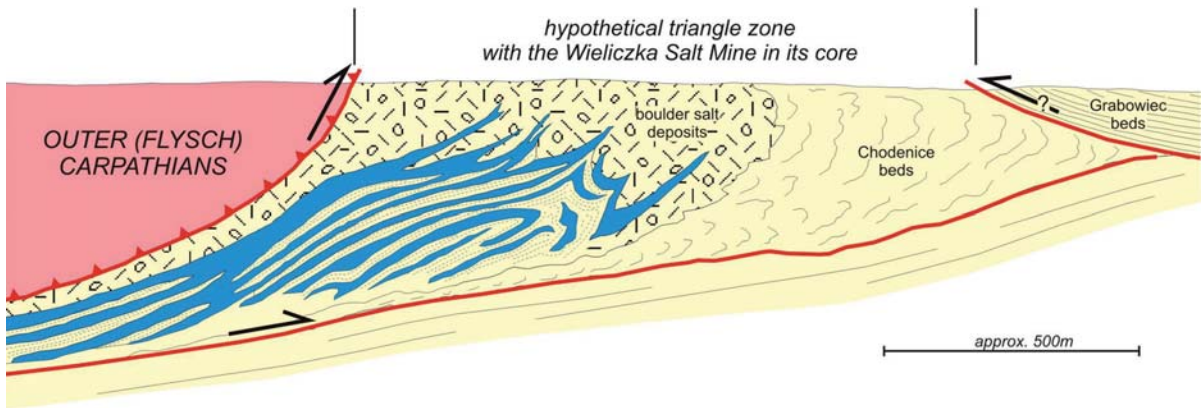
Fig. 10. Wieliczka cross-section (redrawn from Tołwiński, 1957, slightly modified and supplemented). According to this model, the Wieliczka Salt Mine is located within the core of the triangle zone. Blue – stratiform salt deposits, see text for further explanations. Location is shown in Fig. 8. Backthrust of the Grabowiec beds, similar to backthrust observed in the vicinity of Tarnów (Fig. 9), is inferred from the regional geometry shown on the original sketch of Tołwiński (1957), is not supported by structural data and therefore should be regarded as hypothetical

and, towards the foreland, a north-verging thrust representing the most frontal thrust of the entire Carpathian orogenic wedge (Fig. 9; cf Krzywiec, 2001). The intermediate Wojnicz slice is therefore bordered by the north-verging thrust of the Dębno slice and south-verging backthrust of the Biadoliny slice, and could be defined as a triangle zone. All these structures seem to be detached within the anhydrites of the Krzyżanowice formation, that are characterized in this area by relatively small thickness in order of 10–20 m on average. Only locally, rock salt of the Wieliczka formation has been encountered in several wells.

The Wojnicz slice is internally strongly deformed as proved by the observed south-dipping reflectors observed in the northern corner of this tectonic slice, beneath the backthrust defining its northern boundary (Fig. 9). These dipping reflectors are attributed to north-directed thrusts carrying uppermost Badenian - Sarmatian siliciclastic deposits above upper Badenian evaporites (anhydrites of the Krzyżanowice formation). These evaporites are partly infilling the paleovalley located beneath the Wojnicz tectonic unit. Well data confirm the involvement of the upper Badenian evaporites (both anhydrite and rock salt) within the northern imbricates of the triangle zone developed within the Zgłobice unit (Połtowicz, 1991).

The described triangle zone of the Wojnicz slice coincides with a deep erosional paleovalley (Fig. 9) that was incised most probably during Palaeogene inversion of the Mid-Polish Trough (cf. Krzywiec, 2002). The formation of the triangle zone above this paleovalley may have been related to accumulation of thicker upper Badenian evaporites in its axial part that have consequently acted as a more efficient detachment level during shortening. The triangle zone pin line coin-

cides with the northern slope of the paleovalley, which may have coincided with either reduction of upper Badenian evaporite thickness or development of locally overlapping evaporitic horizons, which at a later stage may in turn have triggered the initiation of the Biadoliny backthrust.

West from the Tarnów area, in vicinity of Kraków, a partly different style of deformation is observed within the Zgłobice unit built of deformed foredeep deposits which includes the Wieliczka Salt Mine. This mine, active since the XIth Century and being one of the classical areas of compressional salt tectonics (cf. Jackson, 1995) provides excellent information on the internal structure of the frontal Carpathian orogenic wedge. It is particularly important, as in this part of the frontal orogenic wedge no seismic data exists that could provide reliable information on its internal structure.

In the Wieliczka area it was possible to link available surface and subsurface datasets to build a relatively well-constrained cross-section (e.g., Tołwiński, 1956; Poborski and Skoczylas-Ciszewska, 1963; Fig 10. Using a model for the Tarnów area described above and cross-section by Tołwiński (1956) as a proxy, we'd like to propose that the Wieliczka Salt Mine is located within the core of the triangle zone being equivalent to the Wojnicz slice from the Tarnów area. To the south, this triangle zone is bounded by the frontal thrust of the Outer (flysch) Carpathians, and to the north by the frontal backthrust that carries Grabowiec beds to the south on top of the imbricates of the Wieliczka tectonic unit. Tectonic imbricates developed above a detachment level located in the salt unit. Each tectonic imbricate is formed by layers of salt followed by chaotic and irregular salt bodies (tens of meters large) corresponding to tectonic salt-breccias (in-

cluding clays and siltstones) as a product of erosion of basin margins during thrust emplacement (Kolasa & Ślączka, 1985; Ślączka & Kolasa, 1997). Beneath deformed foredeep succession that includes strongly deformed rock salt of the Wieliczka formation, autochthonous evaporites are present, developed as a rather thin and continuous anhydritic layer, similarly to, e.g., the Tarnów area described above (cf. Garlicki, 1979; Połtowicz, 1993). All these elements define a triangle zone similar to the triangle zone of the Wojnicz slice from the vicinity of Tarnów described above. Similarly to the Pyrenean thrust front in the Cardona area, the Wieliczka triangle zone might have formed where lat-

eral changes of evaporitic facies occurred at the transition from relatively thick rock salt of the Wieliczka formation to significantly thinner anhydrite facies of the Krzyżanowice formation.

The main difference between the two segments of the frontal Carpathians described above is the different involvement of evaporitic units in thrust tectonics. In the Wieliczka area relatively thick rock salt units make up almost the entire axial part of the triangle zone, while in the Tarnów area evaporites are very locally present within the core of the triangle zone and serve mainly as a preferred detachment level.
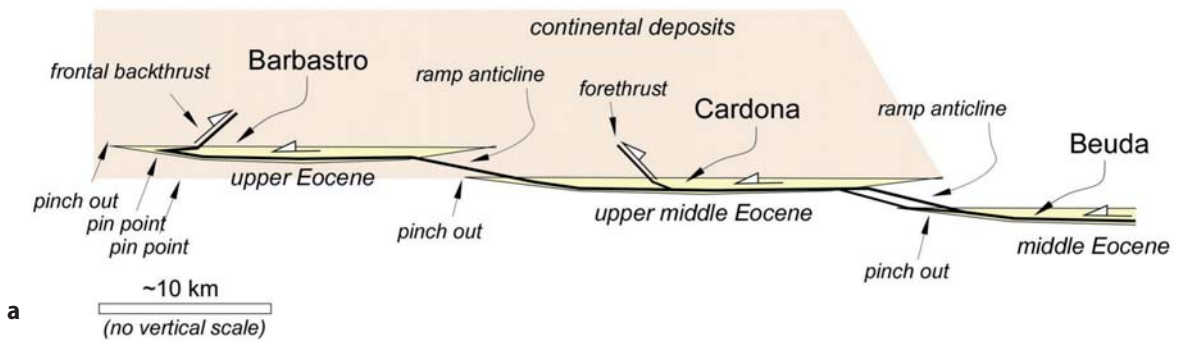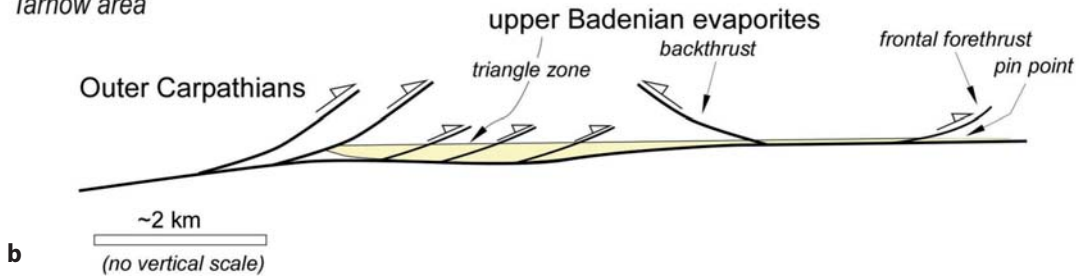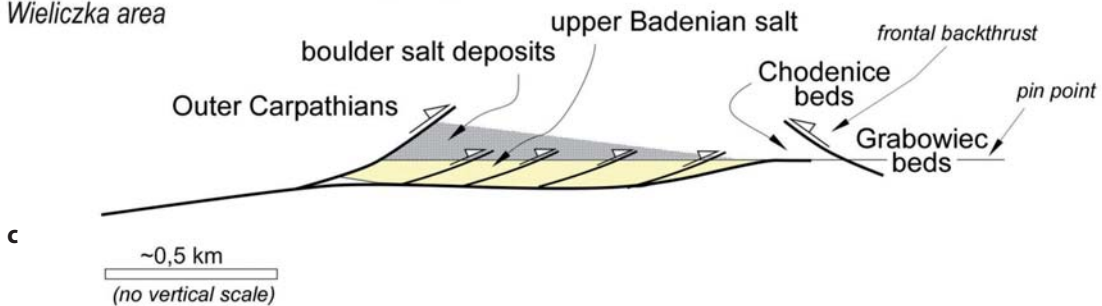
Fig. 11. Schematic models of the frontal thrust structures and influence of evaporitic units upon their development for the S Pyrenees **a**, and the Polish Carpathians: Tarnów area **b** and Wieliczka area **c**

4   Summary and Conclusions

The fronts of the Pyrenees and Carpathians share a common feature that is the presence of syntectonic foredeep / foreland evaporitic levels that developed in the course of foreland progradation of the advancing orogenic wedges. These evaporites exerted a strong control on the evolution of both thrust systems during late stages of their development (Fig. 11).

Within the SE frontal Pyrenees, thick and laterally extent evaporites were deposited from mid-Eocene to early Oligocene times (Cardona and Barbastro formations, respectively). The margins of the evaporitic basins defined the position of tectonic structures like ramps and backthrusts as well as of triangle zones. Zones of overlap of two successive evaporitic levels define location of anticlines on the hangingwall of the thrust ramps, whereas the external pinch outs of the uppermost evaporitic level define the position of backthrusts (Fig. 11A).

The central part of the Polish Carpathian orogenic wedge is characterized by the presence of Middle Miocene foredeep evaporites, that also played an important role in shaping of the orogenic front. The most frontal Carpathian unit built of the Miocene foredeep deposits (i.e. the Zglobice unit) is detached above evaporites of late Badenian age. In the Tarnów area, where evaporites comprise mainly relatively thin anhydrites, this unit is internally deformed by an imbricate thrust system developed between the north-directed frontal Carpathian thrust and the south-directed Biadoliny backthrust (Fig. 11B). This backthrust, carrying upper Badenian evaporites in the lowermost part of its hangingwall, formed at the tip point of the triangle zone of the Wojnicz slice. Location of this tip point may have been controlled either by location of a zone of rapid thinning of anhydrites of the Krzyżanowice formation above the northern slope of the pre-Miocene erosional paleovalley, or by overlap zone of two anhydritic units above this slope.

The Zgłobice unit in the Wieliczka area is characterized by a system of north-directed tectonic slices carrying rock salt interlayered by siliciclastics (Fig. 11C). The possible existence of a south-directed backthrust in the front of the Wieliczka imbricate system, suggested by previously published geological cross-sections based on well and mine data, strongly indicates the existence of a triangle zone equivalent to the triangle zone described within the Wojnicz slice in the Tarnów area. In a similar way as for the Cardona thrust front, the Wieliczka triangle zone might have formed where lateral changes of evaporitic facies occurred at the transition from salt to anhydrite facies.

Acknowledgements

References

Bahroudi A, Koyi HA (2003) Effect of spatial distribution of Hormuz salt on deformation style in the Zagros fold and thrust belt: an analogue modelling approach. Journal of the Geological Society, 160: 719–733.

Costa E, Vendeville B (2002) Experimental insights on the geometry and kinematics of fold-and-thrust belts above weak, viscous evaporitic decollement. Journal of Structural Geology, 24: 1729–1739.

Costa E, Camerlenghi A, Polonia A, Cooper C, Fabretti P, Mosconi A, Murelli P, Romanelli M, Sormani L, Wardell N (2004) Modeling deformation and salt tectonics in the eastern Mediterranean Ridge accretionary wedge. GSA Bulletin, 116(7–8): 880–894.

Cotton JT, Koyi HA (2000) Modeling of thrust fronts above ductile and frictional detachments: application to structures in the Salt Range and Potwar Plateau, Pakistan. GSA Bulletin, 112(3): 351–363.

Davis DM, Engelder T (1985) The role of salt in fold-and-thrust belts. Tectonophysics, 119: 67–88.

Garlicki A (1979) Sedimentation of Miocene salts in Poland. Prace Geologiczne PAN O/Kraków 119, 67pp. (in Polish with English summary).

Jackson M.P.A., 1995, Retrospective salt tectonics. [in]: Jackson MPA, Roberts DG, Snelson S (eds.), Salt Tectonics – A Global Perspective. AAPG Memoir 65: 1–28.

Jones P (1996) Triangle zone geometry, terminology and kinematics. Bulletin of Canadian Petroleum Geology 44(2): 139–152.

Jones P (1997) The Carpathians of the Southern Poland: thrust tectonic or wedge tectonics? AAPG Int. Conf., 7–10.09, Vienna. Abstracts: A27–A28.

Karnkowski P (2001) Geologia i ropogazonośność Przedgórza Karpat. Prace Instytutu Górnictwa Naftowego i Gazownictwa, 109, 79pp.

Kirchner Z, Połtowicz S, (1974) Budowa geologiczna obszaru między Brzeskiem a Wojniczem. Rocznik Polskiego Towarzystwa Geologicznego 44(2–3): 293–320.

Kolasa K, Ślączka A (1985) Sedimentary salt mega-breccias exposed in the Wieliczka mine, Fore-Carpathian Depression: Acta Geologica Polonica, 35: 221–230.

Kotlarczyk J (1985) Evolution of the Carpathian tectogene in the Miocene. [in]: Kotlarczyk J (ed.), Geotraverse Kraków - Baranów - Rzeszów - Przemyśl - Ustrzyki Dolne - Komańcza - Dukla. Guide to excursion 4 of the Carpatho-Balkan Geological Association XIII Congress, 21–32.

Krzywiec P (2001) Contrasting tectonic and sedimentary history of the central and eastern parts of the Polish Carpathian Foredeep Basin - results of seismic data interpretation. Marine & Petroleum Geology 18(1), 13–38.

Krzywiec P. (2002) Mid-Polish Trough inversion - seismic examples, main mechanisms and its relationship to the Alpine – Carpathian collision. [In]: G. Bertotti, K. Schulmann, S. Cloetingh (ed.), Continental Collision and the Tectonosedimentary Evolution of Forelands. European Union of Geosciences, Stephan Mueller Special Publication Series, 1: 151–165.

Krzywiec P, Aleksandrowski P, Florek R, Siupik J (2004) The structure of the Outer Carpathian orogenic front: an example of the Miocene Zgłobice unit between Brzesko and Wojnicz – new data, new models, new questions. Przegląd Geologiczny 52(11): 1051–1059 (in Polish with English abstract).

Książkiewicz M (1977) The tectonics of the Carpathians. [in]: Pożaryski W (ed.) Geology of Poland, IV, Tectonics, 476–620.

Letouzey J, Colletta B, Vially R, Chermette JC (1995) Evolution of Salt-Related Structures in Compressional Settings. [in]: Jackson MPA, Roberts DG, Snelson S (eds.), Salt Tectonics – A Global Perspective. AAPG Memoir 65: 41–60.

MacKay PA, Varsek JL, Kubli TE, Dechesne RG, Newson AC, Reid JP (eds.) (1996) Triangle Zones and Tectonic Wedges: an Introduction. Bulletin of Canadian Petroleum Geology 44(2): 1–5.

Oszczypko N (1998) The Western Carpathian foredeep – development of the foreland basin in front of the accretionary wedge and its burial history (Poland). Geologica Carpathica 49(6): 415–431.

Oszczypko N, Tomaś A (1985) Tectonic evolution of marginal part of the Polish Flysch Carpathians in the Middle Miocene. Kwartalnik Geologiczny 29(1): 109–128.

Oszczypko N, Krzywiec P, Popadyuk I, Peryt T (2005) Carpathian Foredeep Basin (Poland and Ukraine) - its sedimentary, structural and geodynamic evolution. [in]: Picha F, Golonka J (eds.), The Carpathians and Their Foreland: Geology and Hydrocarbon Resources, AAPG Memoir 84, 293–350.

Picha F, Golonka J (eds.) The Carpathians and Their Foreland: Geology and Hydrocarbon Resources, AAPG Memoir 84, 848pp.

Poborski J, Skoczylas-Ciszewska K (1963) Miocene in the zone of the Carpathian overthrust in the area of Wieliczka and Bochnia. Rocznik Polskiego Towarzystwa Geologicznego 33(3): 339–348 (in Polish with English summary).

Połtowicz S (1991) Miocene of the Carpathian zone between Wieliczka and Dębica. Geologia 17(3): 19–57 (in Polish with English summary).

Połtowicz S (1993) Palinspastyczna rekonstrukcja paleogeografii badeńskiego salinarnego zbiornika sedymentacyjnego w Polsce. Geologia 19(4): 203–233.

Połtowicz S (1994) Znaczenie badeńskiej formacji solonośnej w tektogenezie polskich Karpat brzeżnych. Geologia 20(1): 59–75.

Połtowicz S. (1997) Grawitacyjna tektonika jednostki zgłobickiej między Brzeskiem a Wojniczem w świetle wyników badań sejsmicznych. Geologia 23(3): 307–329.

Połtowicz S (2004) The Stebnik and Zgłobice Units in the Polish Carpathian structure. Geologia 30(1): 85–120 (in Polish with English summary).

Ramírez A, Riba O, (1975) Bassin potassique catalan et mines de Cardona. IX Cong. Intern. Sed., Nice, Livret-guide 20: 49–58.

Riba, O., S. Reguant, and J. Villena (1983) Ensayo de síntesis estratigráfica y evolutiva de la cuenca terciaria del Ebro, [in]: J. A. Comba, ed., Libro Jubilar J.M. Ríos, Geología de España, Tomo II, v. II: Madrid, Instituto Geológico y Minero de España, p. 131–159.

Sans, M., 1995, Structural analysis of a thrusted anticline: fold and thrust geometry and fracture distribution, Univ. de Barcelona, p. 1–53.

Sans M, Muñoz JA, Vergés J, (1996) Thrust wedge geometries related to evaporitic horizons (Southern Pyrenees). Bulletin of Canadian Petroleum Geology 44(2): 375–384.

Sans M, Vergés J (1995) Fold development related to contractional salt tectonics: southeastern Pyrenean thrust front, Spain. [in]: Jackson MPA, Roberts DG, Snelson S, (eds.), Salt Tectonics – A Global Perspective. AAPG Memoir 65: 369–378.

Sherkati S, Molinaro M, de Lamonte DM, Letuzey J (2005) Detachment folding in the central and eastern Zagros fold-belt (Iran): salt mobility, multiple detachments and late basement control. Journal of Structural Geology, 27: 1680–1696.

Ślączka A, Kolasa K (1997) Resedimented salt in the Northern Carpathians Foredeep (Wieliczka, Poland). Slovak Geological Magazine, 3: 135–155.

Tołwiński K (1956) Główne elementy tektoniczne Karpat z uwzględnieniem górotworu Salidów. Acta Geologica Polonica 6(2): 75–226.

Vergés, J. (2003) Evolución de los sistemas de rampas oblicuas de los Pirineos meridionales: fallas del Segre y Pamplona: Boletin Geológico y Minero de España, v. 114, p. 87–101.

Vergés J, Muñoz JA, Martínez A. (1992) South Pyrenean fold-and-thrust belt: role of foreland evaporitic levels in thrust geometry. [in]: McClay KR (ed.), Thrust Tectonics, 255–264. Chapman and Hall, London.

Vergés, J., D.W. Burbank, (1996) Eocene-Oligocene Thrusting and Basin Configuration in the Eastern and Central Pyrenees (Spain), in P. F. Friend, and C. J. Dabrio, eds., Tertiary Basins of Spain. The Stratigraphic Record of Crustal Kinematics, v. 6, Cambridge University Press. World and Regional Geology, p. 120–133.

Vergés, J., M. Fernàndez, and A. Martínez (2002) The Pyrenean orogen: pre-, syn-, and post-collisional evolution, in J. G. Rosenbaum, and G. S. Lister, eds., Reconstruction of the evolution of the Alpine-Himalayan Orogen, Journal of Virtual Explorer, 8, p. 55–84.

Wdowiarz S (1976) O stosunku Karpat do zapadliska przedkarpackiego. Przegląd Geologiczny 6: 350–357

Reservoir Properties of Miocene Sandstones in Rzeszow Area (Carpathian Foredeep, Poland)

Grzegorz Leśniak · Piotr Such · Piotr Dziadzio

Abstract. An integrated sedimentological, petrophysical and petrological study has been carried out in the Miocene succession in the southern Carpathian Foredeep basin of SE Poland, involving examination of ca. 800 m of cores combined with analysis of wire line logs from 14 wells. Our main goal was to identify regional trends in development of reservoir properties of the Miocene. Very good reservoir sandstones occur only in channel fill facies association, the top of which accounting for the best reservoir and filtration properties of sandstones and gas accumulations.

Keywords. Miocene sandstones, facies association, reservoir properties, compaction, cementation, Carpathian Foredeep

1   Introduction

Many gas reservoirs were discovered in the Miocene sandstones of the eastern part of the Carpathian Foredeep. Gas research conducted in recent years showed that new discoveries are more difficult because of complex architecture of the basin and ambiguity of seismic interpretation caused by small amplitudes of structures. So, a new prospecting impulse was needed. The central idea of the paper is to define a set of necessary conditions for existence of reservoir traps in this area, its sedimentary architecture and petrographic studies being the main prospecting factors in Miocene research.

The area of interest is shown in Fig.1.

2   Methodology

Totally 154 cores from 14 wells were investigated. A set of investigations were carried out consisting of facies, well log, sequence stratigraphy analyses and classical petrography, computer analyses of microscopic images, cathodoluminescence and scan microscopic analyses as well as investigations of pore space parameters (density, porosity, permeability, mercury porosimetry) (Fig. 2) (Such 2002).

3   Geological Setting

The Carpathian Foredeep basin developed in Miocene times in front of the Carpathian orogenic wedge, at the junction between the Precambrian East European and Palaeozoic platforms. The filling of eastern parts of the Carpathian Foredeep, as in most foredeep basins, took place in two main stages:

1. Underfilled flysch stage-lasting from the early Badenian to the lower part of late Badenian (Moravian - Wieliczian).
2. Overfilled molasse stage - lasting from upper part of the late Badenian to Panonian (Kosovian-Meotian) (Dziadzio et al., 2006) (Figs. 3 & 4, Tab. 1) Classically, this flysch to molasse transition is interpreted as a record of migration of the thrust wedge and foreland basin over the hinge line of the inherited passive margin. Also, the Badenian and Sarmatian successions are characterized by very diverse facies, which were deposited in various depositional environments.

The Badenian and Sarmatian successions are interpreted to have been deposited within 3 third-order depositional sequences: the two first in Badenian time (not recognized in seismic scale), and the third in Sarmatian time, which consists of 4 fourth-order sequences (Dziadzio, 2000 a,b; 2006), total thickness ranging from 800 to over 3000 m.

The oldest part of the stratigraphic succession is made up of the Baranow Beds (Moravian in age; thickness of ca. 0.1–30 m) (Figs. 3 & 4, Tab. 1), deposited in shelfal and near-shore environments during a relative sea level rise followed by a sudden sea level fall (Dziadzio, 2000a,b; Dziadzio et al., 2006). The anhydrite deposits (Wieliczian in age) were deposited during a gradual sea-level rise. The Grabowiec beds (Volhynian) formed in outer shelfal environments during the deepest water phase of the basin's development. During this time in the northern part of the Carpathian Foredeep mainly pelagic deposits occur but in the southern part submarine fan deposits developed. The
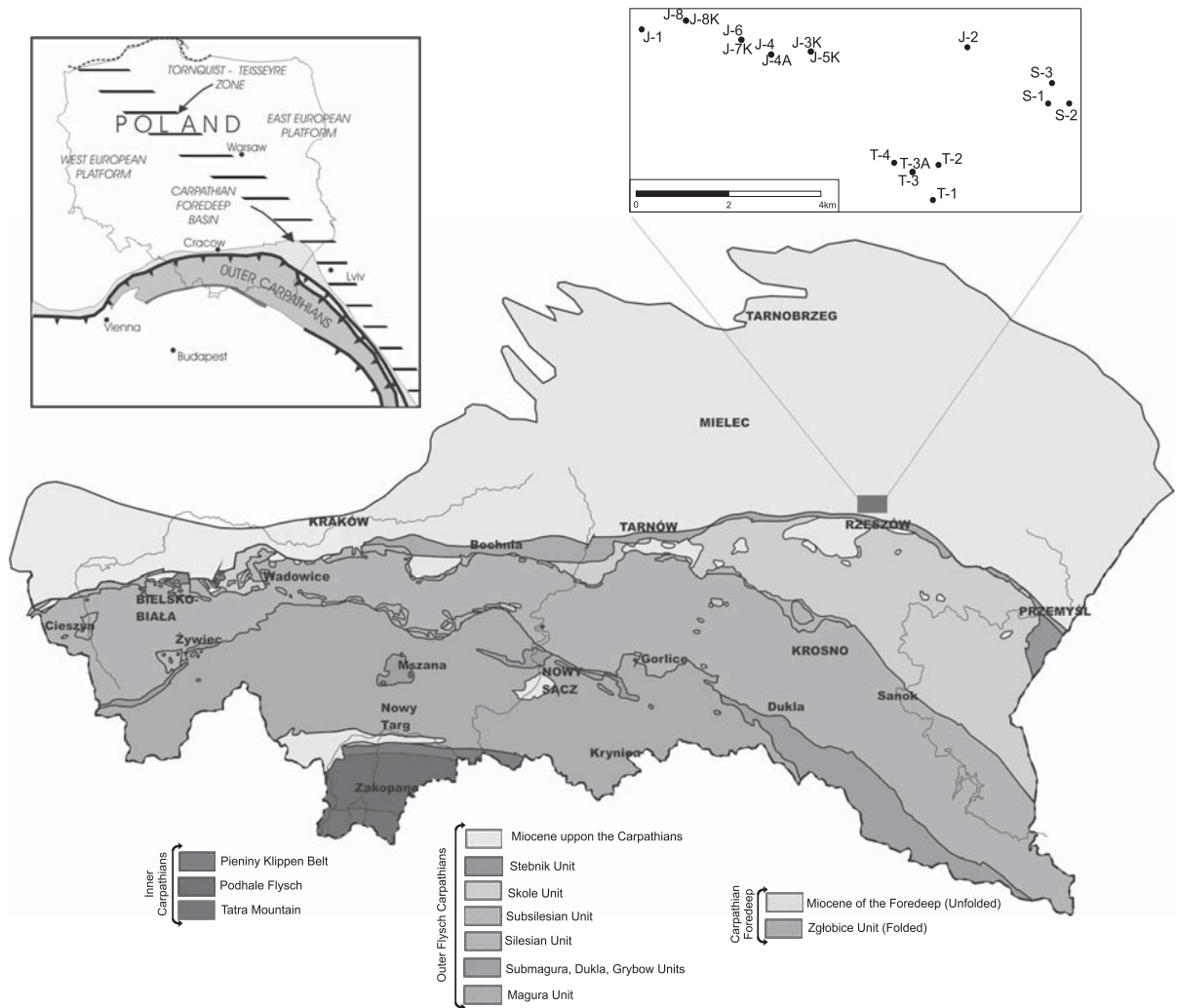
Fig. 1. Location of the studied area: The Miocene sediments in Rzeszow area

Badenian sequences were deposited during two 3rd order sequences. In some areas in the NE part of the Carpathian Foredeep (Fig.4), root structures have been recognized at the top of the Badenian deposits, which are interpreted as associated with a 1st order sequence boundary (Dziadzio, 2000b; Dziadzio et al., 2006).

In the deepest, eastern part of the Carpathian Foredeep, Sarmatian series rest conformably over the Badenian deposits (Fig. 4). The younger Sarmatian deposits onlap to the northwest over the Badenian deposits. The Sarmatian deposits are subdivided into three contrasting depositional environments: I - basin plain complex, II - submarine fan complex, III - deltaic complex with delta fans at the base (Dziadzio, 2000b; Dziadzio et al., 2006) (Fig. 4). These three 'depositional complexes' have different lithological characteristics and different depositional architectures. The basin plain sequence is dominated by fine-grained turbidites

with thick turbidite sandstone bodies at the base, and has been recognized only in the deepest part of the Polish Carpathian Foredeep (Dziadzio, 2000a).

The submarine fan complex was deposited in the southern part of the Carpathian Foredeep (close to the Carpathian orogenic front) as a series of classical fan deposits which extend farther north as widespread tabular-like turbidite sandstone and shale. Deltaic complex is dominated by heterolithic facies intercalated with sandstones. They form a series of offlaping del-

Fig. 2. Composite image combining Miocene cores with sedimentary sketch and well logs. Yellow point on core image shows the core investigated in laboratory. The set of investigations is shown on the left side of figure. It covers classic petrology, cathodoluminescence and SEM investigations, computer analysis of images, capillary pressure and relative permeability investigation
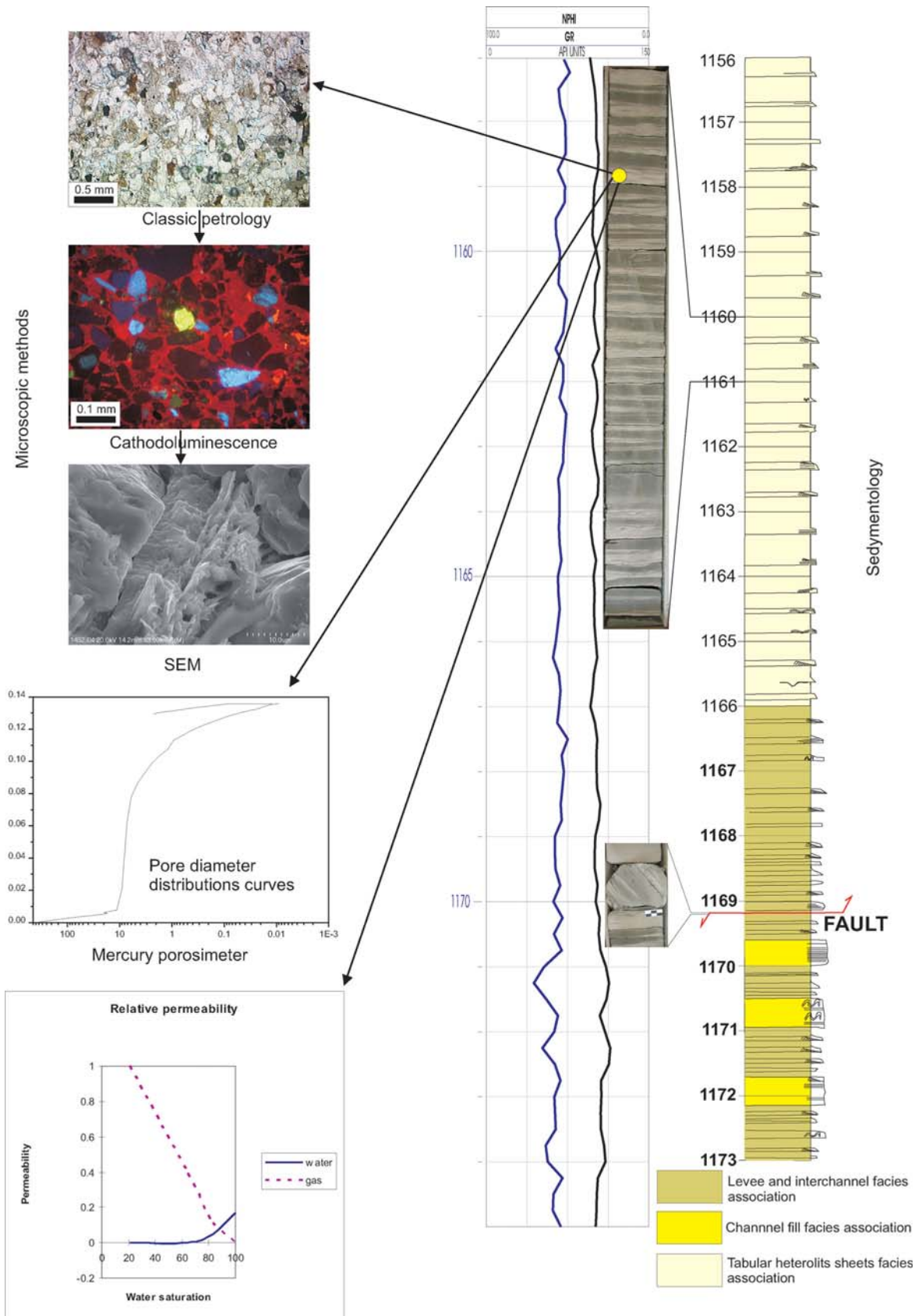
Table 1. Stratigraphic chart of Carpathian Foredeep (after Dziadzio et al., 2006)

Ma. Gradstein et al, 2004	EPOCH		AGE	CENTRAL PARATETHYS (Rögl, 1998)	EASTERN PARATETHYS (Rögl, 1998)			CALCAREOUS NANNOPLANKTON ZONES (Gradstein et al., 2004)	FORAMINIFERA ZONES	LITOSTRATIGRAPHICAL UNITS (eastern part of the Carpathian Foredeep)
7,25										
8	MIOCENE	Upper	TORTONIAN	PANONIAN	Meotian			NN10		Krakowiec clays
9									Trochammina kibleri	
9,8								NN9		
10										
10,6					Chersonian			NN8		
11				SARMATIAN	Bessarabian	U.		NN7	Porosononion granosum	
11,61		Middle	SERRAVALIAN						Elphidium hauerinum/ Varidentella reussi Anomalinoides dividens	
12					Wolhynian	L.				
13				BADENIAN	Kosovian	Upper		NN6	Velapertina indigena	Grabowiec beds
13,65					Wieliczian				Uvigerina costai	Evaporites
14			LANGHIAN		Moravian	Lower		NN5		Baranow beds
15									Candorbulina universa	
								NN4		

taic bodies deposited in a ramp-type basin. They form deltaic successions from prodelta to delta front with thin turbidites in the distal part. Upper part of this complex is dominated by deposits of bay fill environment (Dziadzio, 2000a; Dziadzio et al., 2006). Delta deposits occur in the southern part of the Carpathian Foredeep at the base of third complex fan.

Whole Sarmatian series was deposited during fluctuating relative sea level and their successions exhibit a general shallowing upward trend.

Main transport direction during sedimentation of III Sarmatian depositional complexes was from the Carpathian orogen toward the foreland, with opposite trends (from NW to SE) in younger deposits (Dziadzio, 2000b).

In the study area the traps are made up of multihorizon compactional structures of the Sarmatian deposits over the basement highs (Figs. 5–7), mainly in the widespread turbidites.

4   Facies Analysis

Facies analysis was devoted mainly to sand and mud facies because clay-building trap sealings are practically present everywhere. Six facies were distinguished, including: (a) massive to laminated sandstone; (b) thin-bedded, graded, and laminated sandstone; (c) thin-bedded sandstone with low-angle cross-lamination; (d) calcium carbonate-cemented sandstone; (e) siltstone; and (f) mudstone (Figs.7 & 8).

4.1 Facies Description

4.1.1   Facies (A): Massive to Laminated Sandstone (Fig. 8 a – f)

This facies is represented by thick-bedded to massive homogenous sandstones, locally containing thin lamina of mudstone or claystone. The sandstones are very fine- to coarse-grained, with total content of clay matrix below 20%, or entirely devoid of clay fraction.

The thickness of individual sandstone beds from the cored intervals ranges from 4 to 10 m, usually ca. 1 m. Bed amalgamations as well as changes in grain size of sandstones are frequent. Some thick sandstone beds are massive and show a normal or inverse grading. In some beds, fining-up top grading into very fine sandstone, or mudstones with Tb-d, seldom Te divisions (Bouma, 1962), are present. In many cases, climbing ripples (Jopling and Walker, 1968) occur near the top part of sandstone beds, and are interpreted here as Bouma Tc division (Bouma, 1962; King and Browne, 2002). Deformed bedding and convolute lamination are common, as well as clay clasts (often imbricated), water escape structures, and sand dykes. Between or inside the sandstone beds, coalified plant debris occur in laminae few millimeters thick.

Bed soles tend to be sharp, and tops can be either sharp, or gradational in fine-grained facies. Traction structures, such as horizontal lamination and low-angle cross-lamination in the lower or middle part
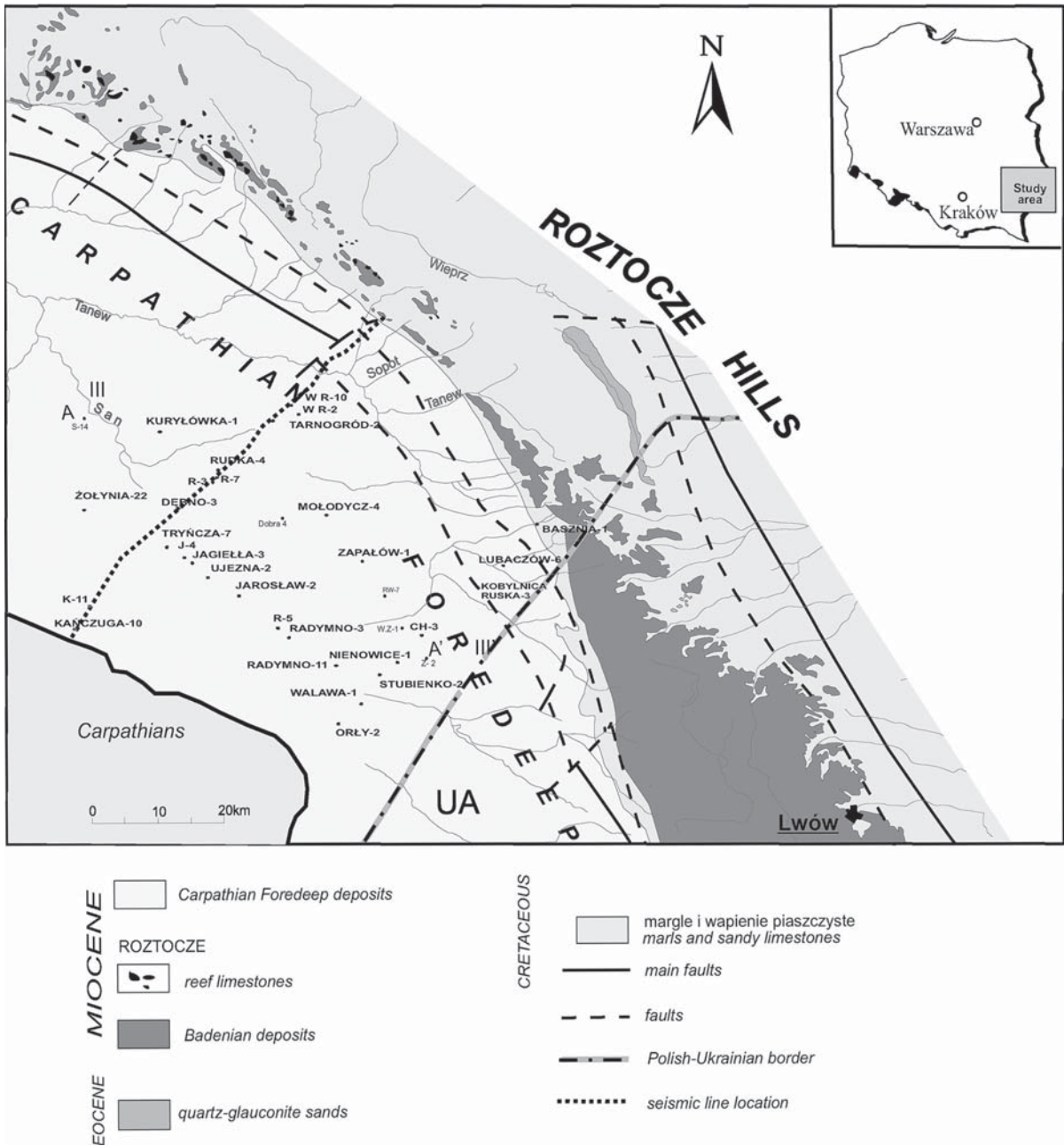
Fig. 3. Map of the eastern part of the Polish Miocene Basin with location of seismic line of Figure 4

of individual sandstone beds are abundant. However, high-angle cross-stratification and through cross-stratification were noted in few cases only.

This facies shares the characteristics of classical turbidites (Bouma, 1962) and high-density turbidites (Lowe, 1982). The presence of clay clasts in different parts of thick sandstone beds and the erosional bases are compatible with highly turbulent flows. Some of the deformed bedding and convolute lamination reflect hydroplastic deformation of unconsolidat-

ed deposits during sedimentation, and resedimentation either down regional slope or towards the channel center. The dish structures and sand dykes formed penedepositionally as a result of pore water displacement (Lowe, 1975).

Facies A occurs within distributary channels, where the energy of turbidity flows was the highest and where the erosion at the base of turbulent flows was very strong.
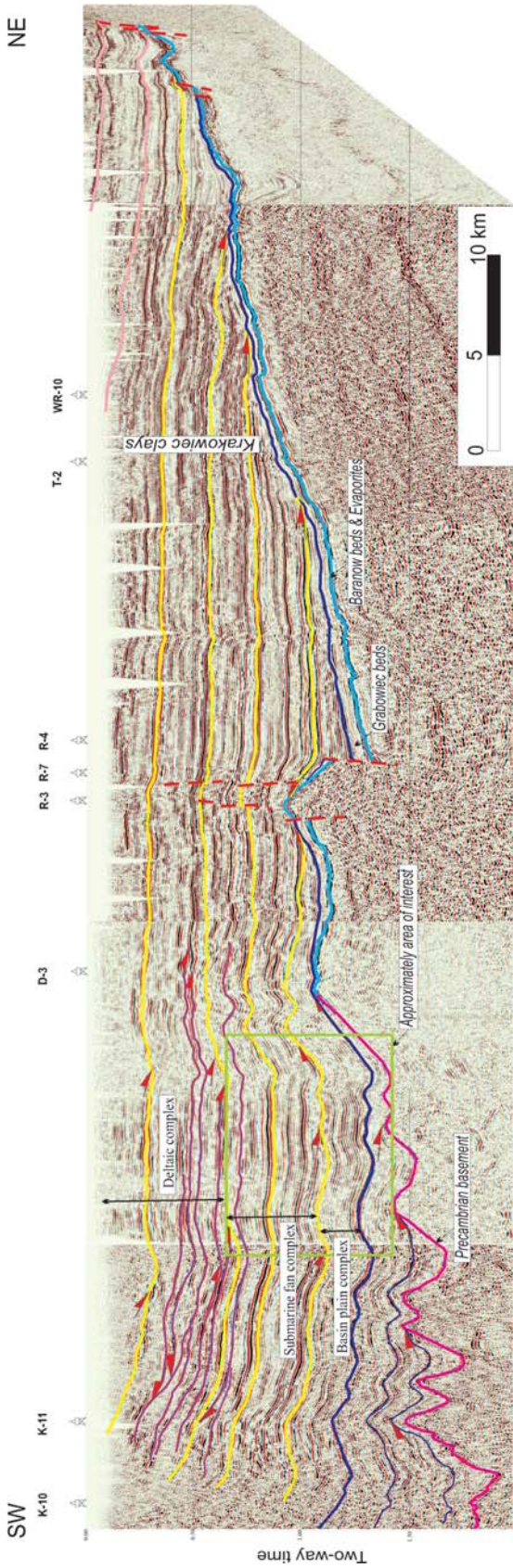
Fig. 4. Seismic line across the Carpathian Foredeep (location as shown in Fig. 3) combined with depositional architectures
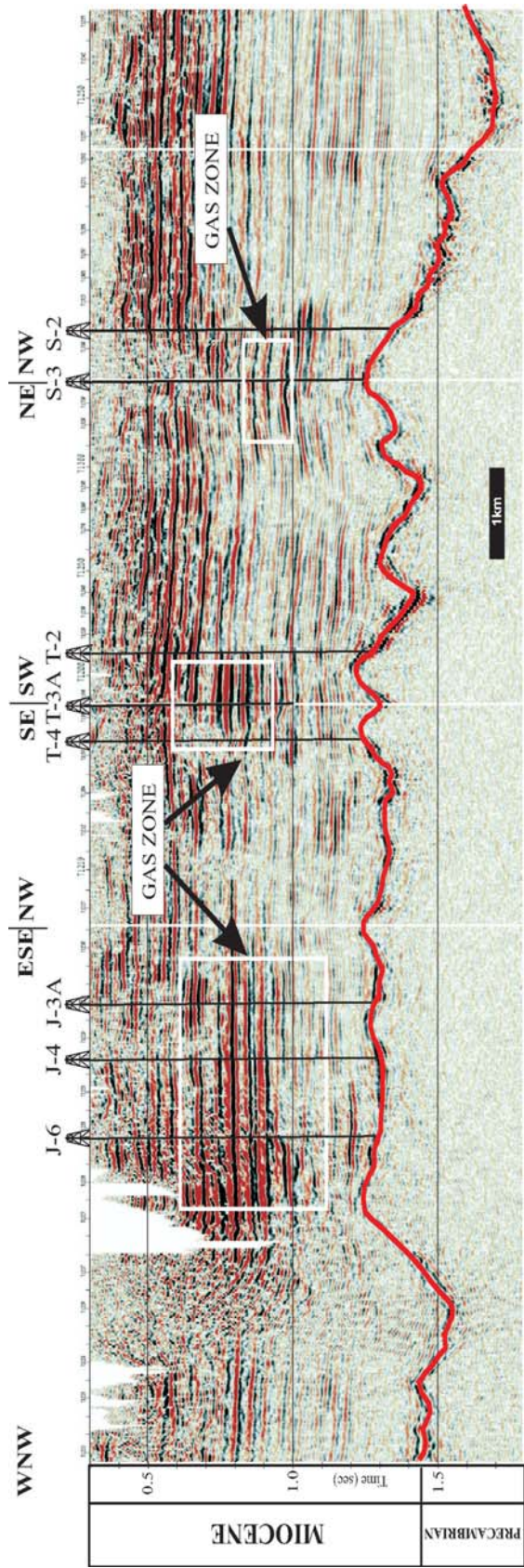
Fig. 5. Reservoir interpretation: the 3D cross seismic line through the Stobierna-Terliczka-Jasionka structure (after K. Madej in Mysliwiec et al., 2006), outlining gas accumulation zones
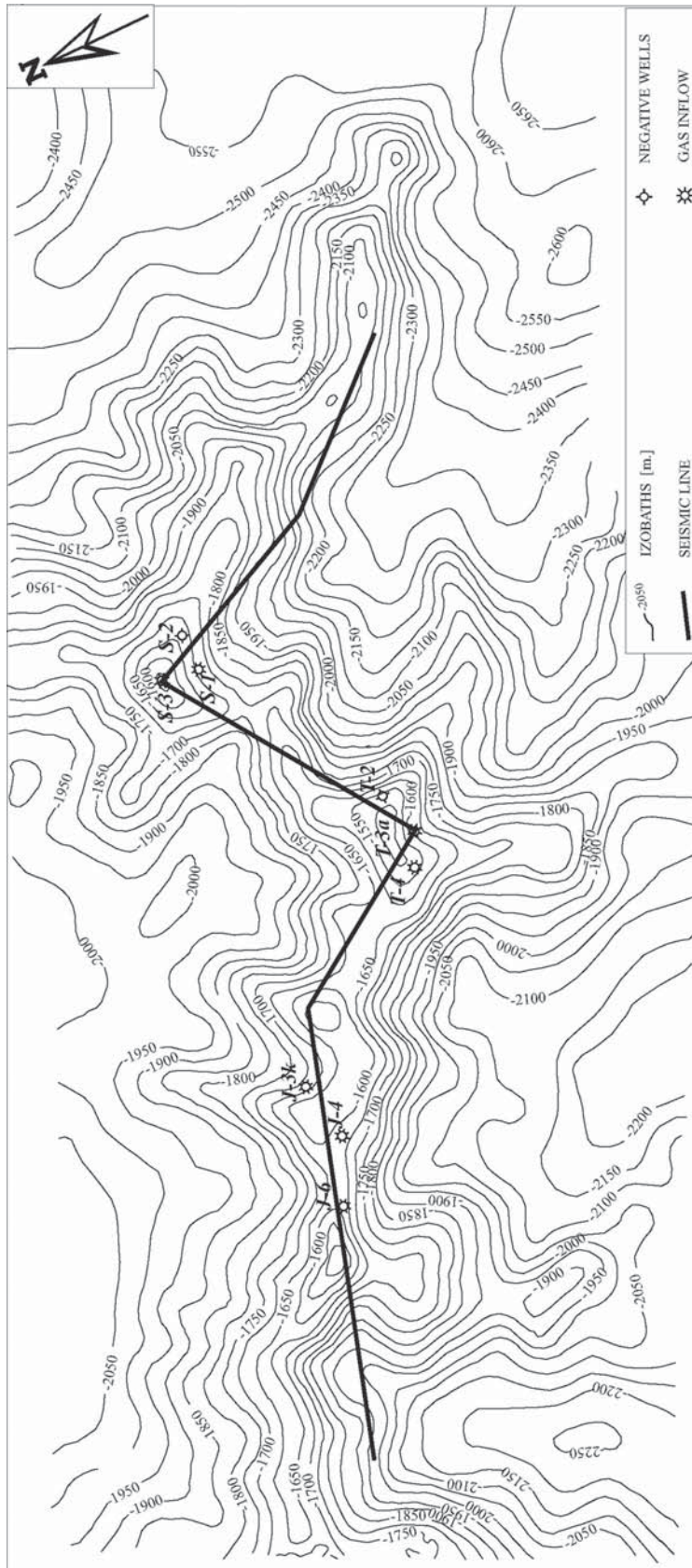
Fig. 6. Contour map of the pre-Miocene basement in the Stobierna-Terliczka-Jasionka area (after K.Madej in Mysliwiec et al., 2006)
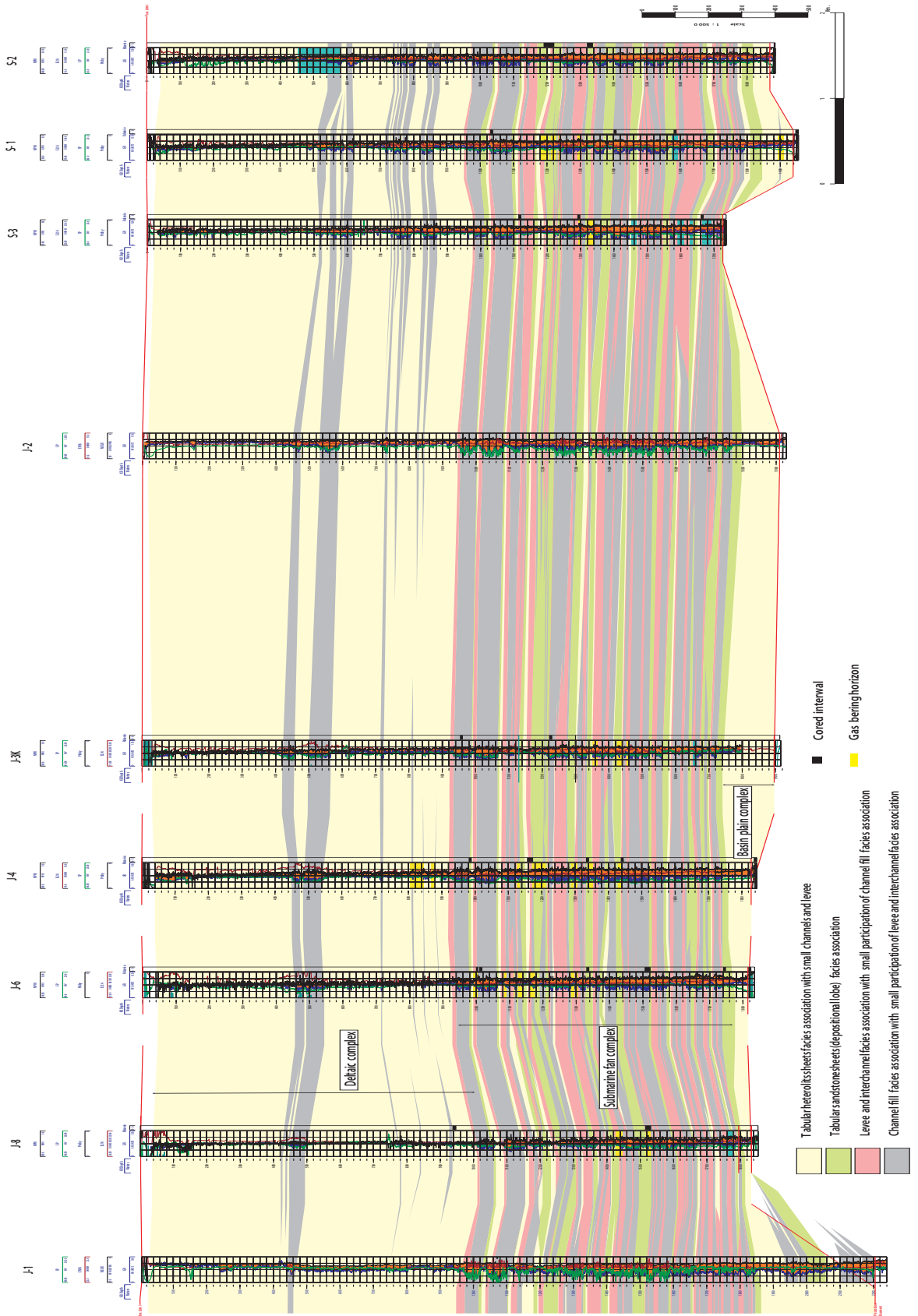
Fig. 7. Synthetic sedimentological sketch: correlation for Jasionka-1 – Stobierna-2 with extracted facies associations, gas bearing horizons, combined with interpreted well logs

4.1.2 Facies (B): Thin-Bedded Graded and Laminated Sandstone (Fig. 8, g, h)

This facies is represented by sandstone beds up to several centimeters in thickness. The beds are very fine-grained to medium-grained and show normal grading, horizontal lamination, cross-lamination, and convolutions, all attributable to Bouma Ta-e, Tb-e, and Tc-e sequences. Some of the sandstone beds reveal only Tc or Td divisions. Climbing ripples of type A, B, S (Jopling and Walker, 1968), and bimodal ripples are present. Wave and flaser bedding occur as well, and show very small mud lenses within ripple troughs. Plant-debris laminae, hydroplastic deformations, and rip-up clay clasts are common. The bases of the sandstone beds are sharp, and tops are gradational.

This facies represents the deposits of classical, though more diluted turbidity currents, laid down in lobe or distal channel-lobe transitions. Deposition was mainly by traction (Tb, Tc, and Td) from flows of declining velocity, followed by suspension settling from the dilute tail of an individual turbidity current.

Sandstone/siltstone with opposite (very often bimodal) ripple cross-laminae could be an effect of deposition from bidirectional currents. The presence of climbing ripples and wavy-bedded fine sand indicates lower flow regime deposition from bottom flows carrying abundant suspended sediment. Intervals that contain rippled beds showing both parallel and transverse sediment transport, were deposited away from the channel.

This facies is interpreted as formed near the top of adjacent channel complexes, and within interchannel and overbank areas.

4.1.3 Facies (C): Thin-Bedded Sandstone With Low-Angle Cross-Lamination (Fig. 8 j, l)

This facies is represented by fine-to-medium-grained, thin-bedded sandstone showing low-angle (<10°) cross stratification. Beds range in thickness from a few to 15 cm and occur in simple or tabular bedsets. Bases and tops of sandstone are sharp and usually against the facies E or F.

Facies C was deposited by turbidity currents passing from upper to lower-flow regime, and extending over many different areas of deposition, such as interchannel, overbanks, lobes with flat top surfaces and as thin drapes mantling an uneven substratum.

4.1.4 Facies (D): Calcium Carbonate-Cemented Sandstone, Siltstone, and Mudstone (Fig 8, i)

This facies is represented by different types of sandstones and siltstones that are cemented by calcium carbonate. The thickness of this facies ranges from several millimeters to a few centimeters. Cemented sandstones and siltstones form individual layers in all recognized facies, but they are particularly abundant in mudstone and claystone facies.

This facies occurs as interbeds among all other facies, but does not assume any specific position within otherwise preferred facies successions. Calcium carbonate forms a primary cement, which suggests that it originated from the recrystallization of micrite emplaced together with siliciclastic detritus.

4.1.5 Facies (E): Laminated Siltstone and Claystone (Fig. 8 m, n)

This facies is represented by silty claystone and claystone showing mm- to cm-thick silt and very fine sand laminae. It is the most frequent facies in all analyzed cores. The thickness of this facies varies from a few millimeters to several centimeters. Horizontal lamination, ripple cross-lamination, and convolute lamination are present in silt-rich parts of this facies, and are attributed to Bouma Tb-d divisions. Some laminae-sets correspond only to Tc or Td divisions. The laminae tend to display sharp bases and sharp or gradational tops. Starved ripples and deformed laminae are common. Siltstone beds contain plant debris, sometimes as very thin (2–3 mm) laminae of coal.

This facies was deposited by low-concentration turbidity currents in distal parts of basin (basin plain) as well as in interchannel and overbank areas.

4.1.6 Facies (F): Mudstone

This facies consist of homogeneous and massive, mostly unbedded claystone and clay shales. Sporadically preserved signs of bedding and lamination are mainly expressed by a color change and very thin silt laminae. The thickness of this facies ranges from a few to tens of centimeters. This facies forms interbeds to sand and silt-dominated facies, all together forming heterolithic deposits.

Massive claystones and clay shales are hemipelagic suspensates that covered the basin floor and overbank areas, and can be interpreted as drape deposits. The presence of isolated laminae of silt or starved ripple lamination indicates deposition from weak traction currents.
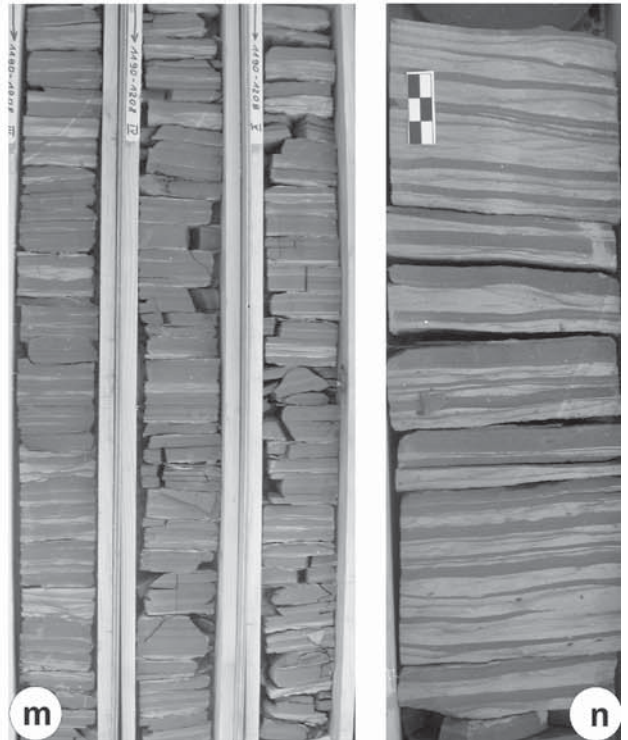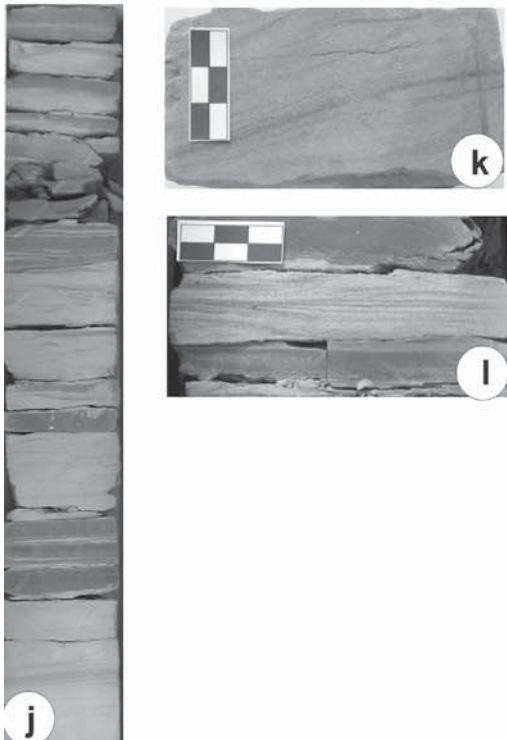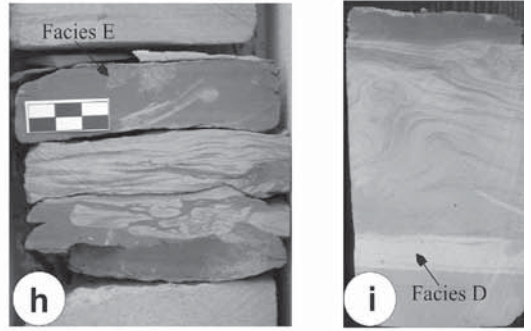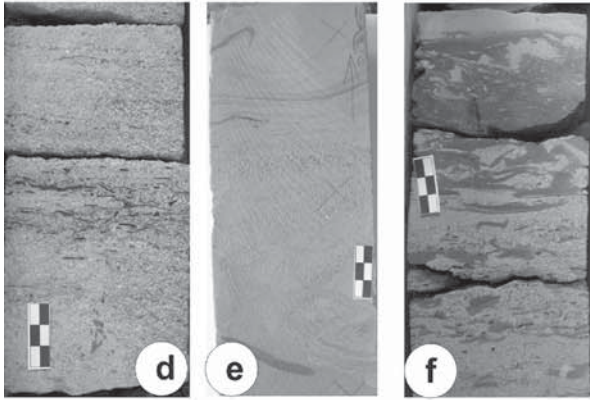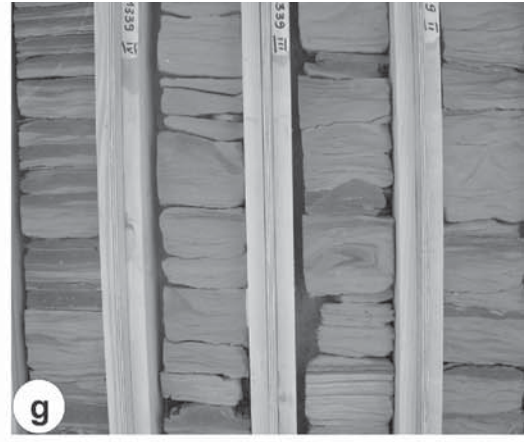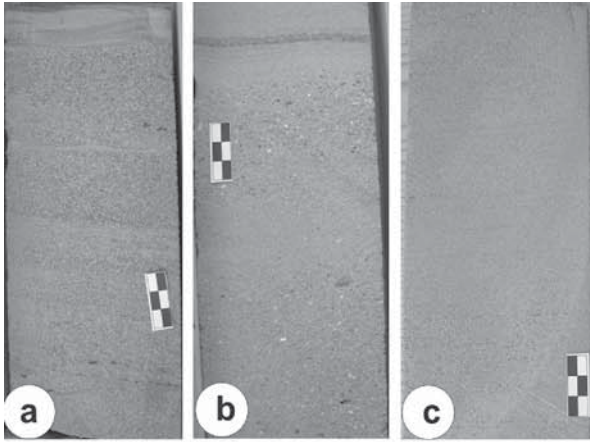
◄ **Fig. 8.** Miocene facies distribution in the studied area.
Facie A - Massive to laminated sandstone
8a - S3 (1298 m) - Levee and interchannel facies association;
8b - S3 (1120 m) - Levee and interchannel facies association;
8c - J4 (1174m) - Levee and interchannel facies association;
8d - J8 (1521m) – Tabular sandstone sheet;
8e - J6 (1338m) - Tabular sandstone sheet;
8f - S3 (1660m) - Levee and interchannel facies association.
Facie B - Thin-bedded graded and laminated sandstone;
8g – J6 (1331 - 1334m) - Tabular sandstone sheet;
Facies E - Laminated siltstone and claystone.
8h - S3 (1116m) - Levee and interchannel facies association.
Facies D Calcium carbonate cemented sandstone, siltstone and mudstone
8g - T3A (1074m) - Tabular sandstone sheet.
Facies C - Thin-bedded sandstone with low-angle cross lamination
8j – T3 (1314m) - Levee and interchannel facies association
8k – T4 - (1015 – Chanel fill facies association;
8l – T3A (1246m) - Chanel fill facies association.
Facies E - Laminated siltstone and claystone
8m – T4 (1192-1194m) – Tabular heterolithic sheet,
8n – J4 (1161m) - Tabular heterolithic sheet

4.2 Facies Association

The sedimentary succession in the area has been subdivided into four main facies associations also defined as architecture elements. These associations were distinguished with the use of cores, but all of them show also characteristic trends on wireline logs. This helps to extend the interpretation for uncored areas (Pirson, 1963; Galloway and Hobday, 1996; Emery and Myers, 1996), and to correlate the obtained results with seismic data, thus providing a 3D insight into the studied Miocene succession.

4.2.1   A1: Channel-Fill Facies Association

This facies association consists of massive to laminated sandstone facies (A), thin-bedded, graded and laminated sandstone facies (B) and, sporadically, laminated siltstone and claystone facies (E), and mudstone facies (F). The presence of erosional sandstone bases, rip-up clasts, deformed bedding, dish structures, high-angle cross-lamination or through cross-lamination, all define this type of association.
On wireline logs (GR, Neutron) this type of depositional elements is represented by characteristic shapes of curves. These are mainly blocky or bell-shape, but cylindrical shape is also present. The blocky shape is characteristic for single or stacked channel fills. The bell shape is characteristic for cases where over levee-overbank association is present above a laterally migrated channel.

Depositional elements interpreted as channels from cores have thickness ranging from tens of centimeters to 8 m, but are difficult to interpret from wireline logs alone. Channel complexes interpreted from logs show thickness between 20 and 80 m, seldom up to 100 m.

This association can be present inside the tabular heterolith sheets facies association (see below), but more commonly it occurs as a complex of channel–interchannel (overbank) or as channel-lobe successions. It can also be developed as a multiple complex of channel-overbank (levee) or as channel-lobe successions.

Based on well-log correlation in the study area, the channels appear to be no deep, widespread and create multistory complexes built of channel-interchannel (levee/overbank) or channel-lobe associations.

4.2.2   A2: Levee and Interchannel Facies Association

This facies association consists of most interpreted facies, except facies A. Fine-grained deposits composed of thin, very thin, and medium sandstone, siltstone, mudstone beds are represented by facies B, C, D, E, and F. This facies contains a spectrum of sedimentary structures characteristic of the areas of terminal turbidity current deposition, as well as for the morphologically higher interchannel and levee stretches.

This facies association is several centimeters to a dozen meters thick. It often overlies the A1 association, and may locally reveal a greater share accumulation of facies A and C. In this case, Bouma turbidites are not complete, and usually lacking some of the lowest divisions. On wireline logs, this association is represented by serrated patterns sometimes with a tendency to a bell shape if A2 is overlain by the A1 association. Both associations form channel-interchannel complexes that are often stacked vertically one upon another forming multiple repetitions through the basin fill.

4.2.3   A3: Tabular Sandstone Sheets (Depositional Lobe) Facies Association

Thin to thick sandstone bedsets (facies A, B) vertically separated by siltstone, claystone C, D facies, and forming kilometer-scale layered sandstone sheets are the most abundant association (architectural element) of the Miocene deposits in the study area.
These tabular sheets are interpreted as widespread, thin depositional lobes.

On wireline logs, this association is represented by irregular, symmetrical to funnel shapes, and where its thickness exceeds 20 meters is easily recognizable on the logs.

In such a case, it is possible to interpret the gradual upward decrease in gamma rays, which are characteristic for lobe deposits (Mutti and Normark, 1987; Mutti and Normark, 1991; Galloway and Hobday, 1996).

4.2.4 A4: Tabular Heterolithic Sheets

This association, similar as A1 and A3, constitues the most laterally continuous intervals in the study area, and can be traced over several kilometers. Association A4 is characterized by gray siltstone and occasional thin turbidite sandstones belonging to facies B, C, D, E, which occur in varying proportions. Association A4 tends to pass upwards into tabular sandstone sheets (depositional lobe - association A3), and commonly overlies the latter.

The tabular heterolithic sheets are interpreted as formed from hemipelagic suspensions and low-density gravity flows during periods of fan abandonment, or rise in relative sea level.

In contrast to the association A2 (levee and interchannel facies association), there is a lack of deformed structures and sandstone/siltstone with ripple cross-lamination. On the other hand, thin-bedded sandstones with low-angle cross-stratification are relatively common in association A4. On wireline logs, this association shows irregularity to linear shapes, and often accompanies the tabular sandstone sheets (depositional lobe) facies association.

5   Petrography

Classical thin-section petrologic analyses show that the Miocene sandstones are subarkose, arkose, sublitharenite, and litharenite. Cements are represented by contact clay cement, clay-carbonate matrix, carbonate and quartz cements. Virtually every sample contains all the types of cements. Detrital grains are predominantly poorly sorted. Differences between petrological composition in distinct facies associations are lower than differences between single samples in the same facies association and it was shown that the kind of cement is not a good indicator of rock properties and correlation parameter.

Lunegard theory (Lunegard, 1992) was applied to verify compaction and cementation. Compactional porosity loss (COPL) was calculated by:

$$COPL = P_i - (((100 - P_i) \times P_{mc})(100 - P_{mc}))$$
(1)

$$P_{mc} = P_o + C$$

Where P_i - initial porosity (%), P_o - total optical porosity (%), C volume percent pore filling cement, P_{mc} - minus-cement porosity.

Cementational porosity loss (CEPL) is equal to

$$CEPL = (P_i - COPL) \times (C/P_{mc})$$
(2)

At last also compaction index (ICOMPACT) was calculated by:

$$ICOMPACT = COPL/(COPL + CEPL)$$
(3)

This indicates which process is responsible for porosity loss (Leśniak and Such, 2001). Taking into account a degree of roundness and sorting of the Miocene sandstones, a value of initial porosity equal to 40% was used. The results of COPL/CEPL calculations are shown in Fig. 9. Correlating COPL as a function of depth with total content of cement as a parameter allows us to calculate the curve (dashed line in Fig. 10) of minimal porosity loss in a function of depth (Fig. 10). The next correlation (COPL versus Depth and ICOMPACT versus predominant grain diameter) shows that compaction affects all samples while cementation processes are present mainly in sandstones characterized by a predominant grain diameter of less than 0.125 mm

(Fig. 11). The models of compaction and cementation are the same for all facies associations.

6   Petrophysics

Density, porosity, permeability, mercury porosimetry, and other relative permeability measurements
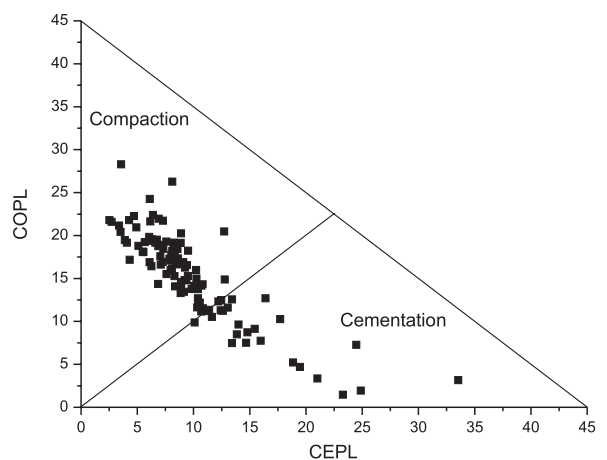
Fig. 9. Lundegard diagram for investigated samples. (Estimating of primary porosity loss) (after Lundegard 1992) COPL - compactional porosity loss, CEPL - cementational porosity loss
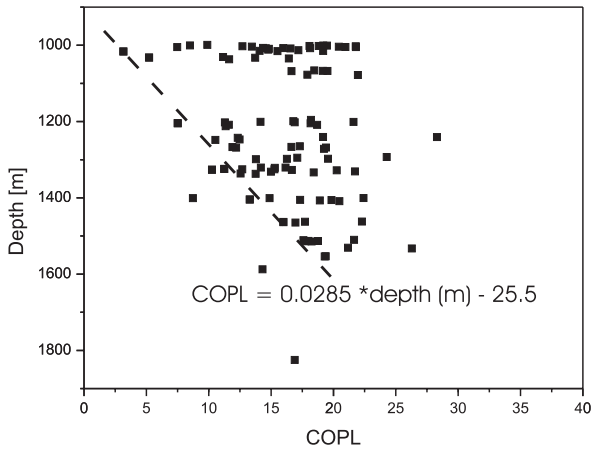
Fig. 10. Compaction porosity loss (*COPL*) versus depth. Trend line shows values of minimal compaction in the function of depth
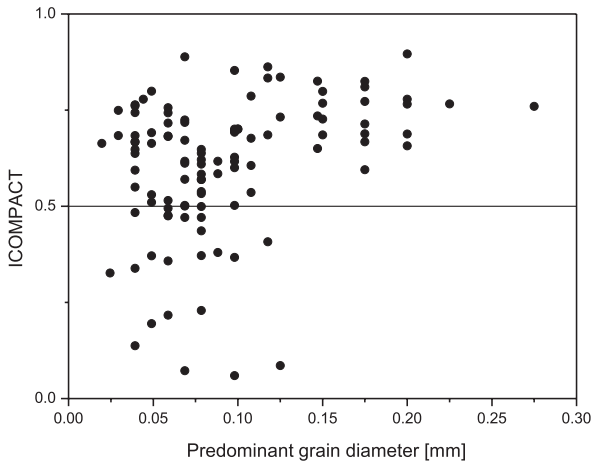
Fig. 11. Cross plot: *ICOMPACT* (compaction index, formula 3) versus predominant grain diameter
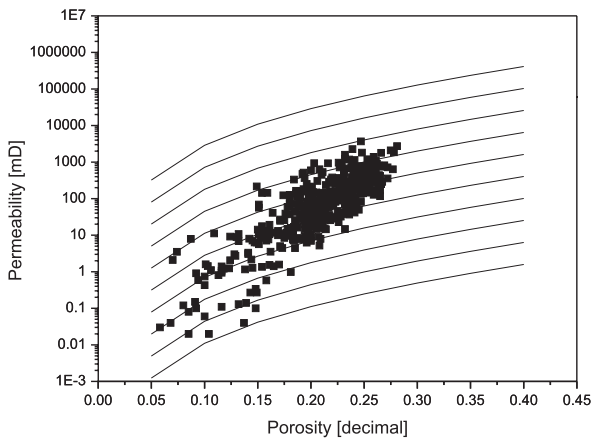
Fig.12. Cross plot porosity – permeability correlated with GHU (Global Hydraulic Unit) sketch

were performed to characterize reservoir and filtration properties.

Generally porosity is good. Cross-plot porosity permeability (Fig.12) combined with Global Hydraulic Unit (GHU) was carried out. Corbett and Potter's (2004) definition of GHU was applied.

At first, Flow Zone Indicator (FZI) was defined as:

$$FZI = \frac{\sqrt{k/Phi}}{\left(Phi/(1-Phi)\right)} \cdot 0.0314 \qquad (4)$$

where *k*- permeability in mD, *Phi* – fraction of porosity.

Permeability equals

$$k = Phi\left[FZI \cdot \left(\frac{Phi}{1-Phi}\right)/0.0314 \right]^2 \qquad (5)$$

Now, Courbett and Porter arbitrarily use *FZI* and define ten Global Hydraulic Units (GHU) as shown in Table 2. Their range covered all porosity-permeability space in a cross-plot for real rocks.

The permeability of Miocene sandstones covered 4 GHU (or 4 – 7) (Corbett and Potter, 2004). Frequency diagrams of porosity and permeability are presented in Figs. 13 and 14.

Analyses of pore space parameters obtained using mercury porosimetry give threshold diameter, fractal dimensions, and percent of pores characterized by pore diameter greater than 1 μm as a base set of parameters describing filtration properties (Such, 2002). Fractal dimensions were calculated by the use of log - log plots obtained from pore diameter cumulative curves (Angulo et al., 1992; Such, 1998). Finally, four classes of similarity of pore space were extracted from the database (Peveraro et al., 2002; Such, 2002). Parameters of classes of similarity are published in Table 3.

Only class I and II represent good reservoir sandstones, other classes are too microporous (threshold

Table 2. Definition of Global Hydraulic Units (GHU) (after Corbett and Potter, 2004). The values of FZI and GHU were calculated with the use of formula 4 and 5

FZI	GHU	FZI	GHU
48	10	1.5	5
24	9	0.75	4
12	8	0.375	3
6	7	0.1875	2
3	6	0.0938	1

Table 3. Extracted classes of similarity on the base of pore space parameters: treshold diameter, fractal dimension and percent of pores greater than 1 µm

Class	Porosity [%]	Treshold diameter [µm]	Fractal dimension	% of pores > 1 µm
I	>25	>20	>2.97	>75
II	>20	10–20	2.94–2.97	>60
III	>15	3–10	2.90–2.94	>45
IV	>15	3–10	<2.9	10–40
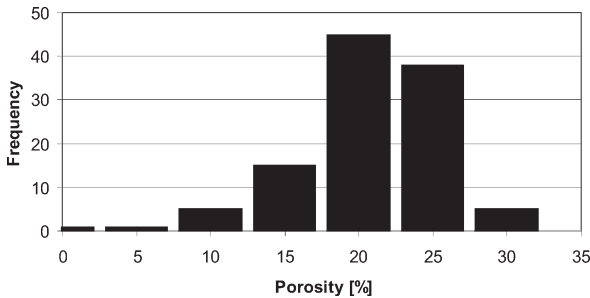
Fig. 13. Frequency diagram of porosity for investigated samples
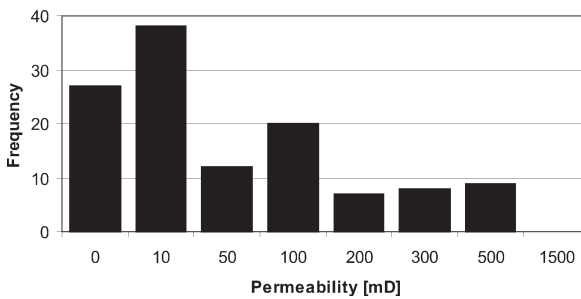
Fig. 14. Frequency diagram of permeability for investigated samples

diameter lower than 10 µm). Permeability analysis allows us to gather extracted classes of similarity with adequate GHU.

The last part of petrophysical investigations consists of anisotropy research and analyses of relative permeability (Bietz et al., 1996; Chen Tielong et al., 1996). The investigated samples showed strong anisotropy (horizontal to vertical permeability equal to 7:1). The main goal of relative permeability measurement was to reveal possible processes affecting pore space in contact with reservoir waters. 15 samples were investigated. The results, especially for relative permeability to gas, covered the range from 0.75 to 0.09. According to earlier investigations of this parameter for the Miocene sandstones (Such and Lesniak, 2001), samples showing relative permeabilities greater than 0.55 can be defined as undamaged samples. Values 0.55 to 0.3 characterized moderately damaged samples. When relative permeability to gas is lower than 0.3 it means that the sample is strongly damaged by flowing water. This effect is coupled with increasing values of residual water saturation of about 15% (cements are destroyed and sand grain collapsed). Five samples from the investigated collection can be defined as strongly damaged (the value of relative permeability to gas being lower than 0.3). The process responsible for pore space damages consists in extracting sand grains by flowing water and sealing pore throats by them. This type of pore space damage is present in sandstones from all facies associations.

7 Computer Analyses of Microscopic Images

Parameters affecting anisotropy were described and numerically parameterized using thin- sections and computer analyses of images. Mainly elongation and circularity were taken into account. The results of microscopic analyses are presented in Table 4.

Parameters presented in Table 4 generally show big differences in min and max values, but can distinguish facies associations. Depositional lobes are the most microporous (range of EqDiameter) while the greatest values of this parameter are characteristic for channel fill associations. Tabular heteroliths sheet samples showed the greatest values of elongation. It is connected with lamination. Several thin laminated samples show the structure of pore space similar to pseudo-fractures. In such type of samples coarse-grained sandstones create a 0.5–7 mm wide path of fluid migrations between fine-grained laminas.

8 Discussion

The Miocene sediments on the studied area present a complex sedimentary and diagenesis history. Detailed sedimentary investigations help identifying elements of depositional architecture recognizable with the use of well logs. These elements are facies associations. Correlation of well logs and 2D seismic cross-sections gave, as a result, the 3D structure of the sedimentary infill and facies associations at basin-scale.

On the other hand, laboratory research identified various processes affecting reservoir properties of rocks. Some of them are the same for all facies associations. They are compaction, cement distribution and poor consolidation. Porosity loss curves obtained (see formula in Fig.10) during compaction analyses and cross-plot porosity permeability (Fig. 12) show that permeable sandstones (permeability greater than 1 mD) can occur only above 2200 m. Increased cement contents occur randomly in all associations. Particularly carbonate cements destroy reservoir properties of

Table 4.
Correlation between facies association and computed shape parameters of pores obtained from computer analysis of microscopic images

Facies association	EqDiameter	Circularity	Elongation
Tabular heterolites sheets	0.0022 – 0.0136	0.803 – 0.981	1.179 – 2.069
Levee and interchannel	0.0032 - 0.0188	0.758 – 0.911	1.452 – 1.659
Depositional lobes	0.0044 - 0.0085	0.783 – 0.869	1.522 – 1.621
Channel fill	0.0028 - 0.0246	0.711 – 0.925	1.455 – 1.700

rocks. Poor consolidated sandstones can be damaged by flowing water. This process is present in all facies associations and is mainly connected with clay-carbonate cements or with very low content of cements and depends on extraction of sand grains by water. Residual saturations of water rise in such type of samples up to 15% in comparison with correlation curves of residual saturation - fractal dimension.

Pore space analysis divides the database into four classes of similarities. The basic parameters used for dividing the samples into disctinct classes include the diameters of pore throats (threshold diameter) and the content of micropores in the pore space (fractal dimension). This last parameter shows rather low values connected with a large number of micropores confirmed by comparison with the percentage of pores connected by channels of diameter lower than 1 μm. Cross-plot porosity permeability coupled with global hydraulic units (GHU) confirm pore level division. GHU from 7 to 4 were obtained. Table 5 contains correlations between the facies associations and the classes of similarity of the pore space as well as those with GHU. It is shown that the best reservoir sandstones (GHU-7) occur only in channel fill facies association (permeability to gas greater than 100 mD).

The properties of other facies associations are decreased by a more microporous character of pore space and especially for tabular heteroliths sheet facies by laminations and elongation of pores.

9   Conclusion

Reservoir sandstones were examined in the Carpathian Foredeep. The first tool applied to the complicated Miocene basin was facies analysis. At last six facies and four facies associations were found. The correlation between facies scheme and well logs shows that facies associations are recognizable on logs.

Petrological investigations show that differences between facies associations are lower than between single samples in the same facies association. The kind of cement is not a good indicator of reservoir properties, despite carbonate cement which strongly reduces porosity and decreases permeability to zero. Small content of cements and clay type of cements make good reservoir sandstones poorly consolidated. Mechan-

Table 5. Correlation between facies associations and class of similarity pore space and GHU

Class	GHU	Association
I	7	Channel fill facies
II	6	Channel fill facies, Levee and interchannel facies
III	5	All
IV	4	Channel fill facies, Levee and interchannel facies Tabular heterolits sheets facies

ical compaction is a dominant process in the Miocene sandstones. Compaction makes sandstones lying deeper than 2220 m practically non-permeable.

Cementation occurs mainly in sandstones characterized by a predominant grain diameter of less than 0.125. Compaction and cementation processes are the same in all facies associations.

Four classes of pore space similarity were distinguished. Only two of them represent good reservoir sandstones. Best reservoir properties (class I) occur only in channel fill facies. Good reservoir properties (class II) occur in levee and interchannel facies and can be gathered with naturally elevated structures built in outer zones of channels.

Unstable sedimentation conditions caused strong anisotropy of filtration properties of sandstones. Extremely changeable conditions created thin-bedded layers which can be treated as "fracture like" type of reservoir rocks.

Generally, type of sedimentation, grain size diameter, and compaction steer the reservoir properties of Miocene sandstones.

References

Angulo, R.F., Alvarado, V., Gonzalez, H., (1992), Fractal Dimensions from Mercury Intrusion Capillary Tests., SPE Paper 23695.

Bietz, R.F., Bennion, D.B., Patterson, J., (1996), Gas Storage Reservoir Performance Optimization through the Application of Drainage and Imbibitions Relative Permeability Data., JCPT, February, 35, 2, 34–40.

Bouma, H.A., (1962) - Sedimentology of some flysch deposits. Elsevier, Amsterdam, 159.

Chen Tielong, Zhao Yong, Peng Kezong, Pu Wanfeng, 1996, A Relative Permeability Modified for Water Control of Gas

Wells in a Low-Permeability Reservoir., SPE Reservoir Engineering, 11, 3, 168–184.

Corbett, P.W.M., Potter, D.K., (2004), Petrotyping: a Basemap and Atlas for Navigating through Permeability and Porosity Data for Reservoir Comparison and Permeability Prediction. SCA Papers 2004-30, 385–396.

Dziadzio, P., (2000a), Variability of sedimentary environments in the southeast part of the Carpathian Foredeep. 20th Regional Meeting, Dublin, Ireland, 13–15 September, Abstracts, p. 92.

Dziadzio, P., (2000b), Depositional sequences in Badenian and Sarmatian deposits in the SE part of the Carpathian Foredeep (SE Poland). English Summary. Przeglad Geologiczny 48, no. 12: 1124–1138.

Dziadzio, P., Maksym, A., Olszewska, B., (2006), Regional recognized of eastern part of the Carpathian Foredeep. Przeglad Geologiczny, v. 54, 413–420.

Emery, D., Myers, K.J., (1996), Sequence stratigraphy, Elsevier, Amsterdam.

Galloway, W.E., Hobday, D.K., (1996), Terrigenous Clastic Depositional Systems. Springer-Verlag Berlin, Heidelberg.

Jopling, A.V., Walker, R.G., (1968), Morphology and origin of ripple-drift cross-lamination with examples from the Pleistocene of Massachusetts. Jour. Sed. Petrol., 38, 971-984.

King, P., Browne, G., (2002), Miocene slope to basin-floor sequences exposed in North Taranaki, New Zealand, New Zealand Petroleum Conference Proceedings, 24–27 February, 483–502.

Leśniak, G., Such, P., (2001), The influence of compaction and cementation on pore space parameters of Miocene sandstones., Mineralogical Society of Poland – Special papers,18, 97–103.

Lowe, D.R., (1975), Water escape structure in coarse-grained sediments. Sedimentology, 22, 157–204.

Low, D.R., (1982), Sediment gravity flows. II. Depositional models with special reference to the deposits of high-density turbidity currents. Jour. Sed. Petrol., 52, 279–297.

Lundegard P. D. (1992), Sandstone porosity loss - a "Big picture" view of the importance of compaction. Jour. Sed. Petr., 62, 250–260.

Mutti E., Normark, W.R., (1987), Comparing examples of modern and ancient turbidite systems; problems and concepts. In: (Leggett, J.K. & Zuffa, G.G., Eds,), Marine clastic sedimentology: Concepts and case studies; Graham & Trotman, 1–38.

Mutti, E., Normark, W.R, (1991), An integrated approach to the study of turbidite system w Seismic facies and sedimentary processes of submarine fans and turbidite systems. Springer-Verlag New York, 75–106.

Myśliwiec, M., Borys, Z., Bosak, B., Liszka, B., Madej K., Maksym, A., Oleszkiewicz, K., Pietrusiak, M., Plezia, B., Staryszak, G., Świętnicka, G., Zielińska, C., Zychowicz, K., (2006), Hydrocarbon Resources of the Polish Carpathian Foredeep Reservoirs, Traps and Selected Hydrocarbon Fields. AAPG Memoir 84, 351–393.

Peveraro, R., van Delden, S., Holwart, J., Geselle, L., Haberland, J., Kloas, F., Lingnau, R., Gupta, R., Larijani,, R., Sementsov, A., Charreyron,, Y., 2002, The development of an integrated reservoir description and simulation model: organization, data integration, development of a shared-earth model, preliminary results and the way ahead, Prace INiG, 110, 129–135.

Pirson, S.J., (1963), Handbook of well log analysis. Prentice-Hall, Inc. Englewood Cliffs, NY.

Such, P., (1998), An Application of Fractal Analysis in Investigations of Reservoir Rocks., Abs. Book Conference and Exhibition: Modern Exploration and Improved Oil and Gas Recovery Methods, Poland, 1–4 September.

Such, P., (2002), Badanie przestrzeni porowej skał zbiornikowych. Prace IGNiG, 113, 78.

Relationship between Hydrocarbon Generation and Reservoir Development in the Carpathian Foreland (Poland)

Irena Matyasik · Michał Myśliwiec · Grzegorz Leśniak · Piotr Such

Abstract. Two similar structures consisting of Devonian carbonates covered by Miocene deposits were observed in the Carpathian foreland near Rzeszow, Poland. They have been penetrated by wells T-3 and J-9. Fractured Devonian carbonates of the T-3 structure are filled by hydrocarbons, while in J-9 well only weakly gas saturated brine was found.

The regional petroleum system was investigated to explain why only one of these two Devonian prospects was filled by hydrocarbons. For this purpose, geological, seismic, well log, petrophysical, and geochemical studies were performed. The karst development, circulation of fluids and various hydrocarbon migration paths are the keys to explain the existence of a HC accumulation in the T-3 structure and the lack of HC pool in the well J-9.

Keywords: Petroleum system, Devonian carbonates, reservoir properties, hydrocarbon generation, karst development.

1 Introduction

Two similar Devonian structures covered by Miocene deposits were detected in the vicinity of wells T-3 and J-9 near Rzeszów (Fig. 1) (Mysliwiec et al., 2004). They were interpreted on the basis of 3D seismic data as a prospective target for oil and gas exploration (Fig. 2) (Mysliwiec et al., 2004). Both structures were tested by wells (Fig. 3). These structures consist of Devonian carbonates deposited directly on top of Precambrian rocks and covered by Miocene siliciclastic deposits. Devonian rocks look like tectonic breccia, although no tectonic activity occurred in this area (Fig. 3). We have compared our data with published examples of various types of breccia resulting from karst development, since both structures were cropping out for a long period before the deposition of the Miocene sedimentary cover. Worth to mention, Miocene claystones that invaded Devonian carbonate rocks were also observed there (George and Powell, 1997; Loucks, 1999; Moore, 2001), the occurrence of which being consistent with the karst development model. Quantitative description of reservoir properties of these rocks have been published by Antonelli and Mollema (2000), and Howard and Nolen-Hoeksma (1990). Devonian carbonates in the T-3 well are filled with hydrocarbons (gas with a small amount of associated liquid hydrocarbons), while the same reservoir rocks in the J-9 well are water saturated in spite of their similar structural and geological position.

Until now, search for gas and oil deposits in the eastern part of the Carpathian foredeep has resulted in the discovery of numerous important accumulations. However, only few discoveries relate to Paleozoic reservoirs beneath the Miocene cover. Miocene gas deposits are located in structural and mixed structural-stratigraphic traps located mostly above well-defined elevations of the pre-Miocene substratum (Borys, 1996). Several hypotheses have been proposed for the origin of gas accumulated in Miocene sediments. Former hypotheses considered that the source rocks accounting for the intra-Miocene gas occurrences were located in the Paleozoic-Mesozoic substratum (Kotarba et al.,1987). More recent geochemical studies of the Miocene gas and organic matter indicate possible generation of hydrocarbons in the Miocene sequence itself (Bessereau et al., 1996; Kotarba et al., 1998; Kotarba, 1998). Isotopic composition of methane in the Miocene strata indicates its bacterial origin. However, the increased $\delta^{13}C$ ($C_2H_6-CH_4$) values reaching 17.9–16.2‰ advocate for a mixture of diagenetic and/or even thermogenic gas (Kotarba, 1992).

Many gas accumulations are associated with liquid hydrocarbons. Microbial methane was generated at depths less than about 2400 m below the Miocene seafloor (Czepiec and Kotarba, 1998).

Four zones can be identified in the outer Miocene basin, according to distinct characteristics for organic matter distribution. The two first zones are located in the foredeep north of the Carpathian thrust front, close to the Tarnów and Mielec-Lezajsk area. The two other zones are located near Rzeszow and Przemysl, in the vicinity of the thrust front and beneath the Carpathian allochthon.

Intensive research conducted between 1998 and 2006 has improved our understanding of hydrocarbon generation in the Miocene sediments of the Carpathian foredeep as well as in the pre-Miocene substratum. Several hypotheses on HC migration paths
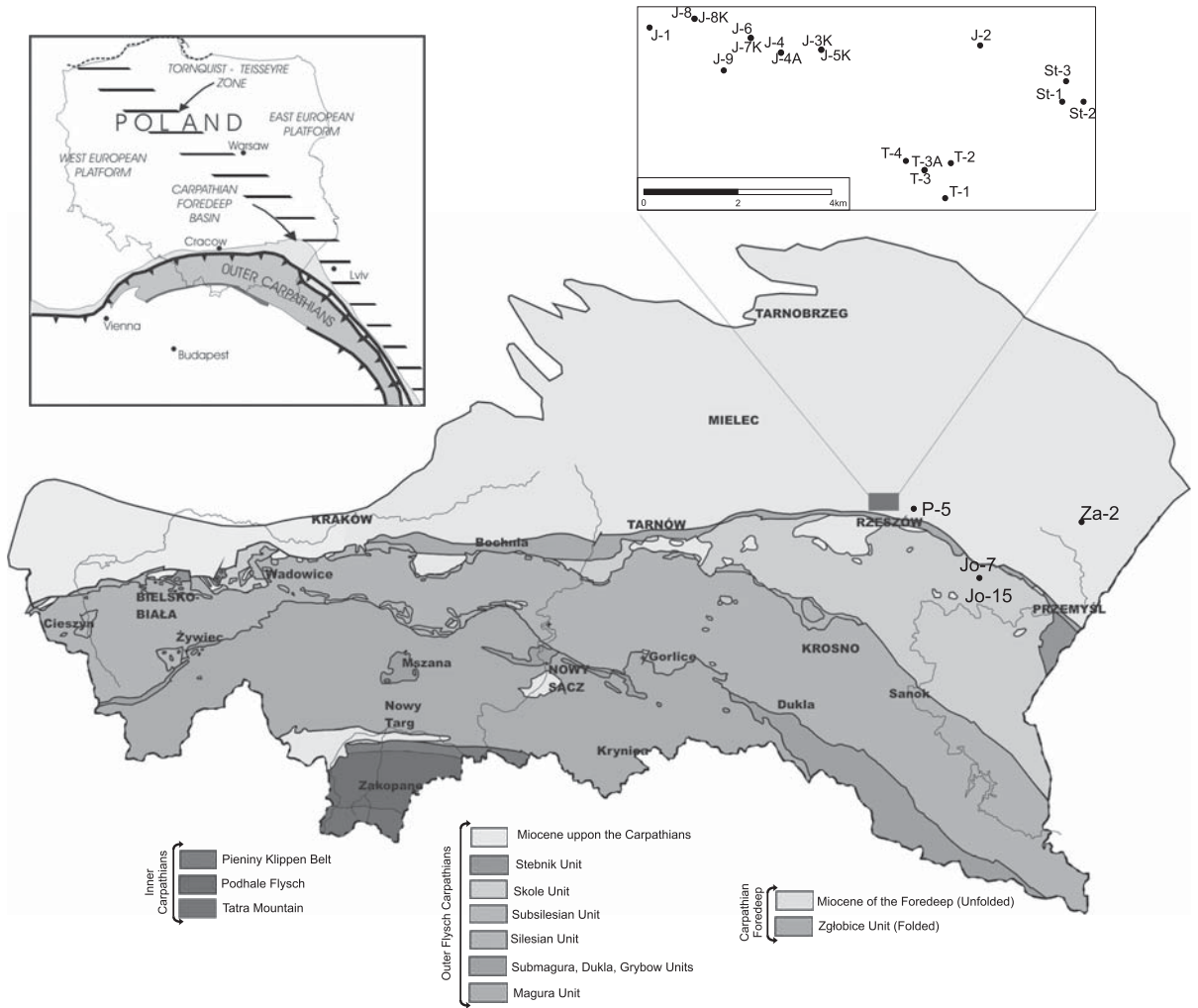
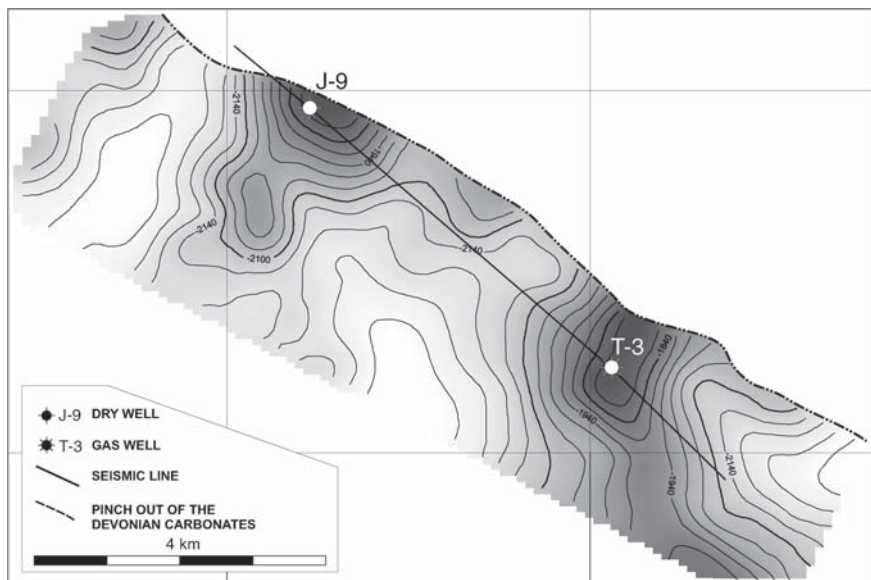**Fig. 1.** Location map of the studied area

Fig. 2. Subcrop map at the top of the Devonian carbonates outlining the T-3 and J-9 structures
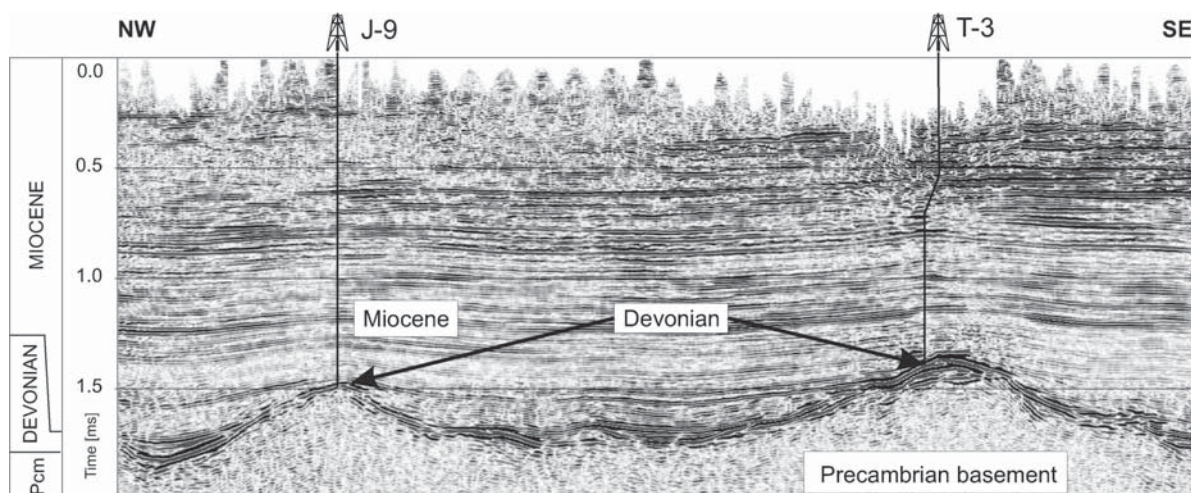
Fig. 3. Seimic section of T-3 and J-9 structures

have been controlled by seismic and geological investigations (Maksym et al., 2003).

New geochemical studies of liquid hydrocarbons from the eastern part of the Carpathian foredeep (Rzeszow area) support the hypothesis of HC generation from early mature Miocene source rocks (Matyasik and Steczko, 2005). Type III kerogen can effectively generate small quantities of liquid hydrocarbons when thermal maturity exceeds about 0.5%Ro. Such a maturity rank has been found in Miocene sediments buried below 2500 m. Moreover, not far from wells J-9 and T-3, more than 50 samples have also been taken from deeper Miocene wells (Za-2, Jo-7 and Jo-15), with type II kerogen being detected in many of them. This has been confirmed by elemental analysis of the kerogen (Kotarba et al., 1998; Matyasik and Steczko, 2005). Our present state of knowledge concerning the quality of organic matter and its genetic links allows for new solutions of the petroleum systems in this part of the Carpathian foredeep. Distribution and thickness of Paleozoic layers including the Devonian, the Silurian and the Ordovician are still only partly known, and part of early generated HC has been probably lost before the deposition of the Miocene cover. Near wells J-9 and T-3, the depth of the Permian-Mesozoic sediments has never been larger than 1200 m, and this suggests that potential source-rocks have never reached oil generation stage before the Miocene. 1D petroleum modelling in the Rzeszow area indicates that the early Paleozoic sediments entered the stage of HC generation only during the early Miocene, at the onset of Carpathian overthrusting (Dudek and Steczko, 2005; Maksym et al., 2003). A Devonian contribution in both the gas and oil in well T-3 would be therefore quite possible.

In addition to 1-D petroleum modelling, detailed laboratory investigations including dual (i.e., fractures and matrix) porosity and permeability analyses of fractured reservoirs, mercury porosimetry and geochemical studies (i.e., correlations between source rocks, gas and oil) were performed, and compared to the known oil and gas occurrences (Such and Lesniak, 2003; 2004). Devonian carbonate reservoirs in well T-3 display a typical brecciated, karst-related fabric which is document in Fig. 5.

2   Geological Data

The rough morphology at the top of the pre-Miocene substratum was created by Precambrian or early Paleozoic, late Paleozoic and Mesozoic erosional episodes, respectively (Roca et al., 1995). Flat spots observed in Fig. 3 outline the top of the Precambrian basement. The Middle Devonian paleorelief was covered by Miocene sediments. Overlying Miocene shale deposits constitute good sealing rocks while sandstone sediments form local reservoirs. The long period of surficial exposure of Devonian carbonates during pre-Miocene times enhanced reservoir properties due to karst development. Miocene shales contain probably enough organic matter to account for HC generation when they have reached a sufficient burial. More than 100 Miocene samples collected from 17 wells were analyzed in recent years. The results of Rock-Eval pyrolysis, extraction and biomarkers studies provide a good geochemical characterization of the organic matter as well as estimates of the petroleum potential of Miocene sediments. Moreover, numerous occurrences of wet gas and light oil, which may be generated at an early stage of maturity from the Miocene sediments, have
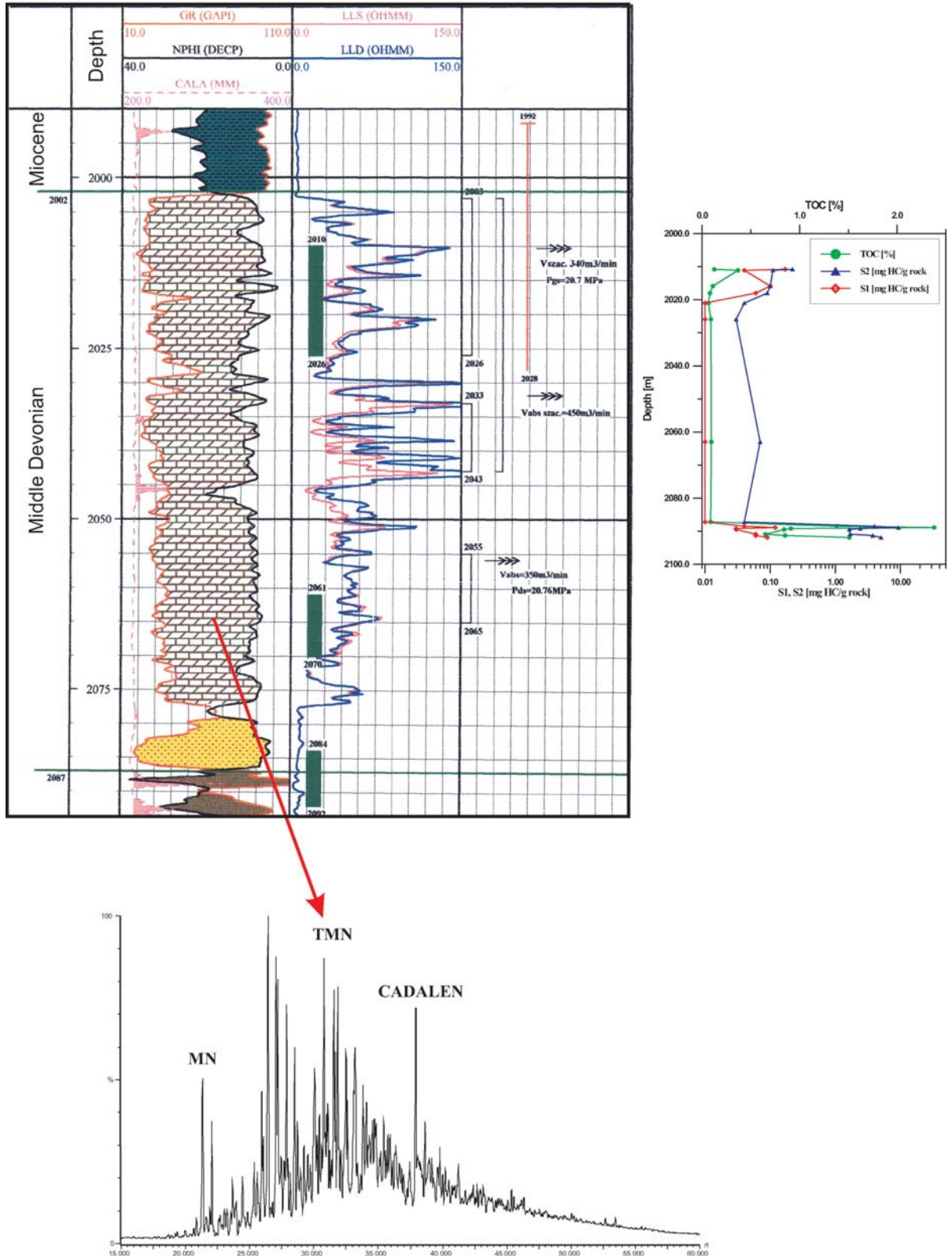
Fig. 4. Electric and geochemical logs of well T-3. Notice also the chromatogram of the oil stored in the Devonian carbonate

Fig. 5. Hand-sample of typical brecciated carbonate reservoir rocks from T-3 well

Fig. 6. Thin-sections of fracture rocks in fluorescent light
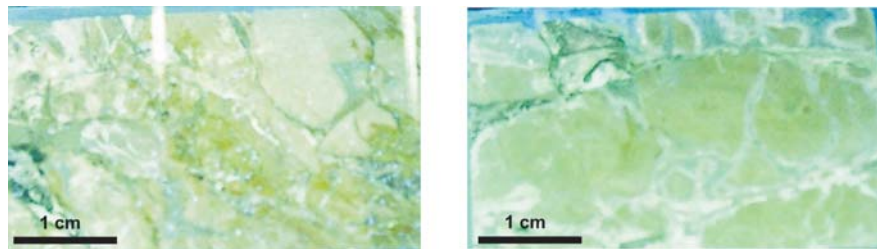
been recognized. During the Paleogene, the current foreland area was uplifted and intensely eroded. Its subsequent Miocene evolution accounts for the present structural grain of the Carpathian foredeep. Thin Miocene sandstone layers constitute the main conduits for hydrocarbon migration paths, part of them onlapping the elevated Devonian structures.

The top of analyzed structures (wells T-3 and J-9) consists of karstified, brecciated and fractured dolomites (Chillingarian, 1992; Lucia, 1995; Moore, 2002) (Fig. 6). The fracture system displays high porosity values because crossing fractures form pseudovugs. Only limited petrological investigations were conducted in this area. However, the fracture system was quantitatively investigated using thin and polished sections saturated with fluorescent resin.

In their lower parts, both structures T-3 and J-9 are made up of Devonian quartz sandstones. Additionally, the base of the T-3 structure comprises also Early Devonian shales.

3 Petrophysical Investigations

Petrophysical parameters of Devonian carbonates and sandstone deposits were measured (Such and Lesniak, 2003). Porosity, permeability and pore space investigations (mercury injection capillary pressure apparatus) were performed. Additionally, fracture porosity and permeability were measured for carbonate rocks, using thin sections, polished sections and full diameter cores as described in Gliniak et al. (2002), Nelson (1989), and Such and Lesniak (2002).

The primary reservoir rocks in both T-3 and J-9 prospects are fractured carbonates. The secondary reservoir rocks are Devonian sandstones found below the carbonates.

Carbonate rocks are similar in both structures. They constitute a typical fracture-porous type of reservoir rocks (Such and Lesniak, 2002). Their basic reservoir parameters are presented in Table 1. Porosity amounts up to 4% inT-3 and 7% in J-9 structures. Permeability is lower than 1 mD. The parameters of frac-

Table 1. Reservoir parameters of Devonian carbonates

Structure	Porosity (%)		Permeability (mD)	
	Fracture	Matrix	Fracture	Matrix
T-3 (1910–1970m)	2–16	<4	11–112	<1
J-9 (1940–2000m)	1–14	<7	2–20	<1

Table 2. Reservoir parameters of the Devonian sandstones

Structure	Porosity (%)	Permeability (mD)	Threshold diameter (µm)
T-3	8–21	8–100	6–30
J-9	<3	<0.1	<3

ture systems were estimated using oriented thin sections and polished sections. Fracture porosity equals 2–16% in T-3 and 1–14% for J-9, respectively. Permeability reaches 112 mD in T-3 and 20 mD in J-9. The range of investigated parameters (particularly the high value of porosity) is characteristic of breccias (Lucia, 1995; George and Powell, 1997).

Petrophysical parameters of Devonian sandstones are presented in Table 2. Apart from porosity and permeability, the values of threshold diameter are also presented. This parameter describes filtration properties of rocks sharing the greatest diameter of pores in which oil can flow through the pore space. The value of threshold diameter lower than 3 µm is a good indicator for no permeable rocks. Petrophysical parameters of sandstones are quite different in T-3 and J-9 structures. Sandstones from T-3 are good reservoir rocks. Their porosity ranges from 8 to 21%, the permeability varies from 8 to 100 mD and the threshold diameter amounts to 30 µm, while in J-9 structure the sandstones are impermeable (porosity lower than 3%, permeability lower than 0.1 mD and values of threshold diameter lower than 3 u m). These sandstones differ also by their quartz cement content.

4   Geochemical Investigations

4.1 Source Rocks Characterization

Rock-Eval, bitumen and biomarkers analyses were performed to characterize source rocks potentials of Miocene (26 samples), Middle (17 samples) and Early Devonian (7 samples) series in the T-3 and J-9 wells. Samples were analyzed for organic carbon and 8 samples were chosen for further study of the organic extracts. Only 6 of the 8 samples had sufficient amounts of organic matter for kerogen isolation and these were studied in greater detail using elemental analysis of kerogen, GC (gas chromatography), and GC-MS (gas chromatography-mass spectrometry). Carbonate and

shale facies source rocks were identified both in the Early Devonian (well T-3) and the Miocene deposits (well J-9).

4.2 Early Devonian

TOC content of the Early Devonian source rocks is usually rather low and varies greatly from 0.65 to 2.38%. Nevertheless these samples present relatively high HI values (above 200 mg HC/g TOC) and the type established on the base of kerogen HI vs OI diagram indicates predominance of oil-prone organic matter (type II). The level of maturity determined from Rock-Eval pyrolysis suggests that the original organic carbon values were higher than the measured values and have been reduced by hydrocarbon generation and expulsion (Table 3, Fig. 7).

The elemental analysis of isolated kerogen reveals a pattern similar to that of the Rock-Eval pyrolysis data suggesting presence of Type II kerogen with atomic H/C ratios ranging from 1.32 to 1.43 (Table 4).

Optical analysis of kerogen reveals that the Lower Devonian series is dominated by liptinite material, but alginite and resinite macerals are also present.

Extract yields were low, ranging from 100 to 980 ppm EOM (Extractable Organic Matter), and dominated by hydrocarbons. Hydrocarbon/non-hydrocarbon ratios range from 1.23 to 3.33, whereas maltene fractions are dominated by saturate compounds (Table 5).
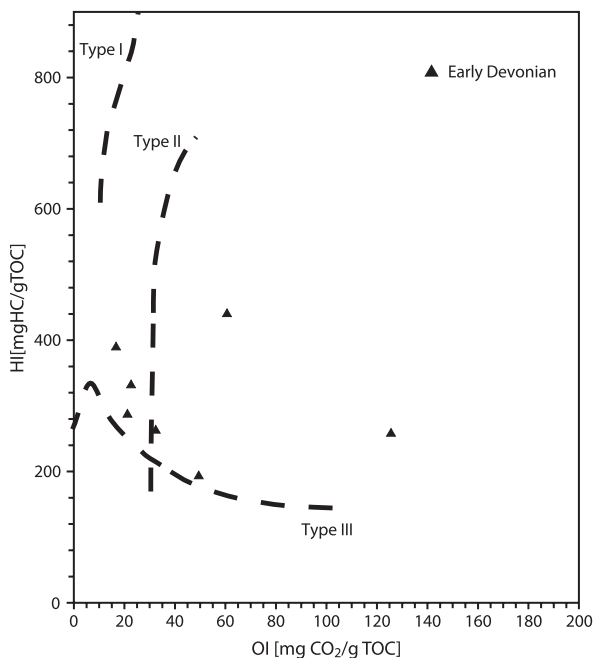
Fig. 7. Hydrogen Index versus Oxygen Index plot used to characterize the Devonian organic matter

Table 3. Rock-Eval pyrolysis data for Middle Devonian and Early Devonian samples from T-3 and J-9 wells

Sample No.	Depth [m]	T_{max} [°C]	S_1 [mg HC/ g rock]	S_2 [mg HC/ g rock]	S_3 [mg CO$_2$/ g rock]	PI [$S_1/(S_1+S_2)$]	PC [%]	RC [%]	TOC [%]	HI [mg HC/ g TOC]	OI [mg CO$_2$/ g TOC]
Middle Devonian T3											
1	2010.8		0.17	0.22	0.56	0.55	0.06	0.07	0.13		
2	2011.1		0.04	0.10	0.52	0.32	0.03	0.34	0.37		
3	2015.8		0.10	0.09	0.66	0.50	0.04	0.07	0.11		
4	2018.0		0.06	0.04	0.37	0.40	0.02	0.06	0.08		
5	2021.0		0.01	0.03	0.29	0.20	0.02	0.05	0.07		
6	2063.0		0.01	0.07	0.62	0.13	0.02	0.08	0.10		
Middle Devonian J9											
7	1946.1		0.02	0.06	0.35	0.23	0.02	0.14	0.16		
8	1948.2		0.02	0.04	0.40	0.29	0.02	0.17	0.19		
9	1954.7		0.02	0.05	0.29	0.26	0.02	0.12	0.14		
10	1962.2		0.02	0.09	0.37	0.20	0.02	0.13	0.15		
11	1974.6		0.02	0.06	0.56	0.25	0.20	0.18	0.20		
12	1983.6		0.02	0.07	0.35	0.24	0.02	0.09	0.11		
13	1984.6		0.02	0.08	0.45	0.24	0.02	0.11	0.13		
14	1990.5		0.03	0.22	0.40	0.13	0.02	0.09	0.13		
15	1996.3		0.03	0.10	0.50	0.22	0.04	0.16	0.19		
16	2042.3		0.03	0.06	0.44	0.31	0.03	0.05	0.07		
17	2046.9		0.03	0.20	0.31	0.12	0.04	0.34	0.38		
Early Devonian T3											
18	2088.5	444	0.04	3.99	0.30	0.01	0.04	1.35	1.38	289	22
19	2088.9	448	0.12	9.32	0.41	0.01	0.81	1.57	2.38	392	17
20	2089.2	443	0.03	2.41	0.30	0.01	0.22	0.69	0.91	265	33
21	2089.5	441	0.03	1.64	0.42	0.02	0.16	0.68	0.84	195	50
22	2090.9	442	0.06	1.69	0.82	0.03	0.18	0.47	0.65	260	126
23	2091.3	446	0.06	3.76	0.52	0.02	0.34	0.51	0.85	442	61
24	2091.9	447	0.09	5.04	0.35	0.02	0.45	1.06	1.51	334	23

Gas chromatograms of the saturated fractions show unimodal, light-end skewed distribution, centered around nC_{19} with no odd- or even-number predominance among the n-alkanes (Fig.8). Pristane/phytane ratios are in the range of 0.91–1.58. The very poor signal-to-noise ratios observed in the GC-MS data when using standard sample preparation and method of analysis indicate low concentrations of hopane and sterane.

4.3 Middle Devonian

TOC content of Middle Devonian samples from wells J-9 and T-3 is very low, ranging from 0.02 to 0.38%. This suggests that there are no source rocks in the Middle Devonian series in the studied area (Table 3).

4.4 Miocene

Miocene source rocks show homogeneous character in terms of organic matter content and quality of kerogen. TOC values are usually rather low and range from 0.05 to less than 1%, except for one high TOC value of 11.53% in well J-07 (Table 6, Fig. 9). The Hydrogen Index ranges from 99 to 152 mg HC/g TOC in all Miocene samples (in several samples HI exceeds 261 mg HC/g TOC). Tsub is generally within the range of 428–439°C, indicating marginally mature kerogen.

Table 4. Geochemical data from isolated kerogen extracts from Miocene, Middle Devonian and Early Devonian samples close from T-3 and J-9 structures

Depth [m]	Ash [%]	Mineral matter [%]	Elemental composition without mineral matter [%]				Sulphur [%]	Atomic ratios	
			C	H	N	O		H/C	O/C
Miocene									
1508.5	17.2	20.6	77.1	5.7	1.9	15.0	3.7	0.867	0.145
1665.4	16.0	20.4	76.2	5.3	2.0	15.0	5.7	0.834	0.147
2621.5	35.5	58.4	53.3	4.4	3.3	6.5	36.5	0.992	0.091
Middle Devonian									
2010.8	31.7	52.9	59.7	3.8	0.5	8.7	34.0	0.772	0.109
Early Devonian									
2088.9	45.1	64.5	65.9	7.9	0.5	13.7	18.2	1.432	0.156
2091.9	42.1	69.8	50.5	5.5	0.6	10.8	29.8	1.317	0.160

Table 5. Quantitative data for extractable organic matter from Miocene, Middle Devonian and Lower Devonian closed to the T-3 and J-9 structures *TOC* (total organic carbon) was taken from the whole rock; *EOM*: extractable organic matter; *Sat*: saturate; *Arom*: aromatic; *Res*: resins; *Asph*: asphaltenes; *Rc1*: vitrinite reflectance values calculated based on MPI-1 index

Depth	TOC (%)	EOM (ppm)	Precent Total Extract				Pr/Ph	Pr/nC_{17}	Ph/nC_{18}	Rc1
			Sat	Arom	Res	Asph				
Miocene										
1508.5	0.66	210	21.7	14.3	44.0	20.0	1.10	2.66	1.68	0.57
1763.6	0.78	160	17.7	20.0	41.5	20.8	1.44	2.58	1.59	0.59
1665.4	0.61	180	14.2	15.0	47.5	23.3	1.20	3.39	2.55	0.62
Middle Devonian										
2010.8	0.13	100	49.3	5.8	39.1	5.8	0.61	0.54	0.76	0.89
Early Devonian										
2088.9	2.38	980	55.6	18.9	22.1	3.4	1.55	0.24	0.15	0.63
2089.5	0.84	140	48.6	15.0	30.7	5.7	0.91	0.24	0.27	0.63
2091.3	0.85	540	48.7	24.1	23.2	4.0	1.25	0.50	0.38	0.67
2091.9	1.51	660	60.1	16.8	19.9	3.2	1.58	0.24	0.15	0.66
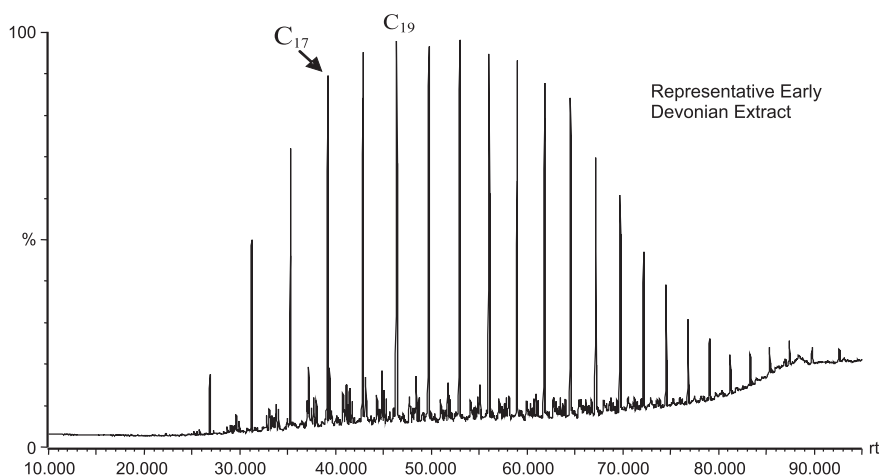
Fig. 8. Saturated hydrocarbons chromatogram of a representative Early Devonian source rock extract

Table 6. Rock-Eval pyrolysis data for Miocene samples from J9 structure

Sample No	Depth [m]	T_{max} [°C]	S_1 [mg HC/ g rock]	S_2 [mg HC/ g rock]	S_3 [mg CO_2/ g rock]	PI [S_1/ (S_1+S_2)]	PC [%]	RC [%]	TOC [%]	HI [mg HC/ g TOC]	OI [mg CO_2/ g TOC]
					Miocene J3K						
1	1339.5	434	0.02	0.81	1.18	0.02	0.12	0.58	0.70	116	169
					Miocene J7K						
2	1505.5	435	0.08	0.99	1.56	0.07	0.15	0.69	0.84	118	186
3	1508.5	432	0.16	1.0	0.78	0.14	0.16	0.50	0.66	152	270
4	1801.5	433	0.02	0.64	0.72	0.03	0.09	0.49	0.58	110	124
5	1873.3		0.01	0.04	0.26	0.20	0.01	0.03	0.04		
					Miocene St 3						
6	1660.7	432	0.02	0.71	0.66	0.03	0.09	0.54	0.63	113	105
7	1662.6	432	0.02	0.70	0.63	0.03	0.09	0.49	0.58	121	109
8	1665.4	434	0.02	0.78	0.58	0.03	0.10	0.51	0.61	128	95
9	1734.4		0.01	0.05	0.24	0.17	0.01	0.04	0.05		
					Miocene P5						
10	1733.5	436	0.03	0.85	0.62	0.03	0.10	0.57	0.67	127	93
11	1734.6	434	0.02	0.79	0.62	0.02	0.10	0.57	0.67	118	93
12	1737.6	436	0.02	0.66	0.67	0.03	0.09	0.58	0.67	99	100
13	1739.6	435	0.02	0.70	0.53	0.03	0.08	0.58	0.66	106	80
14	1743.6	433	0.02	0.73	0.70	0.03	0.10	0.57	0.67	109	104
15	1748.8	434	0.02	0.82	0.58	0.02	0.10	0.67	0.77	106	75
16	1750.4	433	0.02	0.71	0.60	0.03	0.09	0.53	0.62	115	97
17	1763.6	437	0.02	0.81	0.53	0.02	0.10	0.68	0.78	104	68
18	1770.3	434	0.04	0.85	0.57	0.04	0.10	0.64	0.74	115	77
19	1774.4	433	0.02	0.85	0.61	0.02	0.11	0.64	0.75	113	81
20	1778.7	434	0.02	0.70	0.56	0.03	0.08	0.58	0.66	106	85
					Miocene Jo7						
21	2973.5	437	0.33	17.39	2.03	0.05	1.69	9.84	11.53	151	18
					Miocene Jo15						
22	3078.5	436	0.03	0.77	0.66	0.03	0.10	0.65	0.75	121	103
23	3175.0	436	0.03	0.91	0.71	0.03	0.11	0.61	0.72	126	99
					Miocene Za 2						
24	2516.7	438	0.07	1.58	0.64	0.05	0.17	0.68	0.85	193	78
25	2544.4	439	0.08	1.20	0.54	0.06	0.13	0.67	0.80	165	73
26	2621.5	436	0.15	1.41	0.52	0.10	0.15	0.40	0.55	261	96

Saturated fractions chromatograms exhibit an immature signature with bimodal distribution (Fig. 10). Isoprenoid hydrocarbons dominate the chromatogram in the C_{15} to C_{19} molecular weight range while biomarker compounds, primarily steranes and hopanes, dominate the chromatogram in the C_{27} to C_{31} molecular weight ranges. Normal alkanes are minor components in Miocene samples. Pristane/phytane ratios are in the range 1.10–1.44. The n-alkane distribution demonstrates a rather low degree of thermal maturity (marginal maturity). This is in agreement with abundance of cadalene and retene in aromatic fractions (Fig. 11).
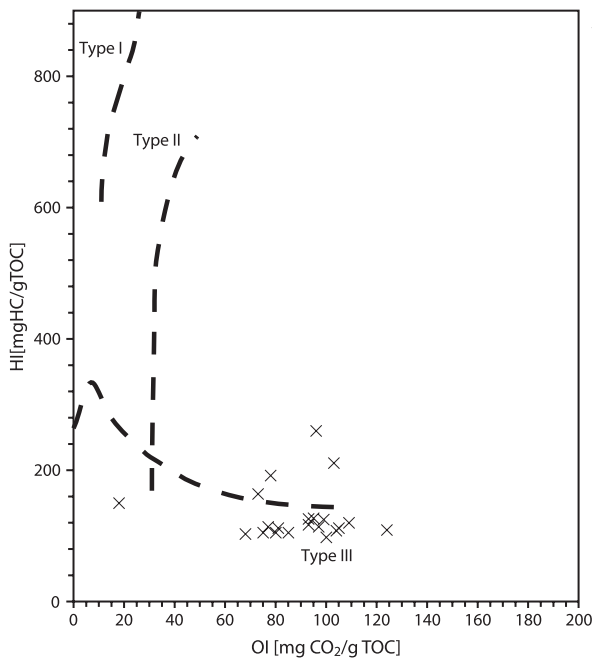
◄ **Fig. 9.** Hydrogen Index versus Tsub plot used to characterize the Miocene organic matter
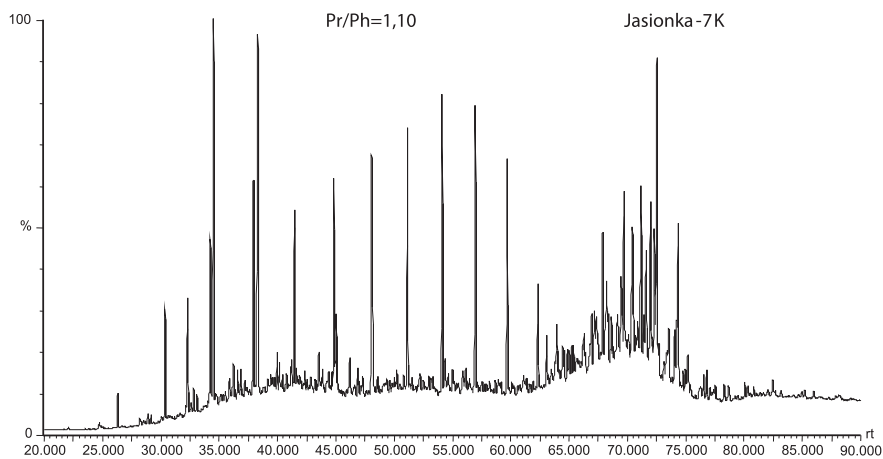
Fig. 10. Saturated hydrocarbons chromatogram of a representative Miocene source rock extract from Jasionka 7-K well, depth 1508.5 m
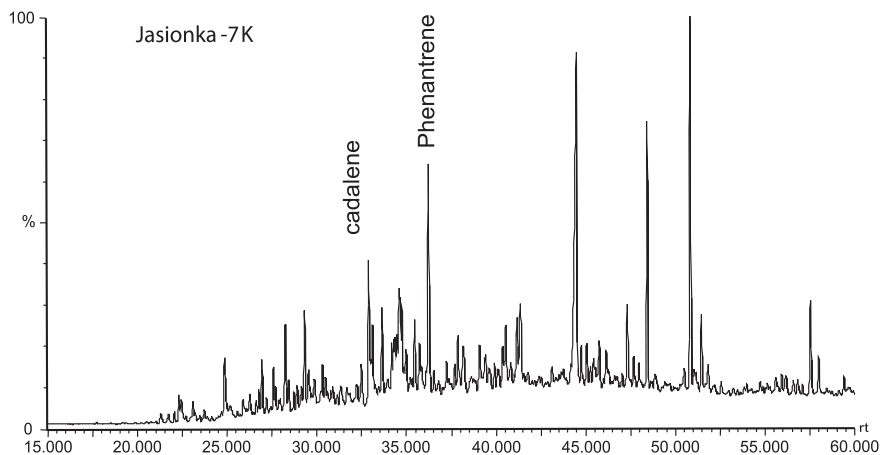
Fig. 11. Aromatic hydrocarbons chromatogram of a representative Miocene source rock extract from Jasionka 7-K well, depth 1508.5 m

This data suggest Type III organic matter connected with gas generation, but it is known (Bordenave, 1993) that in the first phase of thermogenic processes both gas and liquid hydrocarbons are generated.

4.5 Characterization of Oil

Oil accumulated in the Middle Devonian reservoir rocks is light (39°API) with very low sulphur (0.10%) and asphaltene contents (0.6%). Saturated fractions distribution is dominated by isoalkanes, especialy pristane and phytane (Figs. 12 and 13). Pristane/phytane ratio amounts to 1.03, which suggests suboxic depositional environment of source matter for this oil. High values of Pr and Ph compared to n-alkanes could indicate low maturity oil or biodegraded oil. However, biodegradation can be hardly considered at these depths. The only possible process in this case is the process of fractional vaporisation (Canipa-Morales et al., 2003; George et al., 2002). This type of process is known and
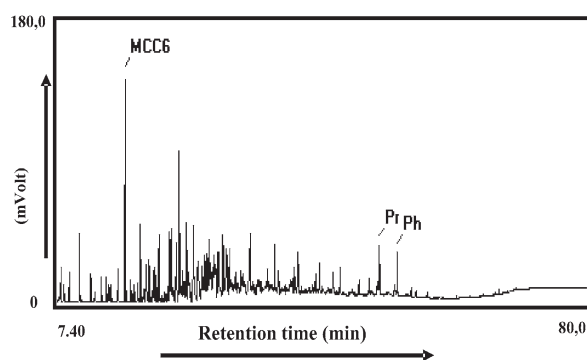
Fig. 12. Capillary gas chromatogram (whole-oil analysis) of crude oil from T-3 well

can be connected with rising pressures in an oil reservoir. Residual oil from Early Devonian source rocks is left in the oil reservoir, while gas stream mobilizes lighter hydrocarbons. Such types of hydrocarbon accumulations are present in the Miocene rocks in the studied area.

The Aromatic fraction of this oil contains cadalene, which is evidence for input of higher plants (Fig. 14).

4.6 Source Rock/Oil Correlation

Oil accumulated in the Middle Devonian reservoir rocks shows more than one origin of generation. This is supported by isotopic and biomarker composition (Figs. 12, 13, 14 and 15). Correlation of T-3 oil with source rocks organic extracts shows a good match with the Miocene shales (Figs. 9 and 10) and is confirmed by the occurrence of cadalene. This biomarker is one component of resins and can be correlated with the Miocene source rocks. Additionally, proportions of pristane to phytane in relation to n-alkanes are characteristic of the Miocene sediments. On the other hand, the presence of steranes with dominating C_{27} sterane can be considered as one of the parameters for identifying input from marine organic matter from the Lower Devonian (Fig. 15).

The mixing character of these hydrocarbons is confirmed by stable carbon isotopes composition measured in accumulated oil and gas. $\delta C^{13}CH_4$ from T-3 equals to -61‰ whereas the characteristic value of this parameter for pure Miocene gas amounts to -68–-89‰. A great deviation of δC^{13} parameter is also observed in oil composition, which is also characteristic for multi-origin oils (δC^{13} Sat = -29.04‰, δC^{13}, δC^{13}Arom = -25.82‰)

Fig. 13. Total ion chromatogram of C_{15+} saturated fractions of oils from T-3 well
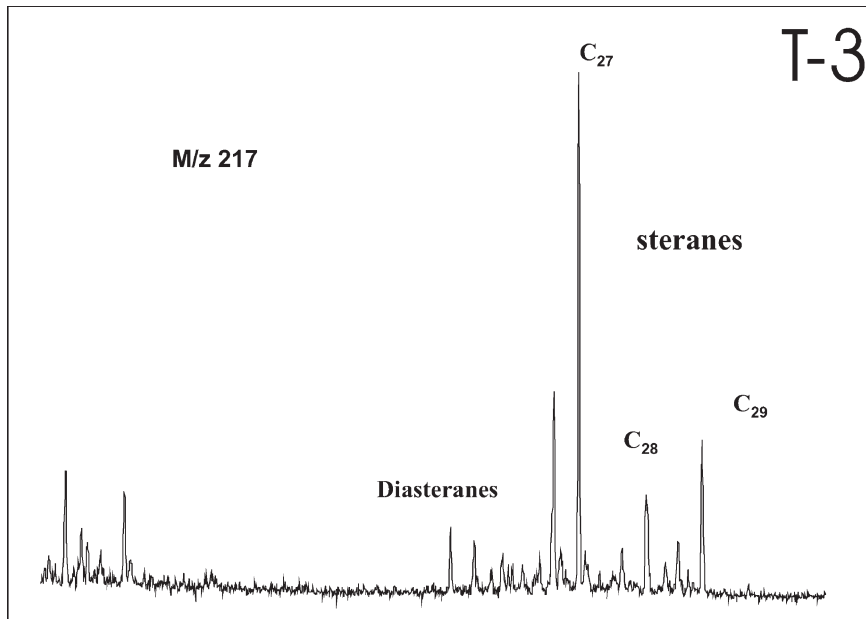
Fig. 14. Mass fragmentogram (m/z 217) showing sterane distributions in oil from T-3 well
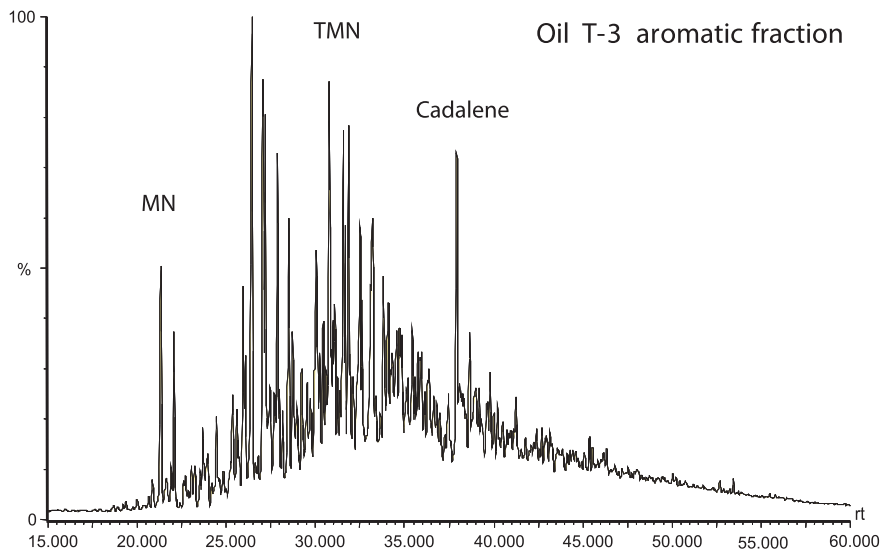
Fig. 15. Total ion chromatogram of the aromatic fraction of oil from T-3 well

5   Development of T-3 and J-9 Traps

Various models of accumulation of HC in the T-3 trap from the Devonian and other source rocks were analysed. First, the long-distance migration of oil from a distal, deeply buried Devonian source and/or from the Paleogene Carpathian Flysch was analysed. These models were rejected for two reasons. The reason to reject a distal Devonian source is that generation would have taken place earlier than the Miocene, i.e. already during the Paleogene episode of rapid subsidence and deposition of the overlying Carpathian Flysch basin,

at a time when the Miocene seal did not yet exist in the foreland. The present regional geological architecture is also against the hypothesis of a Paleogene source, because the Carpathian Flysch is currently structurally more than 1 km higher than the top part of the T-3 trap, thus precluding any further forelandward HC migration since the onset of thrust emplacement of the Carpathian allochthon.

In other words, only the generation from local and isolated Lower Devonian source rocks near the T-3 well during the Miocene and coeval generation and lateral migration from the Miocene infill of the foreland basin can account for the HC accumulated in the well T-

Table 7. Comparative structural and geological features in T-3 and J-9 structures

	T-3	J-9
Presence of source rocks	+	–
Permeable sandstones in lower part of structure	+	–
The Karst phenomena	+	+
Fracture system looking as tectonic breccia	+	+
Presence of the Miocene claystones in fractures and caverns	+	+
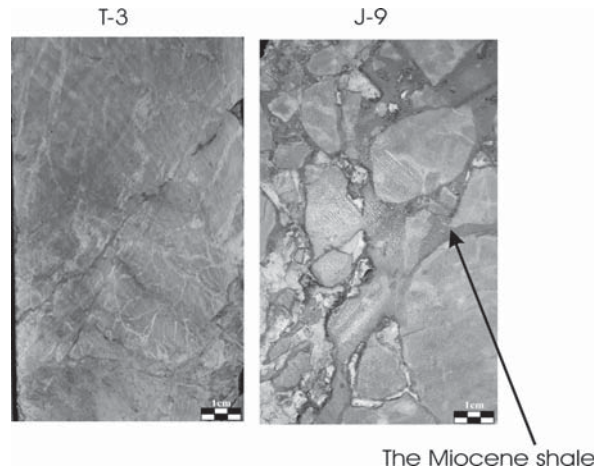
Fig. 16. Polished sections of hand samples outlining the contrasted cementation of fracture systems in T-3 and J-9 brecciated reservoirs. Notice the clay cementation in J-9

Fig. 17. Sketch of development of T-3 and J-9 structures
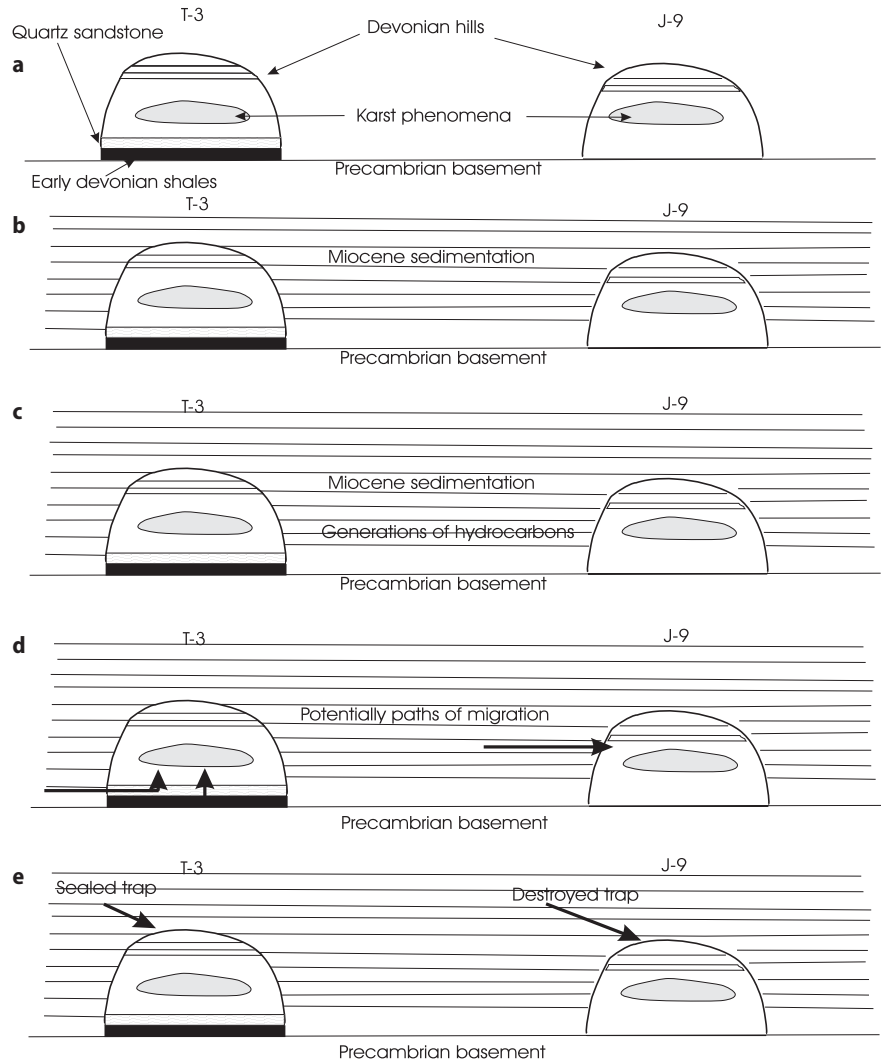
3. Detailed geochemical studies confirm the presence of both components in this oil and gas prospect.

Petrophysical and geochemical studies as well as types of fracturing and presence of claystones in caverns and fractures help to compare and differentiate the evolution and prospectivity of the two Devonian structures identified in wells T-3 and J-9. Table 7 summarises the main similarities and discrepancies between them. Similar geological position induced the same karst development in the two prospects, which display similar fracture system and presence of Miocene claystones in fractures and caverns, although a smaller content of Miocene claystones is observed in well J-9 (Fig. 16).

Two major factors differentiate the T-3 and J-9 structures, i.e. (1) the pore space parameters of underlying Devonian sandstones, and (2) the presence of Early Devonian shales at the base of the T-3 structure only. We consider that these two factors are the key to account for the distinct petroleum potential of both structures.

Before the Miocene sea transgression, these two Devonian elevations developed a meteoric karst (Fig. 17a). After transgression, water filled all voids in carbonate rocks. In the next step, the Miocene clay and mud sediments covered and isolated them (Fig. 17b). At the same time, poorly consolidated Miocene clay and mudstones invaded caverns and large fractures (Tucker and Wright 1990; Loucks, 1999; Moore, 2001). This process is better visible in well J-9 but it is also present in well T-3 (Fig. 16). Up to this stage the history of both structures is similar. The differences appeared when the Lower Devonian source rocks reached the oil window. Hydrocarbons generation started in source rocks in T-3 (Fig. 17c). Permeable sandstones in the T-3 structure created paths of migration for generated hydrocarbons towards fractured structures. Migrated hydrocarbons stopped circulation of water and preserved sealing of the T-3 trap. Simultaneously, HC generation started also in the Miocene sediments. Permeable Miocene sandstones onlapping the T-3 structure could transport the Miocene hydrocarbons aside to the T-3 trap (Fig. 17d). Biomarkers composition and possibility of fractional vaporisation of oil are in agreement with this hypothesis. There was no Lower Devonian source rocks in J-9 structure, and it is the main reason of the absence of oil in this well. Additionally, free circulation of water in the J-9 structure destroyed the trap (Fig. 17e).

6   Conclusion

The development of two similar structures was examined. Reservoir properties in both structures resulted

from meteoric karstification of the Devonian carbonates. Reservoir traps were formed while the Miocene mudstones and claystones sealed these rocks. Two other factors induced HC trapping in the T-3 structure only, i.e. (1) the local occurrence of Lower Devonian source rocks and basal permeable sandstones. The Early Devonian source rocks in T-3 generated hydrocarbons, which were subsequently transported to the overlying reservoir across porous sandstones conduits. Devonian permeable sandstones created the only way also for the Miocene hydrocarbons migration. J-9 trap could be penetrated only by lateral migration dominated by water, which was proved not sufficient to generate a hydrocarbon pool there.

References

Antonellini M., Mollema P. N., 2000. A natural analog for a fractured and faulted reservoir in dolomite: Triassic Sella Group, Northern Italy. AAPG Bull, 84/3, 314–345.

Bessereau G., Roure F., Kotarba M., Kuśmierek J. and Strzetelski W., 1996. Structure and Hydrocarbon habitat of the Polish Carpathians. In Ziegler P.A. and Horvath F., eds., Peri-Tethys Memoir 2, Structure and Prospects of Alpine Basins and Forelands, Mém. Museum Hist. Nat., Paris, 343–373.

Bordenave M.L.,1993. Applied petroleum geochemistry. Editions Technip, Paris, 524.

Borys Z., 1996. Problems in hydrocarbon prospecting in the eastern part of the Polish Carpathian Foredeep. Przegląd Geologiczny (Geological Review), 44 (10) : 1019–1023.

Canipa-Morales N.K., Galan-Vidal C. A., Guzman-Vega M. A. and Jarvie D. M., 2003. Effect of evaporation on light hydrocarbons parameters. Organic Geochemistry, 34, 813–826.

Chilingarian G.V., Mazzullo S.J. and Rieke H.H., 1992. Carbonate reservoir characterization: A geologic-engineering analysis, part I. Elsevier, Amsterdam.

Czepiec I. and Kotarba M.J.,1998. Paleoecology and organic matter in the Late Badenian and Early Sarmatian marine basin of the Polish part of the Carpathian Foredeep. Przegląd Geologiczny (Geological Review), Wydawnictwa Geologiczne (Polish Geological Institute), Warsaw, Poland, 46 (8/2) 732–736.

Dudek L. and Steczko A., 2005. Thermal maturity for modelling of hydrocarbon generation and expulsion processes in sedimentary basins. Nafta-Gaz, 61, 10, 411–421.

George A.D. and Powell C. Mca., 1997. Paleokarst in an Upper Devonian reef complex of the Canning Basin, Western Australia. Journ. of Sedimentary Research, Section A, Sedimentary Petrology and Processes, 67, 5, 935–945.

George S.C., Boreham C.J., Minifie S.A. and Teerman S.C., 2002. The effect of minor to moderate biodegradation on C_5 to C_9 hydrocarbons in crude oils. Organic Geochemistry, 33, 1293–1317.

Gliniak P., Laskowicz R., Leśniak G., Urbaniec A. and Such P., 2002. Factors affecting reservoir properties of Upper Jurassic and Lower Cretaceous carbonate rocks in central part of Carpathian Foreland. In Deformation History, Fluid Reconstruction and Reservoir Appraisal in Foreland Fold and Thrust Belts, May 14–18, AAPG Hedberg Conference, Palermo, Italy, 19.

Howard, J.,H. and Nolen-Hoeksma R.C., 1990. Description of natural fracture systems for quantitative use in petroleum technology. AAPG Bull., 72, 2, 151–163.

Kotarba M., Szafran S. and Espitalié J., 1987. A study of organic matter and natural gas of the Miocene sediments in the Polish part of the Carpathian Foredeep. Chemical Geology, 64, 3–4, 197–207.

Kotarba M., 1992. Bacterial gases in Polish part of the Carpathian Foredeep and the Flysch Carpathians: isotopic and geological approach. In Vially R., ed., Bacterial Gas, Editions Technip, Paris, 133–145.

Kotarba M.J., 1998, Composition and origin of gaseous hydrocarbons in the Miocene strata of the Polish part of the Carpathian Foredeep. Przegląd Geologiczny (Geological Review), Wydawnictwa Geologiczne (Polish Geological Institute), Warsaw, Poland, 46, 8/2, 751–757.

Kotarba M.J., Burzewski W., Wilczek T., Słupczyński K., Kossakowski P. and Botor D., 1998. Model of gaseous hydrocarbon generation In the Miocene strata of Polish part of the Carpathian Foredeep. Przegląd Geologiczny (Geological Review), Wydawnictwa Geologiczne (Polish Geological Institute), Warsaw, Poland, 46, 8/2, 737–742.

Loucks R.G., 1999. Paleocave carbonate reservoirs: Origin, burial depth modifications, spatial complexity, and reservoir implication. AAPG Bull., 83, 1795–1834.

Lucia F. J., 1995. Rock-fabric/Petrophysical classification of carbonate pore space for reservoir characterization. AAPG Bull., 79, 8, 1275–1300.

Maksym A., Śmist P., Pietrusiak M., Staryszak G. and Liszka B., 2003. New data on development of the Lower Paleozoic sediments in the Sędziszów Małopolski-Rzeszów region based on Hermanowa-1 borehole. Przegląd Geologiczny (Geological Review), Wydawnictwa Geologiczne (Polish Geological Institute), Warsaw, Poland, 51, 5, 412–418.

Matyasik I. and Steczko A., 2005. Can we correlate liquid hydrocarbons accumulations with Miocene source rocks in eastern part of the Carpathian Foredeep, Poland? Organic Geochemistry, Challenges for the 21st century, Seville, Spain, Abstracts, 1, 452–453.

Moore C.H., 2001. Carbonate reservoirs: Porosity evolution and diagenesis in a sequence stratigraphic framework. Elsevier, Amsterda, Developments in Sedimentology, 55.

Mysliwiec M., Madej K. and Bys I., 2004. The Miocene gas fields discovered in the Rzeszów area, Carpathian Foredeep, on the basis of the direct hydrocarbons indicators. Przegląd Geologiczny (Geological Review), 6, 501–506.

Nelson A.R., 1989. Geologic analysis of naturally fractured reservoirs. Gulf Publ. Comp. Houston.

Roca E., Besserau G., Jawor E., Kotarba M. and Roure F., 1995. Pre-Neogene evolution of the Western Carpathians: Constrains from the Bochnia-Tatra Mountain section (Polish Western Carpathians). Tectonics, 14, 4, 855–873.

Such P. and Leśniak G., 2004. A filtration of reservoir fluids in fractured rocks in the light of correlation investigations. Nafta-Gaz, 6/2004, 283–286.

Such P. and Leśniak G., 2003. Pore space parameters of reservoir rocks. Works of IGNiG, 119, 63.

Such P. and Leśniak G., 2002. Complex correlation for characterization of transport system in fracture rocks. Proceedings of 12 th Improved Oil Recovery Symposium, Kazan 2002, 502–505

Tucker M. E. and Wright V.P., 1990. Carbonate Sedimentology. Blackwell Science, Oxford

Part VII
Tectonics, Sedimentation and Denudation in Thrust Belts

Foreland Fold-and-Thrust belts constitute natural laboratories to study source-to-sink and uplift-erosion-unroofing processes as well as neotectonics. Part VII of the volume outlines three case studies, each of them being dedicated to one of these challenging topics.

In their paper, Artoni et al. (Chapter 23) describe the architecture and timing of the sedimentary infill of a Late Miocene piggyback basin in the Northern Apennines, and discuss these sedimentary records with respect to such forcing forces as the tectonics and climate.

De Grave et al. (Chapter 24) have applied apatite fission-track thermochronology to unravel the tectonic and unroofing agenda of the Southern Siberian Altaï Mountains in central Asia, accounting for a two stage cooling of Paleozoic basement, first during a rapid Late Jurassic-Cretaceous episode, and possibly also during Late Cenozoic thrusting.

Scrocca et al. (Chapter 25) discuss the significance of the Central Adriatic deformation zone with respect to the Apenninic thrust front and overall geodynamic model, as well as the distribution and timing of Quaternary growth structures in the Northern Apennines and adjacent Po Plain.

Tectonic and Climatic Controls on Sedimentation in Late Miocene Cortemaggiore Wedge-Top Basin (Northwestern Apennines, Italy)

A. Artoni · F. Rizzini · M. Roveri · R. Gennari · V. Manzi · G. Papani · M. Bernini

Abstract. At the foothills of the north-western Apennines, the Cortemaggiore Wedge-Top Basin (CWTB) is bounded by the buried and arcuate Cortemaggiore anticline, to the north, and by the polyphased and complex Salsomaggiore tectonic window, to the south. The CWTB started to form in response to a late Tortonian tectonic pulse that uplifted the Cortemaggiore anticline and established euxinic conditions. A major intra-Messinian tectonic pulse further shortened the CWTB and triggered the emplacement of gravity-driven mass-wasting deposits above which turbiditic, shelfal deposits evolve upward to fluvio-deltaic deposits. The former, Late Messinian hypohaline succession, is characterized by a well-developed cyclical pattern which falls in the range of astronomically-controlled climate changes with precessional periodicity modulated by obliquity and eccentricity periodicity. Tectonic and climate controls on sedimentary succession of the CWTB act at different frequencies. Based on the refined and high-resolution late Miocene chronostratigraphy of coeval Mediterranean sedimentary succession, it is possible to time constrain the tectonic and climatic events and their cyclicity. Tectonics control acts at low frequency (order of 2 Myr) and produces major and fast morphologic changes of the basin. Climate acts at variable higher frequency (order of 20-100 kyr); it both distributes laterally and stacks vertically and cyclically the sediment supplied to transport by erosion of tectonically uplifted rocks. The tectonic and climatic controls should have acted concomitantly over the entire Northern Apennines foreland basin system and the Mediterranean area, because cyclicity and depositional characters of late Miocene succession present common features. Tectonic uplift causes basin-wide hydrologic and hydrogeologic changes that might induce increased evaporation; in the CWTB, two drier climate events, corresponding to the lower and upper evaporites of the Mediterranean region, are closely preceded by tectonic pulses. However, during late Miocene, climate changes occurred also outside the Mediterranean region. Thus, it is argued that the 2 Myr is a periodicity common both to tectonics pulses and climate changes; it is a low-frequency cyclicity that, related to astronomical forces, drives simultaneous action of tectonic pulses and climate changes within the CWTB.

Keywords. Tectonics, climate, foreland basin, orogen, Apennines.

1 Introduction

Tectonic movement and climate are regarded as first-order controlling factors on volumes, vertical-lateral architectures and distribution of sedimentary successions; the two factors strictly affect the amount of sediment supplied to both transportation and final deposition within sedimentary basins and the capacity to preserve their sedimentary flux (Allen and Allen, 2005; Jones and Frostick, 2002; Leeder, 1999). Numerical and analogue modelling have addressed tectonic and climate interplay, mainly reduced to amount of erosion, in sedimentary basins fill (Beaumont et al., 1992; Willett et al., 1993). In foreland basins, with worldwide and extensively studied examples (Allen and Homewood, 1986; Allen et al, 1992; Bertotti et al., 2003; Mascle et al., 1998; Sinclair, 1997; Van Wagoner and Bertram, 1995), tectonic control on the sedimentary fill has been always emphasized and modelled (Allen and Allen, 2005; Beaumont et al., 1992; Flemings and Jordan, 1990; Zoetemeijer et al., 1992). Instead, climatic control is implied in applying sequence stratigraphic analysis (Haq, 1991; Van Wagoner et al., 1988) where various orders of eustatic variations, variable amount of sediment is yielded and delivered from mountain belts and invoked to generate prograding and/or retrograding sedimentary wedges (Plint, 1991; Posamentier and Vail, 1988; Schawn, 1995; Zweingel et al., 1998). Sediment yield is also related to the orogen uplift which, in turn, is supposed to modify atmospheric circulations and thus climate in the long terms (Molnar and England, 1990; Molnar et al., 1993; Raymo and Ruddiman, 1992). If tectonics appears to dominate in controlling the sedimentary basin fill, its interplay and feed-back with climate is still not fully understood (Leeder, 1999; Ruddiman, 1997). It is a common belief that climatic control acts at astronomically forced cyclicities (10–100 kyr), though eustatic cycles, likely climatically-driven, can also last between 1 Myr (3rd order cycles) and 10 Myr (supercycles) (Haq et al. 1988). Whilst, tectonic control is believed to act at much longer time intervals (>10 Myr in Clift et al., 2002a, b; Mascle et al., 1998; Ruddiman, 1997); few ex-

amples report tectonically-driven, very high-frequency sedimentary cycles in the order of 400 kyr (Vakarelov et al., 2006) or even sub-Milankovitchian cycles (Ito et al., 1999). A contribute to better understand tectonic-climatic relationships is certainly represented by accurate time constrain of tectonic phases and climatic changes. Climate and palaeo-climate studies (De Boer and Smith, 1994; Frakes et al., 1992; Lamb, 1995) reveal very high-frequency changes (10–100 kyr) which require extremely detailed stratigraphic studies and datable rocks. The Mediterranean area, whose late Miocene sedimentary record has a refined and high-resolution chronostratigraphic scheme (Hilgen et al., 2000; Van Couvering et al., 2000) is a natural laboratory for time constraining and defining the tectonic and climatic interplay at very short time intervals, less than 2 Myr.

The Mediterranean has been the subject of many case studies of foreland basins (Allen and Homewood, 1986; Mascle et al., 1998; Vai and Martini, 2001), whose overall physiography can be synthetized by the scheme of Giles and DeCelles (1996). In between emerged orogen, mainly under erosion, and foredeep basin, with high sedimentation and subsidence rates in response to the down-flexure of the subducting plate, the wedge-top basins are the most suitable to investigate the tectonic and climate interplay on sedimentary records of foreland basins. The wedge-top basins are sensitive to the accreting pulses of the orogen and they record the variations in sediment delivered from mountain chains which, in response to both climatic changes and uplift pulses, undergoes cyclical erosion.

In this respect, the late Miocene sedimentary record cropping out along the inner border of the Cortemaggiore wedge-top basin of the Northern Apennines foreland basin was previously analysed integrating surface and sub-surface data (Artoni, 2003a; Gennari, 2003; Artoni et al., 2004; Rizzini et al., 2004). The interpretation and revision of these previous data made it possible to precise the tectono-sedimentary evolution of the CWTB and, based on the ages of coeval events in the Mediterranean area, to calibrate in time the tectonic pulses and the climatic changes. Tectonics and climate acted at different cyclicity: the climatic cycles, as short as 20 kyr or even less, are effective during a tectonic cycle of about 2 Myr duration. But tectonic pulses and climatic changes seem to act simultaneously in causing two drier events in the late Miocene.

2   Geological Setting

The Northern Apennines are a collisional orogenic wedge that until the Oligocene was the south-western continuation of the Alpine orogenic wedge (Fig. 1a) (Boccaletti et al., 1990; Gueguen et al., 1998) forming a south-east vergent accretionary prism at the back of the Alpine fronts (Cavazza et al., 2004). Since Oli-
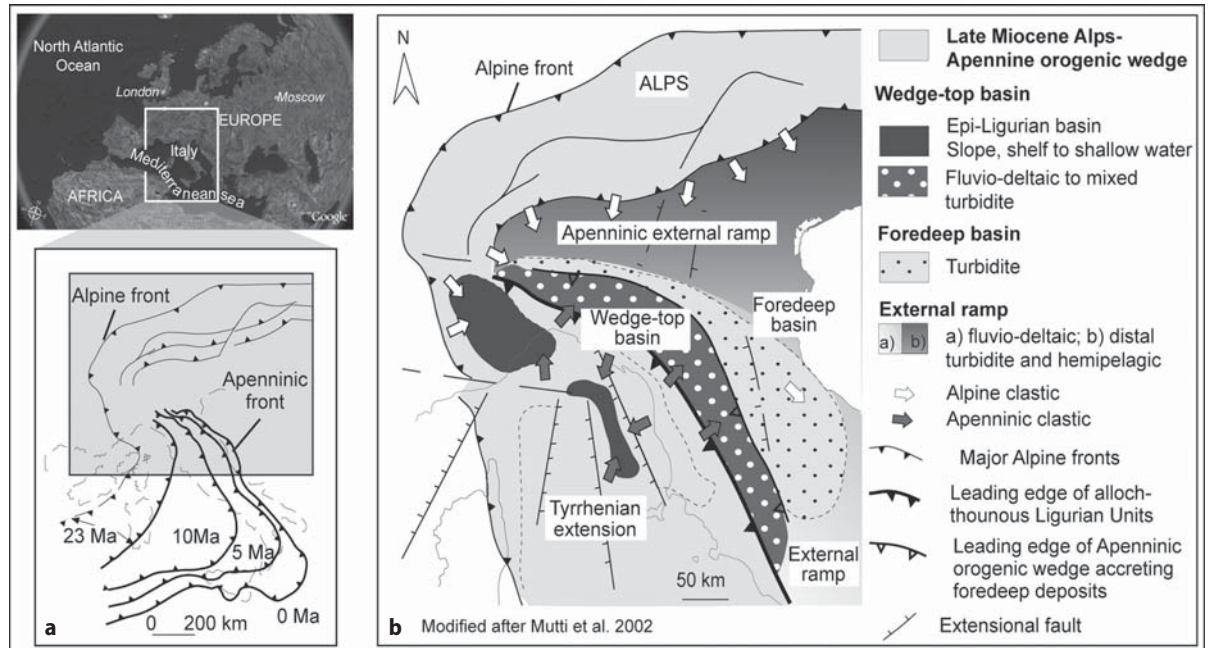
Fig. 1. Location map and **a** Oligocene-Present migration of Apenninic fronts (modified after Gueguen et al., 1998). **b** Schematic paleogeographic map of Apenninic foreland basin system during the late Miocene (modified after Mutti et al., 2002)

gocene to present, the advancing Apenninic orogenic fronts have migrated toward E and NE progressively accreting the foredeep deposits and creating the wedge-top basins (Fig. 1) (Ricci Lucchi, 1986; Argnani and Ricci Lucchi, 2001). At present, the Apenninic orogenic wedge is made of two distinct and superposed structural levels (Fig. 2); the upper and most allochthonous one overrides on top of the Oligocene to recent foredeep and wedge-top deposits, which thus belong to the lower structural level.

The upper structural level is made up of the accreted Ligurian units; i.e. Mesozoic oceanic and forearc deposits derived from the closure of the Ligurian-Piedmont ocean and its continental margins (Abbate et al., 1970; Boccaletti et al., 1971; Elter, 1975; Marroni et al., 2002; Cavazza et al., 2004). On top of the Ligurian units, the epi-Ligurian wedge-top basins are characterized by a middle Eocene-early Messinian succession made up of tectonically-controlled turbiditic, shelfal and slope deposits, passing upward to
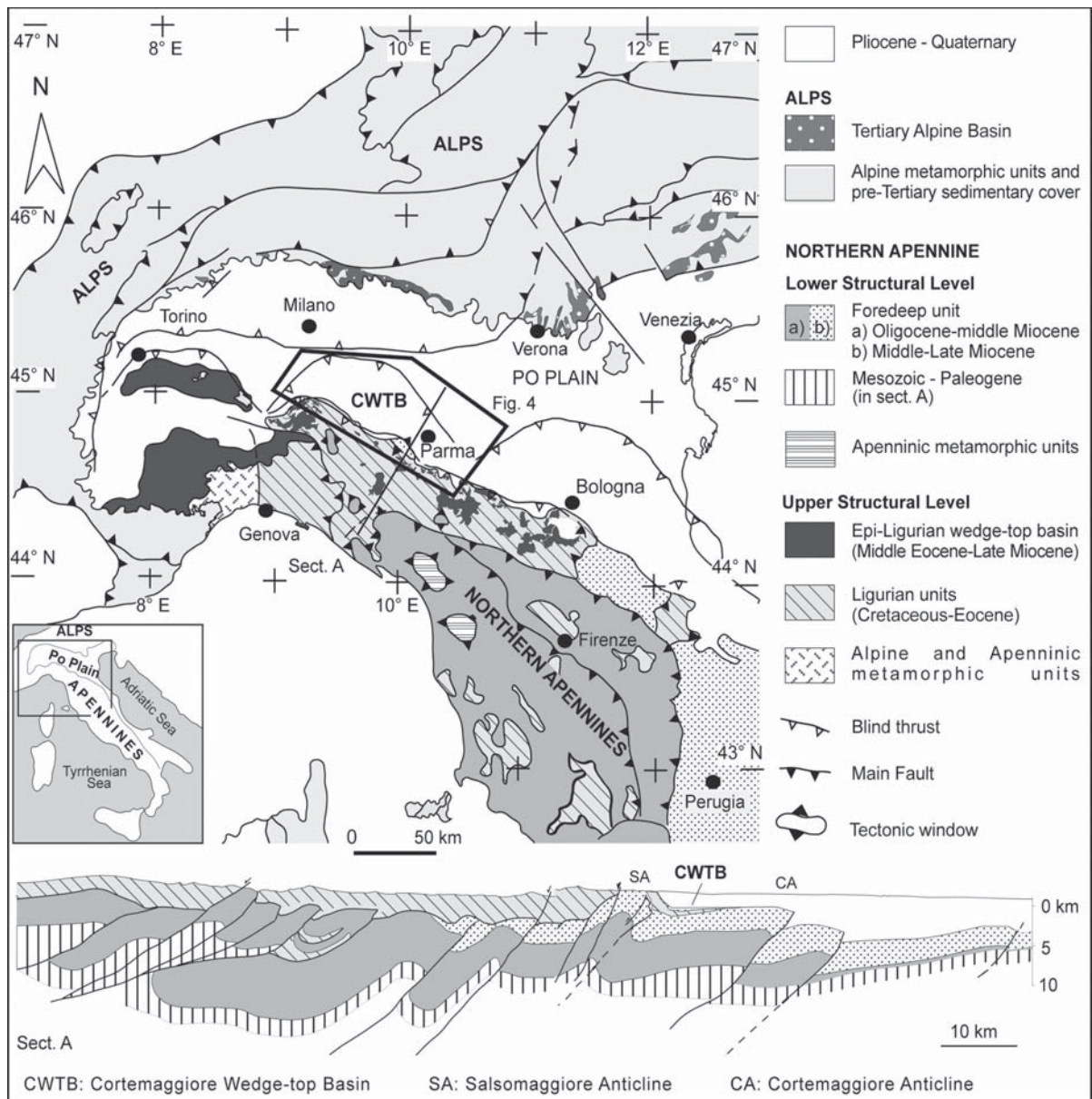
Fig. 2. Geological synthetic map of Northern Apennine (modified after Mutti et al., 2002) and schematic cross section (sect. A) crossing the Cortemaggiore Wedge Top Basin (from Artoni et al., 2004, Fig. 1)

shelfal and, locally, to shallow-water primary evaporitic deposits (Amorosi et al., 1993; Boccaletti et al., 1990; Mutti et al., 1995; Papani et al., 1987; Ricci Lucchi, 1986).

The lower structural level, folded and segmented by thrusts that involve the Palaeozoic basement, consists of Mesozoic-to-Paleogene carbonate successions (Fig. 2), above which Oligocene-to-Recent foredeep and wedge-top deposits record a number of major unconformity-bounded depositional sequences which mark the depocenter's shift; these sequences can be correlated and are coeval to those recorded in the epi-Ligurian wedge-top basins deposits (Ricci Lucchi, 1986).

The leading edges of the two levels progressively propagated toward E-NE; coeval collapse/back-arc extension stretched the orogen to the west and metamorphic complexes were exhumed (Argnani and Ricci Lucchi, 2001; Gueguen et al., 1998). Because of different amounts of shortening and exhumation, the thrust fronts of the lower structural level are completely exposed in the southern area whereas, in the northwestern Apennines, they are buried underneath both allochthonous units and Pliocene-Recent deposits. Consequently, the northwestern Apenninic foredeep and wedge-top deposits crop out only in tectonic windows (Fig. 2).

At the foothills of the northwestern Apennines, the Cortemaggiore Wedge-Top Basin (hereafter CWTB) is bounded by two thrust-related folds of the lower structural level (Fig. 2): the north-east vergent and overturned Salsomaggiore anticline, to the south; the arcuate Cortemaggiore anticline, buried to the north. The sedimentary succession, the architecture and progressive development of the CWTB during the late Miocene could be defined through extensive stratigraphic and structural studies integrating surface and subsurface data (Argnani et al., 2003; Artoni, 2003a; Gennari, 2003; Artoni et al., 2004; Rizzini et al., 2004). The late Miocene events preserved in the CWTB can be also recognized in both the Mediterranean region and in the Apenninic foredeep (Fig. 3). These coinciding events and their precise dating are fundamental for discussing tectonic and climatic interplay in the CWTB. Thus, a brief synthesis is given of late Miocene events and their dating in the Mediterranean region before presenting the evolution of the CWTB in the same time interval.
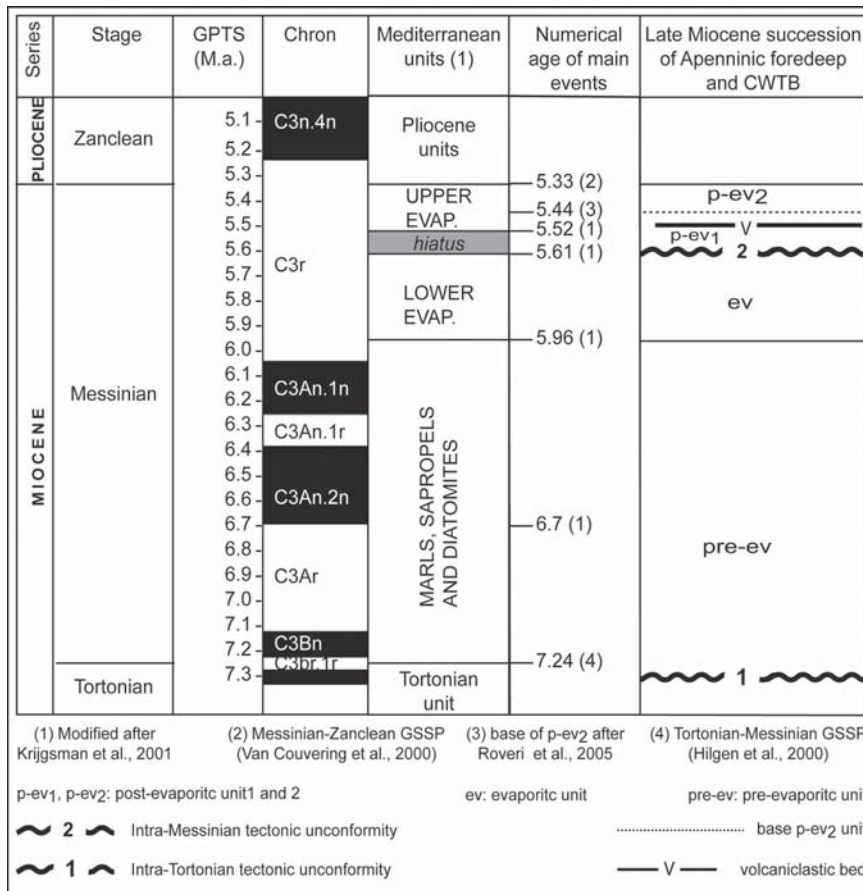
Fig. 3. Chronostratigraphy and stratigraphy of late Miocene succession in Mediterranean region and Apenninic foredeep compared to coeval succession of Cortemaggiore Wedge Top Basin. The chronostratigraphic scheme is defined by integrated magneto-, bio-stratigraphy and astrochronological tuning according to Krijgsman et al. (2001). Numerical ages of main events is based on Global Stratotype and Section Point (GSSP) (Van Couvering et al., 2000; Hilgen et al., 2000) and on integrated stratigraphic studies (Krijgsman et al., 1999; Roveri et al., 2001 and 2005)

3   The Late Miocene Events in the Mediterranean Region and in the Apenninic Foredeep: The Climatic Imprint on the Sedimentary Succession

During the late Miocene, significant transformations occurred in the Mediterranean region. Paleogeographic reconstructions show activity of tectonic processes (Mantovani et al., 1997; Gueguen et al., 1998; Cavazza et al., 2004) that, in the Apennines, produced the advancement of mountain fronts (Fig. 1a) (Ricci Lucchi, 1986; Boccaletti et al., 1990; Patacca et al., 1990; Conti and Gelmini, 1994; Vai and Martini, 2001). Then, the Messinian salinity crisis took place (Hsü et al., 1977) with consequent drastic changes in depositional environments. Nonetheless, it is in the Mediterranean region that absolute dating and G.S.S.P. have been defined for the late Miocene (Hilgen et al., 2000; Van Couvering et al., 2000) and tectono-sedimentary events can be framed in a high-resolution stratigraphic scheme.

Marls, diatoms and sapropelitic deposits characterize the sedimentation in deeper Mediterranean basin at the Tortonian-Messinian boundary and they mainly represent what is named pre-evaporitic units (pre-ev). The inception of euxinic deposits approximate 7 Ma, even if diachroneity has been demonstrated between central and eastern Mediterranean (Hilgen and Krijgsman, 1999). Based on magneto-/bio-/astrochrono-stratigraphy studies on these deposits, the Tortonian-Messinian boundary has been dated at 7.24 Ma (Hilgen et al., 2000) (Fig. 3). This boundary post-dates the intra-Tortonian tectonic pulse which is recorded in the Apenninic Foreland Basin system (Ricci Lucchi, 1986; Boccaletti et al., 1990; Patacca et al., 1990; Conti and Gelmini, 1994; Vai and Martini, 2001) and is part of a period during which important tectonic activity occurred in the Mediterranean area (Mantovani et al., 1997; Gueguen et al., 1998; Cavazza et al., 2004). The age of this tectonic phase is not precisely defined, it must be in between 11 Ma and 7.24 Ma; it is late Tortonian and around 8 Ma in Patacca et al. (1990).

The most known late Miocene event, typical of the Mediterranean area, is the evaporitic event (ev) represented by a widespread diffusion of primary evaporitic precipitates. The inception of this event, or Messinian salinity crisis (MSC), has been posed at 5.96 Ma (Krijgsman et al., 1999) but the causes and modalities of it are still debated (Cita et al., 1975; Hsu et al., 1977; Roveri et al., 2001; Rouchy and Caruso, 2006; Roveri and Manzi, 2006). In the Apenninic foredeep, primary evaporites were deposited in perched epi-Ligurian wedge-top basin on top of the allochthonous units and intra-basinal highs whereas euxinic deposits occupy deeper basin setting (Roveri et al., 2001; Manzi

et al., 2005; Rizzini et al., 2004; Rossi et al., 2001; Roveri et al., 2003).

An unconformity surface, the intra-Messinian unconformity, is the upper boundary of the evaporitic unit. It is well recognized in the northern Apennines (Ricci Lucchi et al., 1982; Roveri et al., 2001) and it also occurs around the Mediterranean region (Krijgsman et al., 1999; Cavazza and DeCelles, 1998; Lofi et al., 2005) (Fig. 3). In the Apenninic foredeep basin, resedimented gypsum are the only physical expression of the intra-Messinian unconformity (Artoni, 2003b; Manzi et al., 2005; Roveri et al., 2001). The intra-Messinian unconformity, which assumes various characters and amount of stratigraphic hiatus depending on marginal or deep basin setting, is dated at 5.6 Ma (Fig. 3) (Krijgsman et al., 1999); erosion and significant sea-level fall, very likely tectonically-driven, lasted until 5.52 Ma (Krijgsman et al., 1999 and 2004) (Fig. 3). Plate motion reorganization corresponds to this surface according to Mantovani et al. (1997).

Above the regional wide intra-Messinian unconformity, siliciclastic rocks appeared again and lacustrine to fluvial, shelfal and turbiditic deposits constitute the post-evaporitic succession (p-ev) that in the Apennine and Mediterranean area is well-known as hypoaline Lagomare succession considered non-marine in response to the closure of the Gibraltar arc (Casati et al., 1976; Cita et al., 1975; Roveri et al., 1998). Sedimentological analysis, carried out on post-evaporitic units all around the Apenninic foredeep (Roveri et al., 1998 and 2001), show that these units generally start with turbiditic, shelfal deposits, which are named p-ev$_1$, and evolves to fluvio-deltaic deposits toward the top. The former are characterized by a well-developed cyclical pattern and named p-ev$_2$ by Roveri et al. (1998). Within the p-ev$_1$ and close to the base of p-ev$_2$ unit a regional volcaniclastic level occurs and it is radiometrically dated at 5.5 Ma (Odin et al., 1997). Locally, in Spain and Sicily, evaporitic precipitation persisted during late Messinian (Decima and Wezel, 1973; Krijgsman et al., 2001) and increased evaporative conditions should have favoured limestone deposition of the Colombacci unit in the Apenninic foredeep (Bassetti et al., 2004; Cosentino et al., 2005). Therefore, the upper evaporites of the Mediterranean region (Hsu et al., 1977; Krijgsman et al., 1999, 2001; Roveri et al., 2001) are correlated to the post-evaporitic unit (Fig. 3). Recently, accordingly to the subdivision of post-evaporitic unit in two subunits (p-ev$_1$ and p-ev$_2$ of Roveri et al., 2001), the base of the p-ev$_2$ unit is tentatively placed at 5.44 Ma, based on comparison with astronomic curves (Roveri et al., 2005) (Fig. 3). The proposed dating agrees with the absolute age of the volcanoclastic marker bed, mentioned above. At regional scale, the post-evaporitic hypohaline unit, with basal stratigraphic hiatus of variable amount was deposit-

ed till the base of the Pliocene (Fig. 3), when open-marine environments were established again. Integrated stratigraphic studies pose the base of the Pliocene at 5.33 Ma (Van Couvering et al., 2000). Thus, the post-evaporitic units are deposited in less than 300 kyr and p-ev$_2$ in less than 200 kyr - a time interval which suggests that these units record a very high-frequency cyclicity.

3.1 The Climatic Cyclicity in Late Miocene Succession of the Mediterranean Region and the Apenninic Foredeep

The tectonics control on late Miocene sedimentary succession of the Mediterranean region has been emphasized by various authors who interpret the major changes in sedimentation driven by tectonic phases (Krijgsman et al., 1999; Roveri et al., 2001; Roveri and Manzi, 2006) or isostatic rebound (Cavazza and De-Celles, 1998). However, it is also generally agreed that late Miocene and in particular Messinian sedimentary cyclicity is related to climate oscillations (Krijgsman et al., 1999; Roveri et al., 1998, 2001; Roveri and Manzi, 2006) which, difficult to reconstruct for ancient sedimentary record (Frakes et al., 1992), are supposed to be strictly related to insolation variations at Earth's surface accordingly to Milankovitch's astronomic cycles. Thus, insolation curve and related eccentricity, obliquity, precession curves (Laskar et al., 2004) have been associated to chrono-magneto-stratigraphy for calibrating astronomically the sedimentary cycles of late Miocene Mediterranean successions (Hilgen et al., 2000; Krijgsman et al., 2001). Detailed and integrated stratigraphic studies demonstrated the presence of astronomically-driven climatic cycles; absolute datings, magneto-chronostratigrapy, biostratigraphy, foraminifera oxygen isotopic curves and sedimentological analysis carried out on late Miocene successions of the Mediterranean area revealed a strict correlation between lithologic and astronomic cycles (Krijgsman et al., 1999, 2000; Sprovieri et al., 2003). Astrochronology became a new method for stratigraphic constraints and it has been integrated in the Neogene chronostratigraphic chart (Gradstein et al., 2004).

3.1.1 Climatic Cyclicity in Pre-Evaporitic (pre-ev) and Evaporitic (ev) units

The cyclicity of pre-evaporitic units is well known in the Mediterranean region (Krijgsman et al., 2001; Sprovieri et al., 2003) where marl/ or carbonate/sapropel couplets appear and contain the Tortonian-Messinian boundary at 7.24 Ma (Hilgen et al., 2000; Krijgsman et al., 2004) (Fig. 3). These couplets are in-

terpreted to be controlled by precession mechanism inducing dry-wet climate oscillations (Krijgsman et al., 1999). Dry periods, characterized by evaporation exceeding precipitations, correspond to precession maxima and insolation minima; carbonates are deposited. Wet periods with increased precipitations and freshwater input correspond to sapropel deposition or precession minima and insolation maxima. The same astronomically-forced climatic oscillations are supposed to generate gypsum/sapropel cycles; the gypsum substitutes the carbonate precipitation of previous cycles because a minimum of eccentricity amplifies the effect of precession maxima at 5.96 Ma (Krijgsman et al., 1999), base of the Lower Evaporites in Mediterranean region (Fig. 3). In the type-area of the Vena del Gesso (Northern Apennines), which is the closest area to the CWTB with primary evaporites, this climatic-controlled cyclicity generates sixteen cycles (Vai and Ricci Lucchi, 1976) containing a characteristic regressive-transgressive facies sequence recently revised by Lugli et al. (2005). In the lower portion of the Vena del Gesso section, up to the 5th cycles, relatively deep setting and low salinity made possible the precipitation of vertical massive selenite which is upward substituted by banded selenite in response to a progressive drowning and a relatively increased salinity with oscillating brine level (Lugli et al., 2005). Between the 6th and 15th cycles of the same section, transgressive facies are given by nodular and lenticular selenite, F5 facies of Vai and Ricci Lucchi (1976). Based on geochemical data, the F5 facies is reinterpreted to form when major influxes of oceanic water were strongly mixed with unsaturated continental waters causing the solution of sulphate precipitates (Lugli et al., 2005). The appearance of F5 facies likely marks and precedes the end of sulphate evaporate precipitation in coincidence with another minimum in Earth eccentricity (Krijgsman et al., 2001) at 5.6 Ma. These astronomically forced climatic oscillations should occur during a glacial period which lasted from 6.2 Ma to 5.5 Ma (Hodell et al., 2001). In fact, in the north Atlantic regions, isotopical stages, coeval to evaporitic and pre-evaporitic units, are interpreted to be representative of a series of glacial-interglacial oscillations which fit the cyclicities recognized in the Mediterranean region by Krijgsman et al. (2001) (Hodell et al., 2001).

After the first main evaporative event, evaporitic deposits were resedimented; gypsum-arenite and gypsum-rudite were formed (Manzi et al., 2005) and they constitute the F6 facies in the 16th cycle of the Vena del Gesso section (Vai and Ricci Lucchi, 1976). In the Sorbas basin, a similar number of gypsum–bearing cycles and magnetostratigraphic-constrained ages between 5.96 Ma and 5.6 Ma, confirm that each cycle has a duration in the order of the precessional astronomic cycles (20.000 yr) (Krijgsman et al., 2001).

3.1.2 Climatic Cyclicity in Post-Evaporitic Units (p-ev)

Climatic cyclicity in post-evaporitic units has been debated because continuous and favourable stratigraphic sections are lacking as a consequence of the intra-Messinian unconformity and the presence of hiatus (Fig. 3), also known as the Messinan gap. Then, the widespread occurrence of non-marine or evaporative deposits are other limiting factors in analyzing climatic changes which are commonly detected by isotopic and palaeoecological analysis of open-marine microfossils. However, recently, the stacking pattern of post-evaporitic units in the Apenninic foredeep has been interpreted as climatic-driven cycles (Roveri et al., 1998; 2001). The occurrence of repeated alternation of coarse- and fine-grained lithofacies of fluvio-deltaic deposits which sedimented in less than 200 kyr (5.5–5.33 Ma) has been regarded as a proof of very high-frequency cycles of dry-wet climate oscillations (Roveri et al., 1998). Uppermost Messinian units of the Mediterranean area show a similar cyclic pattern (Rouchy et al., 2001; Ghibaudo et al., 1985). The p-ev$_2$ unit of Roveri et al. (2001) is made up by three cycles with a duration around 30 kyr which is in the order of precessional/obliquity astronomic cyclicities. Though further cyclo-stratigraphic studies will more precisely express the duration of each cycle, it is difficult to believe that climatic control on sedimentary cyclicity was switched off during the latest Messinian. Earth's precession and obliquity cycles have been demonstrated in pre-evaporitic and evaporitic units (Krijgsman et al, 2001) as well as in Pliocene units (Lourens et al., 1996). In addition, isotopic curves of late Miocene and Pliocene intervals in Atlantic and Pacific regions (Kennett, 1986; Hodell et al., 2001; Zhang and Scott, 1996), likely more sensible to glaciations in polar ice caps, show oscillations also during the time corresponding to Mediterranean post-evaporitic units. The evidences of glacial periods and diffused ice formation also in the Northern hemisphere (Frakes et al., 1992; Hodell et al., 2001) during pre-Pleistocene time imply that climatic changes were driven by astronomical parameters as in Pleistocene time when two polar ice caps were present (Frakes et al., 1992) and Milanktovich cycles occurred.

4   The Late Miocene Stratigraphy and Tectonic Evolution of the Cortemaggiore Wedge-Top Basin

The Miocene paleogeography of the Northern Apennine orogenic wedge and associated foredeep basin is depicted in Fig. 1b. The foredeep, wedge-top and epi-Ligurian wedge-top basins progressively migrated toward E and NE in response to the advancing orogenic fronts (Fig. 1). At the same time, the external ramp was moving and flexing toward more external area of the foreland basin; the external ramp of Apenninic foredeep was also the transfer zone for clastic deposits derived from uplifted Alps (Fig. 1b) (Mutti et al., 2002; Ricci Lucchi, 1975).

The foredeep depocenters were mainly filled by sheet-like turbiditic deposits derived from fluvial and deltaic systems draining the Alps (Fig. 1) (Ricci Lucchi, 1975 and 1986); instead, the epi-Ligurian clastic deposits testify local Apenninic sources (Cibin et al., 2001; Gazzi and Zuffa, 1970). Three different turbiditic systems, that might present continuous gradation among them, strictly correspond to foreland basin physiography (Mutti et al., 2002 and 2003):

1) deltaic turbiditic systems are mainly located on the orogenic wedge and wedge-top basins;
2) mixed turbiditic systems are mainly located to leading edges of the orogenic wedge and inner foredeep;
3) deep marine turbiditic systems are mainly located in axial foredeep depocenters and foreland external ramp.

The articulated physiography of the Tertiary Northern Apennines is demonstrated also by the occurrence of mass-wasting products (slumps, slides, block falls, debris flows) also known as olistostromes (Flores, 1955; Lucente and Pini, 2003; Pini, 1999 and references therein). These complex units derive from masses destabilized along submarine slopes and they are made of both foredeep deposits and Ligurian allochthonous units. They are of various sizes, from few meters to hundreds of meters; they occur either in the epi-Ligurian wedge-top basin, or close to the toe of the orogenic wedge (Artoni et al., 2004; Gelati et al., 1987) and even in the foredeep basins (Lucente and Pini, 2003). They are important marker beds at both local and regional scale as they generally mark destabilization events in the Apenninic foreland basin.

The depositional features and geometry of the sedimentary bodies (Fig. 4), and the regional tectono-stratigraphic analysis (Argnani et al., 2003; Rizzini et al., 2004) similar to the one published for the Cortemaggiore anticline (Mattavelli et al., 1993), demonstrate that the CWTB is a syn-tectonic wedge-top basin from the Tortonian to Pliocene.

4.1 Late Tortonian and Early Messinian Euxinic and Evaporitic Deposits (pre-ev and ev)

During the Tortonian, the Cortemaggiore thrust front was the outer structural high bounding a foredeep basin to the north and the CWTB to the south (Fig. 4).
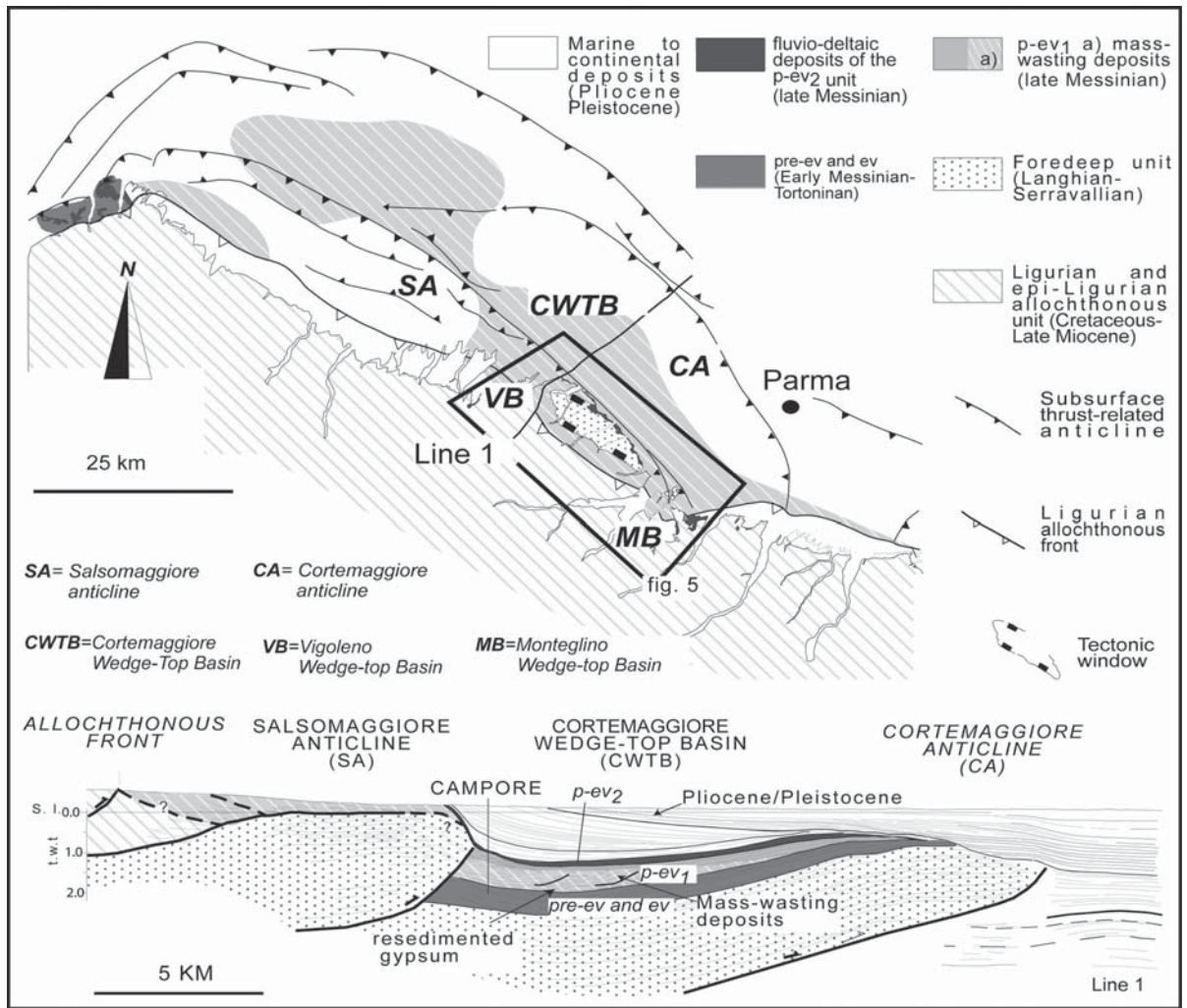
Fig. 4. Structural geological sketch map derived by surface and sub-surface data of Northwestern Apennines. Line drawing from a seismic reflection profile (*Line 1*) crosses the Cortemaggiore Wedge-Top Basin (CWTB) from the Salsomaggiore anticline (SA) to the Cortemaggiore anticline (CA). Late Miocene and Messinian mass-wasting deposits are emphasized (from Artoni et al., 2004, Fig. 4)

The Cortemaggiore thrust front can be considered the leading edge of the Apenninic orogenic wedge formed during the intra-Tortonian tectonic pulse which, in the CWTB, is evidenced by 1) the thinning out of late Tortonian to early Messinian pre-ev and ev units toward the Cortemaggiore anticline hinge (Fig. 4) and 2) the lack of Tortonian unit on the hinge zone of the Salsomaggiore anticline (Figs. 4, 5). In late Tortonian, the Cortemaggiore and the Salsomaggiore anticlines were two intra-basinal highs (Fig. 6a). The intra-Tortonian tectonic pulse should have restricted a limited portion of the foredeep and created the CWTB; euxinic shales on top of hemipelagic marls and thin-bedded turbidites are the first evidence of a confined basin with restricted water circulation established after the deposition of foredeep turbidites (Fig. 7). Anoth-

er, confined basin existed also in a more internal area; the Salsomaggiore anticline, already uplifted during the Serravallian, because of an exposed onlap angular unconformity between the Serravallian sandstone turbidites and the Langhian hemipelagic marl (Fig. 5), constitutes an obstacle to the advancement of the allochthonous units during Tortonian and early Messinian (Argnani et al., 2003; Artoni et al., 2004; Rizzini et al., 2004). On top of the Ligurian allochthonous units, two epi-Ligurian wedge-top basins were present behind the Salsomaggiore anticline: the Vigoleno and Monteglino wedge-top basins (Figs. 4, 5). The Vigoleno epi-Ligurian wedge-top basin preserves shallow-water deposits that record the Tortonian-Messinian boundary according to ostracods fauna assemblages (Miculan, 1992). At present, these shallow-water de-
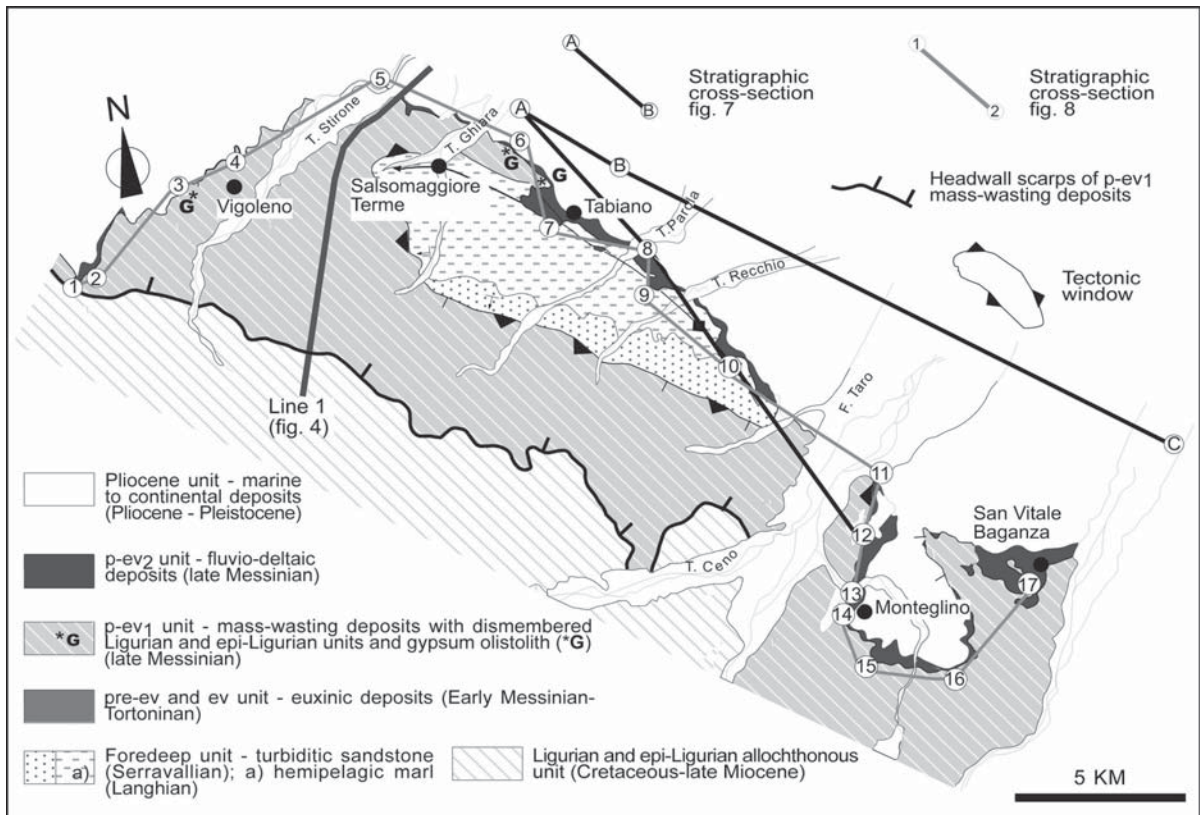
Fig. 5. Geological sketch map of the outcropping southern border of the Cortemaggiore Wedge Top Basin. Location of stratigraphic logs and stratigraphic cross-sections of Fig. 7 and Fig. 8 are reported

posits are part of the late Messinian mass-wasting deposits (Fig. 5). The inception of restricted and anoxic environment as well as the appearance of epi-Ligurian shallow-water deposits constrain the age of the intra-Tortonian tectonic pulse which must precede the 7.24 Ma and possibly is around 8 Ma (see sect. 3).

Concerning the evaporitic deposits (ev), euxinic shale associated to marly and gypsum levels testify that the CWTB was still restricted (Fig. 7). In the CWTB, the primary evaporitic deposits are not preserved in their original position on top of the epi-Ligurian wedge-top basin; they are completely dismembered as resedimented units or tectonically stacked slices, in response to the intra-Messinian tectonic pulse (Figs. 6b, 7).

4.2 The Intra-Messinian Tectonic Pulse and the Associated Mass-Wasting Deposits (p-ev₁)

The intra-Messinian tectonic pulse, a major tectonic phase that affected the whole Northern Apennine (Ricci Lucchi et al., 1982; Roveri et al. 2001) created a regional-scale unconformity (intra-Messinian uncon-

formity) that, erosional and angular in marginal basins, passes to correlative conformity in deeper basins (Roveri et al., 2001). During this tectonic phase, the CWTB, one of the marginal basins, was further shortened and, contemporaneously, filled by gravity-driven mass-wasting deposits derived from destabilized allochthonous units. A major lens-shape body, few kilometers wide, and estimated volumes more than 100 km³, is elongated parallel to the Salsomaggiore anticline and occupies the CWTB's depocenter (Rizzini et al., 2004) (Figs. 4, 7). The masses departed from a denudational area, close to the Salsomaggiore anticline hinge zone, and accumulated in the CWTB where they form imbricate thrust-stacks (Figs. 4, 6b) (Rossi et al., 2001; Artoni et al., 2004). Similarly to what is observed in other areas of the Apennines (Roveri et al., 2003), at the bottom of the chaotic mass, monogenic gypsum arenite and breccia, locally associated to large blocks with primary evaporitic depositional features, are debris flows containing olistoliths derived from nearby epi-Ligurian perched basins and intra-basinal highs (Fig. 6b). Going upward, the largest and widespread volume of the wasted masses is made of pieces and kilometers-wide klippens of dismembered allochtho-
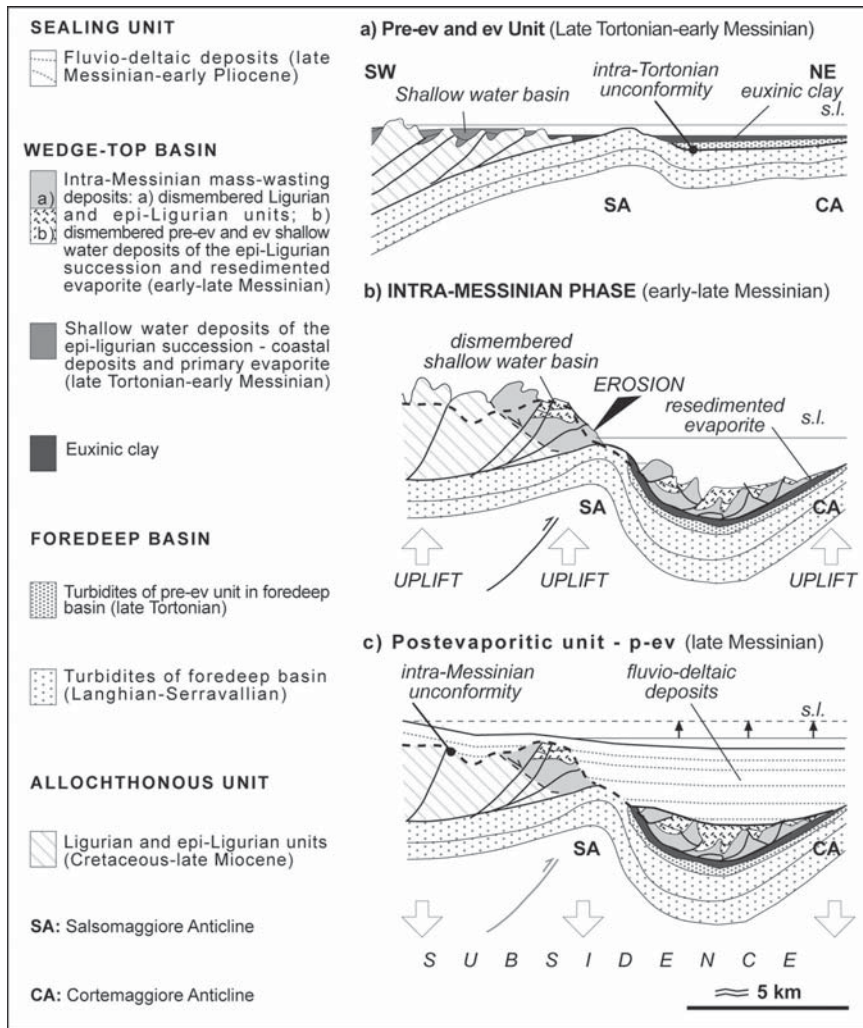
Fig. 6. Stratigraphic and structural evolution of the Cortemaggiore Wedge Top Basin during late Miocene. The *sketches* show the evolution of the CWTB along the cross-section of Fig. 4. See text for details (modified after Artoni et al., 2004)

nous units (Iaccarino and Papani, 1979; Rossi et al., 2001; Artoni et al., 2004) (Fig. 7). The upward increase in dimensions of wasted masses is interpreted to reflect a progressive increase of relief steepness of the inner border of the CWTB in response to the uplift of the Salsomaggiore anticline's hinge zone (Artoni et al., 2004).

The available dates (see sect. 3 and Artoni et al., 2004) restrict the formation of the mass-wasting deposits to a time interval minor than 100,000 years; nonetheless, gyspum debris flows and slide masses might have been multiple and contemporaneous events forming coalescing chaotic masses.

4.3 Late Messinian and Early Pliocene Sealing Siliciclastics Post-Evaporitic Deposits (p-ev)

The mass-wasted deposits, marking the base of the post-evaporitic units, and the intra-Messinian uncon-formity are sealed by late Messinian post-evaporitic (p-ev) units (Figs. 4, 6c, 7, 8).

In the CWTB, similarly to other coeval Apennin-ic basins, the siliciclastic post-evaporitic succession presents extremely variable thickness in response to an irregular and variable substratum shaped by major intra-Messinian tectonic pulses and formation of the wedge-top basin. Because of similar depositional char-acters and because immediately beneath the Miocene-Pliocene boundary, the post-evaporitic units cropping out in the CWTB are correlated to the p-ev₂ unit of Roveri et al. (2001) (Figs. 7, 8) (Artoni, 2003a; Arto-ni et al., 2004). In fact, fluvio-deltaic deposits associat-ed with varved-like alternation of thin claystone beds and marls and micritic limestone are typical of the Co-lombacci units known in the entire Apenninic fore-deep (Casati et al., 1976; Roveri et al., 1998) and of the Lagomare succession of Mediterranean region. Then, the sedimentary cyclicity of post-evaporitic deposits
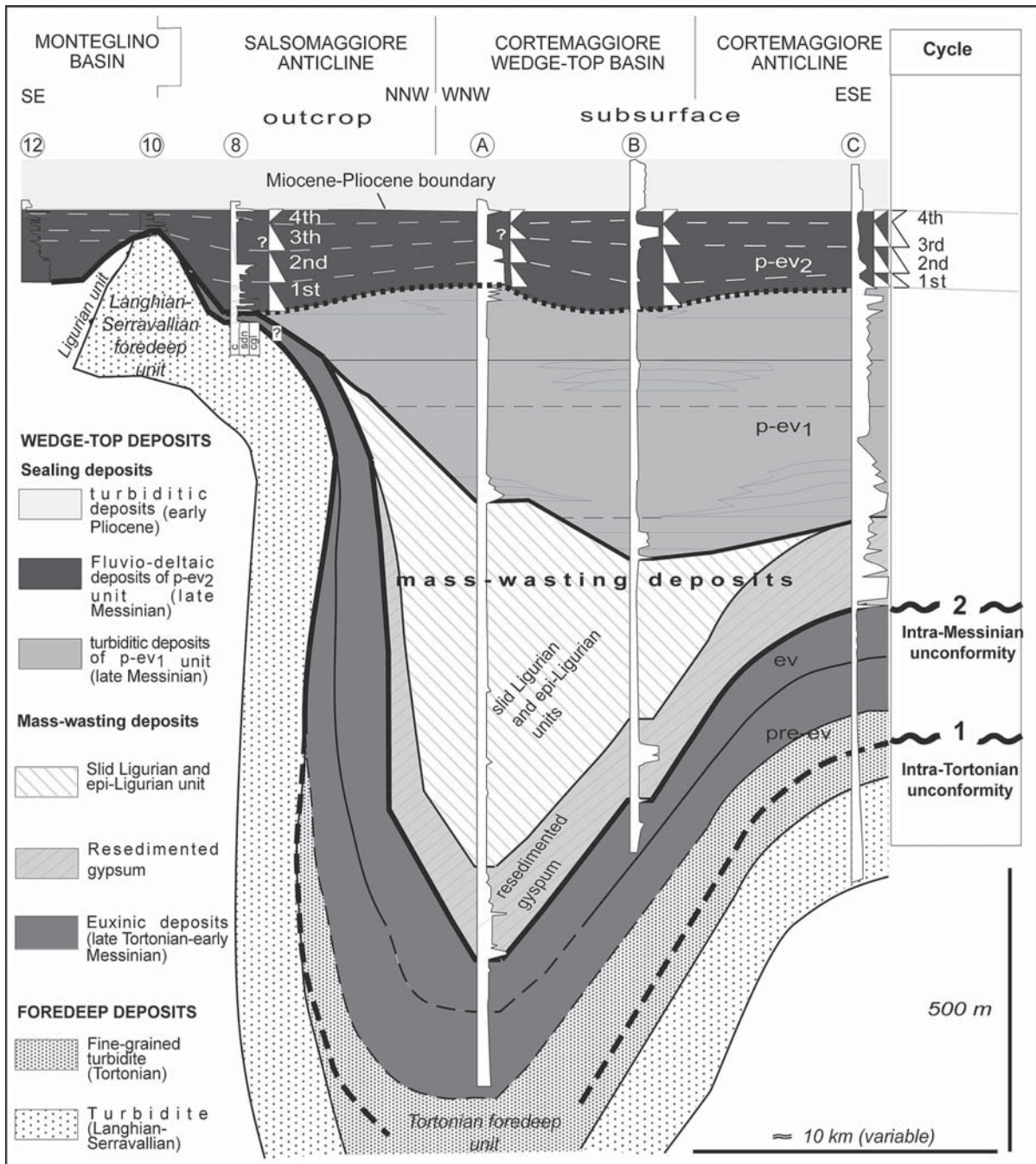
Fig. 7. Stratigraphic cross-section across the Cortemaggiore wedge-top Basin derived from outcrop and subsurface data. The outcropping logs labelled 12, 10 and 8 are the same as in Fig. 8. Stratigraphic log 8 is detailed in Fig. 9. Locations of stratigraphic logs and well logs A, B and C are in Fig. 5. (after Artoni et al., 2004, Fig. 7)

in CWTB is another distinctive character of p-ev₂ unit (Roveri et al., 1998).

During post-evaporitic time, the CWTB is likely undergoing overall subsidence (Fig. 6c) and fluvio-deltaic deposits onlap against and progressively seal both the Salsomaggiore and Cortemaggiore anticlines; then, open marine conditions returned during basal Pliocene (MPL1 biozone in Iaccarino and Papani, 1979).
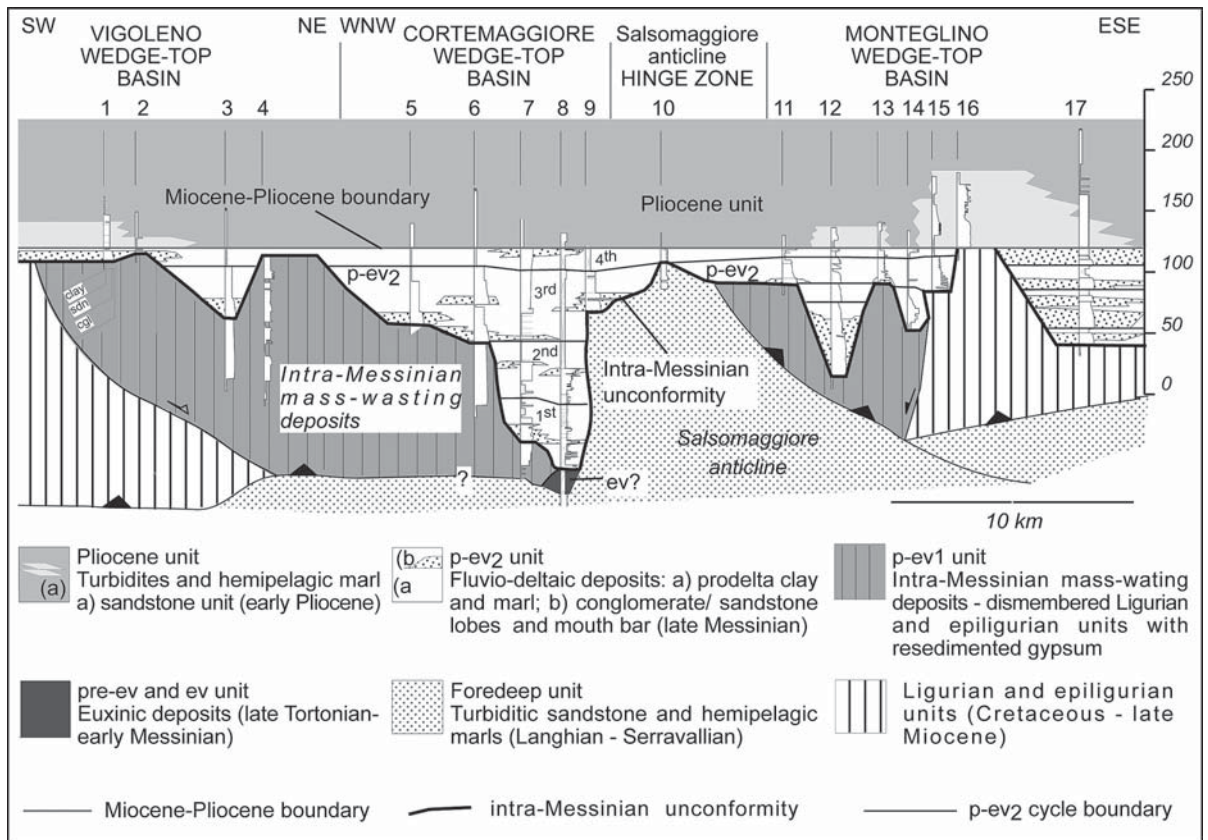
Fig. 8. Stratigraphic cross-section of outcropping late Miocene deposits on the southern border of Cortemaggiore Wedge-Top Basin and more internal Vigoleno and Monteglino wedge-top basins (modified after Artoni et al., 2004). The four sedimentary cycles are correlated across the three sub-basins. Their depositional characters are detailed in log 8 (see Figs. 9 and 10); the main coarse-grained bodies are the guidelines for cycles correlation. See text for detail. (after Artoni et al., 2004, Fig. 9)

5   Sedimentary/Climatic Cycles of Late Miocene Deposits in CWTB

Within the CWTB, pre-evaporitic and evaporitic deposits are cropping out only as remnants and thus their cyclicity can only be derived from coeval deposits in Apenninic foreland basin or other basins of the Mediterranean area (see sect. 3). Instead, the sedimentary cyclicity is well expressed and can be directly studied in late Messinian post-evaporitic units which, as stated before, have been correlated to the p-ev$_2$ unit of Apenninic foredeep. The sedimentary cyclicity of a previously published stratigraphic log (Artoni, 2003a) (Fig. 9) is here revised taking into account the lateral correlation of the newly defined sedimentary cycles cropping out on the southern flank of the CWTB (Fig. 8). The revised cycles are traceable across the stratigraphic cross-section constructed by integrating published stratigraphic logs (Iaccarino and Papani, 1979; Artoni, 2003a; Gennari, 2003) that contain the Miocene-Pliocene boundary which is the datum plane of

the stratigraphic panel (Fig. 8). These new cycles are tentatively traced also in subsurface logs, where alternation of coarse- and fine-grained bodies are evidenced by well-logs spontaneous potential curves (Fig. 7) but no detailed sedimentological data are available.

5.1 Cyclicity in Post-Evaporitic Units of CWTB

The sedimentary cyclicity has been revised in the thickest stratigraphic log 8 of Fig. 8. Previous work was addressed to define the depositional characters preserved in these deposits (Artoni, 2003a). The sedimentological analysis revealed that the prevailing facies are related to fluvio-deltaic systems according to the facies scheme of Mutti et al. (2000, 2003) and the depositonal architectures of coarse-grained deltas of Postma (1990). Coarse-grained bodies derived from hyper-concentrated flows, interpreted to be originated by flood events, pass toward the basin to sandstone lobes, deposited by dense, tractive and turbulent

flows, and finally to distal fine-grained diluted turbulent flows. Other fine-grained deposits show varved-like facies associated with thin, carbonate-rich beds which are interpreted to be deposited in a lacustrine environment.

Based on the above-mentioned facies scheme and other specific depositional facies, nine elementary depositional sequences (EDS sensu Mutti et al., 1994) were defined by tracing boundaries that mark abrupt facies changes. In the case of fluvio-deltaic deposits, the bounding surfaces are defined by more proximal coarse-grained bodies laying on top of distal fine-grained bodies without the interposition of intermediate sandstone lobes. Inside an elementary depositional sequence, lithologic units and depositional facies (lithofacies of Mutti et al., 1994) can change but they represent depositional environments which were genetically related, i.e., they were originally contiguous during their deposition. Sets of elementary depositional sequences, i.e., composite depositional sequences (Mutti et al., 1994), might present vertical stacking pattern which is comparable at different points of the basin; therefore, they are a tool for basin-wide correlation and they represent a higher rank sedimentary unit.

The revised depositional sequences (Fig. 9) are grouped in four higher rank composite depositional sequences based also on their correlability across the exposed portion of the CWTB (Fig. 8). The vertical repetition of similar elementary depositional sequences or similar composite elementary depositional sequences reveals the presence of a cyclicity made of lower rank/higher frequency cycles, which correspond to the elementary depositional sequence, and of higher rank/lower frequency cycles, which correspond to the composite elementary depositional sequence. These sedimentary cycles of different rank and their depositional characters will be described in the following (Figs. 8, 9, 10).

5.1.1 The Sedimentary Cycles and their Depositional characters

The first cycle starts above the finely laminated euxinic clay with few, very fine-grained and thin-bedded sandstone. This euxinic unit, of early Messinian age (Artoni, 2003a), lays unconformably on top of Langhian foredeep deposits; thus, they mark the intra-Tortonian unconformity on the southern border of the CWTB. The conglomeratic units, which erode the euxinic deposits and cover both the Langhian-Serravallian foredeep unit and the allochthonous Ligurian unit, mark the intra-Messinian unconformity that coincides to the base of the first cycle or composite elementary depositional sequences (1st in Fig. 9). The three composing elementary depositional sequences start with a conglomeratic unit that passes upward to a sandstone unit and a topmost clay unit. The conglomeratic unit is ortho-/para-conglomerates with well-rounded cobbles and rare boulders in a sandstone matrix (Fig. 10a). They form decimetric thick beds that start with erosive and massive ortho-conglomerate overlain by para-conglomerate with internal laminations marked by both normal and inverse grading; sometimes, faintly oblique laminations occur. The conglomerates are sourced by the surrounding Ligurian and foredeep unit.

Very coarse- to fine-grained sandstones increase upward within the elementary depositional sequences. The very coarse-grained sandstone contains rare cobbles aligned along low-angle laminae; plants and shells fragments are abundant. The coarse- to fine-grained sandstones form centimeter thick beds that are mainly massive at the base and plane parallel to rippled or hummocky-type cross stratified toward the top (Fig. 10b). The ripples indicate paleocurrents toward the southeastern area, sub-parallel to the Salsomaggiore anticline axis. This implies the location of a feeding system toward NW or SW coherently to the clast's composition.

The clay units at the top of the elementary depositional sequence are given by two main types. A sand-rich type consists of thin to very thin beds of very fine-grained sandstone entirely laminated, plane-parallel and rippled laminated, and gradually passing to massive dark-grey claystone and marls. The second type of clay unit is characterized by massive clay and by alternating thin to very thin beds with variable organic and carbonate contents that produce a typical-banded rock similar to varves (Fig. 10c). Locally, carbonate predominates and massive marly micrite form centimeter thick layers.

The above-described lithofacies, interpreted according to the facies scheme of Mutti et al. (2000, 2003), represent the deposition of conglomeratic hyper-concentrated flows which, consequently to increased concentration by the erosion of the substratum encroached during their movement, are forced to stop. These flows are likely triggered by fluvial floods transferring sediments to shelfal area. The sandstone unit is the down-current evolution of the hyper-concentrated flows, if they were not stopped and were able to move further inside the basin. Very coarse sandstones with sparse cobbles are interpreted as "en masse" deposition of high density flows in proximal areas of shelfal lobes (Mutti et al., 2000). These high-density flows evolve down current to hyper-picnal flows with traction and turbulence that are the origin of the coarse- to fine-grained turbiditic sandstone lobes in delta front or prodelta of fluvial-dominated delta system. Clay units with fine-grained sandstone represent the deposition of turbulent turbiditic flows in the distal
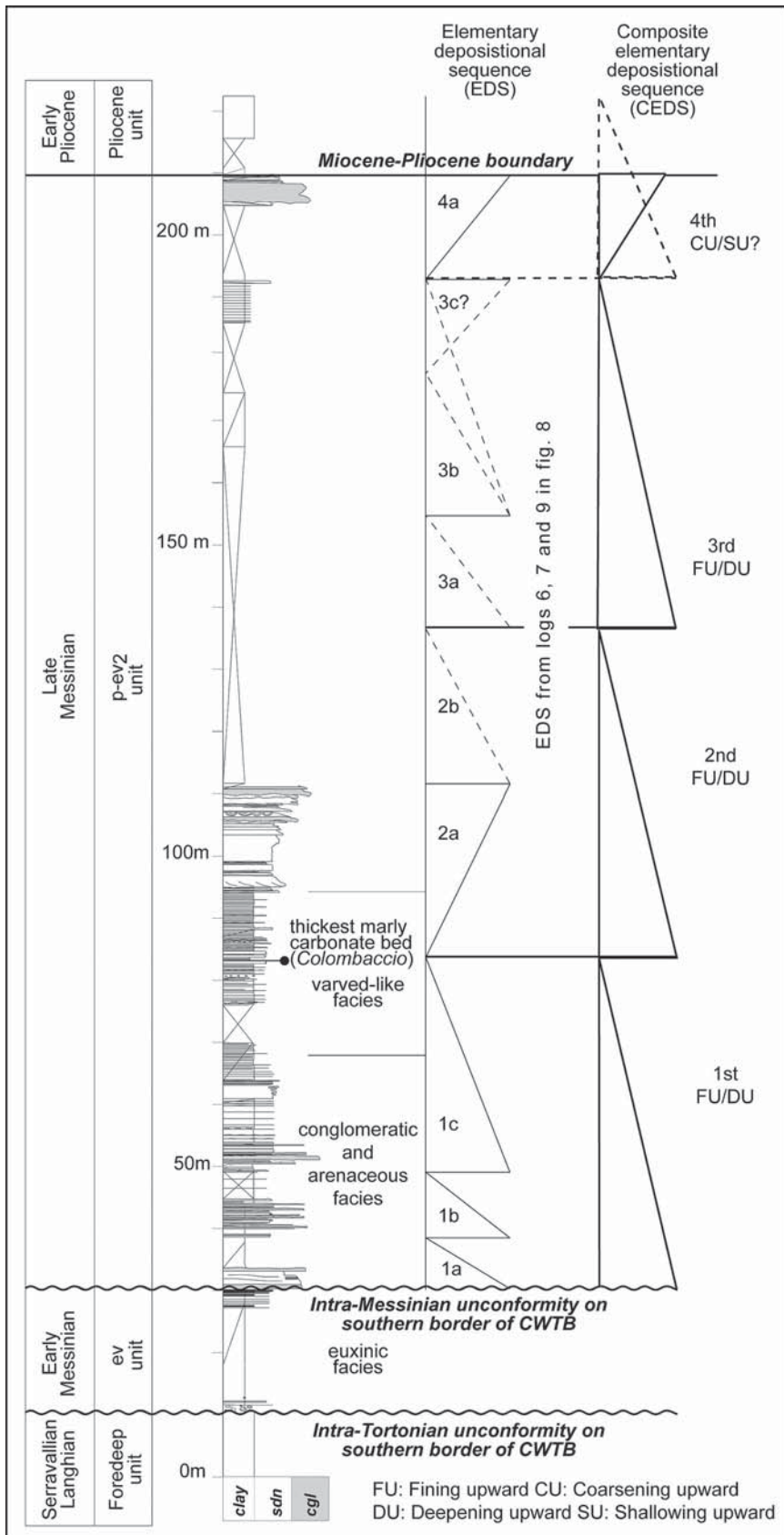
Fig. 9 Detailed stratigraphic log labelled with number 8 in Figs 6 and 7. The depositional sequences were defined in this log and correlated to adjacent logs (see Fig. 8) (modified after Artoni, 2003a)
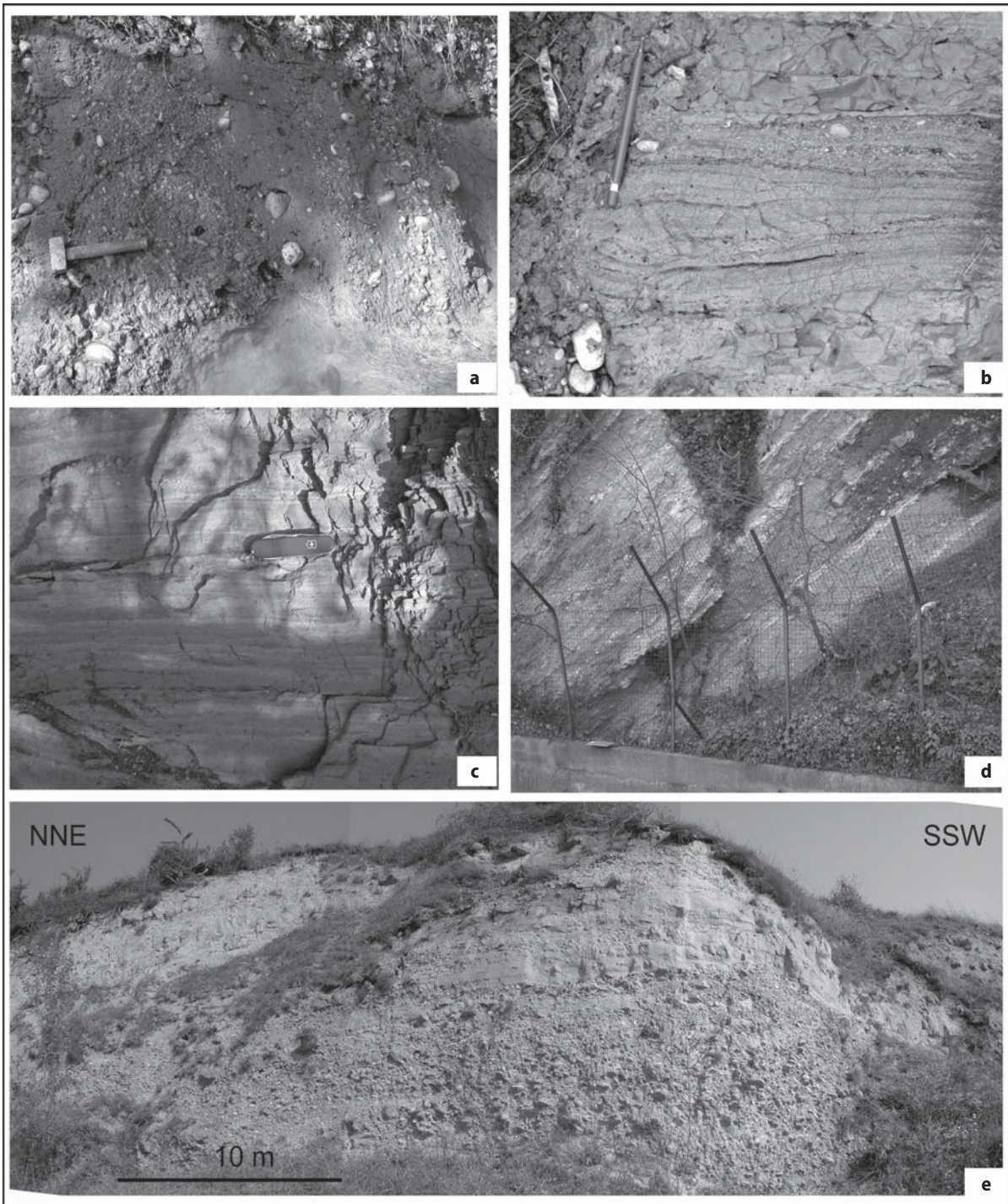
Fig. 10. Examples of fluvio-deltaic facies cropping out on the southern border of CWTB. **a** Ortho-/para-conglomerates with sandstone matrix derived from hyper-concentrated flows triggered by fluvial floods. From the 1a EDS in log 8 of figure 9. **b** Coarse- to fine-grained sandstone with plane parallel and hummochy-type cross stratification in distal sandstone lobes related to fluvial-dominated delatic system. From the 1b EDS in log 8 of figure 9. **c** Varved-like facies; the white bands, are carbonate-rich marl. Fine- to very fine-grained sandstone, dark bands, are the more distal portion of turbiditic sandstone lobes. From the 1c EDS in log 8 of Figure 9. **d** Ortho-/para-conglomerates with sandstone matrix, badly sorted, not well-rounded and massive to crudely laminated. They are intepreted to be deposited in proximal portion of a mouth-bar. From 4th cycle of log 7 in Figures 5 and 8. **e** Ortho-/para-conglomerate units passing upward to coarse-grained sandstone and forming large scale foresets interpreted to be deposited in proximal portion of a fan-delta. The foresets are dipping toward eastern region. From 3rd cycle of log 9 in Figures 5 and 8

part of sandstone lobes where they interfere with the deposition of the second type of clay unit. The latter is interpreted to be originated by fine-grained sediments transported by low-density currents (ipopicnal flows) or falling down from the water column together with precipitates controlled by carbonate concentrations in the water (micritic beds). The occurrence of depositional facies derived from hyper-concentrated flows and the rapid transition to shelfal turbiditic sandstone lobes suggest the presence of a coarse-grained fan delta system (Mutti et al., 2000; Postma, 1990) fed by rivers with small to medium drainage area.

Each of the three elementary depositional sequences (1a, 1b and 1c in Fig. 9) composing the first cycle show a transgressive trend because coarse-grained, more proximal deposits are decreasing upward replaced by more distal prodelta or lacustrine deposits. The higher rank first cycle is fining and deepening upward, accordingly to a retrogradational trend in the vertical stacking of the three composing EDSs (Fig. 9).

The base of the second higher rank cycle (2nd in Fig. 9) has been located at the first sandstone bed above the thickest micritic marly bed which has been named Colombaccio (Fig. 9) (Artoni, 2003a). The base of the 2nd cycle marks an increase of terrigenous input after a phase of prevailing fall-out and vertical settling of fine-grained units which form the varved-like facies. The depositional characters of the first fifty meters of the 2nd cycle are the same in the coarse- to fine-grained sandstone unit of the 1st cycle. Upward, these units gradually pass to medium-/coarse-grained sandstone in 10 to 20 centimeters-thick beds which are massive or with normal grading. Toward the top of thickest beds megaripples and trough cross-bedding occur. On top of these cross-stratified sandstones, there are massive ortho-/para-conglomerate with sandstone matrix. In contrast to the conglomerates of the 1st cycle, these conglomerates are badly sorted and not well-rounded (Fig. 10d). The above depositional facies are interpreted to be generated by hyperpicnal flows in the proximal area of fluvial-dominated delta systems and probably at the mouth of the river because of the trough cross-bedding that corresponds to the top-set of a mouth bar. Textural immaturity of conglomerates also testifies the more proximal depositional area that, associated to tractive facies and deltaic sandstone lobes, are distinctive characters of river-delta systems (Mutti et al., 2000; Postma, 1990).

The conglomerate beds around 150 m of stratigraphic log 8 (Fig. 9) are also the upper portion of a coarsening and shallowing upward EDS (2a in Fig. 9). Above it, fine-grained sandstone and clay of shelfal sandstone lobes are considered lateral equivalent of younger coarse-grained deltaic facies in stratigraphic log 7 (Fig. 8). Fine-grained sandstone and clay, resembling distal sandstone lobes, predominate in the up-per part of the 2nd cycle (Fig. 9). Then, the overall vertical arrangement of the 2nd cycle can be described as fining and deepening upward. In this cycle the lowermost EDS is progradational probably in response to local variations in sediment supply induced by irregular morphology and drainage area of the feeding rivers.

The third cycle is difficult to define on the revised stratigraphic log because of bad quality outcrops; the few outcrops show fine-grained units. The field controls on published stratigraphic logs adjacent to log 8 (Fig. 8) made it possible to recognize the appearance of depositional characters comparable to those of the first cycle. In the well-exposed stratigraphic log 9 (Fig 8) a conglomeratic body was analyzed which erodes the langhian foredeep marl of the Salsomaggiore anticline. Meters-size clasts of the underlying langhian marls are entrained in a disorganized and chaotic pebbly sandstone horizon which marks a 500-meters-wide erosional surface. Above this horizon, ortho-/para-conglomerate units rapidly pass laterally and vertically to coarse-grained sandstone and they form large-scale foresets dipping toward the eastern region (Fig. 10e). Within the foresets, inverse and normal grading is common and the coarse-grained sandstones are either massive or faintly oblique laminated. The sandstone increases upward and they show traction bedforms with pebbles at the base or in concave upward lenses in the middle. As in the 1st cycle, these facies are interpreted to be deposited by hyper-concentrated flows; but, they were laid down in a more proximal area of a fan-delta system because traction structures are dominant. Even though the EDSs cannot be precisely defined, the stratigraphic cross-section (Fig. 8) and the occurrence of similar depositional facies in different logs allow to define at least two EDSs (3a and 3b in Fig. 9) that have a retrogradational trend. A third, doubtful and uppermost EDS (3c in Fig. 9) shows either a progradational trend or is the topmost portion of the underlying 3b EDS. Except this doubt, the third higher rank cycle has an overall fining and deepening upward trend and is retrogradational as the first cycle.

The fourth and uppermost cycle is immediately below the Miocene-Pliocene boundary and it is characterized by the return of coarse-grained sandstone and conglomeratic units deposited in a river-delta system (Artoni, 2003a) which have been also found below the Miocene-Pliocene boundary in the Montegli-no wedge-top basin (stratigraphic log 12 in Fig. 8 from Gennari, 2003). These river delta system facies associations locally pass upward to dark, organic-rich, bioturbated and fine-grained deposits which are interpreted as marsh or palustrine depositional environments. They were found in stratigraphic logs 2, 6, 12 and 13 of fig. 8 (Iaccarino and Papani, 1979; Gennari, 2003).

Marsh on top of river-delta deposits indicates a progradational trend for the uppermost EDS which is coarsening and shallowing upward. It is likely that the topmost EDS (4a in Fig. 9) is part of a higher rank cycle which ends in the Pliocene; thus, the 4a EDS assumes the same meaning of the 2a EDS in the first cycle (Fig 9), i.e., a progradational sedimentary sequence within a higher rank cycle with an overall retrogradational trend. Few scattered data suggest this hypothesis; in fact, deltaic-related sandstone lobes locally persist above the Miocene-Pliocene boundary in the more internal Vigoleno and Monteglino wedge-top basin (Fig. 8).

The entire post-evaporitic succession cropping out in the CWTB can be described as an overall transgressive and retrogradational sequence which precedes the return of open-marine conditions at the base of the Pliocene. The overall transgressive trend is punctuated by downward shift of the deltaic system of different magnitudes and orders. The four higher rank cycles, i.e., composite elementary depositional sequences (Figs. 8, 9), start with a major basinward shift of the deltaic system that, afterward, progressively back-stepped against basin margins and, in deeper setting, prodeltaic and shelfal sandstone lobes or chemical precipitates (Colombacci) were capping the previously deposited proximal deltaic deposits (Figs. 8, 9). The nine lower rank cycles, that correspond to elementary depositional sequences, preserve a similar succession of depositional events: a downward shift of proximal deltaic deposits progressively sealed by distal prodeltaic ones. Locally, the occurrence of a river-delta system creates elementary depositional sequences (2a and 4a EDSs in Fig. 9) which have a progradational trend but they are part of higher rank retrogradational cycles (2nd and 4th cycles Fig. 9) inserted in an overall transgressive succession.

5.2 Astronomic Calibration/Correlation of Post-Evaporitic Unit and Paleo-Climatic Interpretation

Based on the above sedimentary cycles, it has been attempted to calibrate/correlate them to the latest Messinian Earth's insolation and orbit curves of Laskar et al. (2004) which, calculated for the last 50 Myr, are usually employed for astronomical tuning of sedimentary succession and they are indicative of climatic cyclicities (Fig. 11). The calibration should be carried out by means of a time series analysis of detailed sedimentary cyclicity in a continuous, well-exposed and well-dated stratigraphic section (de Boer and Smith, 1994). This is not the case of the stratigraphic log analyzed in the CWTB. In these logs, the numerical ages are attributed by the correlation with the late Miocene events

and Global Stratotype and Section Point defined in the Mediterranean region (Fig. 3). Then, a time series analysis was not pursued. The calibration is essentially based on the comparison between sedimentary cycles and the astronomic cycles in order to verify:

1. The presence of comparable cyclicities
2. A viable correspondence between the paleoclimatic variations expressed by the astronomical curves and the observed variations in depositional features of fluvio-deltaic deposits observed in the stratigraphic logs.

In the CTWB, the sedimentary cyclicity of the p-ev$_2$ unit can be restricted to the post-volcaniclastic marker bed (5.5 Ma) and the base of Pliocene (5.33 Ma). In the exposed portion of the CWTB, the volcaniclastic marker bed does not crop out; but, the p-ev$_2$ unit regionally post-dates this marker bed (Roveri et al., 2001). Assuming that no stratigraphic hiatus exists at the base of the p-ev$_2$ unit in the studied log, the above dates alone pose the above four higher rank cycles in the range of astronomical cycles with periodicity comparable to Earth's axis obliquity (four higher rank cycles in 200 kyr) (Fig. 11). By consequence, the lower rank cycles (EDS) should have a periodicity in the order of precessional cycles or even of sub-Milankovitchian cyclicity. Nonetheless, the following considerations suggest that the four higher rank cycles are precession-driven. First, the p-ev$_2$ unit does not encompass the entire 200 kyr, because it is younger than the 5.5 Ma volcaniclastic bed. It possibly lasts 100 kyr, according to the proposed age of 5.44 Ma for the base of the p-ev$_2$ unit (Roveri et al., 2005). Second, varved-like facies, forming the EDS in the CWTB, have been associated to sub-Milankovitchian and seasonal periodicity in similar facies of the Lagomare unit in the Central Apennines (Cosentino et al., 2005). Third, the calibration/correlation between the four higher rank sedimentary cycles defined above and the precessional cycles (Fig. 11) shows that beneath the Miocene-Pliocene boundary, four precessional cycles might explain the longer period (higher rank) variations in depositional features of the studied stratigraphic log (Fig. 9). These precessional cycles strictly correspond to insolation cycles which provide a more direct connection to paleoclimate being insolation maxima characterized by wetter climate conditions and insolation minima characterized by drier climate conditions.

The correspondence between precessional/insolation/climatic cycles and higher rank depositional cycles has been interpreted as follows. During dry periods, characterized by base-level fall and catastrophic fluvial floods, related to episodic heavy rainfalls, the development of coarse-grained fan-deltas was enhanced (base of 1st and 3rd cycles Fig. 11) as well as
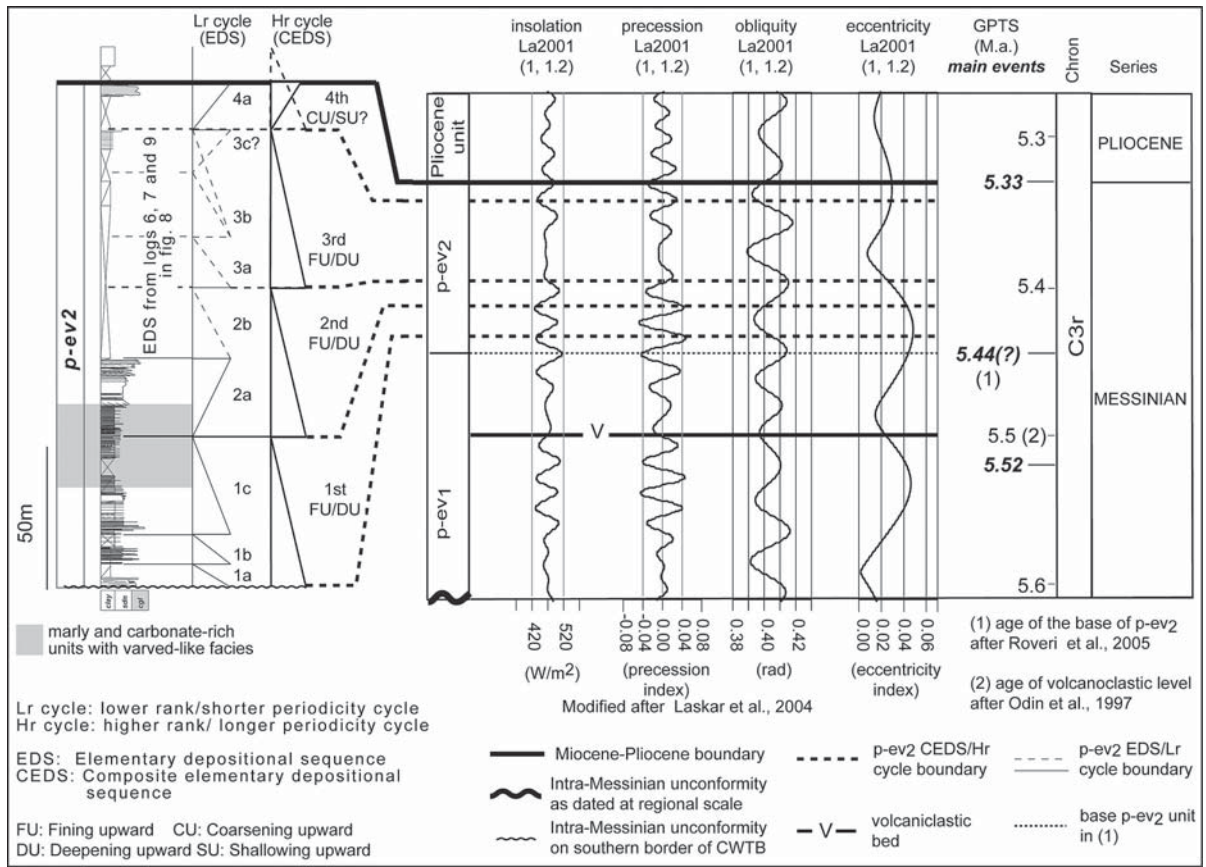
Fig. 11. Cyclicity of post-evaporitic unit. The four cycles, regressive at the base and trasgressive toward the top, are defined in the log 8 (Fig. 9) and correlated to adjacent logs (Fig. 8). They are attributed to the p-ev₂ of Roveri et al. (2001) . Starting from the "datum plane" of Miocene-Pliocene boundary, cyclical variations of depositional characters are calibrated to climatic changes expressed by astronomical curves. See text for details

increased sediment supply (base of 2nd and 4th cycles Fig. 11). These dry periods should correspond to insolation minima and precession maxima (Fig. 11). Instead, wet periods were characterized by base-level rise and subsequent development of back-stepping fan-deltas (upper portion of all four cycles Fig. 11) or river-deltas (lower portion of 2nd and 4th cycles in Fig. 9) and lacustrine deposits (upper portion of 1st cycle Fig. 9). In the insolation curve, wet periods correspond to insolation maxima and precession minima. The coarser-grained deposits mark the more pronounced cyclicity and they seem to occur when the insolation curve presents greater amplitude, i.e., extreme and rapid dry-wet climate changes in the order of precessional cycles.

Other depositional characters seem to correlate to astronomic parameters that have longer periodicity than precession (Fig. 11). Two cycles of Earth's orbit obliquity and one cycle of Earth's orbit eccentricity occur at the time of the four higher rank sedimentary cycles described above. During low angle of the

Earth's axis tilt, obliquity minima, solar radiation increased at mid-latitude and it is more evenly distributed between winter and summer seasons. Formation of polar ice caps or diffused ice formation was enhanced because of increased differences in radiation received at polar and equatorial regions; then, warmer winters were enhancing moisture and snowfall precipitation, which were not melted during cooler summers. During minimum in Earth's orbit eccentricity, evaporation is increased in response to increased solar radiation because of the Earth-Sun's distance at aphelion and perihelion is very similar. Minimum eccentricity in phase with obliquity minimum modulate the reduced amplitude of both precession and insolation curves. In this case, the obliquity acted against the climatic effect of eccentricity causing a relatively minor fall in sea-level: polar ice-cap and diffused ice formation, enhanced by obliquity minimum, is contrasted by increased evaporation/solar radiation, favoured by eccentricity minimum. Thus, the in-phase minima correspond to the deposition of fine-grained

units while coarse-grained deposits are preferentially entrained inside the drainage system. On the contrary, if eccentricity is out-of-phase with obliquity, or eccentricity maximum corresponds to obliquity minimum, the amplitude of precession and insolation curves is increased and coarse-grained deposits prevail (Fig. 11). In fact, obliquity amplifies the climatic effect of eccentricity causing relatively major sea-level falls: polar ice-caps and diffused ice formation were enhanced by amplified excursions in winter-summer solar radiations to the Earth. In the source-to-basin system, the pronounced seasonality favours the delivery of coarse-grained sediments to the depositional area.

From the previous considerations, it results that the astronomical parameters which seem to drive the sedimentary cyclicity are the equinox precession (20 kyr) modulated by the Earth's orbit eccentricity and Earth's axis obliquity. If the latter two parameters had in-phase minima, short-term astronomically-driven climate oscillations have low amplitude and fine-grained units predominate (3rd cycle in Fig. 11); if the minima were out-of-phase, rapid and extreme precession-driven climatic changes favour coarse-grained deposition (1st and 2nd cycles in Fig. 9). Correlation between astronomic curves and sedimentary cycles pursued in other stratigraphic logs and integrated with time series analysis may confirm the above results. For the aim of this paper, it is important to establish an order of magnitude of the periodicities recorded by the sedimentary/climatic cycles; then, climatic and tectonics cyclicities can be compared.

6   Interplay of Tectonic and Climatic Controls on Late Miocene Sedimentation in the CWTB

The structural and sedimentary evolution of the CWTB shows that tectonics and climate exerted a strong control on the architecture and the main depositional characters of the late Miocene succession. Tectonics produces major and likely faster morphologic changes of the basin. The first intra-Tortonian tectonic pulse (Ricci Lucchi, 1986; Boccaletti et al., 1990; Patacca et al., 1990; Conti and Gelmini, 1994), possibly late Tortonian, coincides with the inception of the CWTB and creates a subtle high at the Cortemaggiore anticline (Figs. 6a, 12); the orogenic wedge propagated farther north by creation of a new leading edge. The wedge-top basin confinement was also enhanced by the more internal Salsomaggiore anticline, which continued to be an obstacle to the advancement of the Ligurian allochthonous units. Previous reconstruction proposed that the Ligurian allochthonous units were very close and on top of the Salsomaggiore anticline in late Tortonian (Iaccarino and Papani, 1979) which im-

plies a further confinement of the basin. The location of the emerged land cannot be defined exactly with the available data. Shallow-water deposits of epi-Ligurian Vigoleno wedge-top basin, which indicates the position of late Tortonian-early Messinian palaeo-coastal area, were translated at their present position (Fig. 5) during younger tectonic pulses; therefore, the original position of the coastal area and the extension of the adjacent emerged land remain unknown.

It is the intra-Messinian tectonic pulse that creates the most impressive changes in CWTB morphology (Figs. 6b, 12). The Salsomaggiore and Cortemaggiore anticlines are further amplified and Ligurian allochthonous units almost synchronously moved inside the CWTB (Artoni et al., 2004). Syn-tectonic mass-wasted deposits filled the deepest portion of the wedge-top basin in less than 100 kyrs and they are enclosed between the euxinic deposits (ev) and the post-evaporitic unit (p-ev) (see sect. 4.2 and Fig. 6b). In response to the intra-Messinian tectonic pulse, both the Ligurian tectonic stack and slide masses increased the roughness and irregularities of the relief as the variable thickness of the sealing post-evaporitic units testifies (Figs. 4, 8). The appearance of fan-deltas draining the surrounding Ligurian and epi-Ligurian units indicates that the emerged source areas were closer and sediment transfer system directly reached the CWTB.

On top of the morphologies created by tectonics, climate distributes both laterally and vertically in cyclical stacks the clastic sediments available to erosion and transport. When evaporitic environments developed, chemical precipitation from the water column was controlled by variable salinity conditions related to precessional climatic variations as it is known from Apenninic and Mediterranean surrounding regions (Krijgsman et al., 1999; Hilgen and Krijgsman, 1999; Lugli et al., 2005). In fluvio-deltaic deposits of CWTB, the evidences of base-level changes are the basis for the definition of climatically-driven sedimentary cyclicity. During wetter periods, base-level rise caused the landward shift and entrainment of coarse-grained deltaic deposits in proximal portions of the basin; consequently, sediment supply to the deepest portion of the basin was likely absent or decreased. Whereas, during drier periods, coarse grained deposits were shifted basinward in response to a base-level fall and intense, concentrated rainfalls.

In the CWTB, morphological evolution of the tectonic structures and their feedback with climatic conditions are considered important in controlling the sedimentation. Tectonic pulses created the structures and the mountain orographies which are both obstacles and source for sediment transfer from mountain ranges to the sea; in fact, they formed closed and semi-closed basins in which evaporates precipitated and coarse-grained deposits were trapped (Fig. 12). Once
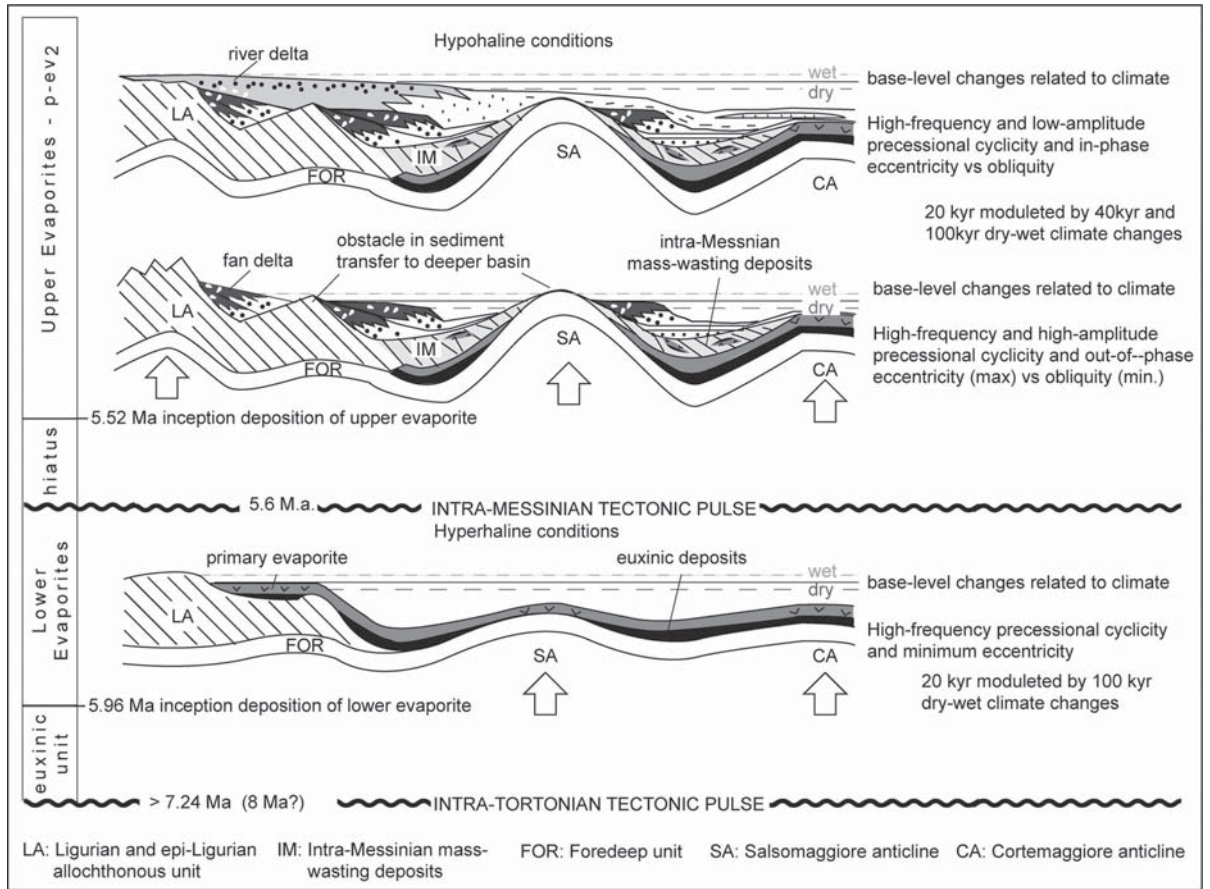
Fig. 12. Tectonic and climatic controls on sedimentation in the CWTB. Tectonic pulse creates the major morphological changes of the basin; climate both laterally distribute and vertically stack the sediment available to be transported, or precipitated in case of evaporitic environment. Note that the tectonic pulses are almost simultaneous or slightly precede the two major evaporative events that in the Mediterranean area are known as Lower and Upper Evaporites. See text for discussion

the climatic changes started to act, alternation of dry and wet periods caused the progressive erosion of emerged structural highs and relief where flood-related hyper-concentrated flows were generated and formed fan-delta system (Fig. 12). These types of deposits were found in the 1st and 3rd higher rank cycles of the p-ev2 unit. At the same time, the submarine tectonic structures, located more toward the basin, were prone to be draped and sealed. This is the case of the Salsomaggiore and Cortemaggiore anticlines which were progressively sealed by fluvio-delatic deposits flowing parallel to their axis. Both erosion and draping of tectonic structures created a smoother morphology. As a consequence, the sediment, still available for transportation, was transferred to the deltaic area more easily and efficiently. River-delta systems with prevailing tractive facies and progradational trend are interpreted to be related to smoother basin morphologies (Fig. 12). Then, these river-delta systems require wetter climate conditions, as derived by the correlation of 2nd

and 4th sedimentary cycles with the insolation curve (Fig. 11).

The accurate dating of Tortonian and Messinian stratotypes in the Mediterranean area, with two GSSP, made it possible to time constrain the tectonic and climate cyclicity in CWTB (Fig. 11). Tectonics control acted at low frequency, at an order of 2 Myr (2.4 Myr precisely). Instead, climate acted at variable higher frequency, at an order of 20–100 kyr; but, 20 kyr precession cyclicity appears to better explain the higher rank sedimentary cycles (Fig. 11). Euxinic and evaporitic deposits lay on top of foredeep or shelf deposits and postdate the intra-Tortonian tectonic pulse (pre 7.24 Ma possibly 8 Ma?); whilst, fluvio-deltaic and lacustrine deposits postdate the intra-Messinian tectonic pulse (~ 5.6 Ma) and lay on top of both allochthonous units and mass-wasting deposits. Each tectonic pulse marks changes in depositional environments (Fig. 12). The tectonic phases closely precede periods character-

ized by more intense evaporation and occurrence of drier climate.

It is already known that orogen uplift induces climate changes but on longer time periods, in the order of 10 Myr (Molnar and England, 1990; Molnar et al., 1993; Raymo and Ruddiman, 1992; Ruddiman, 1997; Clift et al., 2002b). Instead, in the CWTB, the climatic changes seem to be effective immediately or shortly after the uplift produced by tectonic pulses and in time periods of few Myr or less: about 2 Myr between the intra-Tortonian tectonic pulse (~8 Ma?) and the inception of lower evaporites (5.96 Ma); about 100 kyr between the intra-Messinian tectonic pulse (5.6 Ma) and inception of upper evaporites (5.52 Ma). This might be explained by local evaporative/(micro-)climatic conditions induced by the newly created reliefs as envisaged for the Mediterranean region (Krijgsman et al., 1999; Roveri et al., 2001; Roveri e Manzi, 2005). In this respect, the almost immediate response of climate to tectonic processes might result from a shorter term and local-scale observations compared to the longer-term and supra-regional climatic changes induced by the uplift of Alpine-Himalayan orogen (Raymo and Ruddiman, 1992; Ruddiman, 1997; Clift et al., 2002b). But, these climatic conditions are not localized to the CWTB only; the drier events correspond to deposition of lower and upper evaporites in the Mediterranean region (Fig. 3) and a drier period related to expanding ice volumes was proposed for the early Messinian of the North Atlantic and Pacific Ocean (Zhang et al., 1996; Hodell et al., 2001). Thus, another explanation for the evidences that tectonic pulses and climatic changes acted almost simultaneously might be that the two cyclic processes, tectonics and climate, acted in-phase during the late Miocene in the CWTB. This is particularly true for the inception of upper evaporites which started about 100 kyr after the intra-Messinian tectonic pulse.

On the other hand, tectonic and climatic cyclicities have similar periodicities at various orders of the time scale:

1. Global-scale astronomically-driven climatic cycles have been envisaged in continental/lacustrine deposits (Olsen, 1997; Olsen and Kent, 1999) and their duration strikingly coincides with the time separating the two tectonic pulses defined here and in other foreland basins (Johnson et al., 1986; Specht et al., 1991; Burbank et al., 1992);
2. 400 kyr tectonic pulses of Cenomanian in Western Interior of North America (Vakarelov et al., 2006) have a duration strikingly similar to longer-term component of the Earth's orbit eccentricity cycles in the Mediterranean salinity crisis event (Krijgsman et al., 1999);

3. Activity and migration of mountain front and thrust-anticline in the order of 100 kyr (Burbank DW et al., 1992; Calamita et al., 1994; Artoni and Casero, 1997; Tozer et al., 2006) are very similar to obliquity and eccentricity cycles;
4. Tectonically controlled depositional sequences have durations of less than 10 kyr (Ito et al., 1999), i.e., sub-Milankovitchtian periodicity.
5. Earthquakes' frequency in properly oriented plate boundary shows a strict correspondence to Earth's tides in time intervals of few tens of years (Hui and Xiaoming, 2001; Tanaka et al., 2006) which is also a sub-Milankovitchian periodicity.

The above similar periodicities of tectonic and climatic cycles suggest that tectonics and climate might really act simultaneously and in-phase; the tectonic pulses might enhance and amplify climatic changes that would have occurred independently from the tectonic pulse. Similarly, climate changes might favour mountain uplift which would have occurred independently from erosive processes induced by climate changes. This should apply also to the CWTB, where the tectonic pulses are almost simultaneous to the climatic variations that were occurring in the Mediterranean, in the north Atlantic and in the Pacific regions during the late Miocene.

In addition, the almost simultaneous action of tectonics and climate in short time intervals of few Myr might suggest that tectonics and climate were driven by a common mechanism, at least in the CWTB. It is argued that astronomic parameters are driving the almost symultaneous action of tectonics and climate. In fact, an argument for the latter is the widely accepted notion that the Earth's orbit parameters are controlling the cyclicity; whilst, for tectonics, it is usually envisaged that plate motion and the Earth's interior dynamics is controlling the periodicity of tectonic pulses. Nonetheless, if it is considered that 1) the tectonics and climate cycles have comparable periodicity, 2) the moon can affect earthquake recurrence at plate boundaries (Hui and Xiaoming, 2001; Tanaka et al., 2006) and 3) there is evidence of astronomical tuning of plate tectonics (Scoppola et al., 2006 and references therein) it is reasonable to think that the position of the Earth with respect to the Sun and other planets might affect both the tectonic pulses and the amount of solar radiation at the Earth's surface. In this case, the almost simultaneous action of tectonic pulses and climate changes in the CWTB might be the effect of these short(?)-term (~2 Myr) tectonic-climatic cycles which are driven by the same astronomic forces; these forces are able to activate the thrust fronts and, at the same time, to modify the insolation at the Earth's surface. These astronomically-driven tectonic-climatic cycles might also control tectonic pulses and climate

changes on a much shorter time scale (10 to 100 kyr); however, their occurrence should be further investigated in sedimentary successions of other foreland basins and other basin types, also outside the Mediterranean area.

7   Conclusions

During late Miocene, the tectonic and climatic controls should have acted homogeneously and synchronously over the entire Northern Apennine foreland basin system (Roveri et al., 2001) and the whole Mediterranean area (Krijgsman et al., 1999), because marine, evaporitic and fluvio-deltaic deposits show common climatic cyclicity (Krijgsman et al, 1999; 2001; Roveri et al., 2001) and tectonic events (Boccaletti et al., 1990; Patacca et al., 1990; Mantovani et al., 1997; Cavazza et al., 2004) . The same tectonic and climatic events shaped also the Cortemaggiore Wedge Top Basin (CWTB) which, located between emerged orogen and foredeep basins, is appropriate to unravel the tectonic-climatic controls and interplay on sedimentary succession of foreland basins. In the Mediterranean area, the late Miocene chronostratigraphy has the Global Stratigraphic Sections and Points (Hilgen et al., 2000; Van Couvering et al., 2000) which made possible to time-constrain and attribute numerical ages to major and regionally extended depositional and tectonic events. These numerical ages can be also applied to the late Miocene succession of CWTB.

It results that tectonic cyclicity, two tectonic pulses in about 2 Myr, has longer periodicity than climatic cyclicity. The climatic cyclicity, that could be analyzed on exposed sections of late Messinian post-evaporitic units of CWTB, is in agreement with astronomically-driven climatic changes due to Earth's orbit precession cycles (about 20 kyr) as already known in coeval deposits of the Apennine foreland basin (Roveri et al., 1998, 2001). These precessional cycles are modulated by astronomic parameters of longer periodicity: Earth's axis tilt (40 kyr) and Earth's orbit eccentricity (100 kyr). When obliquity's minimum correspond to eccentricity's maxima, a climate characterized by high-frequency and high-amplitude insolation changes is associated to relatively major sea-level falls and coarse-grained deposits supplied to the basin. On the other hand, fine-grained deposits appear related to base-level rise associated to minor amplitude of the insolation and precession curves; in this case, obliquity and eccentricity minima are in phase.

Tectonics produces major and likely faster morphologic changes of the basin; tectonically induced mass-wasting deposits are a case of instantaneous morphological changes of basin topography. Orogen uplift, the other morphologic change guided by tectonics, strongly influenced sedimentation. Basin confined by uplifted thrust fronts contribute to produce euxinic environment after intra-Tortonian tectonic pulse (~8 Ma?); after the intra-Messinian tectonic pulse (~5.6 Ma), the appearance of emerged land is immediately recorded by local-sourced fan-delta systems.

In the CWTB, the tectonics seems to affect the climate in shorter time intervals than the commonly accepted duration of tectonic uplift that induces climate changes (Raymo and Ruddiman, 1992; Ruddiman, 1997; Clift et al., 2002b). In fact, analyzing the interplay between tectonics and climate, it results that tectonics pulses (~8 Ma? and 5.6 Ma) closely precede or they are almost simultaneous to the inception of drier climate testified by the deposition of lower evaporites (5.96–5.6 Ma) and upper evaporites (5.52–5.33 Ma) (Fig. 12). This coincidence suggests that tectonic uplift and thrust front activity caused basin-wide hydrologic and hydrogeologic changes which induced and enhanced the increased evaporation similar to that proposed for the Mediterranean area (Krijgsman et al., 1999; Roveri et al., 2001). But, the occurrence of early Messinian glacial periods also in the north Atlantic and Pacific region (Zhang et al., 1996; Hodell et al., 2001) and the comparable periodicities of tectonics and climate cycles, at different order of time scales, would suggest that tectonic pulses and climatic changes might have acted in-phase during the Messinian Salinity Crisis. At least in the CWTB, two tectonic pulses amplified the effects of two drier climatic events that are recorded also in major oceans outside the Mediterranean region.

In addition, if it is considered that the comparable periodicities of tectonic and climatic cycles might be associated to astronomical tuning of plate movements (Scoppola et al., 2006), including earthquake recurrence controlled by Earth's tides (Hui and Xiaoming, 2001; Tanaka et al., 2006), it can be argued that the position of the Earth with respect to the Sun and other planets might affect both the tectonic pulses and the amount of solar radiation at the Earth's surface. Thus, in the CWTB, the almost simultaneous tectonics pulses and climate changes are not a simple in-phase action of two cyclic processes but it might be the effect of short(?)-term (~ 2 Myr) tectonic-climatic cycles which are driven by the same astronomic forces; the latter are able to move the thrust fronts and change the insolation at the Earth's surface. The occurrence of these short-term astronomically-driven tectonic-climatic cycles and their importance on shorter time scale (10 to 100 kyr) should be verified in sedimentary successions of other foreland basins and other types of basins with a well-defined chronostratigraphy and also outside the Mediterranean area.

References

Abbate E, Bortolotti V, Maxwell JC, Merla P, Passerini P, Sagri M, Sestini G (1970) Development of the northern Apennines geosyncline. Sed. Geol. 4: 201–648.

Allen PA, Allen JR (2005) Basin analysis. 2nd edn. Blackwell, Oxford

Allen PA, Homewood P (eds) (1986) Foreland basins. Blackwell, Oxford. I.A.S. Spec. Publ., 8, pp 453.

Allen PA, Crampton SL, Grotzinger J, Sinclair H (eds) (1992) Thematic set on foreland basin. Bas. Res. 4: 169–352.

Amorosi A, Colalongo ML, Vaiani SC (1993) Le unità epiliguri mioceniche nel settore emiliano dell'Appennino settentrionale. Biostratigrafia, stratigrafia sequenziale e implicazioni litostratigrafiche. Palaeopelagos 3: 209–240.

Argnani A, Ricci Lucchi F (2001) Tertiary siliciclastic turbidite systems of the Northern Apennines. In: Vai GB, Martini IP (eds) Anatomy of an orogen: the Apennines and adjacent Mediterranean basins. Kluwer Academic, London. 327–350.

Argnani A, Rizzini F, Rogledi S, Rossi M, Manzi V, Pini GA, Roveri M, Artoni A, Ricci Lucchi F, Papani G, Panini F, Bassetti MA (2003) Tectonic structures in the subsurface of the Northern Pede-Apennines: implications for Messinian reconstruction. In: Carmina B, Orlando A and Fascio L (Eds), Geoitalia 2003 – 4° Forum Italiano di Scienze della Terra, Bellaria 16–18 settembre. F.I.S.T., Abs., 698–699.

Artoni A (2003a) La sezione stratigrafica del T. Parola (Salsomaggiore, Parma; Appennino Emiliano): confronto con le successioni ipoaline messiniane del margine appenninico padano. Acta Nat. Ateneo Parm. 39: 5–30.

Artoni A (2003b) Messinian events within tectono-stratigraphic evolution of the southern Laga Basin (Central Apennines, Italy). Boll. Soc. Geol. It. 3: 447–465

Artoni A, Casero P (1997) Sequential balancing of growth structures, the late Tertiary example from the Central Apennines. Bull. Soc. Geol. France 168: 35–49.

Artoni A, Papani G, Rizzini F, Calderoni M, Bernini M, Argnani A, Roveri M, Rossi M, Rogledi S, Gennari R (2004) The Salsomaggiore structure (Northwestern Apennine foothills, Italy): a Messinian mountain front shaped by mass-wasting products. GEOACTA. 3: 107–128.

Bassetti MA, Manzi V, Lugli S, Roveri M, Longinelli A, Ricci Lucchi F, Barbieri M (2004) Paleonvironmental significance of Messinian post-evaporitic lacustrine carbonates in the northern Apennines, Italy. Sed. Geol. 172: 1–18.

Beaumont C, Fullsack P, Hamilton J (1992) Erosional control of active compressional orogens. In: McClay KR (ed) Thrust tectonics, Chapman-Hall, London, p 1–18

Bertotti G, Schulmann K, Cloetingh SAPL (eds) (2003) Continental collision and the tectono-sedimentary evolution of forelands. Stephan Mueller Special Publication Series, vol 1, pp. 236

Boccaletti M, Elter P, Guazzone G (1971) Plate tectonics models for the development of the western Alps and northern Apennines. Nature 234: 108–111.

Boccaletti M, Calamita F, Deiana G, Gelati R, Massari F, Moratti G, Ricci Lucchi F (1990) Migrating foredeep-thrust belt system in the Northern Apennines and Southern Alps. Paleogeogr. Paleoclim. Paleoecol. 77: 3–14.

Burbank DW, Vergés J, Muñoz JA, Betham P (1992) Coeval hindward- and forward-imbricating thrusting in the south-central Pyrenees, Spain: timing and rates of shortening and deposition. Geol. Soc. Am. Bull. 104: 3–17.

Calamita F, Cello G, Deiana G, Paltrinieri W (1994) Structural styles, chronology rates of deformation, and time-space relationships in the Umbria-Marche thrust system (central Apennines, Italy). Tectonics 13: 873–881.

Casati P, Bertozzi P, Cita MB, Longinelli A, Damiani V (1976) Stratigraphy and paleoenvironment of the Messinian "Colombacci" Formation in the Periadriatic Trough; a pilot study. In: Catalano R, Ruggieri G, Sprovieri R (eds) Messinian evaporites in the Mediterranean. Memorie della Societa Geologica Italiana16: 173–194

Cavazza W, DeCelles PG (1998) Upper Messinian siliciclastic rocks in southeastern Calabria (southern Italy) : palaeotectonic and eustatic implications for the evolution of the central Mediterranean region. Tectonophysics 298:223–241.

Cavazza W, Roure FM, Spackman W, Stampfli GM, Ziegler PA (eds) (2004) The TRANSMED atlas. The Mediterranean region from crust to mantle. Springer, Berlin Heidelberg.

Cibin U, Spadafora E, Zuffa GG, Castellarin A (2001) Continental collision history from arenites of episutural basins in the Northern Apennines, Italy. Geol. Soc. Am. Bull. 113: 4–19.

Cita MB, Wright RC, Ryan WF, Longinelli A (eds) (1975) Messinian paleoenvironments. Init. Report D.S.D.P., 42. U.S. Gov., Washington, p. 1003–1035.

Clift PD, Kroon D, Gaedicke C, Craig J (eds) (2002a) Tectonic and climatic evolution of the Arabian Sea region. Geol. Soc. London Spec. Publ., 195, pp 525.

Clift PD, Kroon D, Gaedicke C, Craig J (2002b) Tectonic and climatic evolution of the Arabian Sea region: an introduction. In: Clift PD, Kroon D, Gaedicke C, Craig J (eds) Tectonic and climatic evolution of the Arabian Sea region. Geol. Soc. London Spec. Publ., 195, pp 1–5.

Conti S, Gelmini R (1994) Miocene-Pliocene tectonics phases and migration of foredeep-thrust belt system in the northern Apennines. Mem. Soc. Geol. It. 48: 261–274.

Cosentino D, Cipollari P, Lo Mastro S, Giampaolo C (2005) High-frequency cyclicity in the latest Messinian Adriatic foreland basin : insight into paleoclimate and paleoenvironments of the Mediterranean Lago-Mare episode. Sed. Geol. 178 : 31–53.

Decima A, Wezel FC (1973) Late Miocene evaporites of the central Sicilian basin, Italy. Initial Reports of the DSDP, 13, 1234–1241.

De Boer PL, Smith DG (1994) Orbital forcing and cyclic sequences. In: de Boer PL, Smith DG (eds) Orbital forcing and cyclic sequences. I.A.S. Spec. Publ., 19, p. 1–14.

Elter P (1975) Introduction à la géologie de l'Apennin septentrional. Bull. Soc. Geol. Fr. 17: 956–962.

Fleming PB, Jordan TE (1990) Stratiraphic modelling of foreland basin: interpreting thrust deformation and lithospheric rheology. Geology 18: 430–434.

Flores G (1955) Les résultat des etudes pour la recherche pétrolifère en Sicilie: discussion. Proceedings, Fourth World Petroleum Congress, Roma, Casa Editrice Carlo Colombo, section 1/A/2: 121–122.

Frakes LA, Francis JE, Sykes JI (1992) Climate modes of the Phanerozoic. Cambridge University Press, Cambridge.

Gazzi P, Zuffa GG (1970) Le arenarie paleogeniche dell'Appennino emiliano. Mineralogica et Petrographica Acta 16: 97–137.

Gelati R, Rogledi S, Rossi M (1987) Significance of the Messinian unconformity-bounded sequences in the Apenninic margin of the Padan foreland basin, northern Italy (preliminary results). Mem. Soc. Geol. It. 39: 319–323.

Gennari R (2003) Stratigrafia fisica ed evoluzione strutturale al passaggio Miocene-Pliocene nella Valle Sporzana (Appennino settentrionale). Unpublished Laurea Thesis, Università degli Studi di Parma. pp 79.

Ghibaudo G, Clari P, Perello M (1985) Litostratigrafia, sedimentologia ed evoluzione tettonico-sedimentaria dei depositi miocenici del margine sud-orientale del Bacino Terziario Ligure-Piemontese (Valli Borbera, Scrivia e Lemme). Boll. Soc. Geol. It. 104: 349–397.

Giles KA, DeCelles PG (1996) Foreland basin systems. Bas. Res. 8: 105–123.

Gradstein FM, Ogg JG, Smith AG, Agterberg FP, Bleeker W, Cooper RA, Davydov V, Gibbard P, Hinnov LA, House MR, Lourens L, Luterbacher HP, McArthur J, Melchin MJ, Robb LJ, Shergold J, Villeneuve M, Wardlaw BR, Ali J, Brinkhuis H, Hilgen FJ, Hooker J, Howarth RJ, Knoll AH, Laskar J, Monechi S, Plumb KA, Powell J, Raffi I, Röhl U, Sadler P, Sanfilippo A, Schmitz B, Shackleton NJ, Shields GA, Strauss H, Van Dam J, van Kolfschoten T, Veizer J, Wilson D (2004) A geologic Time scale 2004. Cambridge University Press, Cambridge. pp 610

Guegen E, Doglioni C, Fernandez M (1998) On the post-25 Ma geodynamic evolution of the western Mediterranean. Tectonophysics 298: 259–269.

Haq BU (1991) Sequence stratigraphy, sea-level change, and significance for the deep sea. In: Macdonald DIM (ed) Sedimentation, tectonics and eustacy. I.A.S. Spec. Publ., 12, 3–39.

Haq BU, Handenbol J, Vail PR (1988) Mesozoic and Cenozoic chronostratigraphy and cycles of sea-level change. In: Wilgus CK, Hastings BS, Kendall CGStC, Posamentier HW, Ross CA, Van Wagoner JC Sea-level changes: an integrated approach. S.E.P.M. Spec. Publ., 42, p. 71–108.

Hilgen FJ, Krijgsman W (1999) Cyclostratigraphy and astrochronolgy of the Tripoli formation (pre-evaporite Messinian, Sicily, Italy). Terra Nova 11: 16–22.

Hilgen FJ, Iaccarino S, Krijgsman W, Villa G, Langereis CG, Zachariasse WJ (2000) The Global Boundary Stratotype Section and Point (GSSP) of the Messinian stage (uppermost Miocene). Episodes 23: 172–178.

Hodell DA, Curtis JH, Sierro FJ, Raymo ME (2001) Correlation of late Miocene to early Pliocene sequences between the Mediterranean and North Atlantic. Paleoceanography 16: 164–178.

Hsü K J, Montadert L, Bernoulli D, Cita M B, Erickson A, Garrison R E, Kidd RB, Mèlierés F, Müller C, Wright R (1977) History of the Mediterranean salinity crisis. Nature 267: 399–403.

Hui H, Xiaoming L (2001) Research on correlation of positions of celestial objects with earthquakes. Nat. Hazards 23: 339–348.

Iaccarino S, Papani G (1979) Il Messiniano dell'Appennino settentrionale dalla Val D'Arda alla Val Secchia: stratigrafia e rapporti con il substrato e il Pliocene. In: Istituti di Geologia, Paleontologia, Geografia, Petrografia e Giacimenti Minerari, Mineralogia (Ed), Volume dedicato a Sergio Venzo. Università degli Studi di Parma, Parma, p. 15–46.

Ito M, Nishikawa T, Sugimoto H (1999) Tectonic control of high-frequency depositional sequences with durations shorter than Milankovitch cyclicity: an example from Pleistocene paleo-Tokyo Bay, Japan. Geology 27: 763–766.

Lofi J, Gorini C, Berné S, Clauzon G, Tadeu Dos Reis A, Ryan WBF, Steckler MS (2005) Erosional processes and paleo-environmental changes in the Western Gulf of Lions (SW France) during the Messinian Salinity Crisis. Mar. Geol. 217: 1–30.

Lourens LJ, Antonarakou A, Hilgen FJ, Van Hoof AAM, Vergnaud-Grazzini C., Zachariasse WJ (1996) Evaluation of the Plio-Pleistocene astronomical timescale. Paleoceanography 11: 391–413.

Kennett JP (1986) Miocene to early Pliocene oxygen and carbon isotope stratigraphy in the southwest Pacific, DSDP Leg 90. Initial Report DSDP 90: 1388–1412.

Krijgsman W, Hilgen FJ, Raffi I, Sierro FJ, Wilson DS (1999) Chronology, causes and progression of the Messinian salinity crisis. Nature 400: 652–655.

Krijgsman W, Garces M, Agusti J, Raffi I, Taberner C, Zachariasse WJ (2000) The "Tortonian salinity crisis" of the eastern Betics (Spain). Earth and Planetary Science Letters 181: 497–511.

Krijgsman W, Fortuin AR, Hilgen FJ, Sierro FJ (2001) Astrochronology for the Messinian Sorbas basin (SE Spain) and orbital (precessional) forcing for evaporate cyclicity. Sed. Geol. 140: 43–60.

Krijgsman W, Gaboardi S, Hilgen FJ, Iaccarino S, de Kaenel E, van der Laan E (2004) Revised astrochronologyfor the Ain el Beida section (Atlantic, Marocco): no glacio-eustatic control for the onset of the Messinina Salinity Crisis. Stratigraphy 1: 87–101.

Johnson GD, Raynolds RGH, Burbank DW (1986) Late Cenozoic tectonics and sedimentation in the north-western Himalayan foredeep: I. Thrust ramping and associated deformation in the Potwar region. In: Allen PA, Homewood P (eds) Foreland basins. Blackwell, Freiburg, p. 273–291.

Jones SJ, Frostick LE (eds) (2002) Sediment flux to basins: causes, controls and consequences. Geol. Soc. London Spec. Publ., 191, pp 284

Lamb HH (1995) Climate, history and the modern world. 2nd edn Routledge, London

Laskar J, Robutel P, Joutel F, Gastineau M, Correia ACM, Levrard B (2004) A long-term numerical solutin for the insolaion quantities of the earth. Astron. & Astroph. 428: 261–285.

Leeder M (1999) Sedimentology and sedimentary basins. Blackwell Publishing.

Lucente CC, Pini GA (2003) Anatomy and emplacement mechanism of a large submarine slide within a Miocene foredeep in the Northern Apennines, Italy: a field perspective. Am. J. Sci. 303: 565–602

Lugli S, Manzi V, Roveri M, Schreiber CB (2005) The Messinian lower evaporates in the Mediterranean: a new facies model. FIST GEOITALIA 2005, V° Forum Italiano di Scienze della Terra, Spoleto 21–23 settembre 2005, Abstract Vol. 1, 159.

Mantovani E, Albarello D, Tamburelli C, Babbucci D, Viti M (1997) Plate convergence, crustal delamination, extrusion tectonics and minimization of shortening work as main controlling factors of the recent mediterranean deformation pattern. Ann. Geof. XL: 611–643.

Manzi V, Lugli S, Ricci Lucchi F, Roveri M (2005) Deep-water clastic evaporites deposition in the Messinian Adriatic foredeep (northern Apennines, Italy): did the Mediterranean ever dry out? Sedimentology 52: 875–902.

Mattavelli L, Pieri M, Groppi G (1993) Petroleum exploration in Italy: a review. Mar. Petroleum Geol. 10: 410–425.

Marroni M, Molli G, Montanini A, Ottria G, Pandolfi L, Tribuzio R (2002) The external Ligurian units (Northern Apennine, Italy): from rifting to convergence of a fossil ocean-continent transition zone. Ofioliti 27: 119–131.

Mascle A, Puigdefabregas C, Luterbacher HP, Fernàndez M (eds) (1998) Cenozoic foreland basin of Western Europe. Geol Soc. London Spec. Publ., 134, pp. 427

Miculan P (1992) Gli ostracodi del Miocene superiore di Vigoleno (subappennino piacentino). Boll. Soc. Paleont. It. 31: 105–132.

Molnar P, England P (1990) Late Cenozoic uplift of mountain ranges and global climate changes: chicken or eggs? Nature 346: 29–34.

Molnar P, England P, Martinod J (1993) Mantle dynamics, uplift of the Tibetan plateau and the Indian monsoon. Rev. of Geoph. 31: 357–396.

Mutti E, Davoli G, Mora S, Sgavetti M (eds) (1994) The Eastern Sector of South-Central Folded Pyrenean Foreland: criteria for stratigraphic analysis and excursions Notes. In Posamentier HW, Mutti E (organizer) second high-resolution sequence stratigraphy conference, 20–26 june 204, Tremp, Spain. pp 36

Mutti E, Papani L, Di Biase D, Davoli G, Mora S, Segadelli S, Tinterri R (1995) Il bacino terziario epimesoalpino e le sue implicazioni sui rapporti tra Alpi ed Apennino. Mem. Sc. Geol. Univ. Padova 47: 217–244.

Mutti E, Tinterri R, Remacha E, Di Biase D, Fava L, Mavilla N, Angella S, Calabrese L (2000) Delta-front facies associations of ancient flood-dominated fluvio-deltaic systems. Revista de la Sociedad Geologica de España 13: 165–190.

Mutti E, Ricci Lucchi F, Roveri M (eds) (2002) Revisiting turbidites of the Marnoso-arenacea Formation and their basin margin counterparts: problems with classic models. 64th EAGE Conference and Exhibition Excursion Guidebook, Parma University and ENI-AGIP Division, Parma, Italy. pp. 250

Mutti E, Tinterri R, Benevelli G, Di Biase D, Cavanna G (2003) Deltaic, mixed and turbidite sedimentation of ancient foreland basins. Mar. and Petr. Geol. 20: 733–755.

Odin GS, Ricci Lucchi F, Tateo F, Cosca M, Hunziker JC (1997) Integrated stratigraphy of the Maccarone sections, late Messinian (Marche region, Italy). In: Montanari A, Odin GS, Coccioni R (eds) Miocene stratigraphy an integrated approach. Elsevier, Amsterdam, pp. 531–545.

Olsen PE (1997) Stratigraphic record of the early Mesozoic breakup of Pangea in the Laurasia-Gondwana rift system. Ann. Rev. Earth Planet. Sc. 25: 337–401.

Olsen PE, Kent DV (1999) Long-term Milankovitch cycles from the Late Triassic and Early Jurassic of eastern North America and their implications for the calibration of the Early Mesozoic time-scale and the long-term behaviour of the planets. Phil. Trans. Royal Soc. London 357, ser. A-Math. Phys. and Eng. Sc.: 1761–1786.

Papani G, Tellini C, Torelli L, Vernia L, Iaccarino S (1987) Nuovi dati stratigrafici e strutturali sulla Formazione di Bismantova nella "sinclinale" Vetto-Carpineti (Appennino reggiano-parmense). Mem. Soc. Geol. It. 39: 245–275.

Patacca E, Sartori R, Scandone P (1990) Tyrrhenian basin and apenninic arcs: kinematic relations since late Tortonian times. Mem. Soc. Geol. It. 45: 425–451.

Pini GA (1999) Tectosomes and olistostromes in the argille scagliose of Northern Apennines. Geol. Soc. Am. Spec. Paper 335, 70 pp.

Plint AG (1991) High-frequency relative sea-level oscillations in Upper Cretaceous shelf clastics of Alberta foreland basin: possible evidence for a glacio-eustatic control? In: Macdonald DIM (ed) Sedimentation, tectonics and eustacy. Int. Ass. Sed. Spec. Publ., 12, p. 409–428

Posamentier HW, Vail PR (1988) Eustatic controls on clastic depositions, II: sequence and system tract models. In: Wilgus CK, Hastings BS, Kendall CGStC, Posamentier HW, Ross CA, Van Wagoner JC Sea-level changes: an integrated approach. S.E.P.M. Spec. Publ., 42, p. 109–124.

Postma G (1990) Depositional architecture and facies of river and fan deltas: a synthesis. In: Colella A, Prior D Coarse-grained deltas. I.A.S. Spec. Publ., 10, p. 13–27.

Raymo ME, Ruddiman WF (1992) Tectonic forcing of the late Cenozoic climate. Nature 359: 117–122.

Ricci Lucchi F (1975) Miocene paleogeography and basin analysis in the periadriatic Apennines In: Squyres C (ed) Geology of Italy. Petroleum exploration society of Libya, Tripoli, p. 5–111.

Ricci Lucchi F (1986) The Oligocene to Recent foreland basins of the northern Apennines. In: Allen PA, Homewood P (eds) Foreland basins. Blackwell, Freiburg, p. 105–140.

Ricci Lucchi F, Colalongo ML, Cremonini G, Gasperi G, Iaccarino S, Papani G, Raffi S, Rio D (1982) Evoluzione sedimentaria e paleogeografica nel margine appenninico. In: Cremonini G, Ricci Lucchi F (eds) Guida alla geologia del margine appenninico-padano. Soc. Geol. It., pp. 17–46.

Rizzini F, Argnani A, Artoni A, Manzi V, Roveri M, Rossi M, Rogledi S, Papani G, Ricci Lucchi F, Pini GA, Panini F, Bassetti MA (2004) The Northern Apennines messinian deposits: paleogeography and tectono-stratigraphic implications. In: Milli S (ed), GEOSED 2004 - La geologia del sedimentario nella ricerca di base e nelle sue applicazioni, Roma. Atti, p. 106–107.

Rossi M, Rogledi S, Barbacini G, Casadei D, Iaccarino S, Papani G (2001) Tectono-stratigraphic architecture of Messinian piggyback basins of Northern Apennines: the Emilia folds in the Reggio-Modena area and comparison with the Lombardia and Romagna sectors. Boll. Soc. Geol. It. Vol. spec.(1): 437–447.

Rouchy JM, Orszag-Sperber F, Blanc-Valleron MM, Pierre C., Riviere M., Combourieu-Nebout N, Panayides I (2001) Palaeoenvironmnetal changes at the Messinian-Pliocene boundary in the eastern Mediterranean (southern Cyprus basins): significance of the Messinian Lago-Mare. Sedimentary Geology 188–189: 35–67.

Rouchy JM, Caruso A (2006) The Messinian salinity crisis in the Mediterranean basin: a reassesment of the data and an integrated scenario. Sedimentary Geology 145: 93–117.

Roveri M, Manzi V (2006) The Messinian salinity crisis: Looking for a new paradigm? Palaeogeo. Paleogeogr. Paleoclim. Paleoecol. 238: 386–398.

Roveri M, Manzi V, Bassetti MA, Merini M, Ricci Lucchi F (1998) Stratigraphy of the Messinian post-evaporitic stage in eastern-Romagna (northern Apennines, Italy). Gior. Geol. 60: 119–142.

Roveri M, Bassetti M, Ricci Lucchi F (2001) The Mediterranean salinity crisis: an Apennine foredeep perspective. Sed. Geol. 140: 201–214.

Roveri M, Manzi V, Ricci Lucchi F, Rogledi S (2003) Sedimentary and tectonic evolution of the Vena del Gesso basin (Northern Apennines, Italy): Implications for the onset of the Messinian salinity crisis. G.S.A. Bull. 115: 387–405.

Roveri M, Aldinucci M, Bertini A, Biffi U, Capotondi L, Cipollari P, Casentino D, Da Prato S, Dall'Antonia B, Di Stefano A, Donia F, Ferraro L, Florindo F, Foresi LM, Gennari R, Giunta S, Ghiozzi E, Grasso M, Grossi F, Iaccarino S, Lirer F, Lo Mastro S, Maniscalco R, Manzi V, Mazzei R, Morigi C, Negri A, Pipponzi G, Ricci Lucchi M, Riforgiato F, Rossi M, Sandrelli F, Taviani M, Venturini M, Zanchetta G (2005) A high-resolution stratigraphic framework for the Late Messinian Lagomare event in the Mediterranean area: time constraints for basin-wide correlations palaeoenvironmental reconstruction. FIST GEOITALIA 2005, V° Forum Italiano di Scienze della Terra, Spoleto 21–23 settembre 2005, Abstract Vol. 1, 160.

Ruddiman WF (ed) (1997) Tectonic uplift and climatic changes. Plenum Press(now Springer), New York. 535 pp.

Schwan P (1995) Controls on sequence stacking and fluvial to shallow-marine architecture in foreland basin. In: Van Wagoner JC, Bertram GT (eds) Sequence stratigraphy of foreland basin deposits. A.A.P.G. Memoir, 64, p.55–102.

Scoppola B, Boccaletti D, Bevis M, Carminati E, Doglioni C (2006) The westward drift of the lithosphere: A rotational drag? Geol. Soc. Am. Bull. 118: 199–209.

Sinclair H (1997) Tectonostratigraphic model for underfilled peripheral foreland basins; an Alpine perspective. G.S.A. Bull. 109: 324–346.

Specht M, Deramond J, Souquet P (1991) Relations tectonique-sédimentation dans les bassins d'avant-pays: utilisation des surfaces stratigraphiques isochrones comme marqueurs de la déformation. Bull. Soc. Geol. France 162: 553–562.

Sprovieri M, Barbieri M, Bellanca A, Rodolfo N (2003) Astronomical tuning of the Tortonian 87Sr/86Sr curve in the Mediterranean basin. Terra Nova 15: 29–35.

Tanaka S, Sato H, Matsumura S, Ohtake M (2006) Tidal triggering of earthquakes in the subducting Philippine Sea plate beneath the locked zone of the plate interface in the Tokai region, Japan. Tectonophysics 417: 69–80.

Tozer RSJ, Butler RWH, Chiappini M, Corrado S, Mazzoli S, Speranza F (2006) Testing thrust tectonic models at mountain fronts: where are the displacement gone?. Journal of Geol. Soc. London 163: 1–14.

Vai GB, Ricci Lucchi F (1976) The Vena del Gesso in the Northern Apennines: growth and mechanical break-down of gypsified algal crusts. Mem. Soc. geol. It. 16: 217–249.

Vai GB, Martini IP (eds) (2001) Anatomy of an Orogen: The Apennines and Adjacent Mediterranean Basins. Kluwer Academic, London., pp. 656

Vakarelov BK, Battacharya JP, Nebrigic DD (2006) Importance of high-frequency tectonic sequences during greenhouse times of Earth history. Geology 34: 797–800.

Van Wagoner JC, Bertram GT (eds) (1995) Sequence stratigraphy of foreland basin deposits. A.A.P.G. Memoir, 64, pp. 490.

Van Wagoner JC, Posamentier HW, Mitchum RM, Vail PR, Sarg JF, Loutit TS, Hardenbol J (1988) An overview of the fundamentals of sequence stratigraphy and key definitions. In: Wilgus CK, Hastings BS, Kendall CGStC, Posamentier HW, Ross CA, Van Wagoner JC Sea-level changes: an integrated approach. S.E.P.M. Spec. Publ., 42, p. 39–45.

Van Couvering JA, Castradori D, Cita MB, Hilgen FJ, Rio D (2000) The base of the Zanclean Stage and of the Pliocene series. Episodes 23: 179–187.

Zhang J, Scott DB (1996) Messinian deep-water turbidites and glacioeustatic sea-level changes in the North Atlantic: linkage to the Mediterranean Salinity Crisis. Paleoceaongraphy 11: 277–297.

Zoetemeijer R, Sassi W, Roure F, Cloetingh SAPL (1992) Stratigraphic and kinematic modelling of thrust evolution, northern Apennines, Italy. Geology 20: 1035–1038.

Zweingel J, Aigner T, Luterbacher HP (1998) Eustatic versus tectonic controls on Alpine foreland basin fill: sequence stratigraphy and subsidence analysis in the SE German Molasse. In: Mascle A, Puigdefabregas C, Luterbacher HP, Fernàndez M (eds) Cenozoic foreland basin of Western Europe. Geol Soc. London Spec. Publ., 134, p. 299–323.

Willett S D, Beaumont C, Fullsack P (1993) Mechanical model for the tectonics of doubly vergent compressional orogen. Geology 21: 371–374.

Meso-Cenozoic Evolution of Mountain Range - Intramontane Basin Systems in the Southern Siberian Altai Mountains by Apatite Fission-Track Thermochronology

Johan De Grave · Michael M. Buslov · Peter Van den haute · Boris Dehandschutter · Damien Delvaux

Abstract. The Altai Mountains form the northern part of the Cenozoic Central Asian intracontinental orogenic system that developed as a far-field effect of ongoing India-Eurasia convergence. Our study focuses on the southern Siberian Altai Mountains where basement rocks for apatite fission-track (AFT) analysis were sampled. These rocks are mainly Paleozoic granitoids that currently outcrop in several high mountain ranges along reactivated transpressive Paleozoic fault zones. These ranges are in most cases thrust systems adjacent to lacustrine intramontane basins. We present AFT results from the Chuya and Kurai ranges (3 samples) that are thrust over Late Cenozoic sediments of the Chuya-Kurai Basin and from the Shapshal range (4 samples) east of the Dzhulukul Basin. In addition, 5 samples were collected along a transect west of aforementioned study areas in the low-elevation areas of the Siberian Altai or Gorny Altai. Apparent AFT ages were found to be Mesozoic (roughly ranging between 180 and 80 Ma) and AFT length distributions show signs of thermal track fading (mean track lengths vary between 11.3 and 14.1 μm). AFT age and length data were modelled and thermal histories for the different sample sites reconstructed. These yield a two- to three-stage evolution: Late Jurassic-Cretaceous rapid basement cooling, a prolonged period of Late Cretaceous to Paleogene-Neogene stability, and a possible Late Cenozoic cooling to ambient temperatures.

Keywords. Apatite fission-track thermochronology, Siberia, Altai, intracontinental tectonics

1   Introduction

The Altai Mountains are an active intracontinental mountain belt located in the border zone of South Siberia (Russia–Gorny Altai Autonomous Republic), Kazakhstan, Mongolia, and China (Fig. 1). This paper deals with the southern Siberian Altai Mountains, and in particular with the areas around the Chuya-Kurai and Dzhulukul basins (Fig. 1). The Altai Mountains are part of a vast area in Central Asia and Siberia that is subjected to Late Cenozoic and active, mainly transpressive intracontinental deformation. This area includes the Tien Shan, Altai, Sayan, and Baikal rift zone as major constituents. These mountain belts alternate with large, undeformed basins, e.g., Tarim, Junggar, the Mongolian depressions (Great Lakes Depression) (Fig. 1). We refer to this region as the Central Asian Deformation Zone (CADZ), the world's largest intracontinental active orogenic system. Other terminologies have been used to delineate this area. In Russian literature, the area is often called the Ural-Mongolian fold belt, corresponding to the Altaids defined by Şengör et al. (1993). The driving forces for this regional deformation are generated by ongoing indentation of the Indian plate into Eurasia and possibly the Pacific Ocean subduction under eastern Asia (Molnar and Tapponnier, 1975; Tapponnier and Molnar, 1979; Avouac and Tapponnier, 1993). Strain accumulated in the convergence zone is partitioned to Eurasia's continental interior along an intricate pre-existing structural network associated with Central Asian Paleozoic basement and accretion tectonics. Reactivation is hence mostly basement controlled (Dobretsov et al., 1995b; Allen and Vincent, 1997) and involves primarily the easier to deform sutures and mobile belts between rigid units that compose the complex blocky tectonic CADZ collage. The Altai Mountains between the Paleozoic Altai-Mongolia (Fig. 2) and Tuva-Mongolia units are an example of such a reactivated belt.

The Altai ranges (Fig. 1) generally strike NW-SE, while to the north they fan out in E-W ranges in their western part and N-S ranges in the east. Relief and elevation is most outspoken in the South Siberian Altai with peaks exceeding 4000 m (Belukha peak, 4506 m). In the north the Altai border is the West Siberian Basin: the Kuznetsk (east) and Biya-Barnaul (west) sub-basins, in particular. To the SW the Altai are separated from the Zaisan-Junggar basin by the Irtysh shear zone. In Mongolia, the Altai ranges taper out into the E-W trending Gobi Altai. East of Altai are the Sayan Mountains and the Mongolian Great Lake depression.

Despite recent advances in our understanding of CADZ formation and basement evolution, geochronologic and thermochronologic data is sparse, especially in the Altai region. Therefore, an important rationale for this study is to contribute to the chronometry of regional tectonics, and to the Meso-Cenozoic history of
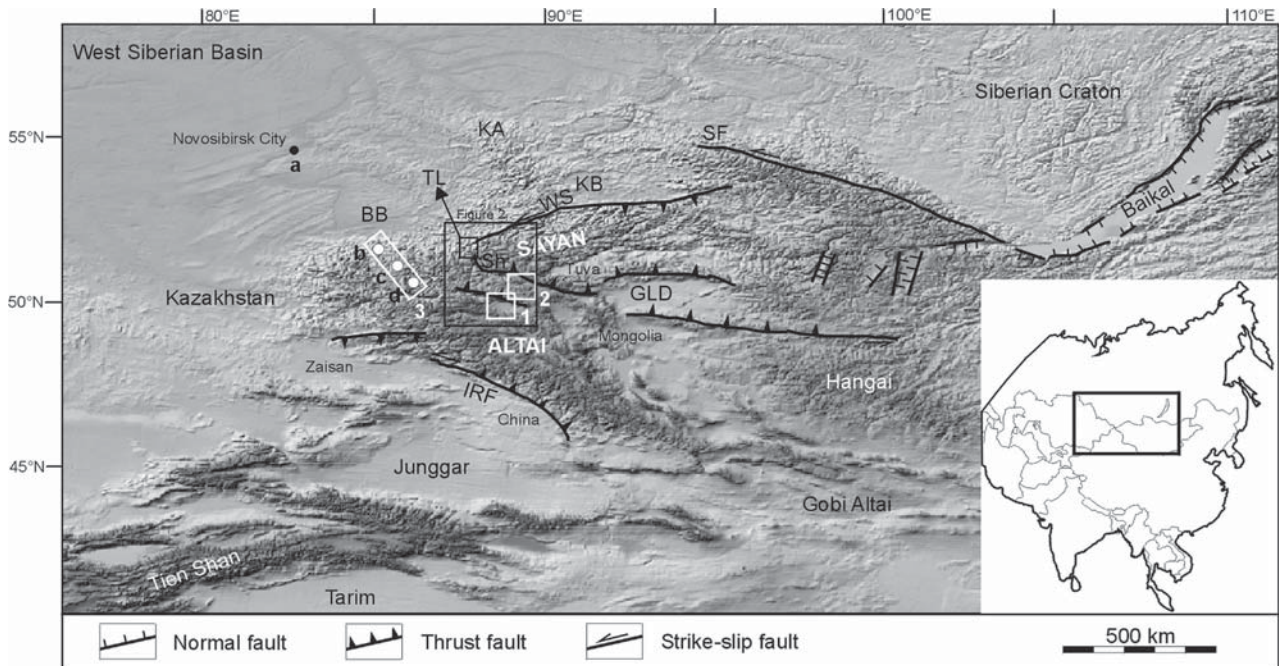
Fig. 1. Map of the Altai region in Central Asia. Sample locations are indicated by numbered boxes: (*1*) Chuya-Kurai Basin area, (*2*) Dzhulukul Basin area, and (*3*) western Gorny Altai transect (*a* = sample No-1; *b* = samples Be-1 and GA 01; *c* = GA 24; *d* = GA 03). *IRF* = Irtysh fault, *SF* = Sayan Fault, *Sh* = Shapshal Fault, *WS* = West Sayan fault. *BB* = Biya-Barnaul Basin, *GLD* = Great Lakes Depression in Mongolia, *KA* = Kuznetsk-Alatau Ridge, *KB* = Kuznetsk Basin

the Siberian Altai. Because especially little is known about the Meso-Cenozoic history of the area, we opted to apply apatite fission-track (AFT) dating and modelling to basement rocks in order to try to find signals in low-temperature techniques that might help us constrain the chronology of the regional basement reactivation. Sediments in intramontane basins flanking our targeted basement-cored uplifts clearly record Meso-Cenozoic tectonic activity; however, from a basement perspective these events remain undisclosed.

2   Geological and Tectonic Setting

2.1 Paleozoic Geodynamics and Basement Structure

The Paleozoic of the Altai Mountains is dominated by the evolution of the Paleo-Asian Ocean (PAO) that extended south of Siberia (Buslov et al., 2001; Khain et al., 2003). During its final stage of evolution, several Paleozoic tectonic units, including terrains of the present-day Altai region, accreted to Siberia (Fig. 2), along an intricate network of sutures that was extensively reactivated with Late Paleozoic and Mesozoic strike-slip movements (Şengör et al., 1993; Buslov et al., 2003). Adding to the crustal growth of Siberia and Eurasia was the emplacement of huge amounts of syn- and

post-collisional plutons (Dobretsov and Vladimirov, 2001; Fig. 2). In the Permian the PAO was consumed completely and subsequently, the Permo-Triassic was characterized by a period of tectonic quiescence, peneplanation, and red bed formation.

2.2 Meso-Cenozoic Reactivation and Formation of the Siberian Altai Orogen

From the Late Triassic and Jurassic on, sedimentary basins formed in a continental active tectonic regime (Dobretsov et al., 1995; 1996; Novikov, 2002). The Altai area was adjacent to several large basins where active subsidence and extension occurred. To the NW the West Siberian Basin, including the Kuznetsk and Biya-Barnaul sub-basins (Figs. 1, 3), was subjected to extension and rifting in the Jurassic-Cretaceous and terrigenous (molasse) and marine sediments were deposited (Pinous et al, 1999; Vyssotski et al., 2006). To the SW the Zaisan and Junggar Basin (Fig. 3) continuously subsided since the Permo-Triassic and accumulated km-scale thick Mesozoic sediments while its basement underwent reactivation in the Jurassic (Allen and Vincent, 1997). East of Altai several basins formed in the Great Lake Depression (GLD) of Mongolia and the Gobi (Fig. 3) where Mesozoic extension is widely documented and Jurassic-Cretaceous terri-
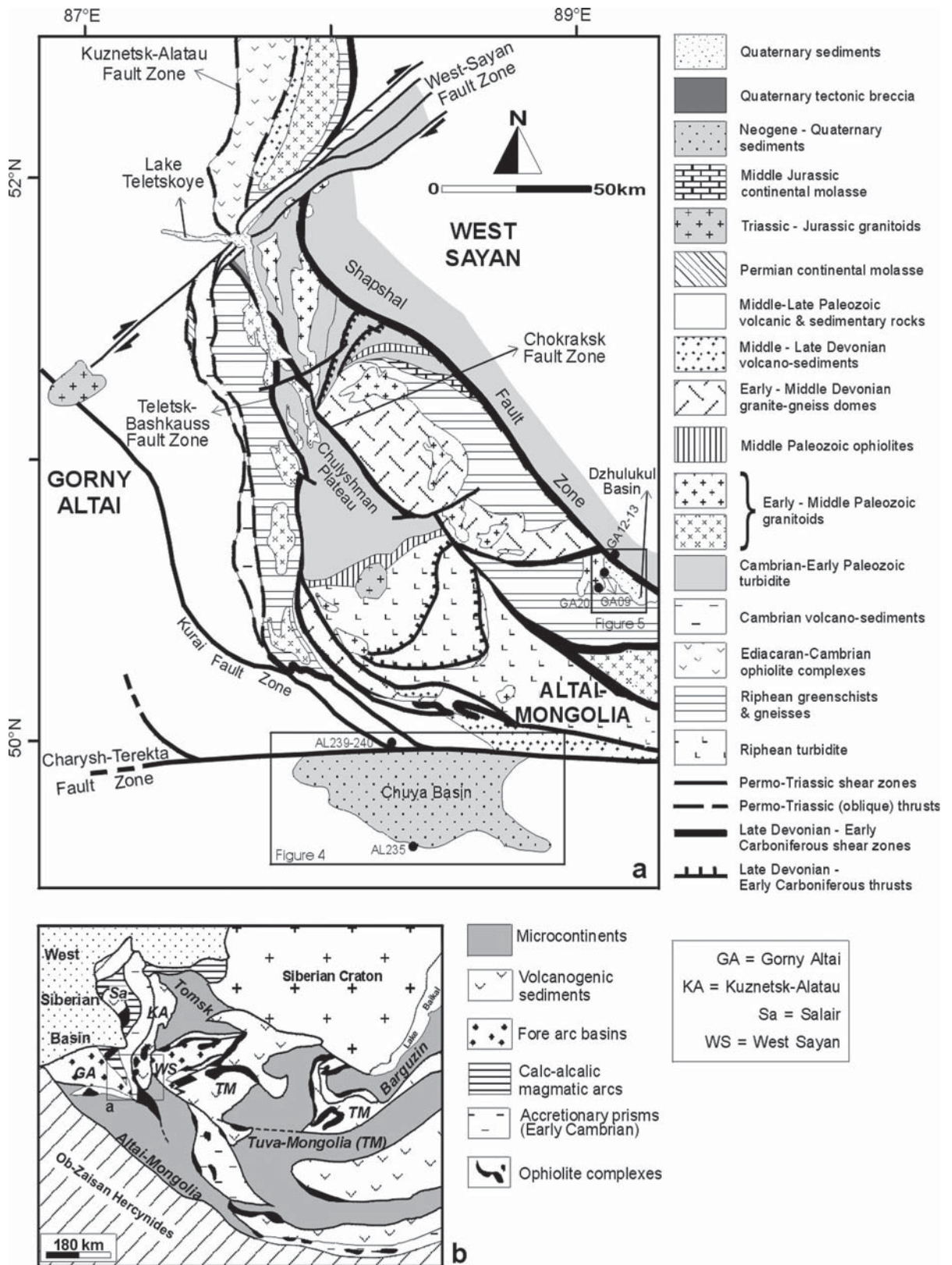
Fig. 2. **a** Simplified geological map of the Siberian Altai Mountains, **b** Schematic map of Paleozoic basement blocks in the Siberian Altai region
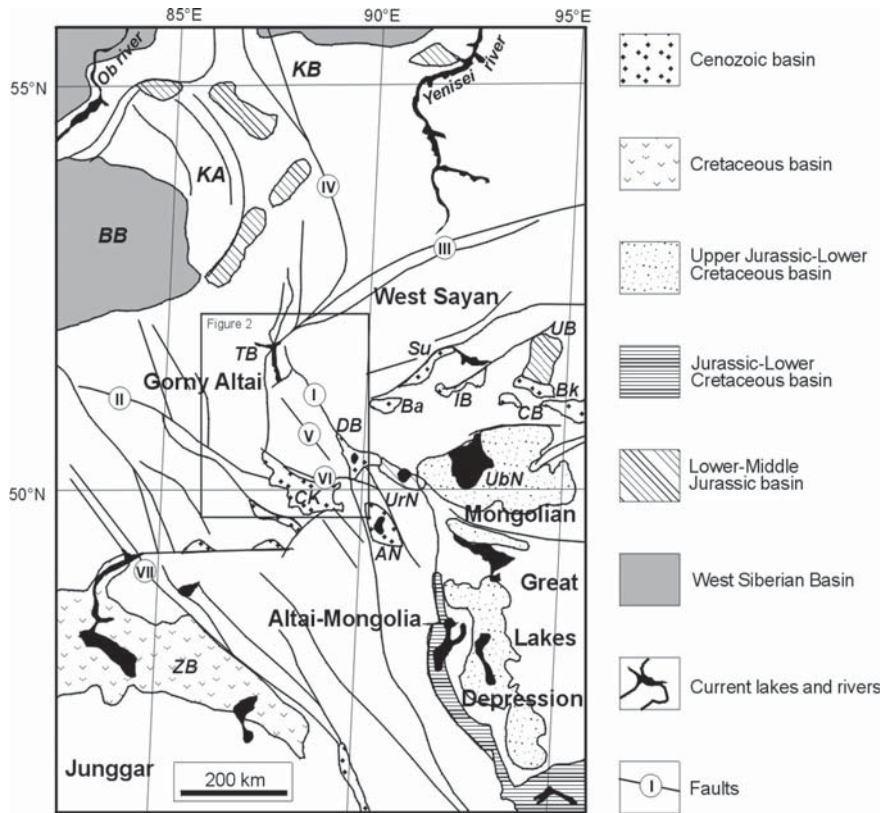
Fig. 3. Meso-Cenozoic basins in the Altai region (after Dobretsov et al., 1996). Basins: *AN* = Achit Nuur, *Ba* = Barlik, *BB* = Biya-Barnaul, *Bk* = Baikhak, *CB* = Chagyshai Basin, *CK* = Chuya-Kurai, *DB* = Dzhulukul Basin, *IB* = Initial Basin, *KA* = Kuznetsk-Alatau thrust, *KB* = Kuznetsk Basin, *Su* = Sutkol, *TB* = Teletskoye Basin, *UB* = Uluchkhem Basin, *UbN* = Ubsu-Nuur, *UrN* = Ureg-Nuur, *ZB* = Zaisan Basin. Faults: *I* = Shapshal; *II* = Charysh-Terekta, *III* = West Sayan, *IV* = Kuznetsk-Alatau, *V* = Chulyshman, *VI* = Kurai, *VII* = Irtysh

geneous sediments accumulated (Graham et al., 2001; Johnson, 2004). North and east of the GLD, the Mongol-Okhotsk Ocean between Siberia and North China–Mongolia (Amuria) closed. Collision of these continents induced the Mongol-Okhotsk orogeny that affected a broad region in Mongolia, North China, and Siberia (Delvaux et al., 1995a; Zorin, 1999; Kravchinsky et al., 2002; Tomurtogoo et al., 2005). The collision was diachronous: the suture is younger from west (Permo-Triassic) to east (Early Cretaceous).

Tectonic forces from the adjacent Mesozoic active provinces affected the Altai basement in the Late Jurassic-Cretaceous. In the Siberian Altai Jurassic fault-controlled basins developed along the Shapshal fault zone and accumulated continental molasse and other coarse Jurassic sediments (Dobretsov et al., 1996; Novikov, 2002; Fig. 2). This implies a Jurassic denudation-sedimentation event in the Siberian Altai, coeval with sedimentation in the larger adjacent basins mentioned. Tectonic activity was accompanied by emplacement of Triassic-Jurassic plutons (Dobretsov and Vladimirov, 2001). In the Cretaceous-Paleogene, tectonic activity subsided and the area experienced peneplanation (Delvaux et al., 1995a and 1995b; Nikolaeva and Shuvalov, 1995; Dehandschutter et al., 2002). Similar Mesozoic tectonic signatures were observed for the Mongolian Altai (Howard et al., 2003).

After Early Cenozoic quiescence, Late Cenozoic and active tectonism related to ongoing indentation of India into Eurasia developed a series of active intracontinental mountain belts through Central Asia. The distant tectonic effects of India-Eurasia convergence have reactivated some of the major Paleozoic structures within the Siberian Altai basement and are responsible for the Late Cenozoic building and morphology of the modern Altai orogen.

The Cenozoic history of the Siberian Altai can be described based on the evolution of the Chuya basin (Fig. 4). A complete ~1.5-km-thick Late Cretaceous to recent stratigraphic section is preserved (Delvaux et al., 1995b; Zykin and Kazansky, 1995; Buslov et al., 1999). The basin is situated in the Gorny Altai tectonic unit (Fig. 2) and its basement is composed of Ediacaran-Cambrian volcanic arc and accretionary prism rocks and Devonian active margin deposits (Buslov and Watanabe, 1996). Remnants of the Cretaceous–Paleogene peneplain are preserved on top of some basement blocks adjacent to the basin (Novikov et al., 1998). Late Cretaceous sediments found in small, remnant basins in the Charysh-Terekta strike-slip fault zone, just west of the Chuya basin (Fig. 4), contain marine radiolaria and foraminifers and represent a transgression from a Cretaceous seaway to the West Siberian Basin (Zykin et al., 1999). Currently these marine sediments are at
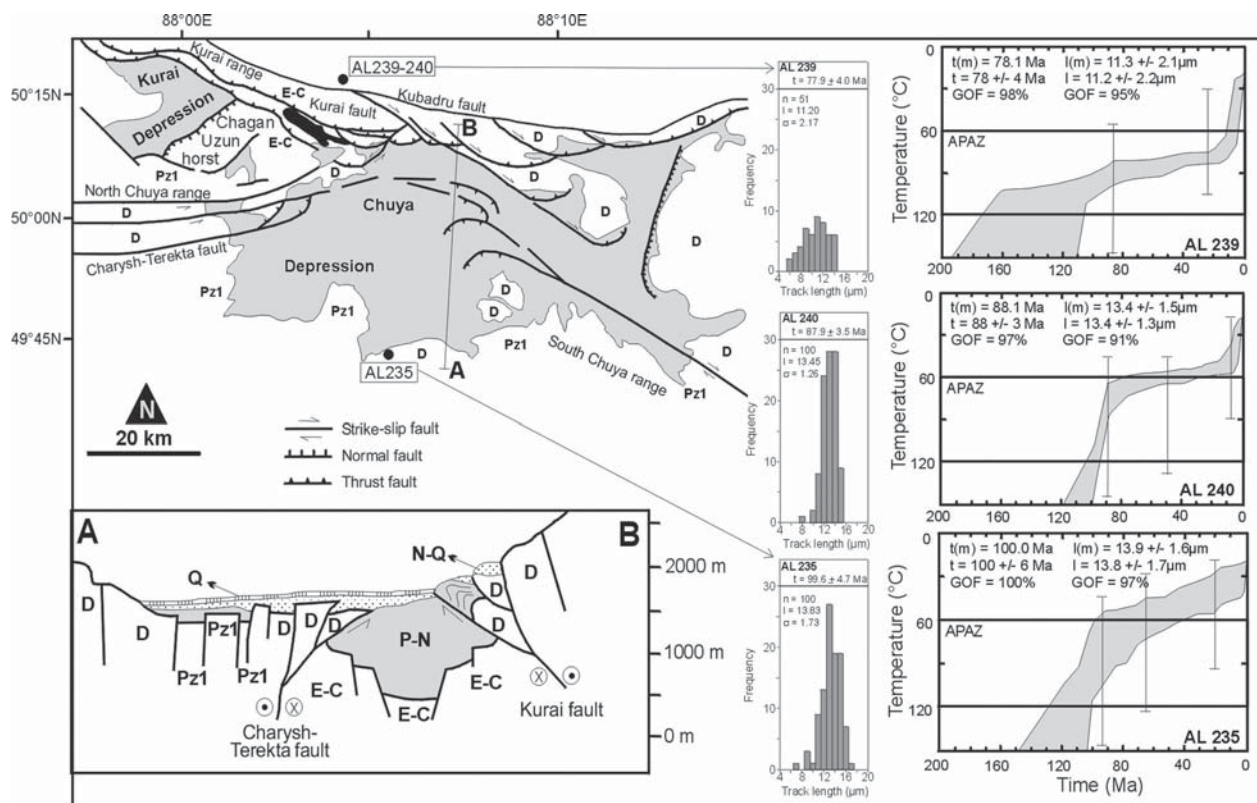
Fig. 4. Structural and geological sketch map and cross-section (AB) of the Chuya-Kurai Basin and Ranges (southern Siberian Altai). Sample locations are indicated by black dots. AFT age and length data are shown: t = AFT age, n = number of measured confined tracks, l = mean track length, σ = standard deviation of track length distribution. Thermal history models for these samples are also indicated. Modelling was performed using Laslett et al. (1987) annealing equations and the AFTSolve software by Ketcham et al. (2000). APAZ = Apatite Partial Annealing Zone; $t\,(m)$ = modeled AFT age, t = observed AFT age, $l\,(m)$ = modeled mean track length, l = observed mean track length; GOF = Goodness of fit. The best statistical tT-path is represented by a line within a statistical good fits envelope (shaded). See text for description and interpretation. For sample details see table 1. $Pz1$ = undivided Lower Paleozoic units, E-C = Ediacaran-Cambrian island arc rocks, D = Devonian active margin units, N-Q = Neogene-Quaternary sediments, Q = Quaternary sediments

an elevation of over 1500 m. Reworked material from these sediments and the Late Cretaceous–Paleogene peneplain are found in the basal Karachum Formation of the Chuya Basin. In these incipient stages, the basin developed as a strike-slip basin (Delvaux et al., 1995b). The basal section is dated to the Late Paleocene–Eocene (perhaps Early Oligocene) based on plant and pollen fossils (Zykin and Kazansky, 1995; Buslov et al., 1999). Oligocene lacustrine sediments are fine (clays, marls, fine sands) and contain pollen fossils that point towards a shallow, low-elevation lake basin, representing an embryonic stage of renewed tectonism. Similar observations were made in the adjacent Mongolian Altai area (Howard et al., 2003). This situation persisted in the Miocene and is encountered in other Siberian Altai locations (e.g. Dzhulukul Basin) (Dobretsov et al., 1996; Novikov, 2002). Towards the Late Miocene–Early Pliocene coarse sands appear and by the Late Pliocene (~3 Ma ago; Buslov et al., 1999),

coarse sands, breccias, and conglomerates dominate and demonstrate basin inversion and growth of the bordering Chuya and Kurai ranges that today house some of the highest Altai peaks (>4000 m). The Late Pliocene is therefore thought to be the time of onset of regional reactivation of the Gorny Altai unit. This reactivation is mainly transpressive with counterclockwise rotation (Thomas et al., 2002) and significant strike-slip. Thrust or reverse faulting positioned hanging wall Paleozoic basement blocks on Plio-Pleistocene glacial sediments during the Late Pleistocene-Quaternary as the Chuya basin evolved to a half- and full-ramp basin (Delvaux et al., 1995b; Buslov et al., 1999). The neotectonic evolution is dominated by reactivation of Paleozoic faults (Kurai and Charysh-Terekta; Fig. 4). A recent (27 Sept. 2003) strong (M = 7.3) earthquake induced by strike-slip along Charysh-Terekta shows its continued activity. Building of the Siberian Altai mountain ranges largely occurred since the

Late Pliocene. This young tectonic activity is mainly manifested along reactivated Paleozoic structures (e.g. Dehandschutter et al., 2002).

Similar Late Cenozoic and active transpressive intracontinental tectonics and orogenic development of the Mongolian and Chinese Altai have been documented by structural (Cunningham et al., 1996), (paleo)seismic (Pollitz et al., 2003; Vergnolle et al., 2003), geomorphologic, remote sensing (Philip and Ritz, 1999) and geodetic methods (Calais et al., 2003). However, in contrast to the Siberian Altai, earlier signs of coarse-clastic erosion and uplift (Miocene and Late Oligocene) are recorded, while the Pliocene is also characterized by the deposition of molasse-type sediments in intramontane basins (Howard et al., 2003). This implies that since the Pliocene an orogen-wide tectonic pulse affected and shaped the Altai as a whole, while earlier (Miocene) signs are recorded in the Mongolian Altai.

3 Samples, Sample Areas, and Analytical Procedures

Sample localities in the Siberian Altai Mountains are grouped in three distinct areas:

1. The Chuya-Kurai Basin and Ranges,
2. The Shapshal Range and Dzhulukul Basin
3. The western Altai transect (Gorny Altai).

All samples (Table. 1) are from Paleozoic basement involved in Late Cenozoic reactivation and characterized by nearby deposition of related Late Cenozoic clastic sediments. The sample sites, especially the Chuya-Kurai and Dzhulukul Basins, are typified by reverse or thrust faults connected to adjacent intramontane basins.

3.1 The Chuya-Kurai Basin and the Chuya and Kurai Ranges

The Chuya-Kurai Basin is located at the junction zone of the Gorny Altai, West Sayan, and Altai-Mongolia tectonic units (Fig. 2). Once a continuous Cenozoic depression, the Chuya and Kurai basins are presently separated by the Chagan-Uzun horst (Fig. 4). Their sediments span the entire Cenozoic as discussed in detail earlier. Cenozoic movements of the Paleozoic rocks from the bordering Kurai and Chuya ranges have deformed the sediments. Fault movements were lateral (strike-slip) with a clear vertical component of either reverse faulting (steep fault plane) or thrusting (low angle fault). The basin is hence bordered by positive, left lateral flower systems, giving the basin a ramp-like morphology (Delvaux et al., 1995b; Buslov et al., 1999). We analyzed two samples (AL 239-240, Table. 1, Fig. 4) from the Kurai Range and a granodiorite sample from the South Chuya Range (AL 235).

Table 1. Location and description of AFT samples from the Siberian Altai Mountains

Sample	Latitude	Longitude	Altitude	Locality	Lithology
1. Chuya-Kurai Basin					
AL 235	49°44′06″N	88°05′50″E	3490 m	Dzankiol pass	pegmatite
AL 239	50°16′31″N	88°04′25″E	2720 m	Ildugemsky pass	mylonite
AL 240	50°16′00″N	88°04′00″E	2440 m	Ildugemsky pass	granodiorite
2. Dzhulukul Basin					
GA 09	50°43′00″N	89°15′17″E	2240 m	Mayrikbazhi massif	gneiss
GA 12	50°45′50″N	89°18′10″E	2785 m	Trechglavaya massif	granodiorite
GA 13	50°45′11″N	89°19′28″E	2500 m	Trechglavaya massif	granodiorite
GA 20	50°37′54″N	89°14′18″E	2015 m	Uzun Uyok river	granitic aplite
3. Western Gorny Altai					
Be 1	51°56′24″N	84°45′24″E	290 m	Belokuriha massif	granite
GA 01	51°55′16″N	85°51′15″E	295 m	Rybalka massif (Sausga)	granodiorite
GA 03	50°38′59″N	86°17′54″E	1100 m	Chiquetaman pass	granodiorite
GA 24	51°19′48″N	85°40′14″E	840 m	Shebalino village	rhyolite
4. Novosibirsk					
No 1	54°59′15″N	82°59′12″E	90 m	Borok quarry, Priobsky complex	monzodiorite

Fig. 5. Structural and geological sketch map and cross-section (AB) of the Dzhulukul Basin (eastern Siberian Altai). Sample locations are indicated by black dots. AFT age and length data are shown: abbreviations and symbols are identical as in Fig. 4. See text for description and interpretation. For sample details see Table 1
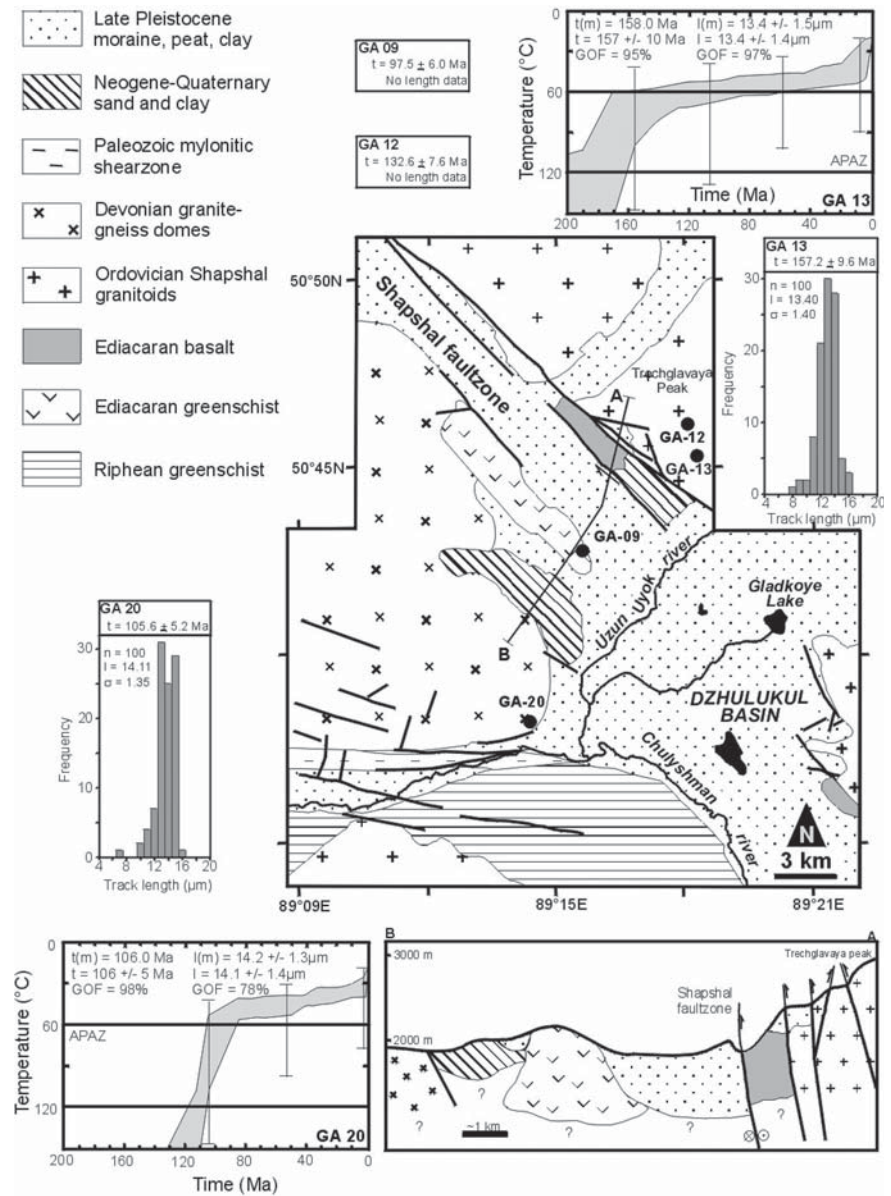
3.2 The Dzhulukul Basin and the Shapshal Range

The Cenozoic Dzhulukul Basin developed along the transpressive reactivated Shapshal fault as a full ramp basin (Figs. 2, 5). Its basement consists of Late Precambrian-Early Paleozoic greenschist and gneiss. At present the Dzhulukul basin resides at an elevation of ~2000 m. Its morphology and sediments are clearly influenced by glacial activity and erosion. The basin is mainly filled with Cenozoic glacial deposits and moraines, intercalated with peat horizons. Novikov (2002) observed that the basin contains small pock-

ets of Jurassic basal units on which the Cenozoic sediments rest unconformably as is the case in many adjacent basins in western Mongolia. To the east the basin is flanked by the Ordovician granitoids of the Shapshal range with Ediacaran basalts at its base. The range is obliquely thrust on Dzhulukul sediments along the Shapshal fault as a result of Late Cenozoic transpressive reactivation. Active tectonic movements along the fault and related structures in Mongolia have resulted in strong historic earthquakes and foreberg formation (Bayasgalan et al., 1999). One Dzhulukul basement gneiss (GA 20) and three Shapshal granitoid samples (GA 09, GA 12, and GA 13) (Table.1, Fig. 5) were obtained.

3.3 The Western Gorny Altai Transect

Also samples in Gorny Altai were collected (general location: Fig. 1) along the main road from the city of Gornyaltaisk to Tashanta at the Mongolian border. This road transects the western Chulyshman and Kurai areas and the lower, hilly foreland areas of NW Gorny Altai. Samples from this area, the 'Western Gorny Altai Transect' come from several Paleozoic plutons and igneous complexes: (1) the Permo-Triassic Belokurikhinsky lacolith (sample Be-1) at the junction between the reactivated modern orogen and the stable Biya-Barnaul Basin, (2) the Devonian Rybalka granitoid-gabbroid massif (GA-01), (3) the Late Devonian Chiquetaman granitoid massif (GA-03), and (4) the Devonian Shebalino rhyolite (GA-24) (active margin sequence). An additional sample (No-1, monzodiorite) was collected near Novosibirsk city (Borok quarry, Permo-Triassic Priobsky batholith), in the eastern part of the flat and stable platform of the West Siberian Basin. No Cenozoic tectonic reactivation is seen here.

3.4 Analytical Procedures

The apatite from aforementioned samples was separated using conventional heavy liquid and magnetic techniques, embedded in epoxy, polished, and dated with the external detector (ED) method. Muscovite mica (Goodfellow clear ruby) was used as an ED. Spontaneous tracks in the apatite were etched with a 2.5% HNO_3 solution for 70 s at 22°C. Induced tracks in the ED were etched with a 40% HF solution for 40 minutes at 22°C. Apatite-ED wafers were irradiated in several batches in the well-thermalized channels of the Thetis research reactor facility at the University of Gent. Depending on the irradiation, thermal neutron fluence values of around 2×10^{15} cm^{-2} were achieved. The thermal neutron fluence was monitored using metal activation monitors, i.e., diluted Au-Al and Co-Al alloys (e.g., Van den haute et al., 1998).

Track counting and length measurements were done using an Olympus BH-2 optical microscope with a 1250× magnification (10× eyepieces with counting grid, 100× dry objective, 1.25× drawing tube attachment) equipped with transmitted and reflected light. At least 1000 spontaneous tracks were counted per sample, spread over minimum 20 separate grains; where possible 100 confined tracks were measured to construct an AFT length-frequency distribution and a mean track length (MTL) was calculated. AFT age and length data were modeled using the Laslett et al. (1987) annealing equations and the AFTSolve modelling software by Ketcham et al. (2000).

The apatites were dated using both an absolute approach based on the procedure factor (Q) and using a fission decay constant (λ_f) of 8.46×10^{-17} a^{-1} (e.g. Wagner, and Van den haute, 1992; Jonckheere, 2003) and the conventional zeta (ζ) method (Hurford and Green, 1983; Hurford, 1990). An overall weighted mean zeta (OWMZ) was calculated on the basis of 32 apatite age standard mounts of Durango and Fish Canyon Tuff apatite (Hurford and Green, 1983). The IRMM-540 dosimeter glass (De Corte et al., 1998) was used and our OWMZ calibration factor was determined as 253.1 ± 2.4. Only conventional mean ζ-ages were used for the thermal history modelling. In all our irradiation packages, apatite age standards co-embedded with dosimeter glass shards, as well as foils of diluted Co-Al and Au-Al metal activation monitors, were included. These were spaced with regular intervals throughout the sample package in order to detect and correct for a possible axial thermal neutron fluence gradient. It also allowed for the interpolation of fluence values (absolute calibration) and induced glass dosimeter track densities (ρ_d for ζ calibration) for each sample individually.

4 AFT Results and Thermal History Modelling

AFT age and length data (Table. 2) is indicated on the sample area maps: Chuya-Kurai basin (Fig. 4), Dzhulukul basin and Shapshal Range (Fig. 5), and the western Gorny Altai transect and Novosibirsk sample (Fig. 6). AFT ages are conventional ζ-ages (Hurford, 1990). Track lengths were measured on natural horizontal confined tracks. Not all samples yielded sufficient confined tracks and hence no length data is reported for those samples. AFT age and length data were modelled using the Laslett et al. (1987) annealing model (with initial track length parameter $l_o = 16.3$ μm) and the AFTSolve thermal history modelling software (Ketcham et al., 2000). Thermal history models and length distributions are shown (Figs. 4, 5, 6). Statistical good fits (Ketcham et al. 2000) are shown as a shaded tT-envelope. Interpretation and discussion is based on the general model trends (good fits envelope). In a first run a model was only constrained by two tT constraints: a low-T (~10°C) benchmark reflecting current ambient temperatures, and a high-T bar-constraint well above 120°C (AFT accumulation threshold) far enough back in time, i.e., significantly predating apparent AFT ages. An age of ~260 Ma was chosen based on Permian amphibole $^{40}Ar/^{39}Ar$ ages (regional Permian strike-slip deformation) from the Teletskoye area in the northern Siberian Altai (Dehandschutter et al., 1997). After an initial run, additional constraints were placed reiteratively along the general thermal history

Table 2. AFT age and length data for the Siberian Altai samples. ρ_s, ρ_i, and ρ_d are respectively, the density of spontaneous, induced tracks and induced tracks in an ED irradiated against a dosimeter glass. The ρ_d-values are interpolated values obtained from regularly spaced glass dosimeters in each of the irradiation packages, expressed as 10^5 tracks/cm^2. Values for ρ_s and ρ_i are expressed as 10^6 tracks/cm^2. N_s, N_i, and N_d are respectively, the number of counted spontaneous, induced tracks and induced tracks in an ED irradiated against a dosimeter glass. N_d is also an interpolated value. $P(\chi^2)$ is the chi-squared probability that the dated grains have a constant ρ_s/ρ_i-ratio, it is given on a 0 to 1 scale. An OWMZ value of 253.1±2.4 a·cm^2 (Durango and Fish Canyon Tuff apatite age standards and the IRMM-540 dosimeter glass) was used for the calculation of t(ζ). AFT length data are reported as a mean track length (l_m) with standard deviation, σ, obtained from the measurement of a number (n) of natural, horizontal confined tracks

Sample	Grains	ρ_s (± 1σ)	N_s	ρ_i (± 1σ)	N_i	ρ_d (± 1σ)	N_d	$P(\chi^2)$	t(ζ) in Ma	l_m (µm)	n	σ (µm)
1. Chuya-Kurai Basin												
AL 235	30	2.175 (0.055)	1580	1.263 (0.042)	912	4.113 (0.080)	2633	0.36	99.6 ± 4.7	13.8	100	1.7
AL 239	50	1.219 (0.032)	1486	0.683 (0.024)	832	3.315 (0.083)	1614	1.00	77.9 ± 4.0	11.2	51	2.2
AL 240	30	1.657 (0.026)	3937	0.950 (0.020)	2257	3.934 (0.111)	1259	1.00	87.9 ± 3.5	13.5	100	1.3
2. Dzhulukul Basin												
GA 09	30	2.009 (0.068)	862	0.992 (0.046)	457	4.054 (0.080)	2595	0.99	97.5 ± 6.0	---	---	---
GA 12	30	3.433 (0.100)	1188	1.407 (0.063)	503	4.049 (0.079)	2592	0.30	132.6 ± 7.6	---	---	---
GA 13	30	2.846 (0.078)	1332	0.872 (0.043)	408	3.851 (0.083)	2169	0.99	157.2 ± 9.6	13.4	100	1.4
GA 20	20	1.197 (0.031)	1532	0.588 (0.021)	753	4.024 (0.079)	2576	0.76	105.6 ± 5.2	14.1	100	1.4
3. Western Gorny Altai and Novosibirsk												
Be 1	30	0.951 (0.030)	979	0.525 (0.022)	551	4.108 (0.080)	2629	0.99	99.1 ± 5.7	13.7	32	1.6
No 1	50	4.246 (0.082)	2682	1.296 (0.046)	788	4.078 (0.080)	2610	0.54	178.6 ± 8.2	---	---	---
GA 01	50	1.739 (0.051)	1144	0.777 (0.034)	510	4.073 (0.080)	2607	1.00	120.4 ± 6.9	13.3	60	2.0
GA 03	40	0.899 0.032)	809	0.447 (0.022)	402	3.858 (0.083)	2173	1.00	98.8 ± 6.5	13.6	58	1.9
GA 24	17	3.551 (0.110)	1044	1.131 (0.062)	338	4.014 (0.079)	2569	0.81	165.5 ± 11.0	---	---	---

Fig. 6. AFT age and length data from the Western Gorny Altai Transect samples: AFT age and length data are shown: abbreviations and symbols are identical as in Fig. 4. See text for description and interpretation. For sample details see Table 1 and Fig. 1
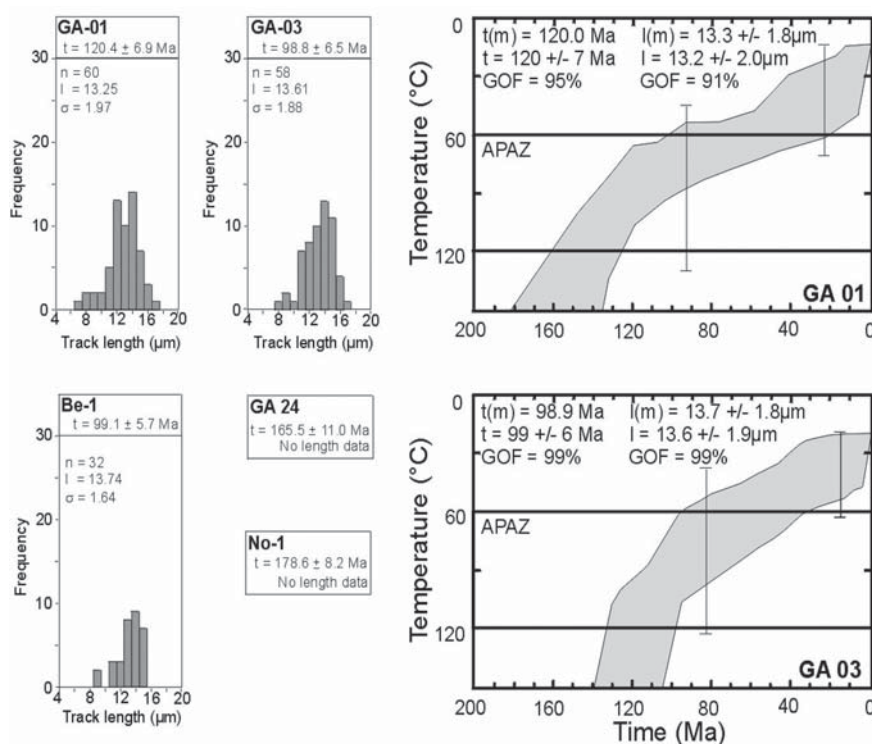
trend to refine the model. Care was taken to place as few constraints as possible, and to let the T-interval be as wide as possible (i.e., wider than the statistically acceptable tT-paths envelope; Ketcham et al., 2000).

No reset Cenozoic AFT ages were found. Apparent AFT ages are Late Jurassic-Cretaceous and range between 80 and 160 Ma, except the Early Jurassic age (179 Ma) for the Novosibirsk sample (No-1, Table. 2). In particular, we obtained the following ages: (1) Chuya-Kurai area: 80–100 Ma (elevations ~2500–3500 m), (2) Dzhulukul: 100–160 Ma (elevations ~2000–2800 m), and (3) western transect: 100–165 Ma (elevations ~300–1000 m). No clear regional trend can be detected, except that lower ages are found in the high elevation area of Chuya-Kurai, higher ages in the lower foreland and intermediate ages in the Dzhulukul area. In general, higher elevation samples from a single area yield higher ages. Mean track lengths (MTL) and length distributions show clear signs of thermal track shortening, suggesting a prolonged stay at APAZ temperatures (120–60°C) (Wagner and Van den haute, 1992). MTL values vary between 11–14 μm (with most around 13 μm), distributions are generally broad ($1.3 < σ < 2.2$ μm), asymmetric, and negatively skewed (Figs. 4, 5, 6).

The AFT age and length data was modelled according to the principles mentioned earlier and a two- and possibly three-stage thermal history model was reconstructed: (1) Cretaceous rapid cooling, (2) Late Cretaceous-Paleogene stability with only slow cooling, and a possible (3) Late Neogene-Quaternary cooling (Figs. 4, 5, 6). The latter event is only clearly registered in sample AL239, while it is only suggested (outside the 120–60°C T-interval) in the other samples. However, the models calculated here are in good agreement with these from samples in the northern Siberian Altai where the younger stage (3) is more outspoken (De Grave and Van den haute, 2002) and the Chinese Altai (Yuan et al., 2006). Sample GA-13, collected east of the Shapshal fault (Fig. 5) shows an earlier onset of Mesozoic cooling, while all other samples show a later onset. These all originate from areas west of the Shapshal fault. This might suggest that cooling of the Altai basement was diachronous, possible related to differential block movements along the Shapshal fault zone in a Mesozoic phase of reactivation.

The Cretaceous event cooled the investigated apatites below the 120°C threshold roughly ~120 Ma ago. Considering a normal geothermal gradient of 25–30 °C/km, this implies that most of our apatite bearing rock samples were brought to depths shallower than ~4 km in the crust. According to the general trend in our thermal history models, the Cretaceous cooling lasted until ~80–90 Ma ago. At the cessation of this cooling, the sampled rocks were at upper APAZ to lower AFT retention temperatures (~80–50°C), cor-

responding to a depth of 3–2 km considering a geothermal gradient of 25–30 °C/km. At these conditions partial AFT annealing persisted and tracks shortened. Variations of these modelled values is predominantly due to their present outcrop altitude, and hence their associated paleo-depth. Additional scatter (e.g., between samples AL239 and 240) might be due to chemical composition differences between individual apatites (Green et al., 1986).

After Cretaceous cooling near-horizontal tT-paths endured from the Late Cretaceous, throughout the Paleogene, until the Late Miocene. This stage in the general thermal history marks a period of stability or slow cooling during which the sampled rocks stayed at upper APAZ/lower retention temperatures. The near-horizontal tT-paths are disturbed by rapid Pliocene to Recent cooling, starting about 15–5 Ma ago. This is evident from sample AL 239, while this event in our models for the other samples falls below the 60°C isotherm. This young rapid cooling eventually brought the samples to ambient surface temperatures and is associated with the exhumation of the apatite bearing rocks to their present outcrop positions. The long APAZ residence time (Late Mesozoic to Late Cenozoic) and associated track annealing and shortening explains the low MTL values and broad, negatively skewed track length distributions (Figs. 4, 5, 6).

A note of caution concerning the Late Cenozoic cooling event should be conveyed here. It has been shown that there exists a potential in AFT thermal history models using specific model parameter values (lo parameter) to produce Late Cenozoic cooling merely as an artefact. This artefact, the 'worldwide recent cooling' (Ketcham et al., 1999; 2000) can further be enhanced by track annealing at ambient temperatures. It is therefore hazardous to interpret Late Cenozoic cooling merely based on AFT thermal history models. It should be meticulously tested against independent geological evidence, as we have attempted to do in this work.

5   Discussion, Tectonic Implications and Conclusions

5.1 The Cretaceous Cooling Event

Cretaceous cooling of the Siberian Altai basement is contemporaneous with an important denudation event in the Jurassic-Cretaceous as recorded in the sediments of intramontane Altai basins and larger orogen-adjacent basins (Figs. 2, 3). We therefore interpret the Mesozoic AFT ages (Table. 2) and the Cretaceous cooling observed in the thermal history models as Siberian Altai basement denudation. Considering a geothermal gradient of 25–30°C/km, the Siberian Al-

tai experienced at least 1 to 3 km of Late Jurassic-Cretaceous denudation recorded by the AFT system.

The derived sediments were mainly fluvially transported to large adjacent basins (GLD, West Siberian Basin, Junggar-Zaisan Basin), and to smaller fault-controlled, intramontane depressions (Dobretsov et al., 1996; Pinous et al., 1999; Howard et al., 2003; Vyssotski et al., 2006). Mesozoic sediments, mainly Jurassic and Early Cretaceous deposits, unconformably overlie the Paleozoic basement of these basins. Mesozoic sediment thickness reaches several kilometers in the large adjacent basins, and in the smaller intramontane basins it locally reaches over 2 km. In these intramontane basins, Mesozoic sediments are often molassic type deposits. The facts that the Altai basement is subjected to significant cooling as seen in the AFT data, that derived sediments are coarse-grained and deposited in thick sequences in large adjacent basins and in fault-controlled basins in the Altai orogen itself, point to denudation of a reactivated orogen. This hypothesis is further underscored by the occurrence of the Late Mesozoic Kuznetsk-Alatau thrust system and related basins at the northern edge (Salair Ridge) of the present-day Altai orogen (Fig. 3), at the Kuznetsk Basin interface (Novikov, 2002; Buslov et al., 2003). The kinematics, and tectonic-geodynamic implications of this thrust system are poorly understood and form the subject of ongoing research. It however clearly indicates Jurassic-Cretaceous tectonic activity in the Siberian Altai.

Accommodation of thick Mesozoic deposits and evidence from geophysical exploration in the large adjacent basins also indicates active extension, and subsidence within these basins: the West Siberian Basin (Pinous et al., 1999; Vyssotski et al., 2006), the Mongolian-Baikal and Junggar basins (Graham et al., 2001; Johnson, 2004). Therefore, denudation and subsequent cooling of the basement as observed in our models, was most likely a complex interaction of extension in large adjoining basins creating accommodation space for Altai deposits on one hand, and tectonic reactivation of the Altai orogen on the other.

Mesozoic tectonic reactivation of the Altai Mountains is coeval with the final stages of closure of the Mongol-Okhotsk (MO) Ocean, and the ensuing MO orogeny. Convergence and ultimate collision of the Siberian and North Chinese-Mongolian continent or Amurian plate, resulted in the development of the MO orogenic belt in the Late Jurassic-Early Cretaceous (Zorin, 1999; Kravchinsky et al., 2002; Tomurtogoo et al., 2005). Incipient collision occurred in the western part of the MO belt (South Baikal - East Sayan - Mongolia area) around the Lias-Dogger transition (170–180 Ma ago). Oblique collision and associated diachronous compressive tectonics lasted until final closure of the MO Ocean in the east during the Early Creta-

ceous (110–140 Ma ago). Deformation was not solely confined to the collision zone proper, but migrated through the hinterland and affected the Mongolian Altai (Dobretsov et al., 1996), the Baikal area (Van der Beek et al., 1996) and reached the Siberian cratonic rim (Zorin, 1999). Our AFT data imply that the Siberian Altai region also experienced far-field effects of the MO orogeny. This induced reactivation and deformation of the ancestral Altai, and to an important phase of denudation as discerned from the Mesozoic tT-cooling paths in our thermal history models. Van der Beek et al. (1996) interpret AFT results of Mesozoic denudation in the Baikal area also in terms of distant effects of the MO orogeny. Their AFT ages and thermal history models show a Late Cretaceous cooling, which is somewhat younger than our results. This is in agreement however with the oblique collision model as outlined above, where initial collision and orogeny affected the western area (Altai) earlier with respect to the central (Baikal) and eastern parts of the MO belt. A similar pattern in pluton emplacement ages along the collision zone corroborates this model (Tomurtogoo et al., 2005). Yuan et al. (2006) however interpret Cretaceous apparent AFT ages and a Cretaceous cooling obtained from thermal history models from the Chinese Altai as a possible consequence of the collision of Eurasia with the Lhasa block (Tibet) and the related Cimmerian orogeny. However, Cimmerian effects in Central Asia are generally older and of Late Jurassic-Early Cretaceous age (e.g. Sobel and Dumitru, 1997; Bullen et al., 2001; De Grave et al., accepted).

5.2 The Period of Late Cretaceous-Paleogene stability

Near horizontal tT-paths at lower APAZ to upper AFT retention temperatures (50–80°C) in the Late Cretaceous-Paleogene reflect a period of prolonged stability in the Siberian Altai. While some samples clearly show a horizontal tT trend (e.g. AL239 or 240), others exhibit a continuous slow cooling (e.g. GA 03). During this period intracontinental Siberia and Central Asia experienced tectonic quiescence and the Mesozoic orogen was subjected to peneplanation. Rocks consequently remained approximately at the position and depth in the crust they reached after the Mesozoic denudation phase. This implies that relaxation of the isotherms occurred and that these rocks stayed at more or less constant temperatures as reflected by the near-horizontal tT-paths in our thermal history models. In Siberia and Central Asia a vast lateritic peneplain with typical red beds developed (Delvaux et al., 1995a and 1995b; Nikolaeva and Shuvalov, 1995; Dobretsov et al., 1996). Remnants of this peneplain are found in many parts of the region, and also in the Siberian Altai

(Novikov, 2002; Dehandschutter et al., 2002). At present the surface is extensively deformed as a result of Late Cenozoic tectonic activity. Remnants are mainly found on plateau-like uplifts, or as basal sequences in Cenozoic intramontane basins (Chuya-Kurai Basin), and are vertically offset by hundreds of meters. This interpretation agrees with observations and interpretations of AFT cooling curves for the adjoining Baikal region (Van der Beek et al., 1996).

5.3 The Late Cenozoic Cooling Event

The Late Cenozoic cooling phase in our thermal history models for the Chuya-Kurai area is associated with the tectonic reactivation of the region and the building and denudation of the modern Altai. The reactivation is thought to be a far-field effect of the India-Eurasia collision and the ongoing indentation of the Indian plate into the Eurasian continent. According to the AL239 model, cooling commenced between 15-5 Ma ago and continues until the present. This corresponds with other indicators that point towards initiation of reactivation in the Late Neogene and clear intensification of transpressive tectonic movements in the Plio-Pleistocene (Cunningham et al., 1996; Dobretsov et al., 1996; Buslov et al., 1999; Dehandschutter, 2002; Novikov, 2002; Howard et al., 2003). This event is more outspoken in earlier AFT studies in the northern part of the Siberian Altai, e.g., in the Teletskoye area (Fig. 1) (De Grave and Van den haute, 2002). Sediments produced by the denudation of the modern Altai orogen are deposited in the large adjacent basins (West Siberian Basin, Mongolian GLD, Junggar-Zaisan Basin) in a similar setting as during the Mesozoic denudation (Fig. 3). Also reminiscent of the Mesozoic denudation, formation of Cenozoic, fault-controlled intramontane basins accommodate part of the Late Cenozoic sediments derived from the growing orogen. The Dzhulukul and Chuya-Kurai Basins are important examples. In these basins, several horizons of coarse Late Neogene to Quaternary sediments are observed (Delvaux et al., 1995b; Buslov et al., 1999; Dehandschutter et al., 2002).

Late Cenozoic reactivation of the Siberian Altai Mountains is substantiated by deformation of the Late Cretaceous-Paleogene peneplain. In comparison to the low-lying inactive hinterland, peneplain remnants are vertically displaced by 2 km or more (Dehandschutter et al., 2002), while in mountain ranges and plateau-like uplifts, adjacent blocks capped with remnants of the lateritic peneplain show vertical offsets of hundreds of meters relative to each other. Preservation of the peneplanation surface however puts an upper limit on the extent of post-Paleogene denudation and on the magnitude of concomitant cooling observed in our AL239 thermal history model. Preservation is local, not regional, indicating that some of the blocks were indeed subjected to considerable denudation. In addition, all samples were collected at the surface and along vertical profiles situated well below the estimated position of the peneplain. In summary, while tectonic and sedimentary evidence indicates a Late Neogene-Quaternary episode of intense tectonic activity with rapid uplift and sedimentation in the Siberian Altai, the AFT models only record the event clearly for sample AL239 in the Chuya region, while other samples suggest this trend, but do not unambiguously record it.

Although to some extent AFT thermal history modelling may overestimate the amount of denudation associated with the Neogene-Quaternary event (Late Cenozoic artefactual cooling discussed earlier) the recent cooling of the Chuya-Kurai basement itself and its timing are accurately reflected. Ample independent geological and tectonic evidence, summarized in previous sections, underscores our observations. We interpret the young cooling event to be related to Late Neogene to recent denudation in a still active transpressive tectonic regime in the area. We conclude that reactivation and building of the modern Altai orogenic edifice is largely constrained to the last 15-5 Ma, or even younger as it is not completely registered in the AFT system.

Late Cenozoic cooling and denudation of Central Asia with respect to reactivation in the framework of ongoing India-Eurasia convergence was reported in AFT studies, in particular of the Tien Shan area (Hendrix et al., 1994; Sobel and Dumitru, 1997; Bullen et al. 2001). Also, closer to the collision zone, in the Altyn Tagh and the northern Tibetan Plateau, this is observed as well (e.g. Jolivet et al., 2001).

Acknowledgements

References

Allen, M.B., Vincent, S.J., 1997. Fault reactivation in the Junggar region, northwest China: the role of basement structures during Mesozoic-Cenozoic compression. Journal of the Geological Society, London 154, 151–155.

Avouac, J.P., Tapponnier, P., 1993. Kinematic model of active deformation in Central Asia. Geophysical Research Letters 20, 895–898.

Bayasgalan, A., Jackson, J., Ritz, J.-F., Carretier, S., 1999. Forebergs, flower structures, and the development of large intra-continental strike-slip faults: the Gurvan Bogd fault system in Mongolia. Journal of Structural Geology 21, 1285–1302.

Bullen, M.E., Burbank, D.W., Garver, J.I., Abdrakhmatov, K,Ye., 2001. Late Cenozoic tectonic evolution of the northwestern Tien Shan: New age estimates for the initiation of mountain building GSA Bulletin 113, 1544–1559.

Buslov, M.M., Watanabe, T., 1996. Intrasubduction collision and its role in the evolution of an accretionary wedge: the Kurai zone of Gorny Altai (Central Asia). Russian Geology and Geophysics 37, 74–84.

Buslov, M.M., Zykin, V.S., Novikov, I.S., Delvaux, D., 1999. Cenozoic history of the Chuya depression (Gorny Altai): Structure and Geodynamics. Russian Geology and Geophysics, 40, 1687–1701.

Buslov, M.M., Saphonova, I.Yu., Watanabe, T., Obut, O.T., Fujiwara, Y., Iwata, K., Semakov, N.N., Sugai, Y., Smirnova, L.V., Kazansky, A.Yu., 2001. Evolution of the Paleo-Asian Ocean (Altai-Sayan region, Central Asia) and collision of possible Gondwana-derived terranes with the southern marginal part of the Siberian continent. Geosciences Journal 5, 203–224.

Buslov M.M., Watanabe, T., Smirnova, L.V., Fujiwara I., Iwata, K., De Grave, J., Semakov N.N., Travin, A.V., Kiryanova, A.P., Kokh, D.A., 2003. Role of strike-slip faults in Late Paleozoic-Early Mesozoic tectonics and geodynamics of the Altai-Sayan and East Kazakhstan folded zone. Russian Geology and Geophysics 44, 49–75.

Calais, E., Vergnolle, M., San'kov, V., Lukhnev, A., Miroshnitchenko, A., Amarjargal, S., Déverchère, J., 2003. GPS measurements of crustal deformation in the Baikal-Mongolia area (1994–2002): implications for current kinematics of Asia. Journal of Geophysical Research 108, 2501, doi:10.1029/2002JB002373, 13 pp.

Cunningham, D., Windley, B., Dorjnamjaa, D., Badamgarov, J., Saandar, M., 1996. A structural transect across the Mongolian western Altai: active transpressional mountain building in Central Asia. Tectonics 15, 142–156.

De Corte, F., Bellemans, F., Van den haute P., Ingelbrecht, C., Nicholl, C., 1998. A new U doped glass certified by the European Commission for the calibration of fission-track dating. In: Van den haute, P. and De Corte, F. (Eds.), Advances in fission-track geochronology, Kluwer Academic Publishers, Dordrecht, pp. 67–78.

De Grave, J., Van den haute, P., 2002. Denudation and cooling of the Lake Teletskoye region in the Altai Mountains (South Siberia) as revealed by apatite fission-track thermochronology. Tectonophysics 349, 145–159.

De Grave, J., Buslov, M.M., Van den haute, P. (2007). Distant effects of India-Eurasia convergence and intracontinental deformation in Central Asia: constraints from apatite fission-track thermochronology. Journal of Asian Earth Science, 29, 188–204.

Dehandschutter, B., Delvaux, D., Boven, A., 1997. The Lake Teletsk tectonic depression (Altai): new kinematic data and chronological relations. Annual Report of the Department of Geology and Mineralogy, Royal Museum for Central Africa, Tervuren, Belgium 1995–1996, 147–167.

Dehandschutter, B., Vysotsky, E., Delvaux, D., Klerkx, J., Buslov, M.M., Seleznev, V.S., De Batist, M., 2002. Structural evolution of the Teletsk graben (Russian Altai). Tectonophysics 351, 139–167.

Delvaux, D., Moeys, R., Stapel, G., Melnikov, A., Ermikov, V., 1995a. Paleostress reconstructions and geodynamics of the Baikal region, Central Asia, Part 1. Palaeozoic and Mesozoic pre-rift evolution. Tectonophysics 252, 61–101.

Delvaux, D., Theunissen, K., Van der Meer, R., Berzin, N., 1995b. Dynamics and paleostress of the Cenozoic Kurai-Chuya depression of Gorny Altai (South Siberia): tectonic and climatic control. Russian Geology and Geophysics 36, 26–45.

Dobretsov, N.L., Vladimirov, A.G., 2001. Continental growth in the Phanerozoic: Evidence from Central Asia. Geology, magmatism and metamorphism of the western part of Altai-Sayan Fold Region. IGCP-420, 3rd Workshop, Field Excursion Guide. Novosibirsk, pp. 139.

Dobretsov, N.L., Berzin, N.A., Buslov, M.M., Ermikov, V.D., 1995. General aspects of the evolution of the Altai region and the interrelationships between its basement pattern and the neotectonic structural development. Russian Geology and Geophysics 36, 3–15.

Dobretsov, N.L., Buslov, M.M., Delvaux, D., Berzin, N.A., Ermikov, V.D., 1996. Meso- and Cenozoic tectonics of the Central Asian mountain belt: effects of lithospheric plate interaction and mantle plumes. International Geology Review 38, 430–466.

Graham, S.A., Hendrix, M.S., Johnson, C.L., Badamgarav, D., Badarch, G., Amory, J., Porter, M., Barsbold, R., Webb, L.E., Hacker, B.R., 2001. Sedimentary record and its implications of Mesozoic rifting in southeast Mongolia. GSA Bulletin 113, 1560–1579.

Green, P.F., Duddy, I.R., Gleadow, A.J.W., Tingate, P.R., Laslett, G.M., 1986. Thermal annealing of fission tracks in apatite.1. A qualitative description. Chemical Geology (Isotopes Geoscience Section) 59, 237–253.

Hendrix, M.S., Dumitru, T.A., Graham, S.A., 1994. Late Oligocene – Early Miocene unroofing in the Chinese Tien Shan: an early effect of the India-Asia collision. Geology 22, 487–490.

Howard, J.P., Cunningham, W.D., Davies, S.J., Dijkstra, A.H., Badarch, G., 2003. The stratigraphic and structural evolution of the Dzereg Basin, western Mongolia: clastic sedimentation, transpressional faulting and basin destruction in an intraplate, intracontinental setting. Basin Research 15, 45–72.

Hurford, A.J., 1990. Standardization of fission track dating calibration: Recommendation by the Fission Track Working Group of the I.U.G.S. Subcommission on Geochronology. Chemical Geology (Isotope Geoscience Section) 80, 171–178.

Hurford, A.J., Green, P.F., 1983. The zeta age calibration of fission-track dating. Geoscience 1, 285–317.

Johnson, C.L., 2004. Polyphase evolution of the East Gobi basin: sedimentary and structural records of Mesozoic-Cenozoic intraplate deformation in Mongolia. Basin Research 16, 79–99.

Jolivet, M., Brunel, M., Seward, D., Xu, Z., Yang, J., Roger, F., Tapponnier, P., Malavieille, J., Arnaud, N., Wu, C., 2001. Mesozoic and Cenozoic tectonics of the northern edge of the Tibetan Plateau: fission-track constraints. Tectonophysics 343, 111–134.

Jonckheere, R., 2003. On the densities of etchable fission tracks in a mineral and co-irradiated external detector with refer-

ence to fission-track dating of minerals. Chemical Geology 200, 41–58.

Ketcham, R.A., Donelick, R.A., Carlson, W.D., 1999. Variability of apatite fission-track annealing kinetics: III. Extrapolation to geologic time scales. American Mineralogist 84, 1235–1255.

Ketcham, R.A., Donelick, R.A., Donelick, M.B., 2000. AFT-Solve: A program for multi-kinetic modelling of apatite fission-track data. Geological Materials Research 2, 1–32.

Khain, E.V., Bibikova, E.V., Salnikova, E.B., Kröner, A., Gibsher, A.S., Didenko, A.N., Degtyarev, K.E., Fedotova, A.A., 2003. The Palaeo-Asian ocean in the Neoproterozoic and early Palaeozoic: new geochronological data and palaeotectonic reconstructions. Precambrian Research 122, 329–358.

Kravchinsky, V.A., Cogné, J.-P., Harbert, W.P., Kuzmin, M.I., 2002. Evolution of the Mongol-Okhotsk ocean as constrained by new paleomagnetic data from the Mongol-Okhotsk suture zone, Siberia. Geophysical Journal International 148, 34–57.

Laslett, G.M., Green, P.F., Duddy, I.R., Gleadow, A.J.W., 1987. Thermal annealing of fission tracks in apatite. 2. A quantitative analysis. Chemical Geology (Isotopes Geoscience Section) 65, 1–13.

Molnar, P., Tapponnier, P., 1975. Cenozoic tectonics of Asia: Effects of a continental collision. Science 189, 419–426.

Nikolaeva, T.V., Shuvalov, V.F., 1995. Mesozoic and Cenozoic evolution of surface topography in Mongolia. Geomorfologiya 2, 54–65.

Novikov, I.S., 2002. Late Paleozoic, Middle Mesozoic, and Late Cenozoic stages of the Altai orogeny. Russian Geology and Geophysics 43, 432–443.

Novikov, I.S., Delvaux, D., Agatova, A.R., 1998. Neotectonics of the Kurai ridge (Gorny-Altai). Russian Geology and Geophysics 39, 970–977.

Philip, H., Ritz, J.-F., 1999. Gigantic paleolandslides associated with active faulting along the Bogd fault (Gobi-Altay, Mongolia). Geology 27, 211–214.

Pinous, O.V., Sahagian, D.L., Shurygin, B.N., Nikitenko, B.L., 1999. High-resolution sequence stratigraphic analysis and sea-level interpretation of the middle and upper Jurassic strata of the Nyurolskaya depression and vicinity (southeastern West Siberia, Russia). Marine and Petroleum Geology 16, 245–257.

Pollitz, F., Vergnolle, M., Calais, E., 2003. Fault interaction and stress triggering of twentieth century earthquakes in Mongolia. Journal of Geophysical Research 108, 2503, doi:10.1029/2002 JB002375, 14 pp.

Şengör, A.M.C., Natal'in, B.A., Burtman, V.S., 1993. Evolution of the Altaid tectonic collage and Palaeozoic crustal growth in Eurasia. Nature 364, 299–307.

Sobel, E.R., Dumitru, T.A., 1997. Thrusting and exhumation around the margins of the western Tarim Basin during the India-Asia collision. Journal of Geophysical Research 102, 5043–5064.

Tapponnier, P., Molnar, P., 1979. Active faulting and Cenozoic tectonics of the Tien Shan, Mongolia, and Baykal regions. Journal of Geophysical Research 84 3425–3459.

Thomas, J.C., Lanza, R., Kazansky, A., Zykin, V., Semakov, N., Mitrokhin, D., Delvaux, D., 2002. Paleomagnetic study of Cenozoic sediments from the Zaisan basin (SE Kazakhstan) and the Chuya depression (Siberian Altai): tectonic implications for central Asia. Tectonophysics 351, 119–137.

Tomurtogoo, O., Windley, B.F., Kröner, A., Badarch, G., Liu, D.Y., 2005. Zircon age and occurrence of the Adaatsag ophiolite and Muron shear zone, central Mongolia: constraints on the evolution of the Mongol-Okhotsk ocean, suture and orogen. Journal of the Geological Society, London 162, 125–134.

Van den haute, P., De Corte, F., Jonckheere, R., Bellemans, F., 1998. The parameters that govern the accuracy of fission-track age determinations: a re-appraisal. In: Van den haute, P. and De Corte, F. (Eds.), Advances in fission-track geochronology, Kluwer Academic Publishers, Dordrecht, pp. 33–46.

Van der Beek, P., Delvaux, D., Andriessen, P.A.M., Levi, K.G., 1996. Early Cretaceous denudation related to convergent tectonics in the Baikal region, SE Siberia. Journal of the Geological Society London 153, 515–523.

Vergnolle, M., Pollitz, F., Calais, E., 2003. Constraints on the viscosity of the continental crust and mantle from GPS measurements and postseismic deformation models in western Mongolia. Journal of Geophysical Research 108, 2502, doi:10.1029/2002JB002374, 15 pp.

Vyssotski, A.V., Vyssotski, V.N., Nezhdanov, A.A., 2006. Evolution of the West Siberian Basin. Marine and Petroleum Geology 23, 93–126.

Wagner, G.A., Van den haute, P., 1992. Fission Track-Dating. Kluwer Academic Publishers, Dordrecht, 285 pp.

Yuan, W., Carter, A., Dong, J., Bao, Z., An, Y., Guo, Z., 2006. Mesozoic-Tertiary exhumation history of the Altai Mountains, northern Xinjiang, China: new constraints from apatite fission track data. Tectonophysics 412, 183–193.

Zorin, Yu.A., 1999. Geodynamics of the western part of the Mongolia-Okhotsk collisional belt, Trans-Baikal region (Russia) and Mongolia. Tectonophysics 306, 33–56.

Zykin, V.S., Kazansky, A.Y., 1995. Main problems of stratigraphy and paleomagnetism of Cenozoic (prequaternary) deposits in the Chuya depression of Gorno Altay. Russian Geology and Geophysics 35, 75–90.

Zykin, V.S., Lebedeva, N.K., Buslov, M.M., Marinov, V.A., 1999. The Discovery of Marine Upper Cretaceous in the Altai Mountains. Doklady Akademii Nauka, Earth Science Section, 367, 610–613.

Slab Retreat and Active Shortening along the Central-Northern Apennines

Davide Scrocca · Eugenio Carminati · Carlo Doglioni · Daiana Marcantoni

Abstract The Quaternary geodynamic evolution and the tectonic processes active along the Central and Northern Apennines thrust fronts and in the adjacent Padane-Adriatic foredeep domains are analysed and discussed.

A reinterpretation of the available geophysical and geological data reveals that the south-eastward prolongation of the Apennines thrust front in the Adriatic Sea is most likely located along the north-eastern side of the Adriatic ridge, i.e., in a more external position with respect to traditional interpretations. Further south, the Apennine thrust front is segmented in correspondence with the Tremiti lithospheric right-lateral transfer zone.

This new interpretation of the Apennine thrust front bears some relevant implications since it rejuvenates to Late Quaternary the most recent contractional deformations in its Adriatic portion. This is consistent with the Late Quaternary activity of the buried thrust-related folds associated with the Apennine front along the Marche coastal belt and in the Po Plain documented by geomorphological analysis and by seismic reflection profiles. Moreover, active shortening associated with the Apennines accretionary prism in the Po Plain and in the central and northern Adriatic Sea is documented by GPS data and by historical and instrumental seismicity.

The Quaternary evolution of one of the active thrust-related folds recognised in the Po Plain subsurface (the Mirandola anticline) has been investigated in detail by backstripping high-resolution stratigraphic data. Our results show decreasing relative uplift rates during the Quaternary. However, tectonic relative uplift rate of about 0.16 mm/a can still be recognised during the last 125 ka. Horizontal shortening faster than 1 mm/a should be expected in agreement with available GPS data.

Furthermore, the SW-ward (or W-ward) increasing dip of the foreland monocline in the Po Plain and in the central-northern Adriatic and the asymmetric distribution of the Quaternary to Recent subsidence indicate a still active flexural retreat of the subducting lithosphere in these domains.

The Quaternary to Recent flexural retreat of the subducting Adriatic lithosphere and the related frontal accretion of the Apennines prism are framed in a coherent geodynamic scenario characterized by a retreating west-directed subduction zone, which is the natural evolution of the Neogene geodynamic history.

1   Introduction

The central and northern segments of the Apennines accretionary prism - foredeep system are among the most studied thrust belts worldwide. The buried geometries of the Northern Apennines frontal thrust system were already nicely imaged below the Po Plain by seismic reflection data at the beginning of the '80s (e.g., Pieri and Groppi, 1981; Pieri 1983). Since then, this structural configuration has served as a classic example for thrust tectonics and growth strata studies (among many others: Doglioni, 1993; Zoetemeijer et al. 1993, Doglioni and Prosser, 1997; Hardy et al., 1996; Ford, 2004). Moreover, by analyzing the Adriatic foredeep domain, fundamental concepts have been developed on the relationships between thrusting and sedimentation as, for instance, the definition of piggy-back basin (Ori and Friend, 1984).

The basic tectonic evolution of the Apennines thrust belt-foredeep system may be considered the result of the late-Oligocene to Present NE-ward rollback of a W-directed slab (among many others: Malinverno and Ryan, 1986; Royden et al., 1987; Doglioni, 1991; Patacca et al., 1990; Faccenna et al., 2003). The subduction depth decreases moving from Calabria to the northern Apennines. Moving along strike, the accretionary prism shows variable depth (3-10 km) of the frontal basal décollement plane (Bigi et al., 2003; Lenci et al., 2004), and variable dip of the foreland regional monocline (Mariotti and Doglioni, 2000). These structural undulations are related either to lateral stratigraphic variations or to inherited Permo-Mesozoic structures (i.e., horst and grabens). The Quaternary geodynamic evolution and the active tectonic processes are, however, still a matter of debate. This scientific controversy provides an interesting opportunity to review and discuss some general issues related to the tectonic evolution of thrust belt-foredeep systems.

Regarding the Central and Northern Apennines thrust front and adjacent Adriatic foredeep domains, the main controversies regard the following points:

- the actual position of the south-eastward prolongation of the Apennine thrust front in central Adriatic domain;
- the age of the most recent tectonic activity along the Apennine thrust front and its present-day seismotectonic behaviour;
- the geodynamic processes responsible for the Quaternary subsidence of the Padane-Adriatic domain.

In this paper, a review of the above issues is carried out. Based on the interpretation of both recently acquired and already available seismic reflection profiles and well data, a new definition of the Apennine thrust front is proposed together with an assessment of the natural subsidence of the Padane-Adriatic region.

The Late Quaternary to Recent tectonic vitality of the Central and Northern Apennine thrust front is discussed by comparing geological and geophysical data in the Adriatic domain and in the Po Plain. Moreover, the Quaternary evolution of one of the active thrust-related folds recognised in the Po Plain subsurface (the Mirandola anticline) is investigated in detail by back-stripping high-resolution stratigraphic data.

The proposed structural interpretation of the Apennine thrust front, its recent activity and seismotectonic behaviour, and the Quaternary natural subsidence of the Padane-Adriatic domain are finally framed in a coherent geodynamic scenario.

2   Geological and Geodynamic Setting

The Apennines thrust belt (Fig. 1) developed in Neogene and Quaternary times in the hangingwall of a west-directed subduction zone, as documented by subcrustal seismicity and seismic tomography (e.g., Spak-
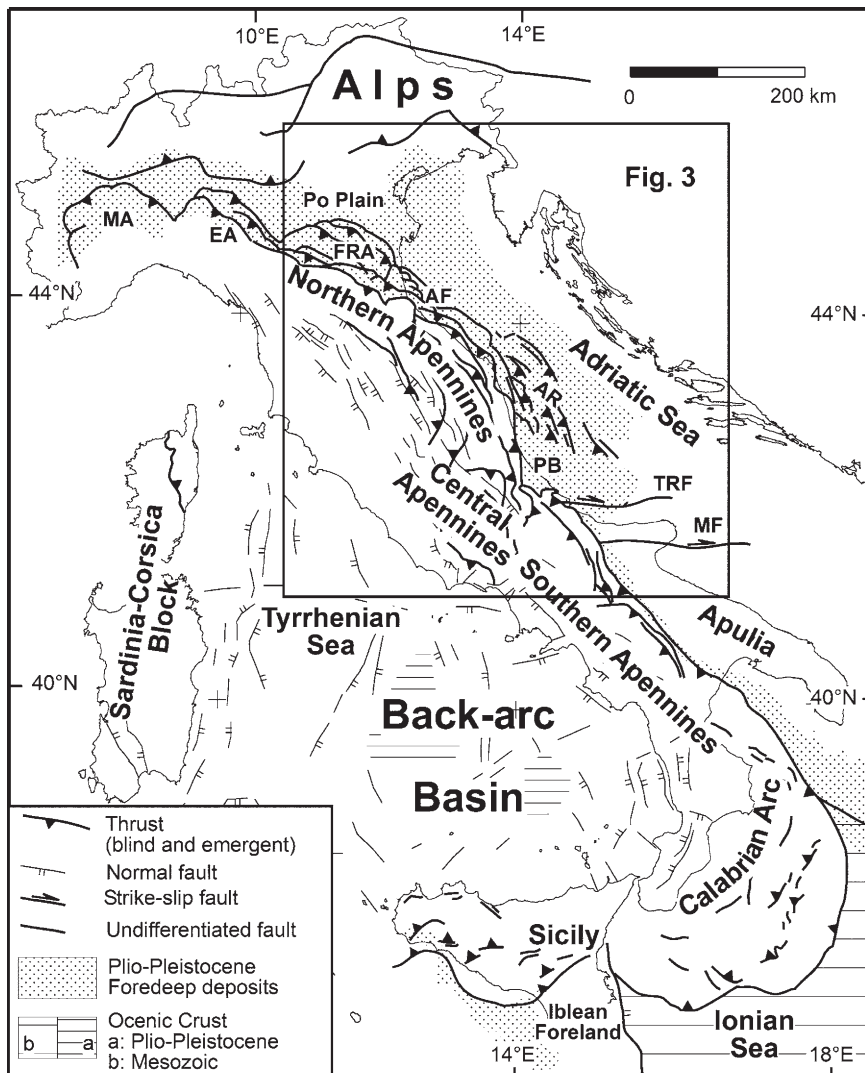
Fig. 1 Main structural features of Italy (modified from Consiglio Nazionale delle Ricerche, 1992). Foredeep deposits are delimited by the -1000 m isobath.
MA = Monferrato Arc;
EA = Emilia Arc;
FRA = Ferrara Romagna Arc;
AF = Adriatic Folds;
AR = Adriatic ridge;
PB = Pescara Basin;
TF = Tremiti Fault;
MF = Mattinata Fault

man, 1990; Amato et al., 1993; Lucente et al., 1999; Chiarabba et al., 2005). The eastward retreat of the subduction is the most plausible explanation for the progressive eastward migration of the thrust fronts, the foreland flexure (and consequent shift of the fore-deep basins) as well as the extensional processes along the internal Tyrrhenian back-arc basins (e.g., Malinverno and Ryan, 1986; Royden et al., 1987; Patacca et al., 1990; Doglioni, 1991; Doglioni et al., 1999a; Faccenna et al., 2003).

Off-scraping and incorporation at the subduction zone of the Meso-Cenozoic passive margin sedimentary covers that overlay the subducted Apulo-Adriatic plate drove to the development of the Apennines accretionary prism. In the Padane-Adriatic domain, these units are made up of clastics, evaporites, and shallow to deep water carbonates sedimentary sequences (Bally et al., 1986; Zappaterra, 1990; Grandić et al., 2002 and references therein).

In the external part of the Apennines, the interaction between the flexural bending of the underthrusting Adriatic plate and the foreland-ward propagation of the contractional deformations produce a zone of active sedimentation above the deforming accretionary wedge (Fig. 2). This "depositional wedge top" (De Celles and Giles, 1996; Ford, 2004) is commonly observed in orogens related to west-directed subduction zones where the fastest subsidence rates occur (Doglioni, 1994). In regions where the depositional wedge top is well developed due to the presence of an effective décollement level, the foredeep sensu stricto (i.e., the area where foredeep deposits overlie undeformed passive margin sedimentary cover) may be restricted to a very narrow band.

Following the pioneering study of Royden et al. (1987) and Royden (1988), who first recognised the segmentation of the subducting Apulo-Adriatic lithosphere, the position of the main lithospheric discontinuities occurring in the Adriatic Sea has been bet-

ter defined by analyzing the tectonic evolution of the Apulo-Adriatic areas. During Pliocene to Pleistocene times, the Central Adriatic underwent high subsidence rates due to eastward rollback of the hinge of the Apennine subduction while the Apulian region experienced uplift since the middle Pleistocene (e.g., Doglioni et al., 1994; 1996). The W-E trending Tremiti lineament has been interpreted as the main right-lateral transfer zone between the two sectors of the subducting Adriatic lithosphere characterized by different amounts of flexural retreat (Milano et al., 2005). The genesis of this transfer zone, occurred mainly during the Pleistocene, has been attributed to the encroachment of the Apulian thick continental lithosphere in the subduction zone (Doglioni et al., 1994; 1996; Gambini and Tozzi, 1996) that has hindered the rollback of the subducting plate in the Apulian region (Figs. 1 and 3).

3   Apennine Thrust Front

The subsurface location of the front of the Northern Apennines accretionary prism below the Po plain is very well defined by seismic and well data (e.g., Pieri and Groppi, 1981; Pieri, 1983; Consiglio Nazionale delle Ricerche, 1992), that constrain a geometry consisting of three arcuate thrusts systems. These three buried arcs, from west to east, are i) the Monferrato, ii) the Emilia, and iii) the Ferrara-Romagna arcs. These arcs are delimited externally by thrust faults which separate them from the Pedalpine monocline. The structure of Ferrara-Romagna arc can be subdivided into three second-order features: the i) Ferrara, ii) Romagna and, more to the east, iii) Adriatic folds (Fig. 3). Moving south-eastward, the prolongation of the Apennine thrust front in the central Adriatic Sea is less evident.

Fig. 2 Schematic cross-section of an orogen due to a W-directed retreating subduction zone (modified after Doglioni et al., 1999a). The shear between the down-going and retreating lithosphere and the eastward compensating mantle is transferred upward, generating the shortening within the accretionary wedge

In the Adriatic domain, the external front of the Apennine accretionary prism is traditionally traced a few kilometres off-shore between the towns of Ancona and Pescara (among many others, Patacca et al., 1990; Doglioni, 1991; Consiglio Nazionale delle Ricerche, 1992; Argnani & Frugoni, 1997; Artoni & Casero,1997; Calamita et al., 2003; Casero, 2004; Lavecchia et al., 2004; Montone et al., 2004). However, as discussed in detail by Scrocca (2006), several lines of evidence suggest a different localization of the Apennine thrust front with respect to the commonly accepted interpretation (Fig. 4a).
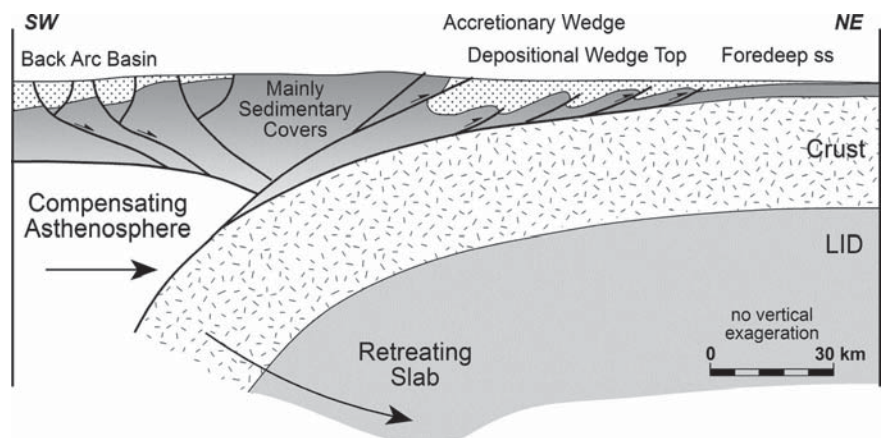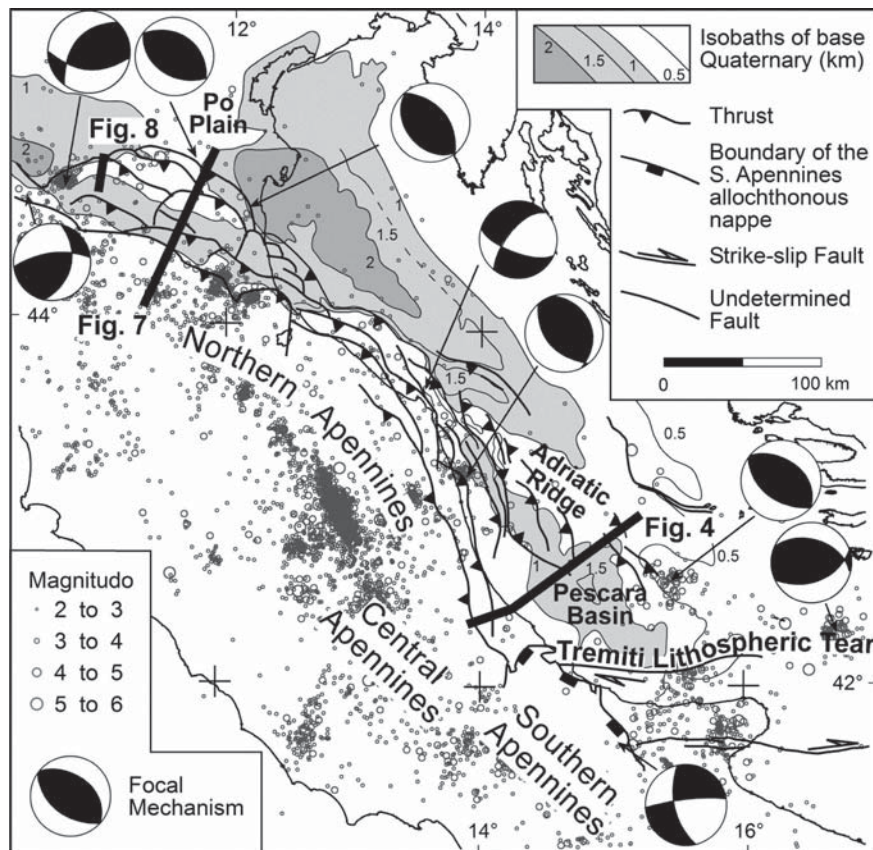
It should be noted that the Central Adriatic Sea is characterized by the presence of a ridge, the so-called "Mid-Adriatic Ridge" (Finetti, 1982) also known as "Central Adriatic Deformation Belt" (Argnani & Gamberi, 1995; Argnani & Frugoni, 1997), made up of structural highs, distributed along a dominant NW-SE to WNW-ESE trend. This Adriatic ridge, well defined by the isobaths of the base of the Plio-Pleistocene deposits (e.g., Consiglio Nazionale delle Ricerche, 1992), extends south-eastward from the town of Ancona for at least 150 km in the central Adriatic Sea (Fig. 4).

The majority of these highs have been interpreted as thrust-related folds although evidence of salt dia-

pirism has been also recognised (e.g., Bally et al., 1986; Ori et al., 1986; De Alteriis, 1995; Argnani & Frugoni, 1997; Calamita et al., 2003; Scrocca, 2006). Some structures combine both compressional and salt tectonics (e.g., Bally et al., 1986).

The interpretation of the CROP M-15 seismic reflection data (Fig. 5), acquired within the framework of the Italian deep crust exploration project (CROP Project; Scrocca et al., 2003), integrated with a review of the multichannel seismic reflection profiles and well data available at the Italian Ministry of Industry, provides a valuable contribution to improve the structural description of the Adriatic ridge.

Some of the Adriatic ridge's folds developed on pre-existing Mesozoic horsts and show seismic and well evidence of tectonic inversion along pre-existing Mesozoic extensional faults at the end of the Lower Cretaceous and in Tertiary times. The origin of the Cretaceous events has been related to the onset of the convergence between Europe and Africa while the Tertiary tectonic inversions have been attributed to far-field effects of the Apenninic and Dinaric compression or to diapirism (e.g., Argnani et al., 1993; De Alteriis, 1995; Gambini et al., 1997; Bertotti et al., 2001).
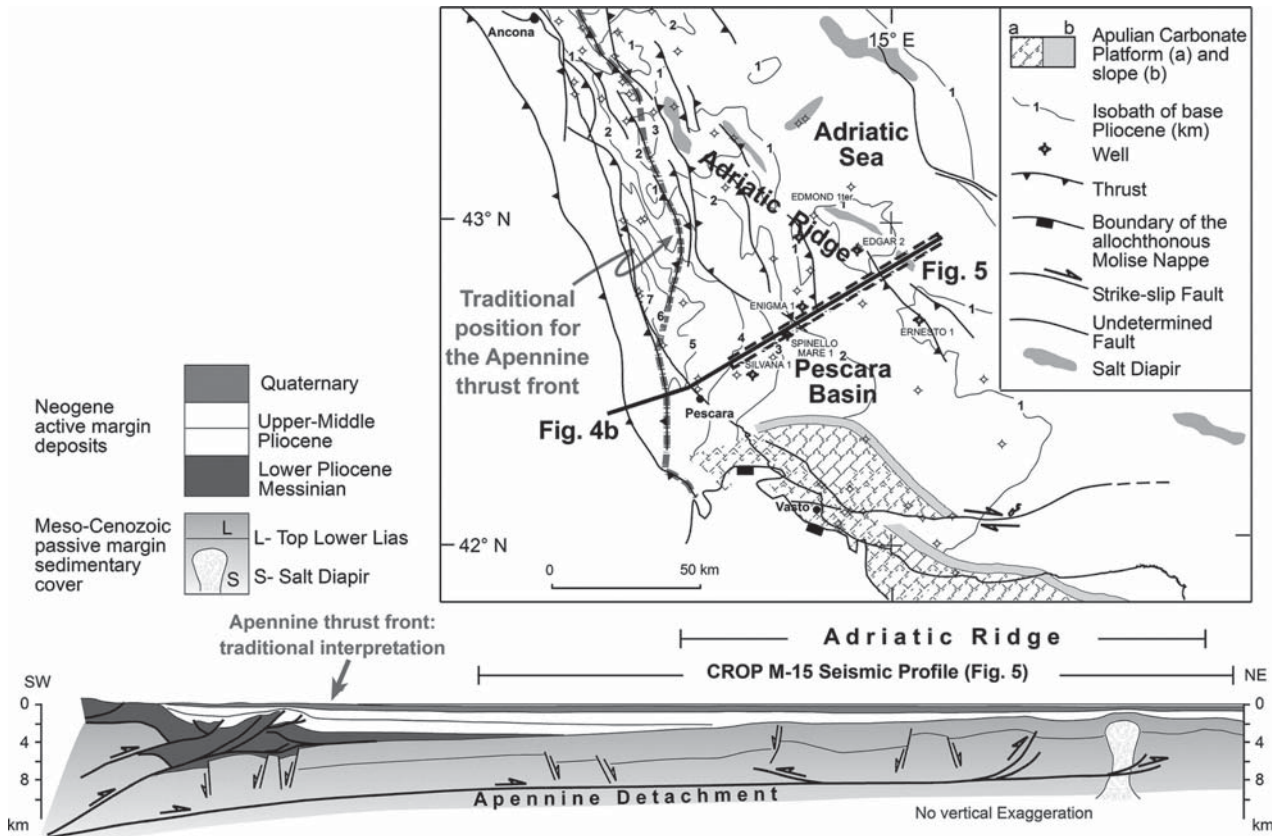
Fig. 4. a Structural map of the central Adriatic. The *grey-dashed* line highlights the commonly accepted position of the external front of the Apennine accretionary prism according to the Structural-Kinematic Map of Italy (Consiglio Nazionale delle Ricerche, 1992). The *thick line* identifies the regional cross section shown in Fig. 4b. The *box* indicates the CROP M-15 seismic profile shown in Figs. 5. b) Geological section across the Apennine thrust front and the Adriatic ridge. The main detachment of the middle/late Pliocene-Quaternary contractional deformations affecting the Adriatic ridge (likely located within the Upper Triassic evaporites) is correlated with the regional detachment of the Apennine accretionary prism

A main tectonic phase affected the Adriatic ridge in middle/late Pliocene-Quaternary, as clearly demonstrated by the widespread occurrence of folded deposits and growth strata. Also this last event has been interpreted by some authors as the result of a thick-skinned tectonic inversion of pre-existing extensional features induced by the Apennine compression (e.g., Argnani and Frugoni, 1997; Bertotti et al., 2001; Calamita et al., 2003). In this thick-skinned tectonic scenario, the reverse faults in the Meso-Cenozoic sedimentary cover do not connect with the thin-skinned Apennine thrust front, which is located farther west, but instead constitute local accommodation features (fish tails) above reactivated high-angle normal faults involving the basement. If the basal detachments accounting for the Adriatic ridge's inversion features and for the western thin-skinned front were connected farther west in the lower crust, the outermost reactivated and/or inverted structures might be considered an example of the "reactivation front" as defined by Lacombe and Mouthereau (1999).

However, the crustal structure of the Apennine accretionary wedge is still a debated issue (see Scrocca et al., 2005 for a discussion) and, in fact, the geodynamic setting of the Apennine orogen as a whole, when compared with other orogens world-wide, suggests that the accretionary prism should be mainly formed by the tectonic stacking of the sedimentary cover (e.g., Doglioni et al., 1999a, 1999b). Although the quality of the available seismic data in not resolutive, we do believe that an alternative thin-skinned interpretation can be put forward in the central Adriatic domain. In the proposed interpretation (Fig. 5), the main detachment of the last middle/late Pliocene-Quaternary contractional deformations can be traced at the base of the Mesozoic sedimentary cover (likely within the Upper Triassic evaporites). These late-stage contractional deformations are thus superimposed on the older Cretaceous and Tertiary inversions of basement-in-
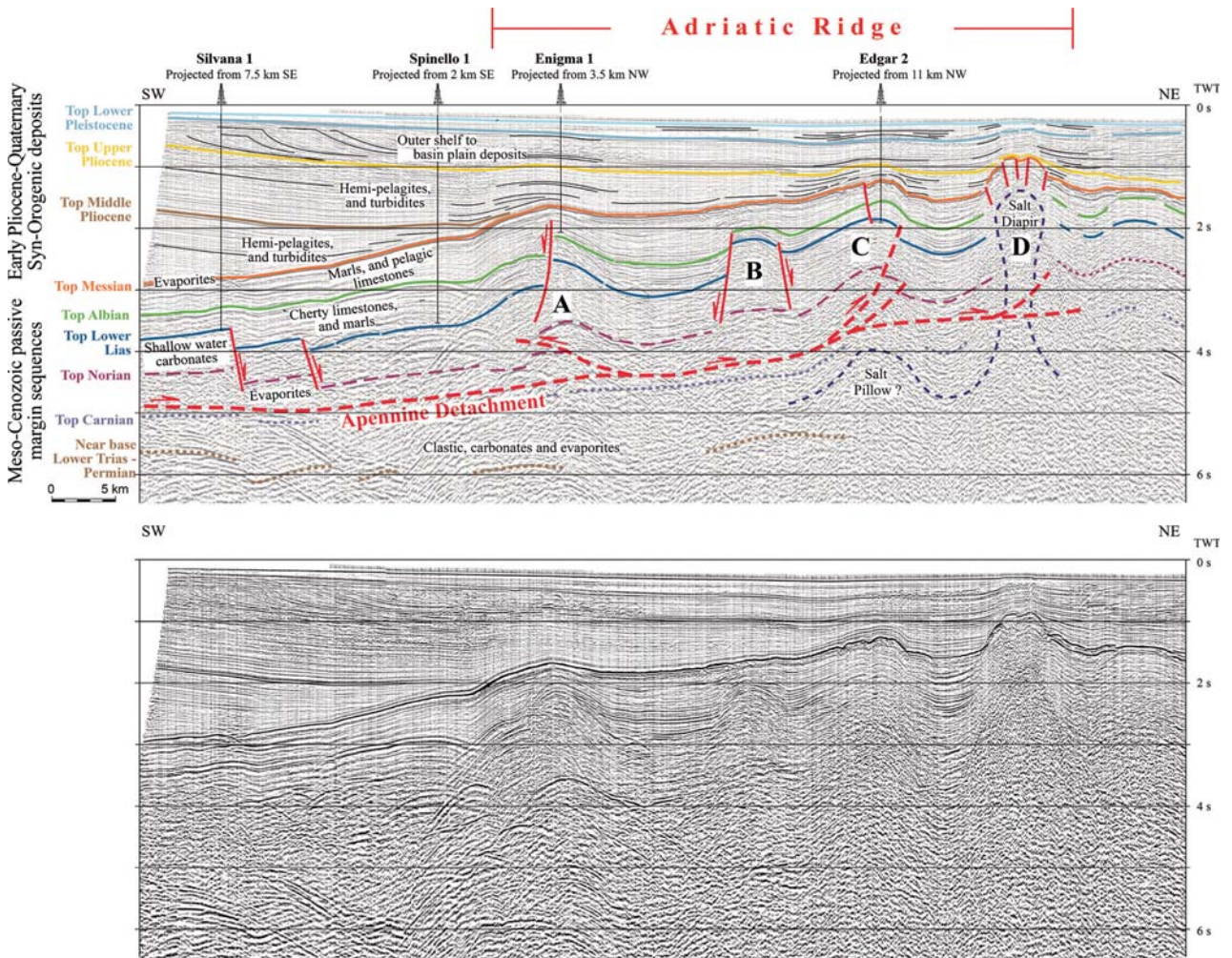
Fig. 5. CROP M-15 seismic profile (location in Fig. 4). Interpreted horizons are *solid* where well constrained, *dashed* where approximate, and *dotted* where speculative. Four structural highs are recognisable on this profile (labelled from *A* to *D*); two of them (*A* and *C*) can be interpreted as thrust related folds with the main detachment likely located within the Upper Triassic evaporites. A diapir (*D*) is also recognisable. The last phase of tectonic activity of the Adriatic ridge (late Pliocene-late Quaternary) can be related to the forelandward propagation of the Apennines detachment. The associated shortening could have enhanced the diapir activity

volving normal faults. Moreover, in our opinion, this detachment can be followed westward and correlated with the regional detachment of the Apennine accretionary prism (Fig. 4), as also already proposed by Bally et al. (1986).

These considerations suggest that the actual Apennines external thrust front should be located on the north-eastern side of the Adriatic compressive belt that, accordingly, should be formally included in the Apennine accretionary wedge. In the proposed interpretation, the Apennine thrust front should not to be regarded as a continuous feature but rather as the envelopment of discrete thrust structures.

Further southward, the Apennines thrust front is segmented in correspondence with the Tremiti litho-spheric transfer zone (Fig. 3), which separates two sectors of the subducting Adriatic plate characterized by different amounts of flexural retreat (Doglioni et al., 1994) and by different amounts of thrust front advance (Scrocca, 2006).

4   Quaternary Tectonic Activity Along the Central and Northern Apennines Thrust Front

Along the Central and Northern Apennines thrust front the last main events of thrust accretion occurred between Pliocene and Early Pleistocene times (e.g., Castellarin et al. 1985; Bally et al., 1986; Ori et

al., 1986), these processes being related to the eastward flexure-hinge retreat of the subducting Adriatic lithosphere.

According to a first group of researchers, following a major geodynamic change, thrusting and related folding at the front of the Apennines ceased in Early Pleistocene times both in the Po Plain and in the adjacent sector of the Adriatic Sea (e.g., Argnani et al., 1997; Bertotti et al., 1997; Di Bucci & Mazzoli, 2002; Argnani et al., 2003 and reference therein). This conclusion is derived from both field studies and seismic reflection lines that, in the interpretation of these authors, show thrusts sealed by Middle Pleistocene to recent deposits.

An alternative scenario has been proposed. Geomorphological analyses, subsurface geology, seismicity and present-day stress field, suggest that the tectonic activity of the frontal part of the Northern Apennine accretionary wedge is still going on (e.g., Meletti et al., 2000; Valensise & Pantosti, 2001; Burrato et al., 2003; Boccaletti et al., 2004 and references therein).

In the following the two conflicting interpretations will be briefly reviewed and compared with the results of our analysis.

4.1 Central-Southern Po Plain

Along the southern edge of the Po Plain, at the morphological boundary with the Apennines, clear evidence of tilted and offset late Quaternary deposits has been described (Boccaletti et al., 1985; Castellarin et al., 1985; Amorosi et al., 1996). Although these features have been also explained with the onset of extensional deformation along SW dipping faults and consequent flexural unloading of their footwall (Bertotti et al., 1997), they are commonly attributed to the activity of a regional thrust (e.g., Castellarin et al., 1985; Amorosi et al., 1996; Benedetti et al., 2003; Boccaletti et al., 2004). This thrust is generally known as the Pede-Apenninic Thrust Front (Boccaletti et al., 1985) or as the Pedeappenine Lineament (Castellarin et al., 1985).

In the area located between the Pede-Apenninic thrust and the external fronts (Emilia and Ferrara arcs), an active compressional tectonic regime is documented by borehole breakout data (Mariucci et al, 1999; Montone & Mariucci, 1999; Montone et al., 2004), showing a roughly N-S maximum horizontal stress, focal mechanism (e.g. Gasperini et al 1985; Boccaletti et al., 2004; Eva et al., 2005), and seismological data (e.g., Frepoli & Amato, 1997; Selvaggi et al., 2001). Furthermore, recent geodetic velocity solutions for Italy and the surrounding areas, obtained from an analysis of continuous and survey-mode Global Positioning System observations (e.g., Battaglia at al., 2004; Serpelloni at al., 2005; Zerbini et al., 2006), show a shortening of a few mm/a between the Medicina site, positioned above the Apennines buried accretionary prism, and the Padova station, located above the Adriatic foreland away from zone of active deformation (Fig. 3).

All the described observations, as well as the results of geomorphological analyses, suggest the presence of growing anticlines driven by active blind thrust faults (e.g., Burrato et al., 2003; Benedetti et al., 2003; Boccaletti et al., 2004; DISS Working Group, 2005). The same conclusion arises from the interpretation of seismic reflection profiles, as discussed by Boccaletti et al. (2004). The active thrust-related folds are spatially arranged along seismogenic belts (Boccaletti et al., 2004; DISS Working Group, 2005) that are nearly coincident with the buried Monferrato, Emilia and Ferrara-Romagna arcs. Some deep faults considered able to produce earthquakes larger than M 5.5 have been already identified along these belts (Valensise & Pantosti, 2001).

In Fig. 7 the relationships between subsurface structure (after Pieri, 1983), seismicity (after Chiarabba et al., 2005) and the interpreted geodynamic setting are shown. According to Eva et al. (2005), in the southwestern half of this section the shallow seismicity (0–10 km of depth) is mainly transtensive, while just below about 10 km in depth, the stress regime converts to transpressional and then to compressive. In our interpretation, the deep compressional events (between 20 and 30 km) are related to the south-western prolongation of the active thrust, developed along the morphological boundary between the Apennines and the Po Plain.

4.2 Central and Northern Adriatic Sea

Moving southwards, along the northern Marche coastal belt, several geomorphic features and the occurrence of several historical and instrumental earthquakes suggest the presence of active and seismogenic thrust-related folds (Vannoli et al., 2004; DISS Working Group, 2005). The lack of contractional deformations in middle Pleistocene to recent deposits in the adjacent Adriatic offshore area, pointed out by Di Bucci & Mazzoli (2002), is reconciled with the geomorphologic and seismologic evidence of tectonic activity by observing that the most external position reached by the Apennine thrust front in Early Pleistocene times does not necessarily coincide with the north-eastern edge of the belt affected by Late Quaternary to recent contractional deformations, which can actually be located in a more internal position (e.g., Vai, 1987).

In the central Adriatic Sea, a very recent activity of the Adriatic ridge's folds is supported by contractional
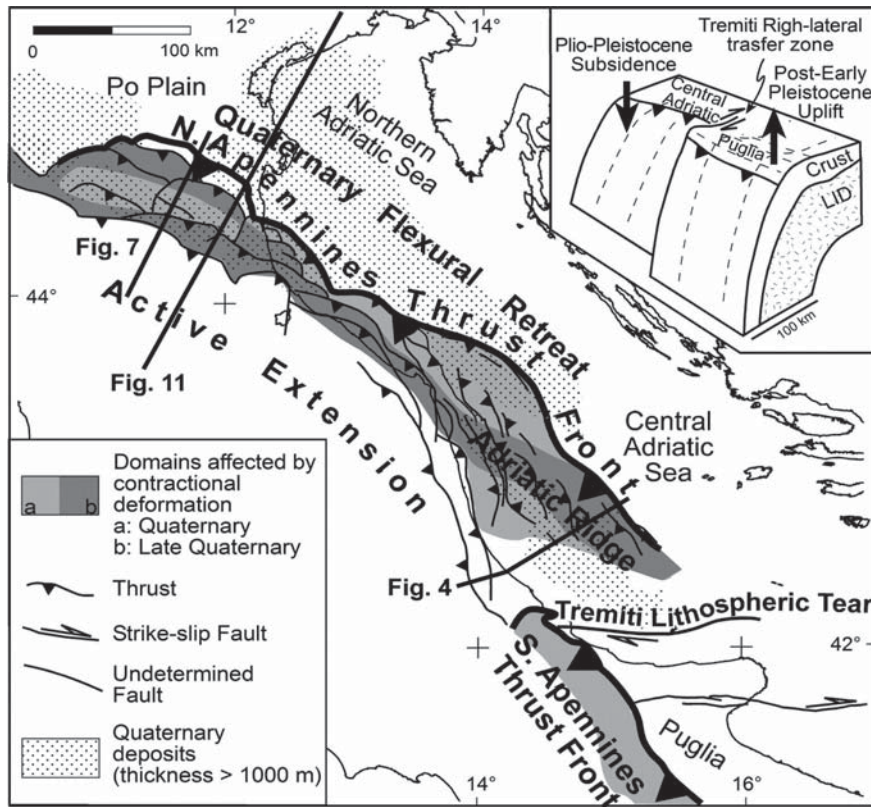
Fig. 6 Tectonic scheme of the Adriatic domain and cartoon showing the 3D slab geometry of the subducting Apulo-Adriatic plate (inset, modified after Doglioni et al., 1994). The Apennine thrust front is located on the NE side of the Adriatic ridge. The differential slab retreat between the central and southern sectors of the subducting Adriatic plate has been accompanied by a different tectonic evolution of the related segments of the accretionary prism that ended up with a segmentation of the Apennine thrust front
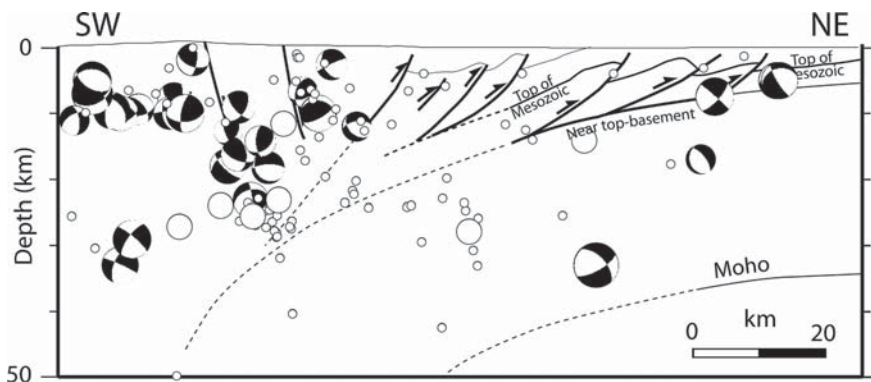
Fig. 7 Simplified geological cross-section showing the relationships between subsurface structure (after Pieri, 1983), interpreted geodynamic setting (after Carminati et al., 2003) and the seismicity (after Chiarabba et al., 2005). Location in Fig. 3. Note that the deep seismicity between 20 and 30 km is mainly represented by compressional events (Boccaletti et al., 2004; Eva et al., 2005) and may be related to the south-western prolongation of the active thrust, developed along the morphological boundary between the Apennines and the Po Plain. The area above is mainly affected by extensional seismicity

deformation affecting late Quaternary strata, induced by buried blind thrusts (Fig. 5), which sometimes have a morphological expression at sea-floor (e.g., Argnani & Frugoni, 1997; Calamita et al., 2003; Scrocca, 2006). This indication is also in good agreement with the distribution of the present-day seismicity (e.g., Chiarabba et al., 2005 and references therein) and with the few

available focal mechanisms (Fig. 3), which indicate a compressional stress field with minor strike-slip component (e.g., Riguzzi et al., 1989; Mariucci et al., 1999; Lavecchia et al., 2004).

Based on the geographic distribution of stress indicators, e.g. borehole break-out and seismological data (e.g., Mariucci et al., 1999; Montone et al., 2004), it be-

comes possible to define a NW-SE oriented belt, that extends south-eastward from the town of Ancona in the central Adriatic Sea for at least 150 km, characterized by a present-day compressional stress field and active contractional structures (Fig. 6).

It should be noted that in the proposed interpretation of the Apennine thrust front, the last phase of tectonic activity of the Adriatic ridge (Late Pliocene-Late Quaternary) relates to the forelandward propagation of the Apennines detachment. Therefore, the late Quaternary to Recent deformations along the Adriatic ridge provide an indication of the most recent tectonic activity of the Apennine thrust front in the Adriatic domain.

4.3 Mirandola Anticline: Relative Uplift Rates

One of the recognised seismogenic sources buried below the Po Plain sediments is the Mirandola anticline, which is located at the western edge of a group of thrust-related folds belonging to the Ferrara arc. This arc represents one of the most external structures of the Northern Apennines thrust front, certainly active during late Pliocene - early Pleistocene times.

Since the Mirandola structure is considered an active seismogenic fault (e.g., Burrato et al., 2003; Boc-

caletti et al., 2004; DISS Working Group, 2005), we have studied in detail its Quaternary evolution by integrating high resolution stratigraphic data (RER & ENI-AGIP, 1998), that provide an accurate description of the tectono-stratigraphic setting relative to the last 0.65 Ma, with other constraints about the overall stratigraphic and structural architecture (AGIP, 1959, 1977; Pieri and Groppi, 1981; Nardon et al., 1990; Consiglio Nazionale delle Ricerche, 1992).

The structural and stratigraphic setting of the Mirandola thrust-related fold (Fig. 8) strongly suggests a syn-sedimentary growth with clear overlapping geometries (i.e., sedimentation rates higher than uplift rates) also in middle to late Pleistocene times.

Since the geometry of the middle to late Pleistocene growth strata is certainly due to a combination of regional subsidence, sedimentation rates, eustatic history, tectonic uplift and compaction effects, we have analyzed and corrected for compaction the available stratigraphic data. As shown in Fig. 9 we have compared the depth of the basement at the crest of the anticline and in the adjacent syncline at different time steps. In this way, although this domain is affected by an overall subsidence, we have estimated a tectonic "relative uplift rates" between the fold crest and the adjacent syncline due to the activity of this thrust-related fold.

Fig. 8 Data used in the decompaction procedure to estimate uplift rates of the Mirandola thrust-related fold. Location in Fig. 3. **a** simplified geological cross-section (drawn after Pieri and Groppi, 1981 and Consiglio Nazionale delle Ricerche, 1992). **b** stratigraphic setting of the Middle Pleistocene to Recent section based on high-resolution stratigraphic data (modified after RER & ENI-AGIP, 1998)
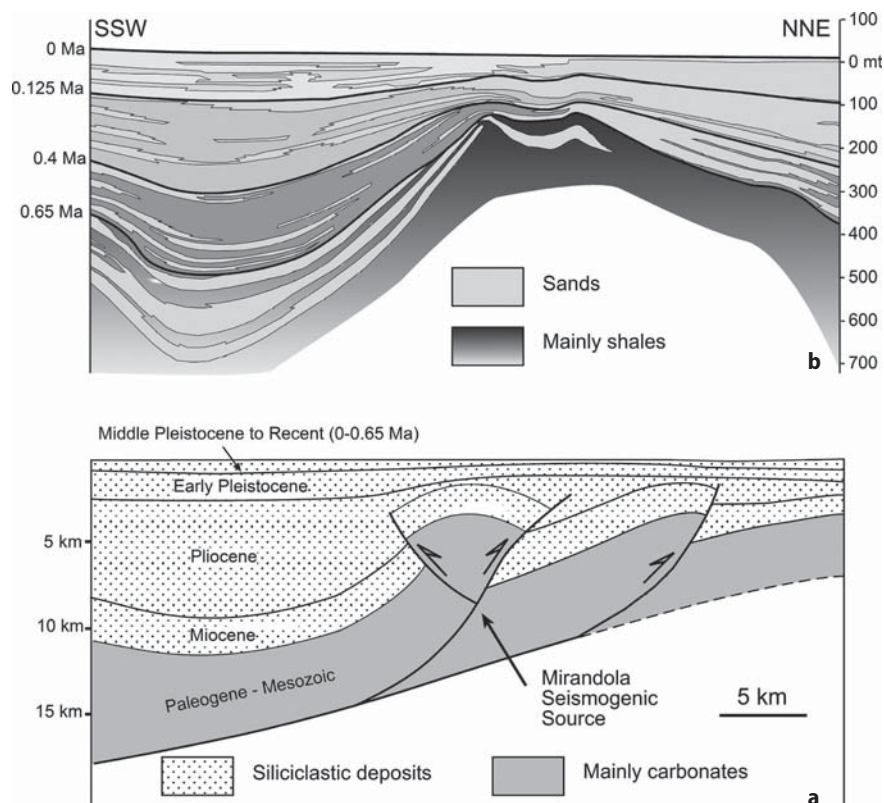
Table 1. Decompaction coefficients, porosities, and densities adopted for the calculations

Profile	c	φ	ρ	Reference
Sand	0.27	0.49	2650	Sclater and Christie (1980)
Shale	0.51	0.63	2720	Sclater and Christie (1980)
Shaley sand	0.39	0.56	2680	Sclater and Christie (1980)

The procedure that we used to decompact sediments follows the backstripping method (Sleep, 1971; Sclater & Christie, 1980). This method allows the restoration of the original (uncompacted) thickness of sediment formations or members starting from the lowest unit in a stratigraphic section and considering in the following steps the younger units. The method assumes that, during progressive burial of sediments in a subsiding basin, the compaction process is mainly depth dependent rather than time dependent (Schmoker & Halley, 1982). The decompaction procedure assumes the exponential porosity-depth relation

$$\phi = \phi_0 \exp^{-cy},$$

where ϕ is the porosity at depth y, ϕ_0 is the original porosity of sediments, and c is an experimentally derived coefficient. The original porosities and the decompaction coefficients adopted for the calculations are shown in Table 1.

In our calculation we have performed both backstripping to 1D sedimentary columns, a technique widely adopted in literature (e.g., Scheck & Bayer, 1999) and 2D section by mean of LithoTect software. At each decompaction time-step the depth of the basement and of the overlying sediments is calculated summing the thicknesses of deposited sediments and adopting corrections for paleobathymetry and eustasy. Theoretically, the corrected depth of a layer (D_{lc}) is calculated following the relation

$$D_{lc} = D_l + D_w - E,$$

where D_l is the uncorrected layer depth (derived only from the thickness of deposited sediments), D_w is the paleobathymetry and E is the relative eustatic change of sea level.

In our calculations paleobathymetries and eustatic sea-level changes are assumed to be equal to zero, since the entire sequence was deposited in shallow marine to continental environments (AGIP, 1959). In other words, after decompaction the tops of the calculated sedimentary columns are located at the zero reference level, i.e., at the average sea level, throughout the entire

analyzed structure. However, the occurrence of a thick (up to 500 m) tabular unit with prograding clinoforms in the shallow part of the considered succession (Pieri, 1983) implies that processes of basin filling (i.e., the occurrence of moderate paleobathymetries) must also be considered.

The assumption of zero water depth is granted for the middle Pleistocene (ca. 600,000 yr ago) to Present sediments, which were deposited in continental environments. The error on subsidence rates calculated for this period due to assumed paleo-water depth is necessarily equal to zero. For the lower Pleistocene sediments, deposited in shallow water, the zero paleobathymetry assumption bears consequences on the calculated subsidence rates, i.e., on the depth of the basement at a certain stage. However, as sketched in Fig. 9, when calculating the relative uplift along the Mirandola anticline, we compare the depth of the basement at the crest of the anticline and in the adjacent syncline. Since the basement position at the two locations would be affected exactly by the same error induced by our paleobathymetric assumption, it is clear that the resulting relative uplift is by no means affected by imposed paleobathymetry.
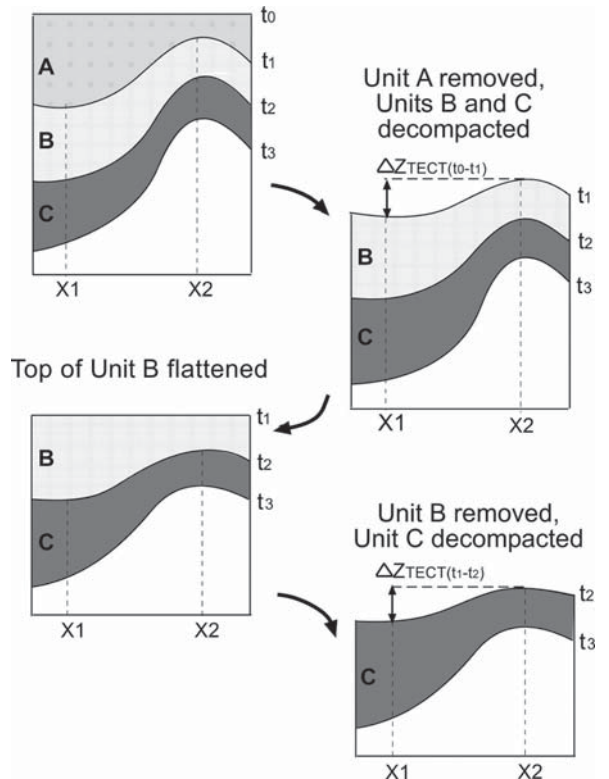
Fig. 9 Decompaction procedure adopted to estimate a tectonic "relative uplift rates" (ΔZ_{TECT}) between the fold crest (X_2) and the adjacent syncline (X_1) at different time steps (t_0, t_1, t_2, etc.)
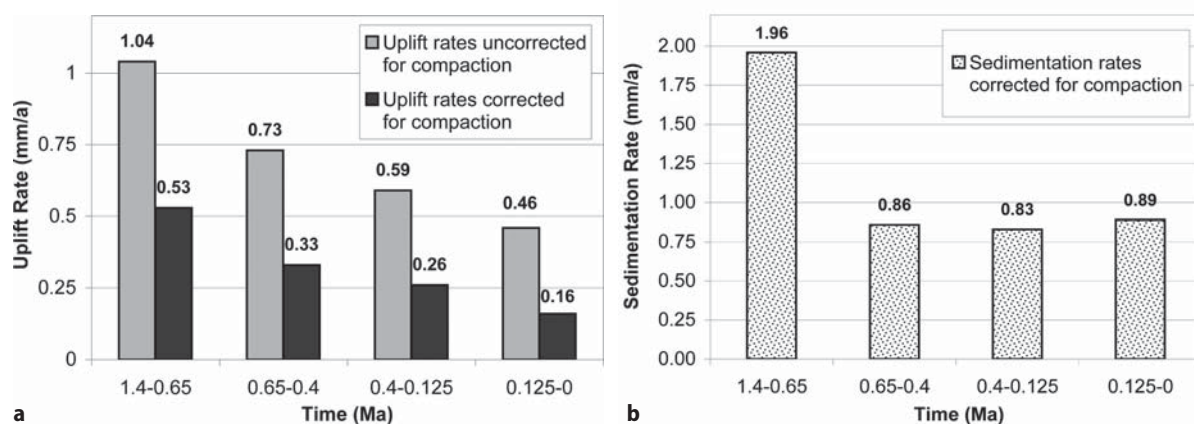
Fig. 10 Mirandola anticline: **a)** uplift rates corrected and uncorrected for compaction during the last 1.4 Ma and **b)**corrected sedimentation rates. Based on the cross-section of Fig. 8, uplift rates have been evaluated on the anticline crest while sedimentation rates have been estimated in the adjacent syncline. Compactable layers include Miocene units while, according to available geological data, lithology is assumed to be 50% shale and 50 % shale

Sensitivity analysis has been carried out varying the lithological composition, although the available geological data indicates an overall 50% shale and 50% sand ratio.

Moreover, the effects of the original porosities ϕ_0 were evaluated. A change of 10% of ϕ_0 determines a change of 2.5% of the calculated uplift rates.

The resulting rates of tectonic uplift decrease during the last 1.4 Ma from values of 0.53 mm/a to values of 0.16 mm/a (Fig. 10a). This means that the Mirandola anticline is still active today, although it moves more slowly than in Pliocene. Anyway, these tectonic uplift rates must be added to a regional subsidence rate of about 1 mm/a, or more (discussed in the following section), resulting in an overall subsidence.

Quaternary sedimentation rates corrected for compaction have been also assessed (Fig. 10b) by simply dividing the decompacted thickness of sediments for the corresponding time interval in the syncline adjacent to the Mirandola anticline.

5   Adriatic Flexural Retreat

The evolution through time and space of Plio-Pleistocene foredeep domain in the Po Plain and in the Adriatic domain has been already analyzed in several studies (among many others, Dondi et al., 1985; Ori et al 1986; Vai, 1987; Royden, 1988; Zoetemeijer et al., 1993; Kruse & Royden, 1994). Below the Apennines foredeep, the regional monocline gradually becomes steeper moving from the foreland domain towards the belt with documented dips of about 20° below the Po Plain (e.g., Pieri, 1983; Mariotti and Doglioni, 2000). Consequently, the thickness of the Plio-Pleistocene foredeep deposits can be as high as 7000 m in the deepest de-

pocenters (Pieri & Groppi, 1975; Consiglio Nazionale delle Ricerche, 1992).

The development of the Plio-Pleistocene Apennine foredeep is usually related to the eastward rollback of the subducting Adriatic plate (among many others, Malinverno and Ryan, 1986; Royden et al., 1987; Patacca et al., 1990; Doglioni, 1993), since it has been shown that the flexural bending of the Adriatic plate cannot be explained by the load of the Apennine orogenic belt (e.g., Royden, 1988).

Other geodynamic processes have been also invoked to explain the evolution of the Apennine foredeep. According to van der Meulen et al. (1998), a lateral shift of foredeep depocenters along the Apennine chain may have been induced by the SE migration of a lithospheric tear which drove to a detachment of the Adriatic slab (Wortel and Spakman, 1992). However, the tomographic analyses that were at the base of this slab detachment model have not been confirmed by other more recent tomographic studies (e.g., Lucente et al., 1999; De Gori et al., 2001) which have pointed out the presence of an almost continuous sub-vertical high velocity body, while also the lateral depocenters migration has been questioned (e.g., Bertotti et al., 2001).

Alternatively, the Quaternary subsidence in the Adriatic Sea has been interpreted as the result of crustal/lithospheric buckling of the Apulo-Adriatic plate with subsidence concentrated in the central part of the main crustal scale synclines (e.g., Bertotti et al., 2001; Calamita et al., 2003).

However, the distribution of the Pleistocene to Recent subsidence rates both in the Po Plain and in the Northern Adriatic domain (Carminati & Di Donato, 1999; Carminati et al., 2003) show a clear subsidence increase moving from the foreland towards the buried
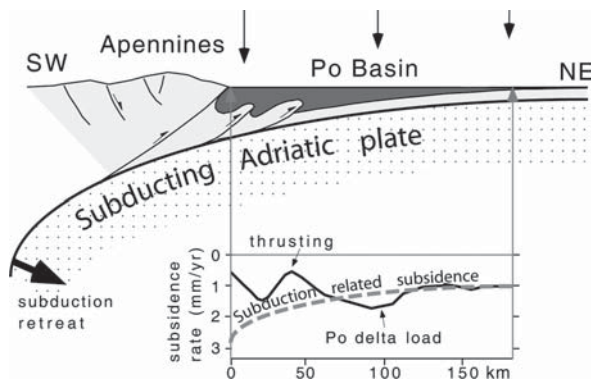
Fig. 11 Schematic profile across the Apennines, Po Basin and Venetian area, showing the curvature of the Adriatic plate in the foreland of the Apennines, associated to the slab retreat. Profile location is shown in Fig. 6. Subsidence rates (modified after Carminati et al., 2003) along the profile trace are also shown (solid line in the graph). Notice that the regular subsidence trend due to subduction retreat is perturbed by thrust tectonics

thrust front (Fig. 11). Recent and asymmetric (faster to the southwest) subsidence is also testified by stratigraphic and geodetic measurements in the whole Po Basin, which is at places below sea-level (Carminati and Martinelli, 2002). Quaternary sedimentation rates in the Po plain can be reasonably assumed to be equal to subsidence rates, since the entire sequence was deposited in shallow marine to continental environments. The obtained subsidence rates range between 0 and 2.5 mm/a, with the largest rates (greater than 1 mm/a) occurring in the southern part of the Po Plain and in the Po Delta. As an example, a significant part of the long-term natural component of the subsidence of Venice (about 0.7–1.0 mm/a) has been related to the north-eastward retreat of the Adriatic subduction (Carminati et al., 2003).

Mean Pleistocene subsidence rates in the Po Basin are comparable to those of other parts of the Apennines foredeep (e.g., the Pescara Basin to the south along the Adriatic coast; Colantoni et al., 1989) where large deltas do not occur.

Moreover, the late Pliocene-Quaternary propagation of the Apennine thrust front in the central Adriatic, and the related development of the Adriatic ridge's folds, strongly influenced the distribution of the Quaternary deposits (post 1.4 Ma), which show two main depocenters (Fig. 3; Dondi et al., 1985; Bartolini et al., 1996). The first sub-basin, at the eastern edge of the Peascara Basin, mainly developed during the Early Pleistocene while the second one, located at the SE edge of the Po Plain basin (i.e., NE with respect to the Adriatic ridge), is characterized by a subsidence maximum in Late Quaternary time (e.g., Calamita et al., 2003).

The asymmetric distribution of the Quaternary subsidence in the Po Plain and in the central-northern Adriatic Sea, and the SW- or W-ward increasing dip of the foreland monocline, suggests a Quaternary-Present flexural retreat of the subducting lithosphere in these domains. The deepest depocenters of the Apennines foredeep tend to match inherited Permo-Mesozoic basins (e.g., Lombard basin, Belluno basin, Umbro-Marchigiano basin, etc.) where the accretionary prism forms salients. These pre-existing features are usually accompanied by subduction-related steeper foreland regional monocline, and the foredeep basin frequently develops on top of the prism (i.e., top-thrust or piggyback basin).

6   Discussion and Conclusion

6.1 Central and Northern Apennines Thrust Fronts

The data exposed and discussed above show that the location of the Apennine thrust front in the Adriatic domain should be located in a more external position with respect to the classical interpretation (e.g., Consiglio Nazionale delle Ricerche, 1992), i.e., along the north-eastern edge of the Adriatic ridge (Fig. 6). This new interpretation bears some relevant implications since the Late Quaternary to Recent contractional deformations in the Adriatic domain, documented by the interpretation of seismic reflection profiles, seismological data and present-day stress indicators, significantly rejuvenate the most recent activity of the Apennine thrust front.

This conclusion is in agreement with the documented Late Quaternary to Recent activity of the buried thrust-related folds associated with the Apennine front along the Marche coastal belt and in the Po Plain (Fig. 6). Although rates of tectonic uplift decreased during the Quaternary, a tectonic uplift rate of about 0.16 mm/a is still recognised during the last 125 ka for one of the most external active thrust-related folds detected along the Ferrara arc. Similar uplift rates (about 0.1 mm/a) have been also estimated by Vannoli et al. (2004) by means of geomorphological analysis for the active blind thrusts that drive the growth of the Marche coastal anticlines.

The decreasing uplift rates must be evaluated taking into account that the Quaternary eustatic low-stand has generated a large increase of sediment supply. This process determines an apparent decrease of thrust activity versus sedimentary chronostratigraphic thickness (Fig. 12). Assuming a steady slip on a thrust surface, a sea-level drop triggers larger volumes of sediment supply into the foredeep that eventually produce a smaller apparent fault throw due to the expan-

Fig. 12 Assuming a steady slip on a thrust surface (*above*), a sea-level drop triggers larger volumes of sediment supply into the foredeep (*bottom left*), determining a smaller apparent fault throw (*bottom right*), due to the expansion of the chronostratigraphic thickness
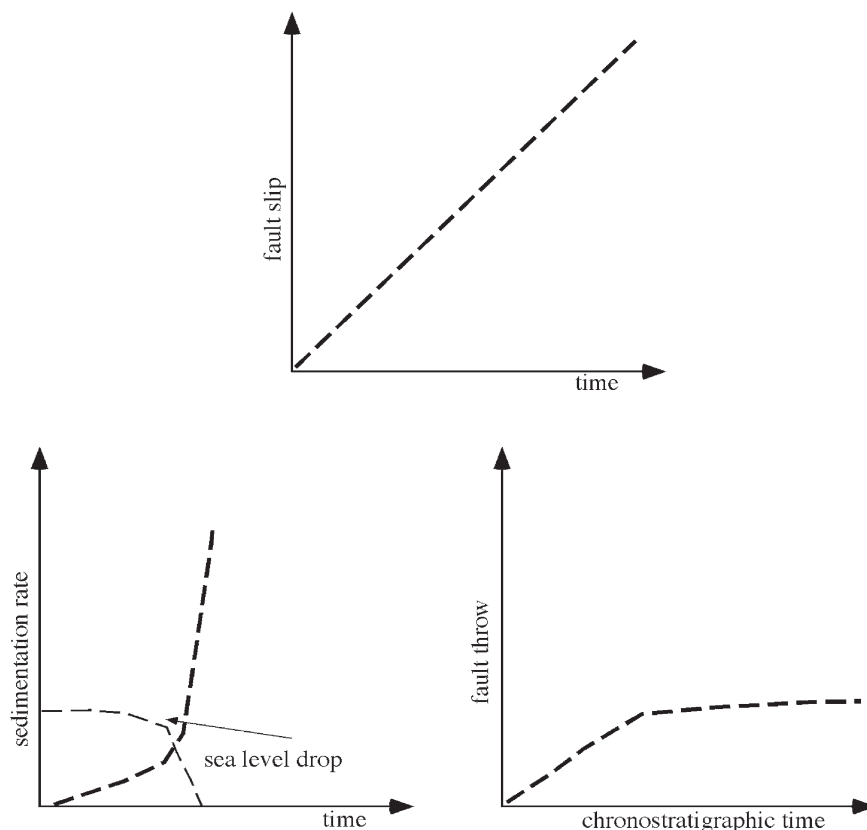
sion of the chronostratigraphic thickness. Moreover, the larger load generated by Pleistocene sediments increases the vertical stress and induces a stabilization of thrusting in compressional settings (e.g., Carminati et al., 2004). Anyway, shortening faster than 1 mm/a are effectively documented by GPS data (Battaglia at al., 2004; Serpelloni at al., 2005; Zerbini et al., 2006) as also expected since uplift rates are one or two orders of magnitude slower than horizontal velocity in all tectonic settings worldwide (e.g., Cuffaro et al. 2006).

The overall tectonic picture is characterized by an active thrust front (in fact made up by the envelopment of discrete thrust structures) running along both the northern Apennine and the central and northern Adriatic domain. Noticeably, the interpreted thrust front delimits the external (north-eastern) edge of a belt where a compressional shallow seismicity and stress field have been detected.

The most external position reached by the Apennine thrust front in Quaternary times does not necessarily coincide with the north-eastern edge of the belt affected by Late Quaternary to Recent contractional deformations, which in some areas is more internal (Fig. 6, Vai, 1987). This evidence reflects the complex interplay between the different parameters controlling the accretionary wedge mechanics (e.g., Davis et al.,

1983; Dahlen et al., 1984; Dahlen, 1990; Boyer, 1995). As an example, an early forward propagation of the thrust along an efficient detachment may have been followed by a shift of the tectonic activity towards inner portion of the wedge in response to an increased dip of the regional monocline.

The internal (south-western) edge of the belt affected by Late Quaternary to Recent contractional deformation is marked by the presence of another active thrust that corresponds to the morphological boundary between the Apennines and the Po Plain. Noticeably, this thrust is also responsible for the rapid uplift of the chain (Doglioni et al., 1999b).

6.2 Quaternary Geodynamic Evolution

We consider that the most internal active thrust together with the external thrust front define the portion of the orogen where accretion of sediments from the subducting plate takes place, as suggested by geodynamic models for west-directed subduction zones (Doglioni, 1991; Doglioni et al., 1999a; 1999b). In this geodynamic model the shear between the downgoing and retreating lithosphere and the eastward compen-

sating mantle is transferred upward, generating the shortening within the accretionary wedge.

Salients and recesses of the thrust front are accommodated by transfer zones with strike-slip or transpressional components all along the buried frontal part of the belt.

The subducting Adriatic plate is characterized by an inhomogeneous flexural behaviour, with the Tremiti lineament representing the main right-lateral transfer zone between the central Adriatic domain, characterized by a more pronounced northeastward retreat, and the Apulian region, affected by uplift (Doglioni et al., 1994; 1996). Accordingly, a foreland-ward advance of the accretionary prism above the more retreated Central Adriatic slab segment could be observed while the Southern Apennines accretionary prism shows a decreased activity (Scrocca et al., 2005). The Apennine thrust front looses its structural continuity in correspondence with the Tremiti transfer zone, that in turn may be considered the actual tectonic boundary between the central and southern segments of the Apennines accretionary prism. It may be argued that the differential slab retreat between the central and southern sectors of the subducting Adriatic plate has induced the segmentation of the Apennine thrust front (Scrocca, 2006).

In our interpretation, both the north-eastward flexural retreat of the subducting Adriatic lithosphere and the related frontal accretion of the Apennine prism have been active throughout the Quaternary and may be considered still active in both the Po Plain and the Central-Northern Adriatic domain, north of the Tremiti lineament (Fig. 6).

In the northern Apennines, the instrumental seismicity at depth of about 20–30 km (Chiarabba et al., 2005), mainly represented by compressional events (Boccaletti et al., 2004; Eva et al., 2005), might relate to the south-western prolongation of the active thrust, developed along the morphological boundary between the Apennines and the Po Plain (Fig. 7). Above this thrust, the seismicity is mainly characterized by extensional events (Boccaletti et al., 2004; Eva et al., 2005).

As a consequence, a large-scale gravity-driven tectonic interpretation of the Northern Apennines (e.g., Argnani et al. 1997; 2003), a model that has been developed for a different class of orogens, does not seem compatible with the vertical juxtaposition of a zone of shallow extensional earthquakes above deeper compressional events. Rather, the proposed structural interpretation, the present-day stress fields and seismicity, and the quaternary natural subsidence could be framed in a coherent geodynamic scenario characterized by a retreating west-directed subduction zone, which represents the natural evolution of the preceding Neogene geodynamic history.

Acknowledgements

References

AGIP Mineraria (1959) I giacimenti gassiferi dell'Europa occidentale. Accademia Nazionale dei Lincei.

AGIP Spa (1977) Temperature sotterranee. Ed. AGIP, San Donato Milanese.

Allen PA, Allen JR (1990) Basin Analysis, Principles and Applications. Blackwell Scientific Publications, Oxford, pp 451

Amato A, Alessandrini B, Cimini GB, Frepoli A, Selvaggi G (1993) Active and remnant subducted slabs beneath Italy: evidence from seismic tomography and seismicity. Ann Geofis 36: 201–214

Amorosi A, Farina M, Severi P, Preti D, Caporale L, Di Dio G (1996) Genetically related alluvial deposits across active fault zones: an example of alluvial fan; terrace correlation from the upper Quaternary of the southern Po Basin, Italy. Sed Geol 102(3–4): 275–295

Argnani A, Gamberi F (1995) Stili strutturali al fronte della catena appenninica nell'Adriatico centro-settentrionale. Studi Geol Camerti Vol Spec 1995/1: 19–27

Argnani A, Frugoni F (1997) Foreland deformation in the Central Adriatic and its bearing on the evolution of the Northern Apennines. Ann Geofis 40: 771–780

Argnani A, Favali P, Frugoni F, Gasperini M, Ligi M, Marani M, Matietti G, Mele G (1993) Foreland deformational pattern in the Southern Adriatic. Ann Geofis 36: 229–247

Argnani A, Bernini M, Di Dio GM, Papani G, Rogledi S (1997) Stratigraphic record of crustal-scale tectonics in the Quaternary of the Northern Apennines (Italy). Il Quaternario 10(2): 595–602

Argnani A, Barbacini G, Bernini M, Camurri F, Ghielmi M, Papani G, Rizzini F, Rogledi S, Torelli L (2003) Gravity tectonics driven by Quaternary uplift in the Northern Apennines: insights from the La Spezia-Reggio Emilia geo-transect. Quat Int 101–102: 13–26

Artoni A, Casero P (1997) Sequential balancing of growth structures, the late Tertiary example from the central Apennines. Bull Soc Gèol France, 168(1): 35–49

Bally AW, Burbi L, Cooper C, Ghelardoni R (1986) Balanced sections and seismic reflection profiles across the Central Apennines. Mem Soc Geol It 35: 257–310

Bartolini C, Caputo R, Pieri M (1996) Pliocene-Quaternary sedimentation in the Northern Apennine Foredeep and related denudation. Geol Mag 133: 255–273

Battaglia M, Murray MH, Serpelloni E, Bürgmann R (2004) The Adriatic region: An independent microplate within the Africa-Eurasia collision zone. Geophys Res Lett 31: L09605, doi:10.1029/2004GL019723

Benedetti LC, Tapponnier P, Gaudemer Y, Manighetti I, Van der Woerd J (2003) Geomorphic evidence for an emergent active thrust along the edge of the Po Plain: The Broni-Stradella fault. J Geophys Res 108(B5): 2238, doi:10.1029/2001JB001546

Bertotti G, Capozzi R, Picotti V (1997) Extension controls Quaternary tectonics, geomorphology and sedimentation of the N-Apennines foothills and adjacent Po Plain (Italy). Tectonophysics 282: 291–301

Bertotti G, Ricotti V, Chilovi C, Fantoni R, Merlini S, Mosconi A (2001) Neogene to Quaternary sedimentary basin in the south Adriatic (central Mediterranean): Foredeeps and lithospheric buckling. Tectonics 20: 771–787

Bigi S, Lenci F, Doglioni C, Moore JC, Carminati E, Scrocca D (2003) Decollement depth vs accretionary prism dimension in the Apennines and the Barbados. Tectonics 22: 1010, doi:10.1029/2002TC001410

Boccaletti M, Coli M, Eva C, Ferrari G, Giglia G, Lazzaretto A, Merlanti F, Nicolich R, Papani G, Postpischl D (1985) Considerations on the seismotectonics of the Northern Apennines. Tectonophysics 117: 7–38

Boccaletti M, Bonini M, Corti G, Gasperini P, Martelli L, Piccardi L, Tanini C, Vannucci G (2004) Seismotectonic Map of the Emilia-Romagna Region, 1:250000. Regione Emilia-Romagna – CNR.

Boyer SE (1995) Sedimentary basin taper as a factor controlling the geometry and advance of thrust belt. Amer J Sci 295: 1220–1254

Burrato P, Ciucci F, Valensise G (2003) An inventory of river anomalies in the Po Plain, Northern Italy: evidence for active blind thrust faulting. Ann Geophys 46(5): 865–882

Calamita F, Paltrinieri W, Pelorosso M, Scisciani V, Tavernelli E (2003) Inherited mesozoic architecture of the Adria continental paleomargin in the neogene central Apennines orogenic system, Italy. Boll Soc Geol It 122: 307–318

Carminati E, Di Donato G (1999) Separating natural and anthropogenic vertical movements in fast subsiding areas: the Po plain (N. Italy) case. Geophys Res Lett 26: 2291–2294

Carminati E, Martinelli G (2002) Subsidence rates in the Po plain (Northern Italy): the relative impact of Natural and Anthropic causation. Eng Geol 66: 241–255

Carminati E, Doglioni C, Scrocca D (2003) Apennines subduction-related subsidence of Venice (Italy). Geophys Res Lett 30(13): 1717, doi:10.1029/2003GL017001

Carminati E, Doglioni C, Barba S (2004) Reverse migration of seismicity on thrusts and normal faults. Earth Science Reviews 65: 195–222

Casero P (2004) Structural setting of petroleum exploration plays in Italy. Special Volume of the Italian Geological Society for the IGC 32 Florence-2004: 189–199

Castellarin A, Eva C, Giglia G, Vai GB (1985) Analisi strutturale del Fronte Appenninico Padano. Giornale Geologia 47(1–2): 47–76

Chiarabba C, Covane L, Di Stefano R (2005) A new view of Italian seismicity using 20 years of instrumental recordings. Tectonophysics 395: 251–268

Colantoni P, Asioli A, Borsetti AM, Capotondi L, Vergnaud-Grazzini C (1989) Subsidenza tardo-pleistocenica ed olocenica nel medio Adriatico evidenziata dalla geofisica e da ricostruzioni paleoambientali. Mem Soc Geol It 42: 209–220

Consiglio Nazionale delle Ricerche (1992) Structural Model of Italy and Gravity Map. Progetto Finalizzato Geodinamica. Quaderni de "La Ricerca Scientifica", 114, Vol. 3

Cuffaro M, Carminati E Doglioni C (2006) Horizontal versus vertical plate motions. EEarth 1: 1–18, www.electronic-earth-discuss.net/1/1/2006/

Dahlen FA (1990) Critical taper model of fold and thrust belts and accretionary wedge. Earth Plan Sci Lett 19: 55–99

Dahlen FA, Suppe J, Davis D (1984) Mechanics of fold and thrust belt and accretionary wedge: Cohesive Coulomb Theory. J Geophys Res 89: 10087–10101

Davis D, Suppe J, Dahlen FA (1983) Mechanics of fold and thrust belt and accretionary wedge. J Geophys Res 88: 1153–1172

De Alteriis G (1995) Different foreland basins in Italy: examples from the central and southern Adriatic Sea. Tectonophysics 252: 349–373

De Gori P, Cimini GB, Chiarabba C, De Natale G, Troise C, Deschamps A (2001) Teleseismic tomography of the Campanian volcanic area and surrounding Apenninic belt. J Volc Geotherm Res 109: 55–75

Di Bucci D, Mazzoli S (2002) Active tectonics of the Northern Apennines and Adria geodynamics: new data and a discussion. J Geodyn 34: 687–707

DeCelles PG, Giles KA (1996) Foreland basins systems. Basin Res 8: 105–123

DISS Working Group (2005) Database of Individual Seismogenic Sources (DISS), Version 3.0.1: A compilation of potential sources for earthquakes larger than M 5.5 in Italy and surrounding areas. http://www.ingv.it/DISS/, © INGV 2005 - Istituto Nazionale di Geofisica e Vulcanologia - All rights reserved

Doglioni C (1991) A proposal of kinematic modelling for W-dipping subductions. Possible applications to theTyrrhenian-Apennines system. Terra Nova 3: 423–434

Doglioni C (1993) Some remarks on the origin of foredeeps. Tectonophysics 228(1–2): 1–20

Doglioni C (1994) Foredeep versus subduction zones. Geology 22(3): 271–274

Doglioni C, Mongelli F, Pieri P (1994) The Puglia uplift (SE Italy): An anomaly in the foreland of the Apenninic subduction due to buckling of a thick continental lithosphere. Tectonics 13: 1309–1321

Doglioni C, Tropeano M, Mongelli F, Pieri P (1996) Middle-Late Pleistocene uplift of Puglia: an "anomaly" in the Apenninic foreland. Mem Soc Geol It 51: 101–117

Doglioni C, Prosser G (1997) Fold uplift versus regional subsidence and sedimentation rate. Marine & Petroleum Geology 14(2): 179–190

Doglioni C, Harabaglia P, Merlini S, Mongelli F, Peccerillo A, Piromallo C (1999a) Orogens and slab vs. their direction of subduction, Earth Science Rev 45: 167–208

Doglioni C, Gueguen E, Harabaglia P, Mongelli F (1999b) On the origin of west-directed subduction zones and applications to the western Mediterranean. In Durand B, Jolivet L, Horváth F, Séranne M (eds) The Mediterranean Basins: Tertiary Extension within the Alpine Orogen. Spec Publ Geol Soc London 156: 541–561

Doglioni C, Carminati E, Cuffaro M (2006) Simple kinematics of subduction zones. Int Geol Rev 48(6): 479–493

Dondi L, Rizzini A, Rossi P (1985) Recent geological evolution of the Adriatic Sea. In: Stanley DJ, Wezel FC (eds) Geological Evolution of Mediterranean Basins. Springer Verlag, New York, pp 195–214

Eva E, Ferretti G, Solarino S (2005) Superposition of different stress orientations in the western sector of the northern Apennines (Italy). J Seism 9: 413–430

Faccenna C, Jolivet L, Piromallo C, Morelli A (2003) Subduction and the depth of convection in the Mediterranean mantle. J Geophys Res 108(B2): 2099, doi:10.1029/2001JB001690

Finetti I (1982) Structure, stratigraphy and evolution of central Mediterranean. Boll Geof Teor Appl 24(96): 247–312

Ford M (2004) Depositional wedge tops: interaction between low basal friction external orogenic wedges and flexural foreland basins. Basin Res 16: 361–375, doi: 10.1111/j.1365–2117.2004.00236.x

Frepoli A, Amato A (1997) Contemporaneous extension and compression in the Northern Apennines from earthquake fault plane solutions. Geophys J Int 129: 368–388

Gambini R, Tozzi M (1996) Tertiary geodynamic evolution of the Southern Adria microplate. Terra Nova 8: 593–602

Gambini R, Thomas R, Morandi S (1997) Inversion Tectonics on the Central Adriatic Sea. FIST, Geoitalia, 5–9 ottobre 1997, Abstracts, Vol. 2: 170–171

Gasparini C, Iannaccone G, Scarpa R (1985) Fault plane solutions for the Italian peninsula. Tectonophysics 117: 59–78

Grandić S, Biancone M, Samaržija J (2002) Geophysical and stratigraphic evidences of the Adriatic Triassic rift structures. Mem Soc Geol It 57: 315–325

Hardy S, Poblet J, McClay K, Waltham D (1996) Mathematical modelling of growth strata associated with fault-related fold structures. In: Buchanan PG, Nieuland DA (eds) Modern Developments in Structural Interpretation, Validation and Modelling. Geological Society of London Special Publication No. 99, pp 265–282

Kruse SE, Royden LH (1994) Bending and unbending of an elastic lithosphere: The Cenozoic history of the Apennine and Dinaride foredeep basins. Tectonics, 13(2): 278–302

Lacombe O, Mouthereau F (1999) Qu'est-ce que le front des orogènes? L'exemple de l'orogène pyrénéen. C R Acad Sci Paris 329: 889–896

Lavecchia G, Boncio P, Creati N, Brozzetti F (2004) Stile strutturale, stato termo-meccanico e significato sismogenetico del thrust Adriatico: dati e spunti da una revisione del profilo CROP 03 integrata con l'analisi di dati sismologici. Boll Soc Geol It 123: 111–125

Lenci F, Carminati E, Doglioni C, Scrocca D (2004) Basal Décollement and Subduction Depth vs Topography in the Apennines-Calabrian arc. Boll Soc Geol It 123: 497–502

Lucente FP, Chiarabba C, Cimini GB, Giardini D (1999) Tomographic constraints on the geodynamic evolution of the Italian region. J Geophys Res 104: 20307–20327

Malinverno A, Ryan WBF (1986) Extension in the Tyrrhenian sea and shortening in the Apennines as a result of arc migration driven by sinking of lithosphere. Tectonics 5: 227–245

Mariotti G, Doglioni C (2000) The dip of the foreland monocline in the Alps and Apennines. Earth Planet Sci Lett 181: 191–202

Mariucci MT, Amato A, Montone P (1999) Recent tectonic evolution and present stress in the northern Apennines. Tectonics 18: 108–118

Meletti C, Patacca E, Scandone P (2000) Construction of a Seismotectonic model: the case of Italy. Pure Appl Geophys 157: 11–35

Milano G, Di Giovambattista R, Ventura G (2005) Seismic constraints on the present-day kinematics of the Gargano foreland, Italy, at the transition zone between the southern and northern Apennine belts. Geophys Res Lett 32(24): L24308 http://dx.doi.org/10.1029/2005GL024604

Montone P, Mariucci MT (1999) Active stress along the NE external margin of the Apennines: The Ferrara arc, northern Italy. J Geodyn 28: 251–265

Montone P, Mariucci MT, Pondrelli S, Amato A (2004) An improved stress map for Italy and surrounding regions (central Mediterranean). J Geophys Res 109: B10410, doi:10.1029/2003JB002703

Nardon S, Marzorati D, Bernasconi A, Cornini S, Gonfalini M, Mosconi S, Romano A, Terdich P (1990) Cavone oil field (Italy): an example of the application of integrated methodologies to reservoir characterization. Mem Soc Geol It 45: 791–805

Ori G, Friend PF (1984) Sedimentary basins formed and carried piggyback on active thrust sheets Geology 12: 475–478

Ori G, Roveri M, Vannoni F (1986) Plio-Pleistocene sedimentation in the Apenninic-Adriatic foredeep (Central Adriatic Sea, Italy). Spec Publ Int Ass Sediment 8: 183–198

Patacca E, Sartori R, Scandone P (1990) Tyrrhenian Basin and Apenninic arcs: kinematic relations since late Tortonian times. Mem Soc Geol It 45: 425–451

Pieri M (1983) Three seismic profiles through the Po Plain. In: Bally AW (ed) Seismic Expression of Structural Styles. A Picture and Work Atlas. Am. Assoc. Pet. Geol. Studies in Geology, 15: 3.4.1/8–3.4.1/26.

Pieri M, Groppi G (1975) The structure of the base of the Pliocene-Quaternary sequence in the subsurface of the Po and Veneto Plains, the Pedeapennine Basin and the Adriatic Sea. In: Ogniben , Parotto M, Praturlon A (eds) Structural model of Italy, Quaderni de "La Ricerca Scientifica" 90: 409–415

Pieri M, Groppi G (1981) Subsurface geological structure of the Po plain, Italy: CNR, Progetto Finalizzato Geodinamica, 414, 13 p.

RER & ENI-AGIP (1998) Riserve idriche sotterranee della Regione Emilia-Romagna. By G. Di Dio. S.EL.CA., Florence, pp 120

Riguzzi F, Tertulliani A, Gasparini C (1989) Study of the seismic sequence of Porto San Giorgio (Marche), 3 July 1987. Nuovo Cimento 12: 453–465

Royden LE (1988) Flexural behaviour of the continental lithosphere in Italy: Constraints imposed by gravity and deflection data. J Geophys Res 93(B7): 7747–7766

Royden LE, Patacca E, Scandone P (1987) Segmentation and configuration of subducted lithosphere in Italy: An important control on thrust-belt and foredeep-basin evolution. Geology 15: 714–717

Scheck M, Bayer U (1999) Evolution of the Northeast German Basin - inferences from a 3D structural model and subsidence analysis. Tectonophysics 313: 145–169

Schmoker JW, Halley RB (1982) Carbonate porosity versus depth: a predictable relation for south Florida. Am Ass Petr Geol Bull 66: 2561–2570

Sclater JG, Christie PAF (1980) Continental stretching: an explanation of the post-mid-Cretaceous subsidence of the central North Sea basin. J Geophys Res 85: 3711–3739

Scrocca D (2006) Thrust front segmentation induced by differential slab retreat in the Apennines (Italy). Terra Nova 18: 154–161

Scrocca D, Doglioni C, Innocenti F, Manetti P, Mazzotti A, Bertelli L, Burbi L, D'Offizi S (eds) (2003) CROP Atlas: seismic reflection profiles of the Italian crust. Mem Descr Carta Geol It 62: 194 pp, 71 plates

Scrocca D, Carminati E, Doglioni C (2005) Deep structure of the Southern Apennines (Italy): thin-skinned or thick-skinned? Tectonics 24, TC3005, doi:10.1029/2004TC001634

Selvaggi G, Ferulano F, Di Bona M, Frepoli A, Azzara R, Basili A, Chiarabba C, Ciaccio MG, Di Luccio F, Lucente FP, Margheriti L, Nostro C (2001) The Mw 5.4 Reggio Emilia 1996 earthquake: active compressional tectonics in the Po Plain, Italy. Geophys J Int 144: 1–13

Serpelloni E, Anzidei M, Baldi P, Casula G, Galvani A (2005) Crustal velocity and strain-rate fields in Italy and surrounding regions: new results from the analysis of permanent and non-permanent GPS networks. Geophysical Journal International 161(3): 861–880, doi: 10.1111/j.1365–246X.2005.02618.x

Sleep NH (1971) Thermal effects of the formation of Atlantic continental margin by continental breakup. Geophys J R Astr Soc 24: 325–350

Spakman W (1990) Tomographic images of the upper mantle below central Europe and the Mediterranean. Terra Nova 2: 542–553

Vai GB (1987) Migrazione complessa del sistema fronte deformativi-avanfossa-cercine periferico: il caso dell'Appennino settentrionale. Mem Soc Geol It 38: 95–105

Valensise G, Pantosti D (eds) (2001) Database of Potential Sources for Earthquakes Larger than 5.5 in Italy. Ann Geof, Suppl to vol. 44(4), pp 180, with CD-ROM, INGV

van der Meulen MJ, Meulenkamp JE, Wortel MJR (1998) Lateral shifts of Apenninic foredeep depocentres reflecting detachment of subducted lithosphere. Earth Planet Sci Lett 154: 203–219

Vannoli P, Basili R, Valensise G (2004) New geomorphic evidence for anticlinal growth driven by blind-thrust faulting along the northern Marche coastal belt (central Italy). J Seism 8: 297–312

Wortel MJR, Spakman W (1992) Structure and dynamics of subducted lithosphere in the Mediterranean region. Proc K Ned Akad Wet 95: 325–347

Zappaterra E (1990) Carbonate paleogeographic sequences of the Periadriatic region. Boll Soc Geol It 109: 5–20

Zerbini S, Matonti F, Doglioni C (2006) Crustal movements in northeastern Italy from permanent GPS stations. European Geosciences Union 2006, Geophysical Research Abstracts 8: 06257

Zoetemeijer R, Cloetingh S, Sassi W, Roure F (1993) Modelling of piggyback-basin stratigraphy; record of tectonic evolution. In: Cloetingh S, Sassi W, Horvath F (eds) The origin of sedimentary basins; inferences from quantitative modelling and basin analysis. Tectonophysics 226: 253–269

Subject Index